ICME2015

International Conference on Mechanical Engineering 2015
(ICME 2015) 18 – 20 December, 2015, Dhaka, Bangladesh

Paper ID : 001

Assessment of Energy Consumption and Emissions of Jute Mill Production Line in Bangladesh

Md. Shazib Uddin[a)], Mahadi Hasan Masud and Soumya Mandal

Department of Mechanical Engineering , Rajshahi University of Engineering and Technology ,Rajshahi-6204, Bangladesh

[a)]Corresponding author: shazib0397@gmail.com

Abstract. This study investigates the electricity consumption and emissions of jute product manufacture stages at Rajshahi Jute mill in Bangladesh. Electricity consumption and emissions at various production stages were estimated. The energy inefficient stages and potential improvement solutions were also investigated to further improve the product manufacture to be an energy efficient way .The result showed that 50% electricity consumption observed in spinning process. The electricity required per day is 28,604 kWh and per ton jute product is 1,345 kWh. Two possible alternative improvement options namely weaving and winding process were investigated. The study showed that daily 3,076 kWh electricity consumptions could be possible to reduce which is 11% of daily total electricity consumption in the Jute mill. The environmental analysis showed that about 1.92 ton CO2 emission per day can be reduced using the alternative improvement options. The analysis of economic benefit showed that the operating cost could be possible to reduced BDT 27,684 per day and BDT 1,318 per ton production of Jute goods. Hence, government can take suggestions from this study to reduce the energy consumption of Jute industry in Bangladesh.

INTRODUCTION

Bangladesh facing a great challenges for the availability and distribution the access of modern energy. Many technical and institutional reforms were taken to improve the energy sectors from 2008, but current status of energy sectors highlighting the insignificant achievement from the year 2008 [1-2]. The electrification of the country is around 50% implies the access of modern energy is not widely distributed over the country [3]. Alarming rate of industrial and infrastructural development of the country painting the energy requirements will be increase in future. At the same time country will contributes on global environmental impacts due to combustion of fossil energy. Jute industry is one of the reputed industries of Bangladesh for the earning foreign currency and export quality jute products. The country is now the second largest exporter of jute and jute-made goods in the world [4]. In the year 2010-2011, the country contributes 85.7% share of Jute goods in the world [5]. These industries energy requirements are mostly depends on the supply of electricity. There are 180 jute mills in the country in which 151 mills are in operation [6]. Jute Mills Corporation (BJMC) reported that Jute mill are extended here rapidly in both private and government sector implies the electricity requirements of Jute mills will be increased in future. A case study of Rajshahi Jute mills mainly reported the economic aspects and shows that the industry is economically poor to achieve its goal. One of the reasons they find out that the machineries of production line is very poor and there is a lacking of modern equipments [7]. Improvement of Jute product quality is reported by Ref [8]. They have taken some compositional modification of Jute yarn. They have shown better mechanical strength and elongation of Jute products. Another study of Jute mills reported the development the spinning of jute yarn. They have replaced conventional mineral oil-based jute conditioning agent by combination of castor oil and glycerin in the spinning process to develop the tensile properties of yarn and yarn hairiness [9]. The above literatures focused are mainly on product quality. The studies on energy consumption in Jute mill of Bangladesh are less well known. Hence, this study aims to investigate the electricity consumption and emissions in Jute mill of Bangladesh and put suggestion for the potential improvement. Rajshahi Jute mill was considered as a case study. The various steps of Jute goods production lines were considered for the

estimation the electricity consumption and corresponding emissions. The energy inefficient steps were detected and possible improvement solutions were studied to further improve the production stages.

METHODOLOGY

Methodology involved identifies the production stages and the machines used in the production line in each stage. The detail is described as follows:

Jute Product Manufacture Stages

There are more than 10 stages for the production of jute products in this study shown in Figure 1. The raw jute is converted from hard to soft in the softening process by the softening machine. The soft jute is then transfer to carding process to make ribbon of uniform weight per unit length of jute called sliver. The drawing process is used to reduce the sliver width and thickness by mixing 4 to 6 sliver together. Multiple number of drawing steps make the sliver more crimpled and suitable for spinning. The spinning process is produce jute yarn from the finished sliver. Winding process provides yam as spools and cops for the requirement of beaming and weaving operations. Yarn form spoil is wounded over a beam of proper width in the beaming process and connect number of ends to weave jute cloth. The interlacement of two series of threads called "Wrap" and "Weft" yarns to produce the fabric of desired quality is done by the weaving process. The rolled woven cloth is unrolled and water is sprinkled on it continuously to provide desired moisture in the damping process. The damped fabric passes through pairs of heavy rollers rendering threads in fabric flattened and improve the quality and appearance is done in the calendaring process. Then fabrics are folded into the required size used in "Bale Press" operation on the lapping machine. The cloth is then cut to the required length for making sack. The raw edges of sacking cloth pieces are shown by folding it with sewing machine and Final product is pressed compactly according to buyers need oil press machine at the final stage.

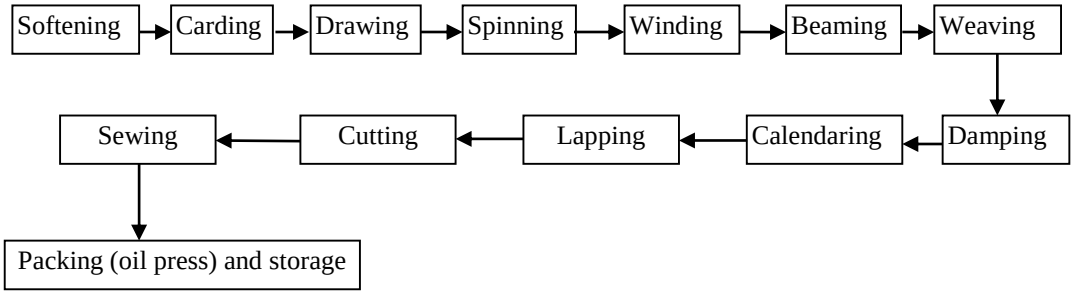

FIGURE 1 . Production stages of jute product manufacture

Data Collection

All the stages contains electricity based machines of different ratings for the manufacture of Jute products. The electricity consumption are estimated from each of the stage taking account the ratings of machine and operating hour per month and day. The mathematical expression is as follows-

Electricity consumption by the machine per month= no. of machine × power rating of machine (kW) × Average operating hour/day × Average operating days/month (1)

The colleted data were then varified with production manager and annual record of the industry for nutrality and consistency. Some stages contains the sub stage are also considered for the data collection. The sub stages are agregated for the estimation of main stage.The estimation was done for the different stages & identify the energy intensive stage. From the analysis of various stages the potential modification options are studied for the improvement.The emissions are estimated taking account the national emission factor per kWh and multiplied with the estimated kWh measured in each steps. The expression is as follows-

Total CO_2 emission of the steps = National emission factor per kWh electricity production × estimated kWh for the steps

RESULTS AND DISCUSSION

This section describes the results and discussions of the study. The section divided into three main parts namely, energy analysis, emission analysis and alternative options study for the potential benefit. Alternative options are divided into energy savings, emission savings and cost savings. The detail of the results are described below:

Energy Analysis

Table 1 shows the electricity consumption through the distinguish steps of the jute product manufacture line. The quantity of electricity consumption is presented per day production and per ton production of jute product. It is seen that spinning is the highest electricity intensive stage contributing 50% of total electricity consumption. Carding, beaming and weaving are also electricity intensive stage. The lowest electricity consumption is the damping stage. The electricty consumption per ton jute product is 1,345 kWh. Figure 2 shows the share of electricity consumption at various stages of jute product manufacture. Figure shows that spinning, weaving, beaming and carding steps are the major contributors of electricity consumption and their magnitude of 50%, 10%, 10% and 14% respectively. Spinning process requires heavy machine of high power rating consumes high quantities of electricity. Beaming and weaving are equal contributors of electricity consumption.

TABLE 1. Electricity consumption in the production steps and per ton jute product

Sl. No.	Steps	Electricity Consumption per Day (kWh)	Electricity Consumption per Ton Production of Jute Goods (kWh)
1	Softening	788	37
2	Carding	3942	187
3	Drawing	1559	74
4	Spinning	14019	667
5	Winding	1445	68
6	Beaming	2744	130
7	Weaving	2875	136
8	Damping	11	0.56
9	Calendaring	184	8.8
10	Lapping	59	2.8
11	Cutting	89	4.2
12	Sewing	167	7.9
13	Pressing	357	17
	Total	28604	1345

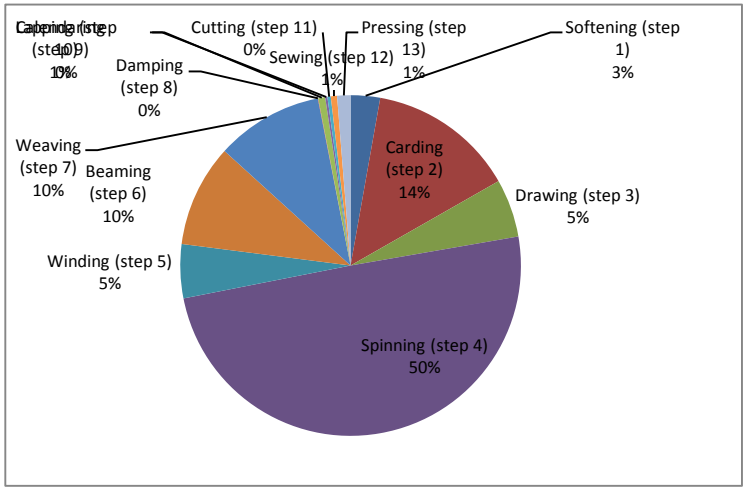

FIGURE 2. Electricity share at various stages of jute manufacture

Emission Analysis

Table 2 shows the estimated emission at the various stages for the manufacture of jute product. It is already discussed that the jute product manufacture equipments are mainly electricity based. Though these machines do not produce direct emission during operation but it produce significant emission indirectly from the power generation plant as the country power generation mainly depends on gas, coal and oil fuel. The emission shows in the table was calculated multiplying the quantities electricity consumes in each stage with their national emission factor. The national emission factor was taken CO2 0.637 kg/kWh, CH4 0.012 gm/kWh and N2O 0.001 gm/kWh [9]. It is seen that total of 845 kg CO2 emission is observed per ton production of jute product. CH4 and N2O emissions are insignificant per ton production of jute product as the magnitudes of their national emission factors are lower. Figure 3 shows the contribution of each type of emission at various production stages during manufacture the jute products. It is seen that the contribution of CO2 and CH4 emission is similar at various production stages and magnitude of major contributing stages are spinning 50%, weaving 10%, beaming 10% and carding 14%. The contributions of other stages are insignificant. Observation of N2O emission shows that spinning process contributes 51% emission where beaming, weaving and carding process contributes 8%, 12% and 16% respectively.

Savings Opportunity

The aforementioned analysis focused only the existing status of the jute product manufacture system. The existing weaving machine is energy intensive. The modern weaving machine is energy efficient and energy consumption is equivalent to one fourth of the existing old weaving machine for the same purpose. On the other hand in winding operation, cope and roll winding is considered but modern setup contains only roll winding for the same purpose. Cope winding is not mandatory and can avoid in the context of energy crisis as it consumes significant electricity. Table 3 shows the potential savings of electricity consumption, corresponding emissions and economic aspect using the above modification. The total electricity saving is 3,076 kWh. The daily emissions savings are CO_2 1.92 ton, CH_4 36 gm and N_2O 3 gm could be possible. The daily monetary saving is BDT 27,684 and per ton production of jute products is BDT 1,318 could be possible using the given strategies.

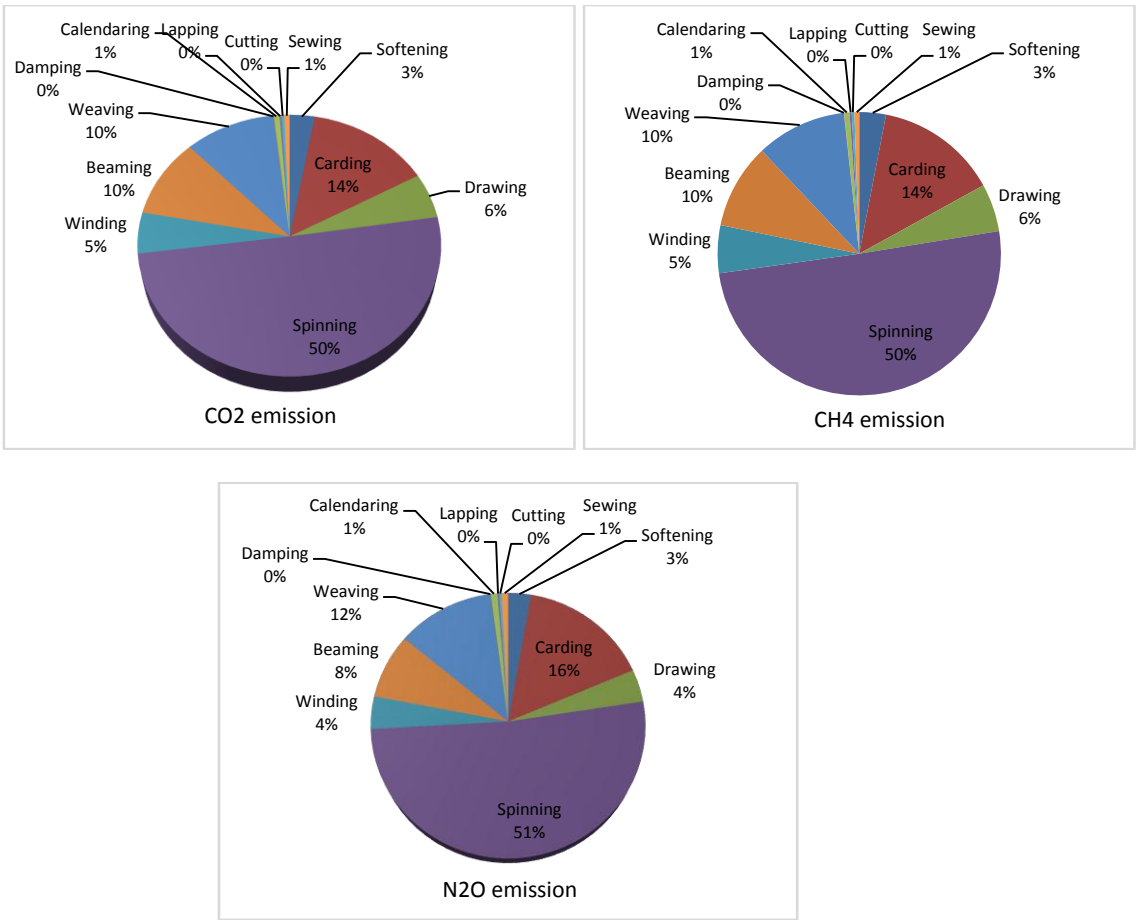

FIGURE 3. Contribution of emissions at various stages during manufacture of jute product

TABLE 2. Emissions at various steps per ton production of jute product

Step No.	Name of the step	CO_2 emission ($kgCO_2$/ton)	CH_4 emission ($gmCH_4$/ton)	N_2O emission (gmN_2O/ton)
1	Softening	23.0	0.5	0.07
2	Carding	119.0	2.3	0.4
3	Drawing	47.0	0.9	0.1
4	Spinning	425.0	8.3	1.3
5	Winding	42.0	0.9	0.1
6	Beaming/Dressing	83.0	1.6	0.2
7	Weaving	87.0	1.7	0.3
8	Damping	0.4	0.01	0.001
9	Calendaring	5.6	0.10	0.02
10	Lapping	1.8	0.04	0.005
11	Cutting	2.7	0.05	0.008
12	Sewing	5.0	0.09	0.02
	Total	845.0	16.0	2.00

TABLE 3. Savings opportunity using the alternative strategies

Strategies	Existing	Proposed	Electricity savings per day (kWh)	Emission savings			Cost savings (BDT/day)	Cost savings (BDT/ton)
				CO_2 (ton/day)	CH_4 (gm/day)	N_2O (gm/day)		
1	Old and inefficient Weaving machine	Modern and efficient weaving machine	2156	1.35	25	2	19,404	
2	Cop Winding and roll winding	Cope winding can be avoided	920	0.57	11	1	8,280	1,318
	Total		3076	1.92	36	3	27,684	

CONCLUSION

Assessment of electricity consumption and emissions in the jute product manufacture of Rajshahi jute mill has been studied. The alternative options are also studied to improve the existing production line in the context of electricity consumption and emissions. The spinning process is the electricity intensive stage consumes 50% of the total electricity consumption. The electricity consumption per ton jute product is 1345 kWh. Two alternative observations are investigated and it is seen that existing weaving machine is old and electricity intensive, it can replace by modern energy efficient weaving machine will reduce the electricity consumption. Cope winding is electricity intensive and not necessary to consider as roll winding can do all the process. These strategies will reduce the electricity consumption by 11.2% of total electricity consumption. The environmental and economic study shows that daily CO_2 emission will be reduced by 1.92 ton and monetary savings will be BDT 27,684 which is significant. The government should take necessary steps in the jute product manufacture sector to reduce the energy consumption, emissions and will achieve economic benefit.

REFERENCES

1. H. Gunatilake and D. R. Holst, "Energy Policy Options for Sustainable Development in Bangladesh", *ADB Economics Working Paper* Series; No. 359, 2013.
2. Asian Development Bank (ADB), "Sector assistance program evaluation for Bangladesh energy sector", *Independent evaluation department*, 2009.
3. Power division Bangladesh, 2014. http://www.powerdivision.gov.bd
4. S. Hossainy, "High interest rate and energy crisis hampering jute and textile industries", The *Independent newspaper*, Bangladesh, 3 June 2011.
5. M. M. K. Akter, "Golden Fiber", *Bangladesh Textile Today* (BTT), 2013. www.textiletoday.com.bd
6. Bangladesh jute mill corporation (BJMC), 2012. http://www.bjmc.gov.bd/home-detail
7. Das & Gobindo, "Production problems in Rajshahi jute mills and its remedies", Undergraduate Thesis, *Rajshahi University of Engineering & Technology*, Bangladesh, 2006.
8. A. K. Uddin, K. M. I. Ali, "Modification of jute yarn by graft-copolymerization with ultraviolet radiation", Institute of Nuclear Science and Technology, *Atomic Energy Commission*, Bangladesh, 1996, Pages 511–517.
9. G. Basu , S.S. De and A.K. Samanta, "Effect of bio-friendly conditioning agents on jute fibre spinning", Industrial Crops and Products, 2009, Pages 281–288.
10. M. Branderl, "Electric factors for grid electricity", *Ecometrica emission factor database*, Technical Paper, 2011. www.emissionfactors.com.

ICME2015

International Conference on Mechanical Engineering 2015
(ICME 2015) 18 – 20 December, 2015, Dhaka, Bangladesh

Paper ID : 029

Heat Line Analysis for MHD Mixed Convection Flow of Nanofluid within a Driven Cavity Containing Heat Generating Block

Salma Parvin[1] and Ayesha Siddiqua[2,a)]

[1]*Department of Mathematics, Bangladesh University of Engineering & Technology,Dhaka-1000, Bangladesh,*
[2]*Department of Mathematics, American International University-Bangladesh, Banani, Dhaka-1213, Bangladesh,*

[a)] Corresponding author: ayesha_math@aiub.edu

Abstract. Mixed convective flow and heat transfer characteristics of nanofluid inside a double lid driven cavity with a square heat generating block is analyzed numerically based on heat line approach. The water- alumina nanofluid is chosen as the operational fluid through the enclosure. The governing partial differential equations with proper boundary conditions are solved by Finite Element Method using Galerkin's weighted residual scheme. Calculations are performed for different solid volume fraction(χ) of nanoparticles $0 \leq \chi \leq 0.15$. Results are shown in terms of stream lines, isothermal lines, heat lines, average Nusselt number, average velocity and average temperature. An enhancement in heat transfer rate is observed with the increase of nanoparticles volume fraction.

INTRODUCTION

Mixed convection flows occur when each of forced convection and natural convection dominates the other. The study of MHD mixed convection in lid-driven enclosures has received a continuous attention, due to the interest of the phenomenon in many technological processes. These include design of solar collectors, thermal design of buildings, air conditioning and, recently the cooling of electronic circuit boards. The present study simulates a reasonable system such as air-cooled electronic equipment with a heat component or an oven with heater.

Heat transfer and flow characteristics for MHD mixed convection in a lid driven cavity with heat generating obstacle is observed by Billah et al. [1]. The authors claimed that only the thermal fields are affected by thermal conductivity ratio K in the cavity at all convective regimes. Rahman et al. [2] made a numerical analysis of Effect of heat-generating solid body on mixed convection flow in a ventilated cavity. A review on the subject shows that a sizeable number of authors had considered MHD mixed convection in enclosures [3, 4]. Rahman et al. [5] investigated the effect of Reynolds and Prandtl numbers effects on MHD mixed convection in a lid-driven cavity along with joule heating and a centered heat conducting circular block. A nano fluid is a fluid containing nanometer sized particles, called nanoparticles.. Muthtamilsevan and Doh [6] examined mixed convection of heat generating nano fluid in a lid driven cavity with uniform and non-uniform heating of bottom wall. Numerical simulation of mixed convection within nano fluid filled cavities with two adjacent moving walls is analyzed by Hemmat Esfe et al. [7]. The results show that when the moving lids have opposite effect, the streamlines contain two main vortices. Recently, Kandasmyet al. [8] performed Nanoparticle volume fraction with heat and mass transfer on MHD mixed convective flow in a nanofluid in presence of thermo-diffusion under convective boundary condition. Again Saedodin et al [9] presented mixed convection heat transfer performance in a ventilated inclined cavity containing heated blocks. Effect of solid volume fraction and tilt angle in a quarter circular solar thermal collectors filled with CNT–water nanofluid was investigated by Rahman et al [10]. The heatline concept was first introduced by Kimuru and Bejan [11] and Bejan [12]. Heatline represents heatflux lines which represent the trajectory of heat flow and they are normal to the isotherms for conductive heat transfer. Tamnay et al [13, 14] also investigated the heatline approach on natural and mixed convection.

To the best knowledge of the authors, a little attention has been paid to problem of mixed conviction in a double lid driven cavity filled with water alumina nanofluid with a square heat generating obstacle. The present work focuses on the heatline analysis for nanofluid concentration effect on MHD mixed convection flow in a double lid driven cavity. It is expected that the present numerical investigation will contribute to the search of finding more efficient and better renewable energy equipment.

PHYSICAL AND MATHEMATICAL MODEL

The schematic of the problem herein investigated is presented in Fig.1(a)-(b). For a steady, two-dimensional laminar and incompressible flow, the governing equations may be written in the non-dimensional form as follows:

$$\frac{\partial U}{\partial X}+\frac{\partial V}{\partial Y}=0, \tag{1}$$

$$U\frac{\partial U}{\partial X}+V\frac{\partial U}{\partial Y}=-\frac{\partial P}{\partial X}+\frac{\gamma_{nf}}{\gamma_f}\frac{1}{Re}\nabla^2 U \tag{2}$$

$$U\frac{\partial V}{\partial X}+V\frac{\partial V}{\partial Y}=-\frac{\partial P}{\partial Y}+\frac{\gamma_{nf}}{\gamma_f}\nabla^2 V+Ri\,\frac{\beta_{nf}}{\beta_f}\theta-\frac{Ha^2}{Re}V \tag{3}$$

$$U\frac{\partial \theta}{\partial X}+V\frac{\partial \theta}{\partial Y}=\frac{1}{Re\,Pr}\frac{\alpha_{nf}}{\alpha_f}\nabla^2\theta \tag{4}$$

For solid obstacle the energy equation is

$$\nabla^2\theta_s+Q=0, \tag{5}$$

where $Re=\frac{V_0 L}{\nu}$, $Pr=\frac{\nu}{\alpha}$, $Ri=\frac{g\beta\,\Delta T\,L}{V_0^2}$, $Ha^2=\frac{\sigma B_0^2 L^2}{\mu}$, $\alpha_{nf}=\frac{k_{nf}}{(\rho c_p)_{nf}}$, $\rho_{nf}=\varphi\rho_s+(1-\varphi)\rho_f$, $(\rho c_p)_{nf}=\varphi(\rho c_p)_s+(1-\varphi)(\rho c_p)_f$, $(\rho\beta)_{nf}=\varphi(\rho\beta)_s+(1-\varphi)(\rho\beta)_f$, $\mu_{nf}=\frac{\mu_f}{(1-\varphi)^{2.5}}$, $\frac{k_{nf}}{k_f}=\frac{k_s+2k_f-2\varphi(k_f-k_s)}{k_s+2k_f+2\varphi(k_f-k_s)}$ and $Q=\frac{q\,L^2}{k_s\,\Delta T}$ are Reyonlds number, Prandtl number, Richardson number, square of the Hartmann number, thermal diffusivity, effective density, heat capacitance , thermal expansion coefficient, effective viscosity, effective thermal conductivity and heat generating parameter in the solid, respectively.

Equations (1)-(5) are non-dimensionalized by using the following dimensionless parameters:

$X=\frac{x}{L}$, $Y=\frac{y}{L}$, $V=\frac{v}{U_0}$, $U=\frac{u}{U_0}$, $\Delta T=T_h-T_c$, $\theta=\frac{T-T_c}{\Delta T}$, $P=\frac{p}{\rho_{nf}U_0^2}$, $\theta_s=\frac{T_s-T_c}{\Delta T}$

The boundary conditions for the present problem are specified as follows:

At sliding double leads: $U=0, V=1, \theta=0$

At horizontal top and bottom walls: $U=V=0, \frac{\partial\theta}{\partial N}=0$

At square block boundaries: $U=V=0, \theta=\theta_b$

At fluid solid interface: $(\frac{\partial\theta}{\partial N})_{fluid}=K\,(\frac{\partial\theta_s}{\partial N})_{solid}$

where N is the non-dimensional distances either in X or Y direction acting normal to the surface and K is the ratio of the solid fluid thermal conductivity K_s/K_f .

The relationships between streamfunction ψ and velocity components *U*, *V* for two-dimensional flows are

$$U=\frac{\partial\psi}{\partial Y} \text{ and } V=-\frac{\partial\psi}{\partial X}$$

which give a single equation

$$\frac{\partial^2\psi}{\partial X^2}+\frac{\partial^2\psi}{\partial Y^2}=\frac{\partial U}{\partial Y}-\frac{\partial V}{\partial X}$$

The no-slip condition is valid at all boundaries as there is no cross-flow. Hence $\psi=0$ is used for boundaries.

The heat flow within the enclosure is displayed using the heatfunction *Π* obtained from conductive heat fluxes $\left(-\frac{\partial\theta}{\partial X},-\frac{\partial\theta}{\partial Y}\right)$ as well as convective heat fluxes (*Uθ*, *Vθ*). The heatfunction satisfies the steady energy balance equation $\frac{\partial\Pi}{\partial Y}=U\theta-\frac{\partial\theta}{\partial X}$ and $-\frac{\partial\Pi}{\partial X}=V\theta-\frac{\partial\theta}{\partial Y}$ which yield a single equation

$$\frac{\partial^2\Pi}{\partial X^2}+\frac{\partial^2\Pi}{\partial Y^2}=\frac{\partial}{\partial Y}(U\theta)-\frac{\partial}{\partial X}(V\theta)$$

The average Nusselt number, average temperature and average velocity may be expressed as

$$Nu = -\frac{1}{S}\int_0^S \left(\frac{k_{nf}}{k_f}\right)\frac{\partial\theta}{\partial N}\, dN \quad , \quad \theta_{av} = \int \theta\, d\bar{V}/\bar{V} \text{ and } V_{av} = \int V\, d\bar{V}/\bar{V}$$

respectively, where S is the non-dimensional length of the surface and $\bar{V}$ is the volume to be accounted.

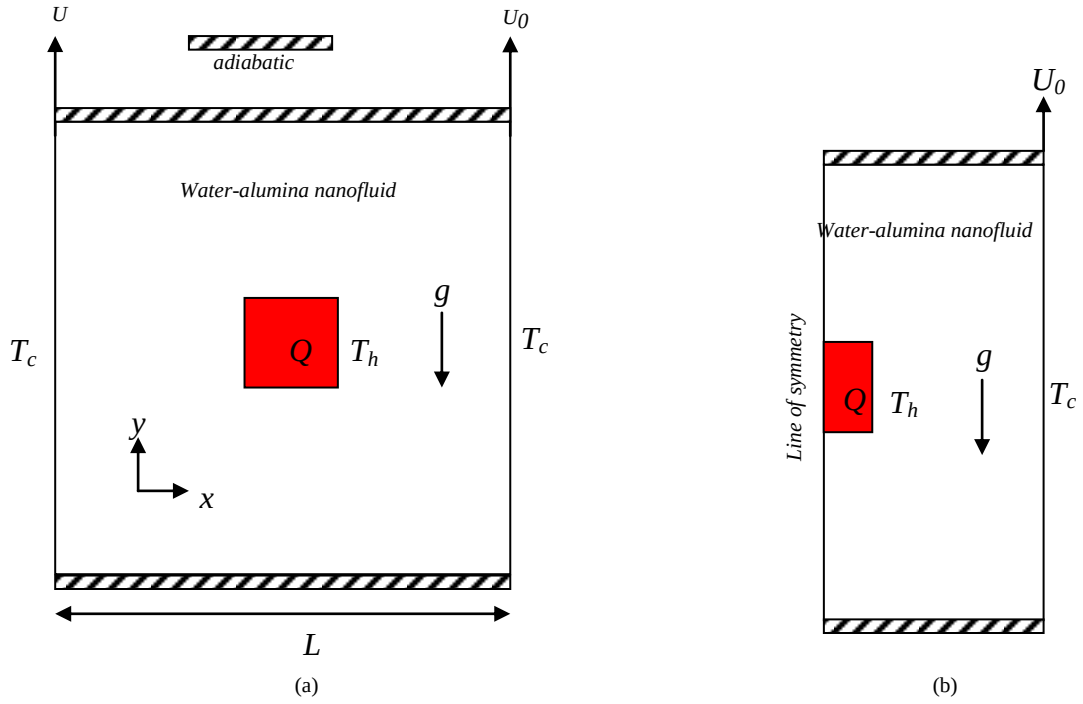

FIGURE 1. (a) Schematic diagram of the problem and (b) computational domain.

COMPUTATIONAL PROCEDURE

The governing equations have been solved by using the Galerking weighted residual finite element method. The fundamental unknowns for the governing equations are the velocity components $(\boldsymbol{U}, \boldsymbol{V})$, the temperature $\boldsymbol{\theta}$ and the pressure $\boldsymbol{P}$. The convergence of solutions is assumed when the relative error for each variable between consecutive iterations is recorded below the convergence criterion ε such that $\psi^{n+1} - \psi^{n} \leq 10^{4}$, where n is the number of iteration and ψ is a function of U, V and θ.

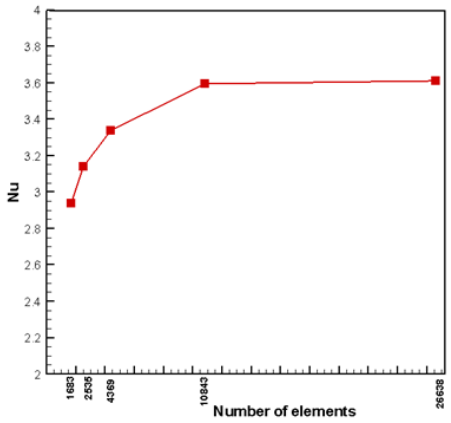

FIGURE 2. Grid sensitivity test

Grid Independent Test

An extensive mesh testing procedure is conducted to guarantee a grid-independent solution for Ri = 1, Re = 100, Pr = 6.2, K = 5, Ha = 10 and Q = 1 and χ = 0.05 in the considered domain. Five different non-uniform grid systems with the following number of elements within the resolution field: 1683, 2535, 4369, 10843 and 26638 are examined. The numerical scheme is carried out for highly precise key in the average Nusselt (*Nu*) number to understand the grid fineness as shown in Fig. 2. The scale of the average Nusselt numbers for 10843elements shows a little difference with the results obtained for the other elements. Hence, considering the non-uniform grid system of 10843 elements is preferred for the computation.

RESULT AND DISCUSSION

MHD mixed convection flow for nanofluid inside a lid driven cavity having a heat generating square obstacle is governed by different parameter namely heat generation Q, solid volume thermal conductivity ratio K, Richardson's number Ri, Reynold's number Re, Prandtl's number Pr, and Hartmann number Ha. Here the solid volume fraction χ is involved to control the heat transfer and fluid flow in this study. The other parameters are kept fixed at Ri = 1, Re = 1, Pr = 6.2, K = 5, Ha = 10 and Q = 1. The results are presented in terms of isotherms, streamlines and heat lines pattern.

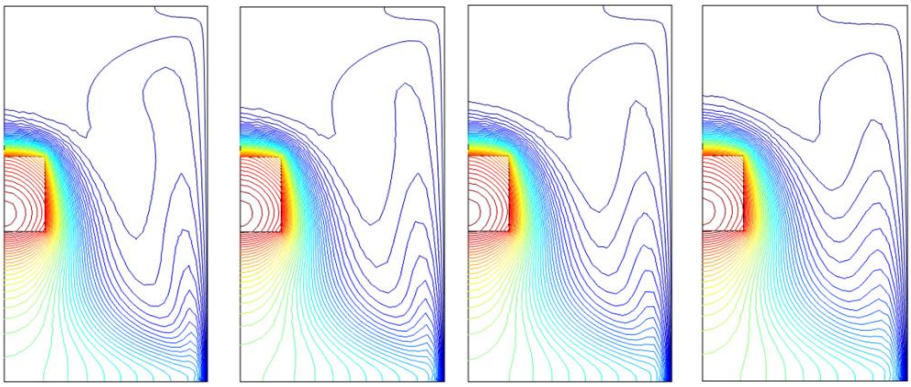

FIGURE 3. Isotherms for various solid volume fraction with *Ri* =1, *Re* = 100, *Pr* = 6.2, *K* = 5, *Ha* = 10 and *Q* = 1.

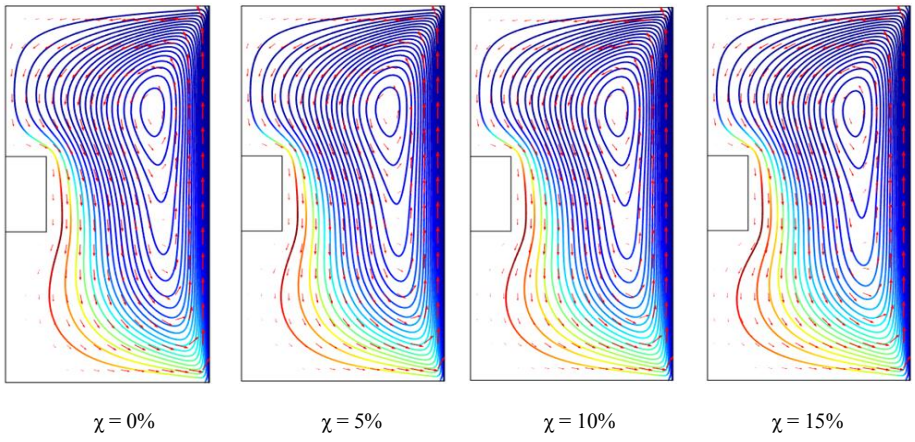

FIGURE 4. Streamlines for various solid volume fraction with *Ri* =1, *Re* = 100, *Pr* = 6.2, *K* = 5, *Ha* = 10 and *Q* = 1.

The isotherms for various solid volume fraction of nano particle inside a double lid driven cavity with a square heat generating block are shown in fig.3. From the figure it can be said that the solid volume fraction of nano particle effects significantly on isotherm structure. If the solid volume fraction is 0% that is for normal fluid isotherms are parabolic near the heat generating block. If solid volume fraction χ is increased from 0% to 15% then the parabolic shaped isotherms increase. Making a comparison of the isotherm lines for various solid volume fractions, the isotherms are slightly shifted from the heat generating block to the side wall.

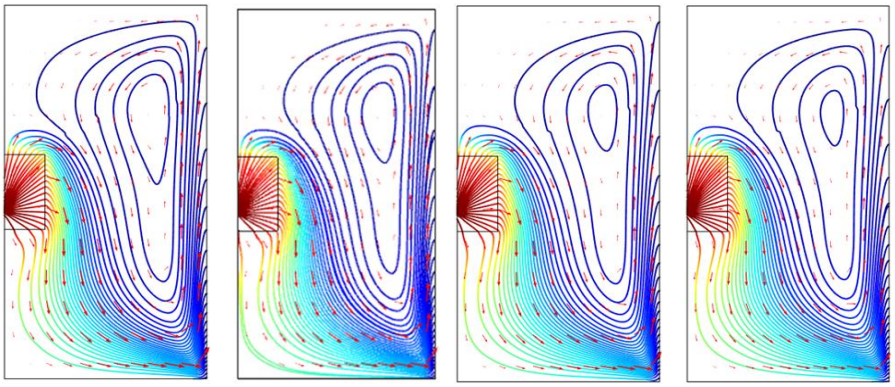

FIGURE 5. Heatlines for various solid volume fraction with *Ri* =1, *Re* = 100, *Pr* = 6.2, *K* = 5, *Ha* = 10 and *Q* = 1.

The flow field inside a double lid driven cavity with heat generating object in terms of computed streamlines for various solid volume fraction χ is shown in fig.4. Here the arrows indicate the direction of the streamlines and the flow field. The size of the vortex as well as the flow strength has a small effect as the solid volume fraction is increased from 0% to 15%. For the given boundary condition there forms a counter clockwise vortex inside the cavity. If the solid volume fraction χ is increased the vortex inside the cavity becomes slightly weaker.

The heat lines for various solid volume fraction χ are shown in fig.5. From the figure it can easily be said that there is well-built effect of solid volume fraction χ on heat line structure. When the solid volume fraction χ is 0% then the hit lines are elliptic at the centre of the circulation and parabolic near the side walls. When the solid volume fraction is increased it is observed that the density of circulations also increases due to convection. When χ is 0% then natural convection contributes to flow the heat due to the boundary condition. Since alumina has relatively high thermal conductivity when the solid volume fraction χ is increased then the heat flow increases. It is found from the figs. 6 (a)-(c) that average Nusselt number increases almost linearly if solid volume fraction increases. It is also applicable for average temperature. But in case of velocity it can be said that if the solid volume fraction increases then average velocity decreases slowly.

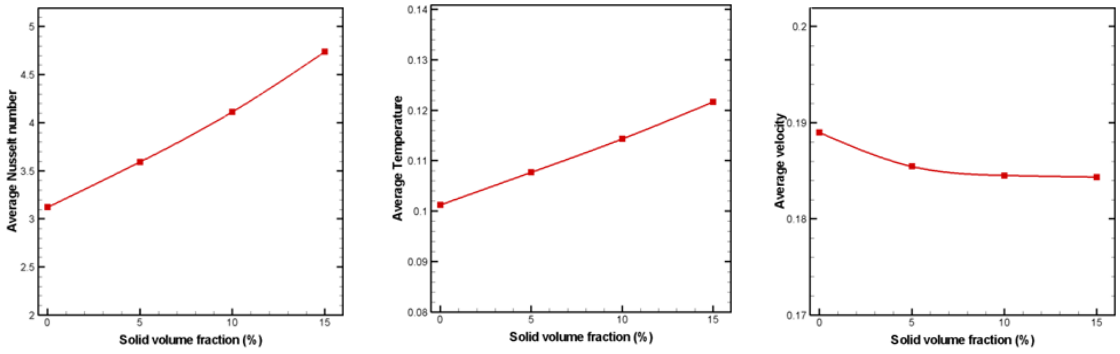

(a) (b) (c)

FIGURE 6. (a) average Nusselt number (b) average Temperature (c) Average Velocity for various solid volume fraction

CONCLUSION

A numerical simulation is performed to investigate the heatlines for MHD mixed convection of water alumina nano-fluid in a double lid driven enclosure with a heat generating block. The following conclusion may be drawn:

- The solid volume fraction effects significantly on the isotherms, steamlines and heatline structure.
- If the solid volume fraction increases from 0% to 15% then the parabolic shaped isotherms become denser near the moving wall, the vortex inside the cavity becomes slightly weaker and the conductive heat flow increases whereas the convective heat flow decreases.
- The average velocity decreases while the average Nusselt number and average temperature increases due to the increment of solid volume fraction of nanofluid.

ACKNOWLEDGEMENT

The present work is fully supported by the department of mathematics BUET.

REFERENCES

1. M. M. Billah, M. M. Rahman, M. H. Kabir and Uddin M. Sharif, Int. J. of energy & technology **3**, 1-8 (2011).
2. M. M. Rahman, S. Parvin, M. Hasanuzzaman, R. Saidur and N.A. Rahim, Heat Transfer Engineering **34**, 1249-1261 (2013).
3. S. Parvin, M.A. Alim and N.F. Hossain, Engineering e-Transaction **7**, 86-95 (2012).
4. S. Parvin and N. F. Hossain, J. of Advanced Science and Engineering Research **1**, 210-223 (2012).
5. M. M. Rahman, M. M. Billah, M. A. H., Mamun, R. Saidur and M. Hassanuzzaman, Int. J. Mechanical and Materials Engineering **5,** 163-170 (2010).
6. M. Muthamilselvan and D. H. Do Appl. Mathematical Modeling **38**, 3164-3174 (2014).
7. M. H. Esfe, A. Z. Ghadi and M. J. Noroozi, Transactions of the Canadian Society for Mechanical Engg. **37**, 1073-1083 (2013).
8. R.K. Kandasmy, C. Jeyabalan and K.K. Sivagnana Prabhu, App. Nanosci, DOI 10.1007/s 13204-015-0435-5 (2015).
9. S. Saedodin, M. Biglari, M.H. Esfe and M.J. Noroozi, J. of Computational and Theoretical Nanoscience **10**, 1-13 (2013).
10. M.M. Rahman, S. Mojumder, S. Saha, S. Mekhief and R. Saidur, Int. Commu. in Heat and Mass Trans. **57,** 79-90 (2014).
11. S. Kimuraand A. Bejan, J. Heat Transfer Trans. ASME **105**, 916-919 (1983).
12. A. Bejan, *Convection Heat Transfer* (3rd ed., Wiley, Hoboken, NJU, 1984).
13. T. Basak, P.V.K. Pradeep, S. Roy and I. Pop, Int. J. of Heat and Mass Trans. **54**, 1706-1727 (2011).
14. T. Basak, G. Aravind and S.Roy, Int. J. of Heat and Mass Trans. **52,** 2824-2833 (2009).

ICME2015

International Conference on Mechanical Engineering 2015
(ICME 2015) 18 – 20 December, 2015, Dhaka, Bangladesh

Paper ID : 030

Experimental Study on the Performance Characteristics and Emission Analysis of a Diesel Engine using Vegetable Oils

Anup Saha [a)], Ekramul Haque Ehite [b)] and M.M.Alam [c)]

Department of Mechanical Engineering, Bangladesh University of Engineering and Technology, Dhaka-1000, Bangladesh.

[a)] Corresponding author: anup106@me.buet.ac.bd
[b)] ehite.haque@gmail.com
[c)] mmalam@me.buet.ac.bd

Abstract. In this research, Vegetable oils derived from Sesame Seed and Rice Bran were used and experimented upon. Using Kerosene as the solvent in varying proportions (30%, 50%, 70% by volume) with the vegetables oils, different blends of Sesame and Rice Bran Oils were produced. The important characteristic properties were found by experimentation and compared with those of Straight Run Diesel. Subsequently, Straight Run Diesel, vegetable oils and their blends were used to run a diesel engine one-by-one and the performance analysis was conducted, followed by an investigation of the exhaust emissions. From the comparative performance analysis, it was found that Rice Bran oil showed better performance as a fuel than Sesame with regards to power production and specific fuel consumption and also resulted in less Carbon Monoxide (CO) emission than Sesame oil blends.

INTRODUCTION

The global energy requirement is increasing in an exponential rate, leading to increased reliance on fossil fuels like coal, gasoline, crude oil etc., especially for the transport sector. Declining crude oil reserve, global warming, air pollution etc. however, is shifting the interest from petrochemical fuels towards alternative fuels, e.g. vegetable oils.

Experiments have been conducted worldwide on numerous occasions regarding the replacements of conventional fuels with alternative ones. Dunn and Jompakdee [1] provided statistical information regarding vegetable oil production, its demand cost analysis in Northern Thailand. Kanthavelkumaran and Seenikannan [2] tested gaseous emissions of CO and NOx when the vehicle is fuelled with new and waste vegetable oils in pure form or in blends (25, 50 and 75%). They concluded that NOx emissions are comparable to those of diesel fuel and CO emission increased a little. R. Altõn et al [3] conducted tests with various biofuels on a diesel engine and found that vegetable oil methyl esters gave better performance and emission characteristics closer to diesel fuel. Misra and Murthy [4] presented a critical review regarding the usage of straight vegetable oils in diesel engine. They posited that stationary diesel engine running at low speed, such as irrigation pumps and electricity generators, are believed to be suitable to pure vegetable oil and their blends without a too high environmental burden. S. Altun et al [5] tested sesame and diesel mixtures on diesel engine and test results revealed comparable power and torque output and less emission using test fuels. Mohant [6] tested biodiesel from rice bran oil on a diesel engine and found satisfactory results in engine performance.

This experimental endeavor focuses on the possibility of using sesame and rice bran oil blended with kerosene in a diesel engine. Results of performance and emission are also presented graphically and compared with diesel fuel.

TEST FUELS AND THEIR PROPERTIES

In this study, Sesame and Rice Bran oils were mixed with Kerosene at varying proportions. Tested blends are listed in Table 1.

TABLE 1. Tested Fuels.

100% Diesel
100% Sesame
100% Rice Bran
30% Sesame + 70% Kerosene (S30)
50% Sesame + 50% Kerosene (S50)
70% Sesame + 30% Kerosene (S70)
30% Rice Bran + 70% Kerosene (R30)
50% Rice Bran + 50% Kerosene (R50)
70% Rice Bran + 30% Kerosene (R70)

Fuel Property Analysis

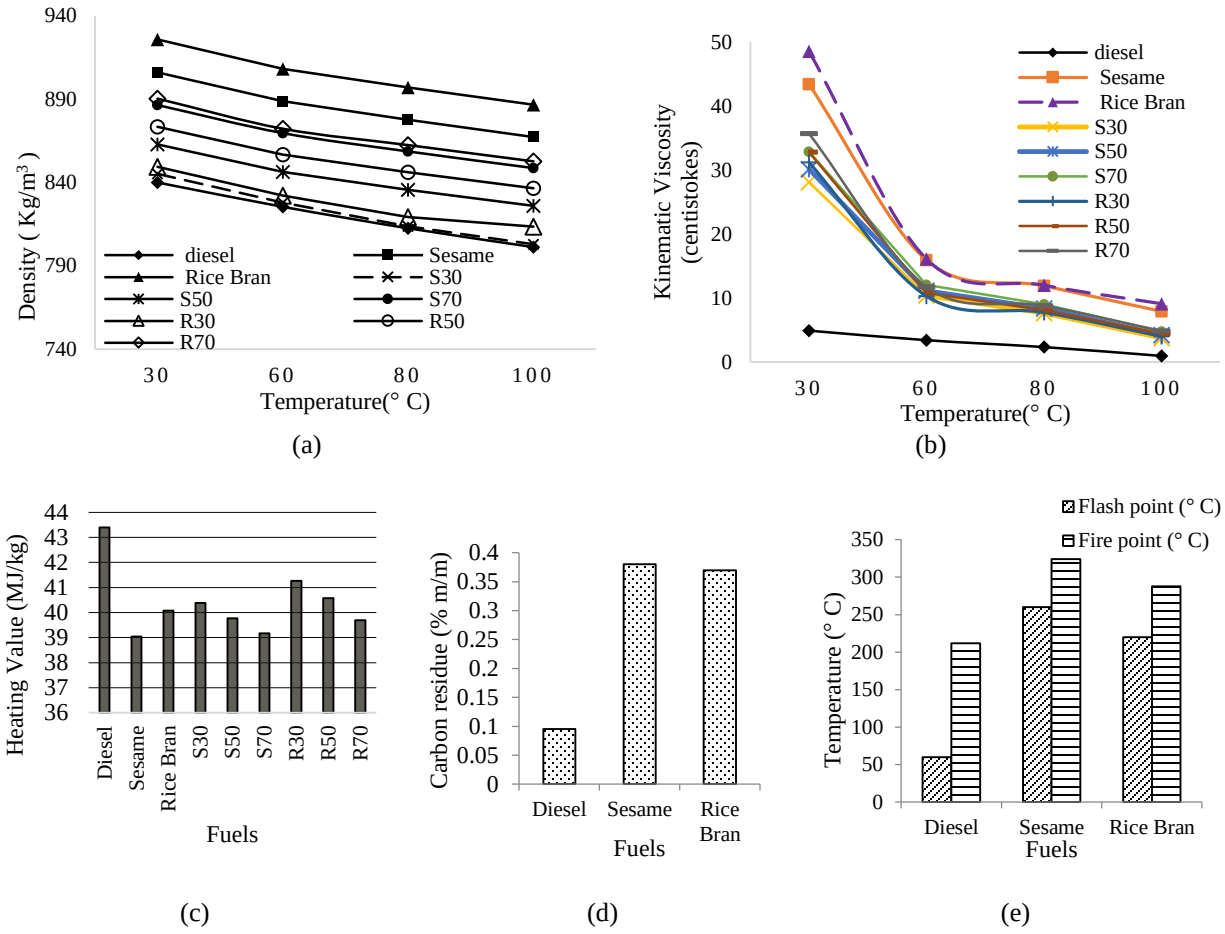

FIGRUE 1. (a) Density, (b) Viscosity, (c) Heating Value, (d) Carbon Residue, (e) Flash Point and Fire Point of test fuels.

To check the compatibility of the test fuels in the engine, several fuel properties have been tested and compared with the corresponding properties of diesel.

Figure 1(a) shows variation of density for different fuel blends. Density decreases with increasing temperature regardless of fuel tested. Undiluted RBO and Sesame exhibit density much higher than diesel. However, as the vegetable oils are diluted with kerosene, their density decrease gradually. RBO and its blends show higher density than Sesame oil and its blends. However density of S30 and R30 blends are close to diesel at all tested temperatures.

ASTM D445 method has been applied to measure the viscosity, shown in Fig. 1(b). Sesame's viscosity is about 8 times higher than that of diesel fuel and Rice Bran is about 9 times higher in the room temperature. Pre-heating the blends to 100° C would cause to achieve comparable viscosity as that of diesel fuel.

From Fig. 1(c), it is observed that, diesel fuel has heating value about 43.4 MJ/Kg. Compared to Diesel, Pure Sesame and Rice Bran have much lower heating values. But as the proportion of kerosene increases, heating values also rise. RBO blends exhibit higher heating values than Sesame blends. Among the blended samples, R30 provides better heating value.

Conradson Carbon Residue (CCR) method has been used to determine the carbon residue in fuels. From Fig. 1(d) it is found that carbon residue for the vegetable oils is higher than fossil diesel. As vegetable oils contain higher amount of Free Fatty Acid (FFA), so their carbon residue is higher than that of petro-diesel.

Standard testing method ASTM D90 has been applied to detect flash point and fire point. Figure 1(e) illustrates that flash point and the fire point for the vegetable oils is much higher than fossil diesel. At lower temperature, not enough vegetable oil fuel evaporates to form a combustible mixture. A higher flash point and fire point results in reduced fire
hazard and increased fuel transportability for the vegetable oil.

ENGINE PERFORMANCE TEST

Experimental Procedure

Performance tests have been performed on a single cylinder, four stroke diesel engine. The engine was maintained at rated rpm of 2200 rpm. Load was varied from 50% of rated load (3.6 kg) to 110% of rated load (around 8 kg). A hydraulic brake dynamometer directly coupled with the engine was used to load the engine. Load was varied by changing the water flow rate. Fuel supply system was modified, so that fuels could be supplied through a graduated burette. Fuel consumption rate was recorded by observing the time using a stop watch for every 30 ml of fuel. Speed was measured by digital tachometer and exhaust, lube oil and fuel inlet temperature was measured by using K-type thermocouple. Preheating was done manually using electric heater. Major engine specifications is shown in Table 2.

TABLE 2. Major Engine Specifications.

Brand Name	CHANGTUO
Model & Engine No	S1100A2 & 50393884
Manufacturer	CHANGCHAI CO. LTD
Type	Horizontal, Single Cylinder, four stroke, water cooled
Combustion Chamber	Swirl combustion chamber type
Rated Output	16 hp
Rated rpm	2200
Cylinder Bore & Piston stroke	100 mm & 115 mm
Net weight	160 kg

PERFORMANCE ANALYSIS

Six performance parameters have been investigated in this experimental study.

- Thermal Efficiency
- Break Horse Power (Bhp)

- Break Mean Effective Pressure (Bmep)
- Break Specific Fuel Consumption (Bsfc)
- Exhaust Gas Temperature
- Lub Oil Temperature.

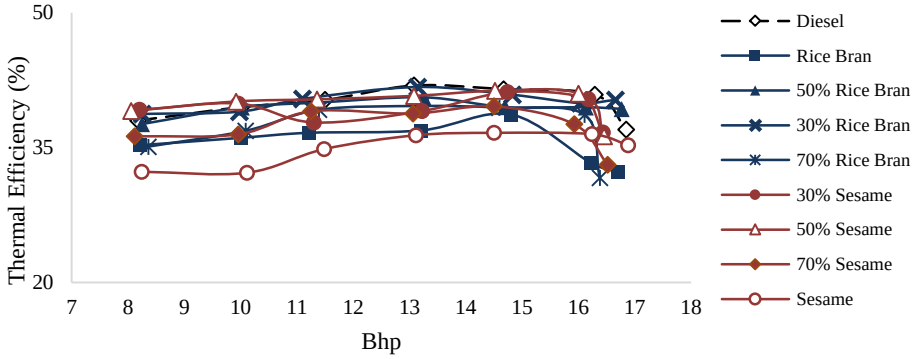

(a)

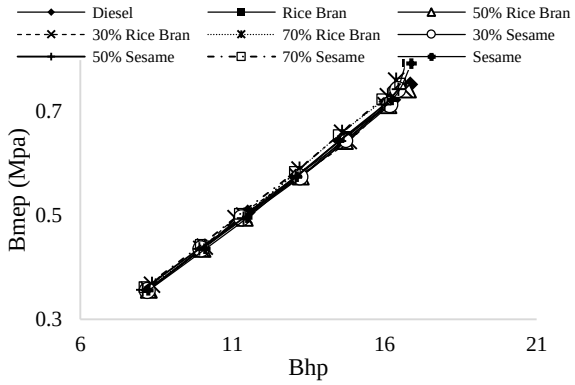

(b)

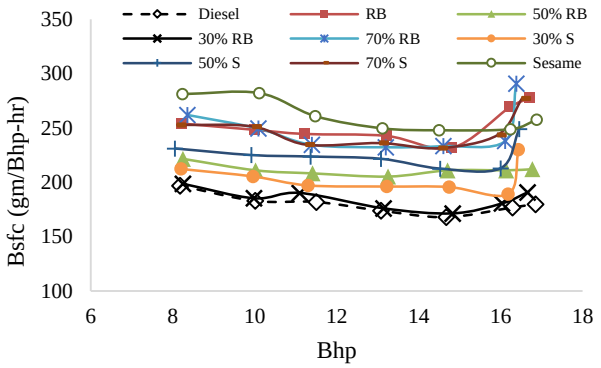

(c)

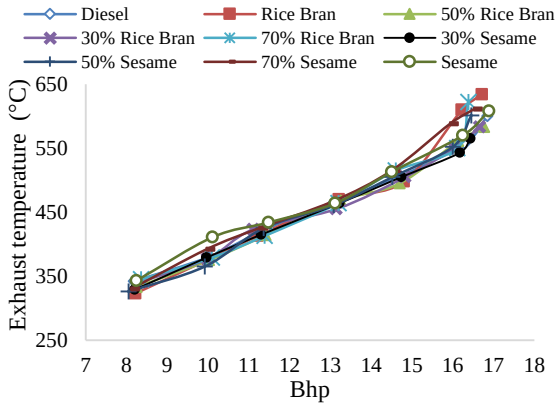

(d)

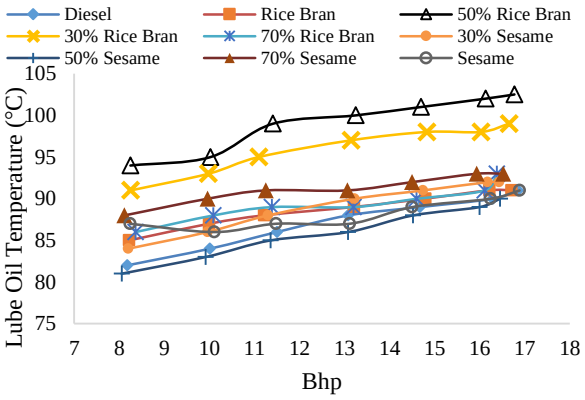

(e)

FIGURE 2. (a) Thermal efficiency vs Bhp, (b) Bmep vs Bhp, (c) Bsfc vs Bhp, (d) Exhaust Temperature vs Bhp, (e) Lub Oil Temperature vs Bhp.

Figure 2(a) shows variation of thermal efficiency with Bhp. It is clear that 100% sesame and RBO exhibit efficiency well below than Diesel. But with increasing percentage of blending agent, efficiency also rises. Among the tested samples, 30% RBO and 30% Sesame shows efficiency close to diesel.

Variation of Bmep is almost similar for all samples at lower load as shown in Fig. 2(b). As the load increases, especially at higher load, there are slight variations in the Bmep values. However, the trends of Bmep do not seem to be changed that much.

Variations of Bsfc with Bhp is shown in Fig. 2(c). As load increases, Bsfc value decreases gradually and after reaching a minimum value, it rises again with load. The load corresponding to minimum Bsfc is particularly important since maximum thermal efficiency is attributed to this load. Sesame & Rice bran oil and blends rich with vegetable oils exhibit higher Bsfc than diesel. However, Bsfc of blend with 30% Rice bran follows that of diesel with a very close proximity.

Exhaust gas temperature (EGT) may be the most critical performance parameter on a diesel engine, because excessive EGT can bring a host of problems that fall under the meltdown category, both figuratively and literally. From Fig. 2(d), it is evident that there is not any significant variation in exhaust temperature using test fuels compared to that of diesel fuel.

Overheated lube oil can have detrimental effects on engine. Therefore it is necessary to investigate the lube oil temperature resulting from various test samples. As in Fig. 2(e), lube oil temperature increasing load for all fuels. 50% RBO and 30% RBO exhibit much higher temperature of lube oil. Other test samples result in comparable lube oil temperature to that of diesel fuel.

ANALYSIS OF CARBON MONOXIDE (CO) IN EXHAUST GAS

Since NO_x emission using vegetable oils is comparable to diesel [2], only CO emission is analyzed in this work with the help of a CO meter whose specifications are given in Table 3. CO meter was held in front of the exhaust pipe outlet at various load conditions. It took 10-12 seconds to stabilize. The reading was displayed in ppm directly.

TABLE 3. Meter Specifications.

Model	CEM CO-180
Measurement Range	0-1000 ppm
Measurement Resolution	1 ppm
Warm up period	< 2 seconds
Battery	9 V, NEDA 1604A
Accuracy	5% or ± 10 ppm
Sensor type	Stabilized electrochemical Gas Specific(CO)
Auto power off	After 15 minutes

Analysis of CO emission has been conducted in two figures. Due to precipitous increase in the emission value at full load, it has been discussed in a separate figure. CO variation up to 90% of full load has been shown in Fig. 8(a). CO emission increases with increasing load, this may be due to the fact that higher load results in richer mixture; so lack of oxygen causes poor combustion and a concomitant rise in CO emission. However, CO emission from all the vegetable oil blends of various origins is higher than that of diesel. Similar results were obtained by Agarwal [7] using Jatropha oil. Due to high viscosity of test fuels, atomization becomes difficult which results in the locally rich mixtures. As volume of the blending agent increases, emission level decreases. Test fuels originated from Sesame results in higher CO emission than those from RBO. CO emission at full load has been shown in Fig. 8(b). CO emission at full load is significantly higher than other loading conditions, but emission characteristics follow similar pattern as of other loading conditions described in Fig. 8(a).

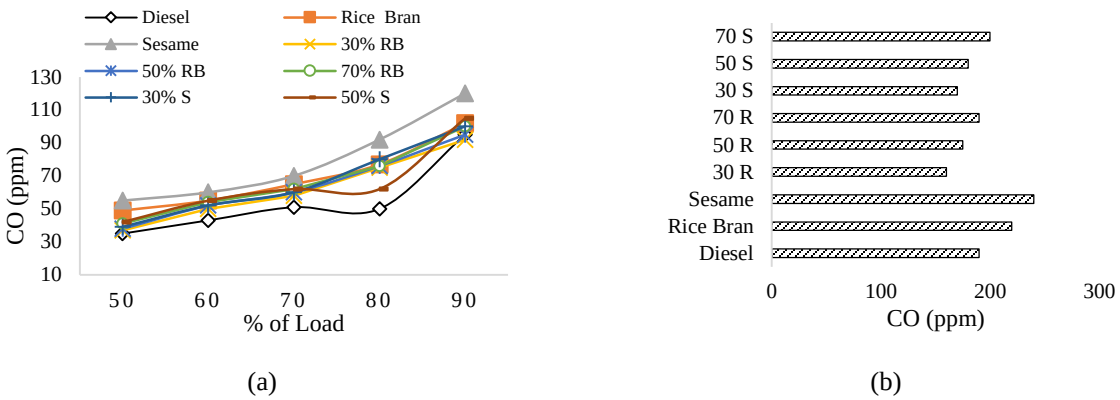

(a) (b)

FIGURE 8. (a) CO variation up to 90% load, (b) CO variation at full load.

.

CONCLUSIONS

- This study showed that Rice Bran and Sesame Oil can be used successfully to operate a direct injection diesel engine without any modification to the engine or the injector system. Preheating of the fuel was necessary to reduce the viscosity of vegetable oils.
- Rice bran oil and its blends with kerosene resulted in better engine performance than those of Sesame and performance parameters were close to diesel. Higher Break specific fuel consumption is observed for sesame than Rice Bran Oil. This may be attributed to lower heating value of Sesame than Rice Bran Oil. As the amount of blending agent (kerosene) in the mixture increases, Bsfc falls accordingly. Among all the test fuels, "30% Rice Bran+70% kerosene" blend shows lowest specific fuel consumption and the values were almost close to Diesel. Bmep values are quite similar for all the tested fuels. A slight decrease in bmep is observed with increasing the amount of kerosene in the mixture. Except 50% Sesame oil blend, all other tested fuels have higher lub oil temperature than diesel. Although there is not wide variation in these values, but lub oil temperature for 30% and 50% Rice bran blends is considerably higher than others.
- CO emission level was higher for the vegetable oil blends than diesel. However, blends originated from Rice bran oil resulted in lower CO emission than those from Sesame.

REFERENCES

1. P.D. Dunn, W. Jompakdee, "The use of vegetable oils as a diesel fuel substitute in Thailand", Proceeding of the Fourth International Conference on Small-Engines and their Fuels, Chiang Mai, Thailand, 21-24 September, 1993.
2. N. Kanthavelkumaran, P. Seenikannan, Research Journal of Applied Sciences, Engineering and Technology **6(15)**, 2886-2890 (2000).
3. R. Altõn, S. Cetinkaya, H.S. Yucesu, Energy Conversion and Management **42**, 529-538 (2001).
4. R.D. Misra, M.S. Murthy, Renewable and Sustainable Energy Reviews **14**, 3005–3013 (2010).
5. S. Altun, H. Bulut, C. Oner, Renewable Energy **33**, 1791-1795 (2008).
6. S. K. Mohant., International Journal of Modern Engineering Research **3(2)**, 920-923 (2013).
7. D. Agarwal, A.K. Agarwal, Applied Thermal Engineering **27**, 2314-2323 (2007).

ICME2015

International Conference on Mechanical Engineering 2015
(ICME 2015) 18 – 20 December, 2015, Dhaka, Bangladesh

Paper ID : 051

Performance and Emission Characteristics of a Four Stroke Spark Ignition Engine with Recirculation of Hot and Cold Exhaust Gases

A.Ganguly[a)], Baidya Nath Murmu[b)] and Somnath Chakrabarti[c)]

Department of Mechanical Engineering, Indian Institute of Engineering Science and Technology, Shibpur, Howrah – 711103, West Bengal, India.

[a)]Corresponding author: aritra@mech.iiests.ac.in
[b)]murmu.baidyanth@gmail.com
[c)]somnathbec@rediffmail.com

Abstract. In the present work, an experiment has been conducted on a four stroke, four cylinder spark ignition engine with and without recirculation of exhaust gas for different loads at a constant speed. Two cases were considered, the first in which 10% and later 20% of the exhaust gas was directly supplied to the intake manifold at a temperature of 820°C, while in the second case the same proportions of exhaust gas (10 and 20%) were cooled in a heat exchanger to a temperature of 210°C before supply to the intake manifold. The various engine performance parameters like brake specific fuel consumption, brake thermal efficiency were evaluated under those conditions and compared with the same engine operating without recirculation of the exhaust gas. The corresponding emission characteristics of the engine were also measured using an exhaust gas analyzer which measured the amount of NO_x, CO, CO_2 and un-burnt HC. Finally, the performance and emissions characteristics of the engine obtained with hot and cold EGR were compared with reference to the same engine operating without EGR. The study revealed that the performance of the engine was better in terms of brake thermal efficiency and brake specific fuel consumption with cold EGR compared to hot EGR. However, the emissions of CO and HC were higher with cold EGR compared to that of hot EGR.

INTRODUCTION

Gasoline engines are widely used in passenger cars, motorcycles and small engines due to their high speed and light weight. The vehicle population is increasing worldwide day by day and this increase is faster in the developing countries of the world like India. The sale of the passenger cars in India have increased from 1,549,882 in 2007-2008 to 2,686,429 in the year 2012-2013 [1]. This significant increase in the vehicle population has increased the emissions of various gases which has aggravated the problem of air pollution. Major constituents of gasoline engine exhaust are oxides of nitrogen (NO_x), carbon dioxide (CO_2), carbon monoxide (CO), unburned hydrocarbon (HC) and particulate matter (PM). The gases coming from the vehicle exhaust have significant effects on the human health. Thus, reducing the emissions of pollutants in conjunction with optimization of performance, comfort and safety is of paramount importance in the development of new engines. Many researchers have worked on the performance of internal combustion engines with Exhaust Gas Recirculation (EGR), but majority of them worked on compression ignition engines. There are only few works available in literature [2-9], which discuss the performance analysis of a spark ignition engine with EGR. Also, no work is available at least in open literature to the authors' knowledge that describes the comparative performance and emission characteristics of a conventional spark ignition engine with hot and cold EGR The aim of the present work is to analyze the influence of exhaust gas recirculation on the performance and emission characteristics of a SI engine with different percentages of hot and cold EGR for different loads. The performance and emissions characteristics of the engine obtained with hot and cold EGR has been compared with reference to the same engine operating without EGR.

The percentage of exhaust gas recirculation (EGR %) is a very important parameter which influences the engine performance and can be defined as the percentage of re-circulated exhaust gas to the total intake mixture.

NOMENCLATURE

EGR	exhaust gas recirculation
bsfc	brake specific fuel consumption
SI	spark ignition engine

EXPERIMENTAL DETAILS

The experiments have been conducted on a four cylinder four stroke, water cooled spark ignition engine. The details of the experimental set up are shown in Fig. 1, while the engine specifications are given in Table 1. The engine is directly coupled to a hydraulic dynamometer of maximum capacity 222.39 N. The water pressure in the hydraulic dynamometer is maintained at a constant value of 1 kg/cm2. The brake power of the engine is measured using the hydraulic dynamometer for different engine loads. The experiments have been conducted with a constant engine speed of 1250 RPM under variable load. The speed of the engine has been measured directly using a mechanical tachometer coupled to the engine. As shown in the figure, a control valve (called EGR valve) is provided in the line of exhaust gas to regulate the amount of exhaust gas re-circulated into the intake manifold. To obtain cold EGR, a heat exchanger is installed in the EGR line to cool the exhaust gas using water before supplying the same to the intake manifold. The amount of water circulated in the heat exchanger may be regulated using a gate valve. In the experimental setup two known diameter orifices have been installed to measure the ambient air flow consumption and the re-circulated exhaust gas flow. Each orifice is connected to a U-tube manometer which can give the pressure differences for different flow rates. From the pressure difference, the flow rate can be estimated. The amount of fuel consumed in a given time can be found by monitoring the drop in the level of fuel in the fuel tank and recording the time using a stop watch. The temperature of the exhaust gas coming out of the heat exchanger (EGR cooler) has been measured directly using a thermometer. The temperature of the exhaust gas has been measured using a K-type thermocouple installed in the exhaust gas line. For analysis of the exhaust gas, Indus make gas analyzer has been used whose specifications are provided in Table 2.

Table 1. Specification of the experimental

Name of the engine	FIAT
No of cylinder	4
No of stroke	4
Total displacement volume	1089 cc
Maximum power	43 hp @5400 rpm
Maximum torque	71 Nm
Bore	68.02 mm.
Stroke	74.93 mm.
Compression ratio	8:1
Cooling Type	Water cooled
Method of loading	Hydraulic Dynamometer

Table 2. Specification of the gas analyser.

Sl.No.	Item	Specifications
1.	Gases Measured	Carbon dioxide, Carbon monoxide Hydrocarbon and Nitric oxide, oxygen
2.	Principle	Non-Dispersive Infrared for CO, CO_2 and electrochemical sensor for O_2 and NO.
3.	Range	CO: 0-15.0%, CO_2: 0-20.00%, O_2: 0-25.00%, NO_x:0-5000 ppm, HC:0-30000 ppm,0-5000ppm
4.	Data Resolution	CO, CO_2 and O_2:0.01%, HC, NO:1ppm
5.	Accuracy	CO: $\pm$ 0.06% Vol, CO_2: $\pm$ 0.5% Vol, HC: $\pm$ 12 ppm Vol, O_2: $\pm$ 0.1%Vol, NO_x : $\pm$ 5 ppm

The exhaust gas analyzer measures the amount of carbon monoxide (CO), carbon dioxide (CO_2), oxides of nitrogen (NO_x) and un-burnt hydrocarbon (HC). The amount of CO and CO_2 are measured as percentage volume, while NO_x and HC are measured in terms of parts per million (ppm). The data has been collected after achieving the steady state condition. For each set of experimental data, three sets of readings were collected, the best or the average of the three readings were considered for the final calculation. The experiments were conducted under three conditions which are as follows:

- Engine operation without recirculation of exhaust gas.
- Engine operation with recirculation of hot EGR (10% and 20%) at a temperature of 820°C.
- Engine operation with recirculation of cold EGR (10% and 20%), the temperature of the gas before recirculation to the intake manifold was reduced to 210°C using a water cooled heat exchanger.

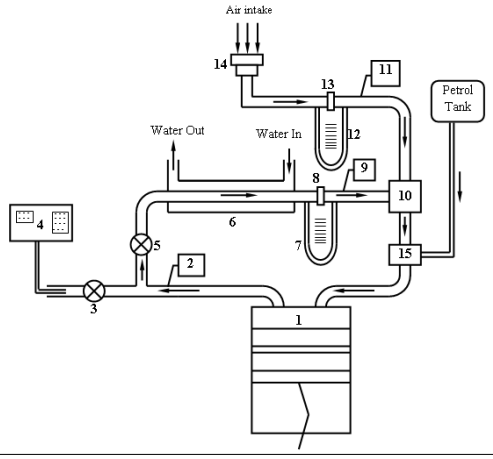

1. Engine; 2. K-type Thermocouple; 3. Gate valve; 4. Exhaust gas analyzer; 5. EGR valve; 6. EGR cooler; 7. U tube manometer; 8. Orifice; 9. Thermometer; 10. Mixing Chamber; 11. Thermometer; 12. U tube manometer; 13. Orifice; 14. Air filter; 15. carburetor

FIGURE1. Schematic layout of the experimental set up.

RESULTS AND DISCUSSIONS

In this section the results obtained from the trial on a four stroke spark ignition engine with different percentages of recirculation of exhaust gas has been discussed in terms of engine performance and emission characteristics.

Figure 2 shows the variation of brake thermal efficiency with brake power for a given engine speed for different percentages of hot and cold EGR. It is found that the performance of the engine in terms of brake thermal efficiency reduces when certain fraction of exhaust gas is re-circulated. This reduction is more prominent with increase in the engine load (brake power). From Fig. 2, it is evident that there is a significant reduction in brake thermal efficiency (about 24%) at a brake power of 4kW when 10% of the hot exhaust gas is directly re-circulated in the intake manifold at a temperature of 820°C. However, under the same conditions of brake power, the reduction in brake thermal efficiency is only about 3.6% (compared to that without recirculation) when the exhaust gas is cooled in a heat exchanger to a temperature of 210°C before recirculation. To study the effect of the proportion of exhaust gas recirculation on the performance of the same engine, the percentage of recirculation of exhaust gas was increased to 20%. It is found that the brake thermal efficiency reduced for both hot and cold EGR when the proportion of gas recirculation was increased to 20%. For the brake power of 4 kW, the brake thermal efficiency with 20% hot EGR is observed to be about 11.5%, while with same proportion of cold EGR, the efficiency value is about 15.9%. The decrease in brake thermal efficiency with EGR (compared to that without recirculation) may be attributed to erratic combustion owing to the dilution of the fuel–air mixture with the exhaust gases. The higher flow rates of EGR reduce the concentration of oxygen in the fresh charge which results in the further reduction in brake thermal efficiency under all conditions of load (brake power). However, with cold EGR the intake charge mixture temperature being lower; the volumetric efficiency is higher than that of hot EGR. So the power developed is more in case of cold EGR which leads to better thermal efficiency compared to that of hot EGR. With cold EGR, the peak engine temperatures during the combustion are also lower and thus the heat rejection to the engine coolant gets reduced. So, more amount of heat is available for power generation which leads to better thermal efficiency compared to that of hot EGR.

Figure 3 shows the variation of brake specific fuel consumption (bsfc) with brake power for a given engine speed for different percentages of hot as well as cold EGR. It is found that the bsfc increases when it is operated with

recirculation of exhaust gas compared to that without recirculation. It is also noted that there is a significant increase in brake specific fuel consumption (about 35%) at a brake power of 4kW, when 10% the hot exhaust gas is directly re-circulated in the intake manifold at a temperature of 820°C(compared to that with 0% EGR). However, under the same conditions of brake power, the increase in brake specific fuel consumption is only about 3.8%, when the exhaust gas is cooled in a heat exchanger to a temperature of 210°C before re-circulation. When the percentage of recirculation of exhaust gas was increased to 20%, the brake specific fuel consumption (bsfc) increased for both hot and cold EGR (compared to that without EGR). At a brake power of 4 kW, the bsfc with 20% hot EGR is about 0.71 kg/kWh, while with 20% cold EGR the same is about 0.52kg/kWh indicating that the performance engine in terms of bsfc is better with cold EGR than that of hot EGR. The increase in bsfc with EGR (compared to that without EGR) is due to the erratic combustion owing to the dilution of the fuel–air mixture with the exhaust gases. However, with cold EGR, the intake charge mixture temperature being lower, the volumetric efficiency is higher than that of hot EGR. So power developed is more in case of cold EGR which leads to a reduction in brake specific fuel consumption.

Figure 4 shows the variation of emission of CO with brake power for a given engine speed for different percentages of hot and cold EGR. It is observed that the emission of CO increases with increase in brake power for all the cases. However, it is found that the emission of CO is higher when the engine is operated with recirculation of exhaust gas. It may be noted that there is a marginal increase in CO emission (about 2.7%) at a brake power of 4kW, when 10% of the hot exhaust gas is directly re-circulated in the intake manifold at a temperature of 820°C. However, under the same conditions of brake power, the increase in CO emission is significantly higher (about 9%), compared to that without EGR when the exhaust gas is cooled before recirculation. When the percentage of recirculation of exhaust gas was increased to 20% the CO emission increased for both hot and cold EGR. It is observed that for a brake power of 4 kW, the CO emission with 20% hot EGR was about 6%, while with same proportion of cold EGR, it was marginally higher about 6.5% by volume compared to that without EGR. The increase in CO emission with EGR is due to the fact that the recirculated exhaust gas replaces some of the oxygen present in the fresh charge which decreases the rate of reactions and promotes incomplete combustion. However, the emission of CO is higher when the exhaust gas is cooled before recirculation for all loads compared to that of hot EGR possibly due to the fact that with cold EGR the peak cylinder temperatures are lower which in turn further reduces the rate of chemical reactions and increases the probability of incomplete combustion.

Figure 5 shows the variation of HC emission with brake power for a given engine speed for different percentages of hot and cold EGR. It is observed that the HC emission increases with increase in brake power and with recirculation of exhaust gas. From Fig. 5, it is evident that there is a marginal increase in HC emission (about 3.5%) at a brake power of 4 kW when 10% the hot exhaust gas is directly re-circulated in the intake manifold. However, under the same conditions of brake power, the increase in HC emission is significantly higher (about 14%), compared to that without EGR when the exhaust gas is cooled in a heat exchanger before re-circulation. When the percentage of recirculation of exhaust gas was increased from 10 to 20%, the HC emission increased for both hot and cold EGR. The increase in the concentration of HC with increase in the rate of EGR is due to the reduction of the availability of oxygen in the inlet charge by the re-circulated exhaust gases in the cylinder. The lack of availability of oxygen in the intake charge is responsible for incomplete combustion and higher emissions of HC. The emission of HC is also associated with the fraction of charge trapped in the crevice volumes in the combustion chamber, quenching near the wall and undergoing partial combustion. In an engine with high levels of EGR, lower temperatures coupled with decreased reactivity results in larger quench distances, leaving more unburned fuel in the region near the wall. The effect of lower in-cylinder temperatures is more prominent with cold EGR due to which the HC emission is higher. Figure 6. shows the variation of oxides of nitrogen emission with brake power for a given engine speed for different percentages of hot and cold EGR. It is observed that the NO_x emission increases with the increase in brake power.

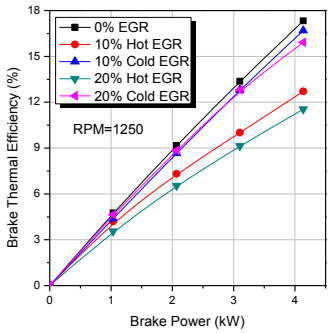

FIGURE 2. Variation of brake thermal efficiency with brake power for different percentage of hot and cold EGR.

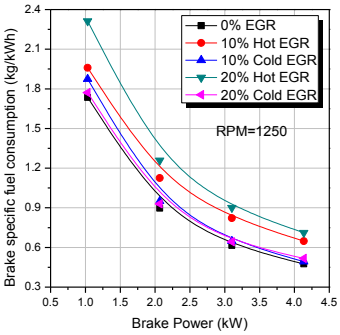

FIGURE 3. Variation of bsfc with brake power for different percentage of hot and cold EGR.

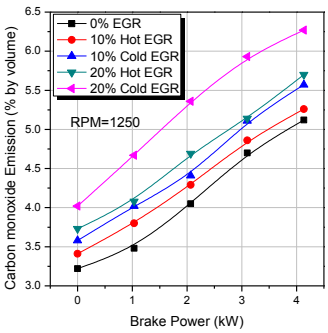

FIGURE 4. Variation of CO with brake power for different percentage of hot and cold EGR.

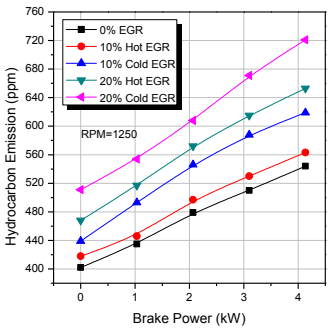

FIGURE 5. Variation of HC with brake power for different percentage of hot and cold EGR.

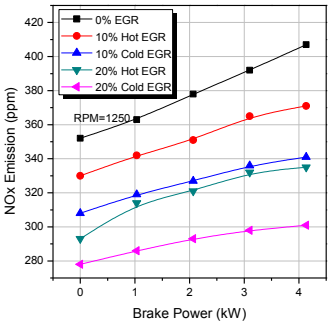

FIGURE 6. Variation of NO_x with brake power for different percentage of hot and cold EGR.

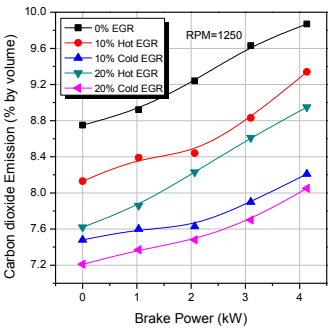

FIGURE 7. Variation of CO_2 with brake power for different percentage of hot and cold EGR.

However, it is found that the emission of NO_x reduces when it is operated with recirculation of exhaust gas. As observed from the figure, the NO_x emission was about 370 ppm at a brake power of 4 kW when 10% of the hot exhaust gas was recirculated in the intake manifold at a temperature of 820°C. However, under the same conditions of brake power, the reduction in NO_x emission was more significant (about 340 ppm), when same proportion of the gas is cooled in a heat exchanger to a temperature of 210°C before re-circulation. It may be noted that when the percentage of recirculation of exhaust gas was increased to 20%, the concentration of NO_x further reduced for both hot and cold EGR compared to that without EGR. The formation of NO_x is highly dependent on the in-cylinder temperature, oxygen concentration and the residence time of the charge for the reactions to take place. Higher the temperature, higher is the tendency for NO_x formation. The NO_x emissions reduce with recirculation of exhaust gas, due to the lowering of the peak combustion temperatures. In case of cold EGR, NO_x emission is expected to be lower than that with hot EGR due to lower gas temperature.

Figure 7 shows the variation of CO_2 emission with brake power for a given engine speed for different percentages of EGR. It is found that the emission of CO_2 increases with the increase in brake power. However, it is found that the emission of CO_2 reduces when it is operated with recirculation of exhaust gas. It is found that there is a reduction in CO_2 emission (about 5.5%), at a brake power of 4kW, when 10% of the exhaust gas is recirculated in the intake manifold at a temperature of 820°C. However, under the same conditions of brake power, the reduction in CO_2 emission is significant, (about 16%) compared to that without EGR when the exhaust gas is cooled in a heat exchanger before recirculation. When the percentage of gas recirculation was increased to 20%, the concentration of CO_2 emission reduced to 8.9%, while with same proportion of cold EGR, the CO_2 emission was about 8% by volume. The CO_2 emission reduced with increase in percentage of EGR, possibly due to the decrease in oxygen

concentration in the gaseous fuel–air mixture. With cold EGR, the rate of oxidation of fuel in the combustion chamber gets further reduced due to lower cylinder temperature, resulting in less emission of CO_2.

CONCLUSION

In this work, an experiment has been conducted on a four stroke, four cylinder SI with and without recirculation of hot and exhaust gas for different loads. Following are the major conclusions that can be drawn from the work:

- The brake thermal efficiency of the engine is found to reduce when the exhaust gas was recirculated back to the intake manifold. However, the brake thermal efficiency is better when the exhaust gas was cooled before recirculation compared to that of the direct recirculation of the hot gas.
- The bsfc is found to increase with increase in percentage of EGR. However, the bsfc is better when the exhaust gas was cooled before recirculation compared to that direct recirculation of the hot exhaust gas.
- The NO_x emission reduced when the exhaust gas was re-circulated back to the intake manifold. However, the NO_x emission is further reduced when the exhaust gas was cooled before recirculation.
- The HC emission increased when the exhaust gas was re-circulated back to the intake manifold compared to that engine operating without EGR. The emission of HC further increased when the exhaust gas was cooled before recirculation compared to that direct recirculation of the hot exhaust gas at a temperature of 820°C.
- The emission of CO concentration is found to be higher when the exhaust gas was re-circulated back to the intake manifold compared to the same engine operating without EGR. However, the emission of CO concentration is further augmented when the exhaust gas was cooled before recirculation.
- The emission of CO_2 concentration decreased when the exhaust gas was recirculated back to the intake manifold compared to that engine operating without EGR. However, the CO_2 concentration further decreased when the exhaust gas was cooled before recirculation compared to that direct recirculation of the hot gas.

REFERENCES

1. Society of Indian Automobile Manufacturers (SIAM), 2014, Industry Statistics, Domestic Sales Trend, Available online at 118.67.250.203//scripts/domestic-sales-trend.aspx. (Accessed on 28th October 2014).
2. M.H. Shojaeefard, M. Tahani, M.M. Etghani, M. Akbari, Cooled EGR for a turbo charged SI engine to reduce knocking and fuel consumption. International Journal of Automotive Engineering. 3 (3) (2013) 474-481.
3. P. Ponnusamy, R. Subramanian, N. Nedunchezhian, An experimental study on the effect of EGR on performance and emission on four stroke SI engine with various catalytic coatings. Elixir Thermal Engineering. 43 (2012) 6586-6589.
4. J. Su, M. Xu, T. Li, Y. Gao, J. Wang, Combined effects of cooled EGR and a higher geometric compression ratio on thermal efficiency improvement of a downsized boosted spark-ignition direct-injection engine. Energy Conversion and Management. 78 (2014) 65–73.
5. T. Li, D. Wu, M. Xu, Thermodynamic analysis of EGR effects on the first and second law efficiencies of a boosted spark-ignited direct-injection gasoline engine. Energy Conversion and Management. 70 (2013) 130–138.
6. J. Cha, J. Kwon, Y. Cho, S. Park, The effect of exhaust gas recirculation (EGR) on combustion stability, engine performance and exhaust emissions in a gasoline engine. KSME International Journal. 15 (2001) 1442 - 1450.
7. G. Fontana, E. Galloni, Experimental analysis of a spark-ignition engine using exhaust gas recycle at WOT operation. Applied Energy. 99 (2012) 534–544.
8. T. Alger, J. Gingrich, C. Roberts, B. Mangold, Cooled exhaust-gas recirculation for fuel economy and emissions improvement in gasoline engines. International Journal of Engine Research. 12 (2011) 254-268.
9. L. Wei, W. Ying, Z. Longbao, S. Ling, Study on improvement of fuel economy and reduction in emissions for stoichiometric gasoline engines. Applied Thermal Engineering. 27 (2007) 2919–2923.

International Conference on Mechanical Engineering 2015
(ICME 2015) 18 – 20 December, 2015, Dhaka, Bangladesh

Paper ID : 070

A Computational Study of Radiation and Gravity Effect on Temperature and Soot Formation in a Methane Air Co-flow Diffusion Flame

Arup Jyoti Bhowal[1, a)] and Bijan Kumar Mandal[2, b)]

[1]*Department of Mechanical Engineering, Heritage Institute of Technology, Chowbaga Road, Anandapur, Kolkata-700 107, West Bengal, India.*
[2]*Department of Mechanical Engineering, Indian Institute of Engineering Science and Technology, Shibpur, Howrah – 711103, West Bengal, India.*

[a)]Corresponding author: arupjyoti.bhowal@heritageit.edu
[b)]bkm375@yahoo.co.in

Abstract. An effort has been made for a quantitative assessment of the soot formed under steady state in a methane air co flow diffusion flame by a numerical simulation at normal gravity and at lower gravity levels of 0.5 G, 0.1 G and 0.0001 G (microgravity). The peak temperature at microgravity is reduced by about 50 K than that at normal gravity level. There is an augmentation of soot formation at lower gravity levels. Peak value at microgravity multiplies by a factor of ~ 7 of that at normal gravity. However, if radiation is not considered, soot formation is found to be much more.

INTRODUCTION

A common problem associated with a diffusion flame is the formation of soot and the flame behaves substantially in a different manner when there is a change in gravity from normal to microgravity level. Microgravity flame offers a better opportunity for a comprehension of the complex phenomena which occur in the reaction zone. In a reduced gravity environment, the shape, size, distributions of emission species and other characteristics of flames change because of lower buoyancy effect. Walsh *et al.* [1] used NASA KC-135 reduced gravity aircraft for experiments with an axisymmetric laminar diffusion flame of methane and air. Their work indicated a possible multiplication in peak soot volume fraction at microgravity, by a factor of 15 of that at normal gravity. Fujita and Ito [2] concluded that the strong thermophoretic force and large residence time caused the soot particles close to the flame zone to move away to a certain narrow area inside the flame and get concentrated there under microgravity. Liu *et al.* [3] studied the effect of radiation on sooting behavior of ethylene-air diffusion flame under normal gravity and microgravity and that the effect was found to be more at microgravity level. Temperature and residence time play a very important role in soot formation. Radiation from gas band and soot decreases flame temperature and thus soot loading also. Keeping this in mind the authors have simulated a methane air diffusion flame under various reduced gravity conditions using an in-house developed code to study the temperature and soot distributions and the effect of radiative heat transfer on those parameters.

NOMENCLATURE

C_j	Concentration of j^{th} species
c_p	Specific heat
g	Acceleration due to gravity
h	Enthalpy

p	Pressure
r	radial distance
λ	Thermal conductivity
μ	Viscosity
v_r	Radial velocity
z	Axial distance
v_z	Axial velocity
ρ	Density
Le_j	Lewis No
$\dot{S}_{c_j}$	Source term
V_t	Thermophoretic velocity
D_{jm}	Mass diffusivity

PHYSICAL AND MATHEMATICAL MODEL

A confined axisymmetric laminar diffusion flame of methane and air has been simulated under normal gravity (1.0 G) and reduced gravity levels of 0.5 G, 0.1 G and 0.0001 G (microgravity). The physical model consists of an annular burner having inner and outer radii of 6.35 mm and 25.2 mm respectively. The details of the burner, computational domain and the grid structure can be seen in the earlier work of the author [5]. The conservation equations of overall mass, radial and axial momentum, energy and species concentration have been taken as the governing equations as follows:

$$\frac{\partial \rho}{\partial t}+\frac{1}{r}\frac{\partial}{\partial r}(r\rho v_r)+\frac{\partial}{\partial z}(\rho v_z)=0 \tag{1}$$

$$\frac{\partial}{\partial t}(\rho v_r)+\frac{1}{r}\frac{\partial}{\partial r}(r\rho {v_r}^2)+\frac{\partial}{\partial z}(\rho v_r v_z) = -\frac{\partial P}{\partial r}+\frac{2}{r}\frac{\partial}{\partial r}\left(r\mu\frac{\partial v_r}{\partial r}\right)-\frac{2}{r}\mu\frac{v_r}{r^2}+\frac{\partial}{\partial z}\left\{\mu\left(\frac{\partial v_z}{\partial r}+\frac{\partial v_r}{\partial z}\right)\right\}-\frac{2}{3}\frac{\partial}{\partial r}\left\{\mu\left(\frac{\partial v_r}{\partial r}+\frac{v_r}{r}+\frac{\partial v_z}{\partial z}\right)\right\} \tag{2}$$

$$\frac{\partial}{\partial t}(\rho v_z)+\frac{1}{r}\frac{\partial}{\partial r}(r\rho v_r v_z)+\frac{\partial}{\partial z}(\rho {v_z}^2) = -\frac{\partial P}{\partial z}+\frac{1}{r}\frac{\partial}{\partial r}\left\{r\mu\left(\frac{\partial v_z}{\partial r}+\frac{\partial v_r}{\partial z}\right)\right\}+2\frac{\partial}{\partial z}\left(\mu\frac{\partial v_z}{\partial z}\right)-\frac{2}{3}\frac{\partial}{\partial z}\left\{\mu\left(\frac{\partial v_r}{\partial r}+\frac{v_r}{r}+\frac{\partial v_z}{\partial z}\right)\right\}+\rho g \tag{3}$$

$$\frac{\partial}{\partial t}(\rho C_j)+\frac{1}{r}\frac{\partial}{\partial r}(r\rho v_r C_j)+\frac{\partial}{\partial z}(\rho v_z C_j)=\frac{1}{r}\frac{\partial}{\partial r}\left(r\rho D_{jm}\frac{\partial C_j}{\partial r}\right)+\frac{\partial}{\partial z}\left(\rho D_{jm}\frac{\partial C_j}{\partial z}\right)+\dot{S_{cj}} \tag{4}$$

$$\frac{\partial}{\partial t}(\rho h)+\frac{1}{r}\frac{\partial}{\partial r}(r\rho v_r h)+\frac{\partial}{\partial z}(\rho v_z h)=\frac{1}{r}\frac{\partial}{\partial r}\left(r\frac{\lambda}{c_p}\frac{\partial h}{\partial r}\right)+\frac{\partial}{\partial z}\left(\frac{\lambda}{c_p}\frac{\partial h}{\partial r}\right)-\frac{1}{r}\frac{\partial}{\partial r}(rq'_{R_r})-\frac{\partial}{\partial z}(q'_{R_z}) +\frac{1}{r}\frac{\partial}{\partial r}\left[r\frac{\lambda}{c_p}\sum_{j=1}^{n}h_j\left({Le_j}^{-1}-1\right)\frac{\partial C_j}{\partial r}\right]+\frac{\partial}{\partial z}\left[\frac{\lambda}{c_p}\sum_{j=1}^{n}h_j\left({Le_j}^{-1}-1\right)\frac{\partial C_j}{\partial z}\right] \tag{5}$$

In the above equations, q'_{R_r} and q'_{R_z} represent the scalar r and z components of the radiative heat flux vector, respectively, and are calculated using an optically thin radiation model following Datta and Saha [6]. The conservation equations for the soot mass concentration and number density can be expressed in general as:

$$\frac{\partial \phi}{\partial t}+\frac{1}{r}\frac{\partial}{\partial r}(rv_r\phi)+\frac{\partial}{\partial z}(\rho v_z\phi)=\frac{1}{r}\frac{\partial}{\partial r}(rV_{t_r}\phi)+\frac{\partial}{\partial z}(V_{t_z}\phi)+\dot{S_\phi} \tag{6}$$

The source term appearing in the above equation for both soot mass concentration and soot number density have been calculated using the semi empirical soot model of Moss et al. [6]. The details however can be obtained from the earlier work of the author [5]. The radiative heat loss terms are dropped for computation without radiation.

BOUNDARY CONDITIONS & NUMERICAL SOLUTION

The conservation equations for the reacting flow have been solved with a numerical algorithm called SOLA. The algorithm is based on primitive variables, defined following a staggered grid arrangement. The temperatures of inlet fuel and air have been taken as 300 K. In conformity with the conditions used by Mitchell et al. [8] and Smooke et al. [9], a fuel velocity of 4.5 cm/s and co-flow velocity of 9.88 cm/s have been taken. Fully developed flow has been considered at the outlet. At the axis, axisymmetric condition, while a no-slip, adiabatic and impervious boundary wall condition have been considered. No soot is entering the computational domain.

RESULTS AND DISCUSSIONS

An experiment on a confined axisymetric and co-flow methane-air diffusion flame has been carried out by numerical simulation under normal and reduced gravity levels. The gravity levels considered are 1.0 G, 0.5 G, 0.1 G and 0.0001 G (which will be referred to as microgravity in all further discussion), when radiation effect is considered. Results have also been obtained without radiation effect considered for gravity levels of 1.0 G and 0.1 G for comparison.

Temperature Distributions at Various Gravity Levels with Radiation Effect Considered

Temperature contours for the aforementioned four gravity levels are presented in figure 1(a) to figure 1(d). It is observed that the very high temperature zone (2000 K or more) is taking a lateral shift away from the axis as the gravity level goes down from normal to microgravity. This is because of lower recirculation due to reduced buoyancy. Also, because of lower buoyancy, residence time increases leading to more soot formation. Higher soot laden zone contributes more towards radiative heat loss from the computational zone. This is manifested in the reduction in length of the high temperature (2000 K or more) zone in the axial direction from a value of approximately 13 cm at normal gravity to about 4 cm in microgravity.

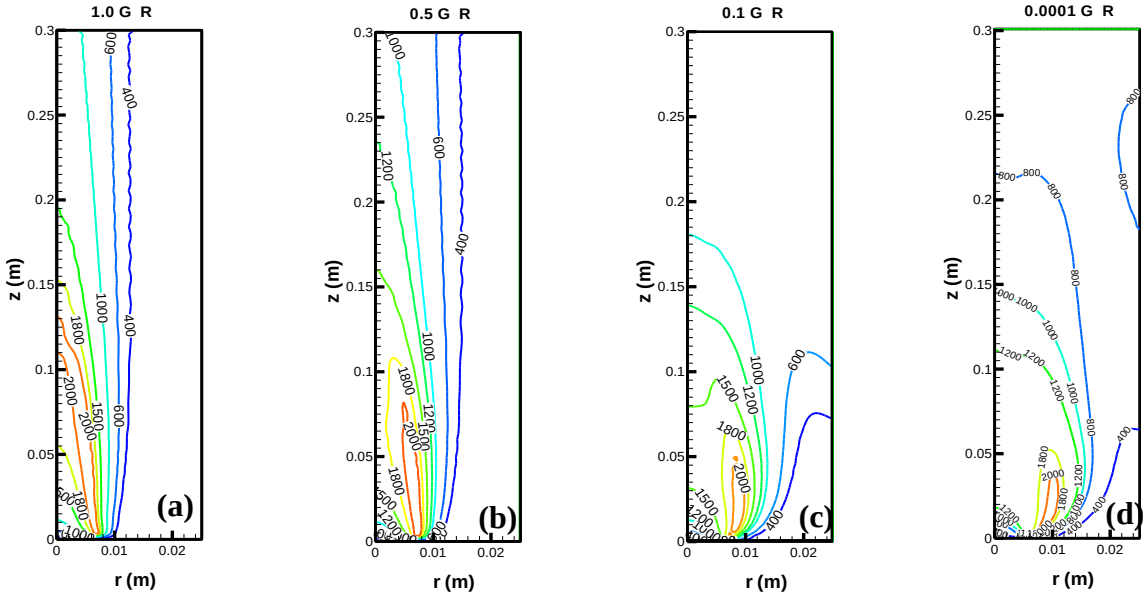

FIGURE 1 Isotherms for gravity levels of (a) 1.0 G, (b) 0.5 G, (c) 0.1 G and (d) 0.0001 G with radiation effect consideration

Soot Volume Fraction Contours for Different Gravity Levels with Radiation Effect Considered

Soot volume fraction contours, as depicted in the figure 2(a) to figure 2(d) for the four gravity levels under consideration, demonstrate the dominant role played by gravity in the distribution of soot. A progressive surge in the values, as the gravity level goes down from normal gravity to microgravity, is clearly visible. Peak value at microgravity multiplies by a factor of ~ 7 of that at normal gravity. This compares well with the experimental work of Ma *et al.* [11] where this factor was found to be 8. Soot is controlled more by diffusion than momentum in microgravity condition. The maximum soot laden zone is seen to take a shift to the wings. From normal to 0.5 G gravity level the soot laden zone grows in size but does not move much along the axis. But at still lower gravity levels of 0.1 G and microgravity, this zone extends along the axis to the exit plane.

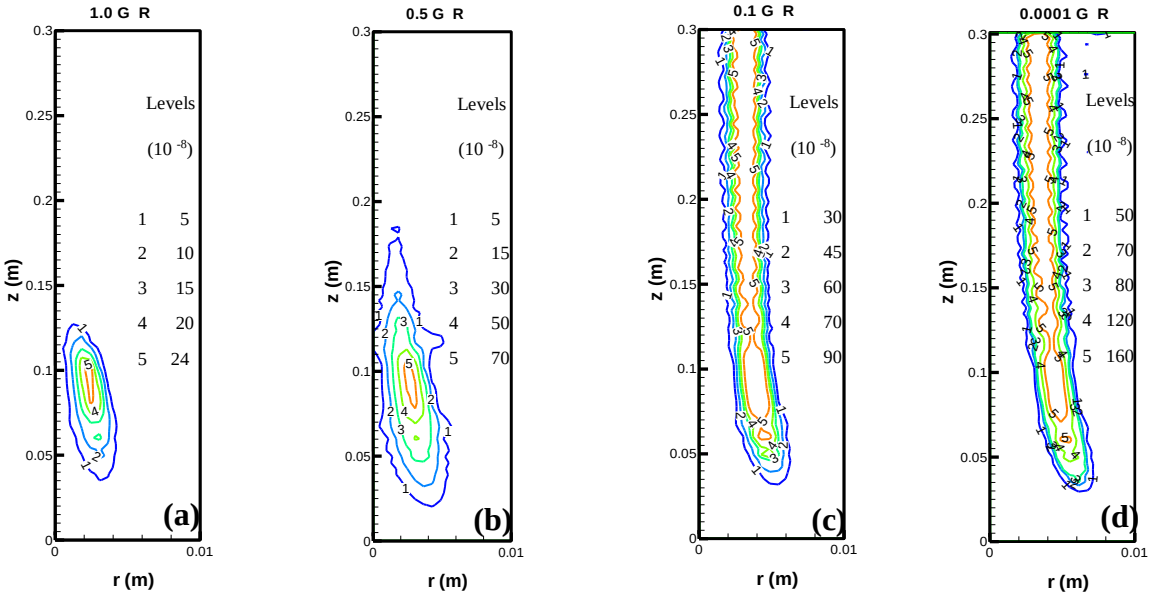

FIGURE 2. Isopleths of soot volume fraction for gravity levels of (a) 1.0 G, (b) 0.5 G, (c) 0.1 G and (d) 0.0001 G with radiation

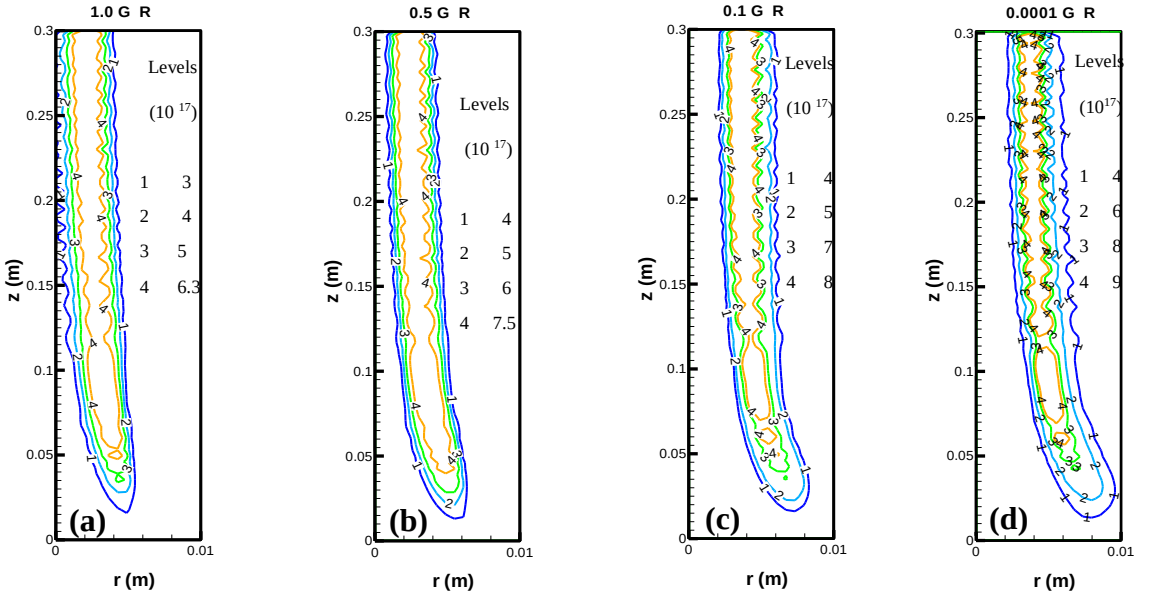

FIGURE 3. Isopleths of soot number density for gravity levels of (a) 1.0 G, (b) 0.5 G, (c) 0.1 G and (d) 0.0001 G

Soot Number Density Contour for Different Gravity Levels with Radiation Effect Considered

Figure 3(a) to figure 3(d) show the contour plots of soot number density at the gravity levels considered for the study. Increase in soot number densities with the decline in the level of gravity is not very appreciable and is indicative of the fact that at microgravity the soot particles increase in size more than they increase in numbers.

Comparison with and without Radiation Effect

Figures 4 and 5 show the temperature and soot volume fraction contours respectively at 1.0 G and 0.1 G gravity levels. Both the figures demonstrate results with and without radiation effect considered, for the purpose of understanding the comparative effect of radiation. Radiation heat loss highly affects the temperature distribution within the computational zone as is observed in figure 4. At 0.1 G gravity level, radiative heat loss has considerably shrunk the high temperature zone, as compared to the situation when radiation effect is in abeyance. Also observed is the reduction in the extent of soot formation with radiation effect present as depicted by lower peak soot volume fraction at any gravity level. At 0.1 G gravity level, peak value of soot volume fraction is ~ 40 times higher when no radiation is considered than when the radiative heat loss is considered. Clearly, soot formation is reduced by a large amount when radiation is considered and the effect is more pronounced at lower gravity levels.

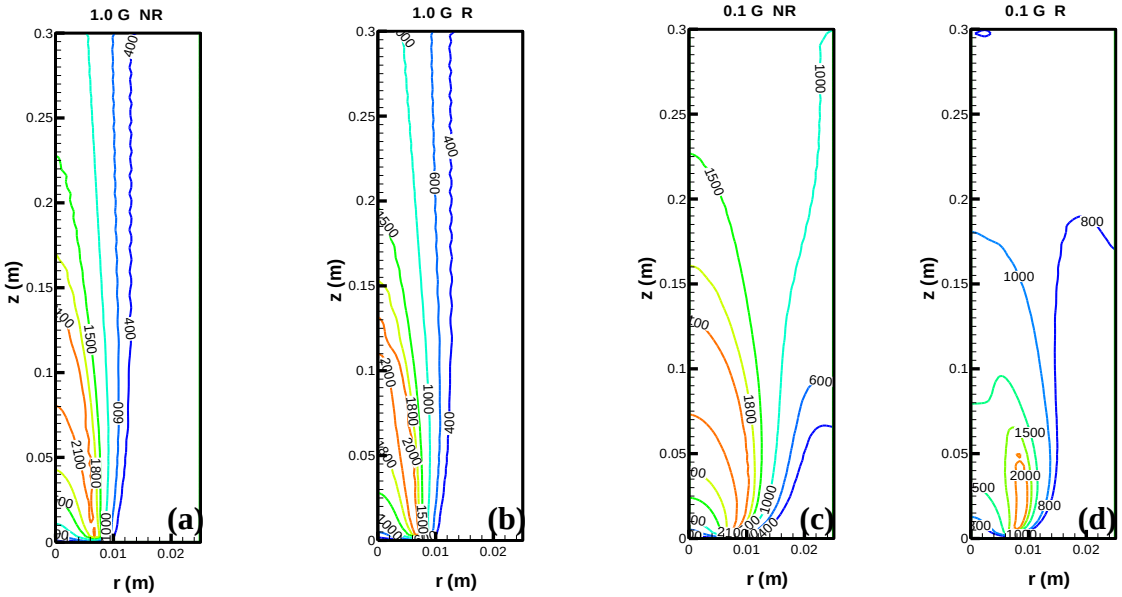

FIGURE 4. Isotherms without radiation at gravity levels of (a) 1.0 G, (c) 0.1 G and with radiation at gravity levels of (b) 1.0 G, (d) 0.1 G

CONCLUSION

Following conclusions can be drawn from this numerical work. Peak temperature at microgravity is found to be lower than that at normal gravity by ~ 50 K. A surge in soot volume fraction is noticed as gravity level is reduced. The peak value of soot volume fraction at microgravity multiplies by a factor of ~ 7 when radiation is considered. Soot number density also increases simultaneously, but not in the same proportion. But, when radiation is not considered, the peak soot volume fraction increases by a large factor of 60 even at 0.1 G gravity level. This suggests that radiation cannot be neglected in soot calculation particularly at microgravity.

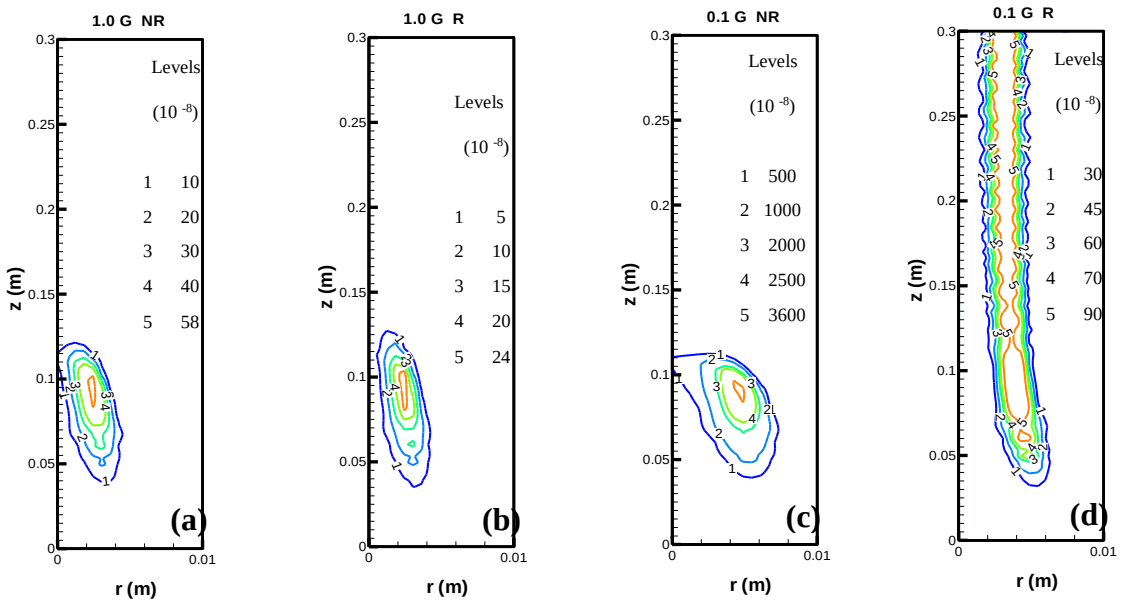

FIGURE 5. Isopleths of soot volume fraction without radiation at gravity levels of (a) 1.0 G, (c) 0.1 G and with radiation at gravity levels of (b) 1.0 G, (d) 0.1 G

REFERENCES

1. K. T. Walsh, J. Fielding, M. D. Smooke and M. B. Long, Experimental and computational study of temperature, species, and soot in buoyant and non-buoyant coflow laminar diffusion flames, Proceedings of the Combustion Institute **28**, 1973–1979 (2000).
2. O. Fujita and K. C. Ito, Experimental Thermal and Fluid Science **26**, 305–311 (2002).
3. F. Liu, G. J. Smallwood and W. Kong, Journal of Quantitative Spectroscopy & Radiative Transfer **112**, 1241 - 1249 (2011).
4. A. J. Bhowal, Soot Formation in Diffusion Flame under Microgravity Conditions, *International Conference on Mechanical Engineering (ICME)*, Dec 18-20, 2011, BUET, Dhaka, Bangladesh.
5. A. Datta and A Saha, Contributions of self-absorption and soot on radiation heat transfer in a laminar methane-air diffusion flame, Proc. IMechE **221**, 955-970 (2006).
6. J. B. Moss, C. D. Stewart and K. J. Young, Combustion and Flame **101**, 491-497 (1995).
7. R. E. Mitchell, A. F. Sarofim and L. A. Clomburg, Combustion and Flame **37**, 227-244 (1980).
8. M. D. Smooke, C. S. McEnally, L. D. Pfefferle, R. J. Hall and M. B. Colket, Combustion and Flame **117**, 117-139 (1999).
9. B. K. Mandal, A. Sarkar and A. Datta, Journal of Engineering for Gas Turbines and Power **131**, 031501-1 031501-9 (2005).
10. B. Ma, S. Cao, D. Giassi, D. P. Stocker, F. Takahashi, B. A. V. Bennett, M. D. Smooke and M. B. Long, An experimental and computational study of soot formation in a coflow jet flame under microgravity and normal gravity, Proc. Combust. Inst. **35**, 839–846 (2015).

ICME2015

International Conference on Mechanical Engineering 2015
(ICME 2015) 18 – 20 December, 2015, Dhaka, Bangladesh

Paper ID : 071

Characterization of a Hemodialyzer in terms of Sherwood Number and Over-all Mass Transfer Co-efficient

Debanjan Das[a)], Rahul Kumar, Somnath Chakrabarti [b)]

Department of Mechanical Engineering, Indian Institute of Engineering Science & Technology, Shibpur, Howrah-711103, India

[a)]Corresponding author: debanjanmech4@gmail.com
[b)]somnathbec@rediffmail.com

Abstract. The present study gives an insight into the performance analysis of a hemodialyzer with the proposed boundary condition of constant concentration of the 'constituent in the blood being removed' in the dialysate fluid flowing outside the dialysis tube. Analytical methods have been used to evaluate the Sherwood number and the overall mass transfer co-efficient for the assumed model considering blood as a Casson's fluid to account for its non Newtonian behavior. The governing differential equations have been solved using series solution assuming steady state one dimensional flow in the axial direction. The expression of Sherwood number for the model have been formulated based on which relevant parameters have been plotted for the characterization of the dialyzer. The diameter of the dialyzer tube required for the optimal functioning of the concerned model has been obtained as 263.5 microns.

INTRODUCTION

The renal replacement therapy, commonly known as Dialysis is a well acknowledged biomedical term involving a procedure that can act as a substitute for many of the normal functions of the kidney. Briefly, it is the artificial process of eliminating waste (diffusion) and unwanted water (ultrafiltration) from the blood across a semipermeable membrane under the conditions when the kidneys are unable to execute their normal physiological functions.The construction of the first working hemodialyzer is attributed to Dr. William Kolff [1] in 1943.

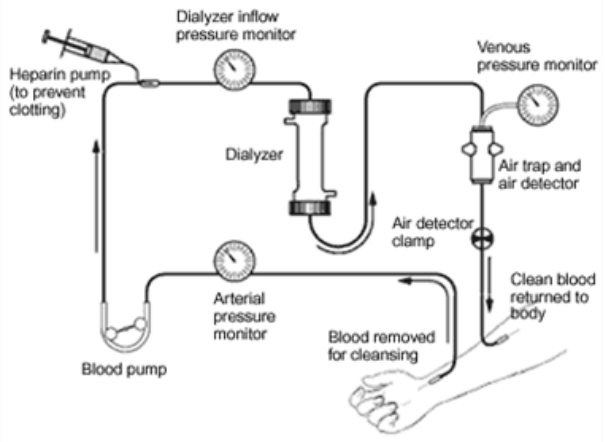

FIGURE 1. Blood circuit in Hemo-dialysis system [2].

Figure 1 shows the various components of a hemodialysis system. It is evident that one of the important aspects of the dialysis system is the ultrafiltration process which takes place in the dialyzer. Ultrafiltration, in principle, uses the phenomenon of convective mass transfer. The mass transfer involves two basic phenomenon, namely, conduction in the radial direction through the filtration membrane following the concentration gradient and advection or transfer by bulk fluid motion in the axial direction. The model considers hollow fibre dialyzer where blood flows inside the core of the dialyzer tube with the dialysate fluid flowing outside the dialyzer tube. The mass transfer takes place in radial direction through the porous walls of the tube.

The concentration of the dialysate fluid in the commonly used dialysis systems keep on varying along the length of the tube due to continuous mass transfer in the system. In other words, the concentration of the component to be removed is least in the dialysate fluid at its point of entrance into the system shown by point 1 in Fig. 2(a) and highest at its point of exit shown by point 3 in Fig. 2(a). At any intermediate point, say point 2, the concentration lies between those of points 1 and 3. The dialysate fluid is filtered after its exit point to prevent it from being exhausted and recirculated in the system. Thus it is ensured that the concentration of the dialysate fluid at a particular point along the tube remain constant with time ideally, although there is a spatial variation in concentration along the tube.

The model considered in the study involves a situation with constant concentration of the dialysate along the tube. It can be realized by the use of a number of localized small filter units (SFU) along the length of the tube instead of a single filter at the exit of the dialysate. As shown in Fig2(b), 2* and 2 are closely located points. The concentration change which take place due to flow of the dialysate fluid and the subsequent mass transfer between the points 1 and 2* has been compensated in the SFU between 2* and 2. Hence the concentration remains same at 1 and 2. Similarly, the SFU between 3* and 3 takes care of the concentration change due to mass transfer between 2 and 3*. Hence the concentration can be maintained same at all the three points, 1, 2, 3.

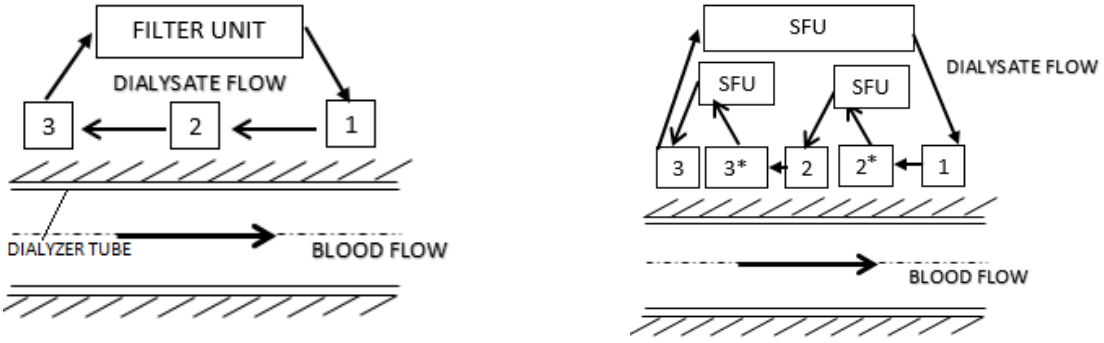

(a) (b)

FIGURE 2. (a) Dialysate flow in commonly used dialysis systems. (b) Method to maintain constant concentration of the dialysate

Thus the change in concentration of the dialysate due to mass transfer from the blood is compensated at several points along the tube by the localized small capacity filters in contrary to the one time filtration by a large capacity filter at the exit. Now, infinite number of such local filters are required to maintain the constant concentration boundary condition ideally.

However, in practice, the condition can be approached closely by installation of quite a few number of such local filters. The accuracy increases with the number of filters used. The foregoing discussion focusses on solving the governing equations applying the constant concentration boundary condition.

METHOD OF SOLUTION

The case in Fig. 3(a) has been considered. Blood is flowing through a dialysis tube with inner radius ri and outer radius ro. The dialysate fluid outside the tube has a constant concentration C_∞ . r and z depict the radial and axial directions for the tube respectively.

The overall mass transfer coefficient based on inner radius is given by

$$\frac{1}{OMTC_i A_i} = \frac{1}{h_{mi} A_i} + \frac{\ln(\frac{r_o}{r_i})}{2\pi DL} + \frac{1}{h_{mo} A_o} \quad (1)$$

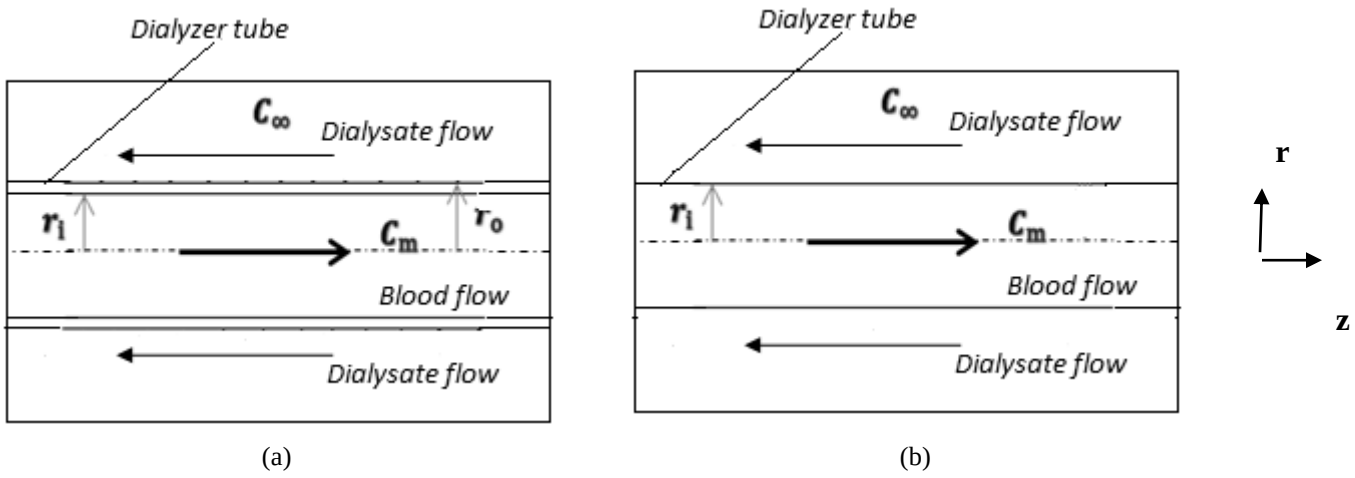

FIGURE 3. (a) Assumed model, (b) An equivalent model.

where $OMTC_i$ is the overall mass transfer co-efficient based on inner surface area, A_i and A_o are the inside and the outside surface areas respectively through which the mass transfer takes place, h_{mi} and h_{mo} are the inside and outside mass transfer co-efficients respectively, L is the length of the tubing, D is the diffusion co-efficient of the membrane and r_i and r_o are the inner and the outer radius of the tubing respectively. The case in Fig 3(b) is equivalent where $OMTC_i$ takes care of the h_{mi}, h_{mo} and D (diffusion co-efficient of membrane) as given by Eqn. 1. These properties are not considered separately and their effects are inherently reflected through the property $OMTC_i$. Now, the case in Fig. 3(b) shows a tube of radius r_i through which the blood is flowing and for which, the constant concentration boundary condition can be applied at $r = r_i$ with $OMTC_i$ as the mass transfer co-efficient without considering h_{mi}, h_{mo} and D separately.

Hence, the boundary conditions are

Boundary Condition 1: At $r=r_i$, $C=C_\infty$

Boundary Condition 2: $\frac{\partial C}{\partial r} = 0$ from symmetry, about the centre line,

where C and r denotes concentration of the constituent being removed and radius of the tube at any point respectively.

It can be reasonably assumed that the mass transfer of a particular constituent which is being removed from blood causes negligible change in the bulk density of blood. Hence, the continuity equation for steady incompressible flow of blood in cylindrical co-ordinates is given by

$$\frac{1}{r}\frac{\partial}{\partial r}(rv_r) + \frac{1}{r}\frac{\partial}{\partial \theta}(v_\theta) + \frac{\partial}{\partial z}(u) = 0 \quad (2)$$

where v_r, v_θ, u in order, denote the velocities in the radial (r), circumferential (θ) and axial direction (z) respectively. Momentum equation in the z direction for steady flow is given by

$$\rho u \frac{\partial u}{\partial z} = -\frac{dp}{dz} + \rho g_z + \frac{1}{r}\frac{\partial}{\partial r}(r\tau) \quad (3)$$

Here, t denotes time, ρ denotes the blood density taken to be 1060 Kg/m^3[3], ρg_z represents body force in the axial direction, τ represents blood shear stress which is related to the strain rate of blood by Casson's equation[4] given below.

$$\tau^{\frac{1}{2}} = a\left(\frac{\partial u}{\partial r}\right)^{\frac{1}{2}} + b^{\frac{1}{2}} \tag{4}$$

where, a is the square root of ultimate Newtonian viscosity with a value of 0.0547 (Pa.s)$^{0.5}$ and b is the yield shear stress of blood taken to be 0.02 Pa.

Assuming fully developed flow and presence of no body force in the axial direction, the convective term on the left hand side and the body force term on the right hand side of Eq (3) have been dropped. Now, Eq (3) and (4) have been solved simultaneously with no slip boundary condition at wall to yield the expression for the velocity profile u(r).

$$u = \frac{1}{a^2}\left[\frac{dp}{dz}\frac{r_i^2}{4}\left\{\left(\frac{r}{r_i}\right)^2 - 1\right\} + b\, r_i\left(\frac{r}{r_i} - 1\right) - r_i^{\frac{3}{2}}\frac{4\sqrt{b}}{3\sqrt{2}}\sqrt{\frac{dp}{dz}}\left\{\left(\frac{r}{r_i}\right)^{\frac{3}{2}} - 1\right\}\right] \tag{5}$$

The mass transfer equation for the assumed steady state one dimensional flow is given by

$$u\frac{\partial C}{\partial z} = D_f\frac{1}{r}\frac{\partial}{\partial r}\left(r\frac{\partial C}{\partial r}\right) \tag{6}$$

Where D_f is the bulk diffusion co-efficient of the constituent to be removed in blood.

Now, due to mass balance, the decrease in concentration of the constituent in the axial direction must equal the amount that have been convected out through the peripheral surface area. Hence, the change in mean concentration Cm in the axial direction can be related to the overall mass transfer co-efficient by the following equation [5].

$$V dC_m = OMTC_t(C_\infty - C_m)P dz \tag{7}$$

which gives

$$\frac{dC_m}{dz} = \frac{OMTC_t(C_\infty - C_m)P}{V} \tag{8}$$

where, V is the volume flow rate of blood, C_m is the mean concentration of blood, P is the perimeter of the tubing.

Now, for fully developed flow, we have [5]

$$\frac{\partial}{\partial z}\left[\frac{C_\infty - C}{C_\infty - C_m}\right] = 0 \tag{9}$$

Which on expansion, and using the fact that C_∞ =constant, gives from equation (8)

$$\frac{\partial C}{\partial z} = \frac{C_\infty - C}{C_\infty - C_m}\frac{dC_m}{dz} = \frac{C_\infty - C}{C_\infty - C_m}\frac{OMTC_t(C_\infty - C_m)P}{V} \tag{10}$$

The expressions for u and $\frac{\partial C}{\partial z}$ are now substituted from Eq (6) and Eq (10) in Eq (7) to have the final differential equation governing mass transfer. This differential equation has been solved analytically using series solution assuming a solution of the form [6,7]

$$\frac{C_\infty - C}{C_\infty - C_m} = \sum_{n=0}^{\infty} X_{2n}\left(\frac{r}{r_i}\right)^{2n} \tag{11}$$

Where, X_{2n} represents series co-efficients. The form of solution is such that it can be shown to satisfy *Boundary condition 2*. By the *Boundary condition 1*, we have

$$\sum_{n=0}^{\infty} X_{2n} = 0 \tag{12}$$

The series co-efficients X_{2n} have been suitably expressed by equating co-efficients of $(r/r_i)^{2n}$ on both sides of the final form of differential equation obtained from Eq(6), after using Eq (10) in it. These series co-efficients, when substituted in Eq (12) yields

$$Sh_D = \frac{OMTC_i d_i}{D_f} = 8 - \frac{f}{32}\frac{\rho u_{avg} d_i}{a^2} \tag{13}$$

Where Sh_D is the Sherwood number based on inner diameter, f is the friction factor and the term $\rho u_{avg} d_i / a^2$ depicts an equivalent Reynold's number (Re).

CHARACTERIZATION AND DISCUSSIONS

The overall mass transfer co-efficient (in have been plotted against d_i, the internal diameter of tubing in Fig. 4(a) based on equation (13). for $D_f = 10^{-11}$ m^2/s[8]which is the diffusion co-efficient of urea with respect to blood for a mass flow rate of 0.0044166 Kg/s and f=0.018.

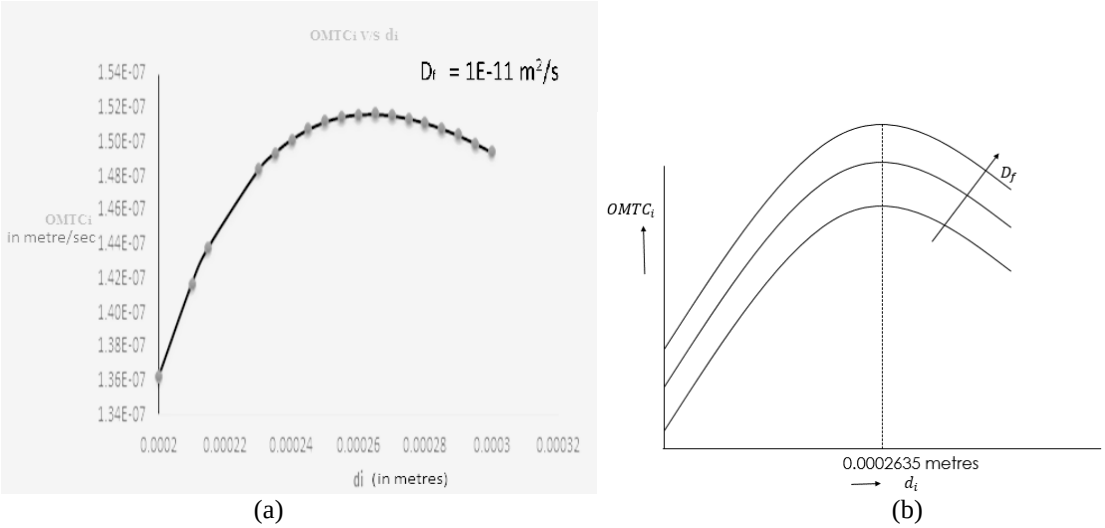

FIGURE 4. Characterization Curves: (a) OMTCi V/s di for Df=1E-11 m^2/s. (b) OMTCi V/s di for various D_f.

Figure 4(b) shows the variation of $OMTC_i$ with di for various values of Df. From these curves, it is evident that over all mass transfer coefficient ($OMTC_i$) initially increases with the increase in the inner tube diameter, reaches an optimum and then decreases. Also, $OMTC_i$ for any particular value of the tube diameter increases with the increase in the value of the diffusion coefficient. The increase in the overall mass transfer co-efficient with the increase in inner diameter is evident from the fact that the tube thickness decreases decreasing the resistance to the radial mass transfer. Hence, the overall mass transfer increases initially. But with the increase of the inner diameter, velocity decreases as per continuity equation which decreases the advection process. At a certain diameter, the decrease in advection dominates the increase in radial conduction and the overall mass transfer start decreasing. Increase in the value of the overall mass transfer co-efficient at a particular diameter with the increase in the diffusion co-efficient is evident since the mass transfer involves both radial diffusion (conduction) through the filter membrane and

advection in the axial direction due to bulk fluid motion with the mass transfer rate, where in case of radial diffusion, it is directly proportional to the diffusion co-efficient by Fick's law of diffusion. Another important observation is that for all the values of the diffusion co-efficients considered, the maximum value of the overall mass transfer co-efficient takes place at the same optimum diameter of 263.5μm. From the study, this diameter may be recommended for the optimal operation of the considered system.

Also, Fig. 5 shows the variation of Sherwood number Sh_D with the equivalent Reynold's number based on Eq (13).

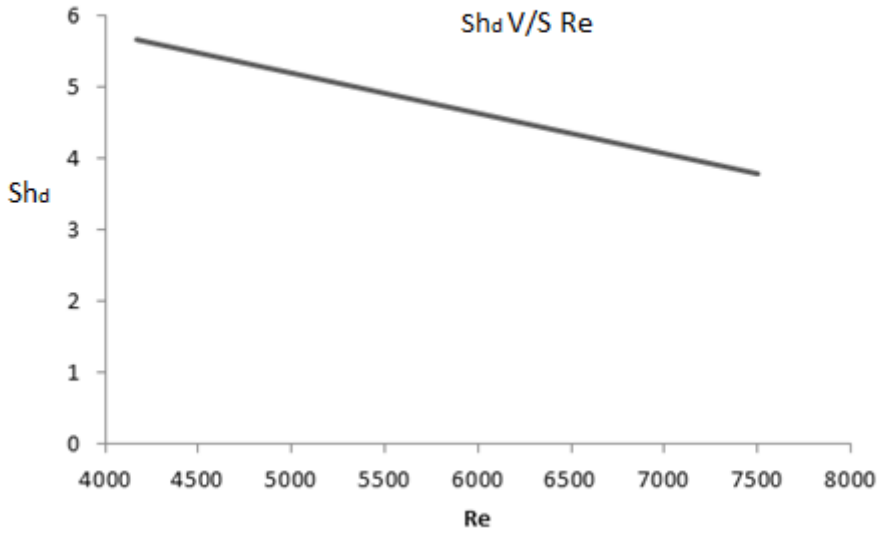

FIGURE 5. Variation of Sh_D with Re.

It is noted from Fig. 5 that the Sherwood number decreases with the increase in equivalent Reynold's number. Thus it yields higher values of Sherwood number at lower values of Reynold's number which is desirable due to laminar flow that actually prevails in tubes having diameter in the order of microns as it is the case with the dialyzer tubing. Reynold's number and Sherwood number, being non dimensional numbers, take into account the various parameters like mass flow rate, inner diameter, diffusion co-efficient etc. and show their trend. For example, since for a given diameter, the mass flow rate is proportional to the Reynold's number, the curve implies a decreasing trend of the Sherwood number, which indicates the decrease in the overall mass transfer co-efficient with increasing mass flow rate. This can be explained as, since the diameter remains constant, increase in mass flow rate increases the velocity and consequently decreases the pressure as by Bernoulli's equation. Since the pressure outside the dialyzer tube on the dialysate side remains constant, the pressure difference across the membrane decreases due to the fall of the inside pressure. Hence mass transfer is expected to decrease with the increase in mass flow rate. Physically it can also have perceived that with increase in mass flow rate more mass of the solute gets accumulated in the tube per unit time which might block the pores affecting the mass transfer. Also, at any particular mass flow rate, the variation of the overall mass transfer co-efficient with the inner diameter is in concordance with what has been obtained in the previous section.

CONCLUSION

In the above discussions, it has been intended to capture certain aspects of the dialyzer model through the characterization. From the overall work, it can be recommended that the optimal diameter of the hemodialyzer may be taken as 263.5μm for the maximum value of overall mass transfer co-efficient. However, in actual conditions, the accurate analysis gets hindered because of factors like difficulties in addressing concentration polarization and

boundary layer effects, effects of variation of humidity and temperature on bio-materials of dialyzers, clotting of blood within the dialyzer due to adhering proteins causing blood pressure rise which may force the dialyzer membrane against the membrane support area exposed to the dialysate. However, the characterization from the work offers the basic guideline about the effect of various relevant parameters on the performance of the considered dialyzer model.

REFERENCES

1. J. F. Maher, *Replacement of Renal Function by Dialysis: A Text Book of Dialysis*., (Springer. 1989), pp. 33.
2. R. Shalak, S. Chien., *Handbook Of Bio-Engineering*, (Tata McGraw-Hill publications, 1987), pp. 39.3.
3. Shmukler, Michael (2004). "Density of Blood" in *The Physics Factbook*. Retrieved 4 October, 2006.
4. E. W. Merrill, *Rheology of Blood, Physiological Reviews*, Department of Chemical engineering, Massachusetts Institute of Technology, Cambridge **49**, 874-875 (1969).
5. F.P. Incropera, D.P. Dewitt, T.L. Bergman, A.S. Lavine, *Fundamentals of Heat and Mass Transfer*, (John Willey & sons, 2007), pp. 494-495, 497-498
6. W. Kays., M. Crawford, *Convective Heat and Mass Transfer*, (Tata McGraw-Hill publications, 1987), pp. 110-117.
7. M.S. Bhatti, *Fully developed temperature distribution in a circular tube with uniform wall temperature*, Unpublished paper, Owens- Corning Fibreglass Corporation, Granville, Ohio, 1985.
8. E. Rambod, M. Beizei, M. Rosenfeld, *an experimental and numerical study of the flow and mass transfer in the model of the wearable artificial kidney dialyzer*, bio-medical engineering online, open access journal, 2010, pp 15.

ICME2015

International Conference on Mechanical Engineering 2015
(ICME 2015) 18 – 20 December, 2015, Dhaka, Bangladesh

Paper ID : 074

Natural Convective Heat and Mass Transfer in a Porous Triangular Enclosure Filled with Nanofluid in Presence of Heat Generation

Raju Chowdhury[1, 2, a)], Salma Parvin[2, b)] and Md. Abdul Hakim Khan[2, c)]

[1]*Department of Natural Science, Stamford University Bangladesh, Dhaka-1217, Bangladesh*
[2]*Department of Mathematics, Bangladesh University of Engineering and Technology, Dhaka-1000, Bangladesh*

[a)]Corresponding author: raju_chy_23@yahoo.com
[b)]salpar@math.buet.ac.bd
[c)]mahakimkhan@gmail.com

Abstract: The problem of natural convective heat and mass transfer in a triangular enclosure filled with nanofluid saturated porous medium in presence of heat generation has been studied in this paper. The bottom wall of the cavity is heated uniformly, the left inclined wall is heated linearly and the right inclined wall is considered to be cold. The concentration is higher at bottom wall, lower at right inclined wall and linearly concentrated at left inclined wall of the cavity. The governing equations are transformed to the dimensionless form and solved numerically using Galerkin weighted residual technique of finite element method. The results are obtained in terms of streamline, isotherms, isoconcentrations, Nusselt number (*Nu*) and Sherwood number (*Sh*) for the parameters thermal Rayleigh number (Ra_T), Heat generation parameter (λ) and Lewis number (*Le*) while Prandtl number (*Pr*), Buoyancy ratio (*N*) and Darcy number (*Da*) are considered to be fixed. It is observed that flow pattern, temperature fields and concentration fields are affected by the variation of above considered parameters.

INTRODUCTION

Natural convective heat and mass transfer in cavities becomes most important issue from industrial and energy perspectives. In the past few decades, experimentally, analytically and numerically extensive researches have been performed on this topic by many researchers [1- 4]. Combined convective heat and mass transfer is referred to the buoyancy driven flows by both temperature and concentration gradients. Combined heat and mass transfer occurs in a wide range of applications in both nature and industry. In nature, such flows are occurred in oceans, lakes, shallow coastal water, and the atmosphere. In industry, these types of flows are the chemical process, crystal growth, solidification, food processing and migration of impurities in non-isothermal material processing applications. Ostrach [5] and Viskanta et al. [6] have reported complete reviews on the subject.

Nanofluids, which are new heat transfer fluids containing a small quantity of nanosized particles suspended in a base fluid, have very high thermal conductivity and many researchers [4, 7] have used this fluid in order to enhance the heat transfer in modern technology. Double-diffusive natural convection in nanofluids is an important fluid dynamics topic that describes the convection driven by two different density gradients with different rates of diffusion [3].

Thermal buoyancy-induced flow and heat transfer inside a porous medium has been investigated enormously in the literature due to its relevance in many natural and industrial applications. Chen and Chen [8] have considered double-diffusive fingering convection in a porous medium. Esfahani and Bordbar [9] have investigated double diffusive natural convection heat transfer enhancement in a square enclosure using nanofluids. Teamah [10] has done numerical simulation on double-diffusive natural convection in an inclined rectangular enclosure with magnetic field and heat source. Bejan [11] has conducted mass and heat transfer by natural convection in a vertical cavity.

Nomenclature		**Greek Letters**	
c	concentration [$mol\ m^{-3}$]	α	thermal diffusivity [ms^{-2}]
C	dimensionless concentration	β_T	volumetric coefficient of thermal expansion [K^{-1}]
Cp	specific heat [$J\ kg^{-1}\ K^{-1}$]	β_s	volumetric coefficient of solutal expansion [$m^3\ kg^{-1}$]
D	mass diffusivity [m^2/s]	λ	dimensionless heat generation parameter
g	gravity acceleration [m/s^2]	μ	dynamic viscosity [$kg\ m^{-1}\ s^{-1}$]
k	thermal conductivity [$W\ m^{-1}K^{-1}$]	θ	dimensionless temperature
l	length of the inclined wall [m]	ν	kinematic viscosity [m^2s^{-1}]
L	height of the triangle [m]	ρ	density [$kg\ m^{-3}$]
N	buoyancy ratio, $\beta_s\nabla c/\beta_T\nabla T$	φ	nanoparticle volume fraction
p	fluid pressure [Pa]	**Subscript**	
P	dimensionless fluid pressure	c	cold
u, v	x, y component of velocity [ms^{-1}]	h	hot
U, V	x, y component of dimensionless velocity	f	fluid
T	Temperature [K]	p	nanoparticle
		nf	nanofluid

Kamotani [12] has examined an experimental work on natural convection in shallow enclosures with horizontal temperature and concentration gradients. Mamou et al. [13] have studied double-diffusive convection in an inclined porous enclosure and used Galerkin finite element formulations.

Heat transfer in a triangular model can be a simple model for many engineering applications. Although many studies have reported natural convection in triangular cavities [14], studies in combined heat and mass transfer in triangular enclosures filled with nanofluid are very limited. The aim of the present study is to investigate the flow pattern, heat and mass transfer in a porous triangular enclosure filled with nanofluid exposed to both temperature and concentration gradients. Double-diffusive conditions is maintained by taking the bottom wall as heated wall and the source for solute concentration, the right inclined wall is cold and lower concentration and the left inclined wall is heated and concentrated linearly.

GOVERNING EQUATIONS

Figure 1 shows the schematic diagram of triangular enclosure subjected to the non-dimensional boundary conditions. The bottom wall of the cavity is heated uniformly at temperature T_h, the temperature of left inclined wall is varying linearly and the right inclined wall is considered to be cold at temperature T_c. The concentration c_h, is higher at bottom wall, lower c_c, at right inclined wall, and the left inclined wall is concentrated linearly. The working fluid consider in the system is a water based Al_2O_3 nanofluid. The properties of water and Al_2O_3 are presented in Table 1. The physical properties of the fluid are assumed to be constant except the density in the buoyancy force term. The non-dimensional governing equations for nanofluids can be written as:

$$\frac{\partial U}{\partial X}+\frac{\partial U}{\partial Y}=0 \tag{1}$$

$$\left(U\frac{\partial U}{\partial X}+V\frac{\partial U}{\partial Y}\right)=-\frac{\partial P}{\partial X}+\frac{\mu_{nf}}{\rho_{nf}\alpha_f}\left(\frac{\partial^2 U}{\partial X^2}+\frac{\partial^2 U}{\partial Y^2}\right)-\frac{\mu_{nf}}{\rho_{nf}\alpha_f}\frac{1}{Da}U \tag{2}$$

$$\left(U\frac{\partial V}{\partial X}+V\frac{\partial V}{\partial Y}\right)=-\frac{\partial P}{\partial Y}+\frac{\mu_{nf}}{\rho_{nf}\alpha_f}\left(\frac{\partial^2 V}{\partial X^2}+\frac{\partial^2 V}{\partial Y^2}\right)-\frac{\mu_{nf}}{\rho_{nf}\alpha_f}\frac{1}{Da}V+Ra_T\,\mathrm{Pr}(\theta+NC) \tag{3}$$

$$\left(U\frac{\partial \theta}{\partial X}+V\frac{\partial \theta}{\partial Y}\right)=\frac{\alpha_{nf}}{\alpha_f}\left(\frac{\partial^2 \theta}{\partial X^2}+\frac{\partial^2 \theta}{\partial Y^2}\right)+\lambda\theta \tag{4}$$

$$\left(U\frac{\partial C}{\partial X}+V\frac{\partial C}{\partial Y}\right)=\frac{1}{Le}\left(\frac{\partial^2 C}{\partial X^2}+\frac{\partial^2 C}{\partial Y^2}\right) \tag{5}$$

where the thermal Rayleigh number $Ra_T = \frac{g\beta_f \rho_f (T_h - T_c)L^3}{\alpha_f \mu_f}$, the solutal Rayleigh number $Ra_s = \frac{g\beta_s \rho_f (c_h - c_c)L^3}{\alpha_f \mu_f}$, Prandtl number $\Pr = \frac{\nu_f}{\alpha_f}$, Darcy number $Da = \frac{K}{L^2}$, heat generation parameter $\lambda = \frac{Q_0 L^2}{(\rho Cp)_{nf} \alpha_f}$, Buoyancy ratio $N = \frac{Ra_s}{Ra_T}$ and Lewis number $Le = \frac{\alpha_f}{D_f}$.

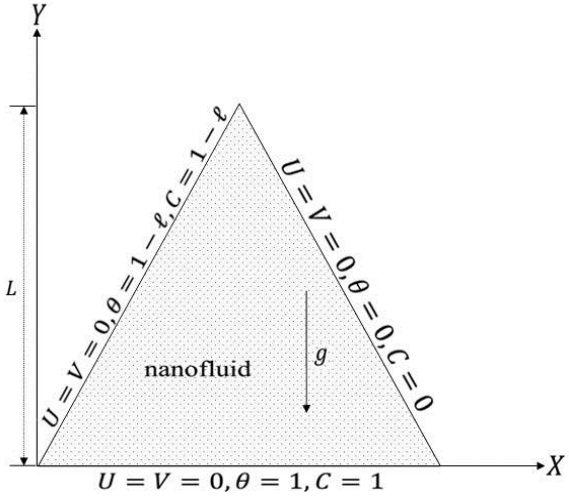

FIGURE 1. Physical model of the problem with corresponding non-dimensional boundary conditions.

The non-dimensional boundary conditions are:
On the right inclined wall: $U = V = 0, \theta = 0, C = 0.$
On the left inclined wall: $U = V = 0, \theta = 1 - \ell, C = 1 - \ell.$
On the bottom wall: $U = V = 0, \theta = 1, C = 1.$

The following dimensionless variables are used to non-dimensionalize the governing equations:

$$X = \frac{x}{L}, Y = \frac{y}{L}, U = \frac{uL}{\alpha_f}, V = \frac{vL}{\alpha_f}, \ell = \frac{l}{L}, P = \frac{pL}{\rho_{nf}\alpha_f^2}, \theta = \frac{T - T_c}{T_h - T_c}, C = \frac{C - C_c}{C_h - C_c} \tag{6}$$

The effective thermal conductivity of the nanofluid is approximated by the Hamilton-Crosser model [13] expressed as

$$k_{nf} = k_f \frac{k_p + 2k_f - 2\varphi(k_f - k_p)}{k_p + 2k_f - \varphi(k_f - k_p)} \tag{7}$$

The viscosity of nanofluid $\mu_{nf} = \frac{\mu_f}{(1-\varphi)^{2.5}}$, volumetric coefficient of thermal expansion $(\rho\beta_T)_{nf} = (1-\varphi)(\rho\beta_T)_f + \varphi(\rho\beta_T)_p$, density $\rho_{nf} = (1-\varphi)\rho_f + \varphi\rho_p$, thermal diffusivity $\alpha_{nf} = \frac{k_{nf}}{(\rho Cp)_{nf}}$ and heat capacitance $(\rho Cp)_{nf} = (1-\varphi)(\rho Cp)_f + \varphi(\rho Cp)_p$.

The local and average Nusselt number along the heated bottom wall can be calculated as

$$Nu_b = -\frac{k_{nf}}{k_f}\left(\frac{\partial\theta}{\partial n}\right), \; Nu = -\left(\frac{k_{nf}}{k_f}\right)\frac{1}{L_s}\int_0^{L_s}\left(\frac{\partial\theta}{\partial n}\right)ds \tag{8}$$

The local and average Sherwood number along the heated bottom wall can be calculated as

$$Sh_b = -\left(\frac{\partial C}{\partial n}\right),\ Sh = -\frac{1}{L_s}\int_0^{L_s}\left(\frac{\partial C}{\partial n}\right)ds \tag{9}$$

NUMERICAL METHOD

The numerical procedure used in this study is based on the Galerkin weighted residual method of finite element method. In this method, the solution domain is discretized into finite element meshes, which are composed of non-uniform triangular elements. Then the nonlinear governing partial differential equations are transferred into a system of integral equations by applying Galerkin weighted residual method. The integration involved in each term of these equations is performed by using Gauss's quadrature method. The nonlinear algebraic equations so obtained are modified by imposition of boundary conditions. These modified nonlinear equations are transferred into linear algebraic equations by using Newton's method. Finally, these linear equations are solved by using Triangular Factorization method.

TABLE 1. Thermophysical properties of water and nanoparticles

Physical Properties	***Cp* (*J/kg K*)**	**ρ (Kg/m^3)**	***k* (*W/mK*)**	**β_T (1/*K*)**
Water	4179	997.1	0.613	21×10^{-5}
Al_2O_3	765	3970	40	0.8×10^{-5}

VALIDATION

A test has been performed to valid the present study by comparing with earlier study Teamah [16]. Figure 2 represents the results in terms of streamlines, isotherms and isoconcentrations obtained by the present code and the results presented by [16]. From the comparison shows in Fig. 2, it can be clearly seen that there is good agreement between the results.

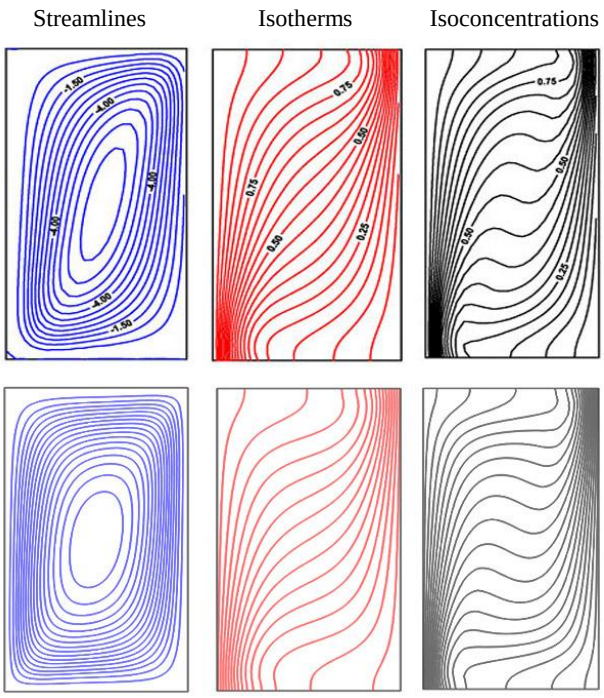

FIGURE 2. A comparison for streamlines (left column), isotherms (middle column) and isoconcentration (right column) between Teamah [16] (top row) and present study (bottom row) for $Ra = 10^5, \Pr = 7.0, \lambda = 0, \varphi = 0, Le = 2, N = -0.8$ and $Ha = 25$.

RESULT AND DISCUSSION

The natural convection inside a porous triangular cavity filled with nanofluid with heat generation effect is influenced by the controlling parameters $10^4 \le Ra_T \le 10^6, 0 \le \lambda \le 10$ and $1 \le Le \le 10$. The results are represented in terms of streamlines, isotherms, isoconcentration, average Nusselt number (*Nu*) and average Sherwood number (*Sh*) for parameters λ and Le varied while $\Pr = 7.0$, $\varphi = 10\%$, $N = 1$ and $Da = 10^{-3}$ are kept fixed.

Figure 3 (a)-(c) represents the streamlines, isotherms and isoconcentrations for different values of heat generation parameter while $Ra_T = 10^5, \Pr = 7.0, \varphi = 10\%, Le = 1, N = 1$ and $Da = 10^{-3}$. At Fig. 3 (a), it can be shown that a triangular shape clockwise flow are formed within the cavity in absence of heat generation, the flow moves upwards near the heated wall and downwards near the cold wall. A secondary vortex is created at the left inclined wall of the cavity with the increase of the value of λ. The size of secondary vortex increases and occupies the space of the cavity for further increasing of heat generation.

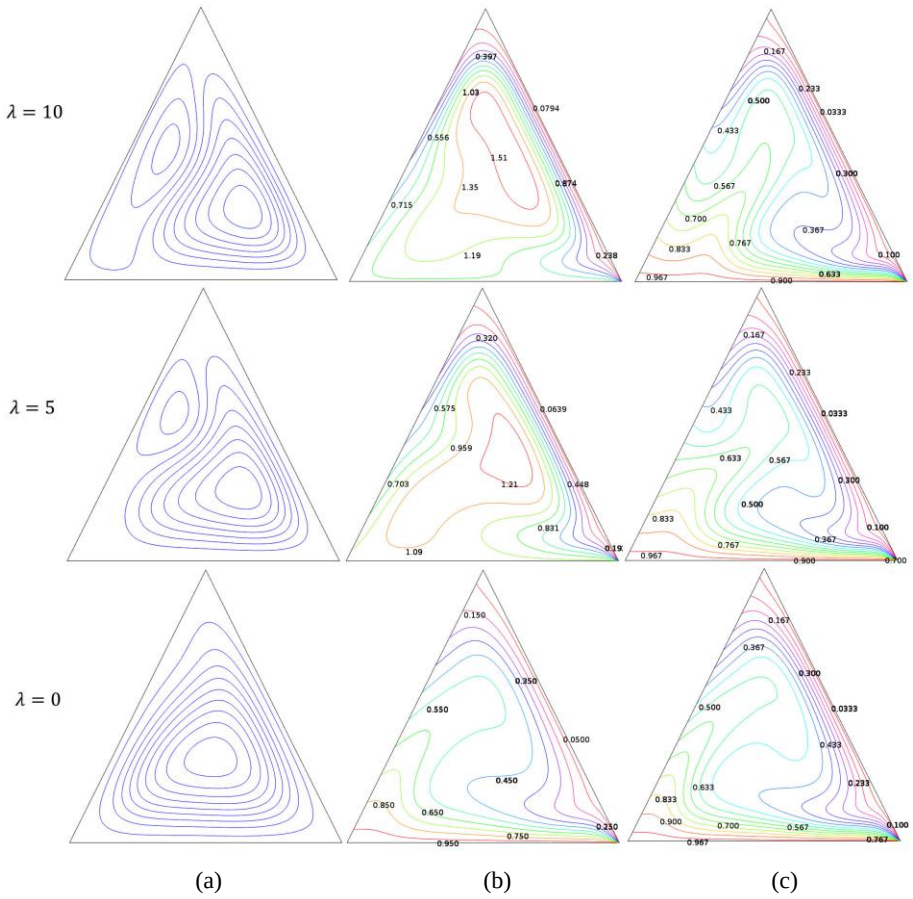

FIGURE 3. (a) Streamlines, (b) Isotherms and (c) Isoconcentrations for different values of heat generation parameter λ with $Ra_T = 10^5, \Pr = 7.0, \varphi = 10\%, Le = 1, N = 1$ and $Da = 10^{-3}$.

As the bottom surface is heated constantly, a heated boundary layer is develops adjacent to the bottom wall that can be shown in Fig. 3 (b). Due to the buoyancy effect, the hot fluid inside the boundary layer moves upward from the bottom left tip. With the increasing of heat generation the temperature gradient in the middle of the cavity also appears to increase. The temperature flows clockwise and moves towards the cold wall and becomes more clustered near the right inclined wall of the cavity for increasing λ Fig. 3 (c) shows the mass transport phenomenon with the increase of heat generation. It can be clearly seen from the figure that the solutal gradient moves from bottom wall to cold for increasing of λ. This is due to the formula that species always transport from the high concentration region to low concentration region.

Figure 4 (a)-(c) represents the flow strength, heat transport and species transport profile for different values of Lewis number varies from 1 to 10 where $Ra_T = 10^5, \Pr = 7.0, \varphi = 10\%, Le = 1, N = 1$ and $Da = 10^{-3}$. As the Lewis number represents the measure of thermal diffusivity to mass diffusivity of a fluid so the larger value of Lewis number represents relatively low mass diffusivity value. The strength of streamline is decreased with the increase of Lewis number that can be shown in Fig. 4 (a). Comparing the Fig. 4 (b) and (c), it can be noticed that for increasing the Lewis number, the thickness of the solutal boundary layer near the heated bottom wall become thinner than thermal boundary layer. This means that the thermal resistance is higher than the solutal resistance and therefore the mass transfer rate is higher than the heat transfer rate.

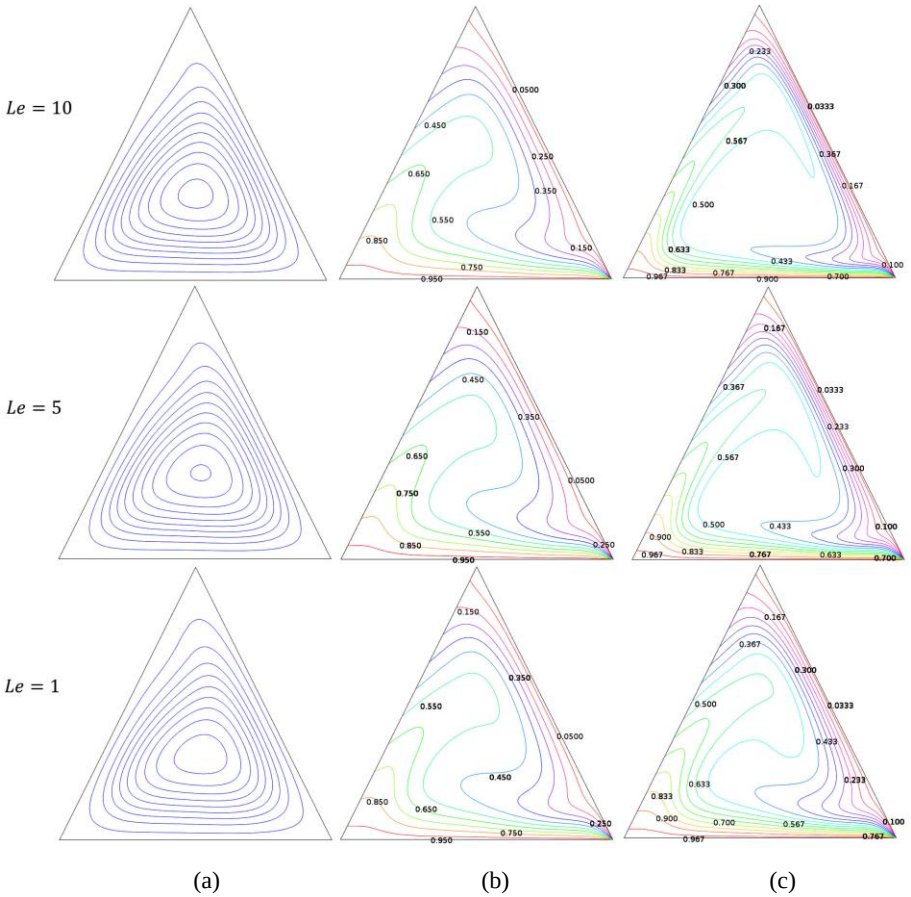

FIGURE 4. (a) Streamlines, (b) Isotherms and (c) Isoconcentrations for different values of *Le* with $Ra_T = 10^5, \Pr = 7.0, \varphi = 10\%, \lambda = 0, N = 1$ and $Da = 10^{-3}$.

Figure 5-6 describes the investigation of the effect of heat generation parameter and Lewis number on the heat and mass transfer rate on the bottom wall which is heated uniformly for different values of Rayleigh number. In the Fig. 5(a) the graph demonstrate that the Nusselt number on the heated bottom wall reduce considerably with the increase of λ for $Ra_T = 10^5$ and $Ra_T = 10^6$. This happens because, the heat generation mechanism develops a boundary layer of hot fluid near the heated wall as a result the increasing rate of internal heat generation negates the heat transfer from the heated surface. However, for lower values of Rayleigh number such as $Ra_T = 10^4$, *Nu* increase remarkably. The Fig. 5(b) shows that the Sherwood number on the heated bottom wall reduce slightly with the increase of λ for $Ra_T = 10^4$ and $Ra_T = 10^5$ but for $Ra_T = 10^6$, *Sh* increase slightly. Graphs from the Fig. 6(a)-(b) demonstrate that the Nusselt number on the heated bottom wall reduce slightly while the Sherwood number rise up remarkably with the increase of Lewis number. From the Fig. 5-6, it can be inferred that both *Nu* and *Sh* are increased considerably when the thermal Rayleigh number is varied from 10^4 to 10^6.

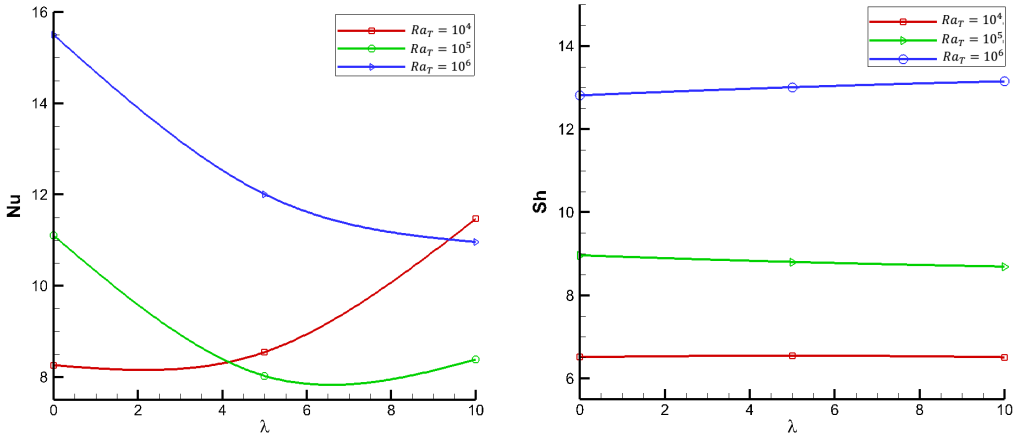

(a) (b)

FIGURE 5. The variation of (a) average Nusselt number (*Nu*) and (b) average Sherwood number (*Sh*) at the heated bottom wall for different heat generation parameter λ and Ra_T with $\Pr = 7.0, \varphi = 10\%, Le = 1, N = 1$ and $Da = 10^{-3}$.

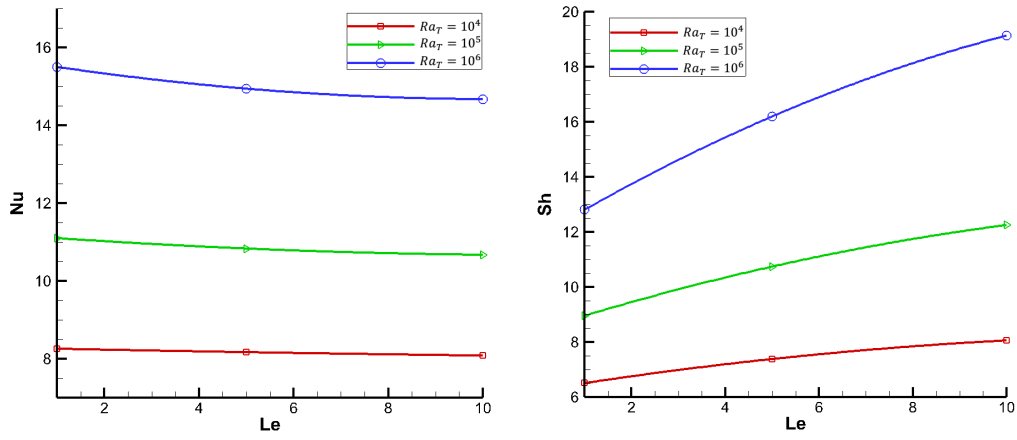

(a) (b)

FIGURE 6. The variation of (a) average Nusselt number (*Nu*) and (b) average Sherwood number (*Sh*) at the heated bottom wall for different *Le* and Ra_T with $\Pr = 7.0, \varphi = 10\%, \lambda = 0, N = 1$ and $Da = 10^{-3}$.

CONCLUSION

In this study, a numerical simulation has been conducted to investigate the effect of heat generation, thermal Rayleigh number and Lewis number on flow pattern, temperature and concentration profile in a triangular cavity filled porous media saturated nanofluid. The outcomes of the existing analysis are as follows:

- The heat generation remarkably affects the fluid flow pattern, heat and mass transfer in the cavity.
- The flow strength is increased for raising the value of heat generation parameter but decrease for increasing values of Lewis number.
- The average Nusselt number and Sherwood number increases for increasing the thermal Rayleigh number.
- The rate of heat transfer reduces remarkably with the increasing of heat generation.
- The heat transfer rate slightly decrease while the mass transfer rate increase significantly for increasing Lewis number and highest mass transfer occurs for $Ra_T = 10^6$.

ACKNOWLEDGEMENTS

This work is supported by the Department of Mathematics, Bangladesh University of Engineering and Technology and Department of Natural Science, Stamford University Bangladesh.

REFERENCES

1. C. Pang, J.W. Lee, Y.T. Kang, Int. J. Therm. Sci. **87**, pp. 49-67 (2015).
2. O.V. Trevisan, A. Bejan, J. Heat Transfer **109**, 104-112 (1987).
3. A. Mojtabi, M.C. Charrier-Mojtabi, "Double-diffusive convection in porous media" In *Handbook of Porous Media* edited by K. Vafai(ed) (New York, Dekker, 2000).
4. K. Khanafer, K. Vafai, M. Lightstone, Int. J. Heat Mass Trans. **46**, pp. 3639-3653 (2003).
5. S. Ohtrach, Physico Chem. Hydrodynamics **1**, 233-247 (1980).
6. R. Viskanta, T.L. Bergman, F.P. Incropera, "Double-diffusive natural convection" in: S. Kakac, W. Aung, R. Viskanta (Eds.), (Natural Convection: Fundamentals and Applications, Hemisphere, Washington, DC, 1985), 1075-1099.
7. G.A. Sheikhzadeh, M. Dastmalchi, H. Khoarasanizadeh, Heat Mass Transfer **49**, 1689-1700 (2013).
8. F. Chen, C. Chen, J. Heat Tran. **36**, 793-897 (1993).
9. J.A. Esfahani, V. Bordbar, J. Nanotec. Eng. Medicine **2**, 021002-1-9 (2011).
10. M.A. Teamah, A.F. Elasfty, E.Z. Massoud, Int. J. Therm. Sci. **52**, 161-175 (2012).
11. A. Bejan, Int. J. Heat Fluid Flow **6**, 149-159 (1985).
12. Y. Kamotani, L.W. Wang, S. Ostrach, H.D. Jiang, Int. J Heat Mass Tran. **28**, 165-173 (1985).
13. M. Mamou, P. Vasseur, E. Bilgen, Int. J. Heat Mass Tran. **41**, 1513-1529 (1998).
14. R. Chowdhury, S. Parvin, M.A.H. Khan, Int. J. Energy Tech. **7**, pp 49-61 (2015).
15. R.L. Hamilton, O.K. Crosser, I & EC Fundamentals **1**,187-191 (1962).
16. M.A. Teamah, Int. J. Therm. Sci. **47**, 237-248 (2008).

ICME2015

International Conference on Mechanical Engineering 2015
(ICME 2015) 18 – 20 December, 2015, Dhaka, Bangladesh

Paper ID :077

Effect of Compression Ratio on the Performance, Combustion and Emission from a Diesel Engine Using Palm Biodiesel

Ambarish Datta[1, a)] and Bijan Kumar Mandal[1, b)]

[1]*Department of Mechanical Engineering, Indian Institute of Engineering Science and Technology, Shibpur, Howrah – 711103, West Bengal, India.*

[b)]Corresponding author: bkm375@yahoo.co.in
[a)]ambarish.datta84@gmail.com

Abstract. The authors have simulated a single cylinder diesel engine using Diesel-RK software to investigate the performance, emission and combustion characteristics of the engine using palm biodiesel and petro-diesel. The simulation has been carried out for three compression ratios of 16, 17 and 18 at constant speed of 1500 rpm. The analysis of simulation results show that brake thermal efficiency decreases and brake specific fuel consumption increases with the use of palm biodiesel instead of diesel. The thermal efficiency increases and the brake specific fuel consumption decreases with the increase of compression ratio. The higher compression ratio results in higher in-cylinder pressure and higher heat release rate as well as lower ignition delay. The NOx and CO2 emissions increase at higher compression ratio due to the higher pressure and temperature. On the other hand, the specific PM emission and smoke opacity are less at higher compression ratio.

INTRODUCTION

Conventional fuels such as petrol and diesel are the primary sources of energy in almost all the automobiles running in the present world. These energy sources are non renewable in nature and the prolonged use of these sources will ensure the extinction of these energy reservoirs and this will lead to a global energy crisis. Again there is the problem of global warming as the uses of these fossil fuels are constantly intensifying the process by contributing green houses gases to the environment. All these have given rise to a crisis situation the only solution of which is the identification and use of an alternate source of energy. In this process of finding of an alternate source of energy biodiesel has attracted the mind of many as they are quite similar to diesel in the physical and chemical prospects. Another reason for biofuels attracting the minds of so many researchers is that it burns cleaner than fossil fuels [1] and thus found to be less harmful to human health and environment.

Many researchers have carried out works to find the compatibility of biodiesels and their blends with an unmodified CI engine. Duraisamy et al. [2] investigated and found that performance of a CI engine increased appreciably by increasing the compression ratio for TPSO (Thevetia Peruviana Seed Oil) blends. Also, it was observed that increase in compression ratio significantly reduced the CO, HC, NOx and smoke emissions. However, a slight increase in CO2 was observed with higher compression ratio. Kassaby and Nemitallah [3] observed that the change of compression ratio from 14 to 18 resulted in 18.39%, 27.48%, 18.5% and 19.82% increase in brake thermal efficiency in case of B10, B20, B30 and B50 respectively. On an average, the CO2 emission increased by 14.28%, the HC emission reduced by 52%, CO emission reduced by 37.5% and NOx emission increased by 36.84% when compression ratio was increased from 14 to 18. The ignition delay period seemed to be lower for biodiesel than that of diesel. The delay period decreased by 13.95% when, compression ratio increased from 14 to 18. Rao et al. [4] experimentally found that there was an increase in brake thermal efficiency, peak cylinder pressure, NOx and CO2 emissions with increase in the compression ratio from 17 to 18; whereas the brake specific fuel consumption,

exhaust gas temperature, CO, HC and smoke emissions decreased for the same. Kumar et al. [5] found that the brake thermal efficiency of a CI engine increased with increase in compression ratio. In case of emissions, it was seen that NOx emission increased and smoke emission decreased with increase in compression ratio.

However, numerical approach to the above investigations will consume less time and money when compared to that of experimental investigations. As such an attempt has been made in this paper to numerically investigate the effect of compression ratio on the performance, combustion and emission characteristics of an unmodified CI engine running with palm stearin methyl ester (PSME). Three different compression ratios have been used in this study, viz. 16, 17 and 18 on a Kirloskar made single cylinder, four stroke, water cooled variable compression ratio TV1 engine running and the various engine characteristics have been simulated, at a constant speed of 1500 rpm, using commercially available software, Diesel-RK.

NOMENCLATURE

$\dot{m}_j$	mass flow rate of j^{th} species
m	total mass within the control cylinder
Y_i^j	stoichiometric coefficients on the product side
Y_i^{cyl}	stoichiometric coefficients on the reactant side
Ω_i	dimensionless integral of order unity dependent on the force interaction during a collision of i^{th} species
θ_d	ignition delay
CRs	compression ratios
bTDC	before top dead center

SIMULATION MODEL

The basic model used in this software is based on the solution of mass, momentum, energy and species conservation equations. The basic governing equations of mass, species and energy used for the simulation using the software are presented in eq. (1) to (3) respectively.

$$\frac{dm}{dt} = \sum_j \dot{m}_j \tag{1}$$

$$\dot{Y}_j = \sum_j \left(\frac{\dot{m}_j}{m} \right) \left(Y_i^j - Y_i^{cyl} \right) + \frac{\Omega_i W_{mw}}{\rho} \tag{2}$$

$$\underbrace{\frac{d(mu)}{dt}}_{\text{Internal Energy}} = \underbrace{-p\frac{dv}{dt}}_{\text{Displacement Work}} + \underbrace{\frac{dQ_{ht}}{dt}}_{\text{Heat Transfer}} + \underbrace{\sum_j \dot{m}_j h_j}_{\text{Enthalpy Flux}} \tag{3}$$

Further details of can be obtained from the previous work of Fiveland and Assanis [6]. During flame propagation, burned and unburned zones are assumed to be separated by an infinitely thin flame front, with no heat exchange between the two zones. The parameters, which have been calculated to find the performance of the engine using the Diesel-RK software are brake power, brake mean effective pressure, brake torque, specific fuel consumption, volumetric efficiency. These parameters are calculated for different fuels and at different compression ratios. CO2 emission is calculated from basic combustion equations. NO is the predominant oxides of nitrogen formed in diesel engine [7] and hence only NO formation is considered in simulation model following Zeldovich mechanism as described by Kuleshov [8]. The model also includes the soot formation model which calculates Hartridge smoke level, Bosch smoke number and factor of absolute light absorption. Particulate matter emission is calculated as a function of Bosch smoke number following Alkidas [9].

ENGINE DETAILS AND PROPERTIES OF FUELS

The performance test is carried out on a single cylinder variable compression ratio DI diesel engine using mineral diesel. The engine is assembled and coupled with an eddy current dynamometer. The compression ratio is varied from 16-18. The load range is taken up to 12 kg. The experiment is conducted at a rated speed of 1500 rpm and fuel injection timing of 23°bTDC. The specifications of the engine are given in table 1. The thermo-physical properties of diesel and palm stearin biodiesel have been shown in table 2.

Table 1. Engine Specifications

Manufacture	Kirloskar
Ignition type	CI (4-stroke)
No of cylinder	1
Type	TV1
Type of cooling	Water cooled
RPM	1500
BHP	3.5 kW
Bore diameter	87.5 mm.
Stroke length	110 mm.
Connecting rod length	234 mm.

TABLE 2. Properties of Palm Biodiesel and Diesel

Property	Palm Biodiesel	Diesel
Mass Fractions (%)		
Carbon	0.77	0.87
Hydrogen	0.115	0.126
Oxygen	0.115	0.004
Low Heating Value (MJ/kg)	36.22	42.5
Cetane Number	60	48
Density at 323K (kg/m^3)	865	830
Dynamic Viscosity coefficient (Pa.s)	0.0055	0.003
Molecular Mass	279	190

RESULTS AND DISCUSSIONS

Experiments have been carried out on the test engine using only mineral diesel at a compression ratio of 17.5:1. The performance and combustion results as recorded by the computer attached to the engine have been compared with the predicted results from the software and a good agreement has been noticed. In order to study the effect of the compression ratio on the performance, combustion and emission characteristics of a diesel engine, numerical simulations of these engine characteristics have been carried out for the test engine running with palm stearin methyl ester at three different compression ratios of 16, 17 and 18. The results obtained have been presented in this section and a comparison with that of pure diesel at a compression ratio of 18 has been made.

Brake thermal efficiency (BTE)

Figure 1 depicts the variation of brake thermal efficiency with brake power for the three different compression ratios of 16, 17 and 18. It can be seen that the brake thermal efficiency increases with an increase in the compression ratio. Due to the reduced ignition delay, the efficiency increases with the increased compression ratio, which can also be seen in figure 3. At higher compression ratio the biodiesel gives much better results than mineral diesel. The efficiency of the engine increases because of low volatility of biodiesel, which results a better combustion at high temperature. The increase in efficiency is also due to the reduction in heat loss and increase of brake power with applied load. Initially the efficiency of biodiesel increases compared to diesel because the biodiesel provides a good lubricity. Also the excess oxygen content of biodiesel leads to a better combustion, which increases the efficiency. Whereas, reduction in compression ratio reduces the efficiency due to lower compression temperature and pressure, slow combustion process and more dilution by residual gases [4].

Brake specific fuel consumption (BSFC)

Figure 2 shows the variation of BSFC with brake power for the three different compression ratios. The difference in the BSFC for biodiesel, as seen in the figure is very minute. However, on closer observation it can be seen that the BSFC decreases with the increase in compression ratio. The possible reason for this trend could be that with an increase in CRs, the maximum cylinder pressure increases due to the fuel injected in hotter combustion chamber and this leads to higher effective power. Therefore, fuel consumption per output power will decrease [10]. The BSFC is lower in case of diesel fuel due to its higher calorific value compare to biodiesel.

Ignition delay

Figure 3 shows the effect of compression ratio on the ignition delay period. It is seen that the delay period decreases with the increase in the compression ratio for biodiesel. The possible reason for this trend could be that the increased compression ratio actually increases the air temperature inside the cylinder helping for early combustion and consequently reducing the ignition delay [3]. However, the ignition delay is much higher in case of mineral diesel due to its lower cetane number in comparison to biodiesel.

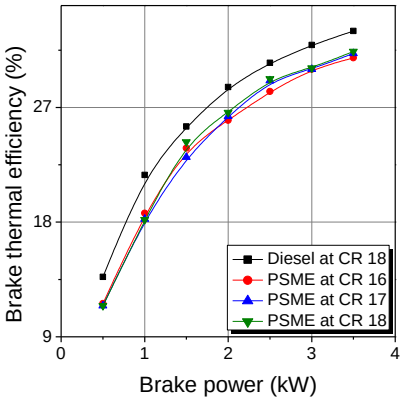

FIGURE 1. Variation of BTE with brake power for different CRs

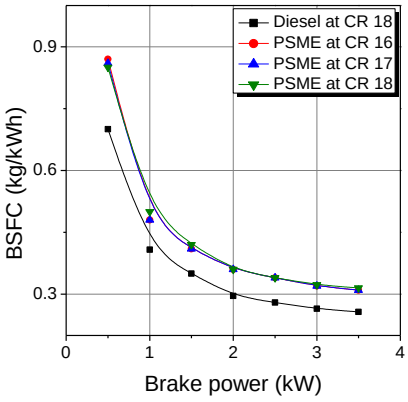

FIGURE 2. Variation of BSFC with brake power for different CRs

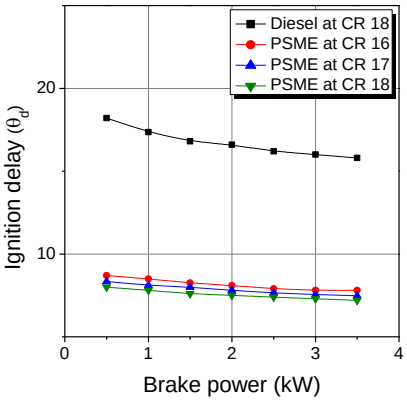

FIGURE 3. Variation of injection delay period with brake power for different CRs

Peak In-cylinder pressure

In a compression ignition engine, increase in compression ratio increases the peak cylinder pressure because the at higher compression ratio the density of fuel air mixture is increased and there is better mixing of the burnt and unburnt charge owing to the higher compression pressure. Whereas, at low compression ratios, cylinder pressure decreases due to slow combustion because of low compression pressure, weak swirl and improper mixing of burnt and unburnt charges [4]. The same trend can be depicted from figure 4 which shows the variation of peak cylinder pressure with brake power for the three different compression ratios. Thus, highest pressure is seen for CR 18 with biodiesel as fuel.

Net heat release rate

Generally, with the increase in the compression ratio in a compression ignition engine, a higher heat release rate is observed due to the fast combustion of the fuel-air mixture which gets injected at a higher compression ratio. On the other hand, lower compression ratio is again attributed by longer ignition delay period during which more fuel is injected, resulting in more time for premixing of air-fuel mixture and this in turn tends to increase the heat release rate [4]. As such, in figure 5 which depicts the effect of compression ratio on the heat release rate, it can be seen that there is a very minute or almost no difference in the heat release rates for all the three compression ratios for biodiesel. In case of diesel, the heat release starts afterwards due to its higher ignition delay, but the peak heat release rate is much higher due to the combustion of accumulated fuel within the combustion chamber.

NO_x emission

Figure 6 depicts the variation of NOx emission with brake power for the three different compression ratios for biodiesel. It can be observed that the trend followed by NOx emission is the same as that of the peak cylinder pressure. As mentioned earlier, NOx formation is a function of cylinder pressure and temperature. Higher in-cylinder temperature and pressure lead to the formation of more valance oxygen and nitrogen atoms from dissociation of air, which eventually produces more NOx emission at tailpipe. Thus, higher cylinder pressure and temperature owing to higher compression ratios results in higher NOx emission. As a result, highest NOx is given

by compression ratio of 18 and the lowest emission is given by compression ratio of 16 for biodiesel. It can be noted that NOx emission for diesel fuel is much lower even at the compression ratio of 18.

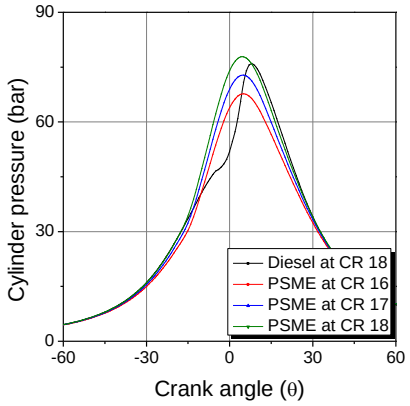

FIGURE 4. Variation of cylinder pressure with crank angle for different CRs

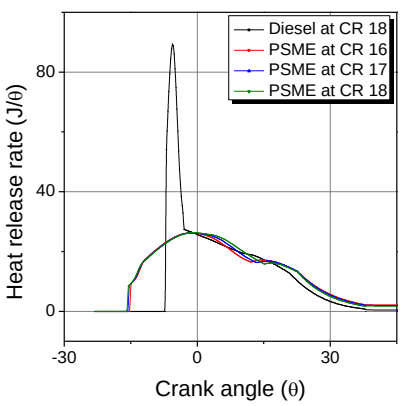

FIGURE 5. Variation of heat release rate with crank angle for different CRs

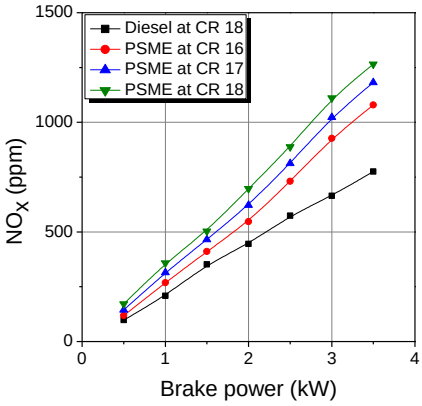

FIGURE 6. Variation of NO_x emission with brake power for different CRs

CO_2 emission

The trend followed by CO_2 emission, as shown in figure 7, is the same as that of peak cylinder pressure and NO_x emission. Higher cylinder pressure and temperature will result in higher CO_2 emission due to formation of higher valance oxygen atoms which oxidizes the carbon monoxide to CO_2. Thus, higher compression ratios, giving rise to higher peak pressure and temperature inside the cylinder will tend to increase the CO_2 emission. Subsequently, figure 7 shows the highest CO_2 emission at the compression ratio of 18 and the lowest by compression ratio of 16 for biodiesel and it is always more than that with mineral diesel due to more complete combustion.

Particulate matter (PM) and smoke emissions

As stated earlier, the primary reason of the PM emission from CI engine is improper combustion and combustion of heavy lubricating oil. Smoke formation occurs primarily in the fuel-rich zone of the cylinder, at high temperatures and pressures [11]. Thus, higher compression ratio decreases the smoke and PM formations. This is due to better oxidation environment and existence of higher temperature and pressure at higher compression ratio [2] for biodiesel. The variation of smoke and specific PM emissions with brake power for the different compression ratio has been shown in figure 8 and figure 9 respectively and the improvement over diesel fuel is also observed.

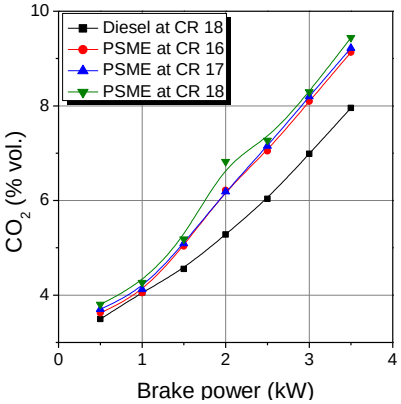

FIGURE 7. Variation of CO_2 emission with brake power for different CRs

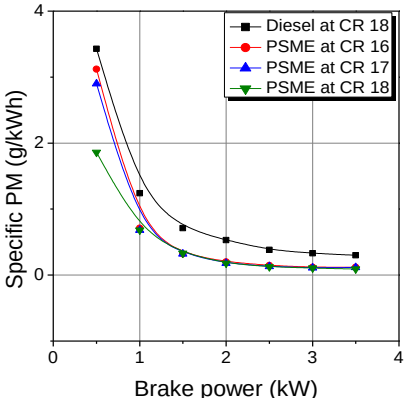

FIGURE 8. Variation of Specific PM emission with brake power for different CRs

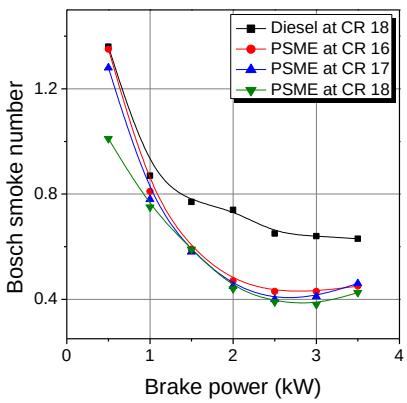

FIGURE 9. Variation of smoke emission with brake power for different CRs

CONCLUSION

It can be concluded that the performance of the engine deteriorates when diesel is replaced by biodiesel (PSME) as fuel. The performance of the biodiesel fueled engine is improved and emission characteristics become poorer with the increase of compression ratio. The ignition delay period is reduced when biodiesel is used, but it increases slightly when compression ratio is reduced. The peak pressure rise inside the cylinder during combustion is higher for biodiesel at high compression ratio. However, in case of net heat release rate no such deviation is observed with respect to compression ratio for biodiesel. On an average, NOx emission increases by 50% with the use of biodiesel over diesel at the same compression ratio. At the same time, CO2 emission increases by 18%, when compared between the extreme values of diesel with that of biodiesel. A significant reduction is observed in case of specific PM and smoke in the exhaust when biodiesel is used and the corresponding values are found to be 70% and 32.53% respectively.

REFERENCES

1. National Policy on Biofuels, A Report by Government of India, Ministry of New & Renewable Energy, http://mnre.gov.in/file manager/UserFiles/DIREC_2010_Report.pdf.
2. M. K. Duraisamy, T. Balusamy and T. Senthilkumar, ARPN Journal of Engineering and Applied Sciences **7(2)**, 229-234 (2012).
3. Md. El-Kassaby, and M. A. Nemit-allah, Alexandria Engineering Journal **52**, 1–11 (2013).
4. N. D. Rao, B. S. Premkumar and S. Jaganath, International Journal of Mechanical Engineering and Technology **4(4)**, 357-365 (2013).
5. N. R. Kumar, Y. M. C. Sekhar, and S. Adinarayana, International Journal of Applied Science and Engineering **11(1)**, 41-49 (2013).
6. S. B. Fiveland and D. N. Assanis, SAE Paper No. 2000-01-0332 (2000).
7. J. B. Heywood, Internal Combustion Engine Fundamentals, *Copyright by McGraw-Hill Co.*, 1988.
8. A. S. Kuleshov, SAE Technical Paper 2006-01-1385, 2006.
9. A. C. Alkidas, SAE Technical Paper 840412, 1984.
10. Md. N. Nabi, Md. M. Rahman, and Md. S. Akhter, Applied Thermal Engineering **29**, 2265–2270 (2009).
11. Y. Ulusoy, Y. Tekin, M. Cetinkaya, and F. Karaosmanoglu, Energy Sources **26**, 927-932(2004).

ICME2015

International Conference on Mechanical Engineering 2015
(ICME 2015) 18 – 20 December, 2015, Dhaka, Bangladesh

Paper ID : 078

Numerical Investigation on the Effects of EGR on CI Engine Characteristics Using Soyabean Biodiesel

Ambarish Datta[1, a)] and Bijan Kumar Mandal[2, b)]

[1, 2]*Department of Mechanical Engineering, Indian Institute of Engineering Science and Technology, Shibpur, Howrah – 711103, West Bengal, India.*

[b)]Corresponding author: bkm375@yahoo.co.in
[a)]ambarish.datta84@gmail.com

Abstract. In this work an attempt has been made to numerically investigate the effect of soyabean biodiesels on an unmodified CI engine and then to study and reduce the NOx emission by the introduction of exhaust gas recirculation (EGR) technique at the rates of 10% and 20% . Compared to no EGR condition for the neat biodiesel, the NOx emission is reduced by 44% and 70% with 10% and 20% EGR respectively. But the increase in the EGR rate deteriorates the engine performance and increases the emissions, other than NOx. Thus, EGR helps in reducing NOx emission but its rate of introduction has to be bounded by a limit.

INTRODUCTION

The main driving source of present day transportation system is the conventional fossil fuels, which are classified as non-renewable sources of energy. With the recent rise in the demand of these fossil fuels due to increasing number of vehicles, the extinction of these fuels in the near future is quite evident. In addition to this, other harmful effects of these fuels include global warming, which has become a serious agenda for the present world. The human health is also very susceptible to the emissions from the vehicles which are run by traditional fossil fuels. All these lead to the search for an alternate and clean source of energy that can reduce our dependency on the conventional energy sources and also at the same time reduces pollutant formation during combustion. Among all the viable replacements tried in the past few decades, biodiesels have found a suitable spot due to their similarity in the physical and chemical properties with that of conventional diesel fuel. Moreover, in a country like India it is observed that biodiesel can be a viable alternative automotive fuel and India has huge potential for biodiesel production from non-edible type oil seeds, like karanja and ratanjyot [1-3].

Many works have been carried out by various researchers to investigate the compatibility of biodiesels and their blends with conventional diesel in an unmodified CI engine. Investigations have shown that biodiesels may be promising fuels for CI engines in the near future. However, the use of biodiesels deteriorates the engine performance, but gives a cleaner exhaust, except for NO_x emission which tends to increase. A suitable way to reduce this drawback of biodiesels is the introduction of exhaust gas recirculation (EGR) technique. Exhaust gas recirculation (EGR) is a nitrogen oxide (NO_x) emissions reduction technique used in petrol and diesel engines. EGR works by recirculating a portion of an engine's exhaust gas back to the engine cylinders [4]. In a diesel engine, the exhaust gas replaces some of the excess oxygen in the pre-combustion mixture [5]. Because NO_x forms primarily when a mixture of nitrogen and oxygen is subjected to high temperature, the lower combustion chamber temperatures caused by EGR reduces the amount of NO_x the combustion generates (though at some loss of engine efficiency) [4]. Machacon *et al.* [6] studied the effect of EGR with O_2 enrichment on the exhaust emissions of diesel engine. They concluded that higher EGR with O_2 enrichment gives lower NO_x emissions and smoke. Ghazikhani *et al.* [7] found an increase in CO and HC emissions with the use of the effect of EGR in a HCCI engine. Hribernik and Samec [8] experimentally found that for his heavy duty turbocharged diesel engine, NO_x emission decreased substantially at 7.6% EGR and at 21.5% EGR and it was as high as 65%. The O2 percentage decreased and HC

emissions increased slightly; whereas the CO and particulate emissions tripled with 21.5% EGR. In case of the combustion parameters, it was seen that the peak cylinder pressure decreased with the increase in the EGR rates. It was further observed that 14.2% EGR was optimum as it reduced NOx emission by 50% with a satisfactory increase in CO and particulate emissions.

Literature is rich with experimental work on EGR and numerical works are very few. Again when compared between the two, numerical work consumes much less time and cost than the experimental ones. As such the primary motive of this work will be to numerically investigate the effect of biodiesels on an unmodified CI engine and then to study and reduce the NOx emission by the introduction of EGR. The test engine used in this work is a 4-stroke, water cooled, single cylinder TV1 engine which is fueled with pure diesel and pure soyabean biodiesel at standard condition (no EGR) initially and then 10% and 20% EGR rates, while running with pure biodiesel. The performance, combustion and emission characteristics of the engine have been simulated using commercially available software, Diesel-RK.

NOMENCLATURE

$\dot{m}_j$	mass flow rate of j^{th} species
m	total mass within the control cylinder
Y_i^j	stoichiometric coefficients on the product side
Y_i^{cyl}	stoichiometric coefficients on the reactant side
Ω_i	dimensionless integral of order unity dependent on the force interaction during a collision of i^{th} species
P	cylinder pressure
T_z	temperature in a burnt gas zone
R	gas constant
ω	angular crank velocity
$[NO]_e$	equilibrium concentrations of oxide of nitrogen
$[N_2]_e$	equilibrium concentrations of molecular nitrogen
$[O]_e$	equilibrium concentrations of atomic oxygen
$[O_2]_e$	equilibrium concentrations of molecular oxygen
V	current volume of cylinder
q_c	cycle fuel mass
dx/dt	heat release rate

SIMULATION MODEL

The simulation is carried using commercial software Diesel-RK which is based on the numerical solution of different conservation equations. Following Fiveland and Assanis [9], the conservation equations for overall mass, different species and energy are presented in Eq. (1), Eq. (2) and Eq. (3) respectively.

$$\frac{dm}{dt} = \sum_j \dot{m}_j \tag{1}$$

$$\dot{Y}_j = \sum_j \left(\frac{\dot{m}_j}{m}\right)\left(Y_i^j - Y_i^{cyl}\right) + \frac{\Omega_i W_{mw}}{\rho} \tag{2}$$

$$\underbrace{\frac{d(mu)}{dt}}_{\text{Internal Energy}} = \underbrace{-p\frac{dv}{dt}}_{\text{Displacement Work}} + \underbrace{\frac{dQ_{ht}}{dt}}_{\text{Heat Transfer}} + \underbrace{\sum_j \dot{m}_j h_j}_{\text{Enthalpy Flux}} \tag{3}$$

Out of all the oxides of nitrogen, NO is predominant in diesel engine [10]. Therefore; only NO formation is considered. NO can also be formed through different mechanisms, but the model used here has taken care of NO

formation through only thermal or Zeldovich mechanism. Similar NO formation model has been used by Kuleshov [11] for simulation of direct injection diesel engine. The oxidizing of nitrogen is on the chain mechanism and basic reactions are as follows:

$$\begin{aligned} O_2 &\leftrightarrow 2O \\ N_2 + O &\leftrightarrow NO + N \\ N + O_2 &\leftrightarrow NO + O \end{aligned} \tag{4}$$

Rate of this reaction depends on concentration of atomic oxygen. The concentration of NO in combustion products can be obtained by using the following equation [12]:

$$\frac{d[NO]}{d\theta} = \frac{p.2.333*10^7.e^{-\frac{38020}{T_Z}}[N_2]_e.[O]_e.\left\{1-([NO]/[NO]_e)^2\right\}}{R.T_Z.\left(1+\frac{2365}{T_z}.e^{\frac{3365}{T_z}}.\frac{[NO]}{[O_2]_e}\right)}.\frac{1}{\omega} \tag{5}$$

Soot formation rate in a burning zone and Hartridge smoke level are calculated as:

$$\left(\frac{d[C]}{dt}\right)_K = 0.004\frac{q_c}{V}\frac{dx}{dt} \tag{6}$$

$$\text{Hartridge} = 100[1 - 0.9545\exp(-2.4226[C])] \tag{7}$$

Similar equations are used to calculate Bosch smoke number and Factor of Absolute Light Absorption (*K).* Particulate matter emission is calculated by using an equation from the work of Alkidas [13] as:

$$[PM] = 565\left(\ln\frac{10}{10-\text{Bosch}}\right)^{1.206} \tag{8}$$

ENGINE DETAILS AND PROPERTIES OF FUELS

The experiment is carried out on a Kirloskar made, single cylinder, constant speed, variable compression ratio TV1 engine with pure diesel without EGR to generate data for the validation of the numerically simulated results. The specifications of the test engine are given in table 1. The thermo-physical properties of diesel and soyabean biodiesel used for this work have also been shown in table 2.

TABLE 1. Engine Specifications

Manufacture	Kirloskar
Ignition type	CI (4-stroke)
No of cylinder	1
Type	TV1
Type of cooling	Water cooled
RPM	1500
BHP	3.5 kW
Bore diameter	87.5 mm.
Stroke length	110 mm.
Connecting rod length	234 mm.

TABLE 2. Properties of Soyabean Biodiesel and Diesel

Property	Soybean Biodiesel	Diesel
Mass Fractions (%)		
Carbon	0.77	0.87
Hydrogen	0.115	0.126
Oxygen	0.115	0.004
Low Heating Value (MJ/kg)	36.22	42.5
Cetane Number	60	48
Density at 323K (kg/m^3)	865	830
Dynamic Viscosity coefficient (Pa.s)	0.0055	0.003
Molecular Mass	279	190

RESULTS AND DISCUSSIONS

The Diesel-RK software is first run with neat mineral diesel without any EGR and the predicted values are compared with those of experimental results for the same operating conditions. The comparison has shown a good agreement. Expecting that the validation will hold good for the EGR conditions also, numerical simulation of various performance, combustion and emission parameters of the test engine fuelled with soyabean oil methyl ester at three different exhaust gas recirculation (EGR) rates, viz. 0% EGR or pure soyabean biodiesel with no EGR, 10% EGR and 20% EGR, has been carried out. The results of which, along with their comparison with pure diesel as baseline fuel, have been presented in this section.

Brake thermal efficiency (BTE)

Figure 1 shows the variation of brake thermal efficiency with brake power for the three different EGR rates. It is seen that increase in the EGR rate decreases the brake thermal efficiency. This may be due to the oxygen deficiency caused by using EGR, which leads to incomplete combustion [14]. Thus, the highest brake thermal efficiency of 31.5% is shown by the 0% EGR condition and the lowest efficiency of 29.8% is shown by 20% EGR condition. The efficiency of the engine with diesel fuel is found to be more than any conditions of biodiesel considered here.

Brake specific fuel consumption (BSFC)

As mentioned above, usage of EGR reduces the engine power due to incomplete combustion owing to the oxygen deficiency in the intake. Thus, in order to produce the same power output as that of 0% EGR condition, more fuel is required which eventually increases the brake specific fuel consumption (BSFC). Thus, highest BSFC is that of 20% EGR condition and the lowest is that of without any EGR, but the change is small throughout the load range as observed in figure 2. However, it can also be observed that the BSFC obtained for pure diesel without EGR is less than with biodiesel fuel without EGR. This can be explained from the fact that the lower heating value of diesel (42.5 MJ/kg) is approximately 16.5 % higher than that of soyabean biodiesel.

NO_x emission

The formation of NO_x is dependent on the peak cylinder pressure and temperature. When EGR system is used, it dilutes the fresh charge at the intake and lowers the flame temperature [15], resulting in a decrease in cylinder pressure and temperature. This eventually contributes in a significant reduction in NO_x emission as can be seen in figure 3; highest NO_x is formed at 0% EGR condition. Whereas, 10% EGR rate reduces NO_x emission by almost 40% and 20% EGR reduces NO_x by more than 65%. It can be further noted that NO_x emission with biodiesel is much higher than that with the mineral diesel at no EGR conditions and even 10% EGR lowers down the NO_x emission below the level obtained using diesel without EGR.

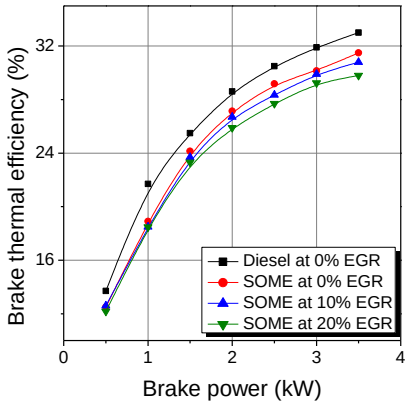

FIGURE 1. Variation of BTE with brake power for different EGR rates

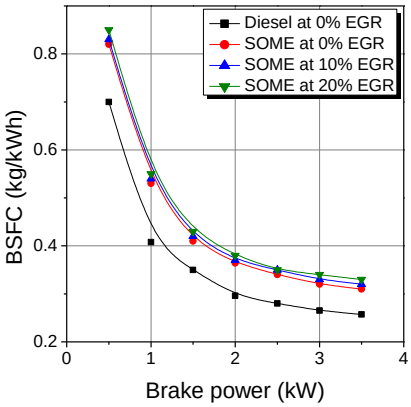

FIGURE 2. Variation of BSFC with brake power for different EGR rates

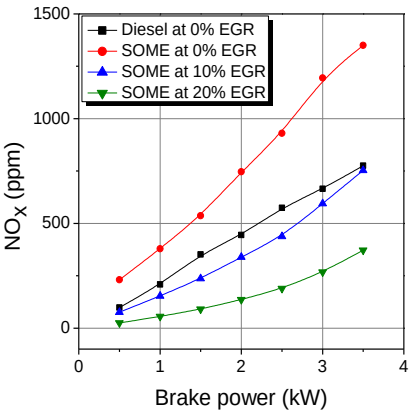

FIGURE 3. Variation of NO_x emission with brake power for different EGR rates

CO_2 emission

Figure 4 shows the variation of CO_2 emission with brake power for the three different EGR rates. It can be seen that the increase in EGR rates gives rise to a slight increase in the CO_2 emission. Though usage of EGR system leads to poor combustion that will in return suppress the oxidization of carbon monoxide to CO_2, the increase in CO_2 emission may be due to the presence of CO_2 already present in the exhaust gas re-circulated and the oxidization of carbon monoxide present in the fraction of the exhaust gas due to the relative higher intake temperature.

Particulate matter and smoke emission

The variations of smoke and specific PM emissions with brake power for the different EGR rates with diesel and biodiesel (SOME) have been shown in figure 5 and figure 6 respectively. As particulate emission (PM) from CI engine are primarily due to improper combustion and combustion of heavy lubricating oil and smoke formation occurs primarily in the fuel-rich zone of the cylinder, at high temperatures and pressures [16]. Introduction of EGR system will tend to increase PM and smoke emissions with biodiesel (SOME) as it leads to poorer combustion. Exhaust gas re-circulation reduces the overall air-fuel ratio which enhances the increase in particulates. Also, the re-circulated exhaust gas contains particulates which further contribute in raising PM and smoke level [14]. Thus, the lowest PM and smoke emission is shown by 0% EGR condition and the highest is shown by 20% EGR condition while fueled with biodiesel (SOME). However, the values are much less than with diesel.

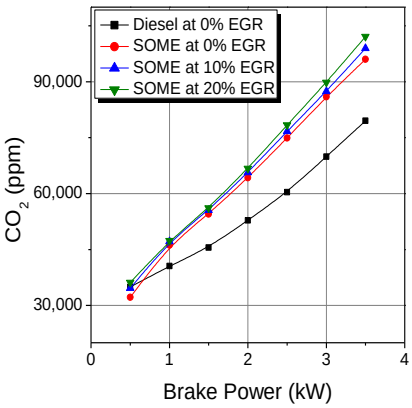

FIGURE 4. Variation of CO_2 emission with brake power for different EGR rates

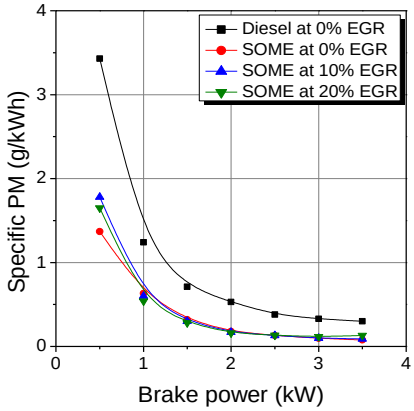

FIGURE 5. Variation of specific PM emission with brake power for different EGR rates

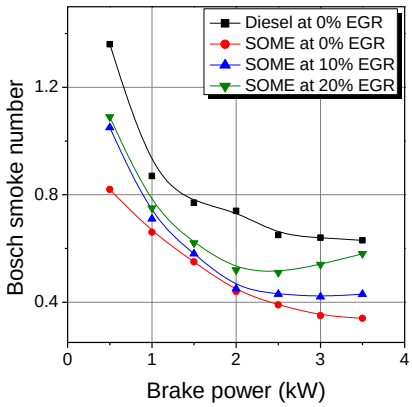

FIGURE 6. Variation of smoke emission with brake power for different EGR rates

CONCLUSION

The following conclusions can be drawn from this numerical investigation of the CI engine characteristics using soyabean biodiesel (SOME) with exhaust gas recirculation technique. The use of SOME deteriorates the engine performance but gives a cleaner exhaust, compared to that of diesel. However, SOME gives a significant rise in NO_x emission (1350 ppm) compared to diesel (775 ppm). Compared to no EGR condition for the neat biodiesel, the NO_x emissions are reduced by 44% and 70% with 10% and 20% EGR respectively. On the contrary, brake thermal efficiency decreases with the increase in EGR rate. Brake specific fuel consumption (BSFC) increases by 3.2% and 6.5% respectively for the same. Particulate matter (PM) emission increases by 15.4% and 66.6% and smoke emission increases from 0.34 BSN (bosch smoke number) to 0.43 BSN and 0.58 BSN for 10% and 20% EGR respectively. So, the introduction of EGR helps in reducing the NO_x emission which is a major problem when a CI engine is run with biodiesel. However, there is a limit to the EGR rates to be used as the EGR reduces the NO_x emission at the cost of engine performance and other harmful exhaust at the tailpipe.

REFERENCES

1. National Policy on Biofuels, a Report by Government of India, Ministry of New & Renewable Energy, http://mnre.gov.in/file manager/UserFiles/DIREC_2010_Report.pdf.
2. Karanja-A Potential Source of Biodiesel, a Report by National Oilseeds and Vegetable Oils Development Board, Government of India, Ministry of Agriculture, 2008, http://www.novodboard.com/Karanja%20English.pdf.
3. Report of the Committee on Development of Bio-Fuel, Planning Commission, Government of India, 2003, http://planningcommission.nic.in/reports/genrep/cmtt_bio.pdf.M.
4. http://en.wikipedia.org/wiki/Exhaust_gas_recirculation#cite_ref-yahooegr_2-0
5. http://www.imperialclub.com/Repair/Lit/Master/308/page08.htm
6. H. T. C. Machacon, S. Shiga, T. Karasawa and H. Nakamura, Effect of EGR on the Particulate and Its Component Emissions in a D. I. Diesel Engine. Bulletin of the M. E. S. J, **25(2)** 77-83 (1997).
7. M. Ghazikhani, M. R. Kalateh, Y. K. Toroghi and M. Dehnavi, An Experimental Study on the Effect of EGR and Engine Speed on CO and HC Emissions of Dual Fuel HCCI Engine, World Academy of Science, Engineering and Technology (2009).
8. A. Hribernik and N. Samec, Effect of Exhaust Gas Recirculation on Diesel Combustion, Journal of KONES Internal Combustion Engines **11(1-2)**, 223-231 (2004).
9. S. B. Fiveland and D. N. Assanis, A Four-Stroke Homogeneous Charge Compression Ignition Engine Simulation for Combustion and Performance Studies, SAE Paper No. 2000-01-0332 (2000).
10. J. B. Heywood, Internal Combustion Engine Fundamentals, *McGraw-Hill Co.*, US, 1988.
11. A. S. Kuleshov, Use of Multi-Zone DI Diesel Spray Combustion Model for Simulation and Optimization of Performance and Emissions of Engines with Multiple Injection, SAE Technical Paper, 2006-01-1385; doi:10.4271/2006-01-1385.
12. A. A. Westenberg, Kinetics of NO and CO in Lean, Premixed Hydrocarbon-Air Flames, Combustion Science and Technology **4(1)** 59-64 (1971).
13. A. C. Alkidas, Relationship between smoke measurements and particular measurements, SAE Technical Paper, 1984, 840412, doi:10.4271/840412.
14. P. V. Walke, N. V. Deshpande and R.G. Bodkhe, Impact of Exhaust Gas Recirculation on the Performances of Diesel Engine, *Proceedings of the World Congress on Engineering*, 2008, Vol. II WCE 2008, July 2 - 4, 2008, London, U.K., ISBN:978-988-17012-3-7.
15. A. Pal, C. Samanchi and S. Sharma, The Effects of Exhaust Gas Recirculation on Exhaust Emission and Combustion Characteristics of a CI engine operated on Diesel and WCO Biodiesel, International Journal of Engineering Research and Development, e-ISSN : 2278-067X, p-ISSN : 2278-800X.
16. Md. N. Nabi, Md, M. Rahman and Md. S. Akhter, Biodiesel from cotton seed oil and its effect on engine performance and exhaust emissions, Applied Thermal Engineering, **29** 2265–2270 (2009).

ICME2015

International Conference on Mechanical Engineering 2015
(ICME 2015) 18 – 20 December, 2015, Dhaka, Bangladesh

Paper ID : 080

Numerical Study of Unsteady Heat and Fluid Flow through a Rotating Curved Rectangular Duct: The Case of Positive Rotation

Sajal Kanti Rudro[1], Poly Rani Shaha[1], Rabindra Nath Mondal[1, a)] and Shinichiro Yanase[2]

[1]*Department of Mathematics, Jagannath University, Dhaka-1100, Bangladesh*
[2]*Department of Mechanical and Systems Engineering, Okayama University, Okayama 700-8530, Japan*

[a)]Corresponding author: rnmondal71@yahoo.com

Abstract. The present study addresses numerical prediction of unsteady fluid flow and heat transfer through a rotating curved rectangular duct of aspect ratio 2 and curvature 0.001. Spectral method is used as a basic tool to solve the system of non-linear partial differential equations. The emerging parameters controlling the flow characteristics are the rotational parameter i.e. *Tr*, (incorporating Coriolis force), the Grashof number, *Gr*, (incorporating buoyancy force), the Prandtl number (Pr = 7.0) and the pressure-driven parameter i.e. the Dean number *Dn* (incorporating centrifugal force). The flow structures are examined for $0 < Tr \leq 1500$ at $Dn = 100$ and $Gr = 500$. The rotation of the duct about the center of curvature is imposed in the positive direction and the effects of rotation (*Coriolis force*) on the unsteady flow characteristics are investigated, and it is found that the steady-state flow turns into chaotic flow through periodic or multi-periodic flows, if *Tr* is increased in the positive direction. Time evolution calculations as well as their phase spaces show that the unsteady flow undergoes in the scenario '*steady-state* $\rightarrow$ *periodic* $\rightarrow$ *multi-periodic* $\rightarrow$ *chaotic'*, if *Tr* is increased. Typical contours of secondary flow patterns and temperature profiles are obtained at several values of *Tr*, and it is found that the unsteady flow consists of two- to six-vortex solutions. Convective heat transfer is also investigated, and it is found that the chaotic flow enhances heat transfer more effectively than the steady-state or periodic solutions due to many secondary vortices generated at the outer wall of the duct.

INTRODUCTION

Fluid flow through curved ducts and channels has been extensively used with a key base of heat transfer and mixing enhancement. Today, the flows in curved non-circular ducts are of increasing importance in many engineering applications, such as in turbo-machinery, refrigeration, air conditioning systems, heat exchangers, rocket engine, internal combustion engines and blade-to-blade passages in modern gas turbines. In a curved duct, centrifugal forces are developed in the flow due to channel curvature causing a counter rotating vortex motion [Dean [1]]. After that, many theoretical and experimental investigations have been made; here, the articles by Berger *et al*. [2] and Ito [3] may be referred to.

It is well known that, the fluid flowing in a rotating curved duct is subjected to two forces: the Coriolis force due to rotation and the centrifugal force due to curvature. When a temperature induced variation of fluid density occurs for non-isothermal flows, both Coriolis and centrifugal type buoyancy forces can contribute to the generation of vortices. The effect of system rotation is more subtle and complicated and yields new; richer features of flow and heat transfer in general, bifurcation and stability in particular, for non-isothermal flows. Selmi et al. [4] examined the combined effects of system rotation and curvature on the bifurcation structure of two-dimensional flows in a rotating curved duct with square cross section. Wang and Cheng [5], employing finite volume method, examined the flow characteristics and heat transfer in a curved square duct for positive rotation and found reverse secondary flow for the co-rotation cases. Yamamoto et al. [6] studied on the flow in a rotating curved rectangular duct. Very recently, Mondal et al. [7] performed numerical investigation on combined effects of centrifugal and Coriolis instability of flow through a rotating curved rectangular duct of moderate curvature, and obtained four branches of symmetric/asymmetric steady solutions with two- and multi-vortex solutions. However, exact transient behavior of the unsteady solutions is still

unresolved for the flow through a rotating curved rectangular channel with strong rotational speed, which motivated the present study to fill up this gap. In the present paper, a comprehensive numerical study is presented for the unsteady solutions with convective heat transfer in a rotating curved rectangular duct of small curvature. Studying the effects of rotation on the unsteady flow characteristics, caused by the combined action of the centrifugal, Coriolis and buoyancy forces, is an important objective of the present study.

PHYSICAL MODEL AND GOVERNING EQUATIONS

Consider a fully developed 2-D flow of viscous incompressible fluid through a rotating curved rectangular duct. The coordinate system is shown in Fig. 1. The system rotates at a constant angular velocity Ω_T around the y' axis. It is assumed that the outer wall is heated while the inner wall cooled. The flow is uniform in the z-direction.

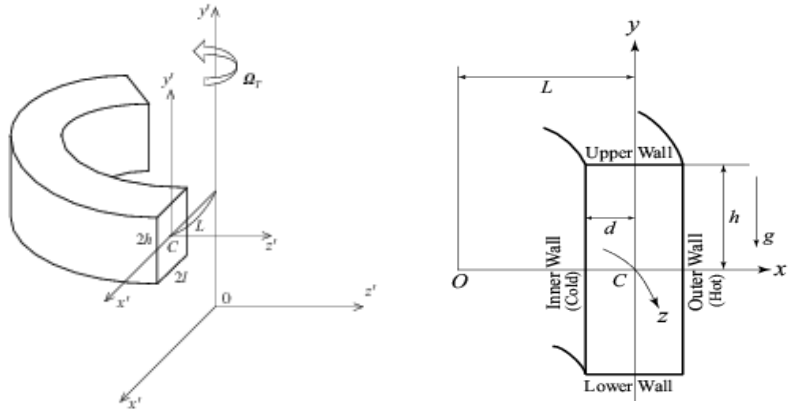

(a) (b)

FIGURE 1. (a) Coordinate system of the rotating curved duct, (b) Cross section of the curved duct

Since the flow field is uniform in the z -direction, the sectional stream function ψ is introduced as

$$u = \frac{1}{1+\delta x}\frac{\partial \psi}{\partial y}, \qquad v = -\frac{1}{1+\delta x}\frac{\partial \psi}{\partial x} \tag{1}$$

Then the basic equations for w, ψ and T are derived from the Navier-Stokes and the energy equations as,

$$(1+\delta x)\frac{\partial w}{\partial t} = Dn - \frac{1}{2}\frac{\partial(w,\psi)}{\partial(x,y)} - \frac{\delta^2 w}{1+\delta x} + (1+\delta x)\Delta_2 w - \frac{1}{2}\frac{\delta}{(1+\delta x)}\frac{\partial \psi}{\partial y}w + \delta\frac{\partial w}{\partial x} - \delta Tr\frac{\partial \psi}{\partial y} \tag{2}$$

$$\left(\Delta_2 - \frac{\delta}{1+\delta x}\frac{\partial}{\partial x}\right)\frac{\partial \psi}{\partial t} = -\frac{1}{2}\frac{1}{(1+\delta x)}\frac{\partial(\Delta_2\psi,\psi)}{\partial(x,y)} + \frac{1}{2}\frac{\delta}{(1+\delta x)^2}\left[\frac{\partial \psi}{\partial y}\left(2\Delta_2{}^2\psi - \frac{3\delta}{1+\delta x}\frac{\partial \psi}{\partial x} + \frac{\partial^2 \psi}{\partial x^2}\right) - \frac{\partial \psi}{\partial x}\frac{\partial^2 \psi}{\partial x \partial y}\right]$$
$$+ \frac{\delta}{(1+\delta x)^2}\times\left[3\delta\frac{\partial^2 \psi}{\partial x^2} - \frac{3\delta^2}{1+\delta x}\frac{\partial \psi}{\partial x}\right] - \frac{2\delta}{1+\delta x}\frac{\partial}{\partial x}\Delta_2\psi + w\frac{1}{2}\frac{\partial w}{\partial y} + \Delta_2{}^2\psi - Gr(1+\delta x)\frac{\partial T}{\partial x} - \frac{1}{2}Tr\frac{\partial w}{\partial y}, \tag{3}$$

$$\frac{\partial T}{\partial t} = \frac{1}{\Pr}\left(\Delta_2 T + \frac{\delta}{1+\delta x}\frac{\partial T}{\partial x}\right) - \frac{1}{(1+\delta x)}\frac{\partial(T,\psi)}{\partial(x,y)} \tag{4}$$

The non-dimensional parameters Dn , Tr , Gr and Pr, which appear in equations (2) to (4) are defined as:

$$Dn = \frac{Gd^3}{\mu\upsilon}\sqrt{\frac{2d}{L}}, \quad Gr = \frac{\beta g \Delta T\, d^3}{\upsilon^2}, \quad Tr = \frac{2\sqrt{2\delta}\,\Omega_T d^3}{\upsilon\delta}, \quad \Pr = \frac{\upsilon}{\kappa} \tag{5}$$

The no slip boundary conditions for w and ψ are used as

$$w(\pm 1, y) = w(x, \pm 1) = \psi(\pm 1, y) = \psi(x, \pm 1) = \frac{\partial \psi}{\partial x}(\pm 1, y) = \frac{\partial \psi}{\partial y}(x, \pm 1) = 0 \tag{6}$$

and the temperature T is assumed to be constant on the walls as

$$T(1, y) = 1, \quad T(-1, y) = -1, T(x, \pm 1) = x \tag{7}$$

In the present study, we take Dn = 100, Gr = 500, δ = 0.001 and Pr = 7.0 (for water) for the aspect ratio 2.

METHOD OF NUMERICAL CALCULATIONS

Equations (2) to (4) are solved numerically by using the spectral method. By this method, the expansion functions $\phi_n(x)$ and $\psi_n(x)$ are expressed as

$$\left.\begin{aligned} \phi_n(x) &= (1 - x^2)\, C_n(x), \\ \psi_n(x) &= (1 - x^2)^2 C_n(x) \end{aligned}\right\} \tag{8}$$

where $C_n(x) = \cos\left(n \cos^{-1}(x)\right)$ is the n-th order Chebyshev polynomial. $w(x, y, t)$, $\psi(x, y, t)$ and $T(x, y, t)$ are expanded in terms of $\phi_n(x)$ and $\psi_n(x)$ as

$$\left.\begin{aligned} w(x, y, t) &= \sum_{m=0}^{M} \sum_{n=0}^{N} w_{mn}(t)\, \varphi_m(x)\, \varphi_n(y) \\ \psi(x, y, t) &= \sum_{m=0}^{M} \sum_{n=0}^{N} \psi_{mn}(t)\, \psi_m(x)\, \psi_n(y) \\ T(x, , y, t) &= \sum_{m=0}^{M} \sum_{n=0}^{N} T_{mn}\, \varphi_m(x)\, \varphi_n(y) + x, \end{aligned}\right\} \tag{9}$$

where M and N are the truncation numbers in the x and y-directions respectively. Then in order to calculate the unsteady solutions, the Crank-Nicolson and Adams-Bashforth methods together with the function expansion (9) and the collocation methods are applied to Eqs. (2) to (4).

RESISTANCE COEFFICIENT

We use the resistance coefficient λ as one of the representative quantities of the flow state. It is also called the *hydraulic resistance coefficient*, and is generally used in fluids engineering, defined as

$$\frac{P_1^* - P_2^*}{\Delta z^*} = \frac{\lambda}{dh^*} \frac{1}{2} \rho \left\langle w^* \right\rangle^2, \tag{10}$$

The main axial velocity $\left\langle w^* \right\rangle$ is calculated by

$$\langle w^* \rangle = \frac{\nu}{8\sqrt{2\delta}} \int_{-1}^{1} dx \int_{-1}^{1} w(x, y, t)\, dy \tag{11}$$

Since $\left(P_1^* - P_2^*\right) / \Delta z^* = G$, λ is related to the mean non-dimensional axial velocity $\langle w \rangle$ as

$$\lambda = \frac{16\sqrt{2\delta}\, Dn}{3\langle w \rangle^2} \tag{12}$$

where $\langle w \rangle = \sqrt{2\delta} d / \nu \left\langle w^* \right\rangle$. In this paper, λ is used to calculate the unsteady solutions by numerical computations.

RESULTS AND DISCUSSION

Positive Rotation, $0 < Tr \le 1500$

We investigated unsteady solutions for positive rotation of the duct over a wide range of Tr for $0 < Tr \le 1500$ and it is found that the unsteady flow is a steady-state solution for $0 < Tr \le 490$. Figure 2(a) shows unsteady solution for Tr = 100. To observe the structure of vortex generation, typical contours of secondary flow patterns and temperature profiles are shown in Fig. 2(b) for Tr = 100, and it is found that the steady-state solution possesses asymmetric two-vortex solution. These vortices are generated due to the combined action of the *centrifugal*, *Coriolis* and *buoyancy forces* (Wang and Cheng [5]). If Tr is increased further, for example $495 \le Tr \le 530$, the steady-state solution turns into periodic oscillating flow, which is justified as shown in Fig. 3.

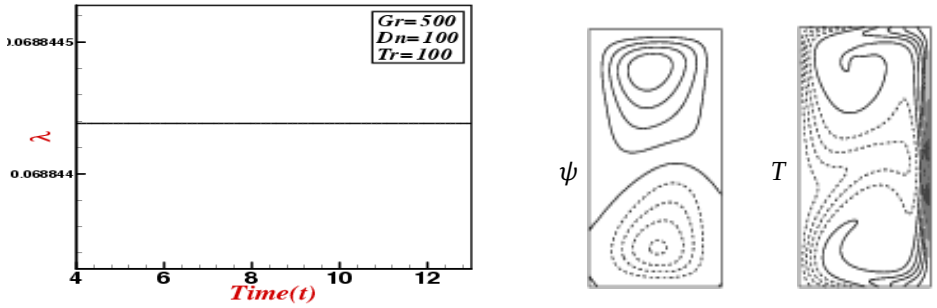

FIGURE 2. Unsteady results for Tr = 100 at Gr = 500 and Dn = 100. (a) Time evolution of λ, (b) Contours of secondary flow patterns (top) and temperature profiles (bottom) at t = 10.

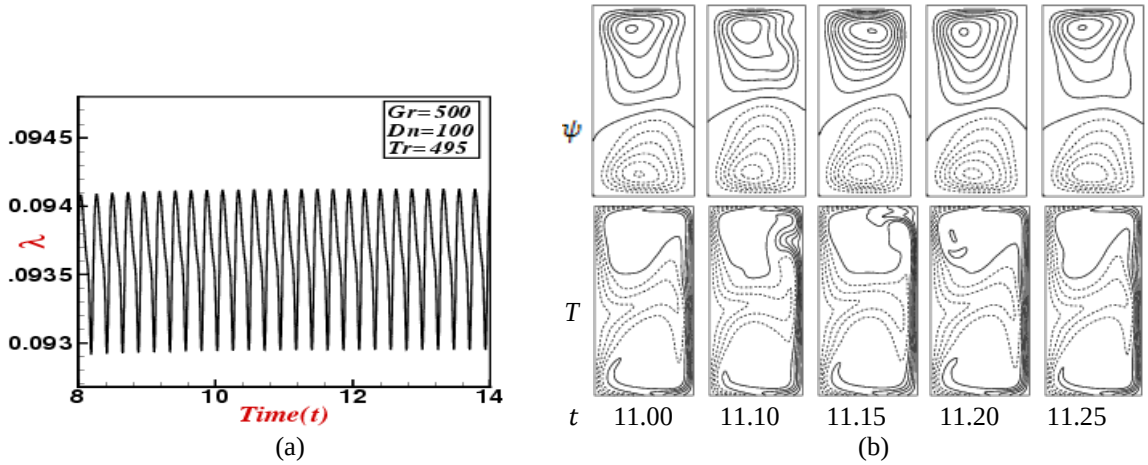

FIGURE 3. Unsteady results for Tr = 495 at Gr = 500 and Dn = 100. (a) Time evolution of λ, (b) Contours of secondary flow patterns (top) and temperature profiles (bottom) for $11.0 \le t \le 11.25$.

Figure 3(a) shows that the unsteady flow is a periodic solution for Tr = 495. Thus it is found that the transition from steady-state to periodic oscillation occurs between Tr = 490 and Tr = 495. Typical contours of secondary flow patterns and temperature profiles are shown in Fig. 3(b), which shows that the unsteady solution at Tr = 495 oscillates in the two-vortex solution. It is observed that if Tr is increased further, the periodic flow turns into multi-periodic flow and the transition from periodic to multi-periodic occurs between $Tr = 530$ and $Tr = 550$. Figure 4(a) shows time-dependent solution for $Tr = 590$, which shows that the flow is also multi-periodic. Then typical contours of secondary flows and temperature profiles are shown in Fig. 4(b) and it is found that the unsteady flow at $Tr = 590$ oscillates between two- and four-vortex solutions. If Tr is increased further the multi-periodic oscillation turns into chaotic solution. In fact, the periodic oscillation, obtained in the present study, is a traveling wave solution as justified

by Yanase *et al*. [8] for a 3D travelling wave solutions as an appearance of 2D periodic oscillation. Figure 5(a) shows the time evolution result for *Tr* = 1000, which shows that the flow is chaotic. Typical contours of secondary flow patterns and temperature profiles are shown in Fig. 5(b) for *Tr* = 1000 and it is found that unsteady solution at $Tr = 1000$oscillates in an irregular pattern between two- and four-vortex solutions. It is found that, the transition from multi-periodic oscillation to chaotic state occurs between *Tr* = 590 and *Tr* = 600. The chaotic flow at small *Tr*, is called `*weak chaos*` and that for large *Tr* `*strong chaos*`. In this study, it is found that secondary flow enhances heat transfer in the flow particularly when Dean vortices emerge at the outer wall.

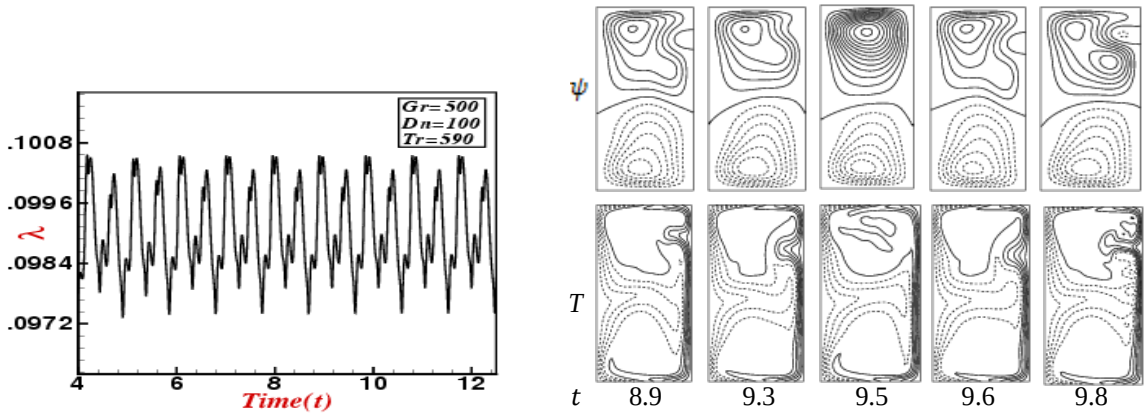

(a) (b)

FIGURE 4. Unsteady results for *Tr* = 590 at *Gr* = 500 and *Dn* = 100. (a) Time evolution of λ, (b) Contours of secondary flow patterns (top) and temperature profiles (bottom) for $8.9 \le t \le 9.8$

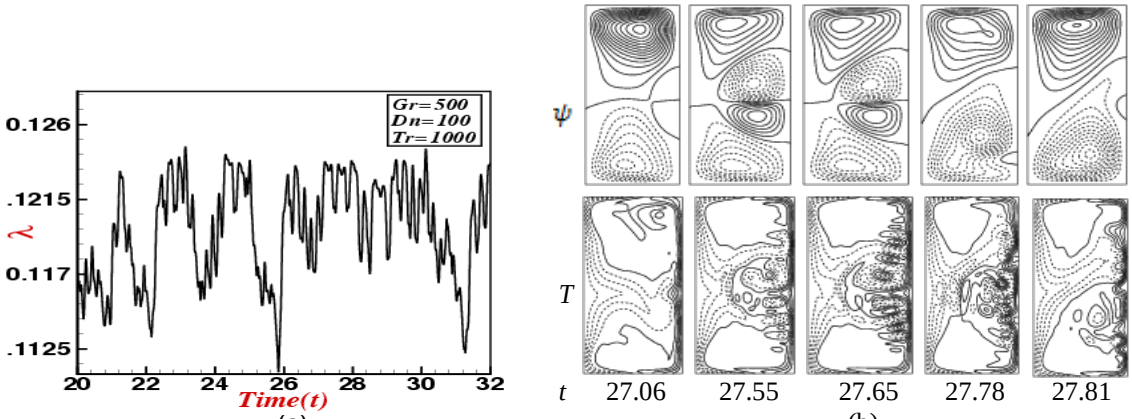

(a) (b)

FIGURE 5. Unsteady results for *Tr* = 1000 at *Gr* = 500 and *Dn* = 100. (a) Time evolution of λ, (b) Contours of secondary flow patterns (top) and temperature profiles (bottom) for $27.06 \le t \le 27.81$.

Phase Spaces in the $\lambda - \gamma$ Plane

In order to well justify the flow transition, we draw phase spaces of the time evolution results obtained at various *Tr*. Figure 6(a) shows phase plots for *Tr* = 495, which shows that the flow is periodic. However, by time evolution calculation, we could not well justify whether the flow is multi-periodic or chaotic for *Tr* = 590. Then by drawing the phase space as shown in Fig. 6(b), we see that the flow is not multi-periodic but transition to chaos. This type of flow is termed as '*transitional chaos*'. Finally, we draw the phase spaces for *Tr* = 1000 as shown in Fig. 6(c), which shows that the flow is strongly chaotic. This type of flow oscillations are termed as *strong chaos*.

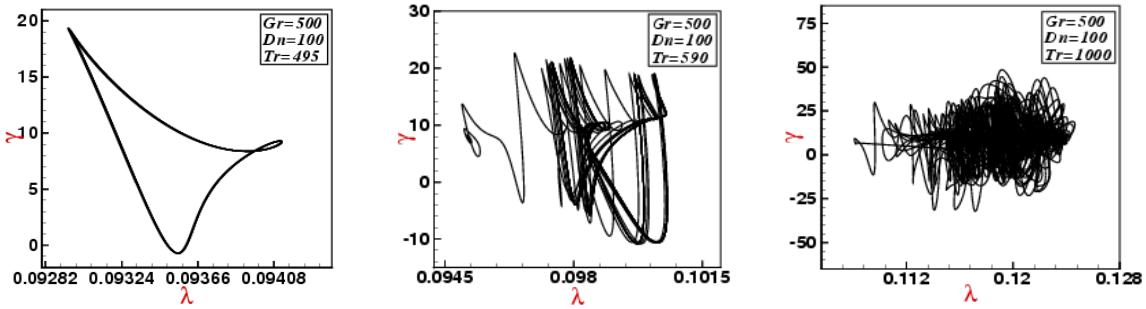

FIGURE 6. Phase Plots in the $\lambda - \gamma$ plane for *Dn* = 100 and *Gr* = 500. (a) *Tr* = 495, (b) *Tr* = 590, (c) *Tr* = 1000.

CONCLUSIONS

In this paper, a spectral-based numerical study is presented for the fully developed two-dimensional flow of viscous incompressible fluid through a rotating curved rectangular duct of curvature 0.001. Numerical calculations are carried out for the Dean number *Dn* = 100 covering a wide range of the Taylor number $0 < Tr \leq 1500$. Furthermore, a temperature difference is applied across the vertical sidewalls for the Grashof number *Gr* = 500. In this study, we investigated unsteady solutions and obtained typical contours of secondary flow patterns and temperature profiles. To study unsteady solutions, we performed time evolution calculations, and it is found that the unsteady flow undergoes in the scenario '*steady-state* $\rightarrow$ *periodic* $\rightarrow$ *multi-periodic* $\rightarrow$ *chaotic'* if *Tr* is increased. To well justify the transitional behavior of the unsteady solutions from one state to another we also obtained phase spaces of the time evolution results. It is found that secondary flow is a symmetric two-vortex solution for $0 < Tr \leq 490$, asymmetric two-vortex for $495 \leq Tr \leq 510$, asymmetric two- to four-vortex for $520 \leq Tr \leq 670$, and two- to multi-vortex solutions for $675 \leq Tr \leq 1500$. In this study, it is found that secondary flow enhances heat transfer in the flow particularly when Dean vortices emerge at the outer wall and that if the flow is periodic and then chaotic, as *Tr* increases, heat transfer is enhanced significantly. This study also shows that there is a strong interaction between the heating-induced buoyancy force and the centrifugal-Coriolis instability of the flow that stimulates fluid mixing and consequently enhance heat transfer in the fluid.

ACKNOWLEDGMENTS

Rabindra Nath Mondal would gratefully acknowledge the financial support from the Japan Society for the Promotion of Science (JSPS), No. L15534, while Shinichiro Yanase expresses his cordial thanks to the Japan Ministry of Education, Culture, Sports, Science and Technology for the financial support through the Grant-in-Aid for Scientific Research, No. 24560196.

REFERENCES

1. W. R. Dean, Philos. Mag. **4**, 208–223 (1927).
2. S. A. Berger, L. Talbot and L. S. Yao, Annual. Rev. Fluid. Mechanics **35**, 461–512 (1983).
3. H. Ito, JSME International Journal **30**, 543–552(1987).
4. M. Selmi, K. Namdakumar and W. H. Finlay, J. Fluid Mechanics **262**, 353–375 (1994).
5. L. Q. Wang and K. C. Cheng, Physics of Fluids **8**, 1553–1573 (1996).
6. K. Yamamoto, S. Yanase and M. M. Alam, J. Phys. Soc. Japan **68**, 1173–1184(1999).
7. R. N. Mondal, S. C. Ray and S. Yanase, Open Journal of Fluid Dynamics **4**, 1–14(2014).
8. S. Yanase, T. Watanabe and T. Hyakutake, Physics of Fluids **20**, 124101, 1–8 (2008).

ICME2015

International Conference on Mechanical Engineering 2015
(ICME 2015) 18 – 20 December, 2015, Dhaka, Bangladesh

Paper ID : 085

Numerical Investigation of Thermal Performance of a Water-Cooled Mini-channel Heat Sink for Different Chip Arrangement

Amitav Tikadar[1, a)], Md. Mahamudul Hossain[1] and AKM M. Morshed[1]

[1]*Department of Mechanical Engineering, Bangladesh University of Engineering and Technology, Dhaka,1000*

[a)] Corresponding Author: amitav453@gmail.com

Abstract. Heat transfer from electronic chip is always challenging and very crucial for electronic industry. Electronic chips are assembled in various manners according to the design conditions and limitations and thus the influence of chip assembly on the overall thermal performance needs to be understand for the efficient design of electronic cooling system. Due to shrinkage of the dimension of channel and continuous increment of thermal load, conventional heat extraction techniques sometimes become inadequate. Due to high surface area to volume ratio, mini-channel have the natural advantage to enhance convective heat transfer and thus to play a vital role in the advanced heat transfer devices with limited surface area and high heat flux. In this paper, a water cooled mini-channel heat sink was considered for electronic chip cooling and five different chip arrangements were designed and studied, namely: the diagonal arrangement, parallel arrangement, stacked arrangement, longitudinal arrangement and sandwiched arrangement. Temperature distribution on the chip surfaces was presented and the thermal performance of the heat sink in terms of overall thermal resistance was also compared. It is found that the sandwiched arrangement of chip provides better thermal performance compared to conventional in line chip arrangement.

INTRODUCTION

Micro-channel heat sink has been studied extensively both numerically and experimentally since its early introduction by Tuckerman and Pease [1] who designed a new, very compact, water-cooled integral heat sink for silicon integrated circuits. At a power density of 790 W/cm2, an utmost substrate temperature increase of 71°C above the input water temperature was found. Toh et al. [2] carried out three-dimensional fluid flow and heat transfer phenomena in heated micro-channels by using the finite-volume method. Qu and Mudawar [3] studied three-dimensional fluid flow and heat transfer in a rectangular micro-channel heat sink numerically using water as the cooling fluid.

Flow Reynolds number also affects the length of the flow developing region. Peterson and Cheng [4] carried out a detailed numerical simulation of forced convection heat transfer occurring in silicon-based micro-channel heat sinks by using a simplified three-dimensional conjugate heat transfer mode (2D fluid flow and 3D heat transfer). Their findings indicate that thermo physical properties of the liquid can significantly influence both the flow and heat transfer in the micro-channel heat sink.

Although micro-channel heat sinks are capable of dissipating high heat fluxes, the small flow rate produces a large temperature rise along the flow direction in both solid and liquid. Lee and Garimella [5] investigated convection parameters in the entrance region of micro-channels of rectangular cross-section at different aspect ratios under circumferentially uniform wall temperature and axially uniform wall heat flux thermal boundary conditions and proposed analytical correlation between the Nusselt number and non-dimensional flow length for developing flow in micro-channel. In the developing zone heat transfer rate is very high compared to the developed zone. From the result of Al-Bakhit et al. [6], entrance region the developing velocity profiles lead to higher values of overall

heat transfer coefficient. Valafi and Zhu [7] first studied double layer with counter current flow heat sink for electronics cooling application for the power supply system.The two-layered design is not significantly more complicated than the single-layered design and demonstrated that two layered micro-channel heat sink design is a substantial improvement over single layer conventional heat sink. Wei. X. and Y. joshi [8-9] investigated two layered micro-channel for the parallel and counter flow arrangement and reported that for smaller inlet flow velocity, a micro-channel stack requires less pumping power to remove a certain rate of heat than a single-layered micro-channel, because it provides a larger heat transfer area. They also found that, the thermal resistance as low as 0.09ºC/W/cm2 for both counter flow and parallel flow configurations and at a fixed pumping power the overall thermal resistance for a two-layered micro-channel is 30% less than that of a single-layered micro-channel. Lei and Ning [10] have studied multilayer copper and silicon carbide (SIC) mini-channel heat sink experimentally and numerically both in single and two phase flow and established that multi layer heat sinks have significant advantages over single-layer equivalents with reductions both in thermal resistance and pressure drop. They also claimed that multilayer heat sinks have less stability at high heat flux, which lead to increased surface temperature. Cheng [11] investigated multi layered micro-channel with enhanced mixing passive micro structure and demonstrated better performance over smooth single layered micro-channel. Dixit et. al. [12] demonstrated that the heat dissipation rate of electronic devices is significantly increased by the silicon micro/nanopillars, which are grown in the micro-channels by utilizing the micro-masking effect in deep reactive ion etching. The overall thermal resistance of micro-channel heat sink was found to be reduced from 1.13 K/W to 0,98 K/W, while the average heat dissipation rate of heat sink was shown to be increased by 16% as compared to one without silicon pillars due to the smaller diameter (0.5–2 μm) and larger height (∼100 μm) of silicon pillars.

Xu et. al. [13] demonstrated the heat transfer in micro-channel can be enhanced by a composition of parallel and transverse micro-channels which divide the whole flow length into some independent flow region in each of which thermal boundary layer is redeveloping. The redeveloping flow is repeated for all of the independent zones, thus the overall heat transfer is increasing along with the pressure drops are decreased compared. Venkatadri et al. [14] reviewed the recent advances in thermal management in three dimensional chip stacks in the electronic system, and discussed the 3D integration technologies, thermal management challenges and advanced 2D thermal management. They demonstrated that three dimensional (3D) integration offers numerous electrical advantages like shorter interconnection distances between different dies in the stack, reduced signal delay, reduced interconnect power and design flexibilities. Xie Gongnan, Zhang Feng [15] designed a mini-channel heat sink for electronic cooling with three kinds of chip arrangement and studied: diagonal arrangement, parallel arrangement, and stacked arrangement. They made a conclusion about the best cooling performance of the heat sink that contains diagonal arrangement of chips.The aim of this paper is to identify the thermal performance of the mini-channel heat sink for five arrangements of chip

NOMENCLATURE

D_h	hydraulic diameter (mm)	Q	volume flow rate (m^3/s)
u	velocity (m/s)	q	heat flux chip (w/cm^2)
C_p	specific heat (kj/kg-K)	Pr	Prandtl number
k	thermal conductivity (w/m-K)	Δp	pressure difference (pa)
R_t	thermal resistance ($K/w\text{-}cm^2$)	***Symbols***	
h_x	local heat transfer coefficient($w/m^2\text{-}K$)	*in*	inlet
		out	outlet
Re	Reynolds number	f	fluid
Nu_x	local Nusselt number	pp	pumping power
$T_{w,max}$	maximum temperature of the Heat sink(k)	***Greek symbols***	
		ρ	density (kg/m^3)
$T_{i,f}$	inlet temperature of coolant (k)	μ	liquid dynamic viscosity (kg/m-s)
$T_{x,w}$	local temperature of the heat sink (K)		

SIMULATION METHODOLOGY

A three dimensional fluid flow and heat transfer characteristics were analyzed for chip arrangement numerically by using the commercial computational fluid dynamics (CFD) package, FLUENT. The single mini-channel was chosen as the baseline to perform the numerical analysis. The computational domain for different chip arrangement is shown in Fig.1.The size of heat sink model was 35 mm ×35 mm×6 mm The computational domain was consisted of 20 channels with size of 35 mm ×1 mm×4mm each. The channels were separated by wall of 0.75 mm.Five different chip arrangements were studied and a simple notation was introduced as: Case-1 (diagonal arrangement), Case-2 (parallel arrangement), Case-3 (stacked arrangement), Case-4 (longitudinal arrangement) and case-5 (sandwiched arrangement). The chip dimension was 15 mm × 15 mm×1 mm.The chips were located on top of the substrate. In Case-1 and case-2, the distance between the chips and the boundary was 2 mm, and the distance between the two chips was 1mm. In Case-2, the left (right), front (back) distance between the chip and boundary were 10 mm and 2 mm, respectively. In Case 3, the distance of the first chip from the bottom surface was 3mm and the distance of the second chip from the bottom was 1mm. In case-5 the lower and upper chips located at the center of both substrates. The substrate thickness was 0.5 mm for Case -1, Case -2, Case-4, and Case-5 and 4.5mm for the case-3. In case-4 the distance between two chips was 1 mm and each chip was 10 mm away from the left boundary of the heat sink.

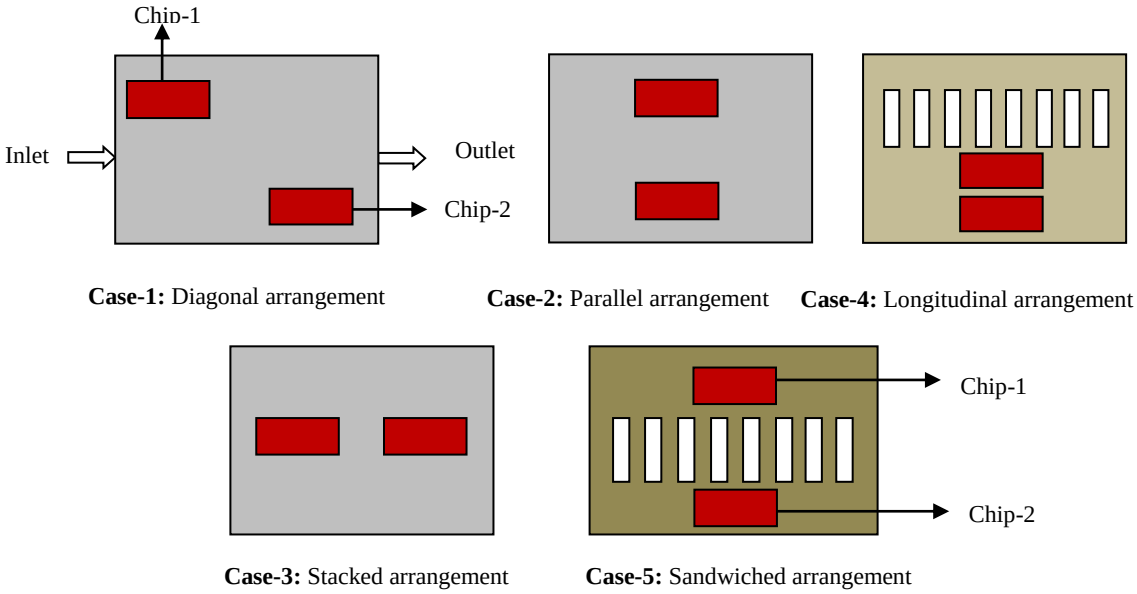

Case-1: Diagonal arrangement **Case-2:** Parallel arrangement **Case-4:** Longitudinal arrangement

Case-3: Stacked arrangement **Case-5:** Sandwiched arrangement

FIGURE 1.Different chip arrangement

MATHEMATICAL FORMULATION

Several assumptions were incorporated before establishing governing equations for the fluid flow and heat transfer in the mini-channel such as Incompressible fluid, Laminar flow in the mini-channel, Negligible radiation and natural convection heat transfer from the mini-channel heat sink, Negligible axial conduction.The incompressible governing equations used to describe the fluid flow and heat transfer in the system are expressed as follows. The conservation equations consist of

Continuity

$$\nabla \vec{V} = 0 \tag{1}$$

Navier-Stokes equation:

$$\rho\frac{\partial\vec{V}}{\partial t}+\ \rho\left(\vec{V}\cdot\nabla\vec{V}\right)=-\nabla P+\ \nabla\cdot\left(\mu\nabla\vec{V}\right) \tag{2}$$

Energy equation:

$$\rho C_p\frac{\partial T}{\partial t}+\ \rho C_p\left(\vec{V}\ \cdot\ \nabla T\right)=k\ \nabla^2 T \tag{3}$$

The overall thermal resistance can be defined by-

$$R_t=\frac{T_{w,max}-T_{i,f}}{q} \tag{4}$$

The pumping power required to drive the coolant through the mini-channel is given by

$$PP=(P_{in}-P_{out})\times Q \tag{5}$$

Local Nusselt number is calculated using the following equation

$$Nu_x=\frac{h_x D_h}{k} \tag{6}$$

A uniform velocity was applied at the channel inlet Thus

$$u=u_{in}\ ,v=0\ ,w=0 \tag{7}$$

The inlet velocity varied from 0.1m/s to 2.0m/s. The inlet temperature of the cooling water was set to a constant value at the channel inlet. To investigate the thermal characteristic of the heat sink, heat generation rate of 6.667×108 w/m3 was considered for each chip (150w) of all the configurations. Inlet velocity of the coolant varied from 0.06 to 2 m/s and the pressure at the outlet was considered atmospheric. Silicon was used as the heat sink material of thermal conductivity 148 w/m-K. Heat transfer from the upper and lower surface to the outside is neglected and laminar, single phase flow is considered through the channel. At the inlet 293K temperature was applied The property of the coolant and heat sink material was considered as a constant value. Convergence criterion set for the computation was 10-6.

MODEL VALIDATION

The computational model was verified using grid independence test and two different mesh number had been tested at different velocities from 0.06 to 2m/s for parallel arrangement of chip. It was observed that the temperature deviation for two different mesh sizes, was maximum is 0.34 % (Fig.3.5).Thus, to keep a balance between computational economy and prediction accuracy, the meshes including 0.7M chosen for all the arrangement.

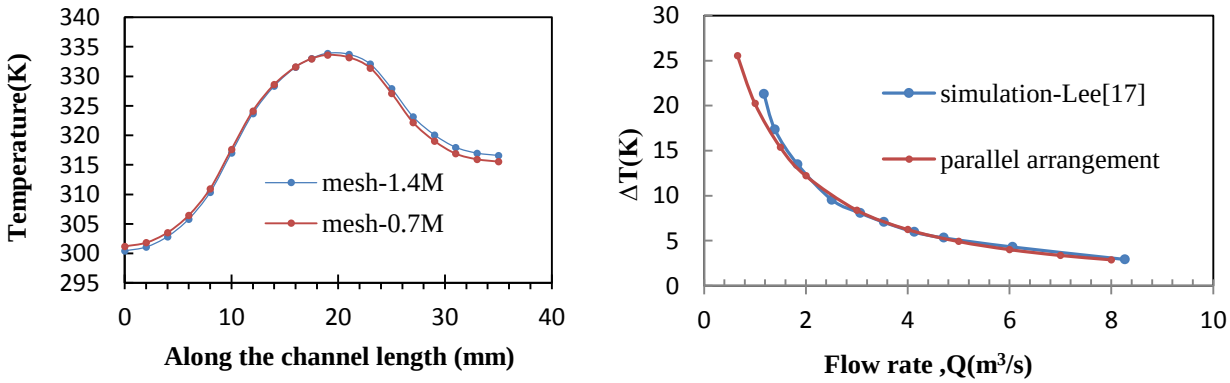

(a) (b)

FIGURE 2.(a) Mesh independence test (b)Comparison of numerical simulation and experimental result from Lee[16]

To validate the model, a temperature difference of the inlet and outlet was calculated and compared with that of Lee [16] for thermally developing flow. Fig.2(b) shows the temperature difference vs. flow rate for the proposed

model and lee's experiment. The two results almost superimpose to each other which give us confidence for further investigation. and found in excellent agreement, which validates the computational model used in this study.

RESULTS AND DISCUSSION

Chip arrangement has a significant effect on the chip temperature distribution while other parameters remained constant. To protect the chip from burned out the temperature of the chip surface should be below the limiting temperature.Temperture map of a surface represnt the temperature distribution over the surface and provides a way to compare thermal performance of electronics cooling device. So to compare the different arrangement of chip the substrate's top surface temperature map was observed for the coolant velocity of 0.25m/s for all the configurations as presented in Fig.3. From the temperature map it was obvious that the temperature distribution over the substrate's top surface was not uniform. Due to lower diffusion rate the centre of each chip showed very high temperature than the periphery of each chip.

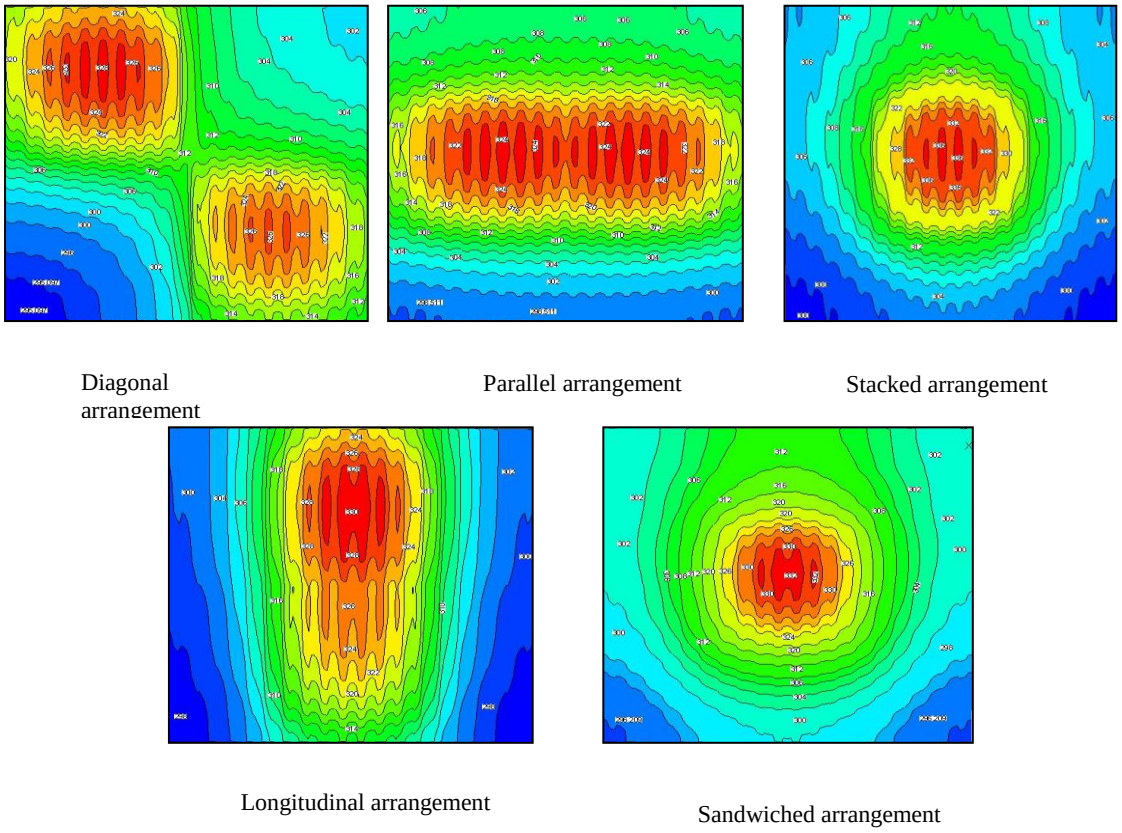

FIGURE 3. Temperature map of substrates for the five arrangements of chips

However the first chip for all the configurations showed relatively lower temperature distribution than the second one as expected. But due to high diffusion rate both the parallel and sandwitched arrangement showed relatively lower temperature than the other arrangement for both the chips.The bottom chip of stacked arrangement showed the highest temperature among all the configurations due to very lower diffusion rate. Howeverut the magnitude of the temperature in the ascending order was sandwiched arrangement, Parallel arrangement, longitudinal arrangement, diagonal arrangement and stacked arrangement

For further analyzing the chip surface, the second chip of each arrangement was splited into three parts and the average temperature distribution along the middle portion (m) of the chip surface was investigated. The temperature

distribution along the middle portion of the chip length was presented in fig.4. The temperature distribution along the chip showed non linear variation for all the configurations.

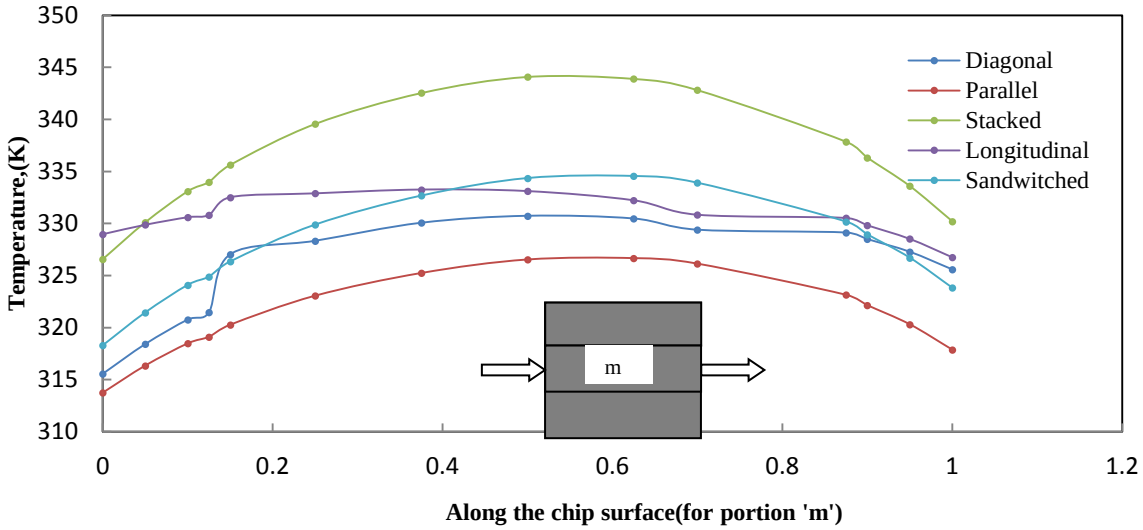

FIGURE 4. Chip slice temperature distribution along the flow direction

The local temperature for the Parallel arrangement was lowest among all other configurations due to higher diffusion rate. Stacked arrangement showed very high temperature(345K) and there was a possibility to burn the second chip.The local temperature for the diagonal , sandwitched and longitudinal arrangement was acceptable although they showed higher temperature than the parallel arrangement.

Pumping power requirement was also taken into consideration in this study. High pumping power requirements can offset the heat transfer enhancement. Although the heat transfer rate increases with the coolant velocity as well as it also incorporate high pressure penalty. The variation of overall thermal resistance for different configurations of the heat sink for different pumping power was demonstrated in Fig.5.

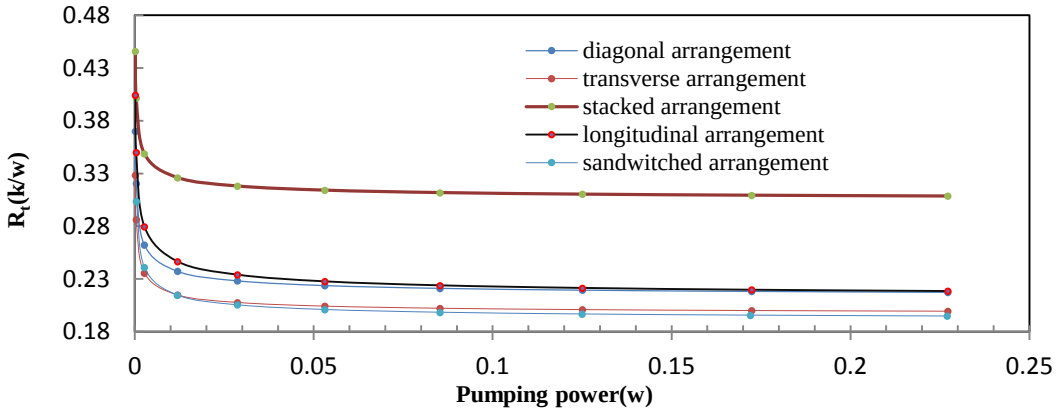

FIGURE 5. Thermal resistance as a function of pumping power for different configurations of electronic chip

For a given pumping power the thermal resistance of the heat sink should be sufficiently lower for effective chip cooling. It has been observed that the overall thermal resistance was decreased with pumping power for all the chip configurations. However interestingly the sandwitched arrangement showed different phenomena by showing lower thermal resistance as compared to other configurations. The overall thermal resistance for sandwiched arrangement was 1.87% less than the parallel arrangement ,10.28% less than diagonal arrangement, 11.38% less than the longitudinal arrangement, and 36.4% less than the stacked arrangement of chip.

The rate of reduction of overall thermal resistance with velocity for the parallel arrangement of the chip was shown in Fig.6.For increase of velocity from 0.1 to 0.25 (pumping power 0.000383 to 0.00265) the thermal resistance decreases about 18 % (Fig.7) for the parallel chip. On the other hand to increase of velocity from 1 to 1.25 the overall thermal resistance decreases by only 1% and for further increases of velocity has little effect on reducing overall thermal resistance. So optimum pumping power must be considered for the economy of the heat sink.

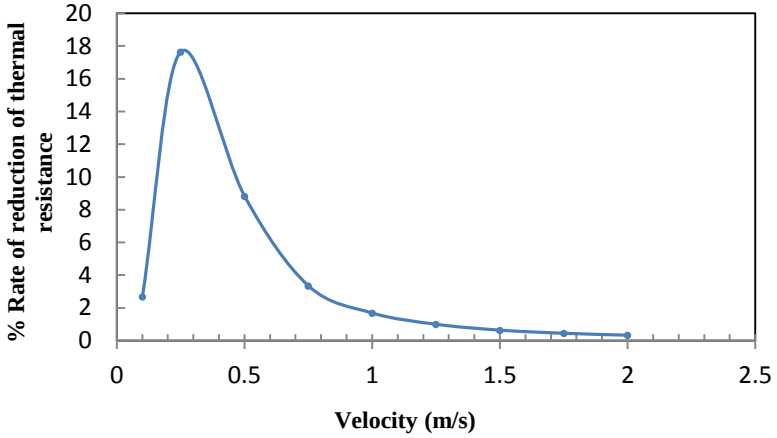

FIGURE 6.% Rate of reduction in thermal resistance for parallel/transverse arrangement of chip

CONCLUSION

The mini-channel heat sink is an attractive way to cool electronic chips. In this study, numerical simulations were performed for water-cooled mini-channels heat sink with various chip arrangements.To observe the effect of the electronic chip arrangement, five cases were considered. From the simulation results following conclusions can be drawn:

- For the stacked chip arrangement, teperature rise on the second chip is very high and may be burned.
- The chip surface temperature is not uniform and generally temperature is very high at the center and reduces along the edge of the chip.
- The magnitude of local temperature was lower for parallel arrangement.
- Sandwitched arrangement was found to have superior themal performace compared to the inline and stacked arrangement by providing lowest thermal resistnace.
-

REFERENCES

1. Tuckerman, D.B. and R. Pease, Electron Device Letters, IEEE **2(5)**, 126-129 (1981).
2. Toh, K., X. Chen, and J. Chai, International Journal of Heat and Mass Transfer **45(26),** 5133-5141 (2002).
3. Qu, W. and I. Mudawar, International Journal of heat and mass transfer **45(19)**, 3973-3985 (2002).
4. Li, J., G. Peterson, and P. Cheng, International Journal of Heat and Mass Transfer **47(19)**, 4215-4231 (2004).
5. Lee, P.-S. and S.V. Garimella, International journal of heat and mass transfer **49(17)**, 3060-3067 (2006).
6. Al-Bakhit, H. and A. Fakheri. ASME 2005 Summer Heat Transfer Conference collocated with the ASME 2005 Pacific Rim Technical Conference and Exhibition on Integration and Packaging of MEMS, NEMS, and Electronic Systems. 2005. American Society of Mechanical Engineers.
7. Vafai, K. and L. Zhu, International Journal of Heat and Mass Transfer **42(12)**, 2287-2297 (1999).
8. Wei, X., Y. Joshi, and M.K. Patterson, Journal of Heat Transfer **129(10),** 1432-1444 (2007).
9. Wei, X. and Y. Joshi, IEEE Transactions on **26(1)**, 55-61 (2003).
10. Lei, N., The University of Arizona,(2006).
11. Cheng, Y., International communications in heat and mass transfer **34(3)**, 295-303 (2007).

12. Dixit, P., et al., A Physical **141(2)**, 685-694 (2008).
13. Xu, J., et al., International Journal of Heat and Mass Transfer **48(9)**, 1662-1674 (2005).
14. Venkatadri, V., Sammakia, B., Srihari, K., Santos, D.,ASME J. Electronic Packaging, , paper no.040011,133 (2011).
15. Xie, G.N., Liu, J., Liu, Y.Q., Sunden, B., Zhang, W.H., ASME J Electronic Packaging , paper no. 021008. 135(2013).
16. Lee, P.S., Ho, J.C., Xue, H., ITherm 2002. Eighth Inter society Conference on Thermal and Thermomechanical Phenomena in Electronic Systems, 379-386, (2002).

ICME2015

International Conference on Mechanical Engineering 2015
(ICME 2015) 18 – 20 December, 2015, Dhaka, Bangladesh

Paper ID : 091

Simulated Performance of Biomass Gasification Based Combined Power and Refrigeration Plant for Community Scale Application

S. Chattopadhyay[1,a)], P. Mondal[2,b)]and S. Ghosh[3, c)]

[1]*Department of Mechanical Engineering, NIT, Agarpara, Kolkata – 700109, West Bengal, India.*
[2,3] *Department of Mechanical Engineering, IIEST, Shibpur, Howrah – 711103, West Bengal, India.*

[c)]Corresponding author: sudipghosh.becollege@gmail.com
[a)]suman.mech09@gmail.com
[b)]mondal.pradip87@gmail.com

Abstract. Thermal performance analysis and sizing of a biomass gasification based combined power and refrigeration plant (CPR) is reported in this study. The plant is capable of producing 100 kWe of electrical output while simultaneously producing a refrigeration effect, varying from 28-68 ton of refrigeration (TR). The topping gas turbine cycle is an indirectly heated all-air cycle. A combustor heat exchanger duplex (CHX) unit burns producer gas and transfer heat to air. This arrangement avoids complex gas cleaning requirements for the biomass-derived producer gas. The exhaust air of the topping GT is utilized to run a bottoming ammonia absorption refrigeration (AAR) cycle via a heat recovery steam generator (HRSG), steam produced in the HRSG supplying heat to the generator of the refrigeration cycle. Effects of major operating parameters like topping cycle pressure ratio (r_p) and turbine inlet temperature (TIT) on the energetic performance of the plant are studied. Energetic performance of the plant is evaluated via energy efficiency, required biomass consumption and fuel energy savings ratio (FESR). The FESR calculation method is significant for indicating the savings in fuel of a combined power and process heat plant instead of separate plants for power and process heat. The study reveals that, topping cycle attains maximum power efficiency of 30%in pressure ratio range of 8-10. Up to a certain value of pressure ratio the required air flow rate through the GT unit decreases with increase in pressure ratio and then increases with further increase in pressure ratio. The capacity of refrigeration of the AAR unit initially decreases up to a certain value of topping GT cycle pressure ratio and then increases with further increase in pressure ratio. The FESR is found to be maximized at a pressure ratio of 9 (when TIT=1100°C), the maximum value being 53%. The FESR is higher for higher TIT. The heat exchanger sizing is also influenced by the topping cycle pressure ratio and GT-TIT.

INTRODUCTION

Gasification of solid biomass in oxygen deficient condition results in the production of producer gas mixture from solid biomass in oxygen starved condition [1, 2]. Different biomass gasification systems, coupled with gas engines are now commercially available to transform solid form of biomass energy into electricity [3]. However, these systems suffer from low cost-effectiveness and low efficiency due to complex gas cleaning technologies and higher maintenance cost. Bio-gasification based indirectly heated combined heat and power generating systems are getting intense popularity due to reduced gas cleaning requirements and non requirement of a fired gas turbine or gas engine [4, 5]. However the main drawback of indirectly heated GT system is low thermal efficiency because more than 60% of the thermal energy is lost as waste heat [6]. Integrating cooling and heating subsystems into a conventional indirectly heated gasification based power plant could increase the plant's efficiency up to 80% [6, 7].

In combined power and refrigeration system, the waste heat of power producing GT unit can be used to run an absorption refrigeration cycle for cooling energy demand. In many industries there is a simultaneous need for

electric power and refrigeration. For these industries a CPR plant, which produces electricity as well as process heat to for absorption refrigeration, is considered a sustainable and economic option [8]. The transfer of usable heat from the GT exhaust to the absorption refrigeration plant forms the only linkage between the two systems. In a directly-coupled system, heat of exhaust is used directly in the generator of the absorption cycle [9], whereas in an indirectly-coupled system, waste heat is utilized to produce steam or the hot water which supplies heat to the generator. The advantage of indirect system is that the steam or the hot water can not only be used to drive the absorption refrigeration cycle, but also can be used for other purposes. In recent times ammonia-water absorption refrigeration plant has gained popularity because of simpler construction and wide availability of brine solution.

Effects of major operating parameters, viz., topping cycle pressure ratio (2-16) and turbine inlet temperatures (TIT= 900-1100°C) on the energetic performance of an indirectly heated bio-gasification based combined power and refrigeration plant (CPR) are reported here. Energetic performance of the plant is evaluated in terms of its energy efficiency, specific biomass consumption and fuel energy savings ratio (FESR). The plant is capable of producing 100 kWe of electrical output while simultaneously producing a refrigeration effect, varying from 28-68 ton of refrigeration (TR).

PROPOSED PLANT CONFIGURATION

The schematic diagram of the bio-gasification based indirectly heated combined power and refrigeration plant is shown in Fig.1. Solid biomass (saw dust) is fed to a fixed bed downdraft gasifier (block 4) to convert into producer gas. The producer gas gets combusted in presence of hot air of gas turbine outlet in the combustion chamber (block 5) and the flue gas is generated. The flue gas then enters the heat exchanger (block 6) as hot fluid and flows through the shell side of it. Block 5 and block 6 together called as combustor-heat exchanger duplex (CHX) unit. The atmospheric air enters the compressor (block 7) and gets compressed. The compressed air now enters the heat exchanger and gets heated. The compressed and hot air then expands in the gas turbine (block 8). The hot air after expansion goes to the combustor for combustion of producer gas.

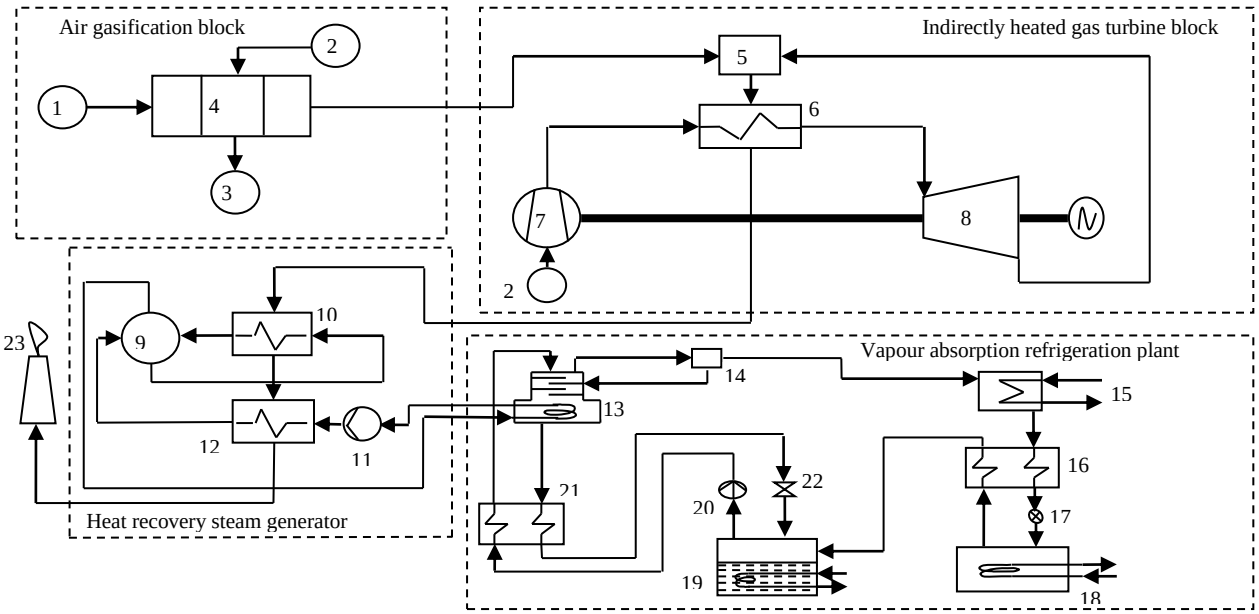

1: Biomass feed **2:** Air feed **3:** Ash out **4:** Gasifier **5:** Combustor **6:** Gas to air heater **7:** Air compressor **8:** Gas/air expander **9:** Drum **10:** Evaporator **11:** Feed pump **12:** Economiser **13:** VAR Generator **14:** Rectifier **15:** Condenser **16:** Refrigerant heat exchanger/precooler **17:** Expansion valve **18:** Evaporator **19:** Absorber **20:** Solution Pump **21:** Solution line heat exchanger **22:** Reducing valve **23:** Stack

FIGURE 1. Schematic diagram of the proposed plant.

A low pressure heat recovery steam generator (HRSG) is used to recover exhaust heat of the topping cycle. The HRSG sub-units are drum (block 9), evaporator (block 10), feed pump (block 11) and economizer (block 12). The steam is used to supply heat in generator (block 13) of vapour absorption refrigeration (VAR) plant.

VAR plant runs on aqua-ammonia absorption cycle. A strong solution of ammonia from absorber (block 19) is pumped (block 20) to the generator (block 13) where heat is supplied from steam of the HRSG. The ammonia vapour is given off from the aqua-ammonia solution at high pressure. The weak solution returns to the absorber through a heat exchanger (block 21) and a pressure reducing valve (block 22). From generator the ammonia vapour goes to condenser (block 15) through rectifier (block 14). Condensate ammonia after passes through the solution line heat exchanger (block 16) throttled by the expansion valve (block 17). In evaporator (block 18) the ammonia evaporates receiving heat from the surroundings and returns to absorber through the heat exchanger (block 16).

MODEL DEVELOPMENT

The model development and thermal performance assessment have been carried out using Cycle-Tempo software [10]. The gasifier, the CHX unit and the GT block have been modeled using standard thermodynamic relations applicable for the configuration and as elaborated in an earlier paper by Mondal & Ghosh [4]. The bottoming VAR cycle is integrated with the GT plant model following mass and energy balance equations applicable for AAR system [8].

Parametric Assumptions

The following assumptions are made for the analyses [4, 8]

- Ultimate analysis of saw dust shows C=48.98, H=4.89, O=36.01 and LHV=18,326 kJ/kg
- The isentropic efficiency of air compressor is 87% and for GT it is 89%.
- For the HRSG, minimum pinch point temperature difference is set to 10°C. The stack temperature is125°C. Isentropic efficiency of HRSG feed pump is 80% and the HRSG operates at a pressure of 3 bar.
- The generator temperature of VAR cycle is 120°C. The inlet water temperature of condenser is 20°C. Isentropic efficiency of solution pump used in VAR cycle is 80%. The aqua-ammonia solution in VAR cycle operates at a pressure of 16 bar and expands to 2.5 bar.

HRSG and VAR Unit

The HRSG unit produces saturated steam in the expense of waste heat of flue gas, which in turn drives the VAR cycle by supplying heat to the generator of the cycle. Standard energy balance equations are employed for each component (economiser, evaporator) of the HRSG unit. The VAR unit is modelled by standard thermodynamic relations and accordingly refrigeration capacity (TR) is calculated.

Performance Parameters

Expression of thermodynamic performance parameters of the proposed plant is shown as follows:

TABLE 1. Performance parameters of the plant

Parameter	Expression	Unit	Remarks
Net work output	$W_{net} = (w_{GT} - w_C)\eta_m\eta_G$	kW	W: work output η: Efficiency
Electrical Efficiency	$\eta_e = \frac{W_{net}}{m_b LHV_b}$	%	m: Biomass flow rate LHV: Lower heating value
Required air flow by mass (RAFM)	$RAFM = \frac{3600 m_a}{W_{net}}$	kg/kWh	
Electrical specific biomass consumption (ESBC)	$ESBC = \frac{3600 m_b}{W_{net}}$	Kg/kWh	
Ton of refrigeration (TR)	$TR = \frac{Q_E}{3.5168}$	TR	Q_E : Heat absorbed by VAR unit

The fuel saving for the combined power and refrigeration plant is expressed considering against a pair of bio-gasification based separate power and refrigeration plant as:

$$\Delta F = \left(\frac{W_{net}}{\eta_{e,ref}} + \frac{Q_G}{\eta_{ref}} \right) - \left(m_b \times LHV_b \right) \quad (1)$$

where, $\eta_{e,ref}$ is the reference electrical efficiency value of GT cycle and η_{ref} is the reference heat efficiency of HRSG. The reference values are set to be 20% and 80% respectively. The FESR is given by:

$$FESR = \frac{\Delta F}{\left(\frac{W_{net}}{\eta_{e,ref}} + \frac{Q_G}{\eta_{ref}} \right)} \quad (2)$$

RESULTS AND DISCUSSIONS

Energetic performance of the proposed plant along with some discussion on the sizing of the major plant components are reported in this section. The influence of major design and operating parameters on the performance of the system are reported. The performance of the gasifier obtained from Cycle-Tempo software using saw dust as biomass feed is shown in Table 2.

For this configuration, a base case is considered where the topping cycle pressure ration is 4, the turbine inlet temperature is 1000°C and generator temperature of VAR cycle is 120°C (rp=4 ,TIT=1000°C and TG=120°C). The performance of the plant at the base case is shown in Table 3. This plant is capable of producing 100 kW electrical power and a refrigeration effect equals to 37.5 TR at base case.

TABLE 2. Performance of the gasifier model and experimental result of Ankur gasifier (experimental)

Gas Composition (% mole fraction)	Present Model	Ankur Gasifier
H_2	21.44	18±3
CO	22.14	19±3
CO_2	10.57	10±3
CH_4	0.54	Upto 3
N_2	39.09	45-50
H_2O	5.76	------
Air-fuel Ratio	1.6	1.5-1.8
LHV (MJ/kg)	5.04	4.40-5.40
Gasification efficiency (%)	82	78-80

TABLE 3. Base Case Performance of the proposed Configurations

Parameter	Unit	Value
GT net Output	kWe	100
Topping Cycle Electrical Efficiency	%	24.545
ESBC	kg/kWh	0.8931
Required Air flow through GT unit	kg/s	0.532
Capacity of Refrigeration	TR	37.5
COP of VAR cycle	-	0.56
FESR	%	48.26

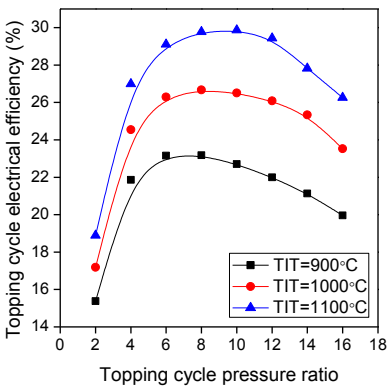

FIGURE 2. Variation of Topping GT cycle efficiency with Pressure Ratio

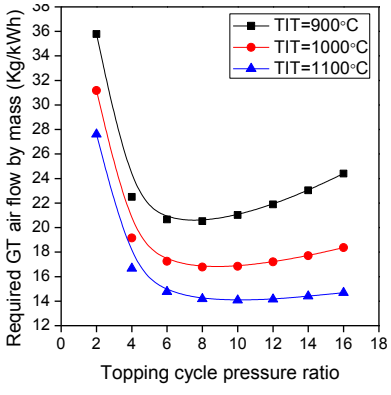

FIGURE 3. Variation in Required Air Flow by Mass, through Topping Cycle with Pressure Ratio

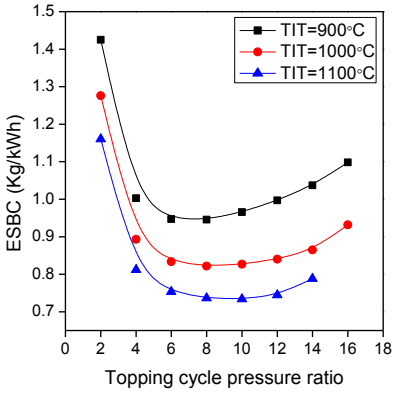

FIGURE 4. Variation in ESBC with Topping Cycle Pressure Ratio

The performance of the plant is found to be influenced greatly by the variations in topping cycle pressure ratio and gas turbine inlet temperature. The variation in topping GT cycle power efficiency with topping cycle pressure ratio at different gas turbine inlet temperatures is shown in Fig. 2. Electrical efficiency of the topping cycle initially increases with increase in topping cycle pressure ratio and then decreases for a fixed TIT as shown in Fig. 2. This is due to fact that the value of specific work output from topping cycle increases upto a certain pressure ratio and then decreases with further increase in pressure ratio. Fig. 2 also indicates that higher TIT results in higher topping cycle efficiency. The maximum efficiency point shifts slightly towards the right as the TIT increases. Now, the net work output from the topping GT cycle is considered to be fixed (100kW) for the present study. It is found that when the pressure ratio increases, the required air consumption (by mass) of the topping cycle initially decreases, gets minimized at a certain range of pressure ratio (8-10), depending on TIT. After then the same increases with increase in pressure ratio, as shown in Fig. 3. This ultimately results in the required ESBC to decrease initially and then to increase with increase in pressure ratio as shown in Fig. 4.

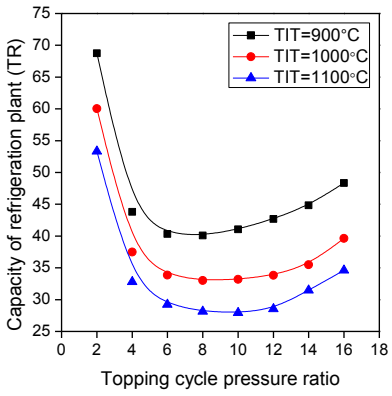

FIGURE 5. Variation in TR with Topping Cycle Pressure Ratio

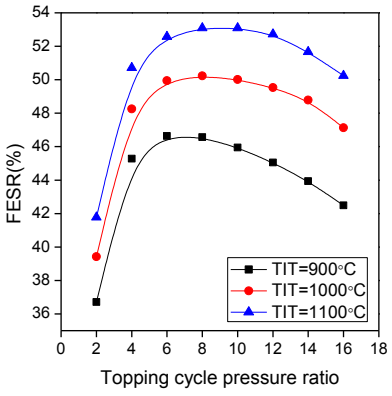

FIGURE 6. Variation in FESR with Topping Cycle Pressure Ratio

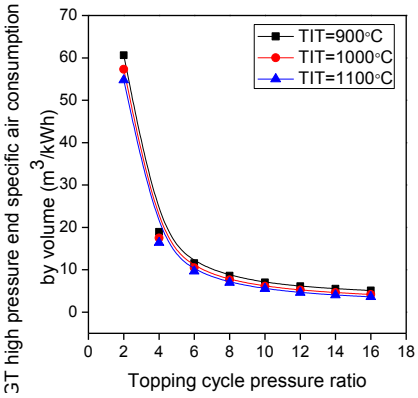

FIGURE 7. Variation in GT high pressure end air consumption by volume with r_p

The performance of the refrigeration plant is greatly influenced by topping GT cycle pressure ratio and TIT. The refrigeration capacity (TR) of the VAR cycle initially decreases upto a certain pressure ratio and then increases with increase in pressure ratio, as shown in Fig. 5. It is also evident from Fig. 5 that the TR of VAR cycle decreases with increase in TIT at particular pressure ratio as the biomass consumption as well as required air consumption of the topping cycle is lower at higher TITs. The COP of refrigeration cycle has no change with topping GT cycle pressure ratio and TIT. The COP of refrigeration cycle is 0.56 throughout the study.

TABLE 4. Performances of the Plant and Sizing of the Heat Exchangers at Different Operating Conditions

Performance Parameters	**Scenario 1: r_p=8, TIT=900°C**				**Scenario 2: r_p=8, TIT=1000°C**				**Scenario 3: r_p=10, TIT=1100°C**			
Required Biomass Flow rate (kg/s)	0.02627				0.02283				0.02039			
Required Air Flow Rate (kg/s)	0.570				0.466				0.391			
Topping Cycle Electrical Efficiency (%)	23.18				26.67				29.86			
Refrigeration capacity (TR)	40				33				27.92			
FESR (%)	46.57				50.23				53.09			
Sizing of the Heat Exchangers	**ΔT_H (K)**	**ΔT_L (K)**	**Q_{tran} (kW)**	**UA (kW/K)**	**ΔT_H (K)**	**ΔT_L (K)**	**Q_{tran} (kW)**	**UA (kW/K)**	**ΔT_H (K)**	**ΔT_L (K)**	**Q_{tran} (kW)**	**UA (kW/K)**
Gas to Air Heater (Block 6)	92.51	185.5	384.1	2.87	73.3	185.4	369.3	3.05	23.74	146.6	340.3	5.043
HRSG Evaporator (Block 10)	349.6	10.0	234	2.45	349.4	10.0	192.8	2.02	349.3	10.0	163	1.706
HRSG Economiser (Block 12)	10.0	18.0	11.96	0.88	10.0	18.0	9.86	0.72	10.0	18.0	8.33	0.612
AAR Generator (Block 13)	13.5	16.0	245.9	16.7	13.5	16.0	202.7	13.7	13.5	16.0	171.3	11.63
AAR Condenser (Block 15)	25.0	21.16	168.8	7.33	25.0	21.16	139.1	6.04	25.0	21.16	117.6	5.106
AAR Evaporator (Block 18)	4.67	8.23	140.3	22.34	4.67	8.23	115.6	18.41	4.67	8.23	97.72	15.56

The variation in fuel energy saving ratio (FESR) with topping GT cycle pressure ratio is shown in Fig.6. The FESR increases with toping cycle pressure ratio upto a certain pressure ratio (6-10) and then decreases with further increase in pressure ratio. The FESR indicates the performance of proposed combined plant. The trend of this graph is same as followed by topping GT cycle power efficiency (Fig.2) but the maximum fuel energy saving occurs at a point which has little difference with GT cycle maximum efficiency.

The required topping cycle air flow rate influences the size of the gas turbine also. The size of the high pressure end of the turbine is determined by specific air consumption by volume and low pressure end of the turbine is determined by the specific air consumption by mass [4]. The size of the tubing's of CHX unit is also determined from specific air consumption by volume trough topping GT cycle. Fig. 7 shows the variation in required air consumption by volume with topping cycle pressure ratio for GT high pressure end to predict the sizes. It is seen from Fig. 7 that the size of the turbine decreases with increase in pressure ratio as well as with higher TITs.

The performance of the plant along with sizing of the heat exchangers used in this plant is shown in Table 4 at different TITs. Sizing of the heat exchanger (block 6) of CHX unit increases with increase in gas turbine inlet temperature because of the log mean temperature difference (LMTD) decreases rapidly with increase in the same. The rate of heat transfer to the topping cycle decreases with increase in gas turbine inlet temperature. The LMTD of the other heat exchangers increases or remain same at different TITs. This ultimately effects the size of other heat exchangers to decrease with increase in gas turbine inlet temperature.

CONCLUSION

This paper presents the performance study of biomass gasification based indirectly heated combined power and refrigeration plant. An ammonia-water absorption refrigeration plant is integrated with a gas turbine plant through the HRSG to utilize the waste heat. The system modeling is performed with the process simulation software Cycle Tempo, which allows flexibility in plant configuration and input variables. The study reveals that, topping cycle efficiency and FESR is maximized at particular values of topping cycle pressure ratio, for a fixed GT TIT. Also, higher TIT results in higher values of cycle efficiency and FESR. Again, ESBC and refrigerating effects gets minimized at particular pressure ratio value. Lower TIT results in higher refrigerating effect and ESBC. From sizing point of view, size of the GT is minimized at particular pressure ratio value and higher TIT results in lower GT size and lower size of the heat exchangers other than the heat exchanger used in CHX unit. From Thermodynamic and sizing point of view it can be concluded that, the plant can be efficiently and economically operated at pressure ratio range 7-10 and at higher GT TITs.

REFERENCES

1. B. Buragohain, P. Mahanta and V.S. Moholkar, Renewable and Sustainable Energy Reviews **14 (1)**, 73-92 (2010).
2. N.S. Barman, S. Ghosh and S. De, Bioresource Technology **107**, 505-511 (2012).
3. Ankur Scientific Energy Technologies Pvt. Ltd. Website: http://www.ankurscientific.com (Website)
4. P. Mondal and S. Ghosh, International journal of Innovative Research in Science, Engineering and Technology **3(2)**, 9285-9294 (2014).
5. S. Soltani, S.M.S. Mahamoudi, M.. Yari and M..A. Rosen, Energy Conversion and Management **70**, 107-115 (2013).
6. M.R. Yap, Biomass Integrated Gasification Combined Cycles (BIGCC), University of New Orleans Theses and Dissertations Paper 206, (2004).
7. J. Bassols, B. Kuckelkorn, J. Langreck, R. Schneider and H. Veelken, Applied Thermal Engineering **22**, 595-602 (2002).
8. P. Colonna and S. Gabrielli, Applied Thermal Engineering **23**, 381-396 (2003).
9. J.C. Bruno, J. Miquel and F. Castells, Applied Thermal Engineering **19**, 1297-1328 (1999).
10. Cycle-Tempo Software, Release 5, TU Delft, Website: http://www.cycle-tempo.nl/. (2012).

ICME2015

International Conference on Mechanical Engineering 2015
(ICME 2015) 18 – 20 December, 2015, Dhaka, Bangladesh

Paper ID : 092

Characterization of Emissions Measure and Thermal Performance of Coal-water Slurry Combustion under O_2/N_2 and O_2/CO_2 Conditions

A. A. Bhuiyan[1, 2, a)], A. Karim[3] and J. Naser [1]

[1]*Faculty of Science, Engineering and Technology (FSET), Swinburne University of Technology, VIC3122, Australia*
[2]*Department of Mechanical & Chemical Engineering, Islamic University of Technology, Gazipur-1704, Bangladesh*
[3]*Department of Mechanical Engineering, Bangladesh University of Engineering & Technology, Dhaka, Bangladesh*

[a)]Corresponding author: arafat@iut-dhaka.edu

Abstract. For energy efficient performance of the power plant, reduction of CO_2 is a challenge. Oxy-fuel combustion is suggested as a promising technology for the expected combustion performance. In order to investigate the phenomenon related to oxy-fuel technique, a physical model of a 5MWth small scale furnace is considered for the 3D combustion of coal-water slurry. Eulerian/Lagrangian model was used for gas/particle phase modeling. For combustion modeling, modified Eddy-Break-up model was considered assuming that the reaction rate is controlled by turbulent mixing. For homogeneous and heterogeneous processes, multi-steps chemical reactions scheme were implemented. WSGGM model is incorporated for radiation calculation using different absorption coefficient for air and oxy-firing cases. SIMPLE algorithm was introduced for pressure-velocity coupling for the transient simulation. The combustion cases under air firing (21% O_2/79% N_2) and O_2/CO_2 (22.2% O_2/36.1% CO_2) firing conditions were conducted. Both the cases were simulated under high pressure. Comparison between temperature (K) and streamline distributions under air-fired and oxy-fired combustion were predicted. Comparatively higher flame temperatures were observed in air firing case compared to recycled case. This is due to heavier flow of coal water slurry in later case. However, a significant increase in the CO_2 concentrations were noted under oxy-fuel combustion conditions. Opposite to CO_2 distribution, it was observed that CO mass fraction for first case was comparatively higher due to higher flame temperature.

INTRODUCTION

In order to reduce the CO_2 emissions and to improve the furnace life, there are several CO_2 capturing technology such as pre-combustion, post-combustion and oxy-fuel combustion [1-4]. Implementation of oxy-fuel combustion is suggested as the efficient option considering its CO_2 capturing capability. Researchers have concentrated to the investigation and the development of oxy-fuel technology experimentally as well as numerically in pilot/laboratory scale and industrial scale for various fuel resources [5-9]. CFD technique provides the opportunity to investigate in details, the combustion phenomena and contaminant development inside the furnace [10, 11]. Also, to the best of author's knowledge, modeling in slagging type combustor shown limited progress in the literature compared to conventional combustion [12]. The study of Chen [13] presented the characteristics of pressurized oxy-coal combustion showing temperature distribution, radiation intensity and coal burning reactions with increasing swirl number (in the range of 0-0.78). Further studies [14-17] concentrated the 3D slag modeling in similar type of combustor. The detailed emissions levels were not highlighted in these studies. In this study, oxy-fuel concept is considered to investigate the effect of coal water-slurry type fuel combustion. Hence, the main objective of this study is to explore the associated emissions level phenomena for combustion of coal mixed with water in a small scale slagging type combustor. This paper will present the fundamental difference between different combustion environment such as air-firing and oxy-firing cases for similar type of combustor. AVL Fire ver. 2009.02 with some user-defined code will be used for the modeling purpose.

FURNACE GEOMETRY AND FUEL PROPERTIES

The physical model of 5MWth coal water slurry scaled combustor given in Ref. [13, 18] was considered in this study. The schematic diagram of the furnace with major components was shown in Fig. 1. A burner is mounted at the center of the front end of the combustor for facilitating the coal/oxidizer flow in to the reaction zone. As the fuel is mixed with water, an atomizer is attached with the burner design. The position of the atomizer is at a small distance down from the burner center. The oxidant flow consist of recycled flue gas such as O_2, N_2, CO_2, H_2O are stabilized by a constant swirling flow to the furnace. The fuel properties used for this study were given in Table 1. For coal, the particles mean diameter of 200μm was used for both air-firing and oxy-fuel cases.

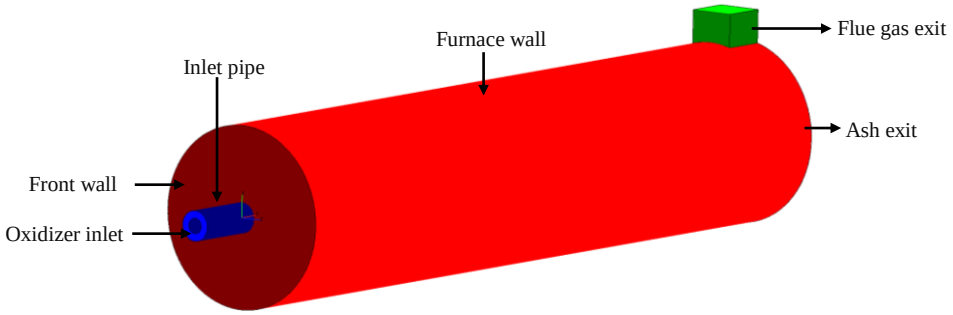

FIGURE 1. Physical model used for coal-water slurry combustion modeling in a small scale furnace.

TABLE 1. Coal-water slurry properties and particle data used for the modeling of combustion under different conditions

Proximate analysis (wt%,ar)		**Ultimate analysis (wt%,ar)**	
Moisture content	6.40	Carbon, C	82.10
Ash content	7.00	Hydrogen, H	05.40
Volatile matter	33.1	Nitrogen, N	01.40
Fixed carbon	53.5	Sulphur, S	00.60
HHV, MJ/kg	29.15	Oxygen, O	11.46

BOUNDARY CONDITIONS AND CASES

The different operating conditions were characterized by air-firing and oxy-firing cases. The compositions of O_2, N_2, CO_2 and H_2O for both the cases are presented in Table 2. For all cases, a constant temperature and high pressure were maintained for oxidizer and atomizer flows. The coal-water slurry mass flow rate is maintained at 0.1 (kg/s) for all the cases simulated. For stability and better mixing of the flow, a constant swirl number of 0.8 was used. For wall, no-slip boundary conditions were assumed and constant wall temperature and emissivity were used for the furnace. At the flue gas and molten ash exit of the furnace, zero gradient for all the variables are assumed.

TABLE 2. Boundary conditions/parameters for different coal-water slurry combustion cases

Cases	**Flow conditions**			**Oxidizer compositions**				**Coal supply conditions**		
	Q (kg/s)	T (K)	P (bar)	O_2 (%)	N_2 (%)	CO_2 (%)	H_2O (%)	T (K)	P (bar)	Q (kg/s)
Air	1.12	305	4.0	0.21	0.79	0.00	0.00	62	15	0.1
Oxy	1.13	305	4.0	0.22	0.037	0.36	0.38	62	15	0.1

NUMERICAL DESCRIPTION

In this study, three dimensional CFD simulation of coal-water slurry combustion is carried out by a commercial CFD code, AVL Fire version.2009.2. To demonstrate the applications of combustion modelling in CFD, a detailed description of the used model is given in [19]. Eulerian/Lagrangian approach is considered for the modelling of fluid

flow. The energy balance equation for radiative and convective heat transfer is used for tracking the particles temperature is given in the following equation:

$$m_p C_{p,p} \frac{dT_p}{dt} = \pi d_p{}^2 . \left(h\left(T_g - T_p\right) + \epsilon_p \sigma \left(T_w{}^4 - T_p{}^4 \right) \right) \quad (1)$$

In this study, Eddy Breakup (EBU) model, a typical mixed-is-burnt combustion model is applied for all the combustion modelling cases. This model determines whether O_2/fuel is in limiting condition or not. The detail of this turbulence controlled combustion model is given in Ref. [10]. This can be expressed by the following equation:

$$\overline{\rho \dot{r}}_{fu} = \frac{C_{fu}}{\tau_R} \bar{\rho} \min \left(\bar{y}_{fu}, \frac{\bar{y}_{ox}}{S}, \frac{C_{pr} \bar{y}_{pr}}{1+S} \right) \quad (2)$$

For turbulence, k-ε model is used for cold and reacting flow [20, 21]. Regarding chemical reactions, three steps homogeneous and heterogeneous chemical reactions [22, 23] are considered as shown in Table 3. Appropriate rate constant for these process were used. SIMPLE algorithm [24, 25] is used for the pressure velocity coupling. A general convergence criterion of absolute residual value set to 10^{-4} for all the variables considered. In order to achieve the level of confidence, grid with 4.65×10^5 cells is considered with minimum computational time with reasonable accuracy in the present study.

TABLE 3. Chemical reactions for devolatilisation and char oxidation modeling.

Reaction steps	Devolatilisation (Homogeneous)	Char combustion (Heterogeneous)
Step-1	$CH_4 + O_2 \rightarrow CO + H_2 + H_2O + \text{Heat}$	$C_{char} + 0.5O_2 \rightarrow CO + \text{Heat}$
Step-2	$CO + H_2O \leftrightarrows CO_2 + H_2$	$C_{char} + CO_2 \rightarrow 2CO$
Step-3	$O_2 + 2H_2 \leftrightarrows 2H_2O$	$C_{char} + H_2O \rightarrow CO + H_2$

RESULT AND DISCUSSION

In this study, thermal and emission characteristics of coal-water slurry combustion has been investigated considering different combustion environment. Results are presented based on flow and temperature distribution, species distribution such as CO_2, O_2, H_2, CO, H_2O and char mass fraction etc. Figure 2 presents the flow distribution of the oxidizer, gas temperature distributions, O2 and associated CO_2 concentration contours for air-firing and oxy-firing cases. These four parameters are closely related to each other. Prediction of mass fraction (kg/kg) distribution of CO_2 and O_2 are important phenomena in oxy-fuel cases which contribute to the heat transfer, flame temperature characteristics. With the presence of higher O_2 in oxy-case, an increase in gas temperature is expected. But a significant decrease in the gas temperature is observed. This can be explained on the basis of higher amount of H_2O and CO_2 fraction having higher heat capacity in the latter case. This dampens the characteristics of better oxidizing capability of O_2 in oxy-firing case. The velocity distribution along the reactor length is presented and no significant variation is observed as mentioned in the flow boundary condition in Table 2. Comparatively lower recirculation is visualized in oxy-firing case which is responsible for lower residence time leading to lower mixing of the fuel with coal. The visualization of temperature shows that peak value is found too far from the burner exit in both cases. This is due to slagging phenomena of the fuel having higher fraction of H_2O in slurry compositions compared to dry coal. As the fuel is not properly burnt, that's why availability of excess oxygen is there compared to air-firing case. The peak temperature for air and oxy-firing cases were found 2085 and 1905 K respectively.

The carbon monoxide (CO), hydrogen (H_2) and water vapour (H_2O) mass fraction (kg/kg) distribution in the direction of furnace length for all the cases considered in this study are presented in figure 3. Based on the chemical reaction mechanism considered and presented in Table 3, different species concentration is formed. The first figure represents the CO mass fraction distribution for both the cases. The decrease in the CO concentrations of the latter case was due to the lower gas temperature of the combustion cases. The gas temperature levels in the air-fired case affected the CO concentrations in the flame regions. The peak CO values expected in the flame region were convoyed by the lowest CO_2 values. The generation of CO mass fraction can be demonstrated by the mechanism of

Boudouard reaction given in [26]. It is observed that H_2 concentration is higher for oxy-firing cases. For air-fired case, lower value of H_2 is found. From the profile of H_2 and O_2 mass fraction, it can be concluded that there is a definite relation between the formation of H_2 and the O_2 concentration.

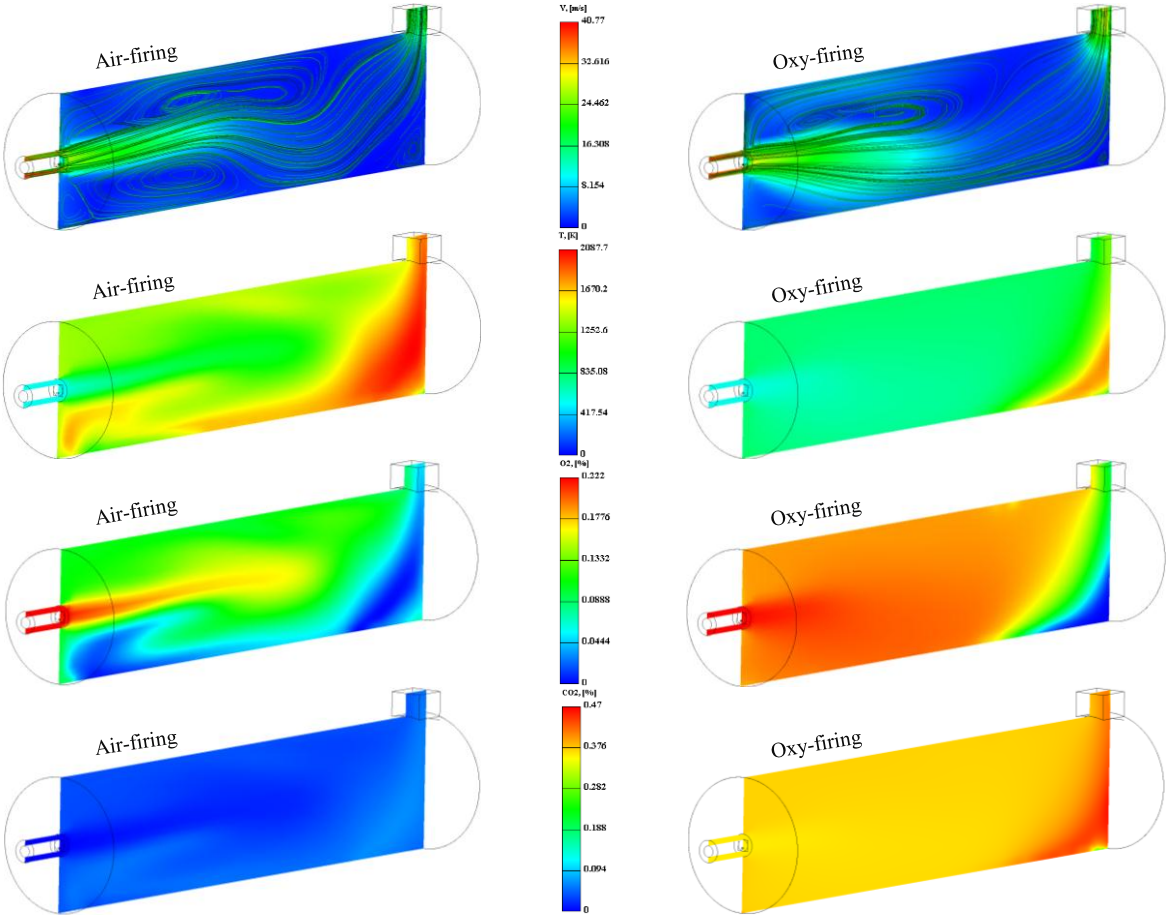

FIGURE 2. Velocity (m/s), temperature (K), oxygen (O_2) and Carbon dioxide (CO_2) mass fraction (%) distribution for different cases

Figure 3 also represents the water vapor mass fraction (kg/kg) distribution for the selected cases in this study. It is seen from the figure that highest value of the water fraction is found in the furnace bottom. The coal-water slurry particles are injected into the furnace which is further entrained on the wall. That's way comparatively higher H_2O is predicted in the bottom zone. Figure 3 also characterizes the mass fraction of char particles in the reactor. Particle tracking mechanism represents that char particles are moving in the bottom part of the reactor due to forces acting on it. The heated particles are burned in the later part of the furnace. The rapid reduction of oxygen concentration in the furnace negatively affected the oxidation of the residual char in the remaining part of the furnace. That's why comparatively higher order of char fraction is predicted in oxy-firing case due lower reduction of O2 as presented.

CONCLUSION

This study presents a CFD modelling study considering coal-water slurry combustion in a 5MW small scale furnace. The characteristic of combustion under air firing and oxy-firing condition was investigated. No significant variation was observed in the flow field; however a decrease temperature was predicted in the range of 150-200 K. This mainly due to presence of CO_2 and H_2O in the latter case. Different species concentrations such as O_2, CO_2, H_2O, H_2, CO were evaluated for both the cases. It was also predicted that burning of char mass particle is delayed in

oxy-firing case compared to air-firing case leading to lower temperature and lower CO generation. Overall, this study will provide a guideline for coal-water slurry type fuel combustion in a typical power plant.

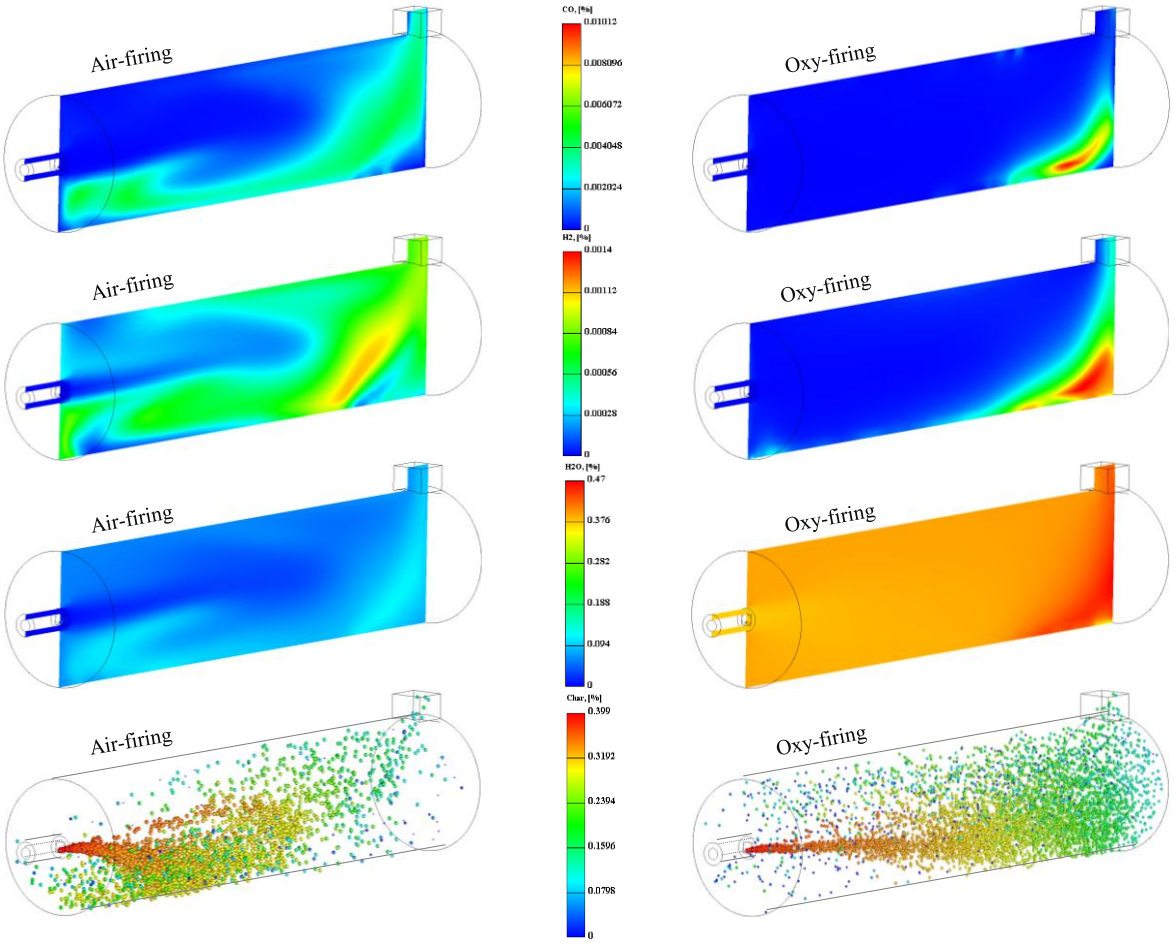

FIGURE 3. Carbon monoxide (CO), Hydrogen (H2), water vapor and char mass fraction (%) distribution for different cases

REFERENCES

1. A.H. Al-Abbas, J. Naser, D. Dodds, "CFD modelling of air-fired and oxy-fuel combustion in a large-scale furnace at Loy Yang A brown coal power station", *Fuel*, 102 (2012) 646-665.
2. A.H. Al-Abbas, J. Naser, E.K. Hussein, "Numerical simulation of brown coal combustion in a 550MW tangentially-fired furnace under different operating conditions", *Fuel*, 107 (2013) 688-698.
3. A.H. Al-Abbas, J. Naser, D. Dodds, A. Blicblau, "Numerical Modelling of Oxy-Fuel Combustion in a Full-Scale Tangentially-Fired Pulverised Coal Boiler", *Procedia Engineering*, 56 (2013) 375-380.
4. A.H. Al-Abbas, J. Naser, "Computational Fluid Dynamic Modelling of a 550 MW Tangentially-Fired Furnace under Different Operating Conditions", *Procedia Engineering*, 56 (2013) 387-392.
5. A.A. Bhuiyan, J. Naser, "Computational modelling of co-firing of biomass with coal under oxy-fuel condition in a small scale furnace", *Fuel*, 143(0) (2015) 455-466.
6. A.A. Bhuiyan, J. Naser, "CFD modelling of co-firing of biomass with coal under oxy-fuel combustion in a large scale power plant", *Fuel*, 159 (2015) 150-168.
7. A.A. Bhuiyan, J. Naser, "Numerical Modeling of Biomass Co–combustion with Pulverized coal in a Small Scale Furnace", *Procedia Engineering*, 105(0) (2015) 504-511.

8. M.R. Karim, J. Naser, "Progress in Numerical Modelling of Packed Bed Biomass Combustion", in: *19th Australasian Fluid Mechanics Conference (19 AFMC),* Australasian Fluid Mechanics Society, 2014.
9. A.A. Bhuiyan, J. Naser, "Thermal characterization of coal/straw combustion under air/oxy-fuel conditions in a swirl-stabilized furnace: a CFD modelling", *Applied Thermal Engineering*, 2016.
10. A.A. Bhuiyan, J. Naser, "Numerical modelling of oxy fuel combustion, the effect of radiative and convective heat transfer and burnout", *Fuel*, 139(0) (2015) 268-284.
11. A.A. Bhuiyan, J. Naser, "Effect of recycled ratio on heat transfer performance of coal combustion in a 0.5MWth combustion test facility", in: *19th Australasian Fluid Mechanics Conference Melbourne*, Australia, 2014.
12. A.A. Bhuiyan, J. Naser, "Modeling of Slagging in Industrial Furnace: A Comprehensive Review", *Procedia Engineering*, 105(0) (2015) 512-519.
13. L. Chen, M. Gazzino, A.F. Ghoniem, "Characteristics of pressurized oxy-coal combustion under increasing swirl number", in: *Proceedings of the 35th international technical conference on clean coal & fuel systems*, 2010.
14. L. Chen, S.Z. Yong, A.F. Ghoniem, "Modeling the slag behavior in three dimensional CFD simulation of a vertically-oriented oxy-coal combustor," *Fuel Processing Technology*, 112 (2013) 106-117.
15. L. Chen, A.F. Ghoniem, "Development of a three-dimensional computational slag flow model for coal combustion and gasification", *Fuel*, 113 (2013) 357-366.
16. S.Z. Yong, A. Ghoniem, "Modeling the slag layer in solid fuel gasification and combustion–Two-way coupling with CFD", *Fuel*, 97 (2012) 457-466.
17. S.Z. Yong, M. Gazzino, A. Ghoniem, "Modeling the slag layer in solid fuel gasification and combustion–Formulation and sensitivity analysis", *Fuel*, 92(1) (2012) 162-170.
18. J. Hong, G. Chaudhry, J. Brisson, R. Field, M. Gazzino, A.F. Ghoniem, "Analysis of oxy-fuel combustion power cycle utilizing a pressurized coal combustor", *Energy*, 34(9) (2009) 1332-1340.
19. A.A. Bhuiyan, M.R. Karim, J. Naser, "Modeling of Solid and Bio-Fuel Combustion Technologies", in: M.M.K.K.M.S. Hassan (Ed.) *Thermofluid Modeling for Energy Efficiency Applications*, Academic Press, 2016, pp. 259-309.
20. A.A. Bhuiyan, A. Islam, M. Amin, "Numerical study of 3D thermal and hydraulic characteristics of wavy fin-and-tube heat exchanger", *Frontiers in Heat and Mass Transfer (FHMT)*, 3(3) (2012).
21. A.A. Bhuiyan, M.R. Amin, J. Naser, A. Islam, "Effects of geometric parameters for wavy finned-tube heat exchanger in turbulent flow: A CFD modelling", *Frontiers in Heat and Mass Transfer (FHMT)*, 6(1) (2015).
22. A.H. Al-Abbas, J. Naser, "Numerical study of one air-fired and two oxy-fuel combustion cases of propane in a 100 kW furnace", *Energy & Fuels*, 26(2) (2012) 952-967.
23. A.H. Al-Abbas, J. Naser, "Effect of chemical reaction mechanisms and NO x modeling on air-fired and oxy-fuel combustion of lignite in a 100-kW furnace", *Energy & Fuels*, 26(6) (2012) 3329-3348.
24. A.A. Bhuiyan, M.R. Amin, A.S. Islam, "Three-dimensional performance analysis of plain fin tube heat exchangers in transitional regime", *Applied Thermal Engineering*, 50(1) (2013) 445-454.
25. A.A. Bhuiyan, M.R. Amin, R. Karim, A.K.M. Sadrul Islam, "Plate fin and tube heat exchanger modeling: Effects of performance parameters for turbulent flow regime", *International Journal of Automotive and Mechanical Engineering*, 9(1) (2014) 1768-1781.
26. A.H. Al-Abbas, J. Naser, D. Dodds, "CFD modelling of air-fired and oxy-fuel combustion of lignite in a 100KW furnace", *Fuel*, 90(5) (2011) 1778-1795.

ICME2015

International Conference on Mechanical Engineering 2015
(ICME 2015) 18 – 20 December, 2015, Dhaka, Bangladesh

Paper ID : 093

Finite Volume Modelling (FVM) of Straw Particles Combustion in a 30 kW Swirl-stabilized Furnace under Different Oxidizing Environments

A. A. Bhuiyan[1, 2, a)], A. Karim[3] and J. Naser [1]

[1]*Faculty of Science, Engineering and Technology (FSET), Swinburne University of Technology, VIC3122, Australia*
[2]*Department of Mechanical & Chemical Engineering, Islamic University of Technology, Gazipur-1704, Bangladesh*
[3]*Department of Mechanical Engineering, Bangladesh University of Engineering & Technology, Dhaka, Bangladesh*

[a)]Corresponding author: arafat@iut-dhaka.edu

Abstract. Global warming is an issue which is related to the increase of CO_2 from fossil fuel based power generation in the developed countries. In order to reduce the greenhouse gas emissions, shifting from coal based power production to biomass energy is must. This study presents the numerical investigation of the co-firing behavior of pulverized straw particles with coal in air and O_2/CO_2 mixtures. Validation is based on experimental work in a semi-technical once-through 30 kW swirl-stabilized furnace. Reference air-fuel (21% O_2) and oxy-fuel (30% O_2) cases were considered for four different coal/straw ratios (100% coal, 20% straw, 50% straw and 100% straw). AVL Fire version 2009.2 is used as a CFD modeling tool. A comprehensive grid independency test was conducted considering three different grid sizes. Ignition performance, emission characteristics, heating profile, residence time were evaluated for different fuel ratios under air and oxy-fuel conditions. This work has shown that no significant changes occur to the fundamental combustion characteristics for straw compared to coal when burned in the O_2/CO_2 atmosphere to air firing case. It was found that with 20% straw sharing, sensible performances were observed similar to that of 100% coal combustion. Also a critical analytical analysis was conducted to investigate the heating performance for straw particle of different sizes (100µm, 330µm and 1000 µm). The heating profiles show significant differences between the three particle sizes assuming isothermal temperature gradient and heating by both radiation and convection. The possibility of burnout of the larger straw particle size is less due to less residence time in air-firing compared to oxy-firing case.

INTRODUCTION

In order to meet the demand of power crisis and to reduce GHG emissions, accumulation of biomass fuel to the regular supply of fossil fuel resource is important. Though biomass is a CO_2 neutral energy sources, but usage of biomass fuel is in the early stage of applications due to its corrosive and slagging issues[1, 2]. Only 62 countries produce electricity using biomass [3]. There are several CO_2 capturing technology available such as pre-combustion, post-combustion and oxy-fuel combustion technology [4-7]. The usage of biomass fuels in furnace with CO_2 emission reduction technique has attracted the researcher's attention. Co-combustion of coal with biomass is a relatively easy way of reducing CO_2 emissions from fossil fuel fired power plants [8]. Oxy-fuel combustion can be applied to biomass as well as coal and the use of CO_2 neutral fuels induces the potential of achieving an overall negative CO_2 emission from the power plant.

Straw is the one of the most available Biomass in the environment. Few experimental investigations have been conducted using straw as a co-fired fuel under air and oxy-fuel environments. Pedersen [9] conducted a detailed experiment on co-firing straw and pulverized coal in a 2.5 MWt pilot-scale burner where fractions of straw in the range of 0-20% on a thermal basis were used in the full-scale experiment and 0-100% on a thermal basis in the pilot-scale experiment. They found that with the increase in fraction of straw in the blend reduces NO and SO_2 emissions. Recent study given in Ref [10] presented the experimental study by introducing biomass in carbon capture power

plants for the combustion of coal and biomass combustion in air and oxy-fuel atmospheres in a swirl stabilized furnace. In another analysis of Kate given in Ref. [11], co-firing coal and straw in a 150MWe power station, has been demonstrated. Karin conducted the experiments on the deposit formation in a 150 MWe Utility PF-boiler during co-combustion of coal and straw at the Danish energy company [12].

CFD technique provides the opportunity to investigate in details, the combustion phenomena and contaminant development inside the furnace. Few researchers attempt to simulate the three dimensional large scale tangentially fired power generation plants using CFD [13-15]. This study presents the fundamental information on straw combustion with coal in a swirl stabilized furnace. AVL Fire ver. 2009.02 with some user-defined code will be used for the modeling purpose. This study will provide a comprehensive guideline for retrofitting a dedicated coal based power plant using renewable fuel sources with CO_2 capturing technology.

PHYSICAL MODEL DETAILS

Furnace geometry and fuel properties

The schematic diagram of the 30 kW vertical furnace is shown in figure 1. The furnace has an inner diameter of 0.315 m and a height of about 1.9 m. On the furnace wall, there are total 8 measuring ports for the measurement of temperature and emissions level. A swirled stabilized burner is mounted on top of the reactor. There are three tubes in the burner, two for primary and secondary oxidant and a separate natural gas inlet. The primary oxidant flow is given directly into the central burner tube. Fuel particles are supplied into the central, primary burner tube. In the present study, coal and straw particles were combusted under different oxidizing conditions. The fuel properties were given in Table 1. The constant total thermal load is settled based on the experimental study [10] considered.

TABLE 1. Fuel properties and particle data used for the modelling of co-firing in a 30kW furnace under different conditions

Proximate analysis (wt%,ar)			Ultimate analysis (wt%,ar)		
	Coal	**Straw**		**Coal**	**Straw**
Moisture	5.03	5.10	Carbon, C	80.70	48.62
Ash	9.62	4. 40	Hydrogen, H	5.41	6.41
Volatile	34.86	72.40	Nitrogen, N	1.69	0.49
Fixed carbon	50.4	18.10	Sulphur, S	0.726	0.094
HHV, MJ/kg	27.09	16.40	Chlorine, Cl	0.016	0.419
Particle size	47	330	Oxygen, O	11.46	43.97

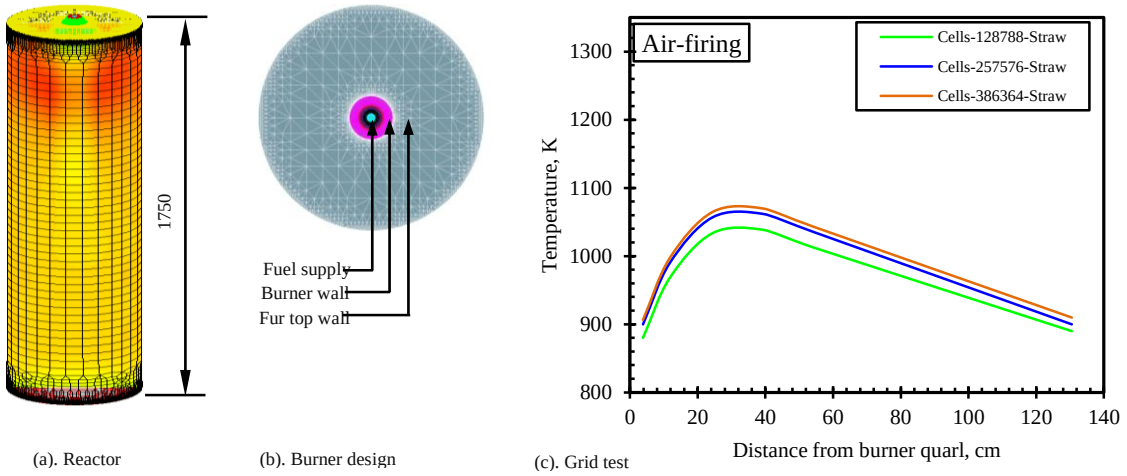

(a). Reactor (b). Burner design (c). Grid test

FIGURE 1. Schematic design of (a) 30kW solid fuel reactor,(b). Burner design and (c) Grid sensitivity result for air firing case.

Boundary conditions and cases

This numerical study has been conducted at several combustion and co-firing conditions. The boundary conditions and data were based on the experimental study of coal/straw combustion given in Ref. [10]. Total four different fuel compositions having different co-firing ratios have been considered. These are 100% coal, 20% straw with 80% coal, 50% straw with 50% coal and 100% straw. The boundary data and property values for determining the heating profile of different sizes of straw particles are given in Table 2. The investigated combustion environments are air-firing and 30% oxy-fuel cases. The operating parameters such as fuel flow and oxidizing flow distributions for different cases were presented in Table. The stoichiometric ratios chosen for this investigation is in the range of 1.19 to 1.30. The swirl number is kept constant at value of 1.8. This is due to stabilization of the flow conditions for both air and oxy-fuel conditions. The boundary condition for different co-firing ratios under air and oxy-firing cases is given in Table 3.

TABLE 2. Boundary data and properties values used for calculation of heating profile for different size of straw particles.

$C_{p,p}$ J/kg.K	$T_{p,0}$ K	ε_p	σ W/m^{2}K^4	Tw °C	P_p, kg/m^3	P_r	Λ_g, W/mK	P_g, kg/m^3	g m/s^2
1000	298	0.85	$5.57X10^{-8}$	1000	500	1.0	0.09	0.3	9.81

TABLE 3. Boundary conditions/parameters for different coal/biomass combustion under air-firing and oxy-fuel conditions

Fuel	Fuel flow Kg/hr	Stoichiometric ratios, λ		Oxidant flow, kg/hr	
		Air-firing	Oxy-fuel	Air-firing	Oxy-fuel
100% Coal	3.99	1.19	1.3	390	620
20% blend	4.33	1.19	1.3	390	620
50% blend	5.00	1.20	1.3	390	615
100 % Straw	6.60	1.22	1.3	390	600

NUMERICAL DESCRIPTION

Combustion methodology

In this study, the combustion methodology used for the modelling of co-firing under air and oxy-fuel combustion has been given in author's previous papers for coal [16-18] and biomass [3, 8, 19, 20] combustion modelling. Eulerian/Lagrangian framework is used for the gas and particle phase modelling. Heat and mass transfer, particle trajectories, turbulence were taken into account by using some source term in the governing equation. Devolatilization and char oxidation were modelled by Badzioch and Hawksley model [21] and global power-law [3]. Three steps chemical reaction modelling is used for homogeneous and heterogeneous phase modelling [22]. The energy balance equation for radiative and convective heat transfer is used for tracking the particles temperature is given in the following equation:

$$m_p C_{p,p} \frac{dT_p}{dt} = \pi {d_p}^2 . \left(h\left(T_g - T_p\right) + \epsilon_p \sigma \left({T_w}^4 - {T_p}^4\right)\right) \quad (1)$$

$$m_p = \frac{\pi}{6} {d_p}^3 \rho_p, h = \frac{Nu\lambda_g}{d_p}, Nu = 2 + mRe_p{}^{.5} . Pr^{.33}, Re_p = \frac{\rho_g u_t d_p}{\mu_g} \quad (2)$$

Validation and grid analysis

In order to reduce the computational time, a comprehensive grid independency test was conducted for the present modelling. Total three grid sizes having number of cell 128788, 257576 and 386364 is considered. A comprehensive analysis as shown in figure 1(c) concludes that the grid size having number of cell 257576 is optimum for further investigation with minimum computational time. The confidence of the numerical study was achieved by comparing the numerical data with the experimental data for different co-firing cases under air-firing and oxy-fuel conditions. Figure 2 shows the comparison of the centreline temperature for both the cases. It is seen from the figures that peak

flame temperatures were observed close to the burner area. For oxy-fuel case, slightly higher temperatures are predicted compared to air-firing. While comparing numerical to experimental data, it was found that variation is within 5% error range.

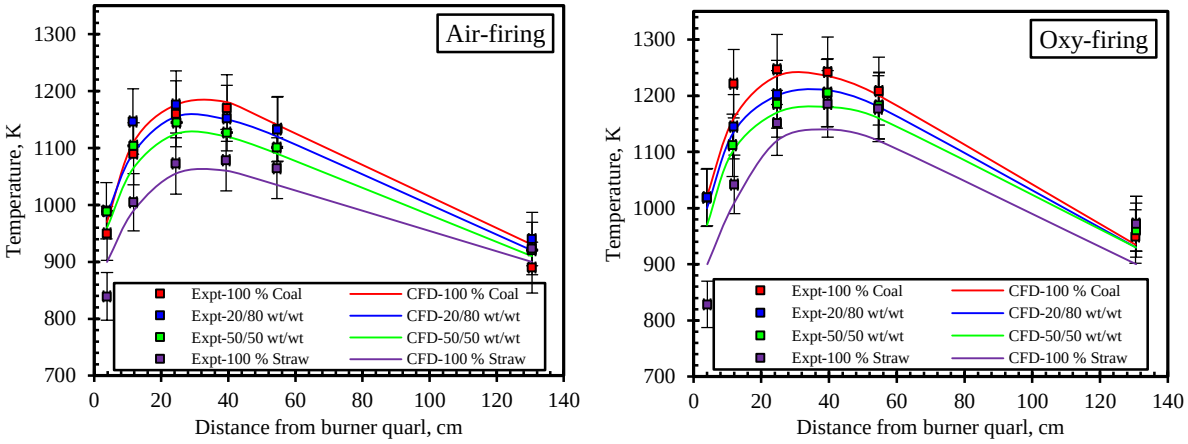

FIGURE 2. Comparison of centerline temperatures for different fuel ratios under air to oxy-firing cases.

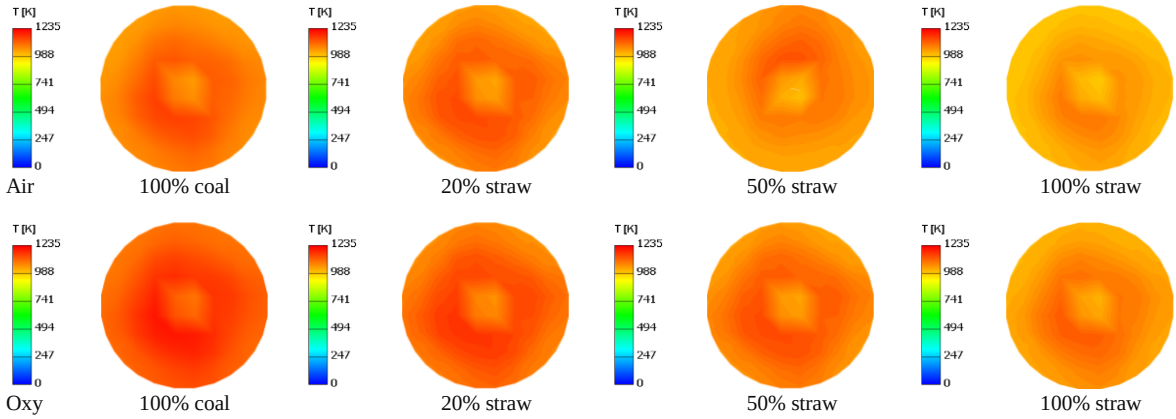

FIGURE 3. Temperature distributions for different co-firing ratios under air to oxy-fuel conditions.

RESULT AND DISCUSSION

Temperature mapping for different co-firing cases

As mentioned earlier that this study was presented four different fuel compositions. So there is a definite variation between the performance of the usage of different fuels such as 100% coal, 20 % and 50 % coal/straw blends, and 100% straw cases. Variation can be observed in terms of the ignition characteristics, flame shape, and temperature profiles. Figure 3 characterizes a comparison of the flame temperature for different cases. The CFD visualization is shown at a position of 0.5 m from the burner exit. It was found that with the increase of straw contribution, peak flame temperature leading to lower value. This can be explained on the basis of higher volatile content and lower heating value. With the increase of straw sharing, volatile fraction increase. The dominant effect of the lower calorific value of straw depresses the effect of volatile content. Thus the principal effect of the lower calorific value of straw is to lower the flame temperature. But compare to air-firing case, a distinct observation is predicted for selected oxy-fuel case. As oxy-fuel case provides better flow mixing compared to air-firing case providing presence of high concentration of O_2 at lower flow rate.

Heating profiles for different sizes of straw particles

Figure 4 shows heating profile for air-firing and oxy-fuel cases for the straw particle sizes of 100 µm, 330 µm and 1000 µm. The heating profile is estimated by using equation (1). The particle temperature along the furnace centerline is taken from numerical result. The different properties and boundary values for the determination of heating profile is given in Table 2. It is found that for different particle sizes, significant variation is observed in heating profile along the reactor centerline. For the first two cases, maximum temperatures were reached very close to the burner exit. But for larger particles, an increased temperature gradient is predicted. Table 4 shows average particle velocities of the investigated particle sizes and their residence time within the furnace. This was predicted at the exit of the furnace. The results clarify the cases when with large straw particles combusted inside the furnace and comparatively lower burnout is observed since the residence time is very limited. Due to the smaller flue gas flow during oxy-fuel combustion the residence time is longer and hence the burnout should increase. The increase in the particle velocity of large particles compared to the smaller size is responsible for less residence time inside the furnace.

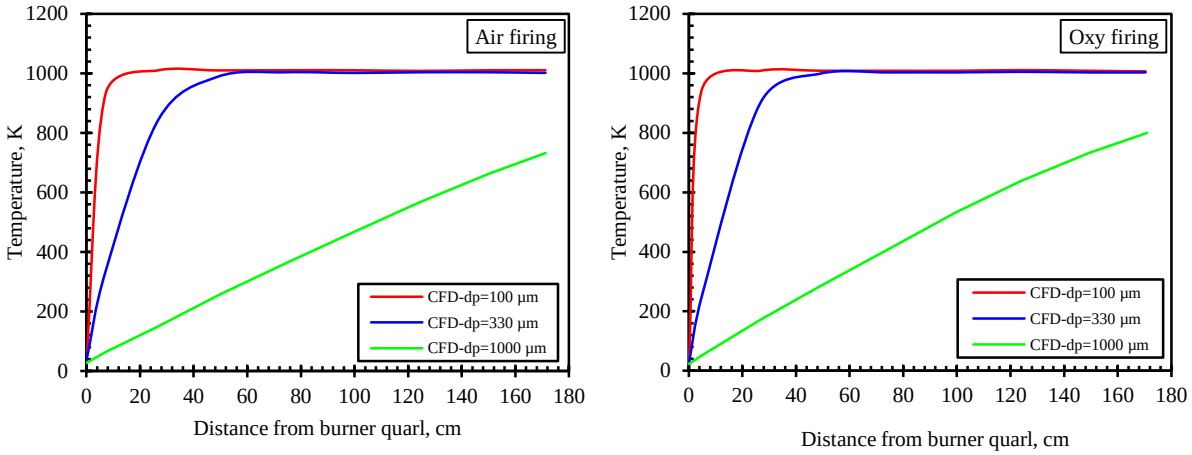

FIGURE 4. Heating profiles for straw particles of different size in the reference air and oxy-fuel atmospheres.

TABLE 4. Predicted particle velocity (m/s) and average residence time (s) of different size of straw particles in furnace.

D_p, (µm)	Air-firing		Oxy-fuel	
	u_t, (m/s)	T_p, (s)	u_t, (m/s)	T_p, (s)
100	0.05	2.42	0.05	3.25
330	0.59	1.38	0.61	1.58
1000	2.61	0.53	2.34	0.61

CONCLUSION

This study presents the coal/straw co-firing modeling under air firing and oxy-firing condition to investigate the combustion performance in a 30kW swirl-stabilized furnace. Validation was achieved by comparing the centerline temperature profile for all the cases considered. Overall, a good agreement was observed and the variation is acceptable. With the increase of straw sharing, flame temperature is significantly reduced. But a similar flame pattern is observed for lower sharing of straw (20% sharing) to the only coal combustion. The heating profiles for different size of straw particle suggest that there is a definite influence on the overall performance of the furnace. Larger particle do not ignite properly due to lower residence time leading to lower burnout.

REFERENCES

1. M.R. Karim, J. Naser, "Progress in Numerical Modelling of Packed Bed Biomass Combustion", in: *19th Australasian Fluid Mechanics Conference (19 AFMC)*, Australasian Fluid Mechanics Society, 2014.

2. A.A. Bhuiyan, J. Naser, "Modeling of Slagging in Industrial Furnace: A Comprehensive Review", *Procedia Engineering*, **105(0**), 512-519(2015).
3. A.A. Bhuiyan, J. Naser, "CFD modelling of co-firing of biomass with coal under oxy-fuel combustion in a large scale power plant", *Fuel*, **159** 150-168,(2015).
4. A.H. Al-Abbas, J. Naser, D. Dodds, "CFD modelling of air-fired and oxy-fuel combustion in a large-scale furnace at Loy Yang A brown coal power station", *Fuel*, **102,** 646-665 (2012).
5. A.H. Al-Abbas, J. Naser, E.K. Hussein, "Numerical simulation of brown coal combustion in a 550MW tangentially-fired furnace under different operating conditions", *Fuel*, **107,** 688-698(2013).
6. A.H. Al-Abbas, J. Naser, "Numerical study of one air-fired and two oxy-fuel combustion cases of propane in a 100 kW furnace", *Energy & Fuels*, **26(2)** 952-967 (2012).
7. A.H. Al-Abbas, J. Naser, D. Dodds, "CFD modelling of air-fired and oxy-fuel combustion of lignite in a 100KW furnace", *Fuel*, **90(5)** 1778-1795 (2011).
8. A.A. Bhuiyan, J. Naser, "Numerical Modeling of Biomass Co–combustion with Pulverized coal in a Small Scale Furnace", *Procedia Engineering*, **105(0)** 504-511(2015).
9. L.S. Pedersen, D.J. Morgan, W.L. Van De Kamp, J. Christensen, P. Jespersen, K. Dam-Johansen, "Effects on SOx and NOx emissions by co-firing straw and pulverized coal", *Energy and Fuels*, **11(2)** 439-446(1997).
10. M. Toftegaard, "Introducing Biomass in Carbon Capture Power Plants: Coal and Biomass Combustion in Air and OxyFuel Atmospheres - Experimental Investigations in a Swirl Burner", in *CHEC Report*, R003 (2011).
11. K. Wieck-Hansen, P. Overgaard, O.H. Larsen, "Co-firing coal and straw in a 150 MWe power boiler experiences", *Biomass and Bioenergy*, **19(6)** 395-409 (2000).
12. K.H. Andersen, F.J. Frandsen, P.F.B. Hansen, K. Wieck-Hansen, I. Rasmussen, P. Overgaard, K. Dam-Johansent, "Deposit formation in a 150 MWe utility PF-Boiler during co-combustion of coal and straw", *Energy and Fuels*, **14(4),** 765-780(2000).
13. A.H. Al-Abbas, J. Naser, D. Dodds, A. Blicblau, "Numerical Modelling of Oxy-Fuel Combustion in a Full-Scale Tangentially-Fired Pulverised Coal Boiler", *Procedia Engineering*, **56** (2013) 375-380.
14. A.H. Al-Abbas, J. Naser, "Computational Fluid Dynamic Modelling of a 550 MW Tangentially-Fired Furnace under Different Operating Conditions", *Procedia Engineering*, **56** , 387-392(2013).
15. A.H. Al-Abbas, J. Hart, J. Naser, "Numerical investigation of pyrolysis of a Loy Yang coal in a lab-scale furnace at elevated pressures", *Heat and Mass Transfer*, **49(12)** (2013) 1725-1732.
16. A.A. Bhuiyan, J. Naser, "Numerical modelling of oxy fuel combustion, the effect of radiative and convective heat transfer and burnout", *Fuel*, **139(0)** (2015) 268-284.
17. A.A. Bhuiyan, J. Naser, "Effect of recycled ratio on heat transfer performance of coal combustion in a 0.5MWth combustion test facility", in: *19th Australasian Fluid Mechanics Conference Melbourne*, Australia, 2014.
18. A.A. Bhuiyan, M.R. Karim, J. Naser, "Modeling of Solid and Bio-Fuel Combustion Technologies", in: M.M.K.K.M.S. Hassan (Ed.) *Thermofluid Modeling for Energy Efficiency Applications*, Academic Press, 2016, pp. 259-309.
19. A.A. Bhuiyan, J. Naser, "Computational modelling of co-firing of biomass with coal under oxy-fuel condition in a small scale furnace", *Fuel*, **143(0)** (2015) 455-466.
20. A.A. Bhuiyan, J. Naser, "Thermal characterization of coal/straw combustion under air/oxy-fuel conditions in a swirl-stabilized furnace: a CFD modelling", *Applied Thermal Engineering*, 2016.
21. S. Badzioch, P.G. Hawksley, "Kinetics of thermal decomposition of pulverized coal particles", *Industrial & Engineering Chemistry Process Design and Development*, **9(4)** (1970) 521-530.
22. A.H. Al-Abbas, J. Naser, "Effect of chemical reaction mechanisms and NO x modeling on air-fired and oxy-fuel combustion of lignite in a 100-kW furnace", *Energy & Fuels*, **26(6)** (2012) 3329-3348.

ICME2015

International Conference on Mechanical Engineering 2015
(ICME 2015) 18 – 20 December, 2015, Dhaka, Bangladesh

Paper ID : 097

Computational Study of Natural Convection in Square Cavity Filled with Water and Heated from the Bottom

Aritra Chatterjee[1,a)] and Bijan Kumar Mandal[2, b)]

[1, 2] *Department of Mechanical Engineering, Indian Institute of Engineering Science and Technology, Shibpur, Howrah – 711103, West Bengal, India.*

[b)]Corresponding author: bkm375@yahoo.co.in
[a)]aritra.snape@gmail.com

Abstract. In this study a numerical investigation of steady two-dimensional laminar motion of water in an enclosed square cavity is carried out, of which the top wall is insulated and the two side walls are kept at lower temperature under cold condition. The middle section of the bottom wall is heated and thus kept at an elevated temperature while the remaining section is insulated. The streamline distributions and the temperature distributions inside the square cavity and the variations for horizontal and vertical fluid velocity along the mid height and mid length of the square cavity have been plotted for three different values of Rayleigh numbers of 100, 200 and 300 respectively. A plot of the temperature, horizontal component and vertical component of velocity at three different heights of the cavity at equal intervals has also been presented for Rayleigh numbers of 100, 200 and 300. The plots indicate an average increase in convective heat transfer in the form of increment in the vorticity of the velocity field and the average temperature inside the cavity with increase in Rayleigh numbers.

INTRODUCTION

Computational study of the pattern and the behavior of the fluid particle motion in the cavity has always been an area of interest for researchers. Numerical algorithms have been implemented with systems of differential equations which describe the thermal and dynamic aspects of the flow, involving particular boundary conditions, providing technically and economically feasible numerical solution of these problems to determine the fluid flow parameters.

Many researchers, in the last few decades, performed extensive work on natural convection in two-dimensional cavities. Robillard and Vasseur [l] performed a numerical study of a cold water-filled square enclosure in which one vertical wall was kept at 0°C while the temperature of the other vertical wall was varied between 4 and 12°C. Thermal boundary conditions on the horizontal walls were either linear in temperature or adiabatic. Poulikakos [2] studied natural convection in a cavity heated and cooled along a single wall, other walls being kept insulated. In their study of natural convective flow, November and Nansteel [3] considered a square cavity with one vertical wall cooled and heated at the base. A numerical study was performed by Ganzarolli and Milanez [4] on the natural convection heat flow in a square cavity which had a heater at the base and cooled by the side walls. Hakeem et al. [5] studied the effect of natural convection in a square cavity induced by the presence of a heated plate. Ambarita et al. [6] carried out a numerical study of laminar natural convection heat transfer in a differentially heated square cavity, which is filled with air along with two insulating baffles attached to its horizontal walls. Saeid and Yaacob [7] performed a numerical study of laminar natural convection in a two-dimensional square cavity filled with pure air with the heated vertical wall having sinusoidal temperature variations about a constant mean value, higher than the cold side-wall temperature.

Most of the studies reported in the literature are with air filled cavity. Water is used in many applications as convective heat transfer medium. Keeping this in mind, the authors have simulated natural convection in a two dimensional water filled square cavity. The top of the cavity is closed with an insulated wall and heated from the middle portion of the bottom wall at a constant temperature. The simulation of the two-dimensional square cavity

has been accomplished using an in-house developed code based on SIMPLE algorithm. The simulated results have been presented in terms of velocity and temperature distributions.

NOMENCLATURE

g	acceleration due to gravity
X	non-dimensional horizontal distance
Y	non-dimensional vertical distance
U	non-dimensional horizontal velocity
V	non-dimensional vertical velocity
Ra	Rayleigh Number
Pr	Prandtl Number
θ	non-dimensional temperature
L	dimension of square cavity
P	non-dimensional pressure

NUMERICAL MODEL

The simulation of the natural convection process has been carried by means of solving the governing equations valid for fluid flow in a square cavity applying appropriate boundary conditions. A representation of the fluid enclosed within the square cavity is demonstrated in figure 1. The two vertical walls are kept under perfectly isothermal conditions. The top wall is insulated and adiabatic and impermeable. The heating element, placed in the middle of the bottom wall, has uniform and constant temperature; while the remaining portion of the bottom wall is insulated and assumed to be adiabatic and impermeable. The working fluid used is water having an average Prandtl number 7.0. The motion inside the cavity can be assumed to be two-dimensional and the effect of the temperature on density is assumed to be confined only to the body force term of the momentum equation and the remaining thermo-physical fluid properties are independent of temperature and pressure (Boussinesq approximation). The temperature and velocity field are coupled through the body force. The fluid flow has been considered to be steady, laminar and incompressible.

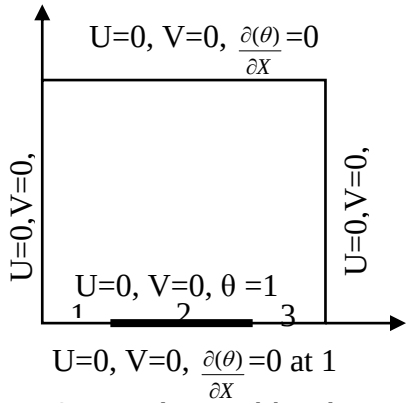

FIGURE 1. Square enclosure with boundary conditions

Governing Equations

On the basis of conservation of mass, linear momentum in x (horizontal) and y (vertical) directions and energy in two dimensions in steady state with some assumption, the governing equation are formulated. The flow is

considered to be steady, laminar and incompressible and other thermo-physical properties are considered constant at the reference bulk temperature. The governing equations for conservation of mass, momentum in x and y directions and energy in non-dimensional form are presented in eq. (1) to (4) respectively.

$$\frac{dU}{dX}+\frac{dV}{dY}=0 \tag{1}$$

$$U\frac{dU}{dX}+V\frac{dU}{dY}=-\frac{dP}{dX}+\Pr\left[\frac{d^2U}{dX^2}+\frac{d^2U}{dY^2}\right] \tag{2}$$

$$U\frac{dV}{dX}+V\frac{dV}{dY}=-\frac{dP}{dX}+\Pr\left[\frac{d^2V}{dX^2}+\frac{d^2V}{dY^2}\right]+Ra.\Pr.\theta \tag{3}$$

$$U\frac{d\theta}{dX}+V\frac{d\theta}{dY}=\frac{d^2\theta}{dX^2}+\frac{d^2\theta}{dY^2} \tag{4}$$

Boundary Conditions

The length and width of the cavity are taken as L. No-slip condition with respect to velocity and impermeable boundary condition are imposed at every wall of the cavity. The non-dimensional temperature of the vertical walls is zero and kept under isothermal conditions. The top surface is insulated. The heating element, placed in the middle of the bottom wall, has a constant temperature; and the remaining portion is insulated. The boundary conditions in the dimensionless form are shown in figure 1.

Numerical Methods

The numerical solution of the non-dimensional conservation equations for mass, momentum and energy for water has been solved with appropriate boundary conditions using finite volume method based on SIMPLE algorithm. Central differencing scheme is used for discretization of the diffusion terms and the advection terms are discretized using hybrid scheme depending on the Peclet number and the power law scheme is adopted. The discretized equations are solved by a line-by-line procedure, combining the tri-diagonal matrix (TDMA) and successive over-relaxation (SOR) iteration. The equations have been solved on a staggered grid arrangement with a uniform grid structure of 102 by 102 in size. A residual mass of 3×10-7 has been taken as the convergence criteria.

RESULTS AND DISCUSSIONS

The results of the simulation in dimensionless forms for Rayleigh numbers of 100, 200 and 300 are represented in the form of temperature contours and velocity streamlines. The temperatures, horizontal components and vertical components of velocity at three different heights of the cavity at intervals 0.25L, 0.5L and 0.75L have been plotted for Rayleigh numbers 100, 200 and 300. The vertical velocity distribution at mid-length of the cavity, horizontal velocity distribution at mid-height of the cavity have also been separately plotted for different Rayleigh numbers.

Temperature Distribution

Isotherms for Rayleigh numbers 100, 200 and 300 have been shown in figures 2, 3 and 4 respectively. At Ra = 100, the spread of the highest isotherms is considerably small and the heat flow across the cavity is mainly affected by conduction. As the Rayleigh number increases, convection becomes dominant. At Ra = 200, the isotherms in the cavity get increasingly deformed as shown in figure 3. At higher Rayleigh number, more heat is added to the fluid to intensify the fluid convection. It can be seen that, at high Rayleigh number, the degree of distortion from the pure

conduction is substantial and some contour lines are almost vertical. Due to central location of the heating element the isotherms are found to be symmetric about the centre of the square enclosure.

Streamline Distribution

The streamline distributions inside the cavity have been shown in figure 5, 6 and 7. Counter clockwise vortices are formed as a result of heating from the middle of the bottom wall and vorticity increases with increase in Rayleigh numbers. The vortex pattern is almost similar in case of Rayleigh numbers 100 and 200 as seen in figure 5 and 6 respectively; however the vortex pattern changes as Ra number becomes 300. The positions of the vortices are symmetrical along the vertical axis passing through the centre of the cavity. As the Rayleigh number increases, the vortices elongate in the vertical direction and then move away from each other, but maintain the axial symmetry.

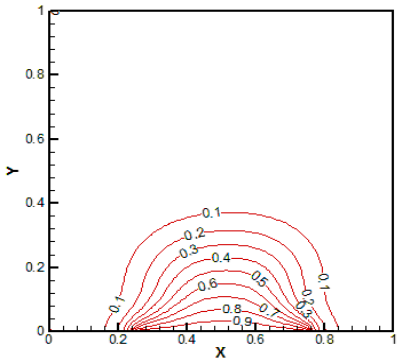

FIGURE 2. Temperature contours plot for Ra=100

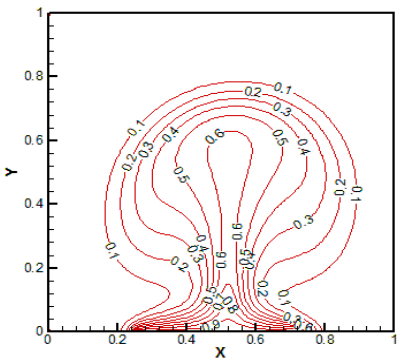

FIGURE 3. Temperature contours plot for Ra=200

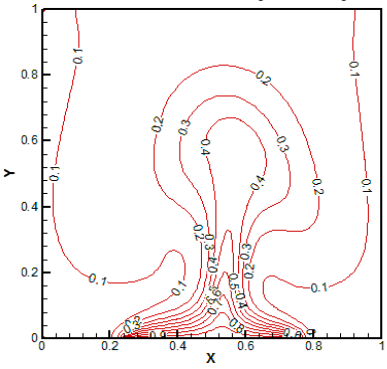

FIGURE 4. Temperature contours plot for Ra=300

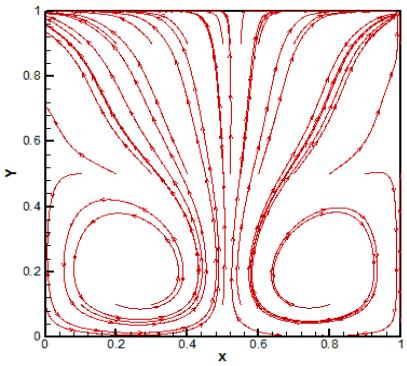

FIGURE 5. Streamline plot for Ra=100

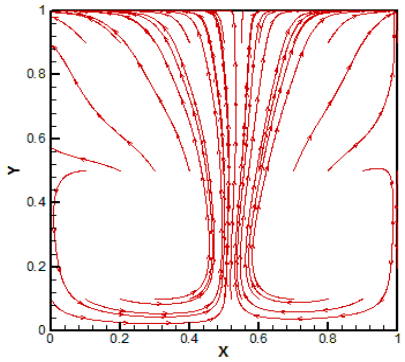

FIGURE 6. Streamline plot for Ra=200

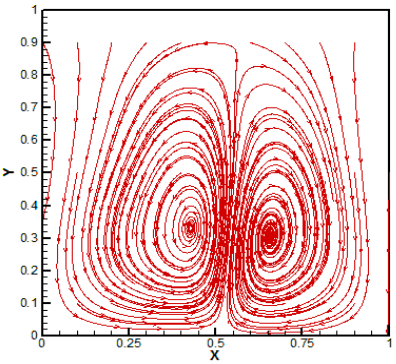

FIGURE 7. Streamline plot for Ra=300

Temperature and Velocity Profile at Different Heights

The variation of temperature at three distinct heights (0.25L, 0.5L and 0.75L) of the cavity has been plotted along the length of the cavity in figures 8, 9 and 10 respectively. The figures indicate that temperature increases with increase in Rayleigh number. At lower Rayleigh numbers conduction is widely prevalent and hence there is a significant temperature difference between heights at 0.25L and 0.5L as shown in figure 8; however with increase in Rayleigh number, the temperature difference decreases and heating becomes more uniform along the cavity. The plots of temperature distribution are expectedly found to be symmetric along the center of the cavity.

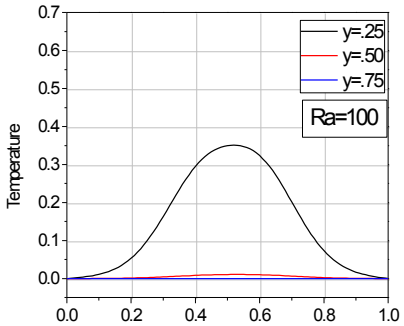

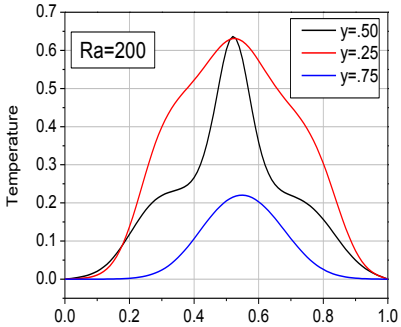

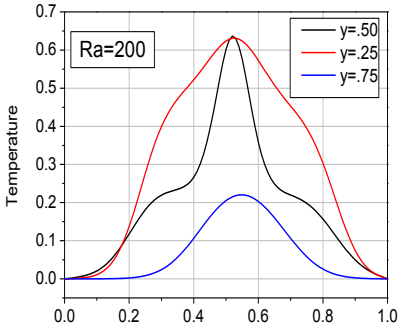

The variation of the horizontal component of velocity at heights 0.25L, 0.5L and 0.75L are plotted in the figures 11, 12 and 13 respectively. The magnitude of horizontal velocity increases with increase in Rayleigh number. For Rayleigh numbers 200 and 300, the direction of velocity at height at 0.25L is opposite to those at higher heights, due to formation of counter clockwise vortices, resulting changes in the direction of velocity at various heights. The anti-symmetric nature of the velocity distribution about the center is due to heating from the middle of bottom wall.

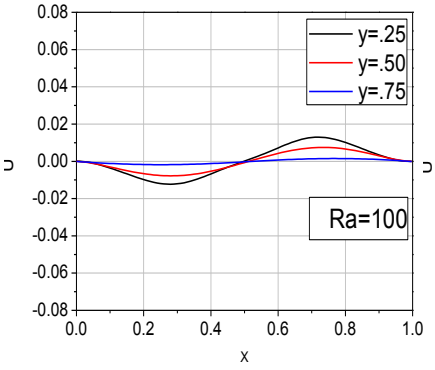

FIGURE 11. Horizontal velocity plot for Ra=100

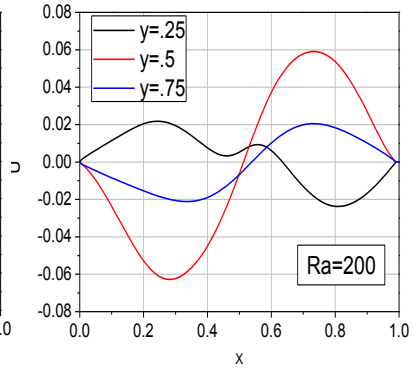

FIGURE 12. Horizontal velocity plot for Ra=200

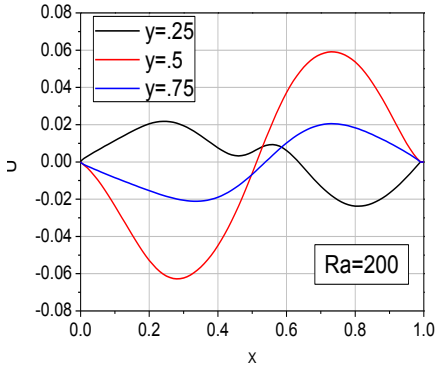

FIGURE 13. Horizontal velocity plot for Ra=300

The variation of vertical velocities plotted in the figures 14, 15 and 16, illustrates the increase in velocity with increase in Rayleigh numbers. The fluid velocity is higher, near the bottom wall due to the presence of the heating element and decreases slowly with increase in height. However the rate of decrease in velocity with increase in height reduces as Rayleigh number increases due to the convection. The plot is also symmetric in nature along the horizontal axis due to the location of the heating element in the middle of the cavity.

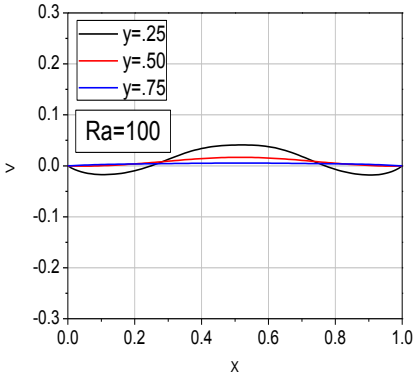

FIGURE 14. Vertical velocity plot for Ra=100

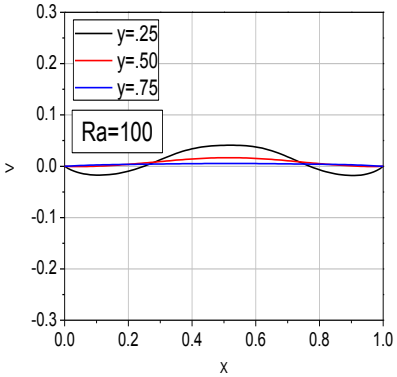

FIGURE 15. Vertical velocity plot for Ra=200

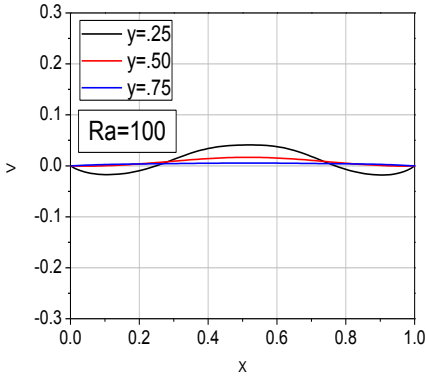

FIGURE 16. Vertical velocity plot for Ra=300

Mid-height and Mid-Length Velocity Distribution

The variation of vertical velocity along the mid-height and that of horizontal velocity along the mid-length of the cavity have been shown in figures 17 and 18 respectively. The magnitude of horizontal velocity increases in both direction, positive and negative, and the width of the zero velocity zone decreases with increasing Rayleigh number due to enhancement of buoyancy effect. Similarly, the vertical velocity is positive along the location of the heating element on the bottom wall and negative in place where the heating element is absent. The magnitude of vertical velocity increases with the increase of Rayleigh number both in the upper and the lower half due to continuity of flow. The vertical velocity distribution is symmetric along a vertical central axis while the plot for horizontal velocity is antisymmetric along the axis passing through the mid height of the cavity.

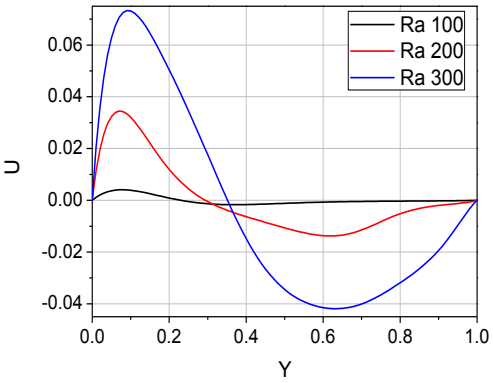

FIGURE 17. .Mid height horizontal velocity distribution

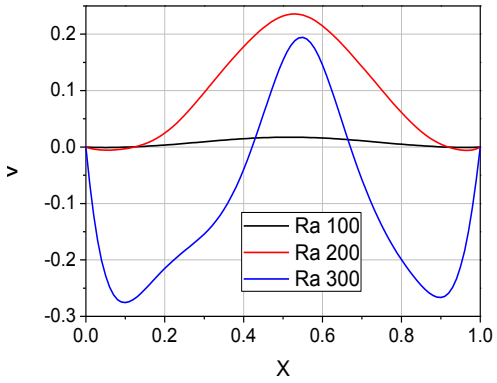

FIGURE 18. Mid length vertical velocity distribution

CONCLUSION

In this numerical study, two-dimensional steady flow analysis on natural convection in a differentially heated square enclosure has been performed. Investigation on the structures of the two-dimensional velocity and temperature fields for three different Rayleigh number 100, 200 and 300 has showed that with increase in Rayleigh number, the flow field changes, the convective activities are found to intensify and accordingly, the vorticity of the velocity field and average temperature inside the cavity also increase with increase in Rayleigh numbers. It is observed that, at higher Rayleigh numbers, the magnitude of temperature and velocity increases substantially at the same height of the cavity owing to higher convective heat transfer.

REFERENCES

1. L. Robillard and P. Vasseur, Effect of maximum density on the free convection of water in a closed cavity, Can. J. Civil Engg. **6(4),** 481-493 (1979).
2. D. Poulikakos, Natural convection in a confined fluid-filled space driven by a single vertical wall with warm and cold regions, Journal of Heat Transfer **107(4)**, 867-876 (1985).
3. M. November and M. W. Nansteel, Natural convection in rectangular enclosures heated from below and cooled along one side, International Journal of Heat and Mass Transfer **30**, 2433-2440 (1987).
4. M. M. Ganzarolli and L. F. Milanez, Natural convection in rectangular enclosures heated from below and symmetrically cooled from the sides, International Journal of Heat and Mass Transfer **32**, 1063-1073 (1995).
5. P. Kandaswamy, J. Lee and A. K. Abdul Hakeem, Natural Convection In a Square Cavity In The Presence Of a Heated Plate, Nonlinear Analysis:Modelling and Control **12 (2)**, 203-212 (2001).
6. H. Ambarita, K. Kishinami, M. Daimaruya, T. Saitoh, H. Takahashi and J. Suzuki, Laminar Natural Convection Heat Transfer in an Air Filled Square Cavity with two insulated baffles attached to its horizontal walls, Thermal Science and Engineering **14(3)**, 35-46 (2006).
7. N. H. Saeid and Y. Yaacob, natural convection in a square cavity with spatial side-wall temperature variation, Numerical Heat Transfer, Part A **49**, 683-697 (2006).

ICME2015

International Conference on Mechanical Engineering 2015
(ICME 2015) 18 – 20 December, 2015, Dhaka, Bangladesh

Paper ID : 098

Validation of FDS for the Burning of PMMA and the Suppression of Fires by Water Mist Spray

H M Iqbal Mahmud[1, 2, a)], KAM Moinuddin[2, b)] and GR Thorpe[2, c)]

[1]*Department of Civil Engineering, Khulna University of Engineering and Technology, Khulna 9203, BANGLADESH*
[2]*Centre for Environmental Safety and Risk Engineering, Victoria University, P.O. Box 14428, Melbourne, Victoria, 8001 AUSTRALIA*

[a)] Corresponding author: iqbal.mahmud@ce.kuet.ac.bd; hm.mahmud@live.vu.edu.au
[b)] khalid.moinuddin@vu.edu.au
[c)] graham.thorpe@vu.edu.au

Abstract. Now-a-days, computational fluid dynamics tools are widely used to simulate the growth and suppression of fires. However, understanding the capabilities of any CFD based tool is necessary in simulating these phenomena. Predicting the growth and suppression of fires are challenging as those involve complex dynamics of fires. Moreover, the mechanisms of suppression of fires by water mist systems are more complex compared to that of the conventional sprinkler systems, as the water mist sprays involve dilution of oxygen by evaporation of water droplets and attenuation of radiation feedback to the unburned fuel from the flame. Additionally, experimental data are required to validate the accuracy of the model. This paper reports a validation work on the accuracy of fire dynamics simulator (FDS 6), a CFD based tool, in predicting the burning rates of fires and finally, its capability in simulating the suppression of fires using water mist spray. Polymethyl methacrylate (PMMA) is used as a solid fuel in simulating the burning of the material and water mist spray is used for the suppression of fire. Published experimental data is taken for the purpose of validation of the model. The steady-state burning rates of the specimen, before and after activation of water mist spray, is calculated by FDS and compared with the experimental data. It has been observed that the predictions of FDS are in reasonable agreement with the experimental data.

INTRODUCTION

In the last two decades, the fire dynamics simulator (FDS) and the coupled three-dimensional visualization program Smokeview, is widely used as a CFD based tool for the prediction of growth and spread, and suppression of fires and for the prediction of smoke and gases movement in buildings generated by fires. However, it is essential to understand the capabilities of any CFD based tool in simulating the pyrolysis of fuel, generation of fire and growth of fire, heat release rate etc. Predicting these phenomena is challenging as it involves complex dynamics and fires involve mechanisms that develop in length scales ranging from millimetres to meters, and time scales from milliseconds to minutes [1]. Moreover, the mechanisms of suppression of fires are more complex for water mist systems compared to that of the conventional sprinkler systems. The mechanisms of suppression of fires using water mist sprays are governed by the dilution of fuel vapours/air ratio by evaporation of water droplets [2-4] and radiation attenuation from the flame [2, 5-7]. Furthermore, experimental data, with appropriate material properties, are required to validate the accuracy of the model.

Therefore, the objective of this work is to validate the accuracy of FDS in predicting the growth and spread of fires, and finally, the capability of this tool in suppression of fire using water mist spray. A better understanding of FDS capabilities in simulating the growth and suppression of fires would help in designing suitable fire control systems. It will also serve as a benchmark in identifying FDS capability in case of burning and suppression of fires produced by solid fuels.

In this study, we have used Polymethyl methacrylate (PMMA) to create fire in the numerical simulation. We have chosen PMMA as a burning material as it is one of the plastic materials widely used in buildings. The experimental data by Magee and Reitz [8] is used for the purpose of validation of the model.

NUMERICAL SIMULATION

In this study the simulation of the burning of the PMMA slabs is conducted using FDS, version 6, and the burning rates of the samples are calculated in the simulation. For PMMA combustion, the MMA monomer (C5 H8 O2) is assumed to be liberated from the sample surface when pyrolysis occurs [9]. In FDS, pyrolysis is assumed to occur as per the Arrhenius equation. The details of the computational domain, grid resolution, external radiation flux on the specimen, and flammability parameters and chemical kinetics of PMMA material are discussed below.

Computational domain

Computational domain with dimensions of 1 m × 2 m × 2 m are created for the simulation of burning and suppression of vertically oriented PMMA slab. The set-up for the computational domain in the numerical simulation is illustrated in Figure 1. For samples with an imposed flux, the cone is located 2.54 cm away from the front surface of the PMMA slab. All sides of the domain are kept open to be consistent with the conditions associated with the experiment.

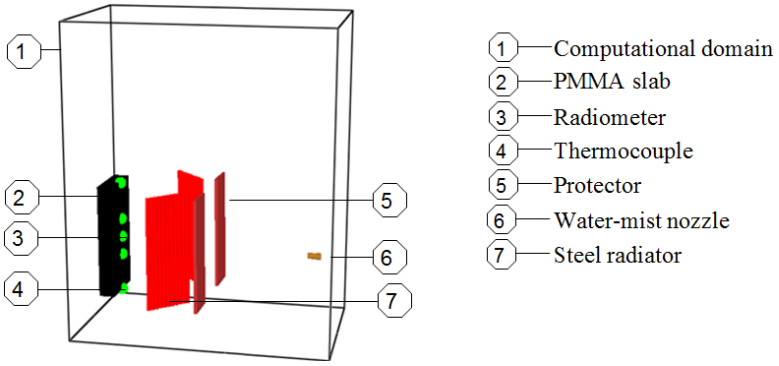

FIGURE 1. Three-dimensional view of the computational domain for the simulation of fires produced by PMMA slab.

The size of the specimen is 17.8 cm wide × 35.6 cm high × 5 cm thick and placed vertically at a height of 20 cm from the floor and 10 cm away from the rear side of the domain boundary. A set of two inclined steel plates is used as a heating source (radiant heaters) to the specimen and they are placed 17.8 cm apart to allow passage of the water spray. They are positioned at a distance of 25 cm away from the front surface of the specimen and inclined at 45^{o} to the plane normal to the centerline of the specimen. The green dots on the specimen surface are the locations where the temperature and radiation rate are calculated. A nozzle is located at a distance of 1 meter from the specimen. Two copper plates are placed in between the steel radiators and the nozzle to protect the radiator from the water spray.

Grid spacing

The numerical results of any CFD model should be grid convergent. A grid sensitivity analysis was performed in a study by Abu-Bakar and Moinuddin [10] using grid spacing of 10 mm, 5 mm and 2.5 mm (in the x, y and z directions). In the simulations, the specimen is subjected to 50 kW/m^2 of radiation. The heat release rates (HRR) of PMMA burning for these three cell sizes are calculated and compared. From the initial coarse grid sizes, the grid sizes are reduced by a factor of two. The results of HRR of these calculations, as illustrated in Figure 2, show that in the case of the 10 mm grid, the HRR is very high compared to that of the two other cell sizes. However, the HRR for the 5 mm and 2.5 mm cell sizes are found to be almost identical. Therefore, a mesh size of 5 mm is used to discretise the computational domain.

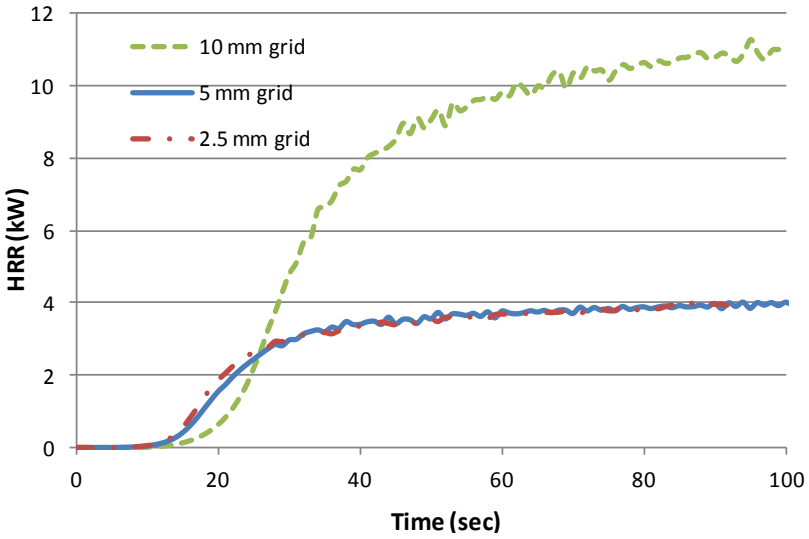

FIGURE 2. Grid convergence test for PMMA fire [10].

External radiation flux

The external radiation flux on the PMMA sample is varied in the simulation as it was in the experiment. In the simulation, the specimen is located underneath two hot steel plates. The distribution of radiant flux over the PMMA surface is calculated by invoking a 'device' on the PMMA surface in the simulation. The heat flux over the PMMA surface resulted from the high temperature of the steel plates. To obtain the desired rate of radiation flux on the PMMA specimen surface, the steel plate temperature is varied and the radiation on the PMMA surface is calculated in the simulation. When the temperature of the steel plates gives the desired rate of radiation flux, that temperature is used as the reference temperature of the steel plates. Radiation heat absorbed by the slab surface is calculated using an emissivity of 0.85 [11] and an absorption coefficient of 2700 (m^{-1}) [12]. The rates of radiation flux used in the simulations are 15.89, 14.65 and 12.55 kW/m^2 for the burning of the specimen.

Flammability parameters and chemical kinetics

The amount of energy consumed per unit mass of reactant in a solid phase reaction is specified by the heat of the reaction/pyrolysis (HoR). The amount of energy released per unit mass of fuel (kJ/kg) from a gas phase chemical reaction is specified as the heat of combustion (HoC) [13]. The HoC and HoR of PMMA were determined in the Fire Dynamics Lab, CESARE, Victoria University using the cone calorimeter test, thermal gravimetric analysis (TGA) and DSC by Abu-Bakar and Moinuddin [10]. The value of the HoR used in the simulation was 1627 kJ/kg for the heating rate of 5 K/min. The HoC data used in this analysis was 19490 kJ/kg for the irradiance of 50 kW/m^2.

To define the solid phase chemistry (Arrhenius reaction), the kinetic parameters of the reaction rate are specified in the simulation. The value of the Arrhenius parameters varies with the variation of the heating rate to the specimen. Here, the values for a heating rate of 5 K/min is used for the simulation as the value for this heating rate gives a better prediction of HRR for PMMA fire. The value of the Arrhenius parameters was determined using TGA in the Fire Dynamic Lab, CESARE by Abu-Bakar and Moinuddin [10]. These are specified in Table 1. The value of specific heat of PMMA material is taken from [14]. The other material properties and combustion parameters of the PMMA used for the simulations are taken from Abu-Bakar and Moinuddin [10].

TABLE 1. Arrhenius parameters.

Arrhenius parameters	Values
Activation energy (E), J/mol	24234
Pre-exponential factor (A)	1.47 ×1018
Reaction order (Ns)	1.64

RESULTS AND DISCUSSION

The burning of the PMMA slab is simulated as coupled pyrolysis and combustion reaction using FDS and the burning rates of the specimen are calculated in the simulation. Figure 3 illustrates a three-dimensional view of the burning of the specimen. The rates of radiation flux on the specimen surfaces for the three different simulations are 15.89, 14.65 and 12.55 kW/m2. The samples are simulated to burn undisturbed until full burning is developed. When the burning rates are observed to be in a steady state, the nozzle activation is simulated in the simulation for the suppression of fires.

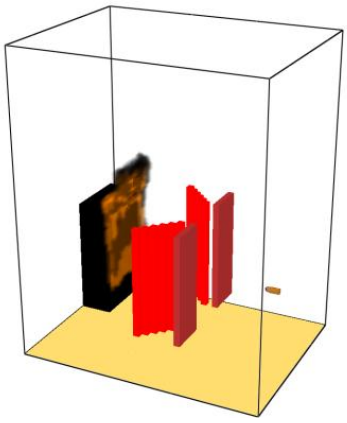

FIGURE 3. Three-dimensional view of the burning of the PMMA slab.

The burning rates of the specimens for the three different rates of radiation flux are presented in Figure 4. In the case of the radiation flux of 15.89 kW/m^2, the specimen is allowed to burn for up to 680 seconds until a steady state burning rate is observed. The water spray nozzle is then activated and, as a result, the burning rate of the sample begins to drop and becomes steady at 1100 seconds. The burning rates of the sample before and after activation of the nozzle in the numerical simulation are 13.6 and 8.0 g/cm^2.s, respectively. These corresponding values in the experimental study by Magee and Reitz [8] are 16.5 and 9.2 g/cm^2.s, respectively, before and after activation of the nozzle. In the analysis, it is found that the numerical value is about 18% and 15% lower than the experimental observation, respectively.

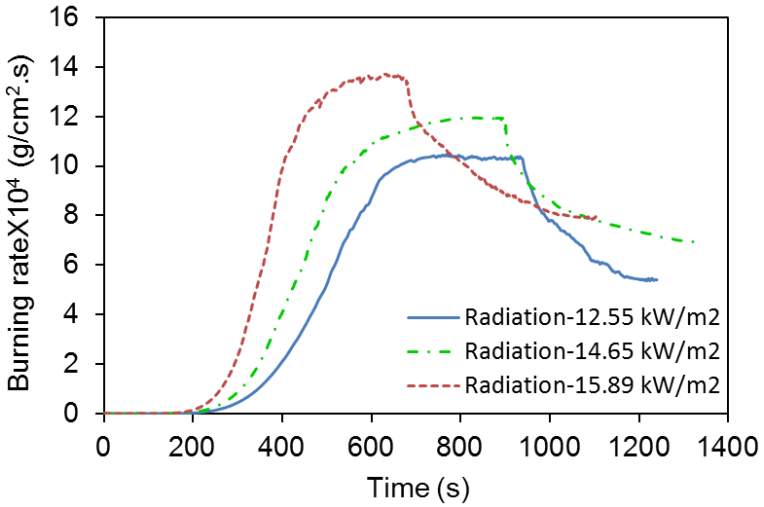

FIGURE 4. Burning rates of the PMMA slabs for the different flux of radiation (kW/m^2) before and after activation of the spray.

The burning rates for the radiation flux of 14.65 and 12.55 kW/m^2 are also calculated in the numerical simulations and the results are presented in the same Figure 4. It is observed that the numerical results underpredict the burning rate in these two cases as has been found for the irradiance of 15.89 kW/m^2. The difference between the numerical predictions and the experimental measurements of the burning rates for the irradiance of 14.65 kW/m^2 is 21% and 13% before and after the activation of the water mist nozzle, respectively. This difference for the radiation flux of 12.55 kW/m^2 is 23% and 14% before and after the activation of the water-mist nozzle, respectively.

The ignition of the sample, development of the fire, burning of the specimen in steady state condition, activation of the water spray and burning of the sample with the water spray in the simulation at a different level of time for the radiation flux rate of 15.89 kW/m^2, are also demonstrated sequentially in Figure 5.

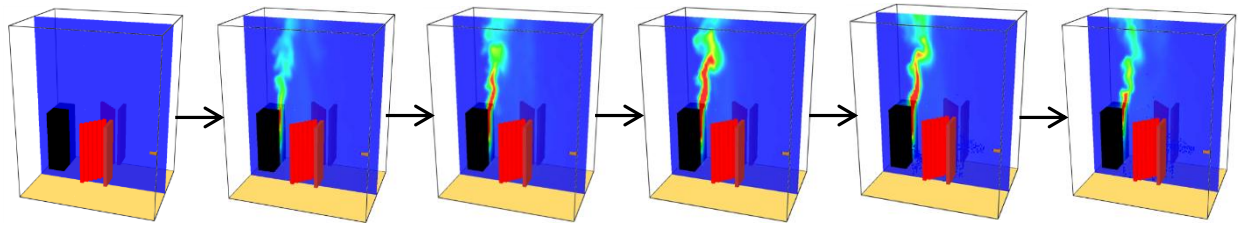

(a) Start of simulation (0 sec) (b) Ignition of sample (400 sec) (c) Fire in growth (500 sec) (d) Fire in steady state (600 sec) (e) Activation of spray (680 sec) (f) Fire with spray (800 sec)

FIGURE 5. Burning and suppression of fire produced by the vertically oriented PMMA for the radiation flux of 15.89 kW/m^2.

CONCLUSIONS

In this study, FDS is used to simulate the burning rates of radiation augmented PMMA fires before and after activation of a water mist spray. Experimental data by Magee and Reitz [8] are used to validate the numerical results. In the simulation, the heating rates on the PMMA specimens are varied and the burning rates before and after the activation of the water mist nozzle is calculated. The steady state burning rates of the specimen by FDS, before and after activation of the water-mist nozzle, are in reasonable agreement with the experimental measurements. The difference between the experimental and numerical values is not more than 23%, and in some cases, this difference is as low as 13%.

ACKNOWLEDGEMENTS

The authors wish to acknowledge the technical and financial assistance provided by Defence Science Technology Organisation (DSTO), Australia.

REFERENCES

1. W. Jahn, G. Rein and J. Torero, “The effect of model parameters on the simulation of fire dynamics,” In Proceedings of the 9th International Symposium on Fire Safety Science, edited by D. T. Gottuk and B. Y. Lattimer (International Association of Fire Safety Science, Karlsruhe, Germany, 21-26 September 2008) pp. 1341-1352.
2. Z. Liu and A.K. Kim, J. of Fire Prot. Eng. **10**, 32-50 (2000).
3. Y. L. Shu, W. J. Jeng, C. W. Chiu and C. H. Chen, Fire Mater. **29**, 295-302 (2005).
4. P. Yang, T. Liu and X. Qin, Build. Environ. **45**, 2309-2316 (2010).
5. J. R. Mawhinney, B. Z. Dlugogorski and A. K. Kim, “A closer look at the fire extinguishing properties of water mist,” In Proceedings of 4th International Symposium on Fire Safety Science, Ottawa, Ontario, Canada, July 13-17, 1994, pp. 47-60.
6. R. Wighus, “Engineering relations for water-mist fire suppression systems,” In Proceedings of Halon Alternatives Technical Working Conference, Albuquerque, New Mexico, 1995, pp. 397.
7. G. Grant, J. Brenton and D. Drysdale, Prog. Energy Comb. Sci. **26**, 79-130 (2000).

8. R. S. Magee and R. D. Reitz, “Extinguishment of radiation augmented plastic fires by water sprays,” In Proceedings of the 15th Symposium on Combustion (The Combustion Institute, Tokyo, Japan, 25-31 August 1974) pp. 337-347.
9. G. Linteris, L. Gewuerz, K. Mcgrattan and G. Forney, “Modeling solid sample buming, In Proceedings of the 8th International Symposium on Fire Safety Science,” (International Association for Fire Safety Science (IAFSS), Beijing, China, 18-23 September 2005) pp. 625-636.
10. A. S. Abu-Bakar and K. A. M. Moinuddin, “Investigation of effects of variation in heating rate on chemical kinetics and heat of reaction for pyrolysis and combustion”, Submitted as a technical paper in Fire and Materials, 2015.
11. J. R. Hallman, J. R. Welker and C. M. Sliepcevich, Polym. Eng. Sci. **14**, 717-723 (1974).
12. P. T. Tsilingiris, Energ. Convers. Manage. **44**, 2839-2856 (2003).
13. K. McGrattan, S. Hostikka, R. McDermott, J. Floyd, C. Weinschenk and K. Overholt, “Fire dynamics simulator (Version 6) - User's guide,” Sixth edition, NIST Special Publication 1019, 2014, pp. 78.
14. H. James, “Measurement of thermal conductivity and specific heat of building construction materials as functions of temperature,” Master’s thesis Centre for Environmental Safety and Risk Engineering, Victoria University, Melbourne, 2014.

ICME2015

International Conference on Mechanical Engineering 2015
(ICME 2015) 18 – 20 December, 2015, Dhaka, Bangladesh

Paper ID : 099

Is Hydrothermal Carbonization a Viable Option For Producing a Solid Fuel With Coal Like Properties From Undervalued Lignocellulosic Biomass?

Animesh Dutta[1, a)], Jamie Minaret[1] and Harpreet Kambo[1]

[1]*University of Guelph, 50 Stone Road East, Guelph N1G 2W1, Canada*

[a] Corresponding author: adutta@uoguelph.ca

Abstract. Biomass is an attractive fuel source for energy production, however its application is limited due to poor physicochemical properties. Dry torrefaction, a pre-treatment used for upgrading biomass, improves most of the physiochemical properties expect for the issues caused from the presence of high moisture and inorganic elements. A thermal pre-treatment process called hydrothermal carbonization (HTC), treats biomass with water under subcritical conditions to produce a solid product (hydrochar) that possesses combustion properties similar to coal and appears remove ash material as well. Studying the effect of reaction temperature, residence time and the phase of water, determined that in order to produce hydrochar with similar properties to coal, the reaction temperature must be at least 250°C. In addition it was also found that HTC using liquid water was more effective at removing ash material compared to water vapour.

INTRODUCTION

Hydrothermal carbonization (HTC) is a unique type of biomass pre-treatment technology, as the process involves completely submerging biomass in water before undergoing a thermal treatment. Therefore the moisture content of biomass is not an issue for the HTC process, meaning even wet biomass containing mainly water can still be carbonized into a black energy dense product (hydrochar). The process typically takes place in a sealed reactor, similar to a pressure cooker, for a temperature range of 180 to 260°C, at either the corresponding saturation pressure of water or at elevated pressures as high as 20 MPa [1-3]. The reaction time for the HTC process can be as quick as 5 to 10 minutes (min) or span up to several hours [4-7]. Additional parameters involved with the HTC process include biomass particle size and biomass to water mass ratio (BWR). Research on HTC has grown exponentially over the last year, with some of the main findings being: an increase in reaction temperature and time span lead to an increase in the carbonization process, while the temperature has been demonstrated to have a more significant effect than the reaction time [4, 6, 8]; a decrease in particle size of biomass leads to an increased mass loss during HTC for shorter residence times [9]; and, the type of biomass undergoing HTC will have an effect on the quality of hydrochar as well.

The HTC process has been compared to dry torrefaction by several researchers with a general consensus that HTC produces an increased energy content, reduced ash content and increased carbon content [10]. This is due to the increase heat transfer experienced during the HTC process compared to torrefaction because of the increased density of water compared to nitrogen (or other inert gases). The goal of this study was to analyse the quality of hydrochar produced from HTC in terms of a solid fuel. The solid product does have several other potential applications as well, which include; soil amendment, metallurgical applications, and wastewater treatment.

METHODS AND MATERIALS

The HTC experiments were performed with the reactor configuration described in a previous study [4] with the addition of a nitrogen cylinder, using corn stover (CS), tomato vines (TV) and willow (Wil) to measure the effect of

various parameters involved in the HTC process. The CS experiments were designed to analyse the effect of temperature and phase of water on the quality of hydrochar, while the Wil experiments were designed to analyse the effect of reaction time. The TV experiments were designed to analyse the effect of adding water during the HTC process for biomass that has a water content above 50%, wet basis (w.b.). This effectively compared two different BWRs, 1:6.7 (no water added) and 1:32 (filled entire reactor with water). The BWR is a ratio of the dry mass of biomass compared to the mass of water contained in the reactor, which is a combination of the water contained in the biomass already and the added water to the reactor. For all HTC experiments, after the raw feedstock and water were added the reactor and the reactor was sealed, the nitrogen cylinder was then attached to the reactor and the reactor was purged to create an inert environment inside. For the CS HTC experiments that used liquid water as the reaction medium, the reactor was pressurized to 2 MPa after being purged, using the same nitrogen cylinder. This allowed the pressure inside the reactor to remain well above the saturation pressure of water during the heating and reaction process, which prevented the water from vaporizing, ensuring that the water remained liquid during the entire process.

The hydrochars produced from the HTC experiments were analysed using various characterization methods, including the solid yield (SY), energy yield (EY), the ultimate analysis, the ash content, and the ash composition. The SY is a measure of the dry mass of hydrochar compared to the dry mass of original raw feedstock used. The EY combines the SY and increase in energy content (often called energy densification) using equation (1), where the higher heating value (HHV) represents the energy content of the biomass (raw) and hydrochar (HTC) in the units MJ/kg.

$$EY = \frac{mass_{HTC} * HHV_{HTC}}{mass_{raw} * HHV_{raw}} \quad (1)$$

Using the EY to compare the hydrochars produced at various conditions gives a good overview of how to quantify the quality of the produced hydrochars, however when considering the hydrochars for use as a solid fuel, it is important to consider more than simply the optimizing the energy contained in the fuel. One of the main components of a solid fuel to consider during combustion is the ash composition and overall content. Since the HTC process uses water as a reaction medium, the potential exists for removing some of the water soluble inorganic compounds that cause issues during combustion.

RESULTS AND DISCUSSION

All of the feedstocks used in the HTC experiments were converted to a black solid that resembled coal when the reaction temperature was increased to 260°C (FIGURE 1). Therefore in order to produce hydrochar that resembled coal it was determined that the reaction temperature must be as close to the maximum HTC temperature as possible, which was 260°C in the case of this study, however other studies use other maximum temperatures such as 250 and 280°C [7, 8, 11]. The argument of maximizing the reaction temperature was also supported by observing the atomic composition of hydrochar using the van Krevelen diagram (FIGURE 2). HTC data from previous literature studies were also included to further demonstrate the effect HTC reaction temperature on the produced hydrochar, where CF, EL, GP, TM, Sp, Bi, EFB, LP, Hop, ES, and MIS represent coconut fibres, eucalyptus leaves, grape pomace, tahoe mix, spruce, birch, empty fruit basket, loblolly pine, common hop, evergreen shrub, and miscanthus, respectively [1, 2, 4, 6, 12-16]. It can be observed that in order for the biomass to transition completely out of both the biomass and peat zones and into the lignite zone, a HTC reaction temperature of at least 250°C must be used. It can also be observed that for most of types of biomass the change in H:C and O:C ratios occur at a nearly linear rate, which would infer that an increase in HTC reaction severity (temperature and residence time) results in an increase in carbon content and decrease in oxygen and hydrogen content at a proportional rate.

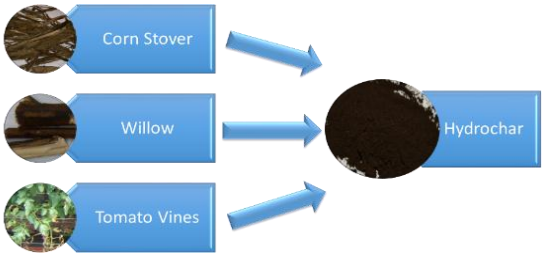

FIGURE 1. Conversion of CS, Wil, and TV to hydrochar via HTC

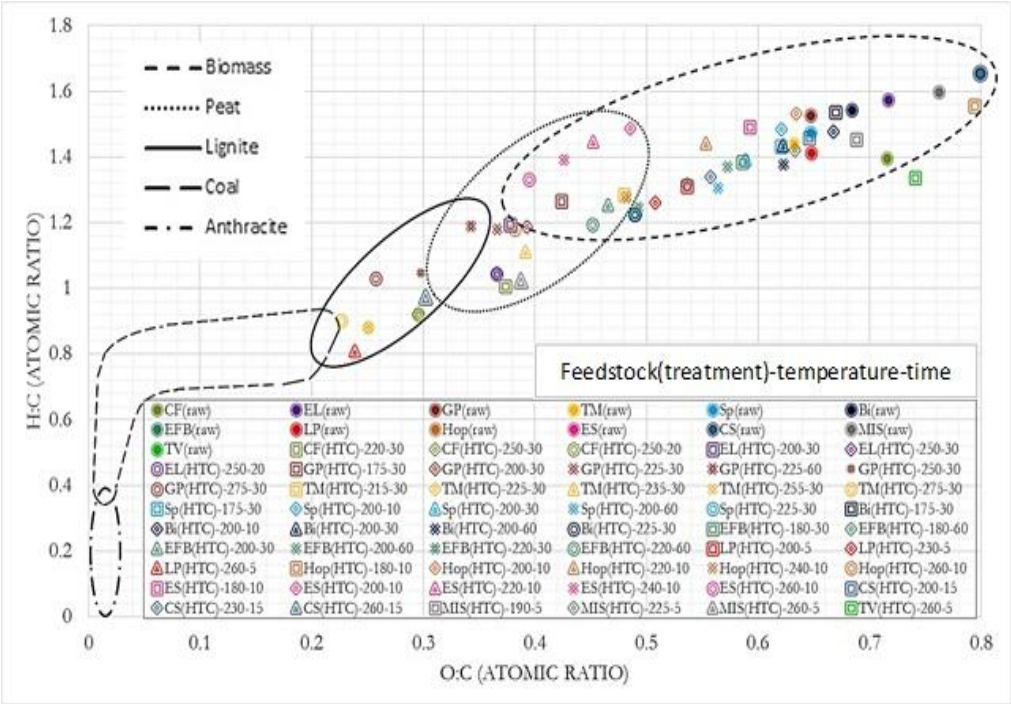

FIGURE 2. van Krevelen diagram of hydrochars produced form a variety of biomass

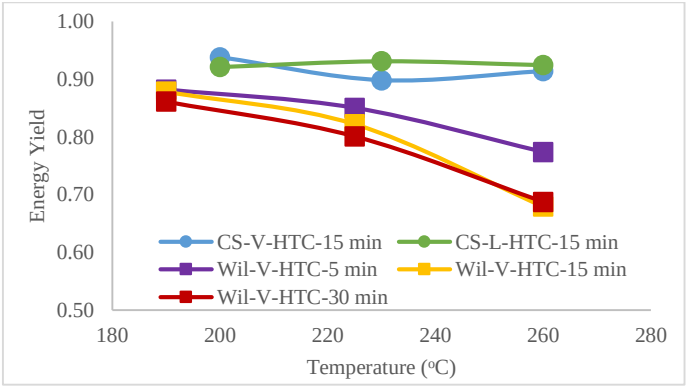

FIGURE 3. Energy yield of CS and Wil hydrochars

The effect of the phase of water, temperature and residence time on the EY of the produced hydrochar were compared to better understand the impact of these parameters and how these parameters effect one another (FIGURE 3). It can be observed for CS experiments that used water vapour as a reaction medium (V-HTC) produced an increased

EY compared to liquid water (L-HTC) for a reaction temperature of 200ºC, while increasing the temperature to 230 and 260ºC resulted in the L-HTC producing an increased EY. It should be noted that the L-HTC produced hydrochars with an increased HHV compared to the V-HTC hydrochars for all reaction temperatures in the CS experiments however the L-HTC also resulted in a decreased SY. Observing equation (1), it is apparent that the decrease in SY for the L-HTC was more dramatic than the increase in HHV compared to the V-HTC for a reaction temperature of 190ºC. However increasing the temperature above 230ºC resulted in a more dramatic increase in HHV compared to the decrease in SY for the L-HTC compared to V-HTC, which ultimately resulted in the increase in EY. The increase in HHV also infers that the L-HTC produced a more coal-like hydrochar compared to the V-HTC.

For the Wil HTC experiments it can observed that at a reaction temperature of 190ºC the hydrochars contained a similar EY for all 3 residence times (FIGURE 3). However increasing the temperature from 225 to 260ºC resulted in a gradual decrease in EY in the hydrochars produced at a residence times of 15 and 30 min compared to the hydrochar produced at 5 min. For all reaction temperatures the hydrochar produced at 5 min contained an increased EY compared to the hydrochars produced at 15 and 30 min. The hydrochar produced at 15 min contained an increased EY compared to the 30 min hydrochar for the lower reaction temperature, while at the highest reaction temperature the 30 min experiment resulted in an increased EY compared to the 15 min. For the Wil HTC experiments it is clear that the optimum residence time was 5 min, meanwhile the EY of the hydrochars produced from the CS experiments were all well above the Wil experiments. Therefore it is clear that the optimum conditions for producing the maximum EY will change depending on the type of biomass being used in HTC.

The TV experiments demonstrated that the use of additional water in the HTC process results in an increase in HHV compared to HTC experiments without water (NW-HTC) even when a lower reaction temperature is used (**Error! Reference source not found.**). The HTC experiments with water did result in a slight decrease in SY, however the greater increase in HHV, resulted in an increased EY compared to the NW-HTC hydrochar. Also in order to remove a significant amount of ash material from the biomass, it was found that additional water is required as the NW-HTC contained a significant increase in ash content compared to both the raw TV and the hydrochar produced with water.

TABLE 1. Data from HTC of TV experiments

Treatment	Raw	NW-HTC-260	HTC-250
HHV (MJ/kg)	12.07	17.34	19.01
Ash (% d.b.)	15.07	17.01	10.82
BWR (1:X)	-	6.7	32
Solid Yield (%)	-	47.09	46.35
Energy Yield (%)	-	67.65	73.00

The composition of the inorganic elements (µg/g) and overall ash (mg/g) of the raw CS, as well as the L-HTC and V-HTC hydrochars were measured and the change in the composition of each hydrochar compared to the original amount contained in the raw CS, were compared to determine which phase of water was more effective at removing ash material (FIGURE 4). Therefore a value of 100% would represent that the hydrochar contained the same composition as the raw CS and if the value is 180% than the hydrochar contains an 80% increase in composition compared to the raw CS, and if the value is 40% than the composition in the hydrochar decreased by 60% compared to the raw CS. The composition of calcium (Ca), magnesium (Mg), and potassium (K) decreased for both the liquid and vapour treated hydrochars at each reaction temperature compared to the raw CS, while the sodium (Na) increased in all cases except for V-HTC produced at 260ºC. The overall ash content of the L-HTC decreased compared to the raw CS for reaction temperatures of 200 and 230ºC, and the V-HTC decreased for only the 200ºC reaction temperature. Observing the ash composition and overall content it can be argued that for the CS experiments the optimum conditions occurred at a reaction temperature of 230ºC using liquid water, since the overall ash content decreased as well as three of the four measured inorganic elements. The L-HTC contained a slightly increased Na composition compared to V-HTC, however the Ca, Mg, and K were all decreased in the L-HTC compared to the V-HTC. In addition the overall ash of the V-HTC increased compared to raw CS, while the L-HTC remained relatively the same as the raw CS. It is important to note that since the hydrochar experienced mass loss during HTC, an ash content or an inorganic element content equal to raw CS, infers that a portion of the mass loss was made of the ash material, or else the content of ash

would have increased in the hydrochars compared to the raw CS. The most notable inorganic compound removed from CS was K, as previous research has found that this element is one of the leading contributors to ash associated combustion issues such as clinking and corrosion [17].

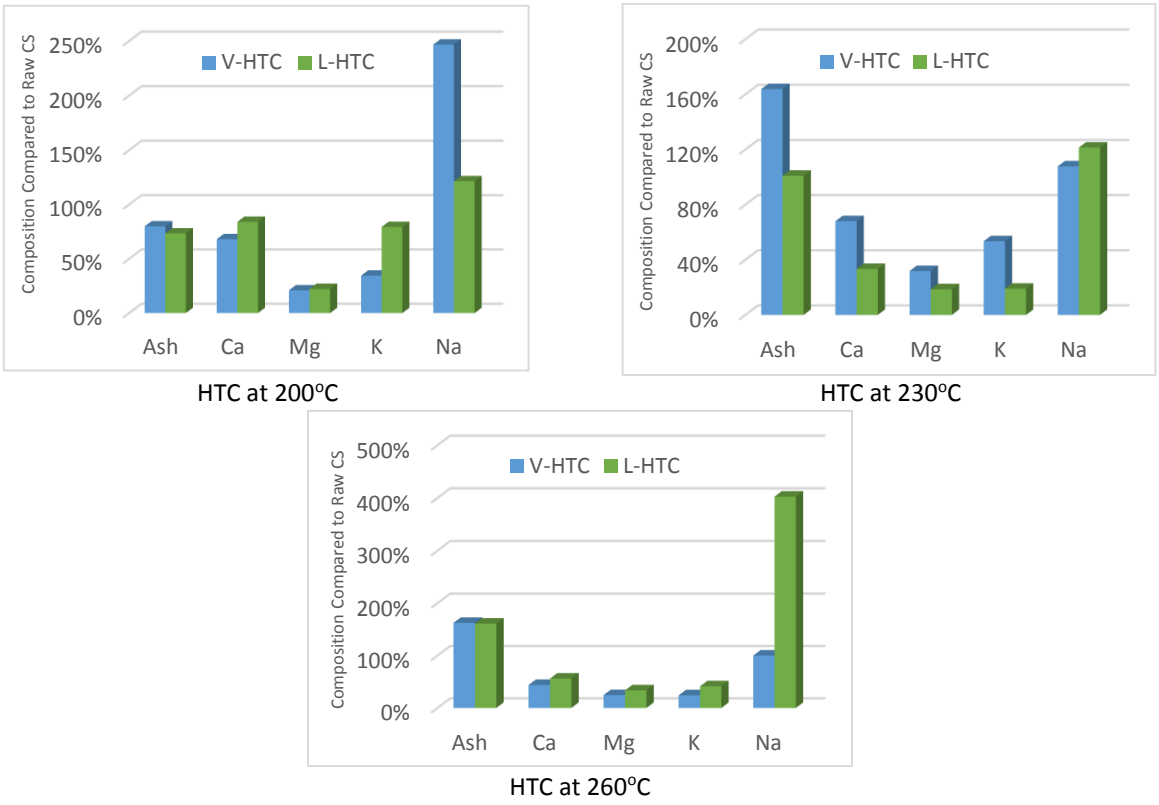

FIGURE 4. Overall ash and ash composition contents of hydrochars produced from CS

CONCLUSION

The HTC experiments conducted on CS, along with data from additional HTC experiments demonstrated that the reaction temperature must be increased to at least 250°C, in order to produce a hydrochar that compares to lignite. The HTC experiments using CS also determined that both liquid and water vapour reaction mediums were able to remove inorganic elements from the biomass during the HTC treatment, and that an increase in reaction temperature resulted in an increase in the removal efficiency of Ca, Mg, and K. The optimum conditions for removing ash material occurred at a reaction temperature of 230°C using liquid water, as these conditions resulted in the best overall removal of ash and inorganic elements. The HTC experiments using Wil demonstrated that at increased reaction temperatures using lower residence times (5 min) resulted in a significant increase in EY compared to higher residence times (15 and 30 min). Increasing the reaction temperature resulted in a decrease in EY for all residence times used, however in order to produce hydrochar with an HHV similar to lignite coal, the reaction temperature needed to be increased to 260°C. This also coincides with the previous findings using the van Krevelen diagram to measure the atomic ratio of hydrochar produced form multiple types of biomass. Performing HTC experiments with TV concluded that additional water was required during the HTC process in order to remove ash material form the biomass, as well as to maximize the increase in HHV of the hydrochar.

ACKNOWLEDGEMENTS

The authors would like to acknowledge the Natural Sciences and Engineering Research Council of Canada (NSERC, Grant no. 400495), and Ministry of the Environment for Best in Science program (Project #1314010).

REFERENCES

1. Bach Q-V, Tran K-Q, Skreiberg Ø, Khalil RA, Phan AN. Effects of wet torrefaction on reactivity and kinetics of wood under air combustion conditions. *Fuel*. 2014;137:375-83.
2. Yang W, Shimanouchi T, Iwamura M, Takahashi Y, Mano R, Takashima K, et al. Elevating the fuel properties of Humulus lupulus, Plumeria alba and Calophyllum inophyllum L. through wet torrefaction. *Fuel*. 2015;146:88-94.
3. Funke A, Reebs F, Kruse A. Experimental comparison of hydrothermal and vapothermal carbonization. *Fuel Processing Technology*. 2013;115:261-9.
4. Kambo HS, Dutta A. Strength, storage, and combustion characteristics of densified lignocellulosic biomass produced via torrefaction and hydrothermal carbonization. *Applied Energy*. 2014;135:182-91.
5. Erlach B. Biomass upgrading technologies for carbon-neutral and carbon-negative electricity generation: techno-economic analysis of hydrothermal carbonization and comparison with wood pelletizing, torrefaction and anaerobic digestion: Berlin, Technische Universität Berlin, Diss., 2014; 2014.
6. Hoekman SK, Broch A, Robbins C. Hydrothermal Carbonization (HTC) of Lignocellulosic Biomass. *Energy & Fuels*. 2011;25:1802-10.
7. Baskyr I, Weiner B, Riedel G, Poerschmann J, Kopinke F-D. Wet oxidation of char–water-slurries from hydrothermal carbonization of paper and brewer's spent grains. *Fuel Processing Technology*. 2014;128:425-31.
8. Funke A, Ziegler F. Hydrothermal carbonization of biomass: A summary and discussion of chemical mechanisms for process engineering. *Biofuels, Bioproducts and Biorefining.* 2010;4:160-77.
9. Bach Q-V, Tran K-Q, Khalil RA, Skreiberg Ø, Seisenbaeva G. Comparative Assessment of Wet Torrefaction. *Energy & Fuels*. 2013;27:6743-53.
10. Kambo HS, Dutta A. A comparative review of biochar and hydrochar in terms of production, physico-chemical properties and applications. *Renewable and Sustainable Energy Reviews*. 2015;45:359-78.
11. Kim D, Lee K, Park KY. Hydrothermal carbonization of anaerobically digested sludge for solid fuel production and energy recovery. *Fuel*. 2014;130:120-5.
12. Liu Z, Quek A, Kent Hoekman S, Balasubramanian R. Production of solid biochar fuel from waste biomass by hydrothermal carbonization. *Fuel*. 2013;103:943-9.
13. Pala M, Kantarli IC, Buyukisik HB, Yanik J. Hydrothermal carbonization and torrefaction of grape pomace: a comparative evaluation. *Bioresour Technol.* 2014;161:255-62.
14. Liu Z, Balasubramanian R. Upgrading of waste biomass by hydrothermal carbonization (HTC) and low temperature pyrolysis (LTP): A comparative evaluation. *Applied Energy.* 2014;114:857-64.
15. Novianti S, Biddinika MK, Prawisudha P, Yoshikawa K. Upgrading of Palm Oil Empty Fruit Bunch Employing Hydrothermal Treatment in Lab-scale and Pilot Scale. *Procedia Environmental Sciences.* 2014;20:46-54.
16. Yan W, Hastings JT, Acharjee TC, Coronella CJ, Vásquez VR. Mass and Energy Balances of Wet Torrefaction of Lignocellulosic Biomass†. *Energy & Fuels*. 2010;24:4738-42.
17. Koppejan J, Van Loo S. The handbook of biomass combustion and co-firing: Routledge; 2012.

ICME2015

International Conference on Mechanical Engineering 2015
(ICME 2015) 18 – 20 December, 2015, Dhaka, Bangladesh

Paper ID :101

Performance Analysis of a Bio-gasification Based Combined Cycle Power Plant Employing Indirectly Heated Humid Air Turbine

S. Mukherjee[a)], P. Mondal[b)]and S. Ghosh[c)]

Department of Mechanical Engineering, Indian Institute of Engineering Science and Technology, Shibpur, Howrah – 711103, West Bengal, India.

[c)] Corresponding author: sudipghosh.becollege@gmail.com
[a)] sankha.deepp@gmail.com
[b)] mondal.pradip87@gmail.com

Abstract. Rapid depletion of fossil fuel has forced mankind to look into alternative fuel resources. In this context, biomass based power generation employing gas turbine appears to be a popular choice. Bio-gasification based combined cycle provides a feasible solution as far as grid-independent power generation is concerned for rural electrification projects. Indirectly heated gas turbine cycles are promising alternatives as they avoid downstream gas cleaning systems. Advanced thermodynamic cycles have become an interesting area of study to improve plant efficiency. Water injected system is one of the most attractive options in this field of applications. This paper presents a theoretical model of a biomass gasification based combined cycle that employs an indirectly heated humid air turbine (HAT) in the topping cycle. Maximum overall electrical efficiency is found to be around 41%. Gas turbine specific air consumption by mass is minimum when pressure ratio is 6. The study reveals that, incorporation of the humidification process helps to improve the overall performance of the plant.

INTRODUCTION

A key way for rural development in India is to provide electricity for rural population. If India has to fulfil its 'Electricity for all' mission by 2022, stand-alone and decentralized power generation system needs to become effective and popular. Biomass gasification based power generation system has a huge potential because of the country's high biomass reserve and its suitability for decentralized generation [1].

Solid biomass undergoes thermo-chemical conversion to generate producer gas which is a hot mixture of H_2, CH_4, CO, CO_2, N_2 and H_2O. Solid residuals are generated in this process which is called tar [2, 3]. If this raw gas is to be fed directly to the gas turbine, gas has to undergo extensive cooling and cleaning to protect GT blades. To avoid this problem a combustor heat exchanger (CHX) duplex unit can be installed [4].Wet cycles is a category of gas turbine power plants that use water to enhance the power plant performance. Mixtures of water and air in thermodynamic cycles have been used for many years and gas turbines have been operated with water during the last few decades [5]. Water is injected into the combustor or humidification tower in the form of direct water or steam [5].The very basic purpose of this system is to densify the working fluid to enhance efficiency [5].

This paper focuses on the thermodynamic modelling and performance assessment of biomass gasification based indirectly heated combined cycle plant employing humid air turbine. Saw dust as fuel feed gets gasified in a downdraft gasifier. A humidification plant has been introduced for water injection in the working fluid, i.e. Air. The topping cycle power output has been kept constant at 1000 kW_e. The plant configuration has been simulated in Cycle Tempo simulation software [6]. A wide range of pressure ratio of GT block as well as air relative humidity (φ =0.2 to 0.99) have been considered. Three sets of turbine inlet temperature (TIT= 1000, 1100 and 1200^0C) for the GT block is also considered during the analysis. The study includes discussion on the sizing of the heat exchanger.

PROPOSED PLANT CONFIGURATION

Fig. 1 shows the schematic diagram of the biomass gasification based indirectly heated combined plant. It incorporates the humid air turbine as well. Solid biomass (saw dust) is fed into the downdraft gasifier (block 2) through hopper (block 1). There it is gasified with the atmospheric air to yield producer gas. The amount of oxygen in the air is less than that of required for complete combustion. The producer gas is fed to the combustor (block 6) where combustion takes place in the presence of pre-heated air. High temperature flue gas is produced in this complete combustion process. The flue gas enters into the shell side of an air heater (shell side) (block 7).The air heater and the combustor together is called combustor-heat exchanger (CHX) duplex unit. The flue gas heats up the topping cycle working fluid, air, in the CHX unit. Then it goes to an air pre-heater (block 14) where it heats up the air used for the combustion of producer gas. The flue gas is finally exhausted to the atmosphere through the stack (block 22).

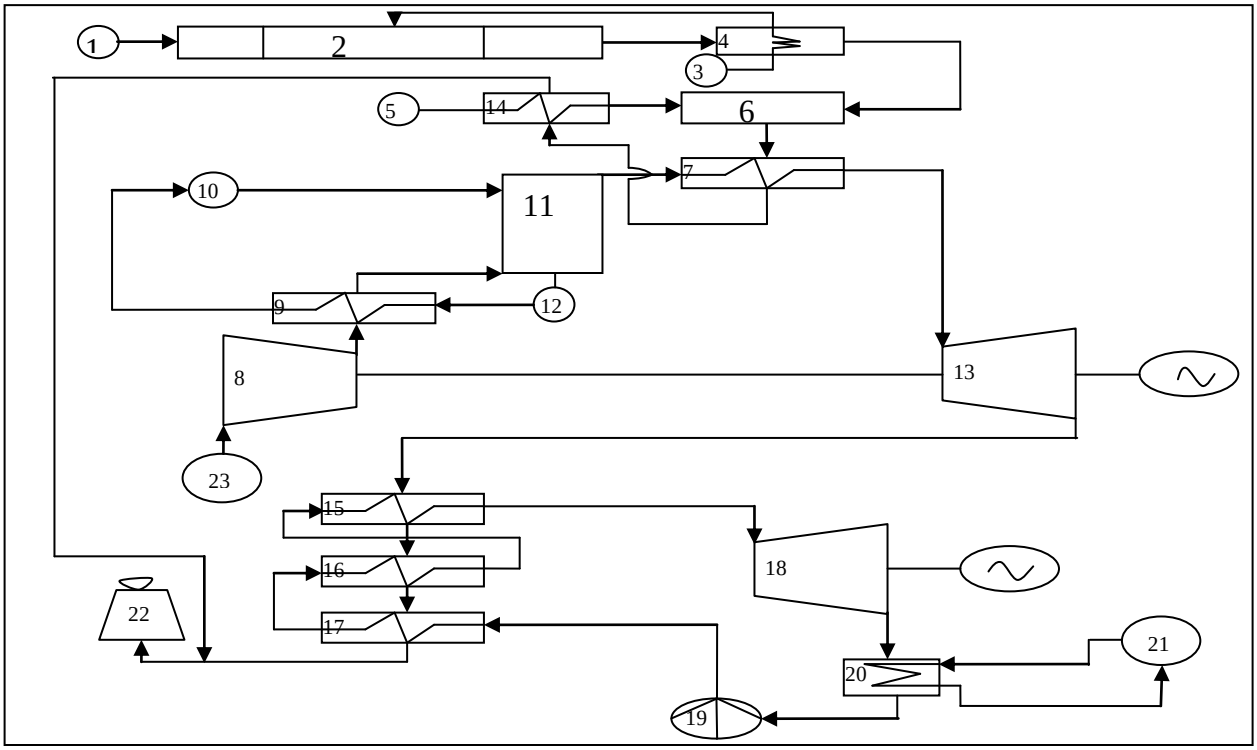

FIGURE 1. Schematic of the bio-gasification based indirectly heated combined cycle plant employing humid air turbine

Atmospheric air after passing through the compressor (block 8) enters into the humidification chamber (block 11). The humid air enters into the CHX unit and gets heated up. The water supplied to the humidifier is heated up in an aftercooler (block 9) using the air coming out of the compressor. The hot high pressure air enters into the turbine (block 13) and is expanded up to atmospheric pressure. It then goes to superheater (block 15) followed by evaporator (block 16) and economiser (block 17) - together called the heat recovery steam generator (HRSG) to produce superheated steam for the steam turbine (block 18). HRSG, steam turbine (block 18), condenser (block 20), feed pump (block 19) and cooling tower (block 21) together complete the bottoming steam power plant. Electric generators are coupled with the gas turbine rotor and steam turbine rotor respectively to produce electricity. Air is finally exhausted to the atmosphere through the stack (block 22).

MODEL DEVELOPMENT

Thermodynamic First Law analysis has been carried out for the given plant configuration, varying certain design and performance parameters. The model development and thermal performance assessment have been carried out

using Cycle-Tempo software. However, detailed thermodynamic analysis considering standard thermodynamic relations can be found out in an earlier paper by *Mondal & Ghosh* [4]. However, the integration of HAT (humid air turbine) cycle as topping cycle is carried out in this study and analysis strategy is given as follows:

Parametric Assumptions

The following assumptions are made for the analyses [4, 7]

- Ultimate analysis of saw dust shows C=48.98, H=4.89, O=36.01 and LHV=18,326 kJ/kg. Tar and char formation has not been considered in the gasification process.
- There is no heat loss in the plant components and in the ducts. There is no pressure loss in any of the fluid circuits.
- The bottoming steam cycle does not incorporate reheat and regeneration. Its operating pressure is 20 bar and steam temperature at turbine inlet is 300^0C. The condenser pressure is 0.08 bar. The isentropic efficiencies of air compressor and GT and bottoming ST are 90%. Humidification process is perfectly isothermal For the HRSG, minimum pinch point temperature difference is set to 10^0C. The stack temperature is 120^0C.

Air Humidification and After-cooler Unit

The compressed air after exchanging heat in the aftercooler enters into the humidifier. Hot water at high pressure is injected. The amount of water evaporated depends on the temperature and pressure of air. Specific humidity of the air at the exit of the humidifier is determined as follows:

$$d = 0.622\frac{\varphi p_{sat}}{p - \varphi p_{sat}} \tag{1}$$

where p_{sat} denotes the saturation vapour pressure of the humidifier in bar and p is the total pressure of wet air in the humidifier in bar. An after-cooler unit is used to extract heat from the hot compressed air to heat up the high pressure water, which will be used in the humidifier. Usually a plate type heat exchanger is used as the aftercooler.

Performance Parameters

Net work output from topping cycle is given by deducting the pump work required from GT work output.

$$W_{net,GT} = (W_{GT} - W_C)\eta_m\eta_G \tag{2}$$

Net work output from the combined cycle is the sum of net work outputs from humid air turbine and from steam turbine.

$$W_{cc} = W_{net,GT} + W_{ST}\eta_m\eta_g \tag{3}$$

The overall electrical efficiency of the combined is expressed as:

$$\eta_e = \frac{W_{CC}}{m_b LHV_b} \tag{4}$$

where, m_b represents the biomass consumption rate equivalent to one formula mol of biomass feed to the plant. Electrical specific biomass consumption-ESBC (kg/kWh) is expressed as:

$$ESBC = \frac{3600 m_b}{W_{cc}} \tag{5}$$

RESULTS AND DISCUSSIONS

The performance assessment result has been reported in this section followed by a brief discussion on thermal designing of the heat exchangers used in this configuration. The performance of the gasifier, considering saw dust as the biomass, is presented Table 1.

A base case is considered where the topping cycle pressure ration is 4, relative humidity of the air after humidifier is 0.99 and the turbine inlet temperature is 1000^0C (r_p=4, φ=0.99 and TIT=1000^0C).The performances of the plant at the base case is shown in Table 2. It is observed form Table 2 that the plant gives 39% combined electrical efficiency (for base case configurations). The ESBC of the configurations is 0.5 kg/kWh.

TABLE 1. Performance of the gasifier model

Gas Composition (% mole fraction)	Present Model
H_2	15.96
CO	18.85
CO_2	11.37
CH_4	0.61
N_2	47.90
H_2O	4.69
Air-fuel Ratio	2.3
LHV (MJ/kg)	3.85
Gasification efficiency (%)	69.18

TABLE 2. Base Case Performance of the proposed Configurations

Parameter	Unit	Value
GT net Output	kWe	1000
ST Output	kWe	665
Combined Cycle Electrical Efficiency	%	39.108
ESBC	kg/kWh	0.50
Required Air flow through GT unit	kg/s	3.128
Steam flow rate	kg/s	0.831
Relative humidity after humidifier	%	0.99

The topping cycle pressure ratio has been varied from 3 to 16 and the humidification process has been kept constant in such a fashion that air is always saturated at the humidifier outlet. Relative humidity of the air after the humidification process has only been varied when the effect of the humidification process on the performance of the plant has been analysed.

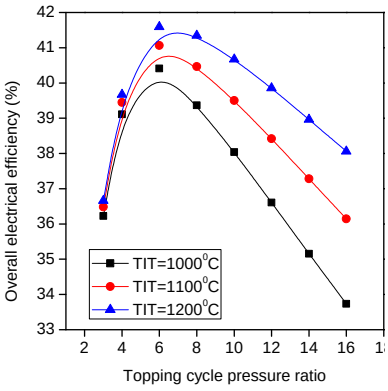

(a)

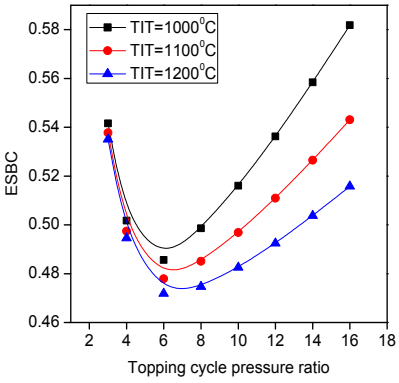

(b)

FIGURE 2. (a) Variation in overall electrical efficiency (b) Variation of ESBC with topping cycle pressure ratio

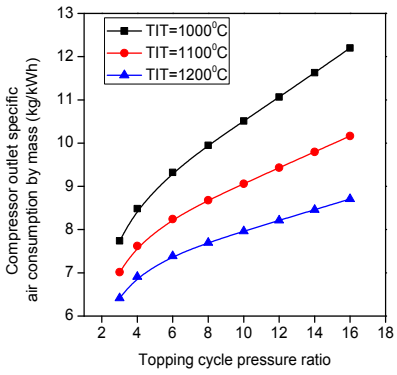

(a)

FIGURE 3. (a) Variation in compressor outlet specific air consumption by mass with topping cycle pressure ratio

The variation of overall electrical efficiency with that of topping cycle pressure ratio has been shown in the Fig. 2a. Initially efficiency increases in each case, reaches maximum value and then starts to reduce. It is observed that the maximum efficiency is achieved when compression ratio of the topping cycle is 6. The efficiency also increases with turbine inlet temperatures (TITs).

The variation in Electric Specific Biomass Consumption (ESBC) with that of topping cycle pressure ratio and TIT has been shown in Fig. 2b. It follows the reverse trend of that of overall electrical efficiency. ESBC is found to be improving with TIT.

Figure 3 shows the variation in compressor outlet specific air consumption by mass with topping cycle pressure ratio and TIT. With the increase in topping cycle pressure ratio, water requirement to saturate the air is reduced

drastically. To compensate the reduction in water addition, compressor mass flow increases continuously to produce specified power output. As the mass flow rate of the air through compressor increases sharply with the pressure ratio, the power input to the compressor also increases. Hence the overall electrical efficiency of the plant is reduced sharply at higher pressure ratio which is reflected in the Fig. 2a.

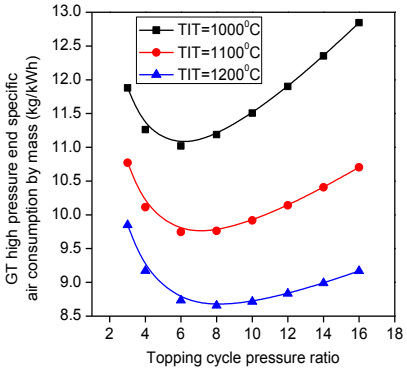

(b)

FIGURE 3. (b) Variation in GT high pressure end specific air consumption by mass with topping cycle pressure ratio

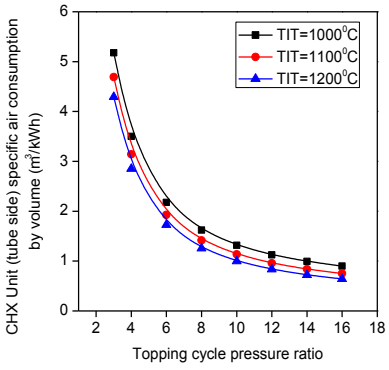

(a)

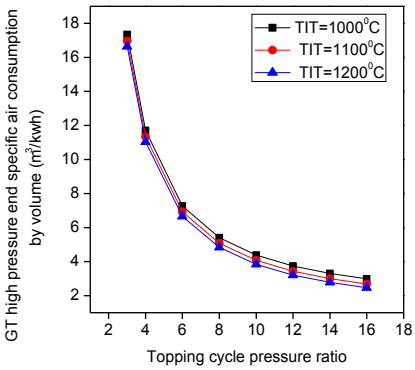

(b)

FIGURE 4. (a) Variation in CHX unit (tube side) specific air consumption by volume (b) Variation in GT high pressure end specific air consumption by volume with topping cycle pressure ratio

Figure 3b shows the variation in GT high pressure end specific air consumption by mass with topping cycle pressure ratio and TIT. The specific air consumption by mass is minimal at optimum pressure ratio 6. For a particular pressure ratio the specific air consumption decreases with the TITs. It is because of the fact that with the increase of TITs, specific energy input to the GT increases which leads to reduction in specific air consumption. The difference of mass flow rate of air through compressor and GT is the amount of water added in the humidifier.

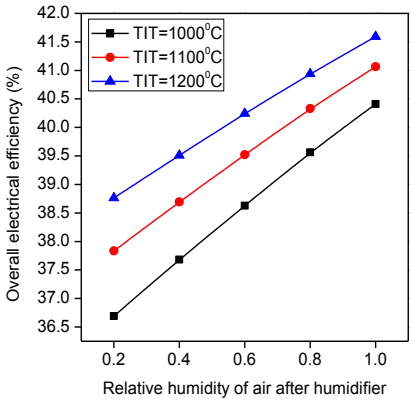

FIGURE 5. Variation in overall Electrical Efficiency with relative humidity of air after humidifier

The required topping cycle air flow rate influences the size of the gas turbine. For the low pressure end of the turbine the size is usually determined by the specific air consumption by mass while that for high pressure end is determined by the specific air consumption by volume [7]. Fig. 4a and Fig. 4b show the variation in required air consumption by volume with topping cycle pressure ratio to predict the sizes. Power output from GT block being constant, volume flow rate reduces monotonically with pressure ratio.

Now, it will be interesting to observe the impact of the humidifier on the performance of the plant. The plant performs best when the topping cycle pressure ratio is 6. Hence for this analysis the topping cycle pressure ratio has been fixed at 6 and relative humidity of the air after humidifier has been varied from 0.2 to 0.99. The variation of overall electrical efficiency with the relative humidity of air after humidification for different turbine inlet temperatures has been shown in Fig. 5. The efficiency increases sharply with the relative humidity due the presence of water vapour in the air. The efficiency also increases with the turbine inlet temperature.

TABLE 3. Performance of the Plant and Sizing of the Heat Exchangers at Different Operating Conditions

Performance of the plant	**r_p=6, TIT=1000^{0}C, φ =0.99**				**r_p=6, TIT=1100^{0}C, φ =0.99**				**r_p=6, TIT=1200^{0}C, φ =0.99**			
Required Biomass Flow rate (kg/s)	0.2036				0.2023				0.2014			
Required Air Flow Rate through GT block (kg/s)	3.061				2.707				2.426			
Required Steam Flow Rate (kg/s)	0.637				0.655				0.671			
Electrical Efficiency (%)	40.413				41.605				41.592			
Sizing of the Heat Exchangers	**ΔT_H (K)**	**ΔT_L (K)**	**Q_{trans} (kW)**	**UA (kW/K)**	**ΔT_H (K)**	**ΔT_L (K)**	**Q_{trans} (kW)**	**UA (kW/K)**	**ΔT_H (K)**	**ΔT_L (K)**	**Q_{trans} (kW)**	**UA (kW/K)**
Flue Gas to GT Air Heater (block 7)	576	156	3473	10.8	476	156	3449	12	376	156	3435	13
Flue Gas to combustor Air Pre-Heater (block 14)	16	94	333	7.5	16	95	331	7.35	16	94	329	7.04
Superheater (block 15)	306	357	142	0.43	380	426	146	0.36	455	495	150	0.31
Evaporator (block 16)	357	10	1202	12.37	426	10	1237	11	495	10	1267	10
Economizer (block 17)	10	78	467	14	10	78	480	14	10	78	492	14
Aftercooler (block 9)	123	85	354	3.44	123	85	313	3.04	123	85	280	2.72
Producer gas to air heater (block 4)	1087	1205	109	0.09	1087	1205	108	0.09	1087	1205	107	0.09

The performance of the entire plant heavily depends on the heat exchangers used in this configuration. Hence thermal performance of these heat exchangers has been analysed to optimize the plant operations. It is observed from the Fig. 2a and Fig. 5 that the plant performs best when r_p=6, φ=0.99 under different turbine inlet temperatures. The performance parameters as well as the thermal design variables have been recorded in table 3 under the best operating conditions mentioned earlier for different TITs. Table 4 shows the size of the heat exchanger (block 7) used in the CHX unit increases with increase in TIT while aftercooler (block 9) size gets reduced accordingly.

CONCLUSION

This paper focus on biomass gasification based combined cycle power plant employing humid air turbine. Indirectly heated scheme has been employed to avoid the complexity of extensive gas cleaning systems. Maximum efficiency is found to be around 42% at pressure ratio 6. GT specific air consumption is minimum at that point. Incorporation of the humidification system improves the overall efficiency by 2-4% when operated with a fixed TIT and topping cycle pressure ratio set at 6. Humidification system also helps to lower the size of the major plant equipment. Constant supply of treated water to the humidification plant is a point of concern which may be addressed with the installation of a water recovery system. Flue gas condensation system will be a right choice for this purpose in big size plants. Proper selection of materials for the CHX unit is also critical for the long-time operational sustainability of the plant.

REFERENCES

1. B. Buragohain, P. Mahanta and V.S. Moholkar, Renewable and Sustainable Energy Rev. **14 (1)**, 73-92 (2010).
2. N.S. Barman, S. Ghosh and S. De, Biores. Tech.**107**, 505-511 (2012).
3. Ankur Scientific Energy Technologies Pvt. Ltd. Website: http://www.ankurscientific.com
4. P. Mondal and S. Ghosh, Int. J. Renewable Energy Research, **5 (2),** 354-366 (2015).
5. M. Thern, "Humidification Processes in Gas Turbine Cycles", Ph.D thesis, Lund University, Lund, Sweden (2005).
6. Cycle-Tempo Software, Release 5, TU Delft, Website: http://www.cycle-tempo.nl/. (2012).
7. A. Datta, R. Ganguli and L. Sarkar, *Energy* **35**, 341-350 (2010).

ICME2015

International Conference on Mechanical Engineering 2015
(ICME 2015) 18 – 20 December, 2015, Dhaka, Bangladesh

Paper ID :102

Comparative Tribological Investigation of Biolubricant Formulated from Non-edible and Edible Oil Source

Mahmudul Hasan[1, a)], Md. Faiyaz Ahmed[1] and Sobahan Mia[1]

[1]*Department of Mechanical Engineering, KUET, Bangladesh*.

[a)]Corresponding author: iammhr@gmail.com

Abstract. Due to the negative effect of petroleum-based lubricant the biolubricant has come to the lime light. Vegetable oils of both edible and non-edible types have some great properties to be considered as an alternative solution to petroleum based lubricants. This paper presents a series of analysis of edible and non-edible oils for the possible use as lubricant. The sample vegetable oils of edible types were used are coconut, rice bran, palm, sesame, linseed, mustard, sunflower, olive oil and non-edibles types were neem and castor oil. It has been observed that every vegetable oil shows very promising characteristics to be used as base oil for biolubricant. It is observed that castor oil has the highest kinematic viscosity followed by neem oil and mustard oil. Almost all of the sample vegetable oils have higher viscosity index than mobil 5W-20 and mobilgear MT 68. It is observed that castor oil has the highest density followed by linseed, neem and mustard oil. All of the vegetable oils have better density than mobil 5W-20 and mobilgear MT 68. It is seen that castor oil has the lowest acid value followed by mustard and rice bran oil. It is found that rice bran oil possesses highest surface tension followed by coconut oil and sesame oil which have almost same surface tension. The surface tension of linseed and castor oil is found in a close range. Castor and linseed oil have shown promising surface tension. Castor oil has the highest flash point followed by rice bran, mustard and linseed oil. Mustard oil has the lowest pour point followed by castor, olive and linseed oil. From the results of this study, it can be concluded that the samples can be used as biolubricant in different purposes.

INTRODUCTION

Many different substances are used as lubricant to lubricate surfaces. Lubricating oils can be of synthetic, vegetable or mineral based as well as any combination of these. But researches have shown that the synthetic or petroleum based lubricating oils are toxic and prone to harm the environment. That's where the term Green Tribology plays an important role. Oleo chemical pollutants are derived from the food industry, petroleum products and by-products such as lubricating hydraulic and cutting oils [1]. Oleo chemical esters of fatty acids such as diesters, polyolesters and complex esters are derived from sunflower, rapeseed, palm and coconut oil. Triglycerides of vegetable oils are more polar than petroleum-based oils, thus they have a higher affinity to metal [2]. Vegetable oils and animal fat are being used as lubricating oil for a long period of time through the history of mankind.With modern technology modification of vegetable oils

with suitable additives can lead to a better alternative to toxic lubricants.The base oils of some high-performance motor oils however contain up to 20% by weight of esters [3]. In this paper, theoretical and experimental results have been compared to make a proper assessment of vegetable oils and petroleum-based oils for comparison.

NOMENCLATURE

ρ = Density (gm/cm^3)
υ = Kinematic viscosity (cSt)
μ = Absolute viscosity of fluid (centipoise)
T = Surface tension (dyne/cm)
m = Mass of oil (gm)
V = Volume (cm^3)

PROCEDURES

Viscosity Measurement by Saybolt Viscometer

The ratio of dynamic viscosity and the mass density is known as kinematic viscosity and is denoted by υ. The approximate relationship between kinematic viscosity and time t for a Saybolt universal viscometer is expressed by

$$\upsilon = 0.0022t - [1.8/t] \quad (1)$$

Where, υ is in stokes and t is in seconds.
Now, the absolute viscosity is given by

$$\mu = \upsilon \times \rho \quad (2)$$

Where,
μ = Absolute viscosity of fluid
υ = Kinematic viscosity of fluid
ρ = Density of fluid

The tap of the outlet passage of oil container was checked, whether it was opened or closed. The tap was opened and it was closed before oil was filled in the container. The oil container was filled with oil. The fluid was poured in the vertical cylinder, whose viscosity was to be measured. The amount of fluid was to be taken in the vertical cylinder was approximately 100 ml. The power supply was given to the thermostat switch and heater. A volumetric flask was placed bellow the capillary tube to receive the fluid discharged from the cylinder. After connecting the thermostat switch to the power supply, the thermostat switch was fixed at the required temperature. Then the heater was working. The heater was fitted at one corner of the container. When the temperature had reached the required temperature, the thermostat switch was automatically disconnected the supply. Then time was given to attain the desired temperature of the fluid. The stop valve was opened. Also the stopwatch was started to record the time in seconds for the flow of 60 ml of fluid through the capillary tube.

After the experiment had been completed, the supply current was disconnected and the oil was

removed from the container.

Viscosity Index Calculation

The viscosity index was calculated using the following formula:

$$V = 100\,\frac{(L-U)}{(L-H)} \tag{3}$$

Where V indicates the viscosity index, U the kinematic viscosity at 40 °C (104 °F), and L & H are various values based on the kinematic viscosity at 100 °C (212 °F) available in ASTM D2270.

Density Measurement

Density ρ,

$$\rho = \frac{M2 - M1}{V} \tag{4}$$

Where,
M1: The mass of empty standard bottle (including cover) (gm)
M2: The mass of filled bottle (gm)
V: Volume of bottle (cm^3)

Pour Point Measurement

ASTM D5853, Standard Test Method for Pour Point of Crude Oils. The specimen was cooled inside a cooling bath (refrigerator). At about 9 °C above the expected pour point, and for every subsequent 3 °C, the test jar was removed and tilted to check for surface movement. When the specimen did not flow when tilted, the jar was held horizontally for 5 sec. If it did not flow, 3 °C was added to the corresponding temperature and the result was the pour point temperature.

It was also useful to note that failure to flow at the pour point might also be due to the effect of viscosity or the previous thermal history of the specimen. Therefore, the pour point might have given a misleading view of the handling properties of the oil. An approximate range of pour point was observed from the specimen's upper and lower pour point.

Flash point Measurement

The outer container of the flash point measuring apparatus was filled with water and inner container with oil through the port. Then the apparatus was switched on. After 4-5 minutes the flame port was opened by pressing the switch and a flame was brought to the flame point. If the flame was flashing the thermometer reading was noted. If not, the waiting time was extended to

another 4-5 minutes.

Acid Value Calculation

Sample oil was taken and weighted in a conical flask. Then 10 ml ethanol was added and shaken well about 20-30 minutes and then titrated with 0.01 or 0.05 M NaOH.

$$Acid\ Value = \frac{56.1 * Strength\ of\ NaOH * Volume\ Of\ NaOH}{Weight\ of\ sample} \quad (5)$$

Phenolphthalein was used as indicator.

Surface Tension Measurement

Capillary tubes of radius r, opened at both ends, were dipped vertically into oil, which wetted the walls. The oil rose up the tube through a height h, the surface of the oil in the capillary tube would assume a spherical shape and for this oil it was concave upward. If it made an angle Θ with the vertical wall of tube, then Θ was the angle of contact and a force T due to surface tension acted along the tangent at A which was the point of contact of the oil with the walls.

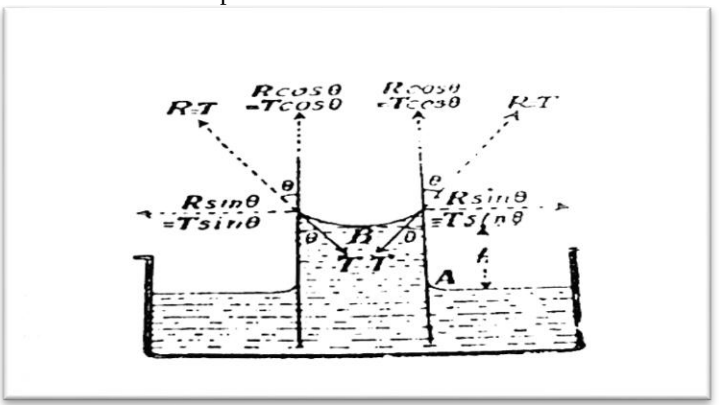

FIGURE 1. Surface tension measurement

The total vertical component of the force acting in the upward direction is 2πrTcosΘ, r being the internal radius of the capillary tube. This upward force supported the weight of the oil column.

$$The\ Volume\ of\ the\ oil = \pi\left(r^2 h + \frac{r^3}{3}\right) \quad (6)$$

If ρ was the density of the oil and g was the acceleration due to gravity then

$$Total\ weight\ of\ oil\ column = \pi r^2 (h + \frac{r}{3})\rho g \quad (7)$$

In equilibrium position,

$$2\pi rT cos\theta \; = \; \pi r^2 \left(h + \frac{r}{3}\right) \rho g \tag{8}$$

$$Surfacetension, T = \frac{r^2 \pi (h + \frac{r}{3}) \rho g}{2\pi r cos\theta} = \frac{r(h + \frac{r}{3}) \rho g}{2cos\theta} \tag{9}$$

If Θ was assumed to be very small, then Θ = 0 and cosΘ = 1

$$T = \frac{\rho g r (h + \frac{r}{3})}{2} dynes/cm \tag{10}$$

RESULTS AND DISCUSSION

This table 1 represents the value of kinematic viscosity of various sample oils in both 40°C and 100°C temperature in comparison with the motor oil and industrial lubricating oil, the measured experimental values by Saybolt viscometer are as follows.

TABLE 1. Kinematic viscosity of sample oils

Name Of Oils	Viscosity at 40°C(cSt)	Viscosity at 100°C(cSt)
Coconut	22.84	5.94
Rice Bran	24.32	6.22
Palm	39.7	8.2
Sesame	39.6	8.34
Neem	48.32	10.5
Castor	243.13	18.5
Linseed	40.12	10.1
Mustard	44.9	10.2
Sunflower	39.9	8.6
Olive	40.3	8.9
Mobil 5W-20	49.8	8.9
Mobilgear MT 68(ISO 68)	68	8.5

One of the most important properties of oil in maintaining a lubricating film between moving parts is its viscosity. The viscosity must be high enough to maintain a lubricating film, but low enough that the oil can flow around the engine parts under all conditions. In this study, figure 1 reveals the data on kinematic viscosity of oils at 40°C and 100°C. Figure 2 represents the data on viscosity index of oils. It is seen that linseed oil has the highest viscosity index followed by rice bran, mustard and neem oil.

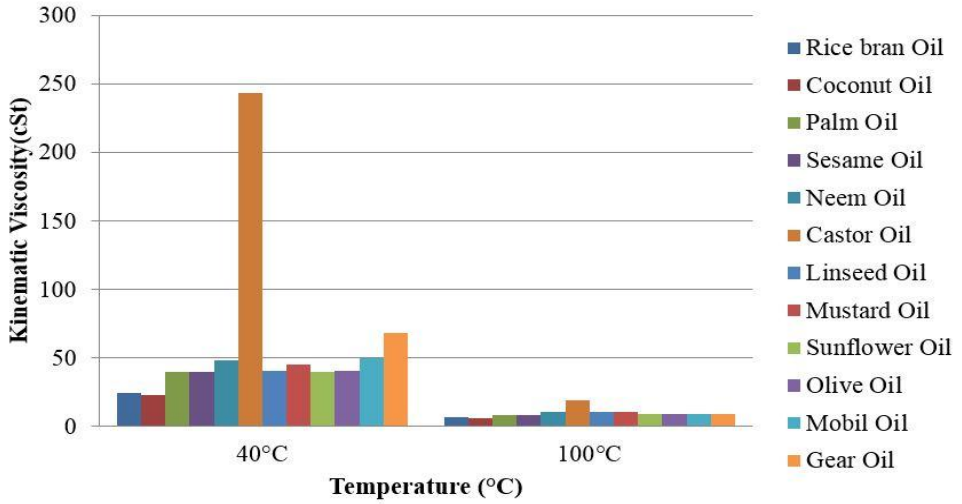

FIGURE 2. Kinematic Viscosity of oils compared with temperature at both 40°C and 100°C showing how viscosity differs with change of temperature

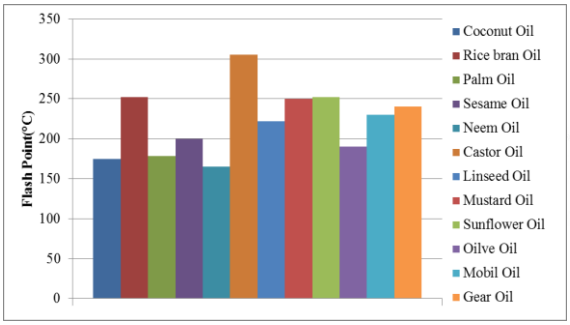

FIGURE 3. Viscosity Index of oils showing comparison between different

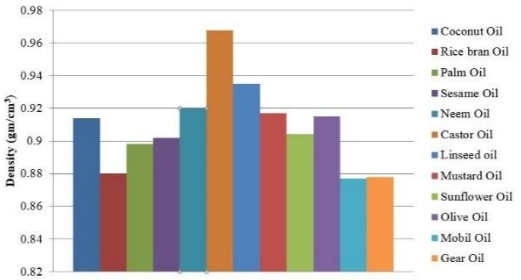

FIGURE 4. Comparison of density of different oils

TABLE 2. Viscosity index, density, acid value, surface tension, flash point and pour point of sample oils

Name Of Oils	Viscosity Index	Density (gm/cm^3)	Acid Value	Surface Tension (dyne/cm)	Flash Point(°C)	Pour Point(°C)
Coconut	226.63	0.914	2.65	25.3	175	22
Rice Bran	224.77	0.880	1.30	31.28	252	1
Palm	187.49	0.898	1.57	5.71	178	16
Sesame	193.67	0.902	3.28	25.70	200	- 6
Neem	214.36	0.920	3.40	8.1	165	10
Castor	82.72	0.968	0.51	15.8	305	-21.7
Linseed	252.32	0.935	3.08	14.23	222	-14.5
Mustard	224.39	0.917	0.70	20.35	250	-28.9
Sunflower	201.66	0.904	3.33	7.81	252	-12
Olive	210.1	0.915	3.80	11.66	190	-15.3
Mobil 5W-20	160.0	0.877	1.20	21.20	230[5]	-43
Mobilgear MT68(ISO 68)	94.2	0.878	1.50	22.70	240[6]	-18

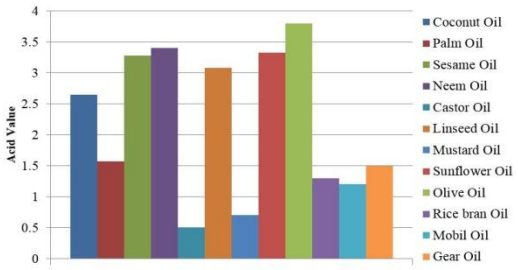

FIGURE 5. Comparison of acid value of different oils.

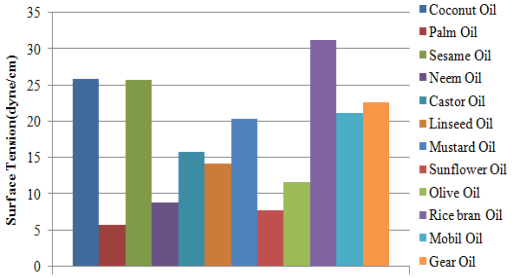

FIGURE 6. Comparison of surface tension of different oils.

The density of sample lubricating oil was determined by density bottle method, the experimental results are provided in table 2. Figure 4 and table 2 reveals the data on density of oils. It is observed that castor oil has the highest density followed by linseed, neem and mustard oil. All of the vegetable oils have better density than mobil 5W-20 and mobilgear MT 68. The acid values of sample oils were determined by titration and are listed in table 2. Acid value is the measure of lubricants acidity. The increase in acidity is an index of deterioration. Figure 5 represents the data on acid value of oils. It is seen that castor oil has the lowest acid value followed by mustard and rice bran oil. Only castor oil and mustard oil have given low acid number than Mobil 5W-20 and mobilgear MT 68. Another important property of oil is its flash point. It is dangerous for the oil to

ignite and burn at ambient temperature, so a high flash point is desirable. Figure 7 reveals the data on flash point of oils and figure 8 represents the data on pour point of oils. The surface tensions of sample oils were acquired from experiment and are listed in table 2. Figure 6 presents the data on surface tension of oils.

The inherent problems of vegetable oils, such as poor oxidation and low-temperature properties, can be improved by using additives. Vegetable oils are a good alternative to petroleum-based oils as lubricants in environmentally sensitive applications.

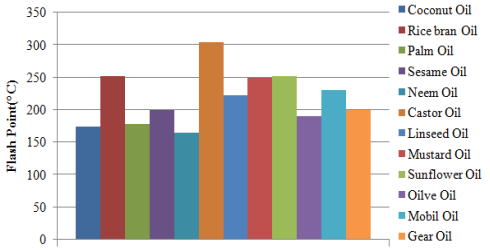

FIGURE 7. Comparison of flash point of different oils.

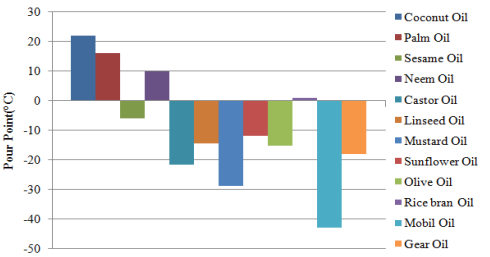

FIGURE 8. Comparison of pour point of different oils.

It is found that rice bran oil possesses highest surface tension followed by coconut oil and sesame oil which have almost same surface tension. From figure 7 it can be concluded that mustard oil has the lowest pour point followed by castor, olive and linseed oil.

CONCLUSION

In this paper various edible and non-edible vegetable oils have been analyzed to find out a better alternative lubricant. In the process of analysis it has been found that some edible and non-edible oils have better lubricating property than petroleum-based lubricants. Some of them have different property other than the petroleum-based oils which is crucial to lubricating agents.Castor oil, mustard oil and neem oil show promising viscosity index and kinematic viscosity. Castor oil, neem oil, mustard oil and linseed oil have high flash point. Castor oil and mustard oil have stunningly low acid number. Coconut oil, rice bran oil, mustard oil and sesame oil show better surface tension than mobil 5W-20.Though the surface tension of castor oil and neem oil is below the highest peak but it's still promising. In case of pour point, coconut oil, palm oil and neem oil fail to sustain its fluidity below 15°C. Castor oil and mustard oil both are well behaved below -20°C, having a viable pour point. It's clear that castor oil along with linseed oil has a great potential for being used as lubricant in almost all weather condition. Mustard oil also shows very good attributes for using as a lubricant in all aspects. Neem oil has good chance to be used as lubricant in above 20°C temperature. So vegetable oils of both edible and non-edible types can be a good alternative to face the challenge of toxic lubricants as well as enhancing the application of green Tribology.

ACKNOWLEDGEMENTS

The authors are very grateful to the Department of Mechanical Engineering, Khulna University of Engineering & Technology for making this study possible and thanks for their continuous support.

REFERENCES

1. Ilija Gawrilow, “Interfacing with the GlobalOils and Fats Business”, 3rd Global Oils and Fats Business Forum USA, 2003.
2. W. Liew Yun Hsien, “Towards Green Lubrication in Machining”, 1st Edition, Springer, USA, 2014..
3. Kornsteiner-Krenn M, Wagner KH, Elmadfa I (2013), "Phytosterol content and fatty acid pattern of ten different nut types", Int J Vitam Nutr Res 83 (5): 263–70. doi:10.1024/0300-9831/a000168, PMID 25305221.
4. Sobahan Mia, Shinichiro Hayashi and Nobuyoshi Ohno (2007), “High pressure Tribological behavior of vegetable oils as lubricant”, ICME 2007, December 2007, Dhaka, Bangladesh
5. http://www.mobil.com/USA-English/Lubes/PDS/GLXXENPVLMOMobil_1_5W-20.aspx
6. http://www.exxonmobil.com/USA-English/Marine/PDS/GLXXENMRNEMMobilgear_SHC_MT_68.aspx

ICME2015

International Conference on Mechanical Engineering 2015
(ICME 2015) 18 – 20 December, 2015, Dhaka, Bangladesh

Paper ID : 104

3-Dimensional Numerical Study of Cooling Performance of A Heat Sink With Air-Water Flow Through Mini-channel

Sambit Majumder[a)], Abhik Majumder[b)] and Swapan Bhaumik[c)]

Department of Mechanical Engineering, National Institute of Technology, Jirania, Barjala, Agartala, Tripura-799046, India

[a)]Corresponding author: sambit.majumder@gmail.com
[b)]onlyabhik@gmail.com
[c)]sbhaumik6519@gmail.com

Abstract. The present microelectronics market demands devices with high power dissipation capabilities having enhanced cooling per unit area. The drive for miniaturizing the devices to even micro level dimensions is shooting up the applied heat flux on such devices, resulting in complexity in heat transfer and cooling management. In this paper, a method of CPU processor cooling is introduced where active and passive cooling techniques are incorporated simultaneously. A heat sink consisting of fins is designed, where water flows internally through the mini-channel fins and air flows externally. Three dimensional numerical simulations are performed for large set of Reynolds number in laminar region using finite volume method for both developing flows. The dimensions of mini-channel fins are varied for several aspect ratios such as 1, 1.33, 2 and 4. Constant temperature (T) boundary condition is applied at heat sink base. Channel fluid temperature, pressure drop are analyzed to obtain best cooling option in the present study. It has been observed that as the aspect ratio of the channel decreases Nusselt number decreases while pressure drop increases. However, Nusselt number increases with increase in Reynolds number.

INTRODUCTION

Thermal management of electronic devices has been an integral part of many industries and it has been a matter of concern in recent years. With the trend of miniaturization of devices, market is demanding for reduction in size and high power density which is expected to increase furthermore in coming years. Devices such as laser diodes, CPU processors, future nuclear fusion, fission reactors and ICs etc. possess high heat flux concentration and thus require thermal management. In this regard micro-channel cooling may be regarded as good solution as it possesses high surface area to volume ratio to remove considerable amount of heat. Most failures in electronics devices occur due to thermal failure such as mechanical stresses, thermal de-bonding and thermal fracture (Kristiansen et al. [1]).

Earlier Tuckerman and Pease [2], used microchannel cooling technique by direct circulation of water in a silicon substrate microchannel. Recently, Biswal et al. [3] have done numerical investigation over vertical microchannels in developing and fully developed regions for large aspect ratio channels with temperature dependent thermo-physical property of the fluid under constant wall temperature boundary condition. They observed increase in thermal entrance length with increase in Rayleigh number and Knudsen number. The average Nu of the flow increased with Rayleigh number and decreased with decrease in Knudsen number. In review article by Shabgard et al [4], put forwarded the advantages of heat pipe heat exchangers in microelectronics industry and research in the field of HVAC. These systems require no power input, cooling water and lubrication systems and as well as are compact, passive, light weight, economical, reliable, contains minimal parts, easy to assemble and install, versatile and adaptable of design. Low thermal resistance, small pressure drop and chemically compatible are some advantages of these systems. Vafai

et al. [5] presented a new technique of electronics cooling by incorporating two-layered micro-channel heat sink with counter-flow arrangement of water along channels. The proposed model of two-layer micro-channel showed reduced temperature rise at base surface and smaller pressure drop is required as compared to conventional one-layered micro-channel. Federov et al. [6] numerically investigated the conjugate heat transfer effect in a 3D micro-channel heat sink. They recognised that water cooled microchannel heat sink possess good potential in cooling electronic systems with small increase in temperature rise of the system and high thermal load capacity. Moreover, large transverse and longitudinal temperature gradients are matter of concern with respect to structural failure and thermal stresses in heat sinks. Croce et al. [7] numerically investigated the conjugate heat transfer and axial conduction effect in low aspect ratio channels. They predicted that heat sink efficiency is a function of Mach number and varies less with axial conduction.

Hadjiconstantinou et al. [8] performed direct simulation Monte Carlo method technique to numerically investigate Nusselt number under constant wall temperature boundary condition in two dimensional micro and nano-channel under hydrodynamically and thermally fully developed condition in slip flow and transition regime. They recognised Nusselt number under axial heat conduction. Xu et al. [9] investigated thermal characteristics over four geometric models-parallel, reticular, toroidal and tree-like structures. Tree- like structure possessed good thermal characteristics and carried out most heat at same inlet flow rate. Hettiarachchi et al. [10] investigated laminar slip flow and heat transfer numerically and observed with increase in Knudsen number pressure gradient decreased. Nu increased due to slip and decreased due to temperature but combined effect may lead to increase or decrease of Nusselt number. Renksizbulut et al. [11] numerically investigated the effect of low Reynolds number, channel aspect ratio and Knudsen number for rarefied gas flow and heat transfer effects in rectangular micro-channels. They observed large reduction in wall friction and heat transfer in entrance region for slip flow condition but it has significant effect with respect to degree of rarefaction and aspect ratio in fully developed region.

A detailed and wide range study were done by many authors (Lyczkowski et al.[12], Wibulswas [13], Chandrupatla et al. [14]) in microchannel flow by varying aspect ratio, geometrical shapes and thermal boundary conditions and provided large data sets. Recently, Majumder et al. [15] investigated numerically effect of fluid flow and heat transfer in a T-junction incorporated with corner radius of various radii in laminar and turbulent flows under H2 boundary condition. It is observed that vortices gradually reduced as corner radii increased and velocity profile showed faster rate of development.

It can be concluded from earlier studies that researchers used either active or passive method of cooling. Moreover, due to increase in trend of miniaturization of devices, microchannel cooling is getting more preference in electronic devices amongst several cooling techniques. The present work aims at incorporating both cooling techniques simultaneously in a heat sink and undergo detailed study of its effect over heat transfer and fluid flow.

METHODS AND PROCEDURE

Three dimensional models researched in this paper are generated in presolver GAMBIT. Rectangular cross section fins are designed with dimension 5x2 mm and heat sink base of dimension 80x80 mm (Fig.1(i)). To incorporate fluid flow through these fins mini-channels are provided with four different aspect ratio as $\alpha^* = 4$, 2, 1.33 and 1 for wide range of investigation as shown in Fig. 1(ii). For fin pitch 2mm, 20 number of fins can be incorporated on heat sink. To introduce forced air flow externally through the heat sink, an air domain is created whose height is 1.5 times the fin height. As these models are symmetric, hence, a half section of the mini-channel fin is selected for the numerical investigation to reduce computational time and cost (shown in Fig. 2(a)).

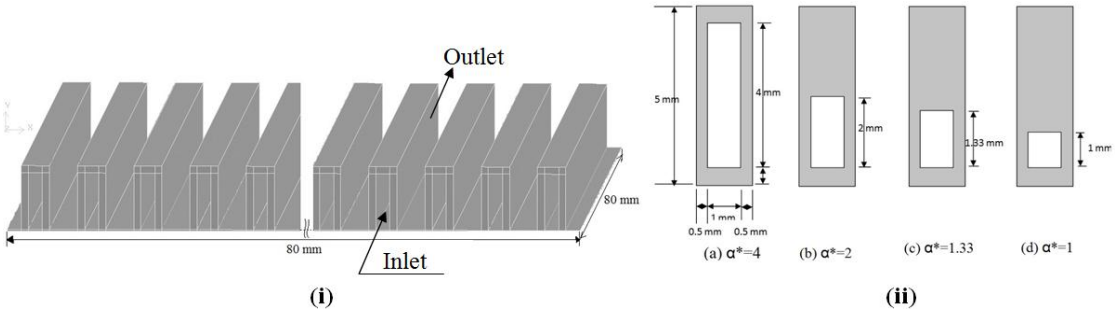

FIGURE 1. (i) Heat sink model; (ii) Different aspect ratio models

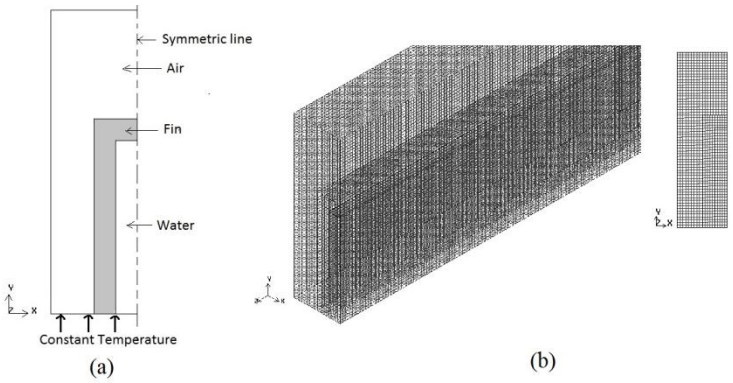

FIGURE 2. (a) Symmetric model; (b) Generated grids.

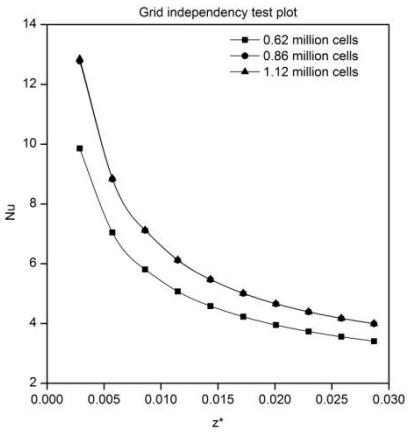

FIGURE 3. Grid independency plot.

A fine mesh produces accurate results while solving fluid flow and heat transfer problems. The grid generation of the models is done in pre-processor GAMBIT. Submapped face meshing is adopted whereas hexahedral element scheme mesh volumes are generated in 3D models as shown in Fig. 2(b). A grid independence study is done over the model to achieve a suitable grid which is a trade-off between numerical accuracy and computational cost. The study is performed for 6.2 lacs, 8.6 lacs and 11.2 lacs number of cells. It is recognised that as number of meshed elements changed from 6.2 lacs to 8.6 lacs cells, the Nusselt number calculated at channel outlet varied by 14.65%, whereas a shift from 8.6lacs to 11.2 lacs elements, the Nusselt number changed by only 0.011% (shown in Fig. 3). Since no significant change is noticed as we moved from second case to third case, hence 8.6 lacs mesh type is selected for rest of the simulation to arrest computational time and cost.

The non-dimensional bulk fluid temperature for aspect ratio ($\alpha^*=1$) with respect to non-dimensional axial length is compared with work done by Wibulswas et al. [13] and plotted in Fig. 4. It is recognised that the present work experienced 5.84% decrement in bulk fluid temperature at channel outlet as compared to Wibulswas [13] for same aspect ratio which revealed a good agreement with earlier works.

In the present study a new technique is introduced where water is passed through the mini-channel fins and air is passed externally along the fins unidirectionally. Water carries huge amount of heat per unit volume and has high thermal conductivity. Moreover air and water are cost effective to be used in cooling purpose. Air and water inlet conditions are provided with uniform velocity inlet boundary condition and copper is chosen as substrate material for heat sink. The model is studied considering steady state, incompressible flow, constant fluid properties and negligible axial conduction, viscous dissipation and radiative effects. The present work is carried out in laminar region where water side Reynolds numbers range from 250 to 1200 to obtain a large number of data for detailed study. The velocity of air at inlet is kept constant (1 m/s) for each model. The numerical model is solved for no slip condition on every wall and pressure outlet at trailing end of the channel. Interface boundary condition is incorporated between wall and fluid interface for heat conduction. Finite volume approach is used for the present study with pressure based, absolute velocity formulation and steady state solver. SIMPLE scheme, pressure velocity coupling is used as iterative algorithm and 10^{-6} convergence criteria. The numerical simulation of the models is carried out in CFD package FLUENT, for constant wall temperature of 323K (T type) boundary condition.

RESULTS AND DISCUSSIONS

The models studied in this work posses hydrodynamically fully developed and thermally developing region. Figure 5 shows the temperature contours of heat sink at outlet for Re=1200. It can be observed from the figure that, $\alpha^*=4$ model has least outlet temperature as compared to other models. Figure 6(a) shows comparison of Nusselt number of present work with Lyczkowski et al. [12] as a function of z^* for $\alpha^*=1$. Figure 6(b) shows comparison of Nusselt number of present work with Chandrupatla et al. [14] for $\alpha^*=1$. These plots reveal that current technique possess good thermal characteristics in hydrodynamically developing region as compared to conventional technique adopted in earlier studies. It can be attributed to the fact that both air and water flow simultaneously through the channel reduce bulk fluid temperature combinedly at large extent and increase Nusselt number to an appreciable extent. Figure 6(c) reveals that pressure difference for water flow increases with increase in Reynolds number.

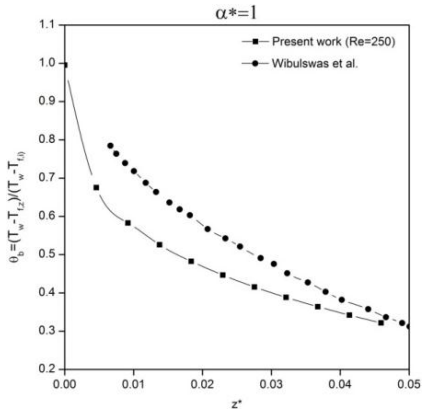

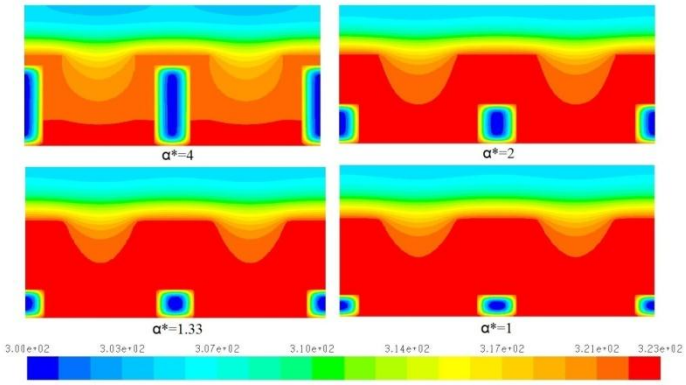

FIGURE 4. Validation of present work with Wibulswas et al[13]. **FIGURE 5.** Temperature contours at sink's outlet (Re=1200).

Moreover, the pressure difference increased with decrease in aspect ratio. It is due to the fact that, as aspect ratio decreases, the flow cross sectional area decreases which result into increase in pressure to drive the flow. The greatest difference is observed in α*=1 models whereas α*=4 models possessed least pressure drop to drive a flow. Hence, an optimization is required. Figure 7(a,b) represent variation of dimensionless bulk fluid (water) temperature as a function of axial length for different Reynolds numbers. Non-dimensional bulk fluid temperature is calculated as

$$\theta_b = \frac{T_w - T_{f,z}}{T_w - T_{f,i}} \quad (1)$$

It can be concluded, as axial length increases, fluid temperature increases and hence θ_b decreases. Moreover, fluid bulk temperature decreases with increase in Reynolds number and increases with decrease in aspect ratio. α*=4 model has least fluid temperature which can be attributed to the fact that heat from sink is distributed among large volume of water.

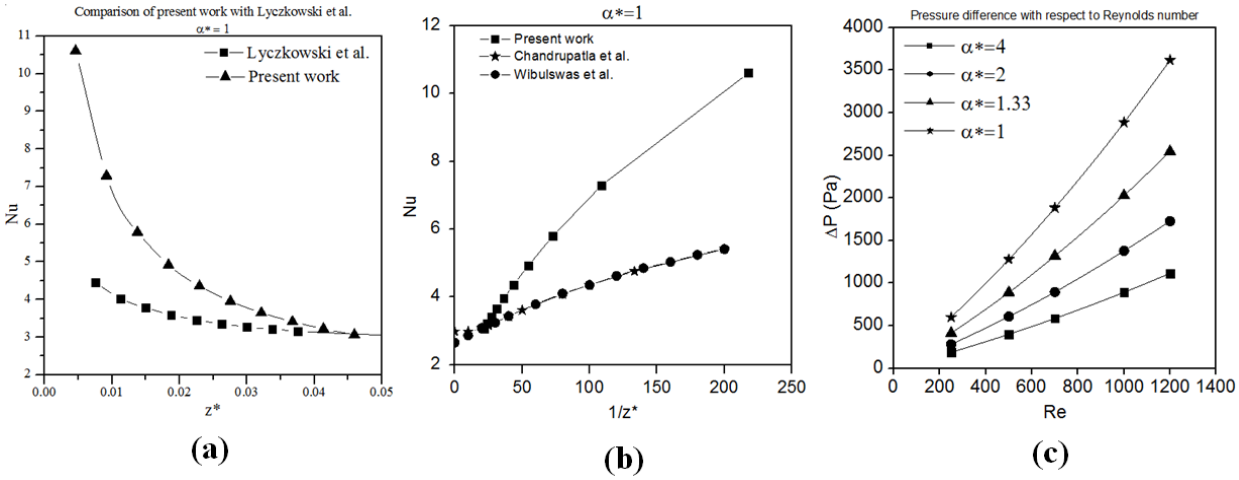

FIGURE 6. (a) Comparison of current work with Lyczkowski et al. [12]; (b) Comparison of current work with Chandrupatla et al. [14] and Wibulswas et al. [13]; (c) Variation of pressure difference with respect to Reynolds number.

Figure 8(a,b) represent the variation of Nusselt number as a function of axial length for different Reynolds numbers. It is observed that the Nusselt number has high gradient initially and gradually arrests to a value in thermally developed zone. Initial high gradient is due to the rapid development of thermal boundary layer. The decrease in Nusselt number is due to decrease in temperature gradient which results into less convection at rear end. Figure 8(c) represents average Nusselt number with respect to Reynolds number. It is revealed from these plots, Nusselt number increases with both increase in Reynolds number and increase in aspect ratio. It is attributed to the fact that with increase in Re, fluid velocity increases and hence convection heat transfer rate increases.

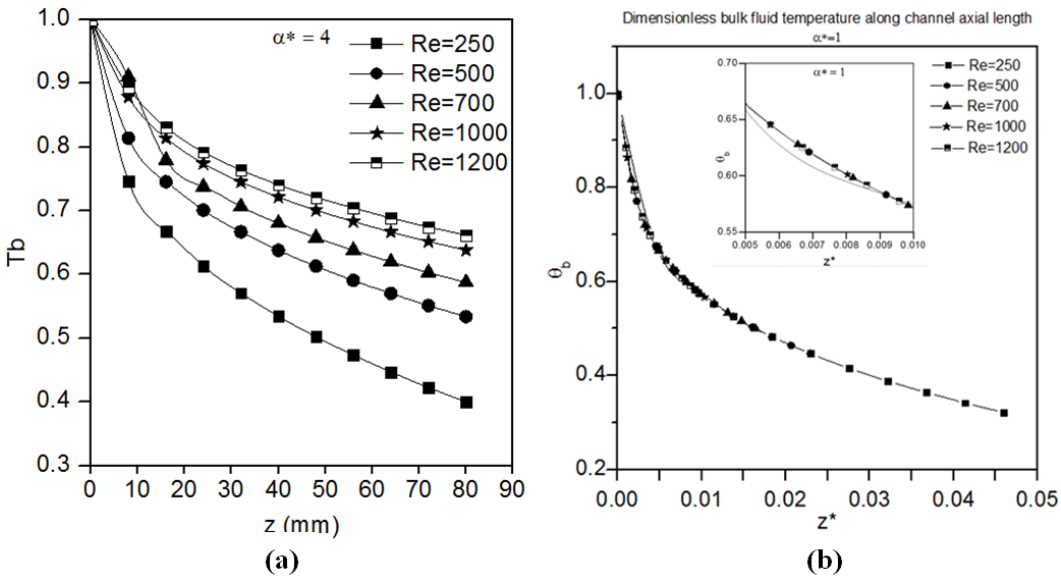

FIGURE 7. (a) Variation of dimensionless bulk fluid temperature along channel axial length (α*=4); (b) Variation of dimensionless bulk fluid temperature along non-dimensionalized channel length (α*=1).

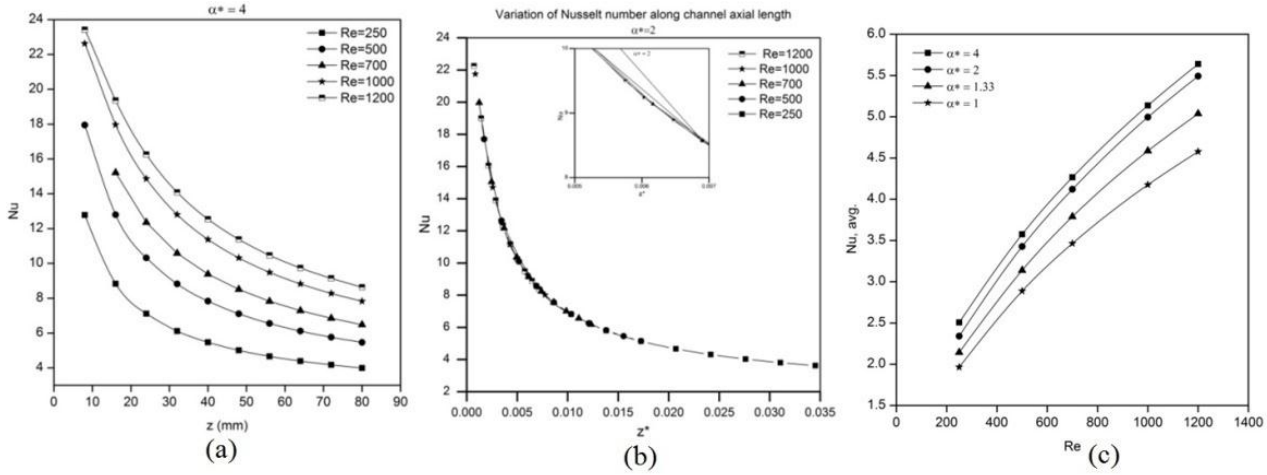

FIGURE 8. (a) Variation of Nusselt number along channel axial length (α*=4); (b) Variation of Nu along non-dimensionalized channel axial length (α*=2); (c) Variation of average Nu with respect to Reynolds number.

CONCLUSIONS

Three dimensional model of heat sink with different aspect ratio minichannel fins are analyzed to investigate cooling performance. Incorporation of air and water simultaneously through minichannel fins enhanced the heat transfer charactersistics. Average Nu increased with increase in Reynolds number and aspect ratio. Aspect ratio 4 minichannel fin possessed least pressure drop. Moreover, minichannel fin with aspect ratio 4 at Re=1200 showed least bulk fluid temperature and hence highest Nu enhancement amongst selected models.

ACKNOWLEDGMENTS

Authors of the paper greatly acknowledge the support received from Department of Mechanical Engineering, National Institute of Technology, Agartala, Tripura, India.

REFERENCES

1. H. Kristiansen, Thermal management in electronics, Chalmers University of Technology, Gotenberg, Swesen , 2001.
2. D.B. Tuckerman, R.F.W. Pease, High performance heat sink for VLSI, IEEE Elect. Dev. Let. **5** (1981) 126-129
3. L. Biswal, S.K. Som, S. Chakraborty, Int. J. Heat Mass Transfer **50** (2007) 1248-1254.
4. H. Shabgard, M.J. Allen, N. Sharifi, S.P. Benn, A. Faghri, T.L. Bergmann, Int. J. Heat Mass Transfer **89,** 138-158 (2015).
5. K. Vafai, L. Zhu, Int. J. Heat Mass Transfer **42 ,** 2287-2297 (1999).
6. A.G. Federov, R. Viskanta, Int. J. Heat Mass Transfer **43**, 399-415 (2000).
7. G. Croce, O. Rovenskaya, P. D'Agaro, J. Heat Transfer **137,** 041701-1 (2015).
8. N.G. Hadjiconstantinou, O. Simek, ASME **24,** 356-364 (2002).
9. S. Xu, G. Hu, J. Qin, Y. Yang, J. Mech. Sci. Tech. **26 (4),** 1257-1263 (2012).
10. H.D.M. Hettiarachchi, M. Golubovic, W.M. Worek, W.J. Minkowycz, Int. J. Heat Mass Transfer **51**, 5088-5096 (2008).
11. M. Renksizbulut, H. Niazmand, G. Tercan, Int. J. Therm. Sci. **45,** 870-881 (2006).
12. R.W. Lyczkowski, C.W. Solbrig, D. Gidaspow, Inst. Gas Technol., Tech. Inf. Center, File 3229, 3424 S.State Street, Chicago, Illinois, 1969.
13. P. Wibulswas, Laminar flow heat transfer in non-circular ducts, PhD Thesis, London University, London, 1966.
14. A.R. Chandrupatla, V.M.K. Sastri, Int. J. Heat Mass Transfer **20,** 1315-1324. (1977)
15. A. Majumder, S. Majumder, Procedia Engineering **105,** 89-95 (2015).

ICME2015

International Conference on Mechanical Engineering 2015
(ICME 2015) 18 – 20 December, 2015, Dhaka, Bangladesh

Paper ID : 108

EXPERIMENTAL STUDY ON PULSATING HEAT PIPE TO EVALUATE THE CHARACTERISTICS FEATURES USING WATER AS WORKING FLUID

Md. Lutfor Rahman[1], Syed Nasif Uddin Ahmed [1a)*], Anindita Dhar[1b)], Sayed Hossain[1], Mohammad Ali[2]

[1]*Military Institute of Science and Technology, Mirpur Cantonment, Dhaka-1216, Bangladesh*
[2]*Bangladesh University of Engineering and Technology, Dhaka-1000*

[a)]*Corresponding author: nasif.anik@yahoo.com*
[b)]*sanjit825@gmail.com*

Abstract. Closed Looped Pulsating Heat Pipe (CLPHP) is now considered as one of the promising technologies for cooling electronic devices. It has attracted researchers because of its simple design, low cost, high thermal performance and rapid response to heat load. This paper emphasizes on determining the characteristics of distilled water as a working fluid in a CLPHP at filling ratios of 40% to 70% with 10% interval and at orientation angles of 0°, 30°, 45° and 60° along the vertical axis. The setup is made of copper tube with 2 mm internal diameter and 2.5 mm outer diameter. The experiment shows that the heat transfer characteristics in a PHP are better at lower filling ratios and 60% is found to be the optimum filling ratio for water. Also the PHP operate at zero and 30°orientation show better heat transfer characteristics.

Keywords. Electronic cooling, closed loop pulsating heat pipe, Distilled water, Thermal performance and heat-transfer coefficient.

TABLE 1. Nomenclature

R_{th}	Thermal resistance, ^{0}C/W	OD	Outer diameter of tube, mm
ΔT	Temperature drop along the device, ^{0}C	ID	Inner diameter of tube, mm
L	Length of heat Pipe, mm	IA	Inclination angle, ^{0}
FR	Filling ratio, %	Q	Heat input, W
D	Diameter of heat pipe, mm	Q	Temperature along the pipe, ^{0}C
Subscripts e evaporator section c condenser section			

1. INTRODUCTION

Although the conventional heat pipes (e.g. mini or micro) are one of the proven technologies, the manufacturing of the complex, miniaturized wick structure/geometry of these heat pipes could become the most cost intensive factor. Another common limitation is the capillary limit, which occurs when the wick cannot return an adequate amount of liquid back to the evaporator. To overcome these difficulties researchers have come up with pulsating heat pipes (PHPs) which work on the principle of oscillation of the working fluid and phase change phenomenon in a capillary tube. Close Loop Pulsating heat pipes (CLPHPs) typically suited for microelectronics cooling consists of a plain meandering tube of capillary dimensions with many U-turns and joined end to end. One end of this tube bundle (evaporator) receives heat and transfers it to the other end (condenser) by a pulsating action of the liquid–vapor/slug-bubble system. The liquid and vapor slug/bubble transport is caused by the thermally induced pressure pulsations occurring inside the device and no external mechanical power is required. The region between evaporator and condenser is adiabatic. The performance of a PHP depends upon many factors like the geometrical parameters of flow channel, the working fluid, the filling ratio, and number of turns, PHP configuration and the inclination angle [2].

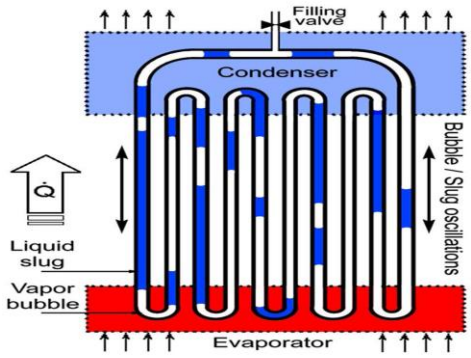

FIGURE A : Closed Loop Pulsating Heat Pipe

In recent years, many experimental studies have been conducted to understand the mechanism of PHP and the factors affecting the performance of PHP. Numerous works had been reported on the effect of various factors like dimensions, tilt angles, number of turns and filling ratio etc. Apart from these parameters, the choice of working fluid is very important. The prime requirements for choosing working fluids are as follows [3-8]: (i) good thermal stability, (ii) moderation of vapour pressure on the operating temperature range, (iii) high latent heat, (iv) high thermal conductivity, (v) high surface tension, (vi) acceptable freezing point, (vii) low liquid and vapour viscosity, and (viii) high $\frac{dp}{dt}$ that means the change of pressure is high with the change of temperature. Majority of the work available in open literature focuses on the effect of working fluid on thermal performance of the device. Very little work has been done to study the effect of working fluid on the start-up parameters of the PHP. Mainly two parameters are used to evaluate the performance of PHP, start-up power and thermal resistance. Tong et al. [9] were the first to explain the importance of start-up and the phenomena in detail.

In view of the technological importance of the thermal performance of pulsating heat pipe, the present work has been focused on the thermal performance of a PHP in terms of heat transfer coefficient and the thermal resistance offered by it. Distilled water is used as working fluid. Water is found to be one of the best working fluid in terms of thermal performance of this type of device under gravitational force. Water, for its thermodynamic attributes in most commercial electronics cooling applications, makes it better than any other fluids for the pulsating heat pipes. High latent heat of water evaporates small amount of liquid resulting low pressure drops and high heat dissipation. Its' high thermal conductivity minimizes the temperature difference associated with conduction through the two phase flow in the PHP. At 25°C the surface tension of water is 72 dynes/cm. As the surface tension of water is higher, it will generate a large capillary action and show better performance in any orientation.

2. EXPERIMENTAL METHOD

2.1. Experimental Setup

The experimental setup is shown in Fig (b) and Fig (c). The PHP consists of a long capillary tube, which is meandered into 8 number of turns. Copper is used as the capillary tube material (ID 2 mm, OD 2.5 mm). The heat pipe is divided into 3 regions- the evaporator (5cm), adiabatic section (12cm) and the condenser (8cm). 8 thermocouples (LM-35sensors, Local Sensor Accuracy (Max) (± C): 0.5, range: -55°C to +150°C) are glued to the wall of heat pipe in evaporator and condensation section. 4 thermocouples were used for each sections. Evaporator section is separated from outside using mica sheets with Nichrome wire wounded inside, which is heated by a power supply unit (AC, 220V, 50Hz) via a Power Supply (3F, 300V, 60 Hz). Wick & asbestos were used to prevent heat loss by convection and radiation. In adiabatic section, glass wool was wrapped over aluminum foil for proper insulation. A band is also used to keep the glass wool at its position and also to ensure proper insulation. A steel structure, along with a cooling fan at the condensation section, is used to hold the PHP. Distilled water is used as working fluid at the amount of FR 40%-70% (by volume) for each setup. For cooling the working fluid, forced convection is used by the AC fan. To avoid complicacy, working fluids are incorporated in the heat pipe by using vacuum suction pump. The other accessories of the setup are adapter circuit, selector switches etc.

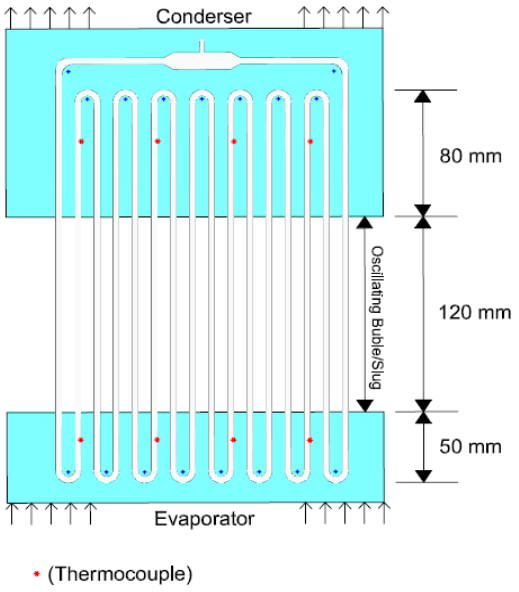

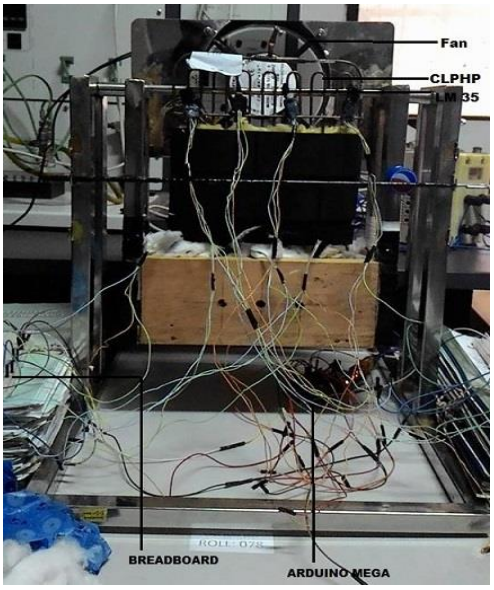

(b) (c)

FIGURE B. Experimental setup. **FIGURE C.** Prototype of Experimental setup.

2.2 Experimental Procedure

- Before filling the working fluid, air is blown inside the heat pipe to ensure that there is no fluid present inside the PHP.
- The heat pipe is filled with required amount of working fluids (Distilled water). Keeping the PHP in different orientation throughout the experiment, the FR is increased gradually from 40% to 70% with 10% increment.
- After the whole setup, the experiment is carried out.
- Different heat inputs (10W to 60W) are provided to the system via variance and temperatures of different sections are measured by thermocouples using Arduino Mega.
- The cooling fan is switched on to cool the condenser.

3. RESULTS AND DISCUSSION

3.1 Characteristics of temperature distribution of time

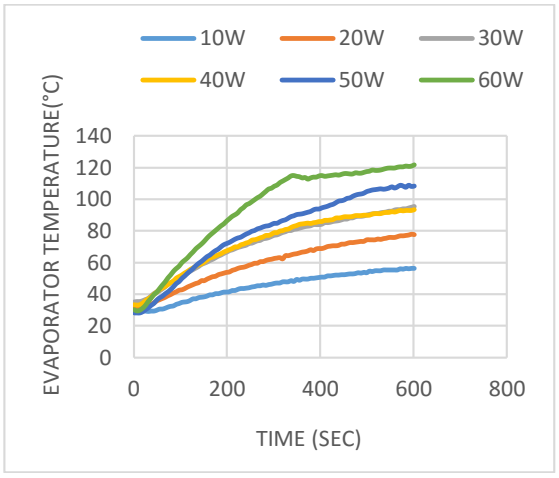

(d)

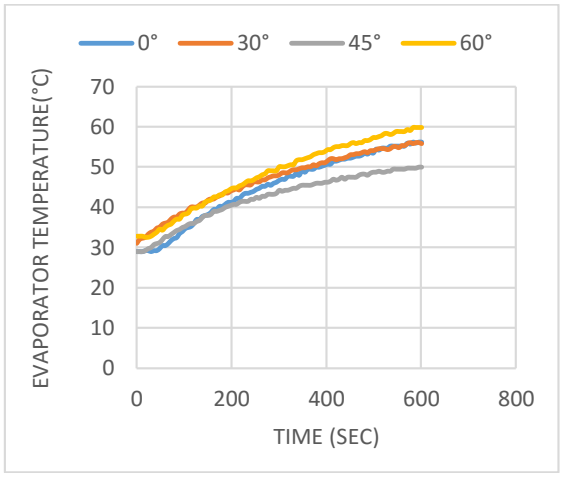

(e)

FIGURE D. Effect of heat input on evaporator temperature in vertical orientation at FR = 50%
FIGURE E. Variation of Evaporator Temperature with time for different orientation at a heat load of 10W and a FR of 50%

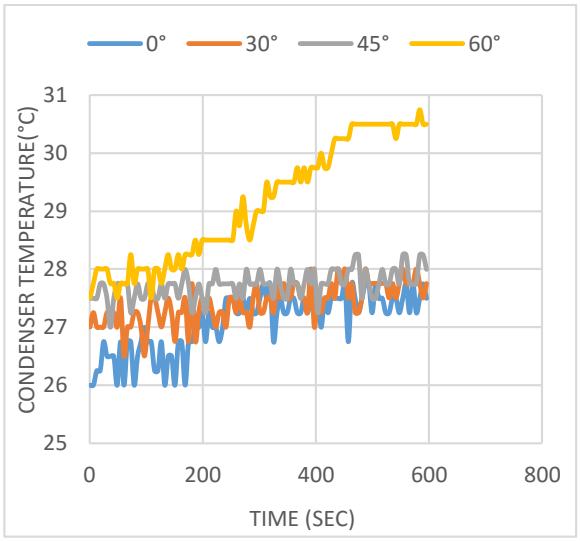

(f)

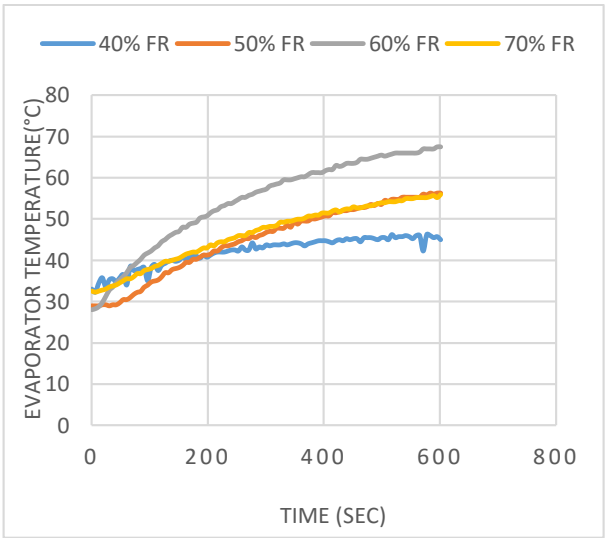

(g)

FIGURE F. Variation of Cond. Temperature with time for different orientation at a heat load of 10W and a FR of 50%.
FIGURE G. Variation of Evaporator Temperature with time at different fill ratio at a heat load of 10 W.

Fig (d) shows the variation of evaporator wall temperature with respect to time in the vertical orientation of operation of PHP at a FR of 50%. It is seen that the curves at first increase rapidly with time and then the rate of increase become slow to some extent. The rate of increase is different for different heat load. After reaching the boiling point the temperature increase in evaporator slows down due to the heat required in phase transfer. It is clear from the figure that till first 100 seconds there is a higher increase rate of evaporator temperature but after 100 seconds the rate decreases. This is because initially after applying a low heat input, liquid slugs cannot move in the tube and this results a temperature climb up in evaporating section. Before the start up condition has reached, the pressure in the vapour bubble is not sufficient to drive the train of liquid plug and vapour bubble above it. The start-up power is the minimum

power needed by the PHP to get started [10]. After the achievement of start-up condition, nucleate boiling starts in the heating section and due to movement of working fluid, temperature of evaporating section becomes almost steady.

Fig (e) and Fig (f) represent the variation of evaporator & condenser temperature with time for different orientation at a heat load of 10W and a FR of 50%. The orientation of PHP plays a very important role in its thermal performance. It is seen that the wall temperature is less at an orientation of 0, 30 and 45 degree compared to 60 degree in both the curves. There is a continuous pressure pulsation during the flow in a PHP. The temperature versus time curve is periodic in nature. But in case of condenser temperature the oscillations become more intensive than in case of evaporator temperature.

Fig (g) shows the variation of evaporator wall temperature with time at different fill ratios at a heat load of 10W. It is reported in the literature that the PHP works as a true pulsating device when the fill ratio is between 20% - 80% [11]. The exact range will differ for different working fluids, operating parameters and construction. From the figure it can be seen that the evaporator temperature is slightly higher at lower fill ratio of 60%. As more vapour phase exists in the PHP at 60% fill ratio, less heat is being transferred from the wall to the fluid. This results in higher evaporator wall temperature at a fill ratio of 60%.

3.2 Variation of Thermal Resistance

Thermal resistance is reciprocal function of heat input and linear function of temperature difference of evaporator and condenser. With the increment of heat input, thermal resistance decreases. The thermal resistance of PHP is given by,

$$R_{th} = \frac{(T_e - T_c)}{Q}$$

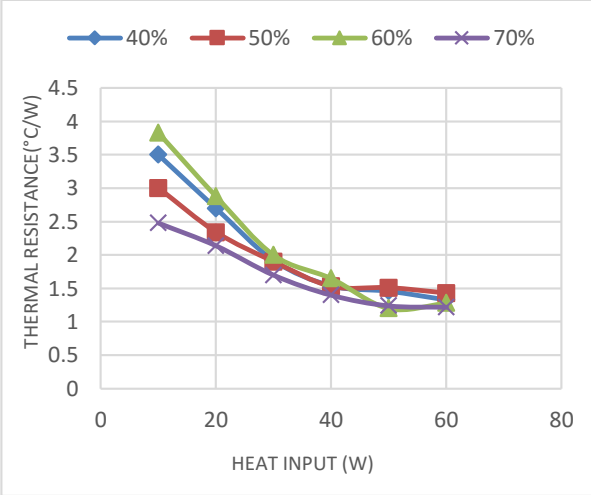

(h)

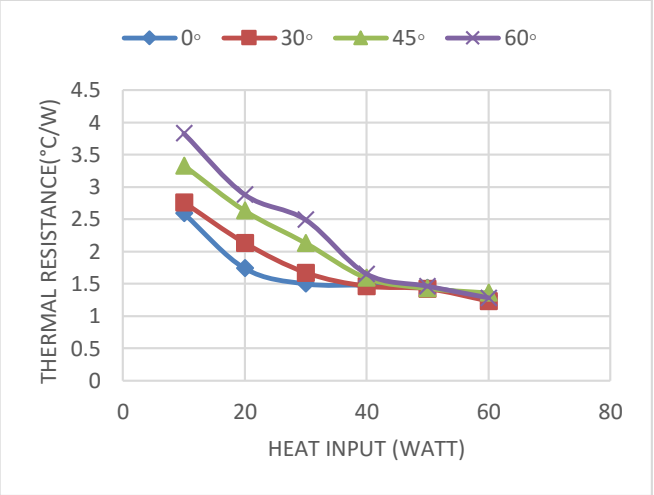

(i)

FIGURE H. Effect of filling ratio on thermal resistance.
FIGURE I. Variation of Thermal Resistance with heat load for different orientation at a FR of 60%.

Figure (h) shows the variation of thermal resistance with heat load in the vertical orientation for different fill ratios. From the figure it is clear that the thermal resistance decreases with increase in heat input at all fill ratios considered. The fill ratio of 60% exhibits the lower values of thermal resistance compared to higher fill ratio of 70%. As the temperature difference between evaporator and condenser is less at lower heat load, the magnitude of thermal resistance is also less. Thus the minimum resistance, 1.2°C/W is obtained at 60% FR and thus 60% is the optimum FR for water. This shows that the heat transfer characteristics in a PHP are better at lower filling ratios. Fig (i) shows the variation of Thermal Resistance with heat load for different orientation at a fill ratio of 60%. It is observed from the figure that the thermal resistance decreases with increase in heat load at all orientations considered. It is also observed that the thermal resistance is less at 0, 30 and 45 degree orientations compared to 60 degree. As the fluid should overcome the effects of gravity more at 60 degree orientation, there is more resistance for heat transfer

and flow at this orientation. Hence, it is desirable to operate the PHP at zero or 30 degree orientations to achieve better heat transfer characteristics.

3.3 Variation of Heat Transfer Coefficient

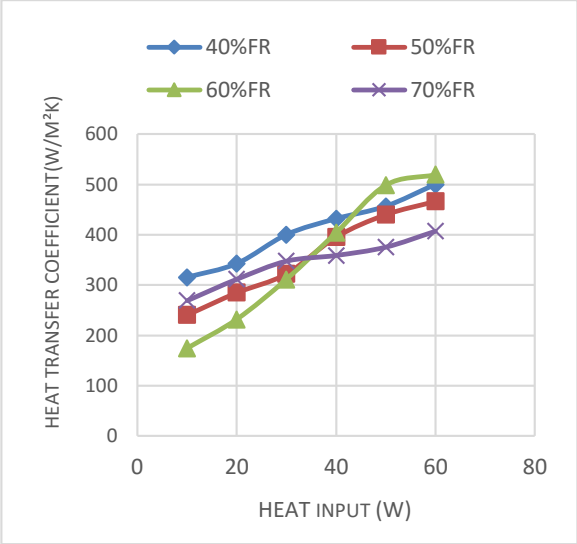

(j)

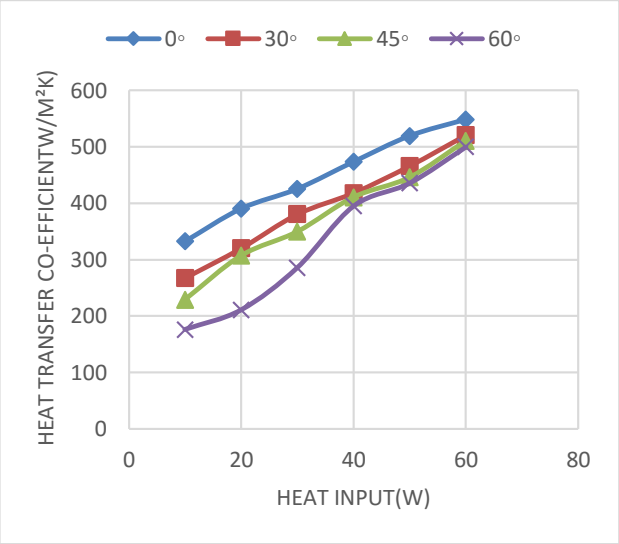

(k)

FIGURE J. Effect of fill ratio on Heat Transfer Coefficient.
FIGURE K. Variation of Heat Transfer coefficient with heat load for different orientation at a FR of 60%.

The heat transfer coefficient of a PHP is given by [12]

$$h = \frac{Q}{A(T_e - T_c)}$$

Fig. (j) shows the variation of heat transfer coefficient with varying heat load in the vertical orientation at different fill ratios. From the figure, it is seen that the heat transfer coefficient increases with increase in heat load at all fill ratios. Higher values of heat transfer co-efficient can be seen at a lower fill ratio of 60% which indicates better performance of PHP. Fig (k) shows the variation of heat transfer coefficient with heat input at various orientations at a FR of 60%. It is observed that the heat transfer coefficient increases with increase in heat load at all orientations considered. It is also seen that the heat transfer coefficient is more at zero and 30 degree orientations than at 60 degree.

4. CONCLUSION

PHPs are highly attractive heat transfer elements, which due to their simple design, cost effectiveness and excellent thermal performance may find wide applications. In the present work, the effects of heat input, working fluid, fill ratio, thermal resistance, and heat transfer co-efficient on the performance of PHP are studied. It is seen from the experiment that the evaporator and condenser wall temperature variation with time is found to be periodic at different orientation. The experimental investigation shows that the minimum resistance, 1.2°C/W offered by 60% FR and thus 60% is the optimum FR for water. Considering gravitational effect, zero and 30° orientation showed better heat transfer characteristics.

5. ACKNOWLEDGEMENTS

The authors feel greatly honored to be able to express their earnest gratitude to the Department of Mechanical Engineering, MIST and BUET for the accomplishment of this research.

6. REFERENCES

1. H. Akachi, “Structure of a Heat Pipe,” US Patent No 4921041, 1990.
2. Y. Zhang and A. Faghri, “Advances and Unsolved Issues in Pulsating Heat Pipes,” Heat Transfer Engineering, Vol. 29, No. 1, 2008, pp. 20-44. Doi: 10.1080/01457630701677114.
3. Wallis, G., “One Dimensional Two-Phase Flow”, McGraw Hill Inc., 1969 (ISBN 0-0706-794-28).
4. Khandekar, S., Schneider, M., Groll, M., “Mathematical modeling of pulsating heat pipes: state- of-the-art and future challenges”, 5th ASME/ISHMT joint International Heat and Mass Transfer Conference, Kolkata, India, 2002, pp. 856– 862 (ISBN 0-07-047443-5).
5. Groll, M., Khandekar, S., “Pulsating heat pipes: a challenge and still unsolved problem in heat pipe science”, Proceedings of the 3rd International Conference on Transport Phenomena in Multiphase Systems, Kielce, Poland, 2002, pp. 35–44 (ISBN 83-88906-03-8).
6. Duminy, S., “Experimental investigation of pulsating heat pipes”, Diploma thesis, Institute of Nuclear Engineering and Energy Systems (IKE), University of Stuttgart, Germany, 1998.
7. Khandekar, S., Schneider, M., Schaafer, P., Kulenovic, R., Groll, M., “Thermofluid dynamic study of flat plate closed loop pulsating heat pipes”, Microsc. Thermophys. Eng. 6 (4) (2002) pp. 303–318 (ISSN 1089-3954).
8. Shafii, M.B., Faghri, A., Zhang, Y., “Thermal modeling of unlooped and looped pulsating heat pipes”, ASME J. Heat Transfer 123 (2001) pp. 1159–1172.
9. B. Y. Tong, T. N. Wong and K.T. Ooi, “Closed Loop pulsating Heat Pipe,” Applied Thermal Engineering, Vol. 21, No. 18, 2001, pp. 1845-1862.
10. W. Qu and H. B. Ma, “Theoretical Analysis of Startup of a Pulsating Heat Pipe,” International Journal of Heat and Mass Transfer, Vol. 50, No. 11-12, 2007, pp. 2309-2316.
11. Khandekar, S. (2004). Thermo Hydrodynamics of Pulsating Heat Pipes. Ph. D Dissertation, University of Stuttgart, Germany.
12. Faghri, A. (1995). Heat Pipe Science and Technology, Washington, USA, Taylor and Francis.

ICME2015

International Conference on Mechanical Engineering 2015
(ICME 2015) 18 – 20 December, 2015, Dhaka, Bangladesh

Paper ID : 109

Effect of Filling Ratio and Orientation on the Thermal Performance of Closed Loop Pulsating Heat Pipe Using Ethanol

M Lutfor Rahman[1], Mehrin Chowdhury [1, a),*], Nawshad Arslan Islam [1, b),] Sayed Muhammad Mufti[1], Mohammad Ali[2]

[1]*Military Institute of Science and Technology, Mirpur Cantonment, Dhaka-1216, Bangladesh*
[2] *Bangladesh Universities of Engineering and Technology, Dhaka-1000, Bangladesh*

a)mehrin.mist11@gmail.com
b)arslan.mechanical@gmail.com

Abstract. Pulsating heat pipe (PHP) is a new, promising yet ambiguous technology for effective heat transfer of microelectronic devices where heat is carried by the vapor plugs and liquid slugs of the working fluid. The aim of this research paper is to better understand the operation of PHP through experimental investigations and obtain comparative results for different parameters. A series of experiments are conducted on a closed loop PHP (CLPHP) with 8 loops made of copper capillary tube of 2 mm inner diameter. Ethanol is taken as the working fluid. The operating characteristics are studied for the variation of heat input, filling ratio (FR) and orientation. The filling ratios are 40%, 50%, 60% and 70% based on its total volume. The orientations are 0° (vertical), 30°, 45° and 60°. The results clearly demonstrate the effect of the filling ratio and inclination angle on the performance, operational stability and heat transfer capability of ethanol as working fluid of CLPHP. Important insight physics in the operational characteristics of CLPHP is obtained and optimum performance of CLPHP using Ethanol is thus identified. Ethanol works the best at 50-60%FR at wide range of heat inputs. At very low heat inputs 40%FR can be used for attaining a good performance. Below 40%FR is not suitable for using in CLPHP as it will give a low performance. The optimum performance of the device can be obtained at vertical position.

Keywords. Closed loop pulsating heat pipe (CLPHP); Thermal performance; Thermal resistance; Heat transfer co-efficient

TABLE1. Nomenclature

Abbreviations		Subscripts	
Thermal resistance, °C/W	R_{th}	Evaporator section	e
Temperature drop along the device, °C	ΔT	Condenser section	c
Length of the pipe, mm	L		
Filling Ratio, %	FR		
Area, mm^2	A		
Diameter of heat pipe, mm	D		
Outer diameter of the tube, mm	OD		
Inner diameter of the tube, mm	ID		
Inclination angle, °	IA		
Heat input, W	Q		
Temperature along the pipe, °	T		

1. INTRODUCTION

In the face of ever improving and evolving electronics thermal management plays a pivotal role in determining the prospects of modern technology. Heat pipes play a vital role for the cooling of different parts like chips, micro processors and other space restricted elements. Pulsating heat pipes (PHPs) or oscillating heat pipes are relatively new addition in the array of heat pipes. The idea of heat pipes was first given by Gaugler[1], invented by Grover [2,3] and pulsating heat pipe was introduced by Akachi[4] in the 1990s [4,5] that became a lucrative system for thermal management. These can be divided into 3 groups at least: (a) closed loop PHP (CLPHP); (b) CLPHP with check valves; (c) open loop PHP (OLPHP), also called closed end PHP (CEPHP) [6]. It is simple in structure with a coil of capillary tubes filled with certain working fluid in it and extended from the heat source to sink. Unlike a conventional heat pipe, PHP having no wick structure prevents the condensate from returning to the evaporator section. PHP works on the principle of fluid pressure oscillations created by means of differential pressure across vapor plugs from evaporator to condenser and back [7]. The vapor formed at the evaporator is pushed towards the condenser in the form of discrete vapor bubbles among packets of fluid at the condenser. At the condenser the vapor gets condensed and releases the latent heat of vaporization and returns to the evaporator to complete the cycle. The performance of a PHP depends upon many factors like the geometrical parameters of flow channel, the working fluid, the filling ratio, and number of turns, PHP configuration and the inclination angle [8].

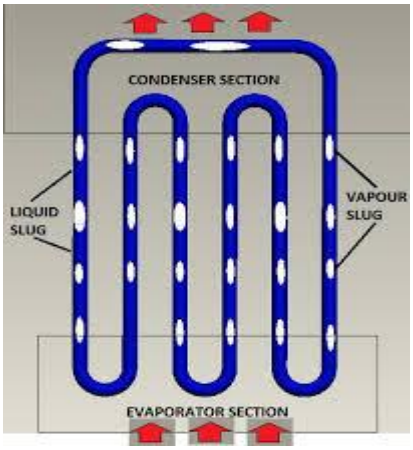

FIGURE 1.Close loop pulsating heat pipe

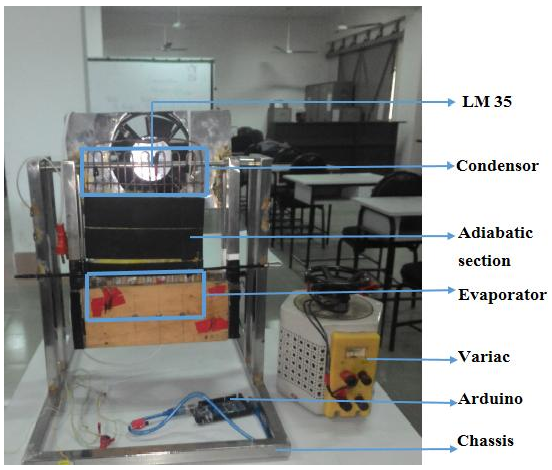

FIGURE 2. Experimental Setup

The present experiment is done with different filling ratio using working fluid ethanol at different orientations. Lee et al. (1999) [9] conducted few performance tests on a multi loop PHP made of brass using Ethanol as working fluid. The PHP was tested for different orientations (30°-90°). Most active oscillations caused by the formation or estimation of bubbles are observed in bottom heating with fill ratio of 40-60%. Lee's experiment was based on flow visualization of the fluid used in CLPHP. Now the present investigation is done to show the effect of ethanol as working fluid on thermal performance of CLPHP based on experimental results. The amount of conduction, convection or radiation of an object determines the amount of heat it transfers.

2. EXPERIMENTAL METHOD

2.1 Experimental setup

In Fig. 1 the model of a CLPHP is shown and in Fig. 2 the experimental setup is shown. The setup is made of a copper heat pipe (ID: 2mm, OD: 2.5mm, L: 25cm, material: copper), having a total of 8 loops. The heat pipe is divided into 3 regions- the evaporator (5cm), adiabatic section (12cm) and the condenser (8cm). 4 thermocouples (LM-35sensors, Local Sensor Accuracy (Max) (+/- C): 0.5, range: -55°C to +150°C) are glued to the wall of heat pipe in evaporator and 4 in condensation section. Insulation of the evaporator section is done by keeping it inside a wooden box. The evaporator section is first wounded by mica and then wounded by nichrome wire above. The setup is heated using a power supply unit (AC, 220V, 50Hz) via a variac (3F, 300V, 60 Hz) connected to nichrome wire

(diameter = 0.25 mm, resistivity: 1.0 × 10−6 Ω-m, specific heat: 450 Jkg-1K−1) wounded over mica sheet, and convective and radiation heat loss is prevented by covering with asbestos and cotton. The heating is uniform throughout the evaporator section as the nichrome wire is wounded around the whole evaporator section. The adiabatic section has been covered by aluminum foil, then filled with glass wool and encircled by insulating tape to ensure a steady adiabatic section. Ethanol is used as working fluid at the amount of 40%-70%FR for each setup. For cooling, forced convection is used by a DC fan. The whole apparatus is set on a Stainless Steel test stand with a wooden box (wood frame) with provision of angular movement of the PHP by an indexing system. Working fluids are incorporated in the heat pipe by using vacuum suction pump. The other accessories of the setup are adapter circuit, selector switches etc.

3. RESULTS AND DISCUSSIONS

The experiment has been carried out for different filling ratios of Ethanol as working fluids used in CLPHP at different orientations. In this investigation the value of thermal resistance is considered as an indication of efficiency, i.e. lower value of R_{th} refers to low resistance to heat flow and eventually indicates a higher efficiency of the system. The evaporative temperatures have been compared first and subsequently other comparisons have been made for different filling ratios at different orientation. The results are compared on the basis of different characteristics.

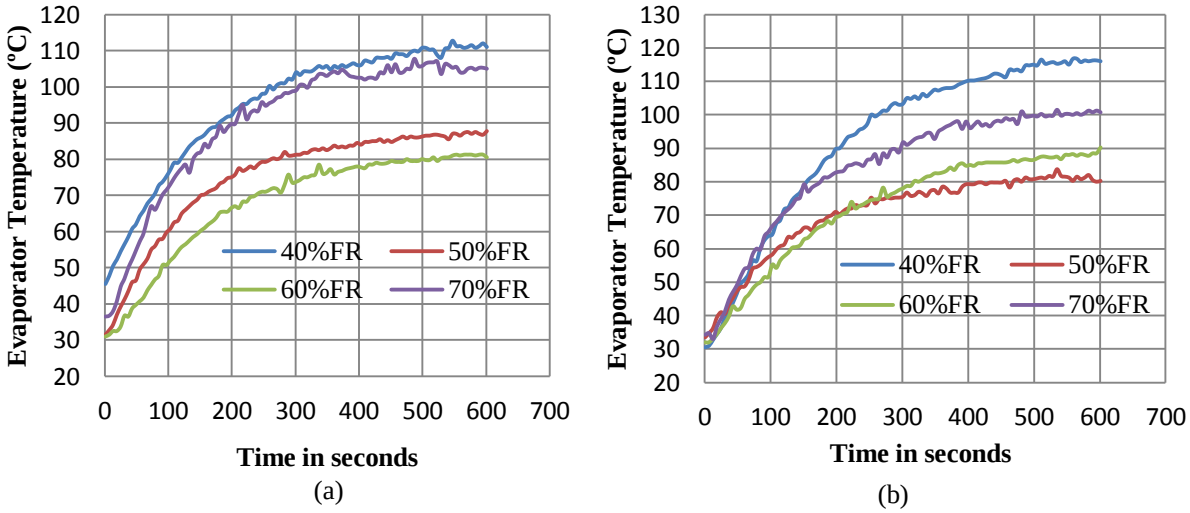

FIGURE 3. Variation of Evaporator Temperature with time at different fill ratio for ethanol at a heat load of 50 W and (a) 0° inclination; (b) 30° inclination.

3.1 Characteristics of temperature distribution

Figure 3(a and b) and Fig.4 (a and b) show the experimental results for time versus evaporator temperature for ethanol at a heat load of 50W, at different inclinations. The results show similar pattern in the evaporator temperature versus time graph for different filling ratios. In almost all the inclinations (i.e. 0°, 30°, 45°, and 60°) the temperature rapidly increases at first and then the rise becomes slow and reaches a near stable state. This happens when ethanol reaches boiling point and thus pulsating effect starts.

The curves in Fig.3 and Fig.4 show large increase of temperature until the start of the pulsating effect. Among all the inclinations, 40%FR and 70%FR have comparatively high evaporator temperatures and greater thermal resistance. At 40%FR more bubbles present cause higher movement but the total amount of fluid for sensible transfer of heat is less. At 70%FR there is less bubble formation and thus less bubble pumping action resulting in higher thermal resistance. Among all the filling ratios 60%FR shows comparatively better result as it reaches the phase changing state earlier and has less variation with a steady rise. In all the curves the initial rise of temperature is very high. After a certain time (start up time), absorbed heat by the working fluid is adequate to commence low

amplitude pulsating motions. Due to movement of working fluid, temperature of evaporating section becomes almost steady. Finally, evaporator's temperature pulsates around a certain value [11]. Also from the curves it is seen that bubble formation decreases with increase of filling ratio.

3.2 Minimum start up time

To evaluate the performance of PHP start-up time and thermal resistance are mainly are used. The start up power is the minimum power needed by the PHP to get started [12]. When the PHP reaches the start up condition, the oscillating motion in the PHP starts. The time required for this is minimum start up time. The start up condition varies for many factors like the tube geometry, wall temperature variation, heat flux level, physical properties of working fluid, filling ratio, heating and cooling modes, transient heat transfer process, initial temperature etc. Figure.3 and Fig.4 show the minimum start up time at different filling ratio for ethanol at different inclinations at 50W. From Fig.3 and Fig.4 it can be seen that initially the temperature of evaporator increases and then becomes constant after which the device starts working in pulsating mode. This is the state when the device starts sensible heat transfer.

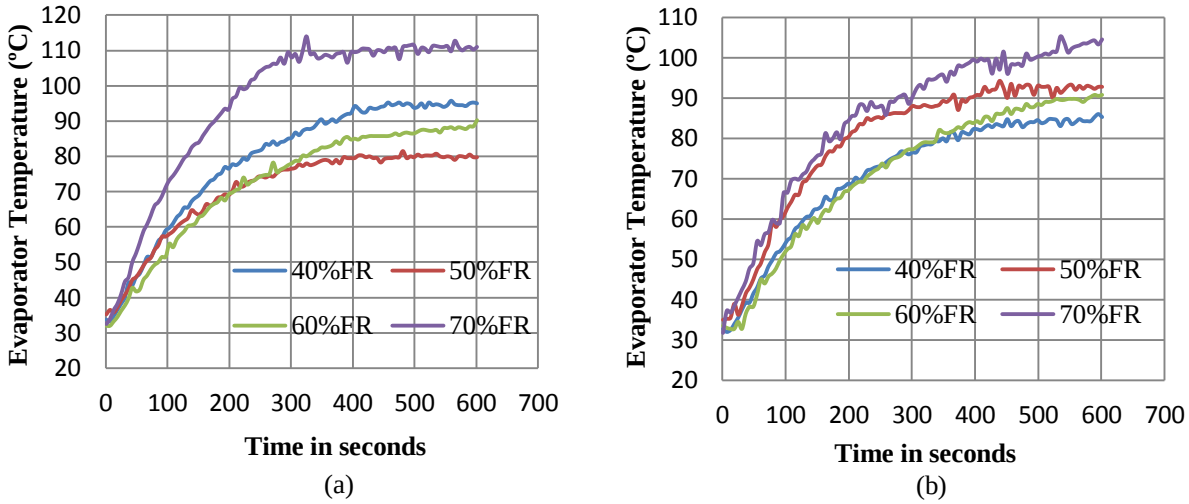

FIGURE 4. Variation of Evaporator Temperature with time at different fill ratio for ethanol at a heat load of 50 W and (a) 45° inclination; (b) 60°inclination

Before the start up, there are insufficient bubbles and after the onset of nucleate boiling, the vapor bubbles and liquid plugs enlarge due to perturbations and start up occurs. Figure 3 and Fig.4 show that for vertical position (0°) start up has occurred in between 200-300seconds mostly. Among the orientations of experimental setup 45° has minimum start up time. This happens for increase of boiling surface with the inclination of PHP. The curves show that 60%FR and 70%FR start pulsating quicker and depict that start up time decreases with increase of filling ratio.

3.3 Variation of thermal resistance

Thermal resistance is defined as the ratio of difference in average temperature of evaporator section and average temperature of condenser section for any instance to the heat input at that time. In mathematical form the thermal resistance of PHP can be expressed as

$$R_{th} = \frac{A(T_e - T_c)}{Q} \tag{3}$$

Thermal resistance refers to the resistance to heat transfer. The lower the resistance the higher will be the heat transfer. In this paper thermal resistance is considered as an indication of heat pipe performance. Thermal resistance has an inverse relation with heat input. The condenser section has been kept at room temperature throughout the experiment and average condenser temperature T_c for calculating thermal resistance is found to be 30°C.

From Fig.5(a) thermal resistance of ethanol at vertical position is plotted against heat input for different filling ratios. It is seen that both 50%FR and 60%FR show low thermal resistances with 60%FR having the lowest thermal resistance. At low heat input, 50%FR shows better performance than 60%FR and at high heat input both show similar performance. This is because at low temperature for 50%FR there is enough bubble formation but for 60%FR there is less bubble formation hindering good heat transfer. However, performance of 60%FR gets better with the increase in heat input for adequate bubble formation. The study shows that 70%FR gives comparatively low performance than other filling ratios. From figure it is seen that 70%FR works poor at 10W or below for in adequate bubble formation and better at medium heat inputs i.e. 20W, 30W and the performance again deteriorates with increase of heat input. This is because there is a lot of liquid present in the PHP for 70%FR and at medium heat inputs there is enough bubble for heat transfer in pulsating mode. As the heat input increases, amount of space for new bubble formation decreases as most of the free space is already occupied by bubbles formed earlier. So performance of the device gets lower at high heat input. At low filling ratios as 40%FR the device works fine at very low heat inputs and shows moderate performance up to 50W. At high heat input the low filling ratio tends to dry out and thus thermal resistance increases. Hence the low filling ratios do not work better at high heat inputs. So the optimum filling ratio for ethanol is 50- 60%FR which give the best outcome at a wide ranges of heat inputs. 40%FR can be used at very low heat input conditions for better performance as well.

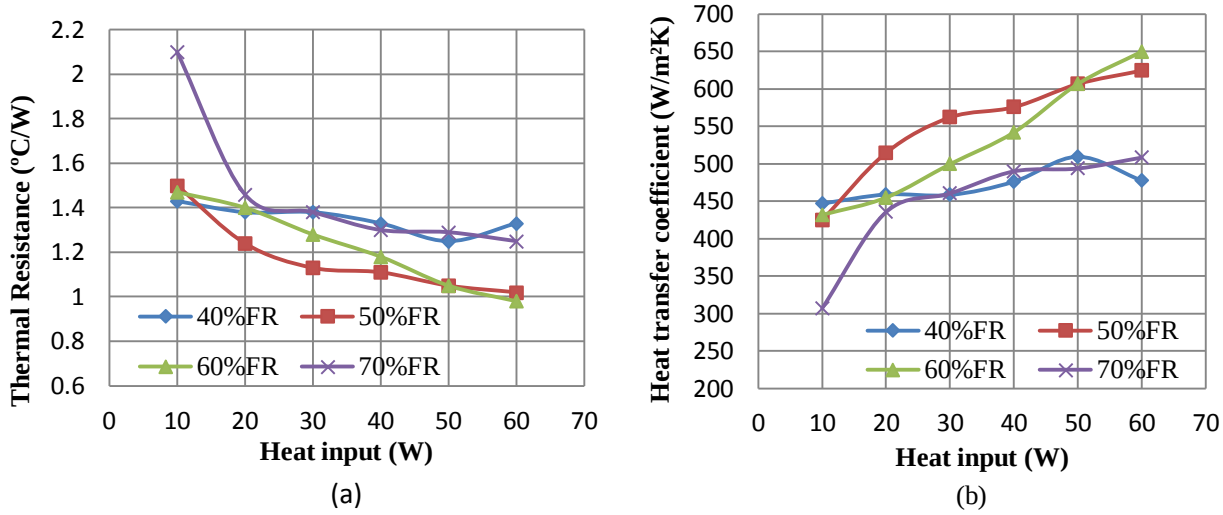

FIGURE 5. (a) Variation of thermal resistance with heat input for ethanol at 0°; (b) Variation of heat transfer coefficient with heat input for ethanol at 0°

3.4 Variation of heat transfer coefficient

The convective heat transfer coefficient of PHP is given by

$$h = \frac{Q}{A(T_e - T_c)} \tag{2}$$

The heat transfer coefficient is essentially the inverse of thermal resistance. As thermal resistance decreases heat transfer coefficient increases indicating the increase in heat transfer. Heat transfer coefficient also has a proportional relationship with heat input. As seen from Fig.5 (b) the 50%FR and 60%FR show greater heat transfer coefficient than the other extreme ones at 0°. Both 50%FR and 60%FR shows almost similar results at high heat inputs such as 50W and above. At medium heat input i.e. up to 50W, 50%FR gives better performance. This occurs due to adequate number of pulsating liquid plugs and vapor bubbles. 70% FR has the lowest heat transfer coefficient and shows the lowest performance and 40%FR has better performance at low heat inputs than at high inputs. These all are due to same reasons that occur with thermal resistance. This implies that the middle FR are the best suited for using in CLPHP which give a better performance for a wide range of heat inputs.

3.5 Effect of inclination

Figure 6 (a and b) show variation of evaporator temperature with time and variation of thermal resistance with heat input for ethanol at 60%FR and 50%FR. For both FR the thermal resistance has gradually decreased from a high value with the periodic increase of heat input. The curves depict that starting from 0°, with the increase in inclinations the initial thermal resistance has increased. By inclining, the space taken by the liquid is increased and thus the space for bubble formation becomes less as well as a decrease in available buoyancy force, which lifts up the bubbles to the liquid surface, also occurs. This results in decreased performance. Figure 6(a and b) show that for 50%FR the lowest thermal resistance of 1.02 °C/W is created at 0° and for 60%FR the lowest value is 0.98°C/W. At 50%FR the variation of thermal resistance occurs as the amount of pulsating fluid is comparatively less, creating impedance for the bubble formation. 60%FR at 0° inclination (vertical) gives the lowest thermal resistance and optimum thermal performance. 50%FR has a close performance to that of 60%FR at all inclination and work better at all heat inputs at vertical position. Thus for the best performance the inclination is the vertical position (0º).

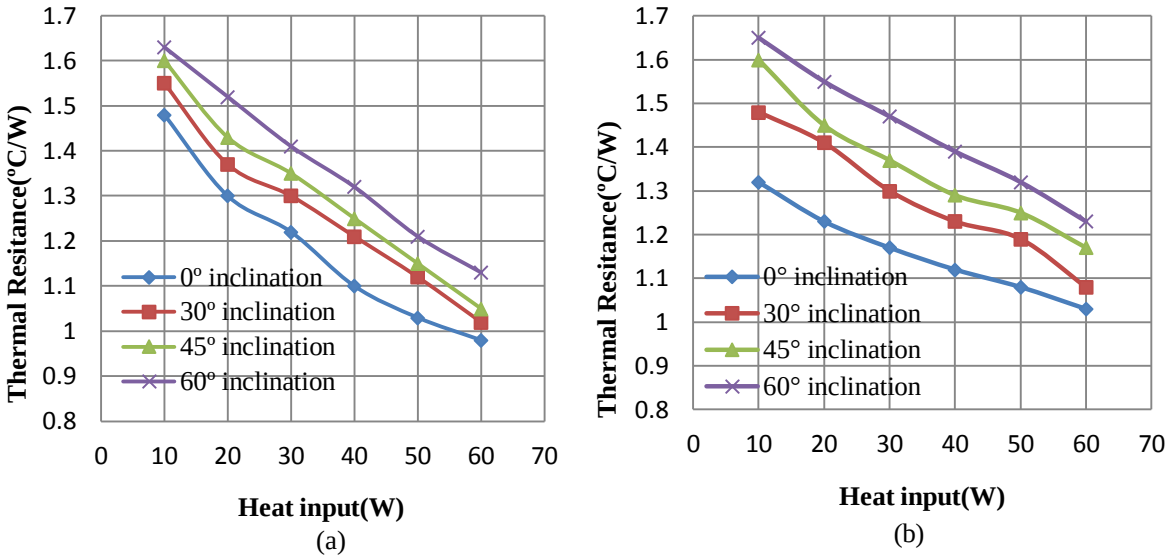

FIGURE 6. Variation of thermal resistance with heat input at different inclination for ethanol at (a) 60%FR; (b) 50%FR

4. CONCLUSION

Closed loop pulsating heat pipes are effective and self-sustained thermally driven devices for heat transfer. Vapor bubble and liquid plug formation speeds up the process whereas excessive liquid slug formation, instabilities and perturbation hinder the process. In this research it is seen that heat transfer capacity of closed loop pulsating heat pipes is governed by several factors including inclination, filling ratio and start up time. The study indicates that for 50-60%FR the thermal performance is optimum as there is sufficient fluid for pulsation effect. The best performance can be obtained at vertical position with these two filling ratios at wide ranges of heat input. At very low heat inputs 40%FR can also render a good performance similar to 50%FR and 60%FR at vertical position. The research also reflects that the CLPHP gives the best pulsating effect at 0° inclination. With the increase in inclination the thermal resistance has increased due to hindrance in lift up of bubbles due to low buoyancy force.

ACKNOWLEDGMENT

The authors feel greatly honored to be able to express their earnest gratitude to the Department of Mechanical Engineering, MIST and BUET for the accomplishment of this research.

REFERENCES

1. Gaugler, R. S US patent 2350348.Appl. 21 Dec, 1972.Published 6 June 1944.
2. Grover, G. M US patent 3229759.Filed 1963.
3. Grover, G.M., Cotter, T.P. and Erickson, G.F. Structures of very high thermal conductance. J. App. Phys., Vol. 35, pp.1190-1191, 1964.
4. H. Akachi, Structure of micro-heat pipe, US Patent 5219020, 1993-06-15.
5. H. Akachi, L-type heat pipe, US Patent 5490558, 1996-02-13.
6. Rittidech S., Terdtoon P., Murakami M., Kamonpet P., Jompakdee W. Correlation to Predict Heat Transfer Characteristics of a Close-End Oscillating Heat Pipe at Normal Operating Condition, *Applied Thermal Engineering*, vol. 23, pp 497-510, 2003.
7. Ch. Sreenivasa Rao, Avssks Gupta, K. Rama Narasimha, Effect of design parameters on the performance of a closed loop pulsating heat pipe"International Journal of Mechanical Engineering and Technology (IJMET), ISSN 0976 –6340(Print), ISSN 0976 – 6359(Online) Volume 4, Issue 3, May - June (2013) © IAEME.
8. Y. Zhang and A. Faghri, "Advances and Unsolved Issues in Pulsating Heat Pipes," *Heat Transfer Engineering*, Vol. 29, No. 1, 2008, pp. 20-44. doi:10.1080/01457630701677114
9. Lee W., Jung H., and Kim J., 1999. Flow Visualization of oscillating capillary tube heat pipe, in Proceeding of the 1th International Heat Pipe Conference, Musashinoshi Tokyo.
10. Xu, J.L., and Zhang, X.M., 2005, "Start-up and Steady Thermal Oscillation of a Pulsating Heat Pipe," Journal of Heat and Mass Transfer, 41(8), 685-694.
11. Xu, J.L., and Zhang, X.M., 2005, "Start-up and Steady Thermal Oscillation of a Pulsating Heat Pipe," Journal of Heat and Mass Transfer, 41(8), 685-694.
12. W. Qu and H. B. Ma, "Theoretical Analysis of Startup of a Pulsating Heat Pipe," *International Journal of Heat and Mass Transfer*, Vol. 50, No. 11-12, 2007, pp. 2309-2316.

ICME2015

International Conference on Mechanical Engineering 2015
(ICME 2015) 18 – 20 December, 2015, Dhaka, Bangladesh

Paper ID : 110

Feasibility Study of Water Emulsified Diesel as CI Engine Fuel and its Stability Analysis

Pijush Kanti Mondal[1,a)] and Bijan Kumar Mandal[2, b)]

[1]*Mechanical Engineering Department, Nazrul Centenary Polytechnic, West Bengal, India*.
[2]*Mechanical Engineering Dept., Indian Institute of Engineering Science and Technology, Shibpur, West Bengal, India*

[a)]Corresponding author: m.pijushkanti@yahoo.com
[b)]bkm375@yahoo.co.in

Abstract. An attempt has been made to review the present status of preparation of water emulsified diesel and performance and emission characteristics of diesel engine using it. It has been seen that the performance is improved and the emissions of different pollutants such as CO, HC, NOx, particulate matter and smoke are significantly reduced. In addition, the stability analysis of emulsified fuel prepared by ultrasonic machine has been carried along with the measurement of two important properties of the fuel, namely density and viscosity. The sample has been prepared mixing 10% water and 2% surfactant by volume with diesel. The sample becomes stable after seven days and its emulsion stability (ES) is calculated to be 88.9%. The density and the viscosity of the water emulsified diesel are found to be more than those of pure diesel.

INTRODUCTION

Diesel engines play important roles in power generation for in-land and marine transportation, agriculture and other industries and power plants. Although the diesel engines are efficient, but these emit different gaseous pollutants such as NO_x, CO, CO_2, SO_x and non-gaseous pollutants like HC, PM and smoke [1]. These pollutants in the atmosphere cause physical, chemical and biological reactions to form noxious substances which are real threat to the ecology and human health [2]. To protect the human life and environment, the local and global bodies are imposing strict regulations on emission standard of automobiles along with the other pollutant emission sources. World Health Organization (WHO) designed air quality guidelines in 1987 and updated in 1997 and 2005 [3]. The CO, NO_x, HC+NO_x and PM emission level permitted by EURO 6 (September, 2014) regulations, for passenger diesel car, are 0.5, 0.08, 0.17 and 0.005 g/km respectively [4]. This has compelled the researchers to work on modification of engine design and utilizing alternative fuel. The alternative fuel includes ethanol, bio-gas, CNG, bio-diesel. Addition of water into the combustion chamber is also considered effective emission control methods for diesel engine. Water can be introduced into the combustion chamber in four ways, namely, inlet manifold water injection, direct water injection with separate nozzle, stratified diesel-water-diesel injection and use of water emulsified diesel (WED) [5]. The use of WED is the effective and economical way to reduce the emissions of NO_x and PM. More important is that the WED which is also considered as the alternative fuel, can be directly used without any alteration of the existing CI engine [6]. Giant companies like MAN B&W Diesel and Wartsila are presently using WED in CI engines. WED are commercially produced in Europe and USA by Elf France, Cam Technology, Lubrizol Corporation, and in Asia by Singapore Emulsion Fuel Pvt. ltd. The stability of the fuel becomes an important issue when additives are mixed with the fuel to improve its characteristics. Keeping this in mind, the authors have prepared an emulsified diesel fuel using water and mixture of two surfactants with the help of ultrasonic machine. The stability profile and emulsion stability (ES) of this prepared emulsion has been investigated. The changes in fuel properties like density and viscosity have also been reported.

WATER EMULSIFIED DIESEL (WED)

Emulsion is the mixture of two immiscible liquids, one is as disperse phase and another is as continuous phase. In WED, water is the disperse phase and diesel is in continuous phase. To increase the stability of the emulsion, surface active agents (surfactants) are used. Surfactant reduces the interfacial tension between water and diesel by absorbing at the liquid-liquid interface and thus stabilizes water diesel emulsion [7]. The Hydrophil-Lipophile Balance (HLB) value of the surfactant indicates the degree to which it is hydrophilic or lipophilic. It is observed that the mixture of one more hydrophilic and one more hydrophobic surfactants results better emulsification effects than a single surfactants having intermediate HLB value [8]. Generally water emulsified diesel are two phase emulsion like water-in-oil (W/O) type or oil-in-water (O/W) type. But three phase emulsion like water-in-oil-in-water (W/O/W) type or oil-in-water-in-oil (O/W/O) type can also be made [7, 9]. The stability of the emulsion depends on the type and quantities of surfactant, amount and size of the water droplets and mixing process parameter like speed, duration, temperature, etc. [1]. The schematic illustration of water-in-diesel dispersion mechanism is shown in Fig. 1. The conventional diesel fuels are having certain characteristics which fulfil the requirement of diesel engine's performance and operations. But due to emulsification of the diesel fuel with water, the characteristics changes. The effects of the water droplets present in the emulsion is to be investigated to understand the change in the emulsified fuel properties. The main characteristics of the base fuel (diesel) and WED with 10% water by weight have been listed in Table 1 as obtained from the literature [10].

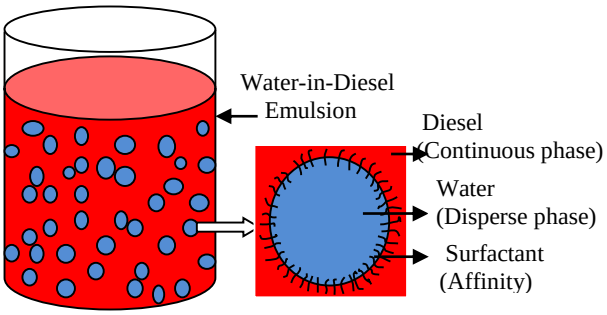

FIGURE 1. Schematic illustration of water-in-diesel dispersion mechanism.

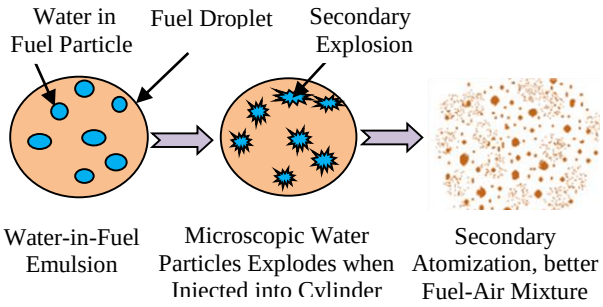

FIGURE 2. Combustion phenomenon of water emulsified diesel [11].

Burning Behavior of WED

When WED is fed into the combustion chamber of IC engine the water particles evaporate first and the diesel droplets surrounding water particles disperse into smaller fuel droplets. This phenomenon is called micro-explosion

TABLE 1. Properties of emulsified fuel and pure diesel [10].

Fuel Type	Density (kg/m^3)	Cetane number	Viscosity (cSt)	Lower Heating Value (MJ/kg)	Adiabatic Flame Temp. (°C)	Summarized Formula
Diesel	839.3	52.4	2.869	42.97	2740.2	$C_{15.243}H_{27.548}N_{0.009}$
WED (10% w/w water)	850.0	44.5	3.210	40.51	2714.4	$C_{15.243}H_{27.548}N_{0.009}$ + 10% w/w H_2O

and formation of tiny fuel droplet due to micro-explosion is called secondary atomization which is shown in Fig. 2 [11]. This results better fuel air mixtures. Due to higher density of the WED, spray jet momentum is more resulting longer travel of fuel and improved air-entraining in the spray also leads to better air fuel mixture. As a result, more complete combustion takes place resulting higher engine efficiency and less pollutant emission [1, 8, 12, 13].

Preparation of WED by Ultrasonocation

Most of the researchers have prepared the emulsified diesel by using mechanical homogenizing machine. In this method, a high speed stirring head mixer is applied into the liquid mixture to violently agitate it. Due to high speed, a large amount of shearing and cutting force generate among the interfaces of the water, diesel and surfactant phases to form the emulsion [7]. The fuel properties and engine performances have been studied by different researchers using WED prepared by mechanical homogenizing methods. A few number of the researchers like Lin et al. [2], Bidita et al.[9] and Kojima et al. [14] used ultrasonic emulsification method to get better emulsified fuel properties and improved engine performance. An ultrasonic wave is made by mechanical vibration and it is propagated through the transmission medium. These vibration waves release large amount of energy into the liquid solution creating mechanical stirring effects, which effectively produces the emulsification of the liquids. Simultaneously, the cavities produced by above mentioned process is compressed by positive pressure created by ultrasonic waves and thus producing collapsing explosion and heat generation among the liquid molecules. When this generated heat is higher than diffusion rate from these cavities then excess heat is absorbed by surrounding liquid which are referred to as heat spot effect [2]. The higher pressure and temperature generated by ultrasonic wave enhance the chemical and physical reaction in the liquid.

Performance and Emission Characteristics with WED

The micro explosion substantially improves combustion of WED and this leads to improvement in engine efficiency [12, 13]. Due to lower calorific value of emulsified fuel, brake specific fuel consumption (BSFC) increases, because a portion of diesel is displaced by equal amount of water. But, if only the amount of diesel is considered as the total fuel of water emulsified diesel, then it will be observed that at any operating condition, there will be a reduction in fuel consumption rate [15]. The evaporation of water present in the emulsified fuel absorbs sensible and latent heats, thus reduces the combustion temperature. The finely dispersed water droplets present in the emulsified fuel work as heat sink [1, 15]. The inner phase water reduces the calorific value of emulsion, so the burning gas temperature reduces in the combustion chamber. The combined effects of lowered combustion temperature and better combustion of emulsified fuel reduces the pollutant emissions [1, 5, 15]. The lowered combustion temperature reduces the formation of NO_x because its generation is highly depends on temperature. The NO_x is primarily formed through oxidation of atmospheric nitrogen (N_2) following Zeldovich mechanism [16]. Improved combustion also reduces the formation and emission of pollutants like CO, unburned HC, PM and smoke. The use of water emulsified diesel in CI engines is the only method which reduces both NO_x and PM simultaneously [16]. The presence of water in WED augments the concentration of OH (hydroxyl) radicals which is a strong soot

TABLE 2. Summary of some previous works using WED as fuel for diesel engine.

Researchers	**Performance Characteristics**			**Emission Characteristics**			
Water by Vol	**BP**	**Thermal Efficiency(η)**	**BSFC**	**CO**	**NO_x**	**PM**	**HC**
Nadeem et al.[1] 5,10&15%	Decreases above engine speed of 4000 rpm	----	Increases	Decreases	Decreases	Decreases	----
Lin et al. [7] 15%	----	----	Increases	Increases, but less at higher load	Decreases	----	----
Attia et al. [12] 17%	----	Increases	----	----	Decreases	----	Decreases
Yang et al. [13] 5%	Decreases	Increases	Increases	No significant difference	Decreases	___	Decreases
Ithnin et al. [15] 5,10,15, 20%	----	----	No Change upto 10% water and then increases.	Increases	Decrease	Decrease	___
Alahmer [16] 5,10,,20, 30%	Increases upto 5% water addition and then decreases	Increases upto 5% water addition and then decreases	Decreases upto 5% water addition and then increases	___	Decreases	___	___
Saravanan et al. [18] 15%	----	No change	Increases	Decreases at higher load	Decreases	___	Decreases

presence of OH radicals in WED. Some researchers found that at low load, the CO formation is higher for WED in comparison to pure diesel. This can be explained by reduction of combustion temperature which limits the oxidizing agent. Ithnin et al. [15] mentioned that the emission of PM is reduced because of better combustion of WED due to micro-explosion, less pyrolysis reaction, reduced flame temperature and enhanced soot oxidation due to presence of OH radicals in WED. Some researchers found that at low load, the CO formation is higher for WED in comparison to pure diesel. This can be explained by reduction of combustion temperature which limits the conversion of CO to CO_2 [15]. With increase of load, the combustion chamber temperature increases and CO is converted to CO_2. Wang et al. [17] analyzed the other effects of water present in the emulsified diesel. The steam generated due to ignition of emulsified fuel works on the piston so that the pressure on the piston increases near TDC. It may be noted that the evaporation of water leads to loss of heat but total enthalpy loss is less because of lower exhaust temperature in case of WED.

Some of the major findings obtained from numerical and experimental investigation by different researchers using emulsified diesel as CI engine fuel, a comparative Table 2 is made to show the performance and emission characteristics of the engine. Although it is difficult to compare among the obtained results because of variation of parameters like fuel quality, engine characteristics and operating parameters, but it gives an overview about the advantages of water emulsified diesel as one of the best promising alternative fuel for diesel engine.

STABILITY ANALYSIS OF EMULSIFIED FUEL

Stability is a major issue in case of any emulsified fuel and it depends on the method of preparation and surfactant used. As a case study, water emulsified diesel is prepared using ultrasonic machine. The actual picture of the machine is shown in Fig. 3 and detail specification of the machine is given in the table 3. In the emulsion, water percentage was 10% by volume, surfactant was 2% by volume and the rest was diesel oil. In this experiment, mixture of surfactants Span 80 (6.7 ml) and Tween 80 (3.3 ml) has been used. The HLB value of the mixture can be calculated using the following relation [19]:

$$HLB_{ST} = \frac{(HLB_S \times W_S) + (HLB_T \times W_T)}{W_S + W_T} \quad (1)$$

where, S and T stands for the surfactants Span 80 and Tween 80, W_S and W_T are weights and HLB_S and HLB_T are HLB values of respective surfactants. Thus the resultant HLB value of the mixture is calculated to be 8.The two important fuel properties namely density and viscosity of the WED have been measured using Pycnometer and Ostwald viscometer respectively.

FIGURE 3. Ultrasonic machine of SONIC (VCX 1500)

TABLE 3. Specification of the Ultrasonic Processing Machine

Manufacturer	SONICS & MATERIALS INC.,
Model No.	VCX 1500
Power Supply	Net power out put : 1500 Watts. Frequency : 20 kHz
Standard Probe	Tip diameter : 1" (25 mm) Length : 9" (230 mm) Processing capability : 4
Electrical Requirements	220 volts, 50/60 Hz, single phase, 15 A

Observation and Discussion

A total volume of 500 ml of the mixture was taken and the volume of the emulsified fuel reduced to 450 ml due to evaporation during preparation. The appearance of the produced emulsion is milky in color. The prepared WED was kept undisturbed for 2 months to observe stability profile and emulsion stability (ES). There was no separation of water during first 24 hours, but after separation started and continued up to 7 days before it became stable. The actual pictures of the emulsion immediately after preparation, after 7 days and after 2 months are shown in Fig. 4(a), 4(b)

and 4(c) respectively. The separated water/ sediments stored at bottom of the biker and diesel at top layer in the biker. Bigger size water globules come down to the bottom of the biker causing separation. After 7 days all the bigger size water globules separated and the emulsion became stable. Stability profile of the water emulsified

(a) (b) (c)

FIGURE 4. Actual pictures of the emulsion (a) immediately after preparation; (b) after 7 days and (c) after 2 months.

diesel prepared by ultrasonic machine is shown in the Fig. 5. The emulsion was formed and water particles were uniformly distributed in the continuous diesel oil phase.

Lin et al. [7] observed that as the larger number of small water particles were formed so higher frictional force and static electric attracting force formed which resulted in higher viscosity and lower separation of water particles from the emulsion. He also reported that the ultrasonic processing produce smaller water granules with higher stability of the emulsion and consume less energy during preparation with compared to mechanical homogenizing process. Bidita et al. [9] concluded from his investigation that the ultrasonic machine used for emulsification should be used at higher amplitude for short time. At lower amplitude, the brake down of large water droplets into small particle may not be completed. And if the machine is operated for long time, the emulsion temperature increases which leads to problem in stability of the emulsion. The emulsion stability (ES) has been evaluated by keeping the emulsion motionless for predetermined time and it is calculated as, $ES=(V_E/V_T)\times100\%$ [14]. In this case, the predetermined time was taken as seven days. After this period, it is observed that 40 ml oil floats at the top and 10 ml is deposited at the bottom as sediment.. ES is calculated to be 88.9% which suggests the high stability of the prepared sample. Table 4 clearly shows that both the density and viscosity of prepared WED are higher than pure diesel. The increase of density is attributed to the higher density of water which is added to the lower density diesel fuel. The higher density adds additional momentum, so fuel jet travel more distance and air-entraining in the spray increases which improves air-fuel mixture resulting better combustion [1, 15]. The viscosity of the WED is increased due to the frictional force and the generated static electricity among the disperse water droplets and continuous diesel fuel [14, 20]. Kojima et al. [14] concluded that the increase of water content and decrease of water particle size led to more water surface area resulting higher viscosity. As the dynamics of the fuel system changes due to flow variation on viscosity variation, so the increase of viscosity tends to advance injection timing in some injection system which allows much more air-fuel mixing time [1, 16]. Increase of viscosity due to frictional force and static electricity improve stability of WED.

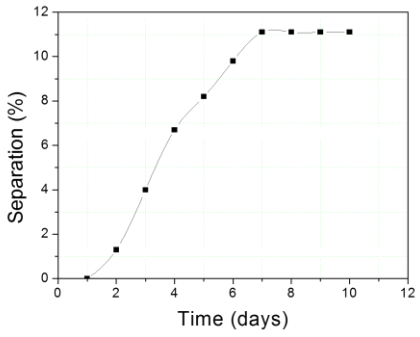

FIGURE 5. Stability profile of the WED prepared by ultrasonication

TABLE 4. Density and viscosity of pure diesel and WED at 35 °C.

Pure diesel was taken from IOCL petrol pump.

The WED was prepared by ultrasonic machine at 80% amplitude containing 10% water and 2% surfactants.

Fuel Type	Density (kg/m^3)	Viscosity (cSt)
Pure Diesel	839.8	2.538
Emulsified Diesel	854.1	4.020

CONCLUSION

The WED is one of the best promising alternative fuels for diesel engine in respect of higher engine performance and low pollutant emissions. Review of the exiting literature shows that emulsified diesel can be prepared most effectively by ultrasonic machine. Although the gain in performances of the engine with WED is marginal, but the improvement in the emission characteristics is remarkable. The experimental part of the present study shows that the prepared sample becomes stable after 7 days and its ES is noted to be 88.9%, indicating a higher stability of the emulsion. The density and viscosity of WED are more than pure diesel.

REFERENCES

1. M. Nadeem, C. Rangkuti, K. Anuar, M.R.U. Haq, I.B. Tan and S.S. Shah, Fuel **85**, 2111–2119 (2006).
2. C. Y. Lin and L. W. Chen, Fuel **85**, 593–600 (2006).
3. "Status of the Vehicular Pollution Control Programme in India", Central Pollution Control Board, India, (March, 2010).
4. P. Haller, A. Jankoowski, C. Kolanek and W.W. Walkowiak, Journal of KONES Powertrain and Transport **19(3**) (2012).
5. Cornelius O' Sullivan, "Investigation of NO_x and PM emissions from a diesel engine operating on nano emulsified fuel. Massachusetts Institute of Technologies", Master of Science in Mechanical Engineering, Massachusetts Institute of Technology, September, 1999.
6. J. Ghojel and D. Honnery; Applied Thermal Engineering **25**, 2072–2085 (2005).
7. C. Y. Lin and L. W. Chen, Fuel **87,** 2154–2161 (2008).
8. A. Lif and K. Holmberg, Advances in Colloid and Interface Science **123–126**, 231–239 (2006).
9. B.S. Bidita, N. Aien, A.R. Suraya, M.A. Mohd Salleh and A. Idris, Journal of Dispersion Science and Technology **35**, 185-192 (2014).
10. O. Armas, R. Ballesteros, F.J. Martos and J.R. Agudelo, Fuel **84**, 1011-1018 (2005).
11. Emulsified Fuel, http://blueoceansoln.com/solutions-2/introduction-to-emulsified-fuel ; Internet, dated: 12.09.2013.
12. A.M.A. Attia and A.R. Kulchitskiy, Fuel **116**, 703–708 (2014).
13. W.M. Yang , H. An, S.K. Chou, K.J. Chua, B. Mohan, V. Sivasankaralingam, V. Raman, A. Maghbouli and J. Li, Applied Energy **112**, 1206–1212 (2013).
14. Y. Kojima, H. Imazu and K. Nishida, Ultrasonics Sonochemistry **21**, 722–728 (2014).
15. A.M. Ithnin, M.A. Ahmad, M.A.A. Bakar, S. Rajoo and W.J. Yahya, Energy Conversion and Management **90**, 375–382 (2015).
16. A. Alahmer, Energy Conversion and Management, **73**, 361–369 (2013).
17. L.P. Wang and W.B. Fu, Fuel Processing Technology **72**, 47–61 (2001).
18. M. Saravanan, A. Anbarasu and B. M. Gnanasekaran, Int J. Adv. Manuf. Technol. **69**, 2531–2544 (2013).
19. C.Y. Lin and K.H. Wang, Fuel **82**, 1367–1375 (2003).

ICME2015

International Conference on Mechanical Engineering 2015
(ICME 2015) 18 – 20 December, 2015, Dhaka, Bangladesh

Paper ID :114

An Experimental Study on the Performance of Closed Loop Pulsating Heat Pipe (CLPHP) with Methanol as a Working Fluid

Md Lutfor Rahman[1], Farah Nazifa Nourin[1,a)*] , Zaimaa Salsabil [1], Nusrat Yasmin[1,b)]
Mohammad Ali[2]

[1] *Military Institute of Science and Technology, Mirpur Cantonment, Dhaka-1216, Bangladesh*
[2] *Bangladesh University of Engineering and Technology, Dhaka-1000, Bangladesh*

[a)]Corresponding author: farahnazifanourin@gmail.com
[b)]nusratyasmin015@gmail.com

Abstract Thermal control is an important topic for thermal management of small electrical and electronic devices. Closed loop pulsating heat pipe (CLPHP) arises as the best solution for thermal control. The aim of this experimental study is to search a CLPHP of better thermal performance for cooling different electrical and electronic devices. In this experiment, methanol is used as working fluid. The effect of using methanol as a working fluid is studied on thermal performance in different filling ratios and angles of inclination. A copper capillary tube is used where the inner diameter is 2mm, outer diameter is 2.5mm and 250mm long. The CLPHP has 8 loops where the evaporation section is 50mm, adiabatic section is 120mm and condensation section is 80mm. The experiment is done using FR of 40%-70% with 10% of interval and angles of inclination 0° (vertical), 30°, 45°, 60° varying heat input. The results are compared on the basis of evaporator temperature, condenser temperature and their differences, thermal resistance, heat transfer co-efficient, power input and pulsating time. The results demonstrate the effect of methanol in different filling ratios and angles of inclination. Methanol shows better performance at 30° inclination with 40% FR.

Keywords Closed loop pulsating heat pipe (CLPHP); Thermal performance; Thermal resistance; Heat transfer co-efficient

TABLE 1. Nomenclature

Symbol	Meaning	Symbol	Meaning
R_{th}	Thermal resistance, °C/W	OD	Outer diameter of tube, mm
ΔT	Temperature drop along the device, °C	ID	Inner diameter of tube, mm
L	Length of heat Pipe, mm	IA	Inclination angle, °
FR	Filling ratio, %	Q	Heat input, W
D	Diameter of heat pipe, mm	T	Temperature along the pipe, °C
e(as subscript)	evaporator section	c (as subscript)	condenser section

INTRODUCTION

With the rapid development of electronic industry, the physical size of the electronic devices is decreased. Hence, thermal management has become and will continue to be one of the most critical technologies in the electronic product development. These small electronic devices have less area for cooling system. To solve the problem of thermal management of microelectronic devices the miniaturization of heat exchanger is needed [1]. A pulsating heat pipe has the best ability to handle above problems. Comparatively, PHP is a young member in the family of heat pipe. The closed loop pulsating heat pipe is made of copper capillary tube, bent into an undulating tube and connected at the ends to form a closed loop with no internal wick structure. The structure of the CLPHP is shown in Fig.1. Compatibility of working fluid is an important factor. Hence, copper is selected as compatible material for methanol heat pipe. As any other two-phase passive thermal control device, heat is gained from the source through the evaporation section transferring it to the working fluid where the slug pumping action is generated. Then the methanol flows by the adiabatic section towards the condensation section. For completing the loop, on a closed loop configuration the fluid is allowed to circulate and after being condensed, methanol returns to the evaporator section. As ID of the tube is very small and meets a capillary scale, methanol forms into liquid slugs alternating with vapor slugs along the total length of the tube [2]. When one end of the CLPHP called evaporator section is subjected to high temperature, methanol which is in liquid slug evaporates, expands and moves through the no heat transferring zone or adiabatic section, toward the cooler section known as condensation section. The vapor slug in condenser section condenses, collapses and releases heat into the environment. Therefore, the vapor slug evaporating in the evaporator section constantly flows to replace the vapor slug collapsing in the condenser. According to this mechanism, methanol circulates and continuously transfers heat in a cycle.

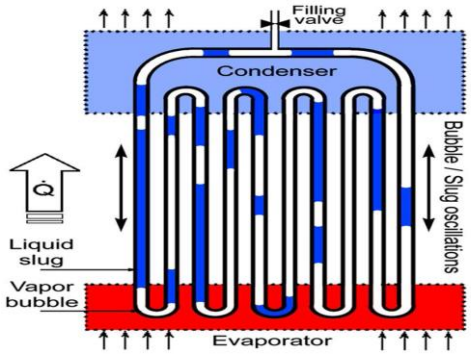

FIGURE 1. Closed Loop Pulsating Heat Pipe

The PHP was first introduced and patented by Akachi et al. [3] as a two phase passive cooling device and captured the attention of many investigators. Various mathematical models have been established to explain the complex behaviour of thermo-fluidic transport phenomena. The mathematical models proposed in field of PHPs need experimental verification as stated by Shafii [4], Zhang [5], and Rama Narasimha et al. [6]. Bai et al. [7] established a steady state mathematical model. Characterization of thermal behaviour in multi-loop PHPs was investigated by Cai [8], Charoensawan [9], Khandekar [10, 11] and Meena et al. [12]. Rama Narasimha et al. [13, 14] investigated the thermal performance of single loop PHP. Experimental results mainly focused on flow visualization studies and the measurement of temperature variation pattern. The primary design parameters such as the effect of working fluid, heat input, tube material, orientation and FR affecting the performance of PHP which was identified by Nagvase and Pachghare [15] needs detailed investigation. Although different studies have been carried out, certain key aspects are poorly understood and even some analytical results obtained by different investigators are to be validated by experiment.

EXPERIMENTAL METHOD

Experimental Setup

Figure 2(b) illustrates the experimental set up. The CLPHP was fabricated by bending copper tubes which has eight turns. The adiabatic section of the copper tube is covered by aluminum foil, then glass wool and finally covered with foam tape for better thermal insulation. The evaporator section is also thermally insulated by using mica sheets with nichrome resistance wire (diameter: 0.25mm, resistivity: 1.0×10^{-6} Ω-m, specific heat: 450Jkg $^{-1}$k $^{-1}$) and asbestos to stop heat loss by convection and radiation. Eight thermocouples (LM-35sensors, Local Sensor Accuracy (Max (+/-C): 0.5, range: -55°C to +150°C) are glued by a glue gun to the wall of heat pipe in evaporator and condensation section; four for each section. Evaporator section is set up inside a box of steel frame which is heated by a power supply unit (AC, 220V, 50Hz) via a variac (3F, 300V, 60Hz).Methanol is used as working fluid at the amount of FR 40-70% (by volume). By using vacuum pump, the copper tube is made vacuum, filling the tube through a syringe at definite filling ratio by opening the top of tube and then the fluid directly enters the tube and finally sealed. For cooling the working fluid, forced convection is used by a DC fan. The whole apparatus is set on a steel test stand. The angular movement is set up manually. For collecting data Arduino Mega (Microcontroller: AT mega 1280, Operating Voltage: 5V, Input Voltage (recommended): 7-12V, Analog Input Pins: 16) is used. The other accessories of the set up are adapter circuit, selector switches, bread board, wire etc.

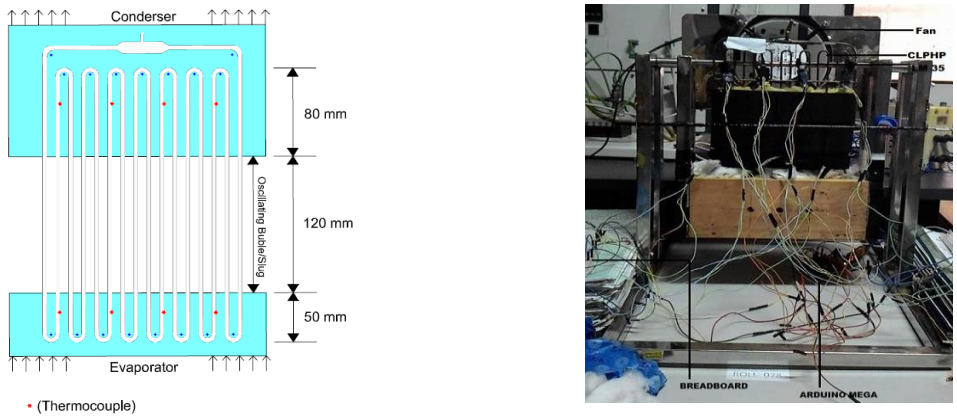

(a) **(b)**

FIGURE 2.a) Experimental setup, **b)** Prototype of experimental setup

Experimental Procedure

The following procedure is adopted for conducting the experiment:

- The experiment is performed for 40-70% filling ratios of Methanol as working fluid and four different angular orientation of heat pipe.
- First the heat pipe is filled with 40% Methanol keeping the PHP in vertical (0°) position.
- 10W – 60W heat inputs are provided to the system and temperature readings are measured by thermocouples using Arduino Mega.
- After recording the readings, a cooling fan is used for cooling the heat pipe.
- Then the angle of inclination is changed to 30°, 45°, 60° and keeping the filling ratio same the above procedure is repeated.
- For other filling ratios, the above procedure is followed for different angles of inclination and heat inputs.

RESULTS AND DISCUSSION

The experiment is carried out for methanol in different filling ratios and different angles of inclination. Considering thermal resistance as an indication of efficiency, this experiment is carried out i. e. lower value of R_{th} refers to low resistance to heat flow and eventually indicates a higher efficiency of the system. The result shows the effect of methanol on the basis of different characteristics.

Effect of Heat Input

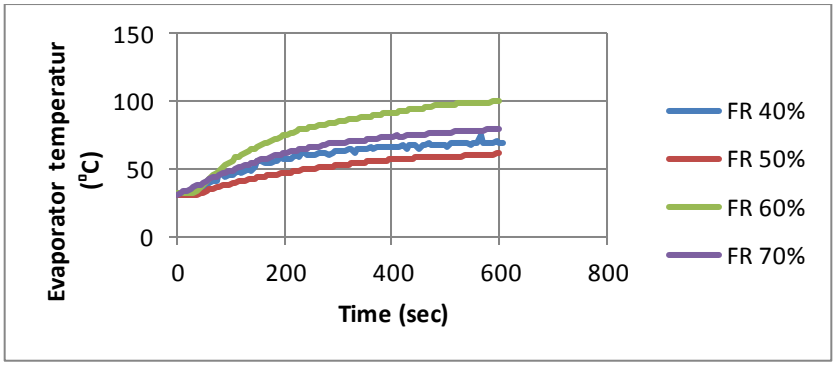

FIGURE 3. Variation of evaporator temperature with time at different FR at 0° inclination at 30W

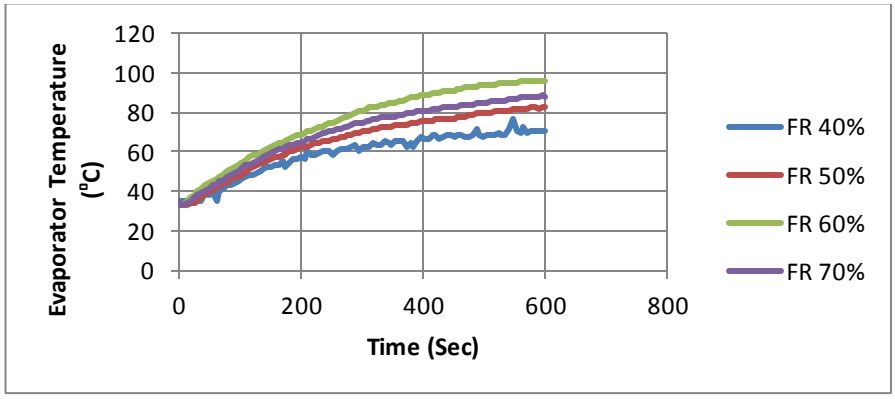

.

FIGURE 4. Variation of evaporator temperature with time at different FR at 30° inclination at 30W

The figures show the variation of evaporator temperature with time for 30W, for all FR at 0°, 30°, 45°and 60° respectively. The variation of temperature with time curve shows a similar pattern for all experimental conditions. In all graphs, the rate of temperature increase is high at beginning and when it reaches boiling point it slows down. The rate of increase is different for different region. The temperature increase in evaporator slows down due to heat requirement in phase transfer. In all figure the rate of temperature increase is higher in 200 sec then the rate slows down. From the graph it can be seen that 40% FR gives the best curve that is pulsating curve. From fig.3, the start up time starts at almost 40 sec and from the graph it can be seen that the start up time decreases with the increase of orientation.

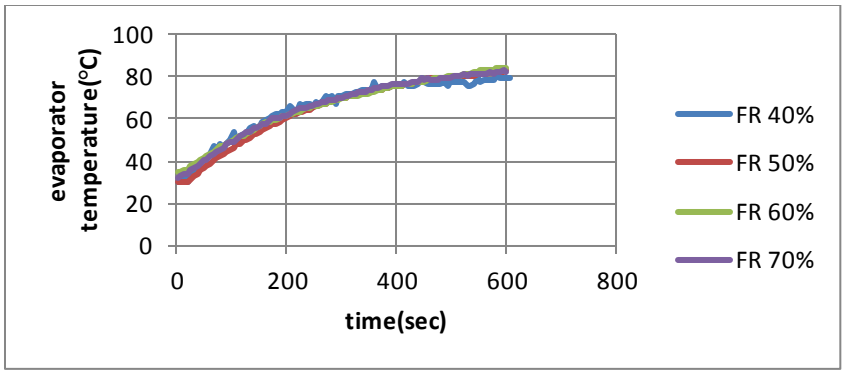

FIGURE 5. Variation of evaporator temperature with time different FR at 45° at 30W

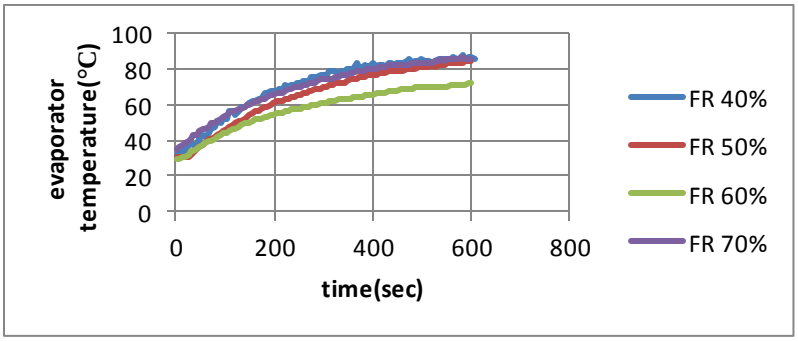

FIGURE 6. Variation of evaporator temperature with time at different FR at 60° at 30W

From fig. it is clear that for the pulsating curve the evaporator wall temperature is higher in case of 40% filling 60w and lower in the case of 40% FR 10 watt. Due to movement of the working fluid, temperature of evaporator section becomes steady. All other filling ratio is smoother curve compared to 40% FR. Only 40% FR gives the best fluctuation.

Effect of Thermal Resistance

For determining the thermal performance, efficiency and understanding the heat transfer characteristics of CLPHP, the wall temperature at different points of CLPHP are measured. Thermal resistance is calculated as thermal resistance=$(T_e - T_{c)})/Q$. After that thermal resistances are plotted against heat input.

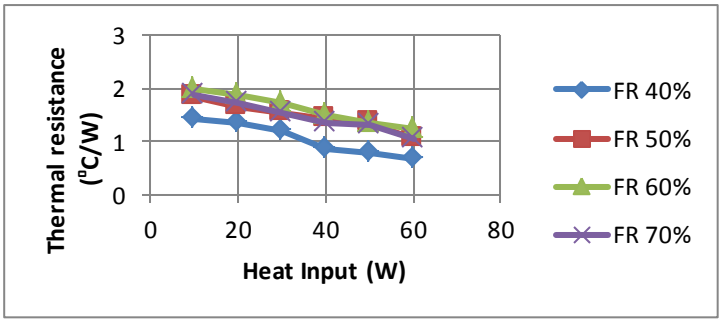

FIGURE 7. Effect of filling ratio on thermal resistance at 30° inclination for methanol

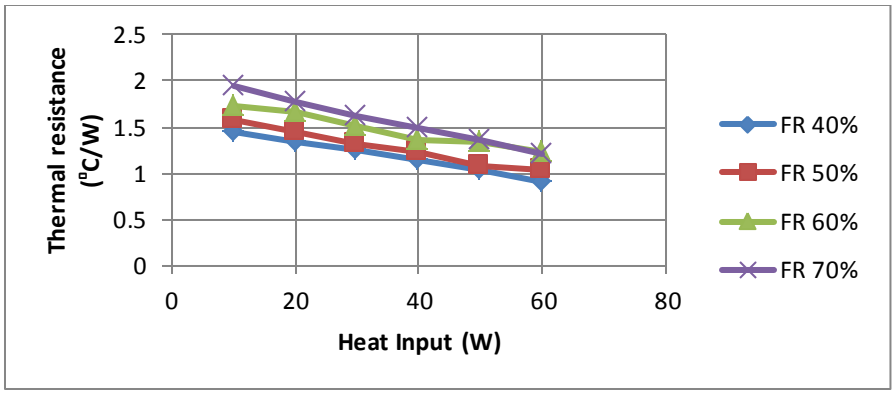

FIGURE 8. Effect of filling ratio on thermal resistance at 45° inclination for methanol

At 30° inclination, the vapor bubbles grow in the evaporator. Buoyancy force helps them to rise up in the tube section. Simultaneously other bubbles which are above in the tube are also helped by their respective buoyant forces. These rising bubbles carry the liquid slugs trapped in between them. In this mode of operation there is a tendency for liquid slugs to travel downwards, helped by gravity force, toward the evaporator. The vapor bubbles also have the natural tendency to travel towards the condenser helped by their buoyancy. Fig.7 and Fig.8 demonstrate the comparison with the variation of thermal resistance with heat input at different filling ratio at 30° and 45° angles of inclination. The curves of thermal resistance are of similar pattern for all the cases. There is inverse relationship between thermal resistance and heat input. In Fig.7, FR 50% and FR 70% show almost same result and FR 40% shows better performance. At low FR, when the heat input is increased the entire surface is covered by the vapor space which leads to the dry out situation. In Fig.8, FR 40% and FR 50% show almost same performance. For FR 60% and FR 70% at 60W thermal resistance meets at the same point. A closer look at Fig 7 and Fig.8, for 30° inclination 40% FR performs better than any other position and FR.

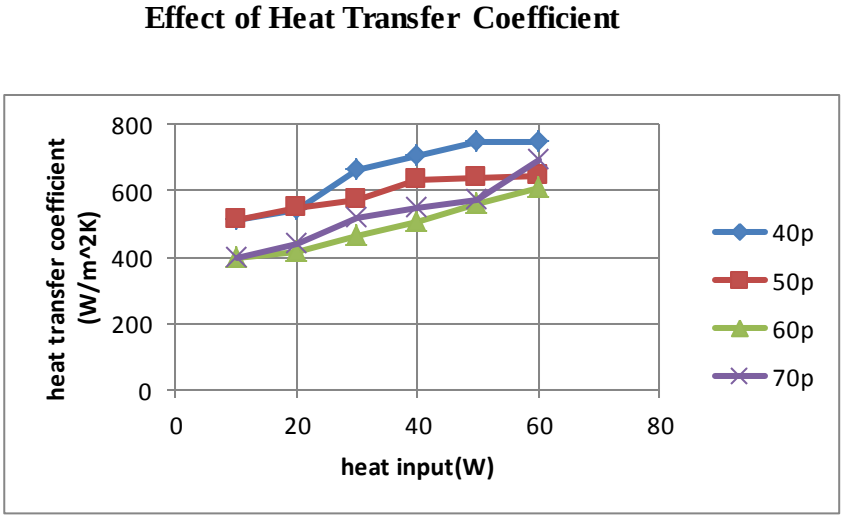

FIGURE 9. Effect of filling ratio on heat transfer co-efficient at 30° inclination for methanol

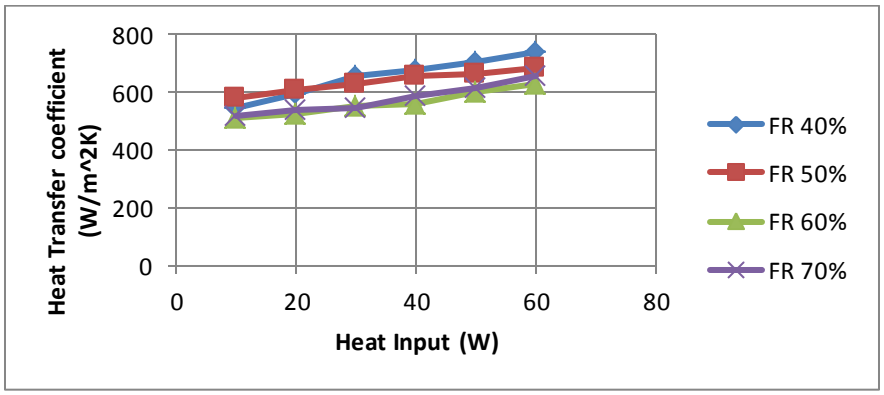

FIGURE 10. Effect of filling ratio on heat transfer co-efficient at 45° inclination for methanol

The convective heat transfer coefficient of CLPHP is given by, $h = \frac{Q}{A(T_e - T_c)}$

Fig.9 and Fig.10 show the variation of heat transfer coefficient with heat input for different filling ratios of methanol at 30° and 45° angles of inclination. Both the figures show that heat transfer coefficient increases with increases in heat input for all the FR. At both the inclination 40% FR shows better heat transfer up to 60W but more precisely it shows better performance at 30° inclination.

CONCLUSION

Form this experimental study some information related to the fundamental characteristics and operational regimes of a CLPHP are generated. The three important factors-bubble formation, phase transfer, pressure are considered to design heat pipe. It can be emphasized the desired thermo-mechanically boundary conditions resulting convective flow boiling condition in the evaporator design. Different heat inputs to these devices give to different flow pattern inside the tube. This in turn is responsible for various heat transfer characteristics. In this investigation, methanol gives better thermal resistance at 30° inclination for 40% filling ratio. For different angles heat transfer coefficient shows better performance at 40% filling ratio. A close comprehensive look is required for designing heat pipes, as their performance is a function of orientation, filling ratios, working fluid and fin. More investigations are needed for most satisfactory pattern of design.

ACKNOWLEDGEMENTS

The authors feel greatly honored to be able to express their earnest gratitude to the Department of Mechanical Engineering, MIST and BUET for the accomplishment of this research by providing laboratory facilities and financial supports.

REFERENCES

1. Moore. g, Craming More Components onto Integrated circuits, Electronics, 1965 38(8)
2. H. Akachi, F. Polasek, and P. Stulc, “Pulsating heat pipes,” in Proc. 5th Intl. Heat pipe Symp, Melbourne, Australia, 1996, pp. 208-217
3. Akachi, H. “Structure of Heat Pipe”, US patent, 4921041, 1990
4. Shaffi, B. M. , Faghri, A., Zhang, Y., “Thermal modeling of unlooped pulsating heat pipes, Journal of Heat Transfer” Vol. 123, No. 6, 2001, pp. 1159-1172.

5. Zhang, Y., Faghri, A.,"Heat Transfer in a pulsating heat pipe with open end, International Journal of Heat Mass Transfer", Vol 45, No. 4, 2002, pp. 755-764
6. Rama Narasimha, K., Rajagopal, M.S., Sridhara, S.N., Seetharamu, K.N., "Parametric studies on Pulsating Heat Pipes", International Journal for Numerical Methods for Heat and Fluid flow,Vol. 20, Issue 4, 2010. pp. 392-415
7. Lizhan Bai, Guiping Lin, Hongxing Zhang, Dongsheng Wen. (2009): "Mathematical modeling of steady state operation of a loop heat pipe". Applied Thermal Engineering, Vol. 29, pp. 2643-2654
8. Cai, Q., Chung-lung Chen, Julie F. Asfia, "Operating Characteristic Investigations in Pulsating Heat pipe", journal of heat transfer, vol.128, 2006, pp.1329-13334.
9. Charoensawan, P., Khandekar, S., Groll, M. and Terdtoon, P. "Closed loop pulsating heat pipes", part-A; Parametric experimental investigations", Applied Thermal engineering, Vol.23 No.6, 2001, pp. 2009-2020
10. Khandekar, S., "Thermo Hydrodynamics of Pulsating Heat Pipe", NTUS-IITK 2nd joint workshop in mechanical, Aerospace and Industrial Engineering, April 5-6, 2008,IIT, Kanpur,India
11. Khandekar,S., "Thermo Hydrodynamics of Pulsating Heat Pipes", Ph.D Dissertation, University of Stuttgart, Germany, 2004.
12. Meena, P., Rittidech, S., Tammasaeng, P, "Effect of inner Diameter and Inclination angles on operation limit of closed loop oscillating heat pipes with check valves", American journal of Applied Sciences, Vol. 1, No.2,2008,pp. 100-103.
13. Rama Narasimha, K., "Studies on Pulsating Heat pipes" Ph.D. Dissertation, Visveswaraya Technological University, India, 200.
14. Rama Narasimha,K., Rajagopal, M. S.,Sridhara, S.N., "Influence of Heat Input, Working Fluid and Evacuation Level on the Performance of a Pulsating Heat Pipe" Journal of Applied Fluid Mechanics, Vol .5 ,No. 2, Issue 10, 2012, Accepted for Publication.
15. Nagvase S.Y.,Pachghare P.R., "Parameters affecting the function of closed loop pulsating heat pipe:A Review", Research Journal of Engineering Sciences, Vol 2(1), 2013,pp.35-39.

ICME2015

International Conference on Mechanical Engineering 2015
(ICME 2015) 18 – 20 December, 2015, Dhaka, Bangladesh

Paper ID : 116

Dean-Taylor Flow with Convective Heat Transfer through a Coiled Duct

Md. Zohurul Islam[1, a)], Raju Roy[2, b)] and Rabindra Nath Mondal[3, c)]

1, 2) Dept. of Mathematics and Statistics, Jessore University of Science and Technology, Jessore-7408, Bangladesh
3) Department of Mathematics, Jagannath University, Dhaka-1100, Bangladesh

[a)] Corresponding author: mz.islam@just.edu.bd
[b)]raju_saha21@yahoo.com
[c)]rnmondal71@yahoo.com

Abstract. The present paper addresses numerical prediction of Dean-Taylor flow through a coiled rectangular duct of curvature 0.1. Spectral method is used as a basic tool to solve the system of non-linear partial differential equation. The emerging parameters controlling the flow characteristics are the rotation parameter i.e. Tr , (incorporating Coriolis force), Grashof number (Gr), Prandtl number ($Pr = 7$), aspect ratio ($a = 2$), and pressure-driven parameter i.e. Dean number Dn (incorporating centrifugal force). The flow structures are examined for the effects of rotation parameter and pressure-driven parameter. We investigated unsteady flow characteristics for two cases of the duct rotation, Case I: Positive rotation and Case II: Negative rotation. For positive rotation, we investigate the unsteady flow for the Dean numbers Dn = 1000 to 2000 over the Taylor number $0 \le Tr \le 500$, and it is found that the chaotic flow turns into steady-state flow through periodic or multi-periodic flows, if Tr is increased in the positive direction. For negative rotation, however, unsteady flow characteristics are investigated over the Taylor number $-700 \le Tr \le -50$, and it is found that the unsteady flow undergoes through various flow instabilities, if Tr is increased in the negative direction. Contours of secondary flow patterns and temperature profiles are obtained at several values of Tr, and it is found that the unsteady flow consists of two-, three-, four-, five-, six-, seven- and eight-vortex solutions. Convective heat transfer is also investigated, and it is found that the chaotic flow enhances heat transfer more significantly than the steady-state or periodic solutions.

TABLE 1

Nomenclature

Dn	: Dean number	d	: Half width of the cross section
Tr	: Taylor number	L	: Radius of the curvature
Gr	: Grashof number	u	: Velocity components in the $x-$direction
P_r	: Prandtl number	v	: Velocity components in the $y-$direction
λ	: Resistance coefficient	w	: Velocity components in the $z-$direction
T	: Temperature	x	: Horizontal axis
t	: Time	y	: Vertical axis
h	: Half height of the cross section	z	: Axis in the direction of the main flow

Greek letters					
δ	: Curvature of the duct	μ	: Viscosity	υ	: Kinematic viscosity
ρ	: Density	κ	: Thermal diffusivity	ψ	: Sectional stream function

INTRODUCTION

Flow and heat transfer through curved ducts and channels have attracted much attention because of their enormous applications in fluids engineering, such as refrigeration, air conditioning systems, heat exchangers, and the blood flow in the human body. In a curved duct, centrifugal forces are developed due to channel curvature causing a counter rotating vortex motion applied on the axial flow through the channel. This creates characteristics spiraling fluid flow in the curved passage known as secondary flow. At a certain critical flow condition and beyond, additional pairs of counter rotating vortices appear on the outer concave wall of curved fluid passages which are known as *Dean vortices*, in recognition of the pioneering work in this field by Dean [1]. After that, many theoretical and experimental investigations have been done by keeping this flow in mind; for instance, the articles by Berger *et al*. [2], Nandakumar and Masliyah [3] and Ito [4] may be referenced. The fluid flowing in a rotating curved duct is subjected to two forces: the *Coriolis force* due to rotation and the *centrifugal force* due to curvature. When a temperature induced variation of fluid density occurs for non-isothermal flows, both Coriolis and centrifugal type buoyancy forces can contribute to the formation of vortices. These two effects of rotation either enhance or counteract each other in a non-linear manner depending on the direction of wall heat flux and the flow domain. Therefore, the effect of system rotation is more subtle and complicated, and yields new richer features of flow and heat transfer for the non-isothermal flows. Ishigaki [5] examined the flow structure and friction factor numerically for both the counter-rotating and co-rotating curved circular pipe with a small curvature. Miyazaki [6] examined the solution when the rotation is in the same direction as the Coriolis force emphasizing the centrifugal force caused by the duct curvature, which is known as co-rotating case. Wang and Cheng [7, 8] and Daskopoulos and Lenhoff, [9] carried out a bifurcation study of the flow through a circular pipe and employed the finite volume method. Unsteady solutions of fully developed curved duct flows were initiated by Yanase and Nishiyama [10] for a rectangular cross section. In that study, they investigated unsteady solutions for the case where dual solutions exist. The time-dependent behavior of the flow in a curved rectangular duct of large aspect ratio was investigated, in detail, by Yanase *et al*. [11] numerically. They performed time-evolution calculations of the unsteady solutions with and without symmetry condition. Wang and Yang [12] performed numerical as well as experimental investigations of periodic oscillations for the fully developed flow in a curved square duct. They showed, both experimentally and numerically, that a temporal oscillation takes place between symmetric/asymmetric 2-cell and 4-cell flows when there are no stable steady solutions. The secondary flow characteristics in a curved square duct were investigated experimentally by using flow visualization method by Yamamoto *et al*. [13]. Three-dimensional incompressible viscous flow and heat transfer in a rotating U-shaped square duct were studied numerically by Nobari *et al*. [14]. However, transient behavior of the unsteady solution is not yet resolved, in detail, for the flow through a rotating curved rectangular duct, which motivated the present study to fill up this gap. To the best of the authors' knowledge, there has not yet been done any substantial work studying the unsteady flow behavior for the non-isothermal flow through a curved rectangular duct in the presence of strong buoyancy force. But from the scientific as well as engineering point of view it is quite interesting to study the unsteady flow behavior in the presence of buoyancy and centrifugal forces, because this type of flow is often encountered in engineering applications. In this paper, we investigate transient flow of viscous incompressible fluid through a curved rectangular duct of aspect ratio 2 by using the spectral-based numerical scheme, and show an enhancement of convective heat transfer by secondary flows. Studying the effects of rotation on the unsteady flow characteristics, caused by the combined action of the centrifugal force, Coriolis force and buoyancy force, is an important objective of the present study.

MATHEMATICAL FORMULATIONS

Consider a hydro-dynamically and thermally fully developed two-dimensional flow of viscous incompressible fluid through a rotating curved duct with rectangular cross section, whose height and width are 2h and 2d, respectively.

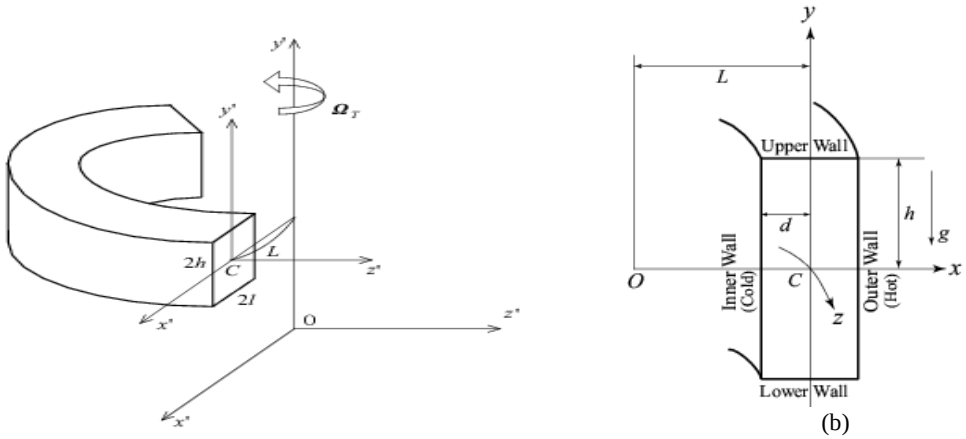

(b)

FIGURE 1. (a) Coordinate system of the rotating curved channel. (b) Cross section of the curved channel.

The coordinate system with the relevant notation is shown in Fig. 1, where x′ and y′ axes are taken to be in the horizontal and vertical directions respectively, and z′ is the axial direction. The system rotates at a constant angular velocity Ω_T around the y′ axis. It is assumed that the outer wall of the duct is heated while the inner wall cooled. It is assumed that the flow is uniform in the axial direction, which is driven by a constant pressure gradient G along the center-line of the duct as shown in Fig. 1. The variables are non-dimensionalized by using the representative length l and the representative velocity U_0.

The sectional stream function ψ is introduced as, $u = \frac{1}{1+\delta x}\frac{\partial \psi}{\partial y}, \quad v = -\frac{1}{1+\delta x}\frac{\partial \psi}{\partial x}.$ (1)

A new coordinate variable y' is introduced in the y direction as $y = ay'$, where $a = h/d$ is the aspect ratio of the duct cross section. From now on y denotes y' for the sake of simplicity. Then the basic equations for the axial velocity w, the stream function ψ and the temperature T are derived from the Navier-Stokes equations and the energy equation under the Boussinesq approximation as,

$$(1+\delta x)\frac{\partial w}{\partial t} + \frac{1}{a}\frac{\partial(w,\psi)}{\partial(x,y)} - Dn + \frac{\delta^2 w}{1+\delta x} = (1+\delta x)\Delta_2 w - \frac{1}{a}\frac{\delta}{(1+\delta x)}\frac{\partial \psi}{\partial y}w + \delta\frac{\partial w}{\partial x} - \delta Tr\frac{\partial \psi}{\partial y} \tag{2}$$

$$\left(\Delta_2 - \frac{\delta}{1+\delta x}\frac{\partial}{\partial x}\right)\frac{\partial \psi}{\partial t} = -\frac{1}{a}\frac{1}{(1+\delta x)}\frac{\partial(\Delta_2\psi,\psi)}{\partial(x,y)} + \frac{1}{a}\frac{\delta}{(1+\delta x)^2}\times\left[\frac{\partial \psi}{\partial y}\left(2\Delta_2\psi - \frac{3\delta}{1+\delta x}\frac{\partial \psi}{\partial x} + \frac{\partial^2\psi}{\partial x^2}\right) - \frac{\partial \psi}{\partial x}\frac{\partial^2\psi}{\partial x\partial y}\right] + \frac{\delta}{(1+\delta x)^2}$$
$$\times\left[3\delta\frac{\delta^2\psi}{\partial x^2} - \frac{3\delta^2}{1+\delta x}\frac{\partial \psi}{\partial x}\right] - \frac{2\delta}{1+\delta x}\frac{\partial}{\partial x}\Delta_2\psi + \frac{1}{a}w\frac{\partial w}{\partial y} - Gr(1+\delta x)\frac{\partial T}{\partial x} - \frac{1}{2}Tr\frac{\partial w}{\partial y}, \ +\Delta_2^2\psi \tag{3}$$

$$\frac{\partial T}{\partial t} + \frac{1}{(1+\delta x)}\frac{\partial(T,\psi)}{\partial(x,y)} = \frac{1}{\mathrm{Pr}}\left(\Delta_2 T + \frac{\delta}{1+\delta x}\frac{\partial T}{\partial x}\right) \tag{4}$$

The non-dimensional parameters Dn, the Dean number, Tr, the Taylor number, Gr, the Grashof number and Pr, the prandtl number, which appear in equations (2) to (4) are defined as:

$$Dn = \frac{Gl^3}{\mu\upsilon}\sqrt{\frac{2l}{L}}, \quad Tr = \frac{2\sqrt{2\delta}\Omega_T l^3}{\upsilon\delta}, \ Gr = \frac{\beta g\Delta T l^3}{\upsilon^2}, \quad \mathrm{Pr} = \frac{\upsilon}{\kappa} \tag{5}$$

In the present study, Dn and Tr are varied while Gr,a, δ and Pr are fixed as Gr =100, a = 2 , $\delta = 0.1$ and Pr = 7.0 (water). The rigid boundary conditions for w and ψ are used as

$$w(\pm 1, y) = w(x, \pm 1) = \psi(\pm 1, y) = \psi(x, \pm 1) = \frac{\partial \psi}{\partial x}(\pm 1, y) = \frac{\partial \psi}{\partial y}(x, \pm 1) = 0 \tag{6}$$

and the temperature T is assumed to be constant on the walls as

$$T(1, y) = 1, \quad T(-1, y) = -1, \ T(x, \pm 1) = x \tag{7}$$

NUMERICAL METHODS

In order to solve the Equations (2) to (4) numerically, the spectral method is used. By this method the expansion functions $\phi_n(x)$ and $\psi_n(x)$ are expressed as

$$\left.\begin{aligned}\phi_n(x) &= (1-x^2)\,C_n(x),\\ \psi_n(x) &= (1-x^2)^2 C_n(x)\end{aligned}\right\} \tag{8}$$

where $C_n(x) = \cos\left(n\cos^{-1}(x)\right)$ is the n^{th} order Chebyshev polynomial. $w(x,y,t)$, $\psi(x,y,t)$ and $T(x,y,t)$ are expanded in terms of the expansion functions $\phi_n(x)$ and $\psi_n(x)$ as

$$\left.\begin{aligned}w(x,y,t) &= \sum_{m=0}^{M}\sum_{n=0}^{N} w_{m\,n}\ \ (t)\ \ \varphi_m\ \ (x)\ \ \varphi_n\ \ (y)\\ \psi(x,y,t) &= \sum_{m=0}^{M}\sum_{n=0}^{N} \psi_{m\,n}\ \ (t)\ \ \psi_m\ \ (x)\ \ \psi_n\ \ (y).\\ T(x,,y,t) &= \sum_{m=0}^{M}\sum_{n=0}^{N} T_{m\,n}\ \ \varphi_{\ m}\ (x)\ \ \varphi_n\ \ (y)\ \ +x\end{aligned}\right\} \tag{9}$$

Where M and N are the truncation numbers in the x and y directions respectively. The accuracy of the numerical calculations is investigated for the truncation numbers M and N used in this study. Four types of grid sizes were used to check the dependence of grid size (i.e. M and N). For good accuracy of the solutions, N is chosen equal to $2M$. The grid sizes are taken as 14×28, 16×32, 18×36, 20×40, and it is found that M = 16 and N = 32 give sufficient accuracy of the numerical solutions. In order to calculate the unsteady solutions, the Crank-Nicolson and Adams-Bashforth methods together with the function expansion (9) and the collocation methods are applied.

TABLE 2

The values of λ and $w(0,0)$ for various M and N at $Dn = 2000$ and $Tr = 320$.

M	***N***	λ	$w(0,0)$
14	28	0.36089734	180.2898
16	**32**	**0.36090702**	**180.4422**
18	36	0.36090845	180.5519
20	40	0.36090815	180.6331

RESULTS AND DISCUSSION

We take a curved rectangular duct of aspect ratio 2 and curvature 0.1 and rotate it around the centre of curvature with an angular velocity ΩT in both the positive and negative directions. In this paper, time evolution calculations of the resistant coefficient λ are performed for the non-isothermal flows (Gr = 100) with stream wise analysis of the secondary flows and convective heat transfer over a wide range of the Taylor Number (Tr) for two cases of the of Dean Numbers, Case I: Dn = 1000 and Case II: Dn = 1500.

Case I: Dean Number, *Dn*=1000

In order to study of the nonlinear behavior of the unsteady solutions, we perform time evaluation of λ for positive rotation of the duct for $0 \le Tr \le 500$ at $Dn = 1000$ and Gr = 100. Fig. 2(a) shows time evolution result for Tr = 0, we found that the unsteady flow oscillates irregularly that means the flow is chaotic which is well justified by

drawing the phase space as shown in Fig. 2(b) in the $\gamma - \lambda$ plane, where $\gamma = \iint \psi dxdy$. From Fig. 2(b) we observe that the orbit of the flow creates different paths which prove that the flow is chaotic. Fig. 2(c) shows typical contours of secondary flow patterns and temperature profiles for Tr = 0, where we observe that the streamlines of the secondary flow consist of two opposite vortices, one is an outward flow is shown by solid line and the other one inward flow shown by dotted line. To draw the contours of secondary flow patterns and temperature profiles, we use the increments $\Delta\psi = 0.8$ and $\Delta T = 0.1$. The same increments of ψ and T are used for all the figures in this study unless specified. Solid lines ($\psi \geq 0$) show that the secondary flow is in the counter clockwise direction while the dotted lines $(\psi < 0)$ is in the clockwise direction as well as the temperature field, solid lines are those for $T \geq 0$ and dotted ones for $T < 0$. Then we perform time evolution of λ for Tr = 105 as shown in Fig. 3(a) and we found the unsteady flow oscillates in regularly but the number of frequency is reduced which prove the flow is a transition to periodic chaos flow. In order to identify the nature of the time evolution solution, in more detail, we draw the phase space diagram for Tr = 105 as shown in Fig. 3(b), which show the flow is periodic flow. From Fig. 3(c), we observe that the unsteady flow is a symmetric two-vortex solution and the stream lines of the temperature contour are symmetrically distributed. Increasing the rotational speed like $105 < Tr \leq 500$ and find that the unsteady flow is a steady-state solution that is shown in Fig. 4(a) for Tr = 120.

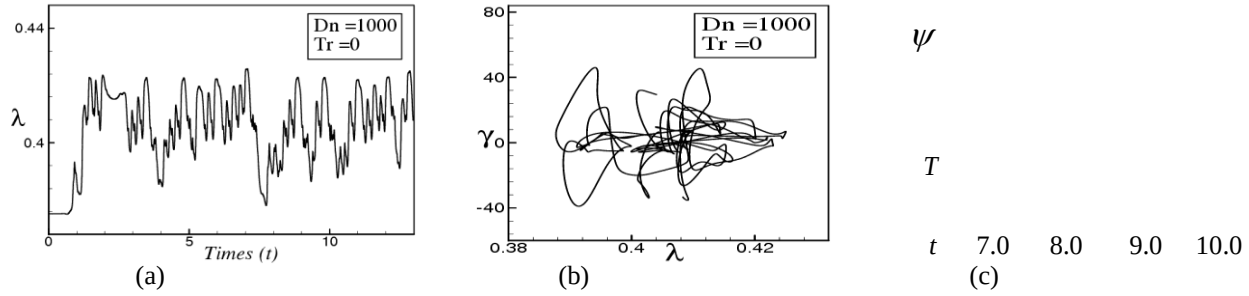

FIGURE 2: (a) Time evolution of λ for Dn = 1000 and Tr = 0, (b) Phase space diagram and (c) Contours of secondary flow (top) and temperature profiles (bottom), at time $7.0 \leq t \leq 10.0$

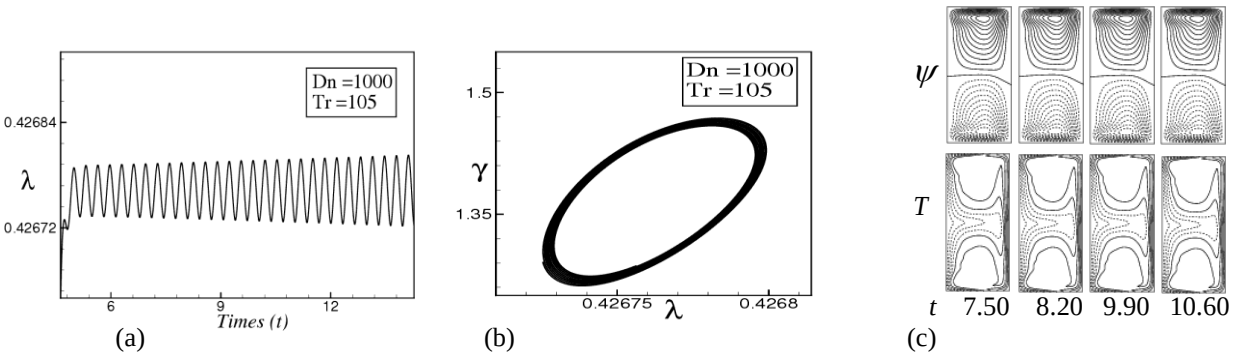

FIGURE 3: (a) Time evolution of λ for Dn = 1000 and Tr = 105. (b) Phase space for Tr = 105, (c) Contours of secondary flow patterns and temperature profiles for Tr = 105 at time $7.50 \leq t \leq 10.60.$

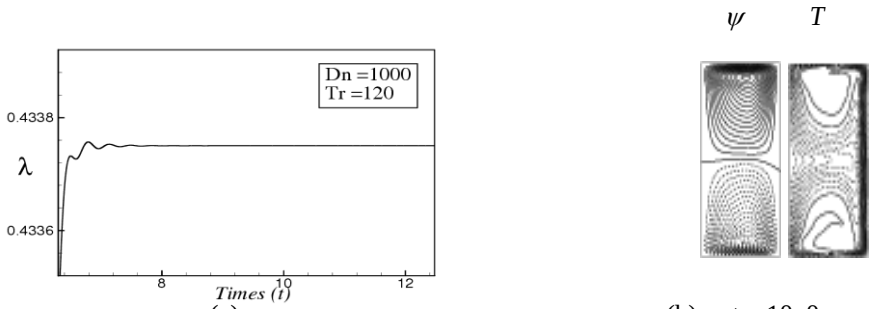

FIGURE 4: (a) Time evolution of λ for Dn = 1000 and Tr = 120. (b) Contours of secondary flow pattern and temperature profile for Tr = 120 at time $t = 10.0$.

Then we investigate on negative rotation for Dn = 1000. Negative rotation is the rotation whose direction is opposite to the main flow. Fig. 5(a) shows time evolution of λ for Tr = -50 that identify the flow is a non-periodic oscillating flow, which oscillates with an irregular pattern that means the flow is chaotic. We have justified it by drawing the phase space is shown in Fig. 5(b). Typical contours of secondary flow patterns and temperature profiles for the corresponding flow parameters are shown in Fig. 5(c), where it is found that the chaotic oscillation is four- to six-vortex solutions. We observe that the steam lines of the secondary flow patterns and temperature distributions are significantly distributed that generates more heat is transferred from the outer wall (heated wall) to the fluid. We then performed time evolution of λ for Tr = -300 is stated in Fig. 6(a). It is found that the flow is a periodic solution. For a clear concept, we depict the phase space of the time evolution result as shown in Fig. 6(b). From Figure the flow creates a couple of orbits instead of a single orbit, so that the unsteady flow at Tr = -300 is a multi-periodic solution. Typical contours of secondary flow patterns and temperature profiles for Tr = -300 are shown in Fig. 6(c), where we found only four-vortex solution. If we increase the rotational speed in the negative direction up to Tr =-340 or more, the flow remains steady-state solution.

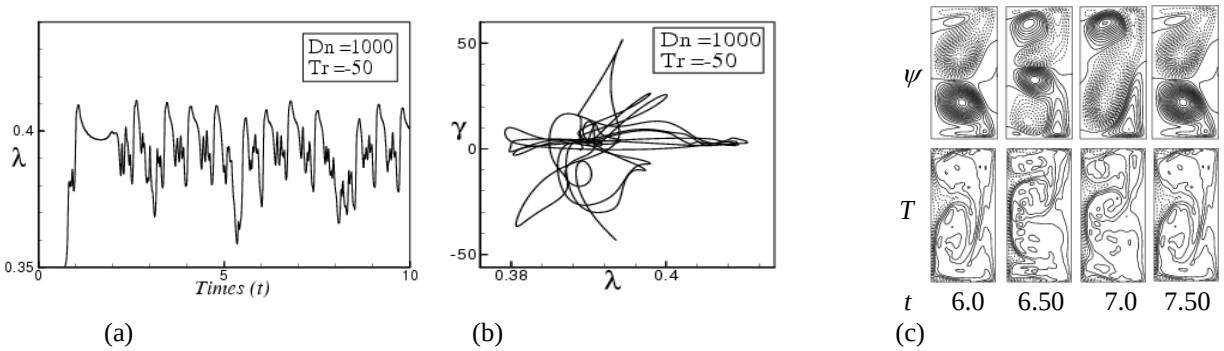

FIGURE 5: (a) Time evolution of λ for Dn = 1000 and Tr = -50. (b) Phase space for Tr = -50, (c) Contours of secondary flow patterns and temperature profiles for Tr = -50 at time $6.0 \le t \le 7.50$.

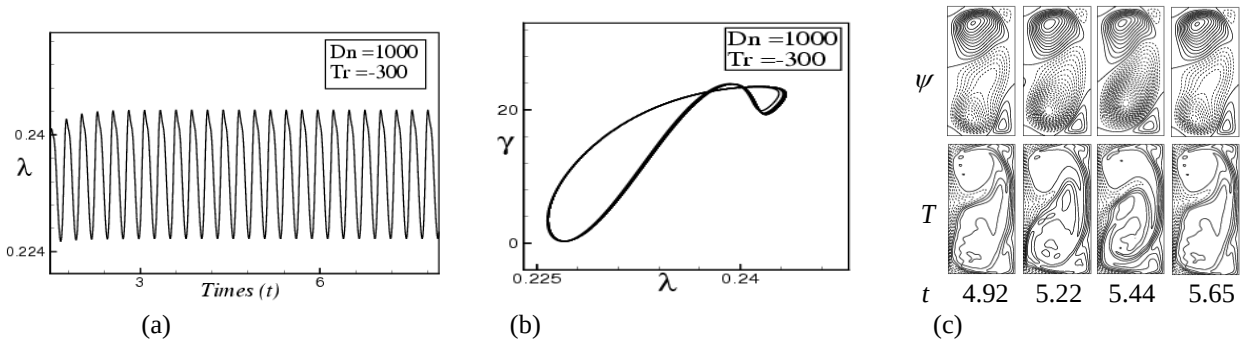

FIGURE 6: (a) Time evolution of λ for Dn = 1000 and Tr = -300. (b) Phase space for Tr = -300, (c) Contours of secondary flow patterns and temperature profiles for Tr = -300 at time $4.92 \le t \le 5.65.$

Fig. 7(a) shows, time evolution results for Tr = -340, where steady-state flows are observed. Corresponding secondary flow patterns and temperature profiles are shown in Fig. 7(b). Observing the figures, we find that if the rotation is increased in the negative direction heat transfer occurs more frequently because of many secondary vortices generated at the outer wall of the duct, and consequently heat transfer increases remarkably in the fluid.

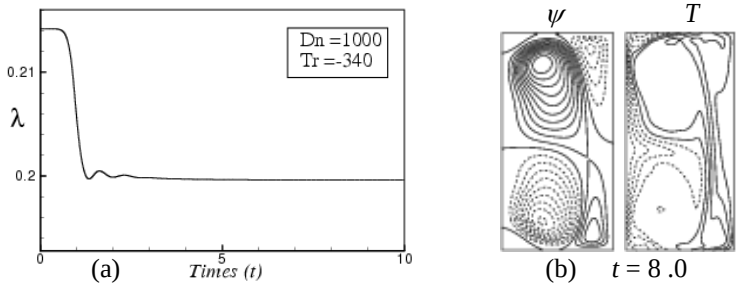

FIGURE 7: (a) Time evolution of λ for Dn = 1000 and Tr = -340. (b) Contours of secondary flow pattern and temperature profile for Tr = -340 at time $t = 8.0.$

Case II: Dean Number, Dn=1500

We perform time evolution of λ for a strong centrifugal force at $Dn = 1500$ for $0 \le Tr \le 500$ at Gr = 100. Fig. 8(a) shows time evolution of λ for Dn = 1500 and Tr = 0 at Gr = 100. It is found that the unsteady flow at Tr = 0 is a strongly chaotic solution, which is well justified by drawing the phase spaces as shown in Fig. 8(b). Fig. 8(c) shows typical contours of secondary flow and temperature profiles, we find that the flow is a four-vortex solution. Then we perform time evolution of λ for Tr = 100 which is presented in Fig. 9(a). From figure the multi-periodic oscillation is well justified by depicting the phase spaces of the time evolution result as shown in Fig. 9(b).

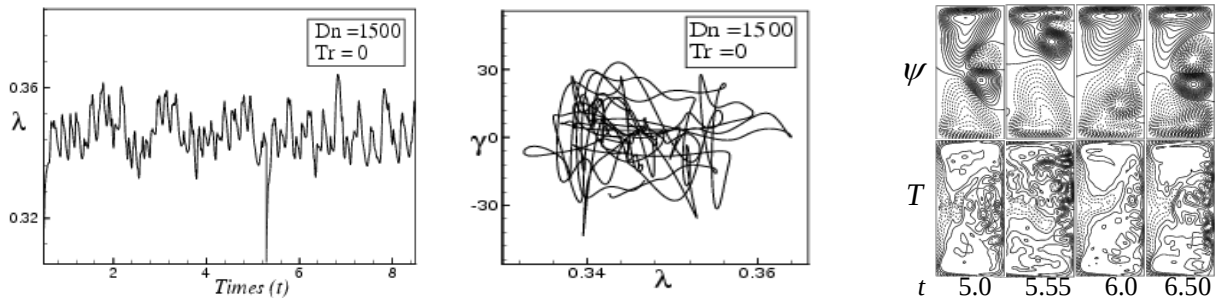

FIGURE 8: (a) Time evolution of λ for Dn = 1500 and Tr = 0. (b) Phase space for Tr =0, (c) Contours of secondary flow patterns (top) and temperature profiles (bottom) for Tr = 0, at time $5.0 \le t \le 6.50$.

Typical contours of secondary flow and temperature profiles are shown in Figs. 9(c). If we increase the rotational speed in the same direction up to Tr = 500, it is found that the flow becomes steady-state. Fig. 10(a) show time evolution results for Tr = 250 and found a single contour of the secondary flow pattern and temperature profile is shown in Fig. 10(b) and also found that the unsteady flow is asymmetric two-vortex solutions. In this study, it is found that combined action of the centrifugal, Coriolis and buoyancy force help to increase the number of secondary vortices, the number of secondary vortices increases and consequently heat is transferred substantially from the wall to the fluid. Finally, we performed time evolution calculation for the negative rotation of the duct at Dn = 1500. Fig. 11(a) shows time evolution of λ for Tr = -50 and Dn = 1500 at Gr = 100. It is found that the unsteady flow is a chaotic oscillation, which is well justified by drawing the phase space as shown in Fig. 11(b). Typical contours of secondary flow patterns and temperature profiles for the corresponding flow parameters are shown in Fig. 11(c).

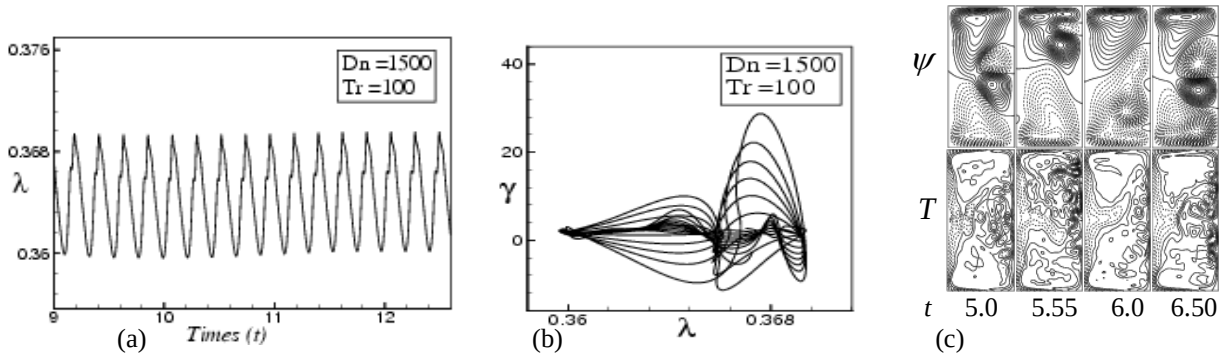

FIGURE 9: (a) Time evolution of λ for Dn = 1500 and Tr = 100. (b) Phase space for Tr =100, (c) Contours of secondary flow patterns (top) and temperature profiles (bottom) for Tr = 100, at time $5.0 \le t \le 6.50$

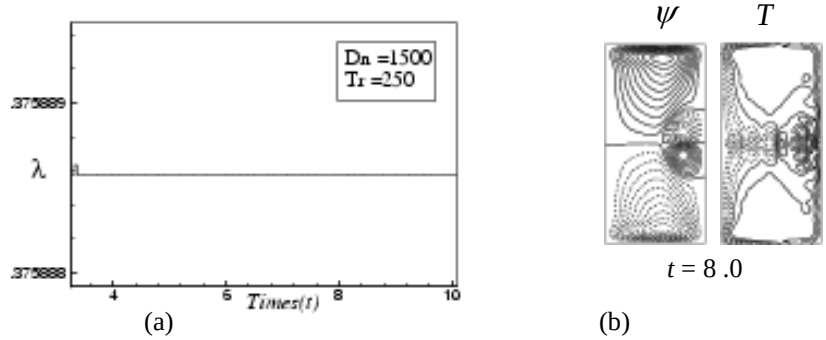

FIGURE 10: (a) Time evolution of λ for Dn = 1500 and Tr = 250. (b) Contours of secondary flow pattern and temperature profile for Tr = 250 at time $t = 8.0$

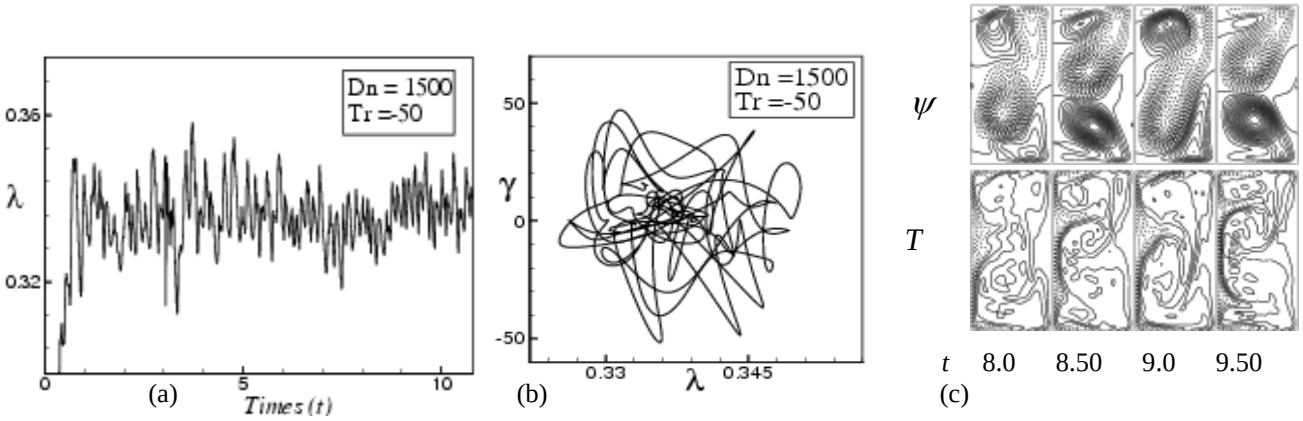

FIGURE 11: (a) Time evolution of λ for Dn = 1500 and Tr = -50. (b) Phase space for Tr = -50, (c) Contours of secondary flow patterns and temperature profiles for Tr = -50 at time $8.0 \le t \le 9.50.$

We observe that stream lines of temperature profiles are consistent with secondary vortices and that the convective heat generation is stronger. We continue this process and perform time evolution of λ for Tr = -680 and Tr = -700 as shown in Figs. 12(a) and 13(a) are fully periodic oscillation and steady state solution.

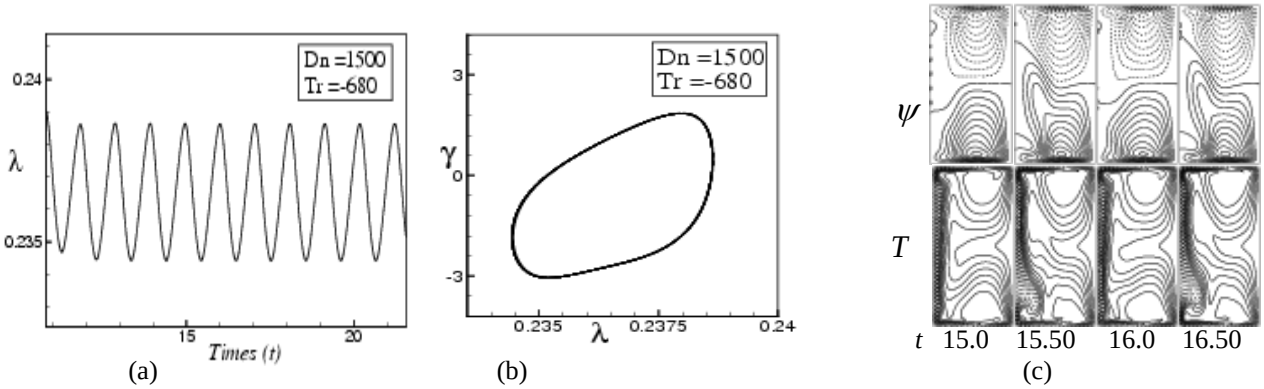

FIGURE 12: (a) Time evolution of λ for Dn = 1500 and Tr = -680. (b) Phase space, (c) Contours of secondary flow patterns and temperature profiles for Tr = -50 at time $15.0 \le t \le 16.50.$

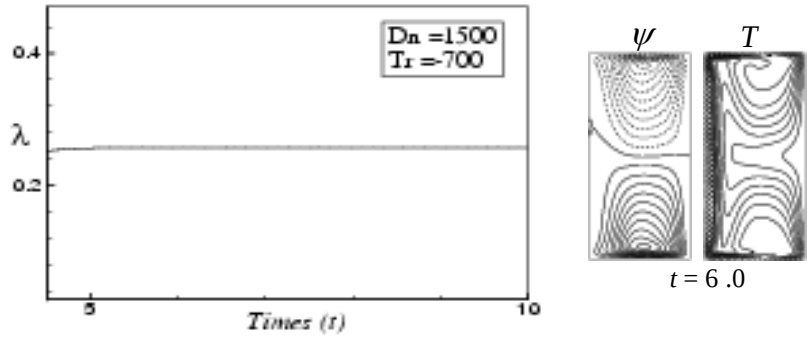

(a) (b)

FIGURE 13: (a) Time evolution of λ for Dn = 1500 and Tr = -700. (b) Contours of secondary flow pattern and temperature profile for Tr = -700 at time $t = 6.0$

CONCLUSION

A spectral-based numerical study is presented for the flow characteristics through a rotating curved rectangular duct. Numerical calculations are carried out for the Dean numbers, Dn = 1000 and Dn = 1500, over a wide range of the Taylor number for both the positive and negative rotation with a temperature difference between the vertical sidewalls for the Grashof number Gr = 100, where the outer wall is heated and the inner wall cooled, the top and bottom walls being adiabatic. We investigated unsteady solutions by time evolution calculations, and it is found that the unsteady flow undergoes in the scenario 'Chaotic $\rightarrow$ multi-periodic $\rightarrow$ periodic $\rightarrow$ steady-state' if Tr is increased in the positive rotation. For negative rotation, however, time evolution calculations show that the unsteady flow undergoes through various flow instabilities. Phase spaces were found to be very fruitful to justify the transition of flow characteristics. Typical contours of secondary flow patterns and temperature profiles are also obtained at several values of Tr, and it is found that there exist two- and multi- vortex solutions. It is found that the temperature distribution is consistence with the secondary vortices, and secondary flows play a significant role in convective heat transfer from the wall to the fluid. It is also found that chaotic flow enhances heat transfer substantially than the steady-state or periodic solutions by creating multi-vortex solutions. The present study also shows that there is a strong interaction between the heating-induced buoyancy force and the centrifugal and Coriolis force in the rotating curved channel that stimulates fluid mixing and consequently enhance heat transfer in the fluid.

ACKNOWLEDGMENTS

Md. Zohurul Islam, one of the authors, would like to acknowledge gratefully for the financial supports to the department of Mathematics and Statistics, Jessore University of Science and Technology, Jessore-7408, Bangladesh.

REFERENCES

1. Dean, W. R.,. Note on the motion of fluid in a curved pipe. *Philos. Mag*., **4**, pp.208–223(1927).
2. Berger, S. A., Talbot, L. and Yao, L. S. Flow in Curved Pipes, *Annual. Rev. Fluid. Mech*., **35**, pp. 461-512(1983).
3. Nandakumar. K and Masliyah, J. H. Swirling Flow and Heat Transfer in Coiled and Twisted Pipes, *Adv. Transport Process*., **4**, pp. 49-112(1986).
4. Ito, H. Flow in Curved Pipes, *JSME Int. J*., **30**, pp. 543-552(1987).
5. Ishigaki H.. Laminar Flow in Rotating Curved Pipes. Journal of Fluid Mechanics, **329**, pp. 373-388(1996).
6. Miyazaki, H.. Combined Free and Force Convection Heat Transfer and Fluid Flow In Rotating Curved Rectangular Tubes. *Trans. ASME C: J. Heat Transfer*, **95**, pp. 64-71(1973).
7. Wang, L. Q. and Cheng, K.C.. Flow Transitions and combined Free and Forced Convective Heat Transfer in Rotating Curved Channels: the Case of Positive Rotation Physics *of Fluids*, **8**, pp.1553-1573(1996).
8. Wang, L. Q. and Cheng, K.C.. *Physics Review* E, **51**, and pp.1555 (1995).
9. Daskopoulos, P. & Lenhoff, A. M.,. Flow in curved ducts. Part 2. Rotating ducts, Journal *of Fluid Mechanics*, **217**, pp. 575-593(1990).
10. Yanase, S. and Nishiyama, K.. On the bifurcation of laminar flows through a curved rectangular tube, *J. Phys. Soc*. *Japan*, **57**(11), pp. 3790-3795(1988).
11. Yanase, S., Kaga, Y. and Daikai, R.. Laminar flow through a curved rectangular duct over a wide range of the aspect ratio, *Fluid Dynamics Research*, **31**, pp. 151-183(2002).
12. Wang, L. and Yang, T.,. Periodic Oscillation in Curved Duct Flows, *Physica D*, **200**, pp. 296-302(2005).
13. Yamamoto, K., Xiaoyun W., Kazuo N., Yasutaka H.. Visualization of Taylor-Dean Flow in a curved duct of square cross-section, *J. Fluid dynamics research.* **38**, pp.1-18(2006).
14. Nobari, M.R.H., Nousha, A. and Damangir, E.. A Numerical Investigation of Flow and Heat Transfer in Rotating U-Shaped Square Ducts. *Int. J. Thermal Sciences*, **48**, 590-601(2009).

ICME2015

International Conference on Mechanical Engineering 2015
(ICME 2015) 18 – 20 December, 2015, Dhaka, Bangladesh

Paper ID : 118

Experimental Investigation On Thermal Performance Of A Closed Loop Pulsating Heat Pipe (CLPHP) Using Methanol And Distilled Water At Different Filling Ratios

Md. Lutfor Rahman[1], Anindita Dhar Swarna [1, a)*], Syed Nasif Uddin Ahmed[1, b)], Sanjida Perven [1], Mohammad Ali[2]

[1]*Military Institute of Science and Technology, Mirpur Cantonment, Dhaka-1216, Bangladesh*
[2]*Bangladesh University of Engineering and Technology, Dhaka-1000*

[a)] Corresponding author: anindita382@gmail.com
[b)] nasif.anik@yahoo.com

Abstract. Pulsating Heat Pipes, the new two-phase heat transfer devices, with no counter current flow between liquid and vapor have become a modern topic for research in the field of thermal management. This paper focuses on the performance of methanol and distilled water as working fluid in a closed loop pulsating heat pipe (CLPHP). This performances are compared in terms of thermal resistance, heat transfer co-efficient, and evaporator and condenser wall temperature with variable heat inputs. Methanol and Distilled water are selected for their lower surface tension, dynamic viscosity and sensible heat. A closed loop PHP made of copper with 2mm ID and 2.5mm OD having total 8 loops are supplied with power input varied from 10W to 60W. During the experiment the PHP is kept vertical, while the filling ratio (FR) is increased gradually from 40% to 70% with 10% increment. The optimum filling ratio for a minimum thermal resistance is found to be 60% and 40% for distilled water and methanol respectively and methanol is found to be the better working fluid compared to distilled water in terms of its lower thermal resistance and higher heat transfer

TABLE 1. Nomenclature

Symbol	Meaning	Symbol	Meaning
R	Thermal resistance, °C/W	OD	Outer diameter of tube, mm
T	Temperature along the pipe, °C	ID	Inner diameter of tube, mm
D	Diameter of heat pipe, mm	FR	Filling Ratio
Q	Heat input, W	th(as subscript)	thermal
h	Heat Transfer Coefficient	a(as subscript)	Adiabatic section
e(as subscript)	evaporator section	c (as subscript)	condenser section

INTRODUCTION

There had been always a great demand for having robust and promising cooling devices in technological fields, due to huge amounts of heat generation in industrial grounds. Thermal management of electronics is a recent issue which is increasingly gaining importance in line with the advancement in packaging technology and attracted the attention of researchers to develop efficient cooling systems.

Several methods such as conventional cooling with air or water, spray cooling, and jet impingement have been applied to dissipate heat from electronic devices [1,2,3].

But the coolant needs to have some properties such as (i) it should be small enough to be placed in restricted spaces, (ii) be able to work in the space when the gravitational force is absent, (iii) be cheap, (iv) has a high value manufacturing capability and (v) low manufacturing complexities. Thereby with the blessings of Grover [4], traditional heat pipes were turned out as high performance coolant rather it is unable to operate in absence of gravitational field. Having wick structure this method is very expensive and may cause problem in some situations [5]. In this regard, Pulsating Heat Pipe (PHP) has emerged a new era in the field of thermal cooling. Close Loop Pulsating heat pipes (CLPHPs), as proposed by Akachi [6], consists of a plain meandering tube of capillary dimensions with many U-turns and joined end to end. The pipe is first evacuated and then filled partially with a working fluid. As the diameter of the tube is so small, the working fluid distributed itself in the form of vapor slug and liquid slug. One end of the CLPHPs tube bundle receives heat (called evaporator section), transferring it to the other (called condenser section) by a pulsating action of the working fluid. In between these two sections there is adiabatic section. The demonstration is shown in Fig. 1.

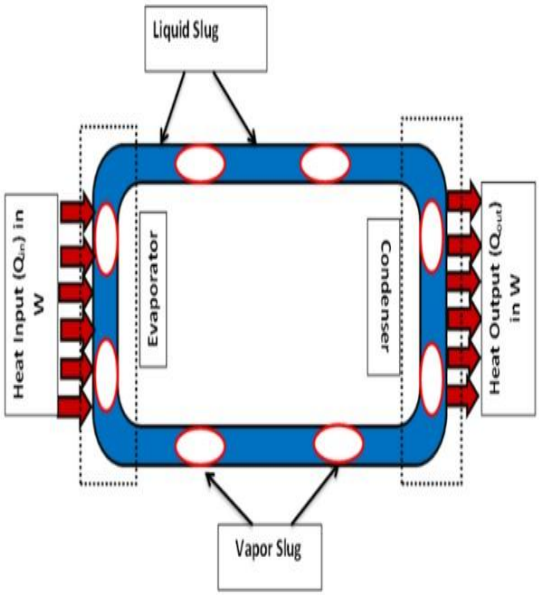

FIGURE 1. Schematic diagram of CLPHPs

The present experiment is done by two different working fluids. One is distilled water and another is methanol. The first consideration in the selection of a suitable working fluid is the operating vapor temperature range. Several possible working fluid may exist within the approximate temperature band, (50 to 150°C) [7]. Different characteristics should be examined to find out the most acceptable of these fluids for the application considered. Water for its thermodynamic attributes in most commercial electronics cooling applications, makes it better than any other fluids for the pulsating heat pipes. High latent heat of water evaporates small amount of liquid resulting low pressure drops and high heat dissipation. Its high thermal conductivity minimizes the temperature difference associated with conduction through the two phase flow in the PHP. At 25°C the surface tension of water and methanol is 72 dynes/cm and 22.51 dynes/cm respectively [8, 9]. As surface tension of water is higher than methanol, water will generate a large capillary action and show better performance in any orientation. Methanol with lower surface tension (about 1/3 rd of water) is a good substitute particularly if the heat pipe is used for sub °C application [10].

EXPERIMENTAL APPARATUS AND METHOD

Experimental Setup

The experimental setup is shown in Fig. 2(a) and Fig. 2(b). The PHP consists of a long capillary tube, which is meandered into 8 number of turns. Copper is used as the capillary tube material (ID 2 mm, OD 2.5 mm). The closed loop pulsating heat pipe is divided into 3 regions having total length of 250 mm. The evaporator, condenser and adiabatic sections are 50 mm, 80 mm and 120 mm respectively. The experiment is conducted in vertical orientations. Eight thermocouples (LM-35sensors, typical accuracies of ±1⁄4˚C at room temperature and ±3⁄4˚C over a full −55 to +150˚C temperature range) are used for the temperature measurement, 4 for each sections. The LM35 does not require any external calibration or trimming. In adiabatic section there is glass wool wrapped over aluminum foil for proper insulation. A band is also used to keep the glass wool at its position in order to minimize heat loss from the system. A steel structure along with a DC fan is used to hold the PHP. Evaporator section is insulated inside a box of steel frame and in order to separate the nichrome wire from the copper tube mica sheets are used. Nichrome wire is coiled in the evaporator and this wire is connected to the variac. By changing the variac voltage, different voltage and current are supplied to the evaporator. Water and methanol are used as working fluid at the amount of FR 40%, 50%, 60% and 70%. For cooling the condenser a cooling fan is used. For data collection Arduino Mega (Microcontroller ATmega1280, Operating Voltage 5V, Input Voltage (recommended) 7-12V, Analog Input Pins 16, Digital I/O Pins 54) is used. The temperature is recorded on a regular time interval.

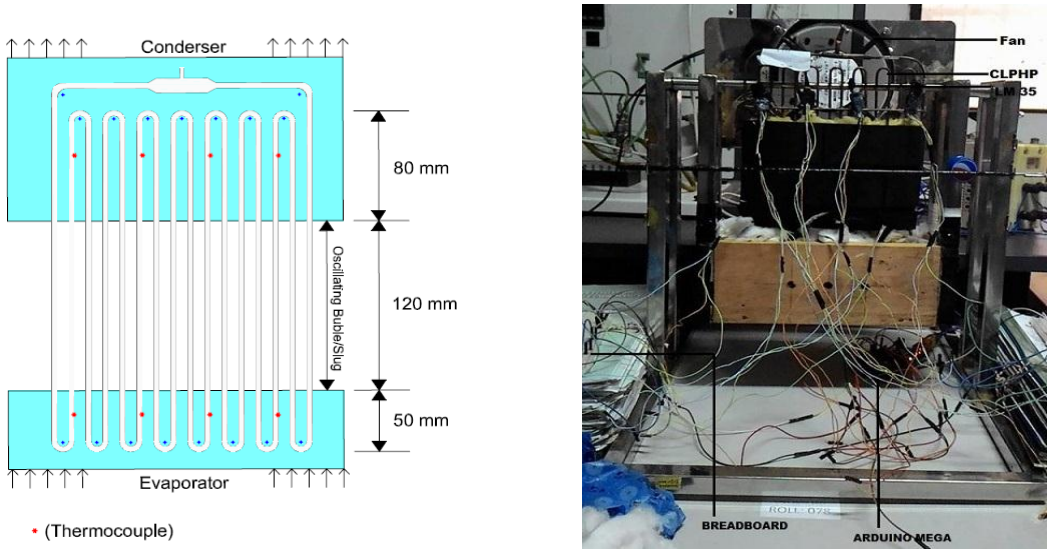

(a) (b)

FIGURE 2. (a) Experimental setup (b) Prototype of Experimental Setup

Experimental Procedure

- Before filling the working fluid, air is blown inside the heat pipe to ensure that there is no fluid present inside the PHP.
- The heat pipe is filled with required amount of working fluids (Distilled water and methanol). Keeping the PHP in vertical orientation throughout the experiment, the FR is increased gradually from 40% to 70% with 10% increment.
- After the whole setup, the experiment is carried out.
- Different heat inputs (10W to 60W) are provided to the system via variance and temperatures of different sections are measured by thermocouples using Arduino Mega. The cooling fan is switched on to cool the condenser.

RESULTS AND DISCUSSION

Effect of Heat Input:

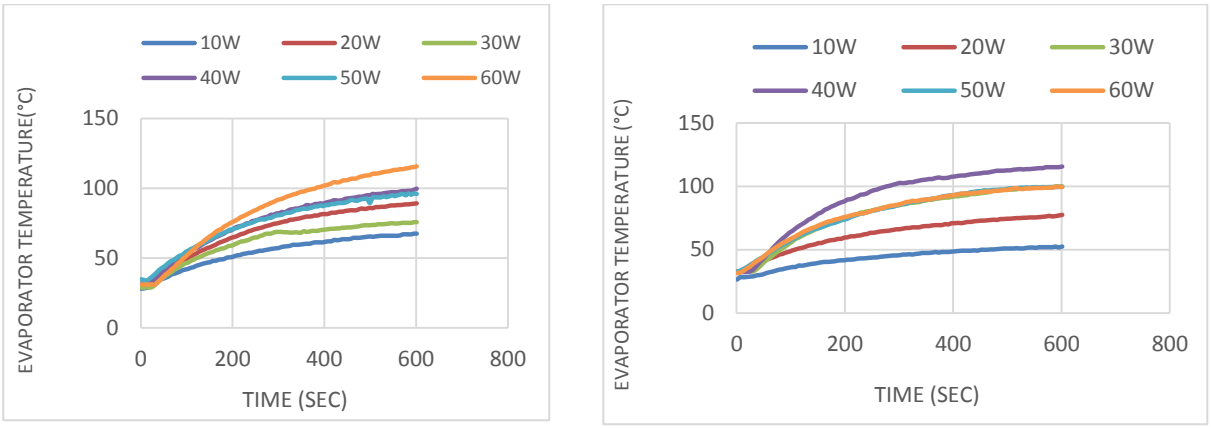

(a) (b)

FIGURE 3. (a) Variation of Evaporator Temperature with time at different heat load for Distilled water at a FR of 60%; (b) Variation of Evaporator Temperature with time at different heat load for methanol at a FR of 60%

Figure 3(a) and 3(b) shows the variation of evaporator wall temperature with time for water and methanol at a FR of 60%. It is evident from the figure that there is a continuous pressure pulsation during the flow in a PHP. The CLPHP is operating with minor flow oscillations up to 200 sec. With the increase in heat load, the oscillations become more intensive in case of water except 60W. More investigation is to be needed for this. At the highest heat load of 60W the evaporation section temperature rises to 115.75°C. So water is more suitable at lower heat loads than 60W. The pulsating effect is almost similar at all heat loads and the evaporator temperature rises gradually at medium heat load (40W) for methanol.

Effect of Fill Ratio on Temperature

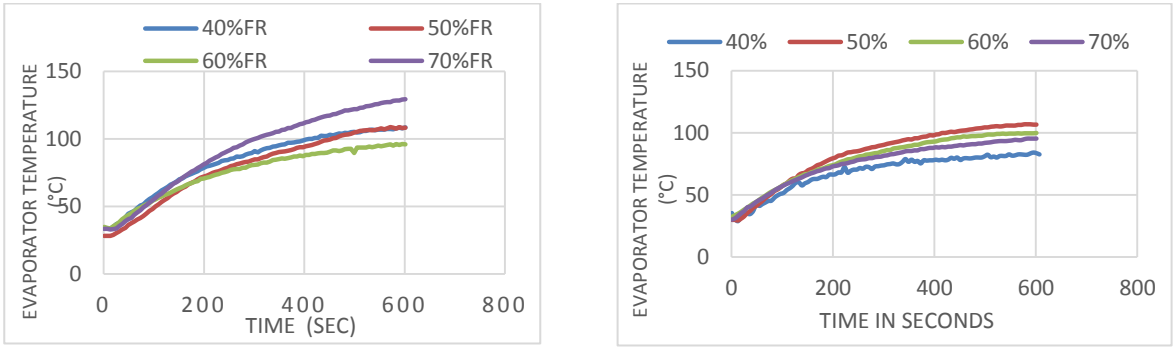

(a) (b)

FIGURE 4. (a) Variation of Evaporator Temperature with time at different fill ratio for distilled water at a heat load of 50W; (b) Variation of Evaporator Temperature with time at different fill ratio for methanol at a heat load of 50 W

The variation of evaporator wall temperature with respect to time for water and methanol at a heat input of 50W is depicted in Fig. 4(a) and 4(b). From Fig. 4(b) it can be seen that the evaporator temperature is slightly higher at

50% FR. As more vapor phase exists in the PHP at 50% FR, less heat is being transferred from the wall to the fluid. From the perspective of distilled water the case is totally opposite.

Effect of Working Fluid

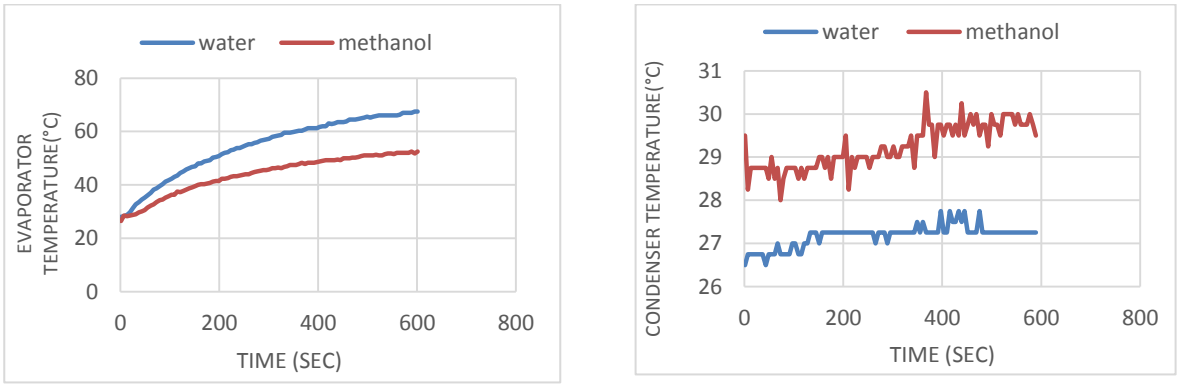

(a) (b)

FIGURE 5. (a) Effect of working fluid on evaporator temperature at Q = 10W and FR = 60%; (b) Effect of working fluid on condenser temperature at Q = 10W and FR = 60%

The variation of evaporator wall temperature with respect to time for different working fluids at a FR of 60% and at a heat input of 10 W is shown in Fig 5(a).It is clear that the evaporator wall temperature is higher in case of water and lower in the case of methanol. It is also observed that the system takes more time to reach the steady state in case of water compared to methanol.

The variation of condenser wall temperature with time for different working fluids at a FR of 60% and at a heat input of 10 W is reported in Fig. 5(b). The fluctuations in the condenser wall temperature are much higher compared to the wall temperature of the evaporator Fig. 5(a). From the figure it is also observed that the condenser wall temperature is lower for water and higher for methanol. As there is an existence of less vapor while entering into the condenser in case of water, only a small amount of heat will be released due to latent heat. Thus water gets sub cooled to a greater extent. However, in case of methanol, the amount of vapor will be more when it enters the condenser and consequently the sub cooling effect will be much lower. This results in higher condenser wall temperature for methanol.

Effect of Heat Input on Thermal Resistance of Water and Methanol with Different Filling Ratio

To know the most appropriate optimum filling ratio, the effect of filling ratio on the thermal resistance of PHP is also studied. Thermal resistance is reciprocal function of heat input and linear function of temperature difference of evaporator and condenser. With the increment of heat input, thermal resistance decreases. The thermal resistance of PHP is given by

$$R_{th} = \frac{T_e - T_c}{Q} \tag{1}$$

Figures 6(a) and 6(b) show the effect of filling ratio on the thermal resistance for PHP with water and methanol as working fluid.

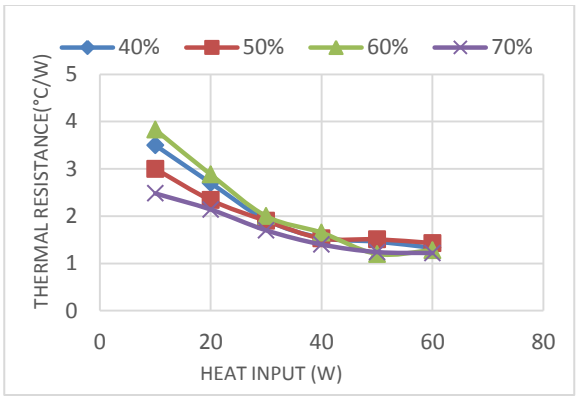

(a)

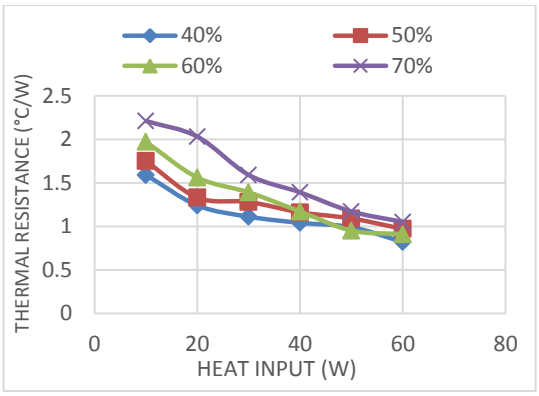

(b)

FIGURE 6. (a) Effect of filling ratio on thermal resistance for Distilled water; (b) Effect of filling ratio on thermal resistance for Methanol

The Figure 6(b) indicates that at very low filling ratios, i.e. 40%, thermal resistance decreases slowly with increasing power. Also the fill ratio of 40% exhibits the lower values of thermal resistance compared to higher fill ratio of 50%, 60% and 70%. In PHP vapor bubbles are supposed to pulse and promote the liquid slug and dispel the heat from evaporator to the condensation section. The low filling ratios are expected to favor the pulsation of the bubble, but as the heat input is increased, the entire surface is covered by the vapor space which leads to dry-out situation. Also the temperature difference between evaporator and condenser is less at lower heat load, the magnitude of thermal resistance is also less. Thereby we can say that the heat transfer characteristics in a PHP are better at lower fill ratios. For methanol, minimum resistance is offered at a filling ratio of 40% whose value is 0.82˚C/W. Fig. 6(a) shows the effect of filling ratio on thermal resistance for water. Thus the minimum resistance, 1.2°C/W is obtained at 60% filling ratio and thus 60% is the optimum filling ratio for water. As, the amount of working fluid is higher, the amount of evaporation is low, bubble formation is lower too which is a hindrance of the pulsation of the bubble and hence the efficiency of heat transfer will not be very good. Thus 60% and 40% are chosen as the optimum filling ratio for water and methanol respectively.

Variation of Heat Transfer Coefficient

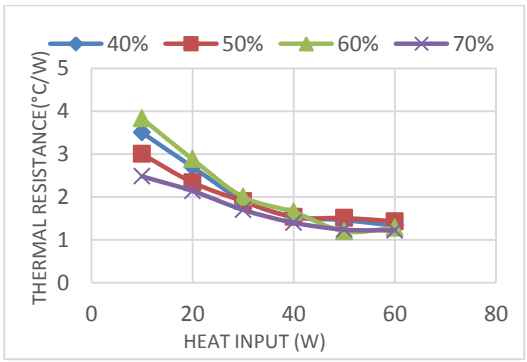

(a)

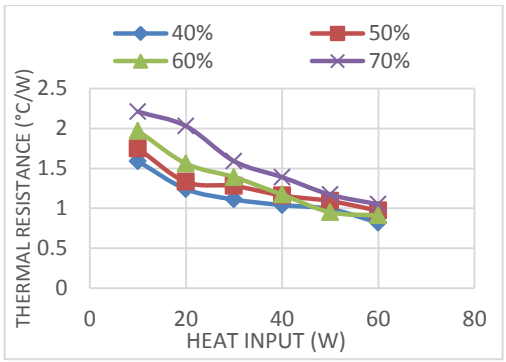

(b)

FIGURE 7. (a) Effect of fill ratio on Heat Transfer Coefficient for Distilled water (b) Effect of fill ratio on Heat Transfer Coefficient for methanol

The heat transfer coefficient of a PHP is given by [11]

$$h = \frac{Q}{A(Te - Tc)} \tag{2}$$

From figures, it is seen that the heat transfer coefficient increases with increase in heat load at all fill ratios. Higher values of heat transfer co-efficient can be seen at a lower fill ratio of 40% which indicates better performance of PHP having methanol as working fluid. This is due to the lower values of temperature difference between evaporator and condenser for methanol. In that case 40% methanol is better than 60% water.

CONCLUSION

PHPs are highly attractive heat transfer elements, which due to their simple design, cost effectiveness and excellent thermal performance may find wide applications. In the present work, the effects of heat input, working fluid, fill ratio, thermal resistance, and heat transfer co-efficient on the performance of PHP are studied. This experimental investigation shows that the evaporator wall temperature variation with time is found to be periodic. The optimum filling ratio for a minimum thermal resistance is found to be 60% for water and 40% for methanol. In vertical orientation of PHP, the resistances observed are 1.2 and 0.82˚C/W for water and methanol respectively. The heat transfer coefficient for methanol at all filling ratio is better than water. Hence it may be concluded that Methanol is found to be the better working fluid compared to water in terms of its lower thermal resistance and higher heat transfer coefficient.

ACKNOWLEDGEMENTS

The authors feel greatly honored to be able to express their earnest gratitude to the Department of Mechanical Engineering, MIST and BUET for the accomplishment of this research.

REFERENCES

1. G. Karimi, and J.R. Culham, "Review and Assessment of Pulsating Heat Pipe Mechanism for High Heat Flux Electronic Cooling," in Thermal Phenomena, 2,2004, Proceedings of International Society Conference,2004, pp. 52-59.
2. S.J. Downs and E.H. James, "Jet Impingement Heat Transfer: A Literature Survey," in Proceedings of ASME, AIChE, and ANS, National Heat Transfer Conference and Exhibition, 24th, Pittsburgh, PA, 1987, ASME Paper No. 87-HT-35.
3. J. Kim, International Journal of Heat Fluid Flow, **28(4),** 753–767 (2007).
4. G.M. Grover, US patent No 3,229,759 (1963)
5. M. Mohammadi, "Experimental Investigation of Pulsating Heat Pipe with Ferro fluid," B.Sc. Thesis, Sharif University of Technology, Iran, 2010.
6. H. Akachi, US Patent No. 4,921,041 (1990)
7. S.G. Khedkar, P. R. Pachghare and Ashish M. Mahalle, International Journal of Emerging Technology and Advanced Engineering, **2(3)** 2250-2459 (2012).
8. N. R. Pallas, and Y. Harrison, "Colloids and Surfaces", (1990)43, pp. 169–194.
9. J.M. Navaza, J.Chem.Eng.Data **40**, 611-614 (1995).
10. G. Karimi t, J.R. Culham "Review and Assessment of Pulsating Heat Pipe mechanism For High Heat Flux Electronic Cooling" Inter society conference on thermal phenomenon 2004.
11. A. Faghri, *Heat Pipe Science and Technology*, (Taylor and Francis, Washington, 1995)

ICME2015

International Conference on Mechanical Engineering 2015
(ICME 2015) 18 – 20 December, 2015, Dhaka, Bangladesh

Paper ID : 120

Effect of Using Ethanol and Methanol on Thermal Performance of a Closed Loop Pulsating Heat Pipe (CLPHP) with Different Filling Ratios

Md Lutfor Rahman[1], Zaimaa Salsabil[1,a)*] , Farah Nazifa Nourin[1,b)], Nusrat Yasmin[1]
Mohammad Ali[2]

1 Military Institute of Science and Technology, Mirpur Cantonment, Dhaka-1216, Bangladesh
2 Bangladesh University of Engineering and Technology, Dhaka-1000, Bangladesh

a)Corresponding author: salsabilzaimaa@ymail.com
b)farahnazifanourin@gmail.com

Abstract This paper presents an experimental study of a closed loop Pulsating Heat Pipe (CLPHP) as the demand of smaller and effective heat transfer devices is increasing day by day. PHP is a two phase heat transfer device suited for heat transfer applications, especially suited for handling moderate to high heat fluxes in different applications. A copper made Pulsating Heat Pipe (PHP) of 250 mm length is used in this experimental work with 2 mm ID and 3 mm OD, closed end-to-end in 8 looped, evacuated and then partially filled with working fluids. The evaporation section is 50 mm, adiabatic section is 120 mm and condensation section is 80 mm. The performance characterization is done for two working fluids at Vertical (0°) orientations. The working fluids are Methanol and Ethanol and the filling ratios are 40%, 50%, 60% & 70% based on total volume, respectively. The results show that the influence of various parameters, the heat input flux, and different filling ratios on a heat transfer performance of CLPHP. Methanol shows better performance as working fluid in PHP than ethanol at present orientation for a wide range of heat inputs and can be used at high heat input conditions. Ethanol is better choice to be used in low heat input conditions.

Keywords: Closed loop Pulsating Heat Pipe, Working fluid, Filling ratio, Electrical cooling, Thermal performance, Methanol, Ethanol.

TABLE 1. Nomenclature

Symbol	Meaning	Symbol	Meaning
R	Thermal resistance, °C/W	T	Temperature along the heat pipe, °C
ΔT	Temperature drop along the device, °C	Q	Heat input, W
L	Length of heat pipe, cm	D	Diameter of heat pipe, mm
OD	Outer diameter of tube	ID	Inner diameter of tube
FR	Filling ratio, %	IA	Inclination angle, °
E_o	Eötvös number	B_o	Bond number
th (as subscript)	thermal	e (as subscript)	evaporator section
a (as subscript)	adiabatic section	c (as subscript)	condenser section

INTRODUCTION

Evolution in the design of the heat pipe; a type of passive two-phase thermal control device, has accelerated in the past decade due to continuous demands for faster and smaller microelectronic systems. An alternative to the capillary heat pipe is the pulsating heat pipe, which consists of one continuous channel that meanders back and forth between the evaporation and condensation regions. The channel can be closed (close looped) or open (open looped). The pulsating/oscillating heat pipe (PHP/OHP) first proposed by Akachi [1] in 1990 is a new type of efficient heat transfer device which has shown promising results for electronic cooling. It is drawing a great deal of attention due to its simple design, small size and excellent thermal performance. In the last decade considerable amount of work has been done out to understand the thermo hydrodynamic characteristics of pulsating heat pipe, but in our experiment we have compared the thermal performance of two most effective working fluids in the field of CLPHP, Ethanol and Methanol. It is different from a traditional heat pipe in working and design. Closed loop pulsating heat pipe (CLPHP) is a new addition to the family of heat pipe. Mainly, it consists of a capillary tube bent in several curves joined to the end to end forming a closed loop parallel passages. It has already found some applications in micro- and power electronics applications owing to favourable operational characteristics coupled with relatively cheaper costs. In recent years, many experimental studies have been conducted to understand the mechanism of PHP and the factors affecting the performance of PHP. Numerous works had been reported on the effect of various factors like dimensions, tilt angles, number of turns, and filling ratio etc. Apart from these parameters, the choice of working fluid is very important. Water, organic solvents and refrigerants have been widely used as working fluid. Nano-fluid has been reported to enhance the thermal performance of PHP, but specific comparison between Ethanol & Methanol has not been done yet. A number of researchers have conducted experimental investigations on PHPs, and the results indicated that the heat transfer capability of PHPs mainly depends on the working fluids, evaporation/condensation lengths, inner diameters, turn numbers, etc. Charoensawan et al.[2] indicate that in vertical orientation for the 2.0 mm devices, water filled devices showed higher performance as compared to R-123 and ethanol; in contrast R-123 and ethanol showed comparable performance in case of 1.0 mm devices with water showing very poor results. Kang et al. [3] demonstrated that silver Nano-fluids temperature difference decreased 0.56–0.65°C compared to DI-water at an input power of 30–50W at the same charge volume by experiment. Qu et al. [4] performed an experimental investigation charged with base water and spherical Al_2O_3 particles of 56 mm in diameter. Compared with pure water, the maximal thermal resistance was decreased by 0.14 °C/W (or 32.5%) when the power input was 58.8W at 70% filling ratio and 0.9% mass fraction. Khandekar et al. [5] reported that ethanol, water and R123 show efficient thermal performance while in vertical mode whereas none of these working fluids were suitable for horizontal mode of PHP operation.

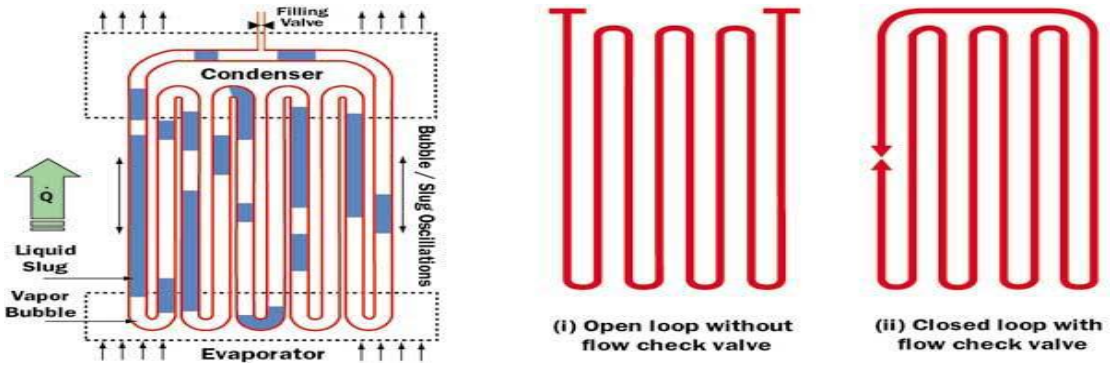

Figure1. Schematic Diagram of Pulsating Heat Pipe

In view of the technological importance of the start-up and thermal performance of pulsating heat pipe, the present work has been focused on studying the effect of working fluid on the start-up and thermal performance of a PHP in terms of heat transfer coefficient and the thermal resistance at different filling ratios offered by it. In this experiment the comparative performance is investigated between Methanol and Ethanol. Ethanol has been found to be one of the best working fluid in terms of thermal performance of device under gravitational force. Methanol has

the highest purity and the air dissolved in the liquid can be neglected. Hence, the methanol and ethanol has been selected as the working fluid for PHP.

EXPERIMENTAL APPARATUS AND METHOD

Experimental setup

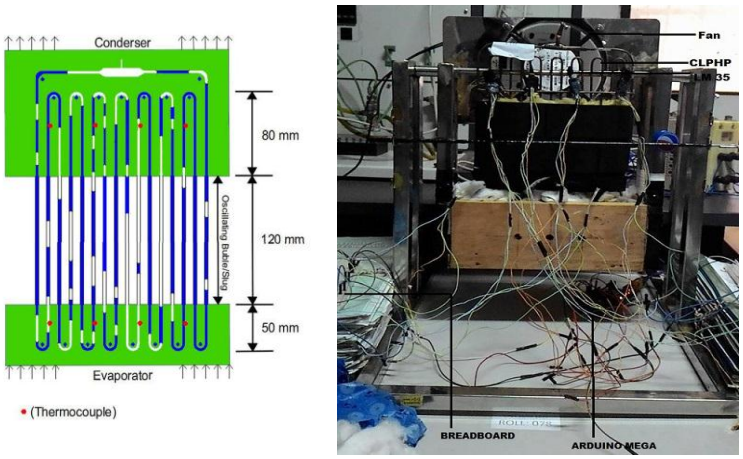

(a) (b)

FIGURE 2.a) Experimental setup, b) Prototype of experimental setup

Figure 2a illustrates the experimental setup and Figure 2b shows the prototype of the setup, consisting of a closed loop PHP assembly, a multi-channel data acquisition system, a power supply unit, and a fan cooling system. The PHP was fabricated by bending copper tubes (ID: 2mm, OD: 2.5mm, L: 25cm), creating a total of 8 turns. The heat pipe is divided into 3 regions- the evaporator (5cm), adiabatic section (12cm) and the condenser (8cm). 8 thermocouples (LM-35sensors, Local Sensor Accuracy (Max) (+/- C): 0.5, range: -55°C to +150°C) are glued to the wall of heat pipe in evaporator and condensation section; 4 for each sections. Evaporator section is insulated inside a box of wood frame, separated from outside using mica sheets with Nichrome wire (diameter = 0.25 mm, resistivity: $1.0 \times 10{-}6$ Ω-m, specific heat: 450 J kg $^{-1}K^{-1}$) was wrapped around the bottom section of tubes, the evaporator. The evaporator was at the bottom and heated by a power supply unit (AC, 220V, 50Hz) via a variac (3F, 300V, 60 Hz). Evaporator section is then again covered by wick & asbestos to stop heat loss by convection and radiation. At the top section, the condenser, cooling was provided by blowing conditioned air at room temperature using a DC fan. Methanol and ethanol are selected as working fluid at the amount of FR 40%-70% (by volume) for each setup. The whole apparatus is set on a Stainless Steel test stand with a wooden box (wood frame) with provision of angular movement of the PHP by an indexing system. Working fluids are incorporated in the heat pipe by using vacuum suction pump. The other accessories of the setup are adapter circuit, selector switches etc.

Experimental Method

Before starting the experiment one condition is maintained, the acceptable diameter of PHP. The theoretical maximum tolerable inner diameter of the PHP capillary tube is given,

$$D_{crit} = 2[\sigma/g\ (\rho_{liq} - \rho_{vap})]^{1/2}$$
$$\text{And} \quad E_o = (B_o)^2$$

At diameters below this value there is a tendency of surface tension forces to predominate and this assists in formation of stable liquid slugs, an essential prerequisite for PHP operation. As the PHP tube diameter increases the surface tension is reduced leading to stratification of phases. Therefore it seems to follow that maximum critical diameter the device will stop functioning as a PHP. After taking the perfect diameter, the experiment would be done on vertical different orientation with Methanol and Ethanol as working fluids, for filling ratios of 40%-70%, 4 CLPHP is used for different filling ratios of Methanol and 4 for Ethanol. Different heat inputs were provided to the system and temperatures reading of different sections were measured by temperature sensor LM-35 using Arduino Mega. Then filling ratio is changed to 50%, 60%, 70% keeping the inclination same and above procedure is repeated later on for both Methanol and Ethanol using CLPHP. For cooling the condenser a DC cooling fan is used. It is connected to an adapter circuit.

RESULTS AND DISCUSSION

An experiment is carried out at different filling ratios of Methanol and Ethanol as working fluids used in CLPHP at vertical orientation. Result is compared between Methanol and Ethanol using CLPHP on basis of different characteristics.

Characteristics of temperature distribution with time

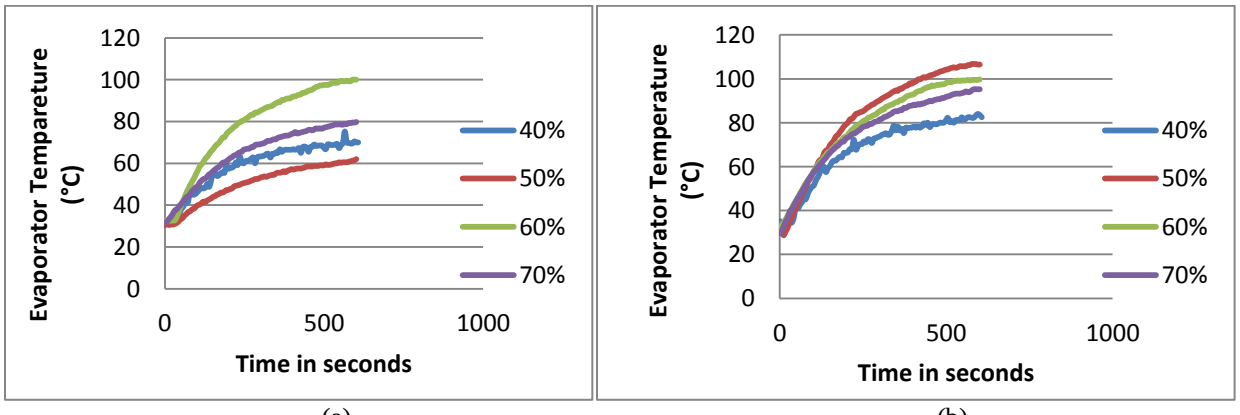

(a) (b)

Figure.3a) Variation of Evaporator Temperature with time at different fill ratio for Methanol at a heat load of 30 W
3b) Variation of Evaporator Temperature with time at different fill ratio for Methanol at a heat load of 50 W

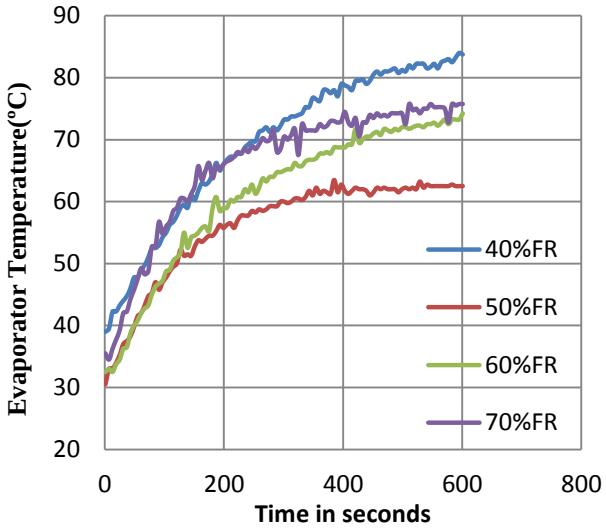

(a)

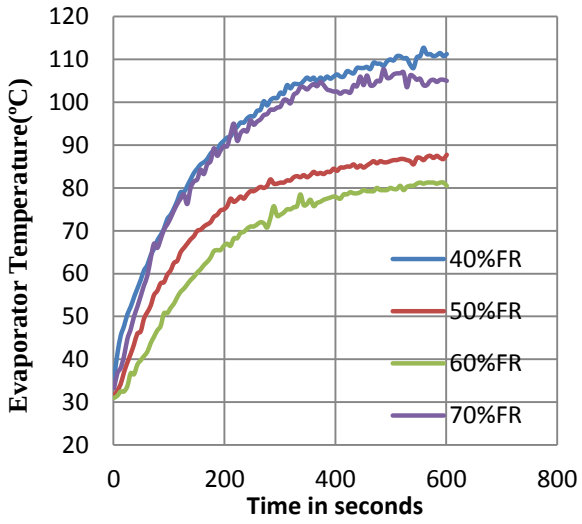

(b)

Figure.4a) Variation of Evaporator Temperature with time at different fill ratio for Ethanol at a heat load of 30 W

4b) Variation of Evaporator Temperature with time at different fill ratio for Ethanol at a heat load of 50W

The variation of temperature with time curve shows a similar pattern for all experimental conditions. The above figures show evaporator temp VS time for all filling ratios for 30 watt & 50watt at orientation 0 degree in fig 3-4 respectively. In the above graphs the rate of temperature increase is high at beginning & when it reaches boiling point it slows down. The rate of increase is different for different region. The temperature increase in evaporator slows down due to heat requirement in phase transfer. In both figure the rate of temperature increase is higher in 220 sec then the rate slows down.

In fig. 3a &b it can be seen that all curve are smooth except 40% filling ratio. At 40% filling very clear pulsating curve can be seen. So 40% filling is better among all filling ratio. The curves start pulsating at 60sec in 30watt and 30 sec in 50watt. This is called the start-up time. The start-up time for 50 watt is lower compared to 30 watt. So 40% filling and 50watt is better. On the other hand from fig.4a&b at 50%FR ethanol gives better pulsation. The start-up time of 30W is lower compared to 50W.So 50%FR and 30W is better for ethanol.

Variation of thermal resistance

Thermal resistance of PHP is defined as the ratio of average temperature difference between the evaporation and condensation sections to the power input. It can be calculated as:

$$R_{th} = \frac{(T_e - T_c)}{Q}$$

Where T_e is the average temperature of the evaporation sections, T_c is the average temperature of the condensation sections. Here the lower value of R_{th} refers to low resistance to heat flow and eventually indicates a higher efficiency of the system.

From the figure 5a&b it can be seen that at very low filling ratios, *i.e.* 40%, thermal resistance increases with increasing power, but, as the power in increased beyond 40 W dry-out occurs. At low filling ratios, as the heat input is increased, the entire surface is covered by the vapor space which leads to dry-out situation. As the filling ratio increases further, the device starts acting in pulsating mode.

In the PHP high fill ratio is responsible to hinder the pulsation of the bubble and hence the efficiency of heat transfer will not be very good. The low filling ratios are expected to favor the pulsation of the bubble, but it is extremely easy to dry out. Thus 40% was chosen as the optimum filling ratio for methanol.

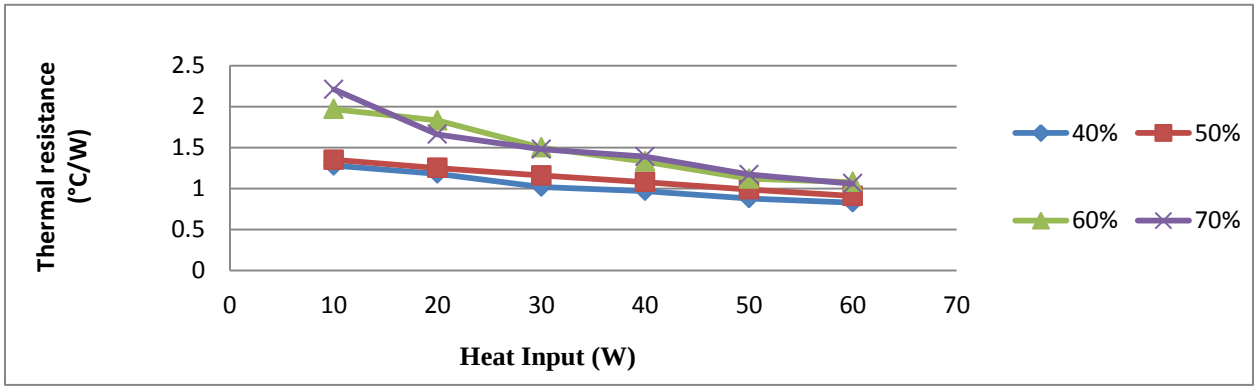

(a)

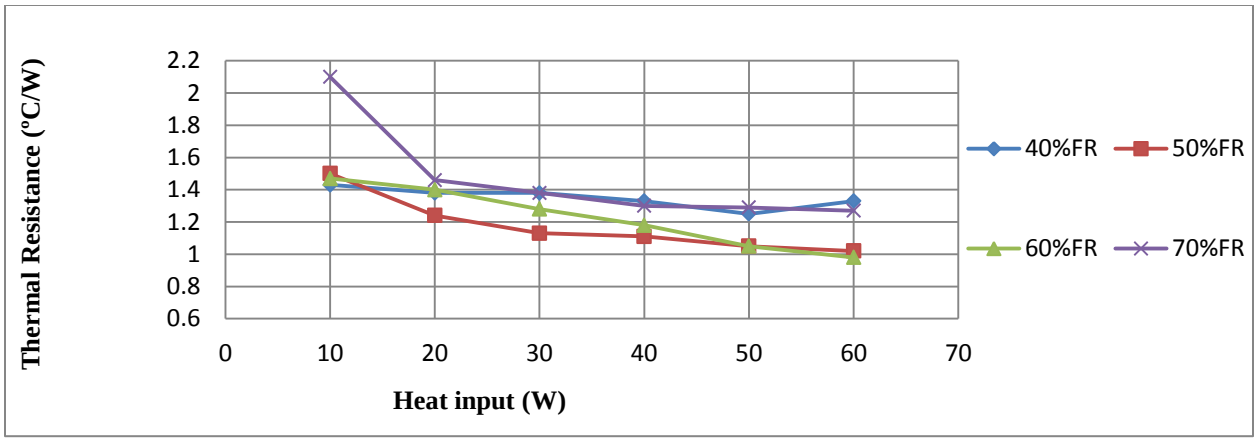

(b)

Figure.5a) Variation of thermal resistance with heat input at 0 degree inclination for methanol
5b) Variation of thermal resistance with heat input at 0 degree inclination for ethanol

For ethanol minimum resistance is offered at a filling ratio of 60% whose value is 1.01°C/W. As the filling ratio increase beyond 60%, the thermal resistance offered by the device tends to increase. At FR 70% few bubbles are present in the PHP decreases, thus a drop in the performance is observed. The performance of methanol is quite comparable to that of ethanol. Methanol offered minimum resistance at 40%FR whose value is 0.83°C/W. The thermodynamic properties of methanol make its performance better. Its high latent heat spreads more heat with less fluid flow. To compare the performance of both the working fluids heat transfer coefficients were calculated.

Variation of Heat Transfer Coefficient

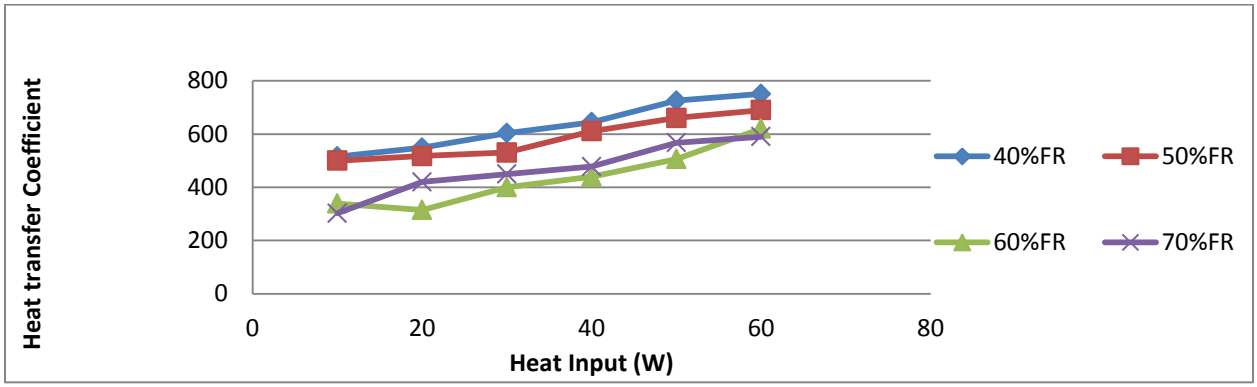

(a)

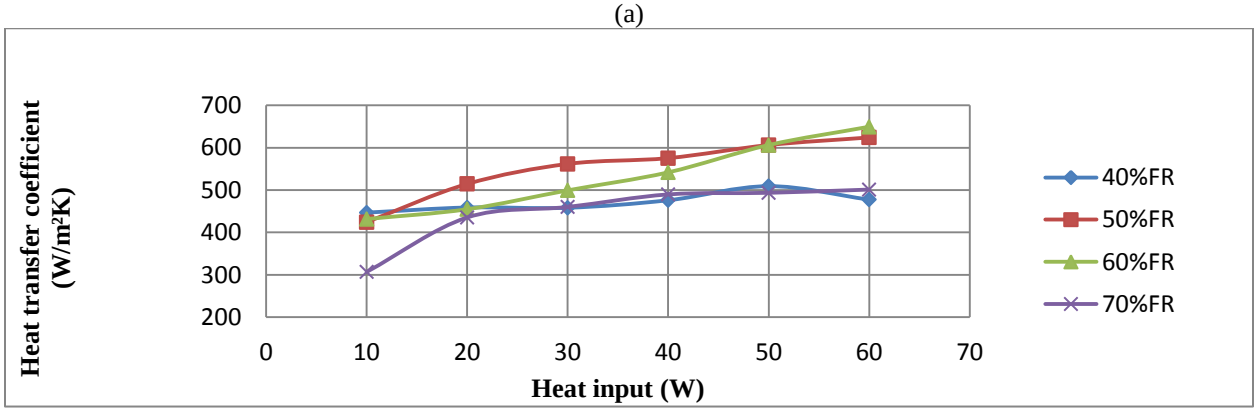

(b)

Figure.6a) Variation of heat transfer coefficient with heat input at 0 degree inclination for methanol

6b) Variation of heat transfer coefficient with heat input at 0 degree inclination for ethanol

The convective heat transfer coefficient of PHP is given by

$$h = \frac{Q}{A(T_e - T_c)}$$

It is seen from fig.6a&b that the heat transfer coefficient of methanol is more compared to ethanol. For ethanol at 60%FR heat transfer coefficient is higher and for methanol it is at 40%FR.So methanol gives better performance because saturation temperature of methanol is higher than ethanol, as the value of heat transfer coefficient is dependent on saturation temperature.

Effect of working fliud

Figure. 7 shows that methanol offers lower thermal resistance than ethanol at 40%FR But for lower heat inputs ethanol shows low thermal resistance. This is because ethanol has a low saturation temperature than ethanol and it starts evaporating sooner than methanol. But as heat inputs increase its performance decreases due to less amount of bubble produced as large portion of liquid is already in vapor state and it tends to dry out but methanol in this case works better. This implies that methanol is a better working fluid than ethanol over a wider range of heat inputs.

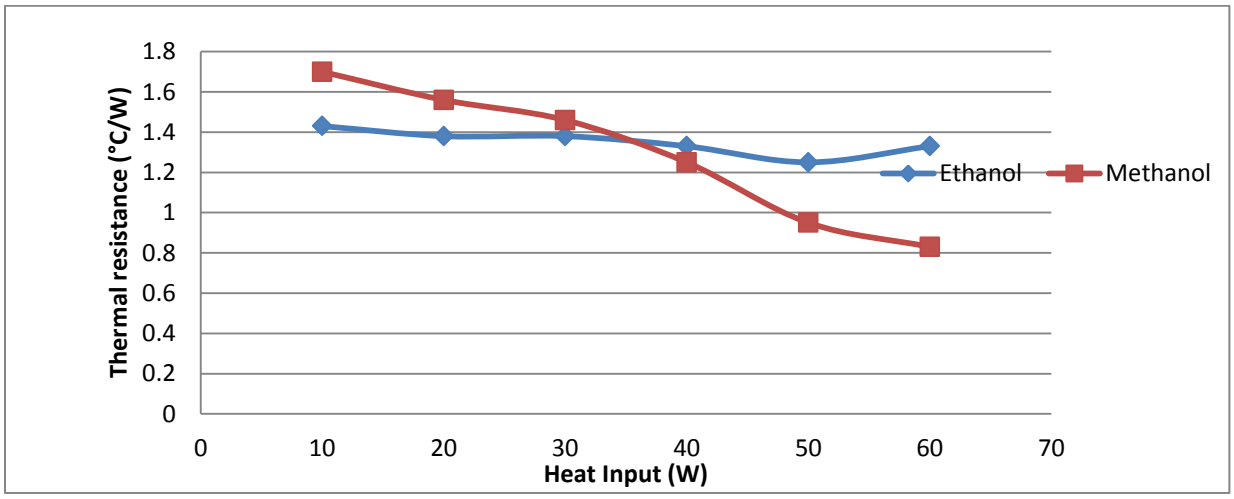

Figure. 7 Variation of thermal resistance with heat input for methanol and ethanol at 40% FR

CONCLUSION

The experimental investigation shows that minimum start-up power for ethanol as working fluid in PHP are at 60% FR while for methanol as working fluid, they are at 40% or below 40%FR. The optimum FR for both the minimum thermal resistance and maximum heat transfer coefficient was found to be 60% for ethanol and 40% for methanol. In vertical orientation of PHP, the resistances observed are 1.01 and .83°C/W and heat transfer coefficients are 750.51 and 627.45 for ethanol and methanol respectively. Hence it may be concluded that the PHP charged with methanol can be considered as better working fluid compared to ethanol.

ACKNOWLEDGEMENTS

The authors are grateful to Department of Mechanical Engineering, MIST and BUET for accomplishment of this research.

REFERENCES

1. Akachi H, Structure of a heat pipe. US Patent No.4921041. 1990.
2. Piyanun Charoensawan, Sameer Khandekar, Manfred Groll, Pradit Terdtoon. (2003): "Closed loop pulsating heat pipes Part A: parametric experimental investigations". Applied Thermal Engineering, Vol. 23, pp. 2009–2020.
3. Lin, Y.H., Kang, S.W., Chen, H.L.: Effect of Silver Nano fluid on Pulsating Heat Pipe Thermal Performance, Applied Thermal Engineering, Vol.12, pp.1312-1317, (2007).
4. Jian Qu, Hui-ying Wu, Ping Cheng. (2010): "Thermal performance of an oscillating heat pipe with Al2O3–water nanofluids". International Communications in Heat and Mass Transfer, Vol.37, pp. 111–115.
5. S. Khandekar, P. Charoensawan, M. Groll, P. Terdtoon. (2003): "Closed loop pulsating heat pipes Part B: visualization and semi-empirical modeling". Applied Thermal Engineering.Vol.23, pp. 2021–2033.

ICME2015

International Conference on Mechanical Engineering 2015
(ICME 2015) 18 – 20 December, 2015, Dhaka, Bangladesh

Paper ID : 123

Effect of Using Acetone and Distilled Water on the Performance of Open Loop Pulsating Heat Pipe (OLPHP) with Different Filling Ratios

Md. Lutfor Rahman[1], Tonima Afrose[1, a)*], Halima Khatun Tahmina[1], Rumana Parvin Rinky[1] and Mohammad Ali[2]

[1] *Military Institute of Science and Technology, Mirpur Cantonment, Dhaka-1216, Bangladesh*

[2] *Bangladesh University of Engineering and Technology, Dhaka-1000, Bangladesh*

[a)]Corresponding author: cadetno41@gmail.com
[b)]tahminakazi@ymail.com

Abstract. Pulsating heat pipe (PHP) is a new innovation in the modern era of miniaturizes thermal management system for its higher heating and cooling capacity. The objective of this experiment is to observe the performance of open loop pulsating heat pipe using two fluids at different filling ratios. This OLPHP is a copper capillary tube of 2.5mm outer diameter and 2mm inner diameter. It consists of 8 loops where the evaporative section is 50mm, adiabatic section is 120mm and condensation section is 80mm. The experiment is conducted with distilled water and acetone at 40%, 50%, 60%, and 70% filling ratios where 0° (vertical) is considered as definite angle of inclination. Distilled water and acetone are selected as working fluids considering their different latent heat of vaporization and surface tension. It is found that acetone shows lower thermal resistance than water at all heat inputs. Best performance of acetone is attained at 70% filling ratio. Water displays better heat transfer capability at 50% filling ratio.

TABLE 1. Nomenclature

Symbol	Meaning	Symbol	Meaning
Bo	Bond number	D_{crit}	Critical Diameter
ρ	Difference in density of the two phases	g	Acceleration due to gravity
a	Acceleration	ρ_l	Density of liquid
L	Characteristic length	ρ_v	Density of vapour
σ	Surface tension	R_{th}	Thermal resistance
T_e	Evaporator temperature	T_c	Condenser temperature
Q	Heat input	FR	Filling ratio

INTRODUCTION

Cooling technology has taken a paradigm shift in the verse of rapid power dissipation as anticipated by Moore's Law [1]. Thermal management system is now playing an important role in today's technology as technology has taken a drift from bipolar to complementary metal-oxide-semiconductor (CMOS). The invention of modern heat pipes has come into existence in order to solve the problems regarding power transportation at longer distance and rapid power dissipation in miniaturised technologies. The concept of heat pipe was first suggested by Gaugler [2]. Grover later on invented capillary base heat pipe by using water as working fluid [3]. Loop heat pipe was first discovered by Akachi [4] was cost effective and overcome the limitations regarding wick structures. Pulsating heat pipe (PHP) which is used in this experiment is a passive two phase thermosyphon without any wick structure. It consists of three sections- evaporator, condenser and adiabatic section. The middle section is made adiabatic to transfer the heat by latent heat absorption from evaporator to condenser. The PHP is partially filled with working fluid. Then the lower end of the tube (evaporator section) is heated. Bubbles are formed when surface temperature is greater than saturated fluid temperature by a certain amount. At a point more nucleation sites develop and bubble coalescence occurs. The bubbles escaped as column and merge to form vapour slugs. Due to increase of temperature and formation of bubbles in the evaporator zone the liquid moves toward the condenser zone. As a result vapour pressure is reduced and bubbles condensed. The vapour plugs generated by the evaporation of liquid push the liquid slugs towards the condenser section and this motion causes flow oscillations that guide device operation [5]. There is a reliable advantage because of the absence of an external mechanical pump [6]. Two different arrangement of PHP is possible- 1) Open loop and 2) Closed loop. The pressure difference and buoyancy force of the liquid drive the vapour slugs upward to the condenser section. Liquid circulation is possible in closed loop but it is believed to be impossible in open loop configuration [7]. In this case it is believed that counter- current liquid-vapour flow occurs in order to promote the proper device orientation [8].

The aim of this experiment is to visualize the performance of open loop pulsating heat pipe using acetone and water as working fluids. An analogy has been made in this experiment by maintaining constant heat input while considering the effect of heat input on the performance of heat pipe. Temperature difference between evaporator and condenser is also discussed to analyze the performance of PHP in this research. The efficiency of OLPHP is determined by taking different filling ratios. The working fluids are selected by considering their high thermal conductivity, high thermal stability, high latent heat, high surface tension and low viscosity. Acetone evaporates quickly than water. The attraction between acetone molecules is weaker than those between water molecules. The normal boiling point of acetone is less than that of water. So vapour pressure of a liquid acetone is higher than the water in a closed container. Superiority of water with its high latent heat and surface is noticeable compared to acetone. Water has a risk of freezing at lower temperature. But both water and acetone are compatible with copper as recommended by their past successful usage. In this research thermal performances of the two working fluids are discussed and differentiated on the basis of their thermodynamic, fluid dynamic and thermal properties. A comparison has also been done by Reihl [9] on the performance of acetone, ethanol, isopropyl alcohol, methanol and water in open loop heat pipe where acetone works best in vertical orientation. Wang et al. [10] compared the performance of DI water and acetone on a copper PHP with respect to start up and found that compared with distilled water the PHP was more readily to be started with acetone as working fluid. A previous literature on thermal and visual observation of water and acetone oscillating heat pipes shows that acetone has higher oscillating frequency but lower thermal amplitude than water. Here thermal amplitude means the temperature variation of the heat pipe wall surface [11].

EXPERIMENTAL SETUP

Design Parameters

Thermal resistance, heat transfer co-efficient, evaporator temperature and difference between evaporator and condenser temperature are important parameters to visualize the thermal performance of a PHP. Along with thermodynamic point of view geometrical properties is also a governing factor. Surface tension should be high in

order to dominate gravitational force. To get higher surface tension and better pulsating action the bond number must be less than 4. Bond number is –

$$\mathrm{Bo} = \frac{\rho a L^2}{\sigma} \tag{1}$$

And the theoretical maximum inner diameter of PHP for formation of stable liquid and vapour slug is defined as-

$$D_{crit} = 2\left[\frac{\sigma}{g(\rho_1 - \rho_v)}\right]^2 \tag{2}$$

The PHP used in our experiment is made of copper tube. Its inner diameter is 2mm and outer diameter is 2.5mm. Water and acetone are selected as two working fluids where the operating range of water is 273K-643K and that of acetone is 250K-475K [12]. The study is carried on vertical position which is 0° orientation. Filling ratios of 40%, 50%, 60% and 70% are taken for both working fluids. The both ends of this open loop heat pipe are closed. No check valve is used as there is no external pumping action.

Construction

The experimental setup is shown in Fig 1(a) and 1(b). The structure which contains the PHP is made of stainless steel except the part which contains evaporator section. The frame which contains evaporator section is made of wood to prevent the unwanted loss and hazards. The PHP consists of long capillary tube bent into 8 U turns. Total 8 thermocouples are used (LM-35 sensors with maximum local sensor accuracy of ∓.5℃). The operating temperature range of each of the thermocouple is -55℃ to 150℃. The evaporator section is wounded with nichrome wire. It is then insulated with asbestos fiber since it is resistant to fire, heat and electricity. Mica sheets are used to wrap the whole pipe because it is a good electrical insulator and a good thermal conductor. The adiabatic section is covered with glass wool to prevent convective heat transfer.

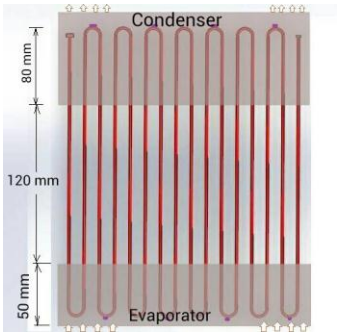

(a) (b)

FIGURE 1. a) The prototype of experimental setup and (b) The structure of open loop heat pipe

Procedure of the Experiment

Firstly the heat pipe is evacuated by a vacuum pump and working fluid is injected with syringe at definite filling ratios. Then both ends of PHP are sealed and the heat pipe is ready for the experiment. Heat is supplied through a

power supply unit (AC, 220V, 50Hz) through a variac (3F, 300V, 60Hz). Cooling is done by forced convective heat transfer through a DC fan. Data collection is done by Arduino Mega (microcontroller: ATmega2580, operating voltage: 5V, input voltage: 7-12V, analogue input pins: 16 is used). Results are collected by repeating the same procedure at 20, 30, 40 and 50W heat input.

RESULTS AND DISCUSSION

Effect of Working Fluids on Evaporator Temperature at Different Filling Ratios

The evaporator temperature is one of the key points to determine performance of a PHP. The evaporator temperature is directly related to startup. Startup is the condition where the oscillating motion of the PHP becomes self-sustained. Figure 2(a) and 2(b) shows the evaporator temperature of water and acetone at 40W and different filling ratios. It is observed from the graph that acetone reach more rapidly at stable pulsating condition than water. The evaporator temperature greatly depends upon heat of vapourization of working fluids. The heat of vapourization of water is larger than acetone. That means water needs much heat to reach the startup condition than acetone. This is the reason acetone takes less time to reach startup temperature. Consequently the startup temperature of acetone is also lesser than water. The startup time and temperature for acetone is lowest at 70% filling ratio. At atmospheric pressure acetone has a boiling point of 56°C and boiling point of water is 100°C. The pressure in the PHP is lower than the atmospheric pressure. This is the reason acetone performs better at 70% filling ratio without any tendency to dry out. But at lower filling ratios and same heat input large number of vapour develops. These excess vapours increase the startup temperature and delays the startup time. This is because the thermal conductivity of vapour is less than liquid. In case of water startup time and temperature is lowest at 50% filling ratio. The reason is that at higher filling ratios water needs more heat to form vapour as heat of vapourization of water is more. As a result water at 70% filling ratio shows higher evaporator temperature**.**

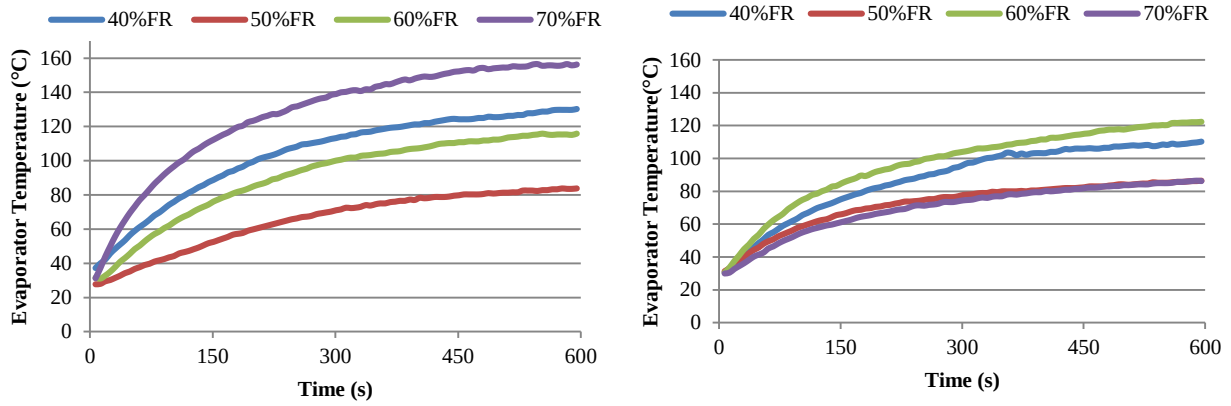

(a) (b)

FIGURE 2. Variation of Evaporator temperature of (a) water (b) acetone with time at different filling ratios

Effect of Working Fluid on Evaporator Temperature at Different Heat Input

Evaporator temperature increases as heat input increases. Figure 3(a) and 3(b) shows the effect of different heat input on evaporator temperature at 70% filling ratio. The maximum evaporator temperature obtained at highest heat input. Higher heat input ensures the startup more quickly than lower level of heat input. At all heat inputs water shows high startup temperature than acetone. This is due to the increase of vapour pressure of acetone. Evaporator temperature is increased by absorbing heat input where there is low vapour pressure difference between condenser

and evaporator. That is evaporator temperature will increase when heat input rate is more than heat transport rate. The graph also shows that at lower heat inputs acetone reach startup condition more quickly.

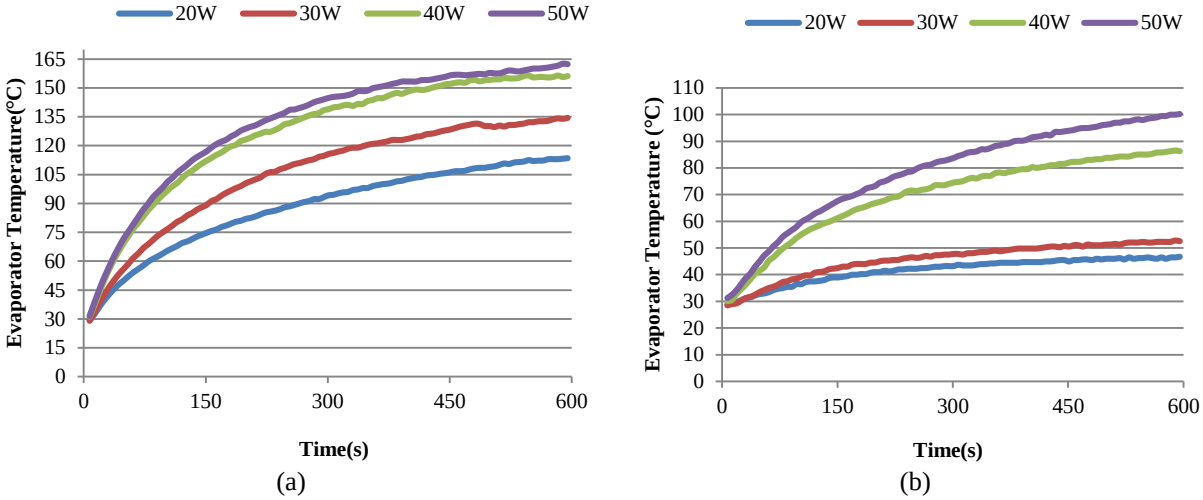

FIGURE 3. Variation of Evaporator temperature of (a) water (b) acetone with time at different heat input

Effect of Working Fluid on Temperature Difference of Evaporator and Condenser

Temperature difference is an important parameter to describe the performance of heat pipe. The comparison is made at 50% and 70% filling ratio of both water and acetone. The 70% and 50% filling ratio is selected because above experimentations show that acetone and water performs best at 70% and 50% filling ratio respectively. The heat transferred in PHP is not only by the latent heat transfer like in other types of heat pipes, but also by sweeping of the hot walls by the colder moving fluid and vice versa[13]. At a certain temperature difference between evaporator and condenser the liquid plugs and vapour bubbles starts to oscillate back and forth [14]. As the graph shows in Fig 4(a) and 4(b) - at 70% filling ratio the temperature difference between evaporator and condenser surface of acetone is much lower than water. At a definite time lower temperature difference indicates better heat transfer from evaporator to condenser surface. In case of acetone with the increase of heat inputs temperature differences also increase. Acetone shows almost uniformity of temperature at lower heat inputs. The reason is at lower heat inputs acetone reaches the startup condition quickly without any possibility to dry out. But at higher input more vapour bubbles form and slow the heat transfer rate. The evaporator temperature of acetone at 50% filling ratio increases due to increase of vapour plug. So the rate of vapour plug formation is more than the rate of heat transport from evaporator to condenser. This is the reason the temperature amplitude increases at 50% filling ratio.

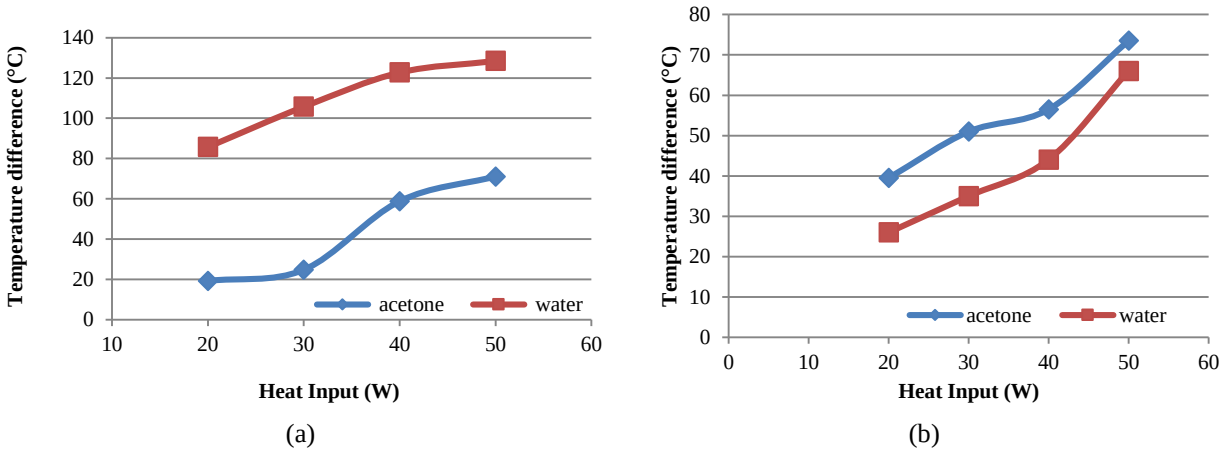

FIGURE 4. Effect of heat input on temperature difference at (a) 70% filling ratio and (b) 50% filling ratio for both acetone and water

Effect of Working Fluid on Thermal Resistance at Different Filling Ratio and Variable Heat Inputs

Thermal resistance is one of the important parameter to describe the performance of PHP. It can be defined by the equation-

$$R_{th} = \frac{T_e - T_c}{Q} \tag{3}$$

Here T_e, T_c are the average evaporator and condenser temperature respectively and Q is the heat input. The thermal resistances at different heat inputs are shown in the Figure 5(a) and 5(b). For both water and acetone the highest thermal resistance is obtained at lower heat input. Thermal resistance of acetone is seen lower than that of water. In case of 70% filling ratio of water PHP starts slowly at low evaporative load and few bubbles generate. As a result at 70% filling ratio and lower heat load water shows high thermal resistance than others. But it is noticeable that the graph is plummeting rapidly as the heat load increases. Because at high heat load and high filling ratio more vapour plugs are tend to generate as a result heat transfer increases. In PHP high filling ratio resist the bubble formation and low filling ratio has a tendency to dry out. In this experiment water is showing best performance at 50% filling ratio. On the contrary acetone is showing lowest thermal resistance at 70% filling ratio. The problems regarding low evaporative load does not affect acetone in this case because acetone has a tendency to evaporate quickly than water. At low filling ratios acetone shows greater thermal resistance because there is a tendency to dry out. Figure 6 shows a comparative view of thermal resistance of acetone and water at 50% and 70% filling ratio. It is found that lowest thermal resistance is obtained at 70% filling ratio of acetone.

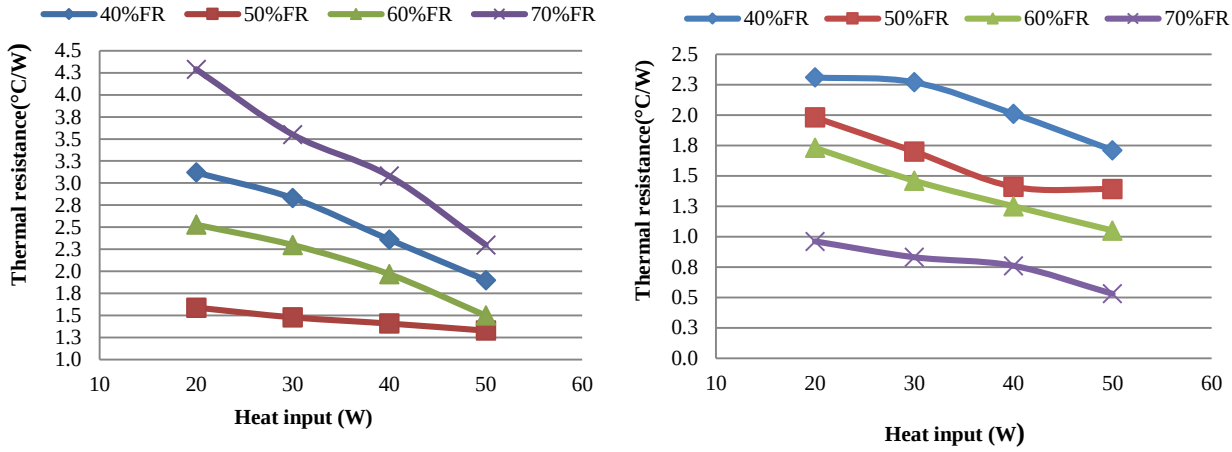

FIGURE 5. Effect of heat input on thermal resistance of (a) water (b) acetone at different filling ratios

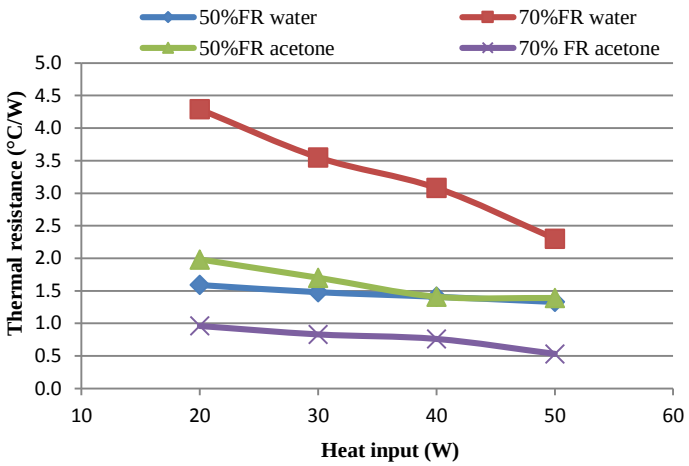

FIGURE 6. Variation of thermal resistance with heat input at 70% and 50% filling ratio of acetone and water

CONCLUSIONS

This paper focused on the potential of acetone and water as working fluid of OLPHP at different filling ratios. In this experimental investigation acetone shows lower thermal resistance than water. Lowest thermal resistance is obtained at 70% filling ratio of acetone. Water shows highest thermal resistance at 70% filling ratio and lowest at 50% filling ratio. Water at 70% filling ratio represents a downward sloping tendency which indicates that it performs better at high heat loads. It is found from the experiment that acetone at lower heat inputs reaches the startup condition earlier than water. This experiment shows that temperature difference between evaporator and condenser surface temperature is almost uniform for acetone at higher filling ratios and lower heat inputs. The evaporator surface temperature of acetone increases rapidly at higher heat inputs. The evaporator surface temperature for acetone remains lower than water at all filling ratios. The evaporator surface temperature is lowest for water at 50% filling ratio and for acetone at 70% filling ratio. From this experimental research it can be summarized that acetone and water performs best at 70% and 50% filling ratio respectively.

ACKNOWLEDGEMENTS

The authors feel sincere gratitude to Department of Mechanical Engineering of MIST and BUET for lab and financial support.

REFERENCES

1. Azar, K. , “The History of Power Dissipation” , Electronics Cooling, Vol.6, No.1, January2006
2. Gaugler, R. S US patent 2350348.Appl. 21 Dec, 1972.Published 6 June 1944.
3. Grover, G. M US patent 3229759.Filed 1963.
4. H. Akachi, “Structure of a Heat Pipe,” US Patent 4921041, 1990.
5. Zhang, Y., Faghri, A., “Heat Transfer in a Pulsating Heat pipe with an Open End”, International Journal of Heat and Mass Transfer, Vol. 45, 2002, pp. 755-764.
6. Khandekar S. and Groll M., On the Definition of Pulsating Heat Pipes: An Overview, Proc. 5th Minsk Int. Conf. (Heat Pipes, Heat Pumps and Refrigerators), Minsk, Belarus, 2003.
7. Riehl, R., "Characteristics of an Open Loop Pulsating Heat Pipe," SAE Technical Paper 2004-01-2509, 2004, doi: 10.4271/2004-01-2509.

8. Riehl, R. R., “Evaluation of the Thermal-Hydrodynamics Behavior of an Open Loop Pulsating Heat Pipe”, National Institute for Space Research (INPE) Report, 2003, 35p.
9. R. R. Riehl, “Characteristics of an Open Loop Pulsating Heat Pipe,” Proceedings of the 34th International Conference on Environmental Systems, Colorado Springs, 19- 21 July 2004
10. X. Wang, T. Han, L. Wang, X. Mao and C. Yang, “Experimental Study on Startup Characteristics of Pulsating Heat Pipe,” Advanced Materials Research, Vol. 354, 2012, pp. 87-91]
11. C.Wilson, B.Borgmeyer, R. A. Winholtz, H. B.Ma, D. Jacobson, D. Hussey “Thermal and Visual Observation of Water and Acetone Oscillating Heat Pipes” ,Heat Transfer: Volume 2, pp. 381-386
12. Heat transfer handbook, Volume 1 by Adrian Bejan, Allan D. Kraus
13. Modelling of pulsating heat pipe by V.S. Nikolayev.
14. Modelling of pulsating heat pipe by V.S. Nikolayev.

ICME2015

International Conference on Mechanical Engineering 2015
(ICME 2015) 18 – 20 December, 2015, Dhaka, Bangladesh

Paper ID : 130

Natural Convection Flow in Porous Enclosure with Localized Heating from Below with Heat Flux

Md. Noor-A-Alam Siddiki[1, a)], Md. Mamun Molla[2, b)] and Suvash C.Saha[3, c)]

[1]*Department of Natural Science, Stamford University Bangladesh,Dhaka, Bangladesh*
[2]*Department of Mathematics & Physics, North South University,Dhaka-1229, Bangladesh*
[3]*School of Chemistry, Physics and Mechanical Engineering, Queensland University of Technology, GPO Box 2434, Brisbane, QLD 4001, Australia*

[b)]Corresponding author : mamun.molla@northsouth.edu
[a)]siddiki@stamforduniversity.edu.bd
[c)]suvash.saha@qut.edu.au

Abstract. Unsteady natural convection flow in a two dimensional fluid saturated porous enclosure with localized heating form below with heat flux, symmetrical cooling from the sides and the insulated top wall has been investigated numerically. The governing equations are the Darcy's law for the porous media and the energy equation for the temperature field has been considered. The non-dimensional Darcy's law in terms of the stream function is solved by finite difference method using the successive over-relaxation (SOR) scheme and the energy equation is solved by Alternative Direction Alternative (ADI) scheme. The uniform heat flux source is located centrally at the bottom wall. The numerical results are presented in terms of the streamlines and isotherms, as well as the local and average rate of heat transfer for the wide range of the Darcy's Rayleigh number and the length of the heat flux source at the bottom wall.

INTRODUCTION

The natural convective heat transfer in porous enclosures has been of interest to engineering applications for many years. Well known examples are the cooling of radioactive waste container, meteorology, geothermal problems, oil recovery, solar power collector, storage of grain etc. These applications require knowledge of natural convection in various geometries to the gravitational field.

The convective heat transfer in the rectangular/square enclosures which has received the attention of many investigations.Ostrach[1]has reviewed the work done on various natural convection flow problems. Most of the published studies on natural convection in rectangular cavities considered the classic problem of the either vertically or horizontally imposed temperature gradient. The corresponding problem, relative to a square cavity heated below and cooled from one side has been studied by Anderson and Lauriat [2, 4]. The authors observed only a single cell in the flow filed and did not observe any Benard type instabilities. The relevance study of the same configuration but heated wall with cooling from side was described by November and Nansteel [3]. It was reported in their studies that the fluid layer adjacent to the bottom wall remains attached up to the turning corner. The authors also claimed that convective heat transfer is shown to be most significant when slightly less than of the lower surface is heated.

Ganzarolli and Milanez [5] presented a numerical study of steady natural convection in a rectangular cavity heated from below and symmetrically cooled from sides. In their numerical model the size of the cavity was varied from square to shallow. There are two heating boundary conditions have been employed on the bottom surfaces, isothermal and heat flux. The authors observed a distinct discrepancy between the isothermal and constant heat flux conditions for shallow cavity. They also observed that the cavity was not always thermally active along its whole length and the flow did not fill the cavity uniform for isothermal heat source condition.

However, the isotherms and streamlines occupy the whole cavity more uniformly, even for low values of the Rayleigh number for the constant heat flux condition.

The natural convection of a square cavity with localized heating from below with symmetric cooling from the sidewalls was investigated by Aydin and Yang [6]. In this work, the top wall and the rest of the non heated portions of the bottom wall were considered adiabatic. The authors have presented the variation of the heat source length and the Rayleigh numbers and shown their simulation results the two counter rotating vortices were formed in the flow domain due to natural convection .The effect of the Rayleigh number and length of the heat source on the average Nusselt number at the heated part of the bottom wall has been shown and discussed .The same problem but with heat flux for heat source of the bottom surface instead of constant temperature has been studied by Sharif and Mohammad [7].

The study of heat transfer in porous media has also got attention of many researchers. The volume of work devoted to this subject has been amply documented in the monographs by Neild and Bejan [8] and Ingham and Pop [9]. There are many published studies related to natural convection in rectangular porous enclosures [10-17] are available in the literature. Most of the work found in literature deals with flow and heat transfer characteristics inside porous enclosures with constant wall temperatures. However, the little work has been carried out on flows saturated porous enclosure driven by localized heating from the below. Although recent work by Basak et al. [18] and Saeid [19] show the effect of a non-uniformly heated bottom wall inside a fluid saturated porous enclosure. But they only consider continuous variation of temperature along the wall. We take their work to the extreme by considering a discontinuous variation of the wall temperature profile.

In the present study, we are interested in investigating the unsteady natural convection laminar flow in a square cavity formed by insulated top and bottom wall, left and right walls being uniformly heated and cooled respectively. The basic equations of motion are transformed into a non-dimensional form, which are solved numerically by using finite difference method with SOR solver for momentum equation and ADI scheme for the energy equation

NOMENCLATURE

g	Acceleration due to gravity	α	thermal diffusivity
H	Enclosure height	β	thermal expansion coefficient
k	Permeability of the porous media	ϵ	width of heat source at bottom wall
Ra	Darcy- Rayleigh Number	ψ	stream function
q_w	Bottom wall heat flux	ν	kinematic viscosity

FORMATION OF PROBLEM

Consider the flow of a Newtonian fluid within porous enclosure with height L as shown in Figure 1. The non-dimensional governing equation are obtain with following assumptions the enclosure is completely filled with porous materials, Darcy's law is assumed to hold, the fluid is assumed to be normal Boussinesq incompressible fluid, negligible inertia effects, the saturated porous medium is to be isotropic in thermal conductivity, the bottom wall has a centrally located heat source which is assumed to be constant heat flux q_w, the side walls are isothermally cooled at a constant temperature T_c while the bottom wall, except the heated part and the top wall are considered to be insulated.

Under the above assumption, the non-dimensional governing equations in terms of the stream function Ψ and temperature θ are as follows:

$$\frac{\partial^2 \psi}{\partial X^2} + \frac{\partial^2 \psi}{\partial Y^2} = -Ra \frac{\partial \theta}{\partial X} \tag{1}$$

$$\frac{\partial \theta}{\partial \tau} + \frac{\partial \psi}{\partial Y}\frac{\partial \theta}{\partial X} - \frac{\partial \psi}{\partial X}\frac{\partial \theta}{\partial Y} = \frac{\partial^2 \theta}{\partial X^2} + \frac{\partial^2 \theta}{\partial Y^2} \tag{2}$$

Where the dimensionless variables are defined by

$$X = \frac{x}{H},\ Y = \frac{y}{H},\quad \tau = \frac{t}{H^2/\alpha},\quad U = \frac{u}{\alpha/H}$$
$$V = \frac{v}{\alpha/H},\quad \psi = \frac{\varphi}{\alpha},\quad \theta = \frac{T - T_c}{q_w H/k},\quad Ra = \frac{g\beta q_w k H}{\alpha \nu} \tag{3}$$

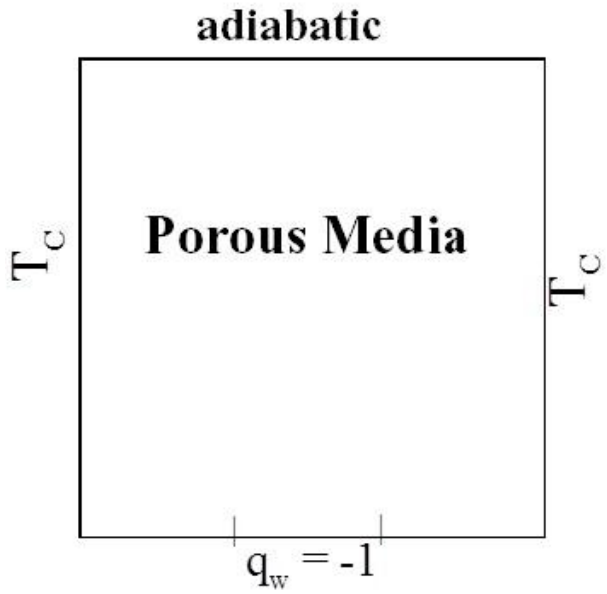

FIGURE 1. Schematic geometry of the computational domain.

The non-dimensional stream function ψ, satisfy the following equations

$$U = \frac{\partial \psi}{\partial Y},\quad V = -\frac{\partial \psi}{\partial X} \tag{4}$$

Equation (1) and (2) are subject to the following boundary conditions:

$$\begin{aligned}
&\psi = \theta = 0, \quad for \quad \tau = 0 \\
&\psi = 0, \quad \theta = 0 \quad for \quad 0 \le Y \le 1 \quad at \quad X = 0 \\
&\psi = 0, \quad \theta = 0 \quad for \quad 0 \le Y \le 1 \quad at \quad X = 1 \\
&\psi = 0, \quad \frac{\partial \theta}{\partial Y} = -1 \quad for \quad \frac{1-\in}{2} \le X \le \frac{1+\in}{2} \quad at \quad Y = 0 \\
&\psi = 0, \quad \frac{\partial \theta}{\partial Y} = 0 \quad for \quad 0 < X < \frac{1-\in}{2} \quad and \quad \frac{1+\in}{2} < X < 1 \quad at \quad Y = 0, \\
&\psi = 0 \quad \frac{\partial \theta}{\partial Y} = 0 \quad for \quad 0 \le X \le 1 \quad at \quad Y = 1
\end{aligned} \tag{5}$$

Where, $\in$ is the non-dimensional heat source length.

Once we know the numerical values of the temperature function we may obtain the rate of heat transfer in terms of the local Nusselt number, *Nu* from the heated portion of the bottom wall using the following relation:

$$Nu(x) = \frac{1}{\theta_w} \tag{6}$$

The average Nusselt number $Nu_{av}$is defined by

$$Nu_{av} = \int_{\frac{1-\epsilon}{2}}^{\frac{1+\epsilon}{2}} Nu(x)dx \tag{7}$$

The governing equation (1)-(2) along with the boundary conditions (5) are solved numerically, employing the finite difference method using the successive over-relaxation(SOR) scheme for Darcy's law and the energy equation is solved by Alternative Direction Alternative(ADI) scheme. After several grid independent test, 101×101 uniform grids is used for the whole computation.

RESULTS AND DISCUSSION

The natural convection in a square cavity with the porous media localized heating from below and symmetrical cooling from the sides has been studied. The effects of Rayleigh number on the flow and thermal patterns are demonstrated in Figures 2 and 3. Streamline and isotherms are shown in the figure for the different values of Darcy's Rayleigh (Ra) numbers and different length of heat source ϵ. Latter, heat transfer performance is also examined in terms of average Nusselt number Nu_{avg}which is shown in the table.

Effects of Rayleigh number

The evolution of the flow and the temperature fields in the enclosure for Ra=10^1, 10^2, 10^3 and $10^4$are shown in Figure 2(a)-(d) for a representative case ϵ =2/5 of. The flow and the temperature fields are symmetric about the vertical centerline of the enclosure up to Ra=10^3. The flow rises in the center of the enclosure due to buoyancy effect and falls along each cold side walls creating mirror image structures that rotate clockwise in the right half and counter clockwise in the left half. It can be seen that the shape of both cells are elliptical. Due to the symmetry, the flows in the left and the right halves of the enclosure are identical except for the sense of rotation. In each case, the flow rises along the vertical symmetry axis from the middle hot portion of the bottom wall and gets blocked at the top adiabatic wall, which turns the flow horizontally towards the isothermal cold walls. Since the Rayleigh numbers are small, viscous forces are more dominant than the buoyancy forces and hence, heat transfer is essential diffusion dominated and the shape of streamline tends to flow the geometry of the enclosure. The maximum values of the co vortex forRa=10^1, 10^2, and10^3 are 0.06, 0.54and 3.86 respectively. On the other hand, the minimum values of the core vortex for Ra=10^1, 10^2 and10^3 are -0.06, -0.54and -3.75 respectively. At Ra =10^4 the flow and temperature field breakdown the symmetry due to the effect of the inertia force and the maximum and minimum values of the core vortex are 16.21 and -12.59 respectively.

Effects of Heat Source Size

The fluid flow and heat transfer behaviors with change of discrete heat source size are investigated by performing numerical simulations for the square enclosure at different discrete heat source lengths of 1/5 to 4/5 are shown in Figure 3, for a representative case of Ra=10^3. It is seen that the flow field are qualitatively identical for different heat source size for a fixed Rayleigh number. However, quantitative results of the maximum values of the stream function are 2.61, 3.86, 4.69 and 5.04 and the minimum values are -2.54, -3.75, -4.49 and-4.82 for ϵ =1/5, 2/, 3/5 and 4/5respectively. On the other hand, the isotherms are affected by the increasing ϵ, as respected. Since the heated part of lower surface increases for the same Rayleigh number, the heating effect will be much more sensible.

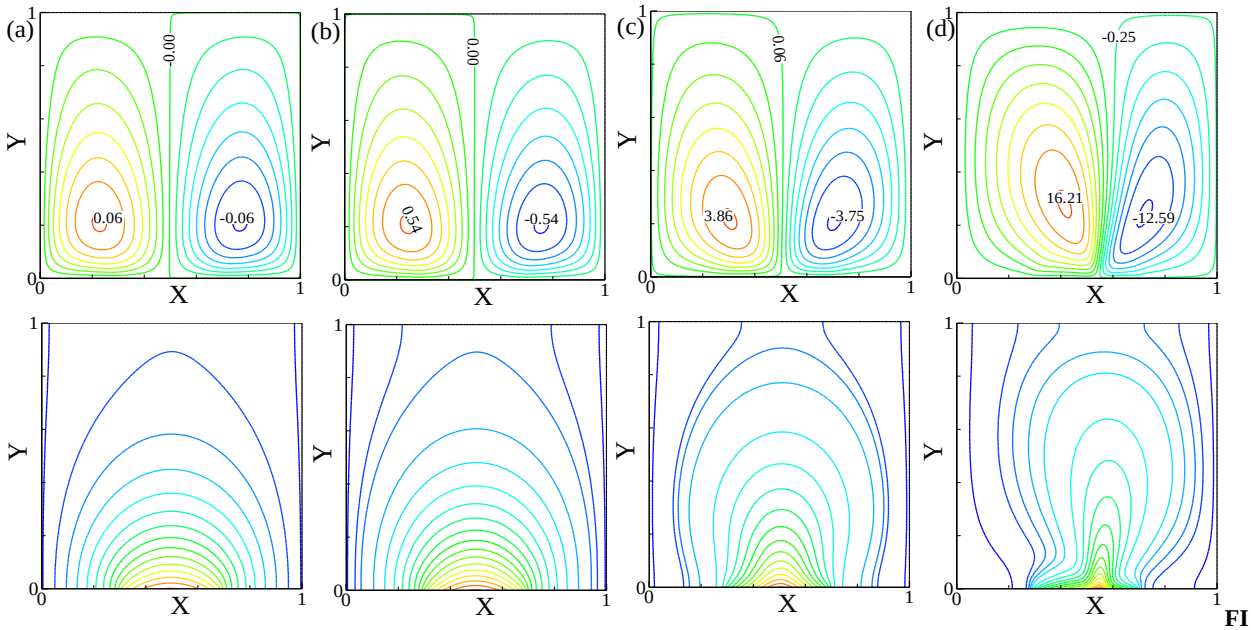

GURE 2.Streamlines (top) and isotherms (bottom) for the different (a) Ra = 10 (b) Ra = 10^2(c) Ra = 10^3 and (d) Ra = 10^4 while ε = 2/5

For a fixed *Ra.*, with increasing ϵ the flow field remains almost the same, while the temperature fields' changes are becoming more stratified for larger values of *Ra*.

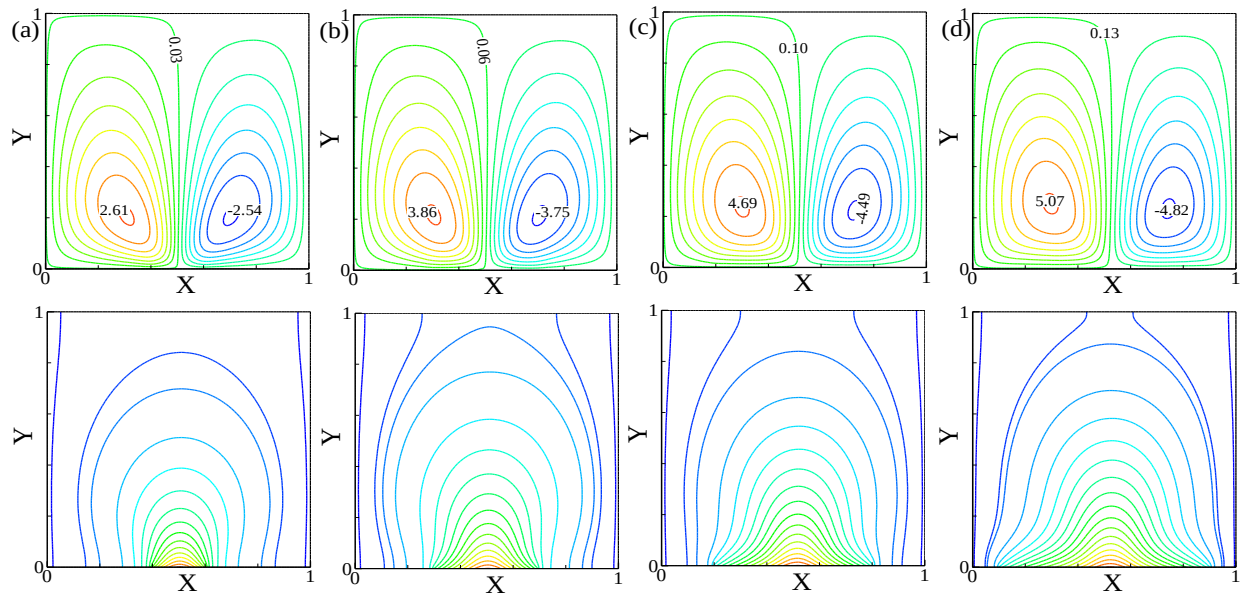

FIGURE 3. Streamlines (top) and isotherms (bottom) for (a) ε = 1/5 (b) ε = 2/5 (c) ε = 3/5 and (d) ε = 4/5 while Ra = 10^3

The average values of the Nusselt number Nu_{av} have been inserted in Table 1 for the different values of *Ra* and the length of heat source ϵ. From this table it is clearly seen that for increasing the Rayleigh number the average rate of the heat transfer increases but for increasing heat source the average rate of heat transfer decreases. It can be concluded that this heat flux case the average Nusselt number is inversely proportional to the length of the heat source.

TABLE 1. Average Nusselt number for the different values of heat source ϵ and Rayleigh number *Ra*

ϵ	Ra=10	Ra = 10^2	Ra = 10^3	Ra=10^4
0.2	5.89	6.15	8.58	25.01
0.4	4.04	4.43	8.21	21.78
0.6	3.59	4.12	8.47	18.39
0.8	3.62	4.12	8.31	17.40

CONCLUSION

In the present study numerical results of buoyancy induced flow and heat transfer in a two dimensional square cavity with localized bottom heating and symmetric cooled side walls has been investigated. Two main parameters, Rayleigh number (Ra) and local heat source size ϵ and their dependency on fluid flow and heat transfer have been analysis. It is revealed that the flow field and the isotherm are laminar up to Ra=10^3. At Ra=$10^4$the flow and temperature field are not symmetric.The increases of Rayleigh number enhance the heat transfer but decrease the rate of heat transfer for increasing heat source size. For lower Rayleigh number the flow is dominant by conduction, however, as the Rayleigh number increases convection takes the role to dominant.

REFERENCES

1. S. Ostrach, Natural Convection in enclosures, J. Heat Transfer **110**, 1175-1190 (1988).
2. R. Anderson and G. Lauriat,The horizontal Natural convection boundary layer regime in a closed cavity, Proceeding of the Eight International Heat Transfer Conference, Vol.4 San Francisco,CA,1986, pp.1453-1458.
3. N. November and M. W. Nansteel, Int. J Heat Mass transfer **30,** 2433-2440 (1986).
4. M. M. Molla, S. C. Saha and M.A.I. Khan, JP J. Heat Mass Transfer **6**, 1-16 (2012).
5. M.M. Ganzarolli and L. F Milnez, Int. J Heat Mass Transfer **38,** 1063-1073 (1995).
6. O. Aydin and W. J. Yang, Int. J Heat Fluid Flow **10(5),** 518-529 (2000).
7. M. A. R. Sharif and T.R. Mohammad, Int. J Thermal Sci. **44**, 865-878 (2005).
8. D. A. Neild and A. Bejan, *Convection in Porous Media* (Springer, New York, 1998).
9. D. B. Ingham and I. Pop, *Transport phenomena in Porous Media* (Elsevier, Amsterdam, 1998).
10. A.C. and I.pop, Int. J Heat Mass Transfer **42**, 1047-1057 (1999).
11. S. L. Moya, E. Ramos and M. Sen, Int. J Heat Mass transfer **30**, 741-756 (1967).
12. A. Bejan, Lett. Heat Mass Transfer **6**, 93-102 (1979).
13. V. Prasad and F.A. Kulacki, J. Heat Transfer **106**,158-165(1984).
14. F.C. Lai and F.A. Kulacki, Int. J. Heat Mass Transfer **31,** 1247-1260 (1988).
15. D. M. Manhole and J. L. Lage, Heat and Mass Transfer in Porous Media HTD **216**, 55-60 (1992).
16. S. Mahmud and R. A. Fraser, Int. J. Heat Mass Transfer **47**, 3245-3256 (2006).
17. K. L. Waker and G. M. Homsy, J. Fluid Mech. **87**, 449-474 (1978).
18. T. Basak, S. Roy, T. Paul and I. Pop, Int. J. Heat Mass Transfer **49**, 1430-1441(2009).
19. N. H. Saied, Int. Comm. Heat Mass transfer **32**, 454-463 (2005).

ICME2015

International Conference on Mechanical Engineering 2015
(ICME 2015) 18 – 20 December, 2015, Dhaka, Bangladesh

Paper ID :131

Mixed Convection Flow of Nanofluid in a Square Enclosure with an Intruded Rectangular Fin

Ran Cong, Xuanyu Zhou, Bruno De Souza Machado, Prodip K. Das [a)]

School of Mechanical and Systems Engineering, Newcastle University,Newcastle upon Tyne, NE1 7RU , United Kingdom

[a)]Corresponding author: prodip.das@ncl.ac.uk

Abstract. Mixed convection flow in enclosures has been a subject of interest for many years due to their ever increasing applications in solar collectors, electronic cooling, lubrication technologies, food processing, and nuclear reactors. In comparison, little effort has been given to the problem of mixed convection in enclosures filled with nanofluids, while the addition of nanoparticles in a fluid base to alter specific material properties is considered a feasible solution for many heat transfer problems. Mixed convection of nanofluids is a challenging problem as the addition of nanoparticles changes the fluid's thermo-physical properties as well as due to the complex interactions among inertia, viscous, and buoyancy forces. In this study, a two-dimensional steady-state numerical model has been developed to investigate mixed convection flow of nanofluids in a square enclosure with an intruded rectangular fin and to optimize the fin geometry for maximizing the heat transfer using the Constructal Design. The model has been developed using ANSYS-FLUENT for various fin geometries. Flow fields, temperature fields, and heat transfer rates are examined for different values of Rayleigh and Reynolds numbers for several geometries of the fin with the aim of maximizing the heat transfer from the fin to the surrounding flow. Outcome of this study provides important insight into the heat transfer behavior of nanofluids, which will help in developing novel geometries with enhanced and controlled heat transfer for solar collectors and electronic devices.

Keywords: Mixed convection, Nanofluids, Numerical modeling, Rectangular fin, Constructal Design.

INTRODUCTION

The study of convective heat transfer inside cavities, such as triangular, trapezoidal, cylindrical, square, wavy, etc. [1-6], has been extensively analyzed due to their application in several engineering problems such as solar collectors, electronic cooling, lubrication technologies, food processing, and nuclear reactors. These studies were essential to provide a better understanding of the physics regarding the fluid dynamics and heat transfer inside the cavities. By narrowing the cavity design to a square lid driven cavity, many studies were carried out for both laminar and turbulent conditions. Nevertheless, due to the equipment miniaturization trend, easily noticed in electronic devices, the technical challenge of increasing the heat transfer inside the cavity without changing the cavity area still remained. Researchers proposed the addition of different types of fin in the cavity and filled with nanofluids, which is the combination of a fluid-base and nanoparticles to enhance certain desired property, in order to increase the heat transfer inside the cavity [7-9].

A large number of experimental and numerical works has been performed for the geometrical optimization of fins and cavities using the Constructal Design [7-11]. Constructal Design is based on the Constructal law, which was

stated by Adrian Bejan as "For a finite-size system to persist in time (to live), it must evolve in such a way that it provides easier access to the imposed currents that flow through it" [12]. It has guided researches toward the discovery of efficient cooling structures for various cavities. However, previous Constructal Design studies are primarily based on air or water filled cavities. It has not been employed to the geometrical optimization of fins and cavities filled with nanofluids. Therefore, the main purpose here is to investigate the geometrical optimization of fins and cavities filled with nanofluids by means of Constructal Design. In the present study, a two-dimensional steady-state numerical model has been developed to investigate mixed convection flow of nanofluids in a square enclosure with an intruded rectangular fin and to optimize the fin geometry for maximizing the heat transfer. The Constructal Design method is used to obtain the optimum geometry, in other words, the one that has the maximum heat transfer between the nanofluid and fin. The fin area and the aspect ratio of fin's height and length are considered the degrees of freedom of the finite flux system. For these degrees of freedom, several values of Rayleigh (Ra) and Reynolds (Re) numbers are considered. For the selected problem, a nanofluid resulted by the mixture of water and 1% of aluminum oxide (Al_2O_3) is utilized. For all the simulations, the Prandtl number (Pr) is kept fixed as Pr = 6.6 for 1% Al_2O_3-water nanofluid.

MATHEMATICAL AND NUMERICAL MODELING

The governing equations for the laminar, two-dimensional, steady state mixed convection fluid flow and heat transfer with the Boussinesq approximation in y-direction are written as:

$$\frac{\partial u}{\partial x}+\frac{\partial v}{\partial y}=0 \tag{1}$$

$$u\frac{\partial u}{\partial x}+v\frac{\partial u}{\partial y}=-\frac{1}{\rho_{nf}}\frac{\partial p}{\partial x}+\frac{\mu_{nf}}{\rho_{nf}}\left(\frac{\partial^2 u}{\partial x^2}+\frac{\partial^2 u}{\partial y^2}\right) \tag{2}$$

$$u\frac{\partial v}{\partial x}+v\frac{\partial v}{\partial y}=-\frac{1}{\rho_{nf}}\frac{\partial p}{\partial y}+\frac{\mu_{nf}}{\rho_{nf}}\left(\frac{\partial^2 v}{\partial x^2}+\frac{\partial^2 v}{\partial y^2}\right)+\frac{(\rho\beta)_{nf}}{\rho_{nf}}g\left(T-T_\infty\right) \tag{3}$$

$$u\frac{\partial T}{\partial x}+v\frac{\partial T}{\partial y}=\frac{k_{nf}}{(\rho C_p)_{nf}}\left(\frac{\partial^2 T}{\partial x^2}+\frac{\partial^2 T}{\partial y^2}\right) \tag{4}$$

where u and v are the horizontal and vertical velocities, p is the thermodynamic pressure, μ_{nf} is the effective dynamic viscosity, ρ_{nf} is the effective density, β_{nf} is the thermal expansion coefficient, T is the temperature, g is the standard gravity, k_{nf} is the heat conductivity, and $C_{p,nf}$ is the heat capacity. The subscript nf represents the effective nanofluid properties, which are computed based on the volume fraction of nanoparticles (φ) in the base fluid. The effective dynamic viscosity of the nanofluid is calculated according to the Brinkman model [13] and the effective thermal conductivity is determined using the Maxwell model [14-16]. Following equations are used to compute the nanofluid properties:

$$\rho_{nf}=(1-\varphi)\rho_f+\varphi\rho_s \tag{5}$$

$$\mu_{nf}=\frac{\mu_f}{(1-\varphi)^{2.5}} \tag{6}$$

$$k_{nf}=k_f\frac{k_s+2k_f-2\varphi(k_f-k_s)}{k_s+2k_f+\varphi(k_f-k_s)} \tag{7}$$

$$(\rho C_p)_{nf}=(1-\varphi)(\rho C_p)_f+\varphi(\rho C_p)_s \tag{8}$$

$$(\rho\beta)_{nf} = (1-\varphi)(\rho\beta)_f + \varphi(\rho\beta)_s \tag{9}$$

where the subscript *s* and *f* represent the solid nanoparticle and base-fluid properties, respectively. It is assumed that base-fluid (in this case water) and nanoparticles (Al_2O_3) are in thermal equilibrium, and nanofluid's thermo-physical properties are constant. Thermo-physical properties of water, Al_2O_3 nanoparticles, and Al_2O_3-water nanofluid (volume fraction of the nanoparticles, φ, is 1%) are listed in Table 1.

TABLE 1. Thermo-physical properties of base-fluid, nanoparticles, and nanofluid.

Physical properties	**Base fluid (water)**	**Nanoparticles (Al_2O_3)**	**Nanofluid**
C_p [J/(kg·K)]	4179	765	4047.01
ρ [kg/m^3]	997.1	3970	1026.83
k [W/m·K]	0.613	40	0.63074
β [1/K]	2.1×10^{-4}	8.5×10^{-6}	2.02×10^{-4}
μ [kg/m]	1.002×10^{-3}	-	1.03×10^{-3}

The numerical solution is obtained by solving the governing equations using commercial finite volume based software, ANSYS-FLUENT. A second order upwind scheme is used for the spatial discretization of the aforementioned equations. Further, the velocity-pressure coupling is done by the SIMPLE algorithm and pressure based solver is used to compute the solution. The solution of governing equations is considered converged when the residuals are smaller than 10^{-7} for mass and momentum equation and smaller than 10^{-8} for energy equation. The numerical simulations are performed using a desktop computer with a quad-core Intel processor with 2.67 GHz clock and 32GB of RAM. In order to select a mesh in which the error associated does not affect significantly the results, a mesh independence test is carried out by comparing the mean Nusselt number between the fin and top wall for various meshes. The results of a mesh independency test are given in Table 2 for mesh densities of 100×100, 120×120, and 160×160 for Ra = 10^5 and φ = 1%. All three meshes produce numerical results that are less than 2% in error, while error in 120×120 mesh is less than 1%. Therefore, the 120×120 volumes mesh is considered to perform the simulations.

TABLE 2. Values of mean Nusselt number for different mesh densities.

Volumes	**Mean Nusselt number**	**% Error**
10000	11.017	1.743
14400	11.106	0.801
25600	11.177	0.638

PROBLEM DESCRIPTION

The selected problem considers a lid-driven square cavity with a fin intruded in its bottom center as shown in Fig. 1. The top surface of the cavity moves through the *x* axis direction and a constant temperature (T_{min}) is defined at it. However, the fin surface has a constant wall temperature (T_{max}) boundary condition. In Figure 1, *H* and *L* are the height and length of the cavity, H_1 and L_1 are the height and length of the fin, and *A* and A_f are the areas of the cavity and the fin, respectively. All exterior surfaces but the top surface are considered adiabatic and no slip condition is valid. The dimensionless velocities (u^* and v^*) and temperature (θ) in Figure 1 are defined as

$$u^* = \frac{u}{u_{max}},\ v^* = \frac{v}{u_{max}},\ \text{and}\ \theta = \frac{T - T_{min}}{T_{max} - T_{min}} \tag{10}$$

The area of the cavity is kept fixed as A = 1 m^2 and different fin areas are tested. The relation of cavity and fin areas is represented by the area fraction of the fin, ϕ, which is the ratio between the fin and cavity areas. In this study, three different values of ϕ are considered: 0.05, 0.10 and 0.15. A set of non-dimensional numbers are used to modify the relation between buoyancy and inertial forces. The Reynolds (Re), Rayleigh (Ra), Prandtl (Pr), and Richardson number (Ri), which are defined as

$$\mathrm{Re} = \frac{\rho_{nf} u_{\max} H}{\mu_{nf}},\ \mathrm{Ra} = \frac{g\beta_{nf}\Delta T L^3}{\nu_{nf}\alpha_{nf}},\ \mathrm{Pr} = \frac{\nu_{nf}}{\alpha_{nf}},\ \text{and}\ \mathrm{Ri} = \frac{\mathrm{Ra}}{\mathrm{PrRe}^2} \tag{11}$$

where α is the thermal diffusivity and ν is the kinematic viscosity. For different buoyancy forces considered in this study, the Rayleigh numbers are varied between 10^3 and 10^8. For different inertial forces, the Reynolds numbers are varied between 100 and 2000. Finally, the averaged Nusselt number (Nu_{avg}) is calculated through the integral of the local Nusselt number (Nu_L) over the fin surface.

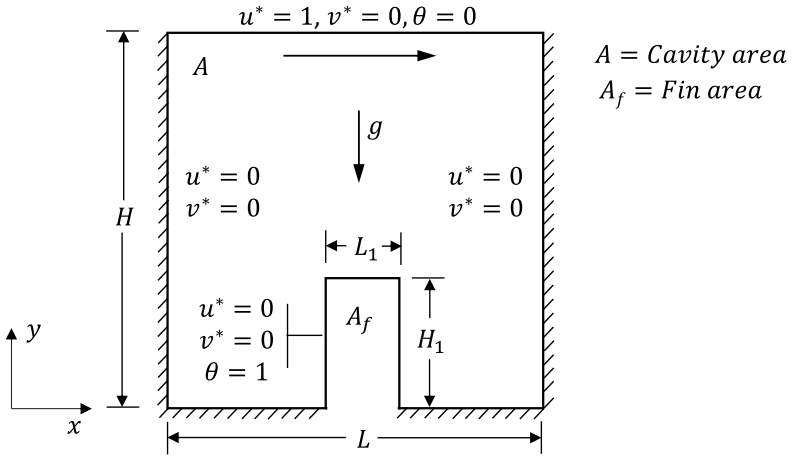

FIGURE 1. Schematic diagram of the cavity flow domain.

RESULTS AND DISCUSSION

In this section, numerical results of mixed convection fluid flow and heat transfer of the Al_2O_3-water nanofluid in a lid-driven square cavity with an intruded rectangular fin are presented. Firstly, the numerical method is evaluated by means of a comparison with other results of literature. A simulation of a convective flow in a partially heated rectangular enclosure filled with a nanofluid is performed. Here a simplified geometry is considered with the omission of intruded fin, which is identical to the geometry used by Oztop and Abu-Nada [17]. This geometry considers a heater on the left wall, which is half the size of wall height and maintained at a constant temperature ($T_{\max}$) higher than the right wall ($T_{\min}$). The top and bottom walls of the enclosure are considered insulated. Figure 2 shows a comparison between present numerical results with the results presented by Oztop and Abu-Nada for different Rayleigh numbers. Here averaged Nusselt number (Nu_{avg}) is estimated by integrating local Nusselt number over the heater surface. It is quite clear that present numerical results for a partially heated rectangular enclosure are in good agreement with the results available in literature [17].

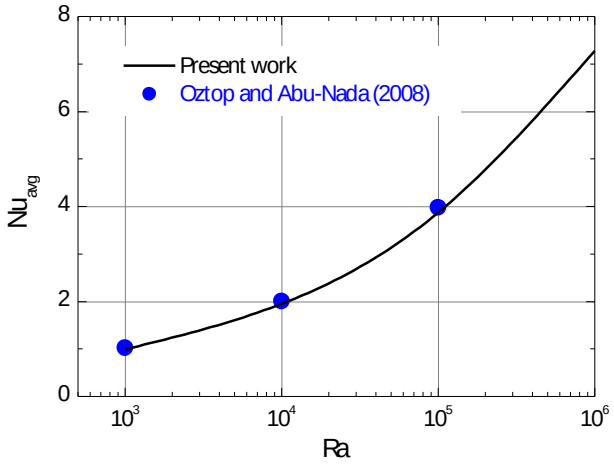

FIGURE 2. Averaged Nusselt number (Nu_{avg}) versus Rayleigh number (Ra) and a comparison with published data.

Effects of Reynolds and Rayleigh Numbers

The influences of Reynolds and Rayleigh numbers on the heat transfer between the fin and nanofluid are shown in Fig. 3. Here Figure 3a shows the effects of Reynolds numbers on the averaged Nusselt number (Nu_{avg}) as a function of fin aspect ratio (H_1/L_1) for the area fraction of 0.05 and Ra = 10^5. It is observed that as the fin aspect ratio increases from 0.1, heat transfer from the fin increases and it reaches at a maximum point and then decreases. Figure 3a reveals that higher Reynolds numbers provide higher heat transfer from the fin to the nanofluid. However, the trend remains the same for all Reynolds numbers primarily due to the forced convection, which can be verified by Fig. 3b as it shows the forced, mixed, and natural convection regimes as a function of Richardson, Reynolds, and Rayleigh numbers for 1% Al_2O_3-water nanofluid. As observed in Fig. 3b, the heat transfer regime for Ra = 10^5 and 500 < Re < 2000 is predominantly the forced convection as the Richardson number remains below 0.1. Figure 3a further reveals that the shape H_1/L_1 = 0.1 has a better heat transfer performance than the shape H_1/L_1 = 10 for all Reynolds numbers. For instance, at Re = 1000, the best shape for this case is obtained for an intermediate ratio of $(H_1/L_1)_{opt}$ = 0.46. For the optimal shape, it is obtained a Nu_{avg} = 24.5 which is nearly 32% and 110% higher than that obtained for the lowest and highest ratios of H_1/L_1, H_1/L_1 = 0.1 and H_1/L_1 = 10, respectively. Clearly, the increase of superficial area (at H_1/L_1 = 10) does not necessarily leads to an increase of heat transfer rate from the fin to the fluid flow. This heat transfer pattern indicates the importance of Constructal Design for optimization of convective flows problems.

The effects of Rayleigh numbers on the averaged Nusselt number for the optimum fin aspect ratio, $(H_1/L_1)_{opt}$, for the area fraction of the fin of 0.05 are shown in Fig. 3c. The averaged Nusselt number for the optimum fin aspect ratio is denoted as $Nu_{avg,max}$. Although increasing Reynolds number increases $Nu_{avg,max}$, the effects of Rayleigh number on $Nu_{avg,max}$ are negligible for the entire range of Reynolds numbers (100 to 2000) for Ra ≤ 10^5. Even for a high Rayleigh number (Ra = 10^6), change in $Nu_{avg,max}$ is small at high Reynolds number (for Re > 1000). This can be further explained by examining Fig. 3b, as it shows that at Re = 1000, changing Rayleigh number from 10^3 to 10^6 does not change the heat transfer regime. For all four cases of Rayleigh number, fluid motion is dominated by the forced convection. Conversely, for low Reynolds number (Re < 500), $Nu_{avg,max}$ increases with Rayleigh numbers as the fluid motion at high Rayleigh numbers is dominated by the mixed convection (0.1 < Ri < 10). For low Re, one can also increase the Richardson number over 0.1 by increasing Rayleigh number, which will shift the heat transfer regime from the forced to mixed convection and then to free convection, as shown in Fig. 3d where $Nu_{avg,max}$ values are shown for several higher Rayleigh numbers (Ra > 10^6). As observed, $Nu_{avg,max}$ increases with Richardson numbers, i.e. with Rayleigh numbers. Here heat transfer from fin's side walls increases as the buoyancy force increases with Rayleigh numbers due to the mixed convection. Clearly, the increase of Rayleigh number can also be effective in the maximization of the heat transfer for low Reynolds numbers (Re ≤ 100) due the buoyancy force

dominance in the flow. When comparing the cases for Ra = 10^3 to Ra = 10^5 for Re = 100, the increase in the heat transfer is over 20% as observed in Figure 3c.

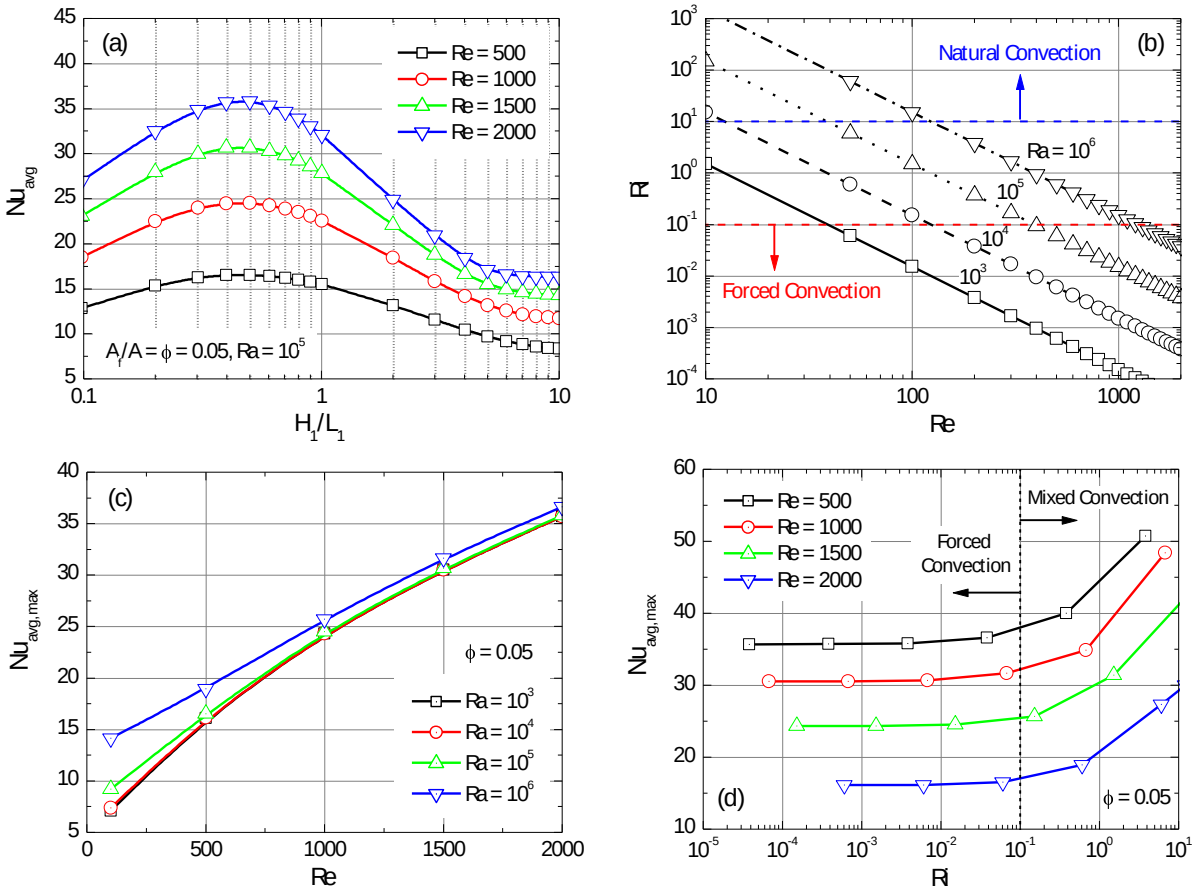

FIGURE 3. Influences of Reynolds and Rayleigh numbers: (a) Effect of fin aspect ratio (H_1/L_1) on Nu_{avg} for various Reynolds numbers at $\phi = 0.05$, (b) Richardson number as a function of Reynolds number for various Rayleigh numbers for Al_2O_3-water nanofluid, (c) Effect of Rayleigh numbers on averaged Nusselt number for the optimum fin aspect ratio, and (d) Effect of Richardson numbers on averaged Nusselt number for the optimum fin aspect ratio ($(H_1/L_1)_{opt}$).

Effect of Fin Aspect Ratio

The optimum fin aspect ratio is the one that maximizes the heat transfer between the fin and nanofluid. No great variation in the optimum fin aspect ratio is observed for the area fraction of the fin of 0.05 for Ra < 10^5, as presented in Fig. 4a as a function of Reynolds number. The optimum aspect ratio stands approximately at $(H_1/L_1)_{opt} = 0.46$ for all Rayleigh numbers when Re ≤ 1000. The increase of the aspect ratio creates recirculation zones in the corner of the cavity, decreasing the heat transfer between the fin and nanofluid. For higher Reynolds number (Re >1000), the optimum aspect ratio decreases slightly, which indicates that a wider fin will have better heat transfer than a taller fin. This is primarily due to forced convection (as illustrated in Fig. 3b for Ra < 10^5 and 500 < Re < 2000) as a taller fin will provide higher flow resistance in the cavity and fluid mixing will be interrupted. For higher Rayleigh number (≥10^7), the optimum fin aspect ratio increases with Reynolds numbers as the heat transfer process is shifting toward the mixed convection regime (see Fig. 3b). A close look to the case of Re = 1000, as illustrated in Figure 4b, depicts that the optimum fin aspect ratio increases at high Rayleigh number (≥10^7) due to the mixed convection. It indicates that the optimum fin aspect ratio is independent of Rayleigh and Reynolds numbers in the forced convection regime, while it is strongly influenced by Rayleigh and Reynolds numbers in the mixed convection

regime. By the means of Constructal Design method, the optimum fin aspect ratio for ϕ = 0.05 is found to be 0.46 for the selected set of degrees of freedom and constrains of Re < 1000 and $10^3 \le Ra \le 10^5$. For Ra = 10^7, the optimum fin aspect ratio is found to be between 0.46 and 0.56 for ϕ = 0.05 as shown in Figure 4a.

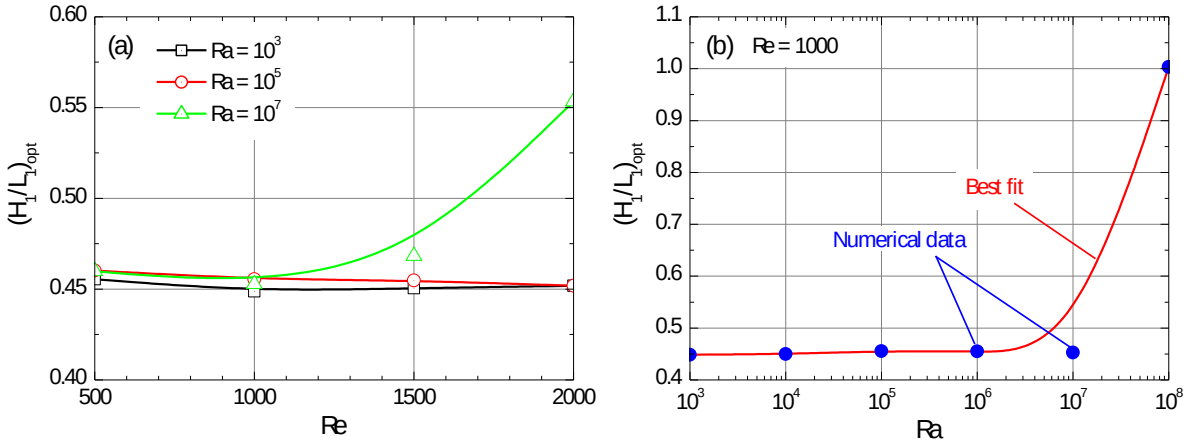

FIGURE 4. Optimum fin dimension as a function of (a) Reynolds number and (b) Rayleigh number for the area fraction of the fin of ϕ = 0.05.

Effect of Area Fraction of the Fin

The size of the fin with respect to the cavity will have an impact on overall heat transfer process. A larger fin may provide higher heat transfer for a fixed temperature gradient due to higher surface area. However, a lager fin may introduce a larger flow resistance due to larger area inside the cavity. Hence, it is important to see how the area fraction of the fin (ϕ) affects the heat transfer. The fin influence on $Nu_{avg,p}$ has been evaluated for two Raynolds numbers as depicted in Figure 5. Since the fin's perimeter changes with the area ratio, a special characteristic length is used here to estimate the spatial-averaged Nusselt number ($Nu_{avg,p}$). The characteristic parameter (p) is estimated by dividing the fin area with the cavity height. It is observed from Figure 5, the qualitative nature of $Nu_{avg,p}$ as a function of fin aspect ratio is almost identical for both Reynolds numbers. $Nu_{avg,p}$ increases with the fin aspect ratio and after the optimum the fin aspect ratio, $Nu_{avg,p}$ decreases for all the area fraction of the fin and for all these area fractions the optimum aspect ratio of the fin remains almost identical.

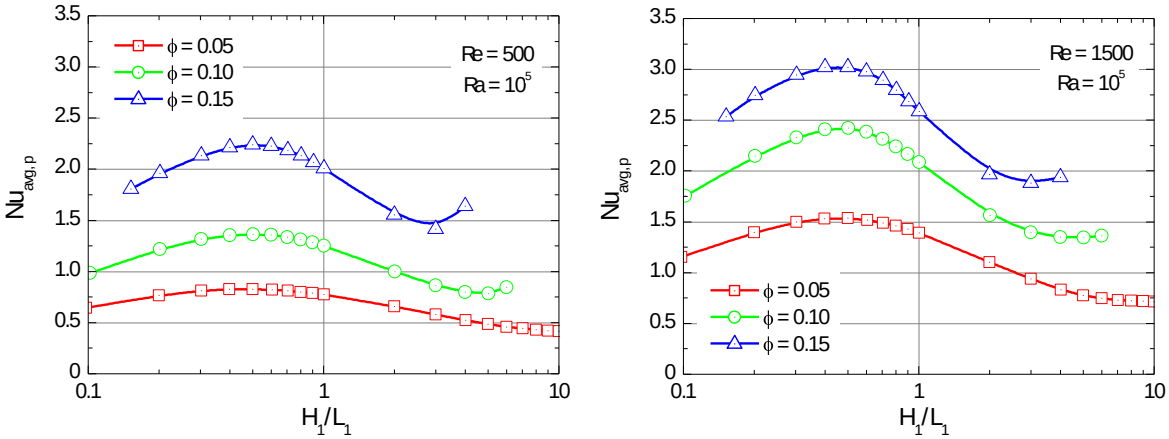

FIGURE 5. Effect of the area fraction of the fin on the spatial-averaged Nusselt number ($Nu_{avg,p}$) for different Reynolds numbers.

CONCLUSIONS

A numerical study has been performed to investigate the mixed convection flow of an Al_2O_3-water nanofluid in a square lid-driven cavity with an intruded rectangular fin and to optimize the fin geometry for maximizing the heat transfer using the Constructal Design method. Some important conclusions can be drawn from the obtained results, such as

- The resistance to the flow caused by the different aspect ratio and also the different area ratio have a big influence in the heat transfer inside the cavity;
- The buoyancy force only presents an effective influence in the heat transfer for high values Rayleigh number, where the convective flow becomes a mixed convection dominant flow;
- The variation of the Rayleigh and Reynolds numbers did not affect significantly the ranging of fin's optimum aspect ratio
- The optimum fin aspect ratio for $\phi = 0.05$ is found to be 0.46 for $Re < 1000$ and $Ra \leq 10^7$and for $Re > 1000$ and $Ra \geq 10^7$, the optimum fin aspect ratio is found to be within 0.46 and 0.56.

In the future, this study can be extended for higher Rayleigh and Reynolds numbers for other types of cavities and nanofluids.

REFERENCES

1. D. Poulikakos and A. Bejan, J. Heat Transfer. **105**, 652–655 (1983).
2. M. Peric, Numer. Heat Transfer, Part A. **24**, 213–219 (1993).
3. S. H. Tasnim, S. Mahmud and P. K. Das, Int. J. Numer. Methods Heat Fluid Flow. 12 (2002) 855–869.
4. S. Mahmud, P. K. Das and N. Hyder, Int. Commun. Heat Mass. **29**, 993–1003 (2002).
5. P. K. Das and S. Mahmud, Int. J. Therm. Sci. **42**, 397–406 (2003).
6. P. K. Das, S. Mahmud, T. H. Tasnim and A.K.M. S. Islam, Int. J. Numer. Methods Heat Fluid Flow. **13**, 1097–1122 (2003).
7. C. Biserni, L. A. O. Rocha, G. Stanescu and E. Lorenzini, Int. J. Heat Mass Transfer. **50**, 2132–2138 (2007).
8. G. Lorenzini, E. D. S. D. Estrada, E. D. dos Santos, L. A. Isoldi and L. A. O. Rocha, Int. J. Heat Mass Transfer. **83**, 75–83 (2015).
9. Y. Xuan and Q. Li, Int. J. Heat Fluid Flow. **21**, 58–64 (2000).
10. A. Bejan and M. Almogbel, Int. J. Heat Mass Transfer. **43**, 2101–2115 (2000).
11. G. Lorenzini, L.A.O. Rocha, Int. J. Heat Mass Transfer. **49**, 4552–4557 (2006).
12. A. Bejan, Int J. Heat Mass Transfer. **40**, 799–816 (1997).
13. H. C. Brinkman, J. Chem. Phys. **20**, 571–581 (1952).
14. J. Maxwell-Garnett, Philos. Trans. Roy. Soc. London Ser. A. **203**, 385–420 (1904).
15. R. L. Hamilton and O. K. Crosser, Ind. Eng. Chem. Fundamen. **1**, 187–191 (1962).
16. P. K. Das, X. Li and Z. S. Liu, Appl. Energy **87**, 2785–2796 (2010).
17. H. F. Oztop and E. Abu-Nada, Int. J. Heat Fluid Flow. **29**, 1326–1336 (2008).

ICME2015

International Conference on Mechanical Engineering 2015
(ICME 2015) 18 – 20 December, 2015, Dhaka, Bangladesh

Paper ID : 135

Natural Convection Flow of Cu-H_2O Nanofluid along a Vertical Wavy Surface with Uniform Heat Flux

Farjana Habiba[1, a)], Md. Mamun Molla[2, b)], M.A. Hakim Khan[3]

[1]*Department of Natural Science, Stamford University Bangladesh, Siddeswari Road, Dhaka-1217, Bangladesh*
[2]*Department of Mathematics & Physics, North South University, Dhaka-1229, Bangladesh*
[3]*Department of Mathematics, Bangladesh University of Engineering & Technology, Dhaka, Bangladesh*

[b)]Corresponding author: mamun.molla@northsouth.edu
[a)]farjanahabiba4@gmail.com

Abstract. A numerical study on natural convection flow of Cu-Water nanofluid along a vertical wavy surface with uniform heat flux has been carried out. The governing boundary layer equations are transformed into parabolic partial differential equations by applying a suitable set of variables. The resulting nonlinear system of equations are then mapped into a regular rectangular computational domain and solved numerically by using an implicit finite difference method. Numerical results are thoroughly discussed in terms of velocity and temperature distributions, surface temperature distribution, skin friction coefficient and Nusselt number coefficient for selected key parameters such as solid volume fraction of nanofluid (ϕ) and amplitude (a) of surface waviness. In addition, velocity vectors, streamlines and isotherms are plotted to visualize momentum and thermal flow pattern within the boundary layer region.

INTRODUCTION

Natural convection heat transfer plays an important role in various branches of engineering, for instance industrial cooling systems, nuclear reactors, solar collectors, transportation industries, biochemical applications, heat exchangers, electronic cooling devices and so forth. Therefore, numerous theoretical and computational investigations have been performed on natural convection heat transfer effect in regular surfaces for saving energy as well as getting better performance and minimizing operating costs. However, flow over roughened surface is very common in industries and in several heat transfer devices since irregular surfaces transfer more heat energy compared to flat surfaces. Thus effects of irregular surfaces on convective heat transfer enhancement have been carried out by several investigators.

Natural convection and mixed convection heat transfer along a vertical wavy surface have been investigated first time by Yao [1, 3] and Moulic and Yao [2] respectively. Later on, Molla et al. [4] studied natural convection flow along a vertical wavy surface with uniform surface temperature in presence of heat generation/ absorption. On the other hand, natural convection and mixed convection heat and mass transfer along a vertical wavy surface are studied by Jang et al. [21] and Jang Yan [22] respectively. Again, Molla and Hossain [5] studied the effect of radiation on mixed convection flow along a vertical wavy surface. Molla et al. [6] also studied natural convection flow along a vertical complex wavy surface with uniform heat flux. All these results showed that the surface geometry plays a vital role in heat transfer effect. In all research works illustrated above, air has been considered as working fluid which has a low thermal conductivity and thus the heat transfer effect is inherently limited. In order to improve the heat transfer performance of conventional fluids (such as water, oil, ethylene glycol), a large number of numerical and experimental research works were conducted by dispersing highly conductive micro-sized solid particles in base fluid since Maxwell's theoretical work was published more than 100 years ago. However, due to the large size and high density of particles, there is no perfect way to prevent the particles in clogging or settling out of suspension sedimentation. To

overcome those, efforts have been made to develop a new innovative type of heat transfer fluid termed as nanofluid by dispersing ultrafine solid particles (small enough not to clog or settle down) in base fluid. Choi [7] is the first who coined the term nanofluid in 1995 and Choi et al. [8] showed that the thermal conductivity of the fluid could be increased up to approximately two times with the addition of small amount (less than 1% by volume) of nanoparticles to conventional fluid. In almost two decades, a number of investigations related to heat transfer enhancement using nanofluids have been conducted.

Xuan and Li [9] introduced a procedure for preparing a nanofluid consisting of water and 5 volume% Cu nanoparticles and revealed a great potential of nanofluid in enhancing the thermal conductivity. Khanafer and Vafai [10] analysed thermophysical characteristics of nanofluids. They introduced several relative correlations for the thermophysical properties of nanofluids based on available experimental data. Khanafer et al. [11] investigated the problem of buoyancy-driven heat transfer enhancement of nanofluids in a two-dimensional enclosure. They analyzed four different models based on the physical properties of nanofluid for a range of Grashof numbers and volume fractions. It was found that the suspended nanoparticles substantially increase heat transfer rate for any given Grashof number. Santra et al. [12] conducted a study of heat transfer augmentation in a differently heated square cavity using copper-water nanofluid. Oztop and Abu-Nada [13] studied natural convection flow in nanofluid-filled partially heated rectangular enclosures with different types of nanoparticles. They found an increase in mean Nusselt number with the volume fraction of nanoparticles and an enhancement in heat transfer at low aspect ratio. Abu-Nada and Oztop [14] studied the influence of inclination angle and volume fraction of nanoparticle on natural convection heat transfer and fluid flow in a two-dimensional square enclosure filled with Cu-nanofluid and noticed a remarkable enhancement in heat transfer for copper nanoparticles.

Basak and Chamkha [15] investigated natural convection of various nanofluids (Cu-water, Al_2O_3-water, TiO_2-water) confined with square cavities with various thermal boundary layer based on visualization of heat flow via heat functions or heat lines. They found that Cu-water and Al_2O_3-water exhibit larger enhancement of heat transfer rates. Besides, Oztop et al. [16] exhibited computational analysis of non-isotherm temperature distribution on natural convection in nanofluid filled enclosures. Lin and violi [17] studied natural convection heat transfer of nanofluid in a vertical cavity. Application of nanofluids for heat transfer enhancement is inspected by Abu-Nada [18] while Wang and Mujumder [19] reviewed heat transfer characteristics of nanofluid. Meanwhile Eastman et al.[20] examined enhanced thermal conductivity through the development of nanofluids. The review of literature clearly indicates that the natural convection flow is mainly related to heated enclosures of regular surfaces filled with nanofluids. So attention has been given to analyze the effect of nanofluid on natural convection flow along a vertical wavy surface. Here Cu-water nanofluid is considered as working fluid due to the excellent thermo-physical properties of Cu-nanoparticles and low cost preparations as well. The thermal characteristics of nanofluid are extracted from Khanafer's model [10]. The Navier-Stokes and energy equations are coupled with nanoparticle volume fraction, Prandtl number and amplitude of surface waviness to describe the phenomenon systematically. These boundary layer equations are solved numerically by using a very efficient implicit finite difference method designated by Yao [1, 3]. Finally, solutions are obtained graphically having Prandtl number Pr=6.2 for various values of solid volume fraction of nanofluid(ϕ) and amplitude of wavy surface (a) in terms of velocity and temperature profiles, skin friction coefficient, surface temperature, average and total Nusselt number coefficients. Moreover, comparisons of all these results are shown between base fluid (pure water) and Cu-H_2O nanofluid. In addition, streamlines, isotherms and velocity vectors are plotted to observe the flow pattern within the boundary layer.

Nomenclature

a amplitude of wavy surface
C_f skin friction coefficient
Gr Grashof number
k thermal conductivity
$\hat{n}$ unit vector normal to the wavy surface
Nu Nusselt number
Pr Prandtl number
q_w uniform heat flux at the surface
T fluid temperature
(u,v) dimensionless velocity component

Greek symbols
β thermal expansion coefficient
θ, Θ dimensionless temperature function
μ viscosity
ρ density
ϕ solid volume fraction of nanofluid
α thermal diffusivity
ν kinematic viscosity
$\sigma(x)$ non-dimensional surface profile
τ shear stress
ψ stream function

MATHEMATICAL FORMULATION

A semi-infinite vertical complex wavy surface immersed in a nanofluid at the ambient temperature T_∞ is shown schematically in Fig. 1 allowing for the surface that is subjected to a uniform heat flux q_w normal to the surface. The boundary layer analysis outlined below allows the shape of the wavy surface, $\hat{\sigma}(\hat{x})$ to be arbitrary. But the detailed numerical work assumes that the surface exhibits a particular sinusoidal-based deformation from the flat surface. Therefore the wavy surface can be described by

$$\hat{y}_w = \hat{\sigma}(\hat{x}) = \hat{a}\sin\left(2\pi\,\hat{x}/L\right) \tag{1}$$

where L is the fundamental wavelength associated with wavy surface and $\hat{a}$ is the amplitude of surface waviness. The fluid oncoming to the surface is a water based nanofluid containing uniform copper nanoparticles. The nanofluid is sufficiently dilute with volume fraction ≤ 0.2 such that fluid is considered incompressible and the flow is also assumed to be laminar and steady. The base fluid (water) and the nanoparticles are assumed to be in thermal equilibrium and no slip occurs between them. The thermo-physical properties are assumed to be constant.

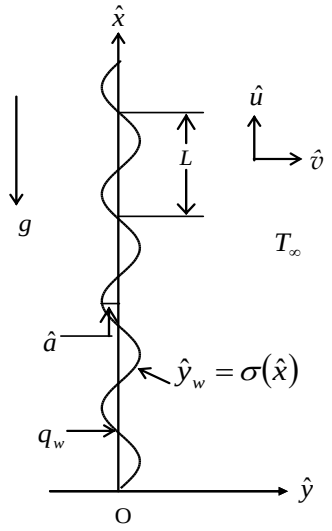

FIGURE 1. Physical model and coordinate system

Governing Equations

The mass, momentum and energy equations in dimensional form are as follows:

$$\frac{\partial \hat{u}}{\partial \hat{x}} + \frac{\partial \hat{v}}{\partial \hat{y}} = 0 \tag{2}$$

$$\hat{u}\frac{\partial \hat{u}}{\partial \hat{x}} + \hat{v}\frac{\partial \hat{u}}{\partial \hat{y}} = -\frac{1}{\rho_{nf}}\frac{\partial \hat{p}}{\partial \hat{x}} + \frac{\mu_{nf}}{\rho_{nf}}\left(\frac{\partial^2 \hat{u}}{\partial \hat{x}^2} + \frac{\partial^2 \hat{u}}{\partial \hat{y}^2}\right) + \frac{(\rho\beta)_{nf}}{\rho_{nf}}g\left(T - T_\infty\right) \tag{3}$$

$$\hat{u}\frac{\partial \hat{v}}{\partial \hat{x}} + \hat{v}\frac{\partial \hat{v}}{\partial \hat{y}} = -\frac{1}{\rho_{nf}}\frac{\partial \hat{p}}{\partial \hat{y}} + \frac{\mu_{nf}}{\rho_{nf}}\left(\frac{\partial^2 \hat{v}}{\partial \hat{x}^2} + \frac{\partial^2 \hat{v}}{\partial \hat{y}^2}\right) \tag{4}$$

$$\hat{u}\frac{\partial T}{\partial \hat{x}}+\hat{v}\frac{\partial T}{\partial \hat{y}}=\alpha_{nf}\left(\frac{\partial^2 T}{\partial \hat{x}^2}+\frac{\partial^2 T}{\partial \hat{y}^2}\right) \tag{5}$$

The boundary conditions are followed by Molla et al. [6]

Effective Thermo-Physical Properties of Nanofluid

Viscosity: $$\mu_{nf}=\mu_f/(1-\phi)^{2..5} \tag{6}$$

Density: $$\rho_{nf}=(1-\phi)\rho_f+\phi\rho_s \tag{7}$$

Heat capacitance: $$(\rho c_p)_{nf}=(1-\phi)(\rho c_p)_f+\phi(\rho c_p)_s \tag{8}$$

Thermal diffusivity: $$\alpha_{nf}=k_{nf}/(\rho c_p)_{nf} \tag{9}$$

Thermal conductivity: $$\frac{k_{nf}}{k_f}=\frac{k_s+2k_f-2\phi(k_f-k_s)}{k_s+2k_f+\phi(k_f-k_s)} \tag{10}$$

TABLE 1. THERMO-PHYSICAL PROPERTIES OF NANOFLUID

Properties	**Pure water**	**Cu**	**Al_2O_3**	**TiO_2**
C_p (J/kg K)	4179	385	765	686.2
ρ (kg/m^3)	997.1	8933	3970	4250
k (W/m K)	0.613	401	40	8.9538
β (1/K)	21×10^{-5}	1.67×10^{-5}	0.85×10^{-5}	0.9×10^{-5}

Transformation of Governing Equations

Following Molla et al. [6], a set of non-dimensional parameters is introduced to reduce governing equations into dimesionless form. Thus for both thermo-physical properties of nanofluid and $Gr\to\infty$ the reduced forms of non-dimensional equations are:

$$\frac{\partial u}{\partial x}+\frac{\partial v}{\partial y}=0 \tag{11}$$

$$u\frac{\partial u}{\partial x}+v\frac{\partial u}{\partial y}=\psi_1\left(1+\sigma_x{}^2\right)\frac{\partial^2 u}{\partial y^2}-\frac{\sigma_x\sigma_{xx}}{1+\sigma_x{}^2}u^2+\psi_2\frac{\sigma_x}{1+\sigma_x{}^2}\theta \tag{12}$$

$$u\frac{\partial \theta}{\partial x}+v\frac{\partial \theta}{\partial y}=\frac{1}{\mathrm{Pr}}\lambda\left(1+\sigma_x{}^2\right)\frac{\partial^2 \theta}{\partial y^2} \tag{13}$$

Here $\psi_1 = \dfrac{1}{(1-\phi)^{2.5}\left[(1-\phi)+\phi(\rho_s/\rho_f)\right]}$, $\psi_2 = \dfrac{(1-\phi)+\phi(\rho_s/\rho_f)(\beta_s/\beta_f)}{(1-\phi)+\phi(\rho_s/\rho_f)}$,

$\lambda = \dfrac{k_{nf}/k_f}{(1-\phi)+\phi(\rho c_p)_s/(\rho c_p)_f}$

The corresponding boundary conditions for the present problem take the form:

$$u = 0, \quad v = 0, \qquad \frac{\partial\theta}{\partial y} = -\frac{1}{\sqrt{1+\sigma_x^2}} \text{ at } y = 0 \tag{14}$$

$$u = 0, \qquad \theta = 0 \text{ as } y \to \infty \tag{15}$$

NUMERICAL METHODS

It has been introduced a set of transformations followed by Molla et al. [6] to obtain a parabolic form of dimensionless equations. Solution of this parabolic system is obtained by using an efficient finite difference method developed by Yao [1,3]. The diffusion terms in continuity, momentum and energy equations are discretized by central difference scheme while a backward difference scheme is adopted for the convection terms. The resulting system of tri-diagonal algebraic equations is solved by Gaussian elimination method. In computation, we start with the energy equation to determine Θ and then use momentum equation to calculate tangential velocity U. Finally the continuity equation is solved directly for normal velocity *V*. The computation is started at $X = 0.0$, and then marches upstream. The size of the computational domain is X=4.0 and Y=80.0. Here the grid size in the y direction is fixed at 0.01 while the step size in x direction is fixed at 0.005. After solving Θ , *U, V* and their derivatives, computations of local skin friction coefficient and Nusselt number are of practical interest.

The skin friction coefficients obtained by using the set of transformations are defined as

$$C_{f_x}(Gr)^{1/5} \Big/ \left\{2(5X)^{2/5}\right\} = \sqrt{1+\sigma_x^2}\,\frac{\partial U}{\partial Y}\Big]_{Y=0} \tag{16}$$

And the average Nusselt number is defined as

$$Nu_m\left(\frac{5X}{Gr}\right)^{1/5} = \frac{X^{1/5}\int_0^X \sqrt{1+\sigma_x{}^2}\,dX}{\int_0^X \sqrt{1+\sigma_x{}^2}\,X^{1/5}\Theta(X,0)dX} \tag{17}$$

RESULTS AND DISCUSSION

In the present study, numerical analysis of natural convection flow of nanofluid along a vertical wavy surface with uniform heat flux has been studied by developing a very efficient numerical code to carry out a number of simulations for a wide range of controlling parameters ϕ (solid volume fraction of nanofluid) and *a* (amplitude of surface waviness). It is to be mentioned here that $\phi = 0.0$ corresponds to the pure water having *Pr=6.2* following Khanafer et al. [11]. Uniform copper nanoparticles are used to analyze the effect of nanofluid on the momentum and thermal features. Moreover, three different nanoparticles Copper (Cu), Alumina (Al_20_3) and Titania (TiO_2) are used to compare their effects on the rate of heat transfer enhancement. Numerical results are presented and interpreted for effects 0f two controlling parameters on velocity and temperature profiles, surface temperature, skin friction coefficients and

Nusselt number coefficients. In addition, streamlines and isotherms are also drawn to analyze the flow pattern. All numerical results are obtained for selected values of ϕ ($0.0 \leq \phi \leq 0.2$). For the variation due to ϕ, a=0.3 is kept fixed.

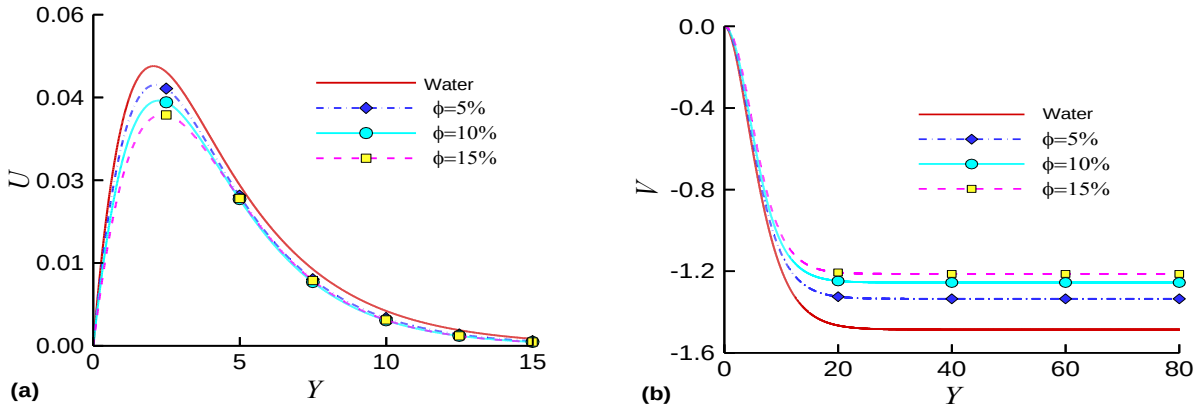

FIGURE 2. Tangential and normal velocity profiles for cu-water nanofluid with a=0.3, Pr=6.2.

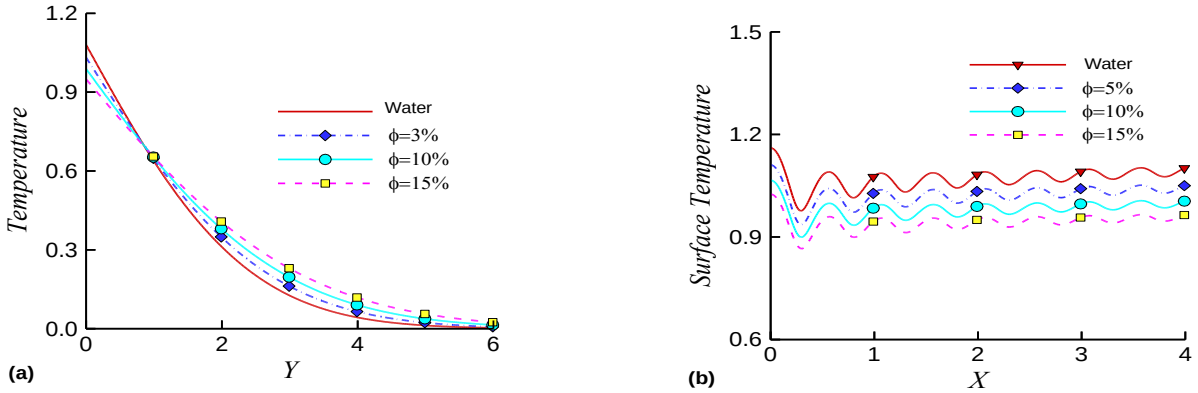

FIGURE 3. (a) Fluid temperature distribution (b) Surface temperature distribution for various values of ϕ with a = 0.3, Pr = 6.2.

The tangential and normal velocity distributions for different values of volume fractions of Cu-water nanofluid have been presented in Fig.2. It is seen that the tangential velocity decreases slightly inside the boundary layer while boundary layer thickness remains almost same with increasing values of solid volume fraction of nanofluid. This is due to the fact that the density and viscosity of nanofluid increases with increasing volume fraction and reduces the fluid flow. Fig.2. also shows that the normal velocity increases significantly away from the surface but no remarkable change is seen near the surface with increasing values of ϕ since ϕ increases energy transport through the fluid within the boundary layer.

The corresponding fluid temperature distribution and surface temperature distribution for different values of ϕ are shown in Fig.3. It is evident that the temperature distribution decreases with increasing ϕ near the surface. But at the position of Y=0.75, temperature profiles take a constant value and then increase with increasing values of ϕ. This is because heat transfer features of a nanofluid increase significantly with ϕ and consequently the movements of particles increase energy exchange rates in the fluid. Hence thermal dispersion is enhanced in the flow of nanofluid. It is also found that the development of surface temperature profiles are oscillatory and these oscillations become weaker as it moves away from the leading edge and decrease gradually along the surface with increasing volume fraction of nanoparticles.

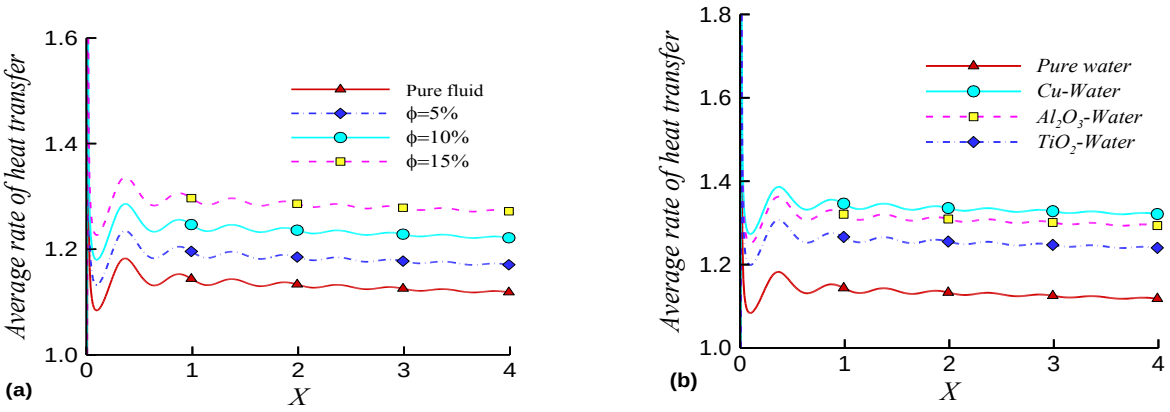

FIGURE 4. Average nusselt number for (a) various volume fractions of nanofluid (a =0.3), (b) various nanofluids (a = 0.3, ϕ =0.2)

The effects of solid volume fraction of nanofluid and several nanoparticles on average rate of heat transfer in terms of average Nusselt number are shown in Fig.4. It is observed that the average rate of heat transfer increases with increasing ϕ since thermal conductivity of nanofluid increases with ϕ. Though the viscosity of nanofluid increases with increasing ϕ and it has reverse effect on heat transfer enhancement rate. But it is clear from Table1. that thermal conductivity of Cu-nanoparticle is higher as compared to its viscosity for any percentage of nanoparticles. Also heat transfer rate is proportional to the temperature gradient which increases with increasing ϕ. Again, three types of nanoparticles such as Cu, Al_20_3 and TiO_2 are used to develop an assessment of their effects on average rate of heat transfer in terms of average Nusselt number for ϕ=0.2. It is found that nanofluid can enhance Nusselt number significantly. The lowest rate of heat transfer is obtained for TiO_2 due to the domination of conduction mode of heat transfer since TiO_2 has the lowest value of thermal conductivity as compared to Cu and Al_20_3 as given in Table1. However, the difference between two impacts of Al_20_3 and Cu nanoparticles on heat transfer enhancement is negligible. The thermal conductivity of Al_20_3 is approximately one tenth of Cu, as given in Table1. But Al_20_3 has a unique property that is its low thermal diffusivity. The reduced value of thermal diffusivity leads to high temperature gradients and therefore huge enhancement in heat transfers. The Cu nanoparticles have heavy thermal diffusivity and thus it reduces temperature gradient which affects the performance of Cu nanoparticles.

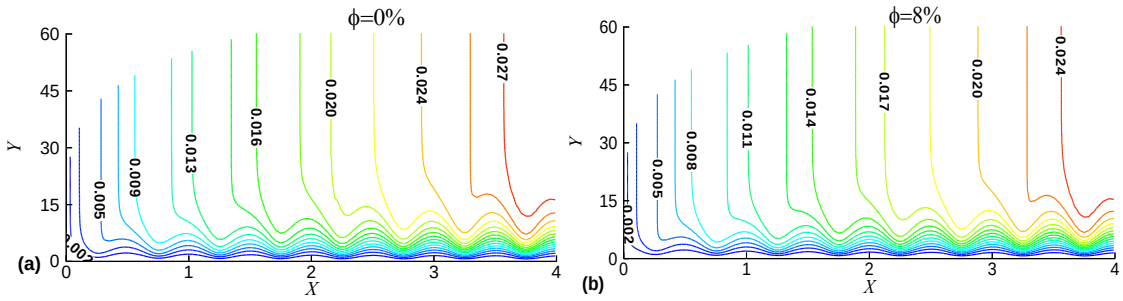

FIGURE 5. Streamline contours for various volume fractions (a = 0.3).

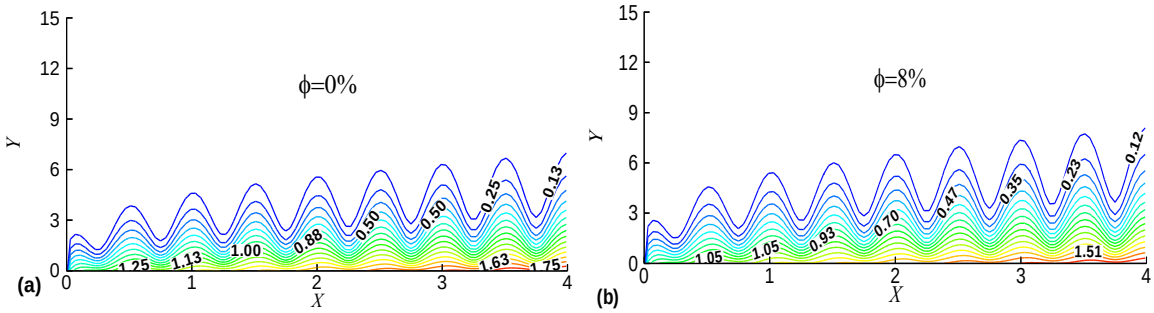

FIGURE 6. Isotherms for various volume fractions (a = 0.3).

Streamlines and isotherms for various volume fractions of Cu-nanoparticles are illustrated in Fig.5. and Fig.6 respectively. It is observed that the strength of flow decreases as ∅ increases. Here ψ_{max}=0.027 and 0.024 for ϕ=0.0 and 0.08 respectively. It is also noticed that the thermal boundary layer reduces for large values of ϕ. This is due to the fact that ϕ amplifies heat transfer enhancement rate. Moreover, huge viscous effect for large ϕ reduces flow rate. It is marked here that isotherm contours exhibit an oscillatory pattern because of amplitude of surface waviness.

The effects of solid volume fraction of nanofluid (ϕ) and amplitude of wavy surface (a) on surface shear stress in terms skin friction coefficients are displayed in Fig.7. It is clear that the skin friction coefficients exhibit a sinusoidal behaviour along the wavy surface. Skin friction coefficient decreases slightly with increasing ϕ as it increases fluid density and consequently reduces fluid motion. It is also seen that skin friction coefficient increases with increasing values of amplitude.

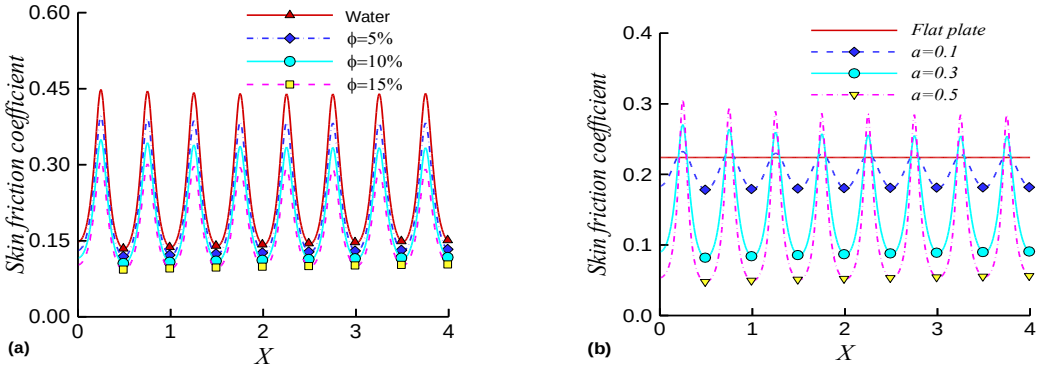

FIGURE 7. Skin friction coefficient for (a) various volume fractions (b) various amplitudes.

CONCLUSION

A numerical study has been performed to investigate the effect of solid volume fraction of Cu-nanoparticles as well as amplitude of surface waviness on natural convection boundary layer flow along a vertical wavy surface with uniform heat flux. Various volume fractions of nanoparticles and different values of amplitude of wavy surface have been considered for momentum and temperature fields as well as skin frictions and heat transfer rates. In addition, contours of streamlines, isotherms and velocity vectors are also drawn to analyze flow pattern. From the present study some findings are summarized as follows:

- The average rate of heat transfer increases with increasing values of solid volume fraction of nanoparticles. The Nusselt number for Cu-nanoparticles was found larger among others.
- The skin friction coefficient decreases with rising values of ϕ and increases with increasing values of a.

- Tangential velocity decreases with increasing values of both ϕ and a. Normal velocity increases slightly with increasing values of a near the surface when it decreases sinificantly away from the surface. It also increases with increasing values of ϕ throughout the boundary layer.
- The surface temperature decreases with increasing ϕ . Moreover, when ϕ increases, the fluid temperature decreases near the surface but increases slightly away from the surface.

REFERENCES

1. Yao, L.S., Natural convection along a vertical wavy surface, ASME J. Heat Transfer vol. 105, pp. 465–468 (1983).
2. Moulic, S.G. and Yao, L.S., Natural convection along a vertical wavy surface with uniform heat flux, ASME J. Heat Transfer vol. 111, pp. 1106–1108 (1989).
3. Yao, L.S., Natural convection along a vertical complex wavy surface, International Journal of Heat and Mass Transfer vol. 49, pp. 281-286 (2006).
4. Molla, M.M., Hossain, M.A. and Yao, L.S., Natural convection flow along a vertical wavy surface with uniform surface temperature in presence of heat generation/ absorption, International Journal of Thermal Sciences vol. 43, pp. 157-163 (2004).
5. Molla, M.M. and Hossain, M.A., Radiation effect on mixed convection laminar flow along a vertical wavy surface, International Journal of Thermal Sciences vol. 46, no. 9, pp. 926-935 (2007).
6. Molla, M.M., Hossain, M.A. and Yao, L.-S., Natural convection flow along a vertical complex wavy surface with uniform heat flux, Journal of Heat Transfer vol. 129, no. 10, pp. 1403-1407 (2007).
7. Choi, S.U.S., Enhancing thermal conductivity of fluids with nanoparticles, in: The proceeding of the 1995 ASME International Mechanical Engineering Congress and Exposition, San Francisco, USA, ASME, FED 231/MD 66, pp. 99-105 (1995).
8. Choi, S.U.S., Zhang Z.G., Yu W., Lockwood F.E., Grulke E.A., Anomalously thermal conductivity enhancement in nanotube suspensions, Appl. Phys. Lett. 79, pp 2252-2254 (2001).
9. Xuan, Y. and Li, Q., Heat Transfer enhancement of nanofluids, Int. J. of Heat and Fluid Flow vol. 21, pp. 58-64 (2000).
10. Khanafer, K. and Vafai, K., A critical synthesis of thermophysical characteristics of nanofluids, International Journal of Heat and Mass Transfer vol. 54, pp. 4410-4428 (2011).
11. Khanafer, K., Vafai, K. and Lightstone, M., Buoyancy-driven heat transfer enhancement in a two-dimensional enclosure utilizing nanofluids, International Journal of Heat and Mass Transfer vol. 46, pp. 3639-3653 (2003).
12. Santra, A.K., Sen, S. and Chakraborty, N., Study of heat transfer augmentation in a differently heated square cavity using copper-water nanofluid, International Journal of Thermal Sciences vol. 47, pp. 1113-1122 (2008).
13. Oztop, H.F. and Abu-Nada, E., Numerical study of natural convection in partially heated rectangular enclosures filled with nanofluids, Int. J. of Heat and Fluid Flow vol. 29, pp. 1326-1336 (2008).
14. Abu-Nada, E. and Oztop, H.F., Effect of inclination angle on natural convection in enclosures filled with Cu-water nanofluid, International Journal of Heat and Fluid Flow vol. 30, pp. 669-678 (2009).
15. Basak, T. and Chamkha, A.J., Heatline analysis on nanural convection for nanofluids confined within square cavities with various thermal boundary conditions, International Journal of Heat and Mass Transfer vol. 55, pp. 5526-5543 (2012).
16. Oztop, H.F., Abu-Nada, E., Varol, Y. and Al-Salem, K., Computational analysis of non-isotherm temperature distribution on natural convection in nanofluid filled enclosures, Superlattices and microstructures vol. 49(4), pp. 453-467 (2011).
17. Lin, K.C. and Violi, A., Natural convection heat transfer of nanofluid in a vertical cavity: Effects of non-uniform particle diameter and temperature on thermal conductivity, Int. J. of Heat and Fluid Flow vol. 31, pp. 236-245 (2010).
18. Abu-Nada, E., Application of nanofluids for heat transfer enhancement of separated flows encountered in a background facing step, Int. J. of Heat and Fluid Flow vol. 29, pp. 242-249 (2008).
19. Wang, X.-Q. and Mujumder, A.S., Heat transfer characteristics of nanofluid: a review, International Journal of Thermal Sciences vol. 46, pp. 1-19 (2007).

20. Eastman, J.A., Choi, S.U.S., Li, S., Thompson, L.J. and Lee, S., Enhanced thermal conductivity through the development of nanofluids, in: 1996 Fall meeting of the Materials Research Society (MRS), Boston, USA, pp. 3-11 (1997).
21. Jang, J.-H., Yan, W.-M. and Liu, H.-C., Natural convection heat and mass transfer along a vertical wavy surface, International Journal of Heat and Mass transfer vol. 46, pp. 1075-1083(20003).
22. Jang, J.-H. and Yan, W.-M., Mixed convection heat and mass transfer along a vertical wavy surface, International Journal of Heat and Mass transfer vol. 47, pp. 419-428(2004)

ICME2015

International Conference on Mechanical Engineering 2015
(ICME 2015) 18 – 20 December, 2015, Dhaka, Bangladesh

Paper ID : 140

Performance Study of a Diesel Engine Operated on Diesel-Tire Pyrolytic Oil Blends

Nirendra N Mustafi [a)], Q.M.Isteeaqul Alam and A.S.M.Rezaun Nabi

Department of Mechanical Engineering, Rajshahi University of Engineering & Technology, Kazla, Rajshahi – 6204, Bangladesh

[a)]Corresponding author: nnmustafi@ruet.ac.bd

Abstract. The aim of the present study is to evaluate the effect of tire-pyrolytic-oil (TPO)-diesel blends on engine performance of a test diesel engine. The raw TPO is first purified and refined and four test fuel blends, TPO10 (contains 10% TPO and 90% diesel fuel in volume basis), TPO30, TPO50, and neat diesel fuel, are prepared to test in a diesel engine. The TPO is derived from waste automobile tires through pyrolysis conversion technique. The crude TPO has a higher viscosity and sulfur content compared to diesel fuel which makes its direct use in diesel engine problematic. In the present work, the crude TPO is desulfurized and then distilled through vacuum distillation. In order to reduce the high sulfur content of the fuel, calcium oxide (CaO), activated Bentonite catalysts are used. Purified oil has a light yellowish color as compared to dark redish color of the raw oil. The fuel properties of the pyrolytic oil including higher heating value, flash point, pour point, viscosity and density are determined. Tests are performed in a single cylinder, four stroke, unmodified, and naturally aspirated DI diesel engine at different operating conditions. The experimental test results show that the DI diesel engine can run with the TPO-diesel fuel blends up to TPO50 without much sacrifice in engine performance. Performance characteristics such as engine power, engine torque, brake specific fuel consumption (bsfc) and exhaust temperature are experimentally investigated and the results are compared between diesel operation and diesel-TPO blend operations. From the experimental results, the blend B10 shows almost similar performance as compared with diesel fuel. TPO fuel content in the fuel blends do not have a significant impact on the engine power, and brake specific fuel consumption (bsfc) with respect to those of the reference diesel fuel.

INTRODUCTION

Searching of alternatives to petroleum fuels for internal combustion (IC) engines has been given prime importance among the energy researchers worldwide in recent times, due to the concerns of rapid depleting reserves and the associated environmental impacts. The waste-to-energy conversion for deriving useful fuels is becoming popular among researchers as it has multiple benefits. Biomass based fuels like methanol, ethanol, biogas, syngas etc. are some of the examples in which waste-to-energy is adopted, and these are used as alternate fuels for the IC engines successfully. Fuel production from waste tires have recently received renewed interests as their disposal is a problematic issue globally. The vehicle population of the world is rapidly increasing. Large countries like China and India have had an explosion in the number of private cars, and with more cars also more scrap tires follow. About 1.5 billion tires were sold worldwide in 2011-12 generating around 20 million tons of scrap tires [1]. These figures include all sorts of tires from car tires to truck tires and the huge tractor and earth moving tires. Waste tires are non-biodegradable materials and their thermo-mechanical properties make them difficult to be directly reused or recycled without mechanical or thermal pre-treatment. On the other hand, scrap tire disposing methods like the landfill, and direct burning can create serious human health and environmental hazards. Rubber from tire has a high heating value (35–40 MJ/kg) and this energy may be recovered by means of waste-to-energy processes which encompass thermo-chemical treatments such as gasification and pyrolysis for power and heat generation and/or fuel production without damaging the environment [2]. Pyrolysis plays a major role for waste tire valorization and is currently considered to be more attractive than other thermo-chemical processes because of its minor environmental impact with attractive fuel recovery [3]. In the pyrolysis process mainly the rubber polymers are heated at high

TABLE 1. Physio-chemical properties of tire derived pyrolytic oil (TPO) [7].

Elements (%wt)	Pyrolytic Oil	Diesel	Physical Properties	Pyrolytic Oil	Diesel
C	86.52	84-87	Density (kg/m^3)	943	820-860
H	9.35	12.8-15.7	Viscosity (cSt)	4.62	2.0-4.5
N	0.53	<3000 ppm	Flash point (°C)	≤30	>55
S	1.3	<7000 ppm	Pour point (°C)	-4	-30 to -40
Ash	0.2	0	Water (wt%)	N/A	≈80ppm
O	2.1	0	pH value	4.3	-
H/C	1.3	1.76-2.24	GCV (MJ/kg)	41.8	44-46

temperatures (300-700°C) in the absence of air (or oxygen) and decomposed to low molecular weight products, like liquid pyrolytic oil, syngas or char. The main interest lies on the production of liquid pyrolytic oil, known as tire pyrolytic oil (TPO) as this can be useful as alternative fuel for combustion in boilers, fueling in engines and turbines, upgrading to transportation fuels or as a renewable feedstock for chemicals and materials [4-5]. Typically, 60–75 wt.% of the feedstock is converted into oil depending on the type of feedstock [6].

The recovered tire pyrolytic oil is a dark-brown liquid having a strong acidic smell. The TPO used in this study is collected from the tire pyrolysis plant developed at RUET and its fuel properties in comparison to diesel are shown in Table 1 [7]. It shows that the TPO has almost similar fuel properties as compared to light diesel fuel. It has similar energy content like diesel fuel indicating possible useful application in diesel engines. It has also lower flash point than diesel flash point temperature and hence an extra care should be taken during storage and transportation. Direct application of TPO in engines is not suggestive due to its acidic nature, high sulfur content, high viscosity, high solid content, and poor ignition properties [6].

Tire derived pyrolytic oil, as an alternative diesel fuel, is one of the attractive research areas for the researchers in recent years. A number of studies have been found in the literature that investigated the effect of TPO fuel/diesel fuel blends on diesel engine performance and emissions [8-11]. The studies in the literature show different results from each other due to different properties of the test fuels and different test engine technology. It was reported that the use of TPO blends with diesel fuel at 20–40–60% and 75% concentrations in a DI diesel engine have shown similar performance and reduced emission as that of the same diesel engine operated in pure diesel. Some reported that HC, NO_X, CO and smoke emissions usually increased with the increasing TPO content in the diesel fuel blends. It has also been reported that the increasing TPO content in the diesel fuel blends can increase the maximum combustion pressure, rate of pressure rise and ignition delay. In addition, engine output power and engine torque decreased while brake specific fuel consumption increased with the increasing TPO content in the diesel fuel blends. In most studies TPO was not upgraded and raw TPO was simply blended with the diesel fuel. However, literature also suggests that engine performance and emissions can be improved by using the upgraded TPO blended with diesel fuel.

The objective of this present study is to upgrade the raw TPO available at RUET and to investigate the effect of this upgraded TPO fuel/diesel fuel blends on engine performance of a single cylinder DI diesel engine at different operating conditions. Results are usually compared with the results obtained for neat diesel operation.

EXPERIMENTAL SECTION

Production of TPO from Waste Automobile Tires

In the present work, an automobile tire is cut into a number of pieces. Thick rubber at the periphery of the tire is alone made into small chips. The tyre chips are washed**,** dried and fed into a fixed-bed fire-tube heating reactor chamber of the pyrolysis plant. Total experimental setup include a gravity feed type reactor feeder, two ice-cooled condensers, a N_2 gas cylinder, N_2 gas pre-heater, an air compressor, TPO collection bottle, char collection bag and thermocouples etc. At a distance of 30mm from the closed bottom of the reactor, a distributor plate is fitted to support the feedstock. Eight equally spaced stainless steel, 10mm diameter fire-tubes containing insulated electric coil of a total capacity 1.60 kW are fixed inside the reactor. The fire-tubes and pre-heated N_2 gas provided uniform heating across the cross-section of the reactor chamber. The experimental setup for tire pyrolysis plant is presented in Fig.1 [7]. The pyrolysis experiments are performed by varying the temperature within the range of 375-575°C at every 50°C for a particular feed size and vapor residence time. The reaction time is 50 min for every pyrolysis run.

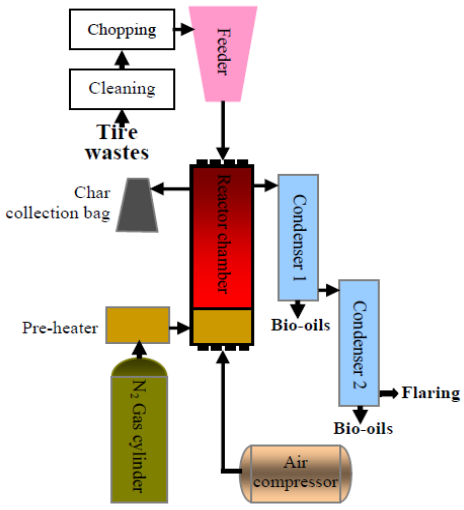

FIGURE 1. A fixed-bed fire-tube heating pyrolysis system [7]

Pyrolysis vapor product is passed through two sets of condenser tubes to quench into liquid and then collected into the glass bottles. The uncondensed gases are flared into the atmosphere. The char product is pushed out from the reactor chamber with the aid of compressed air supplied from the air compressor. Char is collected in the char collection bag. The fuel properties of the raw TPO have already been presented in Table 1[7].

Upgradation Process of Raw TPO

The raw TPO contains impurities like carbon particles, sulfur, and moisture. The liquid product is centrifuged at 3000 rpm for 15 min to remove heavy solid condensate and impurities. Refining and desulfurization process of the raw pyrolytic oil used in this study (Fig. 2) include a few stages [12]: (1) hydro-sulfuric acid (H_2SO_4) treatment, (2) activated bentonite–Calcium Oxide (CaO) treatment, (3) vacuum distillation, (4) Oxidative desulfurization, and (5) washing and drying. All of these stages improve chemical and physical properties of the fuel. The first three stages are known as the hydro-sulfuric acid (H_2SO_4) treatment, which reduces the impurities and sulfur level of the TPO. Initially, the raw TPO is subjected to 8% by weight of H_2SO_4, stirred well by a mechanical stirrer during 4 h and left to settle for 40 h while the temperature of the mixture is maintained at 50°C during stirring process. The mixture was found in two layers 40 h later. The top layer is the clear viscous oil, and the bottom layer is the non-viscous acidic sludge. The clear viscous oil is taken for the activated bentonite–Calcium Oxide (CaO, lime) treatment. Secondly, activated bentonite (100 g activated bentonite for every 1000 ml of acid treated pyrolytic oil) and CaO (50 g for every 1000 ml of acid treated pyrolytic oil) are added to the acid treated pyrolytic oil and mixed by a mechanical stirrer for about 4 h. Temperature of the mixture is maintained at 70°C during stirring process. The contents are kept for 24 h for the settling of the sludge. Whole contents are then filtered by filter-cloth to obtain healed pyrolytic oil for the vacuum distillation. Thirdly, the healed pyrolytic oil is distilled by vacuum distillation.

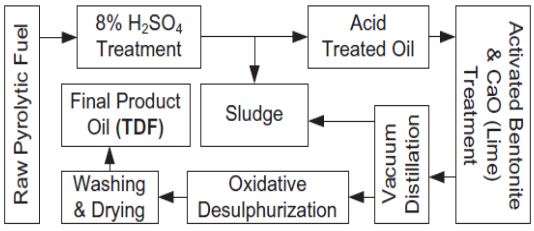

FIGURE 2. The upgradation process of raw TPO [12]

Distilled pyrolytic oil is similar to commercial diesel fuel but still has a high sulfur content. Fourthly, the distilled pyrolytic oil is subjected to the oxidative desulfurization process to reduce the sulfur content more. For the oxidative desulfurization process, thousand milliliters of distilled pyrolytic oil are treated with 100 g of a mixture containing 10 g of 98% formic acid and 20 g of 30% hydrogen peroxide. The mixture is stirred and heated at 60°C for 2 h [12]. Whole mixture is left for settling down overnight. The white precipitate is found between upper (clear oil) and lower layers. The clear pyrolytic oil is separated by separation funnel and washed with distilled water (200 ml distilled water for every 1000 ml of clear oil). Finally, the clear pyrolytic oil is heated up to 110°C during 30 min to remove the moisture. The final product, the upgraded TPO is found to have a production yield of about 25% by volume of its initial volume of raw TPO.

Testing Fuel Properties of Upgraded TPO and the Commercial Diesel

Different fuel properties are evaluated in the lab after the upgradation of raw TPO and the results are presented in Table 2 in comparison to the raw TPO and the conventional diesel fuel. The diesel is purchased from the local supplier and blends are made with the upgraded TPO in various proportions. Four TPO fuel/diesel fuel blends are prepared for engine operation: TPO10 (10% TPO & 90% diesel by vol.), TPO20, TPO30 and TPO50. It is observed that TPO blended easily with reference diesel fuel.

TABLE 2. Fuel properties of the upgraded TPO

Properties	Raw TPO	Upgraded TPO	Diesel fuel
Density (kg/m^3)	975	871	835
K. Viscosity (cSt)	4.2	3.2	2-3
GCV (MJ/kg)	41.8	45.8	46.5
Flash point (°C)	<30	36	>55

Engine Test Procedure

A series of tests is undertaken to investigate the influence of TPO fuel/diesel fuel blends in a single cylinder, 4-stroke, water-cooled, naturally aspirated, DI diesel engine. The test engine details are presented in Table 3. Engine torque is measured by the eddy current dynamometer connected to the engine and speed is measured by a tachometer. The amount of fuel consumption is determined by using a volume burette. The amount of air consumption is calculated by using an air-drum unit equipped with an orifice meter and the exhaust gas temperature is measured by a K-type thermocouple. The engine is run first on neat diesel fuel and on diesel fuel/TPO fuel blends afterwards. For every run, data are recorded after reaching the steady state of test condition. At the end of the tests, the engine is run with neat diesel fuel for a while to flush the engine. The engine is operated on two different conditions: constant speed (at around 910 rpm) with varying loads (17N to 38N) and constant load with varying speeds (800 to 1200 rpm). The experimental uncertainty in the various measurements is within ±5% of the presented values.

TABLE 3. Test engine details.

Model	Peter diesel engine
General	single cylinder, 4-stroke, water-cooled, naturally aspirated, DI diesel engine
Bore × Stroke	80 mm × 110 mm
Swept volume	553 cc
Compression ratio	16.5:1
Rated output	4.48 kW@1800 rpm
Fuel injection time	24°bTDC
Fuel injection pressure	14 MPa (at low rpm) and 20 MPa (at high rpm)

RESULTS AND DISCUSSION

The brake specific fuel consumption (bsfc) with respect to engine load and speed for four different TPO/diesel fuel blends as compared to neat diesel fuel are presented in Figs. 3(a) and 3(b), respectively. It can be mentioned that the reported results (bsfc, exhaust temperature, brake thermal efficiency, power etc.) are just the average values of several observations considered for each run. It can be seen from the figures that although the blended fuels maintain a similar trend to the neat diesel, the value of bsfc of the blended fuels is always higher than that of neat diesel operation for the entire engine load and speed ranges used in this study. This is due to the fact that the blended fuels do not burn properly having higher viscosity and lower heating values as compared to neat diesel fuel.

The brake thermal efficiency (η_b) as a function of engine load and engine speed for different engine fueling conditions is presented in Fig. 4(a) and 4(b), respectively. It can be observed from the figures that the brake thermal efficiency for the blended fuels is always lower than that of neat diesel operation. The efficiency values have a peak at the maximum load point used in this study. The variation of the result between the blended fuels and the diesel fuel is found to be minimum at this point. The η_b for neat diesel at this maximum load is 21.75%, while with TPO10 and TPO50, η_b is 21.4% and 20.5% respectively, which indicates that at high loads, TPO blends have little effect on η_b. On the other hand, as the engine speed increases, the η_b increases up to a value of 910 rpm and then decreases.

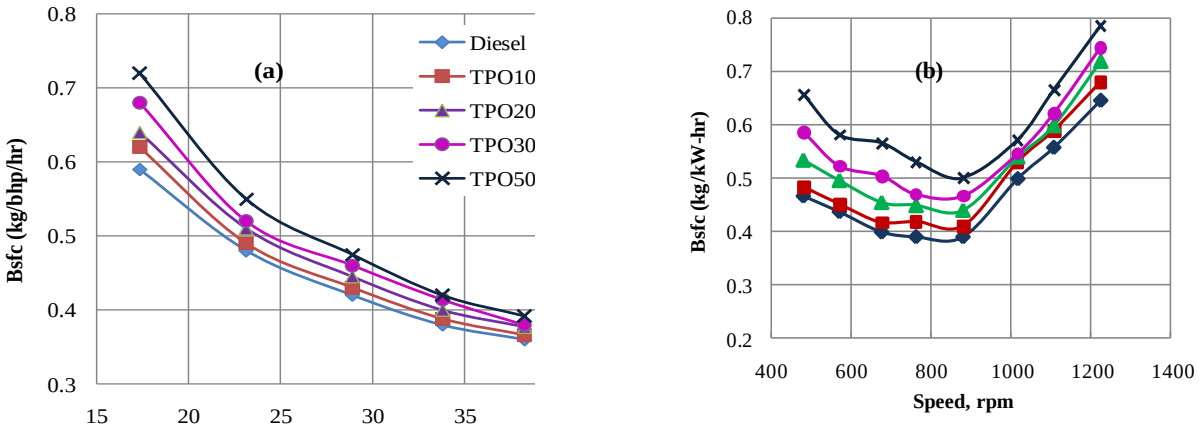

FIGURE 3. Brake specific fuel consumption as a function of (a) engine load and (b) engine speed for neat diesel and different TPO-diesel fuel blends.

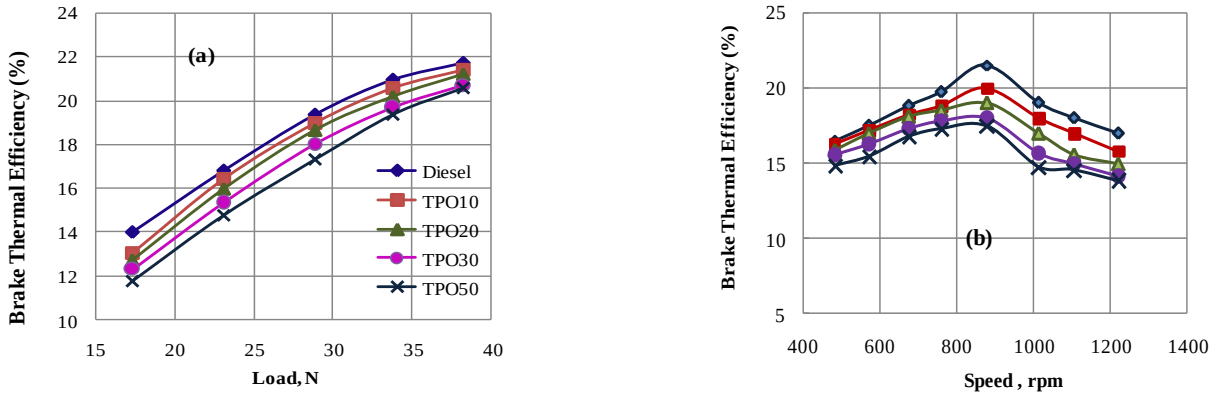

FIGURE 4. Brake thermal efficiency (%) as a function of (a) engine load and (b) engine speed for neat diesel and different TPO-diesel fuel blends.

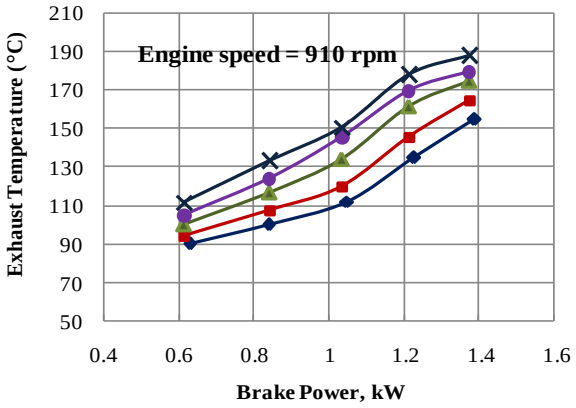

FIGURE 5. Engine exhaust temperature as a function of engine brake power output (or load) for neat diesel and different TPO-diesel fuel blends.

The trend of η_b curves for TPO-diesel fuel blends at varying speeds follows the trend obtained for neat diesel, but with lower values. The ηb is reduced for the blended fuels as the percentage of TPO in the blends is increased resulting from the poor combustion (having lower cetane number) and lower energy content of the fuels.

Researchers have reported in [13] that the ignition delay for the TPO blends usually increases as the percentage of TPO in blends increases in addition to the longer combustion durations.

CONCLUSIONS

Tire derived pyrolytic oil is upgraded for lowering its viscosity and the sulfur content. The fuel properties are determined before and after the upgradation. A diesel engine is operated on neat diesel fuel and on four TPO-diesel fuel blends. The findings may be summarized as follows:

- The upgraded TPO has a production yield of about 25% by volume of its initial raw volume.
- The upgraded TPO is found to have a transparent, clear and light color and its density decreased by 10%, viscosity decreased to the range of diesel fuel, flash point increased to 36°C and the energy content increased by 7% as compared to its raw values.
- The DI diesel engine can run with the TPO fuel blends up to TPO50 without significant sacrifices in engine power output and efficiency. Brake specific fuel consumption (bsfc) usually increases with higher proportions of TPO in TPO-diesel blends, but the effect is lowered at higher engine loads. On the other hand, as engine speed increases, the bsfc for either diesel or TPO-diesel blends increases proportionately. However, at a speed of around 900 rpm, bsfc values show the minimum for all the cases. The highest bsfc values are obtained for TPO50 fuelling. The η_b for neat diesel at maximum load used in this study is 21.75%, while with TPO10 and TPO50, η_b is 21.4% and 20.5% respectively, indicating at higher load, TPO blends have little effect on η_b. The T_{exh} increases as the engine load increases and as the proportion of TPO in TPO-diesel blends. For the blends, T_{exh} is always higher than neat diesel and its value increases by 6 to 20% for different blends as compared to neat diesel operation.

REFERENCES

1. European tyre and rubber manufactures' association (ETRMA). Annual report 2011–2012.
2. G. Harrison and A.B. Ross, Fuel **75**, 1009-1013 (1996).
3. Martinez J, Puy N, Murillo R, Garcia T, Navarro M, Mastral A., Renew. Sust. Energ. Rev. **23**, 179–213 (2013).
4. Bridgwater A.V., Biom. Bioenerg. **38**, 68–94 (2012).
5. Chiaramonti D, Oasmaa A, Solontausta Y, Renew. Sust. Energ. Rev. **11**, 1056–1086 (2007).
6. Bert V. B., Elmar H., Jan F., Appl. Energ. **102**, 190–197 (2013).
7. Islam M. R., Parveen M., Haniu H. and Islam Sarker M. R., Int. J. Environ. Sci. Dev. **1**, 89-96 (2010).
8. Kennedy Z.R, Rathinaraj D., J. Inst. Eng. **88**, 13-18 (2007).
9. Murugan S, Ramaswamy M.C., Nagarajan G., Fuel **87**, 2111–2121 (2008).
10. Murugan S, Ramaswamy M.C., Nagarajan G., Fuel Process Technol. **89**, 152–159 (2008).
11. Ilkılıc C., Aydın H., Fuel Process Technol. **92**, 1129–1135 (2011).
12. Og˘uzhan D., M. Bahattin Çelik, Bülent Ö., Fuel **95**, 340–346 (2012).
13. Murugan S, Ramaswamy M.C., Nagarajan G., Fuel Process Technol. **90**, 67–74 (2009).

ICME2015

International Conference on Mechanical Engineering 2015
(ICME 2015) 18 – 20 December, 2015, Dhaka, Bangladesh

Paper ID : 144

Numerical Investigation of Natural Convection of Nanoparticle Enhanced Ionic Liquids (NEILs) in Enclosure Heated from Below

Titan C. Paul[1], AKM M. Morshed[2] and Jamil A. Khan[1,a)]

[1]*Department of Mechanical Engineering, University of South Carolina, Columbia, SC, USA*
[2] *Department of Mechanical Engineering, Bangladesh University of Engineering & Technology (BUET)*

[a)]Corresponding author: khan@cec.sc.edu

ABSTRACT. The paper presents the numerical simulation of natural convection heat transfer of Al_2O_3 nanoparticle enhanced N-butyl-N-methylpyrrolidinium bis{trifluoromethyl)sulfonyl} imide ([C_4mpyrr][NTf_2]) ionic liquid. The simulation was performed in three different enclosures (aspect ratio: 0.5, 1, and 1.5) with heated from below. The temperature dependent thermophysical properties of base ionic liquids (ILs) and nanoparticle enhanced ionic liquids (NEILs) were applied in the numerical simulation. The numerical results were compared with the experimental result. The numerical results show that at a certain Rayleigh number NEILs has a lower Nusselt number compared to the base IL which are consistent with the experimental results. But the percentage of degradation is much less on the numerical results compared to the experimental. However the numerical results match well with the predicted model of using thermophysical properties of NEILs. From these observations it can be concluded that the extra degradation in the experimental results may occur due the particle-fluid interaction, clustering and sedimentation of nanoparticles.

Keywords: Nanoparticle Enhanced Ionic Liquids (NEILs); Nanoparticle; Numerical Simulation; Nusselt number; Rayleigh number.

INTRODUCTION

High temperature heat transfer fluids (HTF) have the diversified applications such as geothermal heat pumps, pharmaceutical and polymer processing, and concentrated solar power (CSP). Thermophysical properties and thermal performance of the HTF can be enhanced by dispersing small amount of nanoparticles on the base fluids [1]. Ionic liquids (ILs) are organic salts which are liquid at room temperature and it is considered as a potential candidate for HTF [2]. Dispersing nanoparticles on the base ILs termed as the nanoparticle enhanced ionic liquids (NEILs) [3-9]. E. B. Fox et al. [3] have studied different nanoparticles effect on thermophysical properties such as thermal conductivity, viscosity, and thermal stability of NEILs and reported that whisker-shaped Al_2O_3 NEILs show highest thermal conductivity enhancement. Enhanced thermal conductivity and heat capacity of several imidazolium and pyrrolidinium ILs based nanofluids was reported by Nieto de Castro et al. [4-5]. T. C. Paul et al. [7-8] have reported ~6% enhancement of thermal conductivity of NEILs containing 1-butyl-3-methylimidazolium bis{(trifluoromethyl)sulfonyl}imide ([C_4mim][NTf_2]) IL and 1 wt% Al_2O_3 nanoparticles and enhanced forced convection heat transfer coefficient of NEILs compared to base ILs. B. Wang et al. [9] performed their studies on nanofluids containing 1-butyl-3-methylimidazolium hexafluorophosphate ([Bmim][PF_6]) IL and gold nanoparticle and reported enhanced thermal conductivity. Most of the previous study was the thermophysical properties of NEILs.

The experimental investigation of natural convection of NEILs was reported by T. C. Paul et al. [10]. Numerical and experimental studies of nanofluids natural convection are still paradoxical. Numerical investigation of water based nanofluids were reported by several researchers [11-14]. K. Khanafer et al. [11] at first studied numerically the natural convection of nanofluids in a two dimensional enclosure and reported enhanced heat transfer of nanofluids compare to base fluid. K. S. Hwang et al. [12] numerically studied the natural convection of Al_2O_3 nanofluids and reported decreased Rayleigh number with increasing nanoparticle volume fraction. S.-K. Choi et al. [13] reported the deterioration of the natural convection of CuO-water nanofluids which correlates well with the experimental results.

W. Rashmi et al. [14] studied numerically the natural convection heat transfer of Al_2O_3-water nanofluids in a cavity heated by side wall which was found consistent with the experimental results of Putra et al. [15].
In the present paper, numerical analysis of natural convection heat transfer of nanoparticle enhanced ionic liquids (NEILs) by using commercially available Computational Fluid Dynamics (CFD) package, FLUENT, are presented. The NEILs was based on Al_2O_3 and N-butyl-N-methylpyrrolidinium bis{trifluoromethyl)sulfonyl} imide ($[C_4mpyrr][NTf_2]$) ionic liquid. The numerical results of natural convection were compared with the experimental results of literure [10].

NUMERICAL SIMULATION

Geometry

Numerical simulations of natural convection study of NEILs are straight forward in laminar region. The numerical simulation was performed in three enclosures with different aspect ratios (AR-0.5, 1.0, and 1.5) and the dimension of the enclosures are 50×50×25 mm, 50×50×50 mm, and 50×50×75 mm (length×width×height) which are same as the experimental geometrical configuration. The geometry of the natural convection numerical enclosure is shown in Fig. 1. The natural convection enclosure geometry was generated in GAMBIT 2.4.6 (Gambit 2007) and there were 12500 (500×250), 250000 (500×500), and 375000 (500×750) mesh elements for AR-0.5, 1.0, and 1.5 respectively.

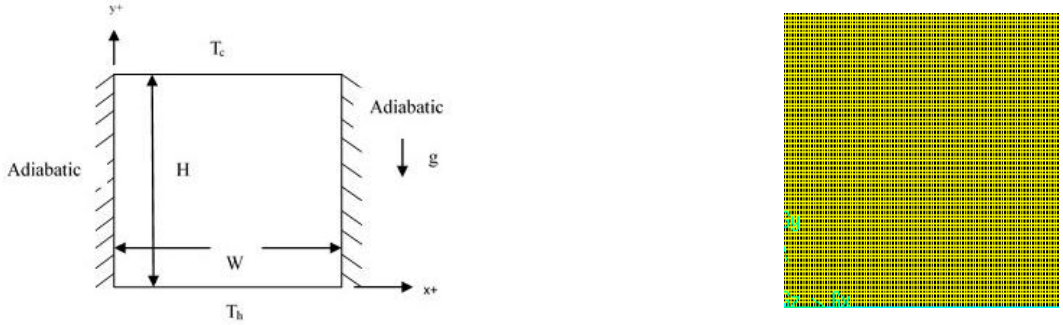

(a) (b)

FIGURE 1. (a) Schematic and coordination system of natural convection configuration (b) The uniform grid of the natural convection enclosure

Boundary condition

The boundary conditions of the numerical simulation are simple bottom wall as a hot surface with constant temperature, top wall as a cold surface with constant temperature, and other walls (left and right) are at adiabatic condition. Also the no slip boundary condition of the all wall was considered. The enclosures are filled with base ILs and NEILs, and NEILs is considered as a single fluid with temperature dependent thermophysical properties.

Simulation Methodology

The numerical problem was solved by using two-dimensional ANSYS Fluent CFD program (FLUENT 2011). NEILs is the combination of ILs and nanoparticles, here the NEILs was considered as a single fluid with thermal equilibrium of nanoparticles and ILs. Also, no relative velocity between nanoparticles and ILs was considered. The governing equations with single phase approximation are as follows:
Continuity equation:

$$\frac{\partial \rho}{\partial t} + \nabla.\left(\rho \vec{V}\right) = 0 \quad (1)$$

Momentum equation:

$$\frac{\partial \rho V}{\partial t} + \nabla.\left(\vec{V}.\vec{V}\right) = -\nabla P + \mu \nabla^2 V - \rho g \beta (T - T_c) \quad (2)$$

Energy equation:

$$\frac{\partial T}{\partial t} + V.\nabla \mathrm{T} = \frac{\partial}{\partial \mathrm{x}}\left(\frac{k}{\rho C_p}\frac{\partial T}{\partial t}\right) + \frac{\partial}{\partial \mathrm{y}}\left(\frac{k}{\rho C_p}\frac{\partial T}{\partial t}\right) \quad (3)$$

The CFD program solves the governing equations by converting those into algebraic equations with control volume theory technique. The laminar viscous model was used with SIMPLE scheme, Green-Gauss Cell Based gradient, and the convergence criteria of the residuals of governing equation variables are 1×10^{-6}. In the pressure and velocity coupling PRESTO was selected as pressure. For momentum and energy equation Second Order Upwind was selected for higher accuracy. All of the temperature dependent thermophysical properties were provided in the materials section. From the applied heat in the bottom wall the total surface wall heat flux was computed by using the area-weighted average surface integrals. The natural convection heat transfer coefficient was calculated by using heat flux and temperature difference between hot and cold walls.

$$h = \frac{\mathrm{q}^{"}}{(T_h - T_c)} \quad (4)$$

where, h is the heat transfer coefficient, $\mathrm{q}^{"}$ is the heat flux computed from the simulation, T_h and T_c are the temperature of the hot and cold surface respectively. The dimensionless Nusselt (Nu), Prandtl (Pr), Grashof (Gr), and Rayleigh (Ra) number are calculated from the following equations:

$$Nu = \frac{hH}{k_f} \qquad Pr = \frac{\nu_f}{\alpha} \qquad Gr = \frac{g\beta\Delta T H^3}{\nu_f^2} \quad (5)$$

$$Ra = Gr.Pr \quad (6)$$

where, H is the height of the enclosure, k_f is the thermal conductivity, ν_f is the kinematic viscosity, $\alpha(=\frac{k_f}{\rho C_p})$ is the thermal diffusivity, β is the volume expansion coefficient, ρ is the density, C_p is the heat capacity of fluid, ΔT is the temperature difference between hot and cold surface fluid, g is the gravitational acceleration, All the fluid properties were evaluated at the average ($T_{av} = \frac{T_c+T_h}{2}$) of the heated and the cooled surface temperature.

RESULTS AND DISCUSSION

Before performing simulation with ILs and NEILs a grid independence study was carried out with different grid sizes using water thermophysical properties. For each aspect ratio four different grid size simulation was performed and it was found that the Nusselt number variation is less than 1% of the final grid size with the previous grid size. Finally, with the sleeted grid size the simulation results were compared with the experimental results from literature [10]. The Fig. 2 shows the simulation results match well with the experimental results of enclosures with aspect ratio 1 and 1.5 and there is no experimental data for aspect ratio 0.5 which is performed for the parametric study to see the natural convection behavior at aspect ratio less 1.

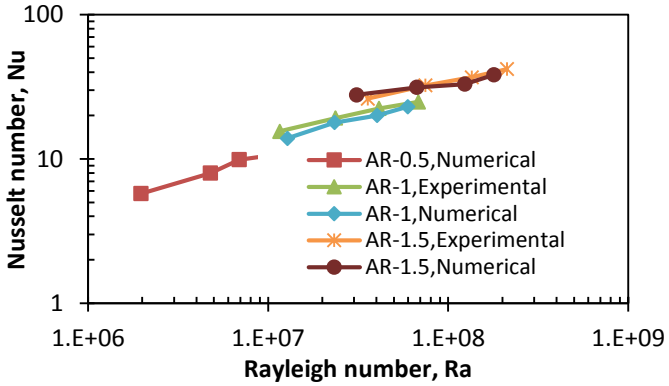

FIGURE 2: Comparison of numerical and experimental data of natural convection of water

After being confident with the simulation of water, numerical simulation was performed for [C_4mpyrr][NTf_2] IL and different concentration (0.5, 1.0, and 2.5 wt%) of Al_2O_3 NEILs. Fig. 3 (a-c) represents the natural convection heat transfer behavior of NEILs and compared with the base IL. It is clear from the Fig. 3 that at a certain Rayleigh number NEILs shows the lower Nusselt number compare to the base IL which are consistent with the experimental results [10]. But the percentage of degradation is much less in the numerical results compare to the experimental.

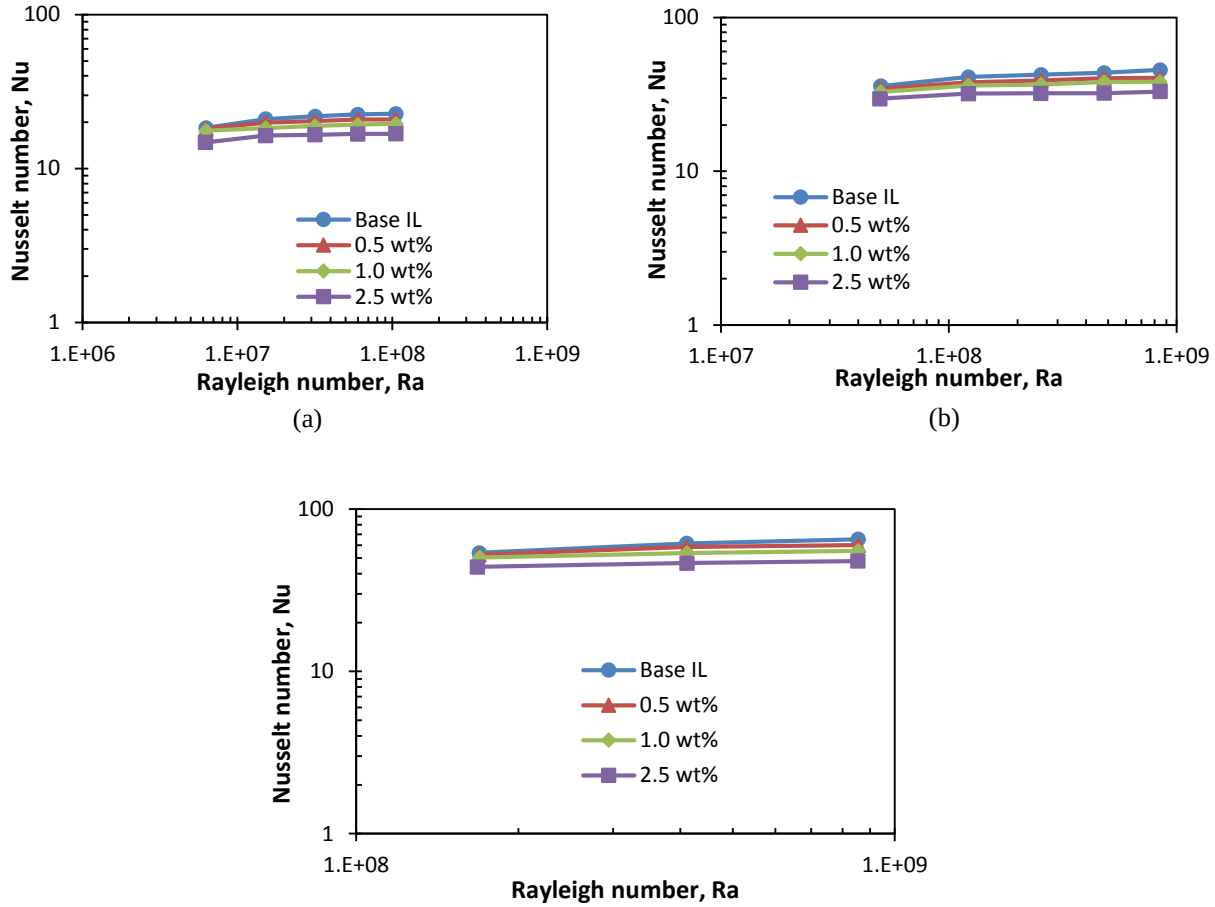

FIGURE 3: Natural convection heat transfer of base IL and NEILs in different enclosures (a) AR-0.5, (b) AR-1, (c) AR-1.5

The Nusselt number and Rayleigh number can be presented in the form of:

$$Nu = cRa^n \tag{7}$$

$$\frac{hH}{k_f} = c\left(\frac{g\beta\Delta TH^3C_p\rho^2}{\mu k_f}\right)^n \tag{8}$$

From the equ.(7-8) normalizing the heat transfer coefficient by dividing the heat transfer coefficient of NEILs to IL we can find the correlation:

$$\frac{h_{NEIL}}{h_{BL}} \sim \left(\frac{\beta_{NEIL}}{\beta_{BL}}\right)^n \left(\frac{\rho_{NEIL}}{\rho_{BL}}\right)^{2n} \left(\frac{C_{p,NEIL}}{C_{p,BL}}\right)^n \left(\frac{\mu_{NEIL}}{\mu_{BL}}\right)^{-n} \left(\frac{k_{NEIL}}{k_{BL}}\right)^{1-n} \tag{9}$$

In the normalized heat transfer coefficient correlation, all of the thermophysical properties except dynamic viscosity have the negative impact on heat transfer coefficient. In the correlation, inserting a typical natural convection correlation exponent value of $n = {}^1/_3$, the normalized heat transfer coefficient was calculated. The numerical results of natural convection heat transfer match well with the theoretical equ. (7-9) where, the theoretical calculated maximum 22% degradation was observed for 2.5 wt% NEILs.

The numerical simulation degradation was found maximum 27% for 2.5 wt% NEILs in the studied Rayleigh number range which is clear at Fig. 4. Fig. 4 represents the normalized Nusselt number (Nusselt number of NEILs divided by the Nusselt number of base IL) at the same Rayleigh number as a function of nanoparticle concentration. It is clear from Fig. 4 that the Nusselt number decreases with increasing the nanoparticle concentration of NEILs and maximum degradation occurs at aspect ratio-0.5 with 2.5 wt% NEILs. This may happen because at a certain Rayleigh number the temperature difference as well as the average temperature is higher in the lower aspect ratio enclosure than a higher aspect ratio. It is clear from the Fig. 5 that the normalized heat transfer coefficient decreases with increases the average

temperature. The reason of the average temperature effect may be the dominant of viscosity enhancement of NEILs compared to other thermophysical properties.

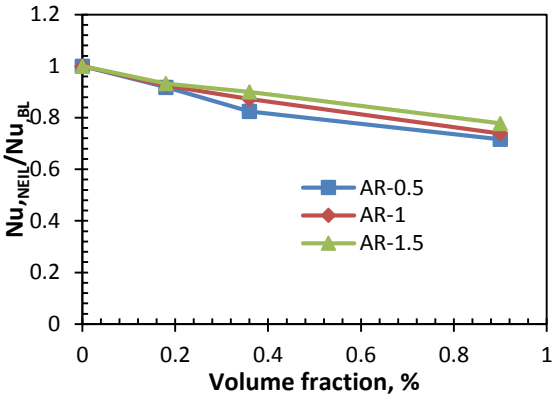

FIGURE 4. Normalized Nusselt number as a function of nanoparticle volume concentration ($Ra = 1.37 \times$

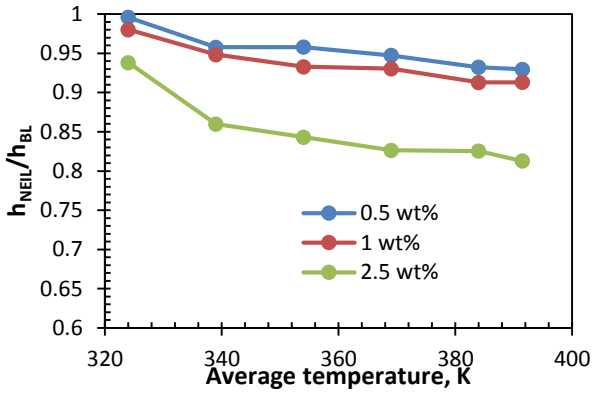

FIGURE 5. Heat transfer coefficient ratio as a function of average temperature (AR-1)

The numerical results can explain the huge degradation of the experimental results in literature [10]. Since the numerical results match well with the theoretical calculation of heat transfer coefficient that means in experimental results the extra degradation may occur for the particle-fluid interaction, clustering and sedimentation of nanoparticles. The present numerical results have contradicted with most of the previous study [11, 16-17]; they reported natural convection heat transfer enhancement of nanofluids compare to base fluids. This is because in their study, they calculate the Nusselt number of nanofluids by using the thermal conductivity of base fluids instead of nanofluids. The present numerical results match well with the literature [13-14, 18].

CONCLUSIONS

Numerical studies of the natural convection of N-butyl-N-methylpyrrolidiniumbis {trifluoromethyl)sulfonyl} imide ($[C_4mpyrr][NTf_2]$) IL and Al_2O_3 NEILs has been performed and compared with the experimental results. NEILs shows degradation of natural convection heat transfer compared to base IL and match well with the predicted model of using thermophysical properties of NEILs. The experimental results show much degradation compared to the numerical results. Thus the extra degradation of the experimental results is from the particle-fluid interaction, clustering and sedimentation of nanoparticles.

ACKNOWLEDGEMENTS

The financial support for this research is from Department of Energy (DOE) Solar Energy Technology Program. Savannah River National Laboratory is operated by Savannah River Nuclear Solutions. This document was prepared in conjunction with work accomplished under Contract No. DEAC09-08SR22470 with the U.S. Department of Energy.

REFERENCES

[1] Choi SUS, Eastman JA. Enhancing Thermal Conductivity of Fluids with Nanoparticles. Developments Applications of Non-Newtonian Flows, ASME, New York, 1995, pp. 99-105.

[2] Wu B, Reddy, RG, Rogers RD. Novel Ionic Liquid Thermal Storage for Solar Thermal Electric Power System. Proceedings of Solar Forum, Solar Energy: The Power to Choose, April 21-25, 2001, Washington, DC.

[3] Fox EB, Visser AE, Bridges NJ, Amoroso JW. Thermophysical Properties of Nanoparticle-Enhanced Ionic Liquids (NEILs) Heat-Transfer Fluids. *Energy Fuels* 2013;27 (6):3385–3393.

[4] Nieto de Castro CA, Lourenco MJV, Ribeiro APC, Langa E, Vieira SIC. Thermal Properties of Ionic Liquids and IoNanofluids of Imidazolium and Pyrrolidinium Liquids. *Journal of Chemical Engineering Data* 2010;55:653–661.

[5] Nieto de Castro CA, Murshed SMS, Lourenço MJV, Santos FJV, Lopes MLM, França JMP, Enhanced thermal conductivity and specific heat capacity of carbon nanotubes ionanofluids. *International Journal of Thermal Sciences* 2012;62:34-39.

[6] Mazumder A, Davis J, Rangari V, and Curry M. Synthesis, Characterization, and Applications of Dendrimer-Encapsulated Zero-Valent Ni Nanoparticles as Antimicrobial Agents. *ISRN Nanomaterials* Volume 2013, Article ID 843709, 9 pages.

[7] Paul TC, Morshed AKMM, Khan JA, Nanoparticle Enhanced Ionic Liquids (NEILs) as Working Fluid for Next Generation Solar Collector. *Procedia Engineering* 2013;56:631–636.

[8] Paul TC, Morshed AKMM, Fox EB, Khan JA. Thermal performance of Al_2O_3 Nanoparticle Enhanced Ionic Liquids (NEILs) for Concentrated Solar Power (CSP) applications. *International Journal of Heat and Mass Transfer* 85 (2015) 585–594.

[9] Wang B, Wang X, Lou W, Hao J. Gold-ionic liquid nanofluids with preferably tribological properties and thermal conductivity. *Nanoscale Research Letters* 2011; 6:259.

[10] Paul TC, Morshed AKMM, Fox EB, Khan JA. Experimental investigation of natural convection heat transfer of Al_2O_3 Nanoparticle Enhanced Ionic Liquids (NEILs). *International Journal of Heat and Mass Transfer* 83 (2015) 753-561.

[11] Khanafer K, Vafai K, Lightstone M. Buoyancy-driven heat transfer enhancement in a two-dimensional enclosure utilizing nanofluids. *International Journal of Heat and Mass Transfer* 46(19) (2003): 3639-3653.

[12] Hwang KS, Lee JH, Jang SP. Buoyancy-driven heat transfer of water-based Al_2O_3 nanofluids in a rectangular cavity. *International Journal of Heat and Mass Transfer* 50(19–20) (2007): 4003-4010.

[13] Choi SK, Kim SO, Lee TH, Hahn D. Computation of the Natural Convection of Nanofluid in a Square Cavity with Homogeneous and Nonhomogeneous Models. *Numerical Heat Transfer, Part A: Applications* 65(4) (2014): 287-301.

[14] Rashmi W, Ismail A, Khalid M, Faridah Y. CFD studies on natural convection heat transfer of Al2O3-water nanofluids. *Heat and Mass Transfer* 47(10) (2011): 1301-1310.

[15] Putra N, Roetzel W, Das SK. Natural convection of nano-fluids. Heat and Mass Transfer 39(8-9) (2003): 775-784.

[16] Ho CJ, Chen M, Li ZW. Numerical simulation of natural convection of nanofluid in a square enclosure: effects due to uncertainties of viscosity and thermal conductivity. *International Journal of Heat and Mass Transfer* 51(17) (2008): 4506-4516.

[17] Oztop HF, Abu-Nada E. Numerical study of natural convection in partially heated rectangular enclosures filled with nanofluids. *International Journal of Heat and Fluid Flow* 29(5) (2008): 1326-1336.

[18] Abouali O, Ahmadi G. Computer simulations of natural convection of single phase nanofluids in simple enclosures: A critical review. *Applied Thermal Engineering* 36 (2012): 1-13.

ICME2015

International Conference on Mechanical Engineering 2015
(ICME 2015) 18 – 20 December, 2015, Dhaka, Bangladesh

Paper ID : 150

A Comprehensive Detailed Chemical Kinetic Model to Predict NO_x for the Combustion of High Hydrogen Content Fuels at Elevated Pressures

Sheikh F. Ahmed[a)], Fahd E. Alam and Tanvir Farouk

Department of Mechanical Engineering, University of South Carolina, Columbia, SC 29208, USA

[a)]Corresponding author: sahmed@email.sc.edu

Abstract. High hydrogen content (HHC) fuel and synthesis gas combustion in gas turbine and other applications is an important aspect of many energy conversion scenarios for generating power. Development and testing of predictive models for NO_x formation continues to be important for the evaluation and design of high efficiency, low emission technologies for HHC fuel and syngas combustion applications. The present study investigates comprehensive detailed chemical kinetic models for describing the oxidation of $CO/H_2/NO_x$ mixtures with the full implementation of NO_x evolution pathways, including thermal, prompt, N_2O and NNH paths. In addition to C_0-C_1 species, the model includes limited amounts of small hydrocarbon species as components for future development of the model towards predicting NO_x in hydrocarbon oxidations. Model predicted behaviors are compared against multiple experimental datasets over a wide range of venues and operating conditions. The experimental venues include shock tube, plug flow reactor, and perfectly stirred reactor experiments that cover pressures from 1 to 100 bar and equivalence ratios from 0.5 to 1.5. The Burke C_0 [Intl. J. of Chemical Kinetics 44, (2012), 444 – 474] and Aramco C_1-C_4 [Intl. J. of Chemical Kinetics 45, (2013), 638 – 675] models are integrated to describe the fuel kinetics. The NO_x kinetic components are developed based on a critical review of NO_x production, and NO-NO_2 interconversion sub-models presently available in the literature. The NO_x sub-model includes N_xH_y reaction paths as well as updated rate expressions and species, such as HNO_2 and $HONO_2$ and the related paths that are found to contribute to NO_x production significantly. In general, the overall model predictions are in good agreement with global combustion target (shock tube ignition delay) as well as with more detailed target data including plug flow reactor reactivity, speciation, and perfectly stirred reactor measurements. Simulations are conducted for a wide range of reacting mixtures ($H_2/O_2/N_2$, $CO/H_2/O_2$ and $CO/H_2O/O_2/N_2$) with initial NO and NO_2 perturbations to consider exhaust gas recirculation (EGR) conditions.

INTRODUCTION

The combustion of high hydrogen content (HHC) fuel and synthesis gas, or syngas in gas turbine and other applications has become an important aspect of many energy conversion scenarios for power generation. Since gas turbines can be operated with a wide range of fuels [1], selection of a cleaner and more efficient fuel has become a topic of current combustion research. Hydrogen is a strong candidate to replace natural gas as a source of clean energy due to its wide flammability limit and CO_2-free emission. However, the widespread application of hydrogen is still challenging due to its high adiabatic flame temperature and fast chemical kinetics leading to unsteady combustion with combustor material degradation [1]. Syngas, a mixture of hydrogen, carbon monoxide in its pure form, water and trace hydrocarbons as impurities, is easier to produce than hydrogen, and intrinsically obviates these impediments due to its wide variation in composition [2]. Therefore, syngas has achieved global interest as a sustainable, low-pollution, secure source

of energy. Syngas is also used as fuel in Integrated Gasification Combined Cycle (IGCC) units to generate electricity, or as a reburning fuel in the reduction of NO_x emissions [3].

A number of detailed and reduced kinetic mechanisms were proposed over the years. The authors critically reviewed a number of recent mechanisms that are available and widely accepted by the combustion community. The GRI-Mech [4] was the first comprehensive methane combustion mechanism with the incorporation of NO formation kinetics that was distributed free across the research community. The updated C_0 reaction mechanism, proposed by Burke et al. [5], has been widely accepted for its hydrogen oxidation chemistry especially at high pressure conditions. Recently a comprehensive C_1-C_4 mechanism has been developed by Metcalfe et al. [6], termed as the Aramco Mech that not only describes the hydrogen and syngas combustion but also smaller hydrocarbon chemistry up to C_4.

As an integral part of all combustion using air as an oxidizer, efficient energy conversion is traded off at the expense of NO_x pollutant emissions, since efficiency and NO_x both increase with higher flame temperature. Development and testing of predictive models for NO_x formation is required for the evaluation and design of high efficiency, low emission technologies for HHC fuel and syngas combustion applications. Dagaut et al. [7], developed a kinetic model of the mutual sensitization of the oxidation of methane and NO in a jet stirred and flow reactor configurations. Rasmussen et al. [8] proposed a detailed mechanism for the oxidation of $CO/H_2/NO_x$ system that encompassed two highly-diverse regimes of chemistry, low temperature atmospheric chemistry and high temperature combustion chemistry. Konnov published his revised version of combustion mechanism [9] in 2009 for hydrogen, carbon monoxide, formaldehyde, methanol, methane, C_2-C_3 hydrocarbon species and their oxygenated derivatives, with possible full implementation of available kinetics of the prompt NO route via NCN. Those revisions related to the NO route allowed better prediction of NO formation.

The current study proposes a comprehensive detailed chemical kinetic reaction mechanism to describe the oxidation of $CO/H_2/NO_x$ mixtures with limited amounts of small hydrocarbon species that will be used as components for predicting NO_x in hydrocarbon oxidation. The NO_x subset of the proposed model includes updated N_xH_y reaction paths as well as species, such as HNO_2 and $HONO_2$ that have been found to contribute to NO_x production significantly. The mechanism has been validated over a wide range of initial conditions and multiple experimental data sets. The experimental venues include shock tube, plug flow reactor, and perfectly stirred reactor data that cover pressures from 1 to 100 bar and equivalence ratios from 0.5 to 1.5. The hydrocarbon and oxygenated-hydrocarbon reactions of the present mechanism are adopted from Aramco Mech [6]. The reaction mechanism reported by Konnov [9] served as the base set of the NO_x kinetics of the present study with necessary revisions and inclusions. In general, the overall model predictions are in good agreement with global combustion targets (shock tube ignition delay) as well as against detailed target data including plug flow reactor reactivity, speciation, and perfectly stirred reactor measurements. A wide range of reacting mixtures with initial NO and NO_2 perturbations are used in validating the present model.

DETAILED MECHANISM FORMULATION APPROACH

The proposed $CO/H_2/NO_x$ model with limited amount of small hydrocarbon species, termed as-UTSR-RASAER (University Turbine Systems Research-ReActing System and Advanced Energy Research) model by the authors, consists of several sub-mechanisms, the C_0-C_1 sub-mechanism, NO_x sub-mechanism and H/N/O sub-mechanism. The details of each sub-mechanism are presented in the proceeding sections.

C_0-C_1 SUB-MECHANISM

The C_0-C_1 sub-mechanism consists of reactions involving H_2/O_2 system, CO/CO_2 system and C_1 species. The present C_0-C_1 sub-mechanism is developed by the integration of the Burke C_0 [5] model and the C_1 species and associated reactions of Aramco [6] model in order to describe the fuel kinetics.

NO_X SUB-MECHANISM

The NO_x kinetic components of the proposed model are developed based on a critical review of existing NO_x formation, and NO-NO_2 interconversion sub-models available in the with the implementation of all possible NO_x evolution pathways, such as *thermal* NO [10], *prompt* NO [11], N_2O paths and NNH paths. The conversion reactions of NO_2 from NO, known as NO_x recycling reactions, play a significant role in the NO_x-related kinetic reaction mechanism. Such conversion can either take place directly or through intermediate formations of HONO, HNO_2 and $HONO_2$ [8]. As suggested by Rasmussen et al. [8], HNO_2, which is a thermodynamically less stable isomer of nitrous acid (HONO), has a noteworthy influence in the combustion process/phenomena. Although the detailed Konnov-mechanism [9] is adroit in predicting both *thermal* and *prompt* NO evolution, unfortunately this NO_x chemistry does not include HNO_2 and $HONO_2$ reaction pathways. Henceforth, the present UTSR-RASAER model is updated based on the complete HONO-subset of Rasmussen et al. [8].

H/N/O SUB-MECHANISM

The H/N/O reactions are important due to their active participation in the formation of NO or N_2 in the flame and also in the systematic formulation of higher hydrocarbons from the lower ones. The N_xH_y reactions of this sub-mechanism are derived from the recent ammonia oxidation model of Skreiberg et al. [12]. In order to ensure a complete NO-NO_2 conversion for the present model, the rate constants of several reactions of NH_2, HNO and NH_2OH are revised based on the detailed NH_3-oxidation and Thermal DeNO_x model of Klippenstein et al. [13].

MODEL PERFORMANCES

Model predicted behaviors of the proposed UTSR-RASAER model are compared against multiple experimental datasets over a wide range of venues and operating conditions. The Chemkin-II package [14] is used for all the simulations of this study.

IGNITION DELAY

Mathieu et al. [15] observed a strong dependence of the ignition delay on the initial NO_2 concentration of a dilute $H_2/O_2/NO_2$ mixture in their shock tube experiments. The present UTSR-RASAER model is used to simulate those experiments for three different operating pressures (1.66, 13.0, 33.6 atm) and the results are illustrated in Fig. 1. An insignificant change in reactivity with the addition of 100 ppm of NO_2 at 1.66 atm is observed, whereas an overall decrease in reactivity is obtained for initial NO_2, higher than 400 ppm, which becomes more prominent with decreasing temperatures. A non-monotonic dependence of ignition delay on initial NO_2 concentration is found at higher pressures (13.0 and 33.6 atm). At 13.0 atm, an increase in overall reactivity is observed by the addition of 100 ppm of NO_2 and this change in reactivity appears to be more prominent at temperatures below 1140 K. A further increase in reactivity is observed below the 1140 K temperature range by the addition of 400 ppm NO_2. However, the overall reactivity decreases along the whole temperature range by the addition of 1600 ppm of NO_2. At the highest investigated pressure (33.6 atm), a significant increase in reactivity is observed by the inclusion of NO_2 up to 400 ppm. An addition of 1600 ppm of NO_2 yields a reactivity, above the pure H_2/O_2 mixture but below the 400 ppm case.

In order to analyze these phenomena, sensitivity analyses at every pressure and NO_2-perturbation were performed for a high and a low-temperature region. The decrease in reactivity with the decrease in temperature for neat H_2/O_2 case can be explained by the most sensitive reactions. At high temperature, the ignition delay becomes more sensitive to the chain branching reaction-$O+H_2=H+OH$ (R41), whereas the chain propagation reaction $H_2O_2+H=H_2+HO_2$ (R42) becomes more sensitive in case of lower temperature, which causes the decrease in reactivity and a consequent increase in ignition delay at lower temperatures. With an addition of small amount of NO_2 (100 ppm) in the mixture, an increase in reactivity is observed for both the temperature zones. With 100 ppm of NO_2, an NO-NO_2 conversion cycle causes the formation of highly reactive OH, H and HONO radicals through the reactions: $NO_2+H=NO+OH$ (R43), $NO+HO_2=NO_2+OH$ (R44) and $NO_2+H_2=HONO+H$ (R1). Flux analysis of NO and NO_2 at 1100 K and 13.0 atm shows that majority of NO_2 are consumed through reaction (R43) producing NO and OH radicals. Again, most of the NO are recycled to NO_2 through (R44) yielding more OH radicals. NO_2 can also be consumed through (R1) to produce HONO, which can again be decomposed into NO and OH through (R11). The formation of the OH radicals through all the above reactions causes a significant increase in the overall reactivity of the mixture.

It can be seen in fig. 1b that the reactivity increases at the lower temperature zone with the addition of 400 ppm of NO_2. With the change in initial NO_2 concentration in this zone from 100 to 400 ppm, the chain branching reaction (R41) becomes more sensitive. In addition, due to higher concentration of NO_2 present in the mixture, (R1) becomes more sensitive, which causes more H radical formation. The higher H concentration will consequently increase the OH concentration through $HO_2+H=2OH$ (R45), which further increases the reactivity when the NO_2 concentration is increased from 100 to 400 ppm. A significant change in the most sensitive reactions and consequently, a much higher ignition delay is observed for the overall temperature range in fig. 1b, when the initial NO_2 concentration is further increases from 400 to 1600 ppm. For example, at lower temperature, it is illustrated in the sensitivity analyses that the most sensitive reaction for 1600 ppm case becomes the propagation reaction $OH+H_2=H+H_2O$ (R46), instead of the branching

reaction $H+O_2=O+OH$ (R47) of the 400 ppm case. In addition, a number of inhibiting reactions, such as, $H+NO(+M)=HNO(+M)$ (R48), $H+O_2(+AR)=HO_2(+AR)$ (R49) and $HO_2+OH=H_2O+O_2$ (R50) become significant for the 1600 ppm case.

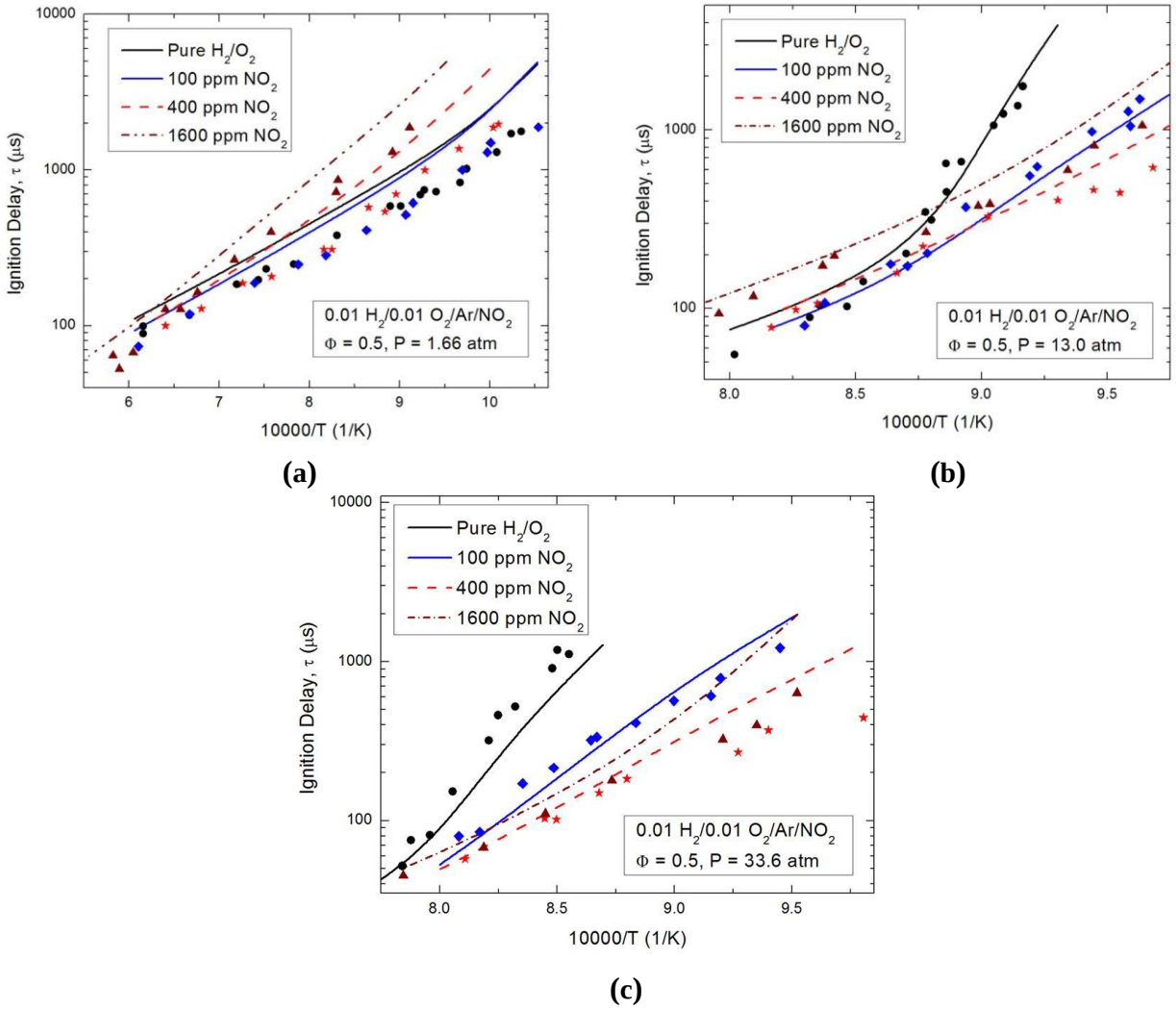

FIGURE 1: Effect of initial NO_2 concentration on τ_{ign} for H_2/O_2 mixtures at (a) 1.66 atm, (b) 13.0 atm and (c) 33.6 atm pressure. Lines represent numerical simulations and symbols represent measurements behind reflected shock waves [15].

PLUG FLOW REACTOR EXPERIMENTS UNDER DILUTE CONDITIONS

Simulations are conducted for $H_2/O_2/N_2$ mixture with initial NO_2 perturbations and compared to the adiabatic flow reactor experiments of Mueller et al. [16], shown in fig. 2a. The improvements in the prediction of the temporal evolution of fuel and NO_x due to the rate constant updates of the H/N/O sub-mechanism are also illustrated in this figure, which ensures an enhancement of the predictive ability of the proposed mechanism by the incorporation of the updates. The important $NO-NO_2$ recycling process, the formation of highly-reactive OH radicals and the NO_x interactions

with the H/O radical pools for the current model for $H_2/O_2/N_2$ mixture with initial NO_2 perturbations at 10 atm are analyzed and the flux analysis are shown in fig. 2b and 2c.

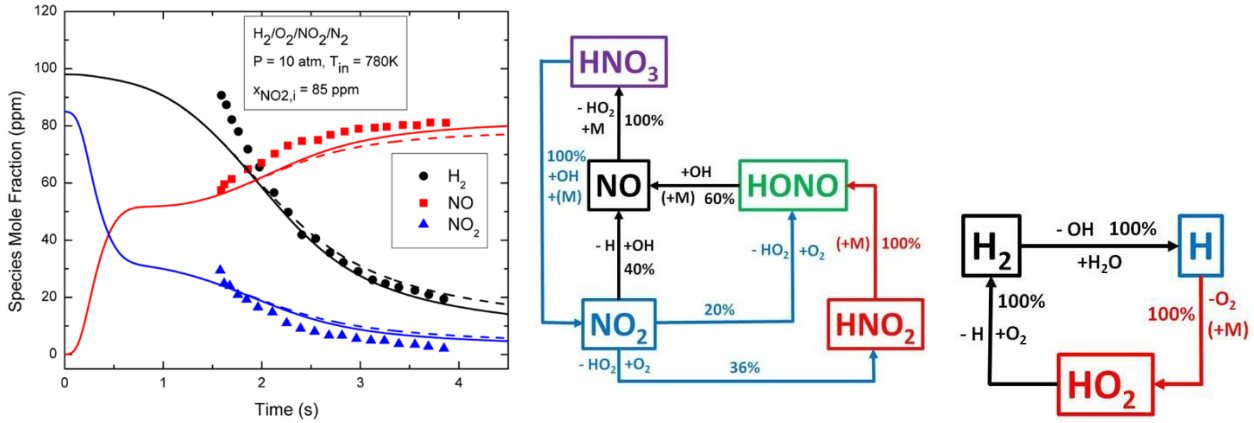

FIGURE 2: (a) Time histories of species concentrations for $H_2/O_2/N_2$ mixture, perturbed with 85 ppm of NO_2 at 10.0 atm and T_{in} = 780 K. Symbols represent experimental data from Mueller et al. [16]. Solid lines represent model predictions generated using the H/N/O reaction rate updates and dashed lines represent predictions generated without the updates. (b) Major reaction pathways of NO-NO_2 conversion and (c) H atom to HO_2 radical conversion.

Model predictions of the fuel, oxidizer, and NO_x (NO and NO_2) species reactivity for $CO/H_2/NO_x$ oxidation are also compared against the isothermal flow reactor experiments at temperature-dependent residence times, performed by Rasmussen et al. [8] at three different pressures of 20, 50 and 100 bars. Figure 3 shows the comparisons at 50 bar. The reactivity predictions of the proposed model are found satisfactory for other investigated pressures as well which are not shown here for brevity.

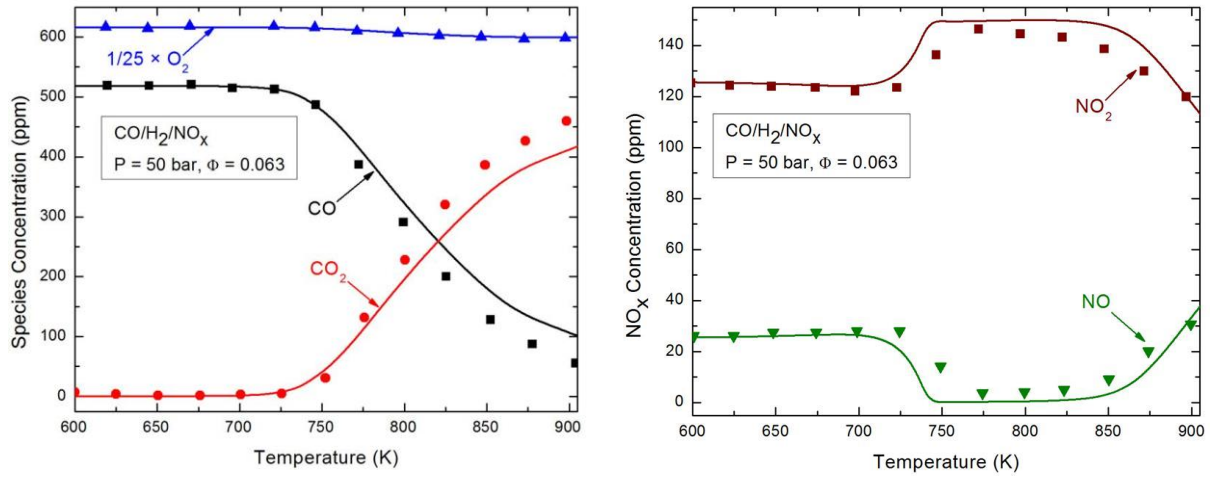

FIGURE 3: Experimental data [8] and numerical simulation results of $CO/H_2/NO_x$ oxidation at 50 bar and 0.063 equivalence ratio.

SUMMARY AND CONCLUSIONS

As an integral part of any combustion process, oxidation of syngas produces pollutant emissions, among which the oxides of nitrogen (NO_x) play an important role in atmospheric pollution. The present study has proposed a comprehensive detailed chemical kinetic mechanism to describe the oxidation of $CO/H_2/NO_x$ mixtures with particular focus on the detailed implementation of NO_x evolution pathways. As components for a future advancement of the model to predict NO_x in hydrocarbon species, the model also includes limited amounts of small hydrocarbon species kinetics. The model emphasizes a precise estimation of NO_x formation by the incorporation of N_xH_y reaction paths as well as species, such as HNO_2 and $HONO_2$ that have been found to play a decisive role in accurate NO_x prediction. In addition, recent updates for the rate constants are also proposed for N_xH_y reactions.

The overall model predictions are in good agreement with multiple experimental datasets over a wide range of venues and operating conditions, including shock tube, plug flow reactor and perfectly stirred reactor experiments that cover pressures from 1 to 100 bar and equivalence ratios from 0.5 to 1.5. In order to replicate the EGR condition, the present study considers a wide range of NO_x-perturbed reacting mixtures, such as $H_2/O_2/N_2$, $CO/H_2/O_2$, and $CO/H_2O/O_2/N_2$. Simulations with such wide ranges of reacting mixtures significantly expanded the acceptability of the proposed model. The study further identifies that NO_x speciation data are extremely critical in developing detailed and validated fuel+NO_x kinetic models as global combustion targets do not provide the necessary constraining conditions.

ACKNOWLEDGEMENTS

This research was funded by the Department of Energy under Award Number DE-FE0012005.

REFERENCES

1. M. C. Krejci, O. Mathieu, A. J. Vissotski, S. Ravi, T. G. Sikes, E. L. Petersen, A. Kérmonès, W. Metcalfe, H. J. Curran, J. Eng. Gas Turb. Power **135**, GTP-12-1293 (2013).
2. R. Chacartegui, D. Sánchez, J. M. Muñoz de Escalona, F. Jiménez-Espadafor, A. Muñoz, T. Sánchez, Fuel Processing Technol. **103**, 134-145 (2012).
3. A. Frassoldati, T. Faravelli, E. Ranzi, Int. J. Hydrogen Energy **32**, 3471-3485 (2007).
4. G. P. Smith, D. M. Golden, M. Frenklach, N. W. Moriarty, B. Eiteneer, M. Goldenberg, C. T. Bowman, R. K. Hanson, S. Song, W. C. Gardiner Jr., V. Lissianski, Z. Qin, <http://www.me.berkeley.edu/gri_mech/>.
5. M. P. Burke, M. Chaos, Y. Ju, F. L. Dryer, S. J. Klippenstein, Int. J. Chem. Kinet. **44**, 444-474 (2012).
6. W. K. Metcalfe, S. M. Burke, S. S. Ahmed, H. I. Curran, Int. J. Chem. Kinet. **45**, 638-675 (2013).
7. P. Dagaut, A. Nicolle, Combust. Flame. **140**, 161-171 (2005).
8. C. L. Rasmussen, J. Hansen, P. Marshall, P. Glarborg, Int. J. Chem. Kinet. **40**, 454-480 (2008).
9. A. A. Konnov, Combust. Flame **156**, 2093-2105 (2009).
10. Y. B. Zeldovich, Acta Physicochim **21**, 577-626 (1946).
11. C. P. Fenimore, Proc. Combust. Inst. **13**, 373-380 (1971).
12. Ø. Skreiberg, P. Kilpinen, P. Glarborg, Combust. Flame **136**, 501-518 (2004).
13. S. J. Klippenstein, L. B. Harding, P. Glarborg, J. A. Miller, Combust. Flame **158**, 774-789 (2011).
14. R. J. Kee, F. M. Rupley, J. A. Miller, "Chemkin-II: A Fortran Chemical Kinetics Package for the Analysis of Gas-phase Chemical Kinetics," Report No. SAND89-8009, Sandia National Laboratories, 1989.
15. O. Mathieu, A. Levacque, E. L. Petersen, Proc. Combust. Inst. **34**, 633-640 (2013).
16. M. A. Mueller, R. A. Yetter, F. L. Dryer, Int. J. Chem. Kinet. **31**, 705-724 (1999).

ICME2015

International Conference on Mechanical Engineering 2015
(ICME 2015) 18 – 20 December, 2015, Dhaka, Bangladesh

Paper ID :153

MHD Mixed Convection Flow Through a Diverging Channel with Heated Circular Obstacle

Md. S. Alam[1, a)], J. Shaha[2, b)], M.A.H. Khan[3] and R. Nasrin[3]

[1]*Department of Mathematics, Jagannath University, Dhaka-1100, Bangladesh*
[2]*Institute of Natural Sciences, United International University, Dhaka, Bangladesh*
[3]*Department of Mathematics, Bangladesh University of Engineering and Technology, Dhaka-1000, Bangladesh*

[a)] Corresponding author Email: sarwardu75@gmail.com
[b)] jsaha@ins.uiu.ac.bd

Abstract. A numerical study of steady MHD mixed convection heat transfer and fluid flow through a diverging channel with heated circular obstacle is carried out in this paper. The circular obstacle placed at the centre of the channel is hot with temperature T_h . The top and bottom walls are non-adiabatic. The basic nonlinear governing partial differential equations are transformed into dimensionless ordinary differential equations using similarity transformations. These equations have been solved numerically for different values of the governing parameters, namely Reynolds number (*Re*), Hartmann number *(Ha)*, Richardson number *(Ri)* and Prandtl number (*Pr*) using finite element method. The streamlines, isotherms, average Nusselt number and average temperature of the fluid for various relevant dimensionless parameters are displayed graphically. The study reveals that the flow and thermal fields in the diverging channel depend significantly on the heated body. In addition, it is observed that the magnetic field increases the rate of heat transfer within the channel.

NOMENCLATURE

B_0	magnetic induction	C_p	specific heat of fluid at constant pressure
g	gravitational acceleration	k_f	thermal conductivity of the fluid
L	length of the channel	Nu	average Nusselt number
p	dimensional pressure	P	dimensionless pressure
T	dimensional temperature	T_h	temperature of heated surface
u, v	velocity components along x, y	U, V	dimensionless velocity components along X, Y direction
Greek Symbols			
α	thermal diffusivity	β	thermal expansion coefficient
θ	dimensionless temperature	ν	kinematic viscosity of the fluid
ρ	density of the fluid	σ	magnetic field intensity

INTRODUCTION

Mixed convection involves features of both forced and natural flow conditions. In mixed convection flows, the forced convection and free convection effects are comparable in magnitudes. Mixed convection problem has got its extensive applications in diversified field of engineering, such as cooling of electronic devices, furnaces, lubrication technologies, chemical processing equipment, drying technologies etc. Actual geometries in practice are often found to have different shapes rather than rectangular one. Moreover, the channel may be in an ideal situation, such as a parallel-plate channel, but a convergent or a divergent channel. There are some situations, such as in electronic equipment cooling, one may not be clear whether what mechanism of divergence or convergence of the channel would make the heat transfer better. Furthermore, MHD flow in diverging channels has important applications in MHD pumps and generators, liquid metal magnetohydrodynamics and physiological fluid flow. Alternation of heat transfer in channels due to introduction of obstacles, partitions and fins in different positions has received sustained massive attention recently. Comprehensive reviews have been conducted by Dennis et al. [1], Drazin [2]. Layek et al. [3] studied steady MHD flow in a diverging channel with suction or blowing, where they analyzed steady two-dimensional divergent flow of an electrically conducting incompressible viscous fluid in a channel formed by two non-parallel walls, caused by a source of fluid volume at the intersection of the walls. Magnetic fields are generally used to control the natural convection of semiconductor melts such as silicon or gallium arsenide to improve crystal quality that is studied by Hadid et al. [4]. Moreover, the steady flow of a viscous incompressible fluid in a linearly diverging asymmetrical channel was studied by Makinde [5]. He expanded the solution into a Taylor series with respect to the Reynolds number and performed a bifurcation study. Alam and Khan [6] in their paper showed the critical analysis of the MHD flow in convergent-divergent channels. They also analyzed the solution to perform the bifurcation study of the parameters and the critical relationship of the parameters. However, studies on natural and mixed convection from converging or diverging channels are limited. A detailed survey of literature on mixed convection in internal flows has been presented in Aung [7]. Sparrow et al. [8] presented the results of an experimental and numerical study on natural convection from isothermal converging channels. The maximum half angle of inclination of the plates considered in their study was 15^0. Sparrow and Ruiz [9] carried out an experimental study of natural convection from a diverging channel and presented a universal correlation for converging, parallel and diverging channel based on the maximum inter-wall spacing. Gau et al. [10] performed an experimental study of both buoyancy assisting and buoyancy opposing mixed convection heat transfer from a converging channel. One of the channel walls was placed vertically and was uniformly heated and the other wall was adiabatic, with an inclination of 3^0. Alternation of heat transfer in channels due to introduction of obstacles, partitions and fins attached to the wall(s) has received considerable attention recently. Billah et al. [11] executed heat transfer and flow characteristics for MHD mixed convection in a lid-driven cavity with heat generating obstacle. The problems of mixed convection in different shapes of encloser with different positions and characterized obstacles are discussed in Costa and Raimundo [12], Bhoite et al. [13], Rahman et al. [14]. From the review of literature, it is clear that comprehensive studies on MHD mixed convection from diverging channel with circular heated obstacle is scarce. The objective of the present study is to investigate the effect of various pertinent controlling parameters on flow and thermal configurations of MHD mixed convection in a diverging channel with a heated circular obstacle. Local Nusselt number and average temperature of the fluid are also presented graphically in this paper.

MODEL CONFIGURATION

The schematic diagram of the problem herein investigated is shown in Fig.1. The system consists of a diverging channel with side of length L. A Cartesian coordinate system is considered with origin at the end of the left inlet of the computational domain. The circular obstacle is heated with temperature T_h and the length of the heated surface is L_c . The top and bottom walls of the channel are non-adiabatic at an angle θ with the axis of x . The length of the inlet and outlet are a and b respectively and the right wall is adiabatic. It is assumed that the incoming flow has a uniform velocity u_i with ambient temperature T_i. The inlet opening is situated at the left end, whereas the outlet opening is at the top and bottom of the right wall of the channel. The uniform magnetic field of strength B_0 is applied to the top wall in vertical direction.

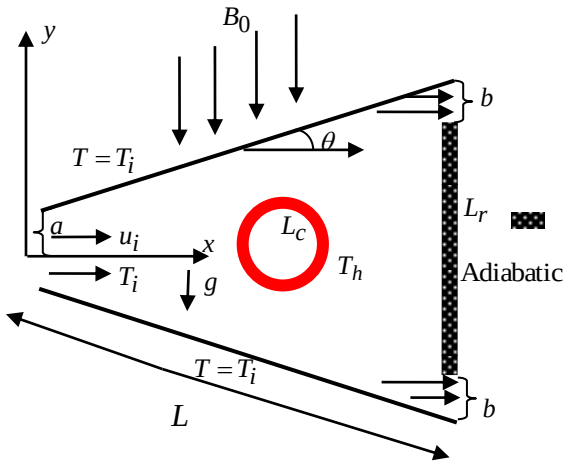

FIGURE 1 Physical model of the diverging channel

MATHEMATICAL FORMULATION

A two-dimensional steady, laminar, incompressible, mixed convection flow is assumed within the channel and the fluid properties are considered to be constant. The radiation and viscous dissipation effects are considered as negligible in this study. The governing equations describing the flow under Boussinesq approximation are as follows:

$$\frac{\partial u}{\partial x}+\frac{\partial v}{\partial y}=0 \tag{1}$$

$$\rho\left(u\frac{\partial u}{\partial x}+v\frac{\partial u}{\partial y}\right)=-\frac{\partial p}{\partial x}+\mu\left(\frac{\partial^2 u}{\partial x^2}+\frac{\partial^2 u}{\partial y^2}\right)-\sigma {B_0}^2 u \tag{2}$$

$$\rho\left(u\frac{\partial v}{\partial x}+v\frac{\partial v}{\partial y}\right)=-\frac{\partial p}{\partial y}+\mu\left(\frac{\partial^2 v}{\partial x^2}+\frac{\partial^2 v}{\partial y^2}\right)+g\rho\beta(T-T_i) \tag{3}$$

$$u\frac{\partial T}{\partial x}+v\frac{\partial T}{\partial y}=\alpha\left(\frac{\partial^2 T}{\partial x^2}+\frac{\partial^2 T}{\partial y^2}\right) \tag{4}$$

The boundary conditions for the present problem are specified as follows:

At the inlet: $u=u_i, v=0, T=T_i$.

At heated circular obstacle boundaries: $u=0, v=0, T=T_h$

At top and bottom walls of the channel: $u=0,\ v=0,\ T=T_i$

At the right adiabatic wall of the channel: $u=0,\ v=0,\ T=T_i$

The above equations are non-dimensionalized by using the following dimensionless quantities

$$X=\frac{x}{L}, Y=\frac{y}{L}, U=\frac{u}{u_i}, V=\frac{v}{u_i},\ P=\frac{p}{\rho {u_i}^2},\ \text{and}\ \bar{\theta}=\frac{(T-T_i)}{(T_h-T_i)},$$

After substituting the above variables into the governing Eqs. (1)-(4), the following dimensionless equations are

$$\frac{\partial U}{\partial X}+\frac{\partial V}{\partial Y}=0 \tag{5}$$

$$U\frac{\partial U}{\partial X}+V\frac{\partial U}{\partial Y}=-\frac{\partial P}{\partial X}+\frac{1}{\mathrm{Re}}\left(\frac{\partial^2 U}{\partial X^2}+\frac{\partial^2 U}{\partial Y^2}\right)-\frac{Ha^2}{\mathrm{Re}}U \tag{6}$$

$$U\frac{\partial V}{\partial X}+V\frac{\partial V}{\partial Y}=-\frac{\partial P}{\partial Y}+\frac{1}{\mathrm{Re}}\left(\frac{\partial^2 V}{\partial X^2}+\frac{\partial^2 V}{\partial Y^2}\right)+Ri\bar{\theta} \tag{7}$$

$$U\frac{\partial \bar{\theta}}{\partial X}+V\frac{\partial \bar{\theta}}{\partial Y}=\frac{1}{\mathrm{RePr}}\left(\frac{\partial^2 \bar{\theta}}{\partial X^2}+\frac{\partial^2 \bar{\theta}}{\partial Y^2}\right) \tag{8}$$

where $Re=\frac{u_i L}{\upsilon}$, $Pr=\frac{\upsilon}{\alpha}$, $Ri=\frac{g\beta\Delta TL}{\mathrm{u_i}^2}$, and $Ha^2=\frac{\sigma {B_0}^2 L^2}{\mu}$ are Reynolds number, Prandtl number, Richardson number and square of Hartmann number respectively.

The corresponding boundary conditions then take the following form:

At the inlet: $U=1, V=0, \bar{\theta}=0.$

At the outlet: Convective boundary condition (CBC), $P = 0$

At heated circular obstacle boundaries: $U=0, V=0, \bar{\theta}=1$

At top and bottom walls of the channel: $U=0,\ V=0,\ \bar{\theta}=0$

At the right adiabatic wall of the channel: $U=0,\ V=0,\ \bar{\theta}=0$

$Nu=-\frac{1}{L_C}\int_0^1 \frac{\partial \bar{\theta}}{\partial n}d\bar{\theta}$, where $L_C=2\pi r$ is the circumference of the circular obstacle, n represents the unit normal vector on the surface of the obstacle. The average temperature of the fluid is defined as $\theta = \int \bar{\theta}\frac{d\bar{V}}{\bar{V}}$, where $\bar{V}$ is the approximate volume of the channel.

NUMERICAL TECHNIQUE

The governing equations along with the boundary conditions are solved numerically employing Galerkin weighted residual finite element techniques. In this method, the solution domain is discretized into finite element meshes, which are composed of non-uniform triangular elements. Then the nonlinear governing partial differential equations are transferred into a system of integral equations by applying Galerkin weighted residual method. The integration involved in each term of these equations is performed by using Gauss's quadrature method. Applying boundary conditions, the obtained nonlinear algebraic equations are modified. These modified non-linear residual equations are solved using Newton-Raphson method to determine the coefficients of the expansions.

CODE VALIDATION

A computational model is validated for mixed convection heat transfer by comparing the results on mixed convection in ventilated cavity with left heated wall performed by Raji and Hasnaoui [15]. In this present work numerical predictions have been obtained on the triangular mesh with 5232 nodes and 3488 elements for the same boundary condition of Raji and Hasnaoui [15]. The model of Raji and Hasnaoui [15] is reproduced at first and the comparison is depicted in Fig. 2. It can be decided that the current code can be used to predict the flow field for the present problem.

RESULTS AND DISCUSSION

MHD mixed convection heat transfer inside a diverging channel with a heated circular body is influenced by various pertinent parameters namely Hartmann number *Ha*, Reynolds number *Re*, Prandtl number *Pr* and Richardson number *Ri*. Figure 3 provides the information about the influence of *Ha* on streamlines and isotherms for mixed convection regime. The flow pattern remains almost similar at the fixed values of $Ha(=0,20)$ at $Ri=1$. However, flow strength increases and the flow field closely symmetric about the two side walls of the channel with higher values of *Ha*. Due to center heating circular obstacle, magnetic field is not so effective parameter on the distribution of temperature. Figures 4 (a)-(c) illustrate the variation of average temperature of the fluid with

Richardson number *Ri* at different values of Hartmann number, Prandtl number and Reynolds number respectively. A quick decrease is observed in Fig 4(a) on average temperature with *Ri* in absence of magnetic field. While the rate of change of θ become sluggish as Hartmann number increases. It can be noticed from the Fig. 4(b, c) that as *Ri* increases θ deceases for higher values of *Pr* and *Re*, as a result, the mean bulk temperature reduces.

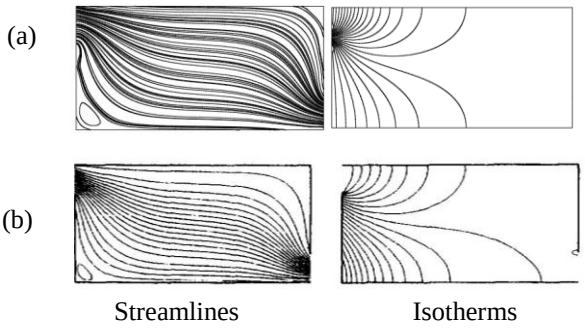

FIGURE 2 Streamline and isotherm comparison of (a) present work with (b) Raji and Hasnaoui [15] for $\mathrm{Re}=10$ and $\mathrm{Pr}=0.71, \mathrm{Ha}=0$.

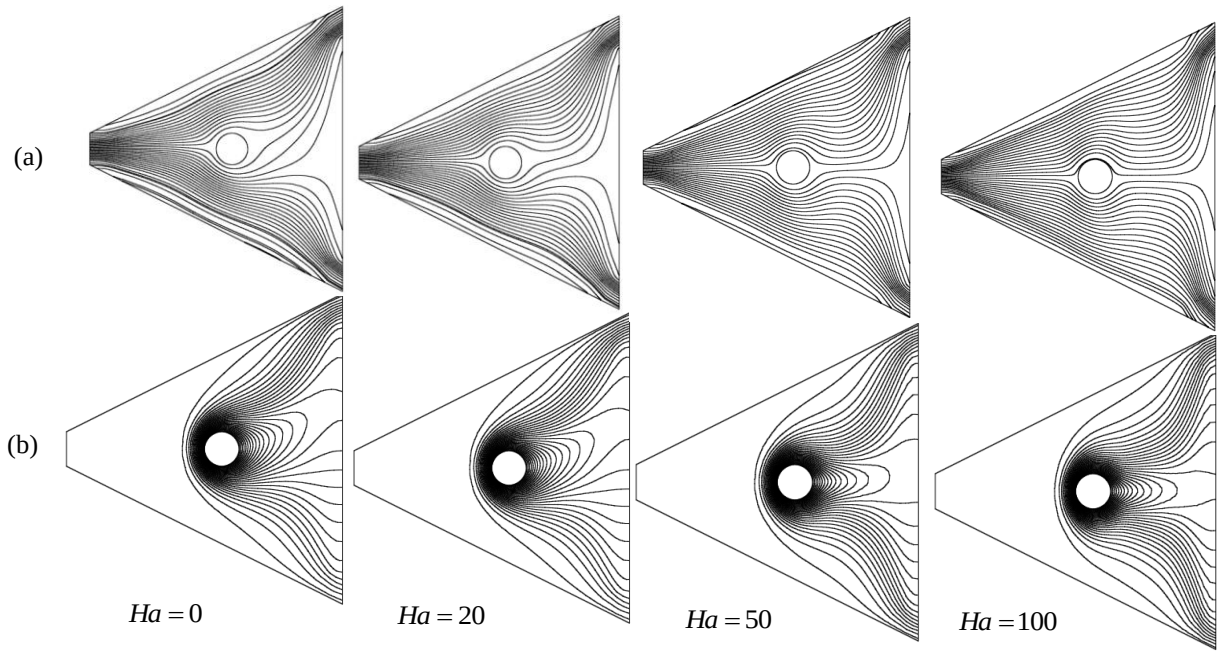

FIGURE 3: (a) Streamlines and (b) Isotherms for various values of *Ha* at $Ri=1.0$, $Pr=7.1$ and $\mathrm{Re}=50$.

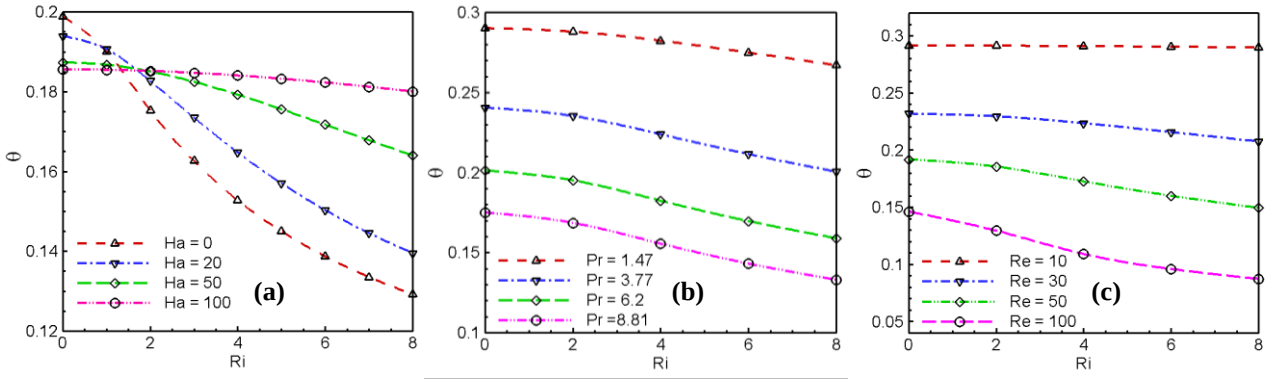

FIGURE 4: Average fluid temperature by the effect of (a) Hartman number *Ha* at $\mathrm{Re}=50,\ \mathrm{Pr}=7.1,$ (b) Prandtl number *Pr* at $\mathrm{Re}=50,\ Ha=30$ and (c) Reynolds number *Re* at $\mathrm{Pr}=7.1, Ha=30$ with $293.15^{\circ}K$.

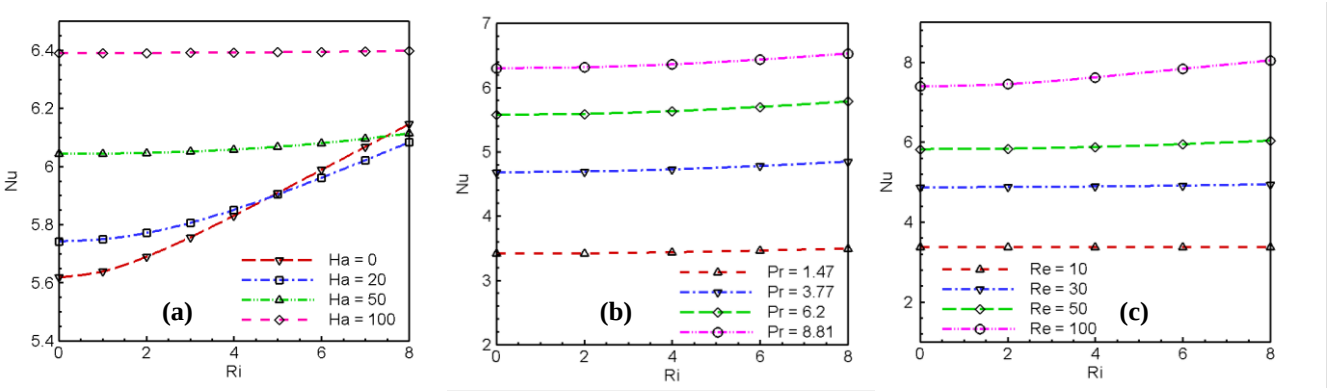

FIGURE 5: Average Nusselt number by the effect of (a) Hartman number *Ha* at $\mathrm{Re}=50,\ \mathrm{Pr}=7.1,$ (b) Prandtl number *Pr* at $\mathrm{Re}=50,\ Ha=30$ and (c) Reynolds number *Re* at $\mathrm{Pr}=7.1, Ha=30$.

Figures 5(a)-(c) show the influence of the parameters on *Nu* with variation of *Ri*. Increasing Hartmann number increases the mean Nusselt number for all values of *Ri.* It can be noticed from the Fig 5(b) that as *Ri* increases *Nu* increases and the rate of heat transfer enhances for higher values of *Pr.* Almost similar results are seen in Fig 5(c) where the effects of Reynolds number on *Nu* with variation of *Ri* is investigated.

CONCLUSION

A numerical analysis is performed to investigate the MHD mixed convection flow in a diverging channel with a heated circular obstacle. Effects of Reynolds number, Hartmann number, Prandlt number and Richardson number are considered to study their impacts on flow structure and heat transfer characteristics. The structure of the flow and thermal field within the channel is found to have significant dependence on the magnetic parameter and Prandtl number. Magnetic field can be a control parameter for the rate of heat transfer and mean temperature of the fluid within the channel for mixed convection. On the other hand, the aforesaid parameters effect strongly on isotherm structures in the channel and around the heated obstacle. The heat transfer rate and the average temperature of the fluid changes rapidly against *Ri* with rising *Re*, *Ha* and *Pr*.

REFERENCES

1. S. C. R. Dennis, W. H. H. Banks, P. G. Drazin and M. B. Zaturska, Journal of Fluid Mechanics **336**, 183-202 (1997).
2. P. G. Drazin, Fluid Dynamics Research **24(6),** 321-327 (1999).
3. G. C. Layek, S. G. Kryzhevich, A. S. Gupta and M. Reza, Z. Angew. Math. Phys. **64(1)** 123-143 (2013).
4. H. Ben Hadid, R. Touihri and D. Henry, Adv. Space Res. **22(8),** 1213-1216 (1998).
5. O. D. Makinde, Computer Assisted Mechanics and Engineering Sciences **4**, 157-165 (1997).
6. M. S. Alam, M. A. H. Khan, Journal of Naval Architecture and Marine Engineering **7(2)**, 83 – 93 (2010).
7. W. Aung, Hand Book of Single Phase Convective Heat Transfer (John Wiley, New York, 1987), chapter 15.
8. E. M. Sparrow, R. Ruiz and L. F. A. Azevedo, Int. J. Heat Mass Transfer **31(5)**, 907-915 (1988).
9. E. M. Sparrow and R. Ruiz, Int. J. Heat Mass Transfer **31(11),** 2197-2205 (1988).
10. C. Gau, T. M. Huang and W. Aung, ASME J. of Heat Transfer **118(3)**, 606-615 (1996).
11. M. M. Billah, M. M. Rahman, M. H. Kabir and U. M. Sharif, Int. J. of Eng & Tech. **3(32)**, 1-8 (2011).
12. V. A. F. Costa and A. M. Raimundo, Int. Journal of Heat and Mass transfer **53**, 1208-1219 (2010).
13. M. T. Bhoite, G. S. V. L. Narasimham and M. V. K. Murthy, Int. J. of Thermal Sciences **44**, 125-135 (2005).

14. M. M. Rahman, M. M. Billah, M. A. H. Mamun, R. Saidur and M. Hassanuzzaman, Int. J. Mechanical and Materials Engineering **5(2)**, 163-170 (2010).
15. A. Raji and M. Hasnaoui, Revue Ge'n e' rale de Thermique **37**, 874-884 (1998).

ICME2015

International Conference on Mechanical Engineering 2015
(ICME 2015) 18 – 20 December, 2015, Dhaka, Bangladesh

Paper ID : 158

A Molecular Dynamics Study of Thermal Transport in Nanoparticle Doped Argon like Solid

Muhammad Rubayat Bin Shahadat[a)], Shafkat Ahmed, AKM M Morshed

Department of Mechanical Engineering Bangladesh University of Engineering and Technology (BUET)Dhaka, Bangladesh

[a)]Corresponding author: rubayat37@gmail.com

Abstract: Interfacial phenomena such as mass and type of the interstitial atom, nano scale material defect influence heat transfer and the effect become very significant with the reduction of the material size. Non Equilibrium Molecular Dynamics (NEMD) simulation was carried out in this study to investigate the effect of the interfacial phenomena on solid. Argon like solid was considered in this study and LJ potential was used for atomic interaction. Nanoparticles of different masses and different molecular defects were inserted inside the solid. From the molecular simulation, it was observed that a large interfacial mismatch due to change in mass in the homogenous solid causes distortion of the phonon frequency causing increase in thermal resistance. Position of the doped nanoparticles have more profound effect on the thermal conductivity of the solid whereas influence of the mass ratio is not very significant. Interstitial atom positioned perpendicular to the heat flow causes sharp reduction in thermal conductivity. Structural defect caused by the molecular defect (void) also observed to significantly affect the thermal conductivity of the solid.

Keywords: Non equilibrium molecular dynamics, interstitial atom, effective thermal conductivity, kapitza conductance.

INTRODUCTION

Micro and nanostructured materials have become very important because of its growing interest and application in micro or nano systems in many fields such as: nanotechnology, advanced material metrology, micro/nano fabrication, microelectronics [1] etc. Thermal properties of nanocomposites have held even greater promise in recent years, especially in their application to thermal interface materials, thermal insulation, and the third generation solar cells [1]. Behavior of micro and nano system is different than that of macroscale due to different surface forces and it needs to have a better understanding. Many noble nanostructured composite materials have been used as thermal interface materials to provide better heat dissipation for ever-increasing power consumption in electronic devices [2]. Very high heat dissipation is possible when there is low thermal resistance at interfaces. This is of particular concern to the development of microelectronic semiconductor devices as defined by the International Technology Roadmap for Semiconductors in 2004 where an 8 nm feature size device is projected to generate up to 100000 W/cm^2 and would need efficient heat dissipation of an anticipated die level heat flux of 1000 W/cm^2 which is an order of magnitude higher than current devices [3]. Doping causes a great enhance of electrical conductivities. The conductivities of $LiFePO_4$ were enhanced by around 1-3 orders by doping rare earth or transition metals [4]. The subject of void structures is no more than two decades old [5]. Ciobanu et al. presents a void structure that confine light in low-index region [5].

Interfacial thermal resistance, also known as thermal boundary resistance or kapitza resistance, is a measure of an interface's resistance to thermal flow. Due to kapitza resistance when an energy carrier attempts to traverse the interface, it will scatter at the interface. The probability of transmission after scattering will depend on the available energy states. Understanding the thermal resistance at the interface between two materials is of primary significance in the study of its thermal properties. Interfaces often contribute significantly to the observed properties of the materials. This is even more critical for nanoscale systems where interfaces could significantly affect the properties relative to bulk materials [7].

While the experimental work becomes relatively difficult, several atomistic simulation techniques have been utilized to model phonon transport in nanostructured materials [6].Two prevailing methods are Monte Carlo (MC) simulation and Molecular Dynamics (MD) simulation. The MC method has been used to solve the Boltzmann transport equation (BTE) for phonon transport under the relaxation time approximation [6]. The distribution function obtained from Boltzmann's equation can be easily related to energy and therefore to temperature. The basic principle of the MC

simulation is to track the phonon energy bundles as they drift and collide through the computational domain [6]. On the contrary Molecular Dynamics Simulation has been used to examine thermal properties in nanostructured materials where phonon-phonon scattering dominates heat transfer [6]. This method is now-a-days very popular method for calculating different transport properties. It is a very powerful toolbox in modern molecular modeling and enables us to follow and understand structure and dynamics with extreme detail-literally on scales where motion of individual atoms can be tracked [8]. This process is simple and can deal with complex geometries. In the most common version, the trajectoriesof atoms and molecules are determined by numerically solving Newton's equations of motion for a system of interacting particles, where forces between the particles and their potential energies are calculated using interatomic potentials or molecular mechanics force fields[5].Molecular Dynamics Simulation can be of two approaches- Equilibrium Molecular Dynamics (EMD) Simulation and Non-Equilibrium Molecular Dynamics (NEMD) Simulation. EMD method calculates heat transfer by Green-Kubo formalism whereas NEMD is a direct approach to calculate thermal conductivity directly from heat flow. As argon-like solids with Lennard-Jones (LJ) potential are used as the model system where electrons are not involved in heat conduction, then the NEMD approach is definitely applicable.

MOLECULAR MODELING

The three dimensional simulation cell of 80 X 15 X 5 nm^3 was constructed of Argon molecules arranged in FCC lattice. Periodic boundary conditions were imposed in all the directions. Four lattices at both ends of the simulation domain were assigned as hot region, and eight lattices in the middle were assigned as cold region. Velocity of the molecules in these regions were scaled to maintain the desired temperature.1200 atoms were created in each region. Three nanospheres each having 68 atoms are place in different positions perpendicular to heat flow direction with a view to observing the effects of nanoparticles on heat transfer. Same observation was for voids too. Simplified Lennard-Jones (LJ) model was appointed to perform the simulation. Previous research reveals that results from the simplified LJ model and atomically realistic models are quantitatively equivalent [9]. Fig. 1(a) presents details of simulation domain of solid argon matrix whereas Fig. 1(b) and Fig. 1(c) for solid matrix with nanospheres andvoidsrespectively.

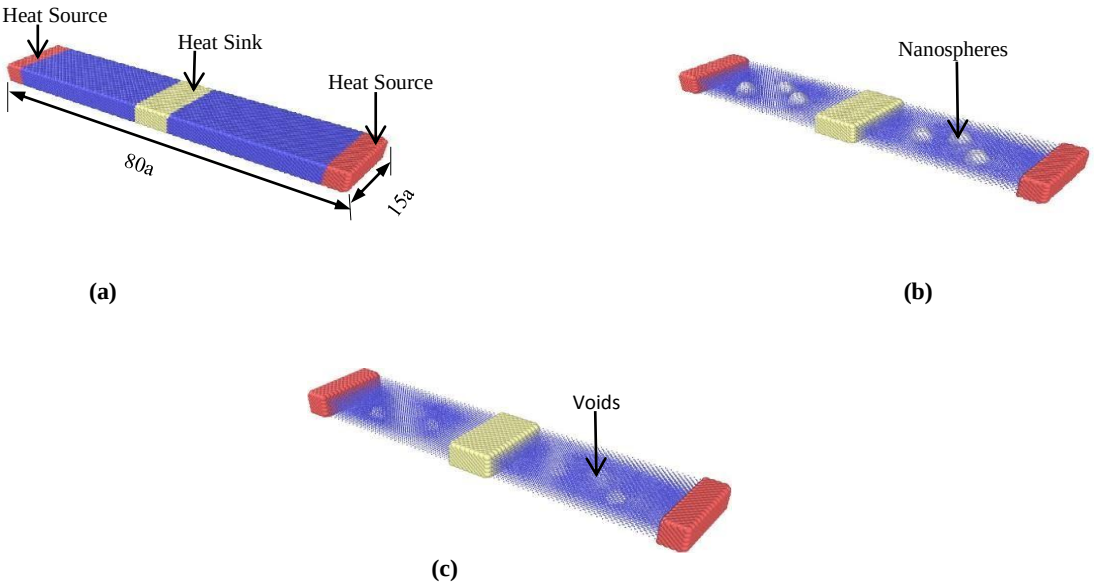

FIGURE 1. Simulation domain (a) Solid argon matrix (b) Solid Argon matrix with three nanospheres (c) Solid argon matrix with three interstitial voids

All the interactions between molecules were calculated by LJ [6-12] potential:

$$\varphi(r) = 4\varepsilon\left[\left(\frac{\sigma}{r}\right)^{12} - \left(\frac{\sigma}{r}\right)^{6}\right] \quad (1)$$

Interaction potential's length and energy parameters were collected from Ref. [14]: Lengths are expressed in terms of σ =0.3405 nm, the energy units are specified by

$\frac{\varepsilon}{K_B} = 120k$, Where ε= 1.67×10^{-21}

The MD time unit corresponds to 2.161×10^{-12} s. Typical time step size is Δt = 0.001ns.The Lenard–Jones potential function was truncated at 2.5σ. The integration of the equations of motions was performed by Varlet algorithm. The simulation was started from its initial configuration with a time step of 2.1fs. The simulation was run with NPT ensemble followed by NVE ensemble. Heat flux required to establish the temperature gradient was measured. Efflux was set 2.78 unit/time step. Thus heat flow started between the cold region and hot region. The simulation was run for 10.5ns to reach a steady temperature gradient.
Once the system reaches steady state temperature, the thermal conductivity of the overall system was calculated by using Fourier's Law:

$$K_{overall} = \frac{1}{R_t} = \frac{\Delta Q}{\tau \frac{\partial t}{\partial x}} \quad (2)$$

Where ΔQ is the total heat flux, τ is the simulation time.
$\frac{\partial t}{\partial x}$ is the linearized temperature gradient of solid argon.

To incorporate the nanoparticles, three nanoparticles each of radius 1.5nm were embedded into the regular atoms as presented in Fig. 1(b). These spheres were set at different planes to have a better understanding. Simulations by keeping voids were performed in the same way which is shown in Fig. 1(c). Nanoparticles mass were varied to 0.125, 0.25 and 0.50 that of solid argon. In each case effective thermal conductivity was calculated and then the results were compared to establish a comparative model. Previous simulation data shows that the effective thermal conductivity of solid argon at near 20K temperature is nearly 0.62 W/m. K [10] whereas our simulation estimates the effective thermal conductivity of solid argon is 0.594 W/m.K. Percentage of deviation is $\frac{0.62-0.594}{0.62} = 4.19\%$. All simulations in this study was performed in LAMMPS [11] and visualizations were done by using OVITO.

RESULTS AND DISCUSSION

For the purpose of thermal transport modeling, MD simulation is advantageous with respect to other theoretical approaches, for example, AMM and DMM [15]. The only inputs needed by MD simulation are the atomic structure and empirical inter-atomic potentials. MD simulations have been used extensively to compute thermal resistance across solid-solid interfaces [15]. The simulation starts from its initial configuration and temperature was scaled to achieve the equilibrium temperature of 20K. Temperature profile of the simulation domain was monitored to check whether the simulation domain was in equilibrium state or not. Once the simulation domain was in equilibrium state, Nose-hoover thermostat was applied to establish the temperature gradient. Initially the temperature difference between the hot and cold section was higher and so the vibration was more. This phenomenon is shown in Fig. 2 (a). As the time goes on, the system reached towards a steady state and hence there is a stability in the graph. This phenomenon is represented in Fig.2(b).

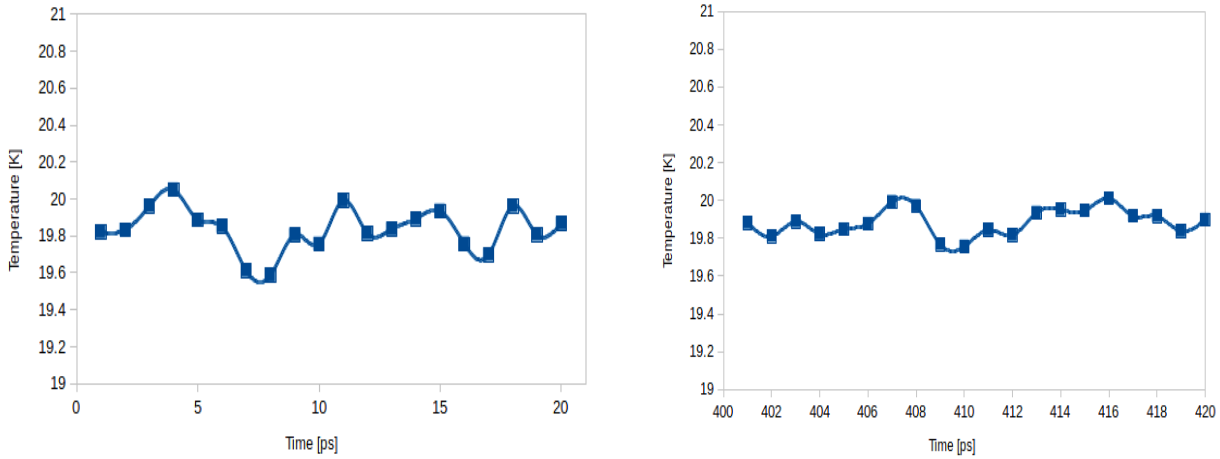

(a) **(b)**

FIGURE 2. (a) Variation of temperature with time at initial stage (b) Stability of temperature with time

Phonon wave packets are formed from linear combinations of vibration eigen states of the perfect crystal. This wave packet is then allowed to propagate towards an interface or a scatterer where it scatters into transmitted and reflected waves [6]. To investigate the effect of voids on the interfacial scattering one void as well as three voids are placed randomly in the perpendicular direction of heat flow and the corresponding results are shown in Fig. 3(a). When a void is placed, at the position of void the particles do not find any other particle to transmit the energy and therefore there is a decrease of thermal conductivity. The effective thermal conductivity in this case is 0.582 W/m.k.

When the number of voids are increased heat transfer is reduced in comparison with one void. By increasing the number of voids, the places where the particles transmit energy will reduce. Therefore there is a decrease of thermal conductivity more than the previous case. Effective thermal conductivity in this case is 0.579 W/mk.

$$\frac{K_{void1}}{K_{void3}} = \frac{0.582}{0.579} = 1.005$$

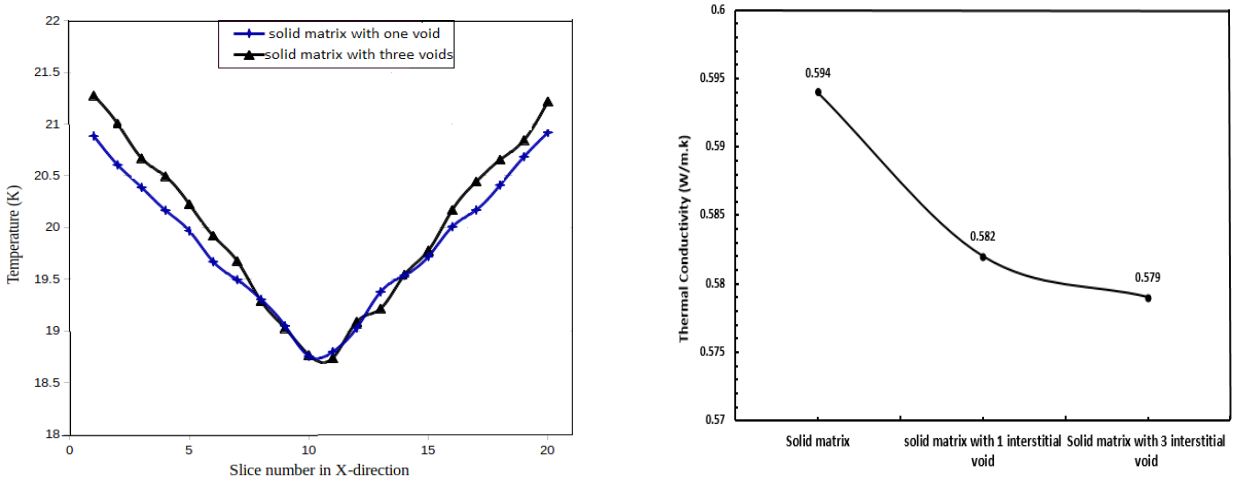

(a) **(b)**

FIGURE 3(a).Temperature profile for a nanocomposite with void (b) Comparison of thermal conductivity

To investigate the interfacial scattering 3 nanospheres as well as the 3 voids are placed in the perpendicular direction of heat flow and the corresponding results are shown in Fig. 4(a)**.** When there is any interstitial atoms or any types of vacancy in the perpendicular direction of heat flow there is a sudden drop of temperature. That means when phonon-interface collisions increases, it creates a hindrance for heat flow. When there is no nanosphere or void, the temperature drop is less as the thermal conductivity of a semi-conducting or insulating single crystal alloy is usually lower than the average of the thermal conductivities of the constituent materials [13]. Effective thermal conductivity in this case k= 0.594 W/m·k.When 3 voids are placed in the direction of heat flow, the phonon-interface collisions increases more and therefore there is a larger drop of temperature than the previous one. Thermal conductivity becomes low in this case. The effective thermal conductivity k is 0.579 W/m.k.

$$\frac{K_{void}}{K_{solid\ matrix}} = \frac{0.579}{0.594} = 0.97$$

Thermal conductivity is 97% of when there is only solid argon matrix.

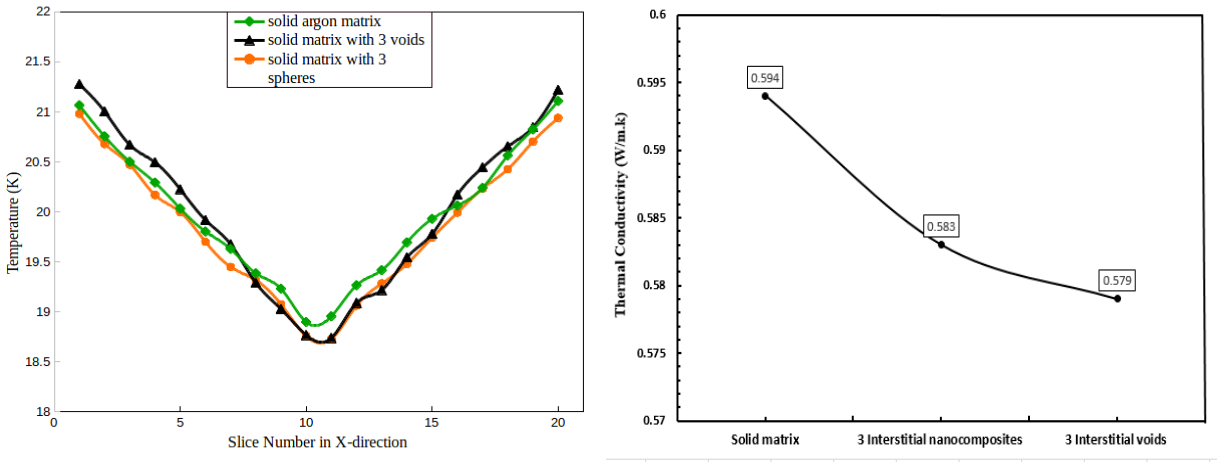

(a) **(b)**

FIGURE 4. (a) Temperature profile of a nanostructure with voids and nanospheres (b)Comparison of effective thermal conductivity among solid matrix, solid matrix with nanospheres and interstitial voids

To understand the effects of nanocomposites on heat flow three nano spheres are set in the structure of pure Argon like solid. The masses particles present in the nano spheres is one-eighth of the mass of argon. Because of kapitza resistance the temperature drop is slightly higher than solid argon matrix. Again as the mass is too small in this case it is observed that there is a little deviation from the graph of three voids. The effective thermal conductivity k is 0.583 W/m.k.

$$\frac{K_{sph}}{K_{solid\ matrix}} = \frac{0.583}{0.594} = 0.981$$

Thermal conductivity in this case is 98.1% of solid argon matrix.

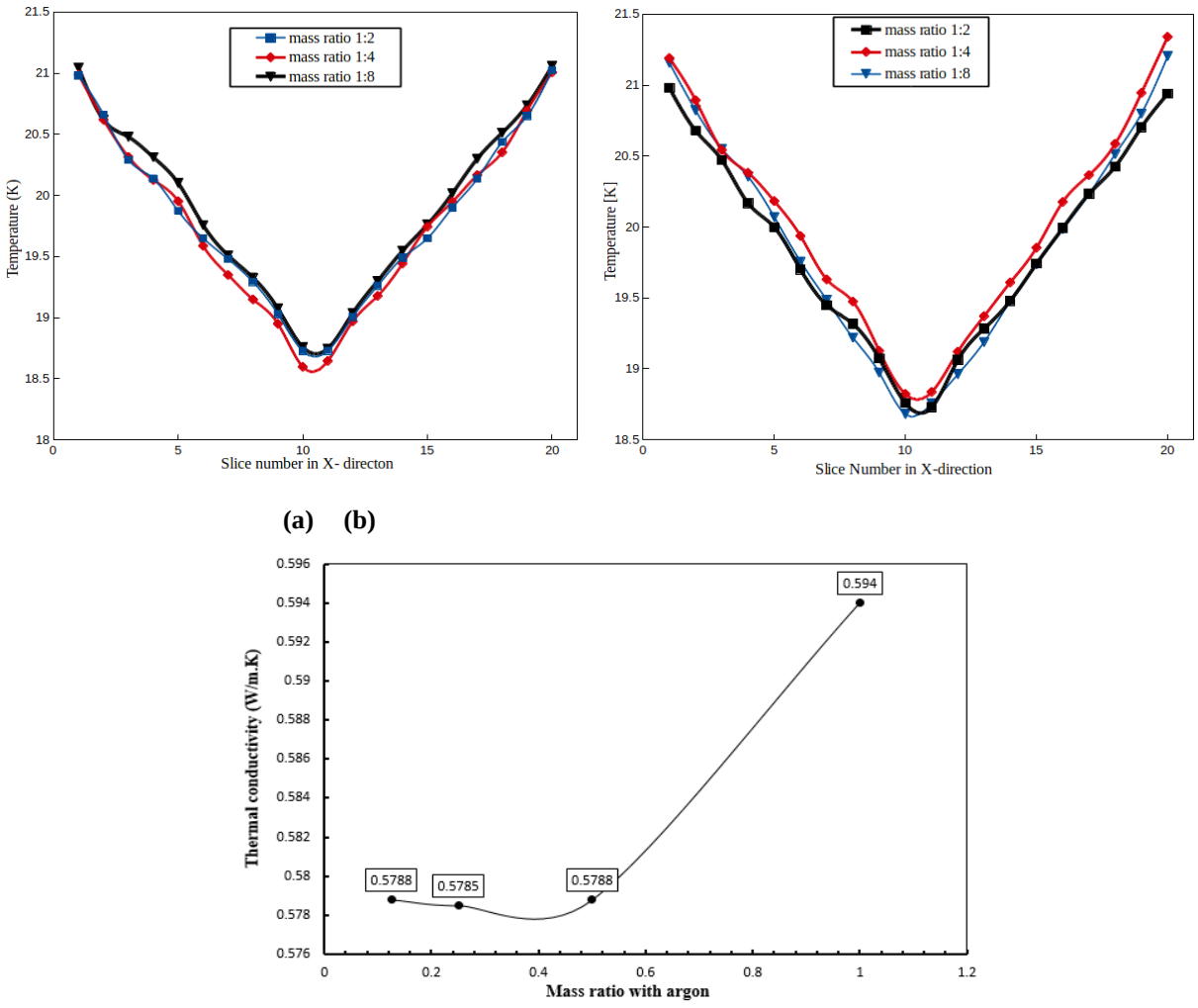

FIGURE 5. (a). Temperature profile for a nanocomposite with one nanosphere of different masses **(b).**Temperature profile for a nanocomposite with three nanospheres of different masses**(c)**Comparison of effective thermal conductivity with one nanosphere of different mass ratio

To investigate the effect of mass change on the interfacial scattering mass ratio of 1:2, 1:4 and 1:8 of argon are placed in the perpendicular of heat flow direction. It is observed that thermal conductivity decreases compared to solid argon modeling because of kapitza resistance. When mass ratio is changed then at the interface the particle of argon will find a particle less than its mass. Therefore it will not be able to transmit energy as before. Hence there will be a decrease of thermal conductivity. Thermal conductivity of mass ratio 1:2, 1:4 and 1:8 are quite same. This change of mass ratio has a very little effect on the thermal conductivity. From the Fig. 5(a) it is observed that the temperature drop in case of mass ratio 1:4 is a little bit larger than the other two cases. Thermal conductivity of mass ratio 1:4 is 0.5785 W/m.k. When mass ratio is 1:2 and 1:8 then thermal conductivity is 0.5788 W/m.k. Which is slightly greater than mass ratio of 1:4. It can be explained when the mass ratio is too large or too small then the change is negligible but in an intermediate mass ratio the thermal conductivity drops a little. Conductivity is mass ratio 1:4 is (.5785/0.594)=0.973 or 97.3% of solid argon matrix. Thermal conductivity of mass ratio 1:2 and 1:8 is (0.5788/0.594)=0.975 or 97.5% of solid argon matrix.

Figure 5(b) shows the effect of change of mass ratio by placing three nanospheres in the perpendicular to heat flow direction. When the number of nanospheres is increased the graph alters. The temperature drop in case of mass ratio 1:4 is slightly less than the mass ratio 1:2 and 1:8. It can explained that when the number of nano particles is increased

the thermal conductivity drop of intermediate mass ratio is less than the larger or smaller mass ratio.

CONCLUSIONS

NEMD simulation was employed to study the effect of nanoparticle doping and nanoscale defects on thermal transport in a solid argon matrix. The matrix material was Argon and the nano spheres were built with argon like solids of different mass ratio. These nano spheres were placed inside the solid matrix perpendicular to the direction of heat flow. Effective thermal conductivity of the nanoparticle doped solid was calculated and compared with that of the pure solid matrix. Nanoscale material defect was also studied by creating nano voids inside the solid matrix. From the simulation results, following conclusions can be drawn:

(1) Nanoparticle doping significantly influences overall thermal conductivity of the solid matrix. With the increase in number of the nanoparticles thermal resistance was observed to increase. However, nanoparticles' mass have less significant effect on the overall thermal conductivity.
(2) Nanoscale material defects represented by the nanovoids have profound effect on the thermal conductivity of the solid matrix. With the increase in the number of voids effective thermal conductivity was observed to reduce following a power law of

$$K = 0.5925e^{-0.013n}$$

Where K is the effective thermal conductivity of solid argon and n is the number of voids.

REFERENCES

[1] W. Tian and R. Yang, Thermal conductivity modeling of compacted nanowire composites, Journal of Applied Physics 101 (2007) 054320
[2] P.K. Schelling, S.R. Phillpot, and P. Keblinski, Kapitza conductance and phonon scattering at grain boundaries by simulation, Journal of Applied Physics 95 (2004) 6082- 6091.
[3] Hu, M., Keblinski, P., Wang, JS., and Raravikar, N., Journal of Applied Physics 104 (2008)
[4] Doping Effects on Electronic Conductivity and Electrochemical Performance of LiFePO4 Jiezi Hu1), Jian Xie2), Xinbing Zhao1)† , Hongming Yu1), Xin Zhou1), Gaoshao Cao1) and Jiangping Tu1)
[5] ELECTRIC FIELD IN VOID NANOSTRUCTURES M. CIOBANU1 , L. PREDA2 , D. SAVASTRU1 , M. TAUTAN1
[6] ZHITING TIAN B.E., Tsinghua University, China, 2007; Nanoscale Heat Transfer In ARGON-Like Solids Via Molecular Dynamics Simulations
[7] K.M. Katika and L. Pilon, The effect of nanoparticles on the thermal conductivity of crystalline thin films at low temperatures, Journal of Applied. Physics 103 (2008) 114308.
[8] Molecular dynamics simulations. Lindahl ER[1]
[9] S. Merabiaa, S. Shenoginb, L. Jolya, P. Keblinskib, J.L. Barrata, Proceedings of National Academy of Sciences 106 (2009) 15113
[10] Thermal conductivity of solid argon by classical molecular dynamics by Hideo kaburaki, Ju Li, Sidney Yip
[11] S. Plimpton, Journal of Computational Physics 117 (1995) 1.
[12] en.wikipedia.org/wiki/Interfacial_thermal_resistance
[13] Y.F. Chen, D.Y. Li, J.R. Lukes, and A. Majumdar, Monte Carlo simulation of silicon nanowire thermal conductivity, Journal of Heat Transfer 127 (2005) 1129-1137.
[14] S. Sarkar, R.P. Selvam, Journal of Applied Physics 102 (2007) 074302
[15]Two-temperature nonequilibrium molecular dynamics simulation of thermal transport across metal-nonmetal interfaces Yan Wang,1 Xiulin Ruan,1,* and Ajit K. Roy2

ICME2015

International Conference on Mechanical Engineering 2015
(ICME 2015) 18 – 20 December, 2015, Dhaka, Bangladesh

Paper ID : 163

Large-Eddy Simulation of Airflow and Heat Transfer in a General Ward of Hospital

Md. Farhad Hasan[1 a)], Taasnim Ahmed Himika[2 b)], Md. Mamun Molla[3c)]
[1,2]*Department of Electrical & Computer Engineering, North South University,Dhaka-1229, Bangladesh*
[3]*Department of Mathematics & Physics, North South University,Dhaka-1229, Bangladesh*

[c)]Corresponding author: mamun.molla@northsouth.edu
[a)]blackarrow810@gmail.com

Abstract. In this paper, a very popular alternative computational technique, the Lattice Boltzmann Method (LBM) has been used for Large-Eddy Simulation (LES) of airflow and heat transfer in general ward of hospital. Different Reynolds numbers have been used to study the airflow pattern. In LES, Smagorinsky turbulence model has been considered and a discussion has been conducted in brief. A code validation has been performed comparing the present results with benchmark results for lid-driven cavity problem and the results are found to agree very well. LBM is demonstrated through simulation in forced convection inside hospital ward with six beds with a partition in the middle, which acted like a wall. Changes in average rate of heat transfer in terms of average Nusselt numbers have also been recorded in tabular format and necessary comparison has been showed. It was found that partition narrowed the path for airflow and once the air overcame this barrier, it got free space and turbulence appeared. For higher turbulence, the average rate of heat transfer increased and patients near the turbulence zone released maximum heat and felt more comfortable.

INTRODUCTION

In the modern research interests, turbulence is still a big challenge. If one wants to know and develop more about this topic, computer simulation has no alternative [1]. In addition, two-dimensional turbulence has exceptional feature that is impossible to understand in nature or laboratory. Although, the realistic turbulence is always three-dimensional, consequently until now many studies still emphasize on two-dimensional turbulence [2].

In the last few decades, Lattice Boltzmann Model (LBM) has emerged as one of the efficient alternatives for simulating and modeling different complicated systems [3]. The implementation of LB is always simpler than that of conventional Computational Fluid Dynamics (CFD) methods. LBM offers those methods not only computational efficiency but also numerical accuracy. Due to these advantages, LBM can be extended to simulate turbulent flows [4-8], to cite only few. For simulating turbulence, LB can be used for direct numerical simulation (DNS) tool or can be combined with the large-eddy simulation (LES) [9]. However, LES is more balanced than DNS in terms of both space and memory.

Since this work is based on the inner side of a hospital room, it should be mentioned that, Lee and Awbi [10] worked on the effect of internal partitioning on room air quality with mixing ventilation but the work was on statistical analysis only using CFD codes. They concluded saying that the partition located towards the exhaust zone and made with a larger height and gap underneath was beneficial to get better room air quality.

However, Zhang and Lin [11] used LBM to study indoor airflows in hospital ward as well. They emphasized much on low Reynolds number indoor airflow fields in a model room with a partition. They found that the computational results of LBM agree with the experimental data in terms of airflow velocities. In addition, LBM has the ability to catch more detailed airflow structures than the traditional steady CFD process. They applied LBM through simulation of airflow in a relatively more complex environment, a model ward with 10 beds. Although their works were solely on fluid flow, they did not include any temperature equations.

This paper focuses on LES of airflow by LBM in a hospital ward with six beds along with temperature equations. Patients on each bed have been considered to release heat continuously in the proposed model since the room temperature is less than the temperature of patients. Before going to the simulation part, mathematical discussions have been added on LES and the Smagorinsky model in Section 2. In Section 3, the results have been added along with discussions in details along with the code validation process, followed by the conclusion in Section 4.

FORMULATION OF THE PROBLEM

For the incompressible flow, if the transport coefficients are independent of the temperature, the energy equation can be decoupled from the mass and momentum equations. For the incompressible thermal problem, *f* and *g* are two functions called flow distribution function and temperature distribution function respectively. These functions are utilized to obtain macroscopic characteristics of the flow like velocity, pressure, temperature etc.

The D2Q9 Model

The general form of the lattice velocity model is expressed as D_nQ_m, where *D* is the spatial dimension and *Q* is the number of connections (lattice velocity) at each node. In this work, the velocity space is discretized in 9 different distribution functions.

The square lattice *D2Q9* for velocity and temperature is expressed as [12-14]:

$$f_i(\bar{x}+\Delta\bar{e}_i, t+\Delta) - f_i(\bar{x},t) = -\frac{1}{\tau_\nu}\left[f_i(\bar{x},t) - f_i^{eq}(\bar{x},t)\right] \tag{1}$$

$$g_i(\bar{x}+\Delta\bar{e}_i, t+\Delta) - g_i(\bar{x},t) = -\frac{1}{\tau_\alpha}\left[g_i(\bar{x},t) - g_i^{eq}(\bar{x},t)\right] \tag{2}$$

where, τ is the single relaxation time that controls the rate of approach to equilibrium, $f_i(\bar{x},t)$ and $g_i(\bar{x},t)$ are the density distribution functions for velocity and temperature respectively along the direction $\bar{e}_i$ at $(\bar{x},t)$, ν is the kinematic viscosity and α is the thermal diffusivity. In physical units, both the lattice spacing and the time step have the value of Δ. The particle speed is $\bar{e}_i$ and density per node is ρ and $\bar{u}$ or $\bar{v}$ is the macroscopic flow velocity.

To calculate the equilibrium distribution functions $f_i^{eq}(\bar{x},t)$ and $g_i^{eq}(\bar{x},t)$, the general expressions have been considered, which are-

$$f_i^{eq} = w_i\rho\left[1+3(\bar{e}_i.\bar{u}) + \frac{9}{2}(\bar{e}_i.\bar{u})^2 - \frac{3}{2}\bar{u}.\bar{u}\right] \tag{3}$$

$$g_i^{eq} = w_i\rho\left[1+3(\bar{e}_i.\bar{u}) + \frac{9}{2}(\bar{e}_i.\bar{u})^2 - \frac{3}{2}\bar{u}.\bar{u}\right] \tag{4}$$

where, $\bar{u} = (u_x, u_y)$ is the velocity, the lattice speed $c = \frac{\Delta x}{\Delta t}$, w_i is the weighting factor and it has different values.

For $i = 1$, $w_i = \frac{4}{9}$; $i = 2,3,4,5$, $w_i = \frac{1}{9}$ and for $i = 6,7,8,9$, $w_i = \frac{1}{36}$.

The macroscopic fluid density ρ and velocity $\bar{u}$ can be found from the moments of distribution functions and they yield to the following:

$$\rho = \sum_{i=0}^{8} f_i \tag{5}$$

$$\bar{u} = \frac{1}{\rho} \sum_{i=0}^{8} f_i \bar{e}_i \tag{6}$$

And for temperature, the general form is:

$$T = \sum_{i=0}^{8} g_i \tag{7}$$

2.2 The Smagorinsky Turbulence Model

To study the steady airflows in place like hospital, Reynolds Average Navier-Stokes (RANS) method is used. However, these types of flows are generally very dynamic as the load or the ventilation changes. So, to simulate dynamic and turbulent flows with the LBM, the basic equation needs to be expanded, as it is limited to low Reynolds number (Re) and it becomes unstable as the relaxation time τ in Eq. (i) and (ii) approach to 1/2 (i.e, the viscosity goes towards 0). For this, it would require very fine lattices and very long simulation times, which will make it impossible to complete the computational works. So, a sub-grid model, like the Smagorinsky model [15], can be applied to demonstrate and model the physical effects that the unresolved sub-grid motion has on the resolved fluid motion. This proposed model uses a positive turbulent eddy viscosity, ν_t, to represent small scale energy damping. ν_t is calculated from the local stress tensor, $\bar{S}_{\alpha\beta}$, as follows:

$$\nu_t = C\Delta^2 |\bar{S}| \tag{8}$$

where, C = 0.01 is the Smagorinsky constant, Δ is the filter width, and is the magnitude of the local stress tensor and $|\bar{S}| = \sqrt{2\bar{S}_{\alpha\beta}\bar{S}_{\alpha\beta}}$ is the magnitude of the local stress tensor and

$$|\bar{S}| = \frac{1}{2}\left(\frac{\partial \bar{u}_\alpha}{\partial x_\beta} + \frac{\partial \bar{u}_\beta}{\partial x_\alpha}\right) \tag{9}$$

The total viscosity of the fluid equals the sum of the physical viscosity and the eddy viscosity

$$\nu_{total} = \nu + \nu_t \tag{10}$$

In the LBM, the effect of the eddy viscosity is put into a local relaxation time τ_s given by [16]:

$$\tau_s = 3\nu_{total} + \frac{1}{2} = 3\left(\nu + C\Delta^2 |\bar{S}|\right) + \frac{1}{2} \tag{11}$$

This upgraded relaxation time is then applied in the relaxation process of the Lattice Bhatnagar-Gross-Krook (LBGK) equations. Each node of the lattice relaxes at different rates. Meanwhile, the local stress tensor is relatively simpler to calculate within the LBM, compared to the traditional procedures (based on finite difference computations) and can be found locally from the non-equilibrium stress tensor,

$$\Pi_{\alpha\beta} = \sum_{i=0}^{8} e_{i\alpha} e_{i\beta} \left(f_i - f_i^{eq}\right) \tag{12}$$

The intensity of the local stress tensor $\bar{S}_{\alpha\beta}$ and relaxation time for temperature distribution function τ_t can be found by the following expressions:

$$\bar{S} = \frac{1}{6C\Delta^2}\left(\sqrt{\nu^2 + 18C^2\Delta^2\sqrt{\Pi_{\alpha\beta}\Pi_{\alpha\beta}}} - \nu\right) \tag{13}$$

$$\tau_t = 3\left(D + D_t\right) + \frac{1}{2} = 3\left(D + C\Delta^2 \frac{|\bar{S}|}{\mathrm{Pr}_t}\right) + \frac{1}{2} \tag{14}$$

here, Pr_t is the turbulent Prandtl number and its value has been kept at 0.5. It is nothing but a non-dimensional term defined as the ratio between the eddy viscosity and the heat transfer eddy diffusivity.

RESULTS AND DISCUSSION

This section has been divided into few subsections. The first part shows the code validation result, followed by simulation results for different situations.

Code Validation

The comparison with the benchmark values by Ghia *et. al* [17] has been presented in graphs in Figure 1. For this validation process, lid-driven square cavity for Re=1000 has been taken. In terms of both *u* and *v* velocity, it can be seen that the present research agrees well with the benchmark values.

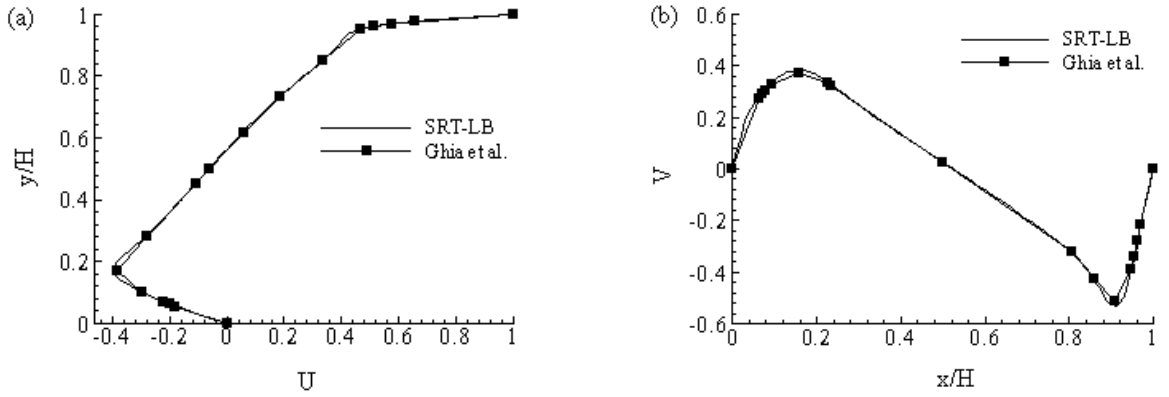

(a) (b)

FIGURE 1. Direct comparison with benchmark values for (a) u velocity at x/H =0.5 and (b) v velocity at y/H =0.5 at Re =1000.

Hospital Ward with a Partition in the Middle

After code validation process, the simulations have been carried out inside hospital ward with a partition in the middle. A schematic diagram has been shown in Figure 2 representing the overall idea. The measurement has been put as well. The lattice size for the whole ward is 400 × 50 and the partition has the dimension of 5 × 40 lattice and it is placed right after the first three blocks. Three different Reynolds numbers: 1250, 1500 and 1800 have been considered to test the behavior of airflow. At the beginning, irregularity in flow can be noticed in the contour as the streamlines appear over there. The airflow nicely crosses the partition without overlapping it and it goes in natural way towards the outlet. Fig. 3 (i) shows the image of the airflow pattern in experiment as well as the velocity contours map generated by LBM. There are more vorticity in the airflow after the partition because the air goes over the partition through a narrow channel and once it gets past that obstacle completely, it gets more space for circulation and same thing happened in that figure. After creating few turbulent flows, air goes towards the outlet, which is also visible in the Fig. 3 (i). In addition, for an increase in *Re*, the highest value of the contour also increases. For example, when Re=1250, the peak value is 3.86. But it becomes 3.96 and 4.09 for Re=1500 and Re=1800 respectively.

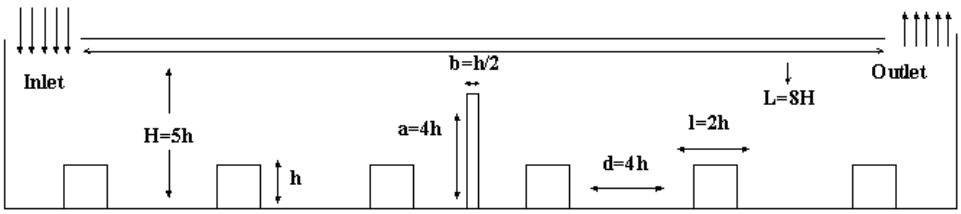

FIGURE 2. Schematic diagram of hospital ward with a partition in the middle.

Patients have been considered on each bed, who are continuously releasing heat that is higher than the room temperature. So, the isotherms have also been kept heated and gaps between the blocks remain cold. Just like the figure in contour, the partition has not been heated. Figure 3 (ii) represents isotherms of different *Re*. *Pr* was kept at 0.71 and turbulent Pr was fixed at 0.5.

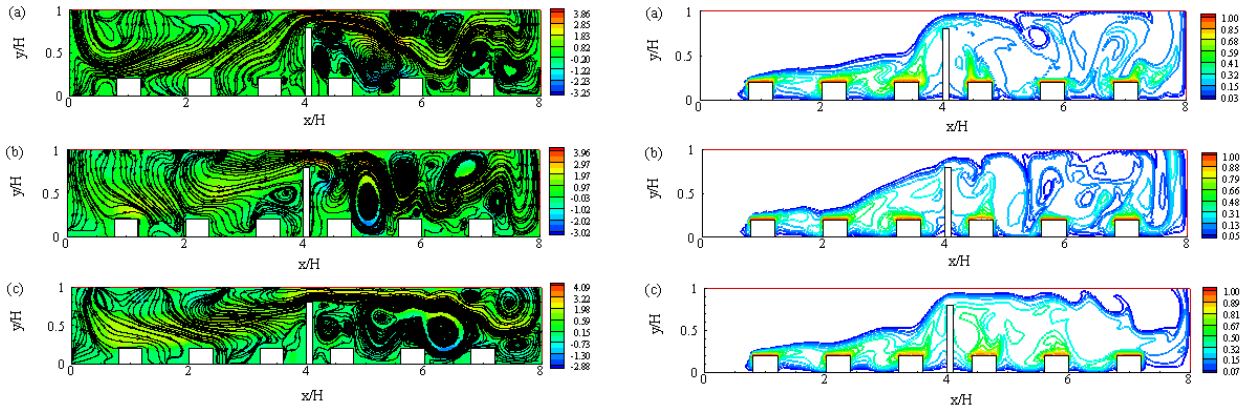

(i) (ii)

FIGURE 3. (i) Streamlines and (ii) isotherms appended for (a) Re=1250, (b) Re=1500, and (c) Re=1800.

Average Rate of Heat Transfer

In this section, Nusselt number has been calculated to observe the changes in average rate of heat transfer for different Re. Table 1 shows such calculation when the partition was placed. To calculate the average $\overline{Nu}$, it is necessary to integrate the expression over the range of interest and thus it implies:

$$Nu(x) = -\frac{\partial\theta}{\partial y}\bigg|_{y=y_2} \qquad \text{i)}$$

Here, y_2 is the surface of each block. To calculate the average Nu_{avg} it is needed to integrate the expression over the range of interest and the following expression is got:

$$Nu_{avg} = \frac{1}{x_2 - x_1}\int_0^{(x_2-x_1)} Nu(x).dx \qquad \text{ii)}$$

As per Table 1, it can be seen the total Nu increases for an increase in Re. For Re=1250, $\overline{Nu}_{avg}$ is 40.77648. After increasing the values of Re to 1500 and 1800, total Nu becomes 44.53272 and 49.02621 respectively. It implies that, if Re keeps increasing, the average rate of heat transfer will increase too. So, from Re=1250 to Re=1500, total Nu gets increased by 8.43% and from Re=1500 to Re=1800, it increases around 9.17%. Now, if the heat transfer for individual block (bed) is considered, changes can be noticed here as well. At block 1, when

Re=1250, $\overline{Nu}_{avg}$ is 7.58013. The value for block 1 remains quite similar in all cases as it is closest to the inlet and the air is just entering into the ward and that is why patient at bed 1 is releasing more heat. Gradually, it keeps getting decreased until block 4. However, at block 5, there is a sudden increase in *Nu*. For example, for Re=1500, value of Nu at block 3 is 3.51671 but for block 4 it spikes to 6.19935. Heat transfer is maximum at block 5 for all conditions. The main reason behind is the vorticity, which was shown in the Fig. 2. As per that figure, vorticity is more visible near block 4 and 5. However, the value was supposed to be at maximum for block 4, but due to partition, the air goes through the narrow path and it gets more free space near block 5 and that is why the patient on that block (bed) will release the maximum heat in that particular ward for all three *Re*. In the end, at block 6, the rate of heat transfer decreases for all case as it is closest to the outlet and the wall. The vorticity also gets reduced. However, if any particular patient needs more air, he or she should be kept on either bed no. 4 or 5, based on their needs.

TABLE 1. Summary of average Nusselt numbers for six blocks individually and total Nusselt numbers, at Pr=0.71.

Re	$\overline{Nu}_{avg}$ **(Indiv.)**		$\overline{Nu}_{avg}$ **(Total)**
1250	Block 1	7.58013	40.77648
	Block 2	4.95634	
	Block 3	3.49007	
	Block 4	5.76506	
	Block 5	11.12709	
	Block 6	7.85778	
1500	Block 1	7.41641	44.53272
	Block 2	5.51089	
	Block 3	3.51671	
	Block 4	6.19935	
	Block 5	13.50099	
	Block 6	8.38837	
1800	Block 1	7.69563	49.02621
	Block 2	6.04786	
	Block 3	4.56460	
	Block 4	7.10631	
	Block 5	15.10631	
	Block 6	8.50575	

CONCLUSION

The main purpose of this paper was to observe the indoor airflow pattern and heat transfer condition in a hospital ward by applying LBM. The airflow was characterized by applying different Reynolds numbers in forced convection. In the first part of this work, code validation had been performed comparing the values of benchmark data and the data achieved from this research. The data agreed well with each other and it implies that the simulations, plotting had been successful. The simulation was then carried out for a general ward with a partition in the middle to observe the patterns and behavior of the airflow. Before going through the simulation process, mathematical discussions had been added on LES.

It can be concluded that placing the partition in the middle made the most vital difference in indoor airflow. After crossing the partition, vortex appeared most in the ward and the rate of heat transfer increased as well. The vorticity is most visible near bed 4 and 5 and that is the reason why values of Nu increased, which was observed earlier in Table 1. Patient on bed 4 should have got more air but the partition in the middle was like a wall and air faced a bit obstacle and then got free space near bed 5, which eventually led to highest heat transfer rate. So, higher re-circulations or vorticity leads to higher rate of heat transfer and patient releasing more heat will feel more comfortable. However, each patient has particular need based on individual disease.

REFERENCES

1. H. Pitsch, Large-Eddy Simulation of turbulent combustion, Annu. Rev. Fluid Mech. 38 (2006) 453–482.
2. C. Zhen-Hua, S. Bao-Chang, Z. Lin, Simulating high reynolds number flow in two-dimensional lid-driven cavity by multi-relaxation-time lattice boltzmann method, Chinese Physics 15 (2006) 1855.
3. Z. Guo, C. Zheng, B. Shi, Lattice Boltzmann equation with multiple effective relaxation times for gaseous microscale flow, Physical Review E 77 (2008) 036707.
4. Y.-H. Dong, P. Sagaut, A study of time correlations in Lattice Boltzmann-based Large-Eddy Simulation of isotropic turbulence, Physics of Fluids (1994-present) 20 (2008) 035105.
5. Djenidi, Structure of a turbulent crossbar near-wake studied by means of Lattice Boltzmann Simulation, Physical Review E 77 (2008) 036310.
6. M. Geier, A. Greiner, J. G. Korvink, Cascaded digital Lattice Boltzmann automata for high Reynolds number flow, Physical Review E 73 (2006) 066705.
7. H. Yu, S. S. Girimaji, L.-S. Luo, Lattice Boltzmann Simulations of decaying homogeneous isotropic turbulence, Physical Review E 71 (2005) 016708.
8. M. Krafczyk, J. To¨ lke, L.-S. Luo, Large-Eddy Simulations with a multiple-relaxation-time LBE model, International Journal of Modern Physics B 17 (2003) 33–39.
9. S. Chen, G. D. Doolen, Lattice Boltzmann Method for fluid flows, Annual review of fluid mechanics 30 (1998) 329–364.
10. H. Lee, H. B. Awbi, Effect of internal partitioning on room air quality with mixing ventilation statistical analysis, Renewable energy 29 (2004) 1721–1732.
11. S. Zhang, C. Lin, Application of Lattice Boltzmann Method in indoor airflow simulation, HVAC&R Research 16 (2010) 825–841.
12. S. Chen, H. Chen, D. Martnez, W. Matthaeus, Lattice Boltzmann Model for simulation of magnetohydrodynamics, Physical Review Letters 67 (1991) 3776.
13. Y. Qian, D. dHumieres, P. Lallemand, Recovery of Navier-Stokes Equations using a Lattice-gas Boltzmann Method, Europhys. Lett 17 (1992) 479.
14. H. Chen, S. Chen, W. H. Matthaeus, Recovery of the Navier-Stokes Equations using a Lattice-gas Boltzmann method, Physical Review A 45 (1992) R5339.
15. J. Smagorinsky, General circulation experiments with the primitive equations: I. the basic experiment*, Monthly weather review 91 (1963) 99–164.
16. S. Hou, J. Sterling, S. Chen, G. Doolen, A Lattice Boltzmann subgrid model for high Reynolds number flows, arXiv preprint comp-gas/9401004 (1994).
17. U. Ghia, K. N. Ghia, C. Shin, High-Re solutions for incompressible flow using the Navier-Stokes Equations and a multigrid method, Journal of computational physics 48 (1982) 387–411.

ICME2015

International Conference on Mechanical Engineering 2015
(ICME 2015) 18 – 20 December, 2015, Dhaka, Bangladesh

Paper ID :166

Turbulent Combined-Convection Boundary Layer with Aiding Flows along a Heated Vertical Flat Plate at Higher Freestream Velocity

Mohammad Zoynal Abedin[1,a)], Mohammed Moinul Islam[1], Md. Abu Hanif[2,b)] and Md. Jahangir Alam[1]

[1]*Department of Mechanical Engineering, Dhaka University of Engineering & Technology, Gazipur-1700, Bangladesh*
[2]*Apex Holdings Limited, Gazipur-1749, Bangladesh.*

[a)]Corresponding author: abedin.mzoynal@duet.ac.bd
[b)]hanifme087@gmail.com

Abstract. A numerical investigation is performed in the turbulent combined-convection boundary layer with aiding flows in air along a heated vertical flat plate at a higher freestream velocity (Re_{δ_0} = 600) by time-developing direct numerical simulation (DNS). At higher freestream velocity, the transition from laminar to turbulent delays for aiding flows and relatively a lower and higher heat transfer rates are observed, respectively, in the laminar and turbulent region compared to that of lower freestream velocity. The wall shear stresses are higher in the laminar region compared to that in the turbulent region, and at higher freestream velocity, the wall shear stress in the transition region shows a higher peak value. The intensity of velocity and temperature fluctuations for aiding flows with higher freestream velocity become appreciably lower than that for lower freestream velocity due to the laminarization of the boundary layer.

INTRODUCTION

The analysis of the boundary layer flows is important not only to clarify the fundamental characteristics of the boundary layer but also to evaluate the basic structures of buoyancy-driven flows practically encountered in many applications. In most cases, freestream velocities are often superimposed on pure thermally-driven boundary layers (combined-convection boundary layers) and the turbulence characteristics of the boundary layers vary with the magnitude and direction of freestream velocity and working fluids [1-3]. However, there are very limited investigations dealing with the time-developing DNS for the turbulent natural- and combined-convection boundary layers along with their characteristics of the turbulent structures [4-7].

The fundamental characteristics of the turbulent combined-convection boundary layers were investigated along various passages [8-10] and the effects of freestream velocity on the turbulent combined-convection boundary layer along a vertical heated plate were extensively investigated by Hattroi et al. [11-13]. Furthermore, few expensive experiments were conducted for the turbulent combined-convection boundary layer with opposing flow (freestream in the direction to the gravitational force) [14, 15]. Due to the difficulty in obtaining the fluctuating characteristics of the boundary layer flows from the experiments, the numerical simulation techniques have been used to evaluate the characteristics of the complex flow phenomenon. Recently, the effects of freestream velocity on the characteristics of boundary layer flows have been numerically analyzed by Abedin and Tsuji [3], and Abedin et al. [6]. However, the effects of the higher freestream velocity on the characteristics of the boundary layer flows in the natural- and combined-convection have not yet been focused sufficiently and are eagerly awaited.

Therefore, in the present analysis, the DNS has been performed to clarify the fundamental characteristics of the turbulent combined-convection boundary layer with aiding flows in air along a heated vertical flat plate at the higher freestream velocity.

NUMERICAL PROCEDURE

A numerical investigation is carried out for the turbulent combined-convection boundary layer with aiding flows for air along a heated vertical flat plate by time-developing DNS. The flow is induced by heating an infinitely long vertical flat plate at a uniform temperature from a given time onward ($\tau = 0$). The calculation domain and coordinate systems are shown in Fig. 1. The coordinates in the vertical, wall-normal and spanwise directions are x, y and z, respectively, and the instantaneous velocities u, v and w are specified in the relevant directions. The instantaneous temperature is t and the wall and ambient temperatures, T_w and T_∞, respectively, are assumed to be constant.

The governing equations with the Boussinesq approximation expressing the conservation of mass, momentum and energy in the tensor notation can be written as follows:

The conservation of mass

$$\frac{\partial u_i^*}{\partial x_i^*} = 0 \tag{1}$$

The conservation of momentum

$$\frac{\partial u_i^*}{\partial \tau^*} + u_j^* \frac{\partial u_i^*}{\partial x_j^*} = -\frac{\partial p^*}{\partial x_i^*} + \frac{\partial^2 u_i^*}{\partial x_j^{*2}} + Gr_{\delta_0}\theta \tag{2}$$

The conservation of energy

$$\frac{\partial \theta}{\partial \tau^*} + u_j^* \frac{\partial \theta}{\partial x_j^*} = \frac{1}{Pr}\frac{\partial^2 \theta}{\partial x_j^{*2}} \tag{3}$$

Where, x_i is the coordinate in tensor notation in meter; τ is the time in second; p is the pressure in Pascal; $Gr_{\delta 0}$ is the Grashof number based on the initial integral thickness of the velocity boundary layer, δ_0; θ is the dimensionless temperature, $(t - T_\infty) / \Delta T_w$; ΔT_w is the temperature difference between wall and ambient in Kelvin; Pr is the Prandtl number. The star symbol "*" is used to normalize the variables with δ_0 and ν. Here, ν is the kinematic viscosity in m^2/s. The periodic boundary conditions have been applied for the x^* and z^* directions and the no-slip boundary conditions in the y^* direction.

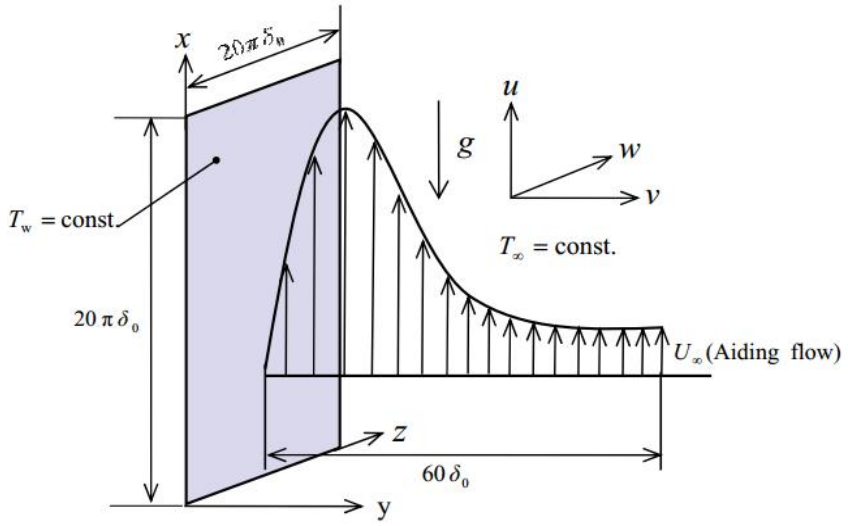

FIGURE 1. Calculation domain and coordinates.

The above momentum and energy equations have been discretized by the second-order accurate central difference scheme on the staggered grids and the detailed numerical simulation techniques are extensively reported in the literature of Abedin et al. [1, 2]. The integral thickness of the velocity boundary layer, δ - which is adopted as a characteristic length scale for the analysis - can be defined as follows:

$$\delta = \int_0^\infty \left| U - U_\infty \right| / \left(U_{\max} - U_{\min} \right) dy \tag{4}$$

Here, U is the mean velocity found by averaging the velocity in the (x - z) plane; U_∞, $U_{\max}$ and $U_{\min}$ are the ambient, maximum and minimum mean velocities in the boundary layer, respectively. For pure natural convection, $U_{\min} = U_\infty = 0$ and for combined convection with aiding flows, $U_{\min} = 0$.

RESULTS AND DISCUSSIONS

Time-developing DNS was advanced by adding various initial disturbances in the laminar boundary layer, which were created by reducing velocity fluctuations observed in the turbulent boundary layer to tiny fluctuations less than 1% for the intensities. Such disturbances have an effect on the calculated results of the characteristics in the turbulent boundary layer region found by Abedin et al. [1, 2]. Therefore, we show the following turbulence statistics as the ensemble averaged values of several iterations with different initial disturbances.

Code Validation

The predicted statistics of the heat transfer rates in boundary layer flows have been well compared and validated with the existing observations. Figure 2 shows the validated heat transfer rates - expressed in terms of the Nusselt number, Nu_δ - in the natural convection boundary layers both in air and water against the Grashof number, Gr_δ based on the integral thickness of velocity boundary layer, δ. As can be seen from Figure 2, the predicted heat transfer rates agree completely well with those obtained by the results in the numerical simulations of Abedin et al. [1] for both air and water. Furthermore, the present predicted results of the heat transfer rates also correspond well, respectively, with the experimental results of Tsuji and Nagano [16] for air, and Vliet-Liu [17] and Tsuji-Kajitani [18] for water. Thereby, it can be henceforth concluded that the present analysis would provide credible information in the characteristics of turbulent combined-convection boundary layer with aiding flows in air along a heated vertical flat plate.

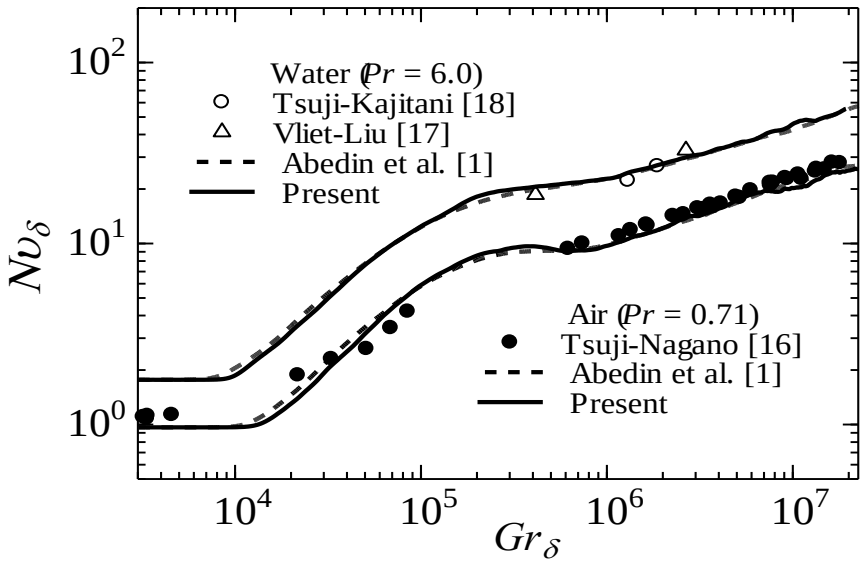

FIGURE 2. Code validation - Heat transfer rates in natural-convection boundary layer on length scale, δ.

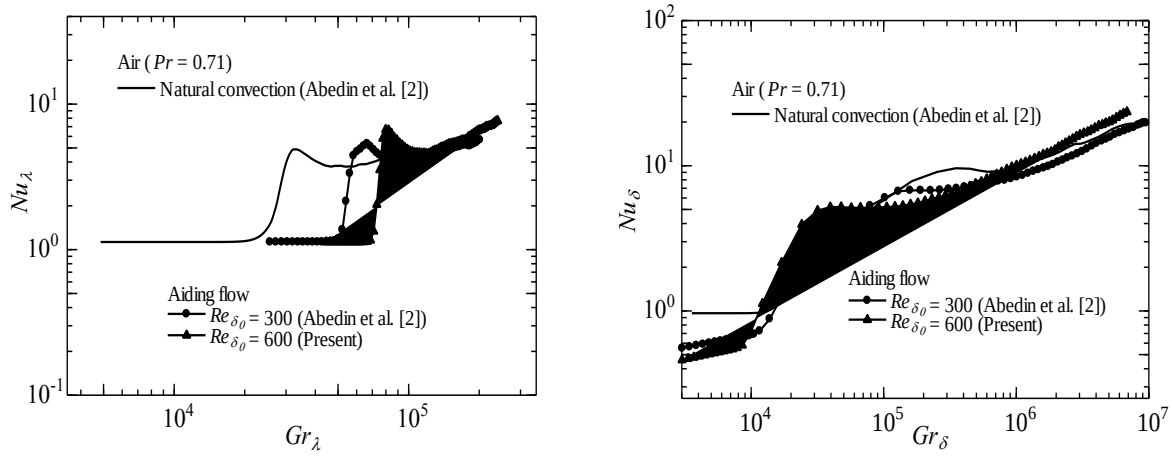

(a) (b)

FIGURE 3. Heat transfer rates in combined-convection boundary layer with aiding flows in air (Pr = 0.7) - (a) Relation between Nusselt and Grashof numbers based on length scale, λ; (b) Relation between Nusselt and Grashof numbers based on length scale, δ

Heat Transfer Rates

The profiles of the heat transfer rates in the natural-convection boundary layer and the combined-convection boundary layer with aiding flows in air (Pr = 0.71) along a heated vertical plate are shown in the relation between the Nusselt number, Nu_λ and the Grashof number, Gr_λ based on the reference length scale, $\lambda = 2\sqrt{\alpha\tau}$ (where, λ is the reference length scale in meter, α is the thermal diffusivity in m^2/s) and in the relation between the Nusselt number, Nu_δ and the Grashof number, Gr_δ based on the integral thickness of the velocity boundary layer, δ in Figs. 3 (a) and (b), respectively.

As can be seen from Fig. 3 (a), with a slight increase in freestream velocity, the transition from laminar to turbulent delays for the combined-convection boundary layer with aiding flow compared to those in the natural-convection boundary layer [2]. At higher freestream velocity, the transition from laminar to turbulent further delays with a higher value of heat transfer in the turbulent region. This implies in consistent with the experimental fact that the transition region moves downstream for aiding flow in the time-developing boundary layer [2].

As can be seen in Fig. 3 (b), the critical Grashof number based on the integral thickness of the velocity boundary layer, δ indicating the transition to turbulence becomes about 10^4 in the natural-convection boundary layer for both air and water (Abedin et al. [1, 2]). And, this critical Grashof numbers show somewhat different values in the combined-convection boundary layer with aiding flows of air for higher freestream velocity. However, at higher freestream velocity, relatively a lower heat transfer rates observed in the laminar region compared to that of the lower freestream velocity.

Wall Shear Stresses

The profiles of dimensionless wall shear stresses in the natural-convection boundary layer and the combined-convection boundary layer with aiding flows in air (Pr = 0.71) along a heated vertical plate are shown in the relation between the dimensionless wall shear stress, $\tau_w/(\rho g\beta\Delta T_w\lambda)$ and the Grashof number, Gr_λ based on the reference length scale, λ and in the relation between the dimensionless wall shear stress, $\tau_w/(\rho g\Delta T_w\delta)$ and the Grashof number, Gr_δ based on the integral thickness of the velocity boundary layer, δ in Figs. 4 (a) and (b), respectively.

As can be seen in Fig. 4 (a), the values of the wall shear stresses, $\tau_w/(\rho g\beta\Delta T_w\lambda)$ are higher in the laminar boundary layer region compared to those observed in the turbulent boundary layer region for both the natural-convection boundary layer and combined-convection boundary layer with aiding flows in air [2]. On the other hand,

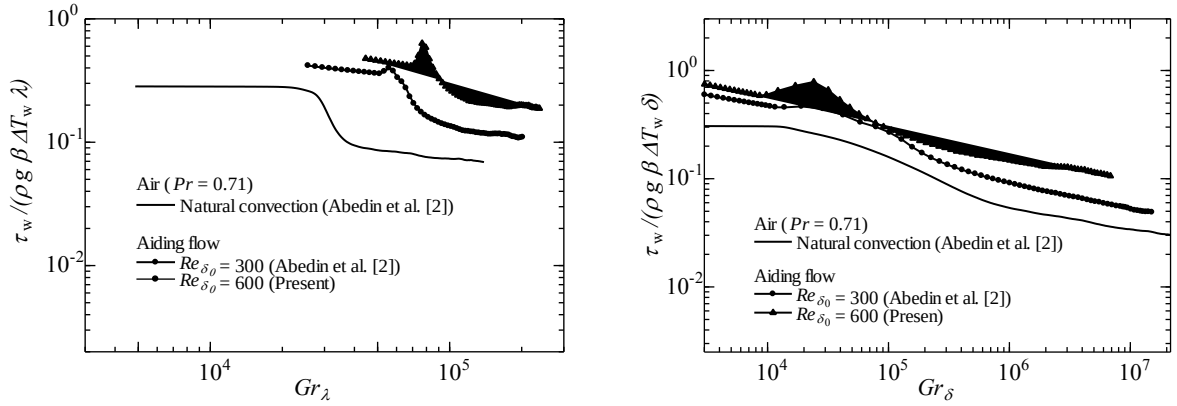

(a) (b)

FIGURE 4. Wall shear stresses in combined-convection boundary layer with aiding flows in air ($Pr = 0.7$) - (a) Relation between wall shear stresses and Grashof number based on length scale, λ; (b) Relation between wall shear stresses and Grashof number based on length scale, δ.

at higher freestream velocity, the wall shear stress in the transition region shows a higher peak value in air compared to those observed in water due to the effect of higher Prandtl number of water (not shown in the figures for water). It is also observed that the transition from laminar to turbulent delays for higher freestream velocity compared to those in the natural convection boundary layer flow and at a lower freestream velocity flow [2] in accordance with the similar nature observed in the heat transfer rates shown in Figs. 3.

As can be seen in Fig. 4 (b), the values of the wall shear stresses, $\tau_w/(\rho g \Delta T_w \delta)$ increase with increase in freestream velocity throughout the boundary layer region. At higher freestream velocity, a higher peak value of the wall shear stress is observed in the transition boundary layer region which is also analogous to the values of the wall shear stresses, $\tau_w/(\rho g \beta \Delta T_w \lambda)$ as shown in Fig. 4(a).

Mean and Fluctuating Velocity Distributions

The mean streamwise velocity profiles, U and the intensity profiles of streamwise velocity fluctuation, u'- both of them are normalized with the velocity difference ($U_{max} - U_{min}$) - predicted for the turbulent natural-convection boundary layer and the turbulent combined-convection boundary layer with aiding flows in air obtained for various Grashof numbers and freestream velocities are displayed against y/δ in Figs. 5 (a) and (b), respectively.

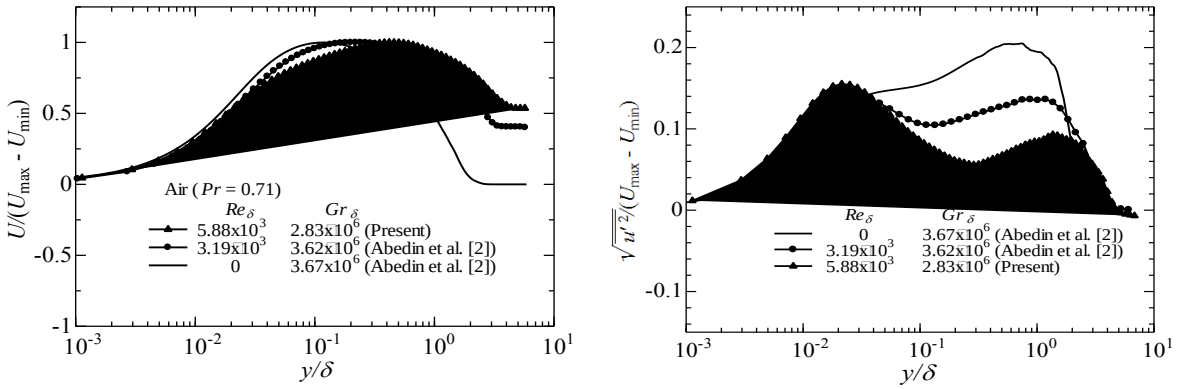

(a) (b)

FIGURE 5. (a) Profiles of mean velocity, (b) Intensity profiles of streamwise velocity fluctuations in turbulent combined-convection boundary layer with aiding flows.

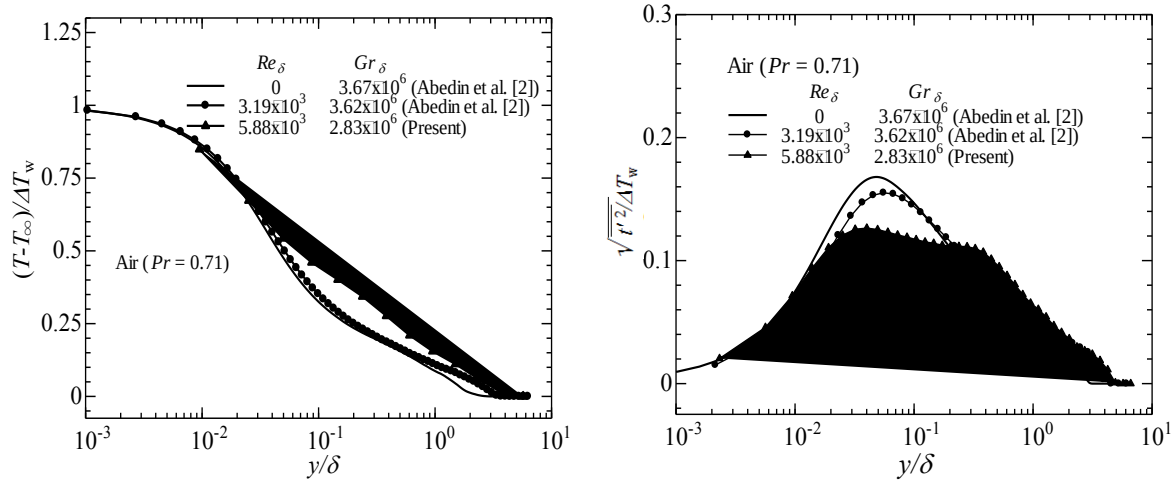

(a) (b)

FIGURE 6. (a) Profiles of mean temperature distribution, (b) Intensity profiles of temperature fluctuations in turbulent combined-convection boundary layer with aiding flows in air (Pr = 0.71).

As can be seen from Fig. 5 (a), the mean velocity changes according to the freestream velocity added to the pure thermally-driven boundary layer flows. However, at higher freestream velocity, the mean velocity profiles has the highest value in the outer boundary layer compared to those observed at lower freestream velocity [2].

As can be seen in Fig. 5 (b), the intensity profiles of streamwise velocity fluctuation, u' for aiding flows of air become once higher with the addition of small freestream than the profiles for pure natural-convection boundary layer. On the other hand, the intensity profile for aiding flow becomes appreciably lower than that for pure natural convection with increasing freestream velocity, and takes two peaks on the sides of the maximum mean velocity location ($y/\delta \approx$ 0.1) indicating the laminarization of the boundary layer. Moreover, at higher freestream velocity, the profiles get decreased compared to those observed in the pure natural-convection boundary layer and combined-convection boundary layer with a lower freestream velocity [2].

Mean and Fluctuating Temperature Distributions

The profiles of the mean temperature distribution and intensity profiles of temperature distribution, t'- both of them are normalized with ΔT_w - predicted for the turbulent natural-convection boundary layer and the turbulent combined-convection boundary layers with aiding flows in air obtained for various Grashof numbers and freestream velocities are plotted against y/δ in Figs. 6 (a) and (b), respectively.

As seen in Fig. 6 (a), the variation of mean temperature profiles is only to a slight degree according to the freestream velocity added to the pure thermally-driven flow. This characteristic of mean temperature leads to the fact that the heat transfer rates remain unchanged in the turbulent combined-convection boundary layer observed in air shown in Fig. 3 (b). However, at higher freestream velocity, the mean temperature profiles gradually and uniformly become zero in air compared to those observed in the natural-convection boundary layer and combined-convection boundary layer flows with a lower freestream velocity [2].

CONCLUSIONS

An investigation is performed for the time-developing combined-convection boundary layer with aiding flows in air along a heated vertical flat plate by DNS in order to clarify the fundamental characteristics of the boundary layer flows. The following conclusions may be drawn from the present analysis.

At higher freestream velocity, the transition from laminar to turbulent delays with higher heat transfer rates in the turbulent boundary layer region. However, the heat transfer rates for the combined-convection boundary layer with

aiding flows become lower compared to that in the laminar region of the pure natural-convection boundary layer flow. At higher freestream velocity, the heat transfer rates become lowest in the laminar region, and the transition from laminar to turbulent happens quickly compared to those for lower freestream velocity.

On the other hand, the wall shear stresses are higher in the laminar region compared to those observed in the turbulent region both in the natural-convection and combined-convection boundary layer flows. Moreover, at higher freestream velocity, the wall shear stress in the transition region shows a higher peak value compared to those observed in water (not shown in the figures for water).

The mean streamwise velocity changes according to the freestream velocity added to the pure thermally-driven boundary layers, and at higher freestream, the mean velocity profiles has the highest value in the outer boundary layer region compared to those observed at the lower freestream velocity. The intensity of velocity and temperature fluctuations for aiding flows with higher freestream velocity become appreciably lower than that for lower freestream velocity due to the laminarization of the boundary layer.

ACKNOWLEDGEMENTS

The authors would like to acknowledge Professor Dr. Toshihiru Tsuji, Nagoya Institute of Technology, Japan, for his invaluable suggestions and great assistances in the time of simulation and experimentation. The Authors would also like to extend their gratitude to Afroza Begum and Ahyan Ruzhan Abedin for their continuous help and cooperation.

REFERENCES

1. M. Z. Abedin, T. Tsuji, Y. Hattori, International Journal of Heat and Mass Transfer, **52,** 4525-4534 (2009).
2. M. Z. Abedin, T. Tsuji, Y. Hattori, International Journal of Heat and Mass Transfer, **53,** 2113-2122 (2010).
3. M. Z. Abedin and T. Tsuji, "Effect of freestream on thermally-driven boundary layers along a heated vertical flat plate," in *Proceedings of the 14th International Heat Transfer Conference* (Washington D.C., USA, TRK-20 of CD-ROM, 2010), pp. 1-8.
4. M. Z. Abedin and T. Tsuji, "Structural characteristics of turbulent combined-convection boundary layers along a vertical flat plate," in *Proceedings of the 7th International Conference on Heat Transfer, Fluid Mechanics and Thermodynamics* (Antalya, Turkey, 2010), pp. 2175-2180.
5. M. Z. Abedin and T. Tsuji, "Transition behavior and turbulence characteristics in combined-convection boundary layers along a heated vertical flat plate," in *Proceedings of the 13th Asian Congress on Fluid Mechanics* (Dhaka, Bangladesh, 2010), pp. 759-762.
6. M. Z. Abedin, T. Tsuji, J. Lee, International Journal of Heat and Fluid Flow, **36,** 92-100 (2012).
7. M. Z. Abedin, T. Tsuji, J. Lee, International Journal of Heat and Mass Transfer, **55**, 3995-4002 (2012).
8. M. J. Watts and C. T. Chou, "Mixed convection heat transfer to supercritical pressure water," in *Proceedings of the 7th International Heat Transfer Conference* (3(MC16), 1982), pp. 495-500.
9. J. Wang, J. Li, J. D. Jackson, International Journal of Heat and Fluid Flow, **25**, 420-430 (2004).
10. N. Kasagi and M. Nishimura, International Journal of Heat and Fluid Flow, **18**, 88-99 (1997).
11. Y. Hattori, T. Tsuji, Y. Nagano, N. Tanaka, International Journal of Heat and Fluid Flow, **21**, 520-525 (2000).
12. Y. Hattori, "Turbulent characteristics and transition behavior of combined-convection boundary layer along a vertical heated plate," Ph.D. thesis, Nagoya Institute of Technology, 2001.
13. Y. Hattori, T. Tsuji, Y. Nagano, N. Tanaka, International Journal of Heat and Fluid Flow, **22**, 315-322 (2001).
14. T. Inagaki and K. Kitamura, Transaction of JSME, **B 54**, 675-680 (1988). (In Japanese)
15. T. Inagaki and K. Kitamura, Transaction of JSME, **B 54**, 2515-2522 (1988). (In Japanese)
16. T. Tsuji and Y. Nagano, Experimental Thermo Fluid Science, **2**, 208-215 (1989).
17. G. C. Vliet and C. K. Liu, Transaction of ASME Journal on Heat Transfer, **C-91**, 517-531 (1969).
18. T. Tsuji and T. Kajitani, "Turbulence characteristics and heat transfer enhancement of a natural convection boundary layer in water along a vertical flat plate," in *Proceedings of the 13th International Heat Transfer Conference* (Sydney, Vol. TRB-08 of CD-ROM, 2006).
19. T. Tsuji and Y. Nagano, International Journal of Heat and Mass Transfer, **31**, 1723-1734 (1988).

ICME2015

International Conference on Mechanical Engineering 2015
(ICME 2015) 18 – 20 December, 2015, Dhaka, Bangladesh

Paper ID : 169

Reduced Thermal Conductivity of a Nanoparticle Decorated Nanowire: A Non-equilibrium Molecular Dynamics Study

Ahmed Shafkat Masnoon[a)], Ferdaushi Alam Bipasha, AKMM Morshed

Department of Mechanical Engineering, Bangladesh University of Engineering and Technology, Dhaka,Bangladesh

[a)] Corresponding author: shafkat.masnoon@gmail.com

Abstract: The effect of nanoparticles decoration on the thermal conductivity of a nanowire is studied using Non Equilibrium Molecular Dynamics (NEMD) simulation. The simulation was conducted using simplified molecular model with Lenard-Jones potential. Argon-like solid was used as the material for both the nanowire and nanoparticles. Nanoparticles were placed on the surface of the nanowire and also embedded inside the structure. Non-equilibrium molecular dynamics simulation was conducted by imposing temperature gradient along the length of the nanowire and thermal conductivity of the nanowire was calculated. Nanowire without any nanoparticles was used as the baseline data. Due to presence of nanoparticles thermal conductivity of the nanowire was observed to decrease and up to 40% reduction in thermal conductivity was observed. With the increase in number of the nanoparticles, thermal conductivity was observed to decrease; however size of nanoparticles has little effect.

Keywords: Molecular dynamics simulation; Nanowire; Thermal conductivity; Nanoparticles; Lenard-Jones potential.

INTRODUCTION

Thermoelectric effect enables direct conversion between thermal and electrical energy and provides an alternative route for power generation and refrigeration [1]. An ideal thermoelectric material should be an excellent electrical conductor having reduced thermal conductivity. Many experimental and theoretical studies have been done on materials such as PbTe, Si, Si-Ge alloy, Bi-alloys, Graphene etc. for thermoelectric material for different applications [2-5]. Most of these materials have shown better performance for nanostructures compared to the bulk. Nanostructured interfaces strongly scatter phonons but only marginally affect the charge carrier transport [6] and thus suitable for reducing thermal conductivity without affecting electrical conductivity.

Nanoparticles which can be used to decorate nanowires or can be embedded inside the nanowire. This additional nanoparticles influences the behavior of the nanowires; more specifically thermal conductivity of the nanowires by phonon scattering at the interface. With the increase of the mass of the nanoparticles mismatch at the interface becomes larger leads to larger temperature drop at the interface. The presence of the nanoparticles provides an effective scattering mechanism for the mid or long wavelength phonons that dominate thermal conduction [7]. Increased phonon-interface collisions prevent the phonons with high energy in the hot region from moving to the cold region and vice versa [8]. This interface scattering means lower energy transport; consequently, the thermal conductivity is low. In many nanocomposite materials, it was observed that the effective thermal conductivity decreases considerably with an increase of the Kapitza resistance. Even though the nanoparticles have a much higher thermal conductivity than the matrix, the nanoparticles may not result in an increased effective thermal conductivity if the nanoparticle size is fairly low and the Kapitza thermal resistance is considerably high [9].

In this study argon-like solids with Lennard-Jones (LJ) potential were used as the model system and NEMD simulation was performed. The simplicity of the interatomic interactions has made argon a benchmark system to test

methodological developments and thus to improve our microscopic understanding [14]. The simulation starts with the simulation of pure argon nanowire. Base line simulation was followed with simulation of nanoparticles embedded nanowire and nanoparticles decorated nanowire. The results are intended to have application in energy conversion devices and applications.

METHODOLOGY

The three dimensional simulation cell of 80a x 6a x 6a was constructed of Ar molecule arranged in FCC lattice, where a is lattice constant of argon which is 5.4 Å. Heat was flowed along the *x* direction as presented in Fig. 1(a) and periodic boundary conditions were imposed in all the directions. Four lattices at both ends of the domain are assigned as the hot region, and eight lattices in the middle are assigned as the cold region. Velocities of the molecules in these regions were scaled to maintain the desired temperature.

The molecular interactions were modeled with simple Lennard-Jones (LJ) potential [10]:

$$\emptyset(r_{ij}) = 4 \in \left[\left(\frac{\sigma}{r_{ij}}\right)^{12} - \left(\frac{\sigma}{r_{ij}}\right)^{6}\right] \quad (1)$$

The values of $\in$ and σ were collected form Allen [10] as $\frac{\in}{k_B}$ =119.8 and σ = 3.405 Å, where k_B is the Boltzmann constant. Only the neighbors of an atom within a certain cutoff radius 2.5σ are included in the force calculation. The simulation was started from its initial configuration with a time step of 2.1 fs. The simulation was run for NPT ensemble followed by NVE ensemble for a time period of 420 ps. Once the simulation cell reaches equilibrium at 20K a fixed amount of heat $\Delta\varepsilon$ = 2.78 unit/timestep is added to the hot region while the same amount of heat is subtracted from the cold region to impose a constant heat flux along the *x*-direction. Thus heat flow started between the cold region and hot region. Default time unit used in LJ calculation is $\tau = 2.1*10^{-12}$ and time step $dt = 2.1*10^{-15}$ was used throughout the simulation. The simulation runs for 10.5ns to reach a steady temperature gradient. After the system approaches a steady state the temperature profile was obtained by time averaging. Thermal conductivity of the nanowire was calculated using:

$$K = \frac{\Delta Q^{\cdot}/\tau}{\partial T/\partial x}\ (W/mK) \quad (2)$$

To incorporate the nanoparticles, two cubic nanoparticles of side 2a were embedded into the regular atoms as presented in Fig. 1(b). Nanoparticles mass were varied to 0.125, 0.25 and 0.50. The numbers of the nanoparticles on each side were also increased to three as presented in Fig. 1(c). To find out the effect of the nanoparticles on the surface, the surface of the nanowire was decorated. Nanoparticles of sizes (2a x 2a x a), (8a x 2a x a), (8a x 4a x a) and (8a x 4a x 2a) were built in four different in Fig. 1(d-g).

All the MD simulations were performed using open source platform LAMMPS and visualizations were performed using OVITO.

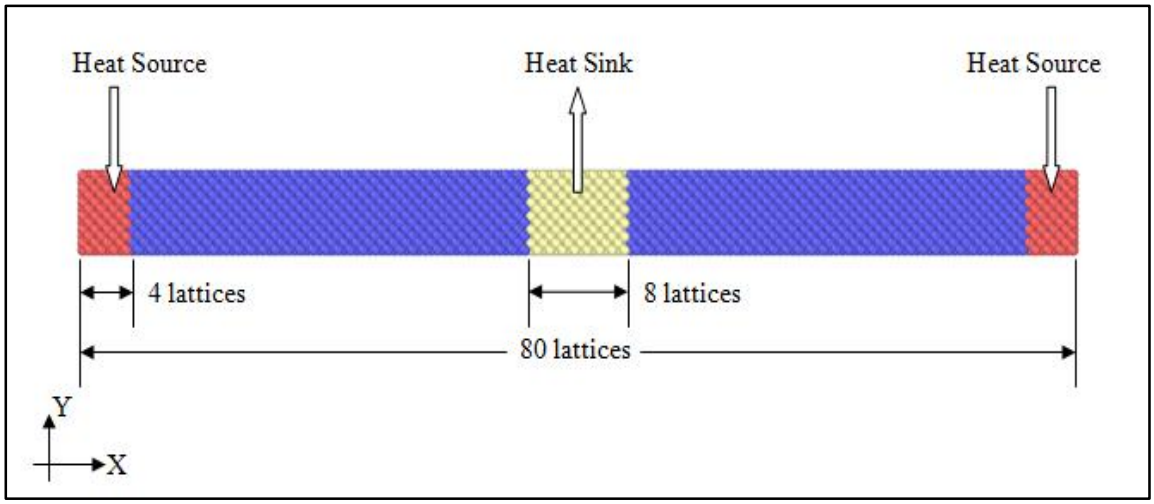

(a)

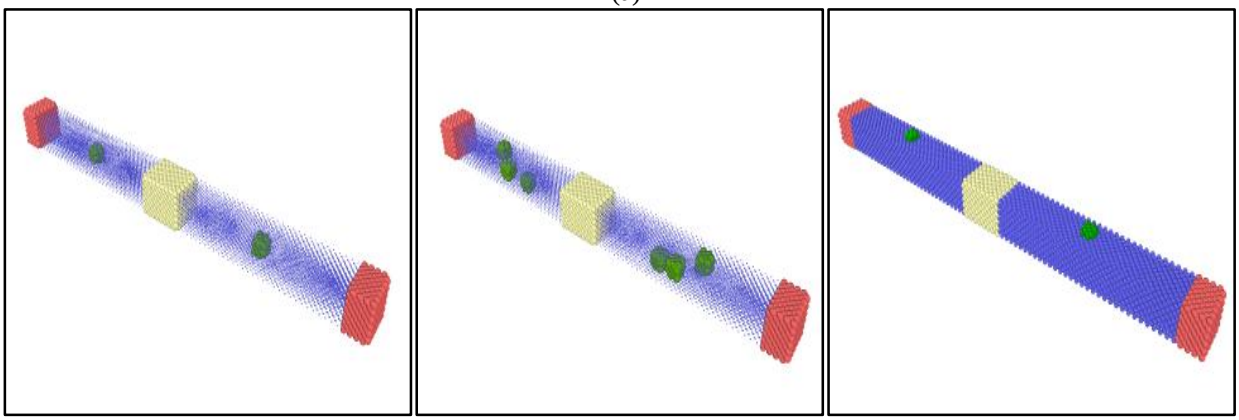

(b) (c) (d)

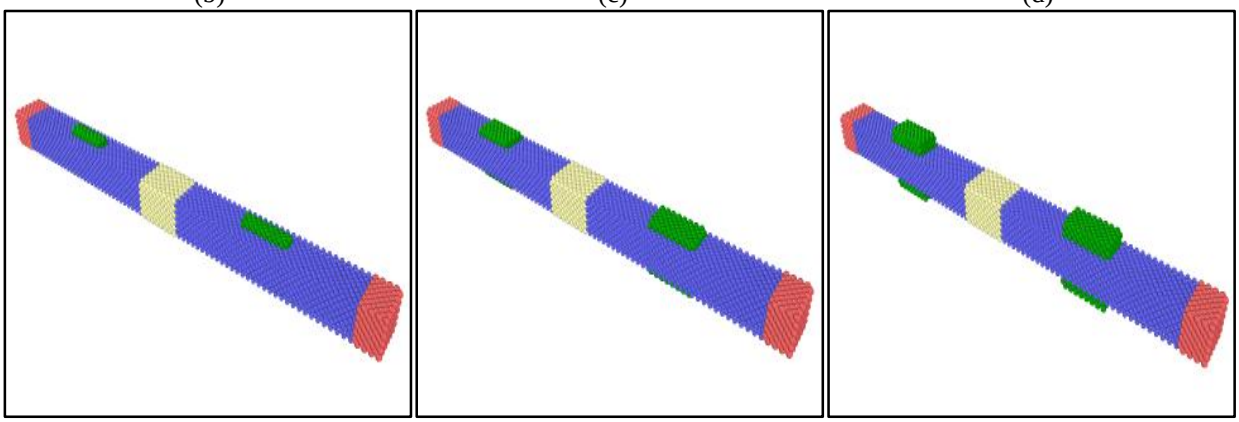

(e) (f) (g)

FIGURE. 1: Simulation cell of (a) solid Ar nanowire, (b) nanowire with 1 embedded nanoparticle, (c) nanowire with 3 embedded nanoparticle; nanowires with surface decorated with nanoparticles of sizes (d) (2a x 2a x a), (e) (8a x 2a x a), (f) (8a x 4a x a), and (g) (8a x 4a x 2a).

3. RESULTS AND DISCUSSION

The simulation starts from its initial configuration and temperature was scaled to achieve the equilibrium temperature of 20K. Once the equilibrium temperature was reached, temperature profile of the simulation domain was monitored to check whether the simulation domain was in equilibrium state or not as presented in Fig. 2.

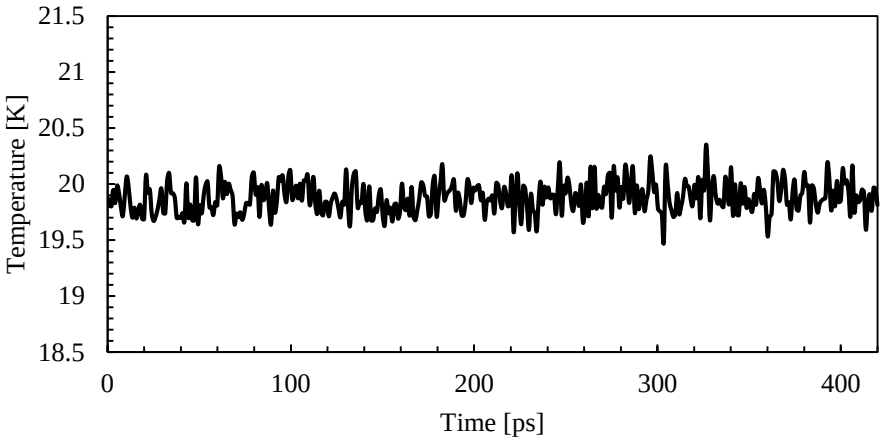

FIGURE. 2: Temperature history of solid Ar nanowire during equilibrium period.

The simulation domain was indeed in equilibrium state and then Nose-Hoover thermostat was applied to establish the temperature gradient. Heat flux along the length of the nanowire was measured and thermal conductivity was calculated from the simulation result as k = 0.53 W/mK which is very close to the thermal conductivity of solid argon of 0.6 W/mK as found from experiment [11]. When a cube shaped nanoparticle with mass 0.125 was doped in the the nanowire, temperature profile was not very smooth as presented in Fig. 3. Due to presence of the nanoparticles, interface scattering in phonon transport is responsible for changes in thermal resistance. Increased phonon-interface collisions prevent the phonons with high energy in the hot region from moving to the cold region and vice versa. This means that the energy transport is low; consequently, the thermal conductivity is low [12-13]. New thermal conductivity is found k = 0.46 W/mK.

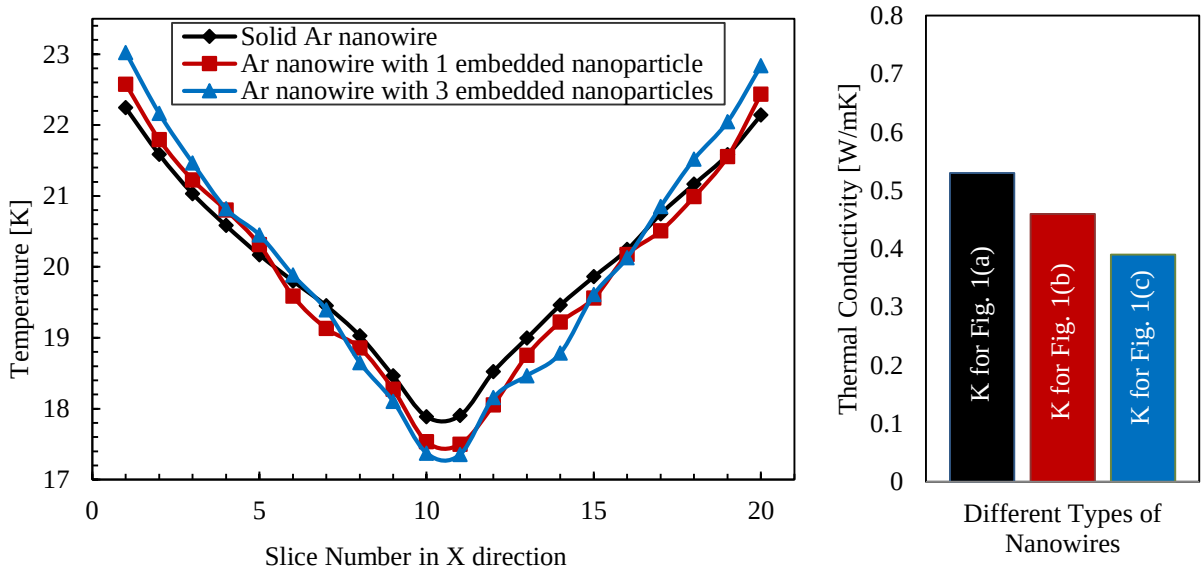

FIGURE. 3: Comparison of temperature profile and thermal conductivity for different nanowires.

With the increase of nanoparticles, thermal conductivity was observed to reduce further due to increase in the phonon scattering. Thermal conductivity of 0.39 W/mK was observed for the 3 nanoparticles embedded nanowire and thus 15% further reduction in thermal conductivity was observed compared to the single nanoparticle embedded nanowire. Temperature profile was observed to be more distorted as the nanoparticles were distributed along length of the nanowires. Embedded nanoparticle's mass also influence thermal conductivity of the nanowire. Nanoparticle with 3 different mass ratios of 0.5, 0.25 and 0.125 was used to investigate its effect on the overall thermal conductivity. With the increase of the mass ratio thermal conductivity of the nanowire was observed to reduce. ~7% reduction in thermal conductivity was observed for the 50% reduction in mass of the nanoparticles as presented in Fig. 2. Nanoparticles with lower mass increases higher interfacial miss match causing higher hindrance in heat flow.

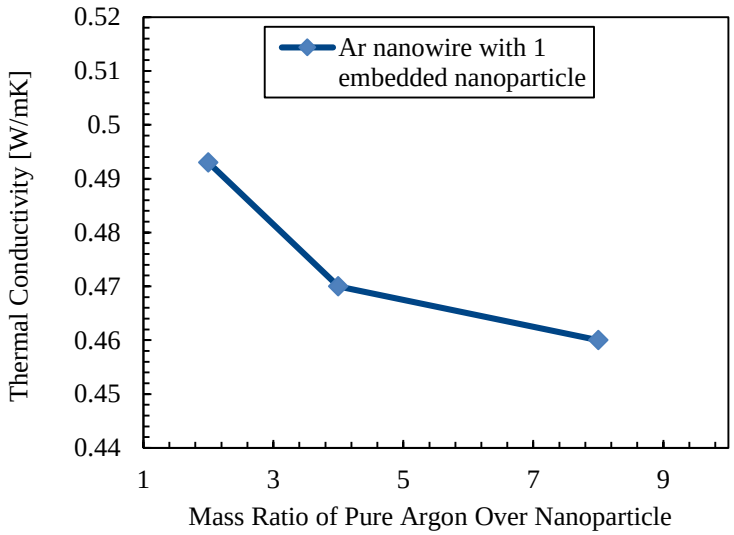

FIGURE. 4: Change of thermal conductivity with mass ratio of nanoparticles.

When the nanoparticles were positioned on the surface of the nanowires different scenario was observed compared to the nanoparticles embedded in the nanowire. For the same size and mass ratio of the nanoparticles, reduction in thermal conductivity was higher for the nanoparticles decorated nanowires compared to the inside embedment. As presented in Fig. 5 and Fig. 6(a). Thermal conductivity for nanowire presented in Fig. 1(d) was found 0.299 W/mK,

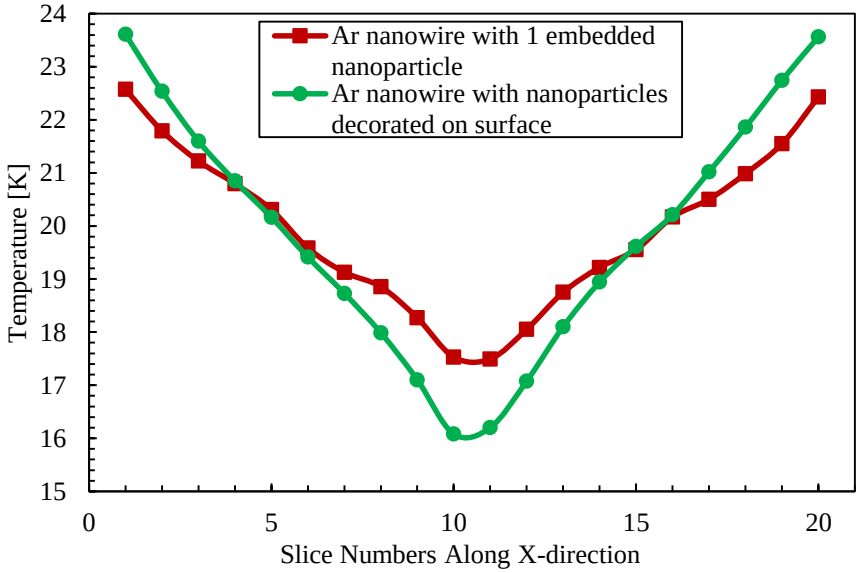

FIGURE 5: Temperature profile for nanoparticle embedded and decorated nanowires.

which is 35% less than the thermal conductivity of single nanoparticle embedded nanowire and almost 40% less than solid argon nanowire.

Due to localized mismatch in mass ratio, phonon frequency changes significantly which hinders phonon of several frequencies to travel along the length of the nanowire resulting in reduction of thermal conductivity. However, size and layering of the nanoparticles have very insignificant effect on the thermal conductivity of the nanowires as presented in Fig. 6(b).

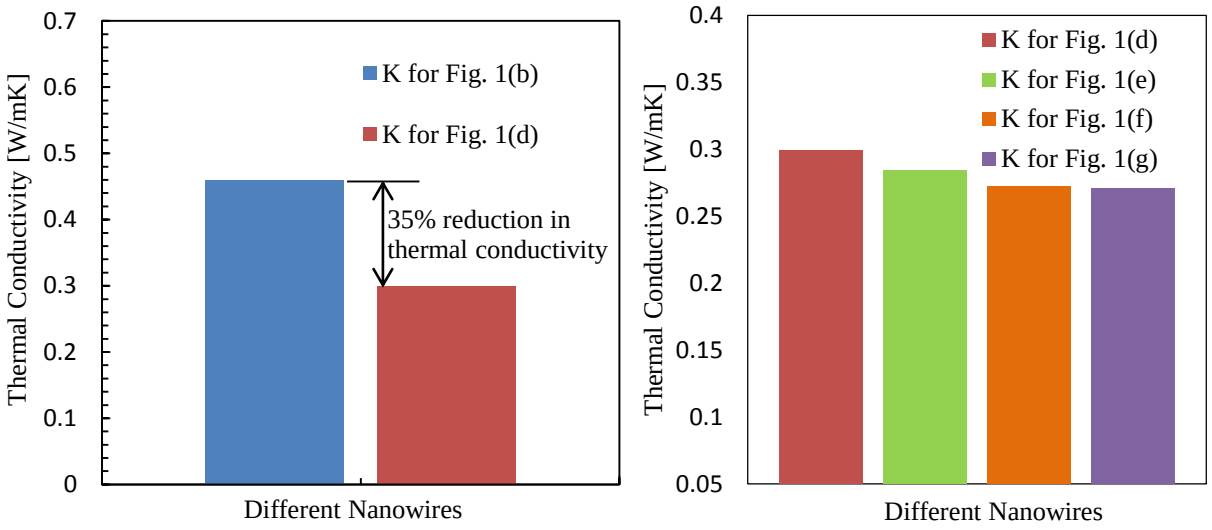

Fig. 6: Comparison of thermal conductivities for different nanowires.

CONCLUSIONS

We have determined the thermal conductivity of solid argon nanowire and doped nanowires in the low temperature regime through NEMD simulations with a LJ model. Nanowires were doped in different ways. From the results of the simulation following conclusions can be drawn:

1. Thermal conductivity of the nanowires reduces for the nanoparticles doping and the reduction increases with the increase of the number of nanoparticles.
2. Nanoparticles mass have influence on the thermal conductivity reduction of the doped nanowire, however the effect is not very significant.
3. Nanoparticle decoration on the outer surface of the nanowire have more profound effect on the thermal conductivity reduction of the nanowire compared to the nanowire embedment inside the nanowire however, the influence is not dependent on the size of the nanoparticle.

REFERENCES

[1] Jing-Feng Li, Wei-Shu Liu; NPG Asia Materials **2**, 152–158 (2010).
[2] Dragoman, D., Dragoman, M.; Applied Physics Letters **91** (20) (2007).
[3] Duck Young Chung, T. Hogan; **459**, XVI ICT (1997).
[4] Heremans, J. P.; Jovovic, V.; Science **321 (5888**): 554–7 (2008).
[5] Pei, Yanzhong; Shi, Xiaoya; Nature **473 (7345):** 66–9 (2011).

[6] F. Sansoz; Nano Lett. **11**, 5378 (2011).
[7] http://web.mac.com/majumdargroup/iWeb/Site/Thermoelectrics.html.
[8] S.H. Choi, S. Maruyama, K.K. Kim, and J.H. Lee, Journal of the Korean Physics Society **43** 747-753(2003).
[9] H.M. Yin, G.H. Paulino, W.G. Buttlar, and L.Z. Sun, Journal of Applied Mechanics **75** 051113(2008).
[10] M. P. Allen, D. J. Tildesley; Computer Simulation of Liquids (Clarendon, Oxford, 1987).
[11] Hideo Kaburaki; Thermal Conductivity of Solid Argon by Classical Molecular Dynamics.
[12] W. Tian and R. Yang, Journal of Applied Physics **101**, 054320(2007).
[13] S.H. Choi, S. Maruyama, Journal of the Korean Physics Society **43**, 747-753(2003).
[14] Tretiakov V., Scandolo; Journal of Chemical Physics **120(8),** 2004.

ICME2015

International Conference on Mechanical Engineering 2015
(ICME 2015) 18 – 20 December, 2015, Dhaka, Bangladesh

Paper ID : 180

A CFD model for biomass combustion in a packed bed furnace

Md.Rezwanul Karim[1, 2], Ifat Rabbil Qudrat Ovi[2] and Jamal Naser[1, a)]

[1] *Faculty of Science, Engineering and Technology, Swinburne University of Technology, VIC 3122, Australia.*
[2] *Department of Mechanical & Chemical Engineering, Islamic University of Technology, Gazipur 1704,Bangladesh.*

[a)] Corresponding author: jnaser@swin.edu.au

Abstract. Climate change has now become an important issue which is affecting environment and people around the world. Global warming is the main reason of climate change which is increasing day by day due to the growing demand of energy in developed countries. Use of renewable energy is now an established technique to decrease the adverse effect of global warming. Biomass is a widely accessible renewable energy source which reduces CO2 emissions for producing thermal energy or electricity. But the combustion of biomass is complex due its large variations and physical structures. Packed bed or fixed bed combustion is the most common method for the energy conversion of biomass. Experimental investigation of packed bed biomass combustion is difficult as the data collection inside the bed is challenging. CFD simulation of these combustion systems can be helpful to investigate different operational conditions and to evaluate the local values inside the investigation area. Available CFD codes can model the gas phase combustion but it can't model the solid phase of biomass conversion. In this work, a complete three-dimensional CFD model is presented for numerical investigation of packed bed biomass combustion. The model describes the solid phase along with the interface between solid and gas phase. It also includes the bed shrinkage due to the continuous movement of the bed during solid fuel combustion. Several variables are employed to represent different parameters of solid mass. Packed bed is considered as a porous bed and User Defined Functions (UDFs) platform is used to introduce solid phase user defined variables in the CFD. Modified standard discrete transfer radiation method (DTRM) is applied to model the radiation heat transfer. Preliminary results of gas phase velocity and pressure drop over packed bed have been shown. The model can be useful for investigation of movement of the packed bed during solid fuel combustion.

Nomenclature

A_p	projected area (m^2)	S	source term (Wm^{-3})
C_p	specific heat ($J\ kg^{-1}\ K^{-1}$)	Sc	Schmidt number (–)
D	diffusivity ($m^2\ s^{-1}$)	Pr	Prandtl number (–)
D_{cil}	cylindrical diameter (m)	T	temperature (K)
$\boldsymbol{d}$	direction vector (–)	V	volume (m^3)
d_{eq}	equivalent diameter of particle (m)	v_∞	gas velocity (ms^{-1})
f_v	porosity (–)	$\boldsymbol{v_s}$	solid velocity (ms^{-1})
G	heat conductance	ρ	density ($kg\ m^{-3}$)
h	convection coefficient ($W\ m^{-2}\ K^{-1}$)	Ɛ	solid fraction (–)
k_m	mass transfer constant (ms^{-1})	ϵ	emissivity (–)
k	thermal conductivity ($W\ m^{-1}\ K^{-1}$)	η	permeability (m^2)
L_{cil}	cylindrical length (m)	μ	gas viscosity ($kg\ m^{-1}\ s^{-1}$)
Re	Reynolds number (–)	ϒ	inertial loss (m^{-1})
$\boldsymbol{s}$	surface vector (–)	ψ	sphericity (–)

INTRODUCTION

Global warming and climate change are recent complex issues which are impacting directly on environment and people around the world. It is changing our economy, health and communities in diverse ways. Emission of CO2 and other greenhouse gases from fossil fuel are main causes of global warming. Along with this, increasing consumption and limited availability of fossil fuels has urged us to look for the renewable energy sources. Biomass and municipal solid wastes are becoming an important source to produce thermal energy and electricity now a day in the energy industry. About 14% of the worldwide major energy source is biomass, and it is fourth largest after coal, oil, and natural gas [1]. Before industrialization biomass has been used as the main energy source for cooking and heating. Energy crisis and environmental impacts of conventional fuels have turned attention in biomass again [2] because it is a carbon dioxide-neutral energy source. Comparing other fossil fuels, biomass consists of lower carbon, higher oxygen, higher volatile contents and lower specific heating value in kJ/kg. So the combustion of solid biomass is a complex phenomenon due to its characteristics. The choice of suitable combustion technology affects the efficient thermal use of biomass fuel. Grate firing of biomass being the most popular technology has the advantage of firing fuels of different moisture content and involves fewer fuel preparation [1]. A fixed bed or packed bed is a place inside the grate furnace where thermal transformation of biomass occurs while the flammable volatiles burn inside the combustion chamber. CFD simulations [3-6] of any combustion system are very helpful to develop an efficient combustion system by combining theoretical model and experimental data.

Comprehensive review of packed bed combustion of biomass has been presented by authors [1, 7, 8] where they have reviewed the up-to-date knowledge on different fixed bed biomass boilers, firing system, important combustion mechanism, recent research and progress and future challenges to be faced. Common modelling approach of packed bed combustion is to divide the simulation in to the bed and the freeboard although there is a strong coupling in between them. Commercial CFD programs (Fluent, Star-CD, CFX, etc.) have been used to model the gas phase but it can't simulate the solid phase of biomass conversion. Different models have been proposed by authors to model the solid phase and linking it with the gas phase but it remains a challenge for researchers. The bed has been modelled using zero-dimensional, one-dimensional, two-dimensional and three-dimensional models [9-15]. Movement of the bed or bed compaction due to particle shrinkage during fuel consumption is a very important phenomenon in fixed bed combustion. Different model have been proposed to solve the bed compaction with or without varying porosity [14-18]. But a complete three-dimensional model for transient combustion of biomass fuel is still under development. In this study a preliminary 3D CFD model for biomass combustion in packed bed is presented. Solid phase is modelled with a set of transport equations through user defined subroutines. Movement of the bed due to local shrinkage of fuel is included through a bed compaction model. This model considers the bed compaction movement in any direction and introduces a solid velocity to consider bed movement. Heat transfer model is used to predict the temperature of solid and gas phases with modified radiative heat transfer solution.

DESCRIPTION OF NUMERICAL MODEL

Preliminary 3D CFD model of biomass combustion in packed bed involves the solution of the solid and gaseous phase and the interface between these phases. Available CFD software can model the gas phase but can't solve the solid conversion process of combustion. Here, CFD simulation will be conducted using a CFD code, AVL Fire 2014 which allow User Defined Functions (UDFs) platform. Solid phase variables are introduced by the User defined subroutines in the CFD. For modelling the biomass combustion in a packed bed, a set of sub models from literature is proposed. Cell based user defined subroutines are written in FORTRAN and coupled to AVL Fire. Some important assumptions of modelling are porous bed is considered as a disperse medium, solid density varies during drying, devolatilisation and char reactions while solid fraction varies during the char reaction only.

Solid Phase Modelling

Solid particles forming the packed bed have a very significant effect on the whole combustion system. Commercially available CFD codes can't model the solid phase, but AVL Fire allows the pairing of FORTRAN sub-routines, which will be used in this work. To characterize the solid phase several user defined scalars have been used by authors [9, 14, 19]. In this work, six variables will be used; these are (1) the solid temperature (T_S), (2) the solid fraction (ε), (3) density of moisture (ρ_m), (4) density of dry biomass (wood) (ρ_w), (5) density of char (ρ_c) and (6) diameter of the particle (d_p). The transport equations of these scalars which have been well established [19] are

shown below. The terms $\dot{\omega}_i'''$ are the growth or consumption rates of the components of biomass (wood), the details of these rates and the energy source of solid energy equation (Eq. (8)) can be found in [19].

$$\text{Solid Temperature } (T_S): \frac{\partial(\varepsilon\rho_p C_p T_S)}{\partial t} = \nabla\left(k_{s,eff} \cdot \nabla T_S\right) + S_s \tag{1}$$

$$\text{Solid fraction } (\varepsilon): \frac{\partial \varepsilon}{\partial t} = -\frac{\dot{\omega}'''_{c,char}}{\rho_p}\,\varepsilon \tag{2}$$

$$\text{Third power of particle diameter (dp3)}: \frac{\lambda d_{p3}}{\lambda t} = -\frac{\dot{\omega}'''_{c,char}}{\rho_p}\,d_{p3} \tag{3}$$

$$\text{Moisture density } (\rho_m): \frac{\partial(\varepsilon\rho_m)}{\partial t} = -\dot{\omega}'''_{moist}\,\varepsilon \tag{4}$$

$$\text{Dry biomass density } (\rho_w): \frac{\partial(\varepsilon\rho_w)}{\partial t} = -\dot{\omega}'''_{wood}\,\varepsilon \tag{5}$$

$$\text{Char density } (\rho_c): \frac{\lambda(\varepsilon\rho_c)}{\lambda t} = \left(\dot{\omega}'''_{G,char} - \dot{\omega}'''_{c,char}\right)\varepsilon \tag{6}$$

$$\text{Total particle density } (\rho_p): \rho_{moist} + \rho_{wood} + \rho_{char} = \rho_p \tag{7}$$

$$\text{Energy equation source: } S_S = S_S^{reac} + S_S^{conv} + S_S^{rad} + S_S^{loss} \tag{8}$$

The main steps of solid fuel conversions are drying, devolatilisation and char conversion. Drying, devolatilisation and char generation are controlled thermally and char consumption can be controlled either kinetically or diffusionally. Moisture evaporation is considered to occur at 373.15K.

Gas Phase Modelling

CFD software's built-in algorithm can solve the gas phase conservation equations like energy, momentum, continuity, turbulence, chemical species etc. The second-order upwind method is used to solve spatial discretisation for all equations. Standard k-epsilon model is used to consider the turbulence effect with enhanced wall treatment. For homogeneous reactions, finite rate Eddy dissipation model is used which uses the lower rate between the Arrhenius rate and Eddy dissipation rate. For this work user defined subroutines will be employed to compute the pressure drop over the packed bed. A source is added in the momentum equation (Eq. (9)) to count the effect of the porous bed on the gas flow. Permeability coefficients and inertial losses are calculated using Eq. (10) and (11), respectively [19]. Where, sphericity and equivalent diameter of the particle are calculated using Eq. (12) and (13).

$$S_{mom} = -\left(\frac{\mu}{\eta} v_\infty + \Upsilon\,\frac{1}{2}\rho_g v^2\right) \tag{9}$$

$$\eta = \frac{\psi^2 d_{eq}^2}{150}\,\frac{f_v^3}{(1-f_v)^2} \tag{10}$$

$$\Upsilon = \frac{3.5}{\psi d_{eq}}\,\frac{(1-f_v)}{f_v^3} \tag{11}$$

$$\psi = \frac{\pi^{1/3}\left(6V_p\right)^{2/3}}{A_p} \tag{12}$$

$$d_{eq} = D_{cil}\left(\frac{3L_{cil}}{2D_{cil}}\right)^{1/3} \tag{13}$$

Gas phase reaction scheme has been modelled through a set of chemical reactions. These reactions are partial oxidation of benzene, methane and hydrogen to carbon monoxide from devolatilisation. Other reactions are CO to CO_2 reaction and two way reactions of water and carbon monoxide. Details of the reaction kinematics are available in literature [9, 14, 15, 19]. Figure 1 shows the code validation of gas phase pressure drop over a packed bed. The packed bed cylindrical furnace model height is 1300 mm, diameter 130 mm and the porous bed height is 580 mm (Fig.1 (a)). Airflow is from the bottom at 0.2 ms^{-1}. Pressure drop has been estimated for three different packed bed having bed particle with equivalent diameter 8.8 mm and bed porosity 0.44 for bed 1, particle equivalent diameter 14.8 mm and bed porosity 0.39 for bed 2, particle equivalent diameter 2.6 mm and bed porosity 0.72 for bed 3. The estimated pressure drop found is 65 Pa, 52 Pa and 166 Pa (Fig.1 (b)) for the three packed bed respectively which are similar to the theoretical values. Velocity profile is shown in Fig.1(c).

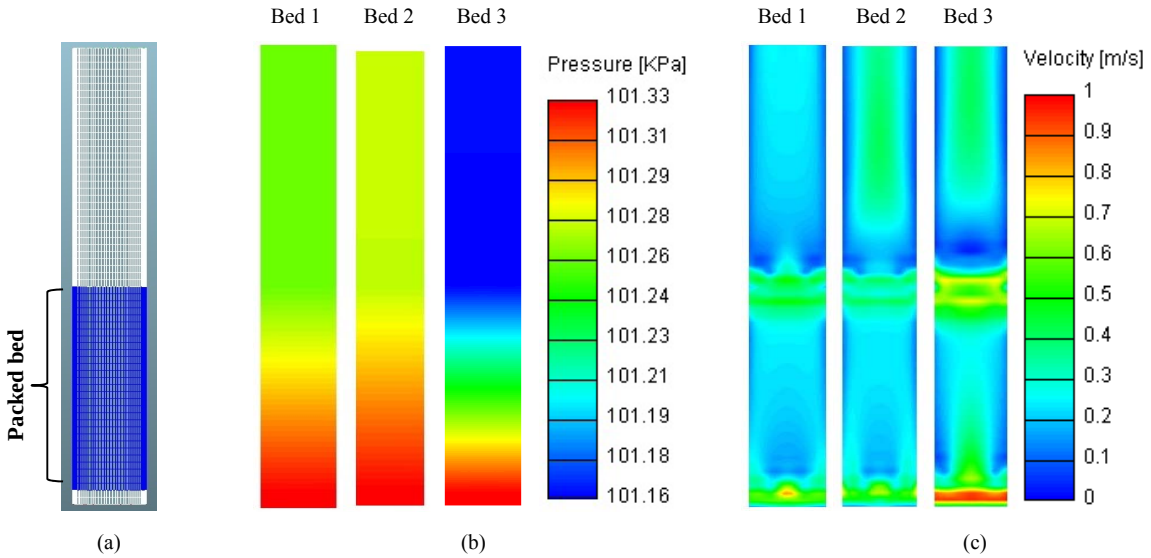

FIGURE 1. Pressure drop and velocity for flow through a packed bed.

Heat and Mass Transfer

Heat and mass transfer is modelled for the solid phase and the interactions of solid with the gas phase. To estimate the effective thermal conductivity ($k_{s,eff}$), Gómez et al.[19] has used Eq.(14) for packed bed. Eq. (14) gives the heat transfer rate through a single cell ($\dot{Q}_C$), where λ is a geometrical parameter and G is the heat conductance through the bed. The convective source term (S_S^{conv}) of energy equation is calculated by Eq. (15) and the opposite value is added in energy source of the gas phase. Heat and mass exchanges have been modelled by the famous Wakao and Kaguei correlations. The calculation of Nusselt (Nu) and Sherwood (Sh) dimensionless numbers are shown in equation (16) & (17) respectively. From these dimensionless numbers, the convective heat transfer coefficient (h) and the mass transfer coefficient (k_m) are calculated (Eq. (18)).

$$\dot{Q}_C = \frac{k_{s,eff} \cdot d_{eq}^2 \cdot \Delta T_S}{\lambda_e d_{eq}} = G \cdot \Delta T_S \tag{14}$$

$$S_S^{conv} = -S_g^{conv} = hA_v(T_g - T_S) \tag{15}$$

$$\mathrm{Nu} = 2 + 1.1\mathrm{Re}^{0.6}\mathrm{Pr}^{1/3} \tag{16}$$

$$Sh = 2 + 1.1Re^{0.6}Sc^{1/3} \tag{17}$$

$$h = \frac{Nu.k}{d_{eq}}, k_m = \frac{Sh.D}{d_{eq}} \tag{18}$$

Radiative Heat Transfer

Heat transfer between the solid particles and gaseous phase is affected significantly by radiative heat transfer. Radiation also takes place between the particles within the packed bed. Radiation transport of non-participative fluids or fluids with low absorptive capacity can be estimated by available CFD codes. But a porous bed consists of solid particle which makes the bed as a medium with high absorption and emission coefficients. So modification is required in these models for estimation of radiation in a porous packed bed. The discrete transfer radiation method (DTRM) included in AVL Fire will be considered in this study. DTRM is suitable for participative medium and has been used in many industrial applications with good directional accuracy [20]. DTRM considers that a distinct ray can estimate the intensity through a solid angle. The total radiation intensities (i'_n) can be calculated through the general solution of radiation transfer equation (RTE) as follows:

$$i'_{n+1} = i'_n\big(1 - \epsilon(T, x_i)\big) + i'_b(T)\epsilon(T, x_i) \tag{19}$$

Where, $\epsilon(T, x_i)$ is the emissivity which depends on the resident temperature and gas composition, the blackbody emissivity of a diffuse fluid contained in the control volume is $i_b = \sigma.T_g^4/4$ and σ is the Stephan–Boltzmann constant. The solution of RTE determines a radiation source term which is used in the enthalpy equation. However this solution can't consider the temperature difference of a multiphase medium. So, a modification is formulated through user defined sub-routines to consider the radiation energy source of the solid phase.

Bed Compaction

Bed shrinkage or bed compaction due to the fuel combustion in packed bed is a very important subject for modelling. Previous models of bed compaction have been done by estimating the particle shrinkage in the bed at a constant porosity. To resolve the problem here a recent model of packed bed compaction [19] has been proposed with further modification which produces a continuous bed movement during solid consumption. This method works on energy and mass transfer between a central cell and neighbour cells. In this model movement of the bed due to compaction has been considered only in gravity direction by discharging the upper cells and filling the bottom cells. Differences in volatile, moisture and char portions are considered for every mass change. In this model, a starting minimum solid fraction (ε_{min}) and a maximum solid fraction (ε_{max}) are considered. It is also considered that if the cell solid fraction is smaller than ε_{min} it becomes weak to collapse whereas if the cell solid fraction reaches ε_{max}, the cell is completely filled and cannot receive more mass. Collapsing cell loses its mass and solid fraction until it becomes empty (ε=0) or until the surrounding cells are completely filled ($\varepsilon=\varepsilon_{max}$).

In this work, the movement of the bed has been considered in all direction instead of gravity direction only. A solid velocity (v_s) has been considered which represents the velocity of the packed bed particles in all direction. So the solid fraction can be transferred to any neighbour cell around except the upper cells. Table 1 shows the bed compaction formula. During bed compaction the solid volume transferred (ΔV_s) from the collapsing cell to the neighbour cell has the amount (Eq. (22)) which is minimum of the two volume, solid volume of the collapsing cell (Eqs. (20.1) and (20.2)) and the solid volume accepted by the receiving cell before being filled up (Eqs. (21.1) and (21.2)). Incoming or outgoing flux ($\boldsymbol{R_{flux}}$) has been calculated by Eq. (24). The transferred volume is multiplied by the incoming or outgoing flux value through any cell face divided by the total flux of all cell faces. This volume is then used to update the solid fraction (Eqs. (23.1) and (23.2)) and other solid phase variables.

Discharging cell		**Receiving cell**	
$V_{s_{col}} = \varepsilon \cdot V \frac{(\boldsymbol{R_{flux}})_{out}}{\sum(\boldsymbol{R_{flux}})_{out}}$	(20.1)	$V_{s_{col}} = \varepsilon \cdot V \frac{(\boldsymbol{R_{flux}})_{out}}{\sum(\boldsymbol{R_{flux}})_{out}}$	(20.2)
$V_{s_{max}} = [\varepsilon_{max} - \varepsilon] \cdot V \frac{(\boldsymbol{R_{flux}})_{in}}{\sum(\boldsymbol{R_{flux}})_{in}}$	(21.1)	$V_{s_{max}} = [\varepsilon_{max} - \varepsilon] \cdot V \frac{(\boldsymbol{R_{flux}})_{in}}{\sum(\boldsymbol{R_{flux}})_{in}}$	(21.2)
$\Delta V_s = min\ (V_{s_{col}}, V_{s_{max}})$	(22)		
$\varepsilon = \varepsilon - \frac{\Delta V_s}{V}$	(23.1)	$\varepsilon = \varepsilon + \frac{\Delta V_s}{V}$	(23.2)
$\boldsymbol{R_{flux}} = (\boldsymbol{d} \cdot \boldsymbol{v_s} \cdot \lvert \boldsymbol{s} \rvert)\ \varepsilon \partial t$	(24)		

TABLE 1. Bed compaction formula.

CONCLUSION

A computational fluid dynamics (CFD) model of packed bed biomass combustion has been presented here. CFD codes available can't model the thermal conversion of solid fuel properly, which is limiting the knowledge on this field. In this work, a sub model of solid fuel conversion is presented considering the interaction between solid and gaseous phase in CFD software AVL Fire 2014. To describe the solid phase a number of variables have been defined. Gas phase modelling includes calculation of the pressure drop over a packed bed and preliminary results have been presented. Modified heat and mass transfer model with special radiative heat transfer model is presented. Bed compaction model has been used to consider the continuous movement of the bed in all direction due to the collapse of region during solid fuel combustion. The proposed model will be validated and developed further to investigate the moving packed bed combustion.

REFERENCES

1. Yin, C., L.A. Rosendahl, and S.K. Kær, "Grate-firing of biomass for heat and power production", in *Progress in Energy and Combustion Science*, 2008. **34**(6): p. 725-754.
2. Demirbas, M.F., M. Balat, and H. Balat, "Potential contribution of biomass to the sustainable energy development"*, Energy Conversion and Management*, 2009. **50**(7): p. 1746-1760.
3. Bhuiyan, A.A. and J. Naser, "CFD modelling of co-firing of biomass with coal under oxy-fuel combustion in a large scale power plant"*, Fuel*, 2015. **159**: p. 150-168.
4. Ström, H. and H. Thunman, "CFD simulations of biofuel bed conversion: A sub model for the drying and devolatilization of thermally thick wood particles", *Combustion and Flame*, 2013. **160**(2): p. 417-431.
5. Bhuiyan, A.A. and J. Naser, "Thermal characterization of coal/straw combustion under air/oxy-fuel conditions in a swirl-stabilized furnace: a CFD modelling", *Applied Thermal Engineering*, 2015.
6. Bhuiyan, A.A. and J. Naser. "Effect of recycled ratio on heat transfer performance of coal combustion in a 0.5MWth combustion test facility", in *19th Australasian Fluid Mechanics Conference,* Australia. 2014.
7. Karim, M. and J. Naser, "Progress in Numerical Modelling of Packed Bed Biomass Combustion", in *19th Australasian Fluid Mechanics Conference (19 AFMC)*, Melbourne, Australia. 2014.
8. Arafat A. Bhuiyan, Karim, M., Jamal Naser, "Modeling of Solid and Bio-Fuel Combustion Technologies", in *Thermofluid Modeling for Energy Efficiency Applications,* edited by M.M.K Khan, N. M.S Hassan (Academic Press, USA, 2015), p. 259-309.
9. Porteiro, J., et al., "Numerical modeling of a biomass pellet domestic boiler", *Energy and Fuels*, 2009. **23**(2): p. 1067-1075.
10. Kær, S.K., "Numerical modelling of a straw-fired grate boiler", *Fuel*, 2004. **83**(9): p. 1183-1190.
11. Porteiro, J., et al., "*Mathematical modelling of the combustion of a single wood particle", Fuel Processing Technology*, 2006. **87**(2): p. 169-175.
12. Van Der Lans, R.P., et al., "Modelling and experiments of straw combustion in a grate furnace", *Biomass and Bioenergy*, 2000. **19**(3): p. 199-208.
13. Yang, Y., et al., "Mathematical modelling of MSW incineration on a travelling bed*", Waste Management*, 2002. **22**(4): p. 369-380.
14. Collazo, J., et al., "Numerical modeling of the combustion of densified wood under fixed-bed conditions", *Fuel*, 2012. **93**: p. 149-159.
15. Collazo, J., et al., "Numerical simulation of a small-scale biomass boiler", *Energy Conversion and Management*, 2012. **64**: p. 87-96.
16. Shin, D. and S. Choi, "The combustion of simulated waste particles in a fixed bed", *Combustion and Flame*, 2000. **121**(1-2): p. 167-180.
17. Hermansson, S. and H. Thunman, "CFD modelling of bed shrinkage and channelling in fixed-bed combustion", *Combustion and Flame*, 2011. **158**(5): p. 988-999.
18. Mehrabian, R., et al., "Multi-physics modelling of packed bed biomass combustion"*, Fuel*, 2014. **122**: p. 164-178.
19. Gómez, M.A., et al., "CFD modelling of thermal conversion and packed bed compaction in biomass combustion", *Fuel*, 2014. **117**: p. 716-732.
20. Bhuiyan, A.A. and J. Naser, "Numerical modelling of oxy fuel combustion, the effect of radiative and convective heat transfer and burnout", *Fuel*, 2015. **139**: p. 268-284.

ICME2015

International Conference on Mechanical Engineering 2015
(ICME 2015) 18 – 20 December, 2015, Dhaka, Bangladesh

Paper ID : 187

Effects of Heat Absorption on MHD Free Convection Flow along a Vertical Wavy Surface in presence of Viscous Dissipation

Nazma Parveen[a] and Sujon Nath[b]

Department of Mathematics, Bangladesh University of Engineering and Technology,
Dhaka-1000, Bangladesh
[a)]Corresponding author: nazma@math.buet.ac.bd
[b)]sujon.buet@yahoo.com

Abstract: The present work investigates the effects of heat absorption on MHD natural convection flow along a vertical wavy surface in presence of viscous dissipation. The governing boundary layer equations with associated boundary conditions are converted to non-dimensional boundary layer equations using the appropriate transformation and the resulting nonlinear system of partial differential equations are reduced to local non similarity equations which are solved numerically by employing the implicit finite difference method, known as Keller-Box scheme. The effects of the pertinent parameters, such as the heat absorption parameter (Q), the magnetic parameter (M), the viscous dissipation parameter (N) on the surface shear stress in terms of the skin friction coefficient C_{fx}, the rate of heat transfer in terms of Nusselt number Nu_x, the velocity profiles, the temperature profiles, the streamlines as well as the isotherms are shown graphically.
Kew words: Heat absorption; MHD; Viscous dissipation; Natural convection; Wavy surface.

1. INTRODUCTION

The study of temperature and heat transfer is of great importance to the engineers because of its almost universal occurrence in many branches of science and engineering. Heat generation or absorption is a volumetric phenomenon. That is, it occurs throughout the body of a medium. Therefore, the rate of heat generation in a medium is usually specified per unit volume. Heat generation is the ability to emit greater than normal heat from the body. The amount of heat generated or absorbed per unit volume is defined as $Q_o(T-T_\infty)$, where Q_o being a constant, which may take either positive or negative. The source term represents the heat generation when $Q_o > 0$ and the heat absorption when $Q_o < 0$. Similarly MHD and viscous dissipation have a great role in science. Few of the investigations are presented here. Gebhart [1] investigated the effects of viscous dissipation in natural convection. Yao [2] studied natural convection along a vertical wavy surface and then he introduced prandtl's transposition theorem [3]. Molla et al. [4] numerically investigated natural convection flow along a vertical wavy surface with uniform surface temperature in presence of heat generation/absorption. Alam et al. [5] studied viscous dissipation effects on MHD natural convection flow over a sphere in the presence of heat generation. Resently, Parveen and Alim [6] investigated MHD natural convection flow along a vertical wavy surface in presence of heat generation/absorption with viscosity dependent on temperature. From the above investigations, heat absorption can be considered in many practical examples in presence of viscous dissipation.

2. FORMULATION OF THE PROBLEM

The boundary layer analysis outlined below allows $\bar{\sigma}(X)$ being arbitrary, but our detailed numerical work assumed that the surface exhibits sinusoidal deformations. The wavy surface may be described by

$$Y_w = \bar{\sigma}(X) = \alpha \sin\left(\frac{n\pi X}{L}\right) \tag{1}$$

where L is the wave length associated with the wavy surface.

The geometry of the wavy surface and the two-dimensional cartesian coordinate system are shown in figure1.

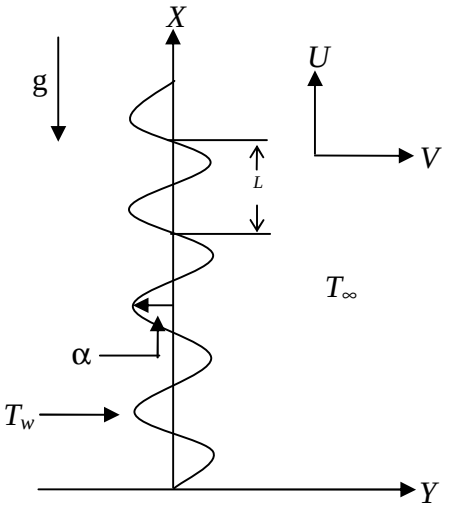

FIGURE 1: The coordinate system and the physical model

The conservation equations for the flow characterized with steady, laminar and two-dimensional boundary layer; under the usual Boussinesq approximation, dimensionless form of the continuity, momentum and energy equations can be written as:

$$\frac{\partial u}{\partial x} + \frac{\partial v}{\partial y} = 0 \tag{2}$$

$$u\frac{\partial u}{\partial x} + v\frac{\partial u}{\partial y} = -\frac{\partial p}{\partial x} + Gr^{1/4}\sigma_x\frac{\partial p}{\partial y} + \left(1+\sigma_x^2\right)\frac{\partial^2 u}{\partial y^2} + \theta \tag{3}$$

$$\sigma_x\left(u\frac{\partial u}{\partial x} + v\frac{\partial u}{\partial y}\right) = -Gr^{1/4}\frac{\partial p}{\partial y} + \sigma_x\left(1+\sigma_x^2\right)\frac{\partial^2 u}{\partial y^2} - \sigma_{xx}u^2 \tag{4}$$

$$u\frac{\partial \theta}{\partial x} + v\frac{\partial \theta}{\partial y} = \frac{1}{\Pr}\left(1+\sigma_x^2\right)\frac{\partial^2 \theta}{\partial y^2} + Q\theta + N\left(\frac{\partial u}{\partial y}\right)^2 \tag{5}$$

Where $\Pr = \frac{C_p\mu}{k}$ is the Prandtl number, $Q = \frac{Q_0 L^2}{\mu Cp Gr^{1/2}}$ is the heat absorption parameter and $N = \frac{\nu^2 Gr}{L^2 C_p(T_w - T_\infty)}$ is the viscous dissipation parameter.

Using Prandtl's transposition theorem to transform the irregular wavy surface into a flat surface as extended by Yao [3] and boundary-layer approximation, the following dimensionless variables are introduced for non-dimensionalizing the governing equations,

$$x = \frac{X}{L}, \quad y = \frac{Y-\overline{\sigma}}{L}Gr^{\frac{1}{4}}, \; p = \frac{L^2}{\rho\nu^2}Gr^{-1}P, \; u = \frac{L}{\nu}Gr^{-1/2}U, \quad v = \frac{L}{\nu}Gr^{-1/4}(V - \sigma_x U),$$

$$\theta = \frac{T-T_\infty}{T_w - T_\infty}, \; \sigma_x = \frac{d\overline{\sigma}}{dX} = \frac{d\sigma}{dx}, \quad Gr = \frac{g\beta(T_w - T_\infty)}{\nu^2}L^3$$

where θ is the non-dimensional temperature function and (u, v) are the dimensionless velocity components.

It can easily be seen that the convection induced by the wavy surface is described by equations (2)–(5). We further notice that, equation (11) indicates that the pressure gradient along the y-direction is $O(Gr^{-1/4})$, which implies that lowest order pressure gradient along x -direction can be determined from the inviscid flow solution. For the present problem this pressure gradient ($\partial p/\partial x = 0$) is zero. Equation (4) further shows that $Gr^{1/4}\partial p/\partial y$ is $O(1)$ and is

determined by the left-hand side of this equation. Thus, the elimination of $\partial p / \partial y$ from equations (3) and (4) leads to

$$u\frac{\partial u}{\partial x}+v\frac{\partial u}{\partial y}=\left(1+\sigma_x^2\right)\frac{\partial^2 u}{\partial y^2}-\frac{\sigma_x\sigma_{xx}}{1+\sigma_x^2}u^2+\frac{1}{1+\sigma_x^2}\theta \tag{6}$$

The corresponding boundary conditions for the present problem are:

$$\left.\begin{aligned} &u=v=0, \quad \theta=1 \qquad at \quad y=0 \\ &u=\theta=0, \quad p=0 \qquad as \quad y\to\infty \end{aligned}\right\} \tag{7}$$

Now we introduce the following transformations to reduce the governing equations to a convenient form:

$$\psi=x^{3/4}f(x,\eta), \quad \eta=yx^{-1/4}, \quad \theta=\theta(x,\eta) \tag{8}$$

Where $f(\eta)$ is the dimensionless stream function, η is the pseudo similarity variable and ψ is the stream function that satisfies the equation (2) and is defined by

$$u=\frac{\partial\psi}{\partial y}, \quad v=-\frac{\partial\psi}{\partial x} \tag{9}$$

Introducing the transformations given in equation (8) and into equation (6) and (5) the following system of non linear equations are obtained,

$$\left(1+\sigma_x^2\right)f'''+\frac{3}{4}ff''-\left(\frac{1}{2}+\frac{x\sigma_x\sigma_{xx}}{1+\sigma_x^2}\right)f'^2+\frac{1}{1+\sigma_x^2}\theta-\frac{Mx^{1/2}}{1+\sigma_x^2}f'=x\left(f'\frac{\partial f'}{\partial x}-f''\frac{\partial f}{\partial x}\right) \tag{10}$$

$$\frac{1}{\Pr}\left(1+\sigma_x^2\right)\theta''+\frac{3}{4}f\theta'+x^{1/2}Q\theta+Nxf''^2=x\left(f'\frac{\partial\theta}{\partial x}-\theta'\frac{\partial f}{\partial x}\right) \tag{11}$$

The boundary conditions (7) now take the following form:

$$\left.\begin{aligned} &f(x,o)=f'(x,o)=0, \qquad \theta(x,o)=1 \\ &f'(x,\infty)=0, \qquad \theta(x,\infty)=0 \end{aligned}\right\} \tag{12}$$

In the above equations prime denote the differentiation with respect to η.

The local *skin* friction coefficient C_{fx} and the rate of heat transfer in terms of the local Nusselt number Nu_x takes the following form:

$$C_{fx}(Gr/x)^{1/4}/2=\sqrt{1+\sigma_x^2}\,f''(x,o) \tag{13}$$

$$Nu_x(Gr/x)^{-1/4}=-\sqrt{1+\sigma_x^2}\,\theta'(x,o) \tag{14}$$

3. NUMERICAL PROCEDURE

The Finite Difference Method is very efficient for programming and rapid convergence among of the three methods. The transformed boundary layer equations are solved numerically with the help of implicit finite difference method together with the Keller-box scheme [7]. The momentum and energy equations are first converted into a system of first order differential equations. Then these equations are expressed in finite difference forms by approximating the functions and their derivatives in terms of the central difference approximations. The above central difference approximations reduces the system of first order differential equations to a set of non-linear difference equations for the unknown at x_i in terms of their values at x_{i-1}. The resulting set of non-linear difference equations are solved by using the Newton's quasi-linearization method. The Jacobian matrix has a block-tridiagonal structure and the difference equations are solved using a block-matrix version of the Thomas algorithm. The whole procedure namely reduction to first order followed by central difference approximations, Newton's Quasi-linearization method and the block Thomas algorithm, is well known as Keller-box method.

4. RESULT AND DISCUSSIONS

Here we have shown the combined effects of viscous dissipation and heat absorption on MHD natural convection flow of viscous incompressible fluid along a vertical wavy surface. The skin friction coefficient C_{fx}, the rate of heat transfer in terms of Nusselt number Nu_x, the streamlines as well as the isotherms are shown graphically.

The influence of the parameter Q, on the skin friction coefficient C_{fx} and local rate of heat transfer Nu_x are illustrated in figures 2.1 (a) and (b) respectively while $\alpha = 0.3$, $N = 0.2$, $M = 0.1$ and Pr = 0.73. From those it is observed that an increase in the heat absorption parameter Q = (0.0, -0.5, -1.0, -2.5) leads to decrease the local skin friction coefficient C_{fx} and increase the local rate of heat transfer Nu_x at different position of x. These are happened, since the increasing values of Q leads to decrease temperature of the fluid flow. Decreasing temperature decreases the viscosity of the fluid. Hence the corresponding shearing stress in terms of local skin friction coefficient decreases. Since the temperature decreases so the rate of heat transfer increases. In figures 2.2 (a) and (b), the skin friction coefficient C_{fx} and local rate of heat transfer Nu_x are illustrated for different values of M while $\alpha = 0.3$, $N = 0.05$, Q = - 0.1 and Pr = 0.73. Here it is observed that an increase in M = (0.0, 0.5, 1.2) leads to decrease the local skin friction coefficient and slightly increase local rate of heat transfer at different position of x. The magnetic field acts against the flow and reduces the skin friction. The variation of local skin friction C_{fx} and the rate of heat transfer in terms of the local Nusselt number Nu_x against x for different values of N while $\alpha = 0.3$, Q = - 0.4, $M = 0.5$, and Pr = 0.73 are illustrated in figure 2.3(a) and (b) respectively. Since the higher value of N accelerates the fluid flow and increases the temperature so from the figure it is noted that for the viscous dissipation parameter N = (0.0, 1.0, 3.0, 5.0, 8.0), the skin friction coefficient increases along the upstream direction of the surface and to decrease of the heat transfer rates.

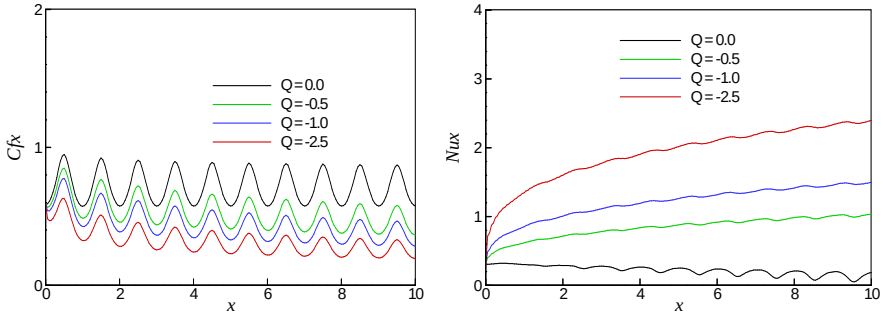

FIGURE 2.1: Skin friction coefficient and rate of heat transfer for different values of Q while Pr = 0.73, $\alpha = 0.3$, $M = 0.1$, $N = 0.2$

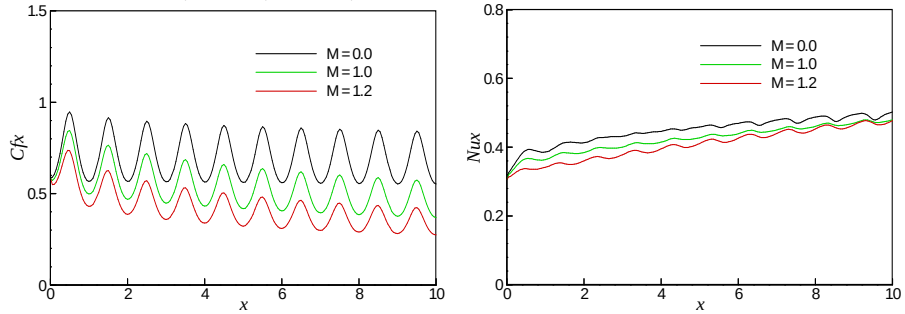

FIGURE 2.2: Skin friction coefficient and rate of heat transfer for different values of M while Pr = 0.73, $\alpha = 0.3$, $N = 0.05$, Q = - 0.1

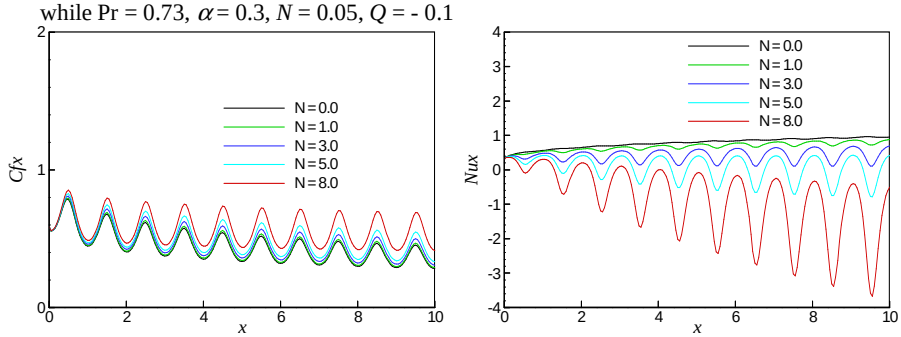

FIGURE 2.3: Skin friction coefficient and rate of heat transfer for different values of N while Pr = 0.73, $\alpha = 0.3$, $M = 0.5$, Q = - 0.4

Figure 2.4 illustrates the effect of variation of the Q equal to 0.0 and -1.0 on the streamlines and isotherms respectively while α = 0.3, N = 0.2, M = 0.1 and Pr = 0.73. Figure 2.4 depicts that the maximum values of ψ decreases while the values of heat absorption parameter Q increases that is ψ_{max} are 8.76 and 2.79 for Q = 0.0 and -1.0 respectively. It is noted from figure 2.4 that as the value of Q decreases the thermal boundary layer becomes thinner gradually. So the isotherms decrease. The effect of variation of the surface roughness on the streamlines and isotherms for the values of M equal to 0.0 and 1.2 are depicted by figure 2.5 while Pr = 0.73, α = 0.3, Q = -0.1 and N = 0.05. The maximum values of streamline decreases steadily while the values of M increases. The maximum values of streamline are 8.24 and 2.49 for M = 0.0 and 1.2 respectively. We observe that as the values of M increases the thermal boundary layer thickness becomes higher gradually. Figure 2.6 shows the effect of viscous dissipation parameter N = (0.0, 3.0) on the formulation of streamlines and isotherms respectively while Pr = 0.73, Q = - 0.4, M = 0.5 and α = 0.3. We find that for N = 0.0 the value of ψ_{max} is 8.76, for N = 3.0 ψ_{max} is 2.79. It is seen that the effect of viscous dissipation parameter N, the flow rate in the boundary layer decreases. From figure 2.6, it is also observed that due to the effect of N, the thermal state of the fluid increases. Finally, the thermal boundary layer becomes thicker.

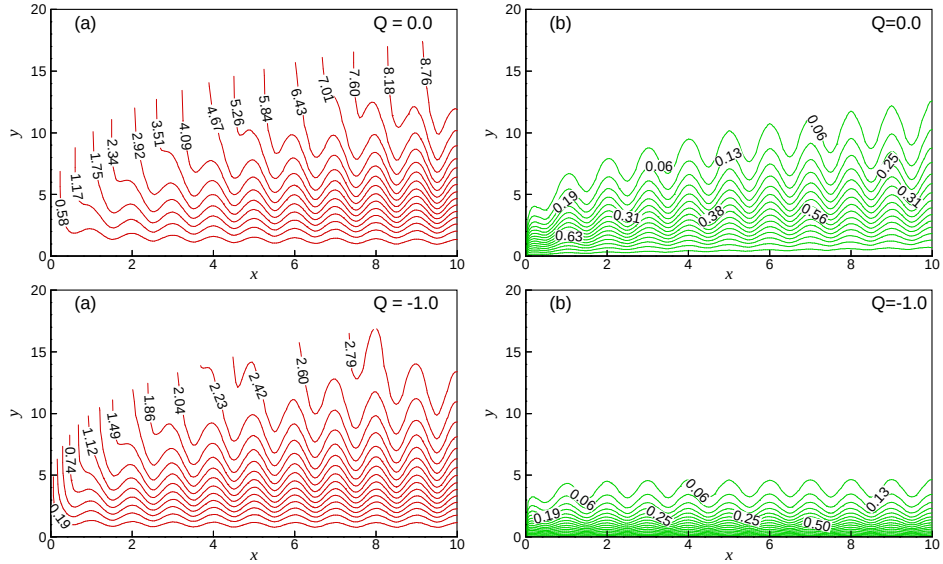

FIGURE 2.4: (a) Streamlines and (b) Isotherms for Q = 0.0 and Q = -1.0 while Pr = 0.73, α = 0.3, M = 0.1, N = 0.2

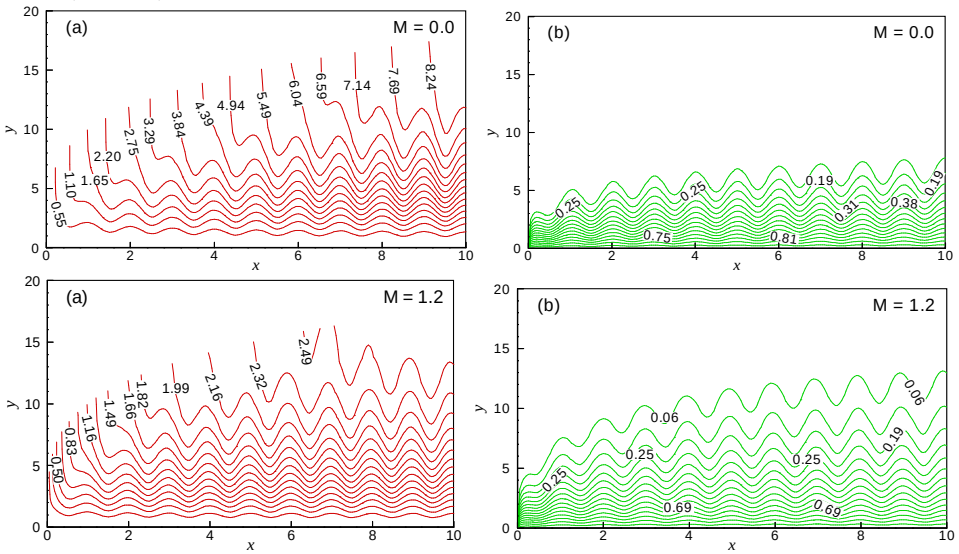

FIGURE 2.5: (a) Streamlines and (b) Isotherms for M = 0.0 and M = 1.2 while Pr = 0.73, α = 0.3, N = 0.05, Q = -0.1

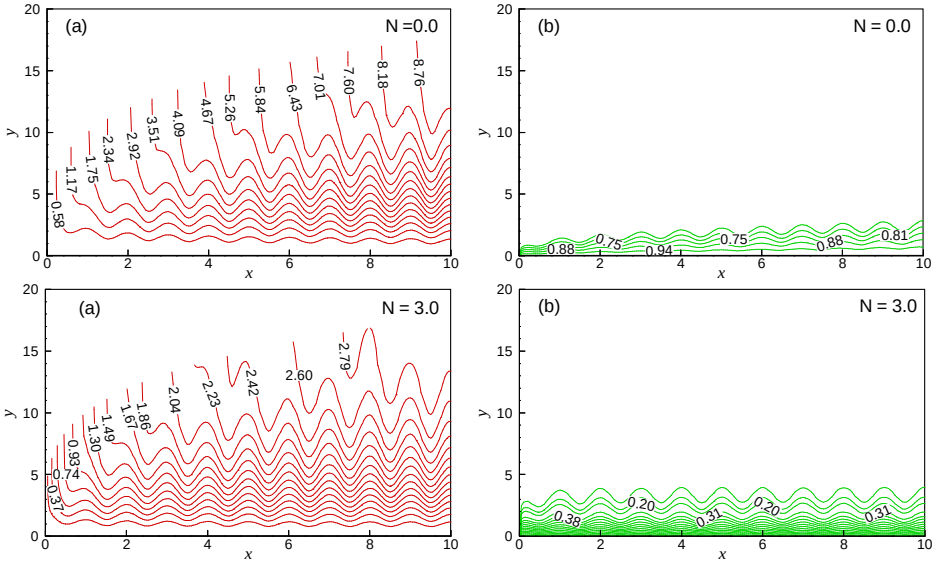

FIGURE 2.6: (a) Streamlines and (b) Isotherms for N = 0.0 and N = 3.0 while Pr = 0.73, α = 0.3, M = 0.5, Q = - 0.4

5. CONCLUSION

From the present investigation the following conclusions may be drawn:

- Increased values of the heat absorption parameter Q leads to decrease in the skin friction coefficient, velocity and thermal boundary layer thickness while the reverse phenomena occurs in the rate of heat transfer
- It is found that the skin friction coefficient, the rate of heat transfer and the velocity boundary layer decrease for increasing values of the magnetic parameter M but the thermal boundary layer becomes thicker gradually.
- The thickness of velocity boundary layer and the rate of heat transfer decrease gradually for the higher values of viscous dissipation parameter N but opposite result is observed in skin friction coefficient and the thermal boundary layer.

REFERENCES

1. B. Gebhart, “Effects of viscous dissipation in natural convection,” J. Fluid Mech., 14(1962) 225–232.
2. L.S.Yao, “Natural convection along a vertical wavy surface,” ASME J. Heat Transfer, 105(1983) 465–468.
3. L.S. Yao, “A note on prandtl’s transposition theorem,” ASME J. Heat Transfer, 110 (1988) 503–507.
4. M.M. Molla, “M.A. Hossain and L.S.Yao, Natural convection flow along a vertical wavy surface with uniform surface temperature in presence of heat generation/absorption,” Int. J. Therm. Sci., 43(2004). 157-163.
5. M.M. Alam, M.A. Alim, M.M.K. Chowdhury, “Viscous dissipation effects on MHD natural convection flow over a sphere in the presence of heat generation,” Nonlinear Analysis: Modelling and Control, 12 (2007) 447-459.
6. N. Parveen and M.A. Alim, **“**MHD natural convection flow along a vertical wavy surface in presence of heat generation/absorption with viscosity dependent on temperature**,** J. Mechanical Engineering, ME 42 (2012) 47–55
7. H.B. Keller, “Numerical methods in boundary layer theory,” Ann. Rev. Fluid Mech., 10 (1978) 417-433.

ICME2015

International Conference on Mechanical Engineering 2015
(ICME 2015) 18 – 20 December, 2015, Dhaka, Bangladesh

Paper ID : 195

Laminar-to-Transitional Flow and Heat Transfer through Nanofluid in a Square Cavity with Localized Heating from Below

Md. Zahangir Hossain[a)], Md. Mamun Molla[b)], Md. Sahadet Hossain, Mustak Mia

Modeling & Simulation Center, Department of Mathematics and Physics, North South University, Dhaka-1229, Bangladesh

[b)] Corresponding author: mamun.molla@northsouth.edu
[a)]zahangir.hossain@northsouth.edu

Abstract. In this paper, a two-dimensional laminar-to-transitional flow of nanofluids confined within a square cavity having localized heat source at the bottom wall has been investigated. The present research is a comparative investigation of the flow and thermal performance between nanofluid and purefluid. The governing Navier-Stokes and energy equations have been non dimensionalized using the appropriate non dimensional variables and then numerically solved using finite volume method with collocated grid. The flow was controlled by a range of Rayleigh numbers Ra = 10^5 to Ra = 10^8, length of heat source, ε and nano particle volume fraction ϕ. The numerical results are represented in terms of isotherms, streamlines, velocity and temperature distribution as well as the local and average rate of heat transfer. It is found that nanofluids are better for heat transfer.

INTRODUCTION

Nanofluids are immersions of nanosized solid particles in a base fluid. It is an innovative and effective way of improving thermal conductivity of fluids. Massive research has been conducted by several researchers explaining the flow and thermal behavior of nanofluids. A comparative study of the fluid flows and thermal performance between pure and nanofluids for high Rayleigh numbers are investigated in a square cavity whose bottom wall is heated by a heat source. The thermal conductivities of nanofluids are expected to be higher than that of common fluids. Xuan et al. [1] studied the procedure of preparing nanofluid. Calcagni et al. [2] conducted an experimental study for the present geometric configuration, that is, localized heating from the bottom and symmetrically cooling from the sides using pure fluid for Pr = 0.71.

An experimental study to investigate the heat transfer and flow behaviour of TiO_2 nanofluids flowing upward through a vertical pipe was investigated by He et al. [3]. It is observed from the experiment that nanofluids increase the convective heat transfer coefficient for both laminar and turbulent flow. It is also observed that enhancement in the laminar flow regime is much smaller than that in the turbulent flow regime. An experimental analysis for two dimensional nanofluids flows with three different nanoparticles was done by Shafahi et al. [4] where water is considered as a base fluid. The analysis showed that for nanofluid flows the temperature gradient along the heat pipe and thermal resistance across the heat pipe are reduced. Pang et al. [5] showed that the clustering of nanoparticles increases the thermal conductivity of nanofluids. Lee et al. [6] also investigated that thermal conductivity increases with increasing volume fraction. An experimental study for the enhancement of Critical Heat Flux (CHF) of

sandblasted surfaces for nanofluids was conducted by Truong et al. [7]. An extended research for further enhancement of enhanced CHF for nanofluids was performed by Dongsheng Wen [8]. In his experiment Wen investigated the possible mechanisms that increases CHF enhancement. Chun et al. [9] conducted an experiment to investigate the effect of nanofluid on a boiling heat transfer for three different nanofluids.

Wen et al. [10] measured the transient and steady heat transfer coefficients for different concentrations of nanofluids under natural convective heat transfer conditions in a high range of Rayleigh numbers from 10^6 to 10^9 and the result shows that the natural heat transfer coefficient decreases with the increasing of nanoparticle concentrations. A similar study for natural convection flow in a vertical cavity was done by Lin et al. [11] and shows that the heat transfer characteristics of nanofluid can be increased by decreasing the mean diameter of nanoparticle. Jung et al. [12] conducted an experimental study to measure the convective heat transfer coefficient and friction factor of nanofluids in a rectangular shaped microchanel.

A numerical study of nanofluids on mixed convection heat transfer was done by Kherbeet et al. [13] and investigated that the Nusselt number increases with the decrease of nanoparticle decrease. The effects of nanofluids on convective laminar flows for different geometries using different types of nanofluids and different Rayleigh numbers are investigated numerically by Vajjha et al. [14], Maiga et al. [15], Oztop et al. [16] and Yang et al. [17]. Abu-Nada et al. [18] investigated the effect of inclination angle on two dimensional natural convection nanofluid flows. Kondaraju et al. [19] investigated the effect of volume fractions on thermal conductivity of nanofluids using Direct Numerical Simulation (DNS) and observed that heat transfer increases with the increases of volume fraction. An exclusive numerical study for determining various types of nanofluid properties with six different types of nanoparticles was conducted by Fan et al. [20]. A comprehensive review of convective heat transfer enhancement with nanofluids is presented by Kakac et al. [21].

The objective of the present study is to investigate a two dimensional laminar-to-transitional flow of nanofluid in a square cavity with localized heat source at the bottom wall.

Nomenclature

α thermal diffusivity	β_f fluid thermal expansion coefficient
σ stress component	β_s solid thermal expansion coefficient
λ thermal conductivity	ϕ solid volume fraction
μ dynamic viscosity	ψ streamline function
ε width of heat source at bottom wall	ν kinematic viscosity

MATHEMATICAL MODELING

A two dimensional square cavity with localized heat source at the bottom wall and the top wall is entirely adiabatic is considered in our study. No slip conditions are imposed on the walls. The governing equation for two dimensional natural convection flows in a square cavity is governed by the following Navier-Stokes and energy equations as follows:

$$\frac{\partial u}{\partial x}+\frac{\partial v}{\partial y}=0 \tag{1}$$

$$\frac{\partial u}{\partial t}+u\frac{\partial u}{\partial x}+v\frac{\partial u}{\partial y}=-\frac{1}{\rho_{nf}}\frac{\partial p}{\partial x}+\frac{\mu_{nf}}{\rho_{nf}}\left(\frac{\partial^2 u}{\partial x^2}+\frac{\partial^2 u}{\partial y^2}\right) \tag{2}$$

$$\frac{\partial v}{\partial t}+u\frac{\partial v}{\partial x}+v\frac{\partial v}{\partial y}\rho=-\frac{1}{\rho_{nf}}\frac{\partial p}{\partial y}+\frac{\mu_{nf}}{\rho_{nf}}\left(\frac{\partial^2 v}{\partial x^2}+\frac{\partial^2 v}{\partial y^2}\right)+\frac{g(\rho\beta)_{nf}(T-T_C)}{\rho_{nf}} \tag{3}$$

$$\frac{\partial T}{\partial t}+u\frac{\partial T}{\partial x}+v\frac{\partial T}{\partial y}=\alpha_{nf}\left(\frac{\partial^2 T}{\partial x^2}+\frac{\partial^2 T}{\partial y^2}\right) \tag{4}$$

where ρ_{nf} is the density, μ_{nf} is the viscosity, β_{nf} is the thermal expansion coefficient, α_{nf} is the thermal diffusivity of nanofluids and g is the acceleration due to gravity.

Nondimensionl Equations

The dimensionless form of the governing equations of fluid flow is very important for numerical simulation. The governing equations are non-dimensionalized by using the following appropriate scales for the dependent and independent variables.

$$X=\frac{x}{L},Y=\frac{y}{L},\varepsilon=\frac{x_h}{L},\mathrm{U}=\frac{\mathrm{uL}}{\alpha_f},\mathrm{V}=\frac{\mathrm{vL}}{\alpha_f},\theta=\frac{T-T_c}{T_h-T_c},\mathrm{P}=\frac{\mathrm{pL}^2}{\rho_f\alpha_f^2},\mathrm{Pr}_f=\frac{\upsilon_f}{\alpha_f},$$

$$Ra=\frac{g\beta(T_h-T_c)L^3\,\mathrm{Pr}_f}{\upsilon_f^2},\tau=\frac{\alpha_f t}{L^2},\nu_{nf}=\frac{\mu_{nf}}{\rho_{nf}},\alpha_{nf}=\frac{k_{nf}}{(\rho C_f)_{nf}} \tag{5}$$

where x_h is the dimensional heat source length of the bottom wall, Pr is the Prandtl number and Ra is the Rayleigh number. The effective viscosity for a suspension containing small spherical solid nanoparticles is given by Brinkman [22] as

$$\mu_{nf}=\frac{\mu_f}{(1-\phi)^{1.5}} \tag{6}$$

The effective density and thermal expansion coefficient of a fluid containing solid nanoparticles are given by

$$\rho_{nf}=(1-\phi)\rho_f+\phi\rho_s \tag{7}$$

$$(\rho\beta)_{nf}=(1-\phi)(\rho\beta)_f+\phi(\rho\beta)_s \tag{8}$$

The effective thermal conductivity of a mixture of base fluid along with particular concentration of nanoparticles is given by Wasp [23] as

$$k_{nf}=\frac{k_s+2k_f-2(k_f-k_s)\phi}{k_s+2k_f+2(k_f-k_s)\phi}k_f \tag{9}$$

Applying the above non dimensional parameters (5) into Eqns. (1)-(4) the dimensionless form of the governing equations are given by:

$$\frac{\partial U}{\partial X}+\frac{\partial V}{\partial Y}=0 \tag{10}$$

$$\frac{\partial U}{\partial \tau}+U\frac{\partial U}{\partial X}+V\frac{\partial U}{\partial Y}=-\frac{1}{(1-\phi)+\phi\frac{\rho_s}{\rho_f}}\frac{\partial P}{\partial X}+\frac{\Pr}{(1-\phi)^{2.5}\left[(1-\phi)+\phi\frac{\rho_s}{\rho_f}\right]}\left(\frac{\partial^2 U}{\partial X^2}+\frac{\partial^2 U}{\partial Y^2}\right) \quad (11)$$

$$\frac{\partial V}{\partial \tau}+U\frac{\partial V}{\partial X}+V\frac{\partial V}{\partial Y}=-\frac{1}{(1-\phi)+\phi\frac{\rho_s}{\rho_f}}\frac{\partial P}{\partial Y}+\frac{\Pr}{(1-\phi)^{2.5}\left[(1-\phi)+\phi\frac{\rho_s}{\rho_f}\right]}\left(\frac{\partial^2 V}{\partial X^2}+\frac{\partial^2 V}{\partial Y^2}\right)$$
$$+Ra\,\Pr\theta\left[\frac{1}{1+\frac{(1-\phi)\rho_f}{\phi\rho_s}}\frac{\beta_s}{\beta_f}+\frac{1}{1+\frac{(1-\phi)\rho_f}{\phi\rho_s}}\right] \quad (12)$$

$$\frac{\partial \theta}{\partial \tau}+U\frac{\partial \theta}{\partial X}+V\frac{\partial \theta}{\partial Y}=\alpha_{nf}\frac{\frac{k_{nf}}{k_f}}{\left[(1-\phi)+\phi\frac{(\rho C_p)_s}{(\rho C_p)_f}\right]}\left(\frac{\partial^2 \theta}{\partial X^2}+\frac{\partial^2 \theta}{\partial Y^2}\right) \quad (13)$$

Boundary Conditions

In order to solve the non-dimensional governing Eqns. (10)-(13) numerically the following boundary conditions are applied:

$$\begin{aligned}
&U=V=0,\quad \theta=0 && \text{at } X=0,1,\ 0<Y<1\\
&U=V=0,\quad \theta=1 && \text{at } Y=0,\ \frac{1-\varepsilon}{2}\le X\le\frac{1+\varepsilon}{2}\\
&U=V=0,\quad \frac{\partial\theta}{\partial Y}=0 && \text{at } Y=0,\ 0\le X\le\frac{1-\varepsilon}{2},\ \frac{1+\varepsilon}{2}\le X\le 1\\
&U=V=0,\quad \frac{\partial\theta}{\partial Y}=0 && \text{at } Y=1,\ 0\le X\le 1
\end{aligned} \quad (14)$$

where ε is the non-dimensional heat source length.

	Cu	Water

$C_p\left(J/kg\,K\right)$	383	4179.0
$k\left(W/mK\right)$	400	0.6
$\rho\left(kg/m^3\right)$	8954	997.1
$\beta\left(1/K\right)$	1.67E-08	21.0E-05

TABLE 1: Physical properties of nanoparticles and base fluids [24].

NUMERICAL METHODS

SIMPLE algorithm is used for solving the governing equations and the finite volume method is used to discretize transformed governing equations which are given in Appendix. The unsteady term is discretized by a three pointbackward difference scheme with a constant time step of $t = 1.0 \times 10^{-4}$. After discretization the obtained systems of linear equations for the variables *U*, *V* and θ are solved with BI-CGSTAB (Bi-Conjugate Gradient Stabilized) solver. The pressure terms are derived with the help of continuity equation that results in a Poisson like equation which is then solved with ICCGSTAB (Incomplete Cholesky Conjugate Gradient Stabilized) solver. In addition, the grid is generated by the in-house code. For resolving the near wall flow refined mesh is used by employing a tanh function.

RESULTS AND DISCUSSION

Code Validation

Calcagni et al. [2] conducted an experimental study for the present geometric configuration, that is, localized heating from the bottom and symmetrically cooling from the sides using pure fluid for Pr = 0.71. A comparison has been done with these experimental results for Ra = 1.205×105 and heat source length $\varepsilon = 4/5$ and $\phi = 0$ (purefluid), a very good agreement was found that is shown in Fig. 1. Numerical simulations have been carried out for different Rayleigh numbers from 105 to 108 and nano particle volume fraction for $\phi = 20\%$ Numerical results for the streamlines, isotherms and local Nusselt number profiles have been presented graphically that represents the effects of the Rayleigh numbers.

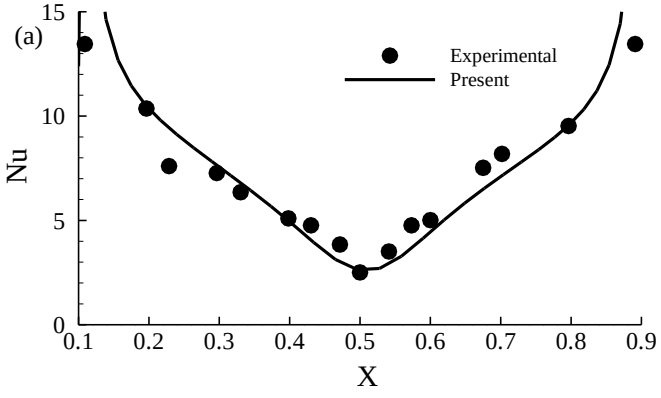

FIGURE 1. Comparison of local Nusselt Number with the experimental results of Calcagni et al. [2] while Pr = 0.71, Ra = 1.205 $\times$105, ε = 4/5 and ϕ = 0 (purefluid)

Streamlines and Isotherms

The streamlines (top) and isotherms (bottom) for Rayleigh numbers 105 to 108 are presented in Fig. 2. The streamlines are spherical loop in shape. From Fig. 2 it is observed that there are two vorticity about the central vertical line of the cavity where the right vortex is moving counter clockwise and the left one clockwise direction. It is clear from the figure that at low Rayleigh numbers (105, 106) the right and left cells are symmetric about the central vertical line of the cavity where as at higher Rayleigh numbers (107, 108) there is a break in symmetry. The maximum magnitudes of the streamlines for different Rayleigh numbers are illustrated in Table 2. From Table 2 we observed that the maximum magnitude of the streamlines increases with increases in Ra, which represent that the rate of fluid flow increases with increases in Ra. It is also observed from the table that the maximum magnitudes of the stream function, $\psi_{\max}$ for the both vortex are almost equal for 105 , 106 while there is a significant difference for 107 , 108 . So, from Fig. 2 and Table 2 we can conclude that for higher Rayleigh numbers the flow break their symmetry and the flow become transitional.

$\psi_{\max}$	**Ra=10^5**	**Ra=10^6**	**Ra=10^7**	**Ra=10^8**
Left vortex	7.47	22.87	40.79	183.05
Right vortex	7.57	22.95	76.37	110.97

TABLE 2. Maximum magnitude of streamline for both vortexes with Rayleigh Numbers.

From Fig. 2 it is observed that the isotherms are also symmetric about the vertical central line of the cavity for Ra=105,106 and the flow becomes chaotic for Ra=107, 108 Therefore the flow becomes turbulent for higher Rayleigh numbers.

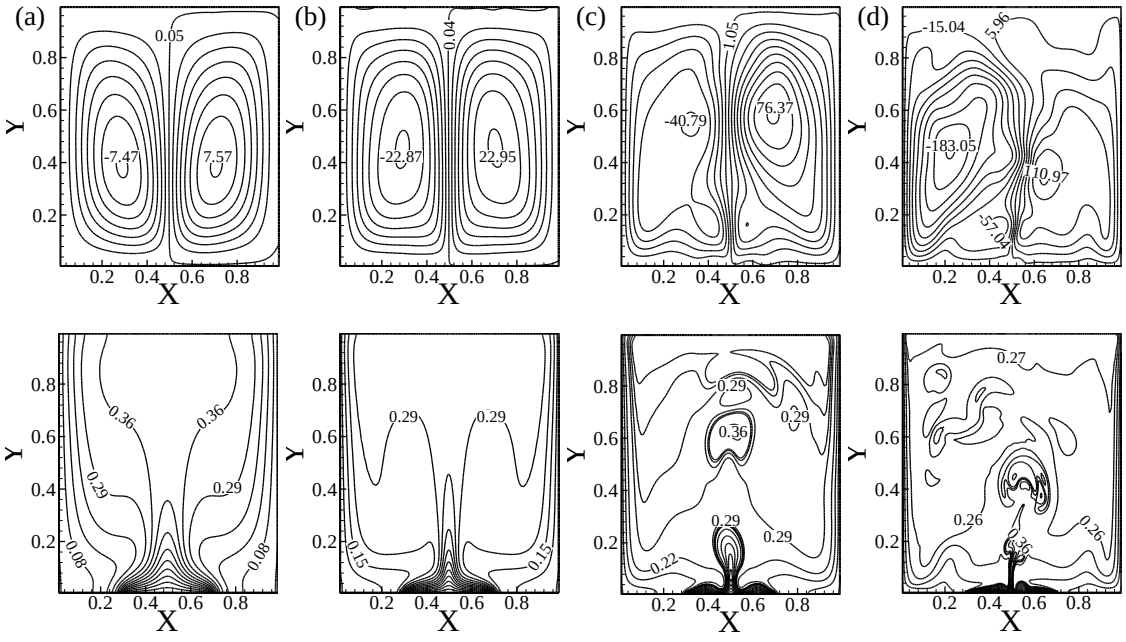

FIGURE 2. Streamlines (top) and isotherms (bottom) for (a) Ra=10^5 (b) Ra=10^6 (c) Ra=10^7 and (d) Ra=10^8 while Pr=6.2, ε = 2/5 and ϕ = 0.2.

Nusselt Number

The variations of local Nusselt number with different Rayleigh numbers are shown in Fig. 3. It is observed from the figure that the lowest heat transfer occurs at low Rayleigh number and highest heat transfer occurs for high Rayleigh number.

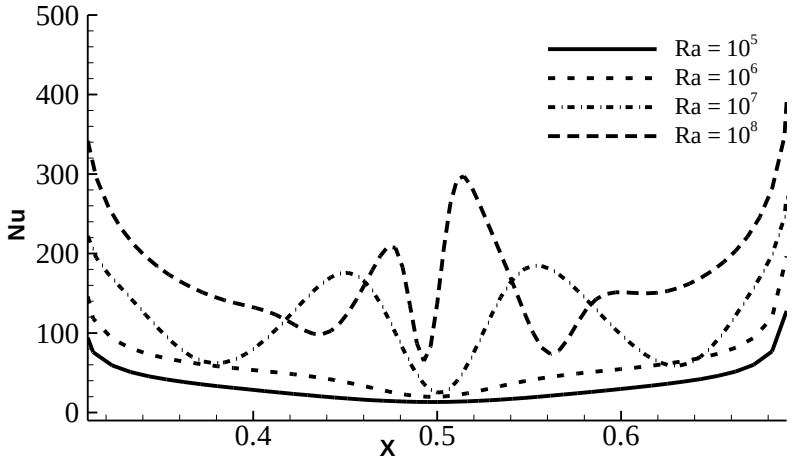

FIGURE 3. Variation of average Nusselt Number with different Rayleigh number while Pr=6.2, $\varepsilon = 2/5$ and $\phi = 0.2$.

From Table 3 it is evident that the average Nusselt number (Nu_{avg})for pure and nanofluids increases with increases in Rayleigh numbers, which is in very good agreement with other research work(Lin et al. [11], Khanafer et al.[25] and Abu-Nada et al.[26]). Use of nanoparticles in fluid increases the average Nusselt number by about 87%, 82%, 127% and 73% for Ra= $10^{5,}$ 10^6 10^7 and 10^8 respectively compared to pure fluid.

Nu_{avg}	Ra=10^5	Ra=10^6	Ra=10^7	Ra=10^8
Pure fluid	8.0436	14.0128	22.7172	43.7015
Nano fluid	15.0454	25.5430	51.7907	75.8391

TABLE 3. Variation of average Nusselt Number with Rayleigh Number (Ra) for pure and nano fluids.

CONCLUSION

The purpose of this work was to study the effects of Rayleigh number and thermal behavior of nanofluid in a square cavity with localized heating from below. The result shows that for higher Rayleigh number the fluid flow behaves like transitional flow. It is found that the rate of fluid flow increases with the increases of Rayleigh number for both pure and nanofluid. It is also observed that for heat transfer nanofluids are superior to pure fluid.

REFERENCES

1. Y. Xuan, Q. Li, International Journal of Heat and Fluid Flow, **21(1)**, 58-64 (2000).
2. B. Calcagni, F. Marsili, M. Paroncini, Applied Thermal Engineering, **25(16)**, 2522-2531 (2005).
3. Y. He, Y. Jin, H. Chen, Yulong Ding, Daqiang Cang, Huilin Lu, International Journal of Heat and Mass Transfer **50(11 – 12)**, 2272 - 2281 (2007).
4. M. Shafahi, V. Bianco, K. Vafai, O. Manca, International Journal of Heat and Mass Transfer **53 (1–3)**, 376-383 (2010).

5. C. Pang, J. Y. Jung, J. W. Lee, Y. T. Kang, International Journal of Heat and Mass Transfer, **55(21—22)** 5597-5602 (2012).
6. S. W. Lee, S. D. Park, S. Kang, I. C. Bang, J. H. Kim, International Journal of Heat and Mass Transfer, 54(1—3), (January 2011), pp. 433-438.
7. B. Truong, L. Hu, J. Buongiorno, T. McKrell, Modification of sandblasted plate heaters using nanofluids to enhance pool boiling critical heat flux, International Journal of Heat and Mass Transfer, 53(1–3), (January 2010), pp. 85-94.
8. D. Wen, Mechanisms of thermal nanofluids on enhanced critical heat flux (CHF), International Journal of Heat and Mass Transfer, 51(19–20), (September 2008), pp. 4958-4965.
9. S.Y. Chun, I. C. Bang, Y.J Choo, C. H. Song, Heat transfer characteristics of Si and SiC nanofluids during a rapid quenching and nanoparticles deposition effects, International Journal of Heat and Mass Transfer,54(5–6), (February 2011), pp. 1217-1223.
10. D. Wen, Y. Ding, Formulation of nanofluids for natural convective heat transfer applications, International Journal of Heat and Fluid Flow, 26(6), (December 2005), pp. 855-864.
11. K. C. Lin, A. Violi, Natural convection heat transfer of nanofluids in a vertical cavity: Effects of non- uniform particle diameter and temperature on thermal conductivity, International Journal of Heat and Fluid Flow, 31(2), (April 2010), pp. 236-245.
12. J.Y. Jung, H.S. Oh, H. Y. Kwak, Forced convective heat transfer of nanofluids in microchannels, International Journal of Heat and Mass Transfer, 52(1–2), (15 January 2009), pp. 466-472.
13. A.S. Kherbeet, H.A. Mohammed, B.H. Salman, The effect of nanofluids flow on mixed convection heat transfer over microscale backward-facing step, International Journal of Heat and Mass Transfer, 55(21–22), (October 2012), pp. 5870-5881.
14. R. S. Vajjha, D. K. Das, P. K. Namburu, Numerical study of fluid dynamic and heat transfer performance of Al_2O_3 and CuO nanofluids in the flat tubes of a radiator, International Journal of Heat and Fluid Flow, 31(4), (August 2010), pp. 613-621.
15. S. E. B. Maïga, S. J. Palm, C. T. Nguyen, G. Roy, N. Galanis, Heat transfer enhancement by using nanofluids in forced convection flows, International Journal of Heat and Fluid Flow, 26(4), (August 2005), pp. 530-546.
16. H. F. Oztop, E. A. Nada, Numerical study of natural convection in partially heated rectangular enclosures filled with nanofluids, International Journal of Heat and Fluid Flow, 29(5), (October 2008), pp. 1326-1336.
17. Y. T. Yang, F. H. Lai, Numerical study of heat transfer enhancement with the use of nanofluids in radial flow cooling system, International Journal of Heat and Mass Transfer, 53(25–26), (December 2010), pp. 5895-5904.
18. E. A. Nada, H. F. Oztop, Effects of inclination angle on natural convection in enclosures filled with Cu--water nanofluid, International Journal of Heat and Fluid Flow, 30(4), (August 2009), pp.669-678.
19. S. Kondaraju, E.K. Jin, J. S. Lee, Direct numerical simulation of thermal conductivity of nanofluids: The effect of temperature two-way coupling and coagulation of particles, International Journal of Heat and Mass Transfer, 53(5–6), (February 2010), pp. 862-869.
20. J. Fan, L. Wang, Heat conduction in nanofluids: Structure–property correlation, International Journal of Heat and Mass Transfer, 54(19–20), (September 2011), pp. 4349-4359.
21. S. Kakaç, A. Pramuanjaroenkij, Review of convective heat transfer enhancement with nanofluids, International Journal of Heat and Mass Transfer, 52(13–14), (June 2009), pp. 3187-3196.
22. H. C. Brinkman, The Viscosity of Concentrated Suspensions and Solutions. The Journal of Chemical Physics, 20(4), (1952), pp. 571-571.
23. E.J. Wasp, J.P. Kenny, and R.L.Gandhi, Solid-liquid flow slurry pipeline transportation, Trans Tech Publications (1977).
24. H. Nemati, M. Farhadi, K. Sedighi, E. Fattahi, A.A.R. Darzi, Lattice Boltzmann simulation of nanofluid in lid-driven cavity, International Communications in Heat and Mass Transfer, 37(10), (December 2010), pp. 1528-1534.
25. K. Khanafer, K. Vafai, M. Lightstone, Buoyancy-driven heat transfer enhancement in a two-dimensional enclosure utilizing nanofluids, International Journal of Heat and Mass Transfer, 46(19), (September 2003), pp. 3639-3653.
26. E. A. Nada and H. F. Oztop, Numerical Analysis of Al_2O_3 / Water Nanofluids Natural Convection in a Wavy Walled Cavity, Numerical Heat Transfer, Part A: Applications, 59(5), (2011), pp. 403-419.

ICME2015

International Conference on Mechanical Engineering 2015
(ICME 2015) 18 – 20 December, 2015, Dhaka, Bangladesh

Paper ID : 202

The Effect of Mass Recovery Adsorption Cooling Cycle to Optimize the Collector Number and Time Allocation

K.M Ariful kabir [1, a)], K.C. Amanul Alam[2], Rifat A. Rouf [3], M. M. A. Sarker[1]

[1]*Bangladesh University of Engineering and Technology (BUET), Dhaka-1000, Bangladesh*
[2]*East West University, Dhaka-1214, Bangladesh*
[3]*Independent University, Bangladesh, Dhaka-1229, Bangladesh*

[a)]Corresponding author: *k.ariful@yahoo.com*

Abstract. The performance of mass recovery for solar adsorption cooling system has been investigated numerically. Solar adsorption cooling appears to have a prospect in tropical region. Though it has a huge installation cost, its long term payback could be a considerable fact. Mass recovery scheme increases Average cooling capacity (ACC) and Coefficient of Performance COP values of the adsorption cooling system. In intension to reduce cost and maximize system performance, a two bed solar driven conventional cooling system run by silica gel and water along with mass recovery process has been investigated mathematically.

INTRODUCTION

Integrating adsorption cooling systems with solar energy can reduce the dependency on fossil fuels making them potential candidates for net zero energy structure operation [1, 2]. Though absorption cycles are predominant in the area of heat driven heat pump pump/refrigeration technologies, adsorption cycles have some distinct advantages over the other systems in viewpoints of their ability to be driven by relatively low temperature heat source [3]. Following are some such examples: Zeolite/ water [4,5], activated carbon/ammonia [6], activated carbon/methanol [7] and silica gel/water [8–10]. Many innovative cycles have been proposed to improve the system performance. Mueiner [11] studied the system performance of cascading cycle in which an activated carbon/methanol cycle topped by zeolite/water. Pons and Poyelle [12] studied the influence of mass recovery process in conventional two beds adsorption cycle. Later, Wang [13] investigated the performances of vapor (mass) recovery cycle with activated carbon-methanol as adsorbent/adsorbate pair and demonstrated that the mass recovery cycle is effective for the low regenerating temperature.

Many researchers studied the adsorption cooling system utilizing solar energy, among them, remarkable studies are made by Pons and Guilleminot [14] and Boubarkri [15] for ice production, Anyanwu and Ogueke [16] and Anyanwu and Ezekwe [17] for refrigeration system, Sumanthy et al.[18], Clauss et al [19] and Alam et al.[20] for air-conditioning system. Recently, Rouf et al. [21] investigated performance of solar driven adsorption chiller for climatic condition of Dhaka, Bangladesh. Later, Alam et el.[22] introduced heat storage tank to the solar driven adsorption cooling system to extend the working hour beyond sunset. As it was discussed that solar driven air-conditioning has a great potential and mass recovery cycle enhances the performance, therefore, solar driven cooling system with mass recovery process will be very effective. From this context, a two bed conventional adsorption cooling system with mass recovery coupled with solar collector, with silica gel-water pair as adsorbent/adsorbate, is analyzed numerically under the climatic condition of Dhaka, Bangladesh in the present study.

Nomenclature

A	area	η	collector efficiency	**Subscript**	
W	weight	U	heat transfer coefficient	cp	collector pipe
C	specific heat	I	solar radiation	cr	collector
T	temperature			$chill$	chill water
$\dot{m}$	mass flow rate				

PRINCIPLE AND OPERATIONAL PROCESS OF THE SYSTEM

In the mass recovery process, the adsorbers are not connected with the evaporator or condenser, the pressurization and depressurization are accomplished by heating and cooling the bed. The partial pressurization and depressurization, however, can occur without heating and cooling the bed. The process is known as the mass recovery process. At the start of mass recovery, the heated adsorber has high pressure while the cooled adsorber has low pressure. By connecting the two adsorbers together, the water vapor will flow from the high pressure heated adsorber to the low pressure cooled adsorber. Because of the pressure differences in the adsorbers, adsorption/desorption process will occur automatically without applying any heating and cooling. Thus, the desorbed water vapour from heated adsorber will move to the cooled adsorber. The mass recovery can further dry the heated adsorber after desorption and reduce the internal pressure. The dryer adsorber can adsorb more water vapour in the next adsorption phase. The process can be made to just connect the desorber and adsorber through a pipe; which allows the vapour to enter from desorber to adsorber. Thus, the mass circulation is increased inside the bed. As a result, the system provides better cooling capacity. There are six thermodynamic steps in the cycle, namely, (i) Pre-cooling (ii) Adsorption/Evaporation (iii) Mass recovery with cooling (iv) Pre-heating (v) Desorption/ Condensation and (vi) Mass recovery with heating. The adsorber (SE1/SE2) are alternately connected to the solar collector to heat up the bed during pre-heating and desorption/ condensation process and to the cooling tower to cool down the bed during pre-cooling and adsorption/ evaporation process.

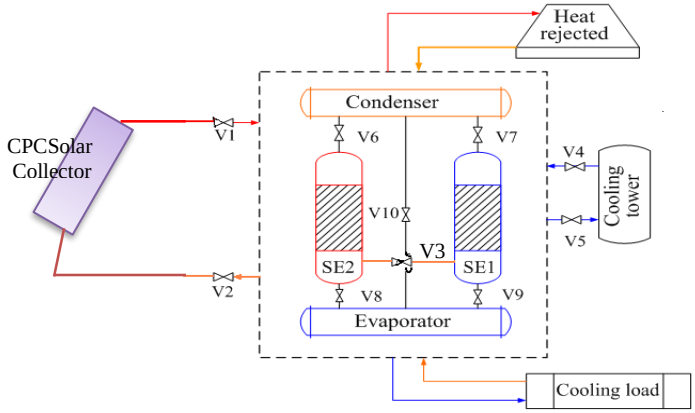

FIGURE1. Schematic diagram of the solar driven adsorption space cooling system with mass recovery

The conceptual P-T-X (Dühring) diagram of the basic mass recovery cycle is presented in Fig. 3.1. From this Fig. it can be seen that greater cooling output than that of conventional cycle can be obtained by utilizing the same resources as used in previous chapters. This process can also be called as an 'internal vapour recovery process' and is reported to enhance the cooling Capacity of the unit without reducing the COP.

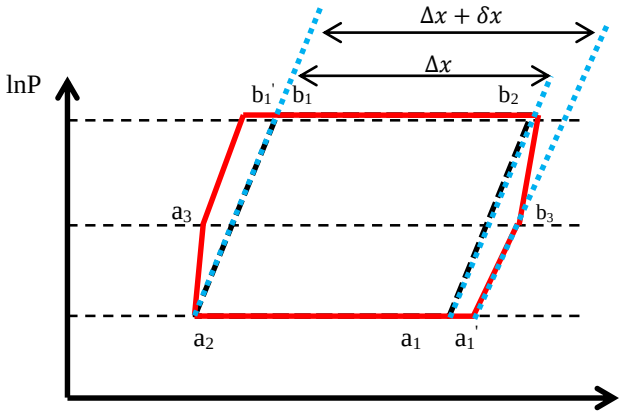

$$-\frac{1}{T}$$

FIGURE 2. Clapeyron diagram of mass recovery cycle

The above figure, Fig. 3.2 (S. Farid[46]) describe an ideal mass recovery cycle. The mass recovery cycle ($a_2 - a_3 - b_1' - b_1 - b_2 - b_3 - a_1' - a_1 - a_2$) is an extended form of a two bed basic cycle shown in Fig. 3.2 and the cycles mass is increased from Δx to $\Delta x + \delta x$, which causes the refrigeration effect to increase.

MATHEMATICAL MODELLING

In the present study, lamped parameter model has been exploited. The temperature and pressure are uniform throughout the whole adsorber. The simulation procedure is elsewhere available in Alam et al [20].

The heat transfer fluid is equally distributed to all the collectors and the combined outlet from all the collectors then enters into desorber. Each collector has nine pipes, water enters through the first pipe and the outlet of the first pipe enters into the next pipe thus the outlet of the ninth pipe of each collector combines together and enters into the desorber. Hence the temperature of the heat transfer fluid in each pipe is calculated separately for all the collectors. The energy balance of each collector can be expressed as [24]:

$$W_{cp,i}\frac{dT_{cr,i}}{dt} = \gamma\{\eta_i A_{cr,i} I + \dot{m}_{f,cr} C_f (T_{cr,i,in} - T_{cr,i,out})\} + (1-\gamma) U_{loss} A_{cr,i} (T_{am} - T_{cr,i}) \quad (1)$$

$$T_{cr,i,out} = T_{cr,i} + (T_{cr,i,in} - T_{cr,i}) EXP(U_{cp} A_{cp,i} / \dot{m}_{f,cr} C_f) \quad (2)$$

The collector efficiency equation is considered to be same as Clauss "et al." [19]. The cyclic average cooling capacity (CACC) is calculated by the equation

$$CACC = \dot{m}_{chill} C_{chill,f} \int_{beginofcycletime}^{endofcycletime} (T_{chill,in} - T_{chill,out}) dt / t_{cycle}. \quad (3)$$

The cycle COP (coefficient of performance) and net solar COP in a cycle (COP_{sc}) are calculated respectively by the equations

$$COP_{cycle} = \frac{\int_{beginofcycletime}^{endofcycletime} \dot{m}_{chill} C_{chill,f} (T_{chill,in} - T_{chill,out}) dt}{\int_{beginofcycletime}^{endofcycletime} \dot{m}_f C_f (T_{d,in} - T_{d,out}) dt} \quad (4)$$

$$COP_{solar,net} = \frac{\int_{Sunrisettime}^{chillerstoptime} \dot{m}_{chill} C_{chill} (T_{chill,in} - T_{chill,out}) dt}{\int_{Sunrisettime}^{chillerstoptime} n\, A_{cr} I\, dt.} \quad (5)$$

Where, I is the solar irradiance, A_{cr} is each collector area and n is number of collectors.

RESULTS AND DISCUSSIONS

The intension of the present study is to reduce collector number and enhance cooling capacity. For the climatic condition of Dhaka at least 14 collectors with 1000s cycle time is needed [7] for the basic adsorption chiller with baser run conditions.

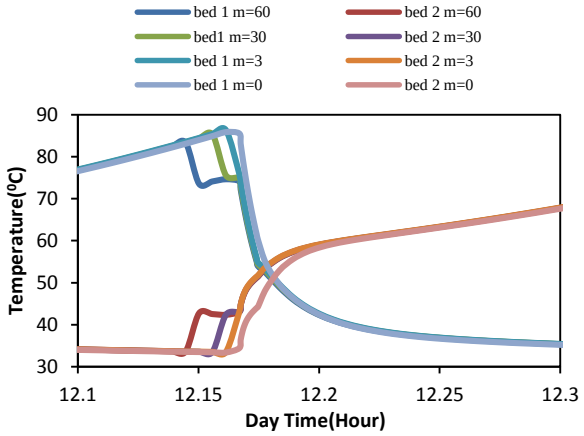

of different
ery.

FIGURE 3(b) Temperature profile for beds of different collector number with mass recovery and without mass

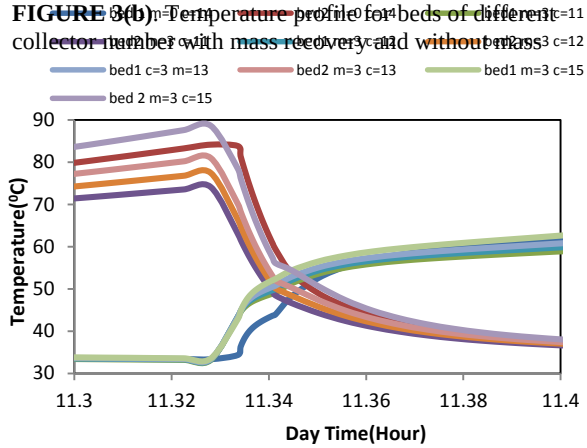

The temperature histories of the adsorption beds with and without mass recovery process are depicted in Figure 3(a) and temperature of different collector number shown in Figure 3(b). It is also seen that increasing mass recovery time produces lower bed (desorber) temperature for the same cycle time. This is due to the mass recovery scheme. As the desorber releases more vapor during the mass recovery process; therefore, hot bed releases more heat as a result of adsorption/desorption characteristic. On the other hand increasing of collector numbers improves bed temperature in both cases.

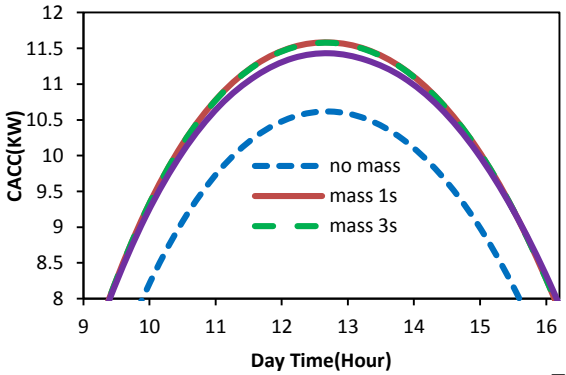

FIGURE 4. Cooling capacity (KW) of different mass recovery time.

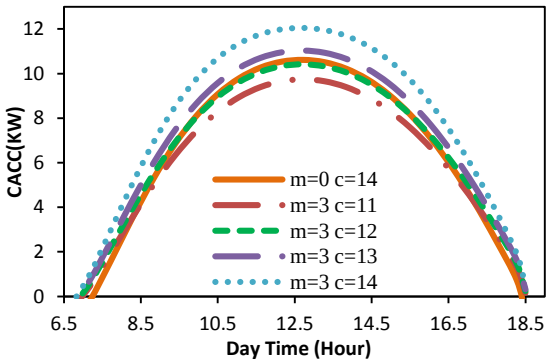

FIGURE 5. Cooling capacity (KW) of different collector number.

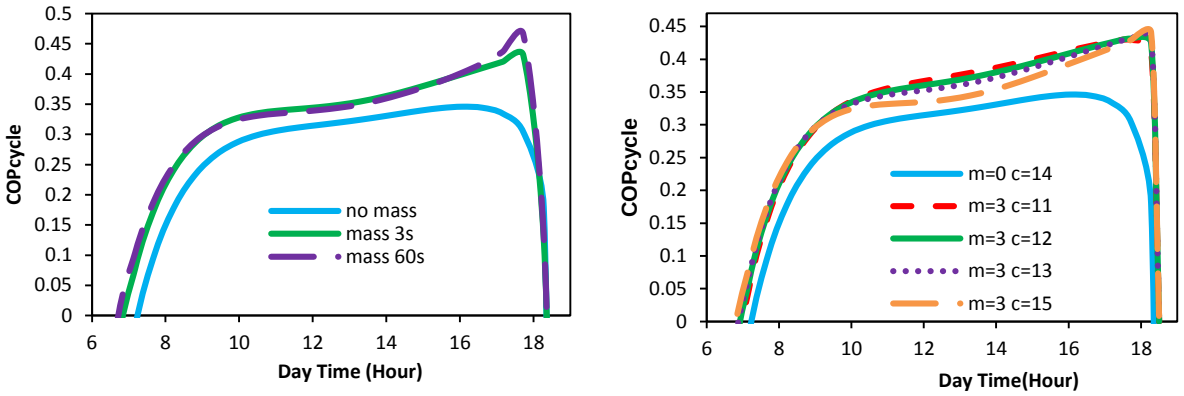

60s)

FIGURE 7. Solar COP in with and without mass recovery in different collector number

Though the bed temperature for without mass recovery cycle is higher than that of mass recovery cycle, better cooling capacity is observed for mass recovery cycle. The cooling capacities of without mass recovery process and with different mass recovery process time are compared in Figure 4. As, optimum adsorption and desorption capacity of silica gel is limited, once saturated enhanced time of mass recovery does not help in more uptake, therefore, there is no further improvement in cooling capacity. Thus, it may conclude that there is an optimum mass recovery process time for the base run conditions. For the present case the optimum mass recovery process time is 3s. As mass recovery process improve the cooling capacity, therefore, it may determine that the collector area could be reduced by introducing mass recovery process in solar driven cooling system. In Figure 5, it is seen that the CACC of 12 collectors with mass recovery is closely equivalent to 14 collectors without mass recovery cycle.

The solar COP in cycle (COPcycle) of different mass recovery and different collector numbers are presented respectively in Figure 5 and Figure 6. It is seen that COP values are improved if mass recovery process is applied in 3s. It is also seen that the COP is better in collector number 11 and 12 with mass recovery. As the mass recovery cycle works effectively with relatively low temperature heat source (Akahira et al. [23]), therefore, the system shows better COP values in the morning and at late afternoon.

CONCLUSION

Based on the analysis of the mass recovery process with the solar heat driven adsorption chiller with direct solar coupling, the following concluding remarks can be made for the base run conditions.

- Mass recover process enhances the performances of the solar driven adsorption chiller. Mass recovery process also enhances the working hour and the optimum mass recovery time is 3s.
- Finally, it may be concluded that the number of collector reduce by employing mass recovery process which is economically very important for adsorption cooling system.

ACKNOWLEDGMENTS

The authors wish to acknowledge the technical and financial support provided by the Bangladesh University of Engineering and Technology (BUET).

REFERENCES

1. Tso C. Y., Chao C.Y.H., Fu S.C., *Performance analysis of a waste heat driven activated carbon based composite adsorbent-water adsorption chiller using simulation model*, Int. J. Heat Mass Tran. 55(2012) 7596-7610.
2. Alam K.C.A, Akahira .A., Y. Hamamoto, Akisawa. A., Kashiwagi.T., *A four-bed mass recovery adsorption refrigeration cycle driven by low temperature waste/renewable heat source*, Ren. Energ. 29 (2004) 1461-1475.
3. Kashiwagi T, Akisawa A, Yoshida Y, Alam K.C.A, Hamamoto Y. *Heat driven sorption refrigerating and air conditioning cycle in Japan. In: Proceedings of the International Sorption Heat Pump Conference*, 24–27 September 2002, Shanghai, China. p. 50–62.

4. Karagiorgas M, Meunier F. *The dynamics of a solid adsorption heat pump connected with outside heat sources of finite capacity*. J Heat Recovery Systems CHP 1987; 7(3):285–99.
5. Tchemev D.I., Emerson D.T.E. *High efficiency regenerative zeolite heat pump.* ASHRAE Trans 1988;94(2):2024–32
6. Critoph R.E., Vogel R. *Possible adsorption pairs for use in solar cooling. Int J Ambient Energy* 1986; 7(4):183–90.
7. Critoph R. E. *Activated carbon adsorption cycles for refrigeration and heat pumping*. Carbon 1989; 27:63–70.
8. Saha B.B, Boelman E.C, Kashiwagi T. *Computer simulation of a silica gel-water adsorption refrigeration cyclethe influence of operating conditions on cooling output and COP*. ASHRAE Trans Res 1995;101(2):348–55.
9. Chua H.T., Ng KC, Malek A, Kashiwagi T, Akisawa A, Saha B.B. *Modeling the performance of two-bed, silica gel-water adsorption chillers*. Int J Refrigeration 1999; 22: 194–204.
10. Alam K.C.A., Saha B.B., Kang Y.T, Akisawa A, Kashiwagi T. *Heat exchanger design effect on the system performance of silica gel-water adsorption system.* Int. J Heat and Mass Transfer 2000;43(24):4419–31.
11. Meunier F. *Theoretical performances of solid adsorbent cascading cycles using the zeolite-water and active carbon methanol pairs: four case studies.* Heat Recovery CHP systems 1986;6(6):491–8.
12. Pons M, Poyelle F. *Adsorptive machines with advantaged cycles for heat pumping or cooling applications.* Int J Refrigeration 1999; 22:27–37.
13. Wang R. Z. *Performance Improvement of Adsorption Cooling by Heat and Mass Recovery Operation*. Int J Refrigeration 2001; 24:602–11.
14. Pons M, Guilleminot J.J., *Design of an experimental solar powered, solid adsorption ice maker*, Journal of Solar Energy and Engineering, (Trans. ASME), 103 (4) (1986) 332-337.
15. Boubakri A., *A new conception of an adsorptive solar powered ice maker*, Ren. Energy, 28 (2003) 831-842.
16. Anyanwu E.E., Ogueke N.V., *Transient analysis and performance prediction of a solid adsorption solar refrigerator, Applied Thermal Engineering*, 27 (2007) 2514-2523.
17. Anyanwu E.E., Ezekwe C.I., *Design, construction and test run of a solid adsorption solar refrigerator using activated carbon/methanol as adsorbent/adsorbate pair*, Energy Conversion and Management 44 (18) (2003) 2879-2892.
18. Sumathy K., Yong Li, Steinhagen H. Muller, Kerskes H., *Performance analysis of a modified two-bed solar-adsorption air-conditioning system*, Int. J. Energ. Res. 33 (2009) 675-686.
19. Clausse M., Alam K. C. A., Meunier F., "*Residential air conditioning and heating by means of enhanced solar collectors coupled to an adsorption system,*" *Solar Energy,* vol.82 (10), pp. 885-892, 2008.
20. Alam K. C. A., Saha B. B. and Akisawa A., Adsorption cooling driven by solar collector: a case study for Tokyo solar data, Applied Thermal Engineering, 50 (2) (2013) 1603-1609.
21. Rouf R. A, Alam K. C. A, Khan M. A. H, Ashrafee T. and Anwer M, "*Solar Adsorption Cooling: A Case Study on the Climatic Condition of Dhaka",* Academy Pub. J. of Computers, v.8, no 5,pp.1101-1108,2013.
22. Alam K. C. A., Rouf R. A., Saha B B., Khan M. A. H. and Meunier F. "*Autonomous Adsorption Cooling – driven by Heat Storage Collected from Solar Heat*", Journal of Heat Transfer Engineering (under review).
23. Akahira A., Alam K.C.A.**,** Hamamoto Y.**,** Akisawa A. and Kashiwagi T., "*Mass recovery adsorption refrigeration cycle—improving cooling capacity*", *Int. J. of Refrigeration*, Vol.27, pp.225-234, (2004).
24. Rouf R. A, Alam K. C. A, Khan M. A., Saha B B., Meunier F., Alim. M. A and Kabir. K .A. "*Advancement of solar Adsorption Coolin by means of heat storage",* Procedia Engineering v. 90, pp. 649-656, 2014.

ICME2015

International Conference on Mechanical Engineering 2015
(ICME 2015) 18 – 20 December, 2015, Dhaka, Bangladesh

Paper ID : 205

Experimental Investigation of the Blends of *Calophyllum Inophyllum* Biodiesel and Gas-To-Liquid Fuel with Diesel in the Context of Fuel Properties and Engine Performance-Emission Parameters

H. Sajjad[1,b)], M.M.R. Khan[2,a)], H. H. Masjuki[1], M. Varman[1], B.M. Masum[1]

[1]*Centre for Energy Sciences, Department of Mechanical Engineering, University of Malaya, Kuala Lumpur, 50603, Malaysia.*
[2] *Department of Textile Engineering, Bangladesh University of Business and Technology, Dhaka-1216.*

[a)]Corresponding author: mahmud.rk@gmail.com
[b)]sajjadhossain13@gmail.com

Abstract. Energy security concerns and environmental sustainability issues have been increasing with the growth of civilization, which have developed the urge to increase energy efficiency with a diminution in environmental pollution. These situations have stimulated the researchers to focus on the alternative transportation fuels like Gas-to-liquid (GTL) fuel and *calophyllum inophyllum* biodiesel (CIBD). This study contains a comparative analysis of fuel properties and engine performance-emission parameters of the two individual blends (20% by volume) of CIBD (CI20) and GTL fuel (G20) with diesel, and ternary blend (DCIG20) of CIBD, GTL and diesel. A four cylinder diesel engine was used to evaluate major engine performance and exhaust emission parameters at constant speed with variable load test condition. The fuel characterization results revealed an improvement of the major fuel properties for G20 and DCIG20 than those of CI20. The engine performance test results of G20 and DCIG20 showed an average increase of brake thermal efficiency (BTE), but lower values of brake specific fuel consumption (BSFC) and brake specific energy consumption (BSEC), when compared to those of CI20. The emission analysis results revealed that all three fuel blends demonstrated significant reductions in CO, HC and smoke emission than those of diesel. In case of NO_x emission, G20 and DCIG20 showed lower values than that of CI20.

INTRODUCTION

Worldwide awareness of the energy crisis in regards of the dwindling of fossil fuel reserves and the heinous environmental effects associated with these fuels have led to the exploration of the alternative energy carriers. Biodiesel and gas-to-liquid (GTL) fuel can be considered as prospective future transportation fuel (1). *Calophyllum Inophyllum* can be regarded as a potential feedstock because of its non-edible origin, higher oil yield than other non-edible feedstocks and the compliance of the biodiesel yield from its crude oil with the US ASTM D6751 and European Union EN 14214 biodiesel standards (2). GTL fuel possesses higher CN, virtually zero sulfur and negligible amounts of aromatic and also demonstrates significantly lower emission than diesel and biodiesel (3, 4). Most of the studies in recent years (1, 5, 6) showed that biodiesel blends with diesel resulted decreasing power, CO, HC and smoke emissions, whereas an increase was observed in fuel consumption and NO_x emissions. The research works in GTL-

diesel blends reported that blending GTL fuel with diesel can certainly improve the fuel properties of the blends, which lead towards better engine performance and exhaust emission than diesel (4, 7). Some recent studies (8, 9) have been reported regarding the combined blends of two alternative fuels with diesel with an aim for further improvement of the fuel properties and engine performance results, but it was only focused within the ternary blends of Palm–jatropha-diesel and palm-coconut-diesel. Analysis of the studies concerning the combined blend of alternative fuels showed that the effect of addition of GTL fuel in this combined blends is still uninvestigated. The objectives of this study are to improve engine performance and emission characteristics, by using a combined blend of non-edible biodiesel (CIBD), GTL fuel and diesel, while comparing to the traditional blends (20% by vol.) of CIBD-diesel and GTL-diesel. This study of the combined blend will ensure the existing emission benefits of biodiesel, along with the improved fuel properties, engine performance-emission parameters of GTL fuel and diesel.

EXPERIMENTAL SET UP AND PROCEDURES

Fuel Blend Preparation and Properties Analysis

In this study, three blends had been prepared as sample fuels. Each binary blend contained 80% diesel and 20% CIBD or GTL fuel, which were designated as CI20 and G20, respectively. The third blend (DCIG20) contained 50% diesel, 30% biodiesel and 20% GTL fuel. While preparing the blends, calculated volumes of diesel and other test fuel were first taken into a sealed magnetic stirrer. Each of the test sample fuel blend was stirred at 4000rpm for 30 minutes. Then the stirred blend was placed in the digital shaker for additional 30 minutes at 400rpm. Finally, the blend sample was removed from the shaker and observed for 12hrs to ensure that no phase separation was occurring.

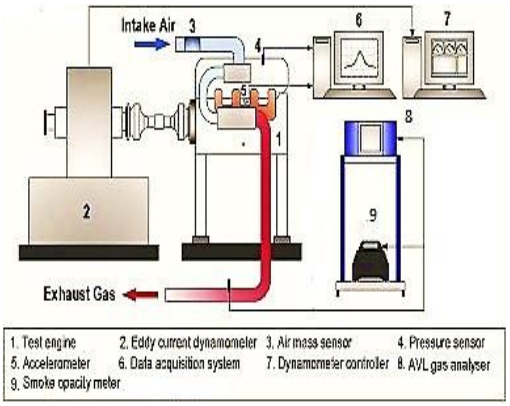

FIGURE 1. Experimental set up

TABLE 1. Engine specification

Engine type	4 Stroke diesel engine
Number of cylinders	4 in-line, longitudinal
Cylinder bore * stroke	91.1 x 95 mm
Displacement	2477 cc
Compression ratio	21:1
Combustion chamber	Swirl type
Rated Power	65 kW at 4200 rpm
Torque	185 Nm, at 2,000 rpm
Valve mechanism	Single overhead camshaft (SOHC)
Injection pressure (kg/cm^2)	157 bar
Aspiration	Turbo charged
Fuel system	Distributor type injection pump
Cooling system	Radiator cooling
Lubrication system	Pressure feed, full flow filtration

Engine Test Rig

A four cylinder, four stroke, water cooled diesel engine was used for experimental investigation. The test rig schematic is depicted in Fig. 1 and the engine specifications are depicted in Table 1. The test engine was directly coupled to Froude-Hoffman AG250 eddy current dynamometer. The initial engine run was performed with diesel before starting the tests with fuel blends. After the test of each sample fuel, the fuel line was purged with diesel to remove that sample and to make it ready for the next sample. In this study, the engine speed was fixed at 2000 rpm, while varying the load percentage (25%, 50%, 75% and 100%). All of the tests were performed under steady-state condition with adequately warmed up exhaust gas and water coolant temperature. To maintain accuracy, each test point was repeated thrice and the mean value was obtained to plot graphs. In addition, each and every test data series (i.e. test point with the same fuel type and at various engine speeds) were recorded on the same day to minimize substantial day-to-day variation in the experimental results. To measure the fuel flow rate, a positive-displacement

type flow meter was installed. For recording the engine test data REO-dCA data acquisition system was incorporated. For exhaust emission analysis, an AVL DICOM 4000 gas analyzer was used to measure the concentration of CO, HC and NO_x. Opacity for smoke measurement was measured with AVL Di-Smoke 4000.

RESULT AND DISCUSSION

Fuel Property Analysis

Table 2 features the fuel properties of the sample fuel blends, which fulfilled the ASTM D7467 specification.

TABLE 2. Physiochemical properties of the sample fuels

Properties	Diesel	CI20	G20	DCIG20
Density Kg/m^3	829.6	840.1	815.8	830.4
Kinematic viscosity at 40°C (mm^2/sec)	3.07	3.85	3.03	3.73
Calorific value	44.46	43.354	45.026	43.475
Cetane number	49	56	65	60
Flash Point (°C)	69.5	76.5	83.5	93.5
CP (°C)	8	8	8	7
PP (°C)	7	4	6	6
Oxidation stability at 110°C , (hr)	59.1	13.55	48.25	37.26

CI20 and DCIG20 demonstrated about 25.4% and 21.5% increased kinetic viscosity than diesel, whereas, G20 showed 1.66% lower values than diesel. Lower kinematic viscosity of fuel ensures less resistance while flows through the fuel system and also leads to better fuel atomization (5). Hence, better combustion efficiency was observed for G20 and DCIG20 than CI20, which ultimately resulted better performance and emission characteristics. G20, CI20 and DCIG20 showed higher flash point about 20.1%, 10.1% and 34.5%, respectively than diesel. In case of the calorific value, CI20 and DCIG20 exhibited about 2.48% and 2.22%, respectively, lower calorific value than diesel, whereas, G20 showed 1.27% higher values than diesel. The higher calorific value of any fuel is desired because it favours the heat release during combustion and improves engine performance (1). DCIG20, CI20 and G20 showed higher CN approximately 22.45% 14.3% and 32.65%, respectively when compared to diesel. The oxidation stability values for DCIG20, CI20 and G20 were 37.26hr, 13.55hr and 48.5hr, respectively. Overall, DCIG20 showed much improvement than CI20. Compared to CI20, DCIG20 showed about 3.12% lower value of viscosity, about 22.22% increased flash point, and about 7.14% higher CN.

Engine Performance Test

Figure 2(a) and 2(b) illustrate the variation of the BSFC and BSEC values of all fuels. On average, CI20 and DCIG20 showed higher BSFC and BSEC values about 5.92% and 3.06%, and about 3.35% and 0.33%, respectively than diesel. Comparing to CI20, DCIG20 showed decreased BSFC and BSEC about 2.71% and 2.94%, respectively. In case of G20, test results revealed approximately 3.7% and 2.92% lower values of BSFC and BSEC than diesel. In this study, the BTE was calculated by equation 1 where η_{bt} is the BTE (%), fc is the BSFC (g/kWh) and H_v is the lower heating value of the fuel (MJ/kg). Figure 2(c) illustrates the variation of the BTE values of all fuel samples. On average, CI20 and DCIG20 showed decreased BTE values about 3.36% and 0.38%, while G20 showed approximately 3.12% increased value, respectively than diesel. Comparing to CI20, DCIG20 showed increased BTE about 3.09%. This trend is also supported by other studies (11, 12). The lower BTE of the other two blends can be ascribed to the combined effect of their lower calorific value and higher kinetic viscosity. The slight improvement of BTE for DCIG20 than CI20 in all test modes can be justified for the presence of GTL fuel in this blend.

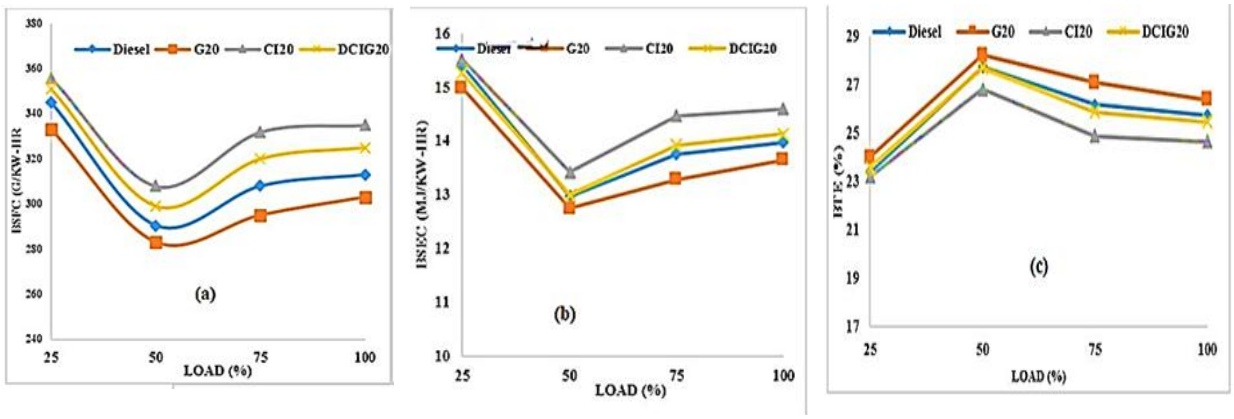

FIGURE 2. Variation of (a) BSFC, (b) BSEC and (c) BTE of all test fuels at 2000 rpm at variable load condition.

Engine Emission Test

Figure 3(a) illustrates the variation of all fuel blends. On average, DCIG20, CI20 and G20 showed decreased CO emission approximately 19.75%, 8.79% and 33.36%, respectively than diesel. When compared to CI20, DCIG20 showed about 12.16% lower CO emission. Improved combustion of G20 attributed to fuel characteristics, like higher hydrogen-carbon ratio, higher CN and very low aromatic content, had contributed to CO reduction. The higher CN of G20 induces shortening of ignition delay that prevents less over-lean zones. Besides, the lower distillation temperature of GTL fuel induces rapid vaporization, which reduces the probability of flame quenching and thus ensures lower CO emission (11, 12). In case of the other two blends, lower CO emissions can be explained by the combined effect of the high oxygen content and higher CN (2). Higher CN results short ignition delay, leading towards better combustion. Moreover, the short ignition delay can also be induced by the longer chain length of biodiesel and thus improves combustion process (10). High oxygen content ensures proper in-cylinder temperature, which also facilitates complete combustion. In case of DCIG20, the combined presence of GTL fuel and CIBD resulted more reduction of CO emission than diesel and CI20.

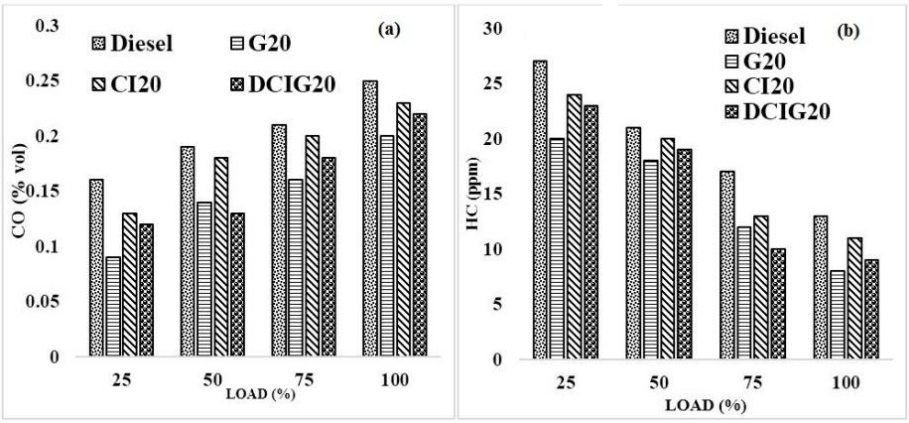

FIGURE 3. Variation of (a) CO emission and (b) HC emission of all test fuels at 2000 rpm at variable load condition.

Figure 3(b) illustrates the variation of the HC emission values of all test fuels. On average, DCIG20, CI20 and G20 showed decreased HC emission approximately 21.81%, 12.82% and 25.64%, respectively than diesel. When compared to CI20, DCIG20 showed about 10.29% lower HC emission. Alike CO emission, reduction of HC emission can be explained regarding the fuel properties and combustion phenomena of GTL fuel. Figure 4(a) presents the variation of the emission values of all fuel blends. On average, DCIG20 and CI20 showed increased NO_x emission

values about 1.62% and 3.11%, respectively than diesel. In case of G20, test results revealed approximately 7.74% decreased values than diesel. When compared to CI20, DCIG20 showed about 1.35% lower NO_x emission. The higher CN of G20 induced shorter ignition delay, followed by a lesser premixed charge, which resulted the lower combustion temperature and pressure (11, 12). It leads towards less thermal NO_x formation. Significant lower aromatic contents of GTL fuel also influenced G20, which prompted to maintain a lower local adiabatic flame temperature and thus assists in NO_x reduction. In case of the other two blends, higher NO_x was observed in all test modes because of their high oxygen content and a higher "premixed part" during combustion, where NO_x is primarily formed (1). For DCIG20, the presence of GTL fuel in this combined blend resulted additional reduction of NO_x content in exhaust emission than CI20.

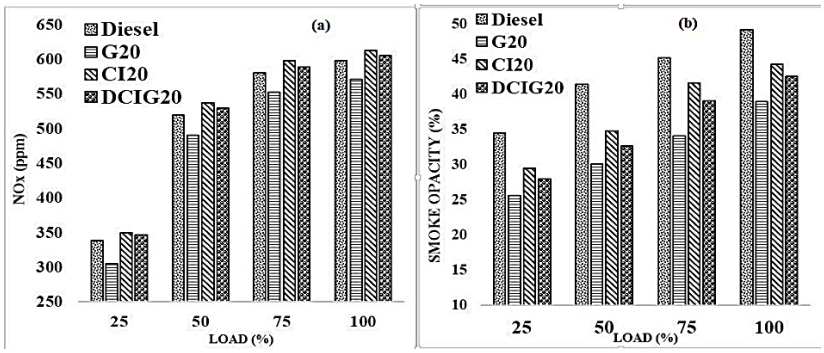

FIGURE 4. Variation of (a) NOx emission and (b) Smoke emission of all test fuels at 2000 rpm at variable load condition.

Figure 4(b) illustrates the variation of the smoke emission values of all test fuels. On average, DCIG20, CI20 and G20 showed decreased smoke emission approximately 16.57%, 11.86% and 19.4%, respectively than diesel. When compared to CI20, DCIG20 showed about 5.35% lower smoke emission. This reduction in smoke emissions in G20, which is in accordance with that observed in the literature (11, 12), can be illustrated by the combined effect of the absence of aromatics (regarded as soot predecessors), low sulphur content and higher hydrogen to carbon ratio of GTL fuel. Regarding the reduction of the other two blends, the higher oxygen content associated with lower sulphur content and impurities can be attributed to such diminution of smoke emission (1). For DCIG20, the incorporation of GTL fuel and CIBD with diesel, demonstrated additional reduction of smoke emission than diesel and CI20.

CONCLUSION

Among all the test fuels, G20 showed the best fuel properties with lower density and kinematic viscosity, but higher calorific values and cetane number, which showed their effects in engine performance and emission. DCIG20 showed improved properties than CI20. G20 showed higher BTE about 3.12%, whereas, lower BSFC and BSEC about 3.7% and 2.92%, respectively, than that of diesel. DCIG20 and CI20 demonstrated higher BSFC about 3.06% and 5.92%; higher BSEC about 0.33% and 3.35%, whereas, lower BTE about 0.38% and 3.36%, respectively than those of diesel. Compared to CI20, DCIG20 showed improvement of BTE, BSFC and BSEC about 3.09%, 2.71% and 2.94%, respectively. On average, G20 showed reduction in CO, HC, NO_x and smoke emission approximately 33.36%, 25.64%, 7.74% and 19.4%, respectively, compared to diesel. On average, DCIG20 and CI20 demonstrated higher NO_x about 1.62% and 3.11%, whereas lower CO about 19.75% and 8.79%; HC about 21.81% and 12.82%; smoke about 16.57% and 11.86%, respectively than those of diesel. Compared to CI20, DCIG20 showed an average reduction in CO, HC, NO_x and smoke emissions about 12.16%, 10.29%, 1.35% and 5.35%, respectively.

ACKNOWLEDGEMENT

The authors would like to appreciate University of Malaya for financial support through High Impact Research grant titled: "Clean Diesel Technology for Military and Civilian Transport Vehicles" having grant number UM.C/HIR/MOHE/ENG/07.

REFERENCES

1. Sajjad H, Masjuki HH, Varman M, Kalam MA, Arbab MI, Imtenan S, et al. Engine combustion, performance and emission characteristics of gas to liquid (GTL) fuels and its blends with diesel and bio-diesel. Renewable and Sustainable Energy Reviews. 2014;30(0):961-86.

2. Sajjad H, Masjuki HH, Varman M, Kalam MA, Arbab MI, Imtenan S, et al. Influence of gas-to-liquid (GTL) fuel in the blends of Calophyllum inophyllum biodiesel and diesel: An analysis of combustion–performance–emission characteristics. Energy Convers Manage. 2015;97(0):42-52.

3. Hossain S, Masjuki H, Varman M, Kalam MA, Rahman SA. Comparative Evaluation of the blends of Gas-to-liquid (GTL) fuels and biodiesel with diesel at high idling conditions: An analysis on engine performance and environment pollutants. RSC Advances. 2015.

4. Sajjad H, Masjuki H, Varman M, Khan MMR, Arbab M, Imtenan S, et al. Comparative Study of Biodiesel, GTL Fuel and Their Blends in Context of Engine Performance and Exhaust Emission. Procedia Engineering. 2014;90:466-71.

5. Arbab MI, Masjuki HH, Varman M, Kalam MA, Imtenan S, Sajjad H. Fuel properties, engine performance and emission characteristic of common biodiesels as a renewable and sustainable source of fuel. Renewable and Sustainable Energy Reviews. 2013;22(0):133-47.

6. Arbab M, Masjuki H, Varman M, Kalam MA, Sajjad H, Imtenan S. Performance and emission characteristics of a diesel engine fueled by optimum biodiesel-biodiesel blend. RSC Advances. 2014.

7. Sajjad H, Masjuki H, Varman M, Kalam M, Arbab M, Imtenan S, et al. Comparative study of gas-to-liquid fuel, B5 diesel and their blends with respect to fuel properties, engine performance and exhaust emissions. RSC Advances. 2014;4(84):44529-36.

8. Sanjid A, Masjuki H, Kalam M, Rahman S, Abedin M, Palash S. Production of palm and jatropha based biodiesel and investigation of palm-jatropha combined blend properties, performance, exhaust emission and noise in an unmodified diesel engine. Journal of Cleaner Production. 2014;65:295-303.

9. Habibullah M, Masjuki H, Kalam M, Fattah IR, Ashraful A, Mobarak H. Biodiesel production and performance evaluation of coconut, palm and their combined blend with diesel in a single-cylinder diesel engine. Energy Convers Manage. 2014;87:250-7.
10. Sajjad H, Masjuki H, Varman M, Kalam M, Arbab M, Imtenan S, et al. Influence of gas-to-liquid (GTL) fuel in the combined blend of Jatropha biodiesel and diesel: an analysis of engine combustion–performance–emission parameters. RSC Advances. 2015;5(38):29723-33.

11. Yongcheng H, Longbao Z, Shangxue W, Shenghua L. Study on the performance and emissions of a compression ignition engine fuelled with Fischer-Tropsch diesel fuel. Proc Inst Mech Eng Pt D: J Automobile Eng. 2006;220(6):827-35.

12. Wu T, Huang Z, Zhang W-g, Fang J-h, Yin Q. Physical and Chemical Properties of GTL−Diesel Fuel Blends and Their Effects on Performance and Emissions of a Multicylinder DI Compression Ignition Engine. Energy Fuels. 2007;21(4):1908-14.

ICME2015

International Conference on Mechanical Engineering 2015
(ICME 2015) 18 – 20 December, 2015, Dhaka, Bangladesh

Paper ID : 220

Investigations on S-bladed Axial Flow Fan for Cooling Bi-directional Electric Motors

Kulkarni Vikram Ashok[1, a)] and M. Govardhan[1, b)]

[1]*Dept. of Mechanical Engg., Indian Institute of Technology, Madras, Chennai 600036, India*

[b)] Corresponding author: gova@iitm.ac.in
[a)] vikram.kulkarni30@gmail.com

Abstract. Use of axial fans for motor cooling is very good alternative as they have less bending losses compared to centrifugal fans. But standard axial fans lack bidirectional operation because of aerofoils used. In current investigation, an axial fan using S-shape blades is studied for suitability in motor cooling. Performance of S-bladed axial fan is analyzed for motor cooling at various mass flow rates for inlet velocities ranging from 10 m/s to 45 m/s at rotational speeds of 1000 and 2000 rpm for forward operation and at 3000 rpm for both forward and reverse operation. After thorough analysis of S-shape blade axial fan in both isolated and motor coupled operation, it is concluded that S-shape axial fan can be good choice for electric motor cooling in bidirectional operation.

INTRODUCTION

Today electrical drives are extensively used as prime movers because of their ease of availability, variety of options and easy operation and maintenance. Stator losses, rotor losses, core and windage losses are main source of heat generation in motor. Majority of motors use air as cooling fluid. With the increase in speed of cooling air flowing through the windings, rotor and stator; the overtemperatures in various components of motor could be reduced. With better cooling techniques for motors, we can go for higher capacities within same size and volumes. This will increase power to weight ratio of electrical motors.

Many motors use centrifugal fans mounted on shaft to supply air. For special requirement of bidirectional operation, impellers with straight blades i.e. both $\beta_1 = \beta_2 = 90°$ are used. They are highly inefficient because of high incidence losses but are used for their bidirectional capability. It gives us scope for improvement in design of cooling fan impeller in electric motors. Though axial fan produces higher velocities and mass flow rate compared to centrifugal fans, they are unsuitable to run in both directions.

A special type of aerofoil named as 'S' type is employed in pumps which alternate as turbine when rotated in opposite direction. But to the best of our knowledge, 'S' type blading has not been employed in electric motor and successful attempt may pave way for efficient cooling of high capacity motors. In this study, an axial flow fan with double cambered S-shape blades has been proposed instead of conventional centrifugal fan. Casacci and Chapus [1] first reported use of blades with S-shape for reversible use in tidal power plants in France. Experiments carried by Ravindran et.al [2] showed that symmetrical S-blades were most suitable for reversible applications. Very few investigators who have dealt with S-blades studies lift-drag ratios, rounding of leading and trailing edges, thickness distribution and incidence effects (Ramchandran et al. [3], Madhusudan [4], Baby Chako et. al. [5], Premkumar et. al. [6]). Till date, very little work has been done on design of actual machine consisting of S-blades for an application, in particular electric motor cooling, which needs reversible operation. Performance study of a reversible axial turbomachine with the use of S-shape blades is still has long a way to go and it will be a great outcome if we succeed

to have an efficient reversible machine with S-blades. Hence, the objective of the investigation is to study performance of S-bladed axial fan coupled to motor in forward and reverse operation.

PROPOSED SETUP

Since the cooling of higher capacity motors is very difficult due to large amount of heat generation, a 3-phase induction motor with rated power output of 200 kW at 3000 rpm is selected. Motor component dimensions are obtained from NEMA specifications and Electrical Machine Design Data book. Dimensions of fan are calculated keeping restrictions posed by motor size in mind using iterative methods. From the results of study by Madhusudan [4], S3525 profile has been chosen for axial fan blades due to its better performance over other geometries.

NUMERICAL METHODOLOGY

Grid Generation and Computational Domain

Computational domain for fan and motor combined system is shown in Fig.1. Grid is created in Ansys Turbogrid 14.5 with for study of isolated fan. The mesh with 639460 number of elements and first layer height above blade surfaces and hub-shroud surface equal to 0.003 mm is used. This number is obtained after conducting grid independent study shown in Fig. 2(a). ANSYS CFX 14.5 solver is used. Inlet total pressure depending upon inlet velocity and exit mass flow rate corresponding to inlet velocity are defined as boundary conditions. Solid walls are defined as no slip walls particularly giving counter rotation to shroud wall. Rotational periodic interface has been used on periodic walls of flow passage. After computational analysis of fan, combined system consisting of S-bladed fan and electric motor has been studied for its performance. Hexahedral grid is made for flow passage through motor components with 1813467 number of elements. Same boundary conditions are applied as that of isolated fan. Motor rotor wall has been given angular velocity same as that of fan. Surface roughness has been defined on rotor and stator surfaces of motor to 100 micron to account for surface irregularities caused due to windings.

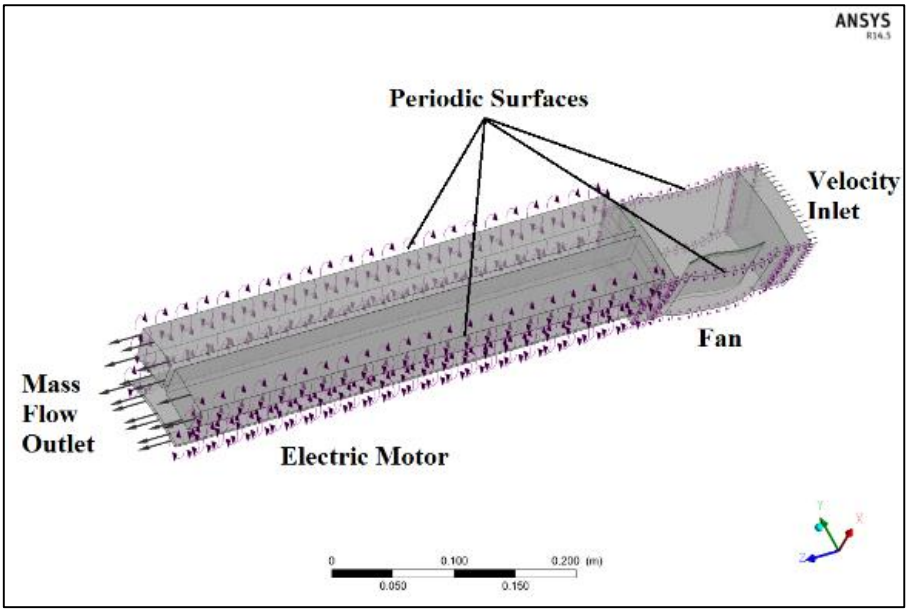

FIGURE 1. Computational domain for fan and motor system

Validation of Computational Results

Comparison of experimental value of pressure coefficient (Ramachandran[3]) to that obtained by computational analysis is shown in Fig.2 (b). Computational results are in good agreement with experimental values. There is little variation between two since exact boundary conditions i.e. inlet velocity is not known and turbulence level can't be predicted.

RESULTS AND DISCUSSION

Different performance parameters used for analysis have been defined as below.

$$\eta = \frac{\rho Q W}{P_{in}} ;\ \gamma = \frac{P}{\frac{\rho}{2} A_0 U_m^3} ;\ C_p = \frac{p - p_{atm}}{\frac{\rho}{2} U_m^2} ;\ \Phi = \frac{C_m}{U_m} \quad (1)$$

where W is fluid specific work, Q is volume flow rate, P_{in} is power input, A_0 flow exit area, U_m is mean blade speed, C_m is meridional velocity. ϕ is flow coefficient, γ is power coefficient and η is efficiency.

After studying the performance of the isolated fan, the S-bladed fan with 16 numbers of blades was selected and complete assembly consisting fan mounted on motor shaft was created. Performance analysis of the fan and motor system is done for several mass flow rates at speed of 3000 rpm in both forward and reverse direction. Performance curves show similar trends in both forward and reverse direction but values are different with some margin. When the fan is operated in forward direction, the air enters the fan from the atmosphere and flows over the motor cooling passage before it exits to the atmosphere. In the reverse direction, the flow passes over the cooling passages before it enters the fan. In this operation, the flow becomes non-uniform and turbulent, hence, the efficiency will be less and will consume more power for most of its operation. It can be observed from Fig. 3a that for isolated fan operation, efficiency is almost constant irrespective of flow coefficient but when fan is coupled with motor, efficiency increases with mass flow rates. Fig. 3b shows that power consumption for system is more compared to isolated fan operation because of more frictional losses. In reverse operation, flow inlet is quite far from fan suction side requiring more power input. But in reverse mode, since suction pressure is lower compared to forward mode, pressure ratio is higher as shown in Fig. 4(a). For both forward and reverse modes, hub to shroud pressure variation is negligible and tendency of separation is also less compared to isolated fan operation which can be seen by negative pressure coefficient in only fan operation in Fig. 4(b).

Figures 5(a) to 5(c) show the variation of static pressure on the blade suction surface (along the blade x-axis) and along blade span (y-axis) for various mass flow rates and various rotational speeds. From Fig.5, it can be seen that as mass flow rate through the S-shape bladed axial fan increases, static pressure on the blade surface has more variation from inlet to outlet compared to lower mass flow rates. The highest local pressure can be observed at inlet section at the tip of the blade while low pressure region is observed at outlet section near blade hub area. Pressure at the mid chord of the blade is almost similar irrespective of flow rate through the fan.

When pressure variation on blade surface for different rotational speeds is compared, Fig.6 shows higher pressure variation from inlet to outlet with increase in rpm. At higher rotational speeds, high pressure zone is seen at shroud tip near inlet section and low pressure zone is observed near hub at outlet section.

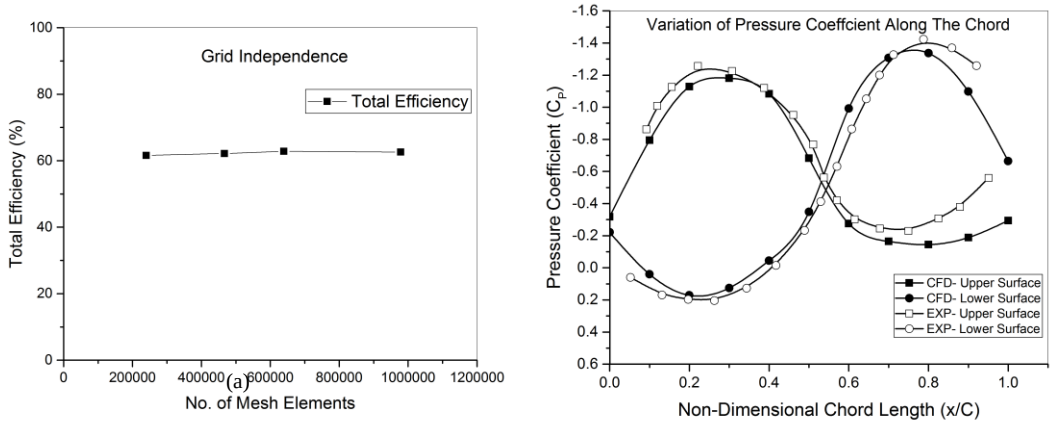

(a) (b)

FIGURE 2. (a) Validation with experimental results; (b) Grid independence study

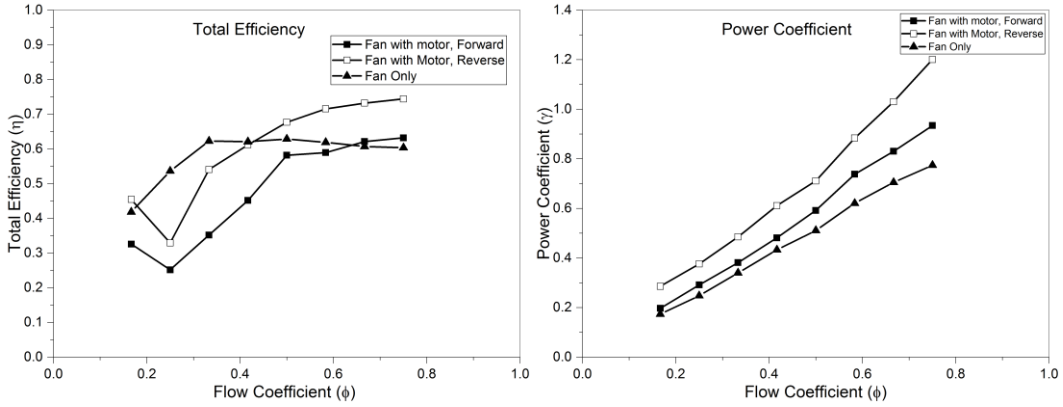

(a) (b)

FIGURE 3. (a) Variation of total efficiency with flow coefficient; (b) Variation of power coefficient with flow coefficient

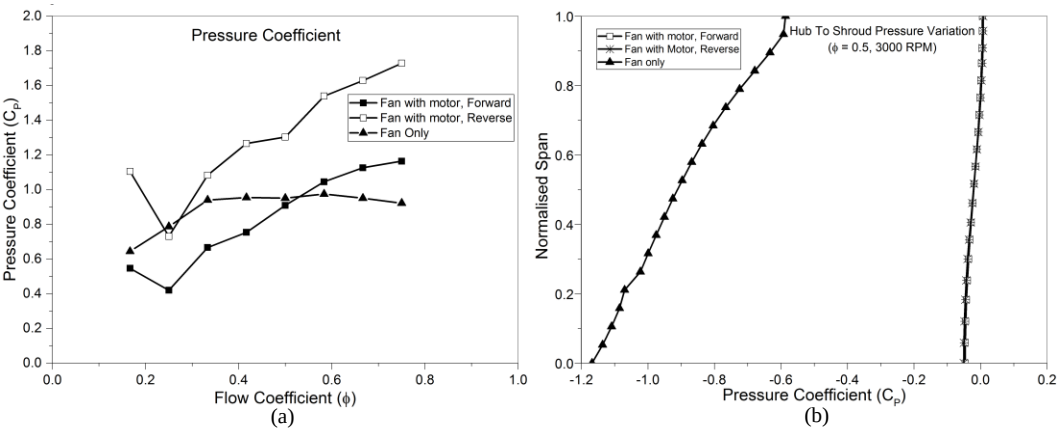

(a) (b)

FIGURE 4. (a) Variation of pressure coefficient with flow coefficient; (b) Hub to shroud pressure coefficient variation for Φ=0.5 for 3000 rpm

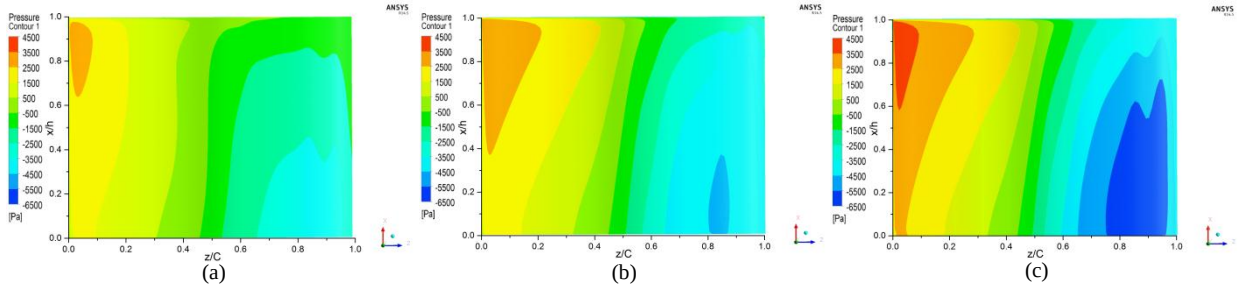

FIGURE 5. Variation of gauge pressure on blade suction surface at (a) Φ =0.25; (b) Φ =0.5; (c) Φ=0.75

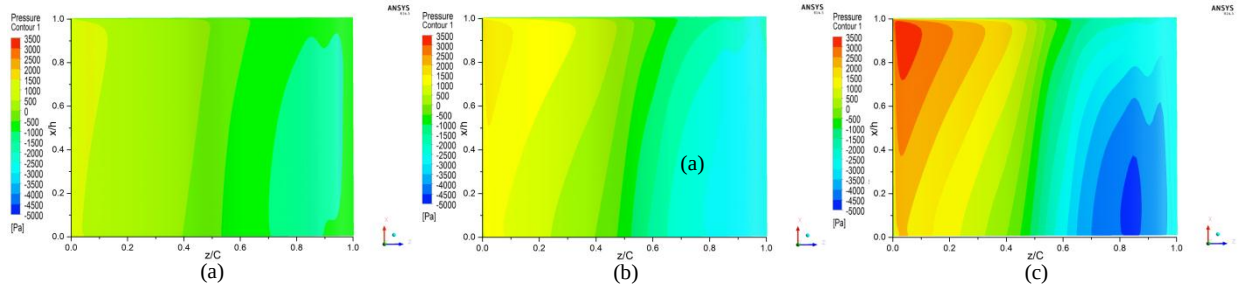

FIGURE 6. Variation of gauge pressure on blade suction surface at (a) 1000 rpm; (b) 2000 rpm; (c) 3000 rpm

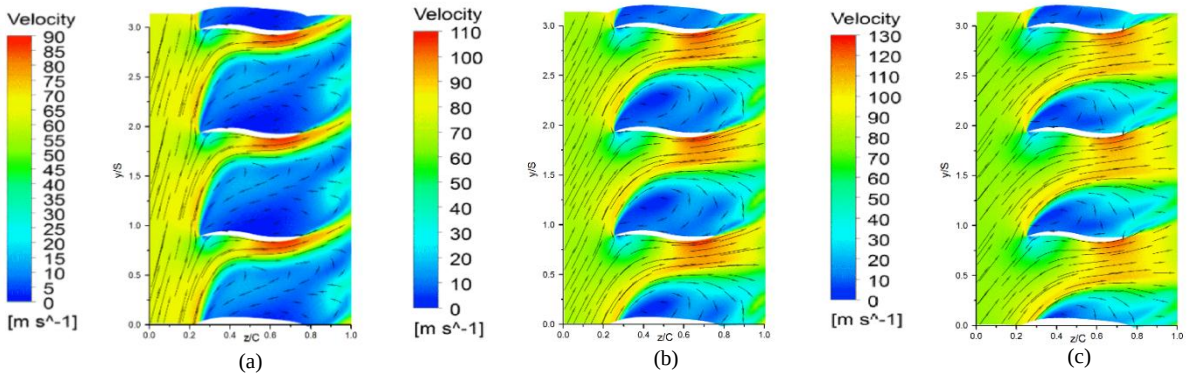

FIGURE 7. Velocity streamlines coloured with velocity at 3000 rpm for (a) Φ =0.25; (b) Φ =0.5; (c) Φ=0.75

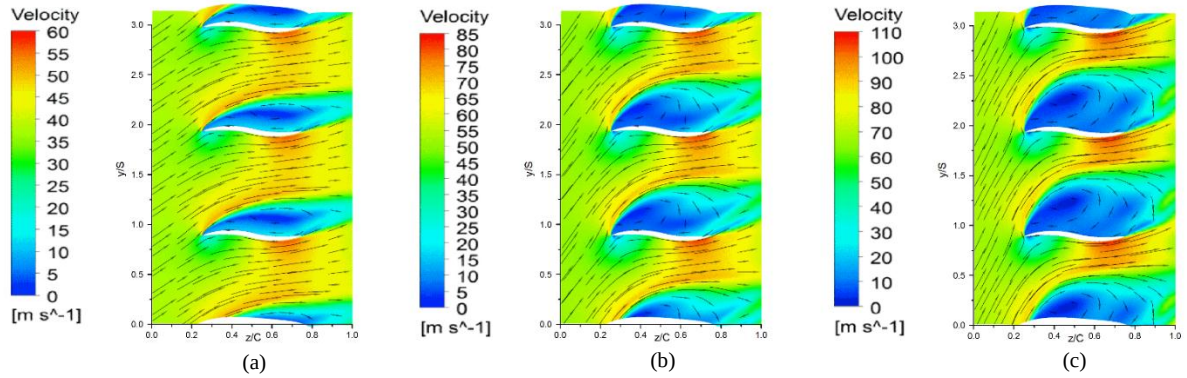

FIGURE 8. Velocity streamlines coloured with velocity for Φ =0.5 at (a) 1000 rpm; (b)2000 rpm; (c) 3000 rpm

Velocity vectors through the fan to study the flow patterns are shown in Figs.7-8. From Fig.7, it is observed that for same rotational speed, the tendency of flow separation reduces as mass flow rate through the fan increases. Highly separated flow can be observed at very low mass flow rates. Running the fan at lower mass rates at higher speeds is not viable. Velocity vectors shown in Fig.8 clearly suggest that at lower rotational speeds, chances of flow separation are less than that at higher speeds for same mass flow rates. From Fig.7 and 8, it can also be stated that the mass flow rate at which flow separation starts reducing is higher for higher rotational speeds. The separated region for $\phi = 0.50$ is quite less at 1000 rpm than it is for $\phi = 0.75$ at 3000 rpm. So running machine at higher mass flow rates for higher rotational speeds can lead to well guided flow.

CONCLUSIONS

1. S-shape bladed fan gives very good performance repeatability in both forward and reverse rotation at design speed.
2. Fan shows flat characteristic over wide flow rate curves at 3000 rpm for which it has been designed. It gives wider operating range for fan with good efficiency. Modifications can be done in design stage itself to make it suitable for other rotational speeds also.
3. Operating fan at higher mass flow rates and higher rpm is best suitable combination from performance point of view.
4. Performance of fan is consistent with very little differences when operated in combination with motor in both forward as well as reverse rotations. Thus the fan is suitable for desired application.

REFERENCES

1. S. X. Casacci and E. E. Chapus, ASME Fluids Engg., (1964).
2. M. Ravindran, and H. C. Radha Krishna. "Influence of blade profiles on the performance of fully reversible axial pump-turbine." Proceedings of the 6th Conference on Fluid Machinery, Budapest, Hungary. 1979.
3. R. M. Ramchandran, H. C. Radha Krishna, and P. A. A. Narayana, Energy Engineering **1**, 37–50 (1986).
4. R. S. Madhusudan, "Flow studies of S-blade for fully reversible axial pump turbine," Ph.D. thesis, Indian Institute of Technology, Madras, 1993.
5. B. Chacko, V. Balabaskaran, E. G. Tulapurkara, and P. A. Aswathanarayana, Energy Engineering, 164–179 (1992).
6. T. M. Premkumar and D. Chatterjee, Renewable Energy **77**, 240–249 (2015).

ICME2015

International Conference on Mechanical Engineering 2015
(ICME 2015) 18 – 20 December, 2015, Dhaka, Bangladesh

Paper ID : 226

Utilization of the waste soles as an energy source through the thermal pyrolysis

Md. Abul Hashem[1, a)], Adhir Chandra Paul[1], Sanzu Hosen[1] and Abir Hasan[1]

[1]*Department of Leather Engineering, Khulna Univerity of Engineering & Technology (KUET), Khulna-9203, Bangladesh*

[a)]Corresponding author: mahashem@mail.kuet.ac.bd

Abstract. Management of industrial process residue has become a great challenge. Disposing of waste thermoplastic rubber (TPR) and poly vinyl chloride (PVC) soles of human used footwear as well as production waste from the footwear industries is a big concern due to its non-biodegradability. In this work, waste thermoplastic rubber (TPR) and poly vinyl chloride (PVC) soles were used as an energy source through the fixed-bed fire-tube heating pyrolysis to reduce the pollution load. The experiments were performed at varying temperature within the range of 2500C to 4500C at every 1000C interval for each case. In pyrolysis, three types of products, e.g. oil, char and gas were obtained from the both TPR and PVC soles. It was observed that with the increasing temperature, percentage of oil was increased from the both the soles. Conversely increasing the temperature, the percentage of char was decreased. The obtained oil was crude in nature which could be used as diesel or gasoline after the proper purification. Noticeably at the same condition TPR soles were produced 12.3% more oil than PVC sole.

INTRODUCTION

Management of industrial process residue has become a great challenge. Disposing of waste thermoplastic rubber (TPR) and poly vinyl chloride (PVC) soles of human used footwear as well as production waste from the footwear industries is a big concern due to its non-biodegradability. In this work, waste thermoplastic rubber (TPR) and poly vinyl chloride (PVC) soles were used as an energy source through the fixed-bed fire-tube heating pyrolysis to reduce the pollution load. The experiments were performed at varying temperature within the range of 2500C to 4500C at every 1000C interval for each case. In pyrolysis, three types of products, e.g. oil, char and gas were obtained from the both TPR and PVC soles. It was observed that with the increasing temperature, percentage of oil was increased from the both the soles. Conversely increasing the temperature, the percentage of char was decreased. The obtained oil was crude in nature which could be used as diesel or gasoline after the proper purification. Noticeably at the same condition TPR soles were produced 12.3% more oil than PVC sole.

Footwear is one of the most important sectors in Bangladesh. Footwear is the wearing apparel for the foot with basic two parts: i) upper part and ii) bottom (sole) part. In most cases the upper part is leather, synthetic and canvas. On the other hand, bottom part (sole) is composed of thermoplastic rubber (TPR), poly vinyl chloride (PVC), ethyl vinyl acetate (EVA), vulcanized rubber (VR), leather etc. In Bangladesh most of the footwear industries are using poly vinyl chloride (PVC) and thermoplastic rubber (TPR) as sole for the footwear production.

Whatever the soles (TPR, PVC, EVA, VR, Leather, etc.) are used in the footwear production after a certain period user indiscriminately discard it as waste. Disposal of organic wastes (tire, sole) from the anthropogenic activity is a growing environmental issue for the modern society, especially in developing country due to its non-biodegradability. In the recent year, footwear industries in Bangladesh are increasing day by day and disposal of waste organic soles (PVC, TPR, etc.) are also increased. Open air dumping of tires, soles may act as the best breeding grounds for disease carrying mosquitoes with the aid of rain water [2]. It is reported that vinyl is the major source of dioxin [3]. Landfill

is the most common ways of disposal of waste soles. But the disposal of landfilling is not viable due to its non-biodegradability. During life span, PVC form organochlorines and emits hazardous substance which is harmful to the environment [4].

To survive the industrial sector waste generation, disposal and minimization have become a great challenge. Cleaner production is the prime need for the forthcoming generation for good health. Increasing population concurrently raising environmental awareness means that waste treatment and disposal practices of past are no longer acceptable. It is reported that every year waste generation per capita is increasing [5]; simultaneously energy consumption is also increased with the limited fossil fuel.

Now-a-days energy crisis is increasing. Renewable energy should be widely investigated in order to renovate energy sources to keep sustainable development. Conversion of waste to energy (WTE) is an important strategy of waste treatment. The method could lead to sanitize the disposal of waste. Pyrolysis is an attractive method of recycling the organic waste, i.e. recycling of tires [2]. Since the soling materials of PVC and TPR are non-biodegradable because it cannot easily return to natural carbon cycle, hence life cycle of soling materials end at the waste disposal facilities [6].

In pyrolysis thermo-chemical process involves the heating of organic waste material at higher temperature in the absence of oxygen to break down them down to simpler organic compounds. Carbon, solid char, oil and gas are produced in the pyrolysis of organic solid wastes [7]. The solid char is carbonaceous materials which be used for the production of activated carbon [8, 9].

In the last few decades various pyrolysis processes have been carried for the rickshaw/ bicycle tires [10–12]. Among the pyrolysis processes, fixed-bed fire-tube heating pyrolysis has been successfully studied by Islam et al. [13] for the rickshaw/bicycle tires. So far, no report has been published for the pyrolysis of the waste TPR or PVC soles. The TPR compounds are articulated by styrene-butadine-styrene (SBS) or styrene-ethylene/butadiene-styrene (SEBS) block copolymers. The chemical composition of SBS and PVC is show in the Fig. 1.

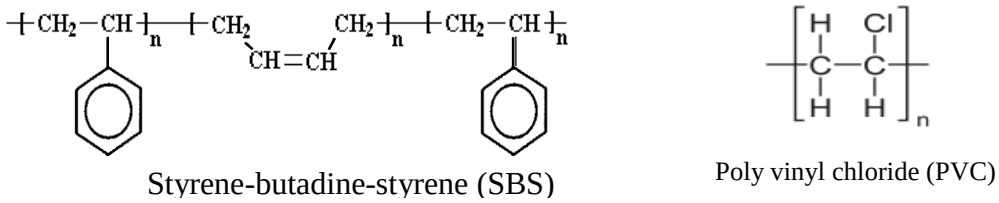

FIGURE 1. Chemical compositions of the SBS and PVC

In this work, waste thermoplastic rubber (TPR) and poly vinyl chloride (PVC) soles were used as an energy source through the fixed-bed fire-tube heating pyrolysis to reduce the pollution load. The benefit of thermal treatment is the reduction of volume of the waste soles over common landfilling.

MATERIALS AND METHODS

Sampling

The waste TPR and PVC soles were collected from a footwear industry, Amar Ekushey Hall, Khulna University of Engineering & Technology as well as a nearby local area of Khulna city, Bangladesh.

Sample preparation

The soles were detached from the upper parts, washed with water to remove dirt, mud, sand and finally the soles were dried in the sun. Then the sun dried soles were cut with a knife into small pieces to facilitate to put into the reactor.

Experimental Set-up

The experimental set-up is shown in Fig. 2. Batch wise fixed-bed fire-tube pyrolysis heating was selected for the experiment. The reactor was made of mild steel (MS) sheet having a dimension of 40 cm L. × 16.0 cm o. d. × 14.25 cm i. d.). Reactor's one side was closed and other side was connected with the flanges which was connected to the electric heater properly by sealed with the high temperature resistance gasket.

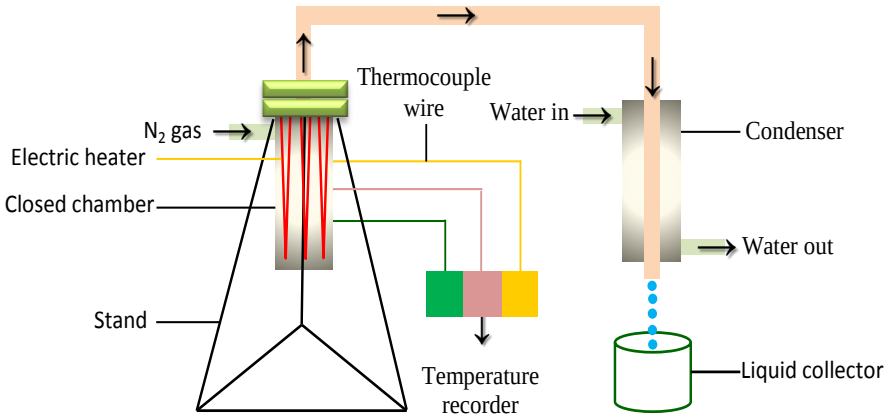

FIGURE 2. Experimental set-up for the thermal pyrolysis

The closed chamber and pipe line were insulated to prevent te loss ofheat. A copper pipe having inner diameter of 0.5 mm was used as a condenser which was wrapped with the foam board to aid the process of condensation of the vapor. Nitrogen (N_2) gas was supplied from a cylinder to make the chamber anaerobic condition. A pressure regulator and N_2 a gas flow meter were used to control the required gas flow rate in the chamber. A thermocouple wire was used in the system which one end was inserted into the chamber and the other end was connected to the temperature recorder to record the temperature.

Methods

The experiments were conducted separately for the TPR and PVC soles. About 1.3 kg waste sole of TPR/PVC sample was taken in the reactor. The pyrolysis process was carried out in the reactor at various temperature ranges from 250°C to 450°C. Before starting the experiment nitrogen (N_2) gas was purged to the reactor making the system anaerobic. The reactor heater was switched on and the temperature of the reactor was allowed to rise to a desire temperature. The experiment was conducted at 250°C, 350°C and 450°C temperature. The thermocouple sensors were placed in the reactor chamber to record the temperature, which was connected to a digital recorder. At the same time, the temperature was controlled by a temperature controller. During the pyrolysis, nitrogen gas was supplied in order to maintain an inert atmosphere in the reactor and also to sweep away the pyrolysis vapor product to the condenser. The vapor from the reactor was condensed by the water condenser and non-condensable gas was vented to the atmosphere. The condensed oil was collected from the outlet of the condenser in a measuring cylinder and weighted. After cooling the reactor, remaining residue was collected and weighted.

Data obtained in the experiment

The TPR and PVC waste soles were separately used for the batch experiment. In each batch about 1.3 kg waste sole was taken in the reactor chamber. The experiments were performed by varying temperature within the range of 250^0C to 450^0C at every 100^0C interval for each case. The experimental conditions and obtained products are shown in the Table 1 and Table 2.

Table 1. Experimental conditions and obtained data for the TPR sole						
No.	TPR sole wt. (kg)	Temp. (^{0}C)	Obtained Products (kg)			Residence Time (min)
			Oil	Char	Gas	
01	1.3	250	0.10	1.14	0.06	50
02	1.3	350	0.25	0.90	0.15	40
03	1.3	450	0.30	0.75	0.25	28

Table 2. Experimental conditions and obtained data for the PVC sole						
No.	PVC sole wt. (kg)	Temp. (^{0}C)	Obtained Products (kg)			Residence Time (min)
			Oil	Char	Gas	
01	1.3	250	0.07	1.18	0.05	45
02	1.3	350	0.12	0.95	0.23	33
03	1.3	450	0.14	0.80	0.36	27

RESULTS AND DISCUSSION

Yield of products

The percentage of the yield of products from the TPR and PVC waste soles are inserted in Fig. 3

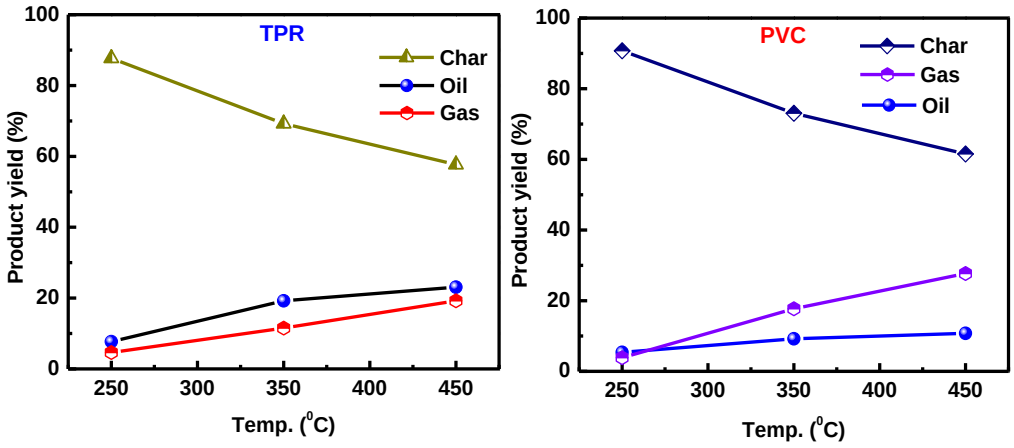

FIGURE 3. Effect of temperature in the pyrolysis process

The TPR and PVC waste soles were used in the pyrolysis. The process was carried out in the temperature range of 250^{0}C to 450^{0}C at interval of 100^{0}C. Three types of products were obtained: oil, char and gas. At the same condition, percentages of yield of the products were varied for the TPR and PVC soles.

Effect of temperature in the pyrolysis

It is clear from the Fig. 3 that in the pyrolysis, significantly temperature was effect on to produce the new products. With increasing the temperature in the pyrolysis, the main yield of products (oil and char) was also increased. In case of TPR sole, at 350°C oil and char were 19.2% and 69.2%, whereas at 450°C oil and char were 23.1% and 57.7%. In case of PVC waste sole, at 350°C oil and char were 9.2% and 73.1%, whereas at 450°C oil and char were 10.8% and 61.5%. It was observed that at 350°C and 450°C temperature TPR was produced oil twice than PVC waste sole. The

probable reason is that in the pyrolysis, the TPR articulated compounds (Fig. 1) were breaking them down into simpler liquid organic compounds. On the other hand, in the pyrolysis of PVC sole was produced more chlorine gas rather than the liquid organic compounds. It was noticed that with an increasing temperature the product of oil was increased from the both soles.

Effect of residence time in the pyrolysis

The effect of residence time on the yield of products is shown in the Fig. 4. It is obvious that at low temperature, more residence time was required to complete the conversion resulting incomplete decomposition of waste soles which produces more char and the least amount of oil. On the other hand, higher the temperature with less residence time was required to complete the conversion of waste soles resulting produces more oil. It could be concluded that higher the temperature with less residence time was suitable to convert the long polymer chain to break them down into smaller organic compounds.

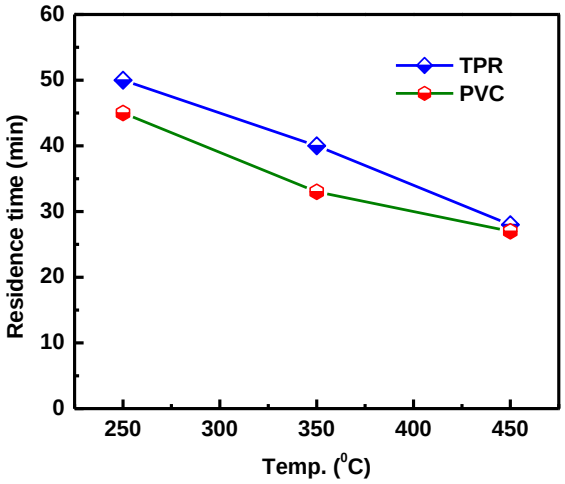

FIGURE 4. Effect of residence time and thermal temperature

CONCLUSION

The thermal decomposition of TPR and PVC soles under anaerobic conditions were produced oil, char and gas. With an increasing the temperature from 250^{0}C to 450^{0}C yield of products oil and gas was increased but with increasing the temperature char was decreased. The obtained oil was crude in nature, which could be used as a diesel or gasoline after proper purification. The TPR sole was provided more effective result than the PVC sole. The process could be optimized in the large scale, which will offer advantages to reduce the environmental impact as well as production of new product from the waste soles.

REFERENCES

[1] A. Isler, S. Sundu, M. Tuter, F. Karaosmanoglu, Transesterification reaction of the fat originated from solid waste of the leather industry, Waste Management 30 (2010) 2631–2635.

[2] M.R. Islam, M.U.H. Joardder, S.M. Hasan, K. Takai, H. Haniu, H, Feasibility study for thermal treatment of solid tire wastes in Bangladesh by using pyrolysis technology, Waste Management 31 (2011) 2142–2149.

[3] J. Thornton, Environmental Impacts of Polyvinyl Chloride Building Materials, A Healthy Building Network Report, Washington, D.C. The United States, 2002.

[4] http://www.bathenclosures.org/press/Fact%20Sheets/Environment/Important%20PVC%20Facts.pdf
[5] A. Tabasová, J. Kropác, V. Kermes, A. Nemet, P. Stehlík, Waste-to-energy technologies: Impact on environment, Energy 44 (2012) 146–155.
[6] G. Luo, T. Suto, S. Yasu, K. Kato, Catalytic degradation of high density polyethylene and polypropylene into liquid fuel in a powder-particle fluidized bed, Polymer Degradation and Stability 70 (2000) 97–102.
[7] A. C. Lloyd, Technology Evaluation and Economic Analysis of Waste Tyre Pyrolysis, Gasification, and Liquefaction, Ph.D. Secretary, California Environmental Protection, 2006.
[8] J. F. Gonzalez, S. Roman, J. M. Encinar, G. Martinez, Pyrolysis of various biomass residues and char utilization for the production of activated carbons, Journal of Analytical and Applied Pyrolysis 85 (2009) 134–141.
[9] M. M. Barbooti, T. J. Mohamed, A. A. Hussain, F. O. Abas, Optimization of pyrolysis conditions of scrap tires under inert gas atmosphere, Journal of Analytical and Applied Pyrolysis 72 (2004) 165–170.
[10] S.-Q. Li, Q. Yao, Y. Chi, J.-H. Yan, K.-F. Cen, Pilot-Scale Pyrolysis of Scrap Tires in a Continuous Rotary Kiln, Industrial & Engineering Chemistry Research 43 (2004) 5133–5145.
[11] M. R. Islam, M. Parveen, H. Haniu, Properties of sugarcane waste-derived bio-oils obtained by fixed-bed fire-tube heating pyrolysis, Bioresource Technology 101 (2010) 4162–4168.
[12] W. Kaminsky, Chemical Recycling of Mixed Plastics by Pyrolysis, Advances in Polymer Technology 14 (1995) 337–344.
[13] Islam, M.R., Haniu, H., Beg, M.R.A., 2007. Limonene-rich liquids from pyrolysis of heavy automotive tire wastes, Journal of Environment and Engineering 2 (2007) 681–695.

ICME2015

International Conference on Mechanical Engineering 2015
(ICME 2015) 18 – 20 December, 2015, Dhaka, Bangladesh

Paper ID :332

Effect of Guide Vane Height on the Performance of a Compression Ignition Engine Run with Biodiesel

S. Bari[1, 2, a)] and Idris Saad[1, 3, b)]

[1]*Barbara Hardy Institute, School of Engineering, University of South Australia, Mawson Lakes, SA 5095, Australia.*
[2]*Department of Mechanical Engineering and Engineering Science, University of North Carolina Charlotte, NC 28223-0001, USA*
[3]*Automotive Research and Testing Cener (ARTeC), Universiti Teknologi MARA, 40450, Shah Alam, Selangor, Malaysia.*

[a)] Corresponding author: saiful.bari@unisa.edu.au
[b)]idrisbinsaad@gmail.com

Abstract. Diesel engines can be run with renewable biodiesel which has the potential to supplement the receding supply of crude oil. However, the viscosity of biodiesels is higher and the calorific value is lower than diesel which cause the performance of diesel engine to be inferior when run with biodiesels. In this research, vane was introduced into the intake runner of a diesel engine to create additional turbulence inside the combustion chamber to improve the mixing of air and higher viscous biodiesel. Vane height was varied experimentally to find the effect of vane height on the performance of a CI engine run with biodiesel. Generally, a reduction of bsfc and increment of engine efficiency were observed when the CI engine was run with biodiesel having guide vanes.

INTRODUCTION

Due to depleting recourses of petroleum-based fuels and environmental concerns, worldwide researchers are looking for alternative fuels to solve or at least reduce the dependency on petroleum-based fuels for IC engines. Among many alternative fuels, neat vegetable oil and biodiesel are found as the promising fuels to replace the diesel fuel since they are renewable and can be used in diesel engines with minor modifications [1, 2]. However, the engine performances such as torque, power, break specific fuel consumption (bsfc), and certain emissions are found to be inferior with biofuel than the engine run with diesel [3-6]. These inferior performances are due to lower calorific value, higher viscosity and heavier molecules present in these biofuels.

Techniques to improve the performance of diesel engines with higher viscous biodiesel and vegetable oil include preheating the fuel before injection [7], blending with diesel [8], and adjusting the injection pressure and timing [9]. Despite improvements of engine performance by these techniques with biofuels, the engine performance is still lower compared to the performance with diesel. Another technique, increasing the turbulence of air inside the combustion chamber to improve the mixing of higher viscous fuels with air will likely improve the performance of the engine [10]. Hence, this research aimed to investigate the effect of guide vanes into the intake manifold on in-cylinder turbulence to improve the performance and emission of diesel engine run with biodiesel.

Based on the literature regarding to the development of guide vane, the design of guide vane depends mainly on four main parameters: vane height, vane angle, vane length and vane number. This research focused on the experimental work to examine the effect of vane height. The various dimensions of the vanes were selected from the previous simulation works by the authors [11-15].

EXPERIMENTAL SETUP

In this study, five guide vane models were fabricated with varied vane heights of 0.1, 0.3, 0.5, 0.7 and 0.9 times the intake runner radius (R) and named as 0.1R, 0.3R, 0.5R, 0.7R and 0.9R, respectively. The vane angle, number and length of the guide vane models were fixed at 35°, four and three time the radius of intake runner (R), respectively, which were found optimum for cold flow simulations without combustion in the authors' previous works [12-14]. Vane height was also varied from 0.1 to 1.0 times the intake runner radius and the cold flow simulation showed highest turbulence of air was created in the injected fuel region by the 0.7R height vane [11].

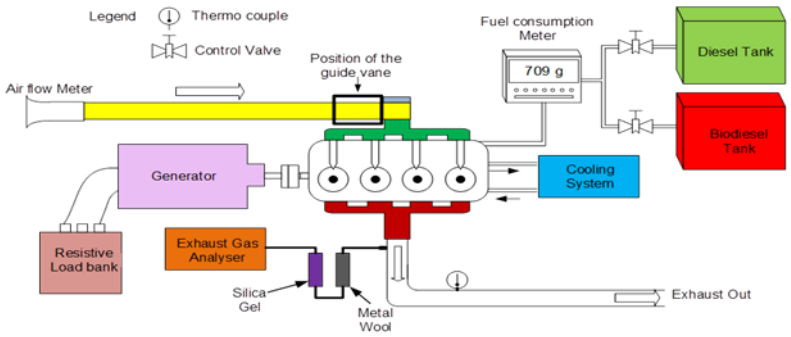

FIGURE 1. Schematic diagram of the experimental setup.

Four cylinders, four-strokes HINO W04D diesel engine of 2 *L* capacity was used in this research which was coupled to a generator. More details of the experimental setup and uncertainty analysis can be found in the author's previous works [16, 17]. The experimental setup is shown in Fig. 1. Initially, the engine was started using diesel and run at 1500 rpm without guide vanes. Then, different loads were applied, and when the engine was at steady state, different readings were recorded. Thereafter, the fuel was switched to biodiesel and after steady state different readings were taken without vanes. Then, the engine was stopped and guide vanes were installed into the intake runner and the engine was started with biodiesel. After reaching steady state, different readings were takes at different loads.

RESULTS AND DISCUSSIONS

The engine performance characteristics and exhaust emissions are presented in this section. The viscosity and calorific value of diesel are 3.21 cSt and 45 MJ/kg, respectively, and the viscosity and calorific value of biodiesel are 5.0 cSt and 38 MJ/kg, respectively. The higher viscosity and lower calorific value of biodiesel are expected to effect the engine performance when run on biodiesel.

Break Specific Efficiency (bsfc)

The experiment result of bsfc is shown in Fig. 2. Typical with diesel engines, the bsfc reduced when the engine load was increased for all runs [18, 19]. However, as expected, the bsfc of biodiesel runs without vanes was higher than diesel due to lower calorific value of biodiesel. On average, the engine consumed approximately 13.87% more biodiesel than diesel with no vanes. With vanes, the bsfc reduced compared to without vanes ran on biodiesel and the reductions were in between 0.96% and 1.77%. This was due to increased turbulence which enhanced the diffusion, mixing and combustion processes. Among different height vanes, the B-0.7R model showed the highest reduction. Lower than this height probably did not produce enough momentum to sustain the turbulence during the injection period and higher than this height probably became obstacle to the airflow than the benefit of higher turbulence.

Efficiency

Figure 3 illustrates the engine efficiency for all runs which are typical to other related research work [1, 2]. The figure shows that biodiesel baseline result was approximately 1.2% higher than the diesel. This is due to the oxygen

content in biodiesel molecule which helped the combustion process [3-7]. With vanes the engine efficiency was further increased between 0.03% and 1.81% due to enhanced diffusion, mixing and combustion processes. Among the vanes, the highest engine efficiency was seen with B-0.7R guide vane model.

Air-fuel Ratio

The results of air-fuel ratio for all runs are given in Fig. 4. The pattern of the graph shows that the air-fuel ratio declined when the load was increased. This condition is due to the requirement of more fuel to maintain the engine speed at 1500 rpm while the load was increased. Comparing the baseline air-fuel ratio results between diesel and biodiesel without vanes, it is found that the air-fuel ratio for biodiesel was lower than diesel runs. This is due to more fuel requirement owing to lower calorific value of biodiesel. Among the guide vane models with biodiesel, the highest air-fuel ratio was recorded with B-0.7R model especially at higher loads due to the effectiveness of the B-0.7R model to generate highest in-cylinder turbulence to improve the mixing of air and fuel which resulted in better combustion.

Carbon Dioxide (CO_2)

The results of CO_2 variation for all runs are portrayed in Fig. 5 which showed that the engine developed more CO_2 as the load was increased. As the load was increased more fuel was required which produced more CO_2. Due lower calorific value, biodiesel runs required more fuel which resulted in higher CO_2 production with biodiesel runs. Biodiesel runs without vanes recorded on average 6.46% increment of CO_2 production than diesel. Among all guide vane models with biodiesel, it is found that reductions of CO_2 in the range between 3.2% and 4.42% were recorded. This reduction is believed to be due to the improvement of diffusion, mixing and combustion processes resulted from the turbulence generated by the guide vanes. The highest reduction of CO_2 was found with the B-0.7R model.

Oxygen (O_2)

Figure 6 presents the percentage of oxygen (O_2) content left in the exhaust gas against loads. Higher engine load requires more fuel and for constant airflow rate this means lower air-fuel ratio (Fig. 4) resulting lower O_2 content in the exhaust gas. This trend is clearly illustrated in Fig. 6. However the graphs of bsfc and air-fuel ratio as presented before suggest that biodiesel should produce lower O_2 than diesel runs. But the figure shows that biodiesel runs contained more O_2 in the exhaust. This is due to oxygen content in the molecule of biodiesel as suggested by other researchers [3, 20, 21]. On average, biodiesel runs showed 4.83% higher O_2 concentration in the exhaust than the diesel runs. In the case of different guide vane runs, a further increment of O_2 concentration were detected by the exhaust gas analyzer in the range of 6.3% and 7.79% with B-0.7R being the least 6.3%.

Nitrogen Oxides (NO_x)

The experimental results of NO_X for all run in ppm versus loads are presented in Fig. 8. The production of NO_X depends on high temperature and O_2 content in the flame front inside the combustion chamber [10, 22]. The figure shows that the NO_X increased as the load increased due to higher temperature for all runs. The biodiesel runs produced more NO_X due to the presence of O_2 in the biodiesel. Biodiesel also contains unsaturated feedstock which also caused higher NO_X [23, 24]. On average, biodiesel without vanes produced 1.46% more NO_X than diesel runs. The introduction of vanes produced more NO_X compared to no vanes when ran with biodiesel. Again, this is due to better combustion owing to higher turbulence due to vanes. The B-0.7R vane model showed the highest increase among the different height vanes. Techniques like exhaust gas recirculation and water injection can reduce these harmful emissions [25-27].

Carbon Monoxides (CO)

Figure 8 presents the percentage variation of CO for all experiment results and plotted against engine loads. Based on theory, the production of CO is due to the incomplete combustion [10, 22]. Naturally, at higher engine loads, more fuel was injected into the cylinder and due to limited time and lower air-fuel ratios, the fuel could not

burn properly producing higher CO emissions. However, the figure shows lower CO for biodiesel runs and this was due to the presence of O2 in the biodiesel molecule. As for the comparison among the five guide vanes models, it is found that further reductions in the range of 1.09 and 3.97% were found, with B-0.7R showing the highest reduction. This is expected due to the better combustion produced by the vanes as mentioned earlier.

Hydrocarbon (HC)

The results of the unburned hydrocarbon (HC) left in the exhaust gas for all runs are illustrated in Fig. 9. Like CO, at higher load due to more injected fuel and lower air-fuel ratios, HC increased. Also, due to better combustion owing to the presence of O2 in the biodiesel, HC content of all biodiesel runs were lower than diesel runs with average reduction of 34.3%. Due to the introduction of vanes which produced higher turbulence, the vane runs with biodiesel CO was lower than no vane and the reduction range was 0.63 to 7.49. The highest reduction was with B-0.7R.

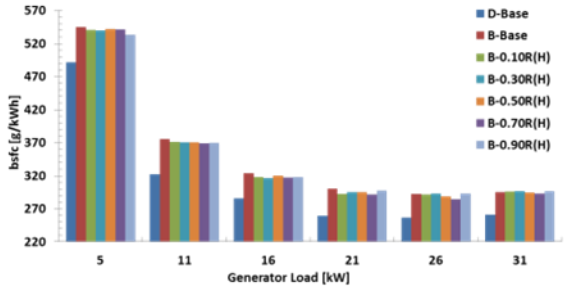

FIGURE 2. Comparison of bsfc versus load.

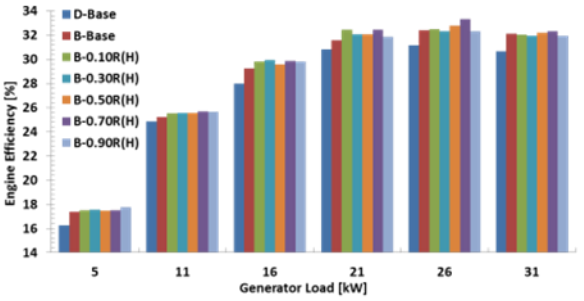

FIGURE 3. Comparison of engine efficiency versus load.

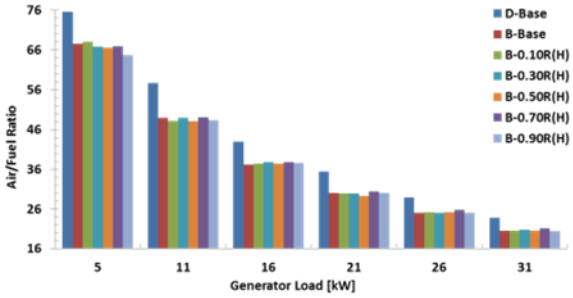

FIGURE 4. Comparison of air-fuel ratio versus load.

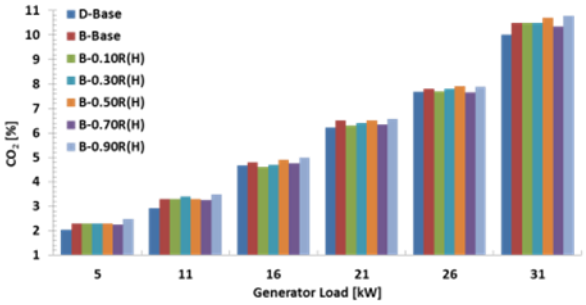

FIGURE 5. Comparison of CO_2 versus load.

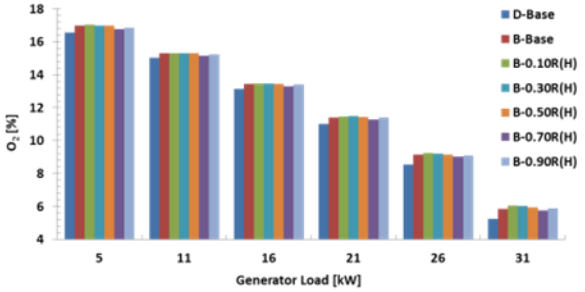

FIGURE 6. Comparison of O_2 versus load.

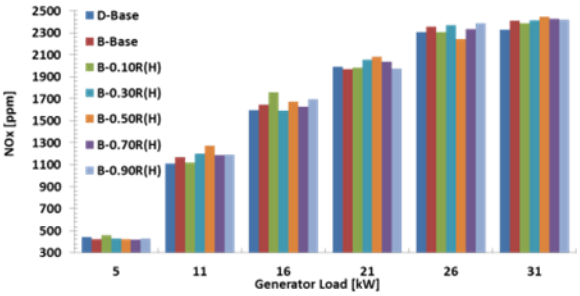

FIGURE 7. Comparison of NO_x versus load.

Optimum Vane Height

The improvements of bsfc were between 0.92% and 1.77% with vanes compared to biodiesel run without vanes. The highest reduction was found with B-0.70R followed by B-0.10R, B-0.50R, B-0.90R and B-0.30R. The engine efficiency of B-Base without vanes was higher than D-Base, which were 32.4% and 31.2%, respectively. With guide

vanes, the improvements of efficiency were in the range of 0.90% and 1.81% from B-Base. The highest efficiency of 33.6% was found with B-0.7R vane. The guide vanes clearly improved the performance and reduced the emissions of the engine with biodiesel. Although, B-0.7R showed better performance than other vanes, but the variations among the vanes were marginal. Therefore, more research needs to be done to confirm this findings, and also other parameters such as vane number, length, angle and shape need to be investigated to find the optimum design of the vanes.

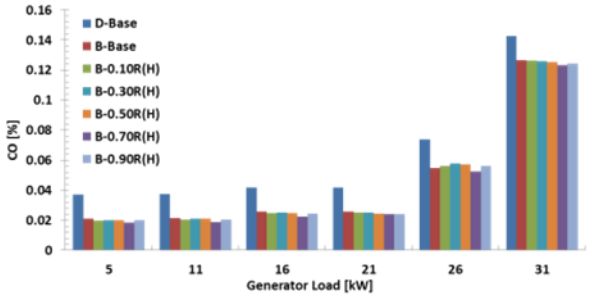

FIGURE 8. Comparison of CO versus load.

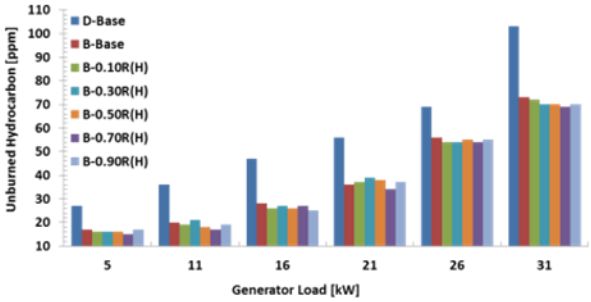

FIGURE 9. Comparison of HC versus load.

CONCLUSIONS

The main objectives of this research are to investigate the effect of adding guide vanes in the intake runner of a diesel engine run with higher viscous biodiesel as well as to determine the optimum vane height. Due to lower calorific values of biodiesel, on average the bsfc with biodiesel without vane was 13.87% higher than diesel. However, introduction of vanes improved the reduction in the range of 0.92 and 1.77%. The highest efficiencies were 33.6%, 32.4% and 31.2% with biodiesel having vane of 28 mm height, biodiesel without vane and diesel, respectively. In terms of emissions, biodiesel produced lower emissions of CO, HC, but produced higher NOX than diesel. Though the variations of engine performance among different heights were marginal, however, the height of 28 mm vane height showed the highest improvements.

REFERENCES

[1] T. M. Yunus khan, I. A. Badruddin, A. Badarudin, N. R. Banapurmath, N. J. Salman Ahmed, G. A. Quadir, *et al.*, "Effects of engine variables and heat transfer on the performance of biodiesel fueled IC engines," *Renewable and Sustainable Energy Reviews*, **44**, pp. 682-691, 2015.

[2] S. Bari and M. M. Roy, "Prospect of rice bran oil as alernative to diesel fuel," presented at the Fifth International Conference on Small Engines, their Fuels and the Environment, pp. 31-36, 1995.

[3] M. Mofijur, M. G. Rasul, and J. Hyde, "Recent Developments on Internal Combustion Engine Performance and Emissions Fuelled With Biodiesel-Diesel-Ethanol Blends," *Procedia Engineering*, **105**, pp. 658-664, 2015.

[4] D. Singh, K. A. Subramanian, and S. K. Singal, "Emissions and fuel consumption characteristics of a heavy duty diesel engine fueled with Hydroprocessed Renewable Diesel and Biodiesel," *Applied Energy*, **155**, pp. 440-446, 2015.

[5] S. Bari, "Investigation into the deteriorated performance of diesel engine after prolonged use of vegetable oil," presented at the ASME Internal Combustion Engine Division 2004 Fall Technical Conference, pp. 447-455, 2004.

[6] S. Bari and I. Saad, "Optimization of Vane Numbers Through Simulation and Experiment, and Investigation of the Effect on the Performance and Emissions of a CI (Compression Ignition) Engine Run with Biodiesel," *Energy*, **79** (0), pp. 248-263, 2014.

[7] S. Vedharaj, R. Vallinayagam, W. Yang, S. Chou, K. Chua, and P. Lee, "Performance emission and economic analysis of preheated CNSL biodiesel as an alternate fuel for a diesel engine," *International Journal of Green Energy*, **12**, pp. 359-367, 2015.

[8] M. A. Wakil, M. A. Kalam, H. H. Masjuki, A. E. Atabani, and I. M. Rizwanul Fattah, "Influence of biodiesel blending on physicochemical properties and importance of mathematical model for predicting the properties of biodiesel blend," *Energy Conversion and Management*, **94**, pp. 51-67, 2015.

[9] N. Panneerselvam, A. Murugesan, C. Vijayakumar, A. Kumaravel, D. Subramaniam, and A. Avinash, "Effects of injection timing on bio-diesel fuelled engine characteristics—An overview," *Renewable and Sustainable Energy Reviews*, **50**, pp. 17-31, 2015.

[10] J. B. Heywood, *Internal Combustion Engines Fundamentals*: McGraw Hill International, 1988.

[11] I. Saad, S. Bari, and S. N. Hossain, "In-Cylinder Air Flow Characteristics Generated by Guide Vane Swirl and Tumble Device to Improve Air-Fuel Mixing in Diesel Engine Using Biodiesel," *Procedia Engineering*, **56**, pp. 363-368, 2013.

[12] S. Bari and I. Saad, "CFD modelling of the effect of guide vane swirl and tumble device to generate better in-cylinder air flow in a CI engine fuelled by biodiesel," *Computers & Fluids*, **84**, pp. 262-269, 2013.

[13] I. Saad, S. Bari. "Effects of guide vane swirl and tumble device (GVSTD) to the air flow of naturally aspirated CI engine," In CD-ROM Proceedings of the 9th International Conference on Mechanical Engineering (ICME), pp. 1-6, 2011.

[14] I. Saad and S. Bari, "Improving Air-Fuel Mixing in Diesel Engine Fuelled by Higher Viscous Fuel using Guide Vane Swirl and Tumble Device (GVSTD)," presented at the SAE 2013 World Congress & Exhibition, Detroit, Michigan, USA, 2013.

[15] I. Saad and S. Bari, "Optimize Vane Length to Improve In-Cylinder Air Characteristic of CI Engine Using Higher Viscous Fuel," *Applied Mechanics and Materials*, **393**, pp. 293-298, 2013.

[16] S. Bari and S. Hossain, "Design and Optimization of Compact Heat Exchangers to be Retrofitted into a Vehicle for Heat Recovery from a Diesel Engine," *Procedia Engineering*, **105**, pp. 472-479, 2015.

[17] S. N. Hossain and S. Bari, "Waste Heat Recovery from Exhaust of a Diesel Generator Set Using Organic Fluids," *Procedia Engineering*, **90**, pp. 439-444, 2014.

[18] A. K. Agarwal and A. Dhar, "Experimental investigations of performance, emission and combustion characteristics of Karanja oil blends fuelled DICI engine," *Renewable Energy*, **52**, pp. 283-291, 2013.

[19] A. K. Agarwal and K. Rajamanoharan, "Experimental investigations of performance and emissions of Karanja oil and its blends in a single cylinder agricultural diesel engine," *Applied Energy*, **86**, pp. 106-112, 2009.

[20] M. A. Kalam and H. H. Masjuki, "Biodiesel from palmoil--an analysis of its properties and potential," *Biomass and Bioenergy*, **23**, pp. 471-479, 2002.

[21] S. Bari, "Performance, combustion and emission tests of a metro-bus running on biodiesel-ULSD blended (B20) fuel," *Applied Energy*, **124**, pp. 35-43, 2014.

[22] W. W. Pulkrabek, *Engineering Fundamental of the Internal Combustion Engine*, 2 ed.: Pearson Prentice Hall, 2004.

[23] G. Karavalakis, E. Bakeas, G. Fontaras, and S. Stournas, "Effect of biodiesel origin on regulated and particle-bound PAH (polycyclic aromatic hydrocarbon) emissions from a Euro 4 passenger car," *Energy*, **36**, pp. 5328-5337, 2011.

[24] S. Bari and I. Saad, "Performance and emissions of a compression ignition (CI) engine run with biodiesel using guide vanes at varied vane angles," *Fuel*, **143**, pp. 217-228, 2015.

[25] A. Ibrahim and S. Bari, "Effect of varying compression ratio on a natural gas SI engine performance in the presence of EGR," *Energy & Fuels*, **23**, pp. 4949-4956, 2009.

[26] W. Marshall, L. G. Schumacher, and S. Howell, "Engine exhaust emissions evaluation of a Cummins L10E when fueled with a biodiesel blend," SAE Technical Paper1995.

[27] A. Ibrahim, S. Bari, and F. Bruno, "A Study on EGR Utilization in Natural Gas SI Engines Using a Two-Zone Combustion Model," SAE Technical Paper2007.

ICME2015

International Conference on Mechanical Engineering 2015
(ICME 2015) 18 – 20 December, 2015, Dhaka, Bangladesh

Paper ID :334

Analyzing Fuel Properties of Bioethanol and Bioethanol Blend Octane and Petrol

Samavi Farnush Bint-E-Naser[1], Laila Hossain[1], Mrittika Debnath[2], Proma Prodipti Barua[1] and Mohidus Samad Khan[1]

[1]*Department of Chemical Engineering, Bangladesh University of Engineering & Technology, Dhaka – 1000, Bangladesh.*
[2]*Applied Chemistry and Chemical Engineering, Dhaka University, Dhaka -1000, Bangladesh.*
[†]*Equally first author: both authors contributed equally*

[a)]Corresponding author: mohid@buet.ac.bd

Abstract. In Bangladesh, the demand of fossil fuel has been consistently increasing with the development of its industrial and agriculture sectors. The annual demand of petroleum products in Bangladesh is met primarily by refining imported crude oils from overseas. To meet the future energy demand and to save foreign exchange, it is essential to look for domestically produced renewable fuel sources. Bioethanol, produced from biomass, could be a potential alternate fuel for Bangladesh. Bioethanol, which is generally obtained from the conversion of carbon-based feedstock, is a quasi-renewable energy source. Although Bangladesh does not commercially produce bioethanol till date, there are few initiatives at the private sector in this regard, and therefore, it is important to understand the fuel properties of bioethanol. This experimental study aims to measure and analyze different fuel properties, namely, specific gravity & API gravity, viscosity, Reid vapor pressure, calorific value, ASTM color, ASTM distillation, copper strip corrosion and water sedimentation, of bioethanol and 5 and 10 percent bioethanol blended with petrol and octane. This study will be highly useful, providing the baseline properties of bioethanol and bioethanol blend octane and petrol as engine fuel.

INTRODUCTION

Ethanol is the most employed liquid biofuel either as a fuel or as a gasoline enhancer [1]. It is generally obtained from the conversion of carbon-based feedstocks which are often locally available and can be converted into secondary energy carriers [2]. Bioethanol is easily biodegradable, and the use of biomass for energy offsets fossil fuel greenhouse gas emissions [3]. Bioethanol is completely miscible with water in all proportions, while the gasoline and water are immiscible [4]. This may cause the blended gasoline to contain water, and further result in the corrosion problems on the mechanical components, especially for components made of copper, brass or aluminum [5].

Bioethanol is a safer alternative to methyl tertiary butyl ether (MTBE), the most common additive to gasoline used to provide cleaner combustion, which is a toxic chemical compound and has been found to contaminate groundwater. In contrast, ethanol has greater octane booster properties, and introduces less contamination to water sources [2]. Ethanol contains 35% oxygen by mass which implies a less amount of required additive and facilitates more complete fuel combustion and reduces the amounts of particulate emission from combustion [3]. For using ethanol as engine fuel, it is important to understand its fuel properties and its effect on the engine performance. In this experimental study, selected physico-chemical properties of the bioethanol sample, and bioethanol blends of octane and petrol prepared in the laboratory, were measured as per ASTM guidelines.

MATERIALS & METHODOLOGY

Sample collection and preparation

The bioethanol sample was collected from Mojj Engineering Systems Limited, India through Sunypun Organics Limited, Bangladesh. The collected bioethanol sample was produced from multi feedstock which was converted to monomeric sugars via enzymatic hydrolysis which was followed by fermentation using yeast for conversion of sugars into ethanol. The produced ethanol was purified in a multi-pressure distillation column with integrated evaporator operating under vacuum at low temperature, and then, dehydrated to obtain the final product. Octane and petrol were collected from local market.

High quality petrol and octane (highest grads) were purchased from local fuel station. The 5 and 10 percent bioethanol blends of petrol and octane were prepared in the laboratory using the collected bioethanol sample, petrol and octane.

Methodology

The fuel properties of all seven samples (pure bioethanol, petrol, octane, 5 and 10% bioethanol blends of petrol and octane) were tested according to ASTM specification. The test methods are listed in Table 1. Each test were carried out for three times (n=3) and the average results were used for further analysis.

Table 1. ASTM test methods.

Parameter tested	ASTM test method
Specific gravity & API gravity	ASTM D 1298-99
Calorific value	ASTM D 2014-96
Reid vapor pressure	ASTM D 323-99a
Viscosity	ASTM D 88-94
ASTM color	ASTM D 1500-03
Copper corrosion	ASTM D 130-04
Distillation	ASTM D 86-04b
Water & bottom sedimentation	ASTM D 1796-97

RESULTS

The results for specific gravity, API gravity, calorific value, Reid vapor pressure, viscosity, ASTM color and Cu strip corrosion test are given in Table 2. Table 3 contains results for ASTM distillation and water sedimentation tests.

Table 2. Results for specific gravity, API gravity, calorific value, Reid vapor pressure, viscosity, ASTM color and Cu strip corrosion test.

Sample	Sample no	Specific gravity	API gravity (^{o})	GCV (*MJ/kg*)	Reid vapor pressure (*kPa*)	Viscosity (*SUS*)	ASTM color	Cu strip corrosion
Bioethanol	1	0.7853	47	29.05	14.25	34.1	0 ASTM Color	Slight tarnish
Petrol	2	0.7553	56	42.10	35.00	28.0	1 ASTM Color	Slight tarnish
Petrol with 5% ethanol	3	0.7652	55	40.00	43.00	28.5	1 ASTM Color	Slight tarnish
Petrol with 10% ethanol	4	0.7572	56	35.86	43.25	29.4	1 ASTM Color	Moderate tarnish
Octane	5	0.7373	61	41.39	50.00	28.2	1 ASTM Color	Slight tarnish
Octane with 5% ethanol	6	0.7627	59	40.81	48.00	28.4	1 ASTM Color	Slight tarnish
Octane with l0% ethanol	7	0.7442	60	39.21	54.00	29.0	1 ASTM Color	Slight tarnish

Table 3. Results for ASTM distillation and water content.

Sample no	ASTM distillation				Water content (%)
	IBP (°C)	FBP (°C)	Total recovery (%)	Percent loss (%)	
1	39.5	87.5	98.50	1.50	1.000
2	54.5	266.5	99.50	0.50	0.400
3	60.5	286.5	99.50	0.50	0.430
4	58.5	242.5	99.50	0.50	0.460
5	46.5	224.5	99.00	1.00	0.250
6	20.5	208.5	99.50	0.50	0.288
7	48.5	248.5	99.00	1.00	0.325

DISCUSSIONS

Specific gravity, API gravity and moisture content

Lighter fuel oils can be transported through pipelines. The greater the specific gravity (SG), the greater the mass of fuel can be stored in a given tank. Fuel density generally increases with increasing molecular weight of the fuel molecules. Generally, an increase in density increases the overall performance of engines [6]. Fig.1. contains graphical representation of experimental and theoretical values [7,8] of SG of the samples. Presence of water resulted in higher values of measured SG of petrol and octane samples than literature values. Blending of ethanol with petrol and octane resulted in higher values of SG. However, the SG of the 5% blends are higher than the SG of the 10% blends in both cases which may be due to experimental deviation. The moisture content in all the samples are shown in Fig.2. The American Petroleum Institute gravity (API gravity), is another means to petroleum lightness with respect to water: if the API gravity is greater than 10, the petroleum fuel is lighter and floats on water; if less than 10, it is heavier and sinks. API gravity is an inverse measure of a petroleum liquid's density relative to that of water (also known as specific gravity), as is shown in Fig.3. API gravity is gradated in degrees on a hydrometer instrument. API gravity values of most petroleum liquids fall between 10 and 70 degrees.

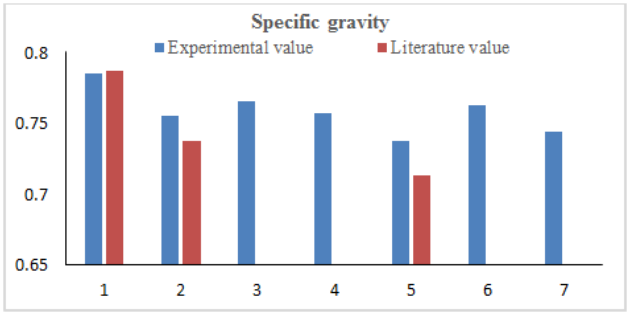

FIGURE 1. Specific gravity of fuel samples

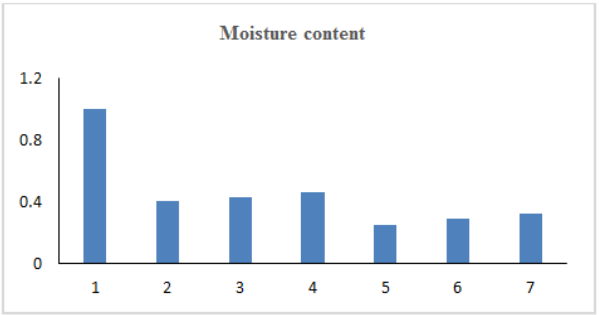

FIGURE 2. Moisture content of fuel samples

Gross calorific value (GCV)

The combustion rate of a fuel is proportional to its calorific value. A low calorific value indicates more water vapor absorption. Gross caloric values of the samples are shown in Fig.4. For sample 1, 2, and 5, the experimentally obtained values are lower than the literature values [9,10]; the possible explanation could be the presence of water which lowers the calorific value of fuel. For samples 3, 4, 6, and 7, blending of ethanol lowers the GCV of petrol and octane. The higher the percentage of ethanol, the lower the GCV.

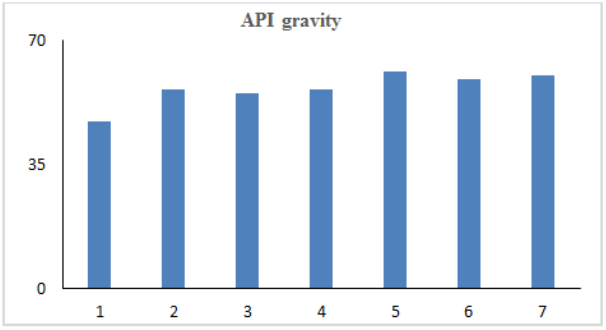

FIGURE 3. API gravity of fuel samples

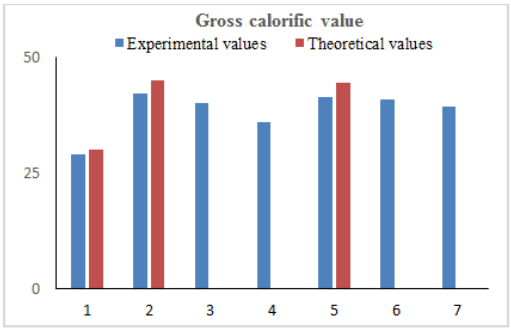

FIGURE 4. Gross calorific values of fuel samples

Reid vapor pressure

Reid vapor pressure (RVP) is frequently used as an indication of volatility of liquid hydrocarbons. The RVP is defined as the absolute pressure (i.e., psia or bar) exerted by a mixture, determined at 100 ºF (37.8 ºC). Motor and aviation gasolines are manufactured as liquids but they are consumed in the vapor phase. Gasoline volatility must be high enough to assure acceptable engine start-up, warm-up, acceleration and throttle response under normal driving (or flying) conditions. On the other hand, the maximum volatility of a gasoline must be restricted to avoid vapor lock, vaporization losses, air pollution, and unsafe storage and handling. According to RFA guidelines, unless other more volatile blending components are used, the addition of ethanol should not create a vapor pressure increase above 1.0 psi in conventional gasoline [11]. The experimental results (Fig.5) showed increase in RVP lower than 1.0 psi (6.89 kPa) for octane blends but slightly higher than 1 psi for petrol blends. The 10% blends showed highest RVP which is similar to the findings of other research groups [12].

Viscosity

Viscosity is a measure of oil's resistance to flow. It decreases (thins) with increasing temperature and vice-versa. Oil's viscosity is measured most commonly by kinematic viscosity, which is measured in the time it takes for a specific volume of oil to flow through a special device called a capillary tube. In this article, kinematic viscosity of all the

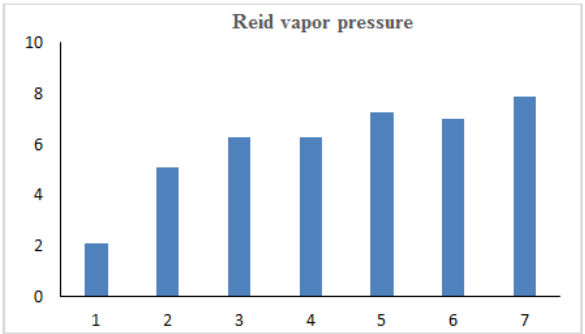

FIGURE 5. Reid vapor pressure of fuel samples

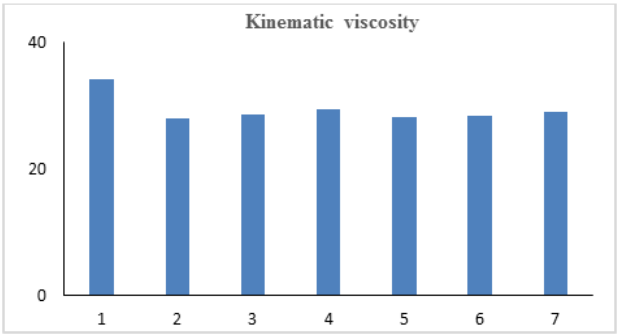

FIGURE 6. Kinematic viscosity of fuel samples

samples has been reported in Saybolt Universal Seconds (SUS). Fig. 6 shows the effect of blending ethanol on the viscosity of petrol and octane. In both cases, viscosity increases with increasing concentration of ethanol.

ASTM distillation

The distillation curves shown in Fig. 7 and Fig.8. The temperatures obtained during the distillation are plotted against the percentages distilled. For efficient combustion, the distillation curve should be smooth and straight. A fluctuation in curve implies an oil that may give erratic operation due to non-uniform conditions [13]. Fig. 7 and Fig. 8 show the degree of spread between the initial boiling point and the end point. Blending of ethanol with petrol and octane lowers the temperature at which any percentage of fuel is evaporated. ASTM D4814 also provides guidance on distillation characteristics.

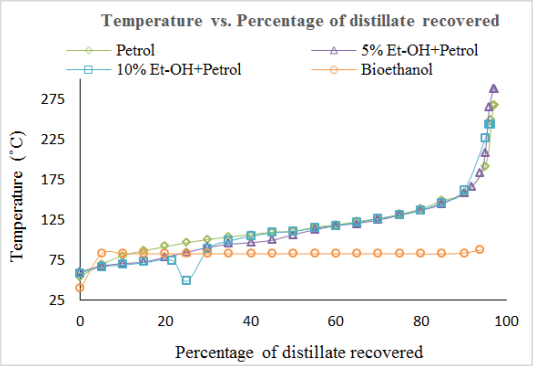

FIGURE 7. Ethanol effect on distillation curve of petrol

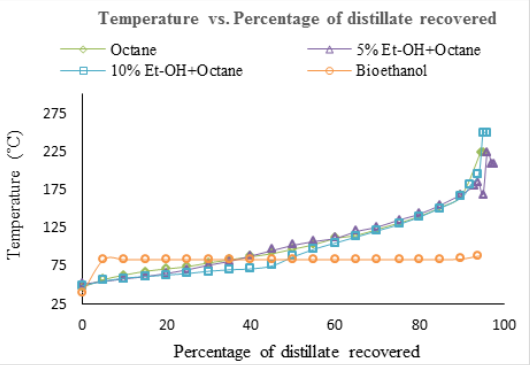

FIGURE 8. Ethanol effect on distillation curve of octane

Cu strip corrosion and ASTM color

Crude petroleum contains sulfur compounds, most of which are removed during refining. However, of the sulfur compounds remaining in the petroleum product, some can have a corroding action on various metals and this corrosivity is not necessarily related directly to the total sulfur content. The copper strip corrosion test (ASTM D130-04) is designed to assess the relative degree of corrosivity of a petroleum product. All samples under test except petrol blend with 10% ethanol (sample 4) caused slight tarnish in color of the copper strip. Sample 4 caused moderate tarnish in the color of the copper strip which may require further investigation. Determination of the color of petroleum products (ASTM D 1500-03) is served as an indication of the degree of refinement of the material and if the color range of a particular product is known, a variation outside the established range may indicate possible contamination with another product. Table 1 shows that blending bioethanol does not contribute in ASTM color.

CONCLUSION

The inevitable depletion of world's energy supply has been increasing worldwide interest in alternative sources of energy to ensure fuel security. In Bangladesh, the present annual demand of petroleum products is about 3.7 MMT. The annual demand is met primarily by refining imported crude oils from overseas, which is processed with a small quantity of oil from Haripur Gas Field. Bangladesh imports about 1.3 MMT of crude oil and another 2.7 MMT (approximately) of refined petroleum products per annum. Considering the limited amount of global fossil fuel reserves, the amount of foreign currency required to import the petroleum products, and concern regarding environmental problems: particularly the greenhouse gas (CO_2) emission, it is vital for Bangladesh to look for alternate renewable fuel for its sustainable development. While renewable energy sources such as solar, wind and hydro energies may be used to generate electricity or heat either directly or indirectly, biomass is the only renewable energy source capable of producing liquid fuels (biofuels) for storage and as a transport fuel [14]. Ethanol blended with petrol and octane is in early stage of development in Bangladesh, and can reduce greenhouse emissions. On an energy basis ethanol has lower calorific value than petrol and octane; hence, it may require relatively higher amount of bioethanol

blended fuel to get similar performance as octane or petrol. The availability of feedstocks of bioethanol can vary considerably from season to season and depend on geographic locations. This experimental study provides baseline properties of bioethanol and bioethanol blend (5% and 10%) octane and petrol as fuel.

ACKNOWLEDGEMENTS

This research was supported by BCEF Academic Research Fund and CASR Research Fund. The authors would like to acknowledge Sunypun Organics Limited, Bangladesh and Mojj Engineering Systems Limited, India for bio-ethanol sample, and Mr. J. Bishwash of Fuel Lab, ChE, BUET, for technical support.

REFERENCES

[1] Oscar J. Sanchez, Carlos A. Cardona, Trends in biotechnological production of fuel ethanol from different feedstocks, Bioresource Technology 99 (2008) 5270-5295.

[2] H. Von. Blottnitz , M. A. Curran, A review of assessments conducted on bio-ethanol as a transportation fuel from a net energy, greenhouse gas and environmental life cycle perspective, Journal of cleaner production 15 (2007) 607-619.

[3] Yan Lin. Shuzo Tanaka, Ethanol fermentation from biomass resources: current state and prospects, Appl. Microbiol. Biotechnol. 69 (2006) 627–642.

[4] Furey, R.L., Perry, K.L., Composition and reactivity of fuel vapor emissions from gasoline-oxygenate blends, SAE Paper 912429, 1991.

[5] Coelho, E.P.D., Moles, C.W., Marco Santos, A.C., Barwick, M., Chiarelli, P.M., Fuel injection components developed for Brazilian fuels. SAE Paper 962350, 1996.

[6] Fuel Density - Universe Communications, web address: http://members.axion.net/~enrique/space_fueldensity.html, Retrieved 11 September, 2015.

[7] Specific Gravity of Liquids Table - CGNetwork, web address: http://www.csgnetwork.com/specificgravliqtable.html, Retrieved 13 September, 2015.

[8] Specific Gravity - Engineering ToolBox, web address: http://www.engineeringtoolbox.com/specific-gravity-liquids-d_336.html, Retrieved 13 September, 2015.

[9] Properties of Polymers - National Physical Laboratory, web address: http://www.kayelaby.npl.co.uk/chemistry/3_11/3_11_4.html, Retrieved 13 September, 2015.

[10] Fuels Higher Caloric Values - Engineering ToolBox, web address: http://www.engineeringtoolbox.com/fuels-higher-calorific-values-d_169.html, Retrieved 13 September, 2015.

[11] RFA Fuel Ethanol Industry Guidelines, Specifications and Procedures, 2010, Pg-12.

[12] Andersen, V. F., Anderson, J. E., Wallington, T. J., Mueller, S. A., & Nielsen, a. O., Vapor Pressures of Alcohol-Gasoline Blends. Energy & Fuels 24 (2010) 3647-3654.

[13] Schimdt, P. F., Fuel Oil Manual, Industrial Press Inc., 1985.

ICME2015

International Conference on Mechanical Engineering 2015
(ICME 2015) 18 – 20 December, 2015, Dhaka, Bangladesh

Paper ID : 338

Effect of Swirl Flow On Heat Transfer Characteristics In A Circular Pipe

Hossain Siddique[a)], Md. Shafkat Bin Hoque[b)] and Mohammad Ali[c)]

Department of Mechanical Engineering, Bangladesh University of Engineering and Technology (BUET), Dhaka 1000, Bangladesh

[a)]Corresponding author: hs_sawrov@yahoo.com
[b)]shafkatbinhoque@gmail.com
[c)]mali@me.buet.ac.bd

Abstract. Swirl flow is of great stature in heat transfer enhancement and in numerous engineering applications. In the present numerical study, the swirl flow of water in a circular pipe is considered. Here the Reynolds Number is kept within 2000. The pipe contains stationary blades to produce the swirl flow. The blades are considered heat resistant. The three-dimensional Navier-Stokes equations for incompressible Newtonian fluid flow are used. The code is corroborated by comparing the simulation results with the established Hagen-Poiseuille law. The comparison is quite satisfactory and thus the code is used for present investigation. In this study, the heat transfer performance of the swirl flow is evaluated. Two cases are considered on the outer surface of the pipe: (i) Constant heat flux and (ii) Constant temperature. This investigation reveals that the swirl flow increases the mean outlet temperature in both cases. The effects of the vane angle, pipe length and diameter on heat transfer characteristics are also evaluated.

INTRODUCTION

Heat transfer augmentation techniques (passive, active or a combination of passive and active methods) are commonly used in areas such as process industries: chemical and mechanical mixing and separation devices, chemical reactors, heating and cooling in evaporators, thermal power plants, combustion chambers, turbo machinery, fusion reactors, pollution control devices, air-conditioning equipment, refrigerators, radiators for space vehicles, automobiles etc. Passive techniques (where inserts are used in the flow passage to augment the heat transfer rate) are advantageous compared with active techniques because the insert manufacturing process is simple and these techniques can be easily employed in an existing heat exchanger. In the design of compact heat exchangers, passive techniques of heat transfer augmentation can play an important role if a proper passive insert configuration can be selected according to the heat exchanger working conditions (both flow and heat transfer conditions).

Better utilization of swirl flows may lead to the heat and mass transfer enhancements. These flows can be generated by means of insertion of various swirl generators such as coiled wires, twisted tapes, axial blades, short length helical inserts, tangential injector, tangential vane and radial blade cascade. Swirl flow is the descriptive term for a fluid flow in which the tangential component of the mainstream velocity is a significant contribution to the resultant velocity. Continuous swirl flow can be generated by inserting coiled wires, twisted tapes and helical vanes into the pipe, by coiling the tube helically or by making helical grooves in the inner surface of the duct. Rotating flow is generated by either a rotating tube or a spinning body in a free stream. Decaying swirl flow arises when a flow with some initial angular momentum is allowed to decay along the length of a tube such as tangential entry

swirl generators and guided vane swirl generators. Tangential entry of the fluid into a duct stream can be achieved by using a single tangential inlet duct or more than one tangential entry. Guided vane swirl generators are of two types: radial guide vane and axial guide vane. Radial generators generate more intense swirls and they cause more complex velocity profiles than axial generators.

The aim of the present investigation is to study the heat transfer phenomena in a circular pipe with the inclusion of swirl flow. Here, the intended goal is to increase heat transfer and to determine the effects of various parameters on the heat transfer characteristics of the swirl flow.

Nomenclature

D	Outer diameter of the pipe [m]
L	Length of the pipe [m]
Q	Heat transfer rate [W]
R	Inner radius of the pipe [m]
V	Radial velocity component [m/s]
W	Tangential velocity component [m/s]
d	Inner diameter of the pipe [m]
f	Friction factor
k	Thermal conductivity [W/m K]
q	Heat flux at the outer surface [W/m^2]
r	Local radius of the pipe [m]
$\dot{m}$	Mass flow rate [kg/s]
μ	Dynamic viscosity [Ns/m^2]
ρ	Density [kg/m^3]
C_p	Specific heat at constant pressure [J/kg K]
T_0	Outlet water temperature [^0C]
T_i	Inlet water temperature [^0C]
U(r)	Axial velocity component [m/s]
U_{max}	Maximum axial velocity of pipe [m/s]
Re	Reynolds number

TABLE 1. Material properties

Properties	Water	Copper
Density, ρ (kg/m^3)	997.13	8930
Dynamic viscosity, μ (Pa s)	8.9×10^{-4}	–
Thermal conductivity, K (W/m K)	0.58	401
Specific heat at constant pressure, C_p (J/kg K)	4.18×10^3	380

NUMERICAL MODEL

The study is carried out to investigate the effects of the heat resistant vanes on heat transfer characteristics of a circular pipe. Two models are considered. One is a circular pipe with heat resistant vanes on the internal surface of the pipe and the other is the straight circular pipe without any vanes. In both cases, the pipe is of copper and water is used as the working medium. The pipe for both models has a length of 42mm, an internal diameter of d = 3mm and an outer diameter of 3.5mm. Though for swirl flow the surface area of the pipe in contact with the water is less than that for laminar because of the presence of the vanes, it is considered the same as the vanes are very thin. Twisting angles of 22^0, 26^0, 30^0 and 35^0 are used to determine its effects on heat transfer. To determine the effects of L/d on heat transfer, pipe length is varied. L/d ratio of 11, 12 and 13 are considered. The initial values are kept constant at 298 K and 1 atm. for both models. Though the inlet velocity is kept constant at 0.01 m/s for most of the findings, it is varied from 0.01 m/s to 0.5 m/s to determine the effects of Reynolds Number on heat transfer characteristics. Inlet pressure is varied from 100 Pa to 700 Pa to determine its effects on heat transfer. Surface heat flux is varied from 2000 W/m^2 to 14000 W/m^2 to observe the changes of heat transfer with the changes of surface heat flux.

MATHEMATICAL MODELING

The governing equations (Continuity equation & momentum equations in cylindrical coordinate system) are as follows:

$$\frac{\partial U}{\partial x}+\frac{\partial V}{\partial r}+\frac{V}{r}=0 \tag{1}$$

$$U\frac{\partial U}{\partial x}+V\frac{\partial U}{\partial r}=-\frac{1}{\rho}\frac{\partial p}{\partial x}+\nu\frac{\partial^2 U}{\partial x^2}+\frac{1}{r}\frac{\partial U}{\partial r}+\frac{\partial^2 U}{\partial r^2} \tag{2}$$

$$U\frac{\partial U}{\partial x}+V\frac{\partial U}{\partial r}=-\frac{1}{\rho}\frac{\partial p}{\partial x}+\nu\frac{\partial^2 U}{\partial x^2}+\frac{1}{r}\frac{\partial U}{\partial r}+\frac{\partial^2 U}{\partial r^2} \tag{3}$$

$$U\frac{\partial W}{\partial x}+V\frac{\partial W}{\partial r}+\frac{VW}{r}=\nu\frac{\partial^2 W}{\partial x^2}+\frac{1}{r}\frac{\partial W}{\partial r}-\frac{W}{r^2}+\frac{\partial^2 W}{\partial r^2} \tag{4}$$

The amount of heat carried away by the water, $Q=\dot{m}C_p(T_o-T_i)$ (5)

Heat supplied to the outer surface of the pipe, $Q=(\pi DL)*q$ (6)

Heat transfer efficiency $=\dfrac{\dot{m}C_p(T_o-T_i)}{(\pi DL)*q}$ (7)

Reynolds Number, $\mathrm{Re}=\dfrac{\rho v d}{\mu}$ (8)

CODE VALIDATION

To validate the numerical code, laminar flow friction factor in a straight, circular pipe without vanes is calculated from the measured pressure drop and flow rates and compared with those given by the Hagen – Poiseuille equation. The comparison, shown in Fig. 1, reveals a good agreement between numerical and theoretical results.

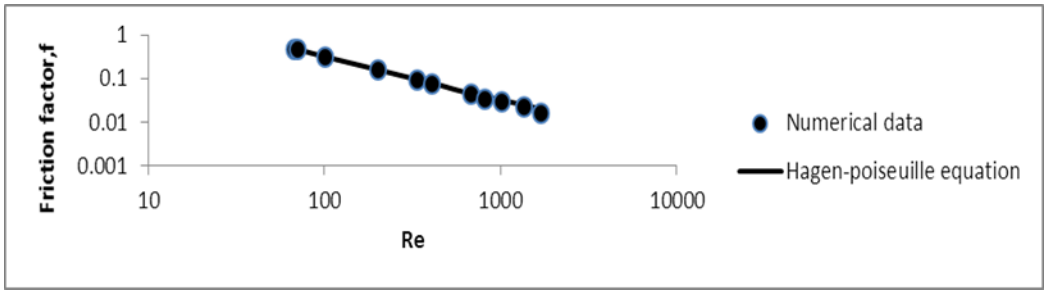

FIGURE 1. Numerical and theoretical friction factor in a straight, circular pipe without vanes

RESULTS AND DISCUSSION

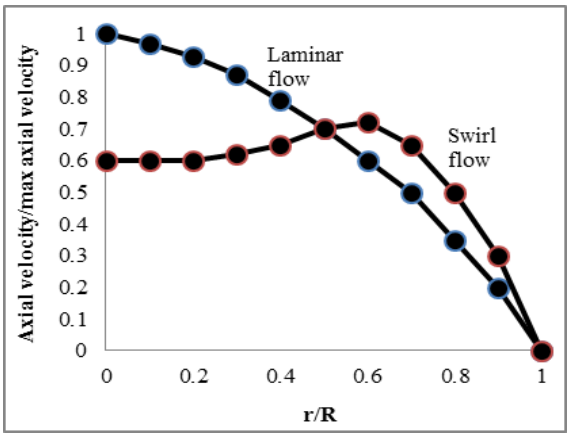

FIGURE 2. Axial velocity distribution for x/d=5.

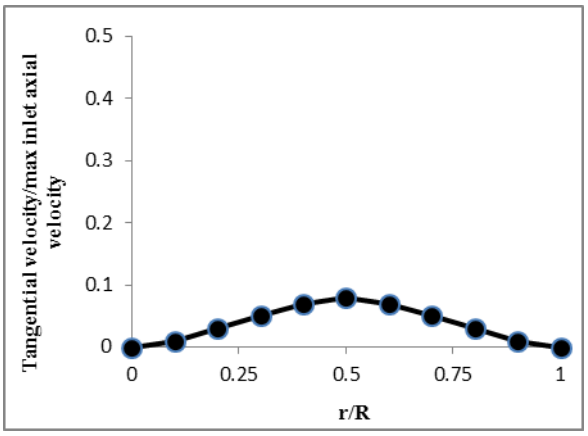

FIGURE 3. Tangential velocity distribution for x/d=5.

The axial velocity distribution in the pipe is presented in Fig. 2, where it is revealed that the fully-developed velocity distribution of laminar flow is altered due to the introduction of the swirl. This is due to the destabilizing effect of the swirl. The actual fully-developed profile of laminar flow will be recovered if the vanes are completely removed and the swirl completely disappears. Figure 3 shows the distribution of the tangential velocity. This trend of tangential velocity was also reported by Chang and Dhir (1995) and Bali (1998) for turbulent swirling flow.

Effects of Swirl Flow

For laminar flow, the maximum local temperature is occurring at the pipe outlet. It is greater than that of swirl flow. This is due to the fact that for laminar flow the water layer adjacent to the pipe always remains closest. So this layer absorbs the highest amount of heat. But for swirl flow different layers of water comes in contact with the pipe at different times. No single layer remains in contact with the pipe at all times. So no water layer of swirl flow can absorb the same amount of heat as that of laminar flow. Swirl increases the heat transfer due to its stirring effect on water. That is why the average water temperature of swirl flow is greater than that of laminar flow as observed from Fig. 4. So swirl flow increases heat transfer rate. With the increase of surface temperature and heat flux, heat transfer increases. This is observed from Fig. 5 and Fig. 6.

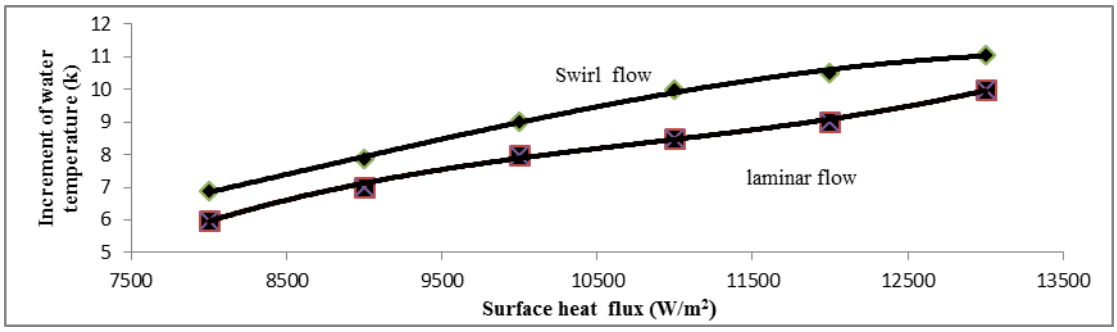

FIGURE 4. Increment of water temperature with respect to surface heat flux

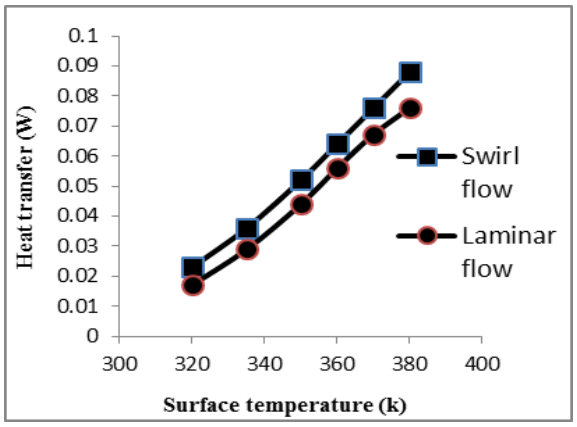

FIGURE 5. Heat transfer with respect to surface temperature

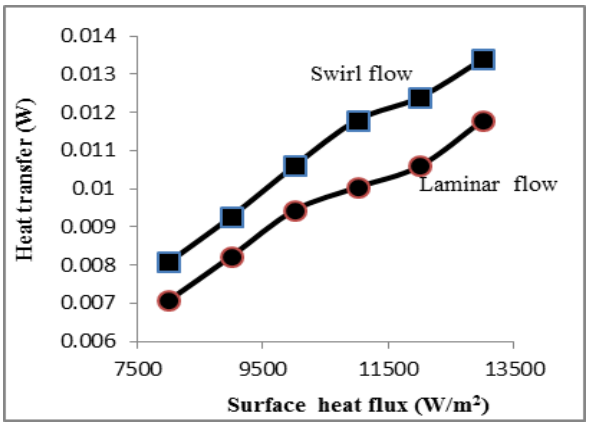

FIGURE 6. Heat transfer with surface heat flux

Effects of Reynolds Number And Inlet Pressure

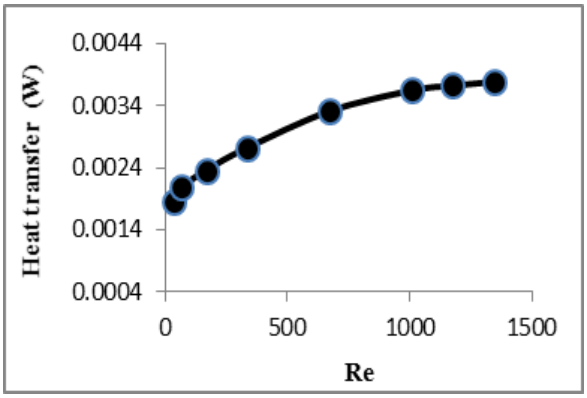

FIGURE 7. Effects of Reynolds Number

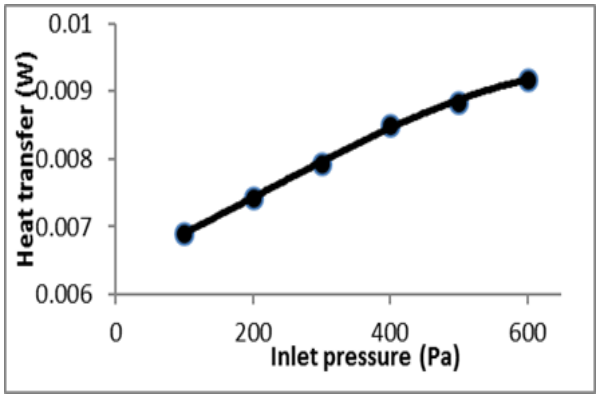

FIGURE 8. Effects of inlet pressure

Heat transfer increases with the increase of Reynolds number due to the increase of mass flow rate. The effects of inlet pressure are similar to the effects of Reynolds number. This is due to the fact that with the increase of inlet pressure, velocity increases. As a result, mass flow rate also increases.

Effects of Twisting Angle

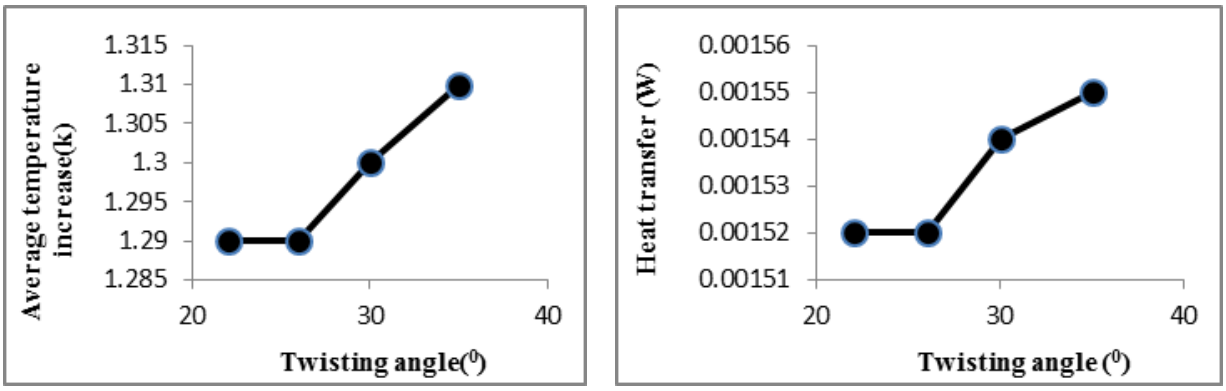

(a) (b)

FIGURE 9. Effects of twisting angle on (a) average temperature increase (b) amount of heat transfer

The effects of twisting angles from 22^0 to 35^0 are studied. As shown in above figures, the heat transfer increases with increasing twisting angle. The increase is negligible at first, but after 25^0, heat transfer increases rapidly. With the increase of twisting angle, the tangential velocity increases at nominal constant values of axial velocity.

Effects of L/d

With the increase of pipe length, the contact area of the pipe with water increases. Thus heat transfer increase almost linearly for L/d ratio of 11 and 12. For L/d ratio of 13, heat transfer increases linearly at first but later higher heat transfer can be observed.

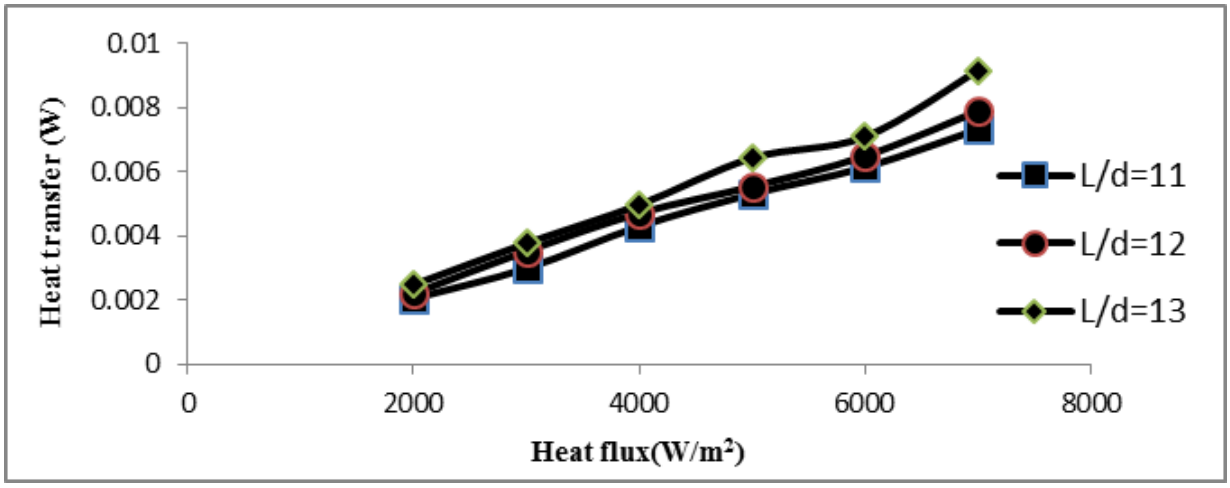

FIGURE 10. Effects of L/d on heat transfer

CONCLUSIONS

The present study is a numerical investigation of heat transfer characteristics of laminar swirling flow through a pipe with continuous vanes. The swirl changes the usual parabolic velocity profile of fully developed laminar flow in the pipe. It is found that swirl flow increases the amount of heat transfer for both surface heat flux and surface temperature. The heat transfer increases with Reynolds Number due to the increase of mass flow rate. The effects of

inlet pressure follow a similar pattern. With the increase of L/d heat transfer increases almost linearly. Increase of twisting angle increases the heat transfer due to the increase of stirring effect of swirl.

ACKNOWLEDGEMENT

The authors acknowledge the contribution of the Department of Mechanical Engineering of Bangladesh University of Engineering and Technology (BUET) for the permission to use computing facilities.

REFERENCES

1. İ. Kurtbaş, A. Durmuş, H. Eren and E. Turgut, *Int. J. Thermal Science* **46**, pp. 300–307 (2007).
2. S. Eiamsa-ard, S. Rattanawong and P.T. Promvonge, *Int. Commun. Heat and Mass Transfer* **36**, pp. 357–364 (2009).
3. A.M. Anderson and R.J. Moffat, *J. Heat Transfer* **113**, pp. 56–62 (1991).
4. M. Yilmaz, O. Comakli, S. Yapici and O. N. Sara, *Energ. Conv. Management* **44 (2)**, pp. 283–300 (2003).
5. A. Durmus, A. Durmus and M. Esen, *Appl. Therm. Engg.* **22 (3)**, pp. 321–332 (2002).
6. A. Durmus, İ. Kurtbaş, F. Gülçimen and E. Turgut, *Int. Commun. Heat and Mass Transfer* **31**, pp. 133–142 (2004).
7. B.A. Saraç and T. Bali, *Exp. Thermal Fluid Science* **32**, pp. 158–165 (2007).
8. E.K. Akpinar, Y. Bicer, C. Yildiz and D. Pehlivan, *Int. Commun. Heat Mass Transfer* **31 (6)**, pp. 857–868 (2004).
9. T. Bali and T. Ayhan, *Int. Commun. Heat Mass Transfer* **26 (1)**, pp. 13–22 (1999).
10. T. Bali, *Int. Commun. Heat Mass Transfer* **25 (3)**, pp. 349–358 (1998).
11. C. Herman and E. Kang, *Int. J. Heat Mass Transfer* **45**, pp. 3741–3757 (2002).
12. F. Chang and V. K. Dhir, *Int. J. Heat and Fluid Flow* **16 (2)**, pp. 78-87 (1995).

ICME2015

International Conference on Mechanical Engineering 2015
(ICME 2015) 18 – 20 December, 2015, Dhaka, Bangladesh

Paper ID : 340

Transient Natural Convection in a Valley Shaped Triangular Cavity Initially Filled with Stratified Water

Sidhartha Bhowmick[1], Feng Xu[2], Suvash C. Saha[3, a)]

[1]*Department of Mathematics, Jagannath University, Dhaka 1100, Bangladesh*
[1,2]*Department of Mechanics, School of Civil Engineering, Beijing Jiaotong University, Beijing 100044, China*
[3]*School of Chemistry, Physics &Mechanical Engineering, Queensland University of Technology, Brisbane QLD 4001, Australia*

[a)]Corresponding author: s_c_saha@yahoo.com

Abstract. Transient natural convection is common in nature such as in a valley. In this paper, transient flows in a valley shaped triangular cavity initially filled with stratified water are investigated using scaling analysis and numerical simulations. The development of the flow on the inclined thermal wall from start-up to a steady-state has been described and discussed. The scaling relations are derived for the thickness, velocity, transitional time and Nusselt number of the thermal boundary layer dependent on the Rayleigh number and the stratified parameter. Moreover, corresponding numerical results are consistent with the scaling results.

INTRODUCTION

With the rapid development of economy, the global environment is being worsen through pollution and frequent disasters. For example, a prominent atmospheric problem, fog and haze, is becoming serious and challenges the human health. In particular, the fog forming in the valley and the corresponding flow have interested a number of investigators. Convective flow over slopes has been studied by Bejan [1]. Palani et al. [2] addressed unsteady natural convection flow on an inclined flat plate considering variation of viscosity and thermal diffusivity. Chen et al. [3] and Ganesan and Palani [4] presented natural convection MHD flow on inclined flat plate with variable wall temperature and concentration and with variable surface heat and mass flux. Studies of steady natural convection flow over inclined flat plate were conducted by Siddiqa et al. [5, 6], one of which describes the effect of radiation on the flow with temperature-dependent viscosity and the other characterizes the flow with internal heat generation and variable viscosity. They have also shown the local skin friction and the local Nusselt numbers. Saha et al. [7-10] have studied extensively the unsteady natural convection flow of inclined flat plate. They considered sudden and ramp heating as well as cooling conditions and also uniform surface heat flux. In their studies, they developed the scaling relations in different flow regimes and validated their results with direct numerical simulations. Using scaling analysis Patterson and Imberger [11] described the different stages of the flow development of the thermal boundary layer, the horizontal intrusion and the flow in the core in a rectangular cavity.

Several researchers conducted laboratory experiments on valley shaped model. Princevac and Fernando [12] performed an experiment study by making an ideal V-type tank fill up with thermally stratified water. They explained that cold air may flow down slope to form a steady layer in the basin valley at night using a tank experiment; in the early morning, this layer is destroyed by the beginning of turbulent convection and upslope flow. They discussed the mechanisms responsible for morning breakup of the steady layer in complex terrain. Field, numerical and water pool experiments in clean climate conditions on complicated terrain had shown in the experiment of Reuten et al. [13]. Their study has shown more complex vertical distributions of temperature, humidity and aerosols than over horizontal terrain. Clark and Hopewood [14] built a Site-Specific Forecast Model (SSFM) using a one-dimensional version of the Met. Office Unified Model as a basis. They described the model

formulation and discussed its behavior by simulating radiation fog in idealized cases and its sensitivity to geotropic wind speed and initial humidity. Two and three dimensional idealized, east-west aligned valley are accomplished with the Regional Atmospheric Modeling System (RAMS) in Lehner and Gohm [15] experiments. The corresponding simulations showed an irregularity in wind flow and tracer circulation between the valley side walls according to the location of the slope with respect to the sun.

Nomenclature			
A	Aspect ratio (h/l)	x, y	Non-dimensional coordinates
H	Height of the cavity	x_s	Termination length
l	Length of the cavity	S	Stratified parameter
L	Length of the inclined surface	s	Non-dimensional Stratified parameter
g	Acceleration due to gravity	***Greek symbols***	
k	Thermal conductivity	κ	Thermal diffusivity
P	Pressure	β	Thermal expansion coefficient
p	Non-dimensional pressure	ν	Kinematic viscosity
Pr	Prandtl number	ρ	Density
Ra	Rayleigh number	ϕ	Angle
T	Temperature	τ	Non-dimensional time
T_w	Inclined surface temperature	τ_s	Steady-state Non-dimensional time
T_f	Fluctuating temperature	δ	Boundary layer thickness scale
$T_a(X)$	local ambient temperature at the distance X	δ_T	Thermal boundary layer thickness
$T_a(0.5L)$	Initial $T_a(X)$ at distance $X = 0.5L$	δ_v	Viscous boundary layer thickness
ΔT	Temperature difference between the surface and the ambient	δ_{Ts}	Quasi-steady state thermal boundary layer thickness
		δ_{vs}	Quasi-steady state viscous boundary layer thickness
t	Time	θ_f	Non-dimensional fluctuating temperature
U, V	Velocity components	θ_w	Non-dimensional inclined surface temperature
u, v	Non-dimensional velocity components	$\theta_a(x)$	Non-dimensional ambient temperature at the distance x
U_0	Non-dimensional velocity scale		
u_s	Steady-state velocity	$\Delta\theta_f$	Non-dimensional temperature difference between the surface and the ambient
X, Y	coordinates		

Similar to the valley case several researchers have studied flows and heat transfer in a triangular enclosure applicable to the attic space. Saha [16] investigated two dimensional transient natural convection flow inside an attic-shaped cavity for Pr >1. For non-instantaneous heating on the inclined walls, the temperature increased linearly up to a given steady value over a given time. The author has developed several flow regimes by scaling analysis, which are validated by direct numerical simulations. Studies for this type of geometric configuration have been conducted on two thermal driving situations; daytime heating [17, 18] and nighttime cooling [19-22].

Jaluria and Gebhart [23] investigated stability and transitional natural convection boundary layer flow in a stable ambient thermal stratified fluid. Henkes and Hoogendoorn [24] presented laminar natural convection boundary layer flow along a heated vertical plate in a stratified fluid for air. The effects of a linear semi-infinite ambient thermal stratification along a vertical plate of an unsteady natural convection boundary layer flow were studied by Lin et al. [25, 26] for small and large Prandtl number. They also developed scaling relations for the vertical natural convection flow in a stably stratified fluid.

In our present study, the development of the unsteady natural convection flows adjacent to uniformly heated inclined surfaces of a valley shaped cavity with linearly stratified fluid is investigated by scaling analysis and numerical simulation for fixed Prandtl number, Pr = 6.63 (water) and aspect ratio, $A = 4/11$with different stratification parameter s and Rayleigh number Ra.

FORMULATION OF THE PROBLEM

A transient two dimensional natural convection flow in a valley shaped triangular cavity with a stratified fluid for $Pr > 1$ has been considered. The physical model with boundary conditions is shown in Fig. 1. The height of the cavity is H and horizontal length is $2l$ and the length of the inclined surface is L. A fixed temperature, T_w has been imposed on both inclined surfaces. Initially the fluid in the ambient is stationary and linearly stratified with a constant temperature stratification number, $S = \frac{dT_a(X)}{dX} = \text{constant}$, where $T_a(X)$ is the fluid temperature dependent on X.

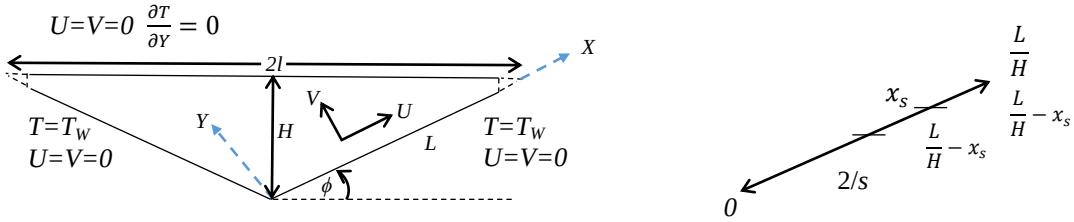

FIGURE 1. Schematic of the computational domain with boundary conditions.

The development of natural convection flows in the cavity is governed by the following two dimensional Navier Stokes with the Boussinesq approximation and energy equation:

$$\frac{\partial U}{\partial X} + \frac{\partial V}{\partial Y} = 0, \tag{1}$$

$$\frac{\partial U}{\partial t} + U\frac{\partial U}{\partial X} + V\frac{\partial U}{\partial Y} = -\frac{1}{\rho}\frac{\partial P}{\partial X} + \nu\left(\frac{\partial^2 U}{\partial X^2} + \frac{\partial^2 U}{\partial Y^2}\right) + g\beta\sin\phi\left(T - T_a(X)\right), \tag{2}$$

$$\frac{\partial V}{\partial t} + U\frac{\partial V}{\partial X} + V\frac{\partial V}{\partial Y} = -\frac{1}{\rho}\frac{\partial P}{\partial Y} + \nu\left(\frac{\partial^2 V}{\partial X^2} + \frac{\partial^2 V}{\partial Y^2}\right) + g\beta\cos\phi\left(T - T_a(X)\right), \tag{3}$$

$$\frac{\partial T}{\partial t} + U\frac{\partial T}{\partial X} + V\frac{\partial T}{\partial Y} = \kappa\left(\frac{\partial^2 T}{\partial X^2} + \frac{\partial^2 T}{\partial Y^2}\right). \tag{4}$$

The Temperature here is considered as, $T = T_f + T_a(X)$ where, T_f is the fluctuating temperature.
$\Delta T = T_w - T_a$ (0.5L); where, T_a (0.5L) = initial T_a (x) at the position, X = 0.5L. Therefore, equation (4) may be written,

$$\frac{\partial T_f}{\partial t} + U\frac{\partial T_f}{\partial X} + V\frac{\partial T_f}{\partial Y} + US = \kappa\left(\frac{\partial^2 T_f}{\partial X^2} + \frac{\partial^2 T_f}{\partial Y^2}\right). \tag{5}$$

The quantities in the above governing equations may be normalized as follows,

$$x = \frac{X}{H}, y = \frac{Y}{H}, u = \frac{U}{U_0}, v = \frac{V}{U_0}, \tau = \frac{t}{H/U_0}, p = \frac{P}{\rho U_0^2}, \theta_f = \frac{(T - T_a(X))}{\Delta T}, \tag{6}$$

where, $U_0 = \frac{\kappa Ra^{1/2}}{H}, Ra = \frac{g\beta\Delta T H^3}{\nu\kappa}, Pr = \frac{\nu}{\kappa}$, $S = \frac{dT_a(X)}{dX} = \frac{\Delta T}{H}\frac{d\theta_a(x)}{dx} = \frac{\Delta T}{H}s \Rightarrow s = \frac{HS}{\Delta T}$.

Non-dimensional form of the governing equations is

$$\frac{\partial u}{\partial x} + \frac{\partial v}{\partial y} = 0, \tag{7}$$

$$\frac{\partial u}{\partial \tau} + u\frac{\partial u}{\partial x} + v\frac{\partial u}{\partial y} = -\frac{\partial p}{\partial x} + \frac{Pr}{Ra^{1/2}}\left(\frac{\partial^2 u}{\partial x^2} + \frac{\partial^2 u}{\partial y^2}\right) + Pr\theta_f\sin\phi, \tag{8}$$

$$\frac{\partial v}{\partial \tau} + u\frac{\partial v}{\partial x} + v\frac{\partial v}{\partial y} = -\frac{\partial p}{\partial y} + \frac{Pr}{Ra^{1/2}}\left(\frac{\partial^2 v}{\partial x^2} + \frac{\partial^2 v}{\partial y^2}\right) + Pr\theta_f\cos\phi, \tag{9}$$

$$\frac{\partial \theta_f}{\partial \tau} + u\frac{\partial \theta_f}{\partial x} + v\frac{\partial \theta_f}{\partial y} + us = \frac{1}{Ra^{1/2}}\left(\frac{\partial^2 \theta_f}{\partial x^2} + \frac{\partial^2 \theta_f}{\partial y^2}\right). \tag{10}$$

SCALING ANALYSIS

A simple scaling analysis of the thermal boundary layer near the inclined surface developing to the steady state is presented. We consider the boundary layer thickness scale δ, length scale L, x-velocity scale u, y-velocity scale v, time scale τ and assume $\delta << L$.

Figure 1 shows the position (x_s) at which the temperature of the wall is equal to that of the neighbouring initially stratified fluid.

$$x_s = 0.5\frac{L}{H} + \frac{\theta_w}{s}, \tag{11}$$

$$\theta_w = \left(x_s - 0.5\frac{L}{H}\right)s = \theta_a(x_s). \tag{12}$$

Then,

$$\theta_a(x) = \left(x - 0.5\frac{L}{H}\right)s. \tag{13}$$

We have $v << u$ and $\delta << x_s$ in the thermal boundary layer above the inclined wall. The analysis is firstly limited to the region $0 \le x \le x_s$ and then it will be extended to the remaining region $x_s \le x \le L/H$.

Balancing the unsteady and diffusion terms in equation (10):

$$\frac{\Delta\theta_f}{\tau} \sim \frac{1}{Ra^{1/2}}\frac{\Delta\theta_f}{\delta_T^2} \qquad => \delta_T \sim Ra^{-1/4}\tau^{1/2} \tag{14}$$

The thickness scaling is effective untill the convection terms become significant. In the equation (8) the order of the unsteady inertia term, the viscous term and the advection term of the x momentum is $O\left(\frac{u}{\tau}\right)$, $O\left(\frac{Pr}{Ra^{1/2}}\frac{u}{\delta_T^2}\right)$ and $O\left(\frac{u^2}{x}\right)$respectively and the buoyancy force is $O\left(Pr\Delta\theta_f \sin\phi\right)$. For sufficiently small time the ratio of the advection to unsteady term in equation (8) is $\frac{\text{advection term}}{\text{unsteady term}} \sim \frac{u^2/_x}{u/_\tau} \sim \frac{u\tau}{x}$ and much smaller. Therefore, advection term is not significant at this stage. The ratio of the inertia to viscous term is $\frac{u/_\tau}{\frac{Pr}{Ra^{1/2}}\frac{u}{\delta_T^2}} \sim \frac{1}{Pr}$. For Pr >>1, inertia term is much smaller than the viscous term. So, the buoyancy term is balanced by the viscous term in equation (8)

$$\frac{Pr}{Ra^{1/2}}\frac{u}{\delta_T^2} \sim Pr\Delta\theta_f \sin\phi \qquad => u \sim \Delta\theta_f(x)\sin\phi\,\tau, \tag{15}$$

where, $\Delta\theta_f(x) = \theta_w - \theta_a(x) = \theta_w - \left(x - 0.5\frac{L}{H}\right)s$.

For the ratio of the advection to diffusion term in x momentum equation (8) over thermal layer thickness is much smaller than unity.

$$\frac{u^2/x}{Pru/Ra^{\frac{1}{2}}\delta_T^2} \sim \frac{uRa^{\frac{1}{2}}\delta_T^2}{Prx} \sim \frac{\Delta\theta_f \sin\phi\,\tau Ra^{\frac{1}{2}}Ra^{-\frac{1}{2}}\tau}{Prx} < 1 \quad => \tau < \left(\frac{Prx}{\Delta\theta_f \sin\phi}\right)^{1/2}, \tag{16}$$

Vorticity is diffused into the core and generating viscous layer of thickness δ_v.

$$\frac{\text{inertia term}}{\text{diffusion term}} \sim \frac{\frac{u}{\tau}}{Pru/Ra^{\frac{1}{2}}\delta_v^2} \sim 1 \quad => \frac{u}{\tau} \sim Pru/Ra^{\frac{1}{2}}\delta_v^2 \quad => \delta_v^2 \sim Pr\tau/Ra^{\frac{1}{2}} \quad => \delta_v \sim Pr^{1/2}\delta_T. \tag{17}$$

That is outer viscous layer dominated by a inertia-viscous balance and inner thermal layer dominated by an buoyancy -viscous balance for $Pr > 1$.

Heat is also being convected adjacent to the inclined surface by the velocity (15) and the boundary layer will grow until conduction balances convection. The order of convection and the conduction terms in the normalised energy equation (10) is $O\left(\frac{u\Delta\theta_f}{x} + us\right)$ and $O\left(\frac{1}{Ra^{1/2}}\frac{\Delta\theta_f}{\delta_T^2}\right)$. Using (14) and (15) this balance yields a time scale of the unsteady thermal boundary layer at distance x in the section $0 \le x \le x_s$.

$$\frac{u\Delta\theta_f}{x} + us \sim \frac{1}{Ra^{1/2}}\frac{\Delta\theta_f}{\delta_T^2} \quad => u\left(\frac{\Delta\theta_f}{x} + s\right) \sim \frac{1}{Ra^{1/2}}\frac{\Delta\theta_f}{Ra^{-1/2}\tau} \quad => \Delta\theta_f \sin\phi\,\tau\left(\frac{\Delta\theta_f}{x} + s\right) \sim \frac{\Delta\theta_f}{\tau},$$

$$=> \tau_s(x) \sim \left(\left(\frac{\Delta\theta_f}{x} + s\right)\sin\phi\right)^{-1/2}. \tag{18}$$

Assume, $\theta_w = 1$, so

$$\tau_s(x) \sim \left(A/\sqrt{1+A^2} + 0.5s\right)^{-1/2} x^{1/2}. \tag{19}$$

At that time the quasi-steady state velocity and boundary layer thickness scale at height x have becomes:

$$u_s(x) \sim \left(A/\sqrt{1+A^2} - \left(x\,A/\sqrt{1+A^2} - 0.5\right)s\right)\left(A/\sqrt{1+A^2} + 0.5s\right)^{-1/2} x^{1/2}, \tag{20}$$

and

$$\delta_{Ts}(x) \sim Ra^{-1/4}\left(A/\sqrt{1+A^2}+0.5s\right)^{-1/4} x^{1/4}. \tag{21}$$

Since, $\tau < \left(\frac{Prx}{\Delta\theta_f \sin\phi}\right)^{1/2}$ for $Pr > 1$, the diffusion of momentum of the inner thermal layer upholds the outer viscous layer; where,

$$\delta_{vs} \sim \frac{Pr^{1/2}\tau_s{}^{1/2}}{Ra^{1/4}} \sim Pr^{1/2}\delta_{Ts}\,, \tag{22}$$

the advection and diffusion of vorticity balance with time τ_s.

When x is in the range $x_s \le x \le L/H$, we can say that the flow models in the boundary layer are almost similar about the horizontal line that passes through the seperation point to those in the region $2/s \le x \le x_s$. So the above scalings are also effective for the region $x_s \le x \le L/H$ but in these equations x should be replaced by $(2x_s - x) = (1+2/s - x)$.

When $s = 0$ and $\phi = \pi/2$, that is the environment is homogenous and the surface becomes vertical, the scaling relations (19) – (21) become $\tau_s \sim x^{\frac{1}{2}},\ u_s \sim x^{\frac{1}{2}},\ \delta_{Ts} \sim Ra^{-1/4}x^{1/4}$.

Lin and Armfield [27] got these scalings for the full development of the thermal boundary layer of natural convection flow in a homogenous fluid in a cavity.

In the region $x_s \le x \le L/H$ heat is completely conducted conversely into the ambient fluid from the region $0 \le x \le x_s$; so the net heat transfer in the upper region $2/s \le x \le L/H$ is almost zero and the mean Nusselt number $\overline{Nu}$ on the inclined surface is

$$\overline{Nu} = \int_0^{2/s} \frac{\partial\theta_f(x)}{\partial x}dx = \int_0^{2/s} \frac{\Delta\theta_f(x)}{\delta_\tau(x)}dx. \tag{23}$$

During the developing stage and fully developed stage $\overline{Nu}$ becomes

$$\overline{Nu} = \frac{Ra^{1/4}}{\tau^{1/2}}\frac{L}{H}, \tag{24}$$

and

$$\overline{Nu} = f(A,s)\, Ra^{1/4}, \tag{25}$$

where

$$f(A,s) = \frac{2^{11/4}}{21}\left[\frac{A}{\sqrt{1+A^2}}+0.5s\right]^{1/4}\left[1+\frac{7}{2}\frac{\sqrt{1+A^2}}{A}s\right]s^{-3/4}. \tag{26}$$

We choose $A = 4/11$and for $1 \le s \le 6$ has an almost linear relation with s. Hence, (25) may be approximated by

$$\overline{Nu} = s\, Ra^{1/4}. \tag{27}$$

NUMERICAL VALIDATION

For the scaling validation, we have performed a number of numerical simulations using the finite volume method with the SIMPLE scheme. To set the linear stratification, Equation (4) has been transformed to Equation (5). We discretized the advection term using the QUICK scheme (see [28]). The viscous terms are discretized using second order central difference scheme. To solve the unsteady term we used second order implicit time-marching scheme. A computational grid is used to divide the domain into discrete control volumes. We integrate the governing equations over the individual control volumes constructing algebraic equations for the discrete dependent variables such as velocities, pressure and temperature.

RESULT AND DISCUSSION

In the Figure 2, the numerical results of the maximum velocity in the initial stage at different positions in $0 \le x \le L/H$ for different values of s with $Ra = 1.99 \times 10^8$ are used to validate with the scaling relation (20). The approximately linear relation between the theoretical and numerical results shows a good agreement. In Fig. 3 $\overline{Nu}\, Ra^{1/4}$ is plotted against s in the initial stage ($\tau = 16$ for $Ra = 1.99 \times 10^8$). The scaling for $\overline{Nu}$ is also in excellent agreement with the numerical results.

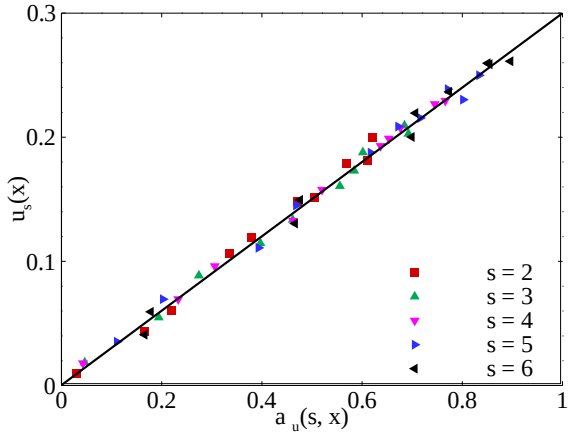

FIGURE 2. $u_s(x)$ plotted against $a_u(s,x)$ at Ra = 1.99 ×10^8, for $0 \le x \le x_s$ and $x_s \le x \le L/H$.

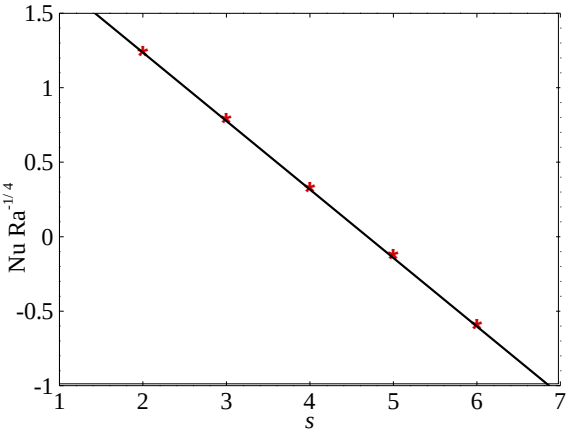

FIGURE 3. $\overline{Nu}\ Ra^{-1/4}$ plotted against s for Ra = 1.99 ×10^8 at initial stage non-dimensional flow time τ = 16.

(a) (b)

FIGURE 4. Streamtrace-Isotherms for (a) Ra = 2.26×10^9 and (b) Ra = 2.26×10^5 at τ = 10 with the same temperature range from θ = 0.0265 to θ = 0.9947.

The streamlines and temperature contours at τ = 10 are plotted in Fig. 4 where $x_s \approx 1.606$ for Ra = 2.26 ×10^9 and $x_s \approx 1.346$ for Ra = 2.26 ×10^5, A = 4/11 and s = 1. Two opposite natural convection boundary layer flows are initiated showing by arrow sign and at each height the thermal boundary layers grow for a period of time in a temperature range θ = 0.0265 to θ = 0.9947.

CONCLUSIONS

Natural convection flows in a valley shaped cavity initially filled by a stratified fluid is investigated using scaling analysis and numerical simulations. The scaling relations are obtained based on the defined stratified parameter s for the mean Nusselt number $\overline{Nu}$ on the inclined surface and the positions x for the maximum velocity inside the boundary layer $u_s(x)$ on the inclined wall. It has been demonstrated that the scaling predictions are consistent with the numerical results.

REFERENCES

1. A. Bejan, *Convective Heat Transfer* (Wiley & Sons, 2004).
2. G. Palani, J. D. Kirubavathi and K. Y. Kim, Thermophysics and Aeromechanics **21,** 65-85 (2014).
3. C. H. Chen, Acta Mechanica **172,** 219-235 (2004).
4. P. Ganesan, and G. Palani, International Journal of Heat and Mass Transfer **47,** 4449-4457 (2004).
5. S. C. Saha, J. C. Patterson, and C. Lei, International Journal of Thermal Sciences **49,** 1600-1612 (2010).
6. S. C. Saha, J. C. Patterson, and C. Lei, Journal of Heat Transfer, **133,** 1-9 (2011).
7. S. C. Saha, J. C. Patterson, and C. Lei, International Journal of Heat and Mass Transfer **53**, 5156-5166 (2010).
8. S. C. Saha, R. J. Brown, and Y. T. Gu, International Journal of Heat and Mass Transfer **55,** 2394-2401 (2012).
9. J. Patterson, and J. Imberger, J. Fluid Mech. **100**, 65-86 (1980).
10. M. Princevac, and H. J. S. Fernando, J. Fluid Mech. **616**, 99-109 (2008).
11. C. Reuten, D. G. steyn, and S. E. allen, Journal of Geophysical Research **112**, 1-17 (2007).
12. P. A. Clark, and W. P. Hopwood, Meteorol Appl. **8**, 279-286 (2001).
13. S. C. Saha, Energy and Buildings **43**, 2908-2917 (2011).
14. R.D. Flack, ASME Journal of Heat Transfer **102**, 770-772 (1980).
15. S.C. Saha, J.C. Patterson, and C. Lei, Heat and Mass Transfer **46**, 621-638 (2010).
16. W. Lin, S.W. Armfield, and P.L. Morgan, International Journal of Heat and Mass Transfer **45**, 451-459 (2002).
17. W. Lin, and S.W. Armfield, International Journal of Heat and Mass Transfer **42,** 4117-4130 (1999).
18. B.P. Leonard, S. Mokhtari, ULTRA-SHARP Nonoscillatory Convection Schemes for High-Speed Steady Multidimensional Flow, NASA TM 1-2568 (ICOMP-90-12), NASA Lewis Research Centre, 1990.

ICME2015

International Conference on Mechanical Engineering 2015
(ICME 2015) 18 – 20 December, 2015, Dhaka, Bangladesh

Paper ID : 343

MHD Mixed Convection Analysis in an Open Channel by Obstructed Poiseuille Flow of Non-Newtonian Power Law Fluid

Khan Md. Rabbi [a)], Tawfiqur Rakib[b)], Sourav Das[c)], Satyajit Mojumder[d)] , Sourav Saha[e)]

Department of Mechanical Engineering, Bangladesh University of Engineering and Technology, Dhaka-1000, Bangladesh

[a)]Corresponding author: khanrabbi92@gmail.com
[b)] tawfiq1448@gmail.com
[c)] dsourav46@yahoo.com
[d)]sjit018@gmail.com
[e)]souravsahame17@gmail.com

Abstract. This paper demonstrates magneto-hydrodynamic (MHD) mixed convection flow through a channel with a rectangular obstacle at the entrance region using non-Newtonian power law fluid. The obstacle is kept at uniformly high temperature whereas the inlet and top wall of the channel are maintained at a temperature lower than obstacle temperature. Poiseuille flow is implemented as the inlet velocity boundary condition. Grid independency test and code validation are performed to justify the computational accuracy before solving the present problem. Galerkin weighted residual method has been appointed to solve the continuity, momentum and energy equations. The problem has been solved for wide range of pertinent parameters like Richardson number (Ri = 0.1 - 10) at a constant Reynolds number (Re = 100), Hartmann number (Ha = 0 - 100), power index (n = 0.6 - 1.6). The flow and thermal field have been thoroughly discussed through streamline and isothermal lines respectively. The heat transfer performance of the given study has been illustrated by average Nusselt number plots. It is observed that increment of Hartmann number (Ha) tends to decrease the heat transfer rate up to a critical value (Ha = 20) and then let increase the heat transfer performance. Thus maximum heat transfer rate has been recorded for higher Hartmann number and Rayleigh number in case of pseudo-plastic (n = 0.6) non-Newtonian fluid flow.

INTRODUCTION

Magneto-hydrodynamic (MHD) mixed convection has been a matter of huge interest and investigation among the researchers [1]. MHD convection through a channel has its wide range of applications especially in the field of blood flow [2, 3] and geothermal system [4]. MHD mixed convection simulation in cavities on different fluids and boundary conditions has been studied by various numerical methods widely [5]. The flow of non-Newtonian power law fluid has largely useful application in many process industries [6] and also in bio-medical Engineering [7] and Peristaltic transports [8]. Mixed convection of non-Newtonian nanofluid in a lid-driven cavity with sinusoidal temperature profile was investigated by Kefayati et al. [9]. It was observed that the introduction of nanoparticle increases heat transfer for various Richardson number and power law index and also showed the augmentation of heat transfer with the drop of power law index. Abo-Eldahab et al. [10] investigated MHD flow and heat transfer of non-Newtonian power-law fluid with diffusion and chemical reaction on a moving cylinder. It was concluded that the effect of magnetic field over power law indices on a moving cylinder. El-Kabeir et al. [11] performed the investigation on heat and mass transfer by MHD stagnation-point flow of a power law fluid towards a stretching surface and represented the result for the velocity, temperature, concentration profile, local Nusselt number and local

Sherwood number illustrating the effect of Hartmann number, power law index and Richardson number. It was found that local Nusselt number and local Sherwood number decreased due to the increase of magnetic field parameter and also increased with the increase of power law index and Richardson number. MHD convection of Poiseuille flow has been a topic for huge investigation and research [12, 13]. Singh et al. [14] analyzed oscillatory rotating MHD Poiseuille flow with injection and Hall currents. It was shown that the increment of Reynolds number increased the variation of velocity profile in case of rotational and non-rotational channel.

This study aims to investigate MHD mixed convection Poiseuille flow through a channel with a rectangular obstacle at the entrance region using non-Newtonian power law fluid. Because of magnetic field as well as the rectangular obstacle in the open channel, average heat transfer shows different phenomena which can be useful in different applications. The flow, thermal field and overall heat transfer has been illustrated by analyzing effect of various Hartmann number and power law index with the alternation of other pertinent parameters with related plots.

PROBLEM SPECIFICATION

The details of the problem are presented in Figure 1. In the figure, rectangular shape geometry of an open channel having *5L* length and *L* breadth is considered. Flow coming in from the left and going out through the right Channel. The obstacle is of 0.6L height and is placed at 1.2*L* length after the inflow in *X* direction. Inlet and top wall of the channel is kept at low temperature ($T = T_c$), while the lower wall is kept adiabatic. External magnetic field of density B is acting on the horizontal negative axis. Gravity is working along the negative *Y* axis.

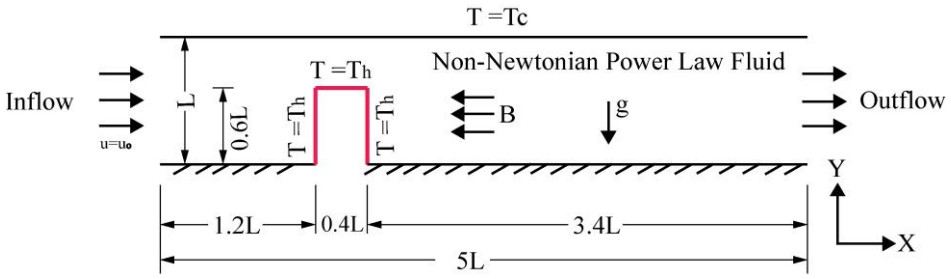

FIGURE 1. Schematic diagram of an open channel with obstruction.

MATHEMATICAL FORMULATION

Conservation equation of mass, momentum and energy in a two dimensional Cartesian coordinate system can be written in non-dimensional form as follows:

$$\frac{\partial u}{\partial x}+\frac{\partial v}{\partial y}=0, \tag{1}$$

$$\left(u\frac{\partial u}{\partial x}+v\frac{\partial u}{\partial y}\right)=-\frac{\partial P}{\partial x}+\frac{\Pr}{\sqrt{Ra}}\left[2\frac{\partial}{\partial x}\left(\frac{\mu_a}{K}\frac{\partial u}{\partial x}\right)+\frac{\partial}{\partial y}\left(\frac{\mu_a}{K}\left(\frac{\partial u}{\partial y}+\frac{\partial v}{\partial x}\right)\right)\right], \tag{2}$$

$$\left(u\frac{\partial v}{\partial x}+v\frac{\partial v}{\partial y}\right)=-\frac{\partial P}{\partial y}+\frac{\Pr}{\sqrt{Ra}}\left[2\frac{\partial}{\partial y}\left(\frac{\mu_a}{K}\frac{\partial v}{\partial y}\right)+\frac{\partial}{\partial x}\left(\frac{\mu_a}{K}\left(\frac{\partial u}{\partial y}+\frac{\partial v}{\partial x}\right)\right)\right]-\frac{\mathrm{PrHa}^2}{\sqrt{Ra}}v, \tag{3}$$

$$u\frac{\partial \Theta}{\partial x}+v\frac{\partial \Theta}{\partial y}=\frac{1}{\sqrt{Ra}}\left(\frac{\partial^2\Theta}{\partial x^2}+\frac{\partial^2\Theta}{\partial y^2}\right), \tag{4}$$

In order to get the numerical solution of the system following scales are implemented to get the non-dimensional governing equations-

$$x=\frac{\bar{x}}{\overline{5L}}, y=\frac{\bar{y}}{\bar{L}}, \mathrm{u}=\frac{\bar{u}}{\left(\frac{\alpha}{\overline{5L}}\right)Ra^{0.5}}, \mathrm{v}=\frac{\bar{v}}{\left(\frac{\alpha}{\bar{L}}\right)Ra^{0.5}}, P=\frac{\bar{P}}{\rho\left(\frac{\alpha}{\overline{5L}}\right)^2 Ra}, \Theta=\frac{T-T_c}{T_h-T_c}, \tag{5}$$

For a purely-viscous non-Newtonian fluid according to Ostwald–DeWaele power-law model [15], the shear stress tensor can be expressed as-

$$\tau_{ij}=2\mu_a D_{ij}=\mu_a\left(\frac{\partial\bar{u}_i}{\partial\bar{x}_j}+\frac{\partial\bar{u}_j}{\partial\bar{x}_i}\right), \tag{6}$$

Here, D_{ij} indicates the rate-of-deformation tensor for the two dimensional Cartesian coordinate and μ_a is the apparent viscosity that is derived for the two-dimensional Cartesian coordinates as

$$\bar{\mu}_a=K\left[2\left[\left(\frac{\partial\bar{u}}{\partial\bar{x}}\right)^2+\left(\frac{\partial\bar{v}}{\partial\bar{y}}\right)^2\right]+\left(\frac{\partial\bar{v}}{\partial\bar{x}}+\frac{\partial\bar{u}}{\partial\bar{y}}\right)^2\right]^{\frac{(n-1)}{2}}. \tag{7}$$

In the above equations $(\bar{u},\bar{v}),T$ and P are the dimensional velocities, temperature and pressure respectively, ρ is the density, σ is the electrical conductivity, B is the uniform magnetic field, and n is the power-law index. Therefore, the deviation of n from unity indicates the degree of deviation from Newtonian behaviour. Boundary conditions used to solve the present problem are mentioned in Table 1.

TABLE 1. Boundary conditions in non-dimensional form.

Boundary Wall	Flow Field	Thermal Field
Top wall	u = 0,v = 0	Θ = 0
Bottom wall excluding the obstacle	u = 0,v = 0	∂T/∂X = 0
Obstacle wall	u = 0,v = 0	Θ = 1
Inlet	u = 8y(y-1),v = 0	Θ = 0
Outlet	u = 0, ∂u/∂x = 0	Convective heat flux

The non-dimensional governing parameters used are Prandtl number (*Pr*), Hartmann number (*Ha*) and Reynolds number (Re) which are defined below-

$$Pr=\frac{\nu}{\alpha}; Ha=\sqrt{\frac{\sigma_n B^2(5L)^2}{\nu_n\rho_n}}; \mathrm{Re}=\frac{\rho uL}{\mu}, \tag{8}$$

The characteristics of heat transfer are obtained by average Nusselt number and can be expressed as-

$$Nu_{av}=-\int_0^1\frac{\partial T}{\partial Y}dX, \tag{9}$$

NUMERICAL PROCEDURE

Numerical Method

The Galerkin weighted residual finite element method (FEM) has been deployed to the present problem to obtain a numerical solution. A set of algebraic equations has been formulated and the iterative process is used to solve this algebraic equation set. Triangular mesh formulation has been used to discretize the entire domain into several elements. Converging nature of the numerical solution has been confirmed and the converging criteria used is $|\mathbf{\Gamma}^{n+1}-\mathbf{\Gamma}^{n}|\le 10^{-6}$, n is the number of iteration and is general dependent variable.

Grid Independency Test and Validation of Code

An extensive mesh testing procedure is conducted to guarantee a grid independent solution. To check the accuracy of the numerical solution several mesh element numbers (1554, 2442, 4426, 6810 and 11698) have been

checked. From the Fig. 2, it is seen that mid-plane Y-velocity profiles after grid elements of 6810 and 11698 almost overlap each other thus making the solution grid independent. So, grid size of 6810 mesh elements is considered to be the optimum for the present study and other numerical simulation has been carried out taking this grid as independent.

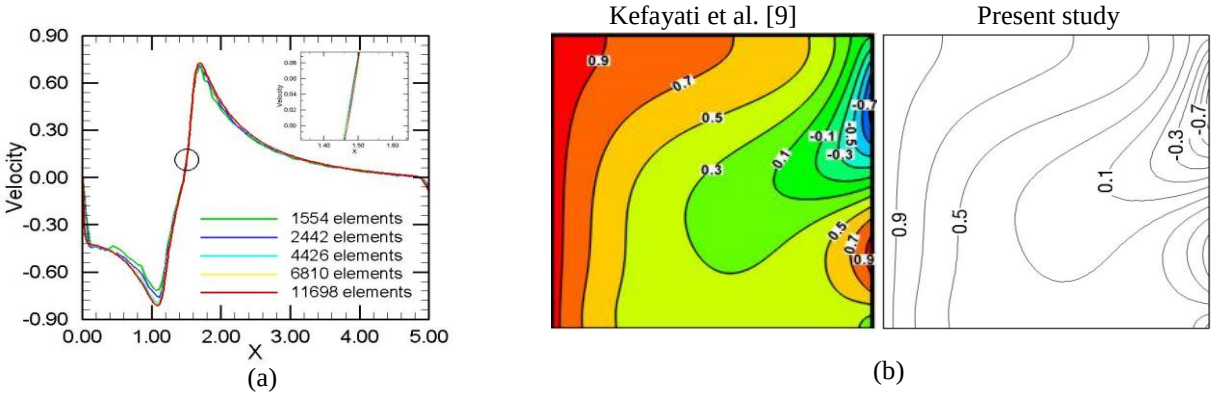

(a) (b)

FIGURE 2. (a) Variation of mid-plane Y velocity (V) with X at *Ha* = 20, *Ri= 1* and *Pr* = 10 and (b) Comparison of the isotherms for $Ra = 10^5$ and *Ha* = 60 between numerical results by Kefayati et al. [9] and the present results.

Code validation is done in light of isotherm and is validated with the consequences of Kefayati et al. [9] at $Ra = 10^5$ and *Ha* = 60 in Fig 2b. From the figure, it is evident that present result is completely in par with the previous study. So, the present numerical code and solution procedure are completely reliable and so is the numerical solution.

RESULT AND DISCUSSION

Effect of Power Law Index and Hartmann Number on Streamline and Isotherm Contours

The flow is represented by the streamlines in Fig. 3 where the effect of Hartmann number and power law index is considered. It is seen that a small vortex is appeared at the left side of the channel in the absence of the magnetic field due to the domination of the buoyancy force. With the increase of Hartmann number, the vortex is disappeared because of retardation of magnetic field in the flow. As the power law index increases, the eddy inside the channel becomes weaker. So it reveals the fact that heat transfer is stronger for pseudo-plastic fluid ($n < 1$) and weaker for dilatant fluid ($n > 1$).The temperature difference is predicted by isotherm in Fig. 4 by considering the effect of Hartmann number and power law index. In the absence of magnetic field, the isothermal lines form a thin boundary layer near the obstacle. But the lines are drastically changed and distorted away from the obstacle with the increase of Hartmann number. Because higher magnetic field distorts by suppressing the buoyancy force and thus ensures better heat transfer. It is also observed that more distorted and intensified isothermal lines are obtained at lower power law index representing convective dominance. So when the power law index is diminished to $n = 1.6$, weaker flow and thermal field is obtained.

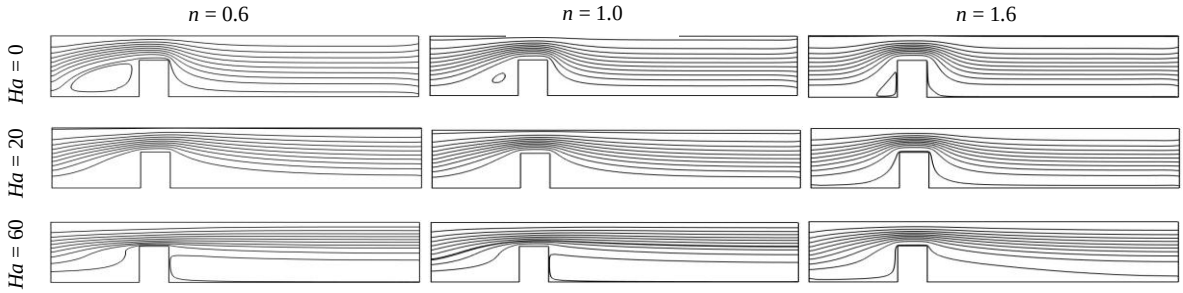

FIGURE 3. Effect of power law index and Hartmann number on streamline contours at *Ri* = 1.

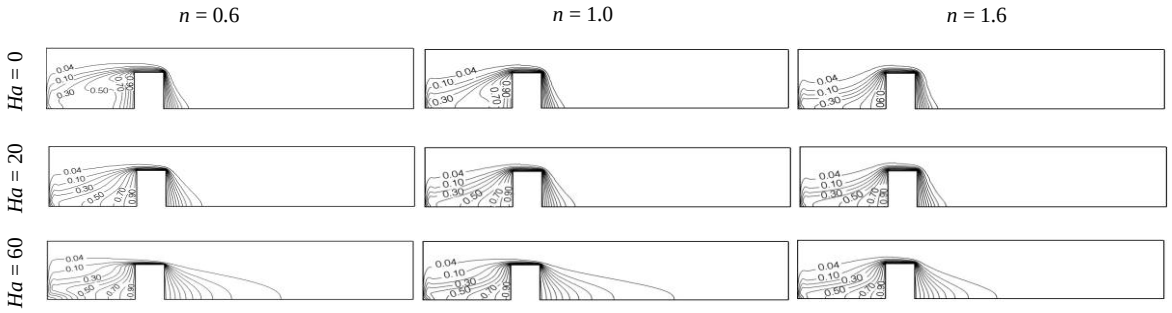

FIGURE 4. Effect of power law index and Hartmann number on isotherm contours at *Ri* = 1

Effect of Hartmann Number on Average Nusselt Number for Different Parameters

In Fig. 5a, average Nusselt number is plotted against different Hartmann number at various power law index (*n* = 0.6, 1.0, 1.6) for *Ri* = 1.0 and *Re* = 100. It is found that heat transfer initially decreases with the increase of Hartmann number. At *Ha* = 10, heat transfer starts to increase with the increase of Hartmann number for pseudoplastic fluid (*n* = 0.6) and Newtonian fluid (*n* = 1.0). This is because of the dominance of magnetic field in the cavity at the respective power law indices. For dilatant fluid (*n* = 1.6), heat transfer remains decreasing even after *Ha* = 10 because of the lower convective flow and thermal gradient. Though, at *Ha* > 60, heat transfer increases slightly due to prominent effect of magnetic field in the cavity. An interesting intersection is found at *Ha* = 10 for Newtonian and dilatant fluid.

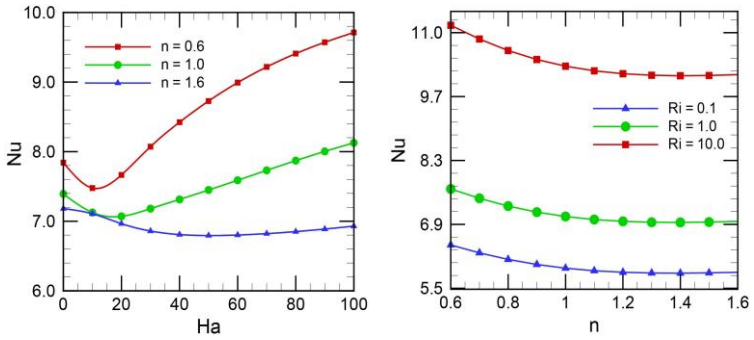

FIGURE 5. Variation of average Nusselt number with (a) Hartmann number at *Ri* = 1, *Re* = 100 and (b) power law index (*n*) at *Ha* = 20.

Effect of Power Law Index on Average Nusselt Number for Different Parameters

The heat transfer is evaluated in terms of Nusselt number (*Nu*) which is illustrated in Fig. 5b showing the effect of power law index at different Richardson number (*Ri* = 0.1, 1.0, 10.0). With the increase of power law index, it is evident that heat transfer decreases due to strong convective flow and high thermal gradient. At *Ri* = 10.0, best possible heat transfer is obtained because of the dominant buoyancy force. With the decrease of Richardson number, flow gradient becomes more effective and thus heat transfer decreases.

CONCLUSION

Addressing to the effect of different pertinent parameters in this study, several concluding remarks are drawn. Pseudo-plastic fluid (*n* < 1) shows better heat transfer rate than Newtonian fluid and dilatant fluid. At *Ha* > 10, the dominance of magnetic field becomes more visible for pseudo-plastic fluid (*n* = 0.6) and Newtonian fluid (*n* = 1.0). At higher strength of magnetic field (*Ha* = 100), non-Newtonian pseudo-plastic fluid shows better heat transfer rate (more than 42%). Thus better heat transfer has been achieved for non-Newtonian pseudo-plastic fluid at higher strength of magnetic field (*Ha* = 100) and higher Richardson number (*Ri* = 10).

ACKNOWLEDGMENTS

The authors would like to take an opportunity to thank Multiscale Mechanical Modeling and Research Network (MMMRN) for their continuous support and thoughtful insight and advice.

REFERENCES

1. M .M. Rahman and S. Parvin and R. Saidur, N.A. Rahim, Int. Commun. Heat Mass Trans. **38**, 184-193 (2011).
2. G.R. Kefayati, Pow. Tech. **253**, 325-337 (2014).
3. M. Hatami and J. Hatami and D. D. Ganji, Comp. Meth. Prog. Bio. **113**, 632-641 (2014).
4. A. J. Chamkha, Int. J. Numer. Meth. Heat Fluid Flow. **11**, 430-448 (2001).
5. O. D. Makinde and A. Aziz, Int. J. Therm. Sci. **49** (2010).
6. R. P. Chhabra and J.F. Richardson, *Non-Newtonian flow in The Process Industries: Fundamentals and Engineering Applications*, (Butterworth-Heinemann, Oxford, 1999).
7. L. M. Srivastava and V. P. Srivastava, Annals Bio. Eng. **13**, 137-153 (1985).
8. S. Srinivas and M. Kothandapani, App. Math. Comput. **213**, 197-208 (2009).
9. G. R. Kefayati, Pow. Tech. **266**, 268-281 (2014).
10. E. M. Abo-Eldahab and A. M. Salem, Heat Mass Trans. **41**, 703-708 (2005).
11. S. M. M. El-Kabeir and A. Chamkha, Int. J. Chem. Reac. Engg. **8** (2010).
12. S. H. Hashemabadi and S. G. Etemad and J. Thibault, Int. J. Heat Mass Trans. **47**, 3985-3991 (2004).
13. A. Setayesh and V. Sahai, Int. J. Heat Mass Trans. **33**, 1711-1720 (1990).
14. K. D. Singh and R. Pathak, Proceedings of the Indian National Science Academy **76**, 201 (2010).
15. H. Ozoe and S. W. Churchill, AlChe. J. **18**, 1196 – 1207 (1972).

ICME2015

International Conference on Mechanical Engineering 2015
(ICME 2015) 18 – 20 December, 2015, Dhaka, Bangladesh

Paper ID : 344

Effect of First and Second Generation Biodiesel Blends on Engine Performance and Emission

A. K. Azad[1, a)], M. G. Rasul[1, b)], M.M.K. Bhuiya[1, c)] and Rubayat Islam[2, d)]

[1]School of Engineering and Technology, Central Queensland University, Rockhampton, QLD 4702, Australia.
[2]*Department of Mechanical Engineering, Bangladesh University of Engineering and Technology, Dhaka-1000, Bangladesh.*

[a)]Corresponding author: azad.cqu@gmail.com / a.k.azad@cqu.edu.au
[b)]m.rasul@cqu.edu.au
[c)]m.bhuiya@cqu.edu.au
[d)]rubayat12@yahoo.com

Abstract. The biodiesel is a potential source of alternative fuel which can be used at different proportions with diesel fuel. This study experimentally investigated the effect of blend percentage on diesel engine performance and emission using first generation (soybean) and second generation (waste cooking) biodiesel. The characterization of the biodiesel was done according to ASTM and EN standards and compared with ultralow sulfur diesel (ULSD) fuel. A multi-cylinder test bed engine coupled with electromagnetic dynamometer and 5 gas analyzer were used for engine performance and emission test. The investigation was made using B5, B10 and B15 blends for both biodiesels. The study found that brake power (BP) and brake torque (BT) slightly decreases and brake specific fuel consumption (BSFC) slightly increases with an increase in biodiesel blends ratio. Besides, a significant reduction in exhaust emissions (except NOx emission) was found for both biodiesels compared to ULSD. Soybean biodiesel showed better engine performance and emissions reduction compared with waste cooking biodiesel. However, NOx emission for B5 waste cooking biodiesel was lower than soybean biodiesel.

INTRODUCTION

World energy demand is increasing day-by-day. Transport sector is one of the energy and emission intensive sector in the world which mainly consumes liquid fuels. The resources of the liquid fuels are decreasing gradually. To mitigate this energy demand, scientists and engineers are exploring alternative source of energy, like biodiesel. It is an eco-friendly and renewable source of energy. It can be a potential and sustainable alternative source of fossil fuel with significant lower emission of greenhouse gases [1]. To find out suitability of this biodiesel as an alternative source of energy for compression ignition (CI) engine is an important research topic now-a-days. The use of biodiesel is increasing day-by-day [2, 3]. This increasing energy demand should be met by different sources of biodiesel such as edible and non-edible sources [4, 5]. Itmainly comes from renewable plant or animal fats (tallow) that contain fatty acids [6, 7]. These fatty acids are converted into biodiesel using transesterification reaction [8, 9]. A wide array of feedstocksare available to produce biodiesel such as waste cooking oil, edible and non-edible oil seeds, wood and wood waste etc. [10-12]. Research and development is also ongoing to produce biodiesel from microalgae also called third generation biodiesel[13], however, this is still in the development stage. Biodiesel can be used directly in diesel engines without any modification of engine combustion chamber [14]. The common way ofusing biodiesel into CI engine is by blending it at different proportion with petroleum diesel fuel [15]. The literatures reported that biodiesel has low emission of greenhouse gases compared with petroleum based diesel fuel [16-18]. It also has bio-lubricity capability which leads total engine life time [19]. So, biodiesel is an ecofriendly fuel which saves environment by reducing harmful emission as well as it can contribute to economy [16, 20, 21]. It has some generations namely, first,

second and third generation [22]. First generation biodiesel is produced from edible food crops such as mustard oil [23, 24], canola oil [25], sun flower oil etc. [26, 27]. Second generation biodiesel is produced from non-edible feedstocks[28-31]. As food crops are not used to make second generation biodiesel, this type of fuel is more commonly used because it is a more efficient and viable option [22, 32, 33]. Third generation biodiesel is produced from microalgae [13]. The research on biodiesel is important from socio, economic and environmental point of view.

Thisstudy investigated the effect of biodiesel blends on diesel engine performance and emission using first generation and second generation biodiesel with ultralow sulfur diesel (ULSD). Brake power (BP), brake torque (BT), and brake specific fuel consumption (BSFC) were determined as engine performance parameters and CO, CO_2, HC and NO_x were studied as emission parameters. There were three types of biodiesel blends namely, B5, B10 and B15 used for this experimental study.

Nomenclature

CO_2 [%]	Carbon-di-oxide emission in exhaust gas
CO [%]	Carbon monoxide emission in exhaust gas
HC [ppm]	Hydrocarbon emission
NOx [ppm]	Nitrogen oxides emission
B5 [-]	5% biodiesel, 95% diesel, by volume
B10 [-]	10% biodiesel, 90% diesel, by volume
B15 [-]	B15% biodiesel, 85% diesel, by volume
BSFC [kg/kw.h]	Brake specific fuel consumption

METHODOLOGY

The Kubota V3300, 4 stroke, 4 cylinder diesel engine coupled with electromagnetic dynamometer was used as the test bed engine for this study. The rated power output of the engine is 50.7 kW at 2600rpm and the rated torque is 230Nm at 1400rpm. The exhaust gas analyzer (EGA) that was used during testing is an Andros 6241A, 5 gas analyzer. This EGA can measure carbon monoxide, carbon dioxide and hydrocarbons using a non-dispersive infrared (NDIR) sensorand nitrogen oxides using an electrochemical sensor. The schematic diagram of the test bed engine is presented in Figure 1. Table 1 presents the detailed specification of the test engine and dynamometer.

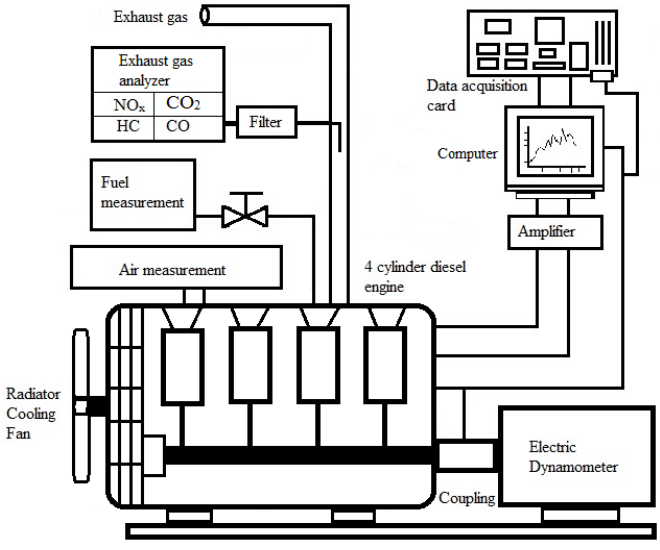

FIGURE 1. Schematic diagram of the test bed engine setup.

TABLE 1: Test bed engine and EGR specification.

Items	**Unit**	**Specifications**
Type	-	V- 4 stroke
No. of cylinder	-	4
Bore x Stroke	mm	98 x 110
Total displacement	L	3.318
Rated speed	rpm	2800
Compression ratio	-	22.6:1
Rated power	kw	53.9
Injection pressure	MPa	13.73

Exhaust gas analyzer (EGR) specification

Measured gas	**Measurement**	
	Range	**Resolution**
HC	0-3e^{4}ppm (n-Hexane)	1 ppm
CO	0-15%	0.001%
CO_2	0-20%	0.01%
O_2	0-25%	0.01%
NO_x	0-5e^4 ppm	1 ppm

CHARACTERIZATION OF BIODIESEL

The physio-chemical fuel properties of the biodiesel is important before use in CI engine. The fuel properties namely density, viscosity, calorific value, certain number, flash point, poor point etc. were measured according to the ASTM D6751 and EN 14214 standards (Table 2). The Table shows that almost every property of the fuels is within the acceptable range. The test biodiesels were blended with ULSD by blending 5% biodiesel and 95% diesel denoted as B5, 10% biodiesel with 90% diesel refried as B10, 15% biodiesel and 85% diesel presented as B15 for both soybean and waste cooking biodiesel fuels.

TABLE 2. Fuel properties of the biodiesels with fossil diesel [9, 34].

Properties	Unit	Diesel	Soybean biodiesel	Waste oil biodiesel	Standard biodiesel
Density at 15°C	kg/m^3	827.2	885	875-900	880
Viscosity	mm^2/s	3.23	4.08	3.77	1.9-6.0
Calorific value	MJ/kg	47.5	39.76	39.78	-
Cetane number	-	58	47-52	39-44	47
Flash point	°C	68.5	69	-	130
Pour point	°C	0	-3	-	- 16
Cloud point	°C	5	-4	-	-3 to -12

RESULTS AND DISCUSSIONS

Performance analysis (BP, BT and BSFC)

The study investigated BP, BT and BSFC as performance parameters for both biodiesel blends. Figure 2 shows the variation of BP and compared with ULSD. For both biodiesels, BP decreases with the increase in biodiesel percentage. This trend is expected as biodiesel has less energy content (Table 1) than ULSD. So, more biodiesel should result in less energy and power. Soybean biodiesel blends (B5, B10 and B15) produced 0.22%, 0.65%, 0.85% less BP compared with ULSD, respectively. On the other hand, waste cooking biodiesel blends (B5, B10, B15) produced 0.33%, 0.94%, 1.22% less BP than ULSD, respectively. It was also found that soybean biodiesel produced more power than waste cooking biodiesel.

Figure 3 illustrates maximum BT variation for both biodiesels. The trend of the curve is consistent which means that the increase of biodiesel blends leads to decrease in BT output. For example, soybean biodiesel blends have lower BT (0.45%, 0.91% and 1.59%, respectively) compared with ULSD. On the other hand, waste cooking biodiesel produced 0.68%, 1.36% and 2.05% less BT than ULSD.

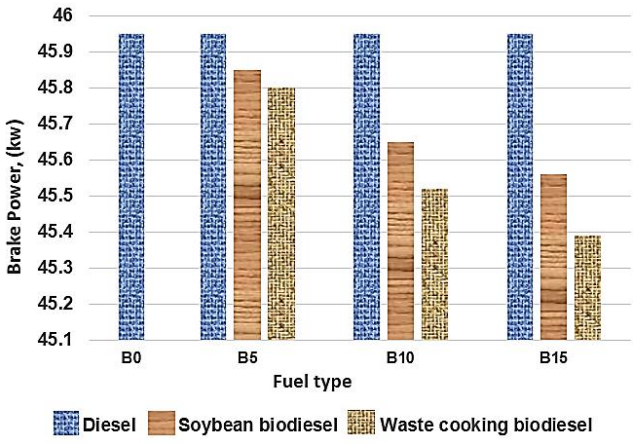

FIGURE 2. Comparison of brake power of diesel and biodiesel blends.

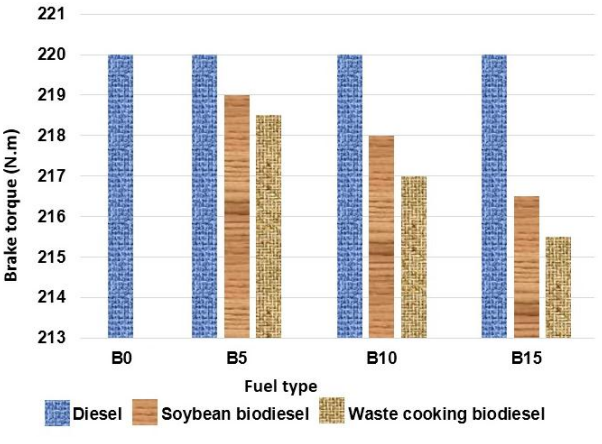

FIGURE 3. Effect of biodiesel blends on brake torque.

BSFC is one of the important factors for engine performance of the fuel. Figure 4 shows the variation of BSFC for different fuel blends over the ISO 8178 test procedure. It can be seen from the Figure that biodiesels have higher BSFC than ULSD. The soybean biodiesel blends have 6.44%, 30.29% and 47.6% more BSFC and waste cooking biodiesel have 27.83%, 48.63%, and 58.21% higher BSFC compared with ULSD, respectively. It can also be seen from the Figure that waste cooking biodiesel blends have more BSFC compared with soybean biodiesel. It is evidenced that BSFC increases with the increase of biodiesel blends [35-37].

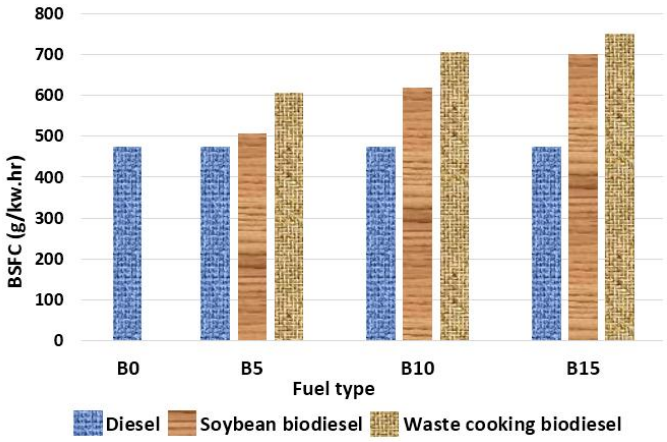

FIGURE 4. Comparison of BSFC for diesel and different biodiesel blends.

Emission study (CO, CO_2, HC, NO_X)

Biodiesel emits lower CO compared with ULSD as shown in Figure 5. The soybean biodiesel blends (B5, B10 and B15) reduced about 15.49%, 24.83% and 30.48% CO emission compared with ULSD, respectively. Besides, waste cooking biodiesel blends have 28.45%, 43.98%, 42.35% lower CO emission than ULSD. It also emits less CO than soybean biodiesel blend. So, the waste oil biodiesel blends are better for CO emission point of view.

Figure 6 shows the CO_2 emissions for the three different test fuels under ISO 8178 test procedure. The literature reported that biodiesel is carbon neutral fuel and the combustion of biodiesel in CI engine emits lower greenhouse gases than fossil diesel [38, 39]. Soybean biodiesel blends reduces about 0.36%, 0.70%, 0.77% CO_2emission compared with ULSD. Waste cooking biodiesel reduces 0.23%, 0.62% and 1.14% CO_2emission than ULSD, respectively. The trend shows the decrease in CO_2 emission compared with diesel which is expected from the experiment.

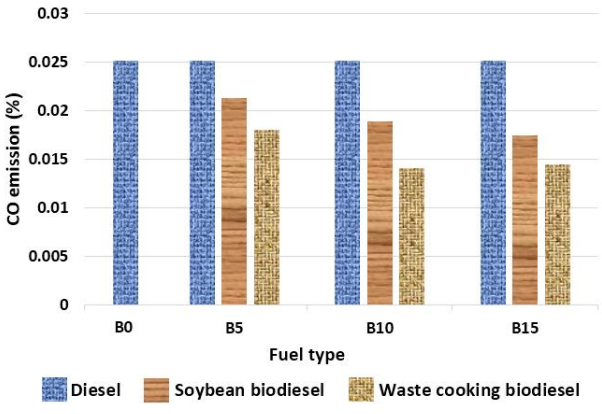

FIGURE 5. Comparative study of CO emission for diesel and different biodiesel blends

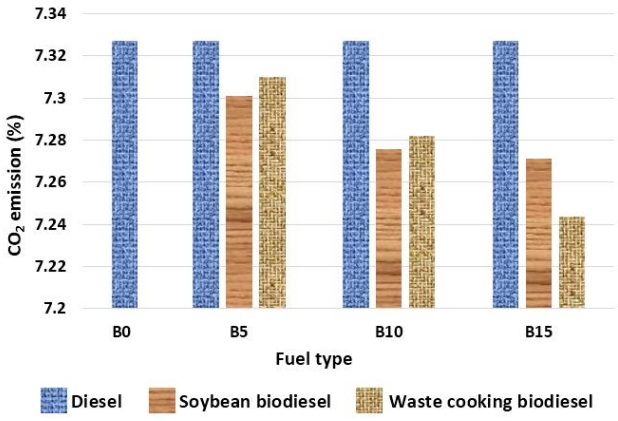

FIGURE 6. Comparative study of CO_2 emission for diesel and different biodiesel blends.

Figure 7 shows the variation of hydrocarbons (HC)emission in the exhaust stream. Incomplete combustion of fuel and flame quenching results in unburned HC emission in CI engine. The United States Environmental Protection Agency (USEPA) determined that with an increase in biodiesel the amount of hydrocarbons in the exhaust stream should decrease. The results shows that soybean and waste cooking biodiesel blends (B5, B10 and B15) reduces about 10.08%, 14.83%, 23.27% and 13.19%, 23.48%, 34.94% HC emission, respectively compared with ULSD.

Figure 8 illustrates NO_x emission by combustion of biodiesels under the ISO 8178 test procedure. It has been evidenced from the previous studies that NO_x emission is one of the most important problems by combustion of biodiesel in CI engine [35]. From the graph, it can be clearly seen that soybean biodiesel blends increases NO_x emission by 13.57%, 19.60%, 21.61% compared with ULSD respectively. Besides, NO_x emission by combustion of B5, B10, and B15 waste cooking biodiesel blends increased emission by 8.94%, 24.82%, 37.59%compared ULSD, respectively.

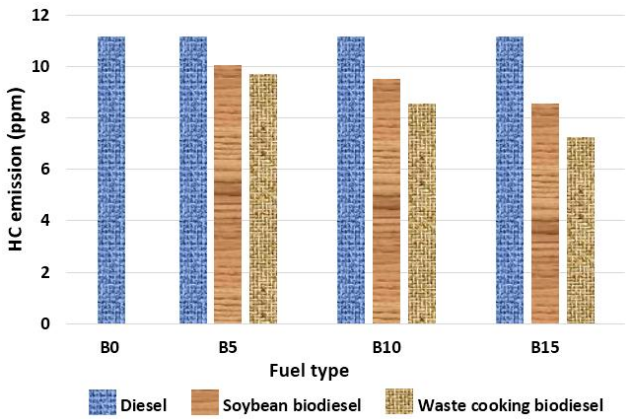

FIGURE 7. Comparative study of HC emission for diesel and different biodiesel blends.

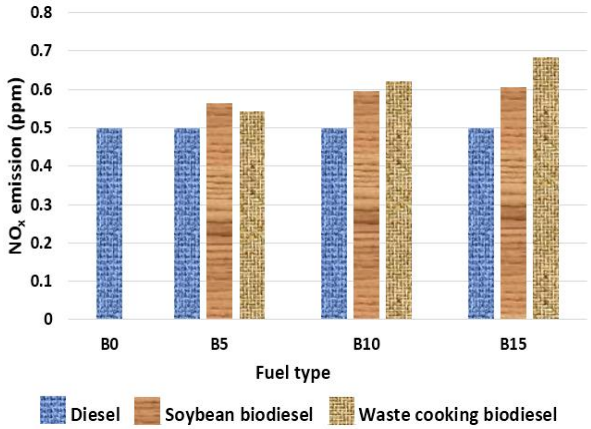

FIGURE 8. Comparative study of NO_x emission for diesel and different biodiesel blends.

CONCLUSIONS

The study experimentally investigated the effect of biodiesel blends on engine performance and emission as an alternative fuel for diesel engine. The fuel properties of the biodiesels and their blends meet the requirement of ASTM D6751 and EN 14214 standards. Under the ISO 8178 test procedure, the study found that biodiesels produced less BP and BT and higher BSFC compared to ULSD. The trend of the performance curves is quite consistent with respect to biodiesel blends. The biodiesel significantly reduces emission of greenhouse gases like CO, CO_2 and HC emission; however, it leads to increase in NO_x emission by increasing blend percentage. The waste cooking biodiesel is better from emission point of view, besides, soybean biodiesel is better from performance point of view. More study is needed on tribological test, corrosion test and combustion performance of these biodiesels before commercial application.

REFERENCES

1. A. K. Azad, M. G. Rasul, M. M. K. Khan, S. C. Sharma and M. A. Hazrat, Renewable and Sustainable Energy Reviews **43**, 331-351 (2015).
2. N. L. Panwar, H. Y. Shrirame, N. S. Rathore, S. Jindal and A. K. Kurchania, Applied Thermal Engineering **30** (2–3), 245-249 (2010).
3. M. M. K. Bhuiya, M. G. Rasul, M. M. K. Khan, N. Ashwath, A. K. Azad and M. A. Hazrat, Renewable and Sustainable Energy Reviews, (In Press) (2016).
4. A. K. Azad, M. G. Rasul, M. M. K. Khan, T. Ahasan and S. F. Ahmed, Journal of Power and Energy Engineering **2** (4), 19-25 (2014).
5. A. Ball, A. Feng, C. McCluskey, P. Pham, G. Stanwix and T. Willcock, (2014).
6. A. K. Azad and S. M. A. Uddin, Journal of Renewable and Sustainable Energy **5** (1), 013118(013111-013112) (2013).

7. M. Mofijur, M. Rasul, J. Hyde, A. Azad, R. Mamat and M. Bhuiya, Renewable and Sustainable Energy Reviews **53**, 265-278 (2016).
8. M. A. Amir Uddin and A. K. Azad, International Journal of Energy Machinery **5** (1), 8-17 (2012).
9. M. Mofijur, A. E. Atabani, H. H. Masjuki, M. A. Kalam and B. M. Masum, Renewable and Sustainable Energy Reviews **23** (0), 391-404 (2013).
10. A. K. Azad, M. G. Rasul, M. M. K. Khan and S. C. Sharma, presented at the International Green Energy Conference, Tainjin, China, 2014 (unpublished).
11. A. E. Atabani, A. S. Silitonga, H. C. Ong, T. M. I. Mahlia, H. H. Masjuki, I. A. Badruddin and H. Fayaz, Renewable and Sustainable Energy Reviews **18**, 211-245 (2013).
12. P. McCarthy, M. Rasul and S. Moazzem, International Journal of Low-Carbon Technologies, ctr012 (2011).
13. A. K. Azad, M. G. Rasul, M. M. K. Khan and S. C. Sharma, presented at the International Green Energy Conference, Tainjin, China, 2014 (unpublished).
14. I. M. Atadashi, M. K. Aroua and A. A. Aziz, Renewable and Sustainable Energy Reviews **14** (7), 1999-2008 (2010).
15. A. K. Azad, S. M. Ameer Uddin and M. M. Alam, International Journal of Automotive and Mechanical Engineering **5**, 576-586 (2012).
16. J. C. Escobar, E. S. Lora, O. J. Venturini, E. E. Yáñez, E. F. Castillo and O. Almazan, Renewable and Sustainable Energy Reviews **13** (6–7), 1275-1287 (2009).
17. S. K. Mondal, K. Ferdous, M. R. Uddin, M. R. Khan, M. A. Islam and A. K. Azad, presented at the 1st international e-conference of energies, Switzerland, 2014 (unpublished).
18. A. K. Azad and M. R. I. Prince, International Journal of Energy and Technology **4** (22), 1-6 (2012).
19. S. Kim and B. E. Dale, Biomass and Bioenergy **29** (6), 426-439 (2005).
20. A. K. Azad, M. G. Rasul, M. M. K. Khan, A. Omri, M. M. K. Bhuiya and M. H. Ali, Energy Procedia, 1902-1906 (2014).
21. A. K. Azad, M. G. Rasul, M. M. K. Khan and S. C. Sharma, presented at the International Conference on Clean Energy Istanbul, Turkey, 2014 (unpublished).
22. M. M. K. Bhuiya, M. G. Rasul, M. M. K. Khan, N. Ashwath, A. K. Azad and M. A. Hazrat, Energy Procedia, 1969-1972 (2014).
23. A. K. Azad, S. M. A. Uddin and M. M. Alam, Global Advanced Research Journal of Engineering, Technology and Innovation **1** (3), 75-84 (2012).
24. S. A. Uddin, A. Azad, M. Alam and J. Ahamed, Procedia Engineering **105**, 698-704 (2015).
25. N. Dizge, B. Keskinler and A. Tanriseven, Biochemical Engineering Journal **44** (2), 220-225 (2009).
26. G. Antolın, F. Tinaut, Y. Briceno, V. Castano, C. Perez and A. Ramırez, Bioresource technology **83** (2), 111-114 (2002).
27. P. McCarthy, M. Rasul and S. Moazzem, Fuel **90** (6), 2147-2157 (2011).
28. A. K. Azad, M. G. Rasul, M. M. K. Khan, S. C. Sharma, M. M. K. Bhuiya and M. Mofijur, International Journal of Global Warming, (In Press) (2016).
29. M. M. K. Bhuiya, M. G. Rasul, M. M. K. Khan, N. Ashwath and A. K. Azad, Renewable and Sustainable Energy Reviews **(In Press)** (2015).
30. M. Bhuiya, M. Rasul, M. Khan, N. Ashwath, A. Azad and M. Mofijur, Energy Procedia **75**, 56-61 (2015).
31. M. Hazrat, M. Rasul, M. M. K. Khan, A. Azad and M. Bhuiya, Energy Procedia **61**, 1681-1685 (2014).
32. B. S. Chauhan, N. Kumar, Y. Du Jun and K. B. Lee, Energy **35** (6), 2484-2492 (2010).
33. A. K. Azad, S. M. Ameer Uddin and M. M. Alam, International Journal of Energy & Environment **4** (2), 265-278 (2013).
34. A. S. Ramadhas, S. Jayaraj and C. Muraleedharan, Fuel **84** (4), 335-340 (2005).
35. M. Mofijur, H. H. Masjuki, M. A. Kalam, A. E. Atabani, M. I. Arbab, S. F. Cheng and S. W. Gouk, Energy Conversion and Management **82**, 169-176 (2014).
36. X. Wang, Y. Ge, L. Yu and X. Feng, Fuel **107**, 852-858 (2013).
37. M. Shahabuddin, H. Masjuki, M. Kalam, M. Mofijur, M. Hazrat and A. Liaquat, Energy Procedia **14**, 1624-1629 (2012).
38. A. K. Azad, M. G. Rasul, M. M. K. Khan, S. C. Sharma and R. Islam, Procedia Engineering **105**, 601-606 (2015).
39. N. Usta, E. Öztürk, Ö. Can, E. Conkur, S. Nas, A. Con, A. Can and M. Topcu, Energy Conversion and Management **46** (5), 741-755 (2005).

ICME2015

International Conference on Mechanical Engineering 2015
(ICME 2015) 18 – 20 December, 2015, Dhaka, Bangladesh

Paper ID : 356

MHD Wall Driven Flow and Heat Transfer through a Porous Tube

Mohammed Mainul Hossain[1,a)] , Md. Sarwar Alam[2] , Md. Abdul Hakim Khan[1]

[1]*Department of Mathematics, Bangladesh University of Engineering and Technology, Dhaka, Bangladesh*
[2]*Department of Mathematics, Jagannath University, Dhaka, Bangladesh*

[a)] Corresponding author: mhcode@live.com

Abstract. Wall driven flow of an incompressible viscous fluid through a porous tube of circular cross section in the presence of magnetic field is considered. The non-dimensional governing equations with boundary conditions for low Reynolds number are solved applying perturbation method together with Hermite-Padé approximation technique. The effect of magnetic field on velocity, temperature, shear stress, rate of heat transfer and stability of the flow is investigated quantitatively.

INTRODUCTION

The study of fluids flow and thermal convection in porous tube and channel have received considerable attention over few centuries due to its wide applications in physical, biological and applied sciences. Berman [2] studied laminar flow in a two dimensional rectangular channel with porous wall. He showed that the corresponding Navier-Stoke equations can be reduced to a nonlinear 3rd order ordinary differential equation with two point boundary conditions. He introduced the perturbation results for extremely small Reynolds number. In a similar way, Makinde [3] considered the computer extension of perturbation series solution, its analysis and analytic continuation in obtaining valuable information on the solution structure at large Reynolds numbers, including bifurcation study for porous tube flow problem. However, Makinde [4] investigated a new series summation and converging improvement technique to study the steady flow of a viscous incompressible fluid flow both in a porous pipe with moving walls and an exponentially diverging asymmetrical channel. The subject of magneto hydrodynamics has also attracted the attention of large number of researchers due to its diverse application. MHD flow in a channel with permeable boundaries is investigated by Makinde et al [6] where they study the combine effect of magnetic field and permeable walls slip velocity. An incompressible symmetric wall driven steady flow of a viscous fluid and heat transfer in a solid tube and porous tube is examined by Odejide et al [9] and Makinde et al [7] respectively.

In this paper, wall driven flow of a viscous fluid with heat transfer through a two-dimensional symmetrical porous tube of circular cross-section in the presence of externally applied homogeneous magnetic field along the normal of the tube's length is investigated. Analytical solutions are constructed for the governing nonlinear boundary-value problem using perturbation method and approximation technique. To investigate the effect of Hartmann number on fluid flow, heat transfer and critical Reynolds number is our objective.

Nomenclature

a	Radius of the tube
u	Velocity along the z axis
v	Velocity along the r axis
B_0	Magnetic field intensity along the normal of the z axis
T_0	Temperature of fluid
T_w	Temperature of wall
ν	Kinematic viscosity
C_P	Specific heat capacity
κ	Thermal conductivity
E	Characteristic velocity
Re	Reynolds Number
Ha	Hartmann Number
Pr	Prandtl Number
σ	Electrical conductivity
ρ	Density of fluid

MATHEMATICAL FORMULATION

Consider laminar flow of an incompressible viscous fluid through a uniformly porous tube of circular cross section. A cylindrical coordinate system r, θ, z is taken where oz lies along the center of the tube.

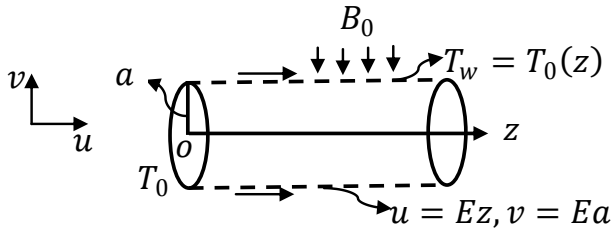

FIGURE 1. Geometry of Problem.

The continuity, momentum and energy equations for axisymetric steady incompressible viscous flow are:

$$\frac{\partial rv}{\partial r} + r\frac{\partial u}{\partial z} = 0 \tag{1}$$

$$u\frac{\partial u}{\partial z} + v\frac{\partial u}{\partial r} = -\frac{1}{\rho}\frac{\partial P}{\partial z} + \nu(\nabla^2 u) - B_0^2\frac{\sigma}{\rho}u \tag{2}$$

$$u\frac{\partial v}{\partial z} + v\frac{\partial v}{\partial r} = -\frac{1}{\rho}\frac{\partial P}{\partial r} + \nu\left(\nabla^2 v - \frac{v}{r^2}\right) \tag{3}$$

$$\rho C_P\left(v\frac{\partial T}{\partial r} + u\frac{\partial T}{\partial z}\right) = \kappa\nabla^2 T \tag{4}$$

The boundary conditions are:

$$\frac{\partial u}{\partial r} = 0, v = 0, \frac{\partial T}{\partial r} = 0 \quad on \quad r = 0 \tag{5}$$

$$u = Ez, \qquad v = Ea, \qquad T_w = T_0\left(1 + \frac{z}{a}\right) \ on \ \ r = a \tag{6}$$

Introducing the stream function ψ and vorticity ω as follows:

$$u = \frac{1}{r}\left(\frac{\partial \Psi}{\partial r}\right), v = -\frac{1}{r}\left(\frac{\partial \Psi}{\partial z}\right) \ \ and \quad \omega = \frac{\partial v}{\partial z} - \frac{\partial u}{\partial r} = -\frac{1}{r}\frac{\partial^2 \Psi}{\partial z^2} - \frac{1}{r}\frac{\partial^2 \Psi}{\partial r^2} + \frac{1}{r^2}\frac{\partial \Psi}{\partial r} \tag{7}$$

Eliminating pressure P from (2) and (3) by using (7) we have

$$\frac{1}{r}\left(\frac{\partial \Psi}{\partial r}\frac{\partial \omega}{\partial z} - \frac{\partial \Psi}{\partial z}\frac{\partial \omega}{\partial r}\right) + \frac{\omega}{r^2}\frac{\partial \Psi}{\partial z} - \frac{B_0^2 \sigma}{\rho}\frac{\partial}{\partial r}\left(\frac{1}{r}\frac{\partial \Psi}{\partial r}\right) = \nu\left(\nabla^2 \omega - \frac{\omega}{r^2}\right) \tag{8}$$

Also using (7) in (4), we obtain

$$\rho C_P \frac{1}{r}\left(\frac{\partial \Psi}{\partial r}\frac{\partial T}{\partial z} - \frac{\partial \Psi}{\partial z}\frac{\partial T}{\partial r}\right) = \kappa \nabla^2 T \tag{9}$$

Introducing the following dimensionless variables

$$\bar{\omega} = \frac{\omega}{E}, \bar{z} = \frac{z}{a}, \bar{r} = \frac{r}{a}, \bar{\Psi} = \frac{\Psi}{Ea^3}, \ \ \bar{T} = \frac{T}{T_0}, Re = \frac{Ea^2}{\nu}, Ha = B_o\sqrt{\frac{\sigma}{\rho E}}, Pr\,Re = \frac{\rho C_P E a^2}{\kappa} \tag{10}$$

We seek a similarity form of solution (Berman, 1953) that is

$$\bar{\Psi} = \bar{z}F(\bar{r}), \ \ \bar{\omega} = -\bar{z}G(\bar{r}), \ \ \bar{T} = \theta(\bar{r}) \tag{11}$$

Equations (7), (8) and (9) become

$$G = \frac{d}{d\bar{r}}\left[\frac{1}{\bar{r}}\frac{dF}{d\bar{r}}\right] \tag{12}$$

$$\frac{d}{d\bar{r}}\left[\frac{1}{\bar{r}}\frac{d(\bar{r}G)}{d\bar{r}}\right] = Re\left[\frac{G}{\bar{r}}\frac{dF}{d\bar{r}} - F\frac{d}{d\bar{r}}\left(\frac{G}{\bar{r}}\right) - Ha^2 G\right] \tag{13}$$

$$\frac{d}{d\bar{r}}\left[\bar{r}\frac{d\theta}{d\bar{r}}\right] = PrRe\left[\theta\frac{dF}{d\bar{r}} - F\frac{d\theta}{d\bar{r}}\right] \tag{14}$$

The boundary conditions (5) and (6) become

$$F = 0, \qquad \frac{d}{d\bar{r}}\left(\frac{1}{\bar{r}}\frac{dF}{d\bar{r}}\right) = 0, \qquad \frac{d\theta}{d\bar{r}} = 0 \quad on \quad \bar{r} = 0 \tag{15}$$

$$F = -1, \qquad \frac{dF}{d\bar{r}} = 1, \theta = 1 \ \ on \ \ \bar{r} = 1 \tag{16}$$

For small Re we seek the solution of the equations (12)-(16) as a perturbation series i.e.

$$\omega(\bar{r}) = \sum_{i=0}^{\infty} \omega_i Re^i \qquad and \qquad \theta(\bar{r}) = \sum_{i=0}^{\infty} \theta_i Re^i \tag{17}$$

Where ω can be either $F(\bar{r}, Re)$ or $G(\bar{r}, Re)$

Solving equations (13) and (14) using (15) and (16), we obtain the first 33 terms of F, G, θ and hence we obtain $u = \frac{1}{r}\frac{dF}{dr}$ and $Nu = -\frac{d\theta}{dr}$ (neglecting the bar symbol for clarity).

Some terms of the stream function $F(r)$, shear stress $G(r)$ and temperature $\theta(r)$ are represented as

$$F_0 = \frac{1}{2}r^2(3r^2 - 5) \tag{18}$$

$$F_1 = \left(-\frac{3}{16} - \frac{1}{16}Ha^2\right)r^2 + \left(\frac{7}{16} + \frac{1}{8}Ha^2\right)r^4 + \left(-\frac{5}{16} - \frac{1}{16}Ha^2\right)r^6 + \frac{1}{16}r^8 \tag{19}$$

$$G_0 = 12r \tag{20}$$

$$G_1 = \left(\frac{7}{2} + Ha^2\right)r + \left(-\frac{15}{2} - \frac{3}{2}Ha^2\right)r^3 + 3r^5 \tag{21}$$

$$\theta_0 = 1 \tag{22}$$

$$\theta_1 = 1 + \left(\frac{7}{8} - \frac{5}{4}r^2 + \frac{3}{8}r^4\right)Pr\,Re \tag{23}$$

APPROXIMATION METHOD

In this paper, the generalization form of the Padé approximation technique (Baker and Graves-Morris) [1] is used for series summation. Let us consider the partial sum is given

$$U_{N-1}(\lambda) = \sum_{i=0}^{N-1} a_i\lambda^i = U(\lambda) + O(\lambda^N) \qquad as\ \lambda \to 0 \tag{24}$$

The solution of the differential equation including critical value can be written as

$$U(\lambda) = \begin{cases} k(\lambda_c - \lambda)^m & for\ m \neq 0,1,2 \ldots\ldots \\ k(\lambda_c - \lambda)^m \ln(\lambda_c - \lambda) & for\ m = 0,1,2 \ldots\ldots \end{cases} \qquad as\ \lambda \to \lambda_c \tag{25}$$

Where k is some constant and λ_c is the critical point with exponent m. Consider, $U(\lambda)$ as the local representation of an algebraic function of λ. So, the expression can be written in form.

$$F_d(\lambda, U_{N-1}) = A_{0N}(\lambda) + A_{1N}^d(\lambda)U^{(1)} + A_{2N}^d(\lambda)U^{(2)} + A_{3N}^d(\lambda)U^{(3)} \ldots\ldots \tag{26}$$

$$Where\ \ N = \frac{1}{2}(d^2 + 5d),\ \ A_{0N}(\lambda) = 1,\ \ A_{iN}(\lambda) = \sum_{j=1}^{d+i} b_{ij}\lambda^{j-1}\ \ and\ \ \ F_d(\lambda, U) = O(\lambda^{N+1})\ \ as\ \ \lambda \to 0$$

The equation (23) forms as a special type of Hermite-Padé approximants. For example, we let

$$U^{(1)} = U, \qquad U^{(2)} = DU, \qquad U^{(3)} = D^2U \qquad \text{Where } D = {}^{d}/_{d\lambda} \tag{27}$$

This enables us to obtain the dominant singularity in the flow field. For detail of this method, interested reader can see Makinde [4,5,8], Tourigny and Drazin[10].

RESULT AND DISCUSSION

The objective of this study is to focus the magnetic effect on the wall driven flow through a porous tube. The magnetic effect on critical Reynolds number, velocity, temperature and rate of heat transfer are discussed applying Hermite-Padé approximants.

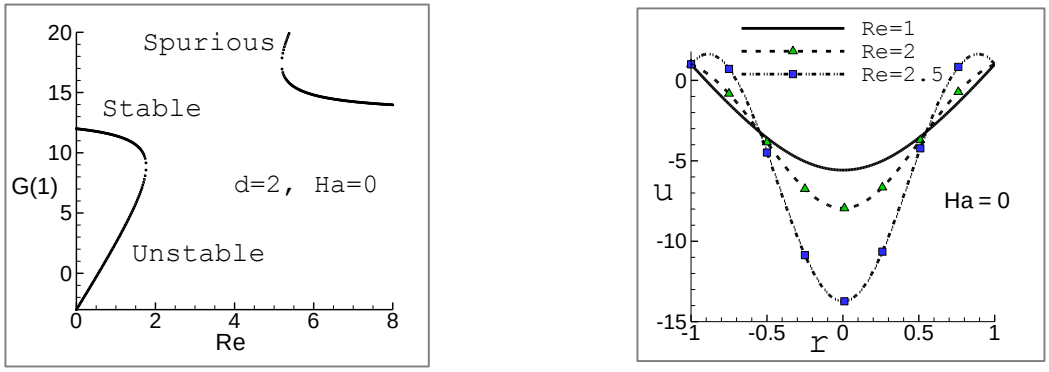

(a) (b)

FIGURE 2. (a) Shear stress versus Reynolds number ; (b) velocity versus radius of the tube

Figure 2(a) represents the shear stress versus Reynolds number. The figure indicates the critical Reynolds number (maximum Reynolds number for laminar flow) is 1.855 and the flow within this critical Reynolds number is stable whereas unstable beyond this Reynolds number. Figure 2(b) demonstrates the velocity versus distance from center on different Reynolds number. It is noticed from the figure that the velocity profile is parabolic and the flow is stable within critical Reynolds number. The Reynolds number of other two curves is higher than the critical limit where velocity profile change its shape, become chaotic and there occurs reverse flow near the walls.

TABLE 1: Critical Reynolds number for different Hartmann number

d	N	Critical Reynolds Number (Re_c)		
		Ha=0	Ha=1	Ha=2
2	7	1.896440	1.660232	1.287847
3	12	1.855555	1.641001	1.239532
4	18	1.855615	1.638108	1.239912

It is very clear from this table that the increase of Hartmann number decrease of the critical Reynolds number and increase the scope of instability.

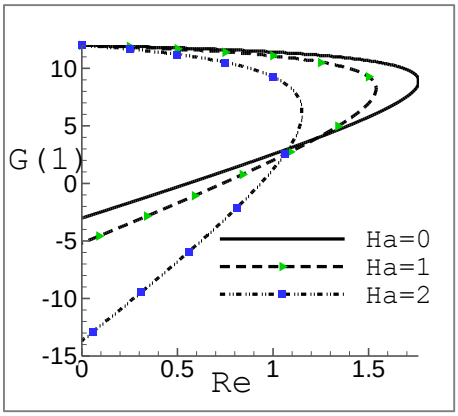

FIGURE 3. Shear stress versus Reynolds number on different Hartmann number

Figure 3 illustrates the Shear stress versus Reynolds number for different values of Hartmann number. It is seen from the figure that the critical Reynolds number transforms towards the origin with the increases of Hartmann number. Moreover, the increase of Hartmann number decreases the critical Reynolds number and enhances the scope of instability.

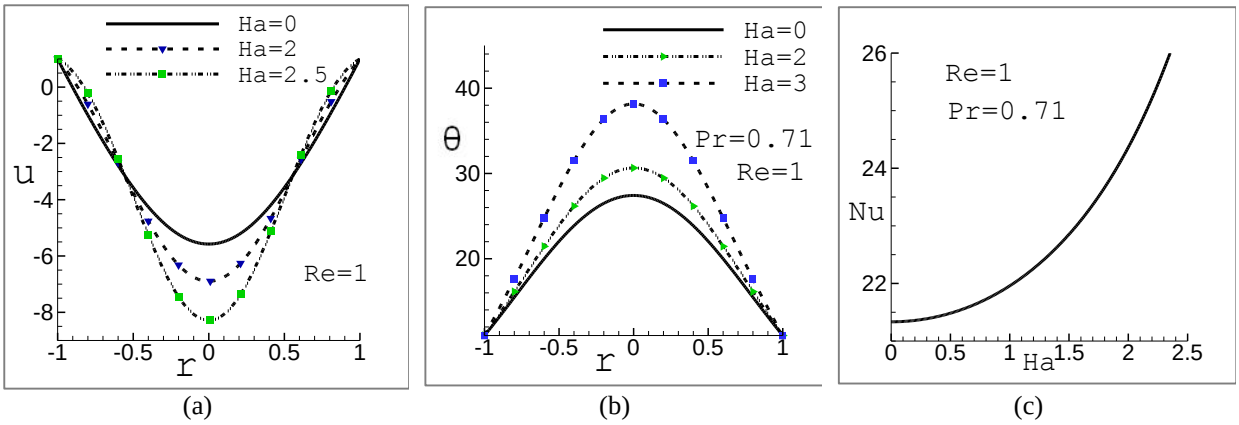

FIGURE 4. (a) Velocity versus radius; (b) Temperature versus radius; (c) Nusselt number versus Hartmann number

Figure 4(a) illustrates the velocity versus characteristics distance for different values of Hartmann number where the velocity reduces with the increase of Hartmann number. On the other hand, Figure 4(b) describes the temperature distributions due to various values of Hartmann number. It can be noted here that the temperature along the centerline increaes with the rising values of Hartmann number due to increase of fluid motion in that region. Figure 4(c) displays the relation between Nusselt number and Hartmann number. As discussed above that Hartmann number enhances the temperature of the fluid, as a result, the rate of heat transfer increases by the increase of Hartmann number.

CONCLUISON

The effect of magnetic field on fluid flow and heat transfer through a porous tube is very significant. Hence the magnetic effect on critical Reynolds number, velocity, temperature and rate of heat transfer are analyzed in this paper. The result reveals the following conclusions.

1) Magnetic parameter decreases the magnitude of critical Reynolds number which leads to early development of instability.

2) The velocity along the centerline increases in the opposite direction and the temperature of the fluid increases when Hartmann number increases.

3) Magnetic field enhances the rate of heat transfer within the tube.

REFERENCES

1. Baker, G.A., Jr., and Graves–Morris, P., Pade Approximants, Encyclopaedia of Mathematics and Its Applications, Cambridge University Press, Cambridge, **59** (1996).
2. A. S. Berman, Laminar flow in channels with porous walls, J. Appl. Phys, **24** (1953) 1232-1235.
3. O. D. Makinde, Computer extension and bifurcation study by analytic continuation of porous tube flow, Jour. Math. Phys. Sci., **30** (1996) 1-24.
4. O. D. Makinde, Extending the utility of perturbation series in problems of laminar flow in a porous pipe and a diverging channel, Jour. of Aus. Math. Soc. Ser. B Applied Mathematics, **41** (1999) 118–128.

5. Makinde, O. D., Strong exothermic explosions in a cylindrical pipe: A case study of series summation technique. Mechanics Research Communications, **32 (**2005) 191-195.
6. O.D. Makinde, E. Osalusi, MHD steady flow in a channel with slip at the permeable boundaries, Rom. Journ. Phys., Bucharest, **51** (2006) 319–328.
7. O. D. Makinde, Y. A. S. Aregbesola and S. A. Odejide, Wall driven steady flow and heat transfer in a porous tube, Kragujevac J. Math. **29** (2006) 193-201.
8. O. D. Makinde, Thermal criticality in viscous reactive flows through channels with a sliding wall: An exploitation of the Hermite-Padé approximation method, Math. and Com. Mod., **47** (2008) 312-317.
9. S.A. Odejide, Y.A.S. Aregbesola, Wall driven steady flow and heat transfer in a tube, International Journal of Pure and Applied Mathematics, **24** (2006) 323-330.
10. Tourigny, Y., and Drazin, P. G., The asymptotic behaviour of algebraic approximants. Proc. Roy. Soc. London A, 456 (2000) 1117-1137.

International Conference on Mechanical Engineering 2015
(ICME 2015) 18 – 20 December, 2015, Dhaka, Bangladesh

Paper ID :365

MHD Natural Convection Flow along a Vertical Wavy Surface with Heat Generation and Pressure Work

M. A. Alim[1,a)], K. H. Kabir[2,b)] and L. S. Andallah[3,c)]

[1]*Department of Mathematics, Bangladesh University of Engineering and Technology, Dhaka-1000, Bangladesh*
[2]*Department of Mathematics, Mohammadpur Kendriya College,Dhaka-1207, Bangladesh*
[3]*Department of Mathematics, Jahangirnagar University, Savar, Dhaka-1342, Bangladesh.*

[a)]Corresponding author: a0alim@gmail.com, maalim@math.buet.ac.bd
[b)] kfzkabir@gmail.com
[c)] andallahls@gmail.com

Abstract. In this paper, the influence of pressure work on MHD natural convection flow of viscous incompressible fluid along a uniformly heated vertical wavy surface with heat generation has been investigated. The governing boundary layer equations are first transformed into a non-dimensional form using suitable set of dimensionless variables. The resulting nonlinear system of partial differential equations are mapped into the domain of a vertical flat plate and then solved numerically employing the implicit finite difference method, known as Keller-box scheme. The numerical results for the velocity profiles, temperature profiles, skin friction coefficient, the rate of heat transfers, the streamlines and the isotherms are shown graphically and skin friction coefficient and rate of heat transfer have been shown in tabular form for different values of the selective set of parameters consisting of pressure work parameter Ge, the magnetic parameter M, Prandtl number Pr, heat generation parameter Q and the amplitude of the wavy surface.

INTRODUCTION

The pressure work effect plays an important role in natural convection in various devices which are subjected to large deceleration or which operate at high rotational speeds and also in strong gravitational field processes on large scales (on large planets) and in geological processes. Joshi and Gebhart [1] first investigated the effect of pressure stress work and viscous dissipation in some natural convection flows. The natural convection along a vertical wavy surface was first studied by Yao [2] and using an extended Prantdl's transposition theorem and a finite-difference scheme. He proposed a simple transformation to study the natural convection heat transfer from isothermal vertical wavy surfaces, such as sinusoidal surface. Moulic and Yao [3] also investigated mixed convection heat transfer along a vertical wavy surface. Alam et al. [4] have also studied the problem of free convection from a wavy vertical surface in presence of a transverse magnetic field. Combined effects of thermal and mass diffusion on the natural convection flow of a viscous incompressible fluid along a vertical wavy surface have been investigated by Hossain and Rees [5]. Hossain et al. [6] have studied the problem of natural convection of fluid with temperature dependent viscosity along a heated vertical wavy surface. Natural and mixed convection heat and mass transfer along a vertical wavy surface have been investigated by Jang et al. [7]. Molla et al. [8] have studied natural convection flow along a vertical wavy surface with uniform surface temperature in presence of heat generation/absorption. Saboonchi et al. [9] investigated Thermal contact resistance of wavy surfaces and found that thermal contact conductance of wavy surfaces depends on the order of surface location.

The present study is to incorporate the idea of the effects of pressure work on MHD natural convection flow of viscous incompressible fluid with heat generation along a uniformly heated vertical wavy surface. The governing equations transformed into non-dimensional form and solved numerically with the appropriate boundary conditions using FORTRAN code based on finite difference method. Numerical results in terms of streamlines and isotherms,

local skin friction and rate of heat transfer for a selection of relevant physical parameters have been shown graphically as well as in tabular form and then discussed.

PROBLEM FORMULATION

Steady two dimensional laminar free convection boundary layer flow of a viscous incompressible and electrically conducting fluid along a vertical wavy surface in presence of uniform transverse magnetic field of strength B_0 with physical properties is considered. It is assumed that the wavy surface is electrically insulated and is maintained at a uniform temperature T_w, The fluid is stationary above the wavy plate and is kept at atemperature T_{∞}. The surface temperature T_w is greater than the ambient temperature T_{∞}. The flow configuration of the wavy surface and the two-dimensional Cartesian coordinate system are shown in figure 1

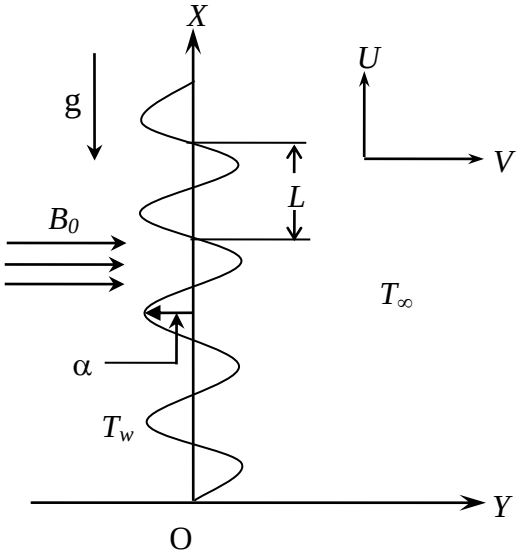

FIGURE 1. Physical model and coordinate system

The boundary layer analysis outlined below allows $\bar{\sigma}(X)$ being arbitrary, but our detailed numerical work assumed that the surface exhibits sinusoidal deformations. The wavy surface may be defined by

$$Y_w = \bar{\sigma}(X) = \alpha \sin\left(\frac{n\pi X}{L}\right) \tag{1}$$

Where, α is the amplitude and L is the wave length associated with the wavy surface. The governing equations of such flow of magnetic field along a vertical wavy surface under the usual Boussinesq approximations can be written in a dimensional form as:

$$\frac{\partial U}{\partial X} + \frac{\partial V}{\partial Y} = 0 \tag{2}$$

$$U\frac{\partial U}{\partial X} + V\frac{\partial U}{\partial Y} = -\frac{1}{\rho}\frac{\partial P}{\partial X} + \frac{1}{\rho}\nabla.(\mu\nabla U) + g\beta(T - T_{\infty}) - \frac{\sigma_0 B_0^2}{\rho}U \tag{3}$$

$$U\frac{\partial V}{\partial X} + V\frac{\partial V}{\partial Y} = -\frac{1}{\rho}\frac{\partial P}{\partial Y} + \frac{1}{\rho}\nabla.(\mu\nabla V) \tag{4}$$

$$U\frac{\partial T}{\partial X} + V\frac{\partial T}{\partial Y} = \frac{k}{\rho C_P}\nabla^2 T + \frac{T\beta}{\rho C_P}U\frac{\partial p}{\partial X} + \frac{Q_0}{\rho C_P}(T - T_{\infty}) \tag{5}$$

where (X, Y) are the dimensional coordinates along and normal to the tangent of the surface and (U, V) are the velocity components parallel to (X, Y), g is the acceleration due to earth gravity, P is the dimensional pressure of the fluid, T is the temperature of the fluid in the boundary layer, C_P is the specific heat at constant pressure, μ is the dynamic viscosity of the fluid in the boundary layer region depending on the fluid temperature, ρ is the density, ν is

the kinematic viscosity, where $\nu = \mu/\rho, k$ is the thermal conductivity of the fluid, β is the volumetric coefficient of thermal expansion, B_0 is the strength of magnetic field, σ_0 is the electrical conductivity of the fluid. The boundary conditions for the present problem are

$$U = 0,\ V = 0,\ T = T_w \text{ at } Y = Y_w = \bar{\sigma}(X);\ \ U = 0, T = T_\infty,\ P = p_\infty \text{ as } Y \to \infty \tag{6}$$

Where, P∞ is the pressure of fluid outside the boundary layer. After introducing the dimensionless variables and the transformations

$$\begin{aligned} &x = \frac{X}{L},\ y = \frac{Y-\bar{\sigma}}{L} Gr^{\frac{1}{4}}, p = \frac{L^2}{\rho\nu^2} Gr^{-1} P,\ u = \frac{\rho L}{\mu} Gr^{-1/2} U, \\ &v = \frac{\rho L}{\mu} Gr^{-1/4}\left(V - \sigma_x U\right), \theta = \frac{T-T_\infty}{T_w - T_\infty}, \sigma_x = \frac{d\bar{\sigma}}{dX} = \frac{d\sigma}{dx}, Gr = \frac{g\beta(T_w - T_\infty)}{\nu^2} L^3 \end{aligned} \tag{7}$$

$$\psi = x^{3/4} f(x,\eta), \quad \eta = y x^{-1/4}, \quad \theta = \theta(x,\eta) \tag{8}$$

The governing equations and boundary conditions reduced to the following form:

$$(1+\sigma_x^2) f''' + \frac{3}{4} f f'' - \left(\frac{1}{2} + \frac{x\sigma_x \sigma_{xx}}{1+\sigma_x^2}\right) f'^2 + \frac{1}{1+\sigma_x{}^2}\theta - \frac{M x^{1/2}}{1+\sigma_x{}^2} f' = x\left(f' \frac{\partial f'}{\partial x} - f'' \frac{\partial f}{\partial x}\right) \tag{9}$$

$$\frac{1}{\Pr}(1+\sigma_x^2)\theta'' + \frac{3}{4} f\theta' - Ge\left(\frac{T_\infty}{T_w - T_\infty} + \theta\right) x f' \ + x^{1/2} Q\theta = x\left(f' \frac{\partial \theta}{\partial x} - \theta' \frac{\partial f}{\partial x}\right) \tag{10}$$

$$\left.\begin{aligned} &f(x,0) = f'(x,0) = 0,\ \ \theta(x,0) = 1 \\ &f'(x,\infty) = 0,\ \ \theta(x,\infty) = 0 \end{aligned}\right\} \tag{11}$$

the local skin friction coefficient C_{fx} and the rate of heat transfer in terms of the local Nusselt number Nu_x are calculated from the following relations:

$$\frac{1}{2}(Gr/x)^{1/4} C_{fx} = \sqrt{1+\sigma_x^2}\ \ f''(x,0) \tag{12}$$

$$Gr^{-1/4} x^{-3/4} Nu_x = -\sqrt{1+\sigma_x^2}\,\theta'(x,0) \tag{13}$$

For the computational purpose the period of oscillations in the waviness of this surface has been considered to be π.

METHOD OF SOLUTION

The governing partial differential equations are reduced to dimensionless local non-similar equations by adopting appropriate transformations. The transformed boundary layer equations are solved numerically using Keller box method described by Keller [10], Cebeci and Bradshaw [11] and used by many other authors.

RESULTS AND DISCUSSIONS

The effect of pressure work on MHD natural convection flow of viscous incompressible fluid along a uniformly heated vertical wavy surface with heat generation has been investigated numerically. In figures 2(a) and 2(b) effects of magnetic parameter *M* on skin friction and the rate of heat transferhave been presented. From figure 2(a) it is found that skin friction decreases significantly for greater magnetic field strength. This is physically realizable as the magnetic field retards the velocity field and consequently reduces the frictional force at the wall. However rate of heat transfer opposite pattern due to the higher values of magnetic parameter *M* which are presented in figure 2(b).

The effect of different values of the pressure work parameter *Ge* on the skin friction coefficients and the rate of heat transfer are shown graphically in figures 3(a) and 3(b) respectively. In this case the values of local skin friction coefficient C_{fx} are recorded to be 0.82727, 0.79101, 0.73628, 0.71794, and 0.68114 for *Ge* = 0.0, 0.02, 0.05, 0.06, 0.08 which occur at same point *x* =1.0. From the figure 3(a), it is observed that at *x* = 1.0, the skin friction

coefficient decreases by 17.66 % due to the higher value of the pressure work parameter *Ge*. However, the values of rate of heat transfer are found to be -0.96988, -0.82646, -0.62225, -0.55731 and -0.43259 for *Ge* = 0.0, 0.02, 0.04, 0.05, 0.08 which occur at same point x = 1.0. The rate of heat transfer coefficient increases by 55.40 % due to the higher value of the pressure work parameter *Ge*. It is seen from the figure 3(b) that for higher values of the pressure work parameter *Ge* the rate of heat transfer increases that is heat transfer rising up for the higher pressure work parameter *Ge*. In Figures 4(a) and 4(b) the skin friction coefficient C_{fx} and local rate of heat transferNu_x for different values of heat generation parameter have been displayed. In this case the values of local skin friction coefficient C_{fx} are recorded to be 0.49625, 0.61549, 0.79101, 1.02766, and 1.32273 for Q = 0.0, 0.5, 1.0, 1.5, 2.0 which occur at same point x =1.0. The values of rate of heat transfer are found to be .34544, -0.10507, -0.82646, -1.95594 and -3.61657 for Q = 0.0, 0.5, 1.0, 1.5, 2.0 which occur at same point x = 1.0. It is seen from the figures 4(a) and 4(b) that for higher values of the heat generation parameter Q skin friction coefficient rising up and local rate of heat transfer decreases. Figure 5(a) and 5(b) show that streamlines and isotherms for selected values of the pressure work parameter *Ge*= 0.0 and 0.05 with amplitude of waviness of the surface α = 0.3, Prandtl number *Pr* = 0.72 and magnetic parameter M = 0.5 respectively.

In Figure 5(a) have been shown the value of stream function ψ is 0.0 near the wall and then ψ increases gradually in the downstream within the boundary layer and away from the wall. The isolines of temperature (isotherms) distribution show that temperature decreases significantly as the values of the pressure work parameter *Ge*increases which have been presented in figure 5(b). The value of isotherm is 1.0 at the wall and isotherms decreases slowly along the y-direction and finally approach to zero. Figure 6(a) and 6(b) show that streamlines and isotherms for selected values of heat generation parameter$Q$= 0.0 and 0.5 with amplitude of waviness of the surface α = 0.3, Prandtl number *Pr* = 0.72 and magnetic parameter$M$ = 0.5 respectively.

Table 1: Skin friction coefficient C_{fx} and the local rate of heat transfer Nu_x against x for different values of the heat generation parameter Q with Pr = 0.72, α = 0.3, M = 0.5 and Ge = 0.03.

	Q = 0.0		Q = 0.6		Q = 1.0		Q = 2.0	
x	C_{fx}	Nu_x	C_{fx}	Nu_x	C_{fx}	Nu_x	C_{fx}	Nu_x
0.00000	0.58972	0.30500	0.58972	0.30500	0.58972	0.305	0.58972	0.305
0.20500	0.63445	0.32164	0.71117	0.08434	0.77726	-0.12417	0.98103	-0.82843
0.40500	0.80870	0.35604	0.94293	0.02450	1.07025	-0.3023	1.48146	-1.51769
0.60500	0.77312	0.37643	0.93096	-0.01895	1.09146	-0.43987	1.61827	-2.08582
0.80500	0.56615	0.37272	0.70853	-0.09092	0.86065	-0.61261	1.36158	-2.74106
1.00500	0.48513	0.37141	0.63029	-0.17629	0.79186	-0.83238	1.3259	-3.64216
1.20500	0.54316	0.38747	0.72573	-0.24239	0.93807	-1.05507	1.64721	-4.70656
1.40500	0.70075	0.41886	0.95248	-0.27295	1.2599	-1.23437	2.3012	-5.71817
1.60500	0.68324	0.43789	0.95477	-0.28969	1.30284	-1.36748	2.49282	-6.54734
1.80500	0.50888	0.43225	0.74057	-0.33159	1.04921	-1.51264	2.10472	-7.32782
2.00000	0.43855	0.42806	0.65700	-0.39167	0.95574	-1.69878	1.97548	-8.23528

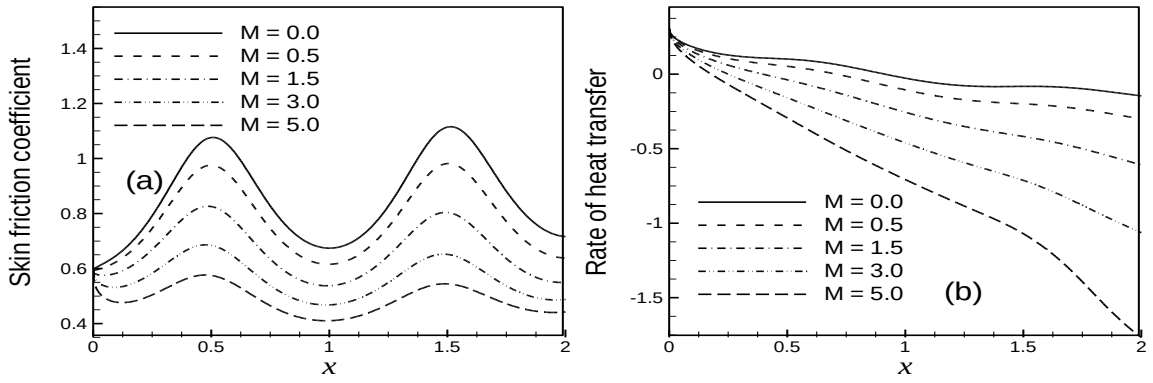

FIGURE 2. (a) Skin friction coefficient and (b) Rate of heat transfer against x for different values of M with α = 0.3, *Pr* = 0.72, Q = 0.5 and *Ge* = 0.02.

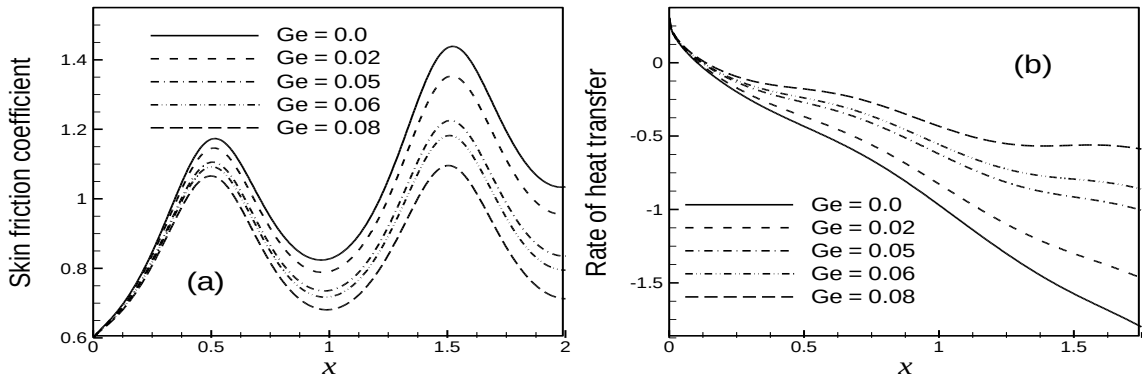

FIGURE 3. (a) Skin friction coefficient and (b) Rate of heat transfer against x for different values of Ge with $\alpha = 0.3$, $Pr = 0.72$, M = 0.5 and Q = 1.0.

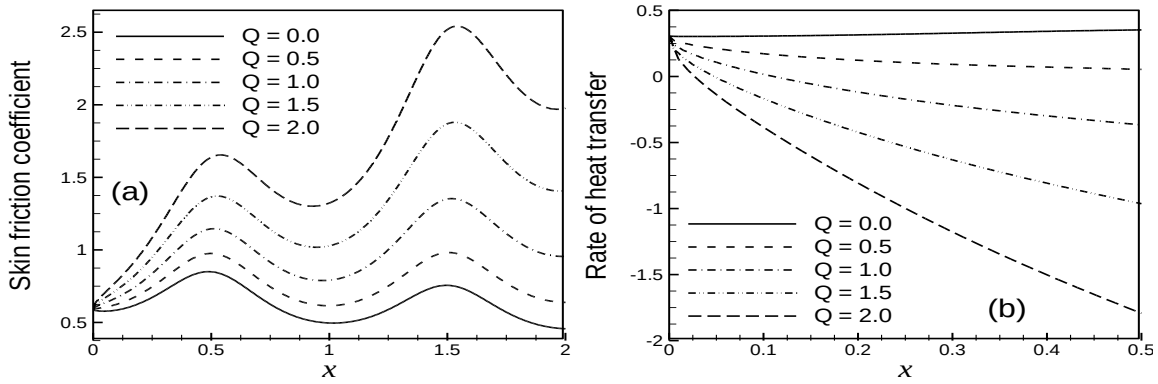

FIGURE4. (a) Skin friction coefficient and (b) Rate of heat transfer against x for different values of Q with $\alpha = 0.3$, $Pr = 0.72$, M = 0.5 and $Ge = 0.02$.

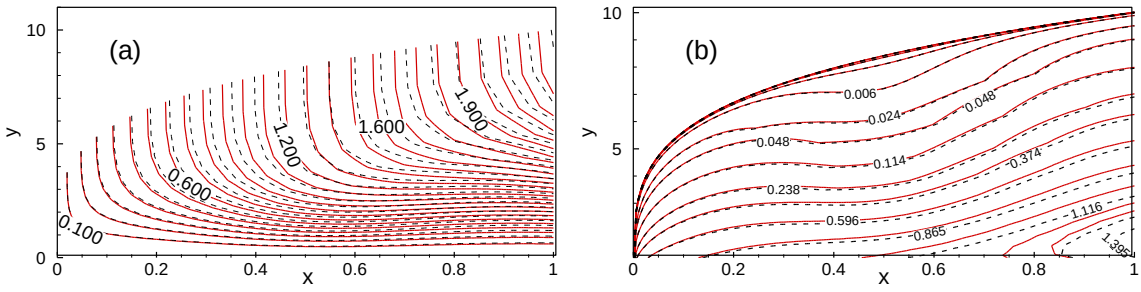

FIGURE 5. (a) Streamlines and (b) Isotherms for Ge = 0.0 (Red solid lines), Ge = 0.05 (Black dashed lines), with $\alpha = 0.3$, $Pr = 0.72$ and $M = 0.5$.

In Figure 9 (a) shows the values of stream function ψ is 0.0 near the wall and then ψ increases gradually in the downstream within the boundary layer and away from the wall. The isolines of temperatures (isotherms) show that temperature decreases significantly as the values of the heat generation parameter Q increases which have been presented in figure 9(b). The value of isotherm is 1.0 at the wall and isotherms decreases slowly along the y-direction and finally approach to zero. Numerical values of skin friction coefficient C_{fx} and rate of heat transfer Nu_x are calculated from equations (22) and (23) for the wavy surface from lower stagnation point at x =0.0 to x =2.0 presented in tabular form in the Table 1.

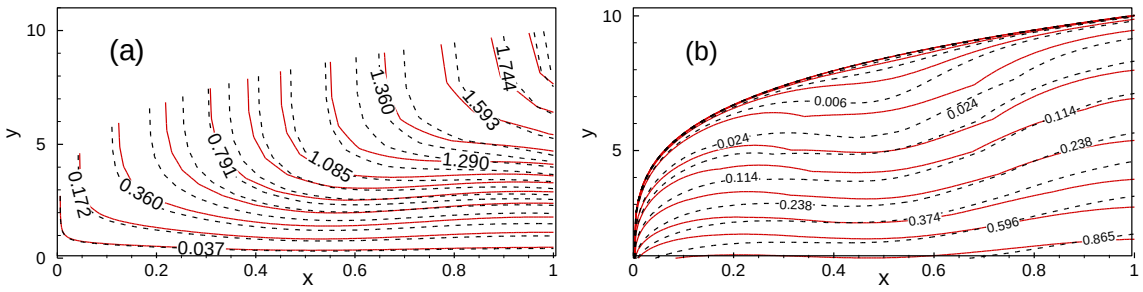

FIGURE 6. (a) Streamlines and (b) Isotherms for Q = 0.0 (Red solid lines), Q = 0.5 (Black dashed lines), with $\alpha = 0.3$, $Pr = 0.72$ and $M = 0.5$.

CONCLUSION

The effects of the pressure work parameter *Ge*, heat generation parameter *Q*, MHD natural convection flow along a uniformly heated vertical wavy surface have been studied numerically. From the present investigations the following conclusions may be drawn:

- The skin friction, the velocity profiles rise up with heat generation parameter Q and reduce for higher values of the magnetic field strength M, pressure work parameter Ge.
- The rate of heat transfer reduces for higher values of the magnetic field strength M, heat generation parameter Q and rise up with the pressure work parameter Ge.
- For increasing values of pressure work parameter Ge the stream function ψ leads to increase. The isolines of temperature (isotherms) show that temperature is 1.0 at the wall and decreases slowly away from the wall and finally approach to zero.

REFERENCES

1. Joshi Y. and Gebhart B, "Effect of pressure stress work and viscous dissipation in some natural convection flows", *International Journal of Heat and Mass Transfer*, Vol. 24 , No. 10, (1981), 1377-1388.
2. Yao, L. S., "Natural Convection along a Vertical Wavy Surface", *ASME Journal of Heat Transfer*, Vol. 105, No. 3, (1983), 465 – 468.
3. Moulic, S. G., Yao, L. S., "Mixed Convection along Wavy Surface", *ASME Journal of Heat Transfer*, Vol. 111, No. 4, (1989), 974 – 979.
4. Alam, K. C. A., Hossain, M. A., Rees, D. A. S., "Magnetohydrodynamic Free Convection along a Vertical Wavy Surface", *International Journal of Applied Mechanics and Engineering*, Vol. 1, (1997), 555-566.
5. Hossain, M. A., Rees, D. A. S., "Combined Heat and Mass Transfer in Natural Convection Flow from a Vertical Wavy Surface", *Acta Mechanica*, Vol. 136, No. 3, (1999), 133-141.
6. Hossain, M. A., Kabir, S, Rees, D. S. A., "Natural Convection of Fluid with Temperature Dependent Viscosity from Heated Vertical Wavy Surface", *Z. Angew. Math. Phys.*, Vol. 53, (2002), 48-57.
7. Jang, J. H., Yan, W. M., Liu, H. C., "Natural Convection Heat and Mass Transfer along a Vertical Wavy Surface", *International Journal of Heat and Mass Transfer*, Vol. 46, No. 6, (2003), 1075-1083.
8. Molla, M. M. , Hossain, M. A. , Yao, L. S, "Natural Convection Flow along a Vertical Wavy Surface with Uniform Surface Temperature in Presence of Heat Generation/Absorption", *International Journal of Thermal Sciences*, Vol. 43, (2004), 157-163.
9. Saboonchi A., Mohammadi Z. M., "Thermal contact resistance of wavy surfaces", *International Journal of Engineering*, Vol. 17, No. 3, (2004), 293-300.
10. Keller, H. B., "Numerical methods in boundary layer theory", *Annual Review of Fluid Mechanics*, Vol. 10, (1978), 417-433.
11. Cebeci, T., Bradshaw, P., "Physical and Computational Aspects of Convective Heat Transfer", Springer, New York, (1984).

ICME2015

International Conference on Mechanical Engineering 2015
(ICME 2015) 18 – 20 December, 2015, Dhaka, Bangladesh

Paper ID : 382

Experimental Investigation of a Diesel-Generator-Set Equipped with a Waste Heat Recovery System

S. Bari[1, 2, a)] and S. N. Hossain[1, b)]

[1]*Barbara Hardy Institute, School of Engineering, University of South Australia, Mawson Lakes, SA 5095, Australia*
[2]*Department of Mechanical Engineering and Engineering Science, University of North Carolina at Charlotte, NC 28223-0001, USA*

[a)]Corresponding author: saiful.bari@unisa.edu.au
[b)]Shekh.Rubaiyat@unisa.edu.au

Abstract. This paper describes the study of a diesel generator-set attached with an exhaust heat recovery system using two heat exchangers. These heat exchangers were manufactured, and tests were performed with water/steam as the working fluid. The optimum pressures of the working fluid were found to be 3, 5, 8 and 15 bar at 10.6, 16.1, 21.5, and 26.6 kW of engine powers, respectively. At these optimum pressures, 0.34, 0.74, 1.78, 2.71 kW additional powers were produced, respectively. A maximum brake specific fuel consumption reduction of 11.1% was achieved due to the additional power of 2.71 kW at the rated power of 26.6 kW. At 40% part load, this bsfc improvement was 3% due to lower exhaust gas temperature.

INTRODUCTION

Internal combustion engines (ICEs) use petroleum fuels to convert available energy into usable work. However, the proven reserve of petroleum fuel has increased by only 26% in the past decade [1]. As a result, the fuel prices will face a price hike in future. This situation implores scientists and researchers to search for different energy sources as well as to increase the efficiency of energy conversion systems such as ICEs [2-5].

Diesel engines are widely used in different fields because of their higher thermal efficiency compared to other ICEs. In remote locations, many towns and agricultural industries rely on diesel-gen-set for electricity. The world installed capacity of power production for this application is about 10-15% [6]. Since the invention of diesel engines, numerous attempts have been tried to improve the efficiency of diesel engines. High injection pressure, Direct Injection (DI), HCCI (homogeneous charge compression Ignition) technologies [7, 8], and the combination of high-boost-pressure and advanced timing of injection [9-11] have been developed to increase the engine performance. Hatazawa et al. [12] studied a water cooled diesel engine and found that about 40% and 25% of the input energy were wasted to the exhaust and coolant, respectively. So, generally, a typical diesel engine rejects around 30-40% of the input fuel energy through the engine's exhaust [14, 16]. Exhaust heat has better recovery prospective than the coolant because it has higher temperature and more exergy content [13]. For typical diesel engines of heavy duty type, the exhaust temperatures vary in between 500 and 700°C [14, 15] whereas the coolant temperature is about 100°C [13].

An effective technique to extract heat from the exhaust gas of a diesel engine is the Rankine Bottoming cycle. Applications of the bottoming Rankine Cycle (RC) to recover exhaust heat from on-road vehicles were first examined during the energy crisis in 1970s [14]. These investigations were mainly for heavy duty (HD) trucks [16-18]. In 1976, Patel and Doyle who worked in Mack Trucks [19] designed, built and tested such a system fitted into the exhaust of a diesel truck engine. They proved the feasibility and economic advantages of the system by conducting 450 km on-road testing. They reported a 12.5% improvement in fuel consumption. In another research, an investigation was carried out by Thermo Electron Corporation [20] utilizing a RC-1 based advanced organic fluid. This is not a pure organic fluid, rather a mixture. The compositions of RC-1 are 40 mole percent hexafluorobenzene and 60 mole percent

pentafluorobenzene. They were able to reduce the bsfc by 3.7%. In 1981, Heywood [21] claimed a fuel consumption reduction by 10% with a Rankine-cycle-based exhaust recovery system for large diesel engines. Srinivasan et al. [22] used basic RC to recover exhaust heat from an advanced-injection low pilot-ignition natural gas (ALPING) engine. He found an improvement of 6.4% in bsfc with low NO_x characteristics of ALPING combustion.

Heat exchangers to extract heat from the exhaust heat is a critical element for the WHR system. Optimization of heat exchanger was carried out for a small capacity engine of 40 kW by the authors in their previous works [23, 24] and an improvement of 12% was found using computer simulations which is much higher than that reported by other research works for small capacity engines (3 – 6% for engines less than 100 kW). This was due to the design optimizations of the heat exchangers, and the pressure of working fluid. In this paper, experimental work of a WHR system with the manufactured optimized heat exchangers is presented.

EXPERIMENTAL SETUP

A 4-cylinder, 4-stroke diesel engine (model HINO W04D) which was attached to an electric generator was used in this current research. The experimental arrangement is presented in Fig. 1. A MPB FlowTrack air flow meter with an accuracy of ±2% was installed upstream of the air intake manifold to calculate the air consumed by the engine. For the measurement of fuel, a stopwatch and a weight-scale having a precision of ±1 g were utilized. The K-type thermocouples with an accuracy of ±1˚C was utilized to collect temperatures at various points. The pressures of the fluids inside the heat exchangers were measured with the help of Burdon tube type pressure gauges. The accuracy of the pressure gauges were ±5 kPa. The mass flow of water/steam, inlet and outlet temperatures of water/steam, and pressures at various points of the heat exchangers were recorded.

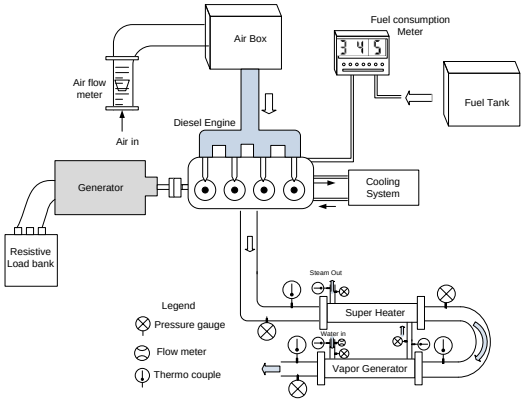

FIGURE 1. Experimental setup.

RESULTS AND DISCUSSIONS

Baseline experiment

Initially, some baseline test of the engine was performed without installing the heat exchangers. The engine performance parameters such as bsfc (brake specific fuel consumption) and thermal efficiency at various engine powers are presented in Fig. 2 which are typical of other related research works [6, 15, 25]. The minimum bsfc and maximum efficiency were found to be 250.4 g/kWh and 31.3%, respectively at the rated power of 26.6 kW. The heat of the exhaust gas of the engine will be used to recovery heat and therefore, a higher exhaust gas temperature is desirable for any heat recovery system. Figure 3 represents the temperature of the exhaust at different engine loads. An approximate exponential relationship between the temperature and the power is found from the figure. At increased engine power more fuel was combusted which produced higher exhaust temperature. Ramadhas et al. [26] reported similar trend in their work. The mass flow rate of fuel was 6.48 kg/h at the rated power of 26.6 kW which produced an exhaust temperature of 479˚C. Rated power is suitable for the engine to run continuously [38]. Thus, this operating point was selected to do the analysis.

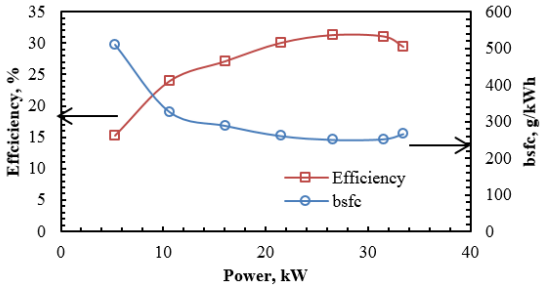

FIGURE 2. Engine performance curves

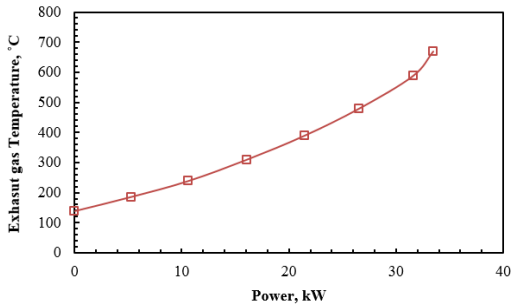

FIGURE 3. Variations exhaust temperature against power.

Experiments with manufactured heat exchanger

As stated earlier, in authors' previous works [23, 24], simulations were carried out to design optimum heat exchangers for this application. The optimum design of the heat exchagers were found to have 31 tubes of 9.4 mm diameter, a shell diameter of 90 mm, a length of 2 m, and 7 baflles with 50% cut. Then, in this research these heat exchagers were manufactured, connected to the exhaust of the engine and tedted.

The water/steam temperature variations with time is presented in Fig. 4. It was found that to generate super-heated steam around 3½ - 5 hrs were required. At any power of the engine, the higher the pressure of the working fluid the higher will be the additional power. However, higher pressure leads to a higher boiling temperature of the water which is limited by the available exhaust temperature and also requires more time for the water to reach that temperature. Therefore, as shown in Fig. 4, at higher powers due to higher boiling temperatures owing to increased working pressures, the time taken to reach the required superheated temperatures were longer.

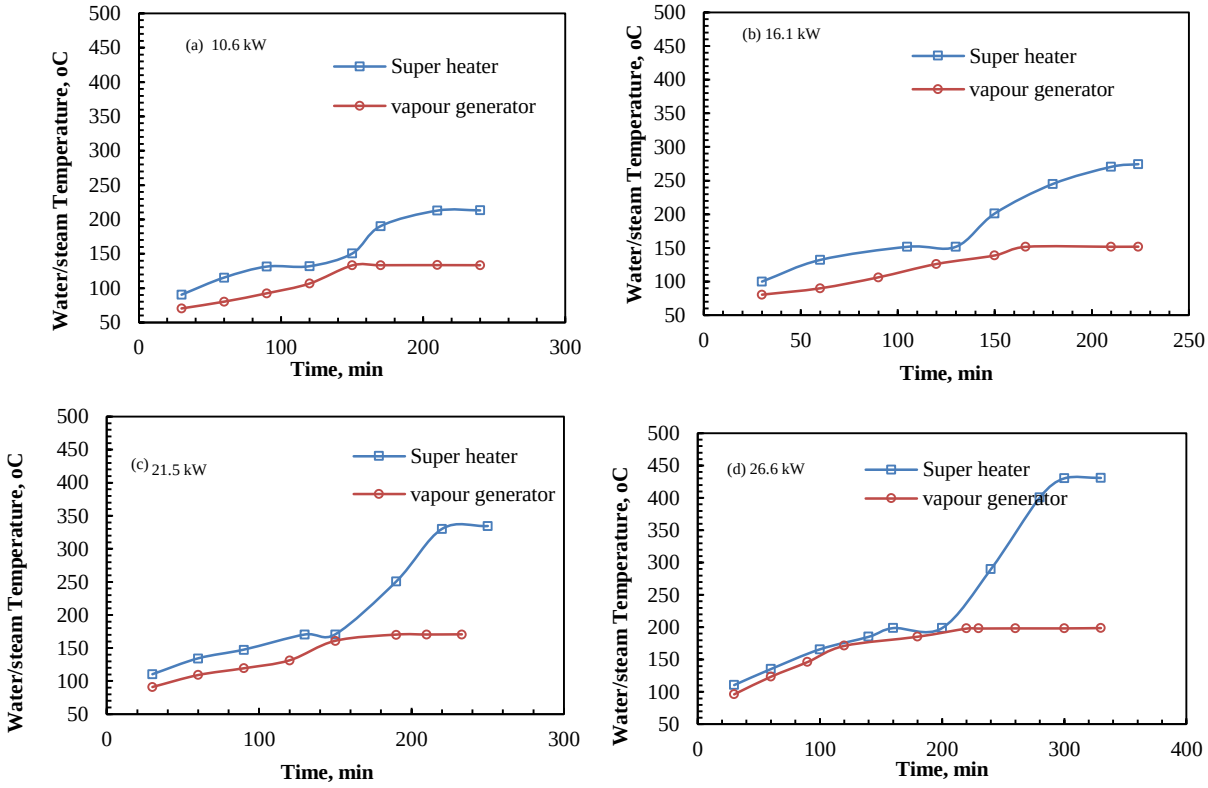

FIGURE 4. Water/steam temperature variations with time at (a) 10.6 kW (b) 16.1 kW (c) 21.5 kW and (d) 26.6 kW power.

In this research, this superheated steam was desirable to expand in a turbine to generate extra power. Although a turbine was not installed in this research, however, the superheated steam was generated at the target turbine inlet temperature at a corresponding working pressure. The superheated steam temperature was higher than the saturation temperature at a particular pressure. Therefore, it was observed that the mass flow rate of steam of super-heater was needed to be lower than the mass flow rate of water of vapour generator to reach superheated and saturated temperatures, respectively with the available exhaust temperature and exhaust gas mass flow rate. Therefore, the optimum mass flow rate of water/steam was the maximum mass flow in the super-heater that could achieve the required superheated temperature at the turbine inlet. These optimum mass flow rates at different powers of the engine as found in experiment are presented in Fig. 5.

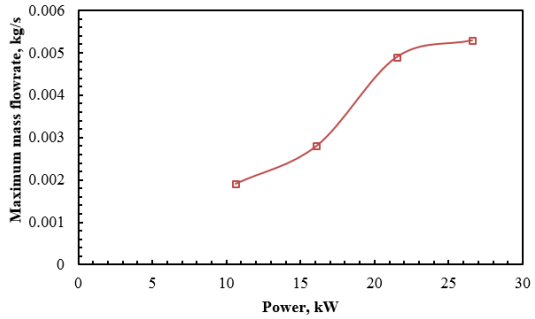

FIGURE 5. Maximum mass flow rate with power of the engine.

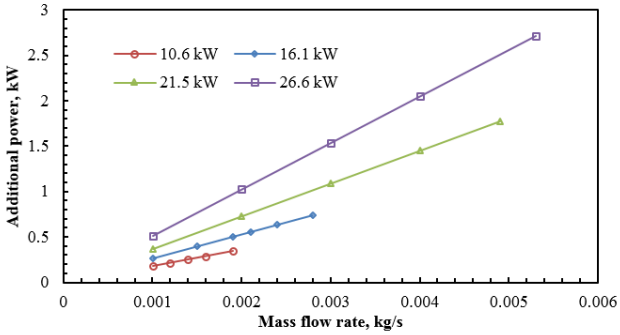

FIGURE 6. Effect of working fluid mass flow rate on additional power.

The effect of the water/steam mass flow rate on additional power generation is presented in Fig. 6. Though, a turbine was not installed in this study, the super-heated steam was generated at the target temperature of the turbine inlet at various working pressures. Then, the additional power generations by the turbine were calculated considering a conservative turbine efficiency of 80% [27]. As previously shown, as the engine power increased the exhaust temperature increased, which allowed the mass flow of the working fluid to increase resulted in higher additional power at higher powers of the engine. For a particular power, the enthalpy drop across the turbine was constant and thus a higher mass flow rate of steam increased the power output linearly. At the maximum power, the mass flow of working fluid was just enough to reach the turbine inlet temperature. Any further increase did not reach the target temperature and therefore, was not shown in the figure. From the figure, it is found that the maximum additional powers calculated at 10.6, 16.1, 21.5 and 26.6 kW engine powers were 0.34, 0.74, 1.78 and 2.71 kW, respectively.

The effect of working pressure on additional power at the rated power of 26.4 kW is shown in Fig. 7. It should be noted here that due to the presence of the heat exchangers the engine experienced negligible amount of power drop from 26.6 kW to 26.4 kW. It is evident from the figure that the additional power generation increased with increasing working pressure. This is due to an increase in the enthalpy drop with increasing working pressure for constant condensing pressure. The maximum additional power generation of 2.71 kW was achieved at the pressure of 15 bar. This is 10.3% additional power at the rated power of 26.4 kW. This maximum pressure was limited by the temperature of the exhaust for this specific engine. It was found in the previous research works by the authors that increased exhaust temperatures for larger size engines of 42 kW managed to use working fluid at a higher pressure of 30 bar and consequently higher additional power of 23.7% was produced [28-30]. For this 26.4 kW rated power engine, the optimum working pressures at part loads of 10.6, 16.1, and 21.5 kW were found to be 3, 5, and 8 bar, respectively.

With the additional power, the bsfc improvements of the engine at rated as well as part loads were calculated from the experimental data and presented in Fig. 8. A maximum improvement of 11.1% was achieved at the rated power. As shown earlier, improvements of 6.4% and 3.8% were achieved by Srinivasan et al [22] and Valentino and Hall [31] for smaller capacity engines of less than 100 kW. The higher improvements found in this research is attributed to the optimizations of the design of heat exchangers and the working fluid pressure.

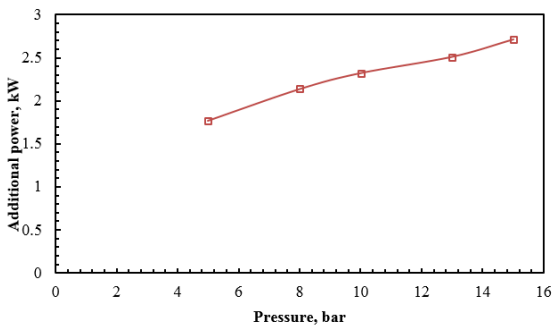

FIGURE 7. Additional power generation at various pressures.

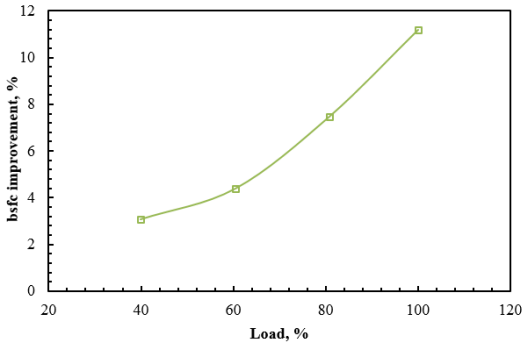

FIGURE 8. Bsfc improvement at various loads.

CONCLUSION

In the current research, a diesel generator-set was used to produce additional power by the heat from the exhaust gas using two heat exchangers. The optimum working fluid pressures were found to be 3, 5, 8 and 15 bar at the engine powers of 10.6, 16.1, 21.5, and 26.6 kW, respectively which resulted into additional powers of 0.34, 0.74, 1.78 and 2.71 kW, respectively. The maximum bsfc improvements were 3% and 11.1% at 40% and 100% loads, respectively. At 40% part load, the exhaust temperatures were lower resulting lower improvement of bsfc.

ACKNOWLEDGEMENTS

Financial and additional help received from Leartek Private Limited to perform this research is greatly appreciated.

REFERENCES

1. L. DeFloriani and G. Nagy, "Representation of Solid Objects by a Modular Boundary Model," in *Computer-Aided Mechanical Assembly Planning*, L. Homem de Mello, S., and S. Lee, Eds., ed Boston: Kluwer Academic, 1991, pp. 41-80.
2. S. Bari and M. M. Roy, "Prospect of rice bran oil as alernative to diesel fuel," presented at the Fifth International Conference on Small Engines, their Fuels and the Environment, pp. 31-36, 1995.
3. S. Bari, "Investigation into the deteriorated performance of diesel engine after prolonged use of vegetable oil," presented at the ASME Internal Combustion Engine Division 2004 Fall Technical Conference, pp. 447-455, 2004.
4. A. Murugesan, C. Umarani, R. Subramanian, and N. Nedunchezhian, "Bio-diesel as an alternative fuel for diesel engines—A review," *Renewable and Sustainable Energy Reviews*, **13**, pp. 653-662, 2009.
5. J. C. de Oliveira Matias and T. C. Devezas, "Consumption dynamics of primary-energy sources: The century of alternative energies," *Applied Energy*, **84**, pp. 763-770, 2007.
6. M. Kanoglu, S. KazIm IsIk, and A. Abusoglu, "Performance characteristics of a Diesel engine power plant," *Energy Conversion and Management*, **46**, pp. 1692-1702, 2005.
7. Z. Şahin, O. Durgun, and C. Bayram, "Experimental investigation of gasoline fumigation in a single cylinder direct injection (DI) diesel engine," *Energy*, **33**, pp. 1298-1310, 2008.
8. K. Sudheesh and J. M. Mallikarjuna, "Diethyl ether as an ignition improver for biogas homogeneous charge compression ignition (HCCI) operation - An experimental investigation," *Energy*, **35**, pp. 3614-3622, 2010.
9. A. Ibrahim, S. Bari, and F. Bruno, "A study on EGR utilization in natural gas SI engines using a two-zone combustion model," SAE Technical Paper, pp. 1294-1303, 2007.
10. D. T. Hountalas, G. C. Mavropoulos, T. C. Zannis, and V. Schwarz, "Possibilities to Achieve Future Emission Limits for HD DI Diesel Engines Using Internal Measures," presented at the SAE Technical Paper Detroit, MI, USA, 2005.

11. A. Ibrahim and S. Bari, "Effect of Varying Compression Ratio on a Natural Gas SI Engine Performance in the Presence of EGR," *Energy & Fuels*, **23**, pp. 4949-4956, 2009.
12. M. Hatazawa, H., Sugita, T.,Ogawa, Y.,Seo, "Performance of a thermoacoustic sound wave generator driven with waste heat of automobile gasoline engine," *Transactions of the Japan Society of Mechanical Engineers (Part B)*, **70**, pp. 292–299, 2004.
13. M. He, X. Zhang, K. Zeng, and K. Gao, "A combined thermodynamic cycle used for waste heat recovery of internal combustion engine," *Energy*, **36**, pp. 6821-6829, 2011.
14. T. Wang, Y. Zhang, Z. Peng, and G. Shu, "A review of researches on thermal exhaust heat recovery with Rankine cycle," *Renewable and Sustainable Energy Reviews*, **15**, pp. 2862-2871, 2011.
15. S. Bari, "Performance, combustion and emission tests of a metro-bus running on biodiesel-ULSD blended (B20) fuel," *Applied Energy*, **124**, pp. 35-43, 2014.
16. E. Doyle, L. DiNanno, and S. Kramer, "Installation of a Diesel-Organic Rankine Compound Engine in a Class 8 Truck for a Single-Vehicle Test," SAE Paper 790646, 1979.
17. C. Leising, G. Purohit, S. DeGrey, and J. Finegold, "Waste heat recovery in truck engines," Society of Automotive Engineers, 400 Commonwealth Dr, Warrendale, PA, 15096, USA, 1978.
18. E. Lodwig, "Performance of a 35-hp Organic Rankine Cycle Exhaust Gas Powered System," *SAE paper*, 1970.
19. P. S. Patel and E. F. Doyle, "Compounding the Truck Diesel Engine with an Organic Rankine-Cycle System," Society of Automotive Engineers, 400 Commonwealth Dr, Warrendale, PA, 15096, USA, 1976.
20. L. DiNanno, F. DiBella, and M. Koplow, "An RC-1 organic Rankine bottoming cycle for an adiabatic diesel engine," Masters Thesis, Waltham, MA, USA, 1983.
21. J. B. Heywood, "Automotive engines and fuels: A review of future options," *Progress in Energy and Combustion Science*, **7**, pp. 155-184, 1981.
22. K. Srinivasan, P. Mago, G. Zdaniuk, L. Chamra, and K. Midkiff, "Improving the efficiency of the advanced injection low pilot ignited natural gas engine using organic Rankine cycles," *Journal of Energy Resources Technology*, **130**, p. 022201, 2008.
23. S. N. Hossain and S. Bari, "Waste heat recovery from the exhaust of a diesel generator using Rankine Cycle," *Energy Conversion and Management*, **75**, pp. 141-151, 2013.
24. S. N. Hossain and S. Bari, "Waste Heat Recovery From the Exhaust of a Diesel Generator Using Shell and Tube Heat Exchanger," in *ASME 2013 International Mechanical Engineering Congress and Exposition*, pp. 1-8, 2013.
25. S. Bari, "Durability issues of running diesel engine with crude palm oil," in *Developments in Renewable Energy Technology (ICDRET)*, pp. 1-4. 2009.
26. A. S. Ramadhas, C. Muraleedharan, and S. Jayaraj, "Performance and emission evaluation of a diesel engine fueled with methyl esters of rubber seed oil," *Renewable Energy*, **30**, pp. 1789-1800, 2005.
27. Y. A. Cengel and M. A. Boles, *Thermodynamics: an engineering approach*: McGraw-Hill Higher Education New York, 2006.
28. S. N. Hossain and S. Bari, "Additional power generation from the exhaust gas of diesel engine by bottoming Rankine cycle," SAE Technical Paper, 2013.
29. S. Bari and S. N. Hossain, "Waste heat recovery from a diesel engine using shell and tube heat exchanger," *Applied Thermal Engineering*, **61**, pp. 355-363, 2013.
30. S. N. Hossain and S. Bari, "Additional Power Generation From Waste Energy of Diesel Engine Using Parallel Flow Shell and Tube Heat Exchanger," *Journal of Engineering for Gas Turbines and Power*,**136**, p. 011401, 2014.
31. R. Valentino, M. J. Hall, and T. Briggs, "Simulation of Organic Rankine Cycle Electric Power Generation from Light-Duty Spark Ignition and Diesel Engine Exhaust Flows," *SAE International Journal of Engines*, **6**, pp. 1299-1310, 2013.

ICME2015

International Conference on Mechanical Engineering 2015
(ICME 2015) 18 – 20 December, 2015, Dhaka, Bangladesh

Paper ID : 407

Atomistic Modelling of Evaporation and Explosive Boiling of Thin Film Liquid Argon over Internally Recessed Nanostructured Surface

Mohammad Nasim Hasan[1, a)], Sheikh Mohammad Shavik[1, b)], Kazi Fazle Rabbi[1, c)] and Mominul Haque[1, d)]

[1] *Department of Mechanical Engineering, Bangladesh University of Engineering & Technology, Dhaka-1000, Bangladesh*

[a)]Corresponding author: nasim@me.buet.ac.bd.com
[b)]shavik@me.buet.ac.bd.com
[c)]rabbi35.me10@gmail.com
[d)]mominulmarup@gmail.com

Abstract. Molecular dynamics (MD) simulations have been carried out to investigate evaporation and explosive boiling phenomena of thin film liquid argon on nanostructured solid surface with emphasis on the effect of solid-liquid interfacial wettability. The nanostructured surface considered herein consists of trapezoidal internal recesses of the solid platinum wall. The wetting conditions of the solid surface were assumed such that it covers both the hydrophilic and hydrophobic conditions and hence effect of interfacial wettability on resulting evaporation and boiling phenomena was the main focus of this study. The initial configuration of the simulation domain comprised of a three phase system (solid platinum, liquid argon and vapor argon) on which equilibrium molecular dynamics (EMD) was performed to reach equilibrium state at 90 K. After equilibrium of the three-phase system was established, the wall was set to different temperatures (130 K and 250 K for the case of evaporation and explosive boiling respectively) to perform non-equilibrium molecular dynamics (NEMD). The variation of temperature and density as well as the variation of system pressure with respect to time were closely monitored for each case. The heat flux normal to the solid surface was also calculated to illustrate the effectiveness of heat transfer for hydrophilic and hydrophobic surfaces in cases of both nanostructured surface and flat surface. The results obtained show that both the wetting condition of the surface and the presence of internal recesses have significant effect on normal evaporation and explosive boiling of the thin liquid film. The heat transfer from solid to liquid in cases of surface with recesses are higher compared to flat surface without recesses. Also the surface with higher wettability (hydrophilic) provides more favorable conditions for boiling than the low-wetting surface (hydrophobic) and therefore, liquid argon responds quickly and shifts from liquid to vapor phase faster in case of hydrophilic surface. The heat transfer rate is also much higher in case of hydrophilic surface.

INTRODUCTION

Rapid liquid to vapor phase transition due to explosive boiling and slow liquid to vapor transition has got significance in various newly emerging technologies, many experimental and numerical studies. This results in protrusion of the use of recessed nanostructured surface, nanostructures embedded over the flat solid surface. In many molecular dynamics studies, heterogeneous phase transition of liquid has become the center of attention for many researchers. Maroo and Chung [3] performed molecular dynamics simulation of platinum heater and associated nano-scale liquid argon film evaporation and colloidal adsorption characteristics. Morshed et al. [4] studied the effect of nanostructures on evaporation and explosive boiling of thin liquid argon films over platinum wall through molecular dynamics simulation. Yamamoto and Matsumoto [5] performed molecular dynamics study on initial stage of nucleate boiling. Yu and Wang [6] simulated evaporation of thin argon liquid films and evaluated the net mass flux. Plawsky

et al. [7] focused on enhancing evaporation using structure on micro and nano level. Weidong et al. [8] monitored the space and time dependences of temperature, pressure, density number, and net evaporation to investigate the phase transition process on a flat surface with and without nanostructures. Hens et al. [9] investigated bubble formation on a platinum substrate with particular emphasis on the surface texture. Sheikh et al. [10] carried out MD simulations to examine explosive boiling of thin liquid argon film on nanostructured surface under different wetting conditions. These studies have confirmed that altering the surface chemistry and surface topography on the micro and the nanoscales can be used to dramatically enhance vaporization and explosive boiling.

Nomenclature

r	Distance between molecules (Å)	*Subscripts*		*Greek symbols*	
t	Time	*Ar*	Argon	ε	Energy parameter of LJ potential (eV)
T	Temperature (K)	*Pt*	Platinum	σ	Length parameter of LJ potential (Å)
P	Pressure (bar)			ϕ	Energy (eV)

SIMULATION METHOD

The three phase system employs solid platinum wall, liquid argon and argon vapor which exists over liquid argon. Figure 1(a) shows the initial configuration of the cuboid simulation box having a dimension of 16.2 nm × 86.9 nm × 8.9 nm (x × y × z). Twenty four monolayers construct the solid wall and are placed at the bottom of the simulation box. The bottom layer of the wall was kept fixed to avoid migration of atoms from simulation box. Next five layers were set as the heat source. Heat is transferred to the liquid argon layers through the remaining layers. The platinum atoms were arranged in FCC (1 0 0) lattice structure corresponding to its density of 21.45×10^3 kg/m^3. The liquid argon layers having a total thickness of 3 nm are placed over the solid wall with a lattice constant corresponding to a density of 1.367×10^3 kg/m^3. The rest of the simulation box is filled with 1035 argon vapor atoms. The total number of atoms in the system was 44480 in the case of simulation consisting recessed surface and 53104 for flat surface. Figure 1(b) shows wall configurations being used. All the interactions between the atoms and the intermolecular forces were evaluated using Lenard–Jones (lj) potential [1].

$$\phi(r) = 4\varepsilon\left[\left(\frac{\sigma}{r}\right)^{12} - \left(\frac{\sigma}{r}\right)^{6}\right] \tag{1}$$

TABLE 1. Lenard-Jones interaction parameters

Parameters	Hydrophilic	Hydrophobic
$\sigma_{Ar\text{-}Ar}$	0.3405 nm	0.3405 nm
$\varepsilon_{Ar\text{-}Ar}$	1.67×10^{-21} J	1.67×10^{-21} J
$\sigma_{Pt\text{-}Pt}$	0.2475 nm	0.2475 nm
$\varepsilon_{Pt\text{-}Pt}$	8.32×10^{-20} J	8.32×10^{-20} J
$\sigma_{Ar\text{-}Pt}$	0.294 nm	0.294 nm
$\varepsilon_{Ar\text{-}Pt}$	2.4×10^{-21} J	8×10^{-22} J

Hens et al. [9] suggested surface wettability based on the condition: when $\varepsilon_{Ar\text{-}Ar} < \varepsilon_{Ar\text{-}Pt}$, the surface can be considered as hydrophilic and when $\varepsilon_{Ar\text{-}Ar} > \varepsilon_{Ar\text{-}Pt}$, surface can be considered as hydrophobic.

The equation of motion for individual particle was integrated using Velocity-Verlet algorithm and Nose-Hoover style non-Hamiltonian equations with 5 fs time step that explicitly evolves positions and velocities. Periodic boundary conditions were applied in the x and z directions. To avoid the escape of gaseous atoms non periodic fixed boundary condition is applied in the y-direction with adiabatic and elastic boundary at the top where the argon atoms are reflected back to the simulation domain from the top boundary without any alteration of momentum and kinetic energy. Three steps have been carried out to realize the simulation. First using constant NVT canonical ensemble thermostat was

turned on at 90 K. Then the fluid domain with NVT ensemble was changed to NVE micro-canonical ensemble and was allowed to equilibrate for 1 ns while the temperature of the wall, liquid and gas were still at around 90 K.

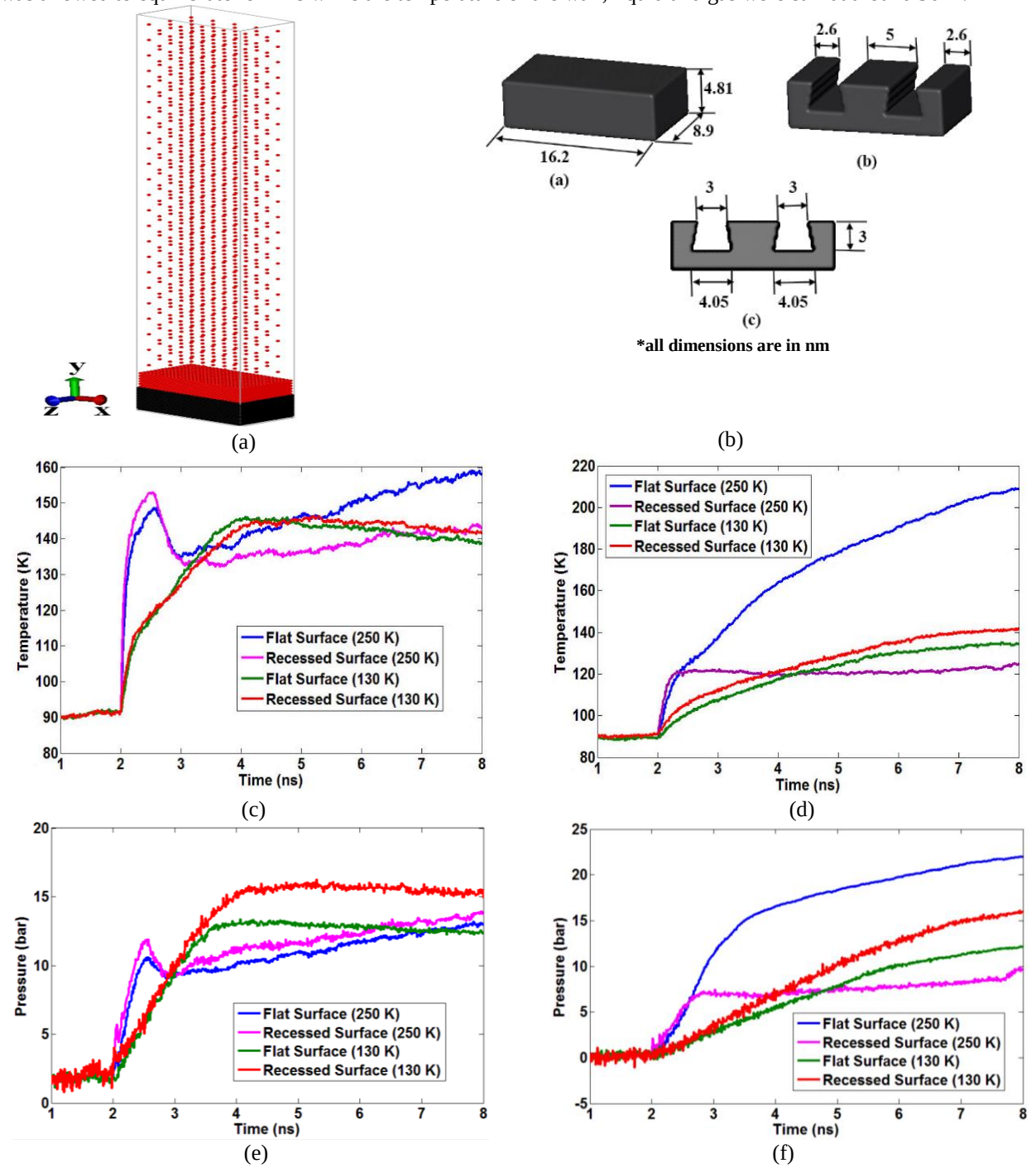

FIGURE 1. Initial configuration of the simulation (a). Solid wall configurations [(a) flat surface; (b) recessed nanostructured surface (isometric view); (c) recessed nanostructured surface (front view)] (b). Temperature history of argon (*Ar*) for hydrophilic surface case (c). Temperature history of argon (*Ar*) for hydrophobic surface case (d). Pressure history of the simulation domain for hydrophilic surface case (e). Pressure history of the simulation domain for hydrophobic surface (f)

The thermodynamic states i.e. temperature, pressure of argon atoms were closely supervised during this period to check the equilibrium of the system. To initiate the phase transition due to explosive boiling and evaporation, the

solid domain was also changed from NVT to NVE and then thermostat was set to 250 K and 130 K respectively. The solid wall (top five layers of the platinum wall) responded and reached equilibrium with the target temperature. The simulation in this condition was run for 6 ns. All the simulations were performed using LAMMPS [11] and visualization was done by VMD (Visual Molecular Dynamics) [12] and OVITO (Open Visualization Tool) [13].

RESULTS AND DISCUSSION

Based on the surface wettability (hydrophilic surface ($\varepsilon_{Ar\text{-}Pt} > \varepsilon_{Ar\text{-}Ar}$) and hydrophobic surface ($\varepsilon_{Ar\text{-}Pt} < \varepsilon_{Ar\text{-}Ar}$)) the wall temperature changes to 250 K and to 130 K in various cases. Figure 1(c) shows temperature history of argon for both the flat and recessed surfaces with hydrophilic wetting condition. When the temperature of the solid wall is suddenly increased from 90 K to 250 K, liquid argon changes phase promptly or explosive boiling occurs. Initially the temperature of the liquid increases abruptly, as liquid layer nearby to the solid wall surpasses the critical temperature and it vaporizes while other layers above are still in the liquid phase. This low density vapor because of its low heat transfer coefficient slowed down energy flow from solid wall. The impulse of this vaporized layer drives the liquid layers upward to separate them from the solid wall. Consequently, the temperature of the argon drops temporarily which indicating that the liquid argon atoms start to get away from the solid wall surface. As shown in Fig. 1(c), for the case of 250 K, argon temperature starts increasing after initial drop for both cases of flat and recessed surface. However, for the lower temperature case with 90 K, the temperature increases at first and then tends to decrease to obtain a balanced state for both surfaces under consideration. Similar result has been reported by Weidong et al. [8] however, complete balanced state has not been found within the simulation time in this study. Figure 1(d) shows the temperature history of the system for the hydrophobic case. In case of hydrophobic surface, solid-liquid interaction is weak. As a result, energy transfer from the solid surface to liquid layer is much lower compared to hydrophilic surface. For flat hydrophobic surface with 250 K wall temperature, explosive boiling does not occur as indicated by the fact that no eminent temperature drop of argon is noticed. Rather, the temperature of the liquid gradually increases with time-indicating a diffusion/evaporation type phase change process. However, addition of nanostructured recess exposes more solid area to liquid which in result offers explosive boiling in case of hydrophobic surface as depicted in Fig. 1(d). As the wall temperature change to 130 K, phase change process takes place as evaporation like in hydrophilic cases for both surface patterns.

Figures 1(e) and 1(f) show the pressure history of hydrophilic and hydrophobic surface respectively. Because of volume constraint with the escalation of temperature, the pressure increases and it exactly follows the temperature trend of the simulation domain in all cases. In high temperature case for hydrophobic case, pressure goes increasing for flat surface and this pressure is higher than recessed surface. This is due to the fact that over the recessed surface the low density vapor presents resistance to energy flow which causes lower temperature and in turn lower pressure. The pressure of the simulation domain for hydrophobic surfaces only increasing trend and is strongly influenced by the presence of nanostructures. Snapshots of simulation domain at different times are depicted in Figs. 2 and 3 for high temperature hydrophilic and hydrophobic case separately. In flat surface and recessed surface disjoining of liquid cluster occurred in between 150-200 ps. As inclusion of recess increases solid surface area, the liquid gets more heated and advances to higher level causing earlier separation from solid recessed wall. With the progression of time liquid cluster get fragmented to smaller clusters. Figures 4 and 5 display snapshots for temperature 130 K. In this case, liquid layers are evenly heated and no cluster is formed.

Figure 6(a) illustrates number density profile at 3ns and shows strong evidence of the existence of cluster for hydrophilic surface cases. Figure 6(a) shows that for explosive boiling the number density is maximum at around 50 nm in case of recessed surface and at around 76 nm for flat surface. In these positions the argon atoms are close to each other and their kinetic energy is lower than other regions, therefore, the temperature of argon atoms in this region is low. But number densities are small at 130 K denoting no sign of cluster and evenly phase change from liquid to vapor. Figure 6(b) depicts the number density profile at 3ns for hydrophobic case and shows that liquid cluster is present only in case of recessed surface at 250 K. Vapor domain, liquid domain and their interface near cluster can be identified from the number density profile by the slope around the peaks.

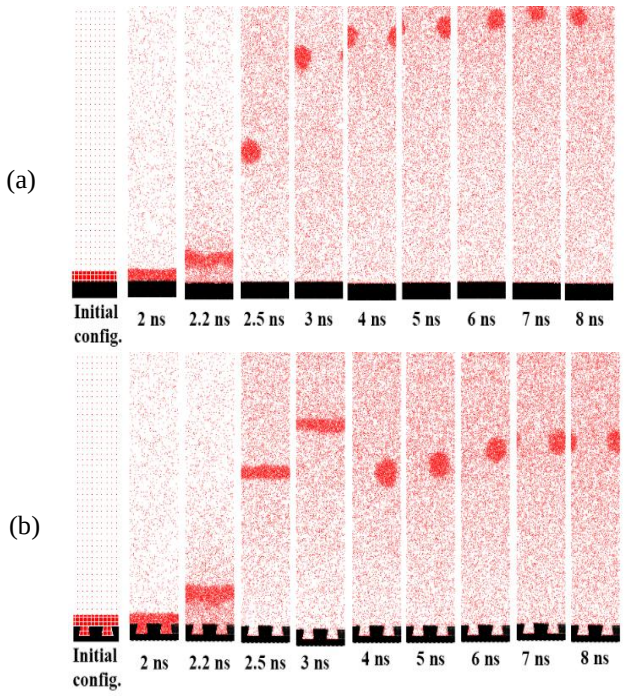

FIGURE 2. Snapshots from the simulation domain for hydrophilic surface case at 250 K, (a) flat surface, (b) recessed surface

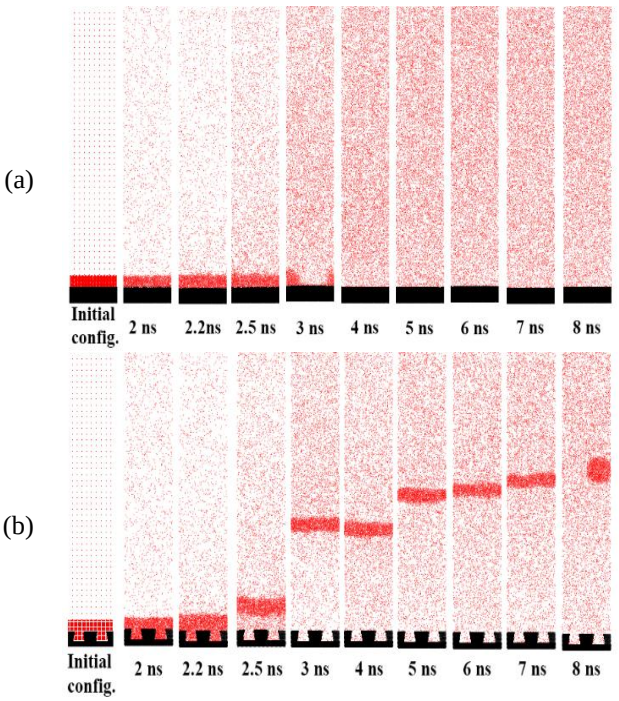

FIGURE 3. Snapshots from the simulation domain for hydrophobic surface case at 250 K, (a) flat surface, (b) recessed surface

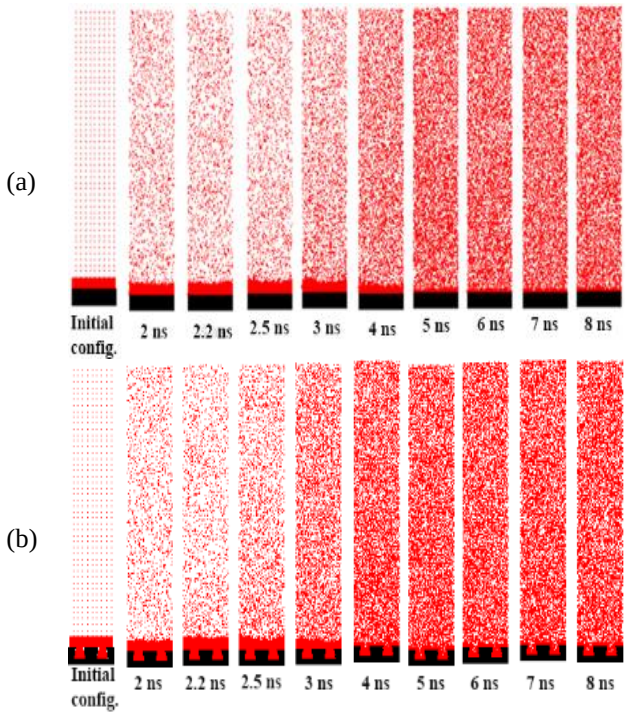

FIGURE 4. Snapshots from the simulation domain for hydrophilic surface case at 130 K, (a) flat surface, (b) recessed surface

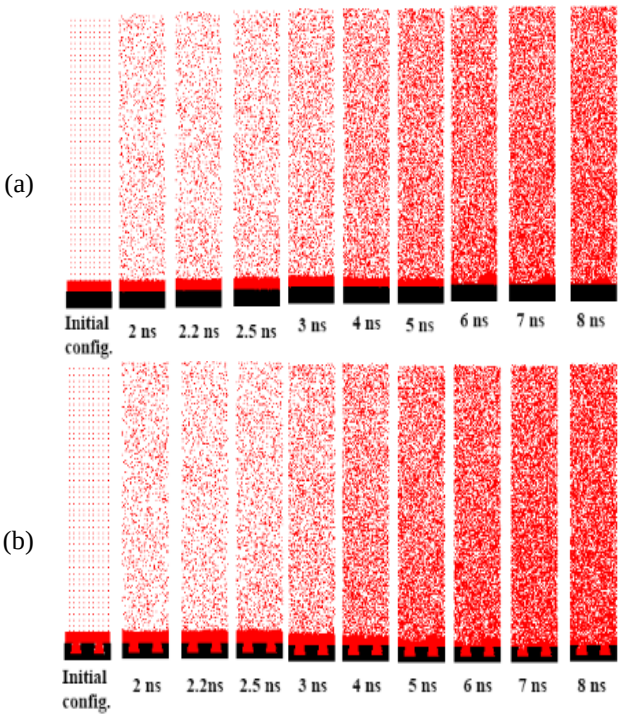

FIGURE 5. Snapshots from the simulation domain for hydrophobic surface case at 130 K, (a) flat surface, (b) recessed surface

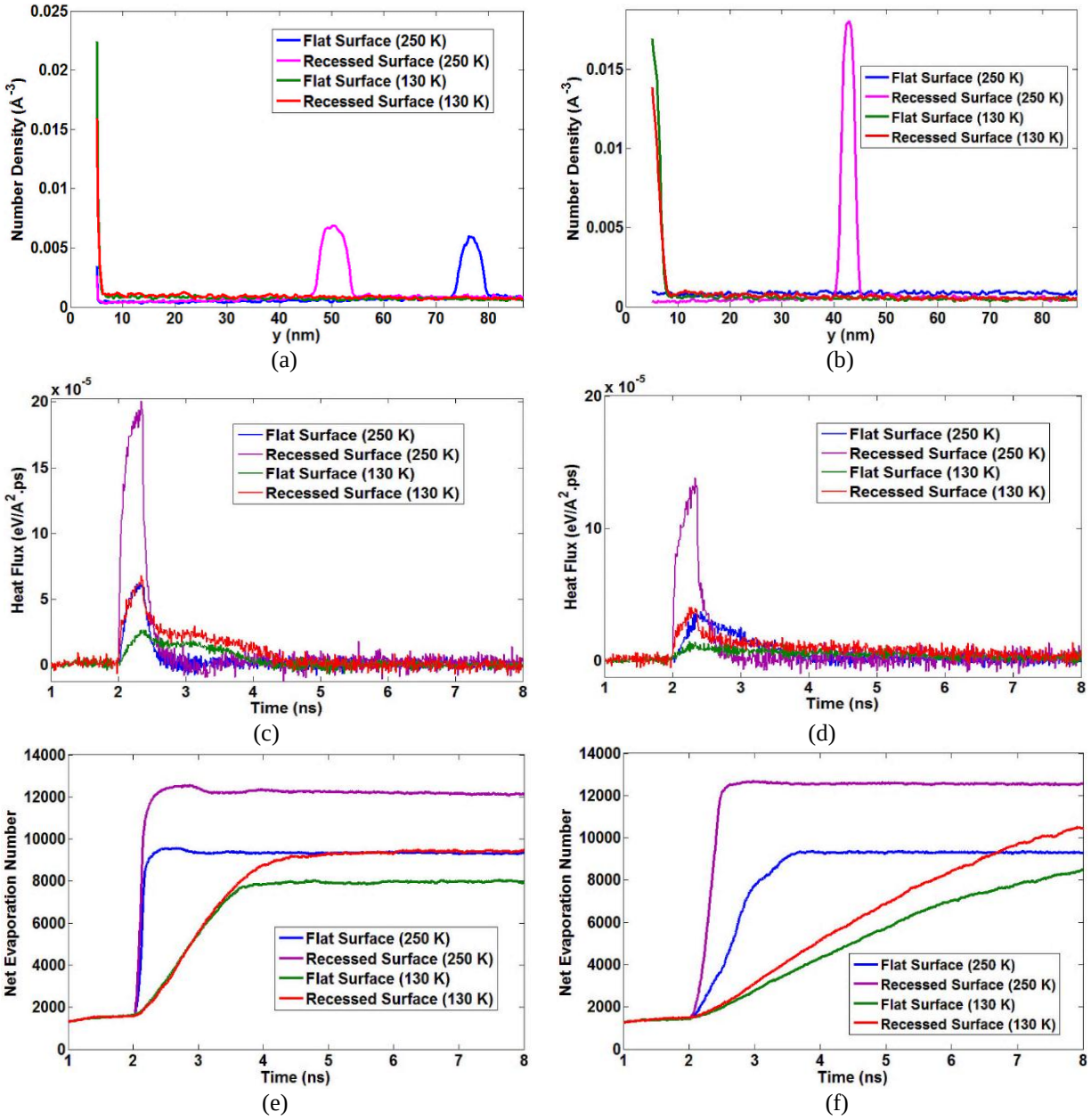

FIGURE 6. Number density profile of argon at 3 ns for hydrophilic surface case along y axis (a). Number density profile of argon at 3 ns for hydrophobic surface case along y axis (b). Heat flux normal to solid wall for hydrophilic surface case (c). Heat flux normal to solid wall for hydrophobic surface case (d). Net evaporation number for hydrophilic surface case (e). Net evaporation number for hydrophobic surface case (f)

To quantify the effectiveness of heat transfer, heat flux normal to the bottom plate were evaluated using per-atom kinetic energy, per-atom potential energy, and per-atom stress as described in [11]. Figures 6(c) and 6(d) depict the heat flux normal to the solid wall (xz plane) for hydrophilic and hydrophobic cases respectively for all cases. For all the cases the trend of the profiles is same. These figures show addition of heat flux when temperature was changed to 250 K for explosive boiling and to 130 K for evaporation. This addition is only for a small period of time and after that it decays near to zero and fluctuates around this value. The heat flux profiles are in good agreement with previous study conducted by Yamamoto and Matsumoto [5]. Unquestionably, explosive boiling over hydrophilic recessed

surface gives higher heat flux than hydrophobic recessed surface. Note that, higher heat transfer occurs in case of recessed surface than flat surface. The most interesting outcome is that the use of recessed surface at 130 K gives higher heat flux than in the case of flat surface at 250 K and this holds for both hydrophilic and hydrophobic case. For different wettability conditions, heat fluxes are computed from Figs. 6(c) and 6(d) that have been tabulated in Table 2. Note that, in case of flat hydrophilic surface the maximum value of the heat flux is higher than the magnitude of theoretical maximum value of heat flux, $q_{max,max} \approx 800$ MW/m^2 as defined by Gambill and Lienhard [2].

TABLE 2. Heat flux for different surfaces based on surface chemistry

Wall Temperature (K)	Surface	Maximum Wall Heat Flux (MW/m^2)	
		Hydrophilic	Hydrophobic
130	Flat	428	229.92
	Recessed	1084.16	644.32
250	Flat	1003.2	596
	Recessed	3209.6	2209.6

Figure 6(e) illustrates net evaporation number for hydrophilic case that has been calculated from the change of argon vapor atoms in vapor region. Evaporation number increases rapidly for 250 K case and then remains constant showing there is no active interaction between solid atoms and liquid atoms. For 130 K case, it reaches equilibrium with a delay. Figure 6(f) shows curves for explosive boiling which follows same pattern as in Fig. 6(e) but at a small delay. For 130 K case, the curves do not reach equilibrium in the simulation time. Evaporation number may differ with pressure in the vapor region, wall–fluid interaction force and the temperature of the wall as suggested by Maroo and Chung [3].

CONCLUSION

The use of recessed surface increases heat transfer rate, shows promising result for hydrophilic case and gives more heat transfer when used at low temperature (130 K) than flat surface at high temperature (250 K). In case of hydrophobic case explosive boiling can be achieved by introduction of recess which can't be obtained in flat surface case. The evaporation rate also increases with the use of recess nanostructure. The usage of hydrophilic recessed surface offers 21.55% more maximum heat flux than the hydrophilic nanostructured surface studied by Sheikh et al. [10] for explosive boiling case. Using hydrophilic surface conditions at 250K and 130K for recessed surface, contributes 45.25% and 68.26% more maximum heat flux than their respective hydrophobic cases. In case of evaporation, there are presence of non-evaporating layers which causes low heat transfer as described in Maroo and Chung [3].

REFERENCES

1. J.E. Lennard-Jones, A.F. Devonshire, Philos. Trans. R. Soc. Lond. Ser. A, Math. Phys. Sci. 163 (1937) 53-70.
2. W. R. Gambill, and J. H. Lienhard, "An upper bound for the critical boiling heat flux," J. Heat Transfer, 111(1989) 815-818.
3. S.C. Maroo, and J.N. Chung, "Molecular dynamic simulation of platinum heater and associated nano-scale liquid argon film evaporation and colloidal adsorption characteristics," J. Colloid Interface Sci. 328 (2008) 134–146.
4. A.K.M.M. Morshed, Taitan C. Paul, Jamil A. Khan, "Effect of nanostructures on evaporation and explosive boiling of thin liquid films: a molecular dynamics study," Applied Physics A 105 (2011) 445-451.
5. T. Yamamoto, and M. Matsumoto, "Initial stage of nucleate boiling: molecular dynamics investigation," J. Therm. Sci. Technol. Jpn. 7 (2012) 334–349.
6. J. Yu, and H. Wang, "A molecular dynamics investigation on evaporation of thin liquid films," Int. J. Heat Mass Transfer 55 (2012) 1218-1225.
7. J. L. Plawsky, A. G. Fedorov, S. V. Garimella, H. B. Ma, S. C. Maroo, L. Chen, and Y. Nam, "Nano- and microstructures for thin-film evaporation—a review."

8. Weidong Wang, Haiyan Zhang, Conghui Tian and Xiaojie Meng, "Numerical experiments on evaporation and explosive boiling of ultra-thin liquid argon film on aluminum nanostructure substrate."
9. A. Hens, R. Agarwal, G. Biswas, "Nanoscale study of boiling and evaporation in a liquid Ar film on a Pt heater using molecular dynamics simulation," Int. J. Heat Mass Transfer 71 (2014) 303-312.
10. Sheikh Mohammad Shavik, Mohammad Nasim Hasan, A.K.M. Monjur Morshed, "Molecular dynamics study on explosive boiling of thin liquid argon film on nanostructured surface under different wetting conditions," InterPACKICNMM2015-48352.
11. LAMMPS User's Manual (http://lammps.sandia.gov – Sandia National Laboratories, USA).
12. Humphrey W, Dalke A, Schulten K. VMD: Visual Molecular Dynamics. J Mol Graph. 1996; 14133: 1996
13. Stukowski A. Visualization and analysis of atomistic simulation data with OVITO-the Open Visualization tool, Model Simul Mater Sci Eng. 2010; 18: 015012

ICME2015

International Conference on Mechanical Engineering 2015
(ICME 2015) 18 – 20 December, 2015, Dhaka, Bangladesh

Paper ID : 411

Entropy Generation inside an Inclined Porous Trapezoidal Enclosure with Wavy Top Surface

Sehrina Muzahid Eshon[1, a)], Rakib Mustafa[1, b)] and Mohammad Nasim Hasan[1, c)]

[1]*Department of Mechanical Engineering, Bangladesh University of Engineering and Technology (BUET) Dhaka-1000, Bangladesh*

[a)]Corresponding author: sehrinamuzahid@yahoo.com
[b)]rakib09me@gmail.com
[c)]nasim@me.buet.ac.bd

Abstract. This work presents the analysis of entropy generation during natural convection inside a tilted trapezoidal porous cavity with wavy top wall. The bottom wall of the cavity is heated sinusoidally whereas the top wall is kept cold at constant low temperature. The sidewalls of the cavity are maintained adiabatic. The physical problem has been represented mathematically by various governing equations along with the corresponding boundary conditions and hence solved by using Galerkin Finite Element scheme. Entropy generation parameters were studied through analysis of entropy generation due to heat transfer irreversibilities (S_θ) as well as fluid friction irreversibilities (S_ψ). Further detailed discussion on variations in total entropy generation (S_{total}) and Bejan number (*Be*) for various Rayleigh numbers (*Ra*), Darcy numbers (*Da*) and angle of inclination (φ) are made. The range of various governing parameters considered in the present study are: $10^4 \leq Ra \leq 10^6$, $10^{-5} \leq Da \leq 10^{-3}$ and $0° \leq \varphi \leq 90°$. It has been found that total entropy generation increases with the increase in Rayleigh number as well as Darcy number. The study of effect of inclination angle revealed angles responsible for minimum and maximum entropy generation inside the cavity. It was also observed that Bejan number (*Be*) is below 0.5 at $Ra = 10^6$ and $Da = 10^{-3}$ which implies dominance of fluid friction irreversibility at higher *Ra* and *Da;* however *Be* being greater than 0.5 at lower *Ra* and *Da* implying dominance of heat transfer irreversibility in these regions.

INTRODUCTION

Natural convection heat transfer has engineering applications in thermal storage, environmental comfort, electronic cooling, etc. Buoyancy induced convection in saturated porous media can be seen widely used in recent years, which involves post accidental heat removal in nuclear reactors, cooling of radioactive waste containers, heat exchangers, solar power collectors, grain storage, food processing, energy efficient drying processes etc. Pioneering works of Neild and Bejan [1] and Darcy [2] contributed a wide overview of heat transfer of porous media. Sompong and Witayangkurn [3] studied the effects of various parameters, Rayleigh number (*Ra*), Darcy number (*Da*), and wave amplitude (a), on natural convection inside a trapezoidal enclosure with wavy top surface. Khansila and Witayangkurn [4] dealt with visualization of natural convection heat transfer in rectangular enclosure filled with porous media and heated sinusoidally on the left vertical wall. These studies provided information about the heat distribution inside the cavity but is not sufficient to account for the loss in available energy or explain the efficiency of the heating processes. Level of efficiency of a convection process can be derived from the study the entropy generation within the system. Entropy is a thermodynamic quantity representing the unavailability of a system's thermal energy for conversion into useful work. It is often interpreted as the degree of disorder of the system. The issue of entropy generation in a tilted saturated porous cavity for laminar natural convection heat transfer was analyzed by Baytas [5] where the mass, momentum and energy balance equations were solved numerically using Darcy's law and Boussinesq-incompressible approximation. Basak et al. [6] carried out an investigation was based on analysis of heat flow visualization and entropy generation during natural convection within inclined square cavities where one of the vertical walls was cold

and the other hot while the top and the bottom walls were kept adiabatic. Bejan [7, 8] introduced entropy generation minimization concept based on the second law of thermodynamics. Mahmud and Islam [9] solved the laminar free convection and entropy generation inside an inclined wavy enclosure and concluded that entropy generation is affected by inclination angle. Bayatas [10] presented a numerical study on the minimization of entropy generation in an inclined enclosure. Bejan [11] showed that the entropy generation for forced convective heat transfer is due to temperature gradient and viscous effect of the fluid. The main objective of the present study is to analyze the entropy generation due to heat transfer and fluid friction during natural convection in a trapezoidal cavity for different system parameters.

Nomenclature

Be	Bejan number	β	volume expansion coefficient (K^{-1})
Da	Darcy number, k/L^2	θ	dimensionless temperature, $(T-T_c)/(T_h-T_c)$
g	acceleration due to gravity (ms^{-2})	μ	dynamic viscosity ($kgm^{-1}s^{-1}$)
k	thermal conductivity ($Wm^{-1}k^{-1}$)	ν	kinematic viscosity (m^2s^{-1})
p	pressure (Pa)	ρ	density of the fluid (kgm^{-3})
P	dimensionless pressure, $pL^2/\rho\alpha^2$	S_θ	Entropy generation due to heat transfer
Pr	Prandtl number	S_ψ	Entropy generation due to fluid friction
Ra	Rayleigh number, $(g\beta(T_h-T_c)L^3Pr)/(\nu^2)$	S_{tot}	Total entropy generation
T	Temperature of fluid (K)	x, y	distance along x, y-coordinate (m)
T_h	maximum temperature of the heated bottom wall (K)	X,Y	distance along dimensionless x, y-coordinate
T_c	temperature of the cold wavy top wall (K)	u, v	velocity component at x, y-direction (ms^{-1})
T_0	Bulk temperature, $(T_h+T_c)/2$ (K)	U,V	velocity along dimensionless x, y-coordinate
α	thermal diffusivity (m^2s^{-1})		

PROBLEM FORMULATION

In the present investigation entropy generation for natural convection inside a tilted porous trapezoidal cavity as shown in Fig. 1 has been considered. The wavy top wall has the profile $\boldsymbol{a + bcos(2\pi X)}$, where a = 0.9 and b = 0.1. The bottom wall of the enclosure is heated with sinusoidal boundary condition, the top wavy wall is kept isothermally cold and the side walls are maintained adiabatic.

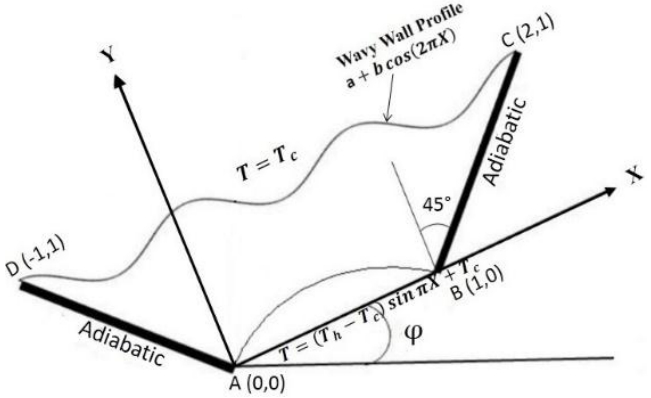

FIGURE 1. Physical model of the 2D inclined porous cavity

MATHEMATICAL MODELING, SIMULATION AND POST-PROCESSING

Velocity and Temperature Distribution

In the present study the Boussinesq approximation is adopted and assumed that the fluid is incompressible and viscous dissipation effects are neglected. The governing equations for steady two-dimensional natural convection flow in an inclined porous trapezoidal cavity using conservation of mass, momentum, and energy may be written with the following dimensionless variables and numbers:

$$\frac{\partial u}{\partial x}+\frac{\partial v}{\partial y}=0 \tag{1}$$

$$U\frac{\partial u}{\partial x}+V\frac{\partial u}{\partial y}=-\frac{\partial P}{\partial X}+\Pr\left(\frac{\partial^2 u}{\partial X^2}+\frac{\partial^2 u}{\partial Y^2}\right)-\frac{\Pr}{Da}U+Ra\,\Pr\theta\sin\varphi \tag{2}$$

$$U\frac{\partial v}{\partial x}+V\frac{\partial v}{\partial y}=-\frac{\partial P}{\partial X}+\Pr\left(\frac{\partial^2 v}{\partial X^2}+\frac{\partial^2 v}{\partial Y^2}\right)-\frac{\Pr}{Da}V+Ra\,\Pr\theta\cos\varphi \tag{3}$$

$$U\frac{\partial \theta}{\partial x}+V\frac{\partial \theta}{\partial y}=\frac{\partial^2 \theta}{\partial X^2}+\frac{\partial^2 \theta}{\partial Y^2} \tag{4}$$

The above equations are normalized using the following dimensionless scales,

$$X=\frac{x}{L},Y=\frac{y}{L},U=\frac{uL}{\alpha},V=\frac{vL}{\alpha},\theta=\frac{T-T_c}{T-T_h},P=\frac{pL^2}{\rho\alpha^2},\Pr=\frac{\gamma}{\alpha},Da=\frac{k}{L^2},Ra=\frac{g\beta(T_h-T_c)L^3\Pr}{\gamma^2} \tag{5}$$

For velocity profile, no-slip boundary conditions (U = V= 0) is assumed for all boundaries.
The boundary conditions for temperature are given as

Top Wall: θ = 0; Bottom Wall: θ = sin (πX); Side Walls: $\frac{\partial\theta}{\partial n}=0$ (where n is in the direction normal to the wall) (6)

Entropy Generation

The entropy generation is due to the irreversible nature of heat transfer and viscous effects, within the fluid and the solid boundaries. According to local thermodynamic equilibrium of linear transport theory, the dimensionless form of local entropy generation rate in porous media due to heat transfer and fluid friction for two-dimensional Cartesian co-ordinates has been derived in Basak et al. [8] which is expressed as

$$S_\theta=\left[\left(\frac{\partial\theta}{\partial X}\right)^2+\left(\frac{\partial\theta}{\partial Y}\right)^2\right] \tag{7}$$

$$S_\psi=\phi\left\{\left[U^2+V^2\right]+Da\left[2\left(\left(\frac{\partial U}{\partial X}\right)^2+\left(\frac{\partial V}{\partial Y}\right)^2\right)+\left(\frac{\partial U}{\partial Y}+\frac{\partial V}{\partial X}\right)^2\right]\right\} \tag{8}$$

Where, S_θ and S_ψ are the local entropy generation due to heat transfer and fluid friction respectively. In the expression for S_ψ Eq. (7), the parameter ϕ is called irreversibility distribution ratio, it is the ratio between viscous and thermal irreversibilities and is defined as

$$\phi=\frac{\mu T_0}{k}\left(\frac{\alpha}{L\Delta T}\right)^2 \tag{9}$$

In the current study, ϕ is taken as 10^{-2} as adopted in Basak et al. [8]. The combined total entropy generation (S_{total}) in the cavity is given by the summation of total entropy generation due to heat transfer ($S_{\theta,total}$) and fluid friction ($S_{\psi,total}$), which in are obtained by integrating the local entropy generation rates (S_θ and S_ψ) over the domain Ω.

$$S_{total}=S_{\theta,total}+S_{\psi,total}=\int(S_\theta)d\Omega+\int(S_\psi)d\Omega \tag{10}$$

An alternative irreversibility distribution parameter called Bejan number (*Be*) is given in dimensionless form as follows:

$$Be = \frac{S_{\theta,total}}{S_{\theta,total} + S_{\psi,total}} = \frac{S_{\theta,total}}{S_{total}} \tag{11}$$

When $Be > 0.5$, the irreversibility due to heat transfer dominates, for $Be < 0.5$, the irreversibility due to viscous effects dominates and when $Be = 0.5$, heat transfer and fluid friction irreversibility are equal. Heat transfer irreversibility is the only origin of entropy generation when $Be = 1$. When $Be = 0$, the fluid friction irreversibility is the only source of entropy generation.

Computational Details and Validation

The continuity equation Eq. (1) represents conservation of mass which can be used to obtain the pressure distribution by penalty formulation. The momentum and energy balance equations Eqs. (2) – (3) are solved using Galerkin weighted residual finite element technique. The present numerical technique will discretize the computational domain into unstructured triangles by Delaunay Triangular method. It is found through grid sensitivity test that 9200 non-regular nodes are sufficient to provide accurate results.

The present code has been validated using the work of Basak et al [12] which dealt with a square cavity filled with a porous medium. The bottom wall is sinusoidally heated with adiabatic top wall keeping the side walls at a constant cold temperature. The contours of S_θ and S_ψ are compared with present study (Fig. 2) and there is excellent agreement between the two works.

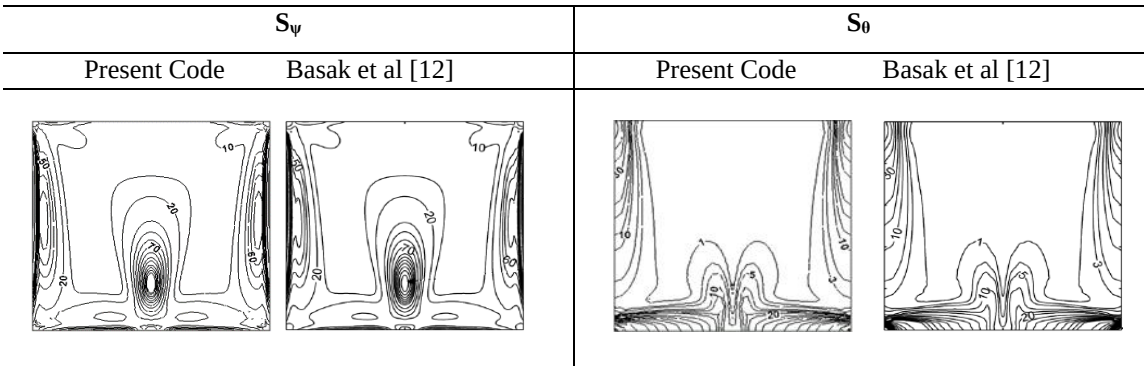

FIGURE 2. Comparison of entropy generation maps (S_ψ, S_θ) for $Ra = 5310^5$ and $Da = 10^{-3}$

RESULT AND DISCUSSION

Entropy generation minimization which allows an increase in overall efficiency has recently been the emerging thermodynamic approach for the optimization of engineering system. In the present study, the range of various governing parameters (*Ra*, *Da*, and φ) are varied as: $10^4 \le Ra \le 10^6$, $10^{-5} \le Da \le 10^{-3}$, $0° \le \varphi \le 90°$. Obtained results are systemically presented in terms of entropy generation due to heat transfer (S_θ) and fluid friction (S_ψ) inside the cavity.

Effect of Rayleigh Number (*Ra*)

Rayleigh number is concerned with the magnitude of buoyancy driven force which affects flow and heat transfer characteristics. Figure 3 shows the entropy generation maps for Prandtl number, $Pr = 7.2$, inclination angle, $\varphi = 0^\circ$ and Darcy number, $Da = 10^{-3}$ where Rayleigh number is varied from $Ra = 10^4$ to 10^6. With the increase in *Ra* convection dominant heat transfer is noticed and a rise in the intensity of fluid flow is experienced. As the bottom wall is heated sinusoidally, maximum entropy generation is located near the bottom wall. For $Ra = 10^4$, $S_{\theta,max} = 38.6$ which is found at the two bottom corners since the isotherms are concentrated at these locations. For low *Ra* (10^4), S_ψ is low due to presence of weak fluid flow field. The magnitude of $S_{\psi,max}$ is 0.0386 for $Ra = 10^4$ which is found near the middle portion

of the bottom wall. At increased *Ra* (10^6), the buoyancy driven forces increase and thus convection dominates inside the cavity. With the enhanced convection process and larger temperature gradient, a high entropy generation is noticed in the cavity.

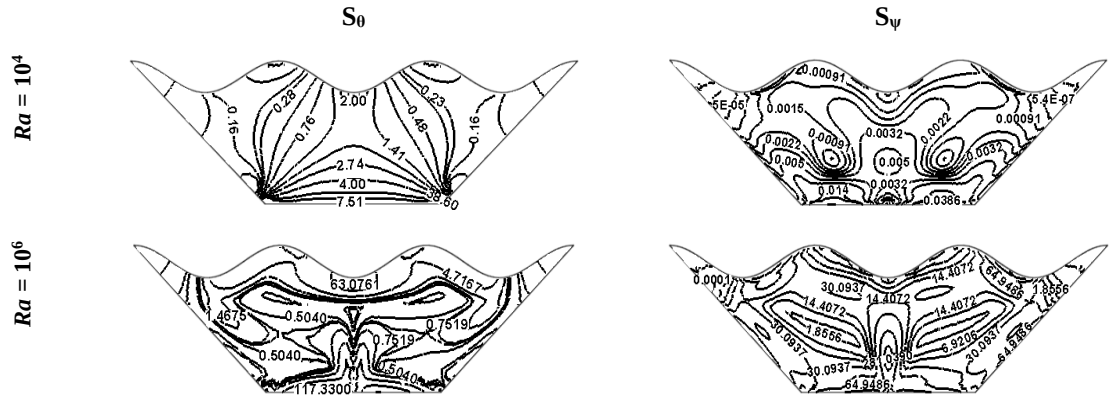

FIGURE 3. Variations of local entropy generation maps (S_θ, S_ψ) for $Da = 10^{-3}$, $\varphi = 0°$, $Pr = 7.2$ at different Rayleigh numbers

At $Ra = 10^6$, $S_{\theta,max} = 117.33$ which is found near the middle region of the bottom wall. Significant increase in S_ψ is observed at $Ra = 10^6$ due to the rise in intensity of the fluid flow. The dense contours of S_ψ occur at the center of the cavity due to the larger velocity gradient where $S_{\psi,max} = 281.039$. In the contours for S_ψ two circulation zones exist on either side of the central region which becomes more elliptical in shape with increasing values of *Ra.*

Effect of Darcy Number (*Da*)

Darcy number is the measure of the permeability through a porous medium. It is defined as the relative effect of the permeability of the medium versus its cross-sectional area. Figure 4 shows the entropy generation maps for $Pr = 7.2$, inclination angle $\varphi = 0^\circ$ and $Ra = 10^6$ varying the Darcy number *Da* between10^{-5} and 10^{-3}. At lower *Da*, the hydraulic resistance of the porous medium is higher and thus the fluid flow is weak. It may be noted that the heat transfer is dominated by conduction regime even at relatively higher *Ra* (10^6) in case of lower values of *Da*. At low Darcy number (10^{-5}), the resistance to thermal permeability is also high. As a result, entropy generation due to heat transfer (S_θ) is low.

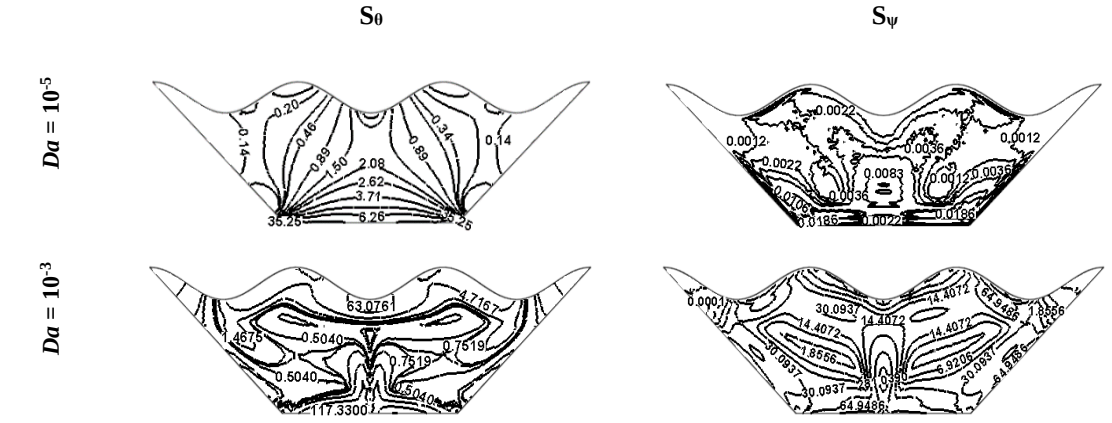

FIGURE 4. Variations of local entropy generation maps (S_θ, S_ψ) for $Ra = 10^6$, $\varphi = 0°$, $Pr = 7.2$ at different Darcy numbers

In the same manner, the entropy generation due to fluid friction (S_ψ) is found to be significantly low due to weak convection in the cavity at low *Da*. So, overall entropy generation is small. As *Da* increases, the hydraulic resistance

of the porous medium decreases and both the heat and fluid flow due to convection is enhanced significantly. Large thermal and velocity gradients are observed. The higher value of *Da* indicates that the permeability of the porous medium is high and hence the fluid velocities are also higher causing both S_θ and S_ψ to have higher values. The entropy generation due to heat transfer is more near the hot bottom wall, where S_θ contours are concentrated. The cold side walls also contribute to S_θ at higher *Da* since large amount of heat is transferred to those regions and they also act as strong sites of entropy generation due to fluid friction at higher *Da*. For $Da = 10^{-5}$, $S_{\theta,max} = 35.25$ and $S_{\psi,max} = 0.0186$. Contours of S_ψ are discontinuous because of higher fluid flow resistance. At higher *Da* (10^{-3}), due to the decreased hydraulic resistance, large temperature gradients are observed. A high value of S_θ is experienced where $S_{\theta,max} = 117.3$ for $Da = 10^{-3}$ is located at the mid-region of the bottom wall. Circulation of fluid inside the cavity is enhanced due to high Rayleigh number (10^6) which causes high magnitude of entropy generation due to fluid friction (S_ψ) as $S_{\psi,max} = 281.04$ for $Da = 10^{-3}$.

Effect of Angle of Inclination (φ)

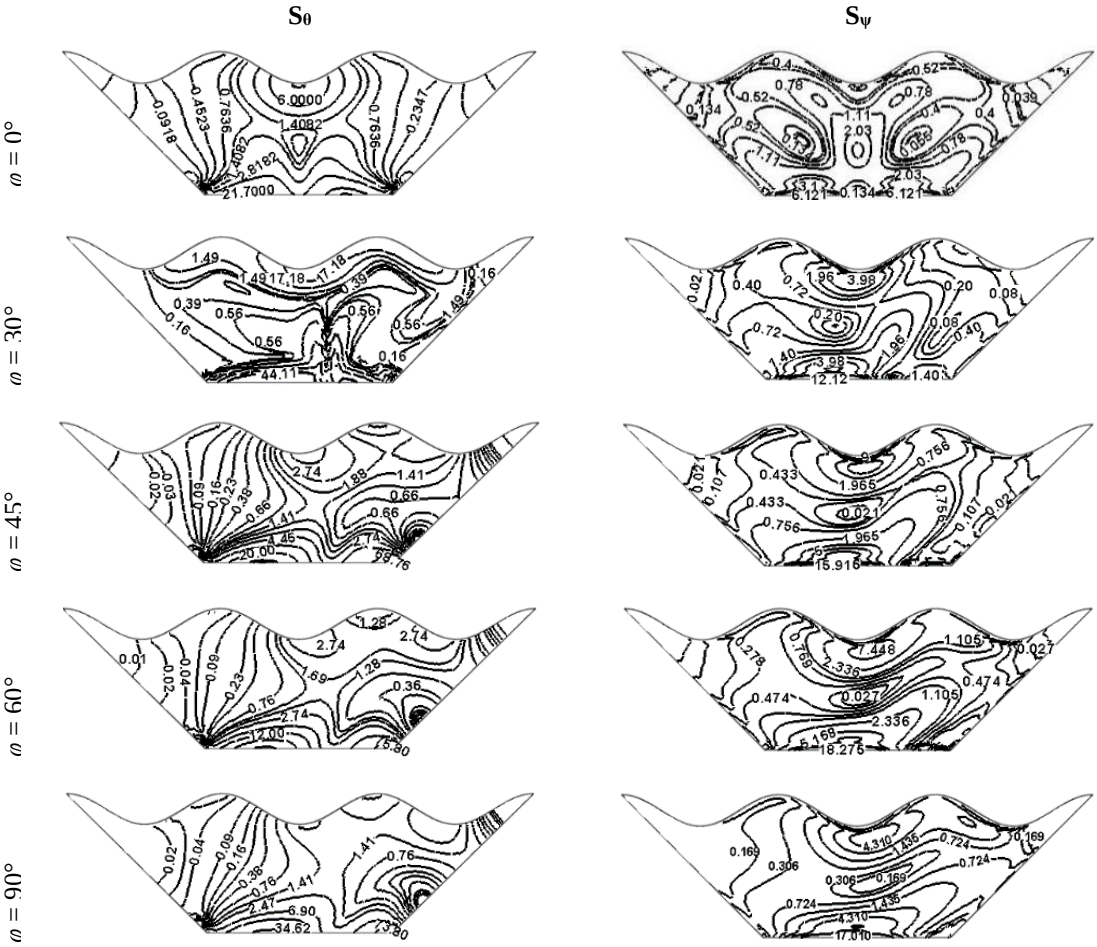

FIGURE 5. Variations of local entropy generation maps (S_θ, S_ψ) for $Da = 10^{-3}$, $Ra = 10^5$, $Pr = 7.2$ at different angles of inclination (φ)

The flow and heat transfer characteristics as well as entropy generation within inclined cavity are largely affected by the tangential and normal components of buoyancy force which arise due to density difference induced by temperature gradients. This trapezoidal cavity is inclined through several angles where $\varphi = 0^\circ, 30^\circ, 45^\circ, 60^\circ$ and 90°.

Effect of different inclination angles on entropy generation are studied keeping Darcy number (Da) and Prandtl number (Pr) constant at 10^{-3} and 7.2 respectively. Rayleigh number is considered 10^5 to ensure convection dominant process. At higher Rayleigh number, entropy generation for both heat transfer and fluid friction irreversibility are higher. Sharp changes in temperature and velocity gradient are observed with the change in angle. Contours of S_θ and S_ψ become denser and as the angle is increased, contours of S_θ and S_ψ shift towards the right side of the core of the cavity due to the higher temperature and velocity gradient in theses region. Figure 4 illustrates the variation of entropy generation with the change of angle. For $Ra = 10^5$, a notable increase in magnitude of S_θ is observed as φ changes from 0° to 45°. Generally the value of local entropy increases with the increase of φ. For φ more than 45°, the rate of increase of S_θ is reduced. Maximum local entropy generation due to heat transfer $S_{\theta,max} = 21.7$ for $\varphi = 0^\circ$ is located at two corner of the bottom wall. $S_{\theta,max} = 44.11$ for $\varphi = 30^\circ$, $S_{\theta,max} = 68.76$ for $\varphi = 45^\circ$, $S_{\theta,max} = 75.8$ for $\varphi = 60^\circ$, and $S_{\theta,max} = 73.80$ for $\varphi = 90^\circ$, these points are located only at the right corner of the bottom wall. The maximum local entropy generation due to fluid friction $S_{\psi,max} = 6.12$ for $\varphi = 0^\circ$ is located near the middle portion of the bottom wall. $S_{\psi,max} = 12.12$ for $\varphi = 30^\circ$, $S_{\psi,max} = 15.92$ for $\varphi = 45^\circ$, $S_{\psi,max} = 18.27$ for $\varphi = 60^\circ$ and $S_{\psi,max} = 17.01$ for $\varphi = 90^\circ$ which are located slightly to the left on the bottom wall. At inclination angle $\varphi = 30^\circ$ to $\varphi = 90^\circ$, a high local entropy generation S_ψ is seen near the mid-region of the cold top wavy wall. Significantly higher values of S_θ and S_ψ are observed near the top wavy cold wall. Insignificant values of S_θ and S_ψ are observed near two adiabatic wall. With the increase of inclination angle at higher Rayleigh number, effect of entropy generation due to fluid friction dominates.

Entropy Generation Characteristics

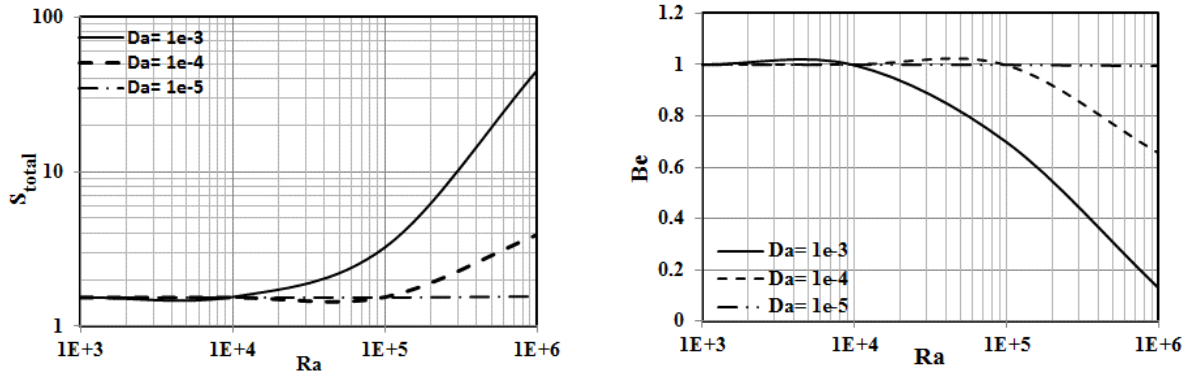

FIGURE 6. Variation of (a) total entropy generation (b) Bejan number with changes in Rayleigh number (Ra) for various Darcy number (Da) at $Pr = 7.2$

Figure 6(a) illustrates the variation in total entropy generation with Ra varying Darcy number. Here the data is taken for $Pr = 7.2$ and $\varphi = 0^o$. At higher Da (10^{-3}), S_{total} initially decreases very slightly and then increases at a steeper rate with increasing values of Ra, $S_{total,max} = 45.37$ for $Da = 10^{-3}$. At $Da = 10^{-4}$, from the graph, it is clear that the value of S_{tot} remains constant up to $Ra = 10^4$ then decreases between $Ra = 10^4$ and $Ra = 10^5$ and again increases but at a lower rate than $Da = 10^{-3}$ reaching a maximum value at $Ra = 10^6$. At lower Da (10^{-5}) the value of S_{tot} does not change much with the increase in Ra. $S_{total,max} = 3.92$ for $Da = 10^{-4}$ and 1.55 for $Da = 10^{-5}$.

Figure 6(b) illustrates the change in Bejan number with Rayleigh number for different Darcy numbers (10^{-5} to10^{-3}) keeping all other parameters fixed ($Pr = 7.2$ and $\varphi = 0^\circ$). For very low Da (10^{-5}), resistance of thermal permeability is very high resulting in very weak convection. Even at higher Ra (10^6), thermal permeability is too low, as a result at $Da = 10^{-5}$, Be remains almost 0.99 to 1 irrespective of Ra. When $Da = 10^{-4}$, same characteristics are observed up to $Ra = 10^5$ after which a drop in Be occurs. At $Ra = 10^6$, Bejan number becomes 0.65 which means that at higher Rayleigh number, irreversibility due to viscous effects is increased and at the same time irreversibility due to heat transfer is reduced. At a higher Da (10^{-3}), the hydraulic resistance of the porous medium is decreased and the heat flow due to convection is enhanced significantly which allows heat fluid friction dominant irreversibility to increase

with the increase of Rayleigh number. At $Ra = 10^5$, $Be = 0.69$ and at $Ra = 10^6$, $Be = 0.128$ for $Da = 10^{-3}$. So, at higher Darcy number Bejan number decreases sharply.

CONCLUSIONS

Loss of available energy is directly related to the total entropy generation. As the total entropy generation increases, the available energy required to heat the fluid decreases. This is due to the fact that, with increase in the entropy generation major part of the available energy is utilized to remove the irreversibilities rather than heating the fluid. From the present study it can be concluded that:

i. The total entropy generation in steady state increases exponentially with the increase of Rayleigh number. At higher *Ra*, S_ψ increases at a much higher rate than S_θ.

ii. Entropy generation due to heat transfer (S_θ) and fluid friction (S_ψ) increases with the increase in φ. Total entropy generation is found to be minimum at $\varphi = 0°$ and maximum at $\varphi = 60°$ for $Da = 10^{-3}$ and $Pr = 7.2$ at convection dominant region ($Ra \geq 10^4$).

iii. Total entropy generation increases with the increase of Darcy number. This is due to the decrease in hydraulic resistance which ensures higher temperature gradient and enhanced fluid flow.

iv. For lower *Da* (10^{-5}), *Be* is less than 0.5 for any Rayleigh number which indicates the domination of heat transfer irreversibility over viscous irreversibility. But at higher *Da* (10^{-3}), *Be* becomes greater than 0.5 as *Ra* increases thus for $Da = 10^{-3}$ predominance of shearing force exists at higher *Ra*.

REFERENCES

1. A. Bejan and D. A. Neild, "Convection in Porous Media," *1st ed., Springer,* 1992.
2. H. P. G. Darcy, *Les Fontaines Publiques de la Ville de Dijon,* 1856
3. P. Sompong and S. Witayangkurn, "Natural Convection in a Trapezoidal Enclosure with Wavy Top Surface," *J. Applied Mathematics,* 2013
4. P. Khansila and S. Witayangkurn, "Visualization of Natural Convection in Enclosure Filled with Porous Medium by Sinusoidally Temperature on the One Side," *Applied Mathematical Sciences,* vol. 97, pp. 4801-4812, 2012.
5. A. C. Baytas, "Entropy generation for natural convection in an inclined porous cavity," *International Journal of Heat and Mass Transfer,* vol. 43, pp. 2089-2099, 2000.
6. T. Basak , A. K. Singh, T. P. A. Sruthi and S. Roy, "Finite element simulations on heat flow visualization and entropy generation during natural convection in inclined square cavities," *International Communications in Heat and Mass Transfer,* no. 51, pp. 1-8, 2014.
7. A. Bejan, "Entropy Generation through Heat and Fluid Flow," *Wiley & Sons,* 1994
8. A. Bejan, "Entropy Generation Minimization," *CRC Press,* 1982.
9. S. Mahmud and A. M. Sadrul Islam, "Laminar free convection and entropy generation inside an inclined wavy enclosure," *Int. J. Thermal Science,* vol. 42, pp. 1003-1012, 2003.
10. A. C. Bayatas, "Optimization in an inclined enclosurefor minimum entropy generation in natural convection," *Int. J Heat Mass transfer,* vol. 22, pp. 145-155, 1997.
11. A. Bejan, "Convection Heat Transfer," *2nd edition, Wiley,* 1995.
12. T. Basak, R. S. Kaluri and A. R. Balakrishnan, "Entropy Generation During Natural Convection in a Porous Cavity: Effect of Thermal Boundary Conditions," *Numerical Heat Transfer, Part A,* pp. 336-364, 2012.

ICME2015

International Conference on Mechanical Engineering 2015
(ICME 2015) 18 – 20 December, 2015, Dhaka, Bangladesh

Paper ID : 412

Evaporation Characteristics of Thin Film Liquid Argon in Nano-scale Confinement: A Molecular Dynamics Study

Mohammad Nasim Hasan [a)], Sheikh Mohammad Shavik [b)], Kazi Fazle Rabbi [c)]
Mominul Haque [d)]

Department of Mechanical Engineering, Bangladesh University of Engineering and Technology (BUET)
Dhaka-1000, Bangladesh

[a)]Corresponding author: nasim@me.buet.ac.bd.com
[b)] shavik@me.buet.ac.bd.com
[c)]rabbi35.me10@gmail.com
[d)]mominulmarup@gmail.com

Abstract. Molecular dynamics simulation has been carried out to explore the evaporation characteristics of thin liquid argon film in nano-scale confinement. The present study has been conducted to realize the nano-scale physics of simultaneous evaporation and condensation inside a confined space for a three phase system with particular emphasis on the effect of surface wetting conditions. The simulation domain consisted of two parallel platinum plates; one at the top and another at the bottom. The fluid comprised of liquid argon film at the bottom plate and vapor argon in between liquid argon and upper plate of the domain. Considering hydrophilic and hydrophobic nature of top and bottom surfaces, two different cases have been investigated: (i) Case A: Both top and bottom surfaces are hydrophilic, (ii) Case B: both top and bottom surfaces are hydrophobic. For all cases, equilibrium molecular dynamics (EMD) was performed to reach equilibrium state at 90 K. Then the lower wall was set to four different temperatures such as 110 K, 120 K, 130 K and 140 K to perform non-equilibrium molecular dynamics (NEMD). The variation of temperature and density as well as the variation of system pressure with respect to time were closely monitored for each case. The heat fluxes normal to top and bottom walls were estimated and discussed to illuminate the effectiveness of heat transfer in both hydrophilic and hydrophobic confinement at various boundary temperatures of the bottom plate.

INTRODUCTION

In recent years many studies have been conducted to understand nanoscale heat transfer mechanisms to develop practical heat transfer solutions due to fast developments in electronics and miniaturization technologies. Molecular dynamics simulation is an effective method to investigate nanoscale heat transfer problems. Molecular dynamics simulation is playing increasingly important roles in investigations of nanoscale heat transfer phenomenon such as evaporation and explosive boiling. Throughout last decades many researchers attempted to study evaporation of thin liquid films on nanoscale surfaces using molecular dynamics simulation. Yi et al. [1] simulated the vaporization phenomenon of an ultra-thin layer of liquid argon on a platinum surface for two different superheat temperatures (150K and 300K). Yu and Wang [2] performed non-equilibrium molecular dynamics (NEMD) simulation to study the evaporation of the thin film, equilibrium vapor pressure as well as non-evaporating liquid layer in a nanoscale triple-phase system. Morshed et al. [3] performed molecular dynamics simulation to study the effect of nanostructures on evaporation and explosive boiling of thin liquid films. Maroo and Chung [4] performed molecular dynamics simulation of platinum heater and associated nano-scale liquid argon film evaporation and colloidal adsorption characteristics. Seyf and Zhang [5] performed non equilibrium molecular dynamics to study effect of nanotextured array of conical features on explosive boiling over flat substrate. Shavik et al. [7] performed molecular dynamics study to investigate the effect of nanostructured surface under different wetting conditions on explosive boiling of thin liquid

argon film. Although above studies modelled the evaporation or boiling of thin liquid films on flat or nanostructured surfaces, studies related to evaporation characteristics of thin liquid film in hydrophilic and hydrophobic confinement are rarely dealt. In the present work, a comprehensive molecular dynamics investigation has been conducted to elucidate the mechanism of thin film evaporation within confined nanospace at different surface temperatures and wettability. In total eight different cases were considered which included four different evaporation temperatures (110 -140 K, with 10 K interval) for both hydrophilic and hydrophobic surface condition. In these molecular dynamics simulations, the heat fluxes corresponding to evaporation at the bottom plate and condensation at the upper plate and also the evaporation rate for different evaporation temperatures and surface wettability were obtained and compared.

Nomenclature

r	Distance between molecules (Å)	*Greek Symbols*		*Subscripts*	
t	Time	ε	Energy parameter of LJ potential (eV)	*Ar*	Argon
T	Temperature (K)	σ	Length parameter of LJ potential (Å)	*Pt*	Platinum
P	Pressure (bar)	ϕ	Energy (eV)		

SIMULATION METHOD

In this study molecular dynamics simulations were performed on a three phase system as illustrated in Fig. 1 which consisted of two parallel platinum plates one at the top and another at the bottom. The system comprised of liquid argon film at the bottom plate and vapor argon in between liquid argon and upper plate of the domain. The simulation domain has a dimension of 7.9nm(x) × 41.75nm(y) × 7.9nm (z). Both the upper and the bottom plate comprised of eight monolayers of platinum atoms. For the bottom plate the first layer was fixed to prevent deformation of the plate atoms; thermostat was applied to the next two layers which functioned as the heat source; the remaining five layers conducted the heat to the liquid argon. For the upper plate the topmost layer was fixed and the remaining layers were for heat conduction. For each plate approximately 6000 platinum atoms were arranged in FCC (100) lattice structure corresponding to its density of 21.45×10^3 kg/m^3. Liquid argon layers of total 3nm height were placed on top of the bottom plate corresponding to its density of 1.367×10^3 kg/m^3. The remaining space of the domain was filled with approximately 170 argon vapor atoms. Periodic boundary conditions were applied to the x and z directions. For the molecular dynamics simulation well known L-J potential [11] was employed to calculate the intermolecular forces:

$$\phi(r) = 4\varepsilon\left[\left(\frac{\sigma}{r}\right)^{12} - \left(\frac{\sigma}{r}\right)^{6}\right] \tag{1}$$

ε and σ in Eq. (1) represents the energy parameter and the length parameter respectively. Hens et al. [9] suggested surface wettability based on the condition: when $\varepsilon_{Ar\text{-}Ar} < \varepsilon_{Ar\text{-}Pt}$, the surface can be considered as hydrophilic and when $\varepsilon_{Ar\text{-}Ar} > \varepsilon_{Ar\text{-}Pt}$, the surface can be considered as hydrophobic. In this study $\varepsilon_{Ar\text{-}Pt} = 3\varepsilon_{Ar\text{-}Ar}$ and $\varepsilon_{Ar\text{-}Pt} = 0.5\varepsilon_{Ar\text{-}Ar}$ were considered for hydrophilic and hydrophobic surface respectively. The L-J potential parameters for argon-argon and argon-platinum used in this study are summarized in Table-1.

TABLE 1. Lennard-Jones interaction parameters

LJ parameter	**Atom**		
	Ar-Ar	**Pt-Pt**	**Ar-Pt**
σ **(nm)**	0.3405	0.2475	0.294
$\varepsilon\times10^{21}$ **(J)**	1.67	83.2	0.835 (hydrophobic); 5.01 (hydrophilic)

The cutoff distance for L-J potential used in this study is $3.5\sigma_{Ar\text{-}Ar}$. Time step of 5fs was chosen for whole simulation. The simulation was started from the initial configuration of the domain (Fig. 1). The equations of motions were integrated using velocity-verlet algorithm. The whole simulation consisted of three stages. In the 1st stage, the entire system was maintained at 90K under equilibrium molecular dynamics under NVT thermostat for 0.5ns. Once the whole system was in equilibrium the thermostat was removed for the fluid domain and NVE ensemble was applied to it. Then in the 2nd stage, the system was run for 1ns. Finally, in the 3rd stage or the final stage the temperature of the bottom plate was set to higher temperature using NVT time integration via Noose/hoover thermostat and simulation

was run for 6.5ns to reach towards an equilibrium state. To check whether the argon is in equilibrium state the temperature, pressure was monitored during the equilibration period. The simulations were performed using LAMMPS [13] and visualization was done by VMD (Visual Molecular Dynamics) [14].

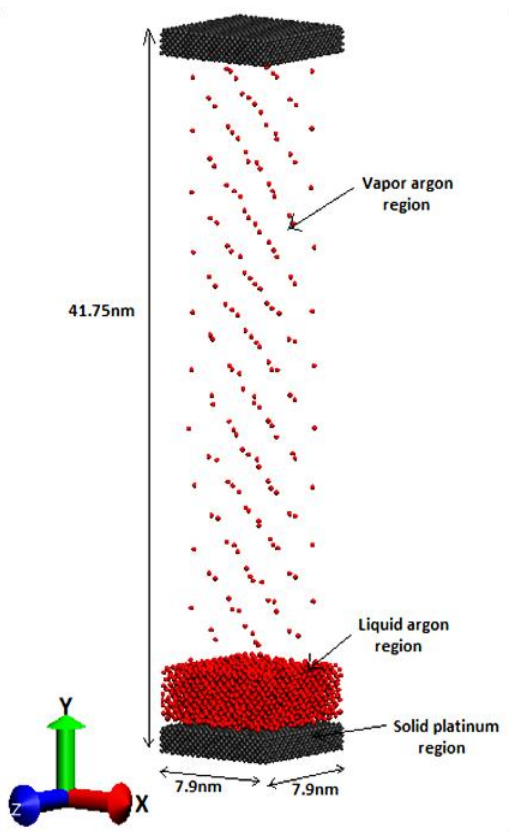

FIGURE 1. Initial configuration of simulation box.

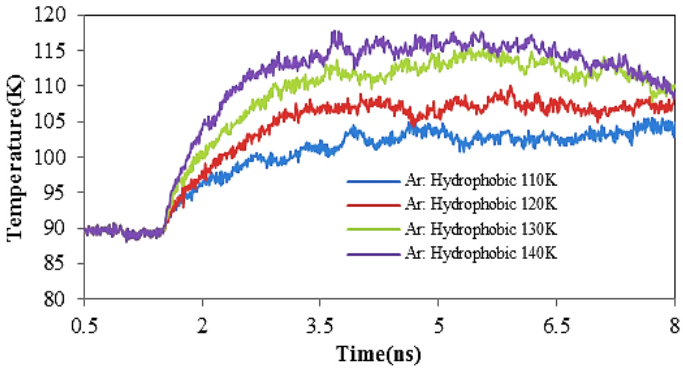

FIGURE 2. Temperature history of argon (*Ar*) for hydrophobic surface case.

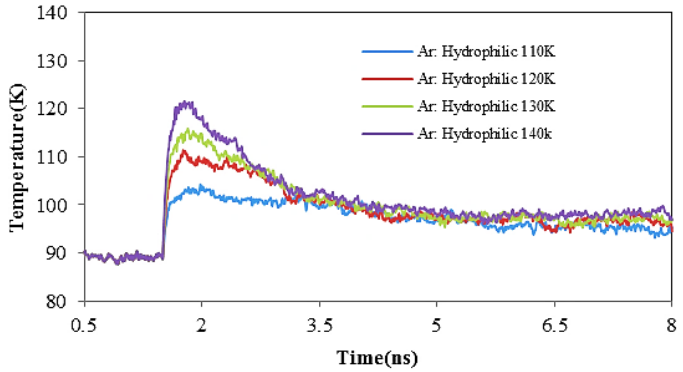

FIGURE 3. Temperature history of argon (*Ar*) for hydrophilic surface case.

RESULT AND DISCUSSION

In this study, both for hydrophilic and hydrophobic surface condition the bottom plate temperature was set to jump from equilibrium temperature (90K) to four different evaporation temperatures (110K, 120K, 130K & 140K) in four different cases. The wettability of the *Pt* surface was controlled by varying the *Pt-Ar* energy parameter $\varepsilon_{Ar\text{-}Pt}$. The two different types of surfaces considered in this study: hydrophilic ($\varepsilon_{Ar\text{-}Ar} < \varepsilon_{Ar\text{-}Pt}$), & hydrophobic ($\varepsilon_{Ar\text{-}Ar} > \varepsilon_{Ar\text{-}Pt}$). Figures 2 and 3 illustrate the temperature history of the argon region for all four cases of bottom wall temperatures for hydrophobic and hydrophilic surface conditions respectively. For the hydrophobic surface condition, Fig. 2 depicts that after the sudden increase of temperature to 130K and 140K of the bottom plate the argon region temperature rise for a while then again start to decrease towards an equilibrium temperature. This is due to the fact that the upper plate is at lower temperature of 90K and the argon vapor loses heat to the upper wall which results in the decrease of its temperature. But in case of evaporation temperature of 110K and 120K as shown in Fig. 2 the argon region temperature instead of increasing sharply increases gradually and approaches towards the equilibrium temperature. Figure 2 illustrates that the argon temperature reaches equilibrium at approximately 102K and 107K after 5ns and 4ns respectively for evaporation temperatures 110K and 120K. But, in case of evaporation temperature of 130K and 140K, for hydrophobic surface the temperature of argon region is around 109K after 8ns and does not reach equilibrium

within this simulation time. For the hydrophilic case as depicted in the Fig. 3 the temperature of the argon region initially rises very sharply due to the sudden increase of the temperature of the bottom plate. Then slowly the argon temperature starts decreasing towards an equilibrium temperature due to the heat loss to the upper plate which is maintained at a lower temperature (90K). Figure 3 depicts that for hydrophilic surface condition for different evaporation temperatures (110K, 120K, 130K and 140K) the argon region temperature reaches equilibrium at approximately 95K, 96K, 97K and 98K respectively after 5ns. So for all the cases with the increase in temperature of the bottom plate the temperature of the argon region increases and equilibrates at a temperature below the temperature of the bottom plate due to the heat loss and condensation at the upper plate. From Figs. 4 and 5 it is very clear that due to volume constraint of the system, increase in temperature results in increase in system pressure and interestingly pressure variation follows the temperature variation trend of the simulation domain.

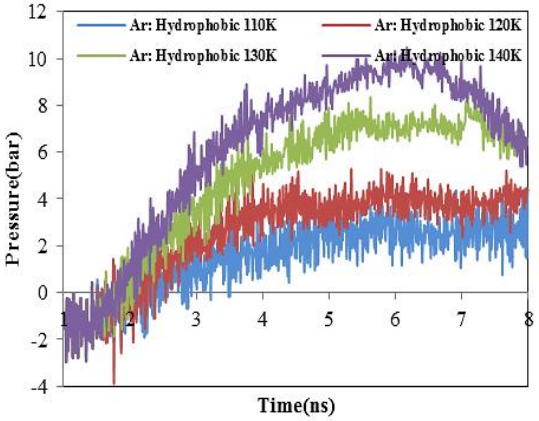

FIGURE 4. Pressure history of the simulation domain hydrophobic surface case

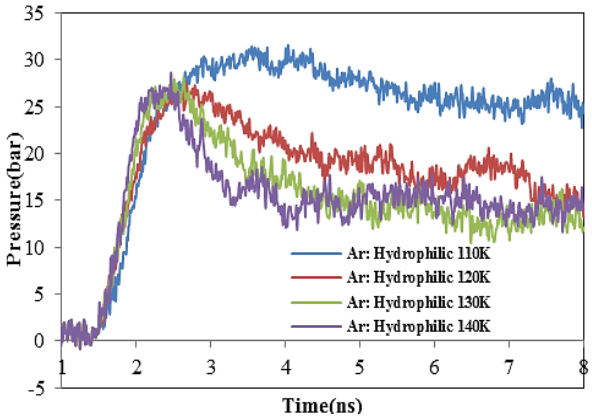

FIGURE 5. Pressure history of the simulation domain for hydrophilic surface case

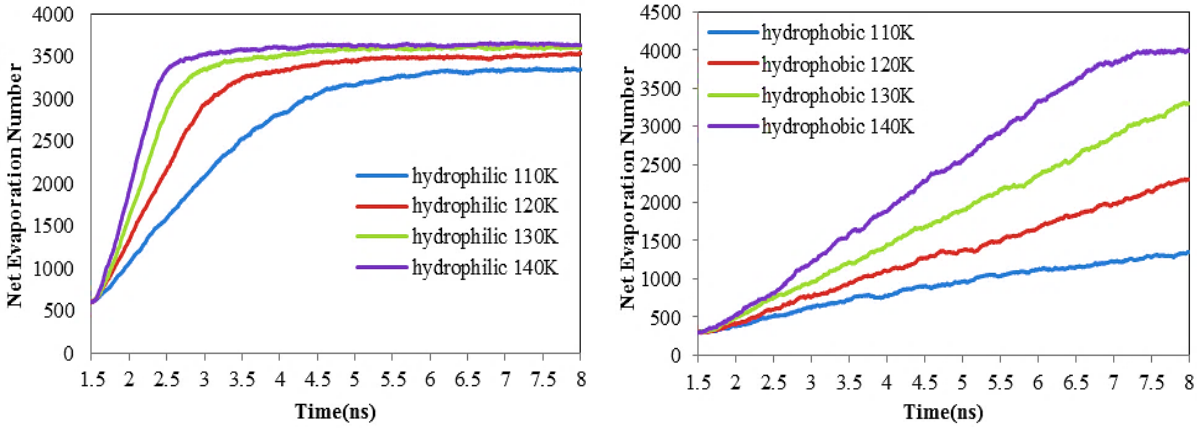

FIGURE 6. Variation of net evaporation number with time (a) For Hydrophilic cases (b) For Hydrophobic cases

The change in number of vapor atoms in the vapor region was counted to calculate the net evaporation rate in the system. By analysing the evaporation number from Fig. 6 it is evident that in case of hydrophilic surface for different evaporation temperatures (110K, 120K, 130K and 140K) around 95% of the total evaporation is completed after 5.5ns, 4ns, 3.5ns, 2.5ns respectively and there isn't any significant evaporation in the system afterwards. On contrary, for hydrophobic surface with evaporation temperature of 140K around 95% evaporation is completed after 7ns and there is no significant evaporation in the system afterwards. But for other hydrophobic cases (110K, 120K, 130K) as the rate of evaporation is comparatively slower, evaporation of liquid argon is far from completion within this 8ns of simulation time.

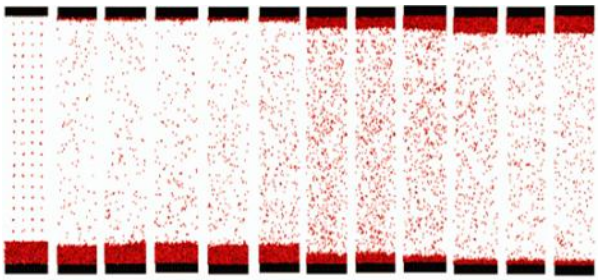

(a) 110 K

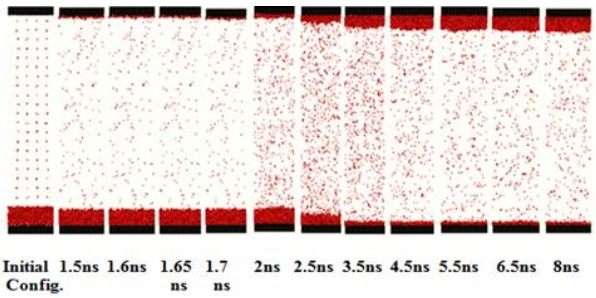

(b) 120 K

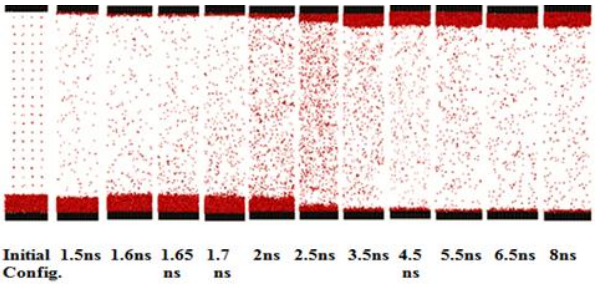

(c) 130 K

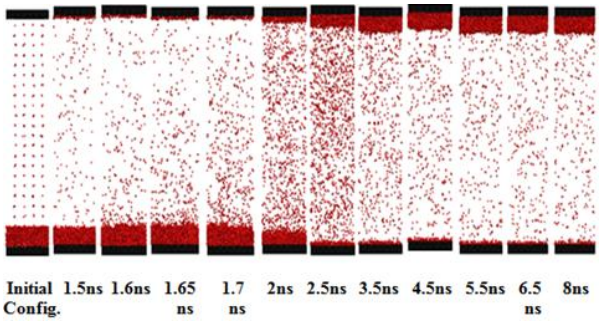

(d) 140 K

FIGURE 7. Snapshots of the simulation domain for hydrophilic surface at various bottom wall temperatures

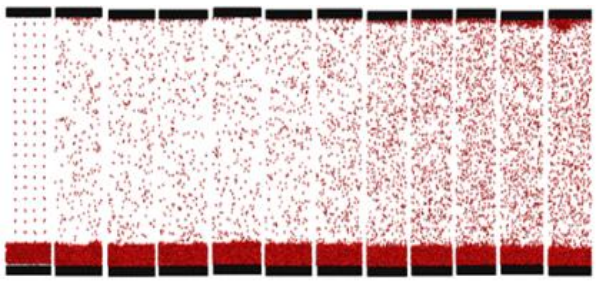

(a) 110 K

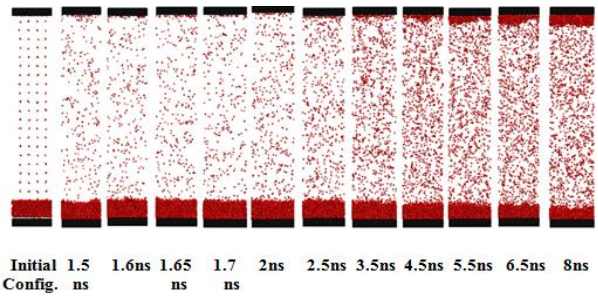

(b) 120 K

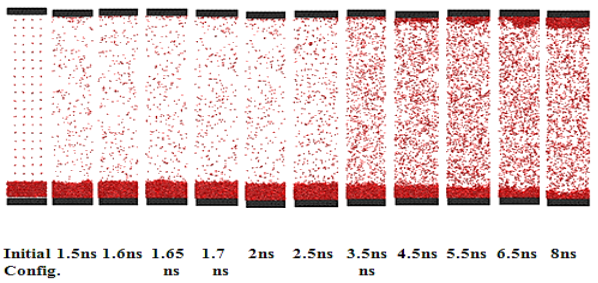

(c) 130 K

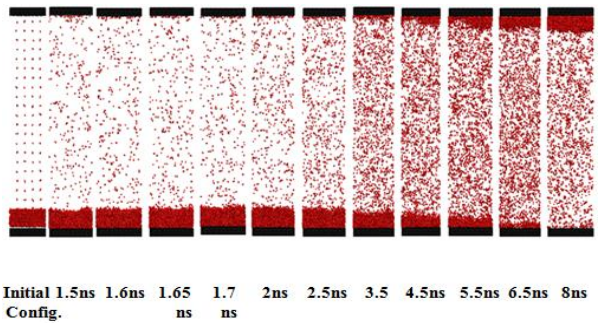

(d) 140 K

FIGURE 8. Snapshots of the simulation domain for hydrophobic surface at various bottom wall temperatures

Figures 7 and 8 illustrate the snapshots of the simulation domain at different times for hydrophilic and hydrophobic cases respectively and give molecular insight into phase transition. From the snapshots as depicted in Figs. 7 and 8, it is clear that for hydrophilic surface evaporation takes place quicker than in case of hydrophobic surface. The snapshots as depicted in Fig. 7 shows that for hydrophilic cases at different bottom wall temperatures (110K, 120K, 130K and

140K) due to variation in the rate of evaporation non-evaporating argon layer forms on the bottom plate after 5.5ns, 3.5ns, 3.5ns and 2.5ns respectively which agrees with Fig. 6(a). Similarly, the snapshots as depicted in Fig. 8 shows that for hydrophobic surface condition at lower evaporation temperatures (110K, 120K and 130K) the evaporation rate is so low that non-evaporating layer does not form even after 8ns of the simulation. So the evaporation rate is higher and the formation of non-evaporating layer is faster in case of higher surface wettability. This is expected as in case of hydrophobic surface solid-liquid interaction is low and as a result energy transfer from solid surface to liquid layer is much lower compared to hydrophilic surface. Figure 8 illustrates that due to lower evaporation rate in case of hydrophobic surface condition for the lower evaporation temperatures (110K,120K,130K) even at the end of simulation liquid argon film remains on the bottom plate and non-evaporating layer on the bottom plate is visible only in case of the higher evaporation temperature (140K) around 8ns. So, the higher the temperature of the bottom plate the higher the rate of evaporation and faster the formation of non-evaporating layer.

For heat transfer phenomena heat flux is an important tool for quantifying the effectiveness of heat transfer. In this study heat flux normal to the solid wall was calculated from the per atom potential energy, the per atom kinetic energy and per atom stress tensor. Figure 9 illustrates the heat flux normal to the bottom plate for all the cases during evaporation. For all the cases the trend of the profiles is same. After the jump in temperature of the bottom plate a high heat flux is added to the liquid argon region within a short time. After this stage heat flux gradually decreases towards zero while oscillating about a mean value. The profiles of the heat flux are in good agreement with a previous study conducted by Yamamoto and Matsumoto [10]. The hydrophilic 110K, 120K, 130K, 140K cases have maximum heat flux values of 367MW/m^2, 480MW/m^2, 697.4MW/m^2, 842.4MW/m^2 respectively. The hydrophobic 110K, 120K, 130K, 140K cases have maximum heat flux values of 140 MW/m^2, 167.3 MW/m^2, 224.5 MW/m^2, 264 MW/m^2 respectively. As expected among all the cases the hydrophilic 140K case has the maximum heat flux close to 842 MW/m^2 which is in order of theoretical maximum value of heat flux $q_{max,\,max}$ = 800MW/m^2 as defined by Gambill and Lienhard [12]. In Fig. 10 from the heat flux loss from the argon region to the upper plate (which is at a lower temperature of 90K than the argon region during evaporation stage) it can be seen that the hydrophilic 110K, 120K, 130K, 140K cases have maximum heat flux values of 243.7 MW/m^2, 315.2 MW/m^2, 362 MW/m^2, 452.1 MW/m^2 and the hydrophobic 110K, 120K, 130K, 140K cases have maximum heat flux values of 111 MW/m^2, 140 MW/m^2, 142 MW/m^2, 193 MW/m^2. So for the hydrophilic surface condition the maximum heat loss to the upper plate is around 50-67% of the heat flux gained from the bottom plate and for the hydrophobic case the maximum heat flux loss to the upper plate is around 65-85% of the heat flux gained from the bottom plate.

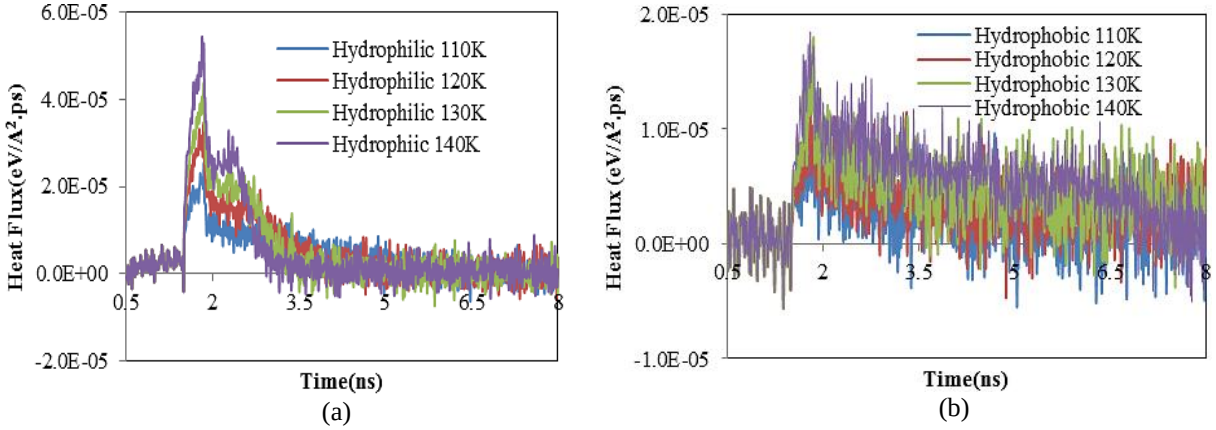

FIGURE 9. Heat flux from the bottom plate (a)For Hydrophilic cases (b)For Hydrophobic cases

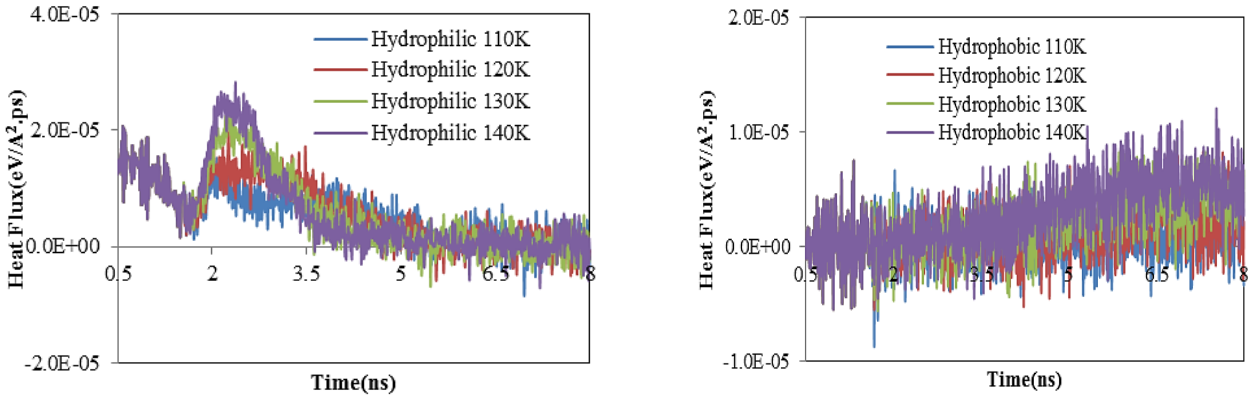

FIGURE 10. Heat flux to the upper plate (a) For Hydrophilic cases (b) For Hydrophobic cases

CONCLUSION

Evaporation of thin liquid film in a confined nano-space at different temperatures and surface wettability using molecular dynamics simulations was studied and the effect of evaporation temperature and surface wettability on the rate of evaporation was investigated. It has been observed that surface wettability highly affects heat transfer through solid liquid interface and hydrophilic surface facilitates heat transfer. For evaporations in all of the four different temperatures the heat flux from the bottom plate to the argon region for hydrophilic surface is higher than hydrophobic surface. From the result of this study it can be seen that even for evaporation in hydrophilic 110K case the heat flux gained from the bottom plate is 367MW/m^2 which is higher than the heat flux 264 MW/m^2 of hydrophobic 140K case. So even at 30K lower temperature hydrophilic surface provided higher heat flux than hydrophobic surface. The maximum heat flux loss from the argon region to the upper plate in case of hydrophilic surface is around 50 to 67% of the maximum heat flux gained from the bottom plate and the maximum heat flux loss from the argon region to the upper plate in case of hydrophobic surface is around 65 to 85% of the maximum heat flux gained from the bottom plate. The argon region within the confined nano-space equilibrates to an intermediate temperature between the high temperature of the bottom plate and low temperature of the upper plate due to heat gain from the bottom plate and heat loss to the upper plate. In case of hydrophilic surface condition evaporation rate is faster than hydrophobic surface condition, which indicates that for higher interaction potential between the surface and the liquid the heat transfer from surface to liquid becomes higher leading to higher rate of evaporation. For higher evaporation temperature the evaporation rate is higher and the vapor-liquid reaches equilibrium state faster than the lower evaporation temperatures. Hence as expected at higher temperature of the bottom plate the argon region approaches toward equilibrium temperature faster in case of hydrophilic surface condition than in case of hydrophobic surface condition.

REFERENCES

1. P. Yi, D. Poulikakos, J. Walther, G. Yadigaroglu, Int. J. Heat Mass Transfer **45**, 2087–2100 (2002).
2. J. Yu, H. Wang, Int. J. Heat Mass Transfer **55** (2012) 1218-1225.
3. A.K.M.M. Morshed, Taitan C. Paul, Jamil A. Khan, Applied Physics A **105,** 445-451 (2011).
4. S.C. Maroo and J.N. Chung, J. Colloid Interface Sci. **328,** 134–146. (2008)
5. H.R. Seyf and Y. Zhang, Int. J. Heat Mass Transfer **66**, 613-624 (2013).
6. Weidong Wang, Haiyan Zhang, Conghui Tian and Xiaojie Meng, "Numerical experiments on evaporation and explosive boiling of ultra-thin liquid argon film on aluminum nanostructure substrate."
7. Sheikh Mohammad Shavik, Mohammad Nasim Hasan, A.K.M. Monjur Morshed, "Molecular dynamics study on explosive boiling of thin liquid argon film on nanostructured surface under different wetting conditions," InterPACKICNMM2015-48352.
8. Sheikh Mohammad Shavik, Mohammad Nasim Hasan, A.K.M. Monjur Morshed, M. Quamrul Islam,

Procedia Engineering **105**, 446-451, (2015).
9. A. Hens, R. Agarwal, G. Biswas, Int. J. Heat Mass Transfer **71**, 303-312 (2014).
10. T. Yamamoto, M. Matsumoto, J. Therm. Sci. Technol. Jpn. **7**, 334–349 (2012).
11. J.E. Lennard-Jones, A.F. Devonshire, Philos. Trans. R. Soc. Lond. Ser. A, Math. Phys. Sci. **163**, 53-70 (1937).
12. W. R. Gambill, and J. H. Lienhard, "An upper bound for the critical boiling heat flux," J. Heat Transfer, 111(1989) 815-818.
13. LAMMPS User's Manual (http://lammps.sandia.gov – Sandia National Laboratories, USA).
14. Humphrey W, Dalke A, Schulten K. VMD: Visual Molecular Dynamics. J Mol. Graph. 1996; 1433: 1996.

ICME2015

International Conference on Mechanical Engineering 2015
(ICME 2015) 18 – 20 December, 2015, Dhaka, Bangladesh

Paper ID : 413

Mixed Convection Heat Transfer inside a Differentially Heated Square Enclosure in presence of a Rotating Heat Conducting Cylinder

Muntasir Alam[a)], Kamruzzaman[b)], Faraz Ahsan[c)], Mohammad Nasim Hasan[d)]

Department of Mechanical Engineering, Bangladesh University of Engineering and Technology (BUET)
Dhaka-1000, Bangladesh

[a)]Corresponding author: muntasiralam91@yahoo.com
[b)] shohag.kamruzzaman@gmail.com
[c)] ahsanfaraz00000@yahoo.com
[d)] nasim@me.buet.ac.bd

Abstract. A numerical study of mixed convection heat transfer phenomena in a square cavity containing a heat conducting rotating cylinder has been investigated. A discrete isoflux heater is placed at the bottom wall of the enclosure while the top wall is kept adiabatic. Left and right sidewalls of the enclosure are assumed to be maintained at constant low temperature. A two-dimensional solution for steady laminar mixed convection flow is obtained by using the finite element scheme based on the Galerkin method of weighted residuals for different rotating speeds of the cylinder varying over the range of 0-1000 keeping the Rayleigh number fixed at 5×10^4 and the Prandtl number at 0.7. The effects of rotating speeds of the cylinder, its radius and conductivity ratio of the rotating cylinder and working fluid on the streamlines, isotherms, local Nusselt number, average Nusselt number and other heat transfer and fluid flow phenomena are investigated. The results indicate that the flow field, temperature distribution and heat transfer rate are dependent on rotating speeds and cylinder size. However, it has been observed that the effect of conductivity ratio is not so prominent.

INTRODUCTION

Mixed convection is a very promising phenomenon now-a-days as it has wide applications in industrial sectors such as heat exchangers, nuclear power plants and cooling of electronic equipments etc. Conjugate heat transfer is studied by many investigators inside a square enclosure with the presence of an active body. In a vertical square enclosure, natural convection is numerically investigated with the presence of a centered, square, heat conducting body in the work of House *et al.* [1]. A mixed convection phenomena has been experimentally observed in the work of Kimura *et al.* [2] but in this case a rotating plate is placed at the center. In [3] the surface of the rotating cylinder is considered as a uniform prescribed temperature and in [4] the cylinder is used as a heat source in a rectangular enclosure. Shuja *et al.* [5] numerically studied mixed convection in a square cavity due to a heat generating rectangular body and the effect of exit port locations is also taken into consideration. V. Costa *et al.* [6] numerically observed steady mixed convection in a differentially heated square enclosure with an active rotating cylinder keeping vertical walls perfectly insulated. Salam *et al.* [7] observed mixed convection in a square enclosure with an active rotating cylinder and also studied the effect keeping the cylinder at different vertical locations.

In this work, the mixed convection problem corresponding to a rotating circular cylinder inside a differentially heated square enclosure is taken into consideration. A discrete isoflux heater is placed at the bottom wall of the enclosure. The top wall of the enclosure is assumed adiabatic whereas the left and right sidewalls are maintained at constant low temperature. A circular rotating heat conducting cylinder with a definite radius and thermal conductivity rotates with a fixed angular velocity in the counterclockwise direction. Air is considered as the fluid inside the square

enclosure with the fixed *Pr*=0.7. In this work, rotational speeds of the cylinder are varied over the range of 0-1000 keeping Rayleigh Number fixed at 5×10^4. Later different heat transfer and fluid flow phenomena are investigated by changing radius and conductivity ratio of the cylinder and it is observed that their effect is very prominent.

Nomenclature

g	gravitational acceleration	q	constant heat flux
C_p	constant pressure specific heat	Ri	Richardson number
k	thermal conductivity		
L	length of enclosure	Greek symbols	
Nu	Nusselt number	θ	dimensionless temperature
p	dimensional pressure	μ	dynamic viscosity
P	dimensionless pressure	υ	kinematic viscosity
Pr	Prandtl number	α	thermal diffusivity
r	dimensional radius of the cylinder	ρ	density
R	non-dimensional radius of the cylinder	ω	angular rotating velocity
Ra	Rayleigh number	Ω	non-dimensional angular velocity
Re	Reynolds number	ε	dimensionless length of heat source
K	thermal conductivity ratio	β	thermal expansion coefficient
T	temperature		
x, y	Cartesian coordinates	Subscripts	
X,Y	non-dimensional Cartesian coordinates	o	value at the centre of the cylinder
u, v	Cartesian velocity components	c	cold
U,V	non-dimensional Cartesian velocity components	s	solid

MATHEMATICAL MODEL

The configuration of the two-dimensional square enclosure with each side L, with an active rotating cylinder is sketched in the Fig.1. In this work, density on the buoyancy term is assumed to be dependent on temperature and Boussinesq approximation is used. All the remaining thermo physical properties of the fluid are assumed to be constant in this work. The dimensionless form of the governing equations can be written as,

$$\frac{\partial U}{\partial X}+\frac{\partial V}{\partial Y}=0 \tag{1}$$

$$U\frac{\partial U}{\partial X}+V\frac{\partial U}{\partial Y}=-\frac{\partial P}{\partial X}+\Pr\left(\frac{\partial^2 U}{\partial X^2}+\frac{\partial^2 U}{\partial Y^2}\right) \tag{2}$$

$$U\frac{\partial V}{\partial X}+V\frac{\partial V}{\partial Y}=-\frac{\partial P}{\partial Y}+\Pr\left(\frac{\partial^2 V}{\partial X^2}+\frac{\partial^2 V}{\partial Y^2}\right)+Ra\Pr\theta \tag{3}$$

$$U\frac{\partial \theta}{\partial X}+V\frac{\partial \theta}{\partial Y}=\left(\frac{\partial^2 \theta}{\partial X^2}+\frac{\partial^2 \theta}{\partial Y^2}\right) \tag{4}$$

For heat conducting solid rotating cylinder, the energy equation is,

$$\frac{\partial^2 \theta_s}{\partial X^2}+\frac{\partial^2 \theta_s}{\partial Y^2}=0 \tag{5}$$

Non-dimensional parameters used in this work are defined as,

$$X=\frac{x}{L},\ Y=\frac{y}{L},U=\frac{u}{\alpha/L},V=\frac{v}{\alpha/L},\theta=\frac{T-T_c}{qL/k},\Pr=\frac{\nu}{\alpha},R=\frac{r}{L},Ra=\frac{g\beta qL^4}{\nu\alpha k},\ P=\frac{pL^2}{\rho\alpha^2},\Omega=\frac{\omega L^2}{\alpha}$$

At all solid boundaries of the square enclosure: $U=0,V=0$ and at left and right vertical wall: $\theta=0$

At the top wall and part of the bottom wall where the wall is at adiabatic condition: $\frac{\partial \theta}{\partial Y} = 0$

At the heated section of the bottom wall: $\frac{\partial \theta}{\partial Y} = -1$

At the solid-fluid vertical interfaces of the block: $\left(\frac{\partial \theta}{\partial X}\right)_{fluid} = K\left(\frac{\partial \theta}{\partial X}\right)_{solid}$

At the solid-fluid horizontal interfaces of the block: $\left(\frac{\partial \theta}{\partial Y}\right)_{fluid} = K\left(\frac{\partial \theta}{\partial Y}\right)_{solid}$

Over the rotating cylinder, velocity components are specified as, $u = -\omega(y - y_o)$ and $v = \omega(x - x_o)$ which can be expressed in the dimensionless form, $U = -\Omega(Y - Y_o)$, $V = \Omega(X - X_o)$

The dimensionless parameter used to evaluate the relative domination of the natural and forced convection is Richardson number which is defined in the following modified way,

$$Ri = \frac{Ra/\Pr}{\left[(\omega r) D/\nu\right]^2} = \frac{Ra \Pr}{4\Omega^2 R^4}$$

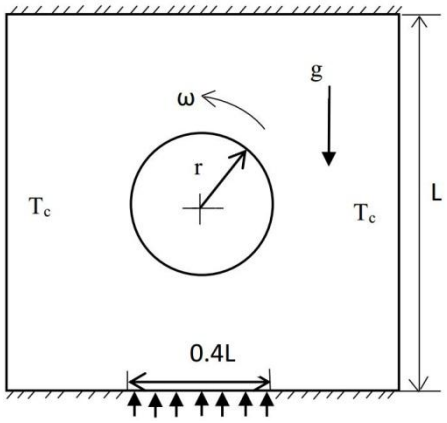

FIGURE 1. A schematic diagram of the considered problem.

Local Nusselt number can be defined as, $Nu_l = \frac{1}{\theta(X)}$ whereas average Nusselt number is, $Nu_{avg} = \frac{1}{\varepsilon}\int_0^{\varepsilon} \frac{1}{\theta(X)} dX$

Here, ε is the dimensionless length of the heat source.

NUMERICAL METHODOLOGY AND CODE VALIDATION

Finite element method is one of the most popular and widely used numerical methods as it can solve complex structural problems. In this work, it is assumed that fluid inside the cavity is viscous and incompressible. To properly study the cavity situation the numerical technique based on the Galerkin weighted residual method of finite element formulation is used in the present work. This method is chosen because the global system matrix is decomposed into smaller matrices and then these sub-matrices are solved using a non-linear parametric solver. Six noded non-uniform triangular mesh elements are used in this work as it results smooth non-linear variations of field variables and the used method ensures fast convergence and also the reliability.

In order to check the validity of developed model, the results were compared with those reported by Kim *et. al* [8] for the case of natural convection in a square cavity with a circular cylinder placed at different vertical locations. Table.1 shows the comparison between the present results with the reported results. For different *Ra* values, surface-average Nusselt number of the inner cylinder is compared between these two results. From Table.1 it can be concluded that, excellent and satisfactory agreement is obtained between these two results.

TABLE 1. Comparison of Average Nusselt number

	Nu_{avg}			
Ra	10^3	10^4	10^5	10^6
Present model	5.04	5.13	7.81	14.18
Kim *et al.* [8]	5.01	5.02	7.78	14.10

RESULTS AND DISCUSSIONS

Temperature Field and Flow Structure Visualization

A numerical analysis has been performed to investigate the effect of rotational speed, radius and conductivity ratio of a rotating circular cylinder in a differentially heated square enclosure. In this work, temperature field and flow field are properly analyzed in terms of distribution of isothermal lines and stream function respectively. Heat transfer visualization is also performed in terms of local Nusselt number (Nu_l) and average Nusselt number (Nu_{avg}).

Effect of rotational speed of the cylinder

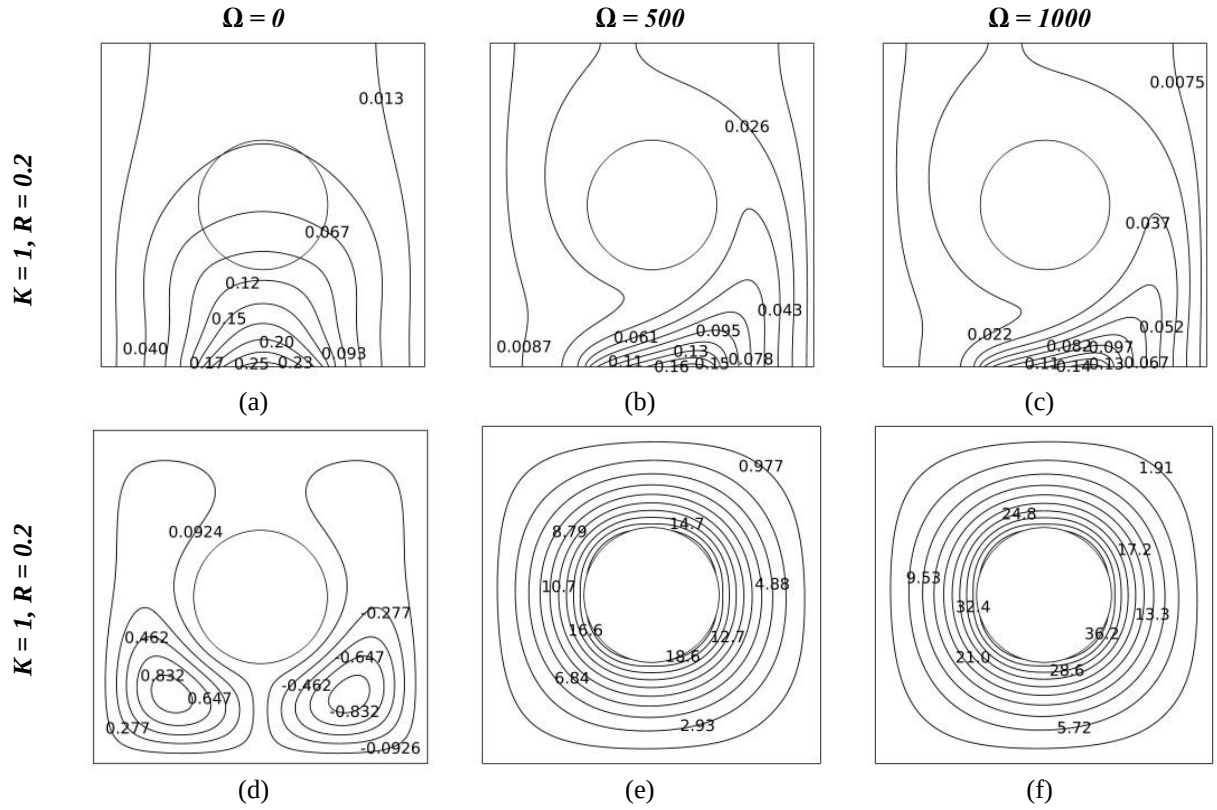

FIGURE 2. Isotherm lines (upper 3) and Stream functions (lower 3) for K = 1, R = 0.2

To demonstrate the effect of speed on isotherm lines and streamlines, the following condition is considered in Fig. 2; K = 1, R = 0.2, Ω = 0, 500, 1000. In the first Fig. 2(a) where Ω=0 refers to natural convection condition. It is also evident from the symmetrical profile of the temperature distribution which is common in natural convection in square enclosure. In Fig. 2(b) where the speed is increased to Ω=500 the symmetry of the temperature distribution is broken and isotherm lines shift to the direction of rotation of the cylinder. The dense isotherm lines on the left side of the heater indicate that higher heat transfer will occur from this region of the heat flux portion. Also the dense temperature

contour at the right side cold wall shows that more heat will be transferred to this wall. The spaced temperature contour at the left side wall indicates that temperature gradient in this side is not as strong as the right side. This is because the convective front created by the rotating cylinder at the left side is opposite to the natural convective flow where it is positive for the right side. In Fig. 2(c) where $\Omega = 1000$ the temperature distribution remains similar to the previous one with more dense isotherm lines. In the space between the enclosure and the cylinder the flow of fluid takes place. In Fig. 2(d) the flow field also shows symmetry about the vertical centerline where natural convection condition prevails. In Fig. 2(e) and 2(f) where $\Omega = 500$ and 1000 the flow field is dominated by the rotation of the cylinder. From the intense streamlines, the strong flow field is evident. The flow field gets closer to the enclosure with the increase of speed.

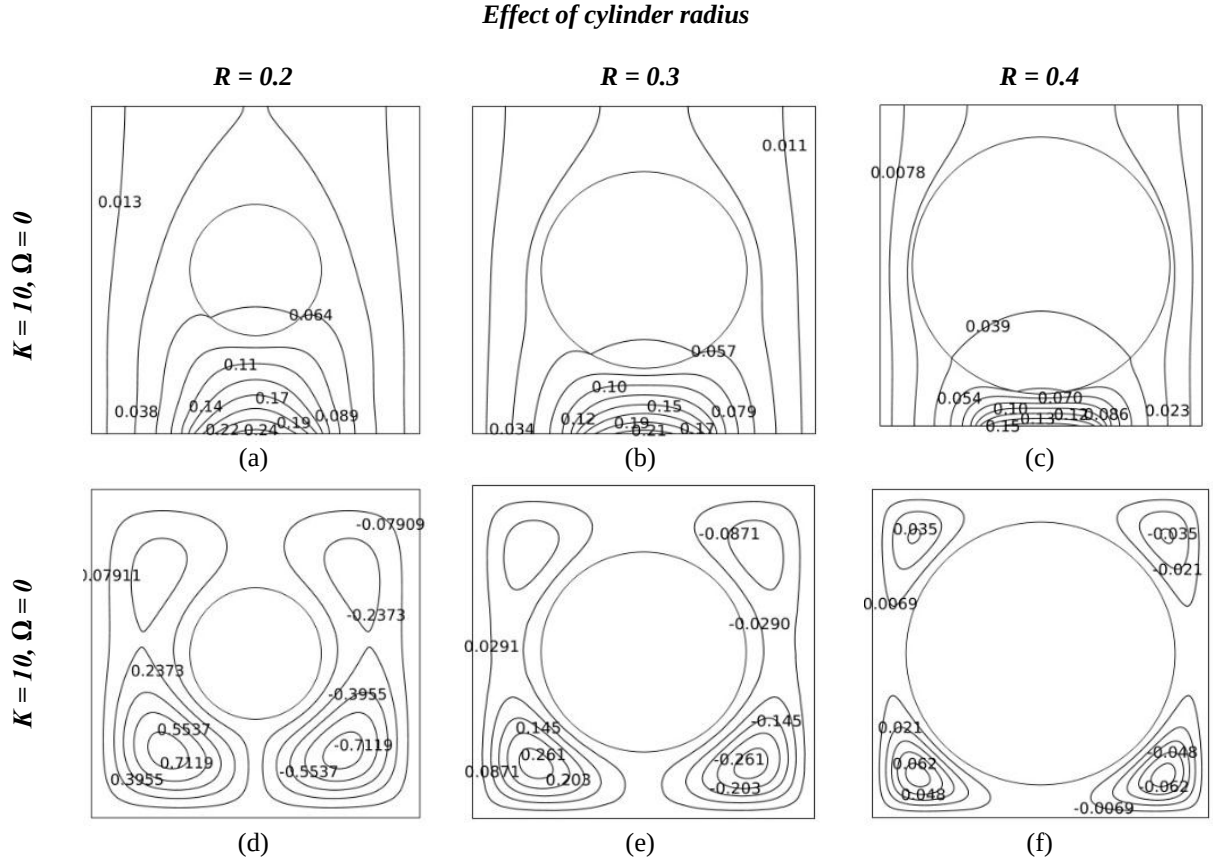

FIGURE 3. Isotherm lines (upper 3) and Stream functions (lower 3) for $K = 10$, $\Omega = 0$

In Fig. 3 the effect of cylinder radius is visualized for $R = 0.2$, 0.3 and 0.4 with $K = 10$ and $\Omega = 0$. As the size of the cylinder increases, the space between the enclosure and the cylinder decreases which hinders the convective flow of the fluid. But for high conductivity of the cylinder heat conducted through the cylinder becomes significant with the increase of cylinder radius. This is also evident from the isotherm lines that shows an increase in temperature gradient with increasing size. With the increase of radius as the space becomes less for fluid flow, separation of flow takes place and fluid flow is present only at the four corner sides of the enclosure. However for the case where Ω is not zero, increased size of the cylinder has a positive effect because strong flow field created by the rotation of the cylinder reaches near the isoflux surface and cold surface except at the corners where the effect of rotating cylinder is weak resulting in higher heat transfer.

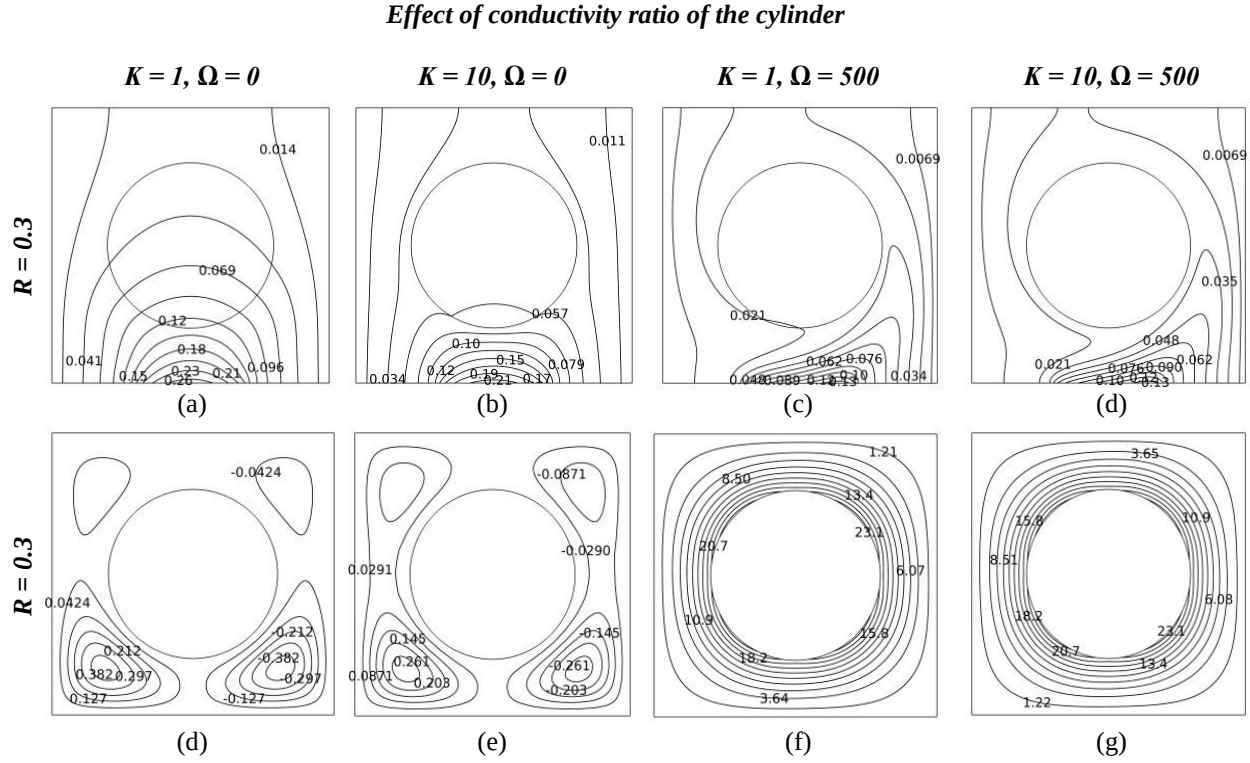

FIGURE 4. Isotherm lines and streamfunctions for R = 0.3 (K = 1, 10 ; Ω = 0, 500).

In Fig. 4 the effect of conductivity ratio on temperature field and flow field is shown for K = 1 and 10 considering R = 0.3 and Ω = 0 and 500. From Fig. 4(a) of isotherm lines where Ω = 0 for K = 1 the slope of the temperature at the solid-fluid interface is identical. Continuity of heat flux present here which means that the heat released by the cylinder is equal to the heat gained by the fluid and vice-versa. In this case temperature is distributed over the cylinder as a stationary fluid. For K = 10 in Fig. 4(b), the temperature slopes at the cylinder-fluid interface vary proportionately with the thermal conductivity ratio of the cylinder. From the figures of streamfunctions (Fig. 4(d), 4(e), 4(f), 4(g)) it is observed that the effect of conductivity on flow field is very small for both natural and mixed convection situtation. From the Fig. 4(c) and 4(d), where Ω = 500, the effect of conductivity ratio on temperature distribution also becomes negligible. This is because as the speed increases, the fluid makes less contact with the conducting cylinder to have the conductivity effect.

Heat Transfer Visualization

The variation of local and average Nusselt number at the heat flux portion of the bottom wall with rotational speed of the cylinder for different radius and conductivity ratios is demonstrated in Fig. 5.

In Fig. 5(a) the distribution of the local Nusselt number (Nu_l) at the heat flux portion is shown for various rotational speeds of the cylinder for R = 0.3 and K = 1. For Ω = 0 the distribution of the Nu_l is symmetric along the heat flux portion. Also the concave upward shape of the curve shows that minimum heat transfer takes place at the middle of the heat flux portion. This is because the convective flow hindrance by the cylinder is larger here. For Ω = 500, the maximum local Nusselt number is observed at the left end of the heat flux portion. This is convenient with the temperature field that shows an intense temperature gradient here. Then the local Nu_l shows a sharp decrease followed by a linear decreasing trend- resulting in a minimum value of Nu_l near the right end of the heat flux portion. At the end of the heat flux portion the local Nusselt number shows an increasing trend. Similar kind of variation of local Nusselt number (Nu_l) with rotational angular speeds is observed for other cylinder radius and conductivity ratios.

From the Fig. 5(b) it is evident that average Nusselt number (Nu_{avg}) is a strong function of rotational speed of the cylinder. Average Nusselt number (Nu_{avg}), increases with rotational speed of the cylinder for all cases under consideration. The conductivity of the rotating cylinder has a positive effect when $\Omega = 0$ but with the increase of speed, conductivity effect is diminished. With the increase of cylinder radius, Nu_{avg} decreases for $K = 1$, $\Omega = 0$. This is because as the cylinder radius is high, the free space left for fluid flow is narrow and it resists the natural convection action. But for higher conductivity ratio $K = 10$ and $\Omega = 0$, heat transfer increases with radius because conduction of heat through the cylinder becomes greater than the hindrance of convective flow by the cylinder. Increase of Nu_{avg} occurs with increasing radius due to the strong flow field near both the isoflux surface and the cold surface.

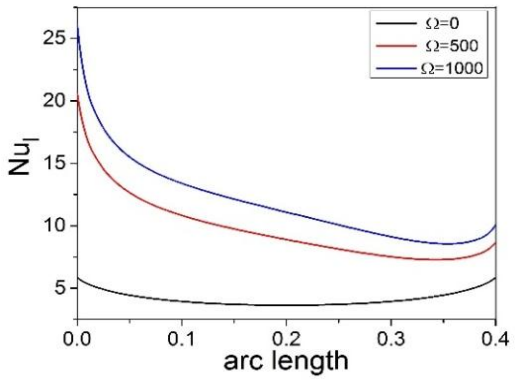

FIGURE 5 (a). Variation of local Nusselt number with angular speeds for arc length at the heat flux portion for ($R = 0.3$, $K = 1$)

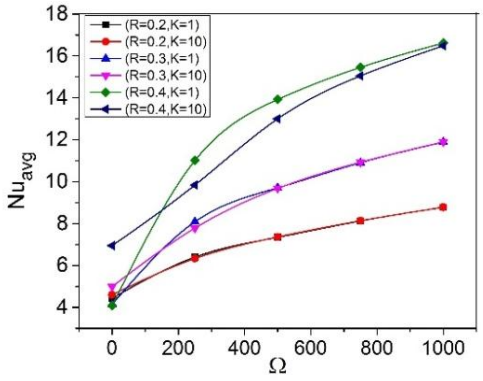

FIGURE 5 (b). Variation of average Nusselt number with angular speeds for different conductivity ratios and radius of the cylinder

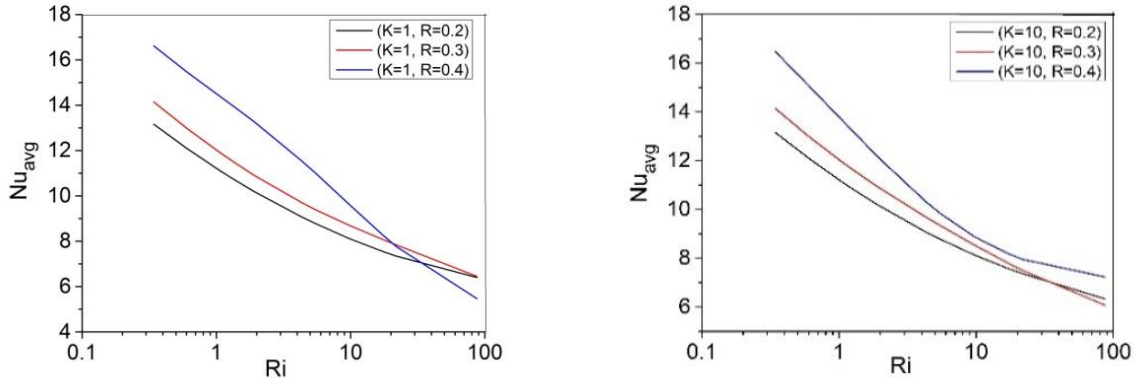

(a) (b)

FIGURE 6. Variation of average Nusselt number with *Ri* (a) $K = 1$ (b) $K = 10$

In Fig. 6 the variation of average Nusselt number with Richardson number for different combination of angular speed and radius of the rotating cylinder is shown. From the curve it is observed that average Nusselt number (Nu_{avg}) decreases with increased *Ri* for all cases irrespective of cylinder radius and conductivity ratio and Nu_{avg} also increases at a very rapid rate in the range of *Ri* (0.3-10). In the region where the value of *Ri* is greater than 10 the effect of forced convection is negligible and main heat transfer takes place by natural convection. Here heat transfer is observed low in this region. Higher value of *Ri* occurs when speed and radius of the cylinder is low. For higher speed and radius of the cylinder *Ri* becomes lower and both the natural convection and forced convection become important and they both dominate the heat transfer phenomena. Heat transfer also increases due to the increasing importance of forced convection. It is also evident that for same value of *Ri* heat transfer is greater for low speed and larger radius than is for higher speed and lower radius.

CONCLUSION

The present study analyzes the variation of isotherm lines and streamlines with the change of rotating speed (Ω), conductivity ratio (K) and cylinder radius (R). For stationary cylinder the temperature profile is symmetric about vertical central axis whereas with the rotation of the cylinder this symmetry is distorted resulting in dense isotherm lines at the right side of the cylinder and thinly distributed isotherm lines at the left side of the cylinder since at the left side the direction of flow of fluid, steered by rotating cylinder, is opposite to that of natural convective flow. The flow field for stationary cylinder is symmetrical, while this flow field gets stronger and gets closer to the enclosure with the increasing speed of the cylinder.

The size of the cylinder has negative effect on heat transfer since the increased size of the cylinder creates more restriction on the convective flow of the fluid. Again the larger the size of the cylinder the greater is the possibility of flow separation which results in fluid flow only at the four corners of the enclosure. On the contrary, for a non-stationary cylinder increased size has positive effect on heat transfer because of rotational speed.

For $\Omega = 0$ and $K = 1$, the continuity of heat flux is denoted by the identical temperature gradient at the solid-fluid interface but the proportionate increase of temperature slope at the solid–fluid interface is observed with the increase of conductivity ratio ($K = 10$). As the rotational speed increases the influence of conductivity ratio on the pattern of isotherm lines diminishes and the flow field is also negligibly affected by the change of conductivity ratio.

REFERENCES

1. House, J.M., Beckermann, C. Smith, T.F, Numer. Heat Transfer, Part A, vol.18, pp. 213-225.
2. T. Kimura, M. Takeushi, N. Nagai, Y. Kataoka, T. Yoshida, Heat Transfer –Asian Res.**32(4),** 342-353 **(**2003).
3. W.-S.Fu, C.-S. Cheng, W.-J.Sheih, Int.J. Heat Mass Transfer **37(13),** 1885-1897 (1994).
4. N.K. Ghaddar, F. Thiele, Num. Heat Transfer A **26,** 701-717 (1994).
5. Shuja, S.Z, Yilbas, B.S. Iqbal, M.O, Int. J. Numer. Methods Heat Fluid Flow **10(8)**, 824-841 (2000).
6. V. Costa, A.M. Raimundo, Int. J. Heat and Mass Transfer **53,** 1208-1219 (2010).
7. Salam Hadi Hussain, Ahmed Kadhim Hussein, International Communications in Heat and Mass Transfer **38,** 263-274 (2011).
8. B. Kim, D. Lee, M. Ha, H. Yoon, International Journal of Heat and Mass Transfer **51,** 1888-1906 (2008).

International Conference on Mechanical Engineering 2015
(ICME 2015) 18 – 20 December, 2015, Dhaka, Bangladesh

Paper ID : 418

Numerical Study of Mixed Convection Heat Transfer from a Rotating Cylinder inside a Trapezoidal Enclosure

Mohammed Khan [a)], Arham Amin Khan[b)], Mohammad Nasim Hasan [c)]

Department of Mechanical Engineering, Bangladesh University of Engineering and Technology (BUET)
Dhaka-1000, Bangladesh

[a)]Corresponding author: khanhridoy23@gmail.com
[b)] arhamakm@gmail.com
[c)] nasim@me.buet.ac.bd

Abstract. This article reports a numerical investigation of mixed convection heat transfer phenomena around an active rotating heated cylinder placed inside a trapezoidal enclosure. The cavity is configured such that top and bottom walls remain thermally insulated while the remaining two sidewalls experience a constant cold temperature. The heated cylinder is located at the centre of the trapezoidal enclosure and undergoes counter clockwise rotation. The numerical solution of various governing equations (i.e. continuity, momentum and energy equations) for the present problem is obtained by using Galerkin finite element method. The present study focused on the influence of the variation of inertia effect of the rotating cylinder as manifested by the parameter, Reynolds number (*Re*) for various Grashof number (*Gr*) ranging from 10^3 to 10^5 while keeping the Richardson number constant as 1, which essentially represents the case of pure mixed convection. An envision of flow field and thermal field has been made by studying the streamlines, isotherms respectively while for the study of heat transfer characteristics, local and average Nusselt number over the heated cylinder has been considered. The result indicates that both the side wall inclination angle as well as the inertia effect of the rotating cylinder has greater impact on heat transfer characteristics compared to the case of motionless heated cylinder placed in a square cavity.

INTRODUCTION

Mixed convection in an enclosure can be a very important phenomenon in many industrial and environmental applications. The actual geometries that are encountered in the engineering field are more complex than a simple enclosure with a convective fluid. Still such studies provide the engineer with fair amount of knowledge that how to solve similar problems in practice. Natural convection in an enclosure has been extensively studied due to its range of application in nuclear reactors, heat exchanger, chemical reactors, cooling of electronic equipment etc. Natural convection in a square enclosure with a circular cylinder at different vertical locations was studied by Kim [1]. The study was performed over the range of varying Rayleigh number from 10^3-10^6. This particular problem can be further improved by rotating the cylinder resulting in mixed convection flow. Costa [2] studied mixed convection in a differentially heated square enclosure with an active rotating circular cylinder. Similar problems have been studied by Fu et al [3], Ghaddar and Thiele [4] and Ghaddar [5], and Liao [6]. Fu et al [3] concluded that direction of cylinder rotation significantly influenced natural convection. Ghaddar and Thiele [4] used spectral element method showing results of a constant heat flux rotating cylinder within an isothermal rectangular enclosure that heat transfer increased with the increase of rotation at low Rayleigh number while heat transfer decrease with the increasing rotation at high Rayleigh number. In literature, heat transfer from a heated rotating cylinder inside trapezoidal cavity is rare. In the present study, mixed convection heat transfer from an active rotating cylinder in a trapezoidal cavity is numerically studied. The enclosure under consideration contains a heated active rotating cylinder at the center whereas the top and bottom walls are kept thermally insulated and the side walls are maintained at a constant low temperature. The study is performed for the case of pure mixed convection that corresponds to a Richardson number of unity while relative contribution of the inertia effect and buoyancy effect on heat transfer is studied by varying the Grashof number. Flow

field, temperature field, and heat transfer characteristics are visualized by streamlines and isotherm distribution and the local and average Nusselt number over the periphery of the cylinder.

Nomenclature

k	Thermal conductivity, (W/m/K)	α	thermal diffusivity, m^2s^{-1}
H	Height, (m)	β	thermal expansion coefficient, (K^{-1})
L	Length, (m)	θ	dimensionless temperature
Pr	Prandtl number	μ	dynamic viscosity, ($kg \cdot m^{-1} \cdot s^{-1}$)
Gr	Grashof number	ν	kinematic viscosity, (ms^{-1})
Ri	Richardson number	ψ	stream function
Ra	Rayleigh number	γ	angular position on cylindrical circumference
Nu	local Nusselt number	$\emptyset$	side wall inclination angle
Re	Reynolds number	ω	angular velocity of the cylinder.
Nu_{avg}	surface averaged Nusselt number		
T_0	Bulk Temperature, $T_0 = (T_h + Tc)/2$ (K)		
u	x component of velocity		
U	x component of dimensionless velocity		
U_o	Peripheral velocity of the cylinder($=\omega R$)		
v	y component of velocity		
V	y component of dimensionless velocity		
x, y	Cartesian coordinates ,(m)		
X, Y	Dimensionless Cartesian coordinates		

MATHEMATICAL MODEL

The schematic configuration considered in the present study is sketched on Fig. 1. Consider the system consists of trapezoidal domain (L/H = 1) having an immersed rotating, heated circular cylinder (T_h) with radius $R = 0.2L$ at the center of the enclosure. The bottom and upper walls of the enclosure are insulated and rest of the walls are at T_c. No slip condition is applied to both the rotating cylinder surface and enclosure walls which essentially make it a mixed convection phenomena. Thermal radiation between walls is negligible and the thermo-physical properties are assumed constant while for the density in the buoyancy term Boussinesq approximation is used. Mixed convection phenomena inside the domain follow the mass, momentum and energy conservation equations that read, in its dimensionless form

$$\frac{\partial U}{\partial X} + \frac{\partial V}{\partial Y} = 0 \tag{1}$$

$$U\frac{\partial V}{\partial X} + V\frac{\partial U}{\partial Y} = -\frac{\partial P}{\partial X} + \frac{1}{Re}\left(\frac{\partial^2 U}{\partial X^2} + \frac{\partial^2 U}{\partial Y^2}\right) \tag{2}$$

$$U\frac{\partial V}{\partial X} + V\frac{\partial V}{\partial Y} = -\frac{\partial P}{\partial Y} + \frac{1}{Re}\left(\frac{\partial^2 V}{\partial X^2} + \frac{\partial^2 V}{\partial Y^2}\right) + \frac{Gr}{Re^2}\theta \tag{3}$$

$$U\frac{\partial \theta}{\partial X} + V\frac{\partial \theta}{\partial Y} = \frac{1}{Re\,Pr}\left(\frac{\partial^2 \theta}{\partial X^2} + \frac{\partial^2 \theta}{\partial Y^2}\right) \tag{4}$$

The dimensionless parameters appear in the forgoing equations are introduced as

$$X = \frac{x}{L}, Y = \frac{y}{L}, U = \frac{u}{U_0}, V = \frac{v}{U_0}, \theta = \frac{T - T_c}{T_h - T_c}, \quad Pr = \frac{\nu}{\alpha}, Re = \frac{U_0 L}{\nu}, Gr = \frac{g\beta(T_h - T_c)L^3}{\nu^2}$$

The heat transfer coefficient in terms of the local Nusselt number (Nu) and average Nusselt number (Nu_{avg}) is defined by

$$Nu = -\frac{\partial \theta}{\partial n} \tag{5}$$

$$Nu_{avg} = \frac{1}{W}\int_0^W Nu\, dS \tag{6}$$

Where n is unit surface normal component, W is the perimeter of the cylinder and dS is small element along peripheral length.

Figure 1. Schematic of the model

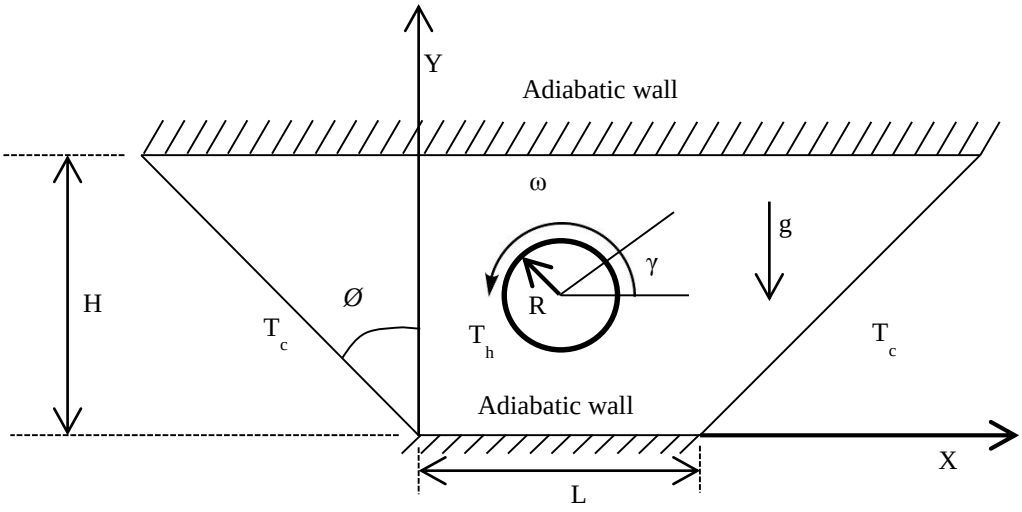

The dimensionless boundary conditions for velocity and temperature are specified as follows:

Top and bottom wall: $U = 0, V = 0, \frac{\partial \theta}{\partial Y} = 0$, Side walls: $U = 0, V = 0, \theta = 0$,

Circular cylinder: $U = \frac{\omega R}{U_0}\sin\gamma, V = \frac{\omega R}{U_0}\cos\gamma,$ where, $0 \le \gamma \le 2\pi$, $\theta = 1$

NUMERICAL SCHEME AND CODE VALIDATION

The Galerkin weighted residual finite element scheme is used to solve the governing equations numerically. In finite element method, the computational domain will discretize into unstructured triangles. The coupled equations (1)-(4) are transformed into a system of integral equations using Galerkin weighted residual technique. To solve these linear equations triangular factorization method is used. To validate the developed model, simulations were carried out to compare the mixed convection problem of a heated rotating cylinder inside a square cavity as reported by Liao and Lin [6]. The summary of comparison has been tabulated in Table 1. As mentioned there, close agreement between the model result and reported result [6] has been obtained.

TABLE 1. Comparison of surface average Nusselt number with Liao and Lin [6] ($Ri = 10^3$, $Pr = 0.71$, $L/R = 5$)

	Nu_{avg}	
Ra	**Present work**	**Liao and Lin [6]**
10^4	9.823	9.8
10^5	6.445	6.5

RESULT AND DISCUSSION

The current study presents the numerical results of mixed convection heat transfer from a rotating circular cylinder placed in trapezoidal enclosure filled with air where $Pr = 0.71$ and $Ri = 1$. The purpose of the study is to investigate the effect of varying side wall inclination angle and Grashof number within a range of $-15^{o} \leq Ø \leq 45^{o}$ and $10^3 \leq Gr \leq 10^5$ on heat transfer characteristics. In order to study this pure mixed convection Reynolds number is changed within limits $31.62 \leq Re \leq 316.23$.

Effect of Grashof number

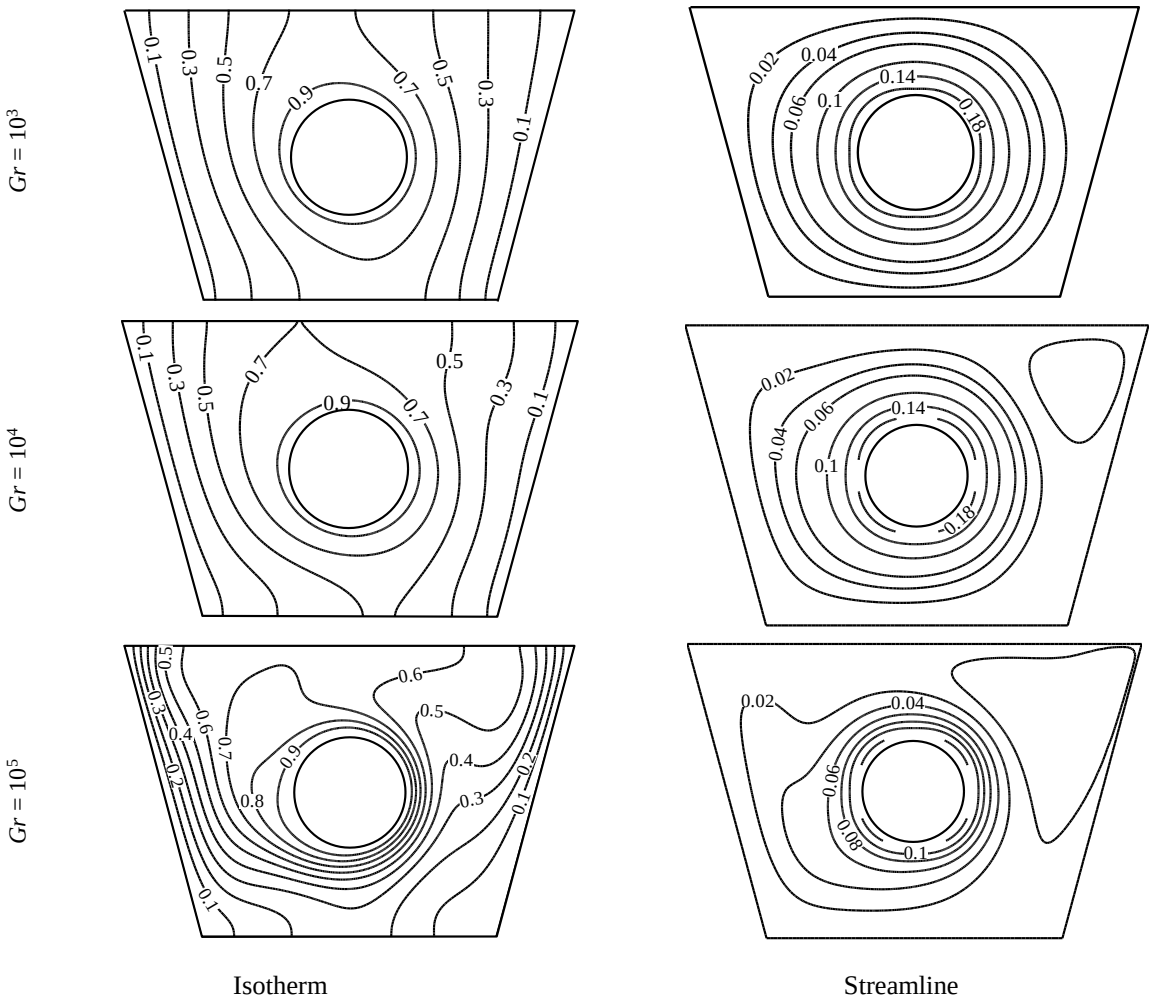

FIGURE 2. Isotherms and Streamlines for various *Gr* for $Ø = 15^{o}$.

The isotherms and streamlines for different Gr are depicted in Fig. 2 for $Ø = 15^{o}$. When Gr = 103, the thermal field is dominated by isotherm patterns which are almost symmetric about a vertical axis passing through the center of the cylinder. Few isotherms tending to form an oval shape around the rotating heated cylinder but prior to the completion of the oval it intersects the upper adiabatic wall perpendicularly. Here heat transfer is conduction dominated. However, the flow structure affected by the rotation of the cylinder, form an almost uniform circular pattern. At Gr = 104, the isotherms start distorting and are asymmetric about a vertical axis through the center of the cylinder. As a result, the

flow structure also moves towards the left creating a plume. At Gr = 105, the isotherms move upward with a plume developing on the upper left portion of the cavity. The shift of the plume structure in the counter clockwise direction is the effect of the rotation of cylinder. As a result, the impingement of the thermal boundary layer on the left wall leads to develop a thinner thermal boundary layer which gives rise to higher heat transfer. A recirculating cell develops at the upper right portion of the cavity resulting in a large change in streamline structure. The significant expansion of the recirculating cell squeezes the flow path. Convective heat transfer associated with the cell brings about higher removal of heat from the heated rotating cylinder.

Effect of Side Wall Inclination Angle

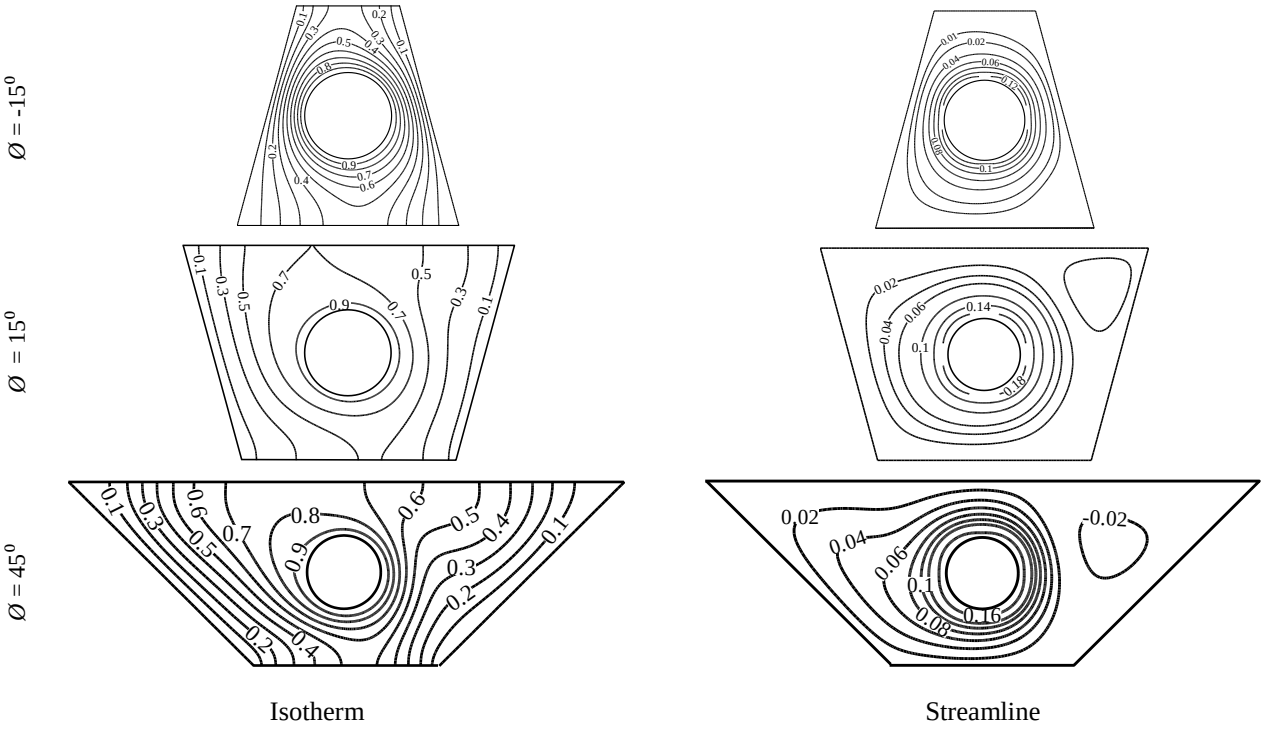

FIGURE 3. Isotherms and Streamlines for $Gr = 10^4$ and various side wall inclination angle.

The flow fields and thermal fields are depicted in Fig. 3 for $Gr = 10^4$ and three different side wall inclination angle .When $Ø = -15^o$ the isotherms are highly congested in the limited space available within the enclosure of the cavity. The thickness of the thermal boundary layer is very small and quite a few number of isotherms have formed complete oval structures around the cylinder. All these lead to high heat transfer rates. A plume generates at the bottom of the cylinder in the isotherm patterns and the flow field has uniform circular orientations. For the case when $Ø = 15^o$ few isotherms split in the upper portion and intersect with the adiabatic wall. The corresponding thermal boundary layer thickness slightly increases near the heat source from the previous case and heat transfer decreases while the flow field is almost identical. For wide side wall inclination angle, $Ø = 45^o$ the isotherms in the upper section widen and some of the oval shape isotherms at the bottom of the cylinder start splitting and intersecting with the bottom wall. The oval shaped isotherms obtain wavy nature with a wider upper mouth, thus the thermal boundary layer thickness further increases and heat transfer decreases significantly. The flow patterns in these cases show a secondary vortex alongside the main streamlines with plume at the left side of the cylinder. But this secondary vortex is not strong enough to reduce the boundary layer thickness. But numerical analysis for $Gr = 10^5$ shows that these vortexes are strong enough to offset the effect of high thermal boundary layer thickness which is consistence with the discussion made with surface averaged Nu_{avg}.

Heat Transfer Characteristics

Plots in Fig. 4 show the distribution of local Nusselt number (*Nu*) over the periphery of the cylinder for three values of Grashof number. The local Nusselt number is plotted in the radial direction. Fig. 4(a) exhibits that *Nu* is maximum at angular positions $\gamma = 20^0$ and $\gamma = 175^0$ for $Ø = -15^0$ and $Gr = 10^3$ while the patterns of *Nu* distribution have a similar shape for rest of the side wall inclination angles. Again Fig. 4(b) illustrates that maximum value of *Nu* is obtained at $\gamma = 180^0$ when $Ø = -15^0$ and $Gr = 10^4$. At this position of the cylinder surface the variation due to side wall angle is maximum but at a position near $\gamma = 300^0$ the variation is negligible. For side wall inclination angle 0^0 to 45^0 the pattern is almost similar but the maximum *Nu* occurs at higher angular coordinate due to the rotational effect of the heated cylinder. At higher Gr the pattern is significantly different from previous two. For these cases, 0^0 angular co-ordinate about the periphery of the cylinder gives maximum value of *Nu* for $Ø = 15^0$ and $Ø = 30^0$.

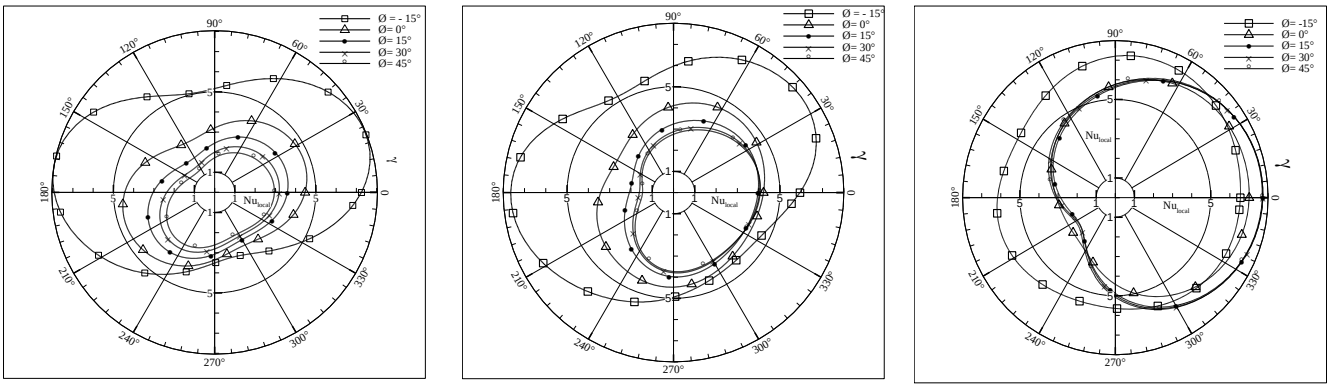

(a) (b) (c)

FIGURE 4. Local Nusselt number depending on the position over the surface of the cylinder for various trapezoidal angle (-15^0 to 45^0), *Pr* = 0.71, (a) $Gr = 1\times 10^3$ (b) $Gr = 1\times 10^4$, c) $Gr = 1\times 10^5$ and *Ri* = 1.

The effect of side wall inclination angle on surface averaged Nusselt number (Nu_{avg}) is illustrated in Fig. 5 with Pr = 0.71 and *Ri* unity. Five Grashof number are selected for comparison. The general outcome from the plot is that Nu_{avg} increases with increasing Grashof number. For a case of $Ø = -15^0$ the Nu_{avg} for $Gr = 10^5$ is 7.8% higher than that of $Gr = 10^3$. While for $Ø = 15^0$ the increase in Nu_{avg} for similar criteria is 42.15% and for $Ø = 45^0$ it is 131%. Thus it can be concluded that the effect of Grashof number on heat transfer is higher in cases of wide side wall inclination angle and less significant in other cases. A deeper insight to this set of data leads to following conclusions. At $Gr = 10^3$, if $Ø = -15^0$, Nu_{avg} increases by 56.52% with respect to the case where $Ø = 0^0$ but when the $Ø = 45^0$ Nu_{avg} decreases by 39.65%. When $Ø = -15^0$ Nu_{avg} is increased by 51% and 49% compared to square cavity for $Gr = 5\times 10^3$ and $Gr = 10^4$, whereas for $Ø = 45^0$ Nu_{avg} is decreased by 33% and 28% respectively. On the contrary in case of high $Gr = 10^5$ the widening of angle to 45^0 increases Nu_{avg} thus heat transfer by 51.58%. Here statement can be made that for side wall inclination angle -15^0 the increase of heat transfer rate compared with respective square cavity decreases with increasing *Gr*. For large side wall inclination angles the heat transfer rate decreases for lower *Gr*, conversely for high *Gr* the effect is reversed.

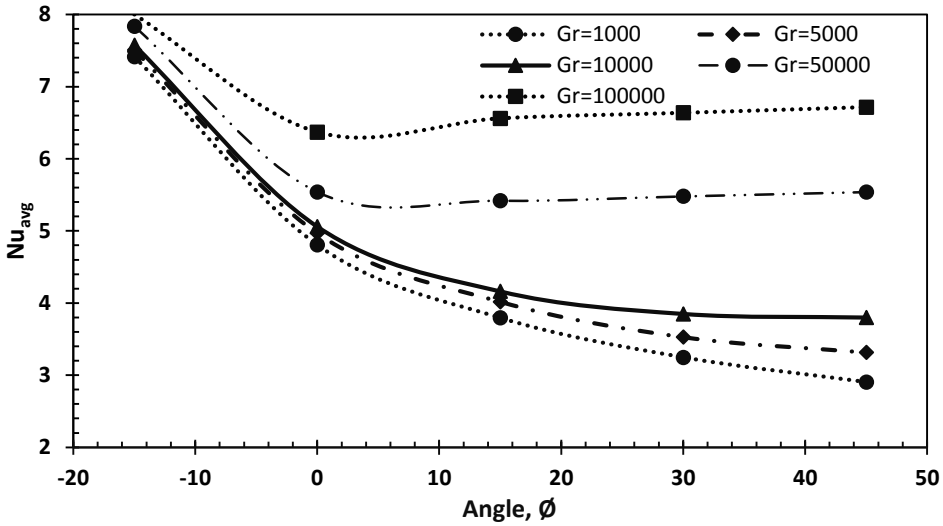

FIGURE 5. Surface averaged Nusselt number as a function of side wall inclination angle with various Grashof number.

CONCLUSION

Numerical studies are carried out for natural and mixed convections with stationary and dynamic complex geometry in simple cavity by using Galerkin method. The method was first validated with results of mixed convection of a heated rotating cylinder in a square enclosure. The relative comparison between buoyancy effect and inertia effect in pure mixed convection is investigated by varying two functions i.e. Grashof number and side wall inclination angle. Based on the results obtained by the investigation, following conclusions can be made. The heat transfer in a trapezoidal cavity differs significantly from the phenomenon observed in a square cavity. For pure mixed convection the heat transfer rates can be changed by varying the relative proportions of *Gr* and *Re*. The effect of Grashof number on heat transfer is higher in cases of wide side wall inclination angle and less significant in other cases. For large side wall inclination angles the heat transfer rate initially decreases with lower *Gr*, conversely for high *Gr* the effect is reversed.

REFERENCES

1. B.S. Kim, D.S. Lee, M.Y. Ha, H.S. Yoon, Int. J. Heat Mass Transfer **51**,1886-1906 (2008).
2. V.A.F,Costa,A.M. Raimundo, Int. J.Heat Mass Transfer **53**, 1208-1219 (2010).
3. W.S. Fu, C.S. Cheng, W.J. Shieh, Int. J. Heat Mass Transfer **37**, 1885-1897 (1994).
4. N.K.Ghadder, F.Thiele, Numer.Heat Transfer A Appl.**26,** 701-717 (1994).
5. N.K. Ghadder, Int. J. Heat Mass Transfer **35**, 2327-2334 (1992).
6. C.C. Liao, C.A. Lin, Int. J. Heat Mass Transfer **72,** 9-22 (2014).

ICME2015

International Conference on Mechanical Engineering 2015
(ICME 2015) 18 – 20 December, 2015, Dhaka, Bangladesh

Paper ID : 465

Prediction of Condensation Heat Transfer of Low GWP Refrigerants inside Smooth Horizontal Tube

Md. Anowar Hossain[1,a)], Hasan MM Afroz[1, b)], Shaon Talukder[1, c)], Akio Miyara[2, d)]

[1]*Department of Mechanical Engineering, Dhaka University of Engineering & Technology (DUET), Gazipur*
[2]*Department of Mechanical Engineering, Saga University, Japan*

[a)]Corresponding author: anowar96me@gmail.com
[b)]hafroz@yahoo.com
[c)]shaon073093@gmail.com
[d)]miyara@me.saga-u.ac.jp

Abstract. The present research work observed the experimental and analytical results of two phase condensation heat transfer of the refrigerants R1234ze(E), R32, R410A, and R1234ze(E)/R32 mixtures inside a smooth horizontal tube. A water heated double tube horizontal heat exchanger with effective length of 3.6m and inner diameter of 4.35mm is used to take place the experiment. Mass flux and the saturation temperature are the design variables under which the experiment is carried out whose values varying from the range 160 to 400 Kg $m^{-2}s^{-1}$ and 30°C to 45°C, respectively. A new correlation for pure refrigerant has been proposed to predict the heat transfer inside a smooth horizontal tube by investigating the experimental data. The newly proposed correlation and some other existing correlations of condensation heat transfer for pure refrigerant have been used to predict the condensation heat transfer of R1234ze(E), R32, R410A and dimethyl ether (DME) and compared the results. The comparison allows that the proposed model of pure refrigerant offered a better performance for all the refrigerants. All the experimental data can be predicted within a 10.2% mean deviation by using the proposed correlation.

INTRODUCTION

The currently used refrigerants in the air conditioning and refrigeration industries are going to be phased out day by day because of high ozone depletion potential (ODP) as well as a new phasing out criteria global warming potential (GWP). As a result, it is essential that to search a new generation refrigerant. The next generation refrigerant must consider the Total Equivalent Warming Impact (TEWI) that balance refrigerant direct GWP, charge level, leakage emissions, and efficiency of the refrigerant in actual systems. This allows the best possible comparison of refrigerants for each application. As a low GWP refrigerant, R1234ze(E) is being focused to be the next generation refrigerant which has a GWP value of 6 (Honeywell Fluorine products, 2008). Design engineers of heat exchangers in refrigeration, air conditioning and heat pump systems are facing problems to find out preliminary information on the heat transfer characteristics of alternative refrigerants, but there has been little research in this field. Cavallini et al. [1] presented a theoretical analysis of the condensation process and a critical review of a number of correlations for predicting the heat transfer coefficients for refrigerants condensing inside various commercially manufactured tubes with enhanced surfaces. A new predictive procedure to compute heat transfer coefficient during condensation inside smooth tubes, covering annular, stratified, and slug flow is proposed by Cavallini et al. [2]. Cavallini et al. [3] reviewed some research relating to condensation inside and outside smooth and enhanced tubes. They concluded that within smooth circular tubes, adequate predicting procedures for heat transfer are in general available to designers, even in the presence of lubricating oils. Experimental data are needed

for condensation of halogenated refrigerants near the critical temperature to possibly extend the confidence on available design tools. Dobson and Chato [4] investigated condensation heat transfer and flow regimes of refrigerants R12, R22, R134a and near-azeotropic blends of R32/R125 (50/50, 60/40 mass%) compositions over the wide range of mass flux in horizontal tubes with diameters ranging from 3.14 mm to 7.04 mm.. They stated that heat transfer coefficient increases with increasing the mass flux and quality in annular flow due to increased shear stress and thinner liquid film than in other flow regimes. They used a two-phase multiplier approach to correlate the heat transfer for annular flow. Haraguchi et al. [5] developed an asymptotic equation of power 2 for condensation heat transfer of the refrigerants HCFC 22, HFC 134a, HCFC 123. The suggested model is based on a predictive study of the flow patterns occurring during the condensation process. Miyara [6] has extensively reviewed condensation heat transfer and pressure drop of hydrocarbons (pure and mixture). For in-tube condensation, heat transfer coefficients of smooth tubes are correlated well with previously proposed equations obtained from experimental data of the fluorocarbons. In the case of condensation on a horizontal tube, heat transfer of smooth tube is explained well by the Nusselt theory. However, different characteristics appear for enhanced tubes due to the effect of properties which are not considered in the Nusselt theory. Hydrocarbons as a candidate for next generation refrigerants are widely used in domestic refrigerators. However, its flammability prevents the extending usage to larger systems, such as residential and packaged air conditioners, car air conditioners, heat pumps, etc. New technologies, such as low refrigerant charge system, reducing the flammability, and preventing the explosion, would be expected. At the same time suitable heat transfer enhancement techniques for condensation of hydrocarbons are required. Hossain et al. [7] experimentally studied the condensation heat transfer and pressure drop in horizontal smooth tube of internal diameter 4.35 mm for R1234ze(E), R32 and R410A and found that heat transfer coefficients of R1234ze(E) are about 30% lower than R32 and about 28% higher than 410A for mass flux of around 300 $kgm^{-2}s^{-1}$.Recently, Condensation heat transfer of low GWP refrigerant HFO1234yf was measured in a horizontal tube (inner diameter: 4 mm) at a mass flux range of 100- 400 $kgm^{-2}s^{-1}$and different saturation temperatures (40, 45, and 50°C), and the results were compared with that of R134a and R32 by Wang et al. [8] .The effects of mass flux and vapor quality on the heat transfer coefficient are primarily observed in the shear force dominated flow regimes when the mass flux is higher the vapor quality is high. The effects of thermo-physical properties on the heat transfer coefficient at different saturations temperature using different refrigerants were analyzed. The results show that the thermal conductivity, density ratio and viscosity ratio play an important role in the variation of the heat transfer coefficient. They found that Haraguchi et al. [5] correlation agrees reasonably with the experimental data values, with a mean deviation of 10.8%.

NOMENCLATURE

Nu	Nusselt number
d	diameter (m)
f	friction factor
G	mass velocity (kg m^{-2} s^{-1})
g	gravitational acceleration
P	pressure (Pa)
ΔP	pressure drop (Pa)
Re	Reynolds number
Pr	Prandtl number
x	vapor quality
X_{tt}	Lockhart-Martinelli parameter [$\left((1-x)/x\right)^{0.9}\left(\rho_v/\rho_l\right)^{0.5}\left(\mu_l/\mu_v\right)^{0.1}$]
T	temperature
Φ	two-phase frictional multiplier
μ	viscosity (Pa s)
ρ	density (kg m^{-3})
ε	void fraction

EXPERIMENTAL DATA

Our previously measured data of condensation heat transfer of R1234ze(E), R32, R410A, inside a horizontal smooth tube have been used for the present analysis. Most of the data have already been used by Hossain et al. [7]. The details of the experimental methodology have been described in Hossain et al. [7] The refrigerant mass flux variation was 147 to 403 kg m^{-2} s^{-1}. The range of inlet saturation temperature of the test section was 35°C to 45°C. The test section was horizontally installed double tube heat exchanger with effective length of 3.6 m as shown in Fig. 1. Refrigerant flows inside an inner tube and heating water flows through the annular space in a counter flow heat exchanger system. In order to measure quasi-local heat transfer, the annular channel is divided into 12 with each subsection length 300 mm. The inner tube is the smooth test tube made of copper and of 4.35mm inner diameter and 6.35 mm outer diameter. The surface roughness of copper test tube is R_a=0.666 µm and R_q=0.849 µm. The outer tube is made of poly-carbonated resin and of 9mm inner diameter and 13mm outer diameter.

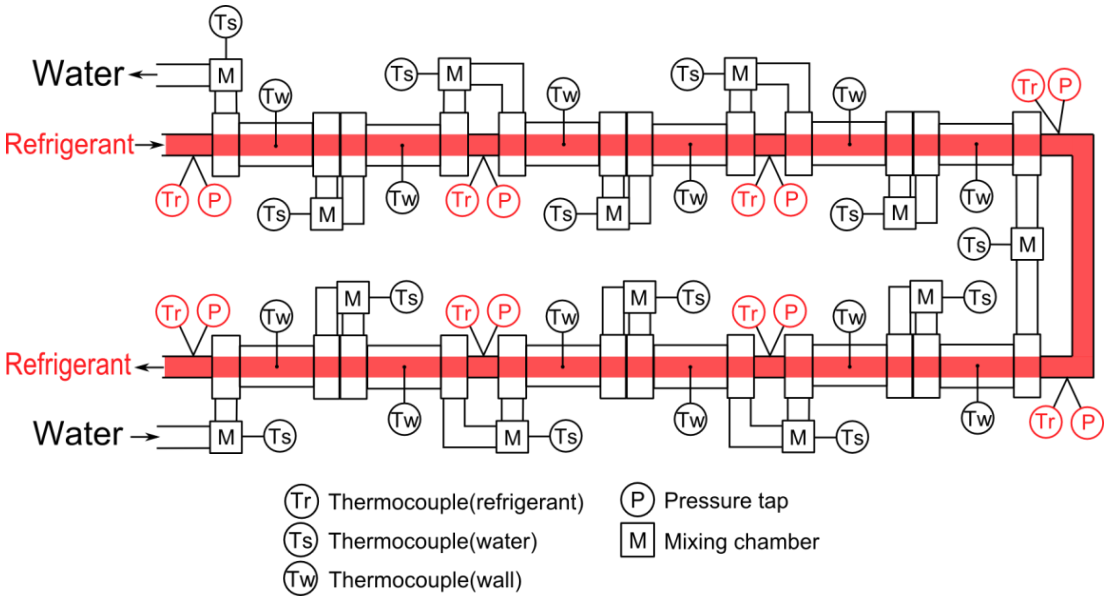

FIGURE 1. Test section

PROPOSED CORRELATION

By using the experimental data of all the refrigerants considered in the present analysis, a correlation of condensation heat transfer has been developed which can be used for low GWP refrigerants.

Developing Model

Haraguchi et al. [5]has developed a asymptotic type equation of power 2 by considering the forced and natural convective condensation as

$$Nu = \alpha d / \lambda_l = (Nu_F{}^2 + Nu_B{}^2)^{1/2} \tag{1}$$

where Nu_F is the forced convective condensation component, and Nu_B is the natural convective condensation component.

From the turbulent liquid film theory, the forced convective condensation component Nu_F can be expressed as follows

$$Nu_F = 0.152(\Phi_V / X_{tt})\,\mathrm{Re}_l{}^{0.9}(\mathrm{Pr}_l / T_i^+) \tag{2}$$

Let,

$$f_1 = 0.152(\Phi_V / X_{tt})\,\mathrm{Re}_l^{\,0.9} \tag{3}$$

Haraguchi et al. (1994) obtained (Pr_l / T_i^+) expression as eq. (4) by curve fitting analysis of $Nu_{F,Exp} / f_1$ versus Re_l graph.

$$(\mathrm{Pr}_l / T_i^+) = Nu_{F,Exp} / f_1 = (0.1 + 0.06\,\mathrm{Pr}_l)\,\mathrm{Re}_l^{-0.13} = f(\mathrm{Pr}_l)\,\mathrm{Re}_l^{-0.13} \tag{4}$$

But, this expression of Haraguchi does not predict our experimental data for example as shown in the Fig. 2 for R1234ze(E) for saturation temperature 40°C.

So, in the following section we have modified the Haraguchi's expression using our proposed Φ_V correlation and present experimental data. To do so first we have plotted the graph of $Nu_{F,Exp} / f_1$ versus Re_l and using curve fitting method, we obtained the value of *a* for every refrigerants and each mass flux of eq. (5) as shown in fig. 3.

$$Nu_{F,Exp} / f_1 = a\,\mathrm{Re}_l^{-0.2} = f(\mathrm{Pr}_l)\,\mathrm{Re}_l^{-0.2} \tag{5}$$

Then we have obtained the expression of $a = f(\mathrm{Pr}_l)$ as eq. (6) using the curve fitting method as shown in fig. 4.

$$a = f(\mathrm{Pr}_l) = 0.17 + 0.125\,\mathrm{Pr}_l \tag{6}$$

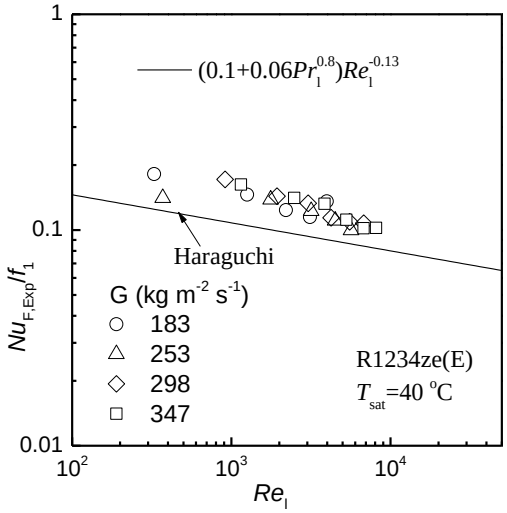

FIGURE 2. Prediction of present experimental data by Haraguchi's expression eq. (4)

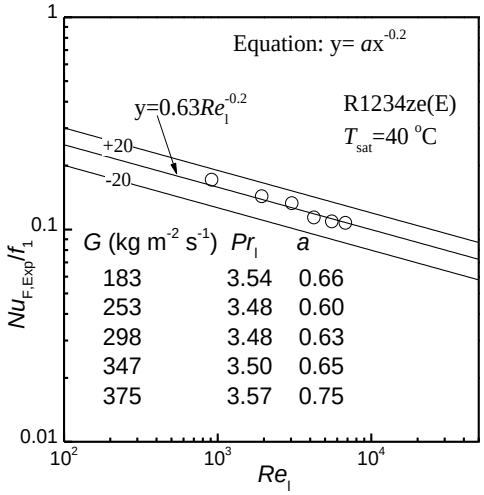

FIGURE 3. Finding the values of *a* in eq. (5)

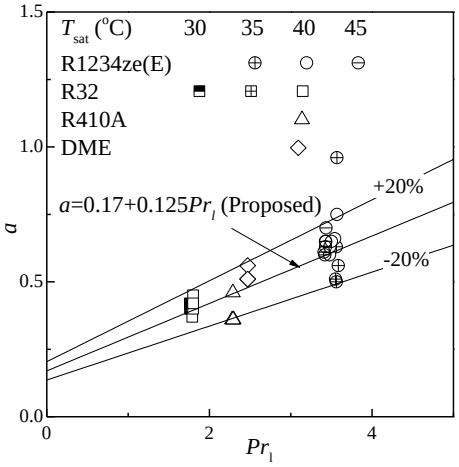

FIGURE 4. Developing the expression of $a = f(Pr_l)$ in eq. (5)

So the final form of the Nu_F expression in the Eq. (2) becomes as

$$Nu_F = 0.0152(0.17 + 0.125\,\mathrm{Pr}_l)(\Phi_V / X_{tt})\,\mathrm{Re}_l^{\,0.7} \tag{7}$$

So, the modified Haraguchi correlation is summarized as

$$Nu = (Nu_F^{\,2} + Nu_B^{\,2})^{1/2}\ ,\ Nu_F = 0.0152(0.17 + 0.125\,\mathrm{Pr}_l)(\Phi_V / X_{tt})\,\mathrm{Re}_l^{\,0.7}\ \&\ Nu_B = 0.725H(\varepsilon)(Ga\,\mathrm{Pr}_L / H_L)^{1/4} \tag{8}$$

where, Φ_V is obtained from the following equations

$$\Phi_{\mathrm{v}}^2 = 1 + CX_{tt}^{\,n} + X_{tt}^{\,2},\ C = 21\left\{1 - \exp\left(-0.28Bo^{0.5}\right)\right\}\left\{2 - 1.9\exp\left(-0.016Fr^{1.4}\right)\right\}\text{and}\ n = \left\{2 - 1.5\exp\left(-0.025Fr\right)\right\} \tag{9}$$

COMPARISON WITH EXPERIMENTAL RESULTS

Figure 5 shows the comparison of modified Haraguchi and Haraguchi's correlation with our present experimental heat transfer coefficient results at T_{sat}=40 $^{\mathrm{o}}$C and different mass fluxes for R1234ze(E) refrigerant. It is seen from this figure that the present modified Haraguchi equation predicted the experimental result with good agreement for all the mass fluxes.

Figure 6 shows the comparative prediction ability of the modified Haraguchi correlation for all the present experimental data. From this figure, it is demonstrated that the modification improves the prediction ability, especially for DME where Haraguchi's correlation could not predict well. We have found that modified Haraguchi predicted 98% data within 30% error whereas Haraguchi's correlation predicted 94% data within 30% error.Experimental results also correlated with other well-known models like Dobson and Chato, Cavallini, Jung, Thome and Shah's correlation. The results for all refrigerants and all models are shown in Table 1. It is seen from this table that among the all models the proposed correlation predicted the experimental data with lowest mean deviation of only 10.2%.

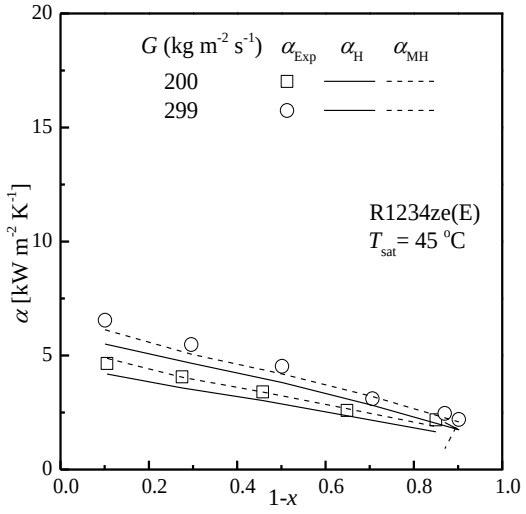

FIGURE 5. Comparison of modified Haraguchi and Haraguchi's correlation with experimental results for different mass fluxes

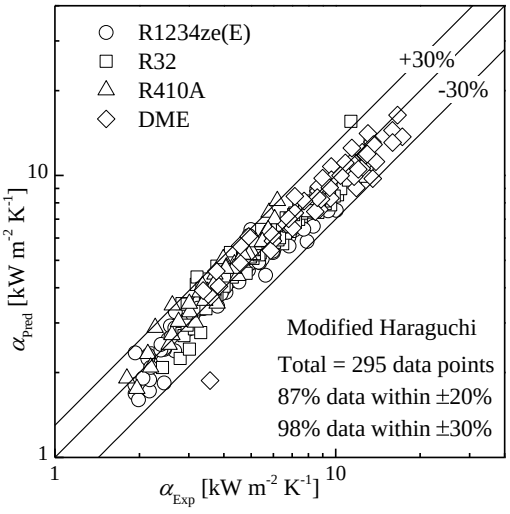

FIGURE 6. Prediction versus experimental results for all the heat transfer coefficient data.

TABLE 1. Deviations of various correlations against the present condensation heat transfer coefficient data

Refrigerant	Haraguchi correlation		Dobson &Chato correlation		Cavallini correlation		Jung correlation		Thome correlation		Shah correlation		Proposed correlation	
	AD[a]	MD[b]	AD[a]	MD[b]	AD[a]	MD[b]	AD[a]	MD[b]	AD[a]	MD[b]	AD[a]	MD[b]	AD[a]	MD[b]
R1234ze(E)	-11.69	12.07	-18.58	18.68	-29.10	29.19	9.90	15.18	-27.55	27.55	-13.74	13.91	-0.89	9.18
R32	-1.52	8.08	-9.68	11.25	-32.50	33.12	8.51	18.84	-35.38	35.38	-27.63	27.63	0.71	8.46
R410A	5.79	10.97	3.19	15.36	-24.39	32.94	28.68	30.67	-28.34	30.52	-16.84	16.84	11.58	12.93
DME	17.60	21.63	-4.91	12.89	-21.82	26.94	3.21	15.22	-24.02	24.57	-21.23	23.11	-3.17	10.38
Total	2.55	13.19	-7.50	14.55	-26.95	30.55	12.58	19.98	-28.82	29.51	-19.86	20.37	2.06	10.24

[a]Average deviation = $\frac{1}{n}\sum_{1}^{n}[(\alpha_{\Pr ed} - \alpha_{Exp})/\alpha_{Exp}]\times 100$ [b] Mean deviation = $\frac{1}{n}\sum_{1}^{n} ABS[(\alpha_{\Pr ed} - \alpha_{Exp})/\alpha_{Exp}]\times 100$

CONCLUSIONS

In the present analytical work, six well-known HTC correlations are used to analyze the experimental results and a new correlation by modifying Haraguchi et al. [5] for pure fluid inside smooth tube is proposed. The results of the work are summarized as follows:

- The prediction of the correlations in the descending mean deviation (MD) order is Cavallini→ Thome→Jung→Shah→Dobson and Chato→Haraguchi.
- The new correlation for pure refrigerants inside smooth tube improves the prediction ability with mean deviations of 10% for all data.

REFERENCES

1. A. Cavallini and R. Jacchin, "A dimensional correlation for heat transfer in forced convection condensation," 5th international heat transfer conference, *Tokyo*, 3, 309-313 (1974).
2. A. Cavallini, G. Censi, D. Del Col, L. Doretti, G.A. Longo and L. Rossetto, "In tube condensation of halogenated refrigerants," paper H-1718 ASHRAE Trans. 108, pt. 1 (2002).
3. A. Cavallini, G. Censi, D. Del Col, L. Doretti, G.A. Longo, and L. Rossetto, Int J Refrigeration **24**,73–87 (2003).
4. M.K. Dobson and J.C. Chato, ASME J Heat Transfer. **120**, 193–213 (1998).
5. H. Haraguchi, S. Koyama and T. Fujii, "Condensation of Refrigerants HCFC 22, HFC 134a and HCFC 123 in a Horizontal Smooth Tube," (2nd Report, Proposals of Empirical Expressions for Local Heat Transfer Coefficient) Trans JSME 60(n.574) 245-52 (in Japanese) (1994).
6. A. Miyara, Int. J. Refrigeration **31**, 621-632 (2008).
7. M.A. Hossain, Y. Onaka and A. Miyara, Int. J. Refrigeration **35**, 927-938S (2012).
8. L. Wang, C. Dang and E.Hihara, Int. J. Refrigeration **35,** 1418–1429 (2012).
9. D. Jung, K. Song, Y. Cho and S. Kim, Int. J. Refrigeration **26**, 4–11(2003).
10. J.R. Thome, J.El. Hajal, and A. Cavallini, Int. J. Heat Mass Tran. **46,** 3365–3387 (2003).
11. M. M. Shah, HVACR research, **15 (5),** p.889-913 (2009).

ICME2015

International Conference on Mechanical Engineering 2015
(ICME 2015) 18 – 20 December, 2015, Dhaka, Bangladesh

Paper ID : 476

Heat Transfer across a Bare Tube Cooling Coil in Staggered Arrangement for Cold Storage Application

Dr. Amiya Kumar Singha[1,a)]

[1] *Associate Professor in Mechanical Engineering*
Department of Jute and Fibre Technology, University of Calcutta,
35 Ballygunge Circular Road, Kolkata-700 019, W.B. India
Tel. +91 33 2461 5444, Fax +91 33 2461 5632

[a)]Corresponding author: amiya_singha@rediffmail.com

Abstract. This paper presents the effects of variations in coil face velocity, coil array and number of rows on the rate of heat transfer, power consumption by the fan and the ratio of heat transfer to fan power for a cooling coil used in cold storage applications. A bare (unfinned) tube cooling coil in a staggered configuration is considered in this study. In this study 25 mm nominal bore seamless steel pipe of outside diameter 26.9 mm and thickness 3.25 mm is considered. The ratio of heat transfer rate and fan power is formulated in a non–dimensional form. A wide range of tube spacing, defined in terms of longitudinal pitch and transverse pitch and also a wide range of face velocities are considered for the study. The highest value of this non-dimensional ratio indicates the optimum coil array that gives maximum heat transfer per unit fan power consumption. From this study it is seen that the non-dimensional ratio of heat transfer rate to fan power consumption is greatly influenced by number of transverse rows, tube array and coil face velocities. It is seen that for every tube array and face velocity there is an optimum number of transverse rows which results in maximum heat transfer per unit fan power consumption. It is observed that four to six numbers of transverse rows give the maximum of this ratio depending upon the coil array. The optimum number of rows decreases as the compactness of the coil increases.

INTRODUCTION

In most cases, design of cooling coil for cold storage application is done keeping in mind the desired compactness of the system. The power consumption by the fan to make the air flow across the cooling coil by overcoming pressure drop has seldom been a criterion for the design. In cold storage applications where space usually does not impose any limitation, the power consumption of the fans should be considered a criteria for designing the cooling coils as the fans are running continuously. The fan, which is placed after the cooling coil induces the air across the cooling coil and the cooled air is fed to the storage space through ducting. The power consumption of the fan is directly proportional to the pressure drop across the cooling coil and the pressure drop depends upon the face velocity and coil array. For example, a 3000 Metric ton capacity potato cold storage where the compressor consumes about

40 kW power, the standard cooling coil fan consumes an almost equivalent amount of power. The high power consumption of the fan is due to the large static pressure drop of the air stream across the cooling coil. Suitable design of the cooling coil array may reduce the pressure drop of the air stream substantially resulting in reduced fan power consumption for the same refrigerating capacity.

The simplest cooling coil is a bare (unfinned) tube cooling coil made from standard size pipes. Heat transfer coefficient and air-side pressure drop can be estimated for various tube arrays using available heat transfer and flow correlations [1, 2]. For every arrangement of the tube array an optimum number of transverse tube rows is expected to give maximum heat transfer per unit fan power consumption for a particular air face velocity. The heat transfer

and fluid flow past a tube bundle are characterized by the tube diameter, the free stream velocity, the tube array and the Reynold's number.

Nomenclature

h	heat Transfer co-efficient (W/m^2K)
hi	internal heat transfer co-efficient (W/m^2K)
ho	external heat transfer co-efficient (W/m^2K)
K	thermal conductivity of air (W/mK)
K_P	thermal conductivity of tube material (W/mK)
Nu	Nusselt number
p	fan power (kW)
Pr	Prandtle number
q	rate of heat transfer per unit area (kW/ m^2K)
R	non dimensional ratio of heat transfer to fan power
Re	Reynolds number
t_e	evaporating temperature of refrigerant (K)
t_i	coil inlet temperature of air (K)
t_o	coil outlet temperature of air (K)
Z	correction factor

MATHEMATICAL FORMULATION

In this section, the heat transfer, fan power and their non dimensional ratio for the flow of air through the unfinned bare tube cooling coil are formulated. In this study the refrigerant considered to be evaporating inside the tube of cooling coil bank is ammonia (NH_3).

In cold storage application, the usual process is the cross flow of air over a tube bundle. The fan is situated after the cooling coil. For this study a staggered configuration of tube bank in cooling coil is considered as shown in Fig. 1. The geometry of tube bank is characterized by the transverse pitch (S_T) and the longitudinal pitch (S_L) between the tube centers as shown in Fig 1.

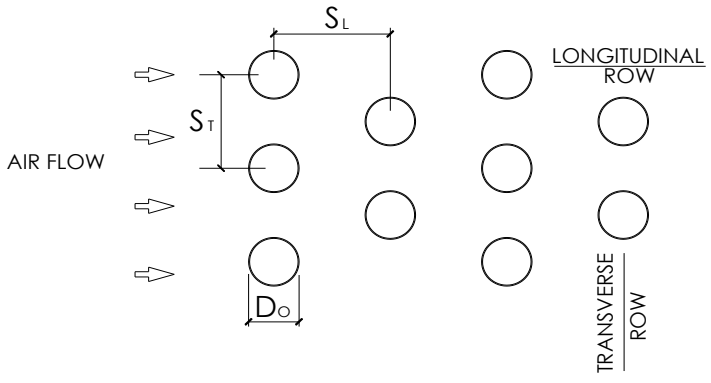

FIGURE 1. Staggered arrangement of a bare tube cooling coil.

External Heat Transfer Coefficient

To determine the external heat transfer coefficient the staggered tube array is considered The Reynolds number for the flow across the tube bank is based on the maximum velocity occurs inside the tube bundle. For this configuration, the maximum velocity occurs on the minimum free flow area available for air flow.

In this case, the maximum velocity is given by

$$V_{\max} = V \frac{S_T}{S_T - D} \tag{1}$$

Where, V is the face velocity of air at coil entrance.

The Reynolds number based on the maximum air velocity occurring within the tube bank is given by

$$\mathrm{Re} = \frac{\rho V_{\max} D}{\mu} \tag{2}$$

Different correlations have been proposed and used by different investigators [3, 4, 5, 6] for evaluating the heat transfer coefficient for flows over tube bundles.

Grimison [3] has proposed a correlation for Nusselt number for a bare tube (unfinned) bank with 10 or more transverse rows as follows:

$$Nu = 1.13\, C_0 \left(\mathrm{Re}\right)^n \left(\mathrm{Pr}\right)^{\frac{1}{3}} \tag{3}$$

Where, the values of the constants C_0 and n have been suggested by Grimison [3] for different tube array.

Zukaukas [4] has proposed another correlation to estimate Nusselt number for a unfinned bare tube bank with 20 or more number of transverse rows as:

$$Nu = C_2 \left(\mathrm{Re}\right)^m \left(\mathrm{Pr}\right)^{0.36} \tag{4}$$

Where, the value of constant C_2 varies from 0.21 to 0.8 and that of exponent m from 0.4 to 0.84, depending on the Reynolds number of the flow [4].

If the number of rows (N) is less than twenty, the Nusselt number can be found from the relation [3]:

$$Nu\big|_{(N<20)} = C_3\, Nu\big|_{(N>20)} \tag{5}$$

Where, the values of the correction factor C_3, as proposed by Zukaukas, are listed in table 1.Correction factor C_3 for an staggered arrangement for Eqn.5 given by Zukaukas [4].

The present analysis is based on Zukaukas model which is a more recent correlation developed as a result of comparison of the experimental data over a wide range of flow rates, Prandtle numbers and tube arrangements. The agreement with the experimental data was shown to be very good [1]. Now, Eq. (4) can be written as:

$$Nu = 0.27 \left(\mathrm{Re}\right)^{0.63} \left(\mathrm{Pr}\right)^{0.36} \tag{6}$$

Internal Heat Transfer Coefficient

The internal heat transfer coefficient for the flow of refrigerant inside the tube can be estimated using well established Dittus-Boelter [7] equation that gives the value of Nusselt number from the relation:

$$Nu_i = 0.023\,(\mathrm{Re})^{0.8}\,(\mathrm{Pr})^{0.4} \tag{7}$$

Overall Heat Transfer co efficient

The overall heat transfer coefficient U can be expressed in the following form.

$$\frac{1}{UA_0} = \frac{1}{h_0 A_0} + \frac{\ln \frac{D}{d}}{2\pi K_P L} + \frac{1}{h_i A_i} \tag{8}$$

For a bare tube cooling coil, air flowing outside and the refrigerant evaporating inside, the overall heat transfer is given by

$$Q_S = m_a C_P (t_i - t_o) \tag{9}$$

and

$$Q_S = UA_S LMTD \tag{10}$$

Equating equations (9) and (10) and we get the rate of heat transfer per unit face area per unit temperature difference becomes

$$q = \rho V_f C_P (1 - e^{-\frac{Nu\pi N}{\mathrm{RePr}(S_T/D)}}) \tag{11}$$

Fan Power Consumption

The pressure drop across the tube bank in cross flow is given by

$$\Delta P = f\,\frac{\rho^2 V_{\max}{}^2}{2}\,N\,Z \tag{12}$$

Where f is the friction factor and Z is the correction factor that depends on tube bank configuration and Z =1 for square tube arrangements.

Fan power per unit face area is given by:

$$p = \frac{\rho\, f\, V_{\max}{}^3 \left(\frac{S_T}{S_T - D}\right)^2}{2\eta}\,N\,Z\,x10^{-3} \tag{13}$$

To find out optimum rows of tube banks for which heat transfer rate per unit area per unit temperature difference (q) is maximum, the ratio of heat transfer (q) to fan power (p) in non-dimensional form can be obtained as:

$$R = \frac{2}{fNZ}\left(1 - e^{-\frac{Nu\pi N}{\mathrm{RePr}(S_T/D)}}\right) \tag{14}$$

The equations (11) , (13) , and (14) give the heat transfer , fan power , and their non-dimensional ratio for a particular set of values for V, S_T and S_L.

RESULTS AND DISCUSSIONS

The performance of the cooling coil in terms of the non dimensional ratio of heat transfer to fan power is studied to ascertain the effect of variations in some design parameters such as number of transverse rows of cooling coil, face velocity of air across cooling coil and longitudinal and transverse pitch of the coil array.

In this study 25 mm nominal bore seamless steel pipe of outside diameter 26.9 mm and thickness 3.25 mm is considered. For longitudinal pitch SL/D = 1.5, 2.0, 2.5 and for transverse pitch ST/D = 1.5, 2.0, 3.0, 4.0 are chosen. Face velocities of 1.5 m/s, 2.0 m/s, 2.5 m/s and 3.0 m/s is considered. Properties related to heat transfer are found at mean bulk temperature.

Fig. 2 shows the variation of non-dimensional ratio with number of transverse rows for different face velocities for ST/D = 3.0 and SL/D = 1.5. The non dimensional ratio R optimizes at a particular value of N for a given face velocity as is apparent from fig. 2.

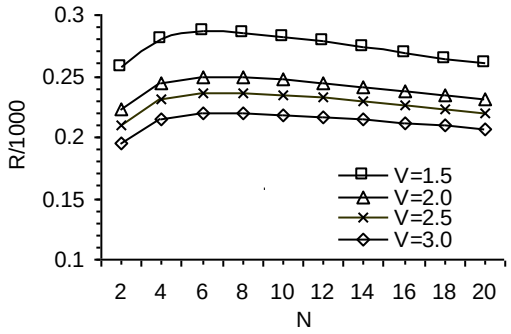

FIGURE 2. Variation of non dimensional ratio R with no of rows ST/D = 3.0 and SL/D = 1.5

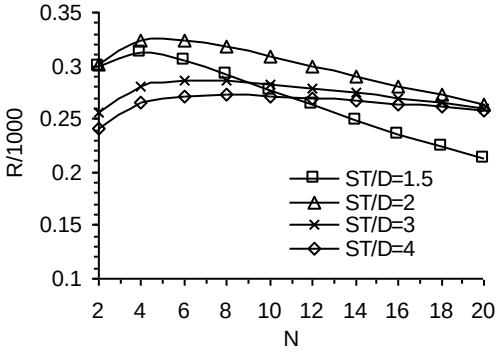

FIGURE 3. Variation of non dimensional ratio R with no of rows ST/D = 1.5 and SL/D = 1.5

Fig. 2 also suggests that lower face velocity gives higher value of this optimum R. This due to the fact that fan power is directly proportional to the square of the face velocity whereas heat transfer is proportional only to the face velocity. It may, therefore inferred that a lower face velocity (1.5 m/s in the current study) is always desirable.

Fig. 3 shows the effect of varying transverse pitch on R. for a given face velocity and longitudinal pitch. It is found that $S_T/D = 2.0$ gives the maximum value of R throughout the considered range of N. Values higher than 2.0 ($S_T/D = 3.0$, $S_T/D = 4.0$) tend to decrease R particularly at lower values of N .

In fig. 4 non dimensional ratio R is plotted with N for different S_L/D for velocity 1.5 m/s and $S_T/D = 3.0$. The plot reveals that R increases as S_L/D decreases. For the assumed S_T/D value, R maximizes at about N=4 for all S_L/D values signifying that SL/D has no significant effect on the optimum number of rows provided other parameters remain unchanged.

In Fig.5, non dimensional ratio R is plotted against S_T/D for N=2, 4, 6 and 8 (since maximum R varies in between N=2, to N=8. as found in Figs. 3 and 4). For Fig.5(a) V=1.5 and for Fig.(b) V=3.0 while S_L/D value

remains same for both of them (1.5). It is seen that at lower S_T/D (<2), optimum value of N is 4 and at higher S_T/D (>2) both N=6 and N=8 give similar results showing maximum values of R. The trend is same for both V=1.5 and V=3.0.

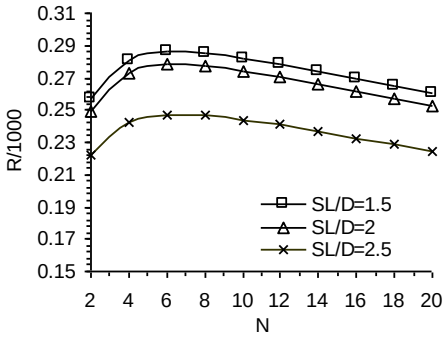

FIGURE 4. Variation of non dimensional ratio R with no of rows ST/D = 1.5 and SL/D = 3.0

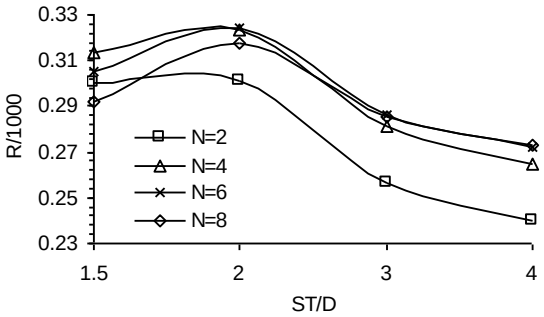

FIGURE 5. Variation of non dimensional ratio R with transverse pitch for pitch ST/D for SL/D =1.5, V=1.5

CONCLUSION

The effect of variations in face velocities across bare tube cooling coil and staggered tube array on heat transfer rate, fan power consumption and their non-dimensional ratio is studied and presented in this paper in a cold storage application. Inside the coil refrigerant is evaporating and air is cooled while passing across the coil. The ration of heat transfer from refrigerant to air and the power consumption by fan is derived in non-dimension form. Increase in non dimensional ratio indicates heat transfer from cooling coil to air is increasing than pressure drop to cause the air flow across coil. It is seen that the non-dimensional ratio of heat transfer rate to fan power consumption is greatly influenced by number of transverse rows, tube array and coil face velocities. It is seen that for every tube array and face velocity there is an optimum number of transverse rows which results in maximum heat transfer per unit fan power consumption. It is observed that lower face velocities give better heat transfer to fan power ratio for any tube array since fan power is directly proportional to the square of the face velocity whereas heat transfer is only proportional to the face velocity. It is also observed that for compact tube bundles (lower values of ST/D and SL/D) the optimum number of rows is four whereas for less compact bundles six to eight rows will give optimum performance. By increasing number of rows beyond eight rows, ratio of heat transfer to power consumption decreases which indicates pressure drop across coil increases compared to heat transfer due to long length of coil along the direction of air flow. The Compactness of cooling coil in the transverse direction affects the heat transfer. The ratio is maximum when transverse pitch is two and decreases sharply on increase in transverse pitch which results more decrease in heat transfer than fan power. It is found that compact cooling coils gives better heat transfer but consumes more fan power indicating higher running cost.

REFERENCES

1. M. N. Ozisik, *Heat Transfer a Basic Approach*, (McGRAW – HILL, 1998).
2. F. P. Incropera and D. P. Dewitt, *Fundamentals of Heat and Mass Tr.*, (John Wiley & Sons , Inc , New York, 1996).
3. E. D. Grimison, Trans. ASME, 583-594 (1937).
4. A. Zukuaskas, Adv. Heat Transfer, 93-160 (1972).
5. P. J. Mago and S. A. Sherif, J. of Heat Tr., 1182-1191 (2002).
6. Y. K. Hoyashi, A. Aoki and H. Yuhara, Heat Tr. Jpn, Res , 79-94(1977).

ICME2015

International Conference on Mechanical Engineering 2015
(ICME 2015) 18 – 20 December, 2015, Dhaka, Bangladesh

Paper ID : 482

Study of Combustion and Emission Characteristics of Fuel Derived From Waste Plastics by Various Waste to Energy (W-t-E) Conversion Processes

M. A. Hazrat[a)], M. G. Rasul and M. M. K. Khan

School of Engineering and Technology, Central Queensland University, Queensland 4702, Australia

[a)]Corresponding author: h.ali@cqu.edu.au

Abstract. Reduction of plastic wastes by means of producing energy can be treated as a good investment in the waste management and recycling sectors. In this article, conversion of plastics into liquid fuel by two thermo-chemical processes, pyrolysis and gasification, are reviewed. The study showed that the catalytic pyrolysis of homogenous waste plastics produces better quality and higher quantity of liquefied fuel than that of non-catalytic pyrolysis process at a lower operating temperature. The syngas produced from gasification process, which occurs at higher temperature than the pyrolysis process, can be converted into diesel by the Fischer-Tropsch (FT) reaction process. Conducive bed material like Olivine in the gasification conversion process can remarkably reduce the production of tar. The waste plastics pyrolysis oil showed brake thermal efficiency (BTE) of about 27.75%, brake specific fuel consumption (BSFC) of 0.292 kg/kWh, unburned hydrocarbon emission (uHC) of 91 ppm and NO_x emission of 904 ppm in comparison with the diesel for BTE of 28%, BSFC of 0.276 kg/kWh, uHC of 57 ppm and NOx of 855 ppm. Dissolution of Polystyrene (PS) into biodiesel also showed the potential of producing alternative transport fuel. It has been found from the literature that at higher engine speed, increased EPS (Expanded Polystyrene) quantity based biodiesel blends reduces CO, CO_2, NOx and smoke emission. EPS-biodiesel fuel blend increases the brake thermal efficiency by 7.8%, specific fuel consumption (SFC) by 7.2% and reduces brake power (Pb) by 3.2%. More study using PS and EPS with other thermoplastics is needed to produce liquid fuel by dissolving them into biodiesel and to assess their suitability as a transport fuel. Furthermore, investigation to find out most suitable W-t-E process for effective recycling of the waste plastics as fuel for internal combustion engines is necessary to reduce environmental pollution and generate revenue which will be addressed in this article.

INTRODUCTION

Fossil fuels are not renewable and limited based on capacity of the supply sources, but provide about 41% of the total worldwide energy demand each year [1]. The emission of these fuels, especially from transport sector, is one of the major sources for environment pollution. Hence, both the energy security concern and the greenhouse gas (GHG) emission have spawned the necessity of producing alternative but clean combustion energy sources. Production of fuel from waste plastics could be considered as one of the major alternative resources of fossil fuels for energy generation. This is known as tertiary or chemical recycling process, which can reduce the bulk amount of non-biodegradable plastics from land filling and incineration. The total worldwide plastic production trend is presented in the Fig. 1, which elucidates the rapid growth of plastic production in last two and half decades. It could be due to increase of population as well as diversified use of plastics in the industrial sectors around the world. In the Table 1, total worldwide annual production of most consumable thermoplastics is shown. This type of plastic production is dominant in the industrial and retail consumption. This amount is increasing rapidly with the increase of consumer demand. Due to this factor, Asia is now producing more than 45 wt% including China's leading production share of 24 wt%, 20 wt% each for European Union and North America and the rest are contributed by the other regions of the world[2]. Both the incineration and landfilling of waste plastics are sources of harmful [3,4] as well as carcinogenic emissions [5]. The global recycling rate of waste plastics was less than 5 wt% of the total new plastics produced in the year 2012 [2]. This small percentage of recycling indicates a grave loss of extracting resource value from the potential waste products.

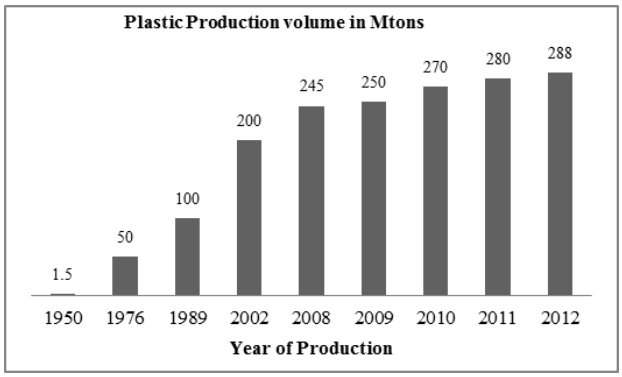

FIGURE 1. Worldwide total plastic production scenario[6]

TABLE 1. Worldwide Annual Thermoplastic Production [7]

Plastic	LDPE	LLDPE	HDPE	PP	PS	PVC	PET	Total	Percent of Total Plastics
World Production (M tons) in 2011	23.3	7.4	25.5	52.2	14.6	43.0	53.3	219.3	78.32%

In this article, pyrolysis and gasification processes are reviewed in terms of waste to energy (W-t-E) conversion processes from the waste plastics. Also combustion and emission characteristics of fuels derived from these processes are presented to indicate the potential of effective waste management as well as production of alternative fuel.

PROCESS TECHNOLOGIES TO PRODUCE FUEL FROM WASTE PLASTICS

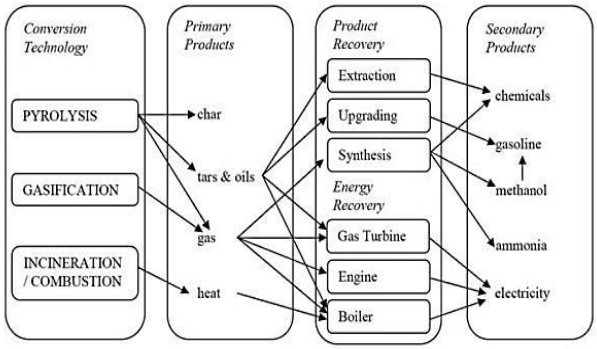

FIGURE 2. Schematic representation of various thermo-chemical conversion processes and their products[8, 9]

As per the analysis from plastic wastes reported by the UNEP [6], polymers that contain carbon and hydrogen molecules (e.g. thermoplastics like PE, PP, PMMA and PS, etc.) only can be considered as good feedstocks to produce liquefied fuel. The foremost quality concerns to convert waste plastics into useful alternative fuel resources can be pointed out as follows [6,7,10]:

- Smoothness of feeding the plastics into the conversion equipment.
- Effectiveness of adopted conversion process to derive fuel products.
- Acceptable level of combustion performance, and emission quality in the user side as per the international standards of fuels and emissions.

Figure 2 is a brief schematic representation of the various thermo-chemical conversion processes by which the plastic wastes can be treated to produce respective products. The attention in this article is to analyze the pyrolysis and gasification processes to produce fuel. These two processes are not culpable for producing hazardous emissions like the landfilling and incineration processes do.

Pyrolysis

The pyrolysis (thermal cracking in absence of oxygen) process yields bio-oil, char and syngas (Fig. 2), modification in the process can lead to production of more oil and syngas products [11-14]. Generally, the bio-oil comprises of gasoline (C_5-C_{10}), kerosene (C_{11}-C_{13}), diesel (C_{13}-C_{18}) and some heavy oil and waxy fractions (C_{20}-C_{37}) mixtures. The ultimate target is to produce more fuel like substances to be used as alternative fuel in the internal combustion engines. To produce anticipated liquid products from pyrolysis process, the selection of reactor is crucial along with the operating parameters. Wong et al. [8], Butler et al. [9] and Gao [15] have reviewed various reactors and their technical capacity on producing more fuel like substances from waste plastics. The researchers reported that, catalytic pyrolysis at low temperature is suitable to produce fuel like liquids. Also, the conical spouted bed reactor (CSBR) can yield more liquid products than that of fluidized bed reactor (FBR). On the other hand, the FBR shows better performance than those of batch and semi-batch reactors in terms of continuous feed. Uniform heat transfer to all plastics in the reactor, mixing quality of catalyst and type of yield products are the primary parameters for reactor selection. The two stage thermo-catalytic conversion of waste plastics into fuel has been identified as one of the effective methodologies; in which selection of the catalyst as well as reactor type contribute the success of total process [16-19]. Besides the solvent based fluidized catalytic cracking (thermo-catalytic) conversion process yields more liquefied products, which is dependent on the type of solvents and ratio (solvent: plastic) used as per desired product [8,20]. The bio-oil is also distilled, hydrogenated or hydrocracked to obtain optimal amount of diesel or gasoline range hydrocarbons from this process [9,21]. The review by Butler *et al.*[9] also suggested that synergism can be observed when the hydroprocessing is performed just after the fluid catalytic pyrolysis of waste plastics.

Wongkhorsub and Chindaprasert [22] conducted pyrolysis of municipal solid waste (MSW) consists of polyethylene (PE) and polypropylene (PP) in an autoclave reactor (300-500^{O}C, 3h). The yield products contain 60-80% oil (C_{10}-C_{30}, 46.2 MJ/kg, 0.815 g/cc, 2.49 cp); 5-10% residue and rest are syngas. The flash point of the oil (100^{O}C) was higher than diesel fuel (70^{O}C). The combustion of MSW plastic (PE+PP) pyrolysis oil produces 12.46% less power at brake specific fuel consumption (BSFC) of 294 g/kW-h than that of diesel fuel combustion. The exhaust gas temperature (no load, full load) of diesel engine with MSW (PE+PP) pyrolytic oil (120^{O}C, 225^{O}C) was reported as lower than that of diesel fuel combustion (119 ^{O}C, 312 ^{O}C) [26]. Also, the smoke opacity varied from 18%-97% with this fuel. Devaraj *et al.* [23] conducted combustion performance analysis with waste plastic pyrolysis oil (WPPO) (45.216MJ/kg, SG 0.798, Cetane Number (CN) 51), and blends of WPPO with 5% as well as 10% diethyl ether (DEE) as designated by WD5 and WD10 respectively. Brake thermal efficiency (BTE) was observed as 28%, 27.75%, 27.51% and 29.12% for diesel, WPPO, WD5 and WD10 respectively. The higher BTE with WD10 was explained due to presence of oxygen in DEE and its better atomization capacity interaction immiscible substances, e.g. WPPO. But at full load, the BSFC was 276 g/kW-h, 292 g/kW-h, 294 g/kW-h, and 301 g/kW-h for diesel, WPPO, WD5 and WD10 respectively. The higher BSFC of WPPO is due to higher density and lower calorific value than those of diesel fuel. WPPO also emitted 91 ppm unburnt hydrocarbon (uHC), 904 ppm NO_x, 0.14% carbon monoxide (CO) and 7.8% carbon dioxide (CO_2) at full load. On the other hand, WD10 emitted 96 ppm uHC, 473 ppm NO_x, 0.12% CO, and 7.2% CO_2 at full load.

TABLE 2. Temperature and catalyst effect on feedstock plastics [11,26].

Plastics	Temperature (^{O}C)	Catalyst	Yield
PE	120-140	O_2	Olefin Oxide
	350-500	H_2, $ZnCl_2$	Gasoline with high RON
	350-450	$Al_2O_3.SiO_2$	Fuel Oil
	400-650	Silica-Alumina	Isobutene
PP	320-380	Y-molecular sieve	Gasoline and diesel oil
	200	Cu	Ethylene chloride
PVC	350	Phosphoric Acid, Sodium silicate	Aromatics
	400-500	$AlCl_3$, $ZrCl_4$, etc.	Gasoline and diesel oil
PS	400-450	Solid acid, solid base, transition metal oxides	Styrene monomer

Sonawane, *et al.* [24] conducted pyrolysis reaction of HDPE plastic in absence and presence of catalysts (Natural zeolite (NZ) and Alumina, 5%wt) in a small fabricated glass based reactor at 550^{O}C. From their analyses, it was observed that with same operating conditions, catalytic pyrolysis produced more oil and less wax in less time (2.5h) than that of non-catalytic pyrolysis (3.5h) process. The oil yields were 70-71%, 65-67% and 60-62% with 5% alumina, 5%NZ and without catalysts respectively. The calorific value (CV) and specific gravity (SG) of the oils were 35.17-

36.43 MJ/kg, 33.49-34.75 MJ/kg, 30.15-30.56 MJ/kg and 0.78-0.785, 0.778-0.782, 0.776-0.779 respectively. Masuda *et al.*[25] have performed catalytic cracking (300-600^{O}C) of bio-oil derived from the pyrolysis (400.0^{O}C, 3h) of PE with Ni-REY catalyst in a career gas of hydrogen stream. At first stage, the oil yield was 74%., which later generated 64% gasoline in the second stage. Further experiments with other catalysts (HY and ZSM-5 zeolites) showed that the Ni-REY catalyst has better retention of catalytic activity than that of others. Table 2 shows the effectiveness of various catalysts for individual plastics on their operating conditions for yield products [11,26]. Hence, the selectivity of catalysts and the operating temperature have to be as per requirement of using the yield products.

Gasification

Gasification process of PSW occurs at higher than 800 ^{O}C and practically at 1000 ^{O}C in a lean air (20%-40% air) or oxygen-deficient reactor [27]. The reactors are mostly moving-bed, fluidized-bed and entrain-bed types. The final product yields are mainly combustible gas mixture (producer gas or syngas) and solid residue as char [28]. Components of gasification of 100% waste plastic yields more gaseous products but in different compositions, methane, light hydrocarbon and CO increases, but H_2 and CO_2 production diminished up to 10 vol% [29]. The air is not allowed into the process to avoid loss of calorific value of the gas products being diluted by the infused nitrogen gas. The main feature of this thermo-chemical process is treating heterogeneous plastics. But the mixture of plastic wastes may result into lower calorific value as observed 43.38MJ/kg, 43.42MJ/kg, 26.34MJ/kg, 39.79MJ/kg and 43.4MJ/kg for PE, PP, PE+PET, PE+PS, and PE+PP respectively [30]. The feedstocks require less pre-treatment and yield syngas for energy utilization [31,32]. The syngas can be converted into diesel fuel by either the Fischer-Tropsch (FT) reaction or by converting the syngas into methanol and then methanol to Gasoline (MTG) for transport application [33-35]. Catalytic (iron or cobalt or nickel) effect on product quality could be observed during these conversion processes. The Gas-t-liquid (GTL) FT process may produce 50-85% of middle distillate liquid fuel (jet fuel/kerosene/diesel) of higher CN [35]. Hydroprocessing could be also performed to convert the GTL-FT products into usable transport grade fuels. This process requires higher capital expenditure as well.

Arena *et al.* [28] have reported that the optimal production of high quality gaseous products can be obtained if the gaseous productions can be continuously removed from the downstream gasifier. They also found that the gasification of plastic wastes in a fluidized bed gasifier consisting of bed material, Olivine, act efficiently in reducing the tar products. Olivine, a neo-silicate of Fe and Mg with an olive-green color, can reduce the attrition of bed material and this is very cheap [36]. Also if the residence time is prolonged for the gas products and temperature is increased beyond 500 °C, the gas yield is increased in the process reaction of plastic wastes [37]. Mainly the gas can be used as combustion raw material in boilers and gas engines/turbines [38]. A secondary reactor (catalytic reactor) has been used to catalytically crack the produced tar after the gasification in presence of Calcined dolomite (at 800–900 °C) to purify the producer gas [39-41]. This has been currently under consideration as an effective purification process.

Straka and Bičáková [42] have investigated co-gasification of mixed waste plastics (LDPE, LLDPE, HDPE, PP, and PS) and lignite at 1200 °C. Due to this high temperature operation, the conversion of polycyclic aromatic hydrocarbons (PAHs) and soot from tar was reduced. As a result, hydrogen rich gaseous products increased. Since the co-gasification shows potential in desired yield gaseous products by reducing the tar in the gas, this process can reduce the coal, biomass and plastic wastes from the environment making the best utilization in terms of fuel production.

Application of liquid fuels obtained from gasification and GTL-FT processes of waste plastics in the internal combustion engines is still to be analyzed. Further investigation may help to assess the viability of this process in plastic waste management policy implementation.

Dissolution into Bio-solvent

In recent years, new methods of converting waste plastics into fuel are investigated. One of the potential and most attractive methods is dissolving these plastic wastes into biodiesel, an effective biodegradable solvent for polymer dissolution [43-45]. Zhang *et al.* [44] have explained in details about the solubility analysis and solubility parameters of PS and LDPE into biodiesel and their fatty acid methyl esters individually. Besides, use of appropriate co-solvent can reduce the dissolution temperature and increase the rate of dissolution in the solvent mixture [45]. There are few experimental results of engine performance and emission analyses are available for the fuels based on this technology. This technology is very promising as the technical setup costs are much less than those of other thermo-chemical processes to convert into fuels. That is how; the waste polymers can be treated as one of the effective additives to boost the fuel quality. The consequences are predicted as, more input towards nation's renewable fuel supply, less

dependence on international market supply, reduction of environment pollution and finally, the beneficial waste recycling method.

Mohammadi *et al.* [46] have investigated the EPS solubility in the waste cooking oil derived biodiesel in present of a homogenized co-solvent, acetone (5 wt% of used biodiesel) at 60°C. 5% EPS-Biodisel solution blended with diesel fuel (EPS-Biodiesel-Diesel blend) was used in the internal combustion engine. At highest speed, increased EPS quantity based biodiesel blend reduced the CO, CO2, NOx and smoke emission. Also, the fuel blend increased the brake thermal efficiency by 7.8% with increased specific fuel consumption (SFC) (7.2%) and reduction of brake power (Pb) (3.2%). Reduction of brake power could be overlooked as it is minimal in comparison to the increased thermal efficiency. Increased SFC was predictable due to the lower heating value discrepancy between plastic and diesel fuel. But, Kuzhiyil and Kong[43] observed that the biodiesel with PS (up to 10 wt% dissolved into the biodiesel) dissolved, can lead to increased NOx in the emission. Though the other emission parameters reduced up to 10 wt% PS dissolved biodiesel, they start increasing with the increase of PS concentration beyond that quantity.

DISCUSSION

Plastics are produced from petroleum based hydrocarbons. The durability and inexpensiveness have influenced the use of plastic products in almost every consumer applications. Therefore, the accumulating wastes should be treated and recycled in such an effective way by which the environment will not be under threat as well as the yield product is valuable. The W-t-E conversion theme is thus effective to consider the waste plastics as feedstocks for energy production. In this condition, the choice of affordable technology and optimal generation of desired fuel based product is important. Pyrolysis process with catalysts and liquefaction of feedstocks could be effective due to complexities of sorting of homogenous plastics from the waste bundles. Temperature, reactor and type of catalyst also regulate the success of gasification process as it does to the fluidized thermo-catalytic cracking process. The handling of gaseous products in the gasification process could make the process expensive but the quality of the end product is good to be used with prospect in the internal combustion engines. The gasification and subsequent GTL-FT process is used for other biomass and waste products to produce hydrocarbon. So, adoption of this technology with waste plastic feedstock could be beneficial as this process does not require the feedstocks to be sorted on homogeneity. Finally, the dissolution of suitable thermoplastics into biodiesel could be also considered as one of the tertiary waste recycling process, thus useful W-t-E processes. Combustion and emission characteristics of catalytic pyrolysis and dissolution processes are presented from various publications along with recent recycling condition in the world. So, the demand of alternative fuel production could consider the waste plastics as potential feedstock.

CONCLUSION

While performing the thermo-catalytic pyrolysis of homogeneous plastics, the low temperature thermal cracking effectively improves the liquid portion. In case of heterogeneous waste plastics and sorting complexities, the solvent based fluidized catalytic cracking provided good results in obtaining more liquefied fuel as final product. Also the use of DEE showed prospect in reducing emission contents, which are shown higher with the combustion of WPPO in the internal combustion engines. Distillation of liquid products from both pyrolysis and gasification process is essential to improve the engine performance as the gasoline range hydrocarbons are not conducive to diesel engine performance improvement. Biodiesel is already established renewable and clean combustible fuel to be used as blend with diesel fuel. Hence the use of biodiesel as solvent could be considered as inexpensive but appropriate methodology of fuel production. Further research is essential to improve the acceptance of this methodology in the commercial sector.

ACKNOWLEDGEMENTS

The authors would like to acknowledge the significant contribution by Central Queensland University in research and development activities.

REFERENCES

1. E. McLamb, in *Fossil Fuels vs. Renewable Energy Resources* (Ecology Global Network, 2011).
2. C. Velis, ISWA Taskforce Report on Globalisation and Waste Management, Report No. NA, 2014.
3. C.-T. Li, H.-K. Zhuang, L.-T. Hsieh, W.-J. Lee and M.-C. Tsao, Environ. Int. **27** (1), 61-67 (2001).

4. M. N. Siddiqui and H. H. Redhwi, J. Anal. Appl. Pyrolysis **86** (1), 141-147 (2009).
5. R. U. Halden, Annu. Rev. Public Health **31** (1), 179-194 (2010).
6. UNEP, Technical Report, Report No. DTI/1230/JP, 2009.
7. M. Chanda and S. K. Roy, *Plastics Technology Handbook*, 4th ed. (CRC Press Taylor & Francis Group, New York, 2006).
8. S. L. Wong, N. Ngadi, T. A. T. Abdullah and I. M. Inuwa, Renewable and Sustainable Energy Reviews **50**, 1167-1180 (2015).
9. E. Butler, G. Devlin, D. Meier and K. McDonnell, Renewable and Sustainable Energy Reviews **15** (8), 4171-4186 (2011).
10. D. R. Askeland, P. P. Fulay and W. J. Wright, *The Science and Engineering of Materials*, 6th ed. (Cengage Learning & Global Engineering, USA, 2011).
11. Y. Xingzhong, in *Feedstock Recycling and Pyrolysis of Waste Plastics, J. Scheirs, W. Kaminsky (Eds.). John Wiley & Sons Ltd., Chichester, West Sussex, England (2006), ISBN: 0-470-02152-7*, edited by J. Scheirs and W. Kaminsky (John Wiley & Sons, 2007), pp. 729-755.
12. J. Scheirs, in *F eeds tock R ecycling and P yrolys is of Was te P las tics: Converting Waste Plastics into Diesel and Other Fuels*, edited by J. Scheirs and W. Kaminsky (John Wiley & Sons Ltd., Chichester, West Sussex, England, 2006), pp. 383-433.
13. G. F. Bennett, J. Hazard. Mater. **147** (1–2), 682-683 (2007).
14. J. Aguado, D. P. Serrano and J. M. Escola, in *Feeds tock Recycling and Pyrolys is of Waste Plastics: Converting Waste Plastics into Diesel and Other Fuels*, edited by J. Scheirs and W. Kaminsky (John Wiley & Sons Ltd., 2006).
15. F. Gao, PhD, University of Canterbury, 2010.
16. M. A. Hazrat, M. G. Rasul and M. M. K. Khan, Procedia Engineering **105**, 865-876 (2015).
17. J. Aguado, D. P. Serrano, G. San Miguel, M. C. Castro and S. Madrid, J. Anal. Appl. Pyrolysis **79** (1–2), 415-423 (2007).
18. M. Artetxe, G. Lopez, M. Amutio, G. Elordi, J. Bilbao and M. Olazar, Chem. Eng. J. **207–208** (0), 27-34 (2012).
19. M. Della Zassa, M. Favero and P. Canu, J. Anal. Appl. Pyrolysis **87** (2), 248-255 (2010).
20. A. Karaduman, E. H. Şimşek, B. Çiçek and A. Y. Bilgesü, J. Anal. Appl. Pyrolysis **62** (2), 273-280 (2002).
21. B. K. Sharma, B. R. Moser, K. E. Vermillion, K. M. Doll and N. Rajagopalan, Fuel Process. Technol. **122** (0), 79-90 (2014).
22. C. Wongkhorsub and N. Chindaprasert, Energy and Power Engineering **5**, 350-355 (2013).
23. J. Devaraj, Y. Robinson and P. Ganapathi, Energy **85**, 304-309 (2015).
24. Y. B. Sonawane, M. R. Shindikar and M. Y. Khaladkar, International Journal of Innovative Research in Science, Engineering and Technology **3** (9), 15903-15908 (2014).
25. T. Masuda, H. Kuwahara, S. R. Mukai and K. Hashimoto, Chem. Eng. Sci. **54** (13–14), 2773-2779 (1999).
26. G. Xi., R. Liang. and Q. Tang., Research of Environmental Sciences **12** (3), 60-61 (1999).
27. A. Brems, R. Dewil, J. Baeyens and R. Zhang, Natural Science **5** (6), 695-704 (2013).
28. U. Arena, L. Zaccariello and M. L. Mastellone, Waste Manage. **30** (7), 1212-1219 (2010).
29. M. P. Aznar, M. A. Caballero, J. A. Sancho and E. Francés, Fuel Process. Technol. **87** (5), 409-420 (2006).
30. V. Wilk and H. Hofbauer, Fuel **107**, 787-799 (2013).
31. S. M. Al-Salem, P. Lettieri and J. Baeyens, Waste Manage. **29** (10), 2625-2643 (2009).
32. J. Scheirs, *Polymer Recycling: Science, Technology and Applications*, First ed. (Wiley-Blackwell, 1998).
33. GTC, in *Gasification Applications and Products* (Gasification Technologies Council, Arlington, VA 2011).
34. Gershman, Brickner and Bratton, Technical report, Report No. GBB/12038-01, 2013.
35. H. Sajjad, H. H. Masjuki, M. Varman, M. A. Kalam, M. I. Arbab, S. Imtenan and S. M. A. Rahman, Renewable and Sustainable Energy Reviews **30** (0), 961-986 (2014).
36. M.-H. Cho, T.-Y. Mun, Y.-K. Choi and J.-S. Kim, Energy **70**, 128-134 (2014).
37. F. Pinto, C. Franco, R. N. André, C. Tavares, M. Dias, I. Gulyurtlu and I. Cabrita, Fuel **82** (15–17), 1967-1976 (2003).
38. U. Arena, F. Di Gregorio, C. Amorese and M. L. Mastellone, Waste Manage. **31** (7), 1494-1504 (2011).
39. J. Corella, A. Orío and J.-M. Toledo, Energy & Fuels **13** (3), 702-709 (1999).
40. C. Brage, K. Sjöström, Q. Yu, G. Chen, T. Liliedahl and C. Rosén, *Biomass Gasification and Pyrolysis*. (1997).
41. N. Abatzoglou, R. Evans, T. A. Milne and n. Biomass Gasifier, *Tars": Their Nature, Formation and Conversion*. (1998).
42. P. Straka and O. Bičáková, Int. J. Hydrogen Energy **39** (21), 10987-10995 (2014).

43. N. Kuzhiyil and S.-C. Kong, Energy & Fuels **23** (6), 3246-3253 (2009).
44. Y. Zhang, S. K. Mallapragada and B. Narasimhan, Polymer Engineering & Science **50** (5), 863-870 (2009).
45. P. R. Harshal and L. M. Shailendra, Research Journal of Engineering Sciences **2** (2), 26-30 (2013).
46. P. Mohammadi, A. M. Nikbakht, M. Tabatabaei and K. Farhadi, International Journal of Automotive Engineering **2** (3), 156-162 (2012).

ICME2015

International Conference on Mechanical Engineering 2015
(ICME 2015) 18 – 20 December, 2015, Dhaka, Bangladesh

Paper ID : 493

Numerical Study of Mixed Convection Heat Transfer in an Inclined Rectangular Channel with Extruding Discrete Multiple Heaters

Araf Al Rafi[a)], Md. Tanvir Akhtar Tonmoy[b)], Mohammad Nasim Hasan[c)]

Department of Mechanical Engineering, Bangladesh University of Engineering and Technology
Dhaka-1000, Bangladesh

[a)]Corresponding author: araf.rafi316@gmail.com
[b)]tanvirtonmoy24@yahoo.com
[c)]nasim@me.buet.ac.bd

Abstract. A numerical investigation ofsteady two dimensional laminar mixed convection heat transfer phenomena in an inclined rectangular channel has been performed in the present study. The upper wall of the channel under consideration is maintained at constant low temperature while the lower wall is being provided with three extruding discrete heaters. The heaters are connected with adiabatic segments and the heater surfaces are assumed to operate at constant heat flux. At inlet, a uniform fluid flow with constant low temperature has been induced. In this study, air has been considered as working fluid. Results have been presented to show how various system parameters such as: Reynolds number, Grashof number, and channel inclination angle affect the resulting flow and thermal field inside the channel as well as the heat transfer performance of individual heater.It has been found that for the pure mixed convection case (Richardson number being equal to 1.0), the better cooling performance can be acheived with increasing the Reynold number forchannel inclination angle in range of 45°-90°.

INTRODUCTION

Advancement of technology has led to the increase of heat dissipation from electronic devices that increased interest in investigating the thermal performance of electronic packages. One of the main problem occurred while designing an electronic device is the prevention of the chips from overheating. Previously a numerical study has been carried out on mixed convection through a rectangular channel with multiple discrete heaters by Guimarães and Menon[4]. Results presented by the numerical investigation of Dogan et al. [2] showed that aspect ratiohas significant impact on temperature distribution. An interesting study by G. M.Rao[3] was reported on mixed convection that consider periodic boundary conditions on a channel with protruding heat generators attached to substrates forming a series of vertical parallel plate. Another similar study has been carried out by Bakkaset al.[6]in which periodic boundary conditions was applied on protruding heaters. In another numerical study Müftüoğlu and E. Bilgen[1] showed that that heaters give best thermal performance if they are placed closer to the bottom and closer to each other at the beginning of fluid flow. Investigation of B. Premachandran and C. Balaji [7] on conjugate convection with surface radiation from horizontal channels with protruding heat sources showed that non-dimensional temperature decreases non-linearly with increase of Reynolds number and decreases linearly with the increase of Grashof number which represents the negligible effect of buoyancy in their study. The study conducted by Nonino and Comini [8] on laminar forced convective heat transfer in ribbed square channels shows that a significant improvement of the average

Nusselt number could be obtained only for angled ribs in antiperiodic configurations and for high values of Reynolds numbers. From the literature review it is evident that most of the investigations were done on natural convection in horizontal channel with flat heaters. In the present study, numerical analysis has been carried out on mixed convection in a channel with extruding multiple heaters.

Nomenclature

B	Heat source length	Ri	Richardson number
D_T	Fluid thermal diffusivity	Fr	Fraud number
g	Gravity acceleration	T	Dimensional temperature
Gr	Grashof Number	T_o	Reference Temperature
H	Channel Height	γ	Inclination Angle
L	Channel length	Θ	Non-dimensional Temperature
M	Heater height	ν	Kinematic viscosity
Nu	Nusselt number	ρ_o	Fluid density
p	Dimensional pressure	ψ	Non-dimensional Streamfunction
P	Non-Dimensional pressure	x, y	Distance along x, y-coordinate (m)
q'	Heat flux	X,Y	Dimensionlessdistance along x, y-coordinate
Pr	Prandtl number	u, v	Velocity component at x, y-direction (ms-1)
Re	Reynolds number	U,V	Dimensionless velocity component at x, y-direction

PROBLEM DEFINITION

Numerical investigation of mixed convection have been carried out in an inclined rectangular channel having length L provided with three discrete heaters at the bottom, each having finite lenght B as shown in Fig. 1. Remaining lower surfaces of the channel and the vertical surfaces of the heaters are consideredadiabatic.Uniform constant velocity (U_o) and temperature profiles (T_o) have been assumed at the inlet.The upper wall of the channel is kept cold at temperature T_c. At outlet,a zero pressure boundary condition has been induced for velocity field while a convective boundary condition for temperature has been considered. Throughout this work, the geometry studiedas shown in Fig. 1 has $x_1 = 2H$, $x_2 = 4H$, $x_3 = 6H$, and $L = 9H$, $M = 0.25H$, where H is the channel height.

Dimensional Analysis and Boundary Conditions

For the present study, non-dimensional forms of Continuity, Navier-Stokes and Energy equation has been formulated. For a 2-D, steady, laminar, constant property fluid flow, adoption of Boussinesq approximation leads to the following non-dimensional governing equations:

$$\frac{\partial U}{\partial X}+\frac{\partial V}{\partial Y}=0; \tag{1}$$

$$U\frac{\partial U}{\partial X}+V\frac{\partial U}{\partial Y}=-\frac{\partial P}{\partial X}+\frac{1}{\mathrm{Re}}\left(\frac{\partial^2 U}{\partial X^2}+\frac{\partial^2 U}{\partial Y^2}\right)+Sin(\gamma)\frac{\theta}{Fr}; \tag{2}$$

$$U\frac{\partial V}{\partial X}+V\frac{\partial V}{\partial Y}=-\frac{\partial P}{\partial Y}+\frac{1}{\mathrm{Re}}\left(\frac{\partial^2 V}{\partial X^2}+\frac{\partial^2 V}{\partial Y^2}\right)+Cos(\gamma)\frac{\theta}{Fr}; \tag{3}$$

$$U\frac{\partial \theta}{\partial X}+V\frac{\partial \theta}{\partial Y}=\frac{1}{\mathrm{Re}\,\mathrm{Pr}}\left(\frac{\partial^2 \theta}{\partial X^2}+\frac{\partial^2 \theta}{\partial Y^2}\right); \tag{4}$$

Various non-dimensional parameters as mentioned in Eqs. (1)-(4) are defined as follows:

$$X=\frac{x}{B};Y=\frac{y}{B};U=\frac{u}{U_o};V=\frac{v}{U_o};P=\frac{p}{\rho_o U_o^2};\theta=(T-T_o)/\left(\frac{q'B}{D_T}\right);\mathrm{Re}=\frac{U_o\rho_o B}{\mu};Gr=\frac{\beta_T g\Delta T B^3}{\nu^2};$$

$$\mathrm{Pr}=\frac{\nu}{D_T};Fr=\frac{\mathrm{Re}^2}{Gr};Ri=\frac{Gr}{\mathrm{Re}^2}; \tag{5}$$

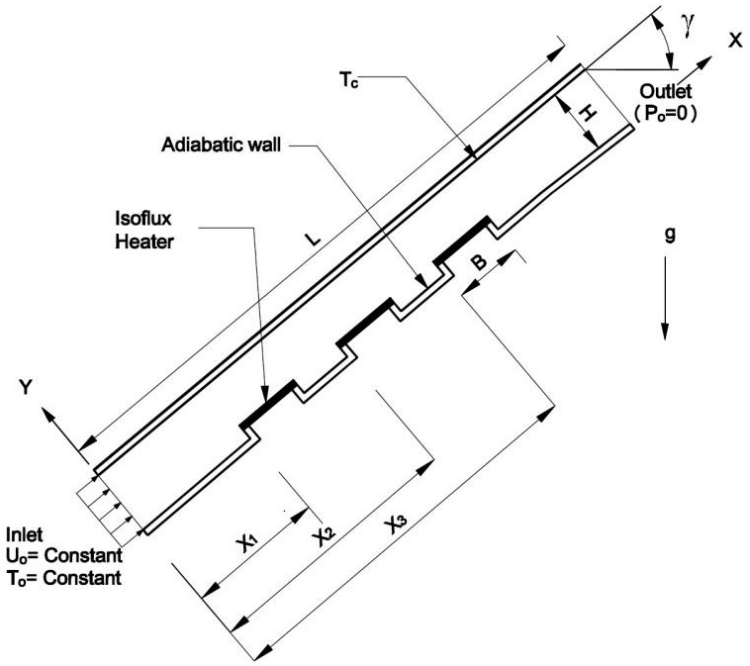

FIGURE 1. Channel Geometry and associated boundary conditions

Various boundary conditions used in this study are summarized in Table 1.

TABLE 1.Boundary conditions

Boundary	Boundary Conditions
Entrance	U=1;Θ=0
Upper wall of the channel	U=V=0;Θ=0
Lower surfaces of the channel	U=V=0;Adiabatic
Vertical walls of the heaters	U=V=0;Adiabatic
Heater module	U=V=0;$\frac{\partial \Theta}{\partial Y}=-1$
Outlet	No viscous stress(P_0=0);Convective flux

For the assessment of heat transfer performance of individual heater, the average Nusselt number (Nu_{avg})over each heater has been considered. For heater module of length '*S*', the average Nusselt number (Nu_{avg})has been defined as:

$$Nu_{avg}=\frac{1}{s}\int_s\frac{1}{\theta}ds \tag{6}$$

SOLUTION PROCEDURE AND VALIDATION

The sets of governing equations (Eqs.(1)-(4))along with the boundary conditions (Table 1) were solved using finite element method. The domain was divided into uniform grid and Galerkine formulation was applied to solve the governing equations.Grid independency test was carried out with different numbers of grids. From the test, it was evident that variation of Nusselt number was very negligible for number of mesh element greater than 6000. To validate the numerical models developed, we compared the heater module temperature distribution of firstheater of P.Guimaraes's[4] study with a flat heater in the model. As mentioned in Table 2, it is evident, that the corresponding values of temperature distribution are quite convincing.

TABLE 2. Comparison of temperature distribution along heater module-1

Dimensionless distance along heater module-1 (X)	Dimensionless temperature (Θ)					
	Re=1,***Gr***=10^5		***Re***=5,***Gr***=10^5		***Re***=10,***Gr***=10^5	
	Present study	P. Guimaraes [4]	Present study	P.Guimaraes [4]	Present study	P.Guimaraes [4]
5	0.076	0.081	0.065	0.068	0.068	0.070
5.6	0.283	0.290	0.226	0.230	0.208	0.210
5.8	0.205	0.210	0.276	0.280	0.229	0.230
5.9	0.164	0.165	0.260	0.261	0.244	0.245

RESULTS AND DISCUSSIONS

Study of the variation of temperature distribution,flow pattern as well as heat transfer characteristics of different heaters has been carried out in this study for a wide range of various system parameters such as Reynolds number($1 \leq Re \leq 100$), Grashof number($103 \leq Gr \leq 106$), Richardson number($0.1 \leq Ri \leq 10$), inclination angle($0° \leq \gamma \leq 90°$). Results obtained in the present study are systematically presented in the next:

Effects on Temperature Distribution

Both Figs. 2(a) and 2(b) show the effect of Reynolds number(*Re*) and Grashof number(*Gr*) on the isotherm distribution whereas Fig. 3 shows the effect of inclination angle(γ) on isotherm distribution under various system configurations. For*Re*=1 and *Gr*=10^3, as shown in Fig. 2(a), heat transfer by natural convectionis very negligible and is mostly due to fluid conduction. This can also be observed by the formation of thermal cells that are confined in regions over the source modules only.With the increase of the Grashof number, natural convection effect increases and for example at Gr=10^5, large plumes of natural convection flow appears over the heater modules which can be perceived from Fig. 2(b)(*Re*=1). One can note from Fig. 2(b) that the thermal plumes are roughly symmetrical about the centerline of the source module. Moreover with the increase of the value of *Re*, the plumes start to shift and stretch towards the direction of flow representing the increased effect of the forced convection.For lower values of *Re*,that is when low fluid velocities, the effect of inclination angle on temperature distribution is stronger as shown in Fig. 3.As depicted in Fig. 3, it is evident that increasing the inclination angle causes the stretching of the thermal plumes towards the outlet without the presence of any aiding flow.

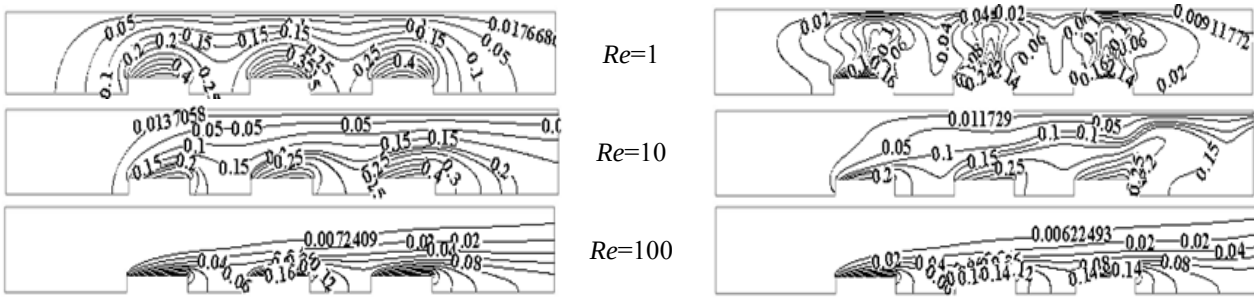

(a) *Gr*=10^3 (b) *Gr*=10^5

FIGURE 2. Variation of isotherm line with *Gr* and *Re* at $\gamma = 0^o$

Effects on Flow Pattern

Figures4(a) and 4(b) illustrate the variation of streamlines with the variation of Grashof number (*Gr*) and Reynolds number (*Re*) respectively. In Fig. 4(a) the distribution of streamlines, for *Gr*=$10^3$and *Re*=1, depicts that the heat transfer mainly occurs in conduction mode in these cases. As the value of *Gr* is increased, convection cells start to form (Fig. 4(a) for *Gr*=$10^4$and *Re*=1) and at higher values of *Gr*(*Gr*=10^5), more concentrated cells are formed indicating the stronger influence of natural convection. On the contrary, if the value of *Re* is increased these convection cells start to

shift and stretch toward the flow direction (Fig. 4(b)) and for higher values of *Re*(*Re*=100) the streamlines become flatten due to the dominance of forced convection flow.

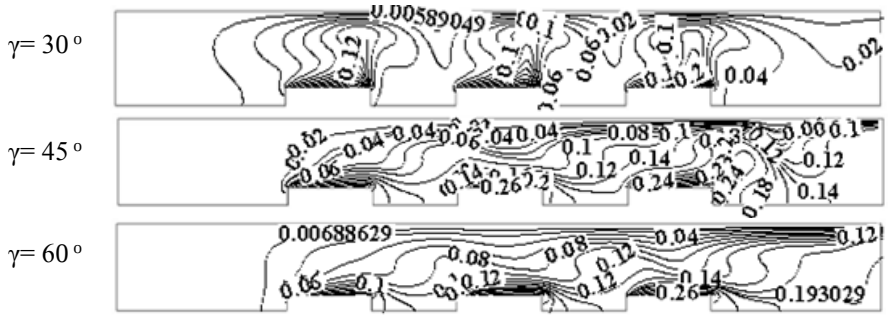

FIGURE 3. Variation of isotherm lines with inclination angle(γ) at Re=1 and Gr=10^5

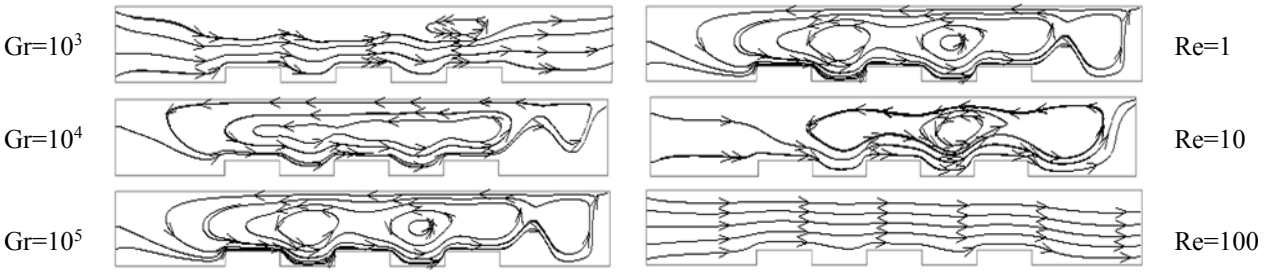

(a) Re=1(b)*Gr=10^5*

FIGURE 4. Variation of streamline with *Re* and *Gr* at γ= 45 °

Effectson Heat Transfer Characteristics

Heat transfer characteristics can be outlinedby evaluating the change ofaverage Nusselt number with the variation of various system parameters.Higher Nusselt number represents the superiority of convection heat transfer.

Effect of Inclination Angle

Figure 5 represents the effect of inclination angle on average Nusselt number at *Gr*=10^5.The results are in good harmony with those found by Guimarães and Menon[4]. From Fig. 5,it is evident that for heater-1 inclination angle has a little impact on the average Nusselt number.

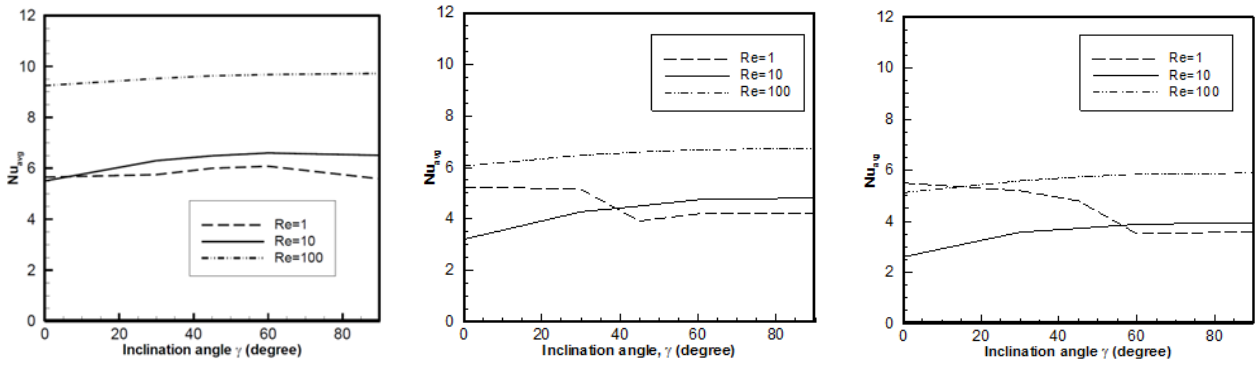

Heater-1 Heater-2 Heater-3

FIGURE 5.Variation of Nusselt number with the inclination angle(γ) at Gr=10^5

For both heater-1 and heater-2, average Nusselt number (Nuavg) increases with the inclination angle for Re=10,100 which characterises the presence of the forced convection. But for Re=1,this behavior is quite different,that is,average Nusselt number falls sharply after γ= 45°.This phenomena occurs becauseat lower Reynolds number, a back flow occurs due to the absence of forced flow that reduces heat transfer rate.

Effect of Reynolds Number

From Fig .6(a) it is evident that,for a fixed Grashof number (*Gr*), the effect of forced convection becomes more prominent when Reynolds number (*Re*) is greater than 100.Forced convection has a little impact on the heat transfer rate at lower values of *Re* as depicted in Fig. 6(a). On contrary, for *Ri*=1 that represents pure mixed convection case, average Nusselt number increases exponentially with the increase of *Re* as demonstrated in Fig. 6(b).This exponential increase of average Nusselt number gloss overs the dominance of pure mixed convection at *Ri*=1.

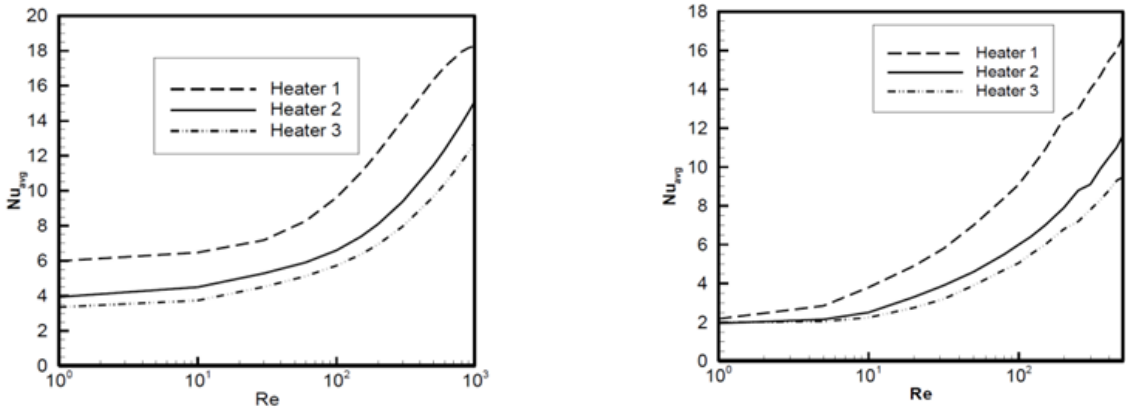

(a)Gr=10^5 (b)Ri=1

FIGURE 6.Variation of Nusselt number with Reynolds number at (a) Gr=10^5 and γ=45° (b) Ri=1 and γ=45°

Effect of Variation of Richardson Number

At higher values of Grashof number(*Gr*=10^5) increasing Richardson number(*Ri*) within the mixed convection region results in significant decreasein the average Nusselt number for all three heater modules as shown in Fig. 7(a). On the other hand at higher values of Reynolds number(*Re*=100) changing the values of *Ri*by changing the Grashof number (*Gr*) does not show any significant variation in the heat transfer rate from the heater module as shown in Fig. 7(b).

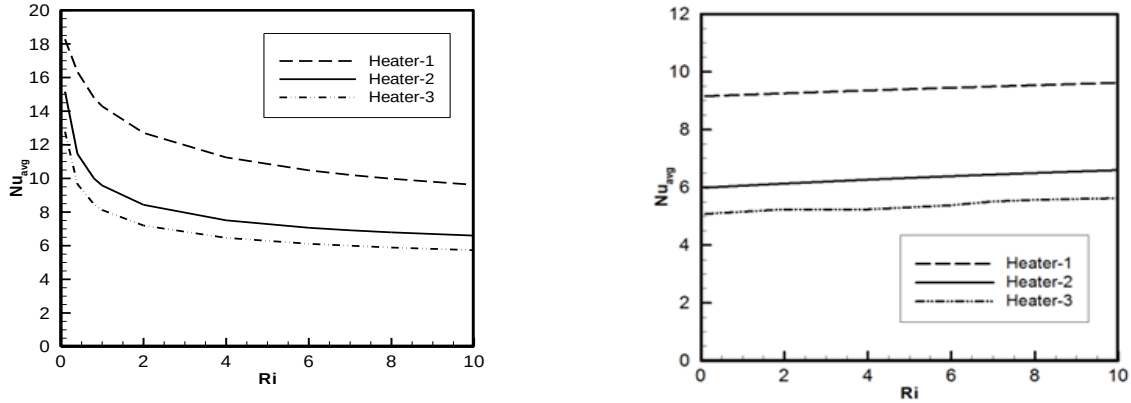

(a)Gr=10^5 (b)Re=100

FIGURE 7.Variation of average Nusselt number with Richardson number (a) Gr=10^5 and γ=45° (b) Re=100 and γ=45°

CONCLUSION

In the present study, analysis of mixed convection heat transfer phenomena in an inclined rectangular channel with multiple discrete heaters have been studied.Inthis work, effects of variation of Reynoldsnumber,Grashof number,Richardson number and channel inclination angle on the distribution of isothermlines andstreamlines as well the average Nusselt number over the heaters have been focused.It have been observed that effect of inclination angle(γ) becomes more prominentat low fluid velocities.Formation of thermal plumes are observed at higher values ofGrashof numbers- such as 105.These plumes start to stretch and shift towards the flow direction with the increase of the value of Reynolds number.In such cases heat sources are reached by hot wakes coming from the previous sources, which increases its temperature. This may cause troubles when cooling is concerned. For mixed convection case,inclination angle between 45°-90° gives the higher values of Nusselt number, therefore enhance heat transfer.Another interesting observation is that- in case of pure mixed convectionthat corresponds to 1 as the Richardson number, increasing the valus of Reynolds numberresults in the highest values of Nusselt number thus the best cooling performance.

REFERENCES

1. A. Müftüoğlu, E. Bilgen . International Journal of Thermal Sciences **47**, 369-377 (2007).
2. A. Dogan, M. Sivrioglu, and S. Baskaya., International Journal of Heat and Mass Transfer **49**, 2652-2662 (2006).
3. G. Madhusudhana Rao, G.S.V.L. Narasimham., Heat and Mass Transfer 50, 3561-3574 (2007).
4. Paul M. Guimarães and Genesio J. Menon, International Communications in Heat and Mass Transfer 35, 1267-1274 (2008).
5. Balachandar, S Yoon ,H S Lee SS Lee JR, Ha MY., Phys Fluids **16(4),** 1097-1117 (2006).
6. M. Bakkas, M. Hasnaoui, A. Amahmid, Energy Conversion and Management **49,** 2757-2766 (2008).
7. C. Balaji B. Premachandran, International Journal of Heat and Mass Transfer 49,8356–3582 (2006).
8. G. Comini C. Nonino, J. Heat Transfer 120,510–514 (1998).

ICME2015

International Conference on Mechanical Engineering 2015
(ICME 2015) 18 – 20 December, 2015, Dhaka, Bangladesh

Paper ID : 519

The Study of the Performance of A Solar Driven Adsorption Refrigeration Chiller Keeping Chilled Water Outlet Temperature Fixed

Fardousi Ara Begum[1,a)] and M.Z.I. Khan[2]

[1] *Department of Mathematics and Natural Sciences, BRAC University, Dhaka-1212, Bangladesh.*
[2]*Department of Mathematics, Bangladesh University of Engineering and Technology, Dhaka-1000, Bangladesh*

[a)]Corresponding author: fardousi08@gmail.com

Abstract. The study deals with the development of a two bed, single stage adsorption chiller driven by thermal heat collected from a solar collector panel. Variation of chilled water mass flow rate with respect to time is observed keeping average chilled water outlet temperature fixed during the daytime for the climatic condition of Dhaka, Bangladesh. Average Cooling Capacity (ACC) and Coefficient of Performance (COP) have also been numerically investigated with different number of collectors with same manner. It is also found that the system with 20 collectors (each of 2.415 m^2) along with 800s cycle time provides better performance.

INTRODUCTION

Energy consumption is increasing around the world. Cooling is one of the reasons of increasing energy demand. To meet the demand in cooling, mechanical vapor-compressor commonly used which can be classified as conventional systems [1]. These systems are very popular due to their high coefficients of performance, small sizes and low weights. They also exhibit some disadvantages such as contributing to global warming and ozone layer depletion and high energy consumptions. This research is focused on one of the sustainable ways to decrease energy demand for cooling which is the solar-powered adsorption cooling system. The advantage and development of adsorption cycle is widely studied by Meunier [2]. Another study was performed by Wang et al. [3]. Different sorption systems were compared thermodynamically by Pons et al. in 1999 in terms of COP using different working pairs [4]. A new design for two-stage adsorption cooling systems with two adsorbent beds was analyzed by Saha et al. [5]. A two-stage adsorption refrigeration chiller using re-heat to determine the influence of the overall thermal conductance of sorption elements and evaporator as well as the adsorbent mass on the chiller performance was investigated by Khan et al. [6]. A simple adsorption cooling cycle was also developed by Chang et al. [7] using a silica gel-water pair. Alam et al. [8] investigated the performance of two-bed conventional adsorption cooling cycle driven by solar heat where CPC solar panel is used under the climatic condition of Tokyo. Later on Alam et al. [9] added a tank to get benefit till late night under the climatic condition of Dhaka. The purpose of this study is to develop a single stage adsorption system which utilizes solar heat source to get a fixed average outlet temperature during the day time. Various numbers of collectors and cycle times have been studied to demonstrate the performance. Here it has also discussed about the variation of chilled water mass flow rate of fluid flow during the day time to get a fixed average outlet temperature.

Nomenclature

C_p	specific heat $(J/(kg \cdot K))$
U	heat transfer coefficient $(W/(m^2 \cdot K))$
q	adsorption capacity or concentration (kg refrigerant/ kg adsorbent)
q^*	concentration at equilibrium (kg refrigerant/ kg adsorbent)
I	solar radiation (W/m^2)
$\dot{m}$	mass flow rate (kg/s)
t	time (s)
T	temperature (K)
W	Weight (kg)
A	Area (m^2)

Subscripts

a/d	adsorber/desorber
s	silica gel
con	condenser
chill	chilled water
cr	collector
eva	evaporator
w	water
l	liquid

SYSTEM DESCRIPTION

The basic adsorption cycle consists of two adsorbent beds, one condenser and one evaporator. Silica gel-water pair has been chosen as adsorbent/ adsorbate. There are four thermodynamic steps in the cycle, namely, (i) Pre-cooling (ii) Adsorption/Evaporation (iii) Pre-heating and (iv) Desorption/ Condensation process. No heat recovery or mass recovery process is considered in the present study. The adsorber (B1/B2) are alternately connected to the solar collector to heat up the bed during pre-heating, desorption/ condensation process and to the cooling tower to cool down the bed during pre-cooling, adsorption/ evaporation process. The heat transfer fluid transport heat from the solar collector to the desorber and returns the collector to regain heat from the collector. The valve between adsorber and evaporator and the valve between desorber and condenser are closed during pre-cooling/ pre-heating period while, these are open during adsorption/ evaporation and desorption/ condensation process.

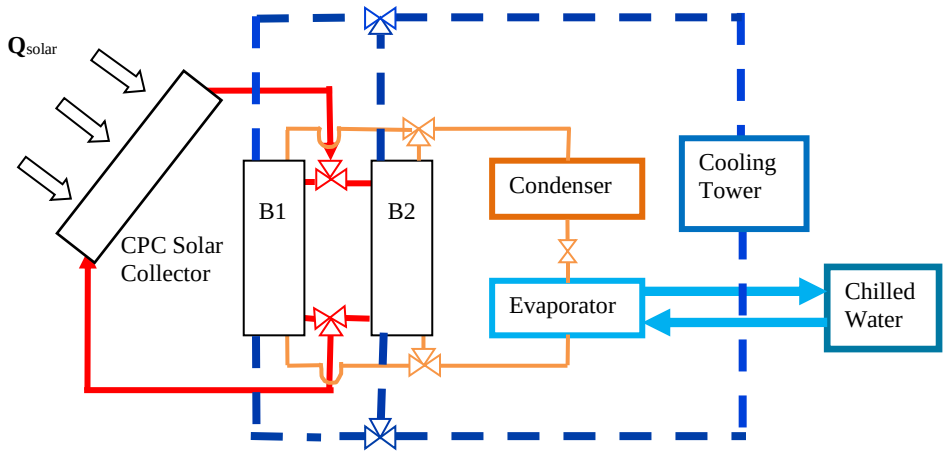

FIGURE1. Schematic of the solar driven adsorption cooling system.

The schematic of the adsorption cooling with solar collector panel is presented in Fig. 1. The operational process of two beds basic adsorption cooling unit can be found in the literature Saha et al. [10].

MATHEMATICAL MODELLING

The model here used is the same model which Alam et al. [8] discussed. More details will be found in that article. It is assumed that the temperature, pressure and concentration throughout the adsorbent bed are uniform.

The cyclic average cooling capacity (CACC) can be evaluated by the following expression:

$$\mathrm{CACC} = \frac{\int_{beginof\ cycletime}^{end\ of\ cycletime} \dot{m}_{chill} C_{chil,f} (T_{chill,in} - T_{chill,out}) dt}{Cycle\ time} \tag{1}$$

The cycle COP (Coefficient of performances) can be calculated by the following equation

$$\mathrm{COP}_{cycle} = \frac{\int_{beginof\ cycletime}^{end\ of\ cycletime} \dot{m}_{chill} C_{chil,f} (T_{chill,in} - T_{chill,out}) dt}{\int_{beginof\ cycletime}^{end\ of\ cycletime} \dot{m}_{f} C_{f} (T_{d,in} - T_{d,out}) dt} \tag{2}$$

Solar COP in a cycle (COP_{sc}) can be expressed as the following expression:

$$\mathrm{COP}_{sc} = \frac{\int_{beginof\ cycletime}^{end\ of\ cycletime} \dot{m}_{chill} C_{chil,f} (T_{chill,in} - T_{chill,out}) dt}{\int_{beginof\ cycletime}^{end\ of\ cycletime} n \cdot A_{cr} I dt} \tag{3}$$

Where, I is the solar irradiance, A_{cr} is each collector area and n is the number of collector.

For the present study the solar radiation data for the station of Dhaka, Bangladesh has been used. The monthly maximum and the minimum average temperature (°*C*) at Dhaka station is supported by the Bangladesh Meteorology Department (BMD) [9]. Implicit finite difference approximation method is applied to solve the set of differential equations. The tolerance for all the convergence criteria is 10^{-4}.

RESULT AND DISCUSSION

For the climatic condition of Dhaka, Bangladesh, 14 collectors each of area 2.415 m^2 with cycle time 800s is enough to raise sufficient bed temperature to run the silica gel-water adsorption cooling system. The temperature profile of 14 collectors for cycle time 800s and 1000s has been presented in Fig.2. Here 22, 20, 18 and 16 no of collectors have been considered to investigate the optimum system performance keeping average outlet temperature at 7°C. It has also seen that the lesser the cycle time lower the driving heat source temperature. It is also observed that the driving temperature may rise with less number of collectors along with higher cycle time; however, it may affect the system performance.

The cyclic average cooling capacity (CACC) with different cycle time and different number of collector has been shown in Fig. 3. CACC (cyclic average cooling capacity) for different number of collectors and cycle time 800s is illustrated at Fig. 4(a).

It is seen that cooling capacity is low at the beginning of the day and it increases until the maximum solar radiation obtained and after that it decreases again. According to the figure it is seen that increasing cycle time does not increase cyclic average cooling capacity. It is also observed that 20 collectors with 800s cycle time provide better cooling capacity.

The COP cycle, COP solar,cycle and COP solar,net for different number of collectors with cycle time 800s have been shown in Fig. 4.(b), (c) and (d) respectively. It is seen that the maximum value of COP cycle is 0.48 where the maximum value of COP solar,cycle and COP solar,net is 0.26 and 0.23 respectively.

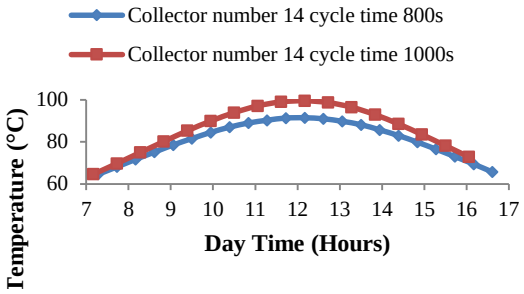

FIGURE 2. Temperature profile of different cycle time with collectors 14

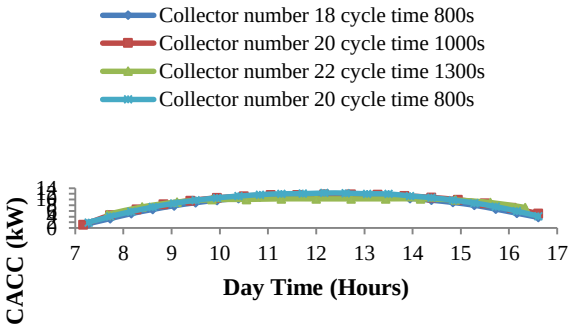

FIGURE 3. Cyclic average cooling capacity for different cycle time with different number of collectors

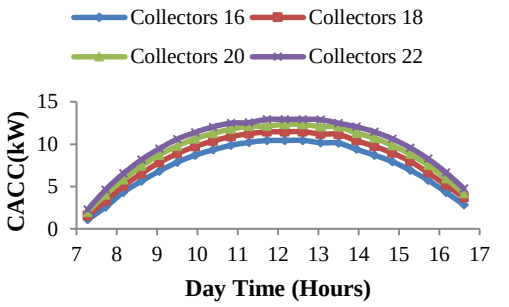

(a)

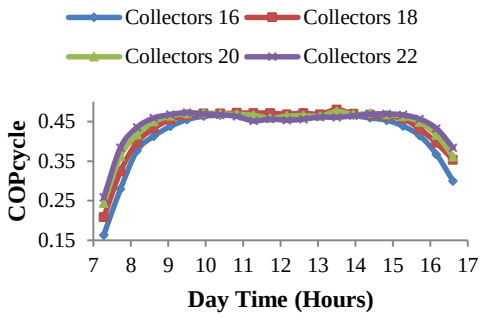

(b)

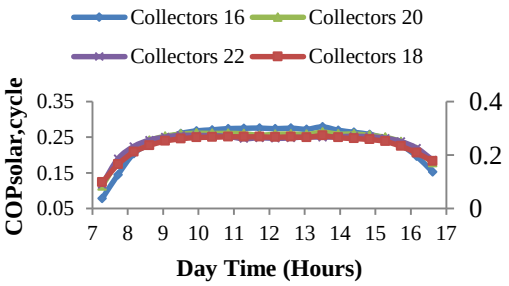

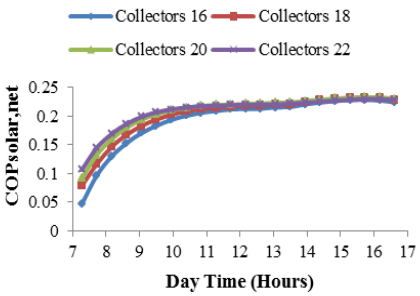

(c) (d)

FIGURE 4. Performance of the chiller for different number of collectors with cycle time 800s (a) CACC, (b) COPcycle, (c) COPsolar,cycle and (d) COP solar,net

The variation of chilled water flow rate is also observed here. It is seen that the maximum chilled water flow rate is 0.42(kg/s) which occurs at 12:00 noon. Chilled water flow rate is depicted at Fig 5.

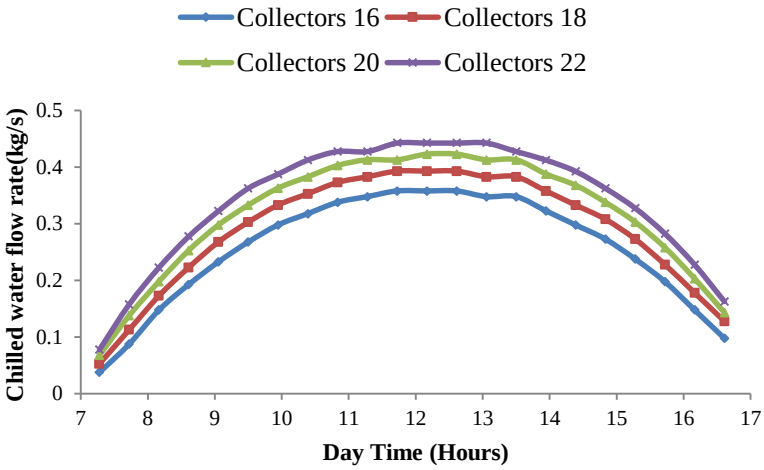

FIGURE 5. Chilled water flow rate for different number of collectors with cycle time 800s

CONCLUSIONS

The present study investigates the followings:

- It is observed that the driving heat source temperature can be raised to 91°C with 800s cycle time for 14 collectors (each 2.415m^2) for the base run conditions.
- Maximum cyclic average cooling capacity is found with 20 collectors and cycle time 800s which is around 12 kW held at 12:00 noon.
- The chilled water flow rate is an influential parameter for an adsorption cooling system run by solar collector and chilled water flow rate can be reduce as the solar radiation increases.
- Maximum value of COPcyle is 0.48 and it occurs during 9:00-15:00.
- Maximum value of COPsolar,cycle and COPsolar,net is 0.26 and 0.23 respectively.

REFERENCES

1. P. L. Dhar, and S. K. Singh, *Studies on Solid Desiccant Based Hybrid Air-Conditioning Systems* (Applied Thermal Engineering, vol. 21, no. 2, 2001), pp. 119-134.
2. F. Meunier, *Solid sorption heat powered cycles for cooling and heat pump applications*, (Applied Thermal Engineering, Vol. 18, 1998), pp. 714-29.
3. W. Wang, R. Z. Wang, Y. X. Xu, J. Y. Wu, and Y. B. Gui, *Investigation on Adsorption Refrigeration with a Single Adsorbent Bed* (International Journal of Energy Research, vol. 22, no. 13, 1998), pp. 1157-1163.
4. M. Pons, F. Meunier, G. Cacciola, R. E. Critoph, M. Groll, L. Puigjaner, B. Spinner, and F. Ziegler, *Thermodynamic Based Comparison of Sorption Systems for Cooling and Heat Pumping* (International Journal of Refrigeration, vol. 22, 1999), pp. 5-17.
5. B. B. Saha, A. Akisawa, and T. Kashiwagi, *Solar/Waste Heat Driven Two-Stage Adsorption Chiller: The Prototype*, (Renewable Energy, vol. 23, no. 1, 200)1, pp. 93-101.
6. M.Z.I. Khan, B.B. Saha, K.C.A. Alam, Y. Hamamoto, A. Akisawa, and T. Kashiwagi, *Parametric study of a two-stage adsorption chiller using re-heat— The effect of overall thermal conductance and adsorbent mass on system performance* (International Journal of Thermal Sciences Vol-45, 2006), pp 511–519.
7. W. S. Chang, C. C. Wang, and C. C. Shieh, *Experimental Study of a Solid Adsorption Cooling System Using Flat-Tube Heat Exchangers as Adsorption Bed*,(Applied Thermal Engineering, vol. 27, no. 13, 2007), pp. 2195-2199.
8. K. C. A. Alam, B. B. Saha and A. Akisawa, *Adsorption cooling driven by solar collector: a case study for Tokyo solar data* (Applied Thermal Engineering, Vol. 50, No. 2, 201), pp. 1603- 1609,.
9. K. C. A. Alam, R. A. Rouf, B. B. Saha, M. A. H. Khan, and F. Meunier, *Adsorption solar cooling- driven by heat storage collected from CPC panel* (Innovative Materials for Processes in Energy Systems IMPRES, 2013), pp. 397- 402.
10. B.B. Saha, E.C. Boelman, T. Kashiwagi, *Computer simulation of a silica gel-water adsorption refrigeration cycle-the influence of operating conditions on cooling output and COP* (ASHRAE Transactions 101 (2) (1995) pp. 348-357.

ICME2015

International Conference on Mechanical Engineering 2015
(ICME 2015) 18 – 20 December, 2015, Dhaka, Bangladesh

Paper ID : 540

A Concentrated Solar Cavity Absorber with Direct Heat Transfer through Recirculating Metallic Particles

M R I Sarker,[1,a)] Manabendra Saha[2, b)] and R A Beg[1]

[1]*Department of Mechanical Engineering, Rajshahi University of Engineering and Technology, Rajshahi-6204, Bangladesh*
[2]*Centre for Energy Technology, School of Mechanical Engineering, The University of Adelaide, Adelaide, SA 5005, Australia*

[a)]Corresponding author*:* islamrabiul@yahoo.com
[b)]manabendra.saha@adelaide.edu.au

Abstract.A recirculating flow solar particle cavity absorber (receiver) is modeled to investigate the flow behavior and heat transfer characteristics of a novel developing concept. It features a continuous recirculating flow of non-reacting metallic particles (black silicon carbide) with air which are used as a thermal enhancement medium. The aim of the present study is to numerically investigate the thermal behavior and flow characteristics of the proposed concept. The proposed solar particle receiver is modeled using two phase discrete particle model (DPM), RNG k- flow model and discrete ordinate (DO) radiation model. Numerical analysis is carried out considering a solar receiver with only air and the mixture of non-reacting particles and air as a heat transfer as well as heat carrying medium. The parametric investigation is conducted considering the incident solar flux on the receiver aperture and changing air flow rate and recirculation rate inside the receiver. A stand-alone feature of the recirculating flow solar particle receiver concept is that the particles are directly exposed to concentrated solar radiation monotonously through recirculating flow inside the receiver and results in efficient irradiation absorption and convective heat transfer to air that help to achieve high temperature air and consequently increase in thermal efficiency. This paper presents, results from the developed concept and highlights its flow behavior and potential to enhance the heat transfer from metallic particles to air by maximizing heat carrying capacity of the heat transfer medium. The imposed milestones for the present system will be helpful to understand the radiation absorption mechanism of the particles in a recirculating flow based receiver, the thermal transport between the particles, the air and the cavity, and the fluid dynamics of the air and particle in the cavity.

INTRODUCTION

Concentrated Solar Power (CSP) systems have the potential to replace the combustion of fossil fuels, and provide a sustainable energy conversion system as solar radiation reaching on the earth's surface is a fairly dispersed, renewable and clean energy source. A typical CSP plant consists of three basic subsystems: solar collector field, solar receiver and a power conversion system. The solar receiver absorbs the concentrated solar radiation by the collectors and then transfers it to the heat transfer fluid (HTF) which is used to feed high temperature heat to a power conversion unit. The current study focuses on the investigation of the performance improvement of the solar receiver. A cavity type solar receiver is investigated in the present study using the internally recirculating metallic solid particles and air as a heat transfer medium to achieve high temperature gas for a Brayton cycle. The solid particle solar receiver concept uses the concentrated solar flux reflected from a field of heliostats into a cavity type absorber where solid particles absorb concentrated direct solar irradiation as well as the

inner cavity wall. It has been demonstrated that the uses of solid metallic particles as a working medium in a high temperature solar particle receiver/reactor provides the efficient absorption of concentrated solar irradiation [1].

The application of metallic particles was initially suggested by Martin et al. [1] in the concept of freely falling particle in an open cavity type solar receiver in which metallic particle enhances the solar irradiation absorption as an effective heat carrying medium. In the sun test experimental demonstration of 2.5 MW freely falling solar particle receiver [2] suggested that the recirculation of the particles can increase the particle temperature in excess of 9000C rather than 2500C in a single pass curtain. It has been noticed that the residence time of the particles into a given solar incident irradiation [3] and the use of recirculation of the heat transfer medium [4, 5] are the two means of increasing particle temperature. The longer exposure time of the solid particles into the solar flux enables the increase of solar energy absorption and hence enhances the convection and radiation heat transfer from the particles to the air. The recirculation characteristics of this concept will lead to an increase in the particles' residence time as well as gas in the solar irradiation and hence result in an improvement of the thermal performance of the solar receiver. Therefore, an increase in the outlet temperature of air is expected using the current developed concept compared with the conventional external type receiver concept. For the receiver or reactor to be operated with particle clouds [6, 7] requires the supplementary excess air to convey and maintain a desired particle concentration into air. This excess gas requires more supplementary solar process heat which results in unacceptable low receiver efficiency of the solar receiver [8, 9]. In the proposed solar receiver, particles' flow with air is controlled by such a system that helps to avoid the supplementary gas supply and a higher thermal efficiency as well as high temperature gas is expected.

The objective of this study is to analyze the impact of continuously recirculating particles in an enclosed cavity type solar receiver on temperature distribution inside the receiver, air outlet temperature and receiver thermal efficiency. Here an explanation of the developed concept and a theoretical steady state three dimensional simulation of the proposed receiver are presented. To predict the temperature of the air and thermal efficiency of the solar receiver, two phase flow of air and particles, radiation transport among the recirculating particle cloud and cavity wall, convection heat transfer between the particles and air and the cavity wall surface are taken into consideration during this investigation. The impact of the mass flow rate of air, particles mass fraction and recirculation rate on thermal performance is investigated to ensure the effect of internally recirculating particles in the solar receiver.

CONCEPT AND MODEL DEVELOPMENT

The proposed solar receiver in this study has two key features, i.e., a recirculating flow field within the receiver and non-reacting metallic particles mixes with the flow. The configuration of the receiver is presented in Figure 3.6. The solar receiver consists of an externally insulated cylindrical cavity with a quartz window aperture at the top, a duct fan combination system to generate the forced recirculation, an inlet for cold gas and an outlet for heated gas. In this solar receiver, metallic particles are initially stored at the bottom of the cylindrical cavity of the solar receiver and then recirculated by a specially designed duct fan combination system. Air is continuously injected into the receiver and recirculated several times before being exhausted from the outlet at a high temperature. Together with the air flow, the metallic particles move upwards from the bottom of the receiver towards the quartz window and then return to the bottom of the receiver as a result of the suction effect of the fan. As shown in Figure 1, the upwards-moving metallic particles absorb solar irradiation directly which results in an increase in particle temperature. When the particles move back to the bottom of the receiver, absorbed solar energy is transferred to the surrounding air flow to form a high temperature mixture of air and particles. This high temperature two-phase mixture is then transported to the bottom of the receiver, where again energy is transferred from the mixture to the injected colder air and particles in the lower part of the receiver. By having such a mechanism within the receiver, irradiation loss is minimized and heat transfer performance is improved, which results in a higher temperature at the outlet.

In order to understand the thermal field of a cavity type solar receiver, a 3D computational fluid dynamics (CFD) model was developed. The commercial CFD package ANSYS Fluent 14.5 was used in this study. The basic geometry, with dimensions and adapted mesh, used in the model is shown in Figure 1. Inlet air was at ambient temperature, pressure was atmospheric at inlet and outlet. Cavity was assumed insulating receiver. The geometry was meshed using a uniform hexahedral mesh grid. The grid sensitivity study showed that 180,000 cells were sufficient to ensure grid independent results. In this analysis, the air and micron size Bauxite (Al_2O_3) metallic particles were used as the HTM for developing a two phase flow model. A uniform particle size of 500 μm diameter

was assumed. Particle size was assumed based on comparative calculation of the terminal velocity and fluidization velocity of the particle and assumed superficial velocity to fly that size particles.

In this study, the flow field was modelled using a steady state RNG $k-\varepsilon$ turbulence model with the standard wall function and used viscous heating with a wall thermal effect. The calculated Reynolds number was above 12,000 based on the mass flow rate of air at the inlet and air flow was assumed to be turbulent in the receiver. Use of the standard wall function provides a commonly used approximation for the near wall velocity for turbulent flow. The effect of buoyancy was also included in the model. The pressures at the inlet and outlet boundaries were assumed to be atmospheric. The turbulence kinetic energy and dissipation rate were calculated using the inlet flow condition. The ducted fan effect was modelled with a momentum disk situated at the bottom of the duct. A discrete phase model (DPM) was used to track trajectories of the non-reacting Al_2O_3 particles in a Lagrangian frame. Stokes' Law was applied for calculation of the drag force. The gravity effect was added to the fluid flow Equation. The particle to particle interaction was assumed to be negligible which is valid for the volume of particles at approximately less than 10%. Two-way turbulence coupling was used for the particles' discrete phase analysis. The initial temperature of particles was assumed to be equal to the ambient temperature. The convection and radiation model (Discrete Ordinate) was coupled with the air flow and particle model. In the Discrete Ordinate (DO) radiation model used for calculating the radiation field inside the receiver, the Irradiative Heat Transfer Equation was solved for a finite element. The magnitude of the solar irradiation flux (W/m^2) was introduced to the cavity through the aperture and calculated using the estimated power input per unit area of the aperture. It was assumed that the wavelength of the solar beam was in the range of (0 - 4.5 μm). A temperature dependent fluid density was assumed in this model considering ideal gas behavior. This temperature was used as an ambient blackbody boundary temperature to calculate re-radiation from the internal walls of the cavity to the aperture. The temperature of the thermally insulated outer receiver boundary was assumed to be 300K.

THERMAL PERFORMANCE OF SOLAR RECEIVER

To investigate the effect of the forced recirculation of solid particles as a heat transfer enhancement medium, three basic cases were studied and compared, namely: (i) only air is utilized as the heat transfer medium without forced recirculation, (ii) only air is utilized as the heat transfer medium with forced recirculation, and (iii) air and particles are employed as the heat transfer medium with forced recirculation. The mass flow rate of the injected air and all other working parameters were kept constant for the studied cases. The investigation was carried out considering the mass flow rate of air 0.00356 kg/s, recirculation rate of air 0.22 kg/s and 10% particle by mass fraction.The temperature contours within the solar receiver for different working conditions are presented in Figure 2.

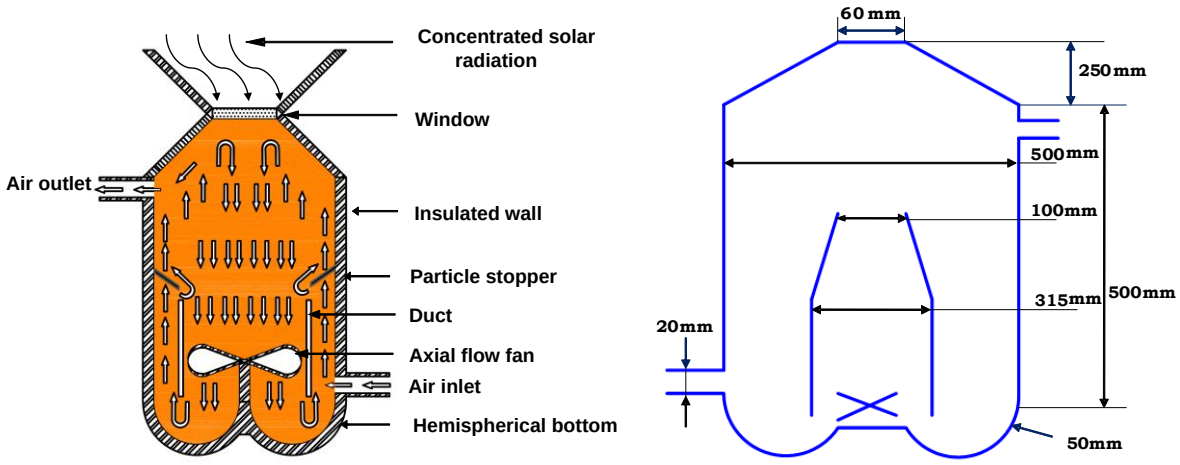

FIGURE 1. Schematic of a cavity type solar receiver model.

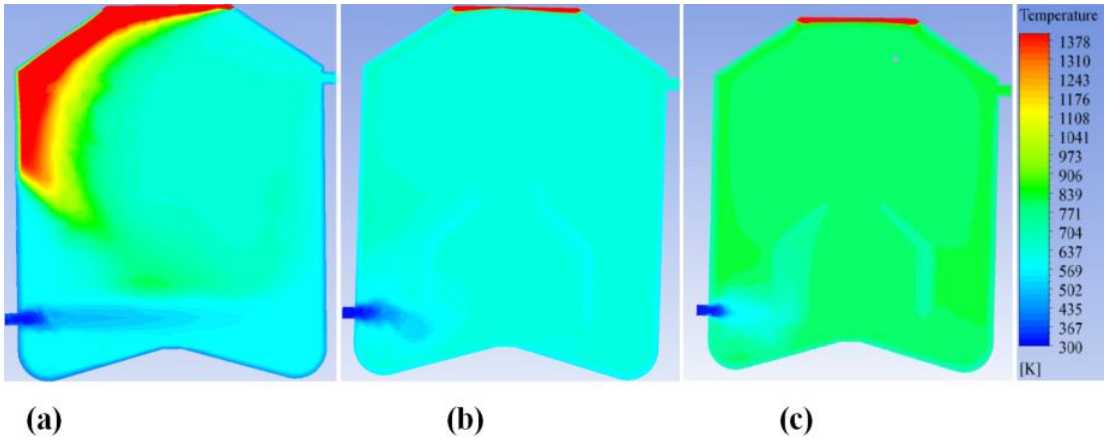

FIGURE 2. Temperature contour within the solar receiver under with (a) only air flow (b) recirculating air flow (c) recirculating air flow with metallic particles.

Figure 2(a) presents the temperature distribution within the receiver without the effect of the fan. In this configuration, a non-uniform fluid temperature distribution was observed as the cavity wall absorbs the solar radiation, and transfers the energy to the fluid via natural convection. A very high temperature region near the aperture was observed due to the lack of cooling effect by slow moving air on the aperture. The overheating of the aperture results in radiation losses and very high thermal stresses on the glass window. It was seen from Figures 2(b) and 2(c) that a more uniform temperature distribution inside the receiver was found as the result of recirculation and the forced convection effect of the flow. The average outlet temperatures of the receiver under different configurations (a, b and c) are 580K, 620K, and 830K, respectively which showed that the solar receiver with the recirculating air flow and metallic particles had the best working performance.

The average exit temperature of the solar receiver with and without metallic particles for the different mass flow rate of 0.00356 kg / s to 0.00872 kg / s, was presented in Figure 3. As shown in the Figure 3(a), the outlet air temperature was reduced with the increase of the air flow rate and the effect of adding metallic particles was indicated by the higher outlet temperature of the receiver with constant heat flux and a specific amount of particles inside.

For a better comparison of the thermal performance of the solar receiver with and without recirculating particles, the temperature and thermal efficiency ratio was calculated and shown in Figure 3(b). These two ratios were between the respective parameters with air only and with air and 10% particle case. For both cases the air was recirculated by a ducted fan to enhance the mixing and convection heat transfer effect. It was noticed that both the temperature and thermal efficiency ratios increased (see Figure 3(b)) with the increase of mass flow rate of the injected air.

Figure 3(b) showed that the outlet air temperature was increased by a factor of 1.28 at an air flow rate of 0.00356kg/s whereas it was increased by a factor of 1.33 at an air flow rate of 0.00872kg/s. The thermal efficiency was increased by a factor of 1.38 at a mass flow rate of 0.00356 where as it was increased by a factor of 1.68 at a mass flow rate of 0.00872 (see Figure 3(b)). It reflects that at higher mass flow rate of air, thermal efficiency was increased more than the increase of outlet air temperature in the case of addition of particles in a recirculating flow case.

The recirculating rate of the internal flow was identified as the mass flow rate of the air flow through the duct which was controlled by varying the fan speed. The impact of the recirculation rate on the working fluid temperature was shown in Figure 4. As seen from the Figure, the outlet temperature is about 580K at a mass flow rate of 0.00356 kg/sec without introducing recirculation (see Figure 2(a) for temperature contours). It is seen from Figure 4(a) that an increase in the recirculation rate results in an increase in the outlet temperature until the recirculation rate exceeds 0.40 kg/sec. For the values higher than 0.40 kg/sec the outlet air temperature of the receiver drops slightly. The effect of the recirculation rate on the thermal efficiency of the receiver is presented in Figure 4(b). As shown in the Figure 4(b), a similar tendency of the receiver thermal efficiency with the recirculation rate was observed.

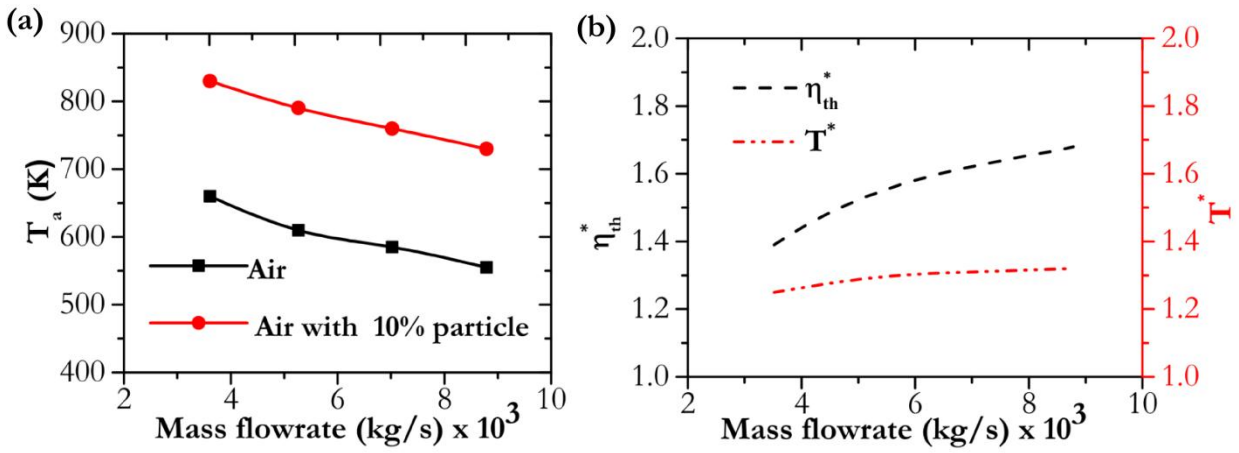

FIGURE 3. Variation of (a) outlet air temperature (b) thermal efficiency ratio (η_{th}^{*}) and temperature ration (T^{*}) with the mass flow rate of air in the solar receiver.

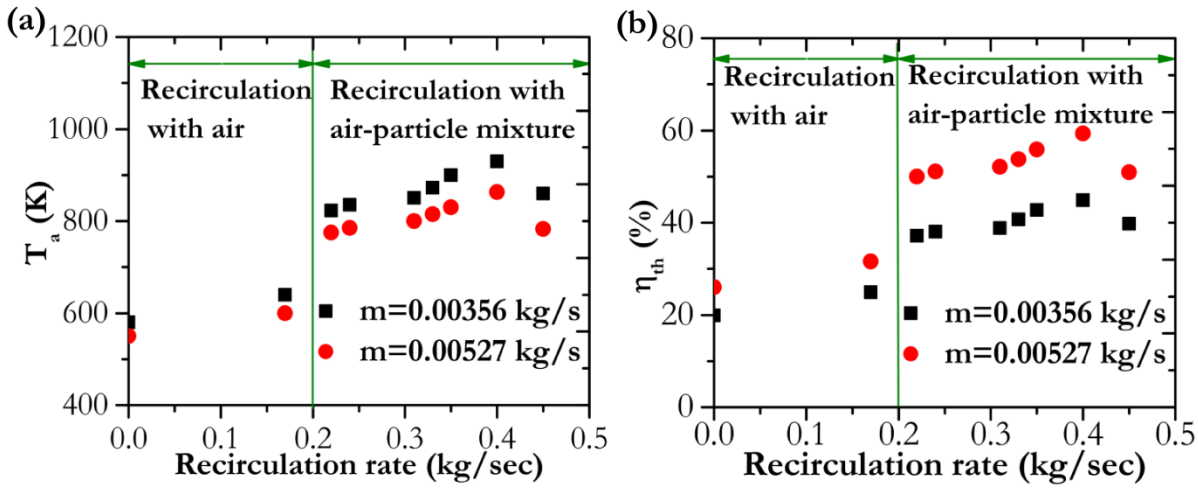

FIGURE 4. Variation of (a) the outlet air temperature (b) thermal efficiency as a function of the recirculation rate.

The temperature of outlet air is increased by 350K compared with the non-recirculation case, whereas the receiver thermal efficiency was increased by 35% which is double compared with the non-recirculation case. The reason behind the increase of the outlet air temperature and receiver thermal efficiency at higher recirculation rates was the recirculation of more particles which in turn absorb more direct irradiation heat flux near the aperture. In addition, higher recirculation rate was increased the energy transfer rate as a result of a more prominent forced convection heat transfer rate. Owing to the increase of the flow velocity and time required for solar energy absorption above the 0.40 kg/sec recirculation rate, the solid particles might not be absorb the maximum solar energy before they return to the bottom of the receiver. This reduction of the energy absorption near the aperture was leaded to the slight decrease in the outlet temperature behind the recirculation rate 0.40 kg/sec. The same tendency of the outlet temperature variation was observed for a mass flow rate of 0.00527 kg/sec.

CONCLUSIONS

A novel concept of recirculating metallic particles' solar receiver was developed to improve the working performance of current solar receivers. Comparative analysis is made to investigate thermal performance of the recirculating flow solid particle solar receiver. The recirculating flow pattern provided a more uniform temperature distribution within the receiver, which reduced the overheating problem of the quartz window on the aperture. The outlet air temperature was decreased and thermal efficiency was increased with the increasing injected mass flow rate of air into the receiver. The outlet air temperature was increased for increasing the particle mass fraction and achieved 250K higher by adding 10% metallic particle at the air flow rate of 0.00356 kg/sec. The outlet air temperature achieves 350K higher at a recirculation rate of 0.40 kg/s, using the air flow rate of 0.00356 kg/sec and 10% particle mixture. Under the same conditions, the thermal efficiency was increased by a factor of 2 compared with a non-recirculation system. However further investigation was required to better optimize the different parameters that the premise of this concept has been found to be highly feasible. An experimental apparatus was under construction to validate these results to optimize the operating parameters better and resolve technical challenges for improved integration of this system into real-life situations.

REFERENCES

1. J. Martin and V. J. Jr., Sandia National Laboratories SAND-82-8203; 1982.
2. N. P. Siegel, C. K. Ho, S. S. Khalsa, and G. J. Kolb, *Journal of Solar Energy Engineering* **132**, 021008 (2010).
3. J. Hruby, Sandia National Labs., Livermore, CA (USA)1986.
4. S. S. S. Khalsa, J. M. Christian, G. J. Kolb, M. Röger, L. Amsbeck, C. K. Ho, N. P. Siegel, and A. C. Moya, "CFD simulation and performance analysis of alternative designs for high-temperature solid particle receivers," in *ASME 2011 5th International Conference on Energy Sustainability*, 2011, pp. 687-693.
5. M. RÃķger, L. Amsbeck, B. Gobereit, and R. Buck,*Journal of Solar Energy Engineering* **133**, 031009 (2011).
6. A. Hunt and C. Brown, "Solar test results of an advanced direct absorption high temperature gas receiver (SPHER)," in *Proceedings of the Solar World Congress*, 1983, pp. 959-63.
7. A. Steinfeld, M. Brack, A. Meier, A. Weidenkaff, and D. Wuillemin, *Energy* **23**, 803-814 (1998).
8. A. Meier, *Chemical Engineering Science***54**, 2899-2905(1999).

9. S. Granz .J, Th., Sturzenegger M., "A new design for volumetric gas/particle reactors for the solar thermal reduction of metal oxides," Annual report 1997.

ICME2015

International Conference on Mechanical Engineering 2015
(ICME 2015) 18 – 20 December, 2015, Dhaka, Bangladesh

Paper ID : 541

Vibration Energy Harvesting in a Small Channel Fluid Flow Using Piezoelectric Transducer

Md. Mehedi Hassan[1], Md. Yeam Hossain[1], Rakib Mazumder[1], Roussel Rahman[1] and Md. Ashiqur Rahman [1, a)]

[1]*Department of Mechanical Engineering, Bangladesh University of Engineering and Technology (BUET), Dhaka-1000.*

[a)]Corresponding author: ashiqurrahman@me.buet.ac.bd

Abstract. This work is aimed at developing a way to harvest energy from a fluid stream with the application of piezoelectric transducers in a small channel. In this COMSOL Multiphysics based simulation study, it is attempted to harvest energy from the abundant renewable source of energy available in the form of kinetic energy of naturally occurring flow of fluids. The strategy involves harnessing energy from a fluid-actuator through generation of couples, eddies and vortices, resulting from the stagnation and separation of flow around a semi-circular bluff-body attached to a cantilever beam containing a piezoceramic layer. Fluctuation of fluidic pressure impulse on the beam due to vortex shedding and varying lift forces causes the flexible cantilever beam to oscillate in the direction normal to the fluid flow in a periodic manner. The periodic application and release of a mechanical strain upon the beam effected a generation of electric potential within the piezoelectric layer, thus enabling extraction of electrical energy from the kinetic energy of the fluid. The piezoelectric material properties and transducer design are kept unchanged throughout the study, whereas the configuration is tested with different fluids and varying flow characteristics. The size and geometry of the obstructing entity are systematically varied to closely inspect the output from different iterations and for finding the optimum design parameters. The intermittent changes in the generated forces and subsequent variation in the strain on the beam are also monitored to find definitive relationship with the electrical energy output.

INTRODUCTION

With the recent growth in the development of low power electronic devices the topic of energy harvesting has received much attention in the past decade [1-11]. Energy harvesting solutions have the ability to provide permanent power sources that do not require periodic replacement. Such systems can operate in an autonomous, self-powered manner, reducing the costs associated with battery replacement, and can easily be placed in remote locations or embedded into host structures [3, 7]. Conventional low-power electronics, such as wireless sensor nodes as well as batteries presents several drawbacks [1]. Though piezoelectric energy harvesting has been thoroughly investigated since the late 1990s, it still remains an emerging technology and critical area of interest. Energy harvesting application fields so far mainly focused on low power devices due to their limited transduction efficiencies. To date, researchers are following distinct ways in developing piezoelectric energy harvesting technology. New materials, configuration approaches and operating modes are under study, and some of these valuable solutions were proposed in order to achieve large bandwidth harvesters that are able to scavenge energy from diverse environments. Research efforts are being focused on the transducer and also on the integration with the downstream conditioning circuitry, power management circuits and application devices [7].

An abundant source of energy is the kinetic energy of naturally occurring flow of fluids, e.g., air flow and water streams. This renewable source of energy is targeted in this work to harvest energy from and the simulation based study was modeled and performed in COMSOL Multiphysics. Our study is based on developing energy from fluid stream with the application of piezoelectric transducers in a micro channel.

FORMULATION OF THE PROBLEM STATEMENT

This study is aimed at developing a way to harvest energy from a fluid stream with the application of piezoelectric transducers in a micro channel. The strategy involved harvesting the energy from a micro fluid-actuator through generation of couples, eddies and vortex shedding following from creation of stagnation points and separation of flow around a semi-circular bluff-body attached with a cantilever beam containing a piezo-ceramic layer. An obstruction of non-aerodynamic shape in the path of a fluid stream resulted in separation of flow and creation of vortices. The cantilever beam protruding from the inverse D- configured obstruction was subjected to the generated lift force; subsequently, deflecting the beam to a significant amount. Fluctuation of fluidic pressure impulse on the beam due to vortex shedding and varying lift forces caused the flexible cantilever beam to oscillate in the direction normal to the fluid flow in a periodic manner. The periodic application and release of a mechanical strain upon the beam effected a generation of electric potential within the piezoelectric layer, thus enabling extraction of electrical energy from the kinetic energy of the fluid. The piezoelectric material properties and transducer design were kept unchanged throughout the study, whereas the setup was tested with different fluids and the size and geometry of the obstructing entity was manipulated with to observe the variation in output from different iterations.

When two or more physical systems interact with each other and the solution of one system is dependent on the solution of another system they are called coupled systems. An example of coupled system is that the fluid structure interaction where none of the system can be solved independently because there are unknown forces to be solved for both the system simultaneously. The forces acted on the structure by the flowing fluid cause deformation in the structure and thus the deformed structure causes a change in the flow pattern of the fluid. In this numerical computation problem, our aim is to generate power or voltage from the deformed structure by using pzt material as solid structure [5]. This is a multi-physics problem where we used COMSOL Multiphysics to simulate result. From COMSOL, we used the Fluid Structure Interaction (fsi) and electromagnetic modeling to model the problem. The fsi can be classified as strongly or weakly coupled problem. Ours is a weakly coupled problem, because in strongly coupled problem, deformation is negligible that it doesn't affect so much the flow pattern. To produce voltage or power the solid structure must be deformed enough. So strongly coupled problem is advisable. For applications with multiphysics problems, we used ALE method that can combine dynamics of both the fluid flow and the structure. This is a combination of classical two description of motion the Lagrangian motion and the Eulerian motion (Fig. 1) [2, 6].

GOVERNING EQUATIONS

The following sections will state and briefly explain the governing equations of the fluid flow, the structure and the coupling between them. The problems under consideration consist of a fluid that is occupying a given domain ΩF and a structure that occupies another domain Ω^s which interact at the common boundary Γ [2].

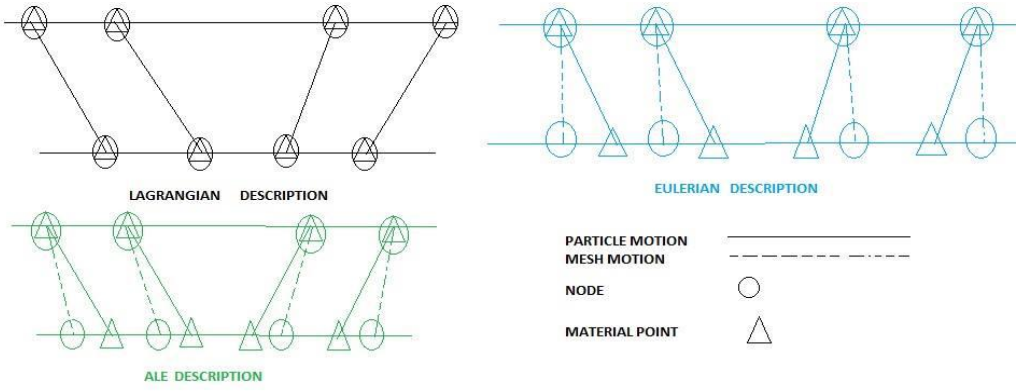

FIGURE 1. Lagrangian and the Eulerian motions

Piezoelectric Sensor Geometry

Strain to Voltage Equations

D(3*1) =dd(3*6) Ó(6*1)

D = Electric displacement
d = Direct piezoelectric co-efficient matrix
Ó = Stress vector

Bimorphs are preferable for pzt sensor design because when force is applied to long pzt beam one side is in tension and other side is in compression. No electrical output can be obtained from this homogeneous beam by bending [4].

Structural equation

The possibly large displacement of the structure is governed by:

$$\rho^s \frac{D^2 y}{Dt^2} \; -\nabla.\left(F.S(u)\right) = \rho^s b^s \quad \text{in } \Omega^s \times (0,T) \tag{1}$$

Where u represents the displacements of the structure, $\boldsymbol{b}^s$ the body forces applied on the structure. S the second Piola-Kirchhoff stress tensor, ρ^s the density of the structure and F represents the deformation gradient tensor [2].

Fluid flow equations

The fluid equations to be solved are the incompressible Navier-Stokes equations expressed in ALE formulation. The Navier-Stokes equations can be derived from the conservation laws for mass and linear momentum and takes in consideration that the fluid is viscous. The equations in ALE formulation take the form:

$$\rho^F \frac{dv}{dt}|_\chi + \rho^F.c.\nabla v - 2\mu\nabla.\varepsilon(v) + \nabla\bar{p} = \rho^F b^F \;\; in\; \Omega^F \times (0,T) \tag{2}$$

$$\nabla.v = 0 in\; \Omega^F \times (0,T) \tag{3}$$

Here v denotes the fluid velocity and p denotes the physical pressure. The fluid density and viscosity is given by respectively μ. The fluid body forces are represented by and $\boldsymbol{\varepsilon}$ ($\boldsymbol{v}$) represents the strain rate tensor. As can be seen in Eqn. (2), the ALE formulation comes in to the equation in the fluid acceleration term and the convective term.

Coupling equations

At the interface Γ, kinematic and dynamic continuity is required. The governing Kinematic coupling equations are:

$$u_\Gamma(t) = d_\Gamma^F(\mathrm{t}) \qquad \dot{u_\Gamma}(t) = v_\Gamma(\mathrm{t}) \qquad \ddot{u_\Gamma}\,(\mathrm{t}) = \dot{v_\Gamma}(t) \tag{4}$$

Here dF「(t) represents the displacement of the fluid mesh nodes at the interface. The dynamic coupling equation takes the form:

$$h^s(t) + h^F(t) = 0 \tag{5}$$

Where $h=\sigma.n$ signifies the traction vector.

PIEZOELECTRIC BEAM MODELING

Piezoelectric materials can be used as transducers which are able to interchange electrical energy and mechanical strain or force. These materials can be used to transfer ambient motion (usually vibration) into electrical energy that

can be stored and used to power other devices. By implementing power harvesting devices, portable systems can be developed that do not depend on traditional methods for providing power, such as the battery, which has a short operating life span [5]. It has been found that a piezoelectric device attached to a beam with cantilever boundary conditions provides an effective method of capturing transverse vibrations and converting them into useful electrical power. Piezoelectric materials become electrically polarized when strained. From a microscopic perspective, the displacement of atoms within the unit cell (when the solid is deformed) results into electric dipoles within the medium. In certain crystal structures, this combines to give an average macroscopic dipole moment or electric polarization. This effect, known as the direct piezoelectric effect, is always accompanied by the converse piezoelectric effect, in which the solid becomes strained when placed in an electric field.

Within a piezoelectric, there is a coupling between the strain and the electric field, which is determined by the constitutive relation:

$$S=s_E\, T + d^T E \quad (6)$$

$$D= dT + \varepsilon_T E \quad (7)$$

Here, S is the strain, T is the stress, E is the electric field, and D is the electric displacement field. The material parameters $s_{E,}$ d, and ε_T correspond to the material compliance, coupling properties and permittivity, respectively.

NUMERICAL MODELING

The simulation is done on COMSOL Multiphysics for performing variations of different geometry of the D-shaped bluff body along with the size of the beam which is deflected under the pressure applied as a boundary load due to formation of vortex resulted from the bluff body. We use Fluid Structure Interaction (fsi) along with the electrostatics under solid mechanics multiphysics for our study. As the displacement of the beam causes change of strain energy on the beam it will produce electrical energy which can be calculated using electrostatics physics in COMSOL. The geometry of our study is shown in Fig. 2. The motion of the deformed mesh is modelled using Winslow smoothing. The Moving Mesh application, which defines the relation between the spatial frame and the reference frame, solves mesh smoothing equations in the fluid domain using the solid displacements to define the coordinate transformations inside the beam. The Moving Mesh application mode confirms the fluid flow domain is deforming along with the bluff structure (Fig. 3).

RESULT AND DISCUSSION

The fluid-flow driven millimetre range energy harvester model simulation provides electrical outputs, deformed shapes, von-Mises stress, variations of lift and drag forces as well as various mechanical outputs. Analysis is performed to find the magnitudes and locations of maximum stress and electrical potential on the cantilever beam for three different shapes of the D-shaped bluff body and of different length of the cantilever beam. Fig. 4 shows two cross-section of the flow channel that expressing velocity field as a directional vector. It is evident that the changes in the fluid-flow due to the D-shaped bluff body have a clear visible effect on the cantilever and fluid-flow itself. Top and bottom surfaces of the cantilever experience increased viscous and pressure forces and create vortex in the flow region.

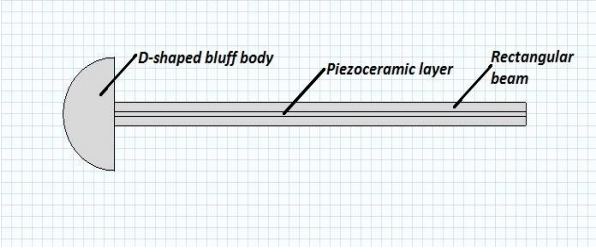

FIGURE 2. Geometry of the structure

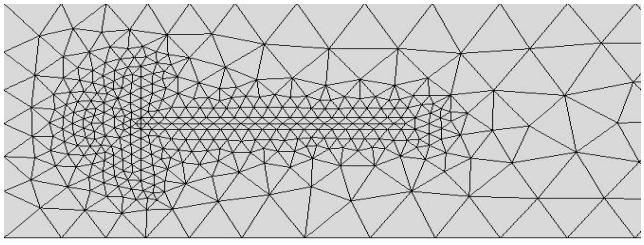

FIGURE 3. Mesh on fluid domain and solid structure

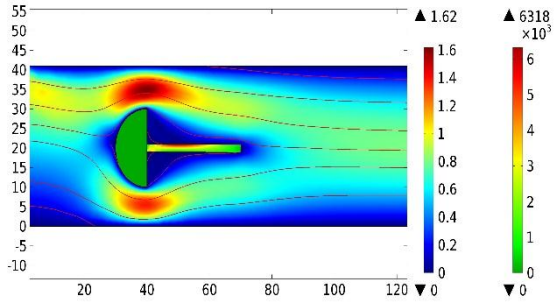

FIGURE 4. Velocity magnitude and von Mises stress with streamline velocity field at t=6 *sec*

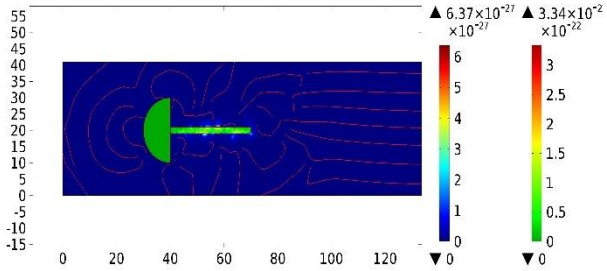

FIGURE 5. vortex formation due to fluid motion *at time=0* sec

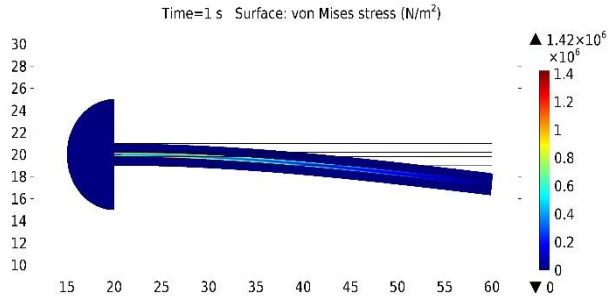

FIGURE 6. Deformation of piezo materials and stress

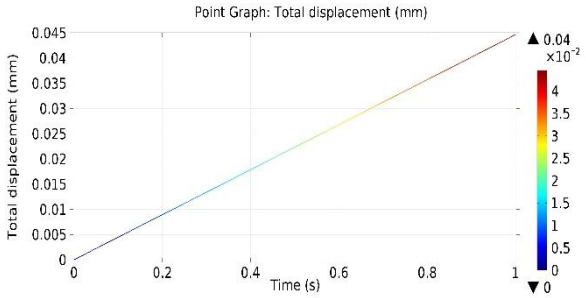

FIGURE 7. Total displacement

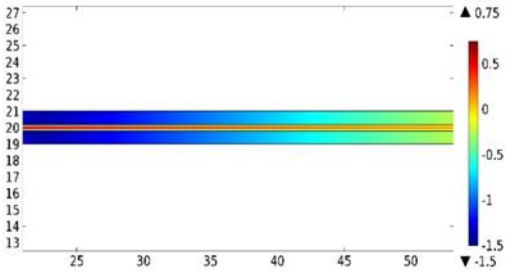

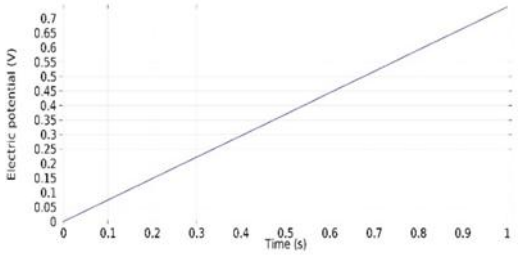

FIGURE 8. From Left to Right, (a) Electric potential in the piezo materials surface (b) Electric potential due to displacement

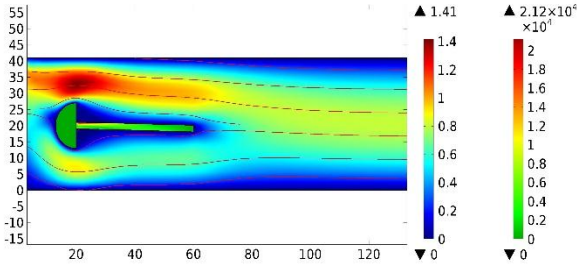

FIGURE 9. Velocity magnitude and von Mises stress with streamlines velocity field at time=6 sec for 7mm bluff body with 40 mm beam

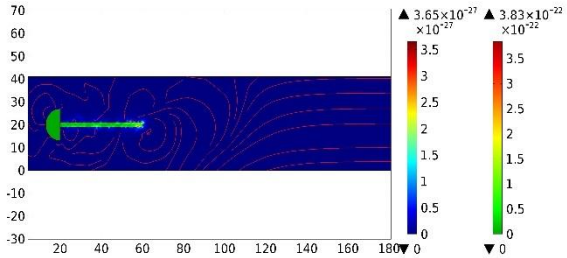

FIGURE 10. Vortex formation due to fluid motion at time=0 sec for 7 mm bluff body with 40 mm beam

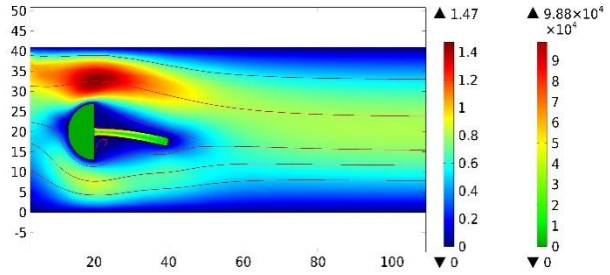

FIGURE 11. Velocity magnitude and von Mises stress with streamlines velocity field at time=6 sec for 7mm bluff body with 20 mm beam

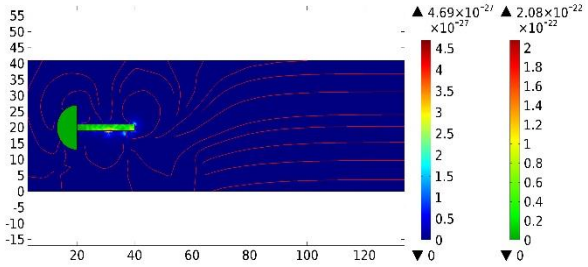

FIGURE 12. Vortex formation due to fluid motion at time=0 sec for 7 mm bluff body with 20 mm beam

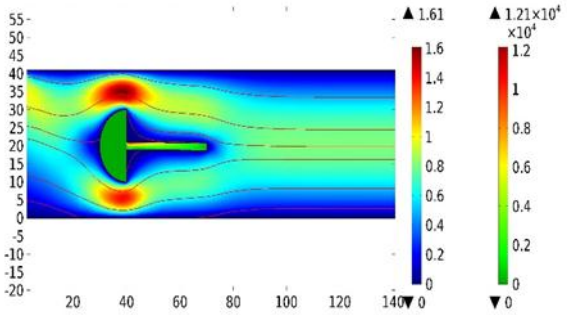

FIGURE 13. Velocity magnitude and von Mises stress with streamlines at time=6 sec for 10mm bluff body with 30mm beam using water

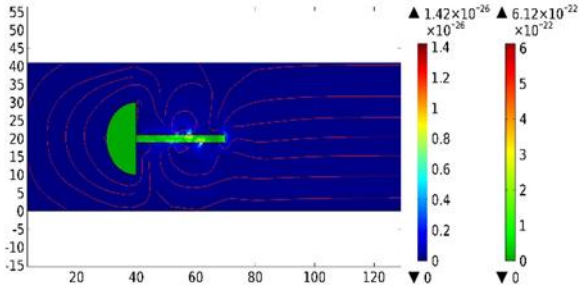

FIGURE 14. Vortex formation due to fluid motion at time=0 sec for 7 mm bluff body with 60 mm beam using water

The viscous and pressure forces act as boundary load on the surfaces of the cantilever, which cause the cantilever bending. As expected, the maximum Von-Mises-stress is determined at the left side of the beam i.e., in the vicinity of the fixed side of the D-shaped bluff-body and the minimum value at the right side of the beam. Fig. 5 shows the vortex created during the flow passed through the Bluff body. The bluff body causes boundary load on the beam surface as well as in tip which causes beam deflection and production of voltage.

Due to the deformation of the piezoelectric crystal layer, which is attached on the top surface of the beam, an electric polarization in the z-direction is created. This polarization is proportional to the deformation and causes an electric potential difference in the piezoelectric crystal as shown in Fig. 6. Fig. 7 shows the total displacement due to applied pressure force on the beam which increases linearly with time. Figs. 8(a) & 8(b) show electric potential in the surface of the piezoelectric body and the value in the point graph. In our case we observe variations of stress and vortex formation due to fluid motion for different shapes of bluff-body along with the different shapes of beam in the Fig. 9 to Fig. 12.Fig.15 shows the variation of vortex formation due to doubling the water velocity where fig.16 present the variation of vortex due to fluid change as Air instead of water.

Figs. 13 & 14 show the variation due to change of working fluid as Air instead of water. The result shows that there are small variations due to these changes. The tip displacement for 10 mm *D*-shaped bluff body is 0.05 mm whereas for 7 mm *D*-shaped body with large rectangular beam will produce more deflection which is in the range of 0.8 mm. For small sized beam vortex formation occur at the tip of the beam. On the other hand for large sized beam it will form vortex in slightly middle as well as in the tip. Due to vortex formation the deflection also increases and the voltage induced for different cases also increases. When we observe the result for air instead of water it shows satisfactory results in the field of tip displacement. In case of air the tip displacement is 1.4 mm range which can be used for better voltage generation for same geometry.

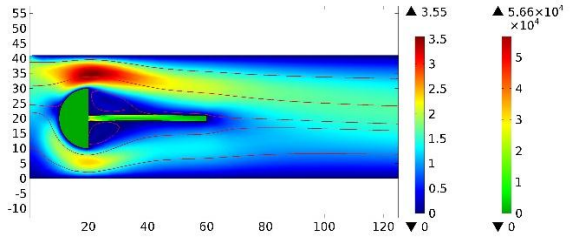

FIGURE 15. Velocity magnitude and von Mises stress with streamlines at time=6 sec for 10mm bluff body with 40mm beam using water at 4(m/s) fluid velocity

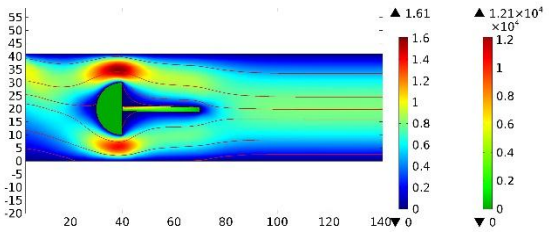

Figure 16. Velocity magnitude and von Mises stress with streamlines at time=6 sec for 10mm bluff body with 40mm beam using Air

CONCLUSION

In this paper, we presented the modeling of an energy harvester that couples mechanical, piezoelectric and fluid domains to convert fluid-flow driven kinetic energy into electricity. The addition of the D-shaped bluff-body made significant improvements in vortex shedding frequency exerting on the cantilever, hence greatly magnified the cantilever deflection. This study investigated energy harvesting from fluid-flow in the form of pressure forces exerted on the cantilever beam for different size of the beam as well as for different fluid domain such as water and air. There exists noticeable change of vortex formation due to change of fluid velocity both for air and water. Simulation result showed that 0.7 V (approx.) could be obtained from the device piezoelectric domain. Because the D-shape bluff-body with the cantilever not optimized yet, therefore the output voltage and consequently output power can be increase after optimization.

REFERENCES

1. Anton R. S., "Multifunctional Piezoelectric Energy Harvesting Concepts," Ph.D. Dissertation, Virginia Polytechnic Institute and State University, 2011.
2. Andersson C. and Ahl. D., "Fluid Structure Interaction Evaluation of two coupling techniques," Technical report, IDE1135, June 2011.
3. Saadon, S., and Sidek O., "A Review of Vibration-based MEMS Piezoelectric Energy Harvesters," Energy Conversion and Management, 52 (2011) 500–504.
4. K.Srinivasa Raoa, K.Girija Sravanib, G.Yugandharc,G.Venkateswara Raod and V.N.Manie, "Design and analysis of fluid structure interaction in a horizontal Micro Channel," Procedia Materials Science, Volume 10, 2015, pp. 768–788.
5. Sodano H. A., Park G., Leo D. J., and Inman D. J., "Model of Piezoelectric Power Harvesting Beam," Proceedings of IMECE, 2003, Washington DC, November 15-21, 2003.
6. Donea J., Huerta A., Ponthot J.-Ph., and Ferran A. R., "Arbitrary Lagrangian–Eulerian Methods," Book Chapter, Encyclopedia of Computational Mechanics, Volume 1: ´ Fundamentals, John Wiley & Sons, Ltd., 2004.
7. Torah, R., Jones P. G., and Tudor M., "Self-powered autonomous wireless sensor node using vibration energy harvesting," Measurement Science and Technology, volume 19, Number 12, 2008.
8. Sloetjes P.J. and De.Boer A., "Vibration Reduction and Power Generation with Piezo-ceramic Sheets Mounted to a Flexible Shaft," Journal of intelligent material systems and structures, Volume 19, 2008, pp. 25-34.
9. Song H. J., Choi Y. T., Werely N. M., Purekar A., "Comparison of monolithic and composite piezoelectric Material-Based energy Harvesting Devices," Journal of intelligent material systems and structures, 2014.
10. Li S. J., and Yao R., "Solution Modification of a Piezoelectric Bimorph Cantilever under Loads," Journal of intelligent material systems and structures, 2014.
11. Bhuyan M.S., Majlis B.Y., Othman M., Ali S.H.M., Kalaivani C., and Islam S, "Development of a Fluid Actuated Piezoelectric Micro Energy Harvester: Finite Element Modeling Simulation and Analysis," Asian Journal of Scientific Research, 6, 2013, pp. 691-702.

ICME2015

International Conference on Mechanical Engineering 2015
(ICME 2015) 18 – 20 December, 2015, Dhaka, Bangladesh

Paper ID : 542

Modelling of Frost Formation and Growth on Microstuctured Surface

Md. Ali Muntaha[1, a)], Md. Mushfique Haider[1, b)] and Md. Ashiqur Rahman[1, c)]

[1]*Department of Mechanical Engineering, Bangladesh University of Engineering and Technology (BUET), Dhaka-1000*

[a)]Corresponding author: rifatdc@gmail.com
[b)]mhraj09@yahoo.com
[c)]ashiqur78@yahoo.com

Abstract. Frost formation on heat exchangers is an undesirable phenomenon often encountered in different applications where the cold surface with a temperature below freezing point of water is exposed to humid air. The formation of frost on the heat transfer surface results in an increase in pressure drop and reduction in heat transfer, resulting in a reduction of the system efficiency. Many factors, including the temperature and moisture content of air, cold plate temperature, surface wettability etc., are known to affect frost formation and growth. In our present study, a model for frost growth on rectangular, periodic microgroove surfaces for a range of microgroove dimension (ten to hundreds of micron) is presented. The mathematical model is developed analytically by solving the governing heat and mass transfer equations with appropriate boundary conditions using the EES (Engineering Equation Solver) software. For temperature, a convective boundary condition at frost-air interface and a fixed cold plate surface temperature is used. Instead of considering the saturation or super-saturation models, density gradient at the surface is obtained by considering experimentally-found specified heat flux. The effect of surface wettability is incorporated by considering the distribution of condensed water droplets at the early stage of frost formation. Thickness, density and thermal conductivity of frost layer on the micro-grooved surfaces are found to vary with the dimension of the grooves. The variation of density and thickness of the frost layer on these micro-grooved surfaces under natural convection is numerally determined for a range of plate temperature and air temperature conditions and is compared with experimental results found in the open literature.

INTRODUCTION

Formation of frost on heat exchanger surface is a very common phenomenon which occurs on cold surfaces of both simple and complex geometry when the surface temperature is below the triple point of water and dew point of surrounding air. Frost formation bring about many detrimental effect on different applications like air conditioning, refrigeration, heat pump, cryogenics and similar other engineering applications. The accumulation of frost offers significant thermal resistance which results in a decrease of heat transfer of the heat exchanger and increases the pressure drop (fan power). Energy efficiency is reduced due to frost accumulation and operation is complicated by the need to defrost the heat exchanger, resulting in an increase in energy consumption.

Many factors including the temperature and moisture content of air, cold plate temperature, surface wettability, frost density, frost surface temperature, air velocity *etc.* affect the frost growth and frost properties on heat transfer surfaces. The prediction of frost properties are essential as because performance of a heat exchanger under frosting condition is characterized by frost properties Therefore many analytical and numerical models are developed to predict frost growth on a cold surface [1-14].

Hoke *et al.* [1] attempted to include the effect of variable wettability on the frost formation and studied how frost properties vary in the early and mature stages of frost growth. Tao *et al.* [2] examined the early growth period of frost formation on a flat plate under forced convection and observed that frost density distribution in the full growth period largely depends on its distribution during the early growth period.

Nomenclature

h_m	convective mass transfer co-efficient (kg/m^{2}s)
h_C	convective heat transfer co-efficient (W/m^{2}k
L	plate length (m)
W	plate width (m)
C_p	specific heat (kj/kg-k)
P	pressure (Pa)
P_v	partial pressure of water vapor at temperature T (Pa)
q	heat flux (W/m^2)
T	temperature (k)
T_f	frost temperature (k)
T_∞	free stream temperature (k)
x	co-ordinate along the frost thickness (m)

Greek Symbol

ω	humidity ratio of moist air, kg (water vapor) / kg(dry air)
ρ_f	frost density
ρ_a	density of dry air
α	thermal diffusivity (m^2/s)

Subscripts

a	dry air
d	diffusion
e	effective medium
f	frost
∞	ambient (free stream)
s	frost surface
t	total
v	water vapour
sen	sensible
lat	latent
w	wall
m	melting

During frost formation, a portion of total mass flux of water vapour causes densification by diffusing through the frost layer and by the phase transformation to ice depositing on the existing frost crystal. The remainder mass flux of water vapor provide thickening of frost layer by freezing at frost surface. Many researchers assumed that at the frost surface the water vapour is saturated. On the contrary, Na and Webb [3] performed a laminar boundary layer analysis and after the detailed investigation, concluded that water vapour at the frost surface is super-saturated rather than saturated. Kandula [4] later suggested that the degree of super-saturation is a strong function of surface wettability. A number of experimental studies suggest that frost properties such as thickness, density and thermal conductivity increase continuously during frost formation [5-14]. Rahman and Jacobi [5] demonstrated in their experimental work that initial droplet distribution during condensation process is largely influenced by surface wettability and the property of frost layer in both stages of frost growth largely depend on it.

No study could be located in the open literature on frost modelling on any microstructure surface incorporating the effect of wettability on frost formation and growth. In this work, an analytical model of frost formation on microgrooved surfaces, incorporating the effect of surface wettability on the frosting and frost properties, has been presented. The findings of the mathematical modellings are then compared with a number of experimental results for a range of operating conditions.

MATHEMATICAL FORMULATION

Mass and Heat Flux at the frost surface and frost layer growth rate

The total mass flux transferred from the moist air to the frost surface can be subdivided into two parts. A portion of total mass flux of water vapor causes densification by diffusing through the frost layer and by the phase transformation to ice depositing on the existing frost crystal. The remainder mass flux of water vapor provide thickening of frost layer by freezing at frost surface.

$$\dot{m}_t = \frac{d}{dt}(x_s \rho_f) + \rho_f \frac{dx_s}{dt} = \dot{m}_e + \dot{m}_d \tag{1}$$

$$\dot{m}_e = \rho_f \frac{dx_s}{dt}; \dot{m}_d = x_s \frac{d\rho_f}{dt} \tag{2}$$

Moreover, total mass flux can be expressed as

$$\dot{m}_t = \rho_a h_m (\omega_a - \omega_s) \tag{3}$$

Here, ω_a and ω_s are the humidity ratios of atmospheric air and frost surface, respectively. Equation (1) and (3) can be rewritten and the frost later growth is obtained as

$$\rho_a h_m(\omega_a - \omega_s) = \rho_f \frac{dx_s}{dt} + x_s \frac{d\rho_f}{dt} \tag{4}$$

The total heat transferred from the air to the frost surface is comprised of two components: sensible heat transfer due to temperature difference, and latent heat of sublimation due to humidity difference. Mathematically,

$$q_t = q_{sen} + q_{lat} \tag{5}$$

$$q_{sen} = h_c(T_a - T_s); q_{lat} = \dot{m}_t L_{sv} \tag{6}$$

Combining of equation (5) and (6) gives the following equation

$$q_t = h_c(T_a - T_s) + \dot{m}_t L_{sv} \tag{7}$$

Equation (7) can be further written by putting the value of $\dot{m}_t$ from equation (1) into it

$$q_t = [h_c(T_a - T_s) + \rho_f L_{sv} \frac{dx_s}{dt}] + x_s L_{sv} \frac{d\rho_f}{dt} \tag{8}$$

The term in between the parenthesis of equation (8) is the heat transfer through the frost surface by conduction, thus can be mathematically represented as

$$q_{cond} = -k_f (\frac{dT}{dx})_s = -[h_c(T_a - T_s) + \rho_f L_{sv} \frac{dx_s}{dt}] \tag{9}$$

After some differentiation and re-arrangement, following Kandula [4], the frost growth rate equation is obtained as follows

$$\frac{dx_s}{dt} = \frac{\rho_a h_m (\omega_a - \omega_s)}{\rho_f (1 + x_s \left[c_2 \left(1 - \xi^{0.5}\right) + \frac{1}{\theta} \right] \frac{1}{(T_m - T_w)} \frac{dT_{fs}}{dx_s})} \tag{10}$$

Where, θ is the dimensionless frost surface temperature and is given by

$$\theta = \frac{T_{s-} T_w}{T_m - T_w}; \xi = \frac{Re}{Re_{cr}} \tag{11}$$

Here, Re_{cr} is the critical Reynolds number for laminar turbulent transition.

An empirical correlation by O'Neal and Tree [13] was used to relate the frost thermal conductivity to its density

$$k_{fst} = 0.001202 \rho_{fst}^{0.963} \tag{12}$$

Heat & Mass transfer coefficient

The convective heat transfer coefficient h_c for laminar flow over a flat plate is determined from the well-known correlation

$$Nu = 0.664 Re^{1/2} Pr^{1/3} \tag{13}$$

The convective mass transfer coefficient h_m is obtained on the basis of Chilton–Colburn analogy between heat and mass transfer which is found to be applicable under frosting conditions

$$ShLe^{2/3} = Nu \tag{14}$$

Where Sh is the Sherwood number and Le is the Lewis number.

$$\omega_s = 0.622 \frac{P_{vs}}{P_t - P_{vs}} \tag{15}$$

P_t is the total pressure in atm, P_{vs} is the saturation vapor pressure corresponding to the frost surface temperature T_{fs}

Saturation vapor pressure is extracted from the following equation prescribed by Lee and Ro [15].

$$lnP_{vs} = \frac{a_1}{T} + a_2 + a_3 T + a_4 T^2 + a_5 T^3 + a_6 T^4 + a_7 lnT \tag{16}$$

Where the values of the constants ($a_1, a_2, a_3, a_4, a_5, a_6, a_7$) are given by Lee and Ro [15].

Boundary and Initial Condition and Temperature distribution in the frost layer

The boundary temperatures are prescribed as:

$$T = T_w \ , x = 0 \tag{17}$$

$$T = T_{fs} \ , x = x_s \tag{18}$$

By integration with the help of appropriate boundary conditions [Equations: 9, 17-18], temperature distribution in the frost layer can be obtained as follows

$$T = T_w + c_1 x + c_2 x^2 \tag{19}$$

$$c_1 = \frac{L_{sv}}{k_f}[h_c(T_a - T_s) + h_m(\omega_a - \omega_s)] \tag{20}$$

$$c_2 = -\frac{L_{sv}}{k_f x_s}[h_m(\omega_a - \omega_s) + \rho_f \frac{dx_s}{dt}\ ] \tag{21}$$

The temperature at the frost surface corresponding to x = x_s can be obtained from

$$T_s = T_w + \frac{x_s}{k_f}[h_c(T_a - T_s)] + \frac{1}{2}\frac{L_{sv} x_s}{k_f}[h_m(\omega_a - \omega_s) + \rho_f \frac{dx_s}{dt}\ ] \tag{22}$$

In this study, the initial values of thickness and density are extracted from the experimental observation of Rahman and Jacobi on a number of microgrooved surfaces [5]. This thickness and density values at the early stages of frost formation are then used in our model to predict the frost growth at the later stages.

Numerical Scheme

The governing equations (4), (10), (12), and (22) were solved simultaneously with the algebraic equations using a commercial software package, Engineering Equation Solver (EES).

RESULTS AND DISCUSSION

The surface wettability affects the frost formation and frost properties, especially at the initial stages of frost growth. In this proposed model, the wettability effect is introduced through the variation of the initial frost thickness and density for the same operating conditions, which resulted from the variation of surface micro-roughness in the form of microgrooves. The validity of the proposed model is verified by a comparison of the predictions of frost properties (density and thickness) with experimental data of Rahman and Jacobi [5] in which the frosting experiments were conducted by introducing wettability effect for different micro-grooved geometry. For a variation in the groove structure (groove depth and pillar width), the shape, size and distribution of the condensed water droplet on the surface and subsequently the frost structure were different. These variations in the initial frost

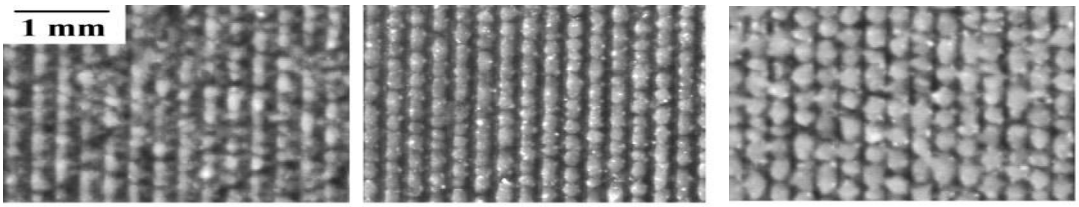

FIGURE 1. Droplet distribution on micro grooved surfaces at the early stages of frost formation, as experimentally obtained by Rahman and Jacoby [2] .The droplets had a brick-wall-like frost pattern on micro grooved surfaces with aspect ratios of (a) 0.21, (b) 0.52, (c) 0.94, for cooling at -18 ℃.

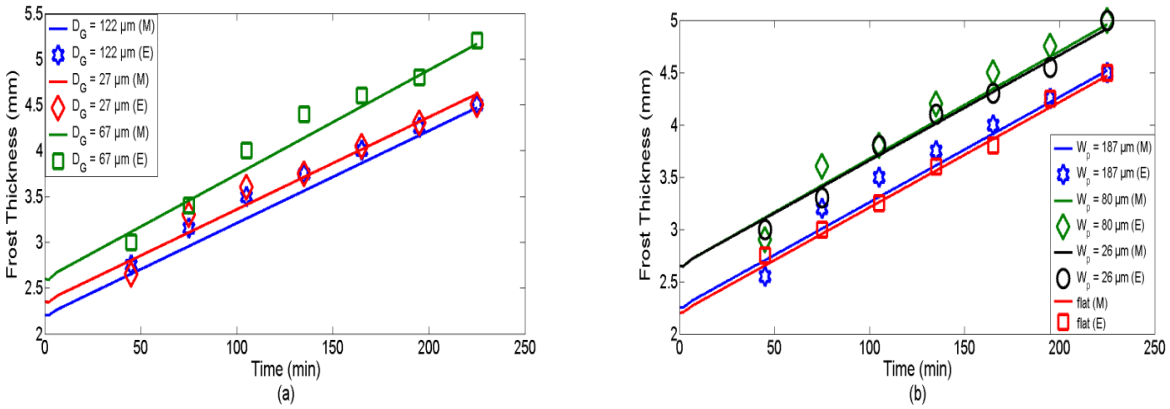

FIGURE 2. Comparison of frost thickness obtained from experiments and the proposed model on one flat baseline surface and three microgrooved surfaces with (a) variable groove depth (WG = 130 µm, WP = 110 µm), and (b) variable pillar width (WG = 130 µm, DG = 67 µm) at a plate temperature of -18 °C. Symbol E and M stands for experiment and model, respectively.

structure have ultimately affected the frost properties (initial frost thickness and density) in the later stages of frost formation and growth. The wettability effect in our model is integrated by incorporating initial frost thickness and density obtained from the experimental observation by Rahman and Jacobi [5].

The experiments were performed on micro-groove brass surfaces for 12 samples having a wide range of groove depth (D_G = 27-122 µm) and pillar width (W_P = 26-187 µm) and a fixed groove width (W_G = 130 µm) under the same operating conditions (air temperature = 22 ± 2 ℃, RH = 30-70 %, Plate temperature = -18 ℃, natural convection). The experimental values of frost thickness and density reported in reference [5] and the numerically obtained results from this study for the same operating conditions are shown and compared in Fig. 2 and 3.

For the frost thickness, we observed in Fig. 2 that for both the variation in groove depth and pillar width, the numerical model can satisfactorily predict the experimental results with a maximum 7% error for both D_G = 122 µm [Fig. 2(a)] and W_P = 80 µm [Fig. 2(b)]. The initial frost density and frost thickness were 85 kg/m^3 and 2.2 mm, respectively, for D_G = 122 µm and were 75 kg/m^3 and 2.65 mm, respectively, for W_P = 80 µm. These values were obtained from the experimentally reported initial frost density and thickness from [5]. For other samples, the values obtained from this model predicted the frost thickness with even higher accuracy for the same operating conditions. The results are reported for a frosting period of 4 hours and are found to predict the frost growth accurately

In our study, we can find that without incorporating the geometry and only including the initial thickness and density, our numerical model can also predicts the frost density. In the case of frost density, the model predicts the experimental result with sufficient accuracy of having maximum error of 14 % for D_G = 122 µm [Fig. 3(a)] and that of 17% for W_P = 80 µm [Fig. 3(b)]. Similar results are observed for the variation of pillar width and groove depth if we can incorporate initial thickness and density accurately. Thus it can suggested that by incorporating the values of

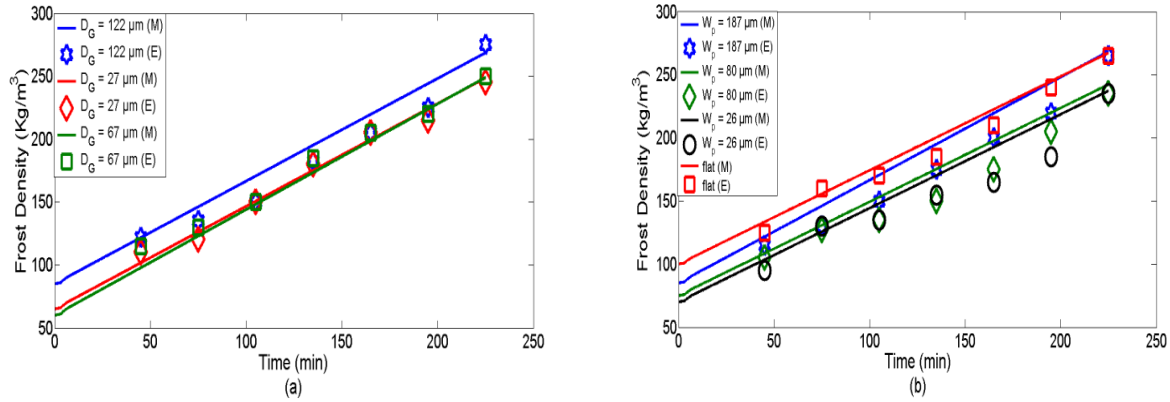

FIGURE 3. Comparison of frost density between experimental data and model on three micro grooved surfaces with variable (a) groove depth (W_G = 130 µm, W_P = 110 µm) and (b) pillar width (W_G = 130 µm, D_G = 67 µm) and one flat surface at a plate temperature of -18 °C.

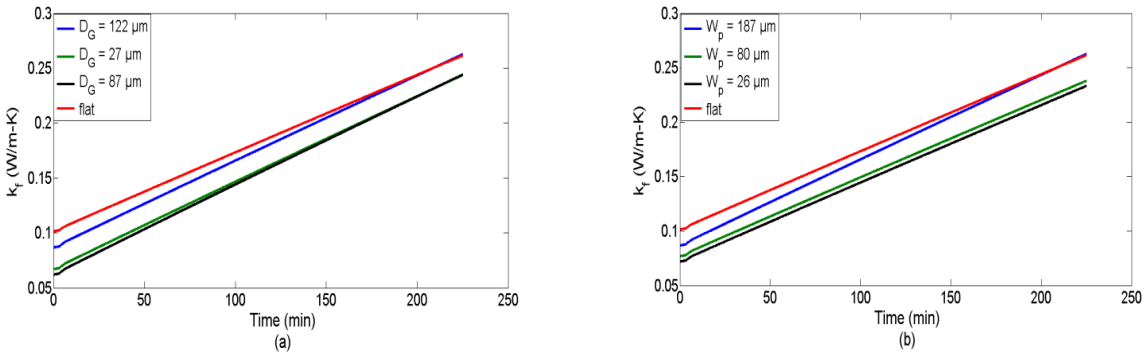

FIGURE 4. Predicted thermal conductivity of frost on one flat and three micro grooved surfaces with variable (a) groove depth (W_G = 130 µm, W_P = 110 µm) and (b) pillar width (W_G = 130 µm, D_G = 67 µm) at a plate temperature of -18 °C.

.

initial frost thickness and density, we could accurately predict the thickness and density for the later part of frost growth.

In our study, we can find that without incorporating the geometry and only including the initial thickness and density, our numerical model can also predicts the frost density. In the case of frost density, the model predicts the experimental result with sufficient accuracy of having maximum error of 14 % for D_G = 122 µm [Fig. 3(a)] and that of 17% for W_P = 80 µm [Fig. 3(b)]. Similar results are observed for the variation of pillar width and groove depth if we can incorporate initial thickness and density accurately. Thus it can suggested that by incorporating the values of initial frost thickness and density, we could accurately predict the thickness and density for the later part of frost growth.

For both cases, maximum error is observed for W_P = 80µm. The experimental frost thickness and density values for this sample were also found to exhibit a random behaviour. The initial frost height difference between the frost layer on the pillar top and the groove base was comparatively higher in this case and as a result, the frost thickness was non-uniform. This might have played a role for the higher error in prediction for this sample.

CONCLUSIONS

A mathematical model for frost growth on periodic microgroove surfaces for a range of microgroove dimension is presented. The model is developed analytically by solving the governing heat and mass transfer equations with appropriate boundary and initial conditions. The effect of surface wettability on the frost formation and frost properties is introduced through the variation of the initial frost thickness and density which result from the variation of surface micro-roughness. In this model, the initial conditions for frost thickness and density are included from the experimental observations of an earlier study. It is found that by incorporating the values of initial frost thickness and density correctly, we can predict the thickness and density for the later part of frost growth with sufficient accuracy. The proposed model of frost formation and growth is validated well with the experimental data and is found to satisfactorily predict the frost thickness with a maximum error of 7% and frost density with a maximum error of 17%. The variation of frost thermal conductivity with the variation of time for the same samples is also calculated. The authors plan to conduct further study to obtain the initial frost thickness and density by numerically analysing the shape, size, and distribution of condensed and frozen water droplets on the surfaces.

REFERENCES

1. J.L. Hoke, J.G.Georgiadis, A.M.Jacobi, Effect of Substrate Wettability on Frost Properties, Journal of Thermo-physics and Heat Transfer , 228-235, 18 (2) (2004)
2. Y.X. Tao, R.W. Besant, K.S. Rezkallah, A mathematical model for predicting the densification and growth of frost on a flat plate, Int. J. Heat Mass Transfer 353–363, 36 (2) (1993)
3. B. Na, R.L. Webb, A new model for frost growth, Int. J. Heat Mass Transfer 925–936, 47 (5) (2004)
4. M. Kandula, Frost growth and densification in laminar flow over flat surfaces, Int. J. Heat Mass Transfer 3719–3731, 54 (2011)

5. M.A. Rahman, A.M. Jacobi, Effects of microgroove geometry on the early stages of frost formation and frost properties, Applied Thermal Engineering 91-100, 56 (2013)
6. A. El Cheikh, A.M. Jacobi , A mathematical model for frost growth and densification on flat surfaces, International Journal of Heat and Mass Transfer 604–611 , 77 (2014)
7. Y. Hayashi, A. Aoki, S. Adashi, K. Hori, Study of frost properties correlating with frost formation types, ASME J. Heat Transfer 239–245, 99 (1977)
8. K.S. Lee, W.S. Kim, T.H. Lee, A one-dimensional model for frost formation on a cold flat surface, Int. J. Heat Mass Transfer 4359–4365, 40 (18) (1997)
9. Y.X. Tao, S. Jia , A Critical review of properties and models for frost formation analysis, HVAC&R Research 10(4) (2004).
10. K.S. Lee, S. Jhee, D.K. Yang, Prediction of the frost formation on a cold flat surface, Int. J. Heat Mass Transfer 3789–3796 , 46 (20) (2003)
11. D.K. Yang, K.S. Lee, Modeling of frosting behavior on a cold plate, Int. J. Refrig. 396–402, 28 (2005)
12. B.W. Jones, J.D. Parker, Frost formation with varying environmental parameters, J. Heat Transfer 255–259, 97 (1975)
13. D.L.O'Neal, D.R. Tree, A review of frost formation on simple geometries, ASHRAE Trans. 91(1985) 267-281.
14. C.J.L. Hermes, An analytical solution to the problem of frost growth and densification on flat surfaces, Int. J. Heat Mass Transfer 7346-7351, 55 (2012)
15. Y.B. Lee a, S.T. Ro, Analysis of the frost growth on a flat plate by simple models of saturation and supersaturation, Experimental Thermal and Fluid Science 685–696, 29 (2005)

ICME2015

International Conference on Mechanical Engineering 2015
(ICME 2015) 18 – 20 December, 2015, Dhaka, Bangladesh

Paper ID : 544

Analytical Modeling of Wetting States and Simulation of Drop Shape on Microstructured Surfaces

Saif Khan Alen[1,a)], Nazia Farhat[1,b)] and Md. Ashiqur Rahman[1,c)]

[1]*Department of Mechanical Engineering, Bangladesh University of Engineering and Technology, Dhaka-1000, Bangladesh*

[c)]Corresponding author: ashiqurrahman@me.buet.ac.bd
[a)]educative.alen@gmail.com
[b)]naziafarhat4@gmail.com

Abstract. Understanding the relationship between surface roughness and wetting state is essential in designing microstructured surfaces with tunable wetting properties. In this work, an analytical model for predicting the wetting state on microgroove geometry is developed and applied to intrinsically hydrophilic brass surfaces with a wide range of groove geometry. To enhance the scope and applicability of the developed model, it is implemented on a number of other aluminum microgrooved surfaces. Before applying any surface minimization algorithm to obtain equilibrium droplet shape, the stable wetting state is determined by comparing the total surface energy of the liquid droplet in Cassie and Wenzel wetting state. It is found that hybridization of the microgrooved surface (PDMS coating on the groove base) reduces the critical microgroove dimensions for exhibiting a Cassie wetting state. The unusual spreading of water droplets, observed experimentally on certain microgrooved surfaces, is predicted more accurately when slightly inclined pillars (with a 7º inclination from vertical) instead of vertical wall are assumed. These results corroborate our earlier claim that the shape and the slope of the pillar edge are responsible for the unusual spreading exhibited by certain surfaces. Moreover, implementation of the experimentally obtained values of droplet elongation ratio in the numerical model further enhances the accuracy of the obtained results. The present mathematical model offers an excellent tool for predicting the wetting state of the rough hydrophilic surface using its roughness geometry, and the numerical approach of implementing inclined pillar and droplet elongation ratio can improve the accuracy of drop shape simulation while predicting the wetting states accurately.

INTRODUCTION

Modification of the intrinsic wetting property of metal surfaces can play a significant role in a range of modern technological developments. A liquid droplet, when placed on a rough surface, can reside in any of the two different wetting states or modes. The first one is the collapsed state, in which the drop enters into the groove or bottom of the surface roughness and completely wets the substrate. For the other case, the drop forms a composite surface under it and does not enter into the valley of the surface roughness. The former collapsed state is termed as 'Wenzel state' and the latter one is called 'Cassie state' of wetting (Fig. 1(a)). The equilibrium wetting state depends on the total energy of the system; if the total system energy of the Cassie wetting state is less than that of the Wenzel wetting state, then Cassie state exists, and vice versa.

When a droplet sits on a microgrooved surface, it can exhibit either a Cassie wetting state or a Wenzel wetting state depending on the droplet volume and microgroove geometry [1-2]. Conditions to be satisfied for the wetting transition (Cassie or Wenzel) on rough surfaces were described by several researchers [3-13]. However, these derived conditions were for intrinsically hydrophobic surfaces. Bormashenko [6] elaborately discussed various types of wetting states, their formation condition, wetting transition conditions and the parameters influencing the wetting. Alberti and DeSimone [8] theoretically analyzed roughness induced wetting of both hydrophilic and hydrophobic surface by homogenization approach. They mathematically showed the contact angle associated with minimum

energy for each type of surface. Bico *et al.* [10] illustrated the wetting phenomenon of rough surfaces by defining a critical angle with solid roughness and solid fraction, which acts as the intermediate transition between wetting and wicking. Patankar [12] proposed an analytical methodology to design superhydrophobic surface that would render such an equilibrium contact angle that would not vary even if the wetting state transitions from Cassie to Wenzel.

Several researchers have reported analytical models for predicting the wetting state of intrinsically hydrophobic surface (whose intrinsic contact angle θ>90°) [14-16]. But this work describes a way of predicting the wetting state of intrinsically hydrophilic surface by analyzing the roughness geometry. Condition for the stable equilibrium wetting state is developed depending on the interfacial energies of the contact surface of solid substrate and liquid droplet.

The Young's equation, and the equations proposed by Cassie and Wenzel regarding the energy associated with the wetting state is given in equations (1-3). Total free energy of the system includes the interfacial energy, the potential energy, and the line tension. The variation of drop potential energy and the effect of the line tension are negligible terms while measuring total system energy. So, the total free energy of the system may be restricted only to the interfacial energies, which can be expressed as equation (4).

$$\cos\theta = \frac{\sigma(sf) - \sigma(sl)}{\sigma(lf)} \tag{1}$$

Where, θ is the Young's contact angle, and σ_{sf}, σ_{sl} and σ_{lf} are the interface surface tensions at the solid-air, solid-liquid and liquid-air, respectively.

$$cos\theta_w = r.cos\theta \tag{2}$$

Where, r is the roughness factor, ratio of true area of the solid-liquid contact surface to the apparent area, and θ_w is the apparent contact angle which corresponds to the stable equilibrium state (i.e. minimum energy state for the system).

$$cos\theta_c = r.f.cos\theta - (1 - f) \tag{3}$$

Where, θ_c is apparent contact angle for stable equilibrium state, f is the Cassie roughness factor which represents the fraction of solid-liquid contact surface area to the apparent area.

$$E_{surface} = \sigma_{sf}.A_{sf} + \sigma_{sl}.A_{sl} + \sigma_{lf}.A_{lf} \tag{4}$$

Where, $E_{surface}$ is the total energy of the drop surface; and A_{sf}, A_{sl} and A_{lf} are the area of the solid-air, solid-liquid, and liquid-air contact surface of the drop periphery, respectively.

When a very small roughness is introduced to a flat surface initially the wetting state is Wenzel. Because practically we can understand that due to the curvature of the spherical liquid drop there is a meniscus curve formed at the bottom of the drop. So until the depth of the groove is increased over a transition point the wetting state of the liquid (water) is Wenzel. In this work, a mathematical model is introduced to predict the wetting state of a rough surface by using the surface geometry. Two mathematical conditions, applicable for intrinsically hydrophilic surfaces, for predicting the critical roughness for transition between Wenzel and Cassie wetting state is developed.

ANALYTICAL MODELING OF CASSIE-WENZEL TRANSITION

First Condition of Wetting Transition

From the thermodynamic point of view, a stable equilibrium shape of the drop exists when the surface free energy is the minimum. Due to fact that potential energy and line tension are negligible, interfacial energy plays key role while defining total free energy. Equation (4) can be employed for calculating the total free energy of both Wenzel and Cassie wetting state. The energy in Wenzel wetting state and Cassie wetting state is represented respectively by equation (5) and equation (6). A generalized expression as in equation (7) is developed by Barbieri [16] which varies in the constant term 'C' for the Cassie and Wenzel wetting state.

$$E_{wenzel} = \sigma_{sf}.r.A_{total} - \sigma_{lf}.r.cos\theta.A_{base} + \sigma_{lf}.A_{external} \tag{5}$$

Where, $A_{external}$ is the external drop surface; A_{base} is the geometric drop base surface; A_{total} is the total solid sample surface.

$$E_{cassie} = \sigma_{sf}.r.A_{total} - \sigma_{lf}\left[f.cos\theta - (1-f) \right] A_{base} + \sigma_{lf}.A_{external} \quad (6)$$

$$E_{surface} = \pi\left(\frac{3V}{\pi}\right)^{2/3} \frac{1}{\left[2 - 3Cos\theta + (Cos\theta)^3\right]^{2/3}} [2\sigma_{lf}.(1-cos\theta) + C.(sin\theta)^2] + \sigma_{lf}.r.A_{total} \quad (7)$$

Where, V is the drop volume; $C=C_{wenzel}$ or C_{cassie}; $C_{wenzel} = -\sigma_{lf}*r*cos\theta$ and $C_{cassie}=-\sigma_{lf}[f.cos\theta-(1-f)]$

Now if we want to minimize the surface free energy, then we need an independent variable with which the energy expression at equation (7) needs to be differentiated. The cosine of intrinsic contact angle, $cos\theta$, is taken as the independent variable. By differentiating that generalized equation (7), we can get the apparent contact angle value for both Wenzel and Cassie wetting states. This obtained apparent contact angle represents the minimum energy level at each wetting regime. The expression for the $cos\theta_w$ and the $cos\theta_c$ obtained from this energy minimization is given respectively in equation (2) and equation (8).

These two equations are called the Wenzel equation and Cassie's law which are based on surface energy minimization. Now we can see that Cassie equation is influenced only by the Cassie roughness factor 'f' which we have defined earlier. At this stage, one point should be noted that for both hydrophobic and hydrophilic surface Cassie state predicts the higher apparent contact angle. That is if we want to increase the hydrophobicity of a surface, then Cassie state is always a favorable wetting state.

In order to compare the two wetting states to define which of them should exist in equilibrium, we need to compare their surface free energy. When the roughness of a surface is continuously increased, then after a critical roughness value, the drop thermodynamically prefers Cassie wetting state over Wenzel wetting state. So, to determine the critical roughness, required for a microgrooved surface exhibiting Cassie wetting state, the cosines of apparent contact angle need to be compared. Equating the cosines of apparent contact angles, as in equation (9), at both Wenzel and Cassie wetting states: $cos\theta_w$ and $cos\theta_c$, we can determine the critical roughness value, as in equation (10), for which the drop will exhibit Cassie wetting state. This obtained r_{cr} is the required transition point between Wenzel and Cassie wetting state. Thus, the condition of transition between Wenzel and Cassie wetting state is presented by the equation (11).

To be very specific about the first condition: by equating the cosines of apparent contact angles of Cassie (θ_c) and Wenzel (θ_w), a thermodynamic criteria can be developed to define which of the two wetting regimes, Cassie or Wenzel, is favored. When the roughness value, induced to the surface, is greater than the critical roughness value, then the wetting state formed by the drop will be Cassie wetting state. It should be mentioned that while equating the cosines of apparent contact angle of Cassie and Wenzel wetting regime, the negative of angle for $\cos\theta_c$, because θ_c>90° is taken.

If we want to analyze the present transition point by plotting the data of $cos\theta$, as in Fig. 1(b), for different intrinsic contact angle of θ varying from 0° to 180°, then we can see that for a roughness value of r=1.5 and f=0.1, the transition point is the intersection of the plot of $cos\theta_w$ and $cos\theta_c$. This relation of equation (11) successfully predicts the stable wetting states for a definite roughness value, which will be shown in one of the next sections. This condition is also capable of accurately predicting the Wenzel to Cassie transition point while changing 'f', Cassie roughness factor.

$$cos\theta_c = f.cos\theta - (1-f) \quad (8)$$

Where, f is the Cassie roughness factor which represents the solid fraction under the drop.

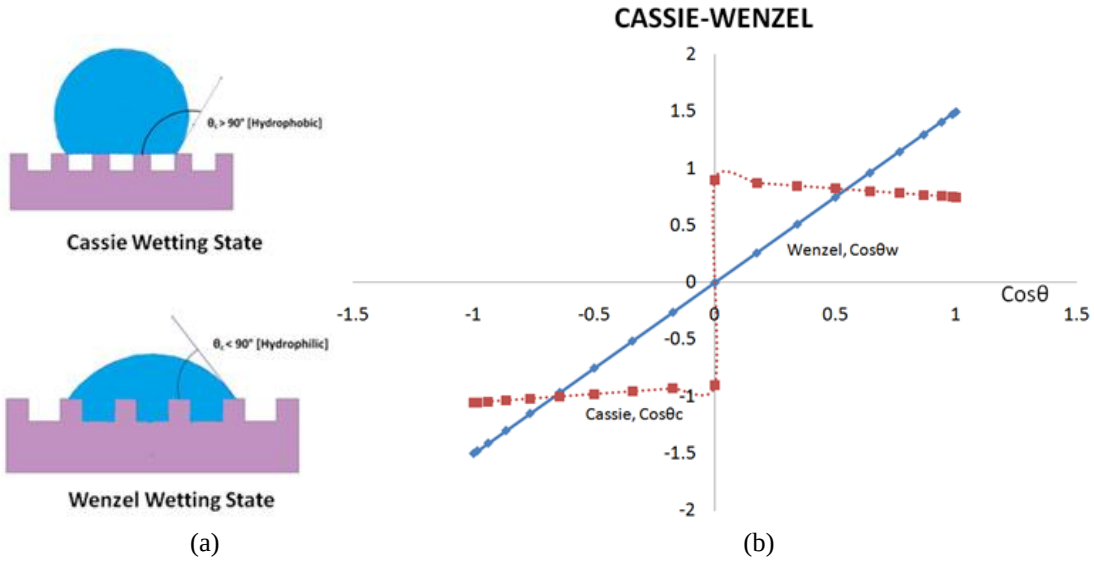

(a) (b)

FIGURE 1.(a) Drop exhibiting Cassie and Wenzel wetting states (b) Distribution of cosines of apparent contact angle of Cassie and Wenzel wetting state with respect to the cosine of intrinsic contact angle

$$cos\theta_w = cos\theta_c \tag{9}$$

$$r_{cr} = \frac{1-f}{1+f}\frac{1}{cos\theta} \tag{10}$$

$$r > \frac{1-f}{1+f}\frac{1}{cos\theta} \tag{11}$$

This is the required first condition to determine the transition between Wenzel and Cassie wetting state.

Second Condition of Wetting Transition

When roughness is introduced to a flat surface, the first wetting regime is Wenzel, and after achieving a sufficient roughness Cassie state occurs. The transition to Cassie wetting is obtained by increasing roughness, and before that critical value of surface roughness, any smaller value of roughness represent the Wenzel wetting regime. For this reason, we consider the apparent contact angle at the point of transition as predicted by Wenzel model.

The second condition for predicting the transition between Wenzel and Cassie wetting state is derived by equating the surface free energies at both Cassie and Wenzel wetting regimes. If we implement this condition to mathematical model, then we get a set of equations from (12) to (18). With the increase of '*r*' we are moving towards Cassie wetting state. So, to obtain the Cassie wetting state the roughness of the surface must exceed the critical roughness value, expressed in equation (18). Using the expression of critical value of the cosine of apparent contact angle and critical roughness, $cos\theta_{cr}$ and $r_{cr,}$ we can obtain the expression of equation (19) and equation (20). A similar work was performed by Bormashenko [4] for the hydrophobic surface at impregnating wetting condition. In short, the second condition, for determining transition between Wenzel and Cassie wetting state, states that for a rough surface exhibiting Cassie wetting state, the value of roughness must be greater than the ratio of cosines of critical apparent contact angle corresponding to that roughness and intrinsic apparent contact angle.

$$E_{casie} = E_{wenzel} \tag{12}$$

$$\sigma_{sf}\left[2H+W\right] - \sigma_{lf}\left[W\right] = \sigma_{sl}\left[2H+W\right] \tag{13}$$

Where, *H* is the height of the parallel microgroove; W is the width of the microgroove.

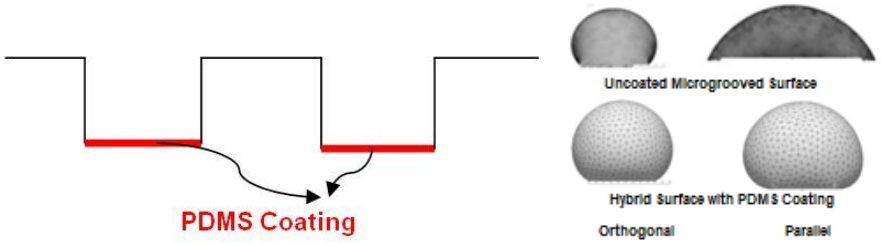

(a) (b)

FIGURE 2.(a) Schematic representation of a hybrid surface (b) Orthogonal and parallel contact angle increased significantly for hybrid microgrooved surface $D_G^{67}W_P^{26}W_G^{130}$

$$\frac{\sigma(sf)-\sigma(sl)}{\sigma(lf)}=\frac{W}{2H+W} \tag{14}$$

$$cos\theta_w=\frac{W}{2H+W} \tag{15}$$

$$cos\theta_w=\frac{1-f}{r-f} \tag{16}$$

$$r.cos\theta=\frac{1-f}{r-f} \tag{17}$$

$$r_{cr}=\frac{1-f}{r-f}\frac{1}{\cos\theta} \tag{18}$$

$$r>\frac{cos\theta\_critical}{cos\theta} \tag{19}$$

$$r>\frac{1-f}{r-f}\frac{1}{cos\theta} \tag{20}$$

This is the required second condition to determine the transition between Wenzel and Cassie wetting state.

Modelling study to determine the Cassie-Wenzel transition point on the intrinsically hydrophilic surface is very rare in the open literature. With this presently developed analytical model, prediction of transition between Cassie and Wenzel state is possible using only the topography of the roughness. In case of an intrinsically hydrophilic surface, if the Cassie roughness factor '*f*' is varied, then the derived first condition of equation (11) is applicable to determine the critical roughness. But if the roughness factor '*r*' is varied, then the derived second condition of equation (20) is valid to determine the transition point.

In addition to the prediction of Cassie-Wenzel transition point of pure metal surfaces, this model is also capable of prediction the exact wetting state when the surface is hybrid. This model is applied on a periodically coated (PDMS) hybrid surface, as shown in Fig. 2(a). The observation was that the critical dimension of roughness for exhibiting Cassie wetting state is changed significantly. When the results of hybrid surface are compared with that of an uncoated microgrooved surface (depth of groove 67 µm and width of groove 130 µm), it can be seen that the width of pillar requirement for exhibiting Cassie wetting state is 27 µm whereas in case of groove coated surface, this dimension is reduced to 20 µm. The sample nomenclature used in this work is in the format $D_G^XW_P^YW_G^Z$, where 'X', 'Y' and 'Z' represent the numerical values of Depth of groove (D_G), Width of Pillar (W_P), and Width of groove (W_G), respectively. For one of the sample surfaces $D_G^{67}W_P^{26}W_G^{130}$, the wetting state from numerical and experimental observation was Wenzel. However, if the groove surface is assumed to be coated with PDMS, then the wetting state becomes Cassie. This Wenzel to Cassie transition of wetting state for the same microgrooved surface gives significant rise in the both orthogonal and parallel contact angle, which is presented in Fig. 2(b). The orthogonal contact angle shifted to 155.2° from 131.6°, also the parallel contact angle increased from 60.8° to 163.2°. Moreover, for the surfaces with width of pillar 112 µm and width of groove 130 µm, the critical dimension of groove depth for wetting transition reduces from 54 µm to 49 µm.

RESULT ANALYSIS

Drop Shape Simulation of Microstructured Aluminum Surface

To verify the universality of the developed numerical model, it is now further applied for several Aluminium surfaces, which was experimentally investigated by Lipping Liu [18]. In their work, Lipping tried to introduce a surface embossing technique to enhance water drainage capability of Aluminium fin stock. They observed that smaller groove width, larger groove depth and steeper groove depths were favourable conditions for drainage enhancement. A similar trend has been observed in our numerical study. Most importantly, the numerical model can predict the orthogonal contact angle with significant accuracy, as we can see from Fig. 3(a). But there remains a significant variation in the case of parallel contact angle, as we can observe from Fig. 3(b); the reason behind this is the limitation while simulating a Wenzel wetting state. This limitation can be overcome by implementing the elongation ratio into the numerical model, which is described in detail in the following section.

Investigating the Unusual Spreading Phenomenon on the Microgrooved Brass Surface

In one of our earlier studies [14], an unusual spreading for the microgrooved surface with highest groove depth (sample $D_G^{122}W_P^{112}W_G^{130}$) was observed. It was hypothesized that for this sample, the cutting tools had to go through the highest number of tool passes for fabricating the deepest grooves surface, which resulted in significant tool wear and consequently surfaces with a high edge angle at the top and low rise angle at the bottom. In the present work, this critical experimental observation and hypothesis are validated analytically. Our analytical model suggests that, due to the machining, if the wall of the pillar is 22° inclined, the droplet will theoretically exhibit Wenzel wetting state. The schematic representation of this inclined pillar wall is given in Fig. 4(a). Moreover, in our earlier work [17], the numerically obtained results (SCA of 138.6° and CA 51.3° in the orthogonal and parallel to grove directions, respectively) showed a significant variation from that of the experimentally obtained results (SCA of 132.7° and 27.3°, respectively). So we put forward a more practical assumption for deep microgrooved surface and assumed a pillar inclination of 7°. For this case, the results were significantly improved (SCA of 135° and 53.4°). The orthogonal and parallel drop shapes of 7° inclined pillar wall are presented in Fig. 4(b,c).

It should be noted here that though the orthogonal CA exhibited an accuracy of 3° for the case of inclined pillar wall, the parallel SCA still exhibits a significant deviation from experimental result. This limitation was overcome when we included the experimentally observed elongation ratio (ratio of drop length in the parallel and orthogonal directions) [19] in the numerical model. For instance, when the experimentally found elongation ratio R=6 was used for the sample $D_G^{122}W_P^{112}W_G^{130}$, the orthogonal and parallel contact angle were 131.2° and 53.4° respectively. This provides a further enhancement of accuracy of the numerical model, capturing the wetting physics and wetting dynamics with more precision.

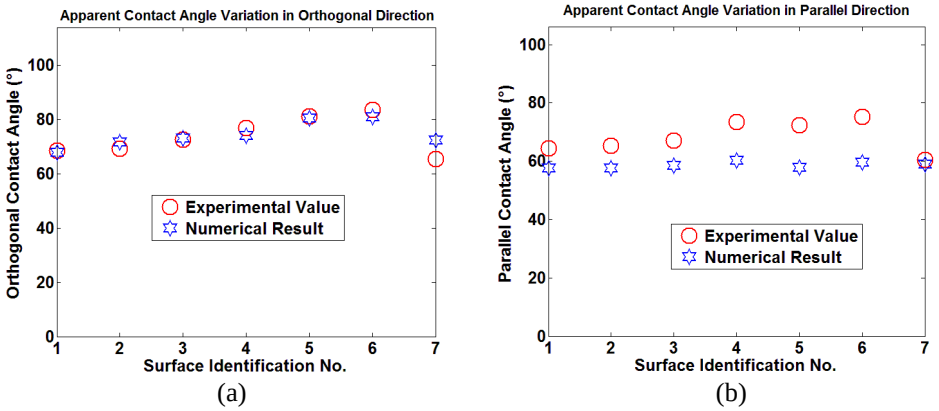

(a) (b)

FIGURE 3. Comparison between experimental and numerically obtained results reported in reference [18] with (a) Variation in the orthogonal direction, and (b) Variation in the parallel direction of grooves for aluminium surfaces with a variation of pillar

width and groove depth and keeping all other parameters constant (for drop volume= 10 µl)

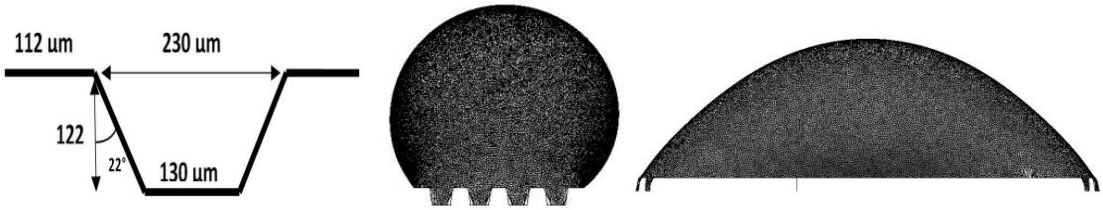

(a) (b) (c)

FIGURE4.(a) Schematic representation of inclined pillar wall for $D_G^{122}W_P^{112}W_G^{130}$ surface (b) Orthogonal view of droplet for $D_G^{122}W_P^{112}W_G^{130}$ surfaceat 7° inclination of pillar wall (c) corresponding paralle view.

SUMMARY

The proposed mathematical model offers an excellent tool for predicting the wetting state of the rough hydrophilic surface using its roughness geometry. The main objective of this work was to capture the wetting state and wetting dynamics accurately on microgrooved aluminium surfaces, along with the same on other designed microstructured surfaces. Wettability of a microgrooved brass or aluminum surface is significantly dependent on the homogeneity of the wetting regime, based on which Cassie (heterogeneous) and Wenzel (homogenous) wetting state can be formed. In this study, an analytical model is developed for both intrinsically hydrophilic and hydrophobic surface to determine the stable equilibrium wetting state (either Cassie or Wenzel) comparing the minimum free energy of each wetting state. This mathematical model is applied to eight microgrooved brass samples and seven microgrooved aluminium surfaces; this model successfully predicts the stable wetting state for each microgroove dimensions using the roughness ratio and the solid fraction, which matches completely with that of the experimental findings. Using this model, it can be observed that hybridization of the microgrooved surface (PDMS coating on the groove base) reduces the critical microgroove dimensions (groove depth and pillar width) for a water droplet to form Cassie wetting state over the substrate. The limitation of simulating Wenzel droplet are overcome by including the elongation ratio (ratio of lengths at the droplet base along the parallel and the orthogonal direction) into the numerical model.

REFERENCES

1. A. B. D. Cassie and S. Baxter, Transactions of the Faraday Society **40**, 546-551 (1944).
2. N. R. Wenzel, Ind. Eng. Chem.**28**, 988-994 (1936).
3. X. Xu and X. Wang, SIAM J. Appl. Math.**70**, 2929-2941 (2010).
4. E. Bormashenko, Advances in Colloid and Interface Science **222**, 92-103 (2015).
5. C. X. Ling and L. Tian, Science in China Series G: Physics, Mechanics & Astronomy **52**, 233-238 (2009).
6. E. Bormashenko, Phil. Trans. R. Soc. A **368**, 4695-4711 (2010).
7. X. Cui and W. Li, Journal of Colloid and Interface Science **347**, 156-162 (2010).
8. G. Alberti and A. DeSimone, Proceedings A: The Royal Society **461**, 79-97 (2005).
9. D. Murakami1, H. Jinnai1 and A. Takahara, Langmuir **30**, 2061-2067 (2014).
10. J. Bico, C. Tordeux and D. Qu´er´, Europhysics Letters **55**, 214-220 (2001).
11. A. Promraksa, Y. C. Chuang and L. J. Chen, Journal of Colloid and Interface Science **418**, 8-19 (2014).
12. N. A. Patankar, Langmuir **19**, 1249-1253 (2003).
13. M. E. Abdelsalam, P. N. Bartlett, T. Kelf and J. Baumberg, Langmuir **21**, 1753-1757 (2005).
14. M. A. Rahman and A. M. Jacobi, Langmuir **28**, 13441-13451 (2012).
15. L. Barbieri, "Wetting properties of flat-top periodically structured superhydrophobic surfaces," Ph.D. thesis, The University of Genoa, 2006.
16. Y. Chen, B. He, J. Lee and N. A. Patankar, Journal of Colloid and Interface Science **281**, 458–464 (2005).
17. N. Farhat, S. K. Alen and M. A. Rahman, Procedia Engineering **105**, 576-585 (2015).
18. L. Liu, "Effects of air-side surface wettability on the performance of dehumidifying heat exchangers," Ph.D. thesis, University of Illinois at Urbana-Champaign, 2011.

19. M. A. Rahman and A. M. Jacobi, Procedia Engineering **90**, 611-617 (2014).

ICME2015

International Conference on Mechanical Engineering 2015
(ICME 2015) 18 – 20 December, 2015, Dhaka, Bangladesh

Paper ID : 546

Water-shedding, retention and absorption characteristics of locally available building-wall coating materials

Nahid Sultan Al-Mamun[1], Md. Zobayer Hossain[1], Md. Ashiqur Rahman[a]

[1]*Department of Mechanical Engineering, Bangladesh University of Engineering and Technology (BUET), Dhaka-1000, Bangladesh*

[a] Corresponding author: ashiqurrahman@me.buet.ac.bd

Abstract. Manipulation of surface wettability by chemical coatings has been attempted for a long time by many researchers to obtain the desired wetting properties and maximize water repellency. In this study, the water-shedding performance of exterior coating materials (paints), which is a very important attribute that indicates the effectiveness of exterior paints subjected to different weather conditions, is systematically examined. A number of samples are fabricated from locally available mud-brick and ceramic brick and by applying normal and weather resistant exterior paints, and interior emulsion paint on both plastered and non-plastered surfaces. Static contact angles (SCA) are found to be in the range of 50° to 80° for different types of paints, bricks and surface conditions. SCA are observed to be higher in the direction of brush stroke during painting, for which direction roughness average is relatively smaller compared to the transverse direction. Sliding behavior of the water droplet is investigated for three different droplet sizes (10, 30, and 45 μL) and the critical sliding angle is found to decrease with the increase of droplet volume. But no significant difference in the sliding behavior of water droplets is observed between weatherproof paints and normal exterior paints. The rate of water retention and absorption are also studied on a dynamic dip test apparatus. Overall, water repellency characteristics are found to be relatively insensitive to paint type. However, the exterior paint-coated surfaces exhibit a significantly lower water absorption rate compared to the same without the coatings. The outcomes of this study can be important in characterizing and improving the water repellency properties of the commonly used building coating materials to prevent water from seeping through and protect the walls behind.

INTRODUCTION

Rain droplets splashing in a puddle, dew drops on leaf in a winter morning, colorful soap bubble formation – all these naturally occurring incidents are related to an important phenomenon termed as wetting. Manipulation of surface wettability has been attempted for a long time to obtain desired the wetting properties in a wide variety of applications ranging from self-cleaning surfaces, micro-fluidic devices, condensate drainage from heat exchangers, drainage of frost melt-water *etc*. It is carried out either by modifying the surface roughness or by applying coating of low/high surface energy over the baseline surface. When a liquid drop rests on a solid surface, it forms a particular shape on the solid surface depending on its wettability and is characterized by a contact angle (θ). Based on the contact angle, surfaces are mainly categorized into hydrophilic (θ<90°) and hydrophobic (θ>90°) surface.

One way to achieve hydrophobic surfaces is to manipulate the surface roughness of the material[1]. Miwa *et al.*[2] used particle deposition and vapor deposition method for creating a super hydrophobic coating of various roughness. In the past, most of the studies were based on Wenzel's and Cassie's surface energy concept[3-5]. A proposal of enhanced droplet mobility induced by increased roughness was proposed by Chan *et al.*[6]. Frenkel[7] first originally studied the sliding motion of liquid drops and presented a theory to estimate the tilting angle at which liquid drops will slide from surface. Water drainage/retention behavior on a surface is also of great importance. Dynamic dip testing approach is now extensively used as a tool for assessing drainage behavior[8-10] as it is considered to be a simple, inexpensive and relatively fast method.

Surface coatings such as emulsion paints are used in building wall not only for decorative purpose but also to protect the wall from dirt, absorption of moisture and rain water etc. Being exposed to adverse environmental conditions, exterior building walls need more protection than interior walls and that is why exterior paints should incorporate some additional features like better water repellence, low water retention and absorption rate. If the water repellency attributes are incorporated into building-wall coating materials, the applied coatings (paint) can act to drain water quickly from the wall surface and therefore, will have less chance for water absorption.

The present study demonstrates the water-shedding performance of commonly available building-wall coatings (paints) in Bangladesh and systematically quantifies and compares their behaviors in terms of wetting, retention and absorption characteristics. To accomplish this objective, SCA and the critical sliding angle (roll-off angle) of water droplets on a number of paint-coated surfaces were determined with specifically fabricated apparatus. Water absorption and retention characteristics were also assessed using a dynamic dip test apparatus.

EXPERIMENTAL METHODOLOGY

Sample Fabrication

A number of samples were fabricated using different types of widely used wall paints in Bangladesh on locally available building wall materials – mud-bricks and ceramic bricks. Table 1 shows the dimensions, nature of paint applied and surface characteristics of these samples. After applying the cement-coat (plastering) over the brick samples, all the samples were polished with fine wall polishing silicon carbide abrasive paper to reduce the roughness and wall putty was used to remove any prominent sized indentation and fill cavity and cracks (if any) on the surfaces. This was done to follow the traditional practice used for cement-plastered building walls in Bangladesh. During applying the different paints, brush stroke was applied uniformly to make the surface characteristics as homogeneous as possible. After preparing the samples, surface roughness was measured in both transverse and parallel direction using a profilometer (*Surtronic 25*).

TABLE 1. Description of the test samples used

Sample Code		Roughness (μm)				Paint Type	Surface Condition
Mud brick	Ceramic brick	Mud-brick		Ceramic brick			
		Transverse	Parallel	Transverse	parallel		
WM01	WC01	6.2	1.8	5.6	3.0	Weatherproof	No cement coat
WM02	WC02	5.2	3.6	7.0	3.0	Weatherproof	No cement coat
EM03	EC03	6.8	5.4	5.2	3.0	Normal Exterior	No cement coat
IM04	IC04	5.2	3.6	4.2	2.8	Interior paint	No cement coat
WM05	WC05	6.2	3.6	5.4	2.8	Weatherproof	No cement coat
WM11	WC11	5.6	2.0	5.6	2.4	Weatherproof	Cement coated
WM12	WC12	4.6	2.6	4.6	2.8	Weatherproof	Cement coated
EM13	EC13	5.2	2.0	7.2	2.8	Normal Exterior	Cement coated
IM14	IC14	5.2	2.6	3.8	2.8	Interior paint	Cement coated
WM15	WC15	5.6	1.8	6.0	2.0	Weatherproof	Cement coated

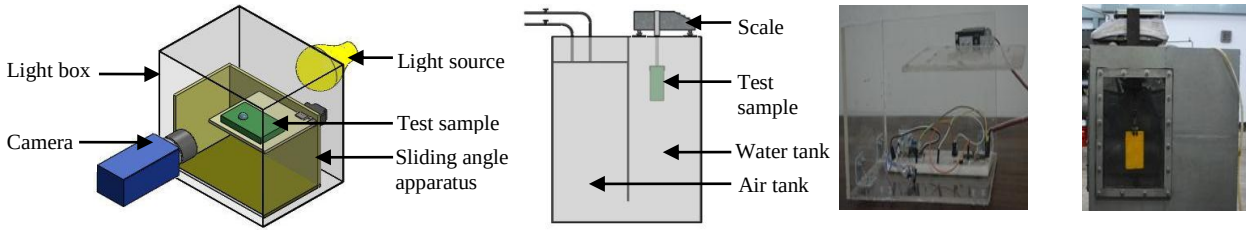

FIGURE 1. Schematic of (a) sliding angle measuring arrangement, and (b) dynamic dip-test arrangement; Specifically designed and fabricated (c) Experimental sliding angle apparatus; (d) Dynamic dip-test apparatus.

Static Contact Angle and Sliding Angle Measurement

SCA was measured by placing sessile water droplets (8 μL) on the horizontal surface of each test sample. Sliding angles were evaluated on a sliding angle apparatus which consisted of a solid platform which could be rotated from a horizontal position to the vertical position at a constant rotational speed (1.5°/sec) by a program controlled servo-motor (Figs. 1(a) & (c)). To find the sliding angle, sessile water droplet was placed on the sample surface which was mounted on a horizontal platform. The platform was then tilted until the droplet slides off the surface completely. Droplet size of 10, 30 and 45 μL were injected on the test surface using micro-syringes. During both SCA and sliding angle measurement, a CCD camera (*pco.1600*) was used to record the full procedure at a rate of 17 frames per second. For improved imaging a light box was used during recording. Images from both SCA and sliding angle procedures were analyzed using standard image processing software *ImageJ*®. SCA and sliding angle both were measured in parallel and transverse direction of brush stroke and repeated at least for four different positions for each test sample.

Water Retention and Absorption Rate Measurement

Water retention and absorption rates were measured using a dynamic dip test apparatus which works on the principle of water-volume displacement (Figs. 1(b) & (d)). It had individual water and air reservoirs. An electronic scale was placed on a platform over the water reservoir and test sample was suspended into the water tank. Pressurized air from compressor was supplied into the air chamber that caused the water level to rise and submerge the test sample. After specific time period pressurized air was released suddenly into atmosphere to drop the water level rapidly and the electronic scale reading was recorded. The samples were submerged for 15 seconds for water retention test and for 30 minutes during water absorption test. Data was recorded in every 2 minutes.

RESULT AND DISCUSSION

Static Contact Angle Results

Wettability of the sample surfaces were quantified in terms of static contact angle (SCA). Overall range for SCA for all sample were found out 50-80 degree (Table 2), which confirmed hydrophilic nature of all coating. For the same surface condition and same coating, SCA for mud brick samples was found to be higher than the ceramic brick samples. Among the weatherproof paints, the maximum SCA value was observed for paint W5 on mud brick for both plastered and non-plastered sample. In case of ceramic brick, maximum SCA was found for W5 &W2 for non-plastered surface and plastered surface respectively. Moreover, the maximum SCA value was found for interior emulsion paint I4.

TABLE 2. Static contact angle data for all the samples in the parallel and transverse directions of brush stroke

Sample Code		Contact Angle, θ(°)						Surface Condition
Mud-brick	Ceramic brick	Mud-brick			Ceramic brick			
		Transverse	Parallel	Average	Transverse	parallel	Average	
WM01	WC01	63.3	65.0	64.1	51.5	62.0	56.7	Non-plastered
WM02	WC02	63.8	68.9	66.3	51.3	61.6	56.5	Non-plastered
EM03	EC03	65.7	67.0	66.4	52.3	64.1	58.2	Non-plastered
IM04	IC04	70.9	77.3	77.1	66.7	72.9	69.5	Non-plastered
WM05	WC05	63.9	66.6	65.2	55.3	62.5	58.9	Non-plastered
WM11	WC11	62.9	69.5	66.2	60.2	59.2	59.7	Plastered
WM12	WC12	65.3	72.1	68.6	53.3	55.4	55.3	Plastered
EM13	EC13	53.6	70.3	61.9	54.6	55.3	55.0	Plastered
IM14	IC14	64.7	73.4	70.0	75.0	75.1	75.0	Plastered
WM15	WC15	65.9	72.5	69.2	57.2	65.0	61.1	Plastered

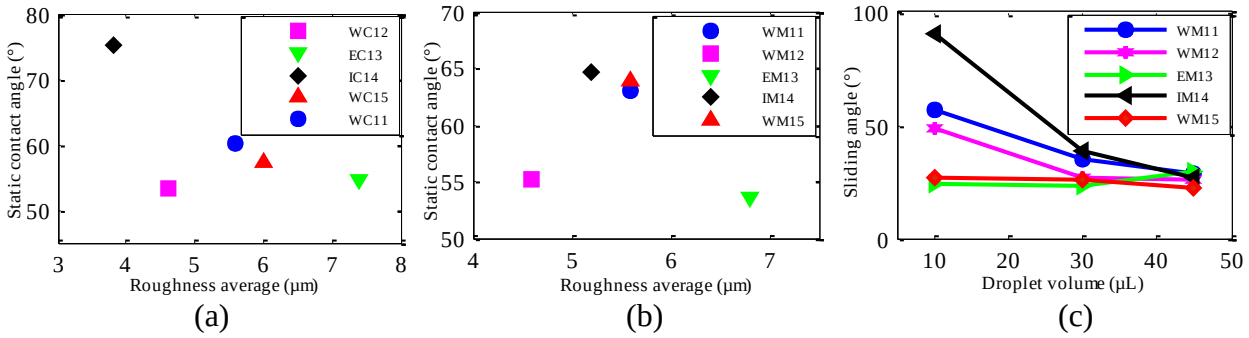

FIGURE 2. Variation of SCA with average surface roughness (Ra) for (a) plastered ceramic and (b) mud brick samples in transverse direction. (c) Variation of sliding angle with droplet volume for plastered mud-brick samples. Sliding angle decreases with the increase of droplet volume.

Variation of SCA for same paint on different surface conditions is caused by three factors: surface heterogeneity, surface roughness and impurities on surface. Variation of surface roughness was induced on the samples due to paint brush stroke. Intensified roughness in transverse direction amplified the hydrophilic property of surfaces which results in lower SCA. Roughness average for any sample without paint is much higher than surface painted with any type of paint. From Figs. 2(a) & (b), it can be seen that the SCA decreased for plastered brick with increasing roughness average. Similar types of results were found for non-plastered samples. In case of samples without any coating on the surface, complete wetting phenomena was observed.

Sliding Angle Results

Effect of Droplet Volume

Figure 2(c) exhibits the variation of sliding angle with droplet volume for plastered mud-brick samples in transverse direction. Augmented gravitational force of higher droplet volume beats out the capillary force at a lower inclination angle and hastens the sliding phenomena. For sample WM11, sliding angles were 56.7°, 35.1°, and 28.8° for water droplet volumes of 10 µL, 30 µL, and 45 µL, respectively. Three other samples also showed same pattern but EM13 shows a different pattern. In case of EM13, the sliding angle at 45 µL was greater than that of at 10 and 30 µL. In case of ceramic-brick samples, sliding angle showed same variety with different volume of droplet. There were also little inconsistencies in those data which are neglected. In general, sliding angle for any surface decreased with increase of water droplet volume regardless of surface condition and types of brick.

Relationship of SCA and Sliding Angle

In general, hydrophilic surfaces are usually associated with lower SCA and higher sliding angle. So there is an inverse relationship between SCA and sliding angle on the same surface. In our study, all samples (except IC14) showed similar relation of SCA and sliding angle at 45 µl droplet. Reason behind this inverse relationship of contact angle and sliding angle is the variations in the adhesive and cohesive energy of various surface. For hydrophilic surfaces, adhesive energy between solid surface and liquid is higher than that of hydrophobic surfaces. This higher adhesive surface energy results in a lower contact angle (<90°).In case of sliding phenomena the higher adhesive energy of surface tries to stick the water droplet to surface even in higher inclination angle of surface. Figs. 3(a) & (b) exhibit variation of sliding angle of 45 µl with SCA for plastered mud and ceramic brick samples .Non-plastered samples also showed similar type of relationship between sliding angle and SCA with some exceptions.

Water Retention Characteristics

The water retention characteristics of the different coatings were examined by submerging the plastered samples under water for a specific period of time (15 seconds) in a Dip-test apparatus. Water retention properties are represented in terms of the amount of water retained per unit area on the sample surface for ease of comparison. Similar to the SCA phenomenon, increased surface roughness in the transverse direction amplified the hydrophilicity of a surface and for a particular coating, a higher sliding angle was found in the transverse direction than the same in

the parallel direction. Variation of sliding angle in transverse and parallel direction for samples WC01 and WM01 are shown in Fig. 3(c). Among the plastered mud-brick samples, maximum retained water per unit area was found for WM11 (2.47 mg/cm^2) and minimum for WM15 (1.85 mg/cm^2). Again, in case of ceramic bricks, maximum value was found for WC12 (2.88 mg/cm^2) and the minimum for IC13 (1.24 mg/cm^2). Figs. 4(a) & (b) show variation of water retention of plastered ceramic and mud brick samples. Slight variation of amount of retained water per unit area were emerged from variation of wetting properties of surfaces. Surfaces with lower SCA (enhanced wetting properties) showed lower water retention than surface of higher SCA (except IC14 & IM14). Sample IC14, with a relatively high SCA in the parallel direction, showed higher water retention characteristic compared to others samples having lower SCA values. This indicates the poor water-shedding behavior of interior paint *4* even though it had higher static contact angle. This might be due to compositional difference in manufacturing process of interior paints with that of the exterior paints.

Water Absorption Characteristics

The effectiveness of using different types of paints in terms of water absorption was investigated for few cement coated samples. There was no significant difference in water absorption for different painted samples. Variation of water absorption with time for coated and uncoated surfaces is shown in fig 4(c). All coated samples exhibited almost similar behavior regardless of the paint type and brick type. The amount of water absorption varies almost linearly with time for minimum 30 minutes and after that absorption rate reduced slowly. All painted surfaces reduced the amount of water absorbed to a significant level compared to any uncoated plastered surface. Any painted surface reduces the amount of water absorption for about 75% than any plastered surface without paint. So painted surface showed a good resistance to seeping of water through the building wall to a good extend but, it did not matter much whether the paint was weatherproof or normal paint.

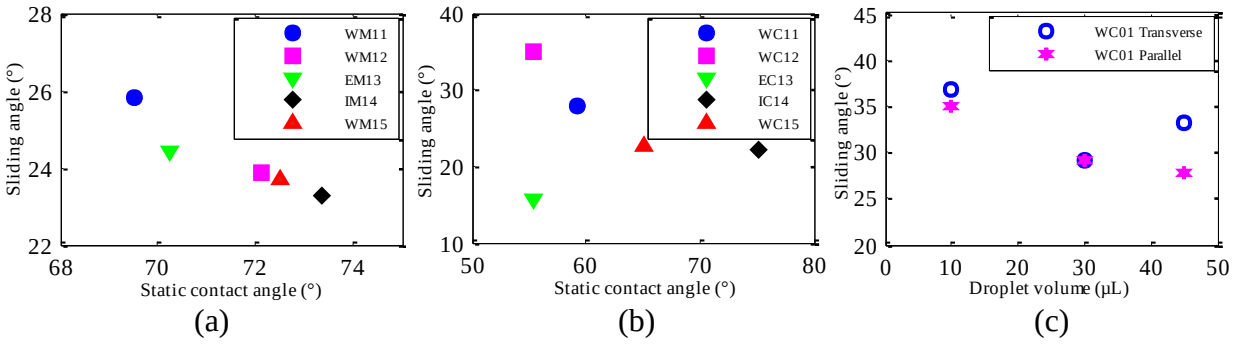

FIGURE 3. Variation of sliding angle (in the parallel direction) with static contact angle for (a) plastered mud and (b) ceramic brick samples at droplet size of 45μl. Sliding angle decreases with increasing static contact angle. (c) Variation of sliding angle with droplet volume in transverse and parallel direction of sample WC01. Sliding angle in the transverse direction is higher than the same in the parallel direction.

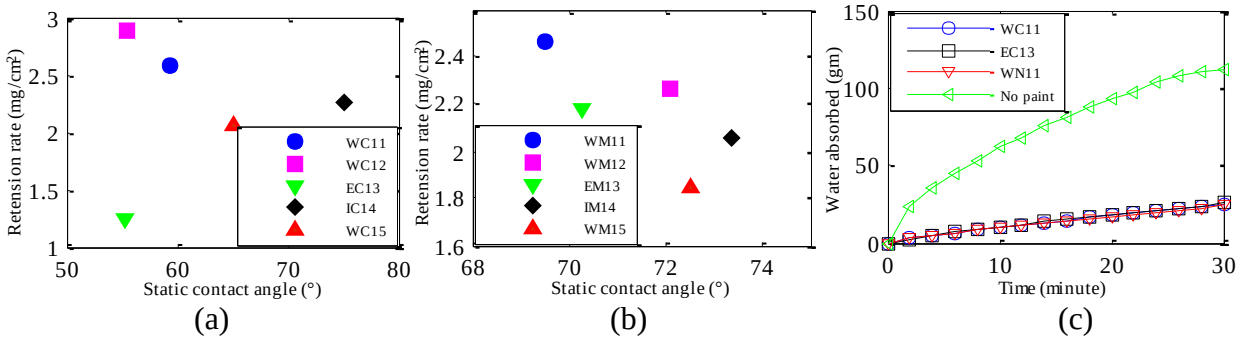

FIGURE 4. Variation of water retention with SCA of (a) ceramic and (b) mud brick in the parallel direction. Retention rate decreases with an increase of SCA. (c) Variation of absorption with time for the coated and non-coated surfaces. Amount of absorbed water increases with time.

CONCLUSION

Water-shedding behavior of exterior building wall coatings (paints) have been studied experimentally to compare the effectiveness of different paint types (weatherproof, normal exterior and interior) in terms of wettability, water retention and absorption characteristics. Sample surfaces and required experimental apparatus for sliding angle measurement and dynamic dip testing were designed and fabricated. Sliding behavior of water droplet on sample surfaces was enhanced with the increase of droplet volume. SCA and sliding angle showed better performance in terms of water-shedding in the parallel direction of paint brush stroke in which direction surface roughness was relatively lower. There was no significant variation in the drainage behavior of water on different paint-coated surfaces. Although the interior paint-coated sample exhibited a higher SCA, in terms of water retention its water-shedding property was found to be poor compared to other exterior paints. A significant (about 75%) reduction in water absorption was found for surfaces with coating than plastered surface without any coating. But all the painted surfaces behaved almost similar in terms of water absorption regardless of the paint type and brick type and followed approximately a linear relationship with time. Usually, weatherproof paints are claimed to be water repellent paint along with its other superior features, but in this study we found that the performance of weatherproof and normal exterior paints was nearly similar in terms of wetting and water retention characteristics.

REFERENCES

1. J. Drelich, A. Marmur, "Physics and applications of superhydrophobic and superhydrophilicsurfaces and coatings," Surface Innovations **2**, 211-227 (2013).
2. M. Miwa, A. Nakajima, A. Fujishima, K. Hashimoto, T. Watanabe, "Effects of surface roughness on sliding angles of water droplets on superhydrophobic surfaces," Langmuir **16**, 5754-5760 (2000).
3. R.N. Wenzel, "Resistance to solid surfaces to wetting by water," Industrial and Engineering Chemistry **28**, 988-994 (1936).
4. A. B. D. Cassie, S. Baxter, "Wettability of porous surface," Transactions of the Faraday Society **40**, 546-551 (1944).
5. R. N. Wenzel, "Surface roughness and contact angle," J. Phys. Colloid Chem. **53**, 1466-1467 (1949).
6. W. Chen, "Ultrahydrophobic and ultralyophobic surfaces: some comments and examples," Langmuir **15**, 3395-3399 (1999).
7. Y. I. Frenkel, "Sliding motion on liquid droplets," J. Exp. Theor. Phys. **18**, 659 (1948).
8. Y. Zhong, A. M. Joardar, Z. P. Gu, A. M. Jacobi, "Dynamic dip testing as a method to assess the condensate drainage behavior from the air-side surface of compact heat exchangers," Exp. Therm. Fluid Sci. **29**, 957–970 (2005).
9. L. Liu, A. M. Jacobi, "Issues affecting the reliability of dynamic dip testing as a method to assess the condensate drainage behavior from the air-side surface of dehumidifying heat exchangers," Exp. Therm. Fluid Sci. **32**, 1512–1522 (2008).
10. J. Kaiser, Y. Zhong, A. M. Jacobi, C. Zhang, "Condensate retention and dynamic drainage from the air-side surface of automotive-style heat exchanger," Proceedings of the International Conference on Compact Heat Exchangers and Enhancement Technology for the Process Industries 361–366 (2003).

ICME2015

International Conference on Mechanical Engineering 2015
(ICME 2015) 18 – 20 December, 2015, Dhaka, Bangladesh

Paper ID : 564

Fuel Properties and Engine Performance of Biodiesel from Waste Cooking Oil Collected in Dhaka City

R B Islam[1, a)], R Islam[1, b)], M N Uddin[1, c)] , Md Ehsan[1, d)] and P H Riley[2]

[1]*Department of Mechanical Engineering, Bangladesh University of Engineering and Technology, Dhaka-1000, Bangladesh.*
[2]*Department of Electrical Engineering, University of Nottingham, Nottingham NG7 2RD, United Kingdom*

[a)]Corresponding author: rifat.buetme145@gmail.com
[b)]masummsm@gmail.com
[d)] ehsan@me.buet.ac.bd

Abstract. Waste cooking oil can be a potential source of biodiesel that has least effect on the edible oil consumption. Increasing number of hotel-restaurants and more active monitoring by health authorities have increased the generation of waste cooking oil significantly in densely populated cities like Dhaka. If not used or disposed properly, waste cooking oil itself may generate lot of environmental issues. In this work, waste cooking oils from different restaurants within Dhaka City were collected and some relevant properties of these waste oils were measured. Based on the samples studied one with the highest potential as biodiesel feed was identified and processed for engine performance. Standard trans-esterification process was used to produce biodiesel from the selected waste cooking oil. Biodiesel blends of B20 and B40 category were made and tested on a single cylinder direct injection diesel engine. Engine performance parameters included – bhp, bsfc and exhaust emission for rated and part load conditions. Results give a quantitative assessment of the potential of using biodiesel from waste cooking oil as fuel for diesel engines in Bangladesh.

INTRODUCTION

As the fossil fuel is depleting day by day importance of alternative fuel is increasing. Biodiesel refers to any diesel fuel substitute derived from renewable biomass. Chemically, it can be defined as a fuel composed of mono-alkyl esters of long chain fatty acids derived from renewable sources, such as vegetable oil, animal fat, and waste cooking oil. Biodiesel is a very good source of alternative fuel. It is renewable, biodegradable and can have better exhaust gas emission [1]. These characters make it a very promising alternative of diesel.

Although in terms of engine performance, exhaust gas emission and it's renew ability, biodiesel is a very good alternative fuel of diesel, but higher cost and limited availability always have been critical issues for biodiesel production [1,2]. High cost of vegetable oil and associated processing costs led to higher production cost of biodiesel than diesel. There have been issues related to the food and heath value of edible oil and reservations regarding its use as an engine fuel [3,4]. On the other hand, several billions of gallons of waste cooking oil (WCO) are produced every year around the world, significant portion of it is wasted and ending up in land-fill sites which is harmful to the environment. Therefore, it makes commercial, technical and environmental sense to re-use this oil for making biodiesel. As the production process of biodiesel from WCO is similar to the production of biodiesel from straight vegetable oil, biodiesel produced from WCO makes biodiesel significantly cheaper [5]. Waste oil is produced by potato processing plants, factories manufacturing foods, and hotel-restaurants. In some factories waste oil is reused but most of the hotel and restaurants dump it in the environment. In densely populated area significant amount of waste oil is produced form hotel and restaurants. So waste cooking oil can be a very good source of biodiesel with lower cost [6]. Properties of waste oil differs from waste vegetable oil and various hotels

and restaurants produce various quality of waste cooking oil. Very little information in this regard is available in public domain.

In this study waste cooking oil samples were collected from different hotels and restaurants within Dhaka city and some important fuel properties like – calorific value, density, viscosity etc. were measured to assess the degree of property variations. Soybean and/or Palm oil are most commonly used for cooking in Dhaka. The WCO sample with best potential was then processed to biodiesel using transesterification method. Two volumetric blends of this biodiesel from WCO (B20 and B40) with diesel fuel were made and tested on a single cylinder CI engine. Engine performance and emission analysis was done at various loads and compared with diesel only operation.

Nomenclature

BHP	Brake Horse Power	Bsfc	Brake Specific Fuel Consumption	HHV	Higher Heating Value
HSU	Hertzian Smoke Unit	SVO	Straight Vegetable Oil	WCO	Waste Cooking Oil

SURVEY ON WCO AND FUEL PROPERTIES

Various hotels and restaurants at Dhaka produce different qualities of waste cooking oils, since they reuse the cooking oils for different cooking conditions and durations. As the properties could vary from case to case, it was important to find out the range of such variations. Based on observation the hotels and restaurants were categorized into three broad groups. High Quality(Group-1), Moderate Quality(Group-2) and Low Quality(Group-3) hotels and restaurants – were grouped based on the level of congeniality of their environment of kitchen and food preparation. 13 samples of waste cooking oil were collected from different hotels and restaurants around Dhaka City, which often required a lot of persuasion. Different fuel properties of the collected samples were measured like - viscosity, density, water content, calorific value etc. and an assessment was made on the range through which properties varied with different categories of hotels and restaurants. The variation of measured properties for each group is given in TABLE 1 - 3. These are compared with commonly used vegetable oils like soybean and palm oil and diesel fuel [7,8].

Although darker in color compared to cooking oil in most cases the measured density of collected WCO samples did not varying significantly (less than ±1%) among samples from all groups. However kinematic viscosity of WCO samples were measured (Saybolt Viscosimeter following ASTM D88) found to vary over a range of 64 to 88 mm^2/sec, showing 54 - 93% increase compared to soybean. Since the variations were found in samples of all groups, the effect of cooking time was further studied on one sample. A group-2 WCO sample was tested after – 1 hour, 2 hour and 3 hour cooking time (TABLE 3). This showed – 46, 54 and 79% increase in kinematic viscosity but small change in density. In most of the hotel vegetable oil was reported to be used for 2-4 hour. Viscosity of the samples were found to be changed significantly over the time of cooking. Heating value measurement (Bomb calorimeter following ASTM D240) of sample collected varied slightly compared to soybean however HHV of sample collected from one group-3 sample was about 4% higher than others probably due to higher proportion of palm oil was used here for cooking. Water content of every sample (Centrifuge following ASTM D1796) was found to be negligible. In general increase of viscosity of WCO was a concern regarding their use as a CI engine fuel directly. Density, viscosity and heating value of the processed biodiesel and its B20 and B40 blend with diesel were tested later to assess their usability in diesel engines.

TABLE 1. Range of density and viscosity found.

Groups	Density (g/cm^3)	Kinematic Viscosity (mm^2/sec)	Viscosity increase compared to Soybean
Soybean	0.916	42	-
Group 1	0.916-0.923	66.9-68.9	59 – 64 %
Group 2	0.922-0.926	64.7-79.2	54 – 88 %
Group 3	0.911-0.924	65.7-81.3	56 – 93 %

TABLE 2. Calorific values

Oil	HHV (Cal/gm)	HHV (MJ/kg)
Diesel	10632	44
Soybean/ Palm Oil	9143.4	38.2 / 41
Waste oil collected from Group-1	8973.1	37.5
Waste oil collected from Group-3	9343.1	39.1

TABLE 3. Properties of cooking oil over time of cooking

Time of cooking (hrs)	Density (gm/cc)	Kinematic Viscosity (mm^2/sec)	Viscosity increase compared to Soybean
Before cooking	0.910	42	-
1 hour after cooking	0.916	61.6	46 %
2 hours after cooking	0.916	64.9	54 %
3 hours after cooking	0.92	75.4	79 %

TABLE 4. Trans-Esterification Data

Sample of waste oil	3.75 L
Method used	Base-Catayl SST
Methanol mixed	0.825 L
KOH	150 gm (2%)
Blending Speed	200 rpm
Blending time	1 hr
Settling time	7 hr
Biodiesel produced	3.6 L
Biodiesel yield (volm)	95 %

PROCESSING

Before use waste cooking oil for engine performance it need to be processed and converted into biodiesel by transesterification. A WCO sample was selected on the basis of availability and property values for transesterification process. After making biodiesel two blends were made and tested in a single cylinder CI engine.

Transesterification

Straight Vegetable Oil(SVO) is not typically used in engines directly as it reduces engine life by the build up of carbon deposits inside the engine and the build up of impurities in the engine lubricant. These issues are attributable to SVO's high viscosity and high boiling point relative to the required boiling range for diesel fuel[9]. Transesterification is the most common process to reduce the high viscosity of the SVO and enable it to use in common engine without much problem [9,10]. Chemically it is the process of exchanging the organic group of an ester with the organic group of an alcohol. This reaction is catalyzed by the addition of an acid or base catalyst. However, in homogeneous catalysis, alkali catalysis (sodium or potassium hydroxide; or the corresponding alkoxides) is a much more rapid process than acid catalysis [11]. Recent study shows that for waste cooking oil KOH is very effective as a catalyst. As alcohol generally methanol is used largely because it is least expensive. Most effective alcohol: vegetable oil molar ratio in terms of cost and reaction speed is 6:1. In order to give the transesterification maximum yield, the alcohol and waste oil should be free of moisture [6,11]. For transesterification process methanol as alcohol and KOH was used as catalyst. Methanol to waste cooking oil ratio

was 5:1. Weight of KOH was 2% of the weight of waste cooking oil. Relevant parameters are shown in TABLE 4.

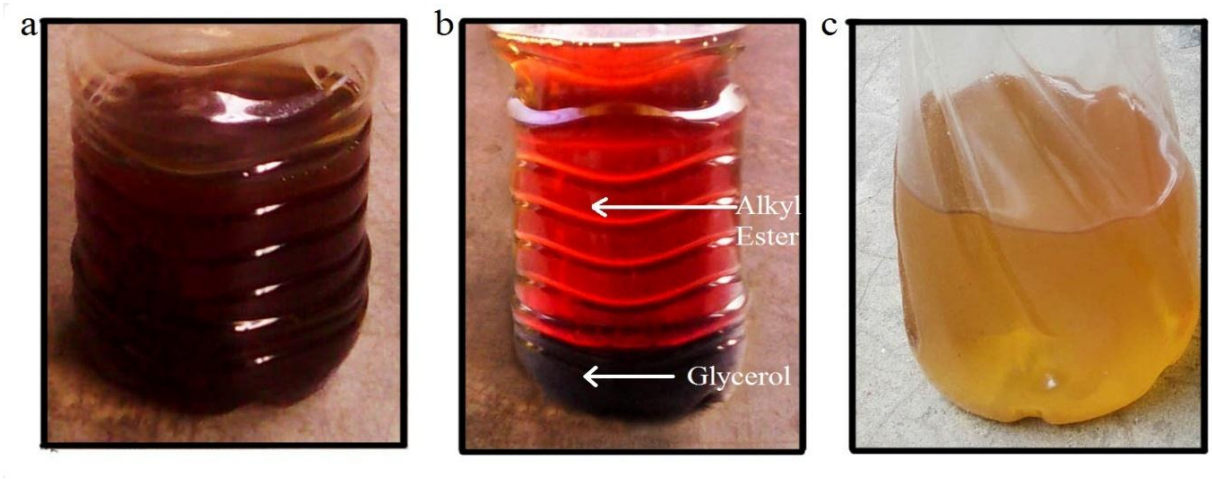

FIGURE 1. (a) waste vegetable oil; (b) Layer of alkyl ester and glycerol during transesterification; (c) Blending of biodiesel and Diesel

Blending

After transesterification two blends of biodiesel were made. One is B20, it is a volumetric mixture of 20% biodiesel with diesel, and the other one is B40, that is 40% volume of biodiesel mixed with diesel. Properties of these blends with biodiesel and waste cooking oil are shown in TABLE 5. Density of the biodiesel produced from the WCO was found to be 8.8% higher compared to Diesel. This would offset the 14% lower heating value of biodiesel to some extent during injection of limited volume of fuel during combustion. However, the viscosity of processed biodiesel was found to be significantly reduced (by about 90%) compared to WCO making it similar to diesel fuel. This indicates the improved usability of biodiesel in diesel engines. Bending of 20% and 40% biodiesel by volume with diesel fuel was made and their heating values were calculated accordingly. B20 has a heating value of 42.6 MJ/kg and B40 has a heating value of 41.3 MJ/kg which is 3.2% and 6.1% less compared to diesel fuel.

TABLE 5. Properties of waste cooking oil, biodiesel and their blends

Item	Density (gm/cm^3)	Kinematic viscosity (mm^2/sec)	Higher heating value (MJ/kg)
Waste cooking oil	0.921	66.7	37.5
100% Biodiesel	0.914	5.4	37.6
Diesel	0840	3.9	44
(B20) 20% blending with diesel	0.855	4.7	42.6
(B40) 40% blending with diesel	0.87	5.2	41.3

ENGINE PERFORMANCE TEST

Engine performance of biodiesel and diesel blends were tested in a 353 cc, water cooled, single cylinder CI engine. Rated power and speed of the engine was 3.5 kW and 1800 rpm. Experimental setup consisted of engine bed, water brake dynamometer, load indicator, supply tank and measurement devices to measure diesel and biodiesel flow rate. K type thermocouples were used to measure the temperature of the exhaust gas and the lubricating oil. Exhaust emission was measured using AVL-1000 smoke meter to access the opacity level of the engine exhaust.

Engine was run with diesel near the rate speed of 1800rpm for a range of variable load conditions and the engine power, speed and fuel consumption rate was calculated. When tested with biodiesel blends the engine was initially run with diesel for about 15minutes before switching to blended mixtures and before turning it off. Laboratory test results were standardized using derating method BS 5514:1987.

Result of the Engine Performance Test

Variation of Bsfc and efficiency with power produced are shown in FIGURE 2 and 3 respectively. Break specific fuel consumption was found to be highest when the engine is running with low power. This decreases when engine power approached the rated power of the engine and then slightly increases at the end. Break specific fuel consumption for diesel was found to be lower than for biodiesel. It increased slightly as the percentage of biodiesel in the blends increases. Biodiesel blends have heating value 3-6% lower than diesel, so more fuel is requires to attain same power as diesel. Since the density and heating values of the diesel and the two blends tried are different, the real comparative picture is exhibited in the variation of thermal efficiency. The thermal efficiency of diesel was found to be highest for diesel and slightly lower for B20 and B40. The small increase in viscosity may be responsible for less uniform dispersion of the fuel injection that has effect on the combustion and heat release. Lubricating oil temperature and exhaust for both diesel and biodiesel blends increases as the engine power increases. The effect of the fuel-blend on the exhaust gas temperature was found to be very small. This indicated that rate of NOx formation for biodiesel blends would not be very different for the formation with diesel operation [12].

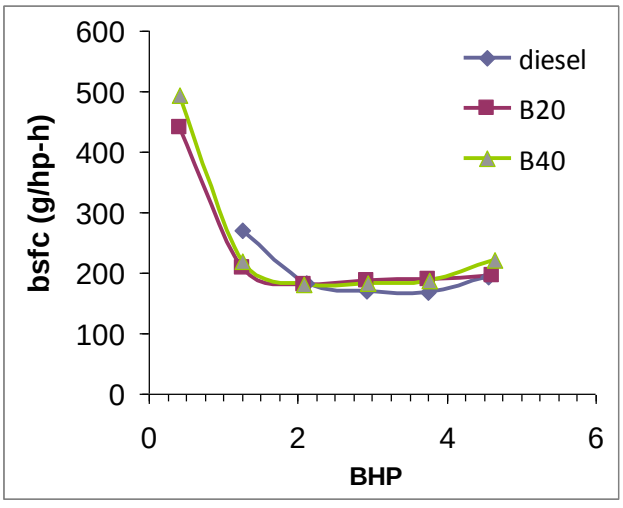

FIGURE 2. Bsfc vs BHP at fixed speed

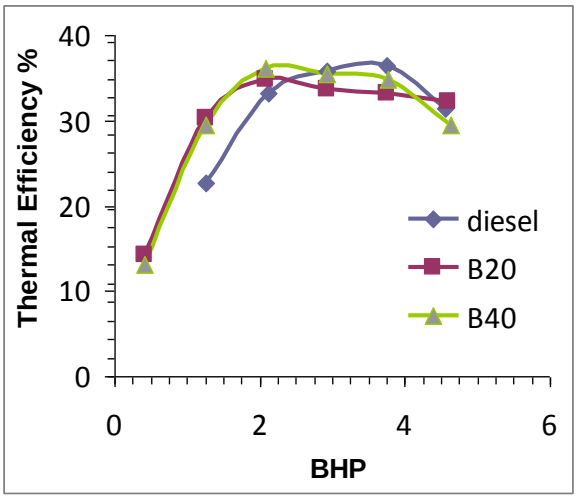

FIGURE 3. Thermal efficiency vs BHP

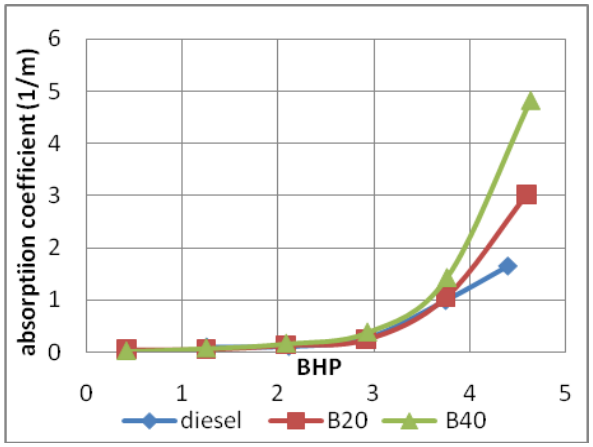

FIGURE 4. Absorption coefficient vs BHP

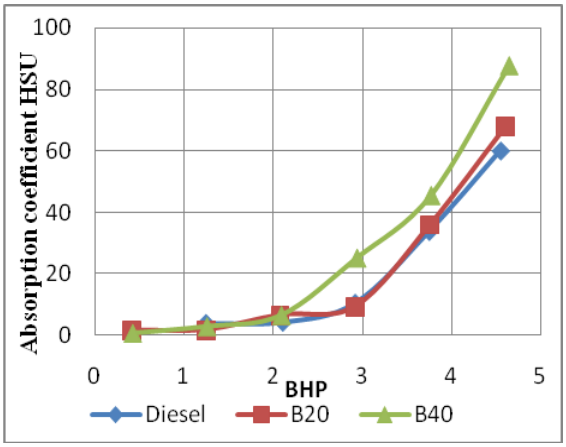

FIGURE 5. Opacity in HSU

Result of Exhaust Emission Measurements

The exhaust gas from diesel engine contains soot and particulate matters which may quickly clog the filters and sampling channel of a 4-gas exhaust analyser, typically used for SI engines. Hence a smoke meter, which operates on the light absorption principle was used to get opacity variation of the diesel exhaust. The opacity is an optical property that refers to the ability to stop light from being transmitted. The opacity variation of the engine exhaust was measured in terms of light absorption coefficient (k-factor). The absorption coefficient determines how far into a material light of a particular wavelength can penetrate before it is absorbed. The measurement was also converted to equivalent Hertzian Smoke Unit (HSU), often referred in emission standards. FIGURE 4 shows the variation of light absorption coefficient of exhaust with engine power. FIGURE 5 shows the same expressed in HSU. Results showed that exhaust gas emission was not affected by the use of biodiesel except near full load. As mentioned earlier due to higher viscosity the dispersion of the fuel injection of the biodiesel blends causes slightly inferior combustion. This is not very evident at lower loads due to the abundance of excess air but becomes significant to affect the opacity and light absorption at higher loads.

CONCLUSIONS

- The kinematic viscosity of waste vegetable oil varies in a wide range and it is even higher than pure soybean and much higher than diesel which makes it difficult to be used directly in CI engine**.** Kinematic viscosity of waste oil depended upon cooking time, it was found to increase as the cooking time increases.
- After transesterification and blending with diesel kinematic viscosity reduces largely to comparable values with respect to diesel, allowing it to be used as a potential diesel fuel replacement in CI engines.
- The higher heating value of waste cooking oil was found to be only slightly less than the values of soybean. It is about 14% less than the higher heating values of diesel. After transesterification and blending higher heating value of B20 blend was found to be 3.2% less and the same of B40 blend was 6.1% less than diesel.
- Engine efficiency and power output from waste cooking oil was found to be comparable with those attined with diesel. However lower heating value of biodiesel blends caused the bsfc values to be a little higher.
- Exhaust gas temperature were very close for different blend of biodiesel and diesel. This indicates using biodiesel from waste cooking oil should not change the rate of NOx formation.

- Emission test result shows that smoke produced from using biodiesel is similar in opacity at lower part loads but higher opacity compared to diesel when engine was operated at higher loads near rated power.

REFERENCES

1. Biodiesel Handbook GehardKnothe, Jon Van Gerpen, Jurgenkrahl. Published by AOCS press 2005.
2. Anh N. Phan, Tan M. Phan. Biodiesel production from waste cooking oils 2008; 87:3490–3496.
3. L. Rubianto, et al., I. J. Engg. Sci. **2,** 28-32 (2013).
4. A. Gnanaprakasam, et al., J. of Energy **1,** 1-10 (2013).
5. M. M. Zamberi, et al., J. Engg. Tech. **2**, 55-65 (2011).
6. Ehsan M., Chowdhury M.H.T., "Production of Biodiesel Using Alkaline Based Catalysts from Waste Cooking Oil: A Case Study", Procedia Engineering 105 (2015), Elsevier Science Direct, pp. 638-645, 6th BSME International Conference on Thermal Engineering (ICTE 2014), IUT, Dhaka 20-21 December, 2014.
7. Knothe G., Steidley K., Fuel **84**, 1059–1065 (2005).
8. B. Esteban et al., Biomass and Bio Energy **142**, 164-17 (2012).
9. A. Demirbas, Energy Conversion and Management. **50**, 923-927 (2008).
10. D. Y. C. Leung, X. Wu, M. K. H. Leung, Applied Energy **87**, 1083-1095 (2010).
11. Y. Zhang, et al., Bioresource Technology **89,** 1-16 (2003).
12. Jinlin Xuea et. al., Elsevier Renewable and Sustainable Energy Reviews **15**, 1098–1116 (2011).

ICME2015

International Conference on Mechanical Engineering 2015
(ICME 2015) 18 – 20 December, 2015, Dhaka, Bangladesh

Paper ID : 570

MHD Heat and Mass Transfer Stratified Fluid Flow Through a Vertical Plate with Viscous Dissipation, Radiation and Thermal Diffusion

M. M. Mukitul Hasan[1,a)] and Md. Mahmud Alam[2,b)]

[1]*Department of Mathematics, Khulna Public College, Khulna-9000, Bangladesh*
[2]*Mathematics Discipline, Khulna University, Khulna-9208, Khulna, Bangladesh*

[b)]Corresponding author: alam_mahmud2000@yahoo.com
[a)]mukitulh@gmail.com

Abstract. The unsteady MHD heat and mass transfer stratified fluid flow through a vertical plate with viscous dissipation, radiation and thermal diffusion have been studied. To obtain dimensionless non-similar coupled nonlinear momentum, energy and concentration equations, usual non-dimensional variables have been used. The explicit finite difference technique has been used to solve the dimensionless equations. Also the stability and convergence analysis have been used for measuring the restriction of usual parameters. The obtained numerical results have been presented graphically and discussed in details. The present results have been compared with the previous results.

INTRODUCTION

Free convection heat and mass transfer for the stratified fluid is a natural phenomenon. Now a day's the international researcher's attention for the heat and mass transfer is on stratified fluid flow due to its endless possibilities in scientific, engineering and Industrial works. Hall current is also important concern in Astrophysics, Geophysical and Engineering applications. The effect of stratification has great impact on heat and mass transfer. Stratification occurred in fluids because of variation of temperature and concentration differences. Recently we can see the application of stratified fluid flow is increasing. It is used in nuclear power plants, Geophysical flows, biomedical technology, ceramics industries, Environmental sciences, food processing, chemical electrolytic reactors etc. Siegel [1] studied transient free convection from a vertical flat plate. Yang et al. [2] explored laminar free convection from a non-isothermal plate immersed in a temperature stratified medium. Jaluria et al.[3] explored stability and transition of buoyancy induced flows in a stratified medium. Free convection from a vertical flat plate to a thermally stratified darcian fluid has been studied by Takhar et al.[4]. Henkes et al.[5] explored laminar natural convection boundary-layer flow along a heated vertical plate in a stratified environment. M.A. Hossain et al.[6]studied viscous dissipation effects on natural convection from a vertical plate with uniform surface heat flux placed in a thermally stratified media. P.Gansen et al.[7] reported viscous heating effects in doubly stratified free convection flow over vertical plate radiation and chemical reaction. The present study, therefore, MHD heat and mass transfer stratified fluid flow through a vertical plate with viscous dissipation, radiation and thermal diffusion. The obtained non-similar partial differential equations have been solved by explicit finite difference method [8]. The obtained results have been shown graphically as well as in tabular form.

MATHEMATICAL MODEL OF FLOW

Consider an MHD free convection heat and mass transfer flow of an electrically conducting viscous, incompressible, stratified fluid through a vertical plate $y = 0$. Considered the Cartesian coordinates x ,measured along the plate surface and y is the coordinate measured normal to the plate surface and z is the coordinate normal to the plate.

The flow is assumed to be in the x direction. At first, the fluid temperature and the plate temperature are same and it is T_∞ and concentration C_∞ .At time $t > 0$, the temperature of the plate is raised to T_w and concentration near the plate is raised to C_w. For the ambient fluid, the temperature and concentration increase linearly with the height, where $T_{\infty,0}$ and $C_{\infty,0}$ being the values at $x = 0$. The Roseland approximation [9] is expressed for radiative heat flux and leads to the form as,

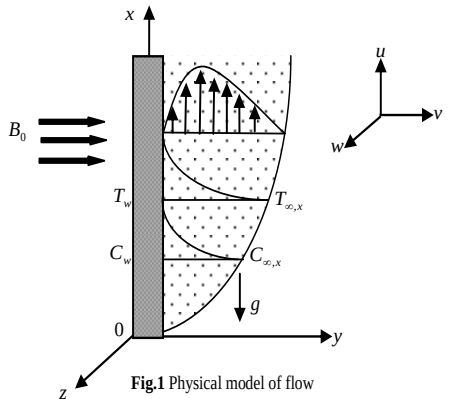

Fig.1 Physical model of flow

$$q_r = -\frac{4\sigma^*}{3k^*}\frac{\partial T^4}{\partial y} \tag{1}$$

Where k^* is the mean absorption coefficient σ^* is the Stefan-Boltzmann constant. The temperature difference with in the flow is sufficiently small. So that T^4 may be expressed as a linear function of the temperature, then the Taylor's series about T_∞ after neglecting higher order terms,

$$T^4 \cong 4TT_\infty^4 - 3T_\infty^3 \tag{2}$$

The dimensionless variables are as follows;

$$X = \frac{x}{L};\ Y = \frac{y}{L}G_r^{\frac{1}{4}};\ U = \frac{uL}{\upsilon}G_r^{\frac{-1}{2}};\ V = \frac{vL}{\upsilon}G_r^{\frac{-1}{4}};\ \overline{T} = \frac{\left(T - T_{\infty,x}\right)}{\left(T_w - T_{\infty,0}\right)};\ \overline{C} = \frac{\left(C - C_{\infty,x}\right)}{\left(C_w - C_{\infty,x}\right)};\ \tau = \frac{t\upsilon}{L^2}G_r^{\frac{1}{2}}$$

By using these non-dimensional quantities into the equations (1)-(5); we get the following dimensionless equations

$$\frac{\partial U}{\partial X} + \frac{\partial V}{\partial Y} = 0 \tag{3}$$

$$\frac{\partial U}{\partial \tau} + U\frac{\partial U}{\partial X} + V\frac{\partial U}{\partial Y} = \frac{\partial^2 U}{\partial Y^2} + \overline{T} + B_f\overline{C} - \frac{M}{\left(1+m^2\right)}\left(U + mW\right) \tag{4}$$

$$\frac{\partial W}{\partial \tau} + U\frac{\partial W}{\partial X} + V\frac{\partial W}{\partial Y} = \frac{\partial^2 W}{\partial Y^2} + \frac{M}{\left(1+m^2\right)}\left(mU - W\right) \tag{5}$$

$$\frac{\partial \overline{T}}{\partial \tau} + U\frac{\partial \overline{T}}{\partial X} + V\frac{\partial \overline{T}}{\partial Y} = \left(\frac{1+R}{P_r}\right)\frac{\partial^2 \overline{T}}{\partial Y^2} + E_c\left\{\left(\frac{\partial U}{\partial Y}\right)^2 + \left(\frac{\partial W}{\partial Y}\right)^2\right\} - S_T U \tag{6}$$

$$\frac{\partial \overline{C}}{\partial \tau} + U\frac{\partial \overline{C}}{\partial X} + V\frac{\partial \overline{C}}{\partial Y} = \frac{1}{S_c}\frac{\partial^2 \overline{C}}{\partial Y^2} + S_r\frac{\partial^2 \overline{T}}{\partial Y^2} - S_M U \tag{7}$$

The corresponding boundary conditions are as;

$$\left.\begin{array}{l} U=0, V=0,\ W=0,\ \overline{T}=1,\ \overline{C}=1 \text{ at } Y=0 \\ U\to 0,\ W\to 0,\ \overline{T}\to 0,\ \overline{C}\to 0 \quad \text{as } Y\to\infty \end{array}\right\} \quad \text{When } \tau>0 \tag{8}$$

The non-dimensional quantities are; $B_f = \dfrac{\beta_C\left(C-C_{\infty,x}\right)}{\beta_T\left(T-T_{\infty,0}\right)}$ (Bouncy frequency), $M = \dfrac{\sigma B_0^2 L^2}{\rho\upsilon} G_r^{\frac{-1}{2}}$ (Magnetic parameter), $P_r = \dfrac{\upsilon}{\alpha}$ (prandtl number), $R = \dfrac{16\sigma^* T_\infty^3}{3kk^*}$ (Radiation parameter), $E_c = \dfrac{\upsilon^2 G_r}{L^2 C_p\left(T_w-T_{\infty,0}\right)}$ (Eckert number), $S_T = \dfrac{\gamma_T L}{\left(T_w-T_{\infty,0}\right)}$ (Thermal stratification parameter), $S_c = \dfrac{\upsilon}{D}$ (Smidth number), $S_r = \dfrac{Dk_t\left(T_w-T_{\infty,0}\right)}{T_m\left(C_w-C_{\infty,0}\right)}$ (Soret number), $S_M = \dfrac{\gamma_C L}{\left(C_w-C_{\infty,0}\right)}$ (Mass stratification parameter), $G_r = \dfrac{g\beta L^3\left(T_w-T_{\infty,0}\right)}{\upsilon^2}$ (Thermal Grashof number), $G_r = \dfrac{g\beta^* L^3\left(C_w-C_{\infty,0}\right)}{\upsilon^2}$ (Mass Grashof number). Where $\gamma_T \equiv \dfrac{dT_{\infty,x}}{dx} + \dfrac{g}{C_p}$ and $\gamma_C \equiv \dfrac{dC_{\infty,x}}{dx} + \dfrac{g}{C_p}$, here $\dfrac{dT_{\infty,x}}{dx}$ represents the vertical thermal advection term and $\dfrac{dC_{\infty,x}}{dx}$ represents the vertical mass advection term. $\dfrac{g}{C_p}$ is the pressure work term known as compression. If the work of compression is very small then we can take $\gamma_T \equiv \dfrac{dT_{\infty,x}}{dx}$ and $\gamma_C \equiv \dfrac{dC_{\infty,x}}{dx}$.

SHEAR STRESS, NUSSELT NUMBER AND SHERWOOD NUMBER

From the velocity field, the effects of different parameters on the shear stress have been calculated. The local and average shear stress, for the primary velocity $\tau_{XL} \propto \left(\dfrac{\partial U}{\partial Y}\right)_{Y=0}$ and $\tau_{XA} \propto \int_0^{100}\left(\dfrac{\partial U}{\partial Y}\right)_{Y=0} dX$. For the secondary velocity, the local and average shear stress are, $\tau_{ZL} \propto \left(\dfrac{\partial W}{\partial Y}\right)_{Y=0}$ and $\tau_{ZA} \propto \int_0^{100}\left(\dfrac{\partial W}{\partial Y}\right)_{Y=0} dX$ respectively. From the temperature field different parameters on Nusselt number have been investigated. The local and average Nusselt number, $N_{uL} \propto \left(\dfrac{\partial \overline{T}}{\partial Y}\right)_{Y=0}$ and $N_{uA} \propto -\int_0^{100}\left(\dfrac{\partial \overline{T}}{\partial Y}\right)_{Y=0} dX$. And from concentration field, the local and average Sherwood number, $S_{hL} \propto \left(\dfrac{\partial \overline{C}}{\partial Y}\right)_{Y=0}$ and $S_{hA} \propto -\int_0^{100}\left(\dfrac{\partial \overline{C}}{\partial Y}\right)_{Y=0} dX$.

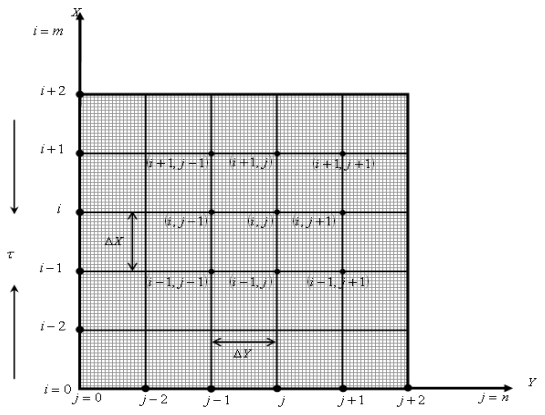

FIGURE 2. Explicit finite difference system grid

NUMERICAL SOLUTIONS

To solve the non-dimensional system by the explicit finite difference method, it is required a set of finite difference equation. To obtain the difference equations the region of the flow is divided into a grid or mesh of lines parallel to X and Y axes where X -axis is taken along the plate and Y -axis is normal to the plate. Here the plate of height $X_{\max}(=100)$ is measured i.e. X varies from 0 to 100 and assumed $Y_{\max}(=25)$ as corresponding to $Y\to\infty$ i.e. Y varies from 0 to 25 .There are $m(=200)$ and $n(=200)$ grid spacing in the X and Y directions respectively as shown Fig. 2. ΔX , ΔY are constant mesh size along X and Y directions respectively and taken as follows, $\Delta X=1.00(0\le X\le 100)$ and $\Delta Y=0.25(0\le Y\le 25)$ with the smaller time-step, $\Delta\tau=0.005$ .Let U', W', $\overline{T}'$ and $\overline{C}'$ denote the values of U, W, $\overline{T}$ and $\overline{C}$ at the end of a time-step respectively.

Using the explicit finite difference approximation, the system of partial differential equations (3)-(7) and the boundary conditions (8), an appropriate set of finite difference equations have been obtained as;

$$\frac{U'_{i,j}-U'_{i-1,j}}{\Delta X}+\frac{V'_{i,j}-V'_{i,j-1}}{\Delta Y}=0 \tag{9}$$

$$\frac{U'_{i,j}-U_{i,j}}{\Delta\tau}+U_{i,j}\frac{U_{i,j}-U_{i-1,j}}{\Delta X}+V_{i,j}\frac{U_{i,j+1}-U_{i,j}}{\Delta Y}=\frac{U_{i,j+1}-2U_{i,j}+U_{i,j-1}}{(\Delta Y)^2}+\overline{T}_{i,j}+B_f\overline{C}-\frac{M}{(1+m^2)}\left(U_{i,j}+mW_{i,j}\right) \tag{10}$$

$$\frac{W'_{i,j}-W_{i,j}}{\Delta\tau}+U_{i,j}\frac{W_{i,j}-W_{i-1,j}}{\Delta X}+V_{i,j}\frac{W_{i,j+1}-W_{i,j}}{\Delta Y}=\frac{W_{i,j+1}-2W_{i,j}+W_{i,j-1}}{(\Delta Y)^2}+\frac{M}{(1+m^2)}\left(mU_{i,j}-W_{i,j}\right) \tag{11}$$

$$\frac{\overline{T}'_{i,j}-\overline{T}_{i,j}}{\Delta\tau}+U_{i,j}\frac{\overline{T}_{i,j}-\overline{T}_{i-1,j}}{\Delta X}+V_{i,j}\frac{\overline{T}_{i,j+1}-\overline{T}_{i,j}}{\Delta Y}=\left(\frac{1+R}{P_r}\right)\left(\frac{\overline{T}_{i,j+1}-2\overline{T}_{i,j}+\overline{T}_{i,j-1}}{(\Delta Y)^2}\right)$$
$$+E_c\left\{\left(\frac{U_{i,j+1}-U_{i,j}}{\Delta Y}\right)^2+\left(\frac{W_{i,j+1}-W_{i,j}}{\Delta Y}\right)^2\right\}-S_TU_{i,j} \tag{12}$$

$$\frac{\overline{C}'_{i,j}-\overline{C}_{i,j}}{\Delta\tau}+U_{i,j}\frac{\overline{C}_{i,j}-\overline{C}_{i-1,j}}{\Delta X}+V_{i,j}\frac{\overline{C}_{i,j+1}-\overline{C}_{i,j}}{\Delta Y}=$$

$$\frac{1}{S_c}\left(\frac{\overline{C}_{i,j+1}-2\overline{C}_{i,j}+\overline{C}_{i,j-1}}{(\Delta Y)^2}\right)+S_r\left(\frac{\overline{T}_{i,j+1}-2\overline{T}_{i,j}+\overline{T}_{i,j-1}}{(\Delta Y)^2}\right)-S_M U_{i,j} \quad (13)$$

With initial and boundary conditions;

$$U^n_{i,0}=1,\ V^n_{i,0}=0,\ W^n_{i,0}=0,\ \overline{T}^n_{i,0}=1,\ \overline{C}^n_{i,0}=1 \quad (14)$$

$$U^n_{i,L}=0,\ V^n_{i,L}=0,\ W^n_{i,L}=0,\ \overline{T}^n_{i,L}=0,\ \overline{C}^n_{i,L}=0,\quad \text{where } L\to\infty$$

Here the subscripts i and j designate the grid points with X and Y coordinates respectively and the subscript n represents a value of time, $\tau=n\Delta\tau$ where $n=0,1,2,3,..$ The stability conditions of the method does not show for the brevity.

RESULTS AND DISCUSSION

In order to investigate the physical significant of the problem, the numerical values of primary velocity, secondary velocity, temperature and concentration within the boundary layer have been computed for different values of various parameters. To obtain the steady-state solutions, the calculations have been carried out up to non-dimensional time $\tau=5$ to 80.It is observed that the numerical values of $U, W, \overline{T}$ and $\overline{C}$ however, show little changes after $\tau=50$. Hence at $\tau=50$ the solutions of all variables are steady-state solutions. In Fig.3 it represents that the local shear stresses in x and $z-$direction is increasing with the increase of Hall parameter. In Fig.4 local shear stress in x and $z-$direction has been illustrated for different values of Thermal stratification parameter. It represents that the local shear stress in x and z- direction are decreasing with the increase of Thermal stratification parameter. Fig.5 indicates the local Nusselt number increasing with the increase of Thermal stratification parameter while the local Sherwood number decreasing with the increase of the different values of Thermal stratification parameter. Fig.6 represents the average Nusselt number and the average Sherwood number for the different values of Thermal stratification parameter. In this figure we can see that the average Nusselt number and Sherwood number is decreasing with the increase of Thermal stratification parameter. Fig.7 represents the local Nusselt number and the local Sherwood number for the different values of Mass stratification parameter. In this figure we can see that the local Nusselt number and Sherwood number is increasing with the increase of Mass stratification parameter.

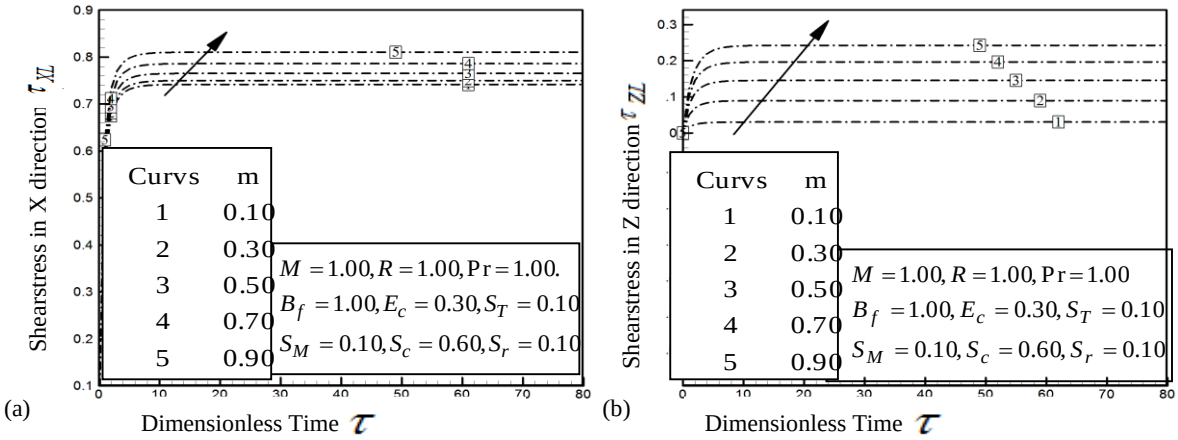

FIGURE 3. (a) Local shear stress in x-direction and (b) Local shear stress in z-direction for the different values of Hall parameter m.

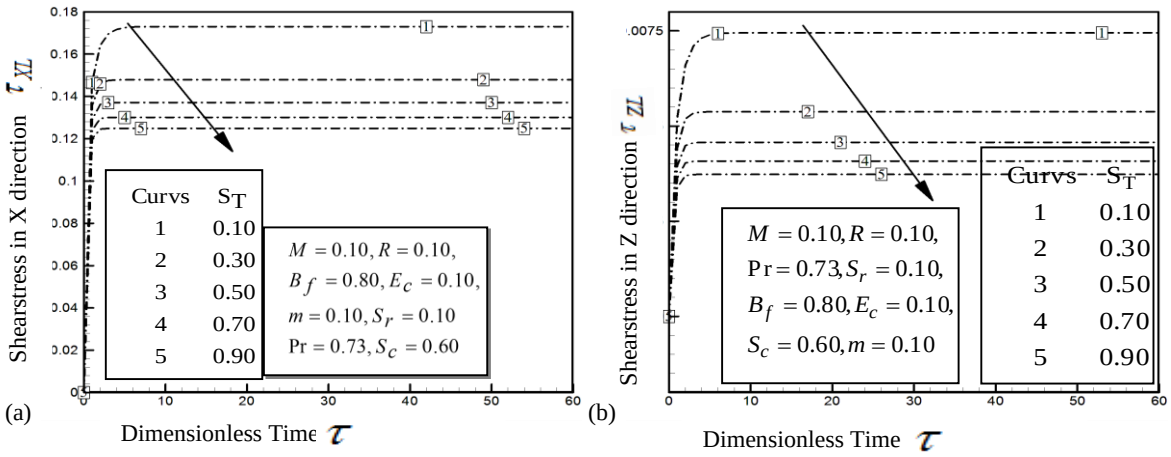

FIGURE 4. (a) Local shear stress in x-direction and (b) local shear stress in z-direction for the different values of Stratification parameter S_T .

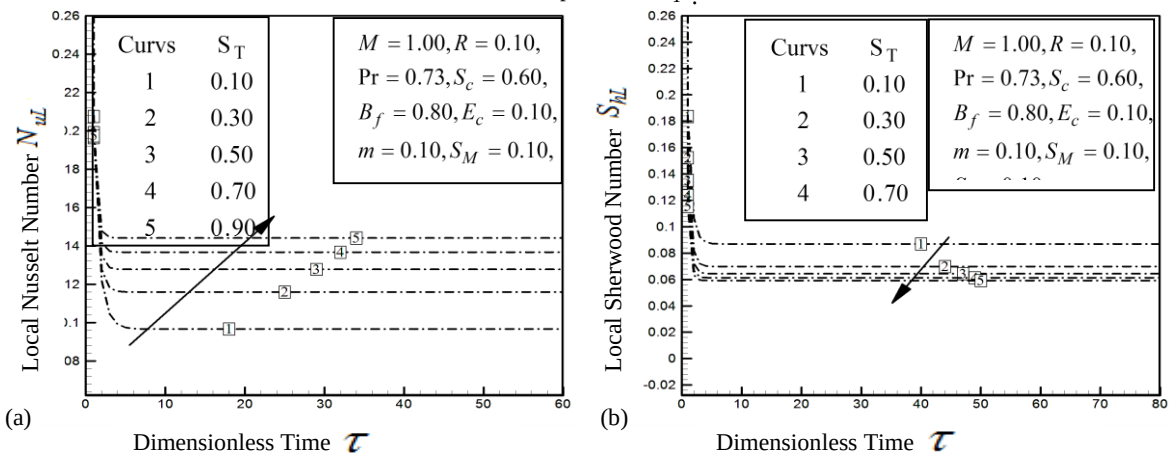

FIGURE 5. (a) Local Nusselt number and (b) Local Sherwood number for the different values of Thermal stratification parameter .

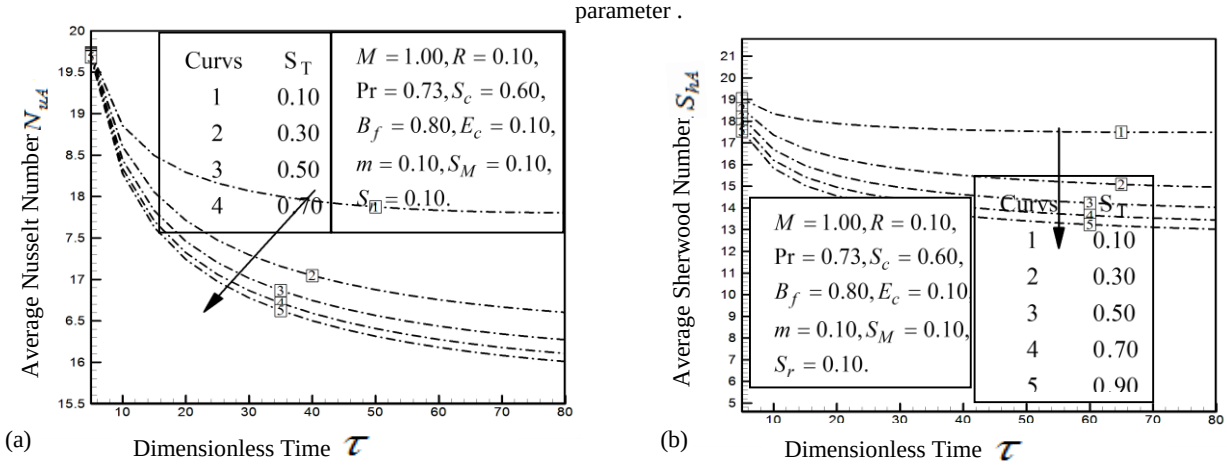

FIGURE 6. (a) Average Nusselt number and (b) average Sherwood number for the different values of Thermal stratification parameter S_T

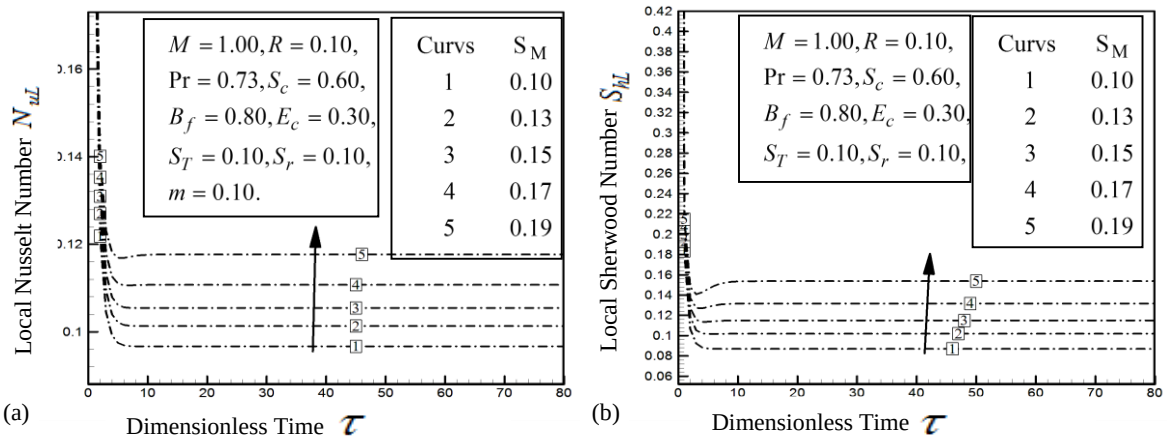

FIGURE 7. (a) Local Nusselt number and (b) local Sherwood number for the different values of Mass stratification parameter.

CONCLUSION

The finite difference solution of MHD heat and mass transfer stratified fluid flow through a vertical plate with viscous dissipation, radiation and thermal diffusion is investigated. The exactness of our outcome is qualitatively good in case of all parameters. Some significant findings of this study are specified below;

(i) The local shear stress in x and $z-$direction is increasing with the increase of Hall parameter.

(ii) The local Shear stress in x and $z-$direction is decreasing with the increase of Thermal stratification parameter.

(iii) The local Nusselt number is increasing with the increase of Thermal and Mass stratification parameter.

(iv) The local Sherwood number is decreasing with the increase of Thermal stratification parameter while the local Sherwood number is increasing with the increase of Thermal stratification parameter.

(v) The average Nusselt number and Sherwood number is decreasing with the increase of Thermal stratification parameter.

REFERENCES

1. R. Siegel, *ASME Journal of Heat Transfer* **80**,347–359 (1958).
2. K.T. Yang, J.L. Novotny, Y.S. Cheng, *International. J. Heat Mass Transfer* **15,** 1097–1109 (1972).
3. Y. Jaluria, B. Gebhart, *J. Fluid Mech*. **65** 593–612 (1974).
4. R. A. W. M.Henkes, and C. J.Hoogendoorn, *Int. J. Heat Mass Transfer* **32**, 147–155 (1989).
5. M.A. Hossain, S.C. Saha, and R.S.R. Gorla, *Int. J. Fluid Mech. Res.* **32,** 269-280 (2005).
6. P.Gansen, R .K.Suganthi,P.Loganathan, *Applied Mathematics and Mechanics(English Edition)* **34 (2)**, 139-152 (2013).
7. Herrmann Schlichting, Boundary Layer Theory,John Wiley and Sons, New York, 1969.
8. W.M. Rohsenow, J.P. Harnett,Y.I. Cho, Handbook of Heat transfer, 3rd edition, McGraw-Hill, New York, 1998.

ICME2015

International Conference on Mechanical Engineering 2015
(ICME 2015) 18 – 20 December, 2015, Dhaka, Bangladesh

Paper ID : 585

Simulation of Reflooding on Two Parallel Heated Channel by TRACE

Md. Ghulam Zakir

Department of Nuclear Engineering,

Chalmers University of Technology, Gothenburg, Sweden.

Paban81@gmail.com

Abstract

In case of Loss-Of-Coolant accident (LOCA) in a Boiling Water Reactor (BWR), heat generated in the nuclear fuel is not adequately removed because of the decrease of the coolant mass flow rate in the reactor core. This fact leads to an increase of the fuel temperature that can cause damage to the core and leakage of the radioactive fission products. In order to reflood the core and to discontinue the increase of temperature, an Emergency Core Cooling System (ECCS) delivers water under this kind of conditions. This study is an investigation of how the power distribution between two channels can affect the process of reflooding when the emergency water is injected from the top of the channels. The peak cladding temperature (PCT) on LOCA transient for different axial level is determined as well. A thermal-hydraulic system code TRACE has been used. A TRACE model of the two heated channels has been developed, and three hypothetical cases with different power distributions have been studied. Later, a comparison between a simulated and experimental data has been shown as well.

1. Introduction

Nuclear energy has become an important part of world electricity generation system. A reasonable portion of total world electricity demand is fulfilled by approximately 440 nuclear reactors located all around the world [1].Almost half of this number of reactors will operate for several decades in the future. The energy demand in both developed and developing countries will be doubled by the end of 2030 and electricity consumption will increase by 50% [2]. The situation will be critical in developing countries where energy crisis results in economic problems, poverty as well as low life standards. Nuclear power can make a significant contribution to eliminate this energy crisis with its low running cost and energy security. In addition to this, abundance of natural uranium resource is 14.8 million tons which can provide nuclear energy for the next 270 years [3]. Furthermore, technical advancements can enhance the efficiency of nuclear power plants and spent nuclear fuel reprocessing techniques can solve the economic problems if Uranium price goes high. So far several technologies have been implemented to convert the nuclear energy into electrical energy. However, light water reactor (LWR) technologies, pressurized water reactor (PWR) and boiling water reactor (BWR), have become well-known since these technologies are used in the majority of power plants of USA and France [4].

Several features such as safe nuclear operation, lower radiation dose to the workers and lower probability of accident in nuclear reactor can make this technology more reliable than before.

Safety is one of the fundamental requirements for development and expansion of nuclear industry. The Safety of nuclear power plants (NPPs) is not only related to safe nuclear operation but also associated with minimizing the consequence of severe nuclear accidents. Nuclear reactor safety is based on the concept of defense-in-depth [5].

One of the crucial aspects in nuclear power plant safety involves the analysis of large break loss-of-coolant accidents (LOCAs). In this kind of scenario, the inventory of core coolant is lost from a break in one of the main pipes. Thus the heat generated because of the decay of the fission products in the core cannot be removed and the temperature of the fuel rods increases. In order to avoid severe damage of the core, an emergency core cooling system (ECCS) is used to provide water on the core. The water delivered by this safety system can stop the temperature increase in the core, and prevent the core from melting.

In BWRs the emergency water can be injected from the top of the core, so that the core can be reflooded and the cooling of the fuel rods can occur.

In this study, a thermal hydraulic complete code TRAC/RELAP Advanced Computational Engine prepared by US Nuclear Regulatory Commission (NRC) is used to execute thermal-hydraulic behavior on LOCA condition in a BWR.TRACE is a consolidation of four main codes: TRAC-P, TRAC-B, RELAP-5 and RAMONA [6]. The plots are prepared by Aptplot which is a Java based plotting tool used to plot the output from trcxtv file of TRACE. Aptplot is better modified version of AcGrace [7].

2. Conservation Equations

Two phase flow equations are composed of mass, energy and momentum conservation for two particular field. The heat transfer from metal surface to the two phase fluid is described by several time and volume averaged equations. Those equations are:

2.1.1 Time averaged mass equations

$$\frac{\partial[(1-\alpha)\bar{\rho}_l]}{\partial t} + \nabla.\left[(1-\alpha)\bar{\rho}_l\vec{\bar{v}}_l\right] = -\Gamma \quad (1)$$

$$\frac{\partial(\alpha\bar{\rho}_g)}{\partial t} + \nabla.\left[\alpha\bar{\rho}_g\vec{\bar{v}}_g\right] = \Gamma \quad (2)$$

2.1.2 Time Averaged Energy Equations

$$\frac{\partial\left[(1-\alpha)\bar{\rho}_l\overline{\left(e_l+\frac{v_l^2}{2}\right)}\right]}{\partial t} + \nabla.\left[(1-\alpha)\bar{\rho}_l\overline{\left(e_l+\frac{v_l^2}{2}\right)\vec{v}_l}\right]$$

$$= -\nabla\left[(1-\alpha)\vec{\bar{q}}_l'\right] + \nabla.\left[(1-\alpha)\left(\overline{T_l.\vec{V}_l}\right)\right] + (1-\alpha)\bar{\rho}_l\overline{g.\vec{V}_l} - \bar{E}_i + \overline{q_{dl}} \quad (3)$$

$$\frac{\partial\left[\alpha\bar{\rho}_g\overline{\left(e_g+\frac{v_g^2}{2}\right)}\right]}{\partial t} + \nabla.\left[\alpha\bar{\rho}_g\overline{\left(e_g+\frac{v_g^2}{2}\right)\vec{v}_g}\right]$$

$$= -\nabla\left[\alpha\vec{\bar{q}}_g'\right] + \nabla.\left[\alpha\left(\overline{T_g.\vec{V}_g}\right)\right] + \alpha\bar{\rho}_g\overline{g.\vec{V}_l} + \bar{E}_i + \overline{q_{dg}} \quad (4)$$

2.1.3 Time Averaged Momentum Equations

$$\frac{\partial\left[(1-\alpha)\bar{\rho}_l\vec{\bar{v}}_l\right]}{\partial t} + \nabla.\left[(1-\alpha)\bar{\rho}_l\overline{\vec{v}_l\vec{v}_l}\right] = \nabla[(1-\alpha)\bar{T}_l] + (1-\alpha)\bar{\rho}_l\vec{g} - \bar{M}_i \quad (5)$$

$$\frac{\partial\left[\alpha\bar{\rho}_g\vec{\bar{v}}_g\right]}{\partial t} + \nabla.\alpha\bar{\rho}_g\overline{\vec{v}_g\vec{v}_g} = \nabla\left[\alpha\bar{T}_g\right] + \alpha\bar{\rho}_g\vec{g} + \bar{M}_i \quad (6)$$

In the above two equations, $\bar{M}_i$represents time averaged interface jump condition to transfer momentum.

2.1.4 Volume Averaged Mass Equations

$$\frac{\partial\overline{[(1-\alpha)\rho_l]}}{\partial t} + \overline{\nabla.\left[(1-\alpha)\rho_l\vec{v}_l\right]} = -\bar{\Gamma} \quad (7)$$

$$\frac{\partial(\overline{\alpha\rho_g})}{\partial t} + \nabla.\left[\overline{\alpha\rho_g\vec{v}_g}\right] = \bar{\Gamma} \quad (8)$$

2.1.5Volume Averaged Energy Equations

$$\frac{\partial\left[\overline{(1-\alpha)\rho_l\left(e_l+\frac{v_l^2}{2}\right)}\right]}{\partial t} + \overline{\nabla.\left[(1-\alpha)\rho_l\left(e_l+\frac{v_l^2}{2}+\frac{P}{\rho_l}\right)\vec{\bar{v}}_l\right]}$$

$$= \overline{-\nabla\left[(1-\alpha)\vec{q}_l'\right]} + \nabla.\left[(1-\alpha)\left(\overline{T_l.\vec{V}_l}\right)\right] + \overline{(1-\alpha)\rho_l g.\vec{V}_l - \Gamma h_l' + W_l} + \overline{q_{dl}} \quad (9)$$

$$\frac{\partial\left[\overline{\alpha\rho_g\left(e_g+\frac{v_g^2}{2}\right)}\right]}{\partial t} + \overline{\nabla.\left[\alpha\rho_g\left(e_g+\frac{v_g^2}{2}+\frac{P}{\rho_g}\right)\vec{\bar{v}}_g\right]}$$

$$= \overline{-\nabla\left[\alpha\vec{q}_g'\right]} + \overline{\alpha\rho_g g.\vec{V}_g} + \overline{\Gamma h_v' + W_g} + \overline{q_{dg}} \quad (10)$$

2.1.6Volume Averaged Momentum Equations

$$\frac{\partial\overline{\left[(1-\alpha)\rho_l\vec{\bar{v}}_l\right]}}{\partial t} + \overline{\nabla.\left[(1-\alpha)\rho_l\vec{\bar{v}}_l\vec{\bar{v}}_l\right]} = \overline{\nabla[(1-\alpha)R_l]} + \overline{(1-\alpha)\rho_l\vec{g} - M_l} \quad (11)$$

$$\frac{\partial\overline{\left[\alpha\rho_g\vec{\bar{v}}_g\right]}}{\partial t} + \overline{\nabla.\left[\alpha\rho_g\vec{\bar{v}}_g\vec{\bar{v}}_g\right]} = \overline{\nabla\left[\alpha R_g\right]} + \overline{\alpha\rho_g\vec{g}} + \bar{M}_i \quad (12)$$

Physical correlations are implemented so that the interaction between vapor and liquid phase and heat transfer at the wall can be taken into account [8]. In addition, special models are also included in order to describe special phenomena such as, critical heat flux or counter current flow limitation.

3. Simulation Procedure

An input model has been developed to study the reflooding phase of LOCA conditions in a BWR. The input model consists of necessary information of the thermal hydraulic components to obtain a certain condition in a BWR. Furthermore, the TRACE code offers several options to obtain more precise and accurate result. All the components and options used in the model are discussed in this portion.

The entire project has been considered as a hypothetical system. Such a system consists of two parallel, vertical, heated channels that resemble two simplified BWR fuel assemblies. In fact the rod bundle used in the GOTA experiments was simulated as bundle similar to BWR [9].

The TRACE model of the hypothetical system is such that:

- A FILL is used to deliver water under normal conditions, from the bottom.
- The FILL component is connected to a lower pipe and this pipe delivers water to the two heated channels through the lower plenum.
- The heated channels are modeled with two PIPE components associated to their own heat structures and power components.
- The heated water is collected from the outlet of the heated channels into the upper PLENUM.
- The upper PLENUM is connected to the upper PIPE, and the PIPE is connected to a pressure boundary condition given by a BREAK component.
- The injection of the emergency coolant from the top of the system is modeled with a FILL component connected to the upper PIPE, and the BREAK component for the pressure boundary condition is connected to the lower PIPE [10]. Entire model is shown in figure:2

Therefore the model consists of in total 16 components. In total four PIPE components, two FILL components, two BREAK components, two heat structures (HTSTR) and two power components have been used in the model. The PIPE component placed on the top is used to maintain thermos-hydraulic flow among FILL, BREAK and PLENUM components and main two PIPE components are used to maintain thermal hydraulic flow between the upper PLENUM and lower PLENUM, another PIPE component on bottom is used to maintain the thermal hydraulic flow among FILL, BREAK and PLENUM components. The two heat structures (HTSTR component) maintain thermal coupling between coolant flows along the channels with two fuel assemblies. All the heat structures and PIPE components are divided into 24 cell volumes. Each fuel assembly contains in total 64 rods. Two adjacent fuel assemblies is shown in figure 1.The materials used for building fuel assembly are given in Table 1.

Table 1**:** Name of the components and the materials used for fuel composition.

Name of the components	Materials
Fuel rod pin	NiCr,Boron Nitride and Inconel-600
Inner channel wall (assumed but no heat structure been used)	Zircaloy

Table 2: All initial parameters used in the model.

Parameter	Nominal
Initial two bundle power on steady state(KW)	300
Inlet flow rate on steady state(kg/s)	7.0
Inlet flow rate on transient state (kg/s)	0.5
Outlet Pressure boundary condition (MPa)	0.1
Inlet water temperature on steady state(℃)	90
Steam venting	Top

The FILL component is connected with the PLENUM by a PIPE component since the FILL component cannot be connected with the PLENUM component directly. Two BREAK components are used in this model: one for outlet boundary condition of coolant flow in steady state condition and another one for outlet boundary condition for coolant flow on reverse direction during the transient state. The following assembly was considered for simulation presents Inconel-600 and boron nitride.

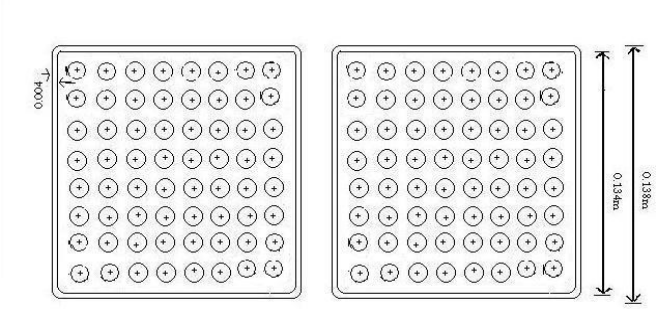

Figure 1: Top view of two parallel channels heated by fuel assembly.

For the critical heat flux, the AECL-IPPE CHF table was used, where the quality is estimated from the CISE-GE correlation. The critical heat flux is an important issue in the current context since it is related to the possible boiling crisis that a channel may suffer because of the degradation of the mass flow rate due to the loss of coolant [11].

For the counter-current flow limitation (CCFL), the Kutateladze correlation was used [9].

$$K_g^{\frac{1}{2}} + m_k K_f^{1/2} = C_K \qquad (13)$$

If we consider the reflooding from the top of the channels, the CCFL is related to the fact that the main emergency flow that moves downwards is limited by a flow of steam moving upwards.

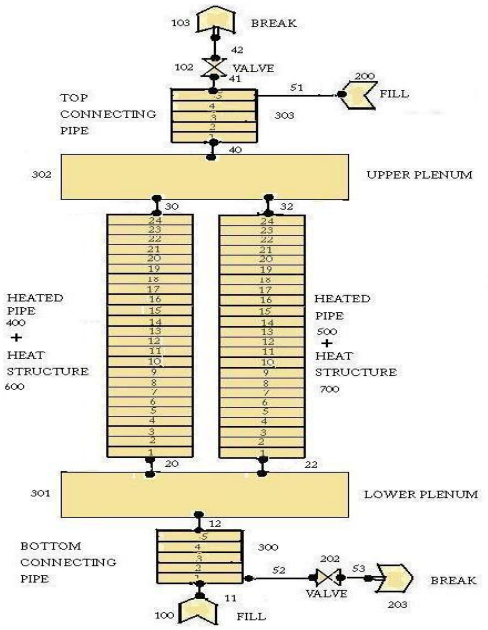

Figure 2: Entire thermal hydraulic model for two channel of BWR.

3.1. Simplifications used in the model

- Heated rods are all the same.
- No radial power distribution (no use of radial peaking factor).
- Axial power profile is considered uniform.

3.2. Limitations of the model

- Bypass channel is not included with the model.
- Axial conduction is not taken into account.
- Radiation from the heat structures is not been included.
- No shroud is included.
- Pressure is assumed to be constant with respect to time.

4. Results

The objective of this work is to perform a preliminary study of the effect of the power distribution between two heated channels on the reflooding phase of a possible LOCA. Based on the assumptions, the input file was prepared to run the TRACE code.

4.1. Description of the analyzed cases.

Three different cases are simulated with different power levels (see the table 3).

Table 3: Initial power for the two heated channels.

Case	Initial power [kW]	
	Heated channel 1	Heated channel 2
1	300	300
2	300	295
3	300	290

Two different power components are used to heat up the channels.

All simulation of the 3 cases is performed in two steps. First step is defined as steady state when emergency cooling system is turned OFF and the coolant flows from the bottom to upward direction and in the second step coolant upward flow is stopped, thus, the transient state appears and emergency cooling system is turned ON to recover from the transient state. More precisely it could be explained that in the first step, spray cooling system kept OFF and the entire hypothetical test facility is operated in the steady state condition and after a while, the transient state is initiated. The spray cooling system is initiated when cladding temperature reaches the peak after 100 seconds of dry state. In the final step, coolant flow is initiated from the top and continued for 2700 seconds, however, in transient state the coolant flows in the opposite direction compared to the flow direction in steady state, meanwhile, coolant flow by FILL-100 from the bottom in steady state is kept OFF. Different states, time periods and state durations are mentioned in Table 4.

First, the steady state is obtained with constant boundary conditions and constant initial power.

Table 4: Different states, the time period and mass flow rate on different states.

State	Time period $[s]$	State Duration $[s]$	Flow Rate $[Kg/s]$
Steady state	0.0-200.0	200.0	7.0
Transient state	200.1-300.0	100.0	0.0
Obtaining the steady state from transient state	300.0-3000.0	2700.0	-0.5

On last column of Table 4 the negative sign refers to the reverse direction of the flow. The fuel pin surface temperatures have been calculated by TRACE code for the following cases.

4.2. Case 1 (300-300 kW)

The upper part of the rod is cooled before the lower part of heat structure (HTSTR-600), at the axial levels 6, 12, 18, 24 and the surface temperature of the rod reaches to the saturation temperature of the fluid.

The same plot is with outer surface rod temperature for heat structures (HTSTR-700), at the same axial levels. As expected, the two heat structures have the same behavior since the two heated channels are equally powered. The results are shown in figure 3.

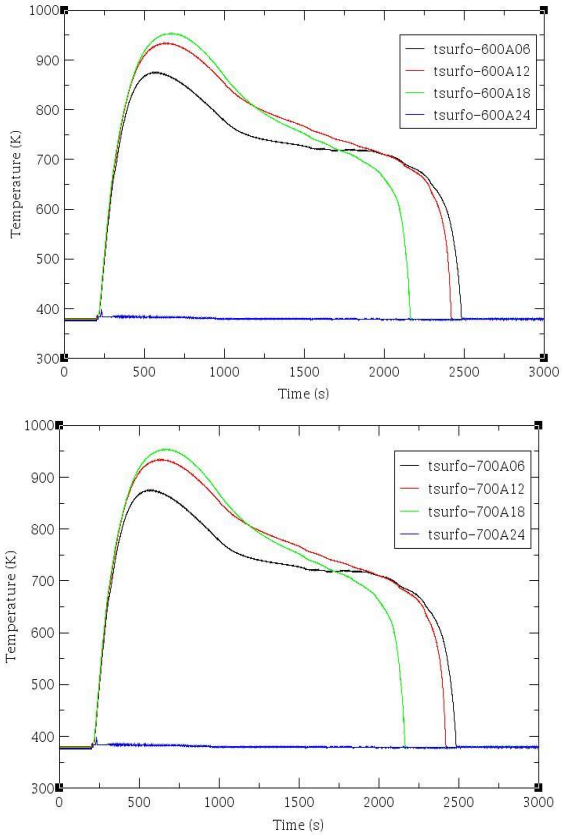

Figure 3: Fuel outer surface temperature on transient state condition for case 1.

4.3. Case 2 (300-295 kW)

Mass flow rate for pipes 400 and 500 at axial level 12 shows that in the colder channel the mass flow rate is larger (in absolute value).

The plots show the outer surface fuel temperature for heat structures 600 and for heat structure 700, at the axial levels 6, 12, 18, 24. Those plots show that the upper part of the rod is cooled before the lower part. The outer surface temperature for HTSTR-700 reaches the saturation earlier than the HTSTR-600.The results are shown in following figure 4.

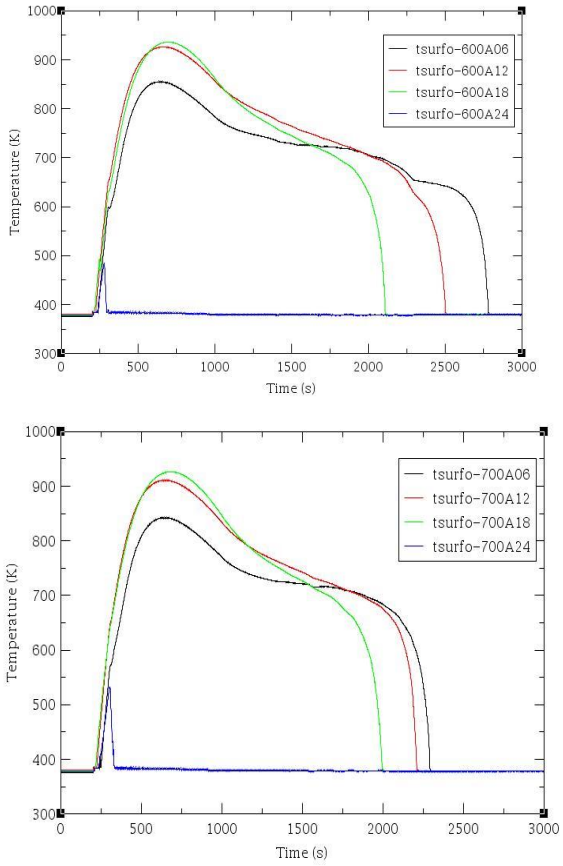

Figure 4: Fuel outer surface temperature on transient state condition for case 2.

4.4. Case 3 (300-290 kW)

Heat structure (HTSTR-600): the same plot includes the outer surf rod temp at axial level 6, 9, 12. It shows that the outer surface rod temperature at level 6 and 9 does not reach the saturation temperature of the fluid, while it does at level 12. This is the hotter rod, the rod at higher power (300 kW). Again, the upper part of the rod is cooled earlier than the lower part.

Heat structure (HTSTR-700): the same plot includes the outer surf rod temp at axial level 6, 9, 12. The point is that these temperatures decrease to the saturation temperature of the fluid. This is the rod at lower power (290 KW). Again, the upper part of the rod is cooled earlier than the lower part.

Since, PIPE 500 has a higher mass flow rate than Pipe 400, so the associated rod HTSTR 700is better cooled.

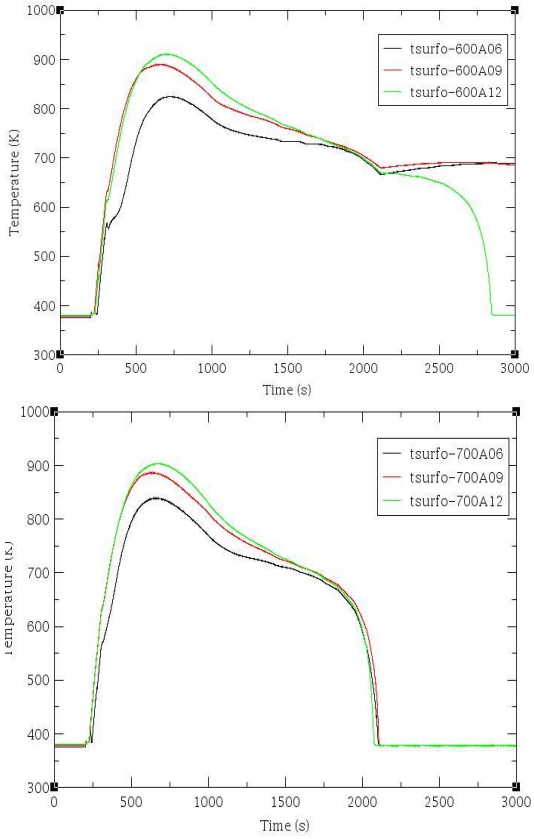

Figure 5: Fuel outer surface temperature on transient state condition for case 3.

4.5Comparison of temperature profile

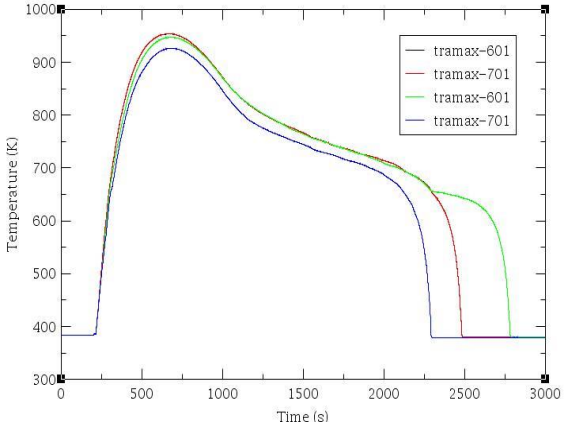

Figure 6: The comparison between the max average temperature by power component 601 and power component 701 for the cases 1 (300-300 kW) and 2 (300-295 kW).

In figure 6, maximum average temperature (tramax) of a particular fuel assembly is presented. Black and red curves indicate the maximum average temperature for case 1 and green and blue curves indicate the maximum average temperature for case 2. The black curve is not visible since the delivered power for two distinct fuel assemblies are same.

In case 1 and case 2, the surface rod temperature is approximately reduced to the saturation temperature of the coolant; in case 2, this reduction occurs later for the hotter channel.

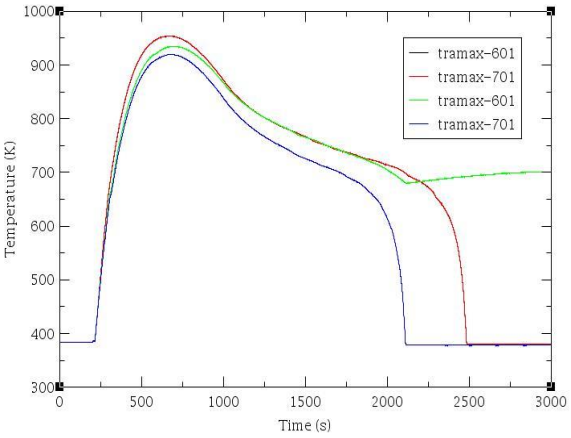

Figure 7: The comparison between the max average temperature by power component 601 and component 701 for the cases 1 (300-300) and 3 (300-290).

In figure 7, black and red curve indicate the max average temperature of two fuel assemblies for case 1 and green and blue curve indicate the max average temperature for case 3. The black curve is not visible since the delivered power for two distinct fuel assemblies for case 1 are same.

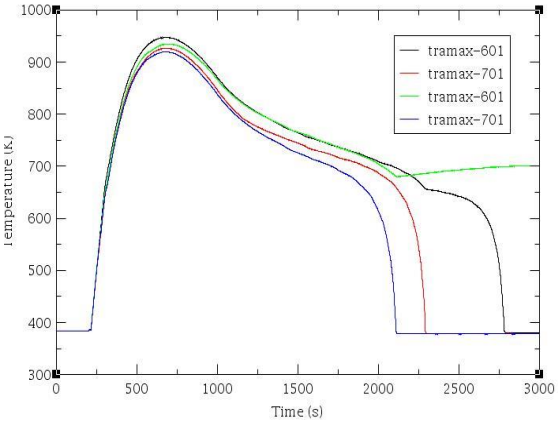

Figure 8: The comparison between the max average temperature by power component 601 and component 701 for the cases 2 (300-295) and 3 (300-290).

In figure 8, black and red curve indicate the max average temperature of two fuel assemblies for case 2 and green and blue curve indicate the maximum average temperature of two fuel assemblies for case 3.

In case 2, the surface rod temperature is approximately reduced to the saturation temperature of the coolant within

the calculation time of 3000 seconds; in case 3, it does not occur for the hotter channel and the mass flow rate is smaller.

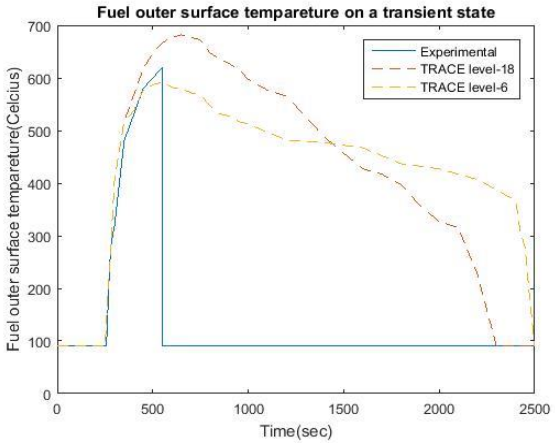

Figure 9: Comparison between experimental and simulation data of fuel outer surface temperature.

It is shown from the above figure 9 that the fuel outer surface temperature is quiet reasonable since curve from experimental data exists between two simulated curves of different level. The experimental data is found a test of STUDSVIK /E4-78/68 [12].

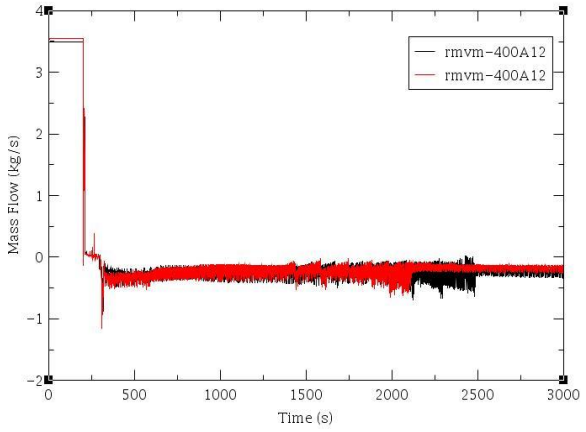

Figure 10: The comparison between the mass flow rate of PIPE 400, at axial level 12, for the cases 1 (300-300) and 3 (300-290).

In figure 10, legend rmvm refers to mass flow rate along a particular channel .400 and 12 respectively refers to the PIPE component number and level number of the component. Black and red curves consecutively indicate the mass flow rate for case 1 and case 3.

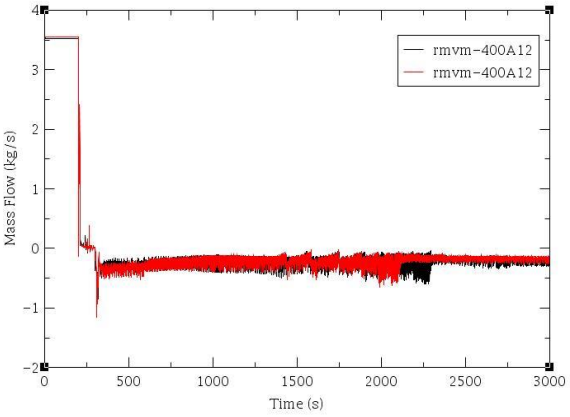

Figure 11: The comparison between the mass flow rate of pipe 400, at axial level 12, for the cases 2 (300-295) and 3 (300-290).

In figure 11, black and red curve consecutively indicate the mass flow rate for case 2 and case 3.

The point is that power differences between the two heated channels lead to differences in the mass flow rates to the channels. This, in turn, affects the reflooding process. In comparison with two above figures, more power causes more boiling and counters current flow .As a result, higher range of magnitude is found for case 1, in comparison with case 2 and case 3. Most importantly, the mass flow rate along the channel is negative since flow direction in transient state is opposite to the steady state.

For instance, it is seen that the maximum average temp in the hotter channel of case 2 is reduced to the saturation temperature of the fluid, while it does not happen in case 3 for the hotter channel during the calculation time of 3000 seconds. In fact, even though the total power of case 2 is higher the more even power distribution between the two channels seems to give better conditions for the decrease of temperature in the hotter channel. In fact, the mass flow rate of pipe 400 in case 2 is higher than the mass flow rate of pipe 400 in case 3.

5. Conclusion

A simplified model was developed for TRACE computer code for two parallel BWR fuel assemblies with an emergency cooling system injecting water from the top. TRACE model was used for two parallel BWR fuel assemblies with an emergency cooling system injecting water from the top. This is applied to investigate possible effects of different power levels in the two channels, on the evolution of the reflooding phase that follows a loss of coolant. Three cases were analyzed. According to these calculations, it was shown that in cases 1 and 2, where the initial power provided to the two channels is more evenly distributed, the maximum average rod temperature of the hotter channel is quenched and decreases to the saturation temperature of the fluid within the simulation time of 3000 seconds. On the other hand, in case 3, where the difference between the power of the two rod bundles is larger (the initial power in the two channels is equal to 300 and 290 kW,

respectively), the temperature of the hotter channel cannot be reduced to the coolant saturation level as quickly as the other cases. However, an extension of this paper could be prepared by addition of sensitivity analysis. Moreover, a bypass channel could be added, radiation from the fuel pin, axial conduction option and a shroud could be included to obtain more accurate result. This simplified model TRACE could be used for other LOCA cases for both BWR and PWR.

Acknowledgement

The entire simulation was done in the Nuclear Engineering Department of Chalmers University of Technology. I'm thankful to the entire nuclear department of Chalmers University of Technology .I'm grateful to publication corporation as well who helped me to prepare this paper.

Abbreviations

AECL:Atomic Energy of Canada Limited,Canada
BWR: Boiling water reactor
CCFL: Counter current flow
CHF: Critical heat flux
CISE:Common Information Sharing Environment
ECCS: Emergency core cooling system
IPPE:Institue of power and physics,Obnisk,Russia
LOCA: Loss of coolant accident
NPP: Nuclear power plant
PCT: Peak cladding temperature
PWR: Pressurized water reactor
TRACE: TRAC/RELAP Advanced Computational Engine
USNRC:US Nuclear Regulatory Commission

References

[1] Lelieveld, Jos, Daniel Kunkel, and Mark G. Lawrence. "Global risk of radioactive fallout after major nuclear reactor accidents." *Atmospheric Chemistry and Physics* 12.9 (2012): 4245-4258.
[2] SourceOECD . *World energy outlook*. OECD/IEA, 2006.
[3] OECD Nuclear Energy Agency and International Atomic Energy Agency (2006), Uranium 2005: Resources, Production and Demand, OECD, Paris, France.
[4] Lester, Richard K., and Mark J. McCabe. "The effect of industrial structure on learning by doing in nuclear power plant operation." *The Rand Journal of Economics* (1993): 418-438.
[5] Sehgal, Bal Raj. "Light water reactor (LWR) safety." *Nuclear Engineering and Technology* 38.8 (2006): 697.
[6] HU, XIAO. "TRACE Analysis of LOCA Transients Performed on FIX-II Facility." (2012).
[7] Walls, Robert Allen. *Boiling Water Reactor Transient Instability Studies of Ringhals 1 Reactor using TRACE coupled with PARCS*. Diss. The Pennsylvania State University, 2009.
[8] Bajorek, S. "TRACE V5. 0 Theory Manual, Field Equations, Solution Methods and Physical Models." *United States Nuclear Regulatory Commission* (2008).
[9] Racca, Stefano, and Tomasz Kozlowski. "Trace code validation for BWR spray cooling injection and CCFL condition based on GÖTA facility experiments."*Science and Technology of Nuclear Installations* 2011.
[10] TRACE V5.0 USER'S MANUAL Volume 2 : Modelling Guidelines by United States Nuclear Regulatory Commission .
[11] TRACE V5.0 USER'S MANUAL Volume 1 : input specification by United States Nuclear Regulatory Commission.
[12] Eriksson, S. O., R. Harju, and R. Pettersson. *BWR emergency core cooling investigations. Spray cooling heat transfer experiment in a full scale BWR bundle mock-up*. Studsvik Energiteknik AB, Nykoeping (Sweden), 1978.

International Conference on Mechanical Engineering 2015
(ICME 2015) 18 – 20 December, 2015, Dhaka, Bangladesh

Paper ID :597

CFD Simulation of Nanofluid Applied Heat Transfer Enhancement in Square Array Subchannel

Jubair A. Shamim, Palash K. Bhowmik, Kune Y. Suh

Department of Nuclear Engineering, Seoul National University, Seoul 151-744, ROK

Abstract. CFD simulation is performed to check the thermo-hydrodynamic performance of alumina (Al_2O_3) nanofluid in square array subchannel featuring pitch-to diameter (*P/D*) ratio of 1.25 and 1.35. Two fundamental aspects of thermal hydraulics i.e. convective heat transfer coefficient and pressure drop are assessed under typical PWR condition for different inlet Reynolds number, *Re* spanning from 3×10^5 to 6×10^5 using pure water and different concentrations (0.5 to 3.0 vol.%) of water/alumina (Al_2O_3) nanofluids as coolant. The realizable k-ε model is implemented to simulate turbulence inside subchannel. Finally, a multiple regression analysis has been performed to propose a new correction factor for an existing correlation of square array subchannel to obtain Nusselt number, *Nu* more accurately for nanofluids in such geometry.

INTRODUCTION

Heat transfer and fluid flow are two pivotal issues that must be taken into consideration while designing a nuclear reactor to save energy, reduce process time, raise thermal rating and increase the working life of reactor pressure vessel. Hence, a major challenge combated by the engineers in this arena is the quantification of the optimal flow of coolant and distribution of pressure drop across the reactor core. While higher coolant flow rates will lead to

better heat transfer coefficients and higher Critical Heat Flux (CHF) limits, it will also result in higher pressure drop across the core, therefore additional demand of pumping powers as well as larger dynamic loads on the core components.

However, recently researchers have come up with a new idea of utilizing nanofluid as coolant instead of pure water to solve the problem of heat transfer enhancement with optimum pressure drop. The improved heat transfer performance of nanofluids is due to the fact that the nanoparticles:

- Increase the surface area and heat capacity of the fluid.
- Improve the thermal conductivity of the fluid.
- Cause more collisions and interactions between the fluid, particles and flow passages.
- Cause more turbulence and mixing of the fluid.

Pak & Cho [1] performed experiments to observe the turbulent friction and heat transfer behaviors of dispersed fluids in a circular pipe using two different metallic oxide particles, γ-alumina (Al_2O_3) and titanium dioxide (TiO_2) with mean diameters of 13 and 27 nm, respectively and proposed following correlation for *Nu* under their experimental ranges of volume concentration (0-3%), *Re* (10^4 - 10^5), and *Pr* (6.54 - 12.33) for the dispersed fluids γ-alumina (Al_2O_3) and titanium dioxide (TiO_2) particles:

$$Nu_{nf} = 0.021 \mathrm{Re}_{nf}^{0.8} \mathrm{Pr}_{nf}^{0.5} \tag{1}$$

Another well cited correlation proposed by Xuan and Li [2] to estimate *Nu* for the turbulent flow of Cu-water nanofluids inside a tube is presented below:

$$Nu_{nf} = 0.0059\left(1.0 + 7.6286\varphi^{0.6886} Pe_P^{0.001}\right) \mathrm{Re}_{nf}^{0.9238} \mathrm{Pr}_{nf}^{0.4} \tag{2}$$

Maiga et al. [3] performed numerical investigation for fully developed turbulent flow of water/ Al_2O_3 nanofluid through circular tube using different concentrations under the constant heat flux boundary condition and the following correlation was proposed to estimate *Nu,* valid for $10^4 \le Re \le 5\times10^5$, $6.6 \le Pr \le 13.9$ and $0 \le \varphi \le 10\%$:

$$Nu_{nf} = 0.085 \mathrm{Re}_{nf}^{0.71} \mathrm{Pr}_{nf}^{0.35} \tag{3}$$

A summary of published experimental investigations on convective heat transfer performance of different nanofluids is presented by Asirvatham et al [4].

Despite numerous studies integrating both scaled experiments and numerical modeling on heat transfer enhancement of nanofluids are available in literature, most of the test sections/ computational domain were comprised of round pipes and also their simulating parameters does not reflect the environment of a nuclear power reactor. Therefore, in this study a numerical simulation has been performed using a commercial CFD tool "STAR-CCM+ (ver.9.06.011)" to develop a new correlation for evaluating heat transfer more accurately in a square array subchannel ($1.25 \le P/D \le 1.35$) for different volume concentrations of water/ alumina (Al_2O_3) nanofluid ($0.5\% \le \varphi \le 3.0\%$). While designing the computational domain and fixing simulating variables, a Korean standard nuclear power plant, "Advanced Power Reactor (APR)-1400" has been considered as reference plant.

MATHEMATICAL MODELLING

Governing Equations

In case of nanofluid, if motion slip between the particles and the continuous phase is considered negligible, the flow inside the subchannel is considered as single phase and incompressible with constant physical properties, both the compression work and viscous dissipation are assumed as negligible and the general conservation equations for mass, momentum and energy can be written in the form of Eq. (4) through Eq. (6) respectively using vector notations:

$$\mathrm{div}\left(\rho v\right) = 0 \tag{4}$$

$$\mathrm{div}\left(\rho v v\right) = -\mathrm{grad} P + \mu \Delta^2 v \tag{5}$$

$$\mathrm{div}\left(\rho v C_P T\right) = \mathrm{div}\left(k\ \mathrm{grad} T\right) \tag{6}$$

In above equations, *v*, *P* and *T* are fluid velocity vector, pressure and temperature respectively.

Thermophysical Properties of Nanofluid

Determination of physical properties of nanofluid is key to any nanofluid research. If the nanoparticles are assumed to be well dispersed in the base fluid; the particle concentration can be considered as constant throughout the domain and effective physical properties of mixture can be evaluated using some classical formulas well known for two phase fluids [5]. In this study, formulas used to determine different properties like density, specific heat, dynamic viscosity and thermal conductivity are presented through Eq. (7) through Eq. (10) respectively:

$$\rho_{nf} = \left(1-\varphi\right)\rho_{bf} + \varphi\rho_P \tag{7}$$

$$\left(C_P\right)_{nf} = \left(1-\varphi\right)\left(C_P\right)_{bf} + \varphi\left(C_P\right)_P \tag{8}$$

$$\mu_{nf} = \left(1+7.3\varphi+123\varphi^2\right)\mu_{bf} \tag{9}$$

$$k_{nf} = \left(1+2.72\varphi+4.97\varphi^2\right)k_{bf} \tag{10}$$

Eq. (7) and Eq. (8) are general relationships have been used in many literatures [1, 5, 6] to recon the density and specific heat for a classical two phase mixture. Regarding dynamic viscosity and thermal conductivity, Maïga et al. performed a least-square curve fitting based on some scarce experimental data available in [7-9] which leads to Eq. (9) and Eq. (10) as presented in [5, 10]. Different properties of base fluid (pure water) and alumina nanoparticles that have been used in this study are tabulated in Table 1.

TABLE 1. Physical properties of base fluid and alumina nanoparticles.

Properties	Base Fluid (Pure Water)	Alumina Nanoparticles
Density (kg/m^2)	734.928	3970
Thermal Conductivity (W/m. K)	0.5701	40
Specific Heat (J/kg. K)	5361.69	880
Dynamics Viscosity (Pa. s)	9.01373E-05	-

NUMERICAL MODELLING

Computational Domain

The computational domain and boundaries considered for this study is shown in Fig. 1, which represents quarter of a 3-D square array subchannel created in Star-CCM+. The diameter of the fuel rod is taken as 9.5 mm and two different rod pitch featuring pitch to diameter (*P/D*) ratio of 1.25 and 1.35 are selected for simulation. The length of the subchannel has been taken as 600 mm which is long enough to establish a fully developed turbulent flow at outlet under single phase forced convection condition up to $Re = 6\times10^5$.

Boundary Conditions

The coolant enters into the subchannel with a uniform inlet velocity, v_0 (m/s) and at inlet temperature 569 K. Different values of v_0 for different coolants that have been used in the simulation are tabulated in Table 2. Different properties of base fluid (pure water) have been calculated at temperature 569 K and at pressure 155.1375 Bar. At outlet, a static pressure equal to 155.1375 Bar has been imposed. On the tube wall, the usual non-slip conditions with

standard wall function are considered with a constant heat flux of 600,000 W/m^2. Considering the established practice from literature and computational time required, realizable *k-ε* model (Shih et al., [11]) has been adopted for turbulence modelling inside a square array subchannel since it has been statistically proved that this model provides the best performance among all the *k-ε* model versions for separated flows and flows with complex secondary flow features [12]. The above parameters and geometric configurations of computational domain are based on the design features of a Korean standard nuclear power plant called "APR 1400".

TABLE 2. Different inlet velocities, $v0$ (m/s) used in simulation.

(a) *P/D* = 1.25

Inlet *Re*	Pure Water	Alumina (Al_2O_3) Nanofluid		
	(φ=0%)	φ=0.5%	φ=1.5%	φ=3.0%
6×10^5	7.829	7.963	8.351	9.196
5.098×10^5	6.651	6.766	7.095	7.813
4×10^5	5.219	5.309	5.568	6.130
3×10^5	3.914	3.982	4.176	4.598

(b) *P/D* = 1.35

Inlet *Re*	Pure Water	Alumina (Al_2O_3) Nanofluid		
	(φ=0%)	φ=0.5%	φ=1.5%	φ=3.0%
6×10^5	5.826	5.926	6.215	6.843
5.098×10^5	4.950	5.035	5.280	5.814
4×10^5	3.884	3.951	4.143	4.562
3×10^5	2.913	2.963	3.108	3.422

CODE VALIDATION

Mesh Convergence

Different mesh settings are selected as presented in Table 3 and values of numerically obtained *Nu* are compared against an existing correlation for square array subchannel and for pure water as presented by Eq. (11) through Eq. (13) to check mesh convergence for computational domain with *P/D* =1.35. Results are plotted in Fig. 2 which clearly states that a mesh setting with base size 0.7 mm, no. of prism layer 2, prism layer thickness 0.3mm and prism layer stretching 3.7 will be sufficient to produce *Nu* within reasonable deviation compared to theoretical prediction made by correlation.

$$Nu = \psi \left(Nu_{\infty} \right)_{c.t.} \tag{11}$$

where,

$$\left(Nu_{\infty} \right)_{c.t.} = 0.023 \,\mathrm{Re}^{0.8}\, \mathrm{Pr}^{0.4} \tag{12}$$

for square array with $1.05 \le P/D \le 1.9$ and for pure water, Presser [13] suggested:

$$\psi = 0.9217 + 0.1478 \,{}^{P}\!/_{D} - 0.1130 e^{-7\left({}^{P}\!/_{D} - 1\right)} \tag{13}$$

Validation of Numerical Model

Since the ultimate test of any numerical simulation is the validation of results against well-known experimental data, the model under consideration in the present study has been validated against correlation of Presser for square array and pure water as presented by Eq. (11) through Eq. (13). Results are plotted in Fig. 3 and Fig. 4 which demonstrates that there is an excellent match between numerical data and theoretical prediction for the specified range of inlet *Re*.

Validation of Turbulence Model for Nanofluid

Despite in the present study it is assumed that nanofluid would behave as a single-phase homogeneous fluid and hence, all of the general conservation equations of mass, momentum and energy can directly be applied in case of nanofluid, however, a successful comparison of numerical *Nu* obtained realizable k-ε model has been carried out against both empirical correlation and experimental data of Pak & Cho [1] for turbulent flow inside a round pipe of inside diameter 10.66 mm using alumina nanofluid (φ=2.78%) as coolant for inlet *Re* spanning from 5.03×10^4 to 1.48×10^4. The results are plotted in Fig. 5 which clearly delineates that this model can perform quite satisfactorily with nanofluids.

TABLE 3. Different mesh settings used to check mesh convergence.

Base Size (mm)	No.	Prism Layers Stretching	Thickness (mm)	*Nu* (Star-CCM+)	*Nu* (Presser)	Deviation (%)
0.5	5	1.5	0.7	742.940		-35.051
0.6	4	1.5	0.5	862.627		-16.313
0.7	3	3.8	0.4	933.92	1003.35	-7.434
0.6	2	3.7	0.3	972.102		-3.214
0.7	2	3.7	0.3	1010.57		0.714

NUMERICAL RESULTS

Heat Transfer at Constant Inlet Re.

A convective heat transfer coefficient and Nusselt number study is carried out in Star-CCM+ for pure water and different concentrations of alumina nanofluid. Values of *Nu* are evaluated at the outlet of the subchannel to assure fully developed turbulent flow condition. Numerical results of *Nu* and *h* for subchannel with different pitch-to-diameter (*P/D*) ratio are presented through Fig. 6 to Fig. 9 respectively and percentage of convective heat transfer increment for different nanofluid coolants are documented in Table 4. From the results, it is obvious that the convective heat transfer coefficient is remarkably increased with the increment of nanoparticle volume concentration and in case of 3.0% volume concentration, convective heat transfer is increased above 22.0% compared to pure water.

Heat Transfer at Constant Mass Flow Rate

Another comparison of convective heat transfer coefficient, *h* with same mass flow rate at inlet boundary for φ=3.0% and *P/D* = 1.35 is carried out and results as depicted in Fig. 10 indicates that values of *h* for nanofluid (φ=3.0%) is somewhat lower (3.95 to 4.34 percent based on inlet mass flow rate) compared to pure water. It implies that nanofluid is capable of increasing heat transfer coefficient at the expense of more pumping power required for the existing nuclear power plants.

Analogy of Numerical Results with Correlations

In case of nanofluid with volume concentration, φ =3.0% numerical results for *Nu* are compared against two well cited correlations of Pak & Cho [1] and Maïga et al. [3] as shown in Fig. 11 (a) & (b) and an attempt has been made whether results of present study can be represented by either of these two correlations.

The results revealed that Pak and Cho correlation severely underestimates the numerical results for *Nu* in subchannel and deviation lies between 17 to 22 percent subject to inlet *Re* and *P/D*.

Regarding correlation of Maïga et al., it shows better approximation compared to correlation of Pak & Cho. Nevertheless, this correlation underestimates the numerical results for the range $5\times10^5 \leq Re \leq 6\times10^5$ and

overestimates for $3\times10^5 \leq Re \leq 4\times10^5$ and deviations are between -0.54 to 6.66 percent depending on inlet *Re* and *P/D*.

TABLE 4. Heat transfer increment (%) for different nanofluid coolants **(a) *P/D* = 1.25**

Inlet *Re*	Increment of *h* (%)		
	φ=0.5%	φ=1.5%	φ=3.0%
6×10^5	2.75	9.62	22.46
5.098×10^5	2.75	9.58	22.37
4×10^5	2.72	9.51	22.16
3×10^5	2.74	9.42	21.89

(b) *P/D* = 1.35

Inlet *Re*	Increment of *h* (%)		
	φ=0.5%	φ=1.5%	φ=3.0%
6×10^5	2.72	9.56	22.35
5.098×10^5	2.72	9.51	22.26
4×10^5	2.71	9.44	22.01
3×10^5	2.69	9.40	21.87

Pressure Drop

Pressure drop along the centre line of the subchannel is evaluated for different coolants and results are presented in Fig. 12 (a) & (b). Percentage of pressure drop increment is documented in Table 5. The results shows that pressure drop is significantly increased with the augmentation of particle volume concentration and for nanofluid with φ=3.0%, pressure drop increment is about 56% higher compared to that of pure water.

TABLE 5. Pressure drop increment (%) for different nanofluid coolants

(a) *P/D* = 1.25

Inlet *Re*	Increment of Δ*p* (%)		
	φ=0.5%	φ=1.5%	φ=3.0%
6×10^5	6.22	21.53	56.60
5.098×10^5	5.82	21.17	56.62
4×10^5	5.79	21.79	56.02
3×10^5	5.24	21.65	55.83

(b) *P/D* = 1.35

Inlet *Re*	Increment of Δ*p* (%)		
	φ=0.5%	φ=1.5%	φ=3.0%
6×10^5	5.82	20.94	56.37
5.098×10^5	5.74	21.29	56.08
4×10^5	5.46	20.90	55.10
3×10^5	5.62	20.88	55.82

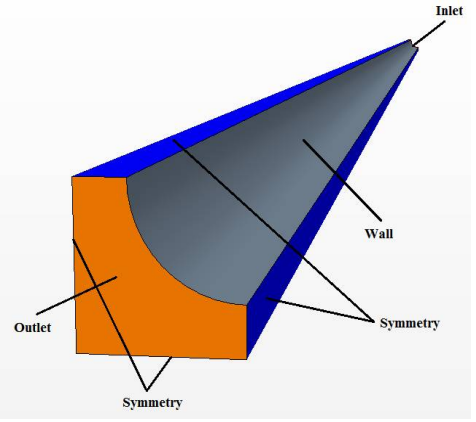

FIGURE 1. Computational domain created in Star-CCM+

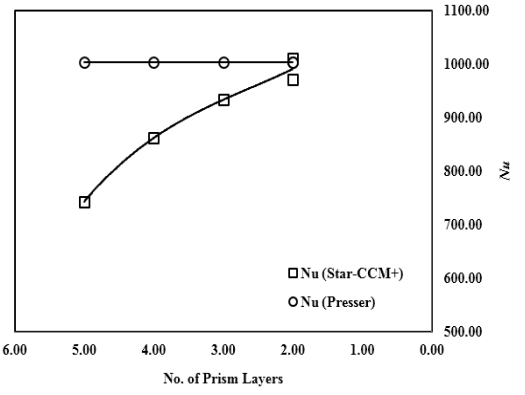

FIGURE 2. Mesh convergence test with different mesh settings

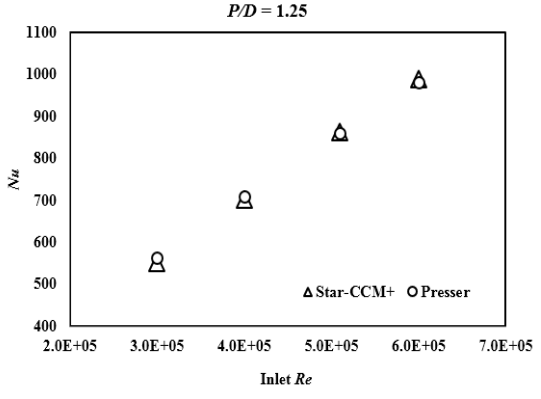

FIGURE 3. Validation of numerical model against correlation for *P/D* =1.25

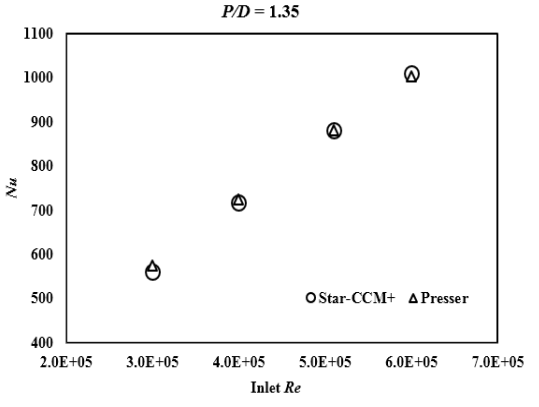

FIGURE 4. Validation of numerical model against correlation for *P/D* =1.35

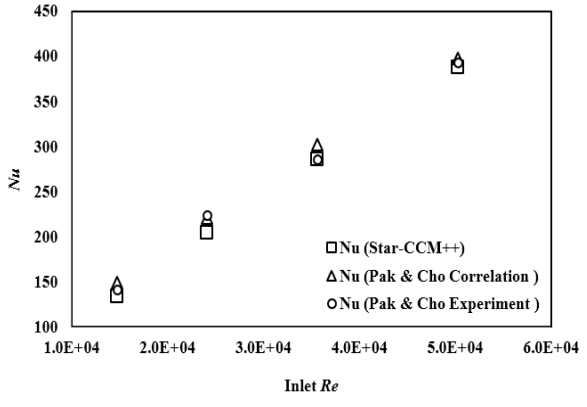

FIGURE 5. Validation of turbulence model against Pak & Cho's correlation

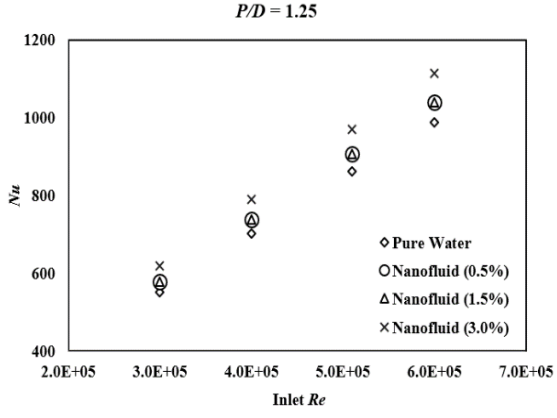

FIGURE 6. Comparison of *Nu* for different coolants in subchannel (*P/D* 1.25)

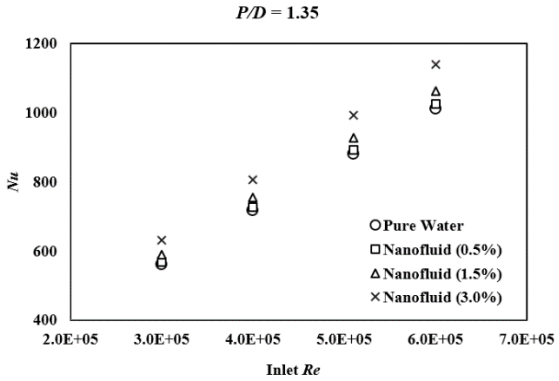

FIGURE 7. Comparison of *Nu* for different coolants in subchannel (*P/D* 1.35)

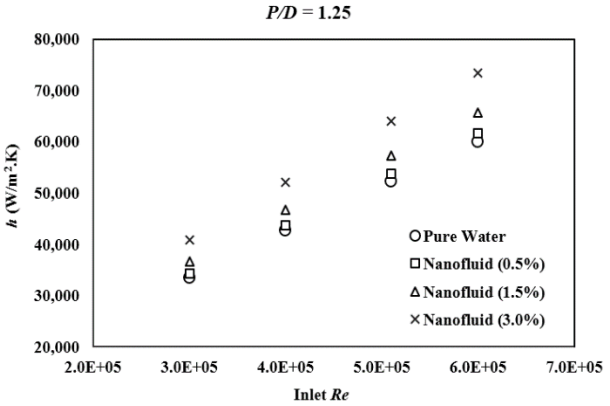

FIGURE 8. Comparison of *h* for different coolants in subchannel (*P/D* 1.25)

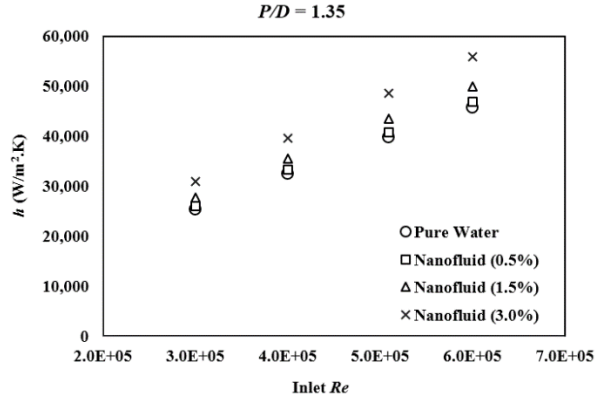

FIGURE 9. Comparison of *h* for different coolants in subchannel (*P/D* 1.35)

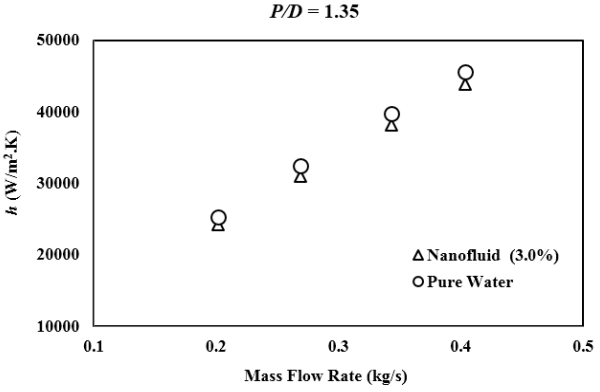

FIGURE 10. Comparison of *h* for same mass flow rate at inlet (φ=3.0% and *P/D* = 1.35)

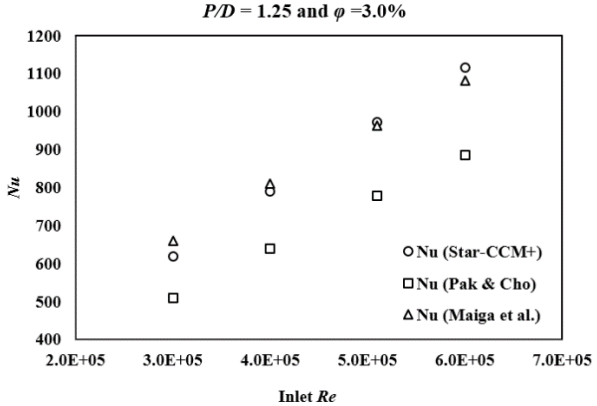

(a) *P/D* = 1.25

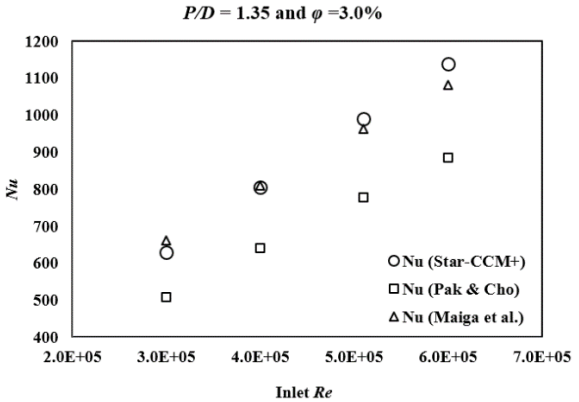

(b) *P/D* = 1.35

FIGURE 11. Comparison of numerical *Nu* against different correlations

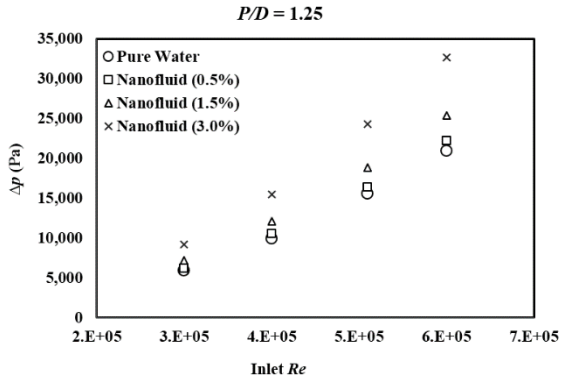

(a) P/D = 1.25

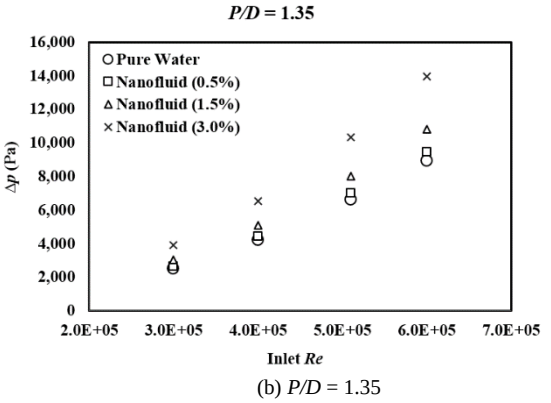

(b) P/D = 1.35

FIGURE 12. Comparison of pressure drop for different coolants

Proposed New Correction Factor for Nanofluid

Finally, a multiple regression analysis is performed with numerical results to propose a new correction factor, β for the existing correlation of square array subchannel with pure water as suggested by Presser [13] so that Nu for nanofluid coolant can be approximated in such geometry. Based on regression results, β can be expressed as follows:

$$\beta = 1 + 0.0247\varphi^{1.39} \tag{14}$$

Nu for nanofluid can be calculated as follows:

$$Nu_{nf} = \beta * \left(Nu_{Presser} \right)_{Water} \tag{15}$$

The validity of above correlation is for $3\times10^5 \le Re \le 6\times10^5$; $0.847 \le Pr \le 1.011$; $1.25 \le P/D \le 1.35$ and $0.5\% \le \varphi \le 3.0\%$ in case of square array subchannel.

CONCLUSIONS

A numerical simulation has been carried out to evaluate thermohydrodynamic characteristics of water/alumina (Al_2O_3) nanofluid in a square array subchannel featuring pitch-to-diameter ratio of 1.25 and 1.35 under steady state, incompressible, single phase turbulent flow condition. Numerical results are compared against available correlations in literature and following conclusions can be conferred from the present study:

- Both convective heat transfer coefficient as well as Nusselt number are increased with increasing volume concentration of water/alumina nanofluid at constant inlet Re.

- The convective heat transfer increment of nanofluid is gained at the expense of larger pressure drop and hence, larger pumping power required. Despite numerical results portray that pressure drop at ϕ=3.0% is higher than 55%, but typical nanoparticle loading for nuclear applications is usually $\le$ 0.1 vol. %. At this low concentration, nanofluid properties are almost similar to that of pure water and pressure drop is much lower but the heat transfer is increased due to higher turbulence produced near the grid spacers by the presence of nanoparticles in base fluid. One limitation of our present study is its inability to consider this phenomena of turbulence enhancement near spacer grids for which further experimentations are required.

- Last but not least, despite analysis of reviewed literature as well as results of present study delineates that nanofluid is capable of augmenting the heat transfer capability remarkably, there is still no satisfactory explanation proposed yet regarding the prevention of clustering in nanoparticle suspensions. Therefore,

while attempting to implement nanofluid coolant in PWR for long term use, clustering phenomenon of nanoparticles may eventually decrease the thermal conductivity and initiate problems like corrosion and wear inside piping and pumps. Hence, the clustering of nanoparticles to be solved first in order to utilize nanofluid as a promising coolant in PWR to achieve both extended life time of associated equipment and higher thermal efficiency.

ACKNOWLEDGEMENT

This work was supported by the National Research Foundation of Korea (NRF) grant funded by the Korean Government (MSIP) under Grant No. 2008-0061900 and partly supported by the Brain Korea 21 Plus under Grant No. 21A20130012821.

REFERENCES

[1] B. C. Pak, Y. I. Cho, Hydrodynamic and heat transfer study of dispersed fluids with submicron metallic oxide particles, Experimental Heat Transfer an International Journal, 11 (1998) 151-170.

[2] Y. Xuan, Q. Li, Investigation on convective heat transfer and flow features of nanofluids, Journal of Heat transfer, 125 (2003) 151-155.

[3] S. El Bécaye Maïga, C. Tam Nguyen, N. Galanis, G. Roy, T. Maré, M. Coqueux, Heat transfer enhancement in turbulent tube flow using Al_2O_3 nanoparticle suspension, International Journal of Numerical Methods for Heat & Fluid Flow, 16 (2006) 275-292.

[4] L. G. Asirvatham, N. Vishal, S. K. Gangatharan, D. M. Lal, Experimental study on forced convective heat transfer with low volume fraction of CuO/water nanofluid, Energies, 2 (2009) 97-119.

[5] S. E. B. Maïga, S. J. Palm, C. T. Nguyen, G. Roy, N. Galanis, Heat transfer enhancement by using nanofluids in forced convection flows, International Journal of Heat and Fluid Flow, 26 (2005) 530-546.

[6] V. Bianco, F. Chiacchio, O. Manca, S. Nardini, Numerical investigation of nanofluids forced convection in circular tubes, Applied Thermal Engineering, 29 (2009) 3632-3642.

[7] S. Lee, S.-S. Choi, S. Li, J. Eastman, Measuring thermal conductivity of fluids containing oxide nanoparticles, Journal of Heat Transfer, 121 (1999) 280-289.

[8] H. Masuda, A. Ebata, K. Teramae, Alteration of thermal conductivity and viscosity of liquid by dispersing ultra-fine particles. Dispersion of Al_2O_3, SiO_2 and TiO_2 ultra-fine particles, 1993.

[9] X. Wang, X. Xu, S. U. S. Choi, Thermal conductivity of nanoparticle-fluid mixture, Journal of thermophysics and heat transfer, 13 (1999) 474-480.

[10] S. E. B. Maïga, C. T. Nguyen, N. Galanis, G. Roy, Heat transfer behaviours of nanofluids in a uniformly heated tube, Superlattices and Microstructures, 35 (2004) 543-557.

[11] T.-H. Shih, W. Liou, A. Shabbir, Z. Yang, J. Zhu, A new k-epsilon eddy viscosity model for high Reynolds number turbulent flows: Model development and validation, 1994.

[12] Introduction to ANSYS FLUENT: Customer Training Material, Release 13, December 2010.

[13] K. H. Presser, Wärmeübergang und Druckverlust an Reaktorbrennelementen in Form längsdurchströmter Rundstabbündel, Kernforschungsanlage, Zentralbibliothek, 1967.

ICME2015

International Conference on Mechanical Engineering 2015
(ICME 2015) 18 – 20 December, 2015, Dhaka, Bangladesh

Paper ID : 598

Nanofluid Heat Transfer and Pressure Drop in Small Modular Reactor Square Array Rod Bundle

Palash K. Bhowmik[1], Jubair A. Shamim[1] and Kune Y. Suh[1,a)]

[1]*Department of Nuclear Engineering, Seoul National University, Seoul 08826, Republic of Korea*
[a)] *Corresponding author: kysuh@snu.ac.kr*

Abstract. Heat transfer and pressure drop characteristics are studied in the so-called NANO (Nine Array Nanofluid Operation) rod bundle under a fully-developed single-phase turbulent upflow condition. The NANO bundle is designed to check on thermo- and hydrodynamic performance of alumina nanofluid in a uniformly-heated square-array rod bundle having a pitch-to-diameter ratio of 1.286, a fuel assembly building block for a small modular reactor sharing commonalities with the current fleet of pressurized water reactors (PWRs). Nine cartridge-type heater rods were installed in the 3×3 square array with four grid spacers utilizing water and alumina as coolant spanning the inlet Reynolds numbers from 21,000 to 100,000. The Nusselt numbers for a wide range of flow inlet velocity and power were obtained and compared against the well-known correlations in the literature. For unheated water the predicted pressure drop generally agreed with the experimental data. For heated nanofluid the pressure drop as well as heat transfer increased with the Reynolds number. The results were compared against the recognized correlations, and any deviations were elucidated quantitatively. A new heat transfer correlation is proposed for the NANO bundle.

INTRODUCTION

Most conventional designs to elevate heat transfer performance are limited to variation of mechanical structures like addition of heat transfer area such as with fins, vibration of the heated surface, injection or suction of fluids, application of electrical or magnetic fields, and so forth. Application of these techniques in a nuclear fuel assembly will require not only designing complex core geometries but also elevating the manufacturing cost, and may as well jeopardize the essential safety features accompanied by reduced lifetime of the reactor pressure vessel. However, recent studies have come up with a new idea of utilizing nanofluid as coolant instead of pure water to solve the problem of heat transfer enhancement with optimum pressure drop [1, 2]. Numerous investigations were carried out to evaluate the pressure drop characteristics in the presence of grid spacers in rod bundles with differing core configurations. DeStordeur [3] experimentally evaluated the pressure drop characteristics of a variety of spacer grids in rod bundle geometry and correlated results in terms of a drag coefficient C_s which is a function of the Reynolds number Re for a given spacer or grid type. Rehme [4] later examined the pressure drop for a hexagonal rod bundle. to conclude that the effect of the ratio of projected frontal area of the spacer to the unrestricted flow area away from the grid spacer is more pronounced than was indicated by DeStordeur [3]. Chun and Oh [5], and Cigarini and Dalle Donne [6] further improved Rehme's correlation by incorporating the effect of mixing devices in conjunction with grid spacers. Suh and Todreas [7] experimentally investigated the effect of lateral drag changes caused by alteration of flow structure due to presence of wire-wrapped spacers in triangular array rod assemblies for liquid metal fast reactor. They correlated the transverse pressure drop data throughout the laminar and turbulent flow regimes.

Xuan and Li [8] utilized 35 nm Cu/deionized nanofluid flowing in a tube with constant wall heat flux to propose the following correlation for the turbulent flow inside a tube:

$$Nu_{nf} = 0.0059\left(1.0 + 7.6286\varphi^{0.6886} Pe_d^{0.001}\right)\mathrm{Re}_{nf}^{0.9238}\,\mathrm{Pr}_{nf}^{0.4} \tag{1}$$

NOMENCLATURE

A_v	unrestricted flow area, m^2	Re	Reynolds number
A_s	projected frontal area, m^2	Nu	Nusselt number
C_v	drag coefficient	Pr	Prandtl number
D	rod diameter, m	Pe	Peclet number
D_h	hydraulic diameter, m	Gr	Grashof number
f	friction factor	C_p	specific heat, J/kg K
g	gravity constant, m/s^2	T_b	bulk temperature of fluid, K
h_f	head loss, m	T_w	surface temperature of heater rod, K
L	length of flow channel, m	h	convective heat transfer coefficient, W/m^2 K
l	heater rod heated length, m	*Greek symbols*	
P	rod pitch, m or pressure, bar	μ	dynamic viscosity, N s/m^2
ΔP	pressure drop, bar	μ_b	fluid viscosity at bulk temperature, N s/m^2
V	flow velocity, m/s	μ_w	fluid viscosity at wall temperature, N s/m^2
Q	total heat input, W	φ	volume concentration of nanoparticles, %
q	heat flux, W/m^2	α	angle with vertical direction of flow, degree
$\dot{m}$	mass flowrate, kg/s	ρ	density, kg/m^3
V_v	average bundle fluid velocity, m/s	*Subscripts*	
ΔZ	changes in elevation of test section, m	*nf*	nanofluid
K_{form}	form loss coefficient	*bf*	basefluid
k	thermal conductivity, W/m K	*p*	particles

Pak and Cho [9] experimentally studied the turbulent friction and heat transfer of dispersed fluids in a circular pipe using two different metallic oxide particles, γ-alumina (Al_2O_3) and titanium dioxide (TiO_2). They proposed the following correlation for $10^4 \le Re \le 10^5$, $6.54 \le Pr \le 12.33$, and $0 \le \varphi \le 3$ %:

$$Nu_{nf} = 0.021 \,\mathrm{Re}_{nf}^{0.8}\, \mathrm{Pr}_{nf}^{0.5} \tag{2}$$

Maiga et al. [10] numerically studied hydrodynamic and thermal characteristics of turbulent flow in a tube using different concentrations of Al_2O_3 nanoparticle suspension under the constant heat flux boundary condition. They proposed the following correlation for $10^4 \le Re \le 5\times10^5$, $6.6 \le Pr \le 13.9$, and $0 \le \varphi \le 10$ %:

$$Nu_{nf} = 0.085 \,\mathrm{Re}_{nf}^{0.71}\, \mathrm{Pr}_{nf}^{0.35} \tag{3}$$

Albeit several studies integrating both scaled experiments and numerical modeling on heat transfer enhancement of nanofluids are presented in literature, most of the test sections or computational domain comprised round pipes. Their simulating parameters did not replicate the environment of a nuclear power reactor, either. This study is aimed at experimental investigation as well as theoretical analysis to more accurately examine the heat transfer in a square array rod bundle which is compatible with a small modular pressurized water reactor (PWR).

THERMOPHYSICAL PROPERTIES OF NANOFLUID

Thermophysical properties of nanofluids such as density, specific heat, viscosity and thermal conductivity are approximated according to the following equations and correlations [11, 12, 13]:

$$\rho_{nf} = (1-\varphi)\rho_{bf} + \varphi\rho_p \tag{4}$$

$$\left(\rho C_p\right)_{nf} = \left(1-\varphi\right)\left(\rho C_p\right)_{bf} + \varphi\left(\rho C_p\right)_p \tag{5}$$

$$k_{nf} = \left(4.97\varphi^2 + 2.72\varphi + 1\right)k_{bf} \tag{6}$$

$$\mu_{nf} = \left(123\varphi^2 + 7.3\varphi + 1\right)\mu_{bf} \tag{7}$$

The alumina nanofluid properties determined by Eqs. 4 through 7 are summarized in Table 1 for particles less than 50 nm in diameter.

TABLE 1. Thermophysical properties of alumina nanoparticles and base fluid (water).

Properties	Alumina Nanoparticles	Water
Specific heat, C_p (J/kg. K)	880	4183
Density, ρ (kg/m^3)	3970	1000
Thermal conductivity, k (W/m. K)	40	0.639~ 0.612

PHYSICAL SETUP, INSTRUMENTATION AND EXPERIMENTATION

Test Loop

The NANO apparatus was constructed to measure heat transfer in, and pressure drop across, a 3×3 square array rod assembly featuring a pitch-to-diameter ratio P/D of 1.286 and hydraulic diameter D_h of 0.010288 m. Fig. 1 shows the NANO test loop. Fig. 2 presents the form loss locations, grid spacers and the inlet flow distributor. The NANO loop consists of a test section, a plate-type heat exchanger (OLAER PWO K Series), a water reservoir, a centrifugal pump (Wilo MHi403EM), flow control valves and stainless steel piping (A269 TP 316L). A total of nine cartridge-type heaters are installed in a 3×3 square array resembling the PWR fuel assembly basic building block. From the pump the coolant enters the plenum connected to the lower part of the vertical test section. The plenum is an empty space upstream of the heated rod bundle which houses a specially designed inlet flow distributor to suppress nonuniformity of the flow generated by pipe fittings. The flowrate is measured by an electromagnetic flow meter (Toshiba LF400, ±0.5 % accuracy) downstream of the pump. Pressure drop along the test section is measured by two identical pressure transducers (Allsensor P601, ±0.25 % FSO accuracy) at the inlet and the outlet. K-type thermocouples are used to measure the coolant bulk and central heater rod surface temperatures. A collecting tank is installed at the upper end of the test section to abate the flow fluctuation. The overall temperature of the fluid can be controlled by changing the heater current input.

Test Procedure

Heat transfer and pressure drop data are taken from the isothermal condition controlling the flowrate of pure water and alumina nanofluid using the data acquisition system (National Instruments SCXI with LabVIEW Signal Express 2009) as follows.

- All valves except the bypass are kept fully open and water is supplied through the main tank (upper left in Fig. 1) until the loop is filled up. Air in the loop is collected in the accumulator tank located above the heater assembly. Once the valve at the top of the pressure damping tank is fully closed, water is added to raise the system pressure to its maximum value.

- Water supply is then stopped to make a closed loop and the pump is turned on. During testing, the bypass valve is closed to maximize the flowrate at the inlet. When the cold circulation is fully established within the loop, then the

heaters are turned on. The heater temperature can be varied by using a power controller. After several minutes, the secondary system coolant water is circulated through the external heat exchanger.

The desired flowrate can be obtained by adjusting the opening of the valve located downstream of the pump. A steady state is achieved by controlling the flowrate of the secondary system coolant. Pressure drop across the test section is recorded by means of two digital pressure transducers.

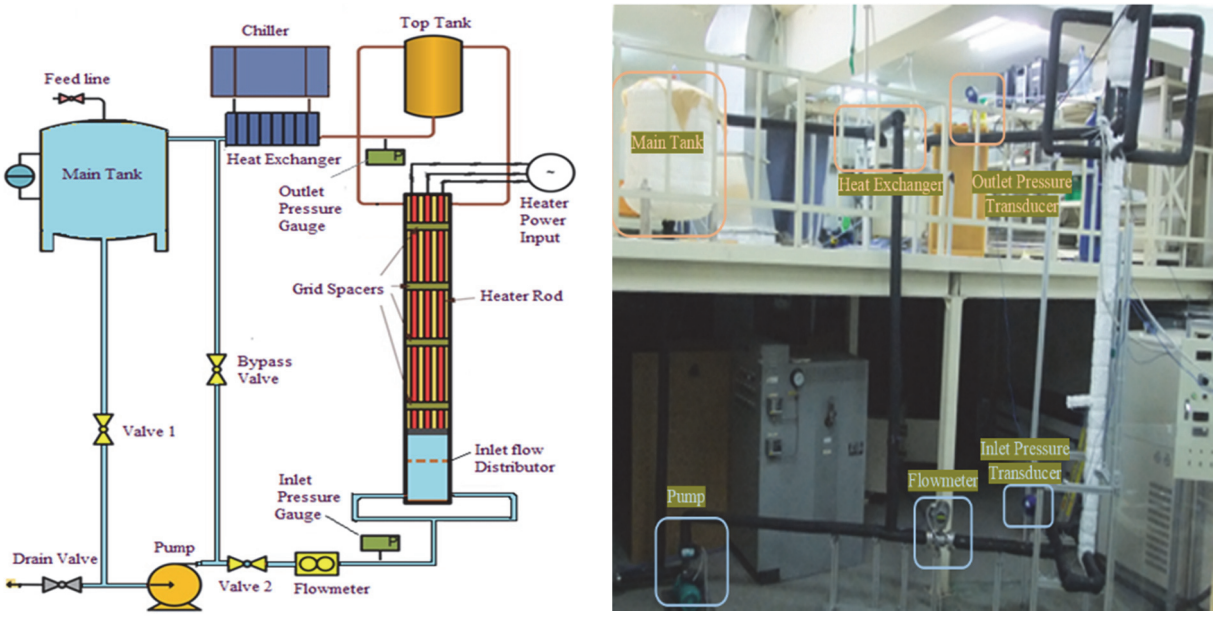

(a) (b)

FIGURE 1. (a) NANO schematic; (b) NANO setup.

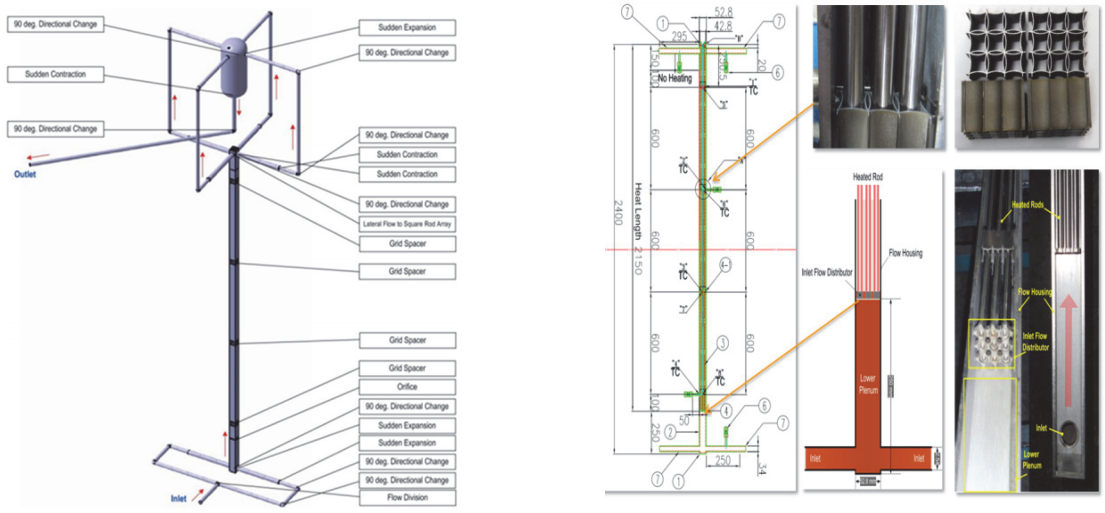

(a) (b)

FIGURE 2. (a) flow direction and form losses; (b) internal configuration of NANO test section.

PREPARATION AND STABILITY OF ALUMINA NANOFLUID

Preparation of Sample Nanofluid Solution

An instrumental aspect of utilizing nanophase particles to upsurge the heat transfer capability of conventional fluids is the precise quality control of the nanofluid solution during the preparation since the nanofluid does not simply refer to a solid-liquid mixture. The Al_2O_3 nanoparticles < 50 nm utilized in this test were manufactured by Sigma-Aldrich. Samples of φ = 0.001 %, 0.01 %, and 0.1 % of alumina nanofluids are prepared with recommend procedure.

Stability of Sample Nanofluid Solution

One central parameter that must be taken into consideration to evaluate the colloidal stability and to prevent flocculation of nanoparticles in the base fluid is the zeta potential which is in fact an indicator of the repulsive force. In general the higher the magnitude of the zeta potential (either negative or positive), the system is more electrically stabilized. A zero zeta potential, or isoelectric point, is where particles tend to agglomerate. In NANO the zeta potential of the sample solutions was monitored by a dynamic light scattering (DLS) device called ZETASIZER (Nano-ZS) up to 40 hours. A sample test result of the zeta potential distribution, pH and conductivity of the alumina nanofluid after 40 hours is shown in Fig. 3 for φ = 0.1 %. The results revealed that all the samples show moderate stability up to 40 hour since the absolute values of the zeta potential are close to 30 mV.

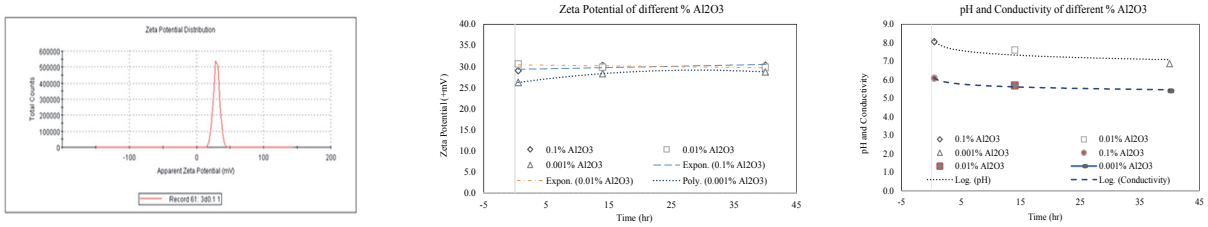

(a) (b) (C)

FIGURE 3. (a) Zeta potential distribution, (b) Zeta potential test results; (c) pH and conductivity test results.

PRESSURE DROP ANALYSIS

Pressure drop across the NANO bundle is measured by means of two digital pressure transducers mounted at the inlet and outlet of the test loop, respectively, as shown in Fig. 4. The test section consist of the inlet piping, elbows, rod bundle with the inlet flow distributor and four grid spacers and the outlet piping with the top accumulator tank which are subjected to the source of flow disturbances. The grid spacers are used to fix the rods in the bundle and the top accumulator tank is employed to stabilize the outlet flow. The pressure drop in the test loop results mainly from the inlet flow distributor, grid spacers, the piping, fittings such as 900 elbows, flow dividers, sudden expansion and contraction, and the gravity. Hence, the theoretical pressure drop (ΔP=Pin – Pout) can be expressed as

$$\Delta P_{Estimated} = \Delta P_{SpacerGrid} + \Delta P_{Friction} + \Delta P_{Gravity} + \Delta P_{Form} \tag{8}$$

Pressure Drop by Grid Spacer and Flow Distributor

The form losses by the flow distributor and grid spacers are singled out from the total form loss in the test loop to get a clearer understanding of the effect of these components on the rod bundle pressure drop. The pressure drop due to spacer grids was calculated by the Rehme correlation [4] as

$$\Delta P_{SpacerGrid} = C_V \left(\frac{\rho V_V^2}{2} \right) \left(\frac{A_S}{A_V} \right)^2 = C_V \left(\frac{\rho V_V^2}{2} \right) \varepsilon^2 \tag{9}$$

where C_v is the modified drag coefficient, V_v the average bundle fluid velocity, A_v the unrestricted flow area away from the grid or spacer, and A_s the projected frontal area of the spacer. The original Rehme correlation was further modified by Cigarini and Donne [6] as

$$C_V = \min\left(3.5 + \frac{73.14}{\mathrm{Re}^{0.264}} + \frac{2.79E10}{\mathrm{Re}^{2.79}}, \frac{2}{\varepsilon^2} \right) \tag{10}$$

The form loss due to the inlet flow distributor is also estimated using the same correlation for the grid spacer. *Re* is calculated in all different sections of NANO spanning the inlet piping, flow distributor, grid spacers, rod bundle, top tank and the outlet piping using the respective D_h, V and μ.

Other Form Losses

The Idelchick correlations [14] are used to estimate the form losses due to the pipe tee and elbows. The pipe tee divides the flow and the 90^0 elbows change the flow directions and causes form losses as

$$\Delta P_{Form} = K_{form} \left(\frac{\rho V^2}{2} \right),\ K_{divider} = 1 + 1.5 \left(\frac{v_{out}}{v_{in}} \right)^2 \text{ and } K_{elbow90^0} = \frac{0.21}{\sqrt{r_{out}/d_{out}}} + 0.0175 \left(90 f_{pipe} \frac{r_{out}}{d_h} \right) \tag{11}$$

The form loss due to sudden expansion and contraction was again determined by the Idelchik correlation [14] as

$$K_{sudden\_expansion} = \left(1 - A_{in}/A_{out} \right)^2 \quad \text{and} \quad K_{sudden\_contraction} = 0.5 \left(1 - A_{out}/A_{in} \right) \tag{12}$$

Frictional and Gravitational Pressure Drops

The frictional pressure drop was calculated by

$$\Delta P_{Friction} = f \left(\frac{L}{D_h} \right) \left(\frac{\rho V^2}{2} \right) \tag{13}$$

where *f* is the average friction factor depending on the channel geometry and flow velocity. For turbulent flow the friction factor for subchannels of square array was been obtained by the Cheng and Todreas correlation [15]. For the circular piping of the NANO apparatus the McAdams and Blasius correlations were used for $30{,}000 \le Re \le 10^6$ and $Re \le 30{,}000$, respectively as

$$C'_{fiT} = a + b_1 \left(P/D - 1 \right) + b_2 \left(P/D - 1 \right)^2, \text{ for turbulent flow} : f_{iT} = \frac{C'_{fiT}}{\left(\mathrm{Re}'_{iT} \right)^{0.18}} \tag{14}$$

$$\text{McAdams} : f = 0.184 \times \mathrm{Re}^{-0.2} \quad \text{and} \quad \text{Blasius} : f = \frac{0.316}{\mathrm{Re}^{0.25}} \tag{15}$$

The gravitational pressure drop was estimated by [16]

$$\Delta P_{Gravity} = \rho g \Delta Z \cos\alpha \tag{16}$$

Discussion of Results

The measured and predicted pressure drops are compared for different inlet *Re* and water coolant in terms of friction, form loss, gravitation and such components as the grid spacers and inlet flow distributor in Figs. 4 and 5. Fig. 4 demonstrates that the estimated pressure drop generally agrees with the experimental value for unheated pure water. Overall the effect of gravity starts to prevail. For the lowest inlet *Re* the gravitational pressure drop accounts for as much as 63 % of the total pressure drop. The contribution of gravitational pressure drop is nearly independent of the inlet velocity. Other pressure losses depend on *Re* at the inlet.

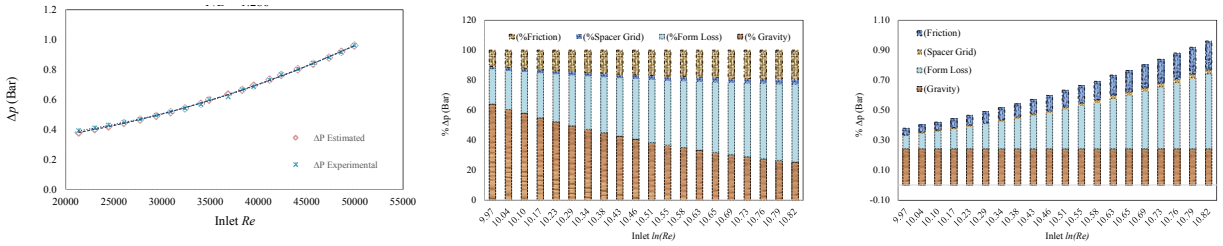

(a) (b) (C)

FIGURE 4. (a) Δ*P* against inlet *Re* without heat source, (b) percentile estimated Δ*P*; (c) estimated Δ*P* by different losses.

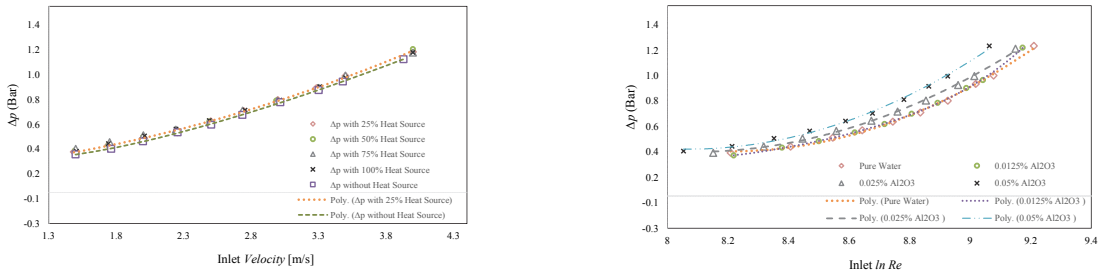

(a) (b)

FIGURE 5. (a) Δ*P* against inlet velocity, (b) Δ*P* influence by Al_2O_3 nanofluid against inlet *Re*.

Fig. 5 shows the significant change in the measured pressure drop due to presence of alumina nanofluid compared against pure water. This difference is amplified at high inlet *Re*. With heat source it is observed that there is greater deviation between the measured and predicted pressure drop than for the unheated case. The discrepancy results from the local cross flow augmented by local heat transfer which is difficult to predict with the correlations used in the analysis.

HEAT TRANSFER ANALYSIS

Estimation of Heat Input

One vital parameter required to quantify heat transfer characteristics in single-phase forced-convection turbulent flow is the heat flux q (W/m^2), which can be defined in terms of the total heat input Q (W) into the flow channel, diameter D (m) and heated length l (m) of heater rods as follows considering the nine rods heated circumferentially:

$$q = \frac{Q}{9\pi Dl}, \quad Q_1 = \sqrt{3}VI\cos\theta \quad \text{and} \quad Q_2 = \dot{m}C_p\,\Delta T_b \tag{17}$$

The total heat input Q is assumed as uniform axially and azimuthally as the thickness of heater rods is unvarying throughout the heated length. It can be obtained either as Q_1, which is measured by the input current I (ampere) and voltage V (voltage) applied to heater rods or as Q_2, which is calculated by considering the coolant flowrate $\dot{m}$ (kg/s),

coolant temperature increase ΔT_b (K) over the flow channel and the specific heat of the coolant C_p (J/kg.K). Here, the heater power supply is three-phase ac and cos θ is the power factor. To validate the estimation of Q, values of Q_1 and Q_2 obtained by Eq. 17 shows fairly good agreement and hence, any of these two values can provide precise estimation of Q. In this study the heater input power Q_1 is used in further calculations.

Evaluation of the Nusselt Number

To compute *Nu* for pure water under single-phase forced-convection turbulent flow regime numerous correlations available in the literature can be implemented subject to geometry of fluid flow channel and fluid mean velocity or *Re*. Among those, the most frequently applied correlations are due to Dittus & Boelter, Sieder & Tate, and Silberberg & Huberquations, as respectively quoted below.

$$Nu = 0.023\,\mathrm{Re}^{0.8}\,\mathrm{Pr}^{0.4} \tag{18}$$

$$Nu = 0.027\,\mathrm{Re}^{0.8}\,\mathrm{Pr}^{0.333}\left(\frac{\mu}{\mu_W}\right)^{0.14} \tag{19}$$

$$Nu = 0.016\,\mathrm{Re}^{0.85}\,\mathrm{Pr}^{0.3} \tag{20}$$

Implementation of the above correlations to estimate *Nu* is justified when the fluid flow sections do not vary significantly from circular. Such channels may include square, rectangular (not too far from square), and probably equilateral or nearly equilateral triangles. In case of fully turbulent flow along the rod bundle, values of *Nu* may remarkably deviate from the circular geometry due to geometric nonuniformity of the subchannels that creates substantial variation of *Nu* azimuthally. Apart from that for a given subchannel in a finite rod bundle, the turbulence may affect the adjacent subchannels depending on the location of subchannels with respect to the duct boundaries. Thus, *Nu* is a function of position within the bundle [16].

Therefore, for rod bundles, the Nusselt number for the fully-developed condition Nu_∞ is expressed as a product of $(Nu_\infty)_{c.t.}$ for a circular tube multiplied by a correction factor ψ as stated below, where $(Nu_\infty)_{c.t.}$ is usually given by the Dittus-Boelter equation unless otherwise stated. For a square array and specifically for water with $1.1 \le P/D \le 1.3$, Weisman [17] has redefined the statement as

$$Nu_\infty = \psi\left(Nu_\infty\right)_{c.t.},\quad \text{Weisman}:\left(Nu_\infty\right)_{c.t.} = 0.023\,\mathrm{Re}^{0.8}\,\mathrm{Pr}^{0.333}\ \text{ where, }\ \psi = 1.826\,{}^{P}\!/_{D} - 1.0430 \tag{21}$$

Since the applicability of the above mentioned correlations are limited to only pure water, *Nu* of alumina nanofluid can be estimated by Eqs. 1 through 3 as has earlier been discussed. All of the above correlations can be simplified as

$$Nu = a\,\mathrm{Re}^{\beta}\,\mathrm{Pr}^{b} \tag{22}$$

The coefficients a, β & b in Eq. 22 for different correlations are tabulated in Table 2. Since *Pr* does not vary significantly during the experiment, it can be assumed as constant for simplification. Eq. 22 can then be presented using a logarithmic function as

$$Nu = \alpha\,\mathrm{Re}^{\beta}\ \text{ where, }\ \alpha = a\,\mathrm{Pr}^{b},\quad \ln\left(Nu\right) = \ln\alpha + \beta\ln\left(\mathrm{Re}\right) \tag{23}$$

The above equation is equivalent to a first degree polynomial, i.e. $y = ax + b$. The value of $\ln\alpha$ is calculated using the average *Pr* and coefficients *a* and *b* are taken from the Weisman correlation Eq. 21 and the average heat transfer profile of the test section is considered to avoid experimental data uncertainty. Now, if we reevaluate *Nu* and *Re* according to the NANO condition and plot Eq. 23, by fitting a first degree polynomial we can obtain the modified coefficients α and β. The experimental *Nu* can be obtained as follows based on D_h of the flow channel and *k* at the

coolant bulk temperature, where h is the convective heat transfer coefficient for fully-developed turbulent flow. T_W and T_b represent the central heater rod wall surface and mean bulk fluid temperatures, respectively.

$$Nu = \frac{hD_h}{k}, \text{ where } h = \frac{q}{T_W - T_b} \tag{24}$$

Heat Transfer Test with Pure Water

The experimental *Nu* for pure water as well as alumina nanofluid is computed using Eq. 24 for a wide range of *Re*. The values thus obtained for pure water are compared against *Nu* obtained by the well-known correlations as presented earlier. Variations of *Nu* with respective *Re* for NANO and different correlations are calculated. Using the logarithmic function in Eq. 23, the experimental *Nu* is plotted against *Re* fitting a curve featuring the first degree polynomial. The estimated coefficients α and β for NANO with pure water and different correlations are presented in Table 2.

TABLE 2. Thermophysical properties of alumina nanoparticles and base fluid (water).

Correlation Name	***a***	***β***	***b***	**Modified, *α***	**Modified, *β***
Experiment	0.030		0.8	0.0387	0.775
Dittus-Boelter	0.023	0.8	0.4	0.0412	0.805
Sieder-Tate	0.027	0.8	0.333	0.5448	0.512
Silberburg-Huber	0.016	0.85	0.3	0.0232	0.804
Weisman (*P/D* 1.286)	0.030	0.8	0.333	0.0488	0.804
Pak & Cho	0.021	0.8	0.5		
Maiga et al.	0.085	0.71	0.35		

The NANO experimental *Nu* agrees well with the Silberbarg-Huber and other correlations as illustrated in Fig. 6.

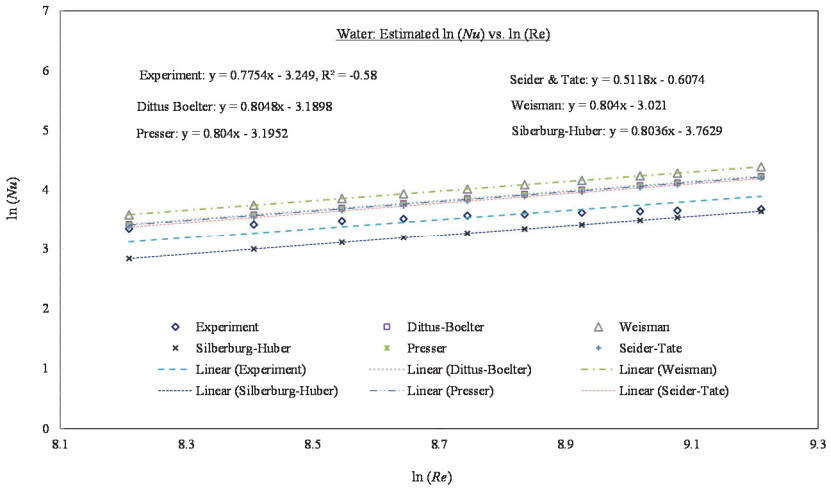

FIGURE 6. Comparison of experimental *Nu* (water) with different correlations.

Heat Transfer Augmentation by Alumina Nanofluid

A similar study as described in last section is carried out to evaluate the effect of alumina nanoparticles inclusion into pure water on heat transfer performance using three different concentrations of alumina/water as coolant. The measured and predicted *Nu* values are presented in Figs. 7 through 9. Fig. 10 shows the increment of *Nu* amalgamation for different concentrations of alumina nanofluid. The result reveals that both *Nu* and convective heat transfer coefficient are increased by 2~5.6 % and 1.46~3.88 %, respectively compared to pure water with the inclusion of only 0.0125 vol. % of alumina nanoparticles and for 0.05 vol. % the increased value becomes 6.56~18% and 3.57~8.74% correspondingly. Note that the percentile increase of *Nu* is slight low while the concentration of alumina nanoparticles increases from 0.0125 vol. % to 0.025 vol. % compare to the increase noticed from 0.0125 vol. % to 0.05 vol. %. This is because, with the increase of vol. % of alumina nanoparticles, the density of the nanofluid was also increased which in turn has lowered the specific heat and *Pr* as well as increase *k* of the solution but still has good agreement with other estimated value of the used correlations. *Nu* obtained by the experiment with different concentrations of alumina nanofluid against the inlet ln*Re* (Fig. 10) and the values of constant coefficients α and β are modified for different coolants as reported in Table 2.

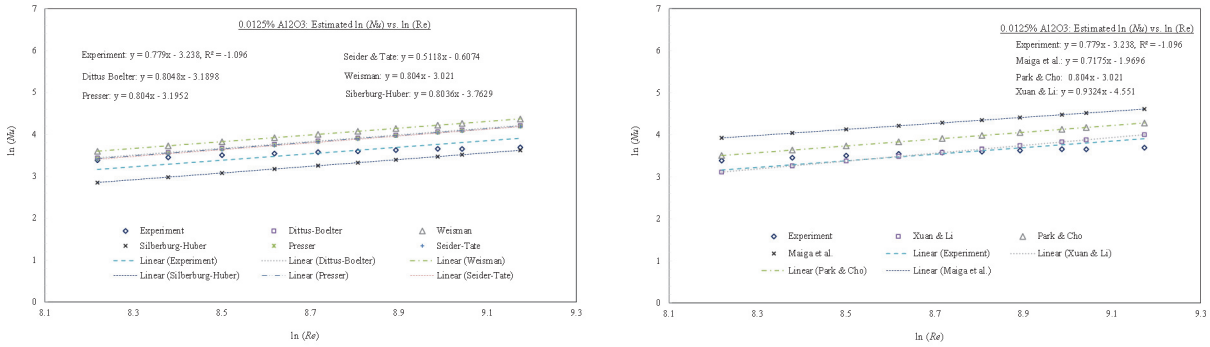

(a) (b)

FIGURE 7. Comparison of experimental *Nu* (0.0125 % alumina nanofluid) with different correlations.

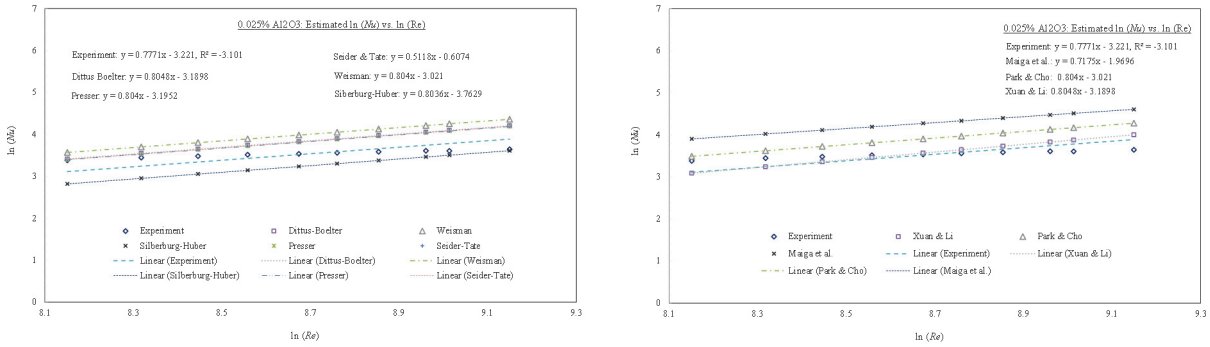

(a) (b)

FIGURE 8. Comparison of experimental *Nu* (0.025 % alumina nanofluid) with different correlations.

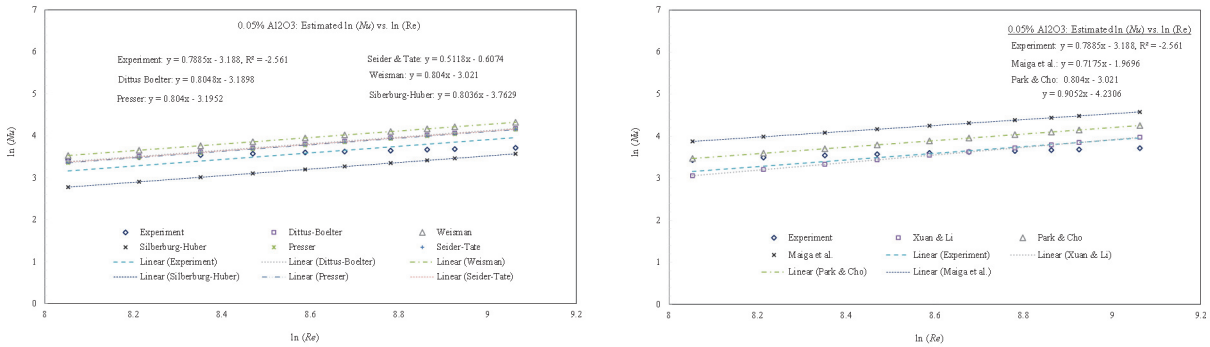

(a) (b)

FIGURE 9. Comparison of experimental *Nu* (0.05 % alumina nanofluid) with different correlations.

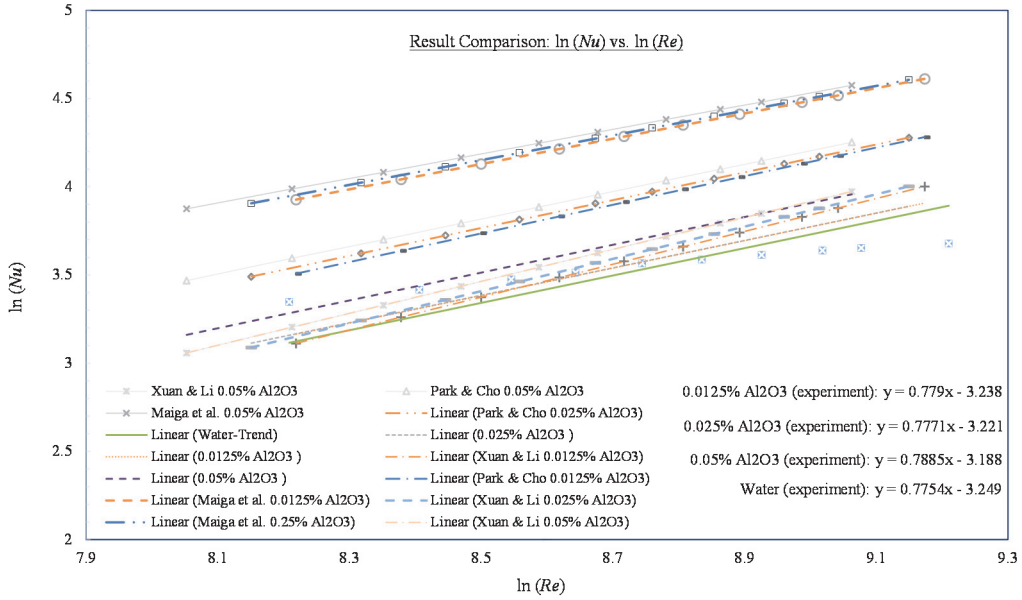

FIGURE 10. Comparison of experimental *Nu* obtained by pure water and different concentration of alumina nanofluid.

CONCLUSION

The present study has been carried out on a 3×3 square array vertical rod bundle housed in a square shell with single-phase turbulent flow covering a wide range of the inlet *Re*. During analysis of convective heat transfer, the applicability of the well-known correlations from literature has been checked and finally the constant coefficients of Dittus-Boelter correlation have been modified for this NANO specific rod bundle using pure water as well as different concentrations of alumina nanofluid. It has been experimentally observed that inclusion of only 0.05 vol. % of alumina nanoparticles in pure water can boost the convective heat transfer coefficient above 7~18 % subject to the inlet *Re*. On the other hand, it has been observed that there is no significant deviation between the experimental and estimated pressure drop spanning the inlet *Re* range of this study, which strongly supports that the NANO apparatus is capable of measuring the pressure drop without any heat source. The heat source introduces little deviation in the measured and estimated pressure drops due to the localized cross flow as well as flow mixing. The pressure drop is increased with the inclusion of alumina nanoparticle, which appears to require higher pumping power. While the difference in elevations plays a vital role in pressure drop when the flowrate is low enough, the innovative design of grid spacer is also of utmost importance to augment heat transfer and to lessen the pressure drop. Above and beyond the geometry

of coolant flow channel, heat transfer performance is also remarkably affected by the coolant flowrate, contact time between the heater rod and the coolant, heated length of the heater rod, the heater capacity, heat loss through insulation, etc. Hence, it is of utmost importance to modify these correlations for any newly constructed rod bundles if one desires to predict the heat transfer more accurately than may be determined by different correlations available in the literature.

ACKNOWLEDGEMENTS

This work was supported by the National Research Foundation of Korea (NRF), funded by the Korean Government (MSIP) under Grant No. 2008-0061900, and partly supported by the Brain Korea 21 Plus under Grant No. 21A20130012821.

ACKNOWLEDGMENTS

This work was supported by the National Research Foundation of Korea (NRF), funded by the Korean Government (MSIP) under Grant No. 2008-0061900, and partly supported by the Brain Korea 21 Plus under Grant No. 21A20130012821.

REFERENCES

1. J. Buongiorno, D. C. Venerus, N. Prabhat, T. McKrell, J. Townsend, R. Christianson et al., A benchmark study on the thermal conductivity of nanofluids. Journal of Applied Physics, 106 (2009), 094312.
2. S. Kakac, A. Pramuanjaroenkij, Review of convective heat transfer enhancement with nanofluids. International Journal of Heat and Mass Transfer 52.13 (2009), 3187-3196.
3. A.M. DeStordeur, Drag Coefficients for Fuel Elements Spacers. Nucleonics, (1961), 19, 6, 74.
4. K. Rehme, Pressure Drop Correlations for Fuel Elements Spacers. Nucl. Technol., (1973), 17-15.
5. T.H. Chun, D.S. Oh, A Pressure Drop Model for Spacer Grids With and Without Flow Mixing Vanes. J. Nucl. Sci. Technol., 35 (1998), 508-510.
6. M. Cigarini, M. Dalle Donne, Thermohydraulic Optimization of Homogeneous and Heterogeneous Advanced Pressurized Reactors. Nucl. Technol. 80 (1998), 107-132.
7. K.Y. Suh, N.E. Todreas, An Experimental Correlation of Cross Flow Pressure Drop for Triangular Array Wire Wrapped Rod Assemblies. Nucl. Technol., 76 (1987), 229.
8. Y. Xuan, Q. Li, Investigation on convective heat transfer and flow features of nanofluids. Journal of Heat transfer, 125 (2003), 151-155.
9. B.C. Pak, Y.I. Cho, Hydrodynamic and heat transfer study of dispersed fluids with submicron metallic oxide particles. Experimental Heat Transfer an International Journal, 11 (1998), 151-170.
10. S. El Bécaye Maïga, C. Tam Nguyen, N. Galanis, G. Roy, T. Maré, M. Coqueux, Heat transfer enhancement in turbulent tube flow using Al_2O_3 nanoparticle suspension. International Journal of Numerical Methods for Heat & Fluid Flow, 16 (2006), 275-292.
11. R.L. Hamilton, O.K. Crosser, Thermal Conductivity of Heterogeneous Two-Component Systems. I & EC Fundamentals, 1(1962) 182-191.
12. M.H. Pirahmadian, A. Ebrahimi, Theoretical Investigation Heat Transfer Mechanisms in Nanofluids and the Effects of Clustering on Thermal Conductivity. Int. J. of Bioscience, Biochemistry and Bioinformatics, 2 (2012), 2, 90-94.
13. L. Yu-Hua, Q.U. Wei, F. Feng Jian-Chao, Temperature Dependence of Thermal Conductivity of Nanofluids. Chinese Phys. Lett., 25 (2008), 9, 3319-3322.
14. I.E. Idelchik, Handbook of Hydraulic Resistance. Hemisphere Publishing Corporation. Washington, 1986.
15. S.K. Cheng, N.E. Todreas, Hydrodynamic Models and Correlations for Wire-wrapped LMFBR Bundles and Subchannel Friction Factors and Mixing Parameters. Nucl. Eng. Design, 92 (1985), 227.
16. N.E. Todreas, M.S. Kazimi, Nuclear Systems I: Thermal Hydraulic Fundamentals. Hemisphere Publishing Corporation, New York, NY, USA, 442-451, 1990.
17. J. Weisman, Heat Transfer to Water Flowing Parallel to Tube Bundles. Nucl. Sci. Eng., 6 (1959), 79.

ICME2015

International Conference on Mechanical Engineering 2015
(ICME 2015) 18 – 20 December, 2015, Dhaka, Bangladesh

Paper ID :599

Effect of Process Parameters on Hardness, Temperature Profile and Solidification of Different Layers Processed by Direct Metal Laser Sintering (DMLS)

Sazzad Hossain Ahmed, Ahsan Mian[a)] and Raghavan Srinivasan

Department of Mechanical and Materials Engineering, Wright State University, Dayton, Ohio 45435, USA

[a)]Corresponding author: ahsan.mian@wright.edu

Abstract. In DMLS process objects are fabricated layer by layer from powdered material by melting induced by a controlled laser beam. Metallic powder melts and solidifies to form a single layer. Solidification map during layer formation is an important route to characterize micro-structure and grain morphology of sintered layer. Generally, solidification leads to columnar, equiaxed or mixture of these two types grain morphology depending on solidification rate and thermal gradient. Eutectic or dendritic structure can be formed in fully equiaxed zone. This dendritic growth has a large effect on material properties. Smaller dendrites generally increase ductility of the layer. Thus, materials can be designed by creating desired grain morphology in certain regions using DMLS process. To accomplish this, hardness, temperature distribution, thermal gradient and solidification cooling rate in processed layers will be studied under change of process variables by using finite element analysis, with specific application to Ti-6Al-4V.

INTRODUCTION

Direct Metal Laser Sintering (DMLS) is a 3D printing technique to fabricate three dimensional parts layer by layer from powdered material by melting induced by a directed laser beam. After fabricating a layer, a new layer of powder is spread and melted on selected regions and this process is repeated until the whole part is fabricated. Medical instruments, dental, aerospace, automotive, surgical implants and in complex manufacturing fields DMLS is widely used [1-5]. During this process, metallic powder changes state from powder to liquid and finally solid. Physical processes involved in this process include heat transfer (conduction, convection and radiation) and sintering of powder [6]. Hardness is an important mechanical property to understand fabricated parts quality. As phase change occurs during this fabrication process and heat is dissipated each time a new layer is formed on top of one another, residual stress is formed in layers and also cooling rate of different layers are not same. These make hardness difference in layers.

In spite of great potential in biomedical and aerospace field, the success of DMLS process is greatly dependent on how better mechanical properties can be achieved in parts fabricated by this process. Microstructure morphology control can be an important factor to manipulate mechanical properties of parts produced by DMLS. Finite element analysis (FEA) using commercial packages have been used to obtain temperature field of selective laser melting process by many researchers [6-10]. Couple of studies has already been done on solidification map of Ti-6Al-4V, microstructure characterization in laser melting process and effects of process parameters on deposited layers [11-13]. In this short study, cooling rate and solidification rate will be calculated from temperature history in different layers

obtained by using parametric simulation by varying process parameters. Distinct feature of this study is to investigate poor layer quality of two multilayer samples fabricated by DMLS process.

HARDNESS TESTING

Two samples are fabricated by DMLS process using Ti-6Al-4V powder, particle sizes from 0-45 μm. Figure 1 (a) shows a 5-layer sample before making a mold. Important process parameters for for sample 1 & 2 are listed in table 1. For both samples laser power is 186 W. Laser moving speed is varied as 800 mm/sec and 1200 mm/sec. Sample 1 has layer thickness of 200 μm and sample 2 has layer thickness of 100 μm. Both from figure 1(c) and 1(d), it is clear that layers are full of defects and in some cases powders are not melted well. The reason of not-well bonded layers and non-melted powders can be explained from transient temperature profiles of different nodal points of a section of these layers.

Vickers hardness of layers has been measured by using a micro hardness tester, MICROMET 1. Before hardness testing, specimens are molded and polished to obtain smooth surface of layers. 500 kgf for 10 seconds has been applied to indent in different layers. Hardness is obtained from the tester by using a computer controlled interface. Hardness is tested on four different places in a single layer to get an average value. Places in a single layer are selected where there are fewer amounts of cracks and voids.

TABLE 1. List of specimens and process parameters

Process Parameters	Sample 1	Sample 2
Laser power	186 W	186 W
Laser beam speed	800 mm/sec	1200 mm/sec
Layer thickness	200 μm	100 μm

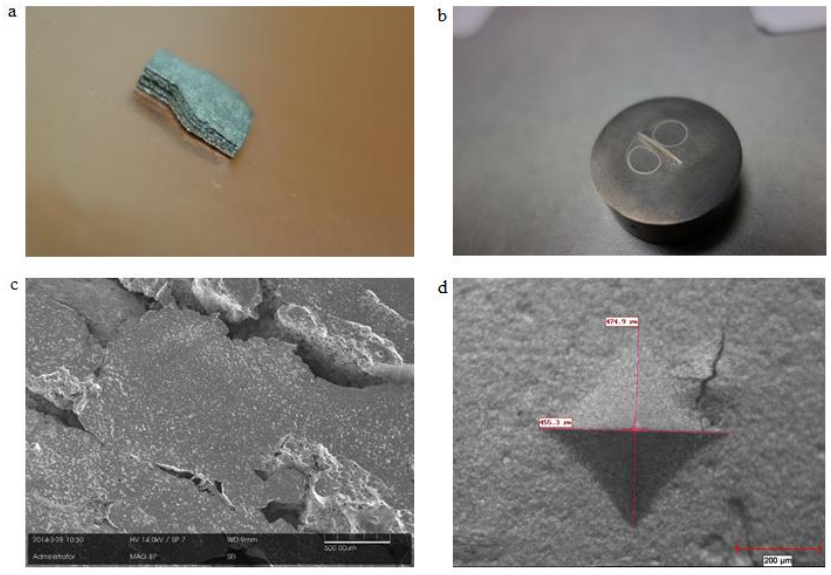

FIGURE. 1. (a) 5 layers specimen; (b) specimen in mold (after polishing); (c) cracks and voids in layers under SEM (d)indentation measurement during micro-hardness testing.

FINITE ELEMENT MODELING

Finite element modelling is done by using ANSYS parametric simulation to simulate layer formation and to find temperature distribution in different layers. Figure 2 is a schematic of layer formation process where laser heat flux Q is moving on powder bed at speed V. The laser energy absorptance on a material

depends on couple of factors: nature of surface, level of oxidation, wave length of laser, surface temperature etc. [14, 15]. Due to uncertainty of absorptance in molten pools of Ti-6Al-4V, absorptance of pure Ti powder is used from [16]. In this FEA modeling nonlinearities due to temperature dependent properties are included by using temperature-dependent specific heat and thermal conductivity of Ti-64. Convection boundary condition is applied on all outer surfaces with ambient temperature of 40 °C and effects of radiation are neglected. From earlier work by Dykhuizen and Dobraich [17] suggests that laser power dissipated by radiation, convection and evaporation is neglected compared to that dissipated by conduction. Element length on top of layers is 25 μm. Thus 100 μm laser spot is divided in four divisions. Average heat flux on the laser spot is obtained by using equation (1), where $\alpha = 0.3$, P = laser power and $r_0 = 50$ μm. The laser scans on top of the powder bed in a single track of length 500 μm. In figure 3(a) and

$$q_{avg} = \frac{1}{\pi r_0^2}\int_0^{r_0} q(2\pi r)dr = \frac{0.865\alpha P}{\pi r_0^2} \quad (1)$$

3(b) FEA model and temperature distribution on top layer at the end step of simulation are shown respectively. In this simulation both substrate and layers are considered as Ti-64.

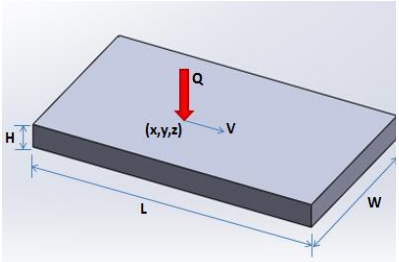

FIGURE 2. Predictive model of DMLS process simulation.

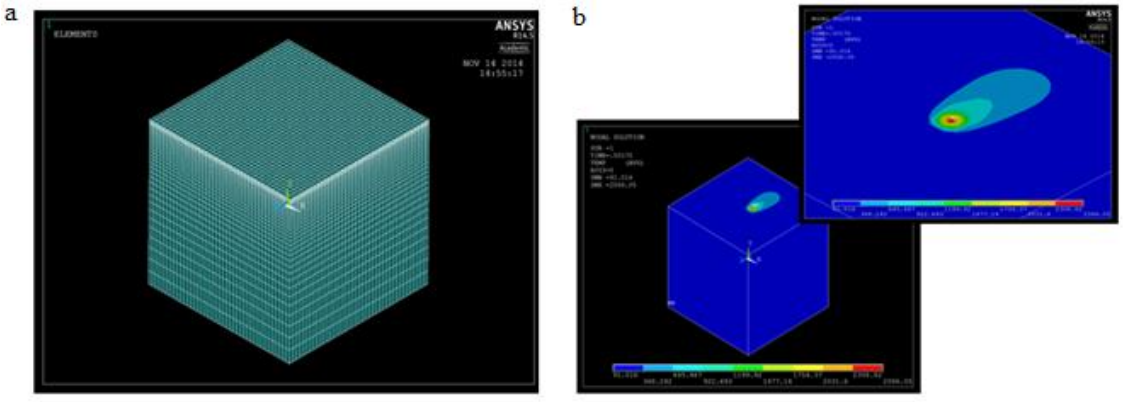

FIGURE 3 (a) Meshing of layers and substrate; (b) Temperature distribution in process simulation (layer thickness = 30 μm, idle time = 0.5 sec, laser power = 186 W, laser moving speed = 1200 mm/sec, preheating temperature = 90 °C and track length = 500 μm).

RESULTS AND DISCUSSION

Experimental

Average hardness of layers in samples 1 and 2 are presented in figure 4. Top layer has 10 to 18 HV higher hardness value from other layers. Cooling rate and residual stress play important roles in hardness. Higher cooling rate increases hardness and also changes microstructure [18]. Top layer has higher scope of heat transfer by convection and radiation. On the other hand, possibility heat transfer by conduction is higher in bottom layers. Top layer also has higher residual stress than other layers. Comparable hardness results have been found in ref [18], where a Ti-6Al-4V component fabricated by DMLS process in different heat treatment conditions.

It is clear from figure 4 that for sample 1, hardness values decreases and then increases that are similar to trends shown in ref [19]. Vickers hardness of bulk Ti-6Al-4V is 349 which is 23% to 32% higher than results of two specimens. It may be mentioned here that samples that are tested in this case were not subjected to any heat treatment such as annealing. This lower hardness may be due to the non-heat treatment of the material and existence of defects like cracks and voids in the layers. It is observed that sample 2 has slightly better mechanical properties than sample 1.

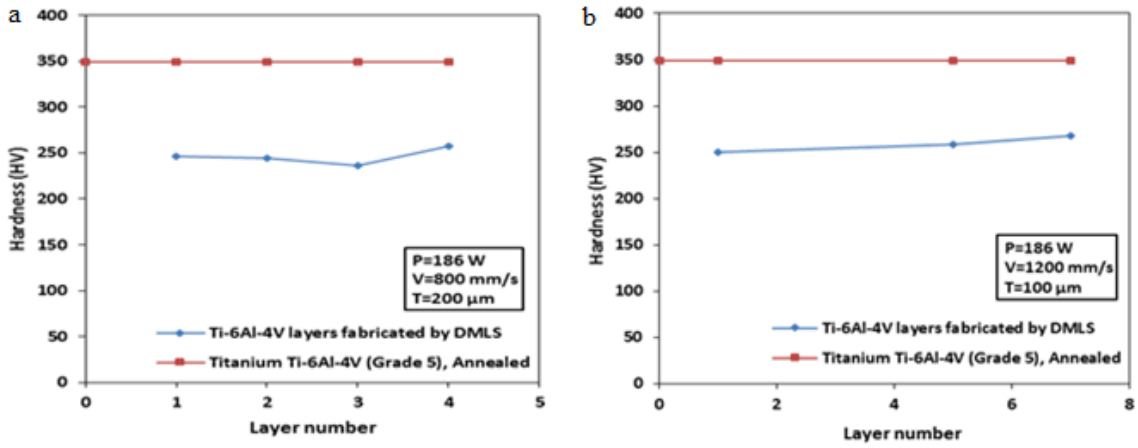

FIGURE. 4. Hardness at different layers: (a) sample 1; (b) sample 2.

Finite Element Analysis

Temperature distribution at 6 nodal points across two layers for 1200, 800 and 600 mm/sec laser speeds are illustrated in figure 5(b), 5(c) and 5(d) respectively. It has been clear that laser speed has significant effects on maximum temperature in different layers. Maximum temperature obtained for 1200, 800 and 600 mm/sec laser moving speeds are 2628, 2693 and 2729 °C which are comparable with ref [6]. Figure 5(a) shows temperature profile at substrate, 1st layer and 2nd layer when laser scanning speed is 800 mm/sec. From figure 5(b) we can clearly see how lower irradiation time or higher laser moving speed for a particular layer thickness and laser power can result non-bonded layers and defects in layers. During formation of 1st layer maximum temperature is below melting temperature of Ti-64 results non-bonded or poorly sintered layers.

The solidification cooling rate and thermal gradient can be extracted from 3D model results at various nodal locations. At any nodal location thermal gradient and solidification cooling rate can be expressed by equations 2 to 4, ref [11].

$$\frac{\partial T}{\partial t} = \left| \frac{Ts - TL}{ts - tl} \right| \tag{2}$$

Where, T_L and T_S are liquidus and solidus temperatures at each node and at times t_L and t_S respectively. This will give us an average cooling rate of solidification. The thermal gradient can be obtained from Fourier's law of heat conduction:

$$G = |\vec{\nabla} T| = \frac{|\vec{q}|}{K} \tag{3}$$

Where, $|\vec{q}|$ is magnitude of heat flux and K is thermal conductivity at liquidus temperature. Then solidification rate can be determined by [11],

$$R = \frac{1}{G} \frac{\partial T}{\partial t} \tag{4}$$

From thermal gradient vs solidification plot in figure 6 at all 6 nodal points, fully columnar microstructure is formed for both 600 mm/sec and 800 mm/sec laser scanning speeds which is expected for poorly bonded layers.

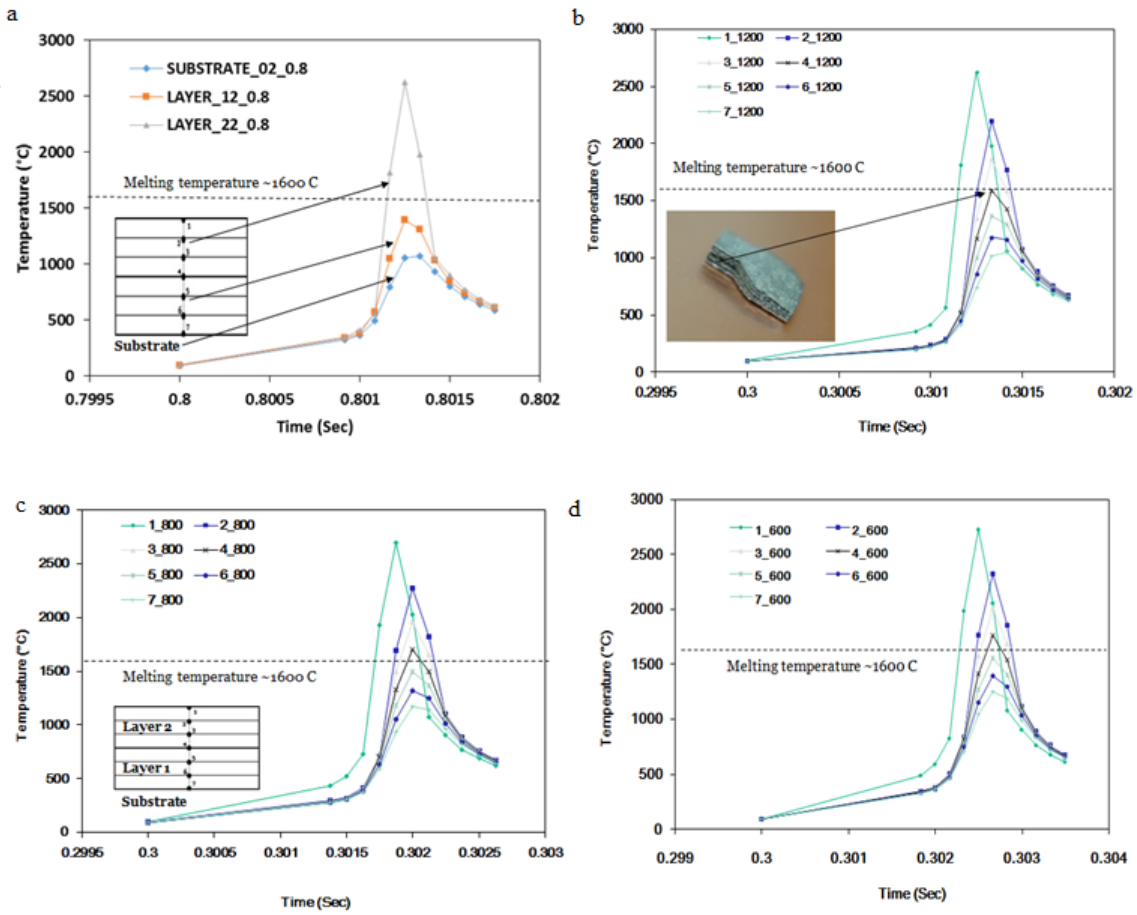

FIGURE 5. (a) Temperature profiles at substrate, layer 1 & 2 at 800 mm/sec laser speed; temperature profiles at different nodal locations across layers at (b)1200 mm/sec, (c) 800 mm/sec and (d) 600 mm/sec laser speeds.

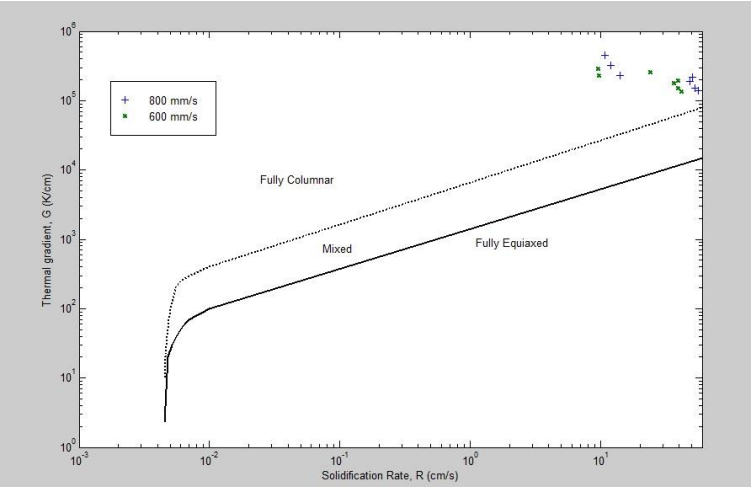

FIGURE 6. Grain morphology across layers at 800 mm/sec and 600 mm/sec laser speeds.

CONCLUSIONS

In this sort study, hardness of different layers fabricated by DMLS process are measured by using micro hardness tester and thermal analysis of different layers for varying process parameters are performed by finite element analysis. Grain morphology across the layers has been found from temperature profiles at different nodal points and solidification map. Process parameters such as laser power and laser scanning speed affect grain morphology of processed layers and ultimately affect mechanical properties of fabricated component.

ACKNOWLEDGEMENTS

The authors thank the Mound Laser and Photonics Center (MLPC) for creating samples for this study.

REFERENCES

[1] A. Simchi, Direct laser sintering of metal powders: Mechanism, kinetics and microstructural features, Materials Science and Engineering, A 428 (2006) 148–158.
[2] Direct metal laser sintering could be ‘better than’ rapid investment casting for aerospace parts, Metal Powder Report, Volume 69, Issue 2, March–April 2014, Pages 41.
[3] L.E. Murra, S.A. Quinonesb, S.M. Gaytana, M.I. Lopeza, A. Rodelaa, E.Y. Martineza, D.H. Hernandeza, E. Martineza, F. Medinac, R.B. Wicker, Microstructure and mechanical behavior of Ti–6Al–4V produced by rapid-layer manufacturing, for biomedical applications, Journal of the Mechanical Behavior of Biomedical Materials Volume 2, Issue 1, January 2009, Pages 20–32
[4] Liciane Sabadin Bertola, Wilson Kindlein Júniora, Fabio Pinto da Silvaa, Claus Aumund-Kopp, Medical design: Direct metal laser sintering of Ti–6Al–4V, Materials & Design, Volume 31, Issue 8, September 2010, Pages 3982–3988
[5] Erhard Brandl, Achim Schobertha, Christoph Leyensb, Morphology, microstructure, and hardness of titanium (Ti-6Al-4V) blocks deposited by wire-feed additive layer manufacturing (ALM), Materials Science and Engineering A 532 (2012) 295– 307
[6] I.A. Roberts, C.J. Wang, R. Esterlein, M. Stanford, D.J. Mynors, A three-dimensional finite element analysis of the temperature field during laser melting of metal powders in additive layer manufacturing, International Journal of Machine Tools & Manufacture 49 (2009) 916–923
[7] A Nisar, M J J Schmidt, M A Sheikh and L Li, Three-dimensional transient finite element analysis of the laser enamelling process and moving heat source and phase change considerations, Proceedings of the Institution of Mechanical Engineers, Part B-Engineering Manufacture, vol.217 (6), 2003, pp.753–764
[8] Contuzzi, N., Campanelli, S. L. & Ludovico, A. D., 3D Finite Element Analysis in the Selective Laser Melting Process, International Journal of Simulation Modelling 10 (2011) 3, 113-121
[9] Chaowen Li, Yong Wanga, Huanxiao Zhan, Tao Han, Bin Han, Weimin Zhao, Three-dimensional finite element analysis of temperatures and stresses in wide-band laser surface melting processing, Materials and Design 31 (2010) 3366–3373
[10] L. Dong, A. Makradi, S. Ahzi, Y. Remond, Three-dimensional transient finite element analysis of the selective laser sintering process, Journal of materials processing technology 209 (2009) 700–706
[11] Srikanth Bontha, Nathan W. Klingbeil, Pamela A. Kobryn, Hamish L. Fraser, Thermal process maps for predicting solidification microstructure in laser fabrication of thin-wall structures, Journal of Materials Processing Technology 178 (2006) 135–142

[12] W. Kurz, C. Bezencon, M. Gaumann, Columnar to equiaxed transition in solidification processing, Society and Technology of Advanced Materials 2 (2001) 185-191
[13] P.A. Kobryn, S.L. Semiatin, Microstructure and texture evolution during solidification processing of Ti–6Al–4V, Journal of Materials Processing Technology 135 (2003) 330–339
[14] W.L. Chen, Y.C. Yang, H.L. Lee, Estimating the absorptivity in laser processing by inverse methodology, Applied Mathematics and Computation 190 (2007) 712 – 721
[15] M.R. Frewin, D.A. Scott, Finite element model of pulsed laser welding, Welding Research Supplement (1999) 15–22
[16] P. Fischer, et al., Sintering of commercially pure titanium powder with a Nd:YAG laser source, Acta Materialia 51 (6) (2003) 1651–1662
[17] D. Dobranich, R. Dykhuizen, Scoping thermal calculations of the LENS process, Sandia National Laboratories Internal Report, 1998
[18] Yisheng Zhao and Xinming Zhang, Effects of Cooling Rate on Metallographic Structure and Hardness of Bearing-B Steel, 2nd International Conference on Electronic &Mechanical Engineering and Information Technology (EMEIT-2012)
[19] L. Chauke, K. Mutombo, C. Kgomo, Characterization of the Direct Metal Laser Sintered Ti6Al4V Components, Material Science and Manufacturing/Light Metals, Council for Scientific and Industrial Research (CSIR), Pretoria, South Africa

International Conference on Mechanical Engineering 2015
(ICME 2015) 18 – 20 December, 2015, Dhaka, Bangladesh

Paper ID : 603

Analysis of Entropy Generation for Double Diffusive MHD Convection in a Square Cavity with Isothermal Hollow Cylinder

Satyajit Mojumder[a)], Sourav Saha[b)] and Sumon Saha[c)]

Department of Mechanical Engineering, Bangladesh University of Engineering and Technology, Dhaka-1000, Bangladesh.

[a)]Corresponding author: satyajit@me.buet.ac.bd
[b)] ssaha09@me.buet.ac.bd
[c)]sumonsaha@me.buet.ac.bd

Abstract. Entropy optimization is a major concern for designing modern thermal management system. In the present work, entropy analysis in a square cavity with an isothermal hollow cylinder at the center is carried out for magneto-hydrodynamic (MHD) double diffusive convection. Galerkin weighted residuals method of finite element formulation is adopted for the numerical solution. Entropies due to fluid flow, heat, and mass transfer are computed for wide range of Hartmann ($0 \leq Ha \leq 50$) and Lewis numbers ($1 \leq Le \leq 15$), and buoyancy ratios ($-5 \leq N \leq 5$) at constant Rayleigh and Prandtl numbers. It is found that the influence of buoyancy ratio is prominent on entropy generation, which also depends on both Lewis and Hartmann numbers. The ratio N = -1 shows minimum entropy generation for any combination of Lewis and Hartman numbers. Visualization of isentropic contours and the variation of total entropy with the governing parameters provide remarkable evidences of entropy optimization.

INTRODUCTION

MHD convection is gaining attention from the scientific community in recent days due to its wide range of applications in nuclear reactors, micro-electronics cooling, crystal growth, refrigeration system, and so on [1, 2, 3]. MHD convection is basically the influence of external magnetic field on convection of magnetically susceptible fluid. When any such fluid passes through an applied magnetic field, Lorentz force is generated, which tries to retard the convective transport. Diego et al. [4] studied natural convection in a square cavity having a heated solid circular obstruction inside. They reported that inner obstacle had profound effect on augmentation of heat transfer. Similar type of investigations having an internal obstacle have been carried out by Laguerre et al. [5], Hussain and Hussein [6], and De and Dalal [7]. Variation of concentration naturally enforces double diffusive convective transport inside a cavity. External magnetic field also has significant impact on such concentration driven flow field. Venkatachalappa et al. [8] investigated the effect of magnetic field on double diffusive heat transfer and reported that higher buoyancy ratio contributed to alter flow and thermal fields.

Magnetic field also has noteworthy effect on entropy generation. Basak et al. [9] studied entropy generation in a square cavity for various thermal boundary conditions and concluded that these boundary conditions along with Rayleigh number had significant impact on entropy generation. Mejri et al. [10] analyzed entropy generation in water-Al_2O_3 nanofluid filled square enclosure with sinusoidal heating boundary condition under MHD convection and suggested proper choice of Rayleigh and Hartmann numbers to maximize heat transfer with optimum entropy generation. Most recently, Meherz et al. [11] carried out numerical simulation on entropy generation in the presence of magnetic field for an open cavity and found that magnetic field had significant influence on entropy generation.

From the above review, it can be concluded that very few works are focused on analyzing entropy generation under external magnetic field in the context of double diffusive heat transfer inside a cavity. The present work aims to analyze the entropy generation for a square cavity with isothermal hollow cylindrical insert at the center in the context of double diffusive MHD convection. All the possible entropies such as entropy due to fluid flow, thermal

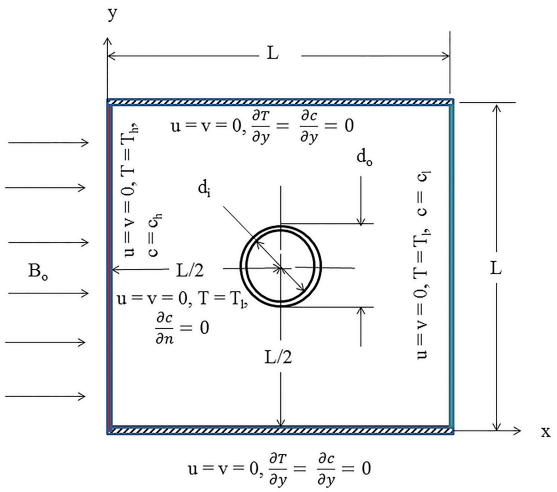

FIGURE 1. Schematic diagram for the present problem with appropriate boundary conditions and coordinate system.

interaction, mass diffusion and combined heat and mass transfer are computed for a wide range of Hartmann and Lewis numbers and buoyancy ratios. The variation of total entropy generation is critically observed to obtain the characteristics features of MHD flows.

PROBLEM FORMULATION

Physical Modeling

The schematic diagram of the physical problem is shown in Fig. 1 with appropriate boundary conditions and co-ordinate system. A square cavity having equal length and height of L is considered, where the left and the right vertical walls are maintained hot ($T = T_h$) and cold ($T = T_l$) conditions, respectively. Top and Bottom horizontal walls of the cavity are insulated. A hollow cylindrical insert with isothermal outer surface ($T = T_l$) is placed at the center position of the cavity. The inner and the outer diameters of the hollow cylinder for the present problem are d_i and d_o, respectively. The physical dimensions of the cylinder are $d_i/L = 0.19$ and $d_o/L = 0.20$, respectively. Higher concentration of air, with mixture of different gases, is considered near left vertical wall ($c = c_h$) and lower concentration is maintained near right vertical wall ($c = c_l$). Both horizontal walls of the cavity and the outer surface of the cylindrical insert are assumed to be impermeable to mass transfer. An external magnetic field with strength B_o is applied on the left side of the cavity acting along the positive x-axis. All the solid boundaries are assumed to be stationary. Viscous heating and radiation effects are neglected for simplifying the problem.

Mathematical Modeling

The working fluid is assumed to be incompressible and Newtonian with constant thermophysical properties except the variation of density. Boussinesq approximation is considered to include the variation of density due to change of temperature. Governing continuity, momentum, energy, and diffusion equations for a laminar flow under steady state condition can be written in the non-dimensional form as follows:

$$\frac{\partial U}{\partial X} + \frac{\partial V}{\partial Y} = 0, \tag{1}$$

$$U\frac{\partial U}{\partial X} + V\frac{\partial U}{\partial Y} = -\frac{\partial P}{\partial X} + Pr\left(\frac{\partial^2 U}{\partial X^2} + \frac{\partial^2 U}{\partial Y^2}\right), \tag{2}$$

$$U\frac{\partial V}{\partial X} + V\frac{\partial V}{\partial Y} = -\frac{\partial P}{\partial Y} + Pr\left(\frac{\partial^2 V}{\partial X^2} + \frac{\partial^2 V}{\partial Y^2}\right) + RaPr(\Theta + NC) - Ha^2 PrV, \tag{3}$$

$$U\frac{\partial\Theta}{\partial X}+V\frac{\partial\Theta}{\partial Y}=\frac{\partial^2\Theta}{\partial X^2}+\frac{\partial^2\Theta}{\partial Y^2}, \tag{4}$$

$$U\frac{\partial C}{\partial X}+V\frac{\partial C}{\partial Y}=\frac{1}{Le}\left(\frac{\partial^2 C}{\partial X^2}+\frac{\partial^2 C}{\partial Y^2}\right), \tag{5}$$

where, X, Y are the non-dimensional spatial coordinates, U and V are the non-dimensional velocities along X and Y directions, respectively, P, Θ and C are the non-dimensional pressure, temperature, and concentration, respectively. Following scales are adopted to obtain the aforementioned non-dimensional equations,

$$X=\frac{x}{L}, Y=\frac{y}{L}, U=\frac{uL}{\alpha}, V=\frac{vL}{\alpha}, \Theta=\frac{T-T_l}{T_h-T_l}, P=\frac{pL^2}{\rho\alpha^2}, C=\frac{c-c_l}{c_h-c_l}. \tag{6}$$

The non-dimensional governing parameters for the present problem are Prandtl (Pr), Rayleigh (Ra), Lewis (Le), Hartmann (Ha) numbers, and buoyancy ratio (N), which can be defined as follows:

$$Pr=\frac{\eta}{\alpha}, Ra=\frac{g\beta_T(T_h-T_l)L^3}{\alpha\eta}, Le=\frac{\alpha}{D}, Ha=B_oL\sqrt{\frac{\sigma}{\rho\eta}}, N=\frac{\beta_c(c_h-c_l)}{\beta_T(T_h-T_l)}, \tag{7}$$

where $\eta, \alpha, g, D, \beta_T, \beta_C, \sigma, \rho$ are kinematic viscosity, thermal diffusivity, gravitational acceleration, mass diffusivity, thermal expansion coefficient, concentration expansion coefficient, electrical conductivity, and density of the working fluid, respectively. The boundary conditions for the present problem are listed in dimensionless form in Table 1.

TABLE 1. Non-dimensional boundary conditions for the present problem.

Boundary wall(s)	**Velocity field**	**Temperature**	**Concentration**
$X=0, 0\le Y\le 1$	$U=V=0$	$\Theta=1$	$C=1$
$X=1, 0\le Y\le 1$	$U=V=0$	$\Theta=0$	$C=0$
$0\le X\le 1, Y=0,1$	$U=V=0$	$\partial\Theta/\partial Y=0$	$\partial C/\partial Y=0$
Outer surface of hollow cylinder	$U=V=0$	$\Theta=0$	$\partial C/\partial n=0$

For double diffusive natural convection case, the associated irreversibilities are due to fluid friction, heat and mass transfer. According to local thermodynamic equilibrium of the linear transport theory,

$$S_\Theta=\left(\frac{\partial\Theta}{\partial X}\right)^2+\left(\frac{\partial\Theta}{\partial Y}\right)^2, \tag{8}$$

$$S_\psi=\Phi_1\left[2\left(\frac{\partial U}{\partial X}\right)^2+2\left(\frac{\partial V}{\partial Y}\right)^2+\left(\frac{\partial U}{\partial Y}+\frac{\partial V}{\partial X}\right)^2+Ha^2U^2\right], \tag{9}$$

$$S_C=\Phi_2\left[\left(\frac{\partial C}{\partial X}\right)^2+\left(\frac{\partial C}{\partial Y}\right)^2\right], \tag{10}$$

$$S_K=\Phi_3\left[\frac{\partial C}{\partial X}\frac{\partial\Theta}{\partial X}+\frac{\partial C}{\partial Y}\frac{\partial\Theta}{\partial Y}\right], \tag{11}$$

where, $\Phi_1=\mu T_0\alpha^2/[kL^2(\Delta T)^2]$, $\Phi_2=(RDT_0/kc_0)(\Delta c/\Delta T)^2$, $\Phi_3=(RD/k)(\Delta c/\Delta T)$ and S_Θ, S_ψ, S_C and S_K are entropy generations due to heat transfer, fluid friction, mass transfer, and combined heat and mass transfer, respectively. Here, T_0 and c_0 are the reference fluid temperature and concentration, k and μ are thermal conductivity and dynamic viscosity of the working fluid, respectively. In these equations, R is the universal gas constant, $\Delta c=c_h-c_l$ and $\Delta T=T_h-T_l$. For the present problem, $\Phi_1=10^{-4}, \Phi_2=0.5$ and $\Phi_3=0.01$ have been considered [9]. Local entropy generation can be represented by the following expression:

$$S^*=S_\Theta+S_\psi+S_C+S_K. \tag{12}$$

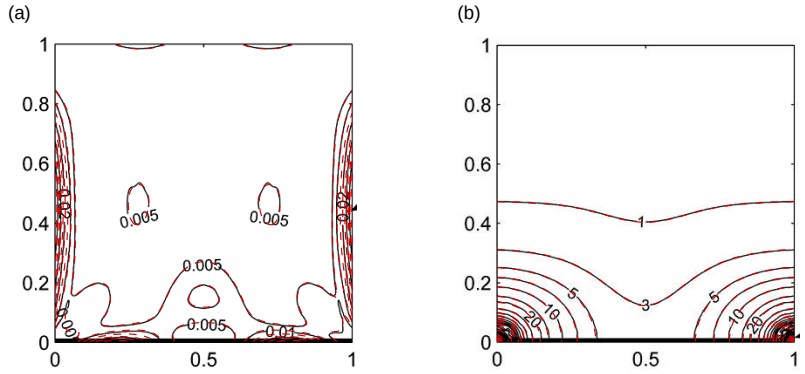

FIGURE 2. Comparison of contour plots of (a) S_ψ and (b) S_Θ with Basak et al. [9] at $Ha = 0$, $Ra = 10^3$ and $Pr = 0.026$ for isothermal boundary condition. Red dashed line represents the present code. (Color online only)

Total entropy generation inside the cavity is now computed as follows:

$$S = \int_\Omega S^* d\Omega, \tag{13}$$

where, $\Omega = 1 - \pi d_o^2/4L^2$ is the non-dimensional domain area inside the cavity normalized by the area of the square cavity (L^2).

NUMERICAL METHODS, GRID SENSITIVITY TEST AND CODE VALIDATION

Galerkin weighted residuals method of finite element scheme is adopted to find numerical solution for the present problem. The entire domain is discretized into nonuniform triangular elements and the governing equations (1-5) are applied with the specified boundary conditions at selected nodes of elements. Energy and diffusion equations are discretized using simplex elements, while Navier-Stokes equations are discretized using six nodded triangular elements. Resulting set of algebraic equations are solved using iteration technique. A convergence criterion is set as $|\gamma^{m+1} - \gamma^m| \leq 10^{-5}$, where γ is the general dependent variable and m is the iteration number. Grid sensitivity tests are performed for $N = 1$, $Ha = 25$, $Le = 10$ at $Ra = 10^4$ and $Pr = 0.71$. The details of the grid refinement test are shown in Table 2. It is found that nonuniform mesh with element number of 4224 is optimum to ensure reasonable numerical accuracy. Thus the mesh size with 4224 element numbers is selected for entire simulation.

TABLE 2. Grid independence test for the present problem at $N = 1$, $Ha = 25$, $Le = 10$, $Ra = 10^4$ and $Pr = 0.71$.

Element numbers	S_ψ	S_Θ	S_C	S_K	**Total entropy (S)**
872	0.885140	2.208530	2.434311	0.015852	5.543833
1152	0.885525	2.208495	2.435795	0.015854	5.545669
2172	0.885746	2.208470	2.436783	0.015855	5.546855
3488	0.885795	2.208475	2.436885	0.015855	5.547010
4224	0.885824	2.208472	2.436994	0.015855	5.547145
6722	0.885838	2.208486	2.437088	0.015855	5.547248

The verification of simulation code is performed to check the reliability of the present results. The present code is validated with the works of Basak et al. [9] for a square cavity with isothermally heated bottom wall. The present results in terms of contour plots of S_ψ and S_Θ are computed for $Ra = 10^3$ and $Pr = 0.026$ and are shown in Fig. 2. The result of Basak et al. [9] are shown in black line, whereas the present simulation is represented by the red dashed line. As it can be seen that both S_ψ and S_Θ contours are identical with the previous work of Basak et al. [9]. Therefore, the present code can guarantee reliable numerical solution.

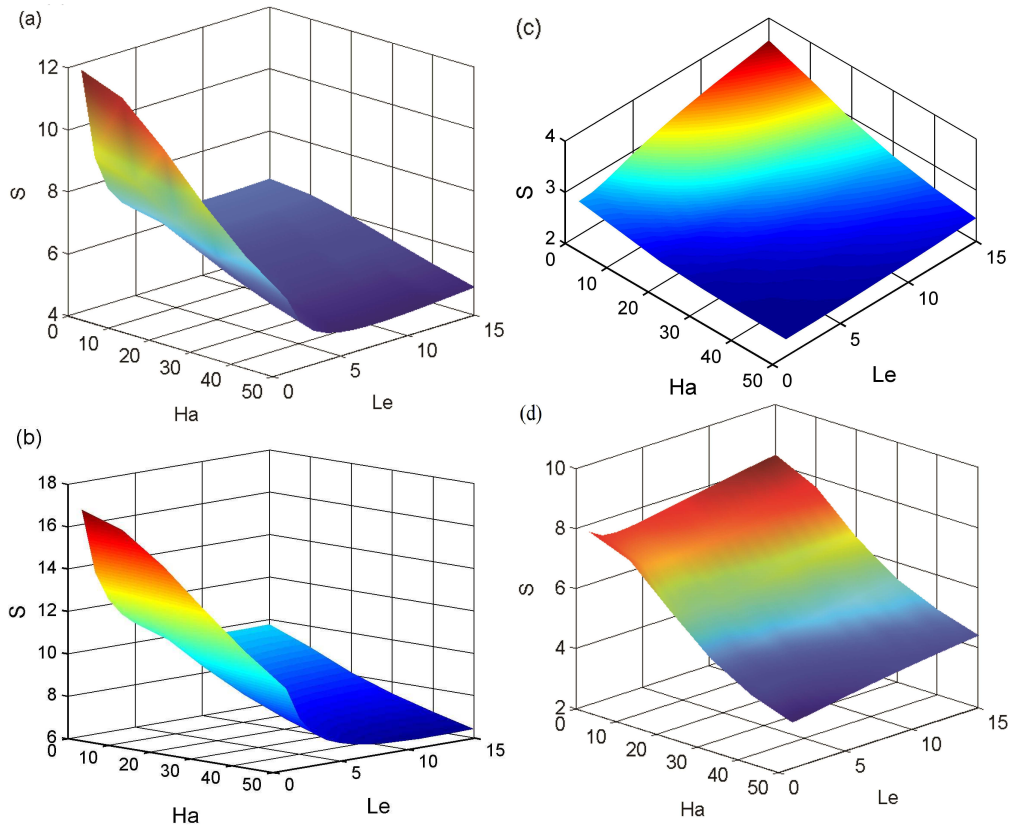

FIGURE 3. Variation of total entropy with *Ha* and *Le* at (a) $N = -5$, (b) $N = 5$, (c) $N = -1$, and (d) $N = 1$.

RESULTS AND DISCUSSION

In the present investigation, generation of entropy for MHD double diffusive convection is studied in a brief manner. Important governing parameters such as *Ha*, *Le*, and *N* are varied to observe how these parameters affect thermodynamic properties of the system under investigation through energy dissipation. Other governing parameters like *Pr* and *Ra* are kept fixed at 0.71 and 10^4, respectively.

Figure 3 (a–d) exhibits 3D plots of total entropy generation (S) against the variation of *Ha* and *Le* for $N = -5$, 5, -1 and 1, respectively. All cases confirm that S decreases with increase of *Ha*. From thermodynamic point of view, when the motion of fluid flow is slowed down by higher value of *Ha*, fluid inside the cavity gains more potential to dissipate energy. These results in lower value of entropy generation and higher exergy. The variation of total entropy due to the increment of *Ha* does not affected by any value of *Le* and *N*. However, the total entropy generation varies differently with the increase of *Le* for any value of *Ha*. Moreover, these variations are also dependent on the selection of buoyancy ratio. It is observed from Fig. 3 that for $N = -5$ and 5, the total entropy generation decreases with *Le*, whereas S increases with increasing *Le* for $N = -1$ and 1. It should be mentioned that for $N = -1$, value of S is the lowest among all the cases. At these buoyancy ratio, both thermal and species diffusion potentials are same. When $N = 1$ or -1, increasing *Le* increases the volume of mass diffusion. This is a spontaneous process and thermodynamically favorable for the increment of entropy generation. Moreover, it is expecting to have critical value of *N* where the effect of *Le* on S is optimum. Hence, it is necessary to observe the effect of *Le* and *Ha* separately on different value of *N*. Further explanation regarding these issues will be discussed next using Fig.4 (a–b) which clearly show these observations to identify the optimum point(s) for entropy generation.

Apart from the effect of *Le* and *Ha*, we also focus on the variation of total entropy generation with respect to buoyancy ratio. Figure 4 (a) portrays the variation of total entropy with *N* for different values of *Le* (= 1, 7, and 15) at constant *Ha* = 25. Similar plot is drawn in Fig. 4 (b) where the variation of total entropy is shown for different values

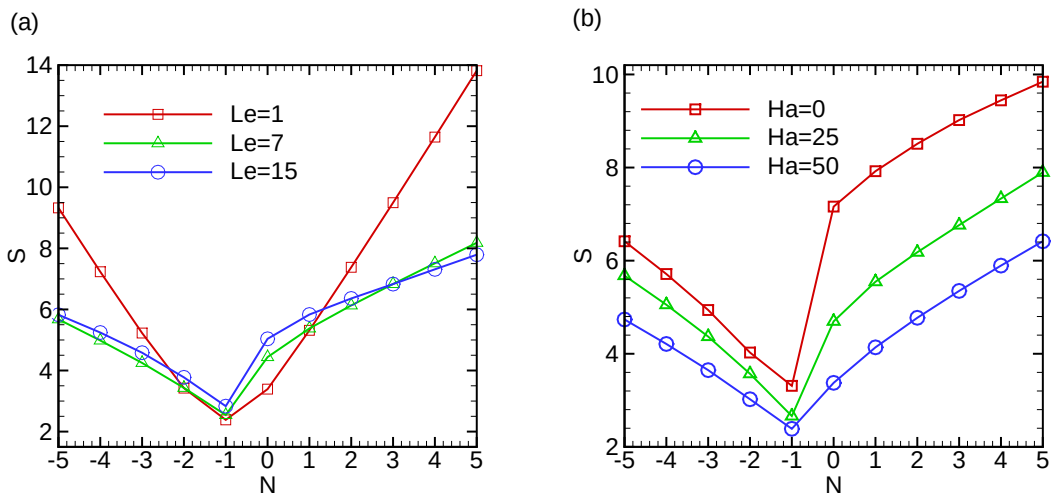

FIGURE 4. Variation of total entropy with N for (a) different Le at $Ha = 25$ and for (b) different Ha at $Le = 10$.

of Ha (= 0, 25 and 50) at constant $Le = 10$. These figures actually imply the impact of thermal and mass diffusion on total entropy. Within the range of N ($-5 \leq N \leq 5$), it is found that total entropy always reaches at minimum when $N = -1$ (as shown both in Fig. 4(a) and (b)). Physical reason of this outcome may be the equity of thermal and mass buoyancies in opposite directions (since N is negative and equal to 1). Consequently, only terms contributing to entropy generation are fluid friction and combined heat and mass transfer, and hence, total entropy at this point becomes minimum. The value of S increases if N is either higher or lower than -1, however, the positive increment always results in higher value of S than the negative increment of N. From Fig. 4(a), it is interesting to observe that the rate of increment of S with either positive or negative increment of N varies differently with the change of Le at constant Ha. However, when the value of Ha changes at constant Le as shown in Fig. 4(b), the rate of change of total entropy (slope of the curve in either positive or negative increment of N) is almost same. This implies a consistent behavior of total entropy as a function of buoyancy ratio for different values of Ha. As a results, some interesting characteristics can be pointed out from Fig. 4(a) for the variation of Le at $Ha = 25$. In fact, the effect of Le on S is totally dependent on the selection of N. Total entropy generation either increase or decrease with increasing Le based on the choice of either positive or negative buoyancy ratio.

A closer observation of Fig. 4(a) reveals some interesting features of entropy generation that depends on the choice of Le and N. When $N = -1$, the value of S increases with increasing Le and it continues to rise both in positive and negative increment of N up to the optimum point based on the choice of Le. At this point (optimum value of N), the values of S for two different values of Le become equal and further increase of N (corresponding increment or decrement of N) opposes the impact of Le on entropy generation. For example, at $N = 1$, the values of S for $Le = 1$ and 7 are same and when $N > 1$, total entropy for $Le = 1$ is always higher than that for $Le = 7$. Similarly, another optimum point at $N = 3$ can be observed for $Le = 7$ and 15. In fact, for each pair of Le (for example, $Le = 1$ and 7), there are two optimum points ($N = 1$ and -2) where the value of total entropy becomes equal for each Le. Beyond this optimum point, total entropy increase with decreasing Le whereas within the optimum region, the enhancement of total entropy occurs with increasing value of Le.

Figures 5 and 6 compare the effects of Lewis number on the isentropic plots for constant N (= 1) and Ha (= 25). Moreover, the buoyancy ratio is selected based on the observation of optimum point as shown in Fig. 4 for $Le = 1$ and 7. At this point, total entropy is same for the above two cases and hence, it would be interesting to investigate the nature of isentropic lines generated due to fluid flow (S_ψ), heat transfer (S_Θ), mass transfer (S_C) and combined heat and mass transfer (S_K). Figures 5(a) and 6(a) reveal that the contour lines of S_ψ are congested near vertical boundary walls of the cavity as considerable amount of energy is dissipated to overcome the viscous effect induced by no-slip wall condition. Moreover, the hydrodynamic boundary layer is developed at those regions. Isentropic lines for fluid flow are also surrounded around insert wall although the insert boundary generates very little entropy. This is a clear indication of separation of flow due to the presence of hollow insert. Both patterns for isentropic plots of S_ψ are similar for $Le = 1$ and 7 as shown in Fig. 5(a) and 6(a). However, data for $Le = 7$ generates lower entropy compare to the case

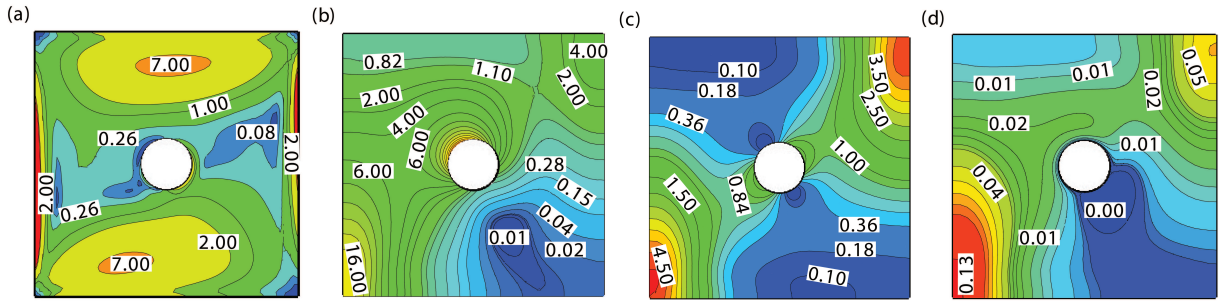

FIGURE 5. Contour plots of (a) S_ψ, (b) S_Θ, (c) S_C, and (d) S_K for representative case of $N = 1$, at $Le = 1$ and $Ha = 25$.

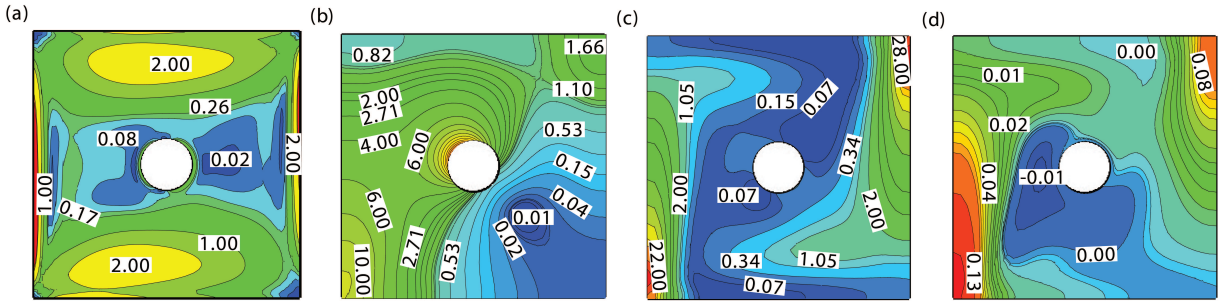

FIGURE 6. Contour plots of (a) S_ψ, (b) S_Θ, (c) S_C, and (d) S_K for representative case of $N = 1$, at $Le = 7$ and $Ha = 25$.

for $Le = 1$. Another similar patterns of isentropic lines for heat transfer are observed in Fig. 5(b) and 6(b). Figure 5(b) shows that isentropic lines with higher values of S_Θ are clustered near the junction of hot and adiabatic walls. Sudden change of thermal condition at this region gives rise to such distribution of S_Θ. Isentropic lines for heat transfer are also become parallel and clustered near the isothermal cold wall of the insert. This patterns represent severe energy transfer at that region. The only difference between Fig. 5(b) and 6(b) is that the nondimensional entropy for case $Le = 1$ has higher value compared to that for case $Le = 7$. Now the contour plot of S_C as shown in Fig. 5(c) indicates that the isentropic lines are clustered near bottom-left and top-right corners of the cavity where steep concentration gradient exists. This gradient causes energy transport via species diffusion. The combined effect of heat and mass transfer is represented by the contour plots of S_K which is illustrated in Fig. 5(d). The contour lines have higher density near the regions of steep temperature and concentration gradients. This changes are due to high propensity of energy transfer (resulting in entropy generation according to the second law of thermodynamics). Now comparing Fig. 5(c) and 6(c), and Fig. 5(d) and 6(d), it is interesting to observe that the isentropic lines evolve more with boundary wall due to increase of Le from 1 to 7. As a results, the patterns of those contour plots change drastically in order to balance the higher values of S_ψ and S_Θ in Fig. 5(a) and 5(b) for $Le = 1$. Since the total entropy for these two cases are same and the contour plots of S_ψ and S_Θ have similar patterns with higher values of entropy for $Le = 1$, it is obvious to maintain the balance between $Le = 1$ and 7 by changing the profiles of S_C and S_K with higher values of entropy for $Le = 7$.

In order to observe the influence of buoyancy ratio on the contour plots of S_ψ, S_Θ, S_C, and S_K, another set of illustrations is presented in Fig. 7 (a)–(d) for $N = 3$, $Le = 7$ and $Ha = 25$. Comparing with Fig. 6(a) due to the increment of N from 1 to 3, it is found that a low entropy core region prevails around the cylindrical insert due to the flow entropy. The patterns of S_Θ do not change substabtially due to the change of N (see Fig. 6(b)), although a slight increase of contour values of S_Θ is noticed near the bottom-left and top-right regions. Similarly, higher values of entropy for S_C contours are found near vertical walls (see Fig. 6(c) and 7(c)), where the concentration gradient is higher. However, the contour profiles of S_K in Fig. 7(d) do not change drastically in compared with Fig. 6(d) due to the increment of N at constant Le.

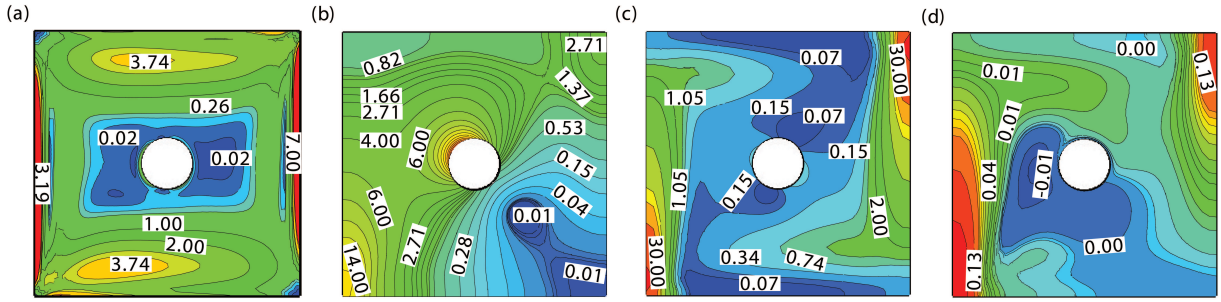

FIGURE 7. Contour plots of (a) S_ψ, (b) S_Θ, (c) S_C, and (d) S_K for representative case of $N = 3$, at $Le = 7$ and $Ha = 25$.

CONCLUSIONS

The present investigation reveals some important aspects of entropy optimization for double diffusive natural convection under an external magnetic field inside a square cavity with isothermal hollow cylindrical insert. Principal sources of energy dissipation considered here are the fluid friction near the walls, and high thermal and concentration gradients near hot and cold walls. Entropy generation due to transfer of heat is dominant among other generation terms. Higher entropy generation indicates loss of exergy which means more efficient use of stored energy in a system. Therefore, if the aim is to maximize the energy transfer of a system, required conditions should be such that entropy generated becomes highest. Increment of *Ha* reduces entropy generation by retarding flow field and reducing heat transfer. These statement is true for any combination of *Le* and *N*. Minimum value of entropy is always found at $N = -1$ for any value of Le and Ha. However, the rate of increment of S with either increasing or decreasing of N from $N = -1$ does not remain the same. Moreover, increment of *Le* enhances entropy generation around a certain range of N within $N = -1$ at fixed *Ha*. The selection of this range of N depends on the selected pairs of *Le* and their intersection point is referred to the optimum point for entropy generation. Beyond the range of N, the trend for entropy generation is completely opposite with increasing *Le* at constant *Ha*.

ACKNOWLEDGMENTS

The authors gratefully acknowledge the support provided by the Department of Mechanical Engineering , Bangladesh University of Engineering and Technology, Dhaka, Bangladesh during this work.

REFERENCES

[1] Z. T. Yu, Y. C. Hu, L. W. Fan, and K. F. Cen, Numer. Heat Tr. A-Appl. **58**, 564–580 (2010).
[2] G. Saha, S. Saha, M. N. Hasan, and M. Q. Islam, IJE Trans A: Basics **23**, 1–10 (2010).
[3] K. Khanafer and S. Aithal, Int. J. Heat Mass Tran. **66**, 200–209 (2013).
[4] A. Diego, L. Paolo, and S. B. Giovanni, Int. J. Heat Mass Tran. **51**, 553–565 (2008).
[5] O. Laguerre, S. Benamara, D. Remy, and D. Flick, Int. J. Heat Mass Tran. **52**, 5691–5700 (2009).
[6] S. H. Hussain and A. K. Hussein, Int. Commun. Heat Mass **37**, 1115–1126 (2010).
[7] A. K. De and A. Dalal, Int. J. Heat Mass Tran. **49**, 4608–4623 (2006).
[8] M. Venkatachalappa, Y. Do, and M. Sankar, Int. J. Eng. Sci. **49**, 262–278 (2011).
[9] T. Basak, R. S. Kaluri, and A. Balakrishnan, Numer. Heat Tr. A-Appl. **59**, 372–402 (2011).
[10] I. Mejri, A. Mahmoudi, M. A. Abbassi, and A. Omri, Pow. Techn. **266**, 340–353 (2014).
[11] Z. Mehrez, A. El Cafsi, A. Belghith, and P. Le Quéré, J. Magn. Magn. Mater. **374**, 214–224 (2015).

ICME2015

International Conference on Mechanical Engineering 2015
(ICME 2015) 18 – 20 December, 2015, Dhaka, Bangladesh

Paper ID : 604

Regulation of Flow through a *T*-Shaped Open Cavity by Temperature Dependent P, PI, and PID Controllers

Sourav Saha[a)], Satyajit Mojumder[b)] and Sumon Saha[c)]

Department of Mechanical Engineering, Bangladesh University of Engineering and Technology, Dhaka-1000.

[a)]Corresponding author: ssaha09@me.buet.ac.bd
[b)]satyajit@me.buet.ac.bd
[c)]sumonsaha@me.buet.ac.bd

Abstract. P (proportional), PI (proportional-integral), and PID (proportional-integral-derivative) controllers are popular means of controlling industrial processes. Due to superior response, accuracy, and stable performance, PID controllers are mostly used in control systems. This paper presents a mathematical model and subsequent response analysis regarding regulation of flow in mixed convection through a *T*-shaped open cavity by temperature dependent controllers. The *T*-shaped cavity has cold top and hot bottom walls, while air is flowing through the inlet at surrounding temperature. The inflow is regulated by a controlled gate which operates according to the signal received from the controller. Values of proportional gain (k_p), integral gain (k_i), and derivative gain (k_d) are varied to obtain the desired system response and to ensure a stable system with fastest response. At first, only P controller is used and eventually PI and finally PID control scheme is applied for controller tuning. Tuning of different controllers (P, PI, and PID) are carried out systematically based on the reference temperature which is continuously monitored at a certain location inside the cavity. It is found that PID controller performs better than P or PI controller.

INTRODUCTION

Continuous controllers are the core of the feedback control systems. These systems are widely used in many process industries because of stringent monitoring requirement over temperature, humidity, quantity, and other parameters. However, practical process control system often involves nonlinear systems making it difficult to formulate a simple mathematical model. Recently, researchers are developing better PID control schemes to monitor industrial processes. Aziz et al. [1] presented a new approach named gravitational search algorithm optimization for PID controller tuning in waste-water treatment process. Ozen et al. [2] proposed two novel approaches for motion control with PID controller. In industries, PI and PID controllers are used for controlling temperature, flow or volume of chemical. Feng et al. [3] designed a self-tuning-parameter fuzzy PID temperature controller for hydraulic system. Yukimoto et al. [4] proposed a new PID controller tuning method to control the flue gas temperature in a gas turbine power plant. Aguilar et al. [5] put forth a mathematical model of robust temperature control in catalytic cracking reactors. Before PID controllers, PI controllers were used for such control systems [6, 7].

Mixed convection has been one of the key topics of research over the years. Many studies regarding mixed convective heat transfer from open cavities are carried out by the researchers. Islam et al. [8] performed a parametric analysis on mixed convection in an open cavity with a flush mounted discrete isoflux heat source on the bottom wall. The influence of Richardson number, discrete heat source size, inclination angle, and aspect ratio of the cavity on the flow and the thermal field were observed and their results indicated that maximum thermal performance was achievable at higher value of discrete heat source size with aspect ratio of 1 as well as at higher value of inclination angle with high Richardson number. Recently, Chamkha et al. [9] studied two-dimensional mixed convection from a heated square solid cylinder that was located at the center of a vented cavity filled with air. Their results showed that the average Nusselt number along the heated surface of the inner square cylinder increased with increasing values of Reynolds and Grashof numbers. Rahman et al. [10] analyzed mixed convection inside a square ventilated cavity with a heat generating solid body located at the center. It was found that heat transfer had a strong dependence on the conductivity ratio between solid and fluid as well as the diameter of the heat generating body. Many similar works can

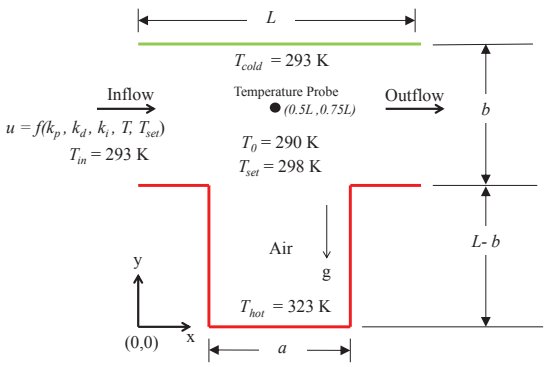

FIGURE 1. Schematic diagram of the T-shaped cavity for the present problem with appropriate boundary conditions and coordinate system.

be found in the previous literatures [11, 12].

Cavity shape is an influential parameter for the analyses of mixed convection. T-shaped cavity is very practical from engineering point of view. However, analysis of mixed convection on this shape of cavity has not been thoroughly studied so far. Rouijaa and Alami [14] studied natural convection in an inclined T-shaped cavity and reported that increase of inclination angle was not favorable for heat transfer augmentation. Similar type of work considering radiation effect inside a T-shape cavity was investigated by Amraqui et al. [15]. They concluded that increment of Rayleigh number enhanced heat transfer rate. Mansour et al. [13] studied natural convection in a T-shaped cavity filled with nanofluid having localized heat source and they came to the conclusion that the narrower part of T-shaped cavity augmented the heat transfer rate. Recently, a new study was performed by Kasaeipoor et al. [16] on mixed convection inside a T-shaped open cavity using Cu-water nanofluid under uniform magnetic field. Their study focused on finding out the impact of governing parameters, such as Reynolds, Richardson, Hartmann numbers, volume fraction of nanoparticles, and aspect ratio of the cavity. Therefore, T-shaped cavity has a huge potential for contributing to the enhancement of heat transfer rate.

The present investigation focuses on finding the influence of different controllers on control of flow through a T-shaped open cavity subjected to mixed convection. Since the velocity of inflow controls heat transfer rate in mixed convection from the open cavity, the obtained numerical results can be extended to solve problems regarding efficient and effective controlling heat transfer rate in mixed convection problems.

PHYSICAL MODELING

The physical model of the problem investigated in this work is shown in Fig. 1 in Cartesian coordinate system with origin at (0, 0). The cavity length L is taken to be 1 cm. The size of the inlet and the outlet openings of the cavity is taken as $b = 0.5L = 0.5$ cm. Similarly, the size of the extended bottom portion of T-shaped cavity is taken as $a = 0.5L = 0.5$ cm. T-shaped cavity with similar dimensions was also considered by Amraqui et al. [15] in their investigation. All walls on the bottom portion of the cavity are heated to temperature of $T_{hot} = 323$ K. The top wall of the cavity is maintained at a temperature of $T_{cold} = 293$ K. Initially, fluid inside the cavity is considered at $T_0 = 290$ K which is continuously monitored by a temperature probe. It is desired that fluid inside the cavity at a central position (0.5 cm, 0.75 cm) to be maintained at $T_{set} = 298$ K. In order to control the temperature inside the cavity, a controller is set to send signal to an inlet valve which controls the inflow speed at $T_{in} = 293$ K. The inlet velocity u_{in} is a function of k_p, k_i, k_d, T, and T_{set}. For the simplified analysis, fluid inside the cavity is taken as air. Thermodynamic properties of air are mentioned in Table 1.

MATHEMATICAL MODELING

Air is assumed as Newtonian fluid with constant thermophysical properties except density. Variation of density is accounted for using Boussinesq's approximation. Radiation and viscous heating are neglected. Continuity, momentum,

and energy equations for the present problem are written as

$$\frac{\partial u}{\partial x} + \frac{\partial v}{\partial y} = 0, \tag{1}$$

$$\frac{\partial u}{\partial t} + u\frac{\partial u}{\partial x} + v\frac{\partial u}{\partial y} = -\frac{1}{\rho}\frac{\partial p}{\partial x} + \eta\left(\frac{\partial^2 u}{\partial x^2} + \frac{\partial^2 u}{\partial y^2}\right), \tag{2}$$

$$\frac{\partial v}{\partial t} + u\frac{\partial v}{\partial x} + v\frac{\partial v}{\partial y} = -\frac{1}{\rho}\frac{\partial p}{\partial y} + \eta\left(\frac{\partial^2 v}{\partial x^2} + \frac{\partial^2 v}{\partial y^2}\right) + g\beta\left(T - T_{cold}\right), \tag{3}$$

$$\frac{\partial T}{\partial t} + u\frac{\partial T}{\partial x} + v\frac{\partial T}{\partial y} = \alpha\left(\frac{\partial^2 T}{\partial x^2} + \frac{\partial^2 T}{\partial y^2}\right), \tag{4}$$

where x, y are the spatial coordinates, u and v are the velocities along the respective coordinates, p and T are pressure and temperature, respectively, η, α, β, g, and ρ are the kinematic viscosity, thermal diffusivity, thermal expansion coefficient, gravitational acceleration, and density of the working fluid respectively. Boundary conditions for the present problem are listed in Table 2. The inlet boundary conditions due to the presence of PID controller are mentioned here. The same equation is used for P and PI controllers by setting $k_i = k_d = 0$ and $k_d = 0$, respectively. Measured temperature by the probe at any time is defined as $T_p = T$ (0.5 cm, 0.75 cm). At $t = 0$, the temperature of the fluid inside the cavity is 290 K, velocity components of the flow field $u = v = 0\ ms^{-1}$, and pressure is equal to the atmospheric pressure.

TABLE 1. Properties of dry air at 300 K taken from Lemmon et al.[18].

Property	Symbol	Unit	Value
Density	ρ	kgm^{-3}	1.225
Kinematic viscosity	η	$m^2 s^{-1}$	1.507×10^{-5}
Thermal Diffusivity	α	$m^2 s^{-1}$	22.05×10^{-6}

TABLE 2. Boundary conditions for the present problem.

Boundary	Thermal field condition	Flow field condition
Top wall	$293K$	$u = v = 0\ ms^{-1}$
Bottom walls	$323K$	$u = v = 0\ ms^{-1}$
Inlet	$293K$	$u = k_p(T_p - T_{set}) + k_i\int(T_p - T_{set})dt + k_d\frac{\partial}{\partial t}(T_p - T_{set})$ if $T_p \geq T_{set}$; for $T_p < T_{set}$, $u = 0$
Outlet	$\partial T/\partial x = 0$	$p = 0$ Pa, $\partial v/\partial x = 0$, $\partial u/\partial x = -\partial v/\partial y$

In order to analyze the result in a convenient way, instead of dimensional temperature, nondimensional temperature response (Θ) is observed with time. This parameter is defined as,

$$\Theta = \frac{T_p - T_0}{T_{set} - T_0}. \tag{5}$$

NUMERICAL SIMULATION

The governing equations and the corresponding boundary conditions are discretized using Galerkin weighted residuals method of finite element analysis. Coupled solution for Navier-Stokes and energy equations is obtained using triangular mesh elements. Time stepping for transient solution is done by using generalized alpha method. Iteration termination criterion for each time step is set to $|\gamma^{m+1} - \gamma^m| \leq 5 \times 10^{-4}$, where γ is the general dependent variable and m is the iteration number. In order to ensure the minimum computational cost, a grid sensitivity test is performed to find out the minimum number of elements required for optimum results (see Fig. 2). From the grid refinement test, it is found that simulation results do not change much if we use element number of 7096 or higher. Hence, the mesh with 7096 elements is selected as the optimum grid size for all subsequent simulations.

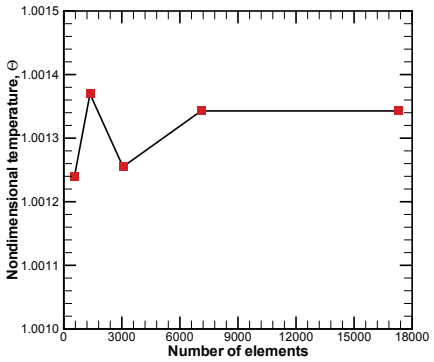

FIGURE 2. Grid sensitivity test in terms of Θ for $k_p = 0.15\ ms^{-1}K^{-1}$, $k_i = 0.3\ ms^{-2}K^{-1}$, and $k_d = 0.001\ mK^{-1}$ at $t = 3\ s$.

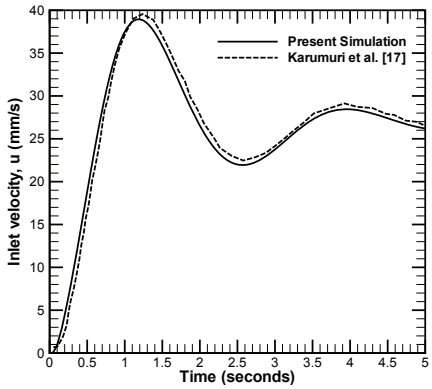

FIGURE 3. Comparison of simulation results with the work of Karumuri et al. [17] in terms of inlet velocity, u for $k_p = 0.1\ m^4mol^{-1}s^{-1}$, $k_i = 1\ m^4mol^{-1}s^{-2}$, and $k_d = 0.001\ m^4mol^{-1}$.

CODE VALIDATION

The present code is validated by regenerating the work of Karumuri et al. [17] in terms of inlet velocity, u, calculated at the vented left opening for $k_p = 0.1\ m^4mol^{-1}s^{-1}$, $k_i = 1\ m^4mol^{-1}s^{-2}$, and $k_d = 0.001\ m^4mol^{-1}$ within 0 to 5 seconds interval. Both results are compared and presented in Fig. 3. It is observed that inlet velocity obtained by the present code closely follows that of Karumuri et al. [17]. This ensures the validity of the current numerical scheme for the computation of the similar types of physical problems.

RESULTS AND DISCUSSION

In this paper, the application of P, PI, and PID controllers on flow control mechanism inside a T-shaped cavity is studied by varying the inlet flow through temperature dependent controller. For the present study, at first only P controller is used with k_p of 0.05, 0.15, and 0.25 $ms^{-1}K^{-1}$ while keeping k_i and k_d equal to zero. Later, keeping $k_p = 0.15\ ms^{-1}K^{-1}$, PI control scheme is employed where k_i is varied as 0.1, 0.2, and 0.3 $ms^{-2}K^{-1}$. Finally, PID controller is employed fixing k_p and k_i as 0.15 $ms^{-1}K^{-1}$ and 0.3 $ms^{-2}K^{-1}$, respectively and taking k_d as 0.00001, 0.005, 0.001 mK^{-1}. The velocity fields in terms of contour surface plots at $t = 0$, 0.32 and 1 s for each case are observed in order to investigate the variation of the flow field inside the cavity. Moreover, the response curves of the system are obtained by continuously monitoring the nondimensional temperature (Θ) at the desired location $(0.5cm, 0.75cm)$.

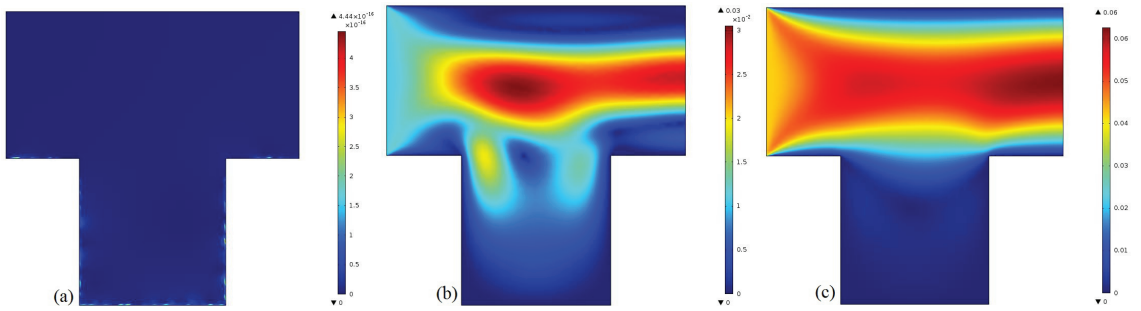

FIGURE 4. Evolution of the flow field inside the cavity at (a) $t = 0s$, (b) $t = 0.32s$, and (c) $t = 1s$ for $k_p = 0.15\ ms^{-1}K^{-1}$, $k_i = 0\ ms^{-2}K^{-1}$, and $k_d = 0\ mK^{-1}$. Vertical color legend on right side of each figure shows the magnitude of velocity in ms^{-1}.

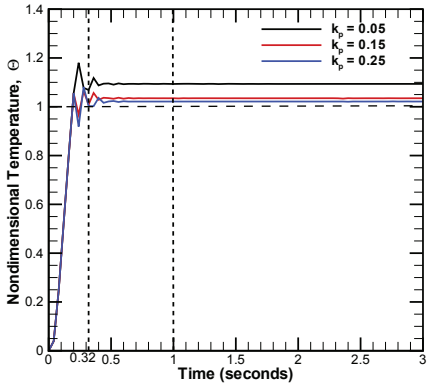

FIGURE 5. System response of the P controller in terms of Θ for $k_p = 0.05$, 0.15, and 0.25 $ms^{-1}K^{-1}$ respectively.

P Controller

At first, we make a systematic observation on the performance of P controller. The working mechanism of P controller is simple enough since it triggers response in direct proportion to error. However, this controller is unable to eradicate steady-state error of the system. This whole scenario is captured by Figs. 4 and 5. Figs. 4 (a), (b), and (c) show velocity field at $t = 0$, 0.32, and 1 s, respectively at $k_p = 0.15\ ms^{-1}K^{-1}$. Initially, there is no flow since the initial temperature T_0 is less than the set temperature T_{set} ($\Theta = 0$). Temperature inside the cavity is raised by heat released from the hot bottom wall. Once the temperature inside the cavity at the specified location $(0.5cm, 0.75cm)$ exceeds T_{set} slightly, the controller sends signal to the inlet valve and the flow is initiated. By letting in outside air at T_{in} ($< T_{set}$), the controller tries to reduce the temperature inside the cavity to T_{set}. This initial flow is visible in Fig. 4 (b). The flow continues until the temperature becomes equal or less than T_{set} ($\Theta \leq 1$). However, P controller is unable to reach the state where the steady-state error is zero or temperature inside the cavity becomes T_{set}. Hence, the flow continues indefinitely (see Fig. 4 (c)). Fig. 5 is the response curve showing the temperature of fluid inside the cavity at the desired location $(0.5cm, 0.75cm)$. From the figure, it can be seen that temperature of the cavity goes above the desired value $\Theta = 1$ within 0.3 s. Although responses from P controllers are generally quite quick, these responses are futile since these controllers yield large steady-state error. Moreover, the initial overshoot is also quite high for each case of k_p (maximum 20% for $k_p = 0.05\ ms^{-1}K^{-1}$). As the value of k_p is increased, overshoot and steady-state error become smaller (overshoot reduces to 6% for $k_p = 0.25\ ms^{-1}K^{-1}$ and steady-state error becomes 2.14%).

PI Controller

Now, we will consider the influence of an integral controller combined with proportional controller. Hence, PI controllers have advantages over P controllers because these controllers eliminate steady-state error. In order to remove discrepancy of temperature of fluid inside the cavity at final state, PI controller is employed. Proportional gain (k_p) is kept at 0.15 $ms^{-1}K^{-1}$ and k_i is selected as 0.1, 0.2, and 0.3 $ms^{-2}K^{-1}$ while k_d is zero for all cases. Figs. 6 (a), (b)

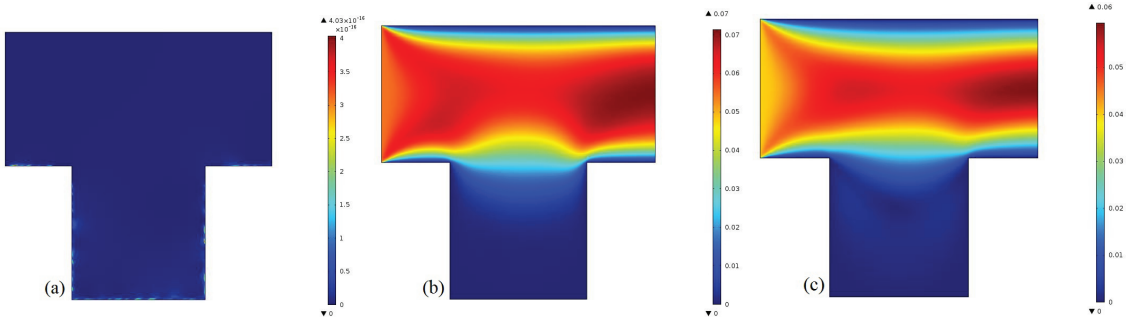

FIGURE 6. Evolution of the flow field inside the cavity at (a) $t = 0s$, (b) $t = 0.32s$, and (c) $t = 1s$ for $k_p = 0.15\ ms^{-1}K^{-1}$, $k_i = 0.2\ ms^{-2}K^{-1}$, and $k_d = 0\ mK^{-1}$. Vertical color legend on right side of each figure shows the magnitude of velocity in ms^{-1}.

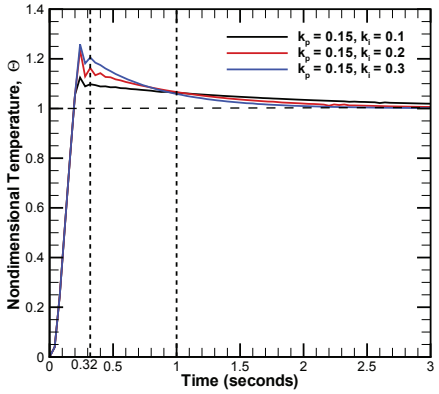

FIGURE 7. System response of the PI controller in terms of Θ for $k_i = 0.1$, 0.2, and 0.3 $ms^{-2}K^{-1}$ at $k_p = 0.15\ ms^{-1}K^{-1}$ and $k_d = 0\ mK^{-1}$ respectively.

and (c) represent the velocity field at $t = 0$, 0.32, and 1 s, respectively for $k_i = 0.3\ ms^{-2}K^{-1}$. Evolution of the velocity field is quite different from P controller at $t = 0.32$ s. Since PI controller actually eliminates the steady-state error, the flow velocity should gradually reduce. Hence, it is found that at $t = 0.32$ s, magnitude of maximum velocity in the cavity is 0.07 ms^{-1} while it becomes 0.06 ms^{-1} at $t = 1$ s. Fig. 7 exhibits the response curves for PI controller showing the effects of varying k_i. The results indicate more overshoot initially due to the selected values of k_p and k_i, and the controller is itself sluggish in response. For all values of k_i, the non-dimensional temperature at the specified point becomes close to unity almost after $3s$. With the increase of k_i at fixed k_p, the overshoot increases continuously, while the response reaches close to the final value at a faster rate.

PID Controller

Finally, we select the PID controller since it contains all the advantages of P and PI controllers (fast response and zero error) and buffer shortcomings of each type. In order to observe the impact of using PID controller, k_p and k_i are kept at 0.15 $ms^{-1}K^{-1}$ and 0.3 $ms^{-2}K^{-1}$ respectively, and k_d is varied to be 0.00001, 0.005, and 0.001 mK^{-1}. The value of k_d is deliberately kept small according to the usual practice in industries. Figs. 8 (a), (b) and (c) show the evolution of velocity field inside the cavity at $t = 0$, 0.32, and 1 s for $k_d = 0.001\ mK^{-1}$. It is evident that there is initially no flow in the cavity and when the temperature Θ becomes equal or greater than 1, the forced flow from the inlet enters into the cavity and starts the cooling process. The response curve as shown in Fig. 9 indicates that compared to P and PI controllers, PID controllers provide the quickest response. It is interesting to see that for any value of k_d, Θ reaches to unity within 2.5 s due to the combined effect of P, I and D controllers. However, the response curve shows excessive overshoot (maximum of 28%) at high value of k_i, which can be tuned down by optimising the value of k_i. Oscillatory behaviour is completely absent in PID response curve and thus makes it more stable system.

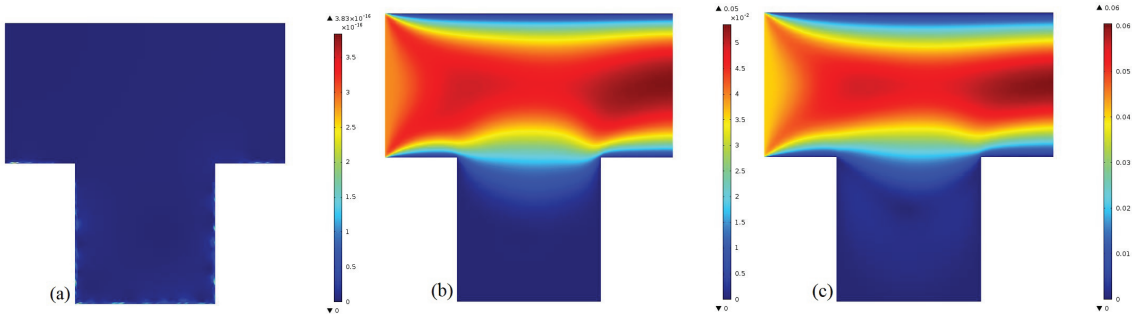

FIGURE 8. Evolution of the flow field inside the cavity at (a) $t = 0s$, (b) $t = 0.32s$, and (c) $t = 1s$ for $k_p = 0.15\ ms^{-1}K^{-1}$, $k_i = 0.3\ ms^{-2}K^{-1}$, and $k_d = 0.001\ mK^{-1}$. Vertical color legend on right side of each figure shows the magnitude of velocity in ms^{-1}.

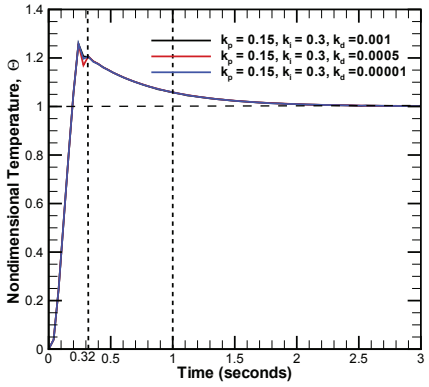

FIGURE 9. System response of the PID controller n therms of Θ for $k_d = 0.001$, 0.0005, and 0.00001 mK^{-1} at $k_p = 0.15\ ms^{-1}K^{-1}$ and $k_i = 0.3\ ms^{-2}K^{-1}$ respectively.

CONCLUSIONS

This paper presents a new concept by controlling convection in a T-shaped open cavity through different controllers. This work pivots around the performance of temperature controlled P, PI, and PID controllers to control flow behaviour and temperature inside a T-shaped cavity. From the present analysis, the following conclusions can be made.

- In regard to steady-state performance, P controller is the worst one since it never able to keep the temperature inside the cavity to the desired value.
- PI controllers are very fast with zero steady-state error when higher k_i is used. However, using very high value of k_i makes the system oscillatory.
- PI controllers are slower compared to P controllers. Stability and performance of PI controllers depend on the values of k_p and k_i.
- PID controller is the best one in all regards. Oscillatory nature of the system can be eradicated by properly tuning of k_p, k_i and k_d in PID controllers. These controllers have the fastest response.

ACKNOWLEDGMENTS

The authors would like to thank the Department of Mechanical Engineering, Bangladesh University of Engineering and Technology, Dhaka, Bangladesh for providing necessary support for this research.

REFERENCES

[1] M. S. I. Aziz, S. W. Nawawi, S. Sudin, N. A. Wahab, M. Faramarzi, and M. A. M. Yusof, Jurnal Teknologi **73**, 103 – 109 (2015).

[2] O. Ozen, E. Sariyildiz, H. Yu, K. Ogawa, K. Ohnishi, and A. Sabanovic, "Practical pid controller tuning for motion control," in *2015 IEEE International Conference on Mechatronics (ICM),* (IEEE, 2015), pp. 240–245.

[3] B. Feng, G. Gong, and H. Yang, "Self-tuning-parameter fuzzy pid temperature control in a large hydraulic system," in *IEEE/ASME International Conference on Advanced Intelligent Mechatronics, 2009. AIM 2009.* (IEEE, 2009), pp. 1418–1422.

[4] M. Yukitomo, Y. Iino, S. Hino, K. Takahashi, and K. Nagata, "A new pid controller tuning system and its application to a flue gas temperature control in a gas turbine power plant," in *Proceedings of the 1998 IEEE International Conference on Control Applications, 1998.*, Vol. 2 (IEEE, 1998), pp. 1373–1377.

[5] R. Aguilar, A. Poznyak, R. Martınez-Guerra, and R. Maya-Yescas, Journal of Process Control **12**, 695–705 (2002).

[6] U.-C. Moon and K. Y. Lee, "Temperature control of glass melting furnace with fuzzy logic and conventional pi control," in *Proceedings of the American Control Conference, 2000.*, Vol. 4 (IEEE, 2000), pp. 2720–2724.

[7] U.-C. Moon and K. Y. Lee, Control Systems Technology, IEEE Transactions **11**, 548–554 (2003).

[8] M. Islam, S. Saha, M. Ali, M. Q. Islam, and G. Saha, Journal of Energy, Heat and Mass Transfer **31**, 73–89 (2009).

[9] A. J. Chamkha, S. H. Hussain, and Q. R. Abd-Amer, Numerical Heat Transfer, Part A: Applications: An International Journal of Computation and Methodology **59**, 58–79 (2011).

[10] M. M. Rahman, S.Parvin, M. Hasanuzzaman, R. Saidur, and A. N. Rahim, Heat Transfer Engineering **34**, 1249 – 1261 (2013).

[11] S. Singh and M. A. R. Sharif, Numerical Heat Transfer, Part A: Applications **44**, 233–253 (2003).

[12] Y. Stiriba, International Communication in Heat and Mass Transfer **35**, 901–907 (2008).

[13] M. A. Mansour, A. Y. Bakier, and M. A. Y. Bakier, American Journal of Engineering Research **2**, 49–61 (2013).

[14] H. Rouijaa and M. E. Alami, Fluid Dynamics and Materials Processing **7**, 57–70 (2011).

[15] S. Amraqui, A. Mezrhab, and C. Abid, Energy Conversion and Management **52**, 1166–1174 (2011).

[16] A. Kasaeipoor, B. Ghasemi, and S. M. Aminossadati, International Journal of Thermal Sciences **94**, 50–60 (2015).

[17] S. R. Karumuri, P. Sri Sairam, and Y. Srinivas, European Journal of Applied Engineering and Scientific Research **1**, 62–66 (2012).

[18] E. W. Lemmon, R. T. Jacobsen, S. G. Penoncello, and D. G. Friend, Journal of Physical and Chemical Reference Data **29**, 331–385 (2000).

ICME2015

International Conference on Mechanical Engineering 2015
(ICME 2015) 18 – 20 December, 2015, Dhaka, Bangladesh

Paper ID : 606

Comparative Performance Study of a CI Engine run by Vegetable oil as an eco-friendly Alternative Fuel

Md Sanuwar Uddin[a)]

Department of Mechanical Engineering, Bangladesh University of Engineering and Technology, Dhaka-1000.

[a)]Corresponding author: sanuwar3803@gmail.com

Abstract. In the view of the energy crisis and emission problems, alternative fuels are promising substitutes to the conventional petroleum based fuels. Among those, vegetable oil seems to be a suitable option of diesel fuel. It has the advantages of being geographically widely produced, in a variety of products & renewable in nature and thereby not adding to the net atmospheric concentrations of green house gas, CO_2 . However, higher viscosity and low volatility are identified as the main constraints of vegetable oils as straight diesel fuel substitute. In this study attempts have been made to evaluate the possibility of using vegetable oils as diesel fuel substitute by modifying their properties. Preheating is one of the promising means to change the fuel viscosity to enhance atomization, mixing with air and better combustion.In the present study, experiments are carried out in a diesel engine at different speeds and loading conditions using diesel fuel to generate base data and afterwards the experiments were repeated by replacing diesel fuel by preheated soybean at three different temperatures. Various performance parameters are obtained to study the effects of the degree of preheating of vegetable oils on the engine performance at different engine speeds. It is observed that, straight soybean oil can be used as an alternative of diesel fuel in CI engines with very little power and efficiency loss. It is also observed that, with the increase in the preheat temperature of the vegetable oils, the overall engine efficiency increases.

INTRODUCTION

Diesel and petrol are the main fuels for any internal combustion engine. The compression ignition (C.I.) engines (i.e. Diesel engines) are generally high performance engines. These are widely used in automobiles and in power generation. However mass production of Internal Combustion (I.C.) engines and the use of petroleum fuels create atmospheric pollution by the exhausts. The exhaust-emission is a major issue to the mankind. Furthermore, it is realized that the petroleum resources will be scarce in the near future. As such, there is an urgent need of establishing the countermeasure, conserving petroleum products through the system design, developing alternative fuels and new energy sources. In this regard vegetable oil can be a promising alternative source of energy, which many of us do not know. However an outstanding question regarding the use of vegetable oil in C.I. engines relates to it,s high viscosity .Due to its high viscosity, in normal conditions, it has few problems, such as incomplete atomization and heavy particulate emissions.

However there are some simple and easy methods (i.e. fuel modification) by which the atomization problem can be eliminated and we can use the vegetable oils as substitute of diesel fuel. Three methods of fuel modification can be applied (e.g. blending, fuel heating, vegetable oil ester) to reduce viscosity and tested. These modified vegetable oils can be used in diesel engine including military vehicles especially when we will run short of fuel in the operation areas.

WHY SHOULD WE LOOK FOR ALTERNATIVE FUEL

Engineering equipment backed by fuel is increasing day by day. Fuel is also depleting day by day besides its incasing cost from the past and will probably continue to be increased in the coming days. Therefore alternative fuel technology may become more common in the next decades.

Another reason for motivating towards the development of alternate fuels technology for the I.C. engine is, regarding the concern over the emission problems. Therefore, additional improvement is needed due to the ever-increasing number of automobiles.

VEGETABLE OIL AS ALTERNATIVE FUEL NEEDS LITTLE MODIFICATIONS.

Raw vegetable oil can be used as fuel in diesel engines with some minor technical effort that reduces viscosity and the methods are:

a. Blending.
b. fuel pre heating,
c. Thermo-emulsification.

Blending

Blending is commonly known as mixing. Certain percentage of vegetable oil can be mixed with diesel without any technical difficulties (e.g. 60% diesel and 40% vegetable oil).

Preheating

Due to preheating of oil, thermal efficiency becomes higher and there is a significant reduction in brake specific fuel consumption (bsfc) when compared with diesel/petrol. Fuel pre-heating also improves the engine performance.

Thermo-emulsification

By thermo-emulsion, Chemical structure / bondage can be changed by means of electrification.

Advantages of Vegetable Oil as Fuel Substitute

Interest for vegetable oil as substitute to diesel fuel is enhanced for following reasons:

a. CO_2 and NO_x emission by vegetable oil is very less compared to conventional fuel.
b. It contains no sulfur (or very negligible amount). So the environmental damages due to sulfuric acid are reduced.
c. It is produced domestically which helps to reduce the cost of petroleum imports.
d. Development of the bio-diesel industry would strengthen the domestic and particularly the rural, agricultural based countries like India and Bangladesh.
e. It is bio -degradable and non-toxic.

Challenges of using Vegetable Oil

The major challenges those are likely to be faced while using vegetable oil as I.C. engine fuels are listed below:

a. Cold weather operation of the engine is not easy with vegetable oil.
b. Continuous availability of vegetable oil needs to be assured before using it in I.C engines.

c. Engine performance, emissions and durability of engine, type and size need to be developed to increase consumer's confidence.
d. Attention is needed to reduce production cost, develop low feedstock and identify potential markets in order to balance cost and availability.

LITERATURE REVIEW ON VEGETABLE OILS

Researchers have tested vegetable oils for short term and long term use in a diesel engine during the maximum power and fuel consumption tests and test reports are as follows:

Safflower Oil

Successful operation of a direct injection diesel engine can be attained with a blend of 25/75% high oleic safflower oil and diesel oil. Deposits of carbon and lacquer with this blend are much lower compared to diesel fuel.

Rapeseed Oil

The study reported a successful use of a 70/30% rapeseed oil and diesel oil blend to operate a small single cylinder, swirl chamber diesel engine for 850 hours with no significant engine performance problems. Blending with 25% diesel oil, reduces the droplet size, improves volatility and thereby reduces carbon deposits.

Sunflower Oil

Scientists compared the performance of 25/75% sunflower oil and diesel oil blend and a sunflower oil methyl ester with pure diesel oil. No significant difference was noted with respect to characteristics such as thermal efficiency, ignition delay, exhaust temperature, CO and NO_x.

Soybean oil

Thermo-emulsification of soybean oil into methyl, ethyl or butyl esters are found to reduce the viscosity and to confer fuel properties similar to diesel fuel. Soybean oil was tested in a diesel engine with an indirect fuel injection system to determine the injector performance such as spray angle, nozzle output, delay in initiation of atomization, carbon deposits, smoke emissions, effect on the lubrication system and engine wear.

Neem Oil

Tests were carried out using neem oil and diesel oil blends of 10, 20 and 30% in diesel engine. Viscosities of these blends were found to be nearly equal to the viscosity of diesel fuel at 25, 30, 44 and 60^0C respectively. The authors suggested heating of fuel by recalculating the exhaust to avoid cold starting problems during winter.

Palm Oil

The palm oil Research institute of Malaysia converted crude palm oil and crude palm stare to methyl esters known as palm oil diesel. The observations revealed higher power outputs than diesel blends. Out of three blends of (palm oil and diesel oil) 25%, 50%, 75%, the blend with the ratio of 1:1 by volume produced the best performance for power, torque and specific fuel consumption.

AN EXPERIMENTAL RESULT OF USING PURE VEGETABLE OIL (SOYBEAN OIL) IN AN IC ENGINE

The experiment consists with a diesel engine run by diesel and vegetable oil supply system with different metering and measuring devices. Due to easy availability, soybean oil was taken for this experiment. Experiments were carried out at three different speeds of 1750, 2000 and 2250 rpm at various load conditions. Data of the different loads were analyzed to have various performance parameters to study the effects of different operating conditions. A comparative result of experiment using diesel & vegetable oil separately is shown by the diagram below.

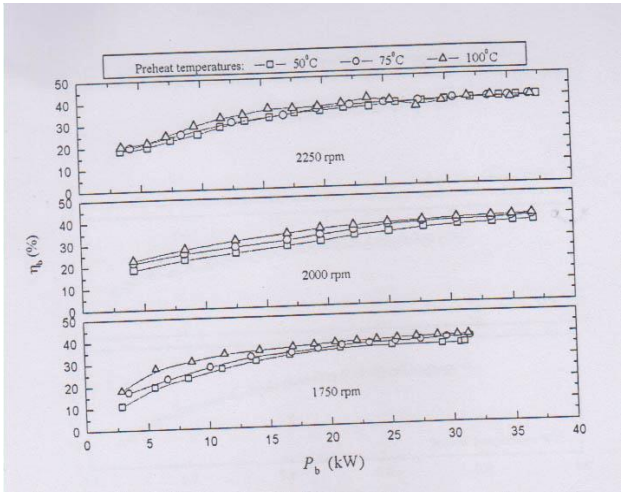

FIGURE 1. Brake Thermal Effiency with engine brake output power at different speeds using soybean oil at different preheated condition

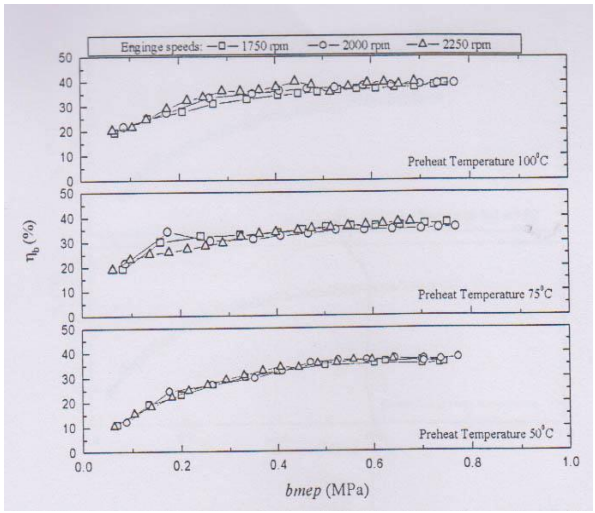

FIGURE 2. Estimated brake thermal efficiency with engine brake mean pressure using soybean oil fuel at different preheat temperatures

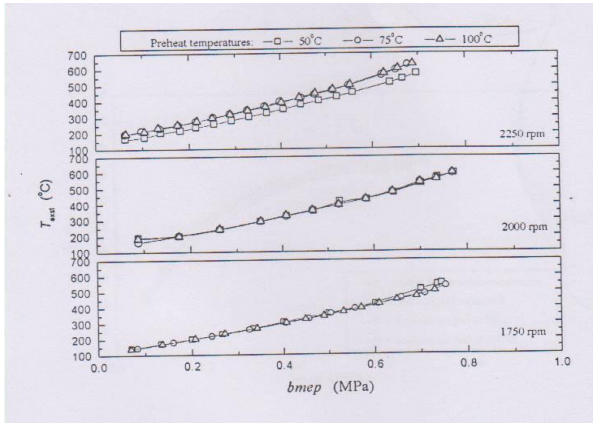

FIGURE 3. Measured exhaust temperature as a function of brake mean effective pressure using preheated soybean oil as fuel

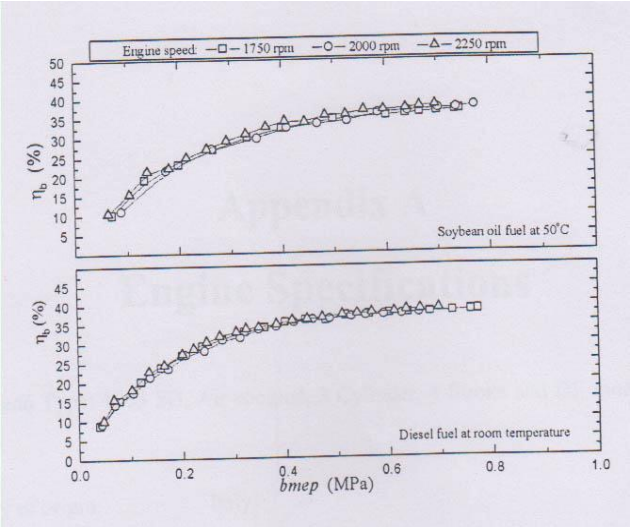

FIGURE 4. Comparison of brake thermal efficiency as a function of brake mean effective pressure run by soybean oil fuel at 50^0C temperature and diesel fuel at room temperature.

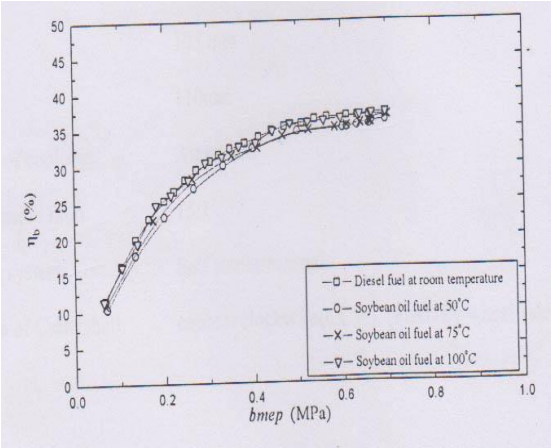

FIGURE 5 . Comparison of brake thermal efficiency as a function of brake mean effective pressures run by diesel fuel and preheated soybean oil both at speed of 2250 rpm

CONCLUSIONS

The use of various vegetable oils as fuels is not a new concept. Over the years the production of the diesel engine has been based on the availability of petroleum-derived fuel. Most of the alternate fuels are very costly at present. Nonetheless unreliability of supply of petroleum oil has created the necessity for the developing countries to find alternative fuels for their requirements. Vegetable oil is a promising substitute fuel for diesel engines in some situations.The outstanding question regarding the use of vegetable oils as fuels for diesel engines relates to the durability problems, which are related to the high viscosity, chemical structures that affect the chemistry of combustion, lubricating oil contamination due to incomplete combustion. Direct injection engines are more dependent upon the ability of the injection system to accomplish a high degree of fuel atomization than the indirect injection engines.Researchers in various countries carried out many experimental works using vegetable oils as I.C engine fuel substitutes. Though, vegetable oils have a lower volumetric energy density than diesel fuel but produce lower exhaust emissions. It is reported that RME had about 40% lower HC emissions, 35% lower CO, 35% lower PM. Vegetable oil

and their methyl esters gave performance and emission characteristics comparable to that of diesel. Hence, they may be considered as diesel fuel substitutes.

References

1. S. Bhattacharyya and C.S Reddy "Vegetable Oils as fuels for IC Engine; A Review" journal of J, agric. Engr Res, Vol 57 page 157-166.
2. Recep Altn, Selim Cetinkya, Huseyin Serdar "The Potential of using Vegetable oil fuels as fuel for Diesel engines" Journal of PERGAMON, Vol 42(2001), Page 529-538.
3. A.S Ramadhas, S, Jayaraj, C, Muraleedharan" Data Bank on Use of Vegetable Oils as I.C Engine Fuels –A Review" Journal of ELSEVIER, Renewable Energy Vol 29(2004), Page 727-742.
4. O.M.I. Nwafor "Emission Characteristics of Diesel Engine running on Vegetable oil with elevated fuel temperature" Journal of ELSEVIER, Biomass and Bio energy Vol 27(2004), Page 507-511.
5. Michael S. Graboski and Robert L. McCormick "Combustion of Fat and Vegetable Oil Derived Fuels in Diesel Engines" Journal of Pergamum, Energy Combustion vol 24, Page 125-164.
6. Md. Zahurul Haq Msc Thesis Paper on "Study of the properties of vegetable oil as an alternative to diesel fuel" BUET, Aug 1995.
7. Onwuzurigbo Martini, Nwafor Thesis Paper of PhD on "Alternative Fuels in Diesel Engine" Engineering University of reading, U.K, September 1994.
8. Md. Habibur Rahman Msc Thesis Paper on "Experimental Investigation of Dual-Fuel Diesel Engine" BUET, March 2003.
9. Md. Zulfiker Ali Bhutto M.Sc Thesis Paper on "Comprehensive Modeling of Diesel Engine with Biogas/Diesel" BUET, 2003.

ICME2015

International Conference on Mechanical Engineering 2015
(ICME 2015) 18 – 20 December, 2015, Dhaka, Bangladesh

Paper ID : 609

Turbulent Flow Heat Transfer Simulation in Interior Sub-channel of a 1000 MW Nuclear Power Reactor

M. A. Ullah[1, a)], K. M. Rabbi[1], M A Altab Hossain and M. A. R. Sarkar[1]

[1] *Department of Mechanical Engineering, Bangladesh University of Engineering & Technology, Dhaka-1000, Bangladesh*

[a)]Corresponding author: asif591232@gmail.com

Abstract. In this study, turbulent flow heat transfer in interior sub-channel of a 1000 MW nuclear power reactor has been investigated. Turbulent flow model (k-ε) has been assumed for simulation. The temperature, velocity, Nusselt number, pressure drop and friction factor have been analyzed for various axial locations ($z = 0 - 37\ D_h$) in the sub-channel. Effect of Reynolds number ($Re = 10^4 - 10^7$) on Nusselt number, relative pressure drop and friction factor has been studied. Grid independency test has been done to find optimum mesh size. Finally, optimization of performance parameters is accomplished in the sub-channel considered.

INTRODUCTION

Principal application of nuclear power reactor is to produce thermal energy which leads to power generation. Nuclear fission reaction in the fuel rod is the primary source of heat. Produced thermal energy in the boundary wall of the fuel rod causes convection heat transfer through coolant. Disturbance and non-uniformity in the flow field cause better heat transfer. Thus, turbulent flow heat transfer can be matter of great concern to predict and evaluate thermal performance of power reactors. Thermal hydraulic characteristics in VVER-1000 nuclear reactor have been investigated and analyzed [1]. C.L Waata [2] studied heat extraction by coolant in the sub-channel of VVER-1000 reactor. It was found that heat transfer rate increased due to increase in axial distance. Markov et al. [3] investigated flow and heat transfer processes fuel assembly model of VVER-1000 reactor. It was observed that proposed model could be used to calculate heat transfer in rod fuel elements of the reactor.

Different nuclear reactors can be a matter of interest. VVER-1000 nuclear reactor has been considered as a choice of research. The VVER-1000 is a Pressurized Water Reactor (PWR) which has a spray steam suppression system. Hexagonal fuel rod assembly is a distinct characteristic of VVERs. In nuclear reactors, heat is generated by the nuclear fission reaction inaugurated by neutrons from any neutron source like Am-Be. This heat is extracted by any coolant such as liquid Sodium, heavy water, light water etc. In VVER-1000, light water is used as coolant. In PWRs, two circuits for coolant are used to avoid radioactive contamination. The primary cooling circuit includes the sub-channels between fuel rods and a heat exchanger submerged in the secondary circuit. Radioactive contaminated water is circulated in the primary cooling circuit and is never allowed to go out. Hexagonal fuel rod assembly has 3 types of sub-channels depending on geometrical shape whose boundary conditions are different. These sub-channels are named as interior, corner and edge sub-channels [4]. In this paper, results for only interior sub-channel in the fuel rod assembly are studied.

Pacio et al. [5] studied thermal-hydraulic behavior of working fluid in a hexagonal rod bundle with grid spacer numerically. It was found that turbulent momentum transport along two bundles leads to more heat transfer rate and better thermal performance. Rehme et al. [6] observed pressure drop in rod bundles using improvising flow experimentally. Correlation for pressure loss due to spacer grid were presented and compared with the experimental dataset. Jian et al. [7] investigated analytical prediction for friction factor and Nusselt number near the rod bundles. It was found that the method was valid for infinite number of rod bundles.

The objective of this paper is to validate the geometry and design of a VVER-1000 reactor taking turbulent flow heat transfer in consideration. Effect of axial distance and Reynolds number on Nusselt number and pressure drop is studied in the interior sub-channel numerically. Constant temperature field, pressure drop and velocity profile are illustrated to study and optimize safety issues in an economic point of view.

Nomenclature			
D	Fuel rod diameter	Re	Reynolds number
P	Pitch between fuel rods, fig 1(b)	Nu	Nusselt number
Z	Axial distance	Nu_{fd}	Fully developed Nusselt number
D_h	Hydraulic diameter	Pr	Prandtl number
p	Perimeter of sub-channel	k	Thermal conductivity of water
A_c	Cross sectional area of sub-channel	μ	Dynamic viscosity of water
v	Velocity of water	f	Friction factor
P_r	Relative pressure drop	P_0	Maximum pressure developed
		P	Local pressure

GEOMETRY AND MESH

In VVER-1000, the number of fuel rods is 163. Fuel rods are assembled in 15 spans are by 14 intermediate spacer grids. One inlet and another outlet spacer grid are also used. Each span is about 222mm long.

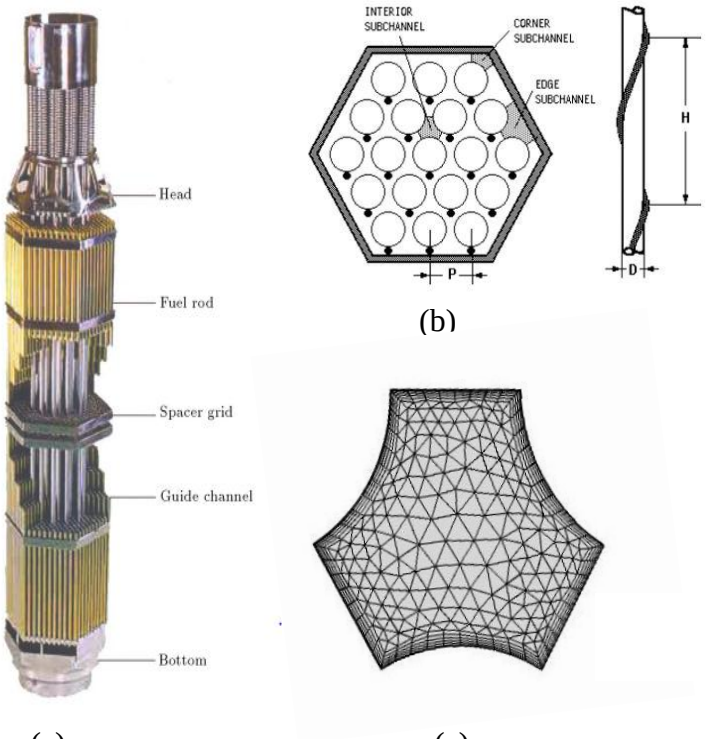

FIGURE 1. (a) Fuel rod assembly, (b) sub-channels and (c) mesh generation.

The cross sectional area of the sub-channel is 37.87mm^2 and the perimeter is 25.24mm. Hydraulic diameter is 6mm. To perform a non-dimensional analysis, geometry is drawn to a ratio of 1 : 6.

For analysis, the portion of first span from inlet to the starting of first intermediate spacer grid is taken. This sub-channel is created first at SolidWorks and is exported to COMSOL MULTIPHYSICS 5.0 to create mesh. The

software gives tetrahedral cells. The mesh is shown in the Fig. 1(c). The specifications of VVER 1000 is listed in Table 1.

TABLE 1. Specification of VVER-1000 reactor[4]

Parameter	Value
Fuel pins	
Number of fuel rods	163
Number of fuel pins	312
Number of guide tubes	18
Number of instrumentation tubes	1
Pin pitch, cm	1.275
Fuel rods	
Pellet diameter, cm	0.772
Clad inside diameter, cm	0.772
Clad outside diameter, cm	0.910
Clad material	Zr
Active fuel length, cm	353.0
Guide tubes	
Inside diameter, cm	1.090
Outside diameter, cm	1.265
Material	Zr
Central instrumentation tube	
Inside diameter, cm	0.960
Outside diameter, cm	1.125
Material	Zr

GOVERNING EQUATION

The governing equations are continuity equations, energy equation and momentum equation. The equations can be written as follows-

Continuity equation-

$$A_{fi}\frac{\partial}{\partial t}(\rho i)+\frac{\Delta \dot{m}_i}{\Delta z}=-\sum_{j=1}^{J}W_{ij} \tag{1}$$

Momentum equation-

$$\frac{\partial}{\partial t}(\dot{m}_i)+\sum_{j=1}^{J}W_{ij}\left\{\begin{matrix}*\\ v_z\end{matrix}\right\}+\frac{\Delta(\dot{m}_i\, v_{zi})}{\Delta z}=-A_{fi}(\rho)g_z-A_{fi}\frac{\Delta\{p\}}{\Delta z}-\sum_{j=1}^{J}W_{ij}{}^{*M}\left(v_{zi}-v_{zj}\right)-\left\{\frac{F_{iz}}{\Delta z}\right\} \tag{2}$$

Energy equation-

$$A_{fi}\frac{\partial}{\partial t}\left[(\rho h)_i\right]+\frac{\Delta \dot{m}_i h_i}{\Delta z}=\left(\dot{q}_i\right)_{rb}-\sum_{j=1}^{J}W_{ij}{}^{*H}\left(h_i-h_j\right)-\sum_{j=1}^{J}W_{ij}\{h^*\}+A_{fi}\left(\frac{Dp_i}{D_t}\right) \tag{3}$$

Relative pressure drop-

$$\mathrm{P_r}=\frac{P-P_o}{P} \tag{4}$$

Friction factor-

$$f = \frac{2gD_h\Delta P}{lv^2} \tag{5}$$

Friction factor using Prandtl correlation [8] –

$$\frac{1}{\sqrt{f}} = 2.0\log_{10}\left(\mathrm{Re}_{D_h}\sqrt{f}\right) - 0.8 \tag{6}$$

BOUNDARY CONDITIONS

The boundary condition has been used for both flow field and thermal field. For flow field, the solid walls are assumed to be of no slip condition. For thermal field, the heat flux is specified at the fuel rod walls. The heat flux of 278.7 KW/m^2 has been used while modeling the domain. For $Re = 10^5$, the inlet velocity and temperature are 5 ms^{-1} and 291° C respectively. The fluid flows upward inside the sub-channel of the fuel rod assembly.

RESULTS AND DISCUSSION

In Fig. 2, temperature profiles in the sub-channel for different axial locations have been shown for $Re = 10^5$. It is found that, temperature gradient becomes more prominent at the farthest distance (z = 30 D_h). Negligible variation in the isothermal contours is observed after z = 16 D_h. This is due to the fact that, coolant enters into the turbulent region at z = 16 D_h. Thus, a critical value of axial distance can be predicted to achieve better thermal contours and higher heat transfer rate.

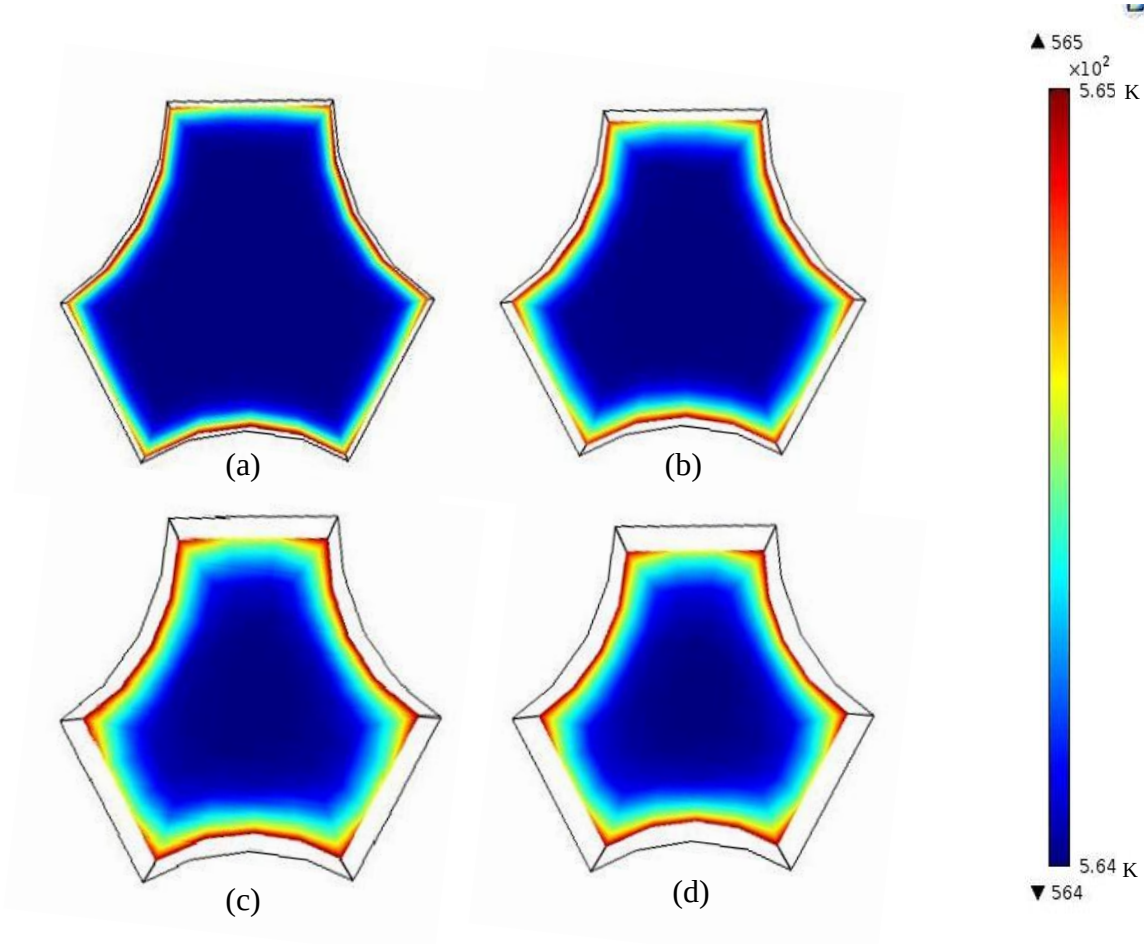

FIGURE 2. Isothermal contours in the sub-channel for (a) z = 6 D_h, (b) z = 12 D_h, (c) z = 24 D_h, (d) z = 30 D_h,.

The contours of the axial velocity of cooling water at various axial locations along the flow direction are shown in Fig. 3(a) to 3(d). It is observed that flow field becomes weaker with the increase of axial distance. Minor variation of velocity profile is observed after axial distance z = 16 D_h.

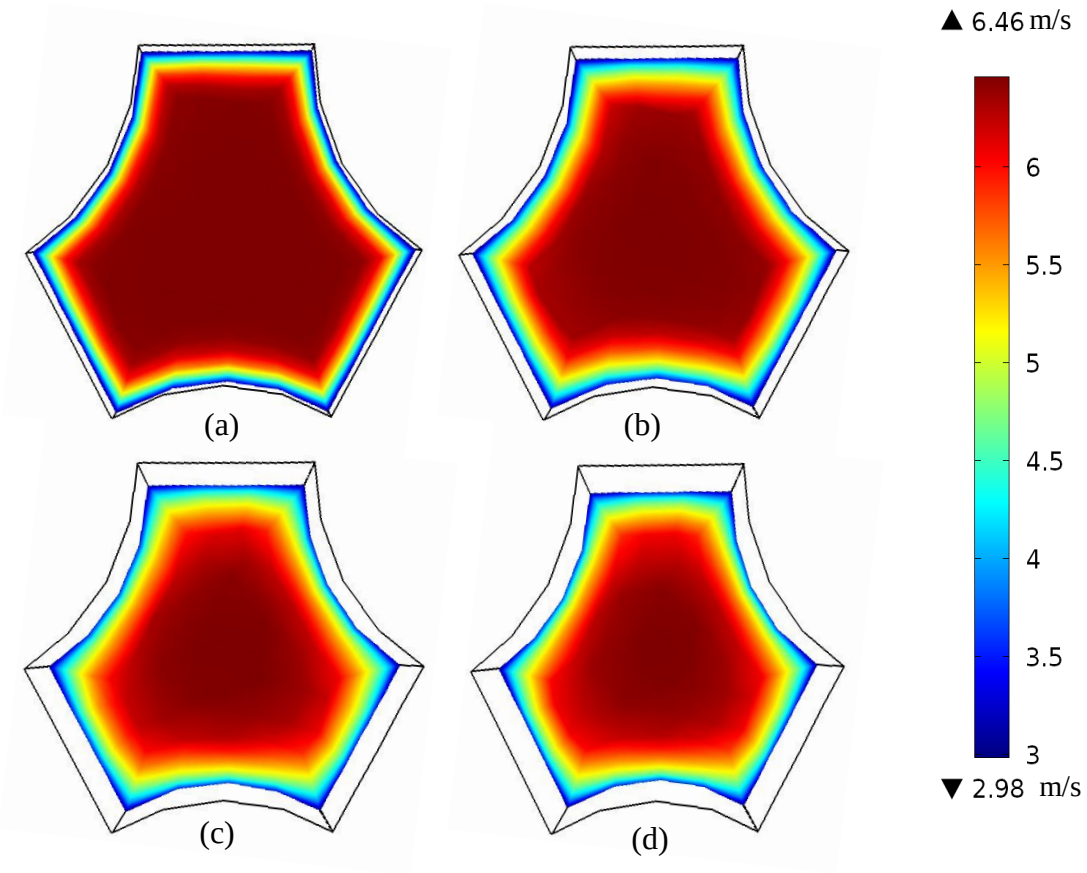

FIGURE 3. Constant velocity contours in the sub-channel for (a) z = 6 D_h, (b) z = 12 D_h, (c) z = 24 D_h, (d) z = 30 D_h,.

Variation of cooling water velocity along the axial distance is shown in Fig. 4 for various Reynolds number. The increase of velocity at the end of the sub-channel is about 0.8 m/s for Re = 10^5. This increase in velocity compensates the loss of velocity due to the blockage in spacer grid.

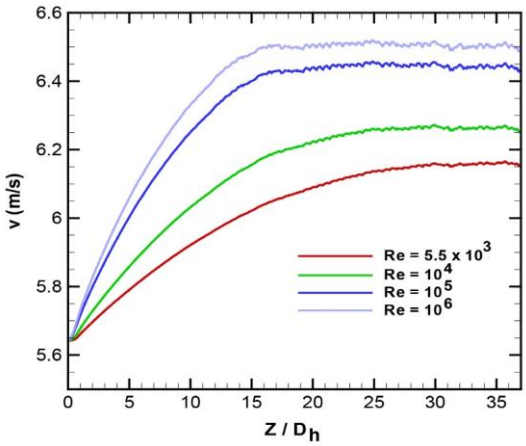

FIGURE 4. Variation of coolant velocity with dimensionless axial distance.

Local Nusselt number variation along the axial distance for various Reynolds numbers is shown in Fig. 5(a). Nusselt number reaches a fully developed value at 16 D_h for Reynolds number of order 5 and 6 but it reaches a fully developed value at 25 D_h for Reynolds number of order 3 and 4. The flow first develops the full turbulence, then the Nusselt number becomes constant. To get proper heat removal, the length of the sub-channel must be fixed considering the minimum length for attaining a fully developed Nusselt number.

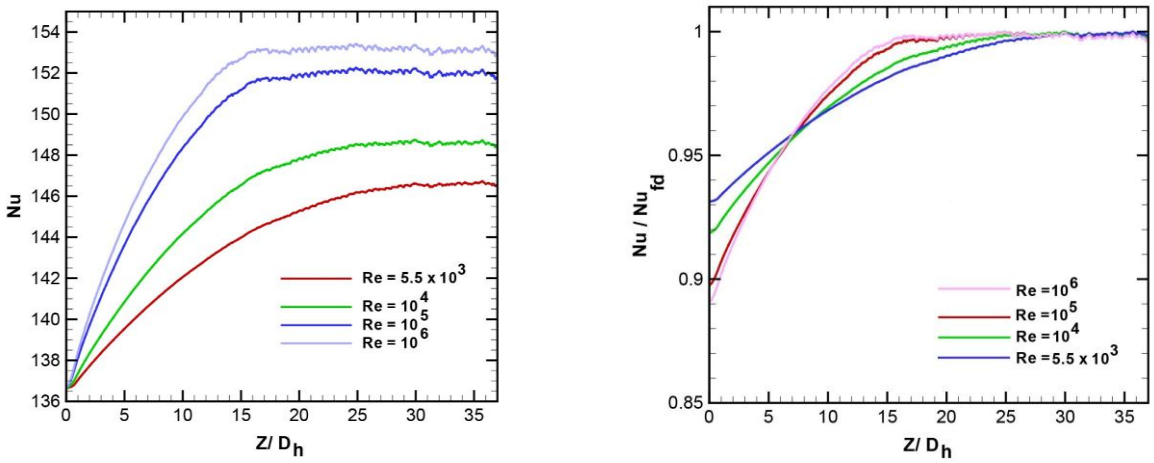

(a) (b)

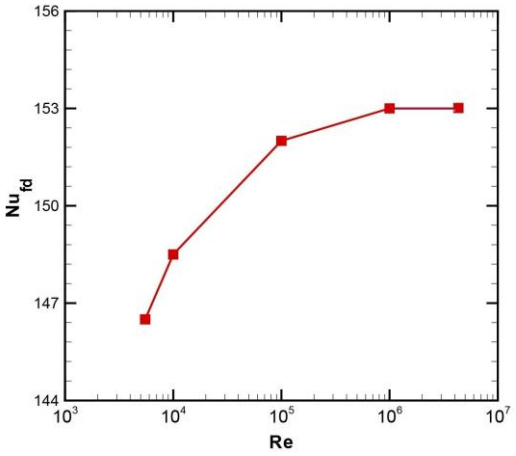

(c)

FIGURE 5. Variation of (a) Nusselt number with dimensionless axial distance (b) normalized Nusselt number with dimensionless axial distance and (c) fully developed Nusselt number with Reynolds number in the sub-channel.

In Fig. 5(b) variation of normalized nusselt number with respect to axial distance in the sub-channel is shown. Difference of normalized Nusselt number in the inlet and outlet is found to be less for lower Reynold's number.

In Fig. 5(c), the variation of fully developed Nusselt number with respect to Reynolds number is shown. Increase in Nusselt number for higher Reynolds number is not so high. To run a reactor economically, the optimization between Reynolds number and fully developed Nusselt number must be done. Higher Reynolds number yields to higher operating cost but higher Nusselt number yields to less production cost for per unit power. From that point of view Reynolds number of order above 6 is not needed.

In Fig. 6(a), it is observed that maximum pressure decreases with the increase of Reynolds number. It is also investigated that for higher Reynolds number, the pressure gradient is lower. Relative pressure drop variation along

the axial distance for two different Reynolds numbers is shown in Fig. 6(b). It is found that, relative pressure drop does not depend substantially on Reynolds number.

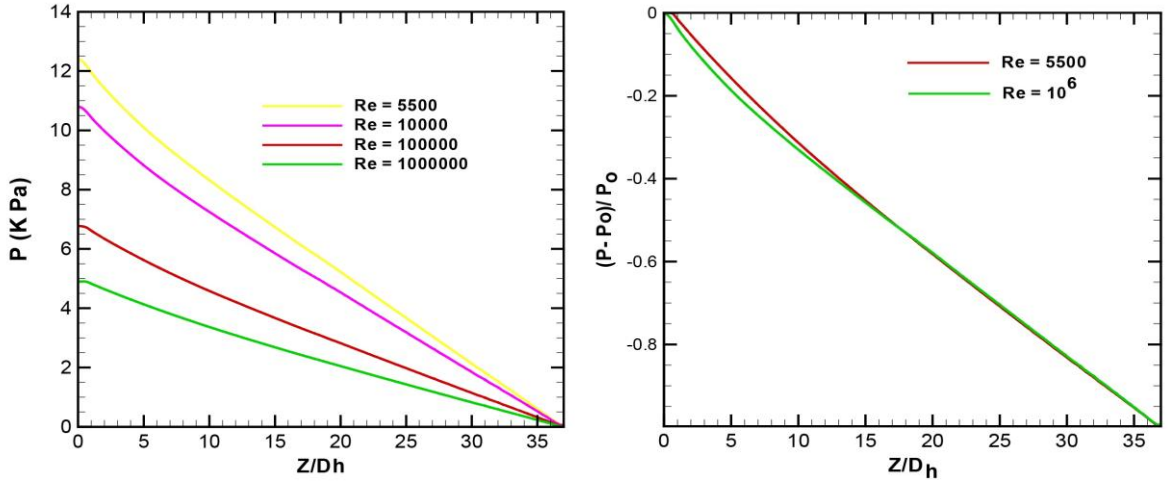

(a) (b)

FIGURE 6. Variation of (a) pressure and (b) relative pressure drop with dimensionless axial distance in the sub-channel.

In Fig. 7(a), variation of friction factors along the axial distance for different Reynolds numbers is shown. The friction factors were obtained from equation 6 using local velocities. The cladding surface is smooth. Friction factor in smooth pipe for a turbulent flow is given by equation 7 which is proposed by Prandtl. In this study, friction factors for two different Reynolds number is calculated by the equation 6 using bulk velocity of water. Obtained values of friction factor in our study is compared with the Prandtl correlation in Fig. 7(b). Obtained values are little less from those of Prandtl correlation.

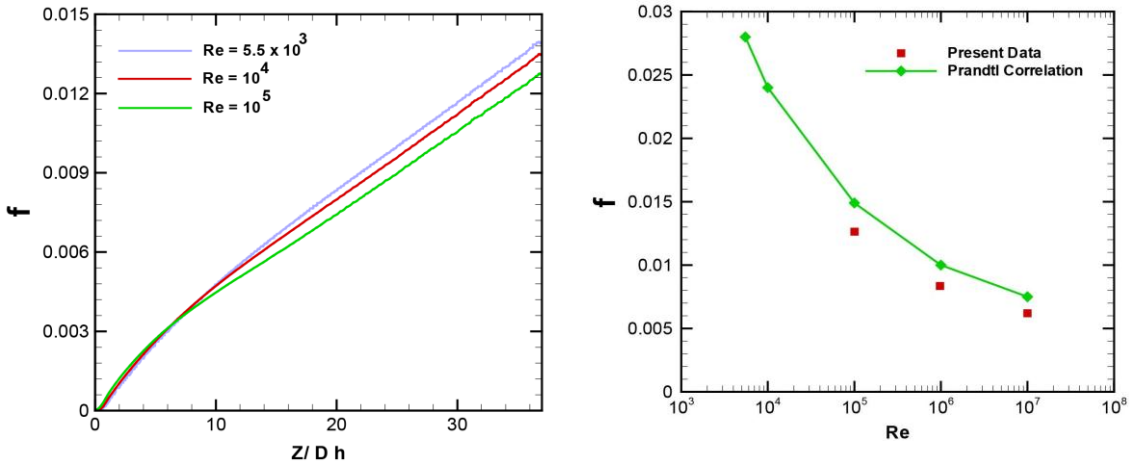

(a) (b)

FIGURE 7. Variation of friction factor with (a) axial distance and (b) Reynolds number.

CONCLUSION

A three-dimensional Computational Fluid Dynamics (CFD) analysis for turbulent flow in the interior sub-channel of hexagonal fuel rod assembly of VVER-1000 is carried out. The following remarks may be drawn from the study-

- The change in temperature and velocity profile in the sub-channel after a critical axial distance is insignificant.
- With the increase of Reynolds number, the minimum axial distance required to achieve a fully developed flow decreases. To remove more heat, sufficient length of sub-channel must be allocated for fully developed Nusselt number. So, for VVER-1000, Reynolds number $\geq 10^5$ may be considered.
- Relative pressure drop is almost the same for various Reynolds numbers.
- Friction factor for the interior sub-channel of hexagonal fuel rod assembly of VVER-1000 is validated with the Prandtl correlation.
- Nusselt number approaches a constant value at $Re \geq 10^6$. For a fixed Reynolds number, Nusselt number becomes constant at a particular axial location. From that location, the probability of nucleate boiling gets higher and two phase flow may occur.

REFERENCES

1. A. A. Falkov, O. B. Samoilov, A. V. Kupriyanov, V. E. Lukyanov, O. N. Morozkin, D. L. Shipov, "Experimental investigation and analysis of thermal-hydraulic characteristics of WWER-1000 alternative FA". 6th International Conference on WWER Fuel Performance, Modeling and Experimental Support. Albena, Bulgaria.
2. C. L. Waata, Coupled Neutronics/Thermal-Hydraulics Analysis of a High-Performance Light-Water Reactor Fuel Assembly, FZKA, Forschungszentrums Karlsruhe, Karlsruhe, Germany **7233** (2005).
3. P. V. Markov, The numerical calculation of heat transfer from stem fuel elements of nuclear VVER, Science and education: science and technology electronic edition, 790-799 (2014).
4. Y. K. Pandey, A. Chauhan, Fuel Management of VVER-1000 Reactors of Kudankulam, Nuclear Power Plant, India, IAEA.
5. J. Pacio, K. Litfin, A. Batta, M. Viellieber, A. Class, H. Doolaard, F. Roelofs, S. Manservisi, F. Menghini, M. Böttcher,Heat transfer to liquid metals in a hexagonal rod bundle with grid spacers: Experimental and simulation results, Nucl. Engg, Design **290**, 27-39 (2015).
6. K. Rehme, G. Trippe, Pressure drop and veclocity distribution in rod bundles with spacer grids, Nucl. Eng. Design, **62** 349-359 (1980).
7. S. Jian, P. Atila, F. Silva, Analytical prediction of friction factors and Nusselt numbers of turbulent forced convection in rod bundles with smooth and rough surfaces, Nucl. Engg, Des. **215**, 111-127 (2002).
8. N. E. Todreas, M. Kazimi, *Nuclear Systems Volume II: Thermal Hydraulic Fundamentals* (Taylor & Francis, New York, 1989), pp. 189–237.
9. J. R. Lamarsh and A. J. Baratta, *Introduction to Nuclear Engineering* (Prentice Hall, New Jersey, USA, 1975).

International Conference on Mechanical Engineering 2015
(ICME 2015) 18 – 20 December, 2015, Dhaka, Bangladesh

Paper ID : 610

Onset of Transition from Laminar to Chaos in MHD Mixed Convection of a Lid-Driven Trapezoidal Cavity Filled with *Cu*-water Nanofluid

Mohammad Azam[b)], Md. Hasanuzzaman[c)] and Sumon Saha[a)]

Department of Mechanical Engineering, Bangladesh University of Engineering and Technology, Dhaka 1000, Bangladesh

[a)]Corresponding author: sumonsaha@me.buet.ac.bd
[b)]azam09mebuet@gmail.com
[c)]hasanuzzaman138@gmail.com

Abstract. The present study investigates the thermal mixing scenarios of steady magneto-hydrodynamic (MHD) mixed convection in a two-dimensional lid-driven trapezoidal cavity filled with *Cu*-water nanofluid. The top wall of the cavity slides with a uniform velocity from left to right direction, while the other walls are fixed. The bottom wall is kept with a constant higher temperature than the top one. The governing mass, momentum and energy equations are expressed in non-dimensional forms and Galerkin finite element method has been employed to solve these equations. Special attention is paid on investigating the onset of transition from laminar to chaos at pure mixed convection case. Hence, the computations are carried out for a wide range of Reynolds numbers ($Re = 0.1 - 400$) and Grashof numbers ($Gr = 10^{-2} - 1.6 \times 10^5$) at unity Richardson number and fixed Hartmann number ($Ha = 10$). The variation of average Nusselt number of the bottom heated wall indicates the influence of governing parameters (*Re* and *Gr*) on heat transfer characteristics. The results are presented and explained through the visualisation of isotherms, streamlines and heatlines.

INTRODUCTION

MHD mixed convection has received considerable attention due to its wide applications in engineering areas such as cooling of nuclear reactor, crystal growth in liquid, micro-electric devices, power plant and solar technology, etc. A frequent studies of mixed convection in lid-driven enclosures of rectangular or square shape have been reported broadly in many recent articles. However, in many practical applications, non-rectangular geometries like trapezoidal enclosures have significant impact on internal fluid flow and heat transfer during mixed convection. Very few studies have considered mixed convection in trapezoidal enclosures. Numerical studies of two-dimensional mixed convection in lid-driven trapezoidal closed cavities were carried out by Hossain, Mamun, and Saha [1], Chowdhury, Saha, and Mamun [2], Hasan *et al.* [3], Mamun *et al.* [4], Saha *et al.* [5], Hasib, Hossen, and Saha [6]. Among those investigations, Saha *et al.* [5] analyzed the onset of transition from laminar to chaos in mixed convection flow and heat transfer characteristics within a lid-driven trapezoidal enclosure filled with water-Al_2O_3 nanofluid at Richardson number, $Ri = 1$. They quantitatively predicted the beginning and the end of transition via the variation of average Nusselt number with both Reynolds and Grashof numbers. However, the characteristic nature of mixed convection (transition from laminar to chaos) in lid-driven square cavity was first observed by Cheng [7] for a wide range of Richardson and Prandtl numbers.

In convection problems, it is also important to visualize the flow of fluid and the flow of energy. The transport of energy through the flow field is a combination of both thermal diffusion and enthalpy flow which can be illustrated by 'Heatline' concept. It was first proposed by Kimura and Bejan [8]. It is a visualization technique such that the net flow of energy (thermal diffusion and enthalpy flow) is zero across each constant heatline. The use of heatlines is the standard technique as isotherms are not a proper heat transfer visualization tool for convection. Hence, to the best knowledge of the authors, no work has paid attention to the problem of onset of transition in MHD mixed convection

in a trapezoidal cavity through the visualization of heatline concept.

The objective of the present study is to investigate MHD mixed convection characteristics in a lid-driven trapezoidal cavity filled with *Cu*-water nanofluid at pure mixed convection case using $Ri = 1$. The selected range of governing parameters ($Re = 0.1 - 400$) and ($Gr = 10^{-2} - 1.6 \times 10^5$) is expected to be sufficient to cover the region of transition from laminar to chaos in mixed convective flow.

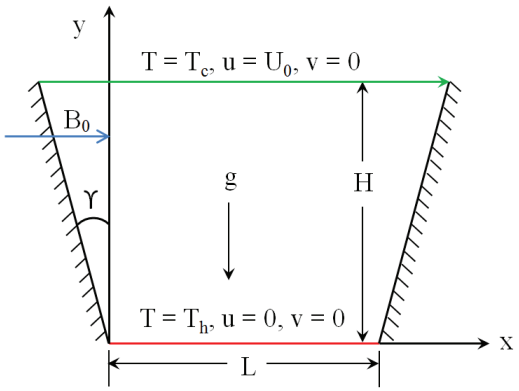

FIGURE 1. Schematic diagram of two-dimensional lid-driven trapezoidal cavity with problem specifications.

PROBLEM DESCRIPTION

The physical domain of the present study is a lid-driven trapezoidal cavity filled with *Cu*-water nanofluid as shown in Fig. 1. The height and the length of the base wall of the cavity are H and L, respectively with aspect ratio of $H/L = \cos 15^\circ$. The top wall is kept at a constant low temperature, T_c whereas the bottom wall is isothermally heated to temperature, T_h ($> T_c$). Besides, only the top wall is moving from left to right with a uniform velocity, U_0. The adiabatic side walls are inclined to $\gamma = 15^\circ$ with y-axis. An external magnetic field with strength B_0 acts horizontally from negative to positive x-axis. There is no induced magnetic field acted on the cavity. *Cu*-water nanofluid is considered as the working fluid which is assumed to be incompressible Newtonian fluid. It is assumed that both the basefluid and the nanofluid are in thermal equilibrium. Moreover, the fluid flow is assumed to be steady and laminar with constant properties except density variations which give rise to buoyancy forces according to the Boussinesq approximation. Single phase model is considered for *Cu*-water nanofluid. Viscous dissipation and the radiation effect are neglected and there is no internal heat generation. The non-dimensional governing equations under the above assumptions are expressed as

$$\frac{\partial U}{\partial X} + \frac{\partial V}{\partial Y} = 0, \tag{1}$$

$$U\frac{\partial U}{\partial X} + V\frac{\partial U}{\partial Y} = -\frac{\partial P}{\partial X} + \frac{\mu_{nf}}{\rho_{nf}\nu_f}\frac{1}{Re}\left(\frac{\partial^2 U}{\partial X^2} + \frac{\partial^2 U}{\partial Y^2}\right), \tag{2}$$

$$U\frac{\partial V}{\partial X} + V\frac{\partial V}{\partial Y} = -\frac{\partial P}{\partial Y} + \frac{\mu_{nf}}{\rho_{nf}\nu_f}\frac{1}{Re}\left(\frac{\partial^2 V}{\partial X^2} + \frac{\partial^2 V}{\partial Y^2}\right) + \frac{(\rho\beta)_{nf}}{\rho_{nf}\beta_f}Ri\Theta - \frac{\sigma_{nf}\rho_f}{\sigma_f\rho_{nf}}\frac{Ha^2}{Re}V, \tag{3}$$

$$U\frac{\partial \Theta}{\partial X} + V\frac{\partial \Theta}{\partial Y} = \frac{\alpha_{nf}}{\alpha_f}\frac{1}{RePr}\left(\frac{\partial^2 \Theta}{\partial X^2} + \frac{\partial^2 \Theta}{\partial Y^2}\right), \tag{4}$$

where the following scales are used to obtain the above non-dimensional governing equations as given below,

$$X = \frac{x}{L}, Y = \frac{y}{L}, U = \frac{u}{U_0}, V = \frac{v}{U_0}, P = \frac{p}{\rho_{nf}U_0^2}, \Theta = \frac{T - T_c}{T_h - T_c}. \tag{5}$$

In the above relation, X and Y are the dimensionless distances in the horizontal and the vertical directions respectively, U and V are the dimensionless velocity components in X and Y directions respectively, P is the dimensionless pressure,

and Θ is the dimensionless temperature. The non-dimensional governing parameters such as Reynolds number (Re), Grashof number (Gr), Prandtl number (Pr), Richardson number (Ri) and Hartmann number (Ha) are defined as,

$$Re = \frac{U_0 L}{\nu_f}, Gr = \frac{g\beta_f (T_h - T_c) L^3}{\nu_f^2}, Pr = \frac{\nu_f}{\alpha_f}, Ri = \frac{Gr}{Re^2}, Ha = B_0 L \sqrt{\frac{\sigma_f}{\mu_f}}. \tag{6}$$

TABLE 1. Nondimensional hydrodynamic and thermal boundary conditions for the present study.

Boundary	Temperature	Velocity
Top wall	$\Theta = 0$	$U = 1, V = 0$
Bottom wall	$\Theta = 1$	$U = V = 0$
Inclined side walls	$\partial\Theta/\partial n = 0$	$U = V = 0$

The boundary conditions for the present problem as shown in Fig. 1 are expressed in nondimensional form using the scales defined in (5). The nondimensional boundary conditions are listed in Table 1. The thermo-physical properties of the nanofluid such as effective density (ρ_{nf}), effective viscosity (μ_{nf}), heat capacitance of nanofluid ($c_{p_{nf}}$), thermal expansion coefficient (β_{nf}), effective thermal conductivity (k_{nf}) effective electrical conductivity (σ_{nf}) can be obtained from the relations listed in Table 2. In the relationship of effective thermal conductivity, k_{nf} the unknown parameters, A_s/A_f and Pe are obtained from the following expression,

$$\frac{A_s}{A_f} = \frac{d_f}{d_s}\frac{\phi}{1-\phi}, Pe = \frac{u_s d_s}{\alpha_f}, u_s = \frac{2k_b T}{\pi \mu_f d_s^2}, \tag{7}$$

where d_s is the diameter of the solid nanoparticles (Cu) that in this study is assumed to be equal to 100 nm, d_f is molecular size of liquid (water) and is taken as $2A^0$ and u_s is the Brownian motion velocity of nanoparticles inside the cavity and k_b is the Boltzmann constant. Using the above expressions as given in Table 2, the thermo-physical properties of Cu-water nanofluid are obtained and listed in Table 3.

TABLE 2. Thermo-physical relationship for the properties of nanofluid. The subscripts 's', 'f' and 'nf' denote the properties of nanoparticles, base fluid and nanofluid respectively.

Property	Relations	Reference
Effective density, ρ_{nf}	$\rho_{nf} = (1-\phi)\rho_f + \phi\rho_s$	Pak and Cho [9]
Effective viscosity, μ_{nf}	$\mu_{nf} = \frac{\mu_f}{(1-\phi)^{2.5}}$	Brinkman [10]
Heat capacitance, $(\rho c_p)_{nf}$	$(\rho c_p)_{nf} = (1-\phi)(\rho c_p)_f + (\phi\rho c_p)_s$	Xuan and Roetzel [11]
Thermal expansion coefficient, β_{nf}	$\beta_{nf} = [(1-\phi)(\rho\beta)_f + \phi(\rho\beta)_s]/\rho_{nf}$	Xuan and Roetzel [11]
Effective thermal conductivity, k_{nf}	$\frac{k_{nf}}{k_f} = 1 + \frac{k_s A_s}{k_f A_f} + ck_s Pe\frac{A_s}{A_f k_f}$, $c = 3.6 \times 10^4$	Patel *et al.* [12]
Effective electrical conductivity, σ_{nf}	$\sigma_{nf} = (1 + 3\phi)\sigma_f$	Cruz *et al.* [13]

TABLE 3. Thermo-physical properties of water, Cu and Cu-water nanofluid used for the present simulation.

Property	Water	Cu	Cu-water nanofluid ($\phi = 0.05$)
c_p (J/kg K)	4179	383	2960.612
ρ (kg/m^3)	997	8954	1394.85
k (W/m K)	0.6	400	0.951734
β (1/K)	2.1×10^{-4}	1.67×10^{-5}	1.4795×10^{-4}
μ (Pa. s)	8.9×10^{-4}	-	1.012×10^{-3}
σ ($1/\Omega m$)	0.05	5.96×10^7	0.0575

The average Nusselt number at the bottom heated wall is expressed as,

$$Nu = -\left(\frac{k_{nf}}{k_f}\right)\int_0^1 \left(\frac{\partial\Theta}{\partial Y}\right)_{Y=0} dX. \tag{8}$$

In order to visualize the thermal field, the dimensionless heat function can be written as,

$$\frac{\partial \Pi}{\partial Y} = \frac{(\rho c_p)_{nf}}{(\rho c_p)_f} RePrU\Theta - \frac{k_{nf}}{k_f}\frac{\partial \Theta}{\partial X}, \quad -\frac{\partial \Pi}{\partial X} = \frac{(\rho c_p)_{nf}}{(\rho c_p)_f} RePrV\Theta - \frac{k_{nf}}{k_f}\frac{\partial \Theta}{\partial Y}, \tag{9}$$

which yield a single equation,

$$\frac{\partial^2 \Pi}{\partial X^2} + \frac{\partial^2 \Pi}{\partial Y^2} = \frac{(\rho c_p)_{nf}}{(\rho c_p)_f} RePr\left[\frac{\partial}{\partial Y}(U\Theta) - \frac{\partial}{\partial X}(V\Theta)\right]. \tag{10}$$

For computation, Dirichlet boundary conditions are set for the adiabatic side walls, whereas the isothermal heating or cooling walls are represented by Neumann boundary conditions which are specified as follows,

$$\mathbf{n}.\Delta\Pi = 0 \quad \text{(for uniformly heated bottom wall)}, \tag{11}$$

and

$$\mathbf{n}.\Delta\Pi = -\frac{(\rho c_p)_{nf}}{(\rho c_p)_f} RePrU\Theta \quad \text{(for uniformly cooled top wall)}. \tag{12}$$

A reference value of Π is assumed to be zero at $X = -sin15^\circ$, $Y = cos15^\circ$ for adiabatic left side wall. Therefore, the heat function, $\Pi = 0$ is the condition for left adiabatic side wall. Similarly, for setting the boundary condition of the right adiabatic side wall, the value of the heat function is determined from Eq. (9), and is written as below

$$\Pi = -\frac{1}{RePr}\frac{(\rho c_p)_f}{(\rho c_p)_n f} Nu. \tag{13}$$

NUMERICAL SIMULATION

The governing equations (1 – 4) are solved by using the Galerkin finite element method. Six noded triangular mesh elements are used to discretize the physical domain since this type of mesh elements smoothly capture the non-linear variations of the field variables. All the six nodes are associated with velocities as well as temperature, only the corner nodes are associated with pressure. The relative tolerance for the error criteria is considered to be 10^{-6}.

Grid Sensitivity Test

Grid sensitivity test is performed to confirm the required numerical accuracy of the solution. Table 4 shows the results of the grid sensitivity test using the variation of Nu. It is found that Nu increases with the increase of mesh element up to 6924 where Nu reaches its maximum value. Now further increment of the element size results lower value of Nu decreases. Hence, mesh elements of 6924 is the optimum mesh size which is selected for the present problem.

TABLE 4. Results of grid sensitivity test obtained for $Gr = 10^3$, $Re = 100$, $Ha = 0$ and $\phi = 0$.

Mesh elements	Nu for bottom heated wall	Mesh elements	Nu for bottom heated wall
2362	6.102556	5130	6.127073
3086	6.103219	6346	6.127164
4024	6.125465	6924	6.127195
4878	6.126239	7160	6.127114

Code Validation

Due to the incommensurate data for the present case, the computational code for heatlines is validated with the previous work of Khorasanizadeh, Nikfar, and Amani [14]. Validation is performed through the observation of heatllines for $Re = 1$, $Ra = 10^4$ and solid volume fraction, $\phi = 0$ (basefluid) and $\phi = 0.05$ (Cu-water nanofluid). Figure 2 shows the comparison of the present work with the result of Khorasanizadeh, Nikfar, and Amani [14]. The heatline contours indicate very good agreement with their work. Thus, the numerical accuracy of the present work is verified.

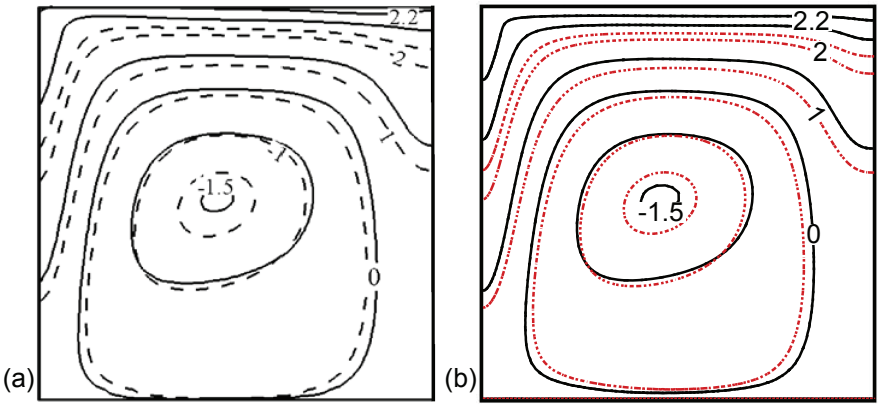

FIGURE 2. Heatlines comparison at $Re = 1$ and $Ra = 10^4$ for basefluid (solid lines) and nanofluid (dashed lines) of $\phi = 0.05$ with (a) Khorasanizadeh, Nikfar, and Amani [14] and (b) the present code.

TABLE 5. List of critical parameters for transition from laminar to chaos of the present problem.

Parameter	**Re (B)** **Gr (B)**	**Re (A)** **Gr (A)**	**Re (B′)** **Gr (B′)**	**Re (A′)** **Gr (A′)**	**Nu (A = A′)** **Nu (B = B′)**	**ΔNu (A − B′)**
$\phi = 0$	92.8 8.61×10^3	123.1 1.515×10^4	152.5 2.325×10^4	183.8 3.378×10^4	5.432268 5.0376043	0.3946637
$\phi = 0.05$	151.8 2.304×10^4	182 3.312×10^4	224 5.0176×10^4	324 1.05×10^5	8.822009 8.410326	0.411683

RESULTS AND DISCUSSIONS

The present investigation is carried out at pure MHD mixed convection condition at $Ri = 1$ and $Ha = 10$ using both base fluid (water) and *Cu*-water nanofluid containing 5% solid-volume fraction of *Cu* nanoparticles. Both Reynolds and Grashof numbers are varied simultaneously for the present problem in order to fix $Ri = 1$. The range of *Re* considered here is $0.1 \leq Re \leq 400$ and the corresponding range of *Gr* is $0.01 \leq Gr \leq 1.6 \times 10^5$. Fig. 3 shows the effect of increasing both *Re* and *Gr* on average Nusselt number for the cases of $\phi = 0$ and $\phi = 0.05$ at constant Richardson number ($Ri = 1$) and Hartmann number ($Ha = 10$). The transition from conduction to convection regime is noticed at $Re \leq 3$ and $Gr \leq 9$ (similar to the findings of Saha *et al.* [5] for water-Al_2O_3 nanofluid) because *Nu* remains almost constant within this range for both basefluid and *Cu*-water nanofluid. Another important observation is the beginning and the end of transition from laminar to chaos. Points *A* (maximum *Nu*) and *B*′ (minimum *Nu*) represent those two cases which is shown in Fig. 3. Within this region a sudden but gradual drop of *Nu* from *A* to *B*′ is observed for both basefluid and nanofluid. In order to explain the drop of *Nu* it is necessary to observe the pattern of isotherms, streamlines and heatlines in the cavity within the transition regime and compare them with points *B* and *A*′ whose *Nu* values are almost equal to points *A* and *B*′ respectively. The summary of all critical parameters describing the characteristics of the transition region is presented in Table 5.

The combined effects of *Re* and *Gr* are represented via the visualization of isotherms, streamlines and heatlines for $Ri = 1$, $Ha = 10$ and $\phi = 0$ depicted in Fig. 4. At points *B* and *A*, Figs. 4 (a) and (b), the isotherms are clustered near the heated bottom wall, which indicate the existence of steep temperature gradients and thin thermal boundary layers in the vertical direction. However, at points *B*′ and *A*′ as shown in Figs. 4 (c) and (d), the temperature gradients close to the bottom wall and right corner are less steep as compare to the case of points *B* and *A*. From Figs. 4 (e), (f), (g) and (h), it is observed that except *B* point, a clockwise rotating buoyancy-driven vortex is created in the right corner of the bottom wall and with the increase of *Re* and *Gr*, the vortex gets stronger and larger which yields a better convection heat transfer scenario. The heat flow distribution inside the cavity is illustrated in Figs. 4 (i), (j), (k) and (l). From these figures, it is easily understood that heat flux is high at the left adiabatic wall and the magnitudes of the heatlines are high at the middle of the cavity. The associated heatlines are introduced from the hot bottom wall and ended to the cold top wall and are parallel to adiabatic side walls. It is also observed from points *B* to *A* that

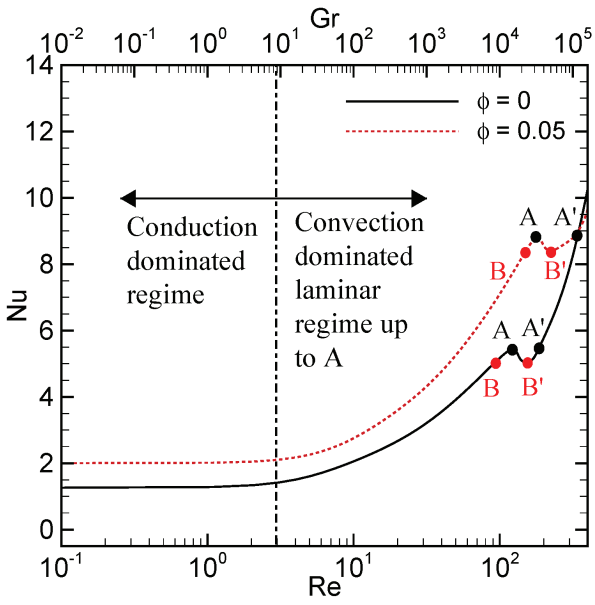

FIGURE 3. Combined effect of *Re* and *Gr* on average Nusselt number of the heated bottom wall at $Ri = 1$ and $Ha = 10$. Solid black line represents basefluid whereas red dotted line represents nanofluid of $\phi = 0.05$. Onset of laminar to chaos transition in mixed convection regime is clearly marked by two black and red points, *A* and *B*′. Comparison is done with same point *A*′ and *B* which points *Nu* number is almost equal to the points of *A* and *B*′.

the vortices of the heatlines are getting enlarged which indicate greater heat transfer rate. Then, from points *A* to *B*′, the vortices of the heatlines are squeezed which indicate lesser heat transfer rate. From points *B*′ to *A*′, again the circulations of the heatlines are getting enlarged which indicates greater heat transfer rate and better thermal mixing inside the cavity. These effects are clearly illustrated in Fig. 3. Figs. 5 exhibits the comparison in the presence of nanoparticles on flow and thermal fields with respect to basefluid as a function of *Re* and *Gr* while $Ri = 1$, $Ha = 10$ and $\phi = 0.05$. The performance of nanofluid is always higher than the basefluid which is shown in terms of isotherms, streamlines and heatlines. Since *Nu* is always higher for nanofluid in compared with basefluid, the resulting variation of critical parameters are influenced by the improved thermo-physical properties of the nanofluid.

CONCLUSION

The present problem of steady MHD mixed convection in a lid-driven trapezoidal cavity filled with *Cu*-water nanofluid is investigated numerically by Galerkin finite element method. The study reveals the phenomena of onset of transition from laminar to chaos in pure mixed convection condition at $Ri = 1$. The effects of both *Re* and *Gr* at $Ri = 1$ and $Ha = 10$ on the average Nusselt number for both nanofluid and basefluid are analyzed. Both quantitative and qualitative predictions for the beginning and the end of transition are carried out by varying the governing parameters, *Re* and *Gr*. The limit of critical parameters relating to the onset of the transition also depends on solid volume fraction of *Cu* nanoparticles. From the present findings, it is shown that with the increase of *Re* up to 3 and their is no significant change of convection heat transfer characteristics in the cavity. Further increase of *Re* up to the the value of *Re*(*A*), the convection heat transfer in the cavity increases rapidly. After that, with the increase of *Re* up to *Re*(*B*′), the value of *Nu* decreases and then further increment of *Re*, the value of *Nu* increases which means enhanced convection heat transfer. In this way, a scenario called onset of transition from laminar to chaos is observed for the present investigation under the influence of MHD mixed convection.

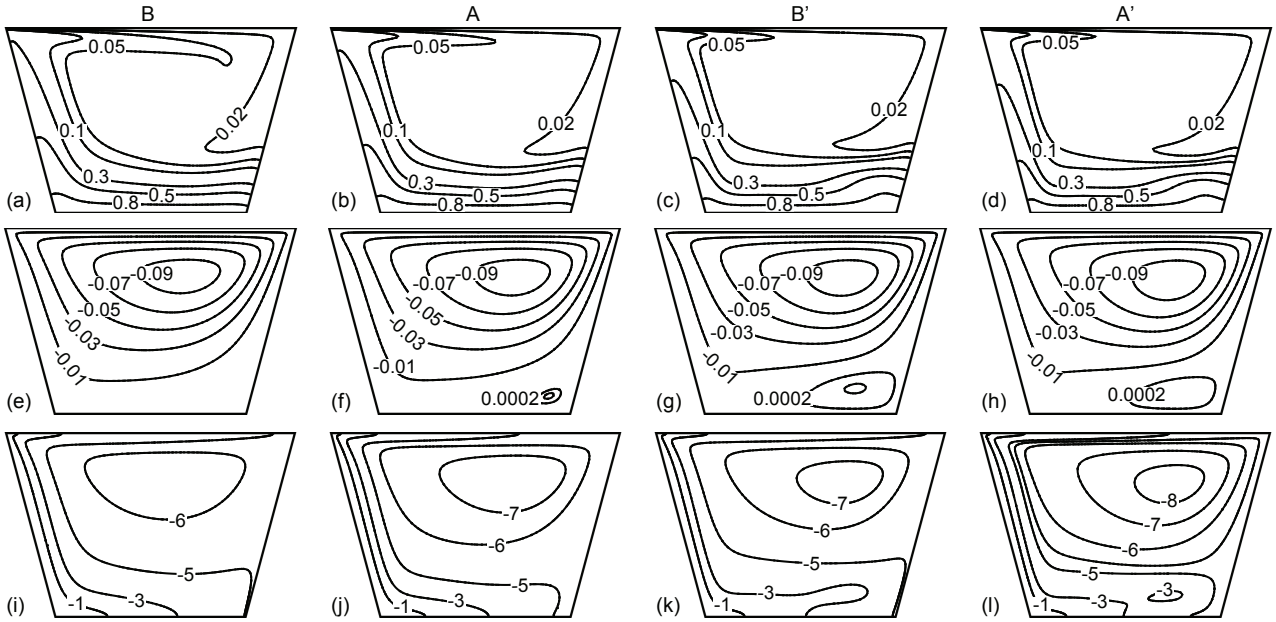

FIGURE 4. (a), (b), (c), (d) – isotherms; (e), (f), (g), (h) – streamlines and (i), (j), (k), (l) – heatlines respectively for basefluid (water) at $Ha = 10$ and $Ri = 1$.

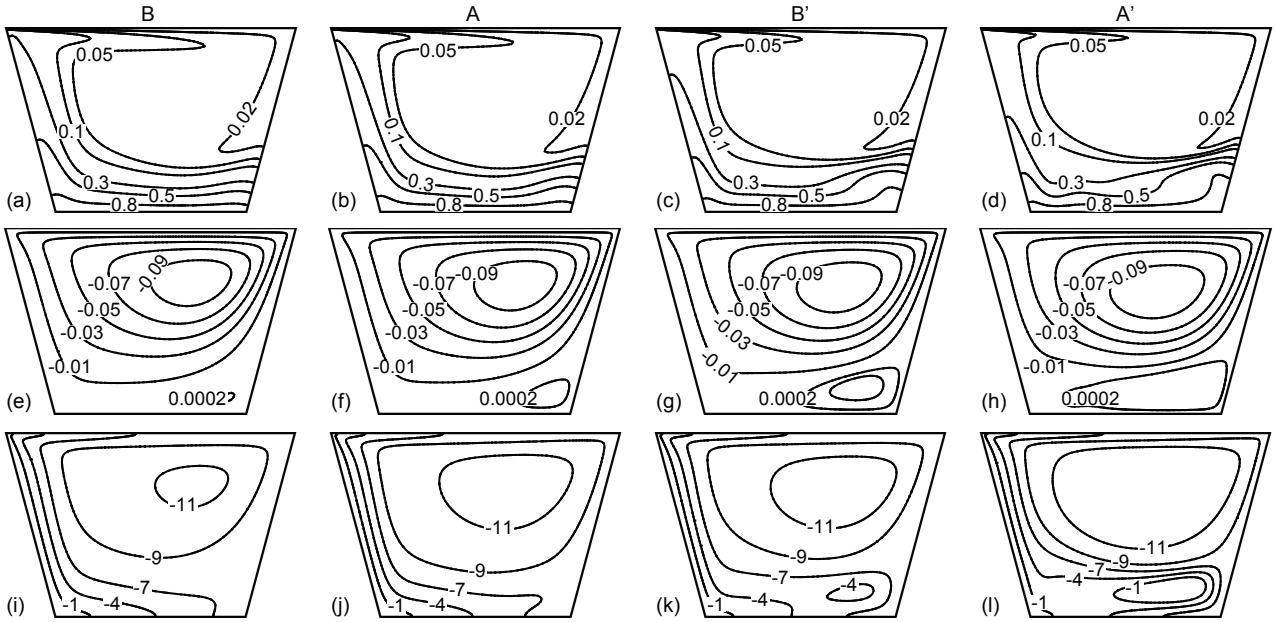

FIGURE 5. (a), (b), (c), (d) – isotherms; (e), (f), (g), (h) – streamlines and (i), (j), (k), (l) – heatlines respectively for *Cu*-water nanofluid ($\phi = 0.05$) at $Ha = 10$ and $Ri = 1$

ACKNOWLEDGMENTS

The authors would like to thank the Department of Mechanical Engineering, Bangladesh University of Engineering and Technology (BUET), Bangladesh for the support provided during this research work.

REFERENCES

[1] M. N. Hossain, M. A. H. Mamun, and S. Saha, "Mixed convection in a trapezoidal cavity with moving lid at top wall and heating from below," in *International Conference on Chemical Engineering* (Dhaka, Bangladesh, 2008).

[2] M. N. H. K. Chowdhury, S. Saha, and M. A. H. Mamun, "Mixed convection analysis in a lid driven trapezoidal cavity with isothermal heating at bottom for various aspect angles," in *8th International Conference on Mechanical Engineering* (Dhaka, Bangladesh, 2009).

[3] M. N. Hasan, S. Saha, G. Saha, and M. Q. Islam, "Effect of sidewall inclination angle of a lid-driven trapezoidal enclosure on mixed convective flow and heat transfer characteristics," in *13th Asian Congress of Fluid Mechanics* (Dhaka, Bangladesh, 2010).

[4] M. A. H. Mamun, T. R. Tanim, M. M. Rahman, R. Saidur, and S. Nagata, International Journal of Mechanical and Materials Engineering **5**, 18–28 (2010).

[5] S. Saha, S. Hossen, M. H. Hasib, and S. C. Saha, "Onset of transition in mixed convection of a lid-driven trapezoidal enclosure filled with water-Al_2O_3 nanofluid," in *19th Australasian Fluid Mechanics Conference* (Melbourne, Australia, 2014).

[6] M. H. Hasib, M. S. Hossen, and S. Saha, Procedia Engineering **105**, 388–397 (2015).

[7] T. Cheng, International Journal of Thermal Sciences **50**, 197–205 (2011).

[8] S. Kimura and A. Bejan, Journal of Heat Transfer **105**, 916–919 (1983).

[9] B. C. Pak and Y. I. Cho, Experimental Heat Transfer an International Journal **11**, 151–170 (1998).

[10] H. C. Brinkman, The Journal of Chemical Physics **20**, 571–571 (1952).

[11] Y. Xuan and W. Roetzel, International Journal of Heat and Mass Transfer **43**, 3701–3707 (2000).

[12] H. E. Patel, T. Sundararajan, T. Pradeep, A. Dasgupta, N. Dasgupta, and S. K. Das, Pramana **65**, 863–869 (2005).

[13] R. C. Cruz, J. Reinshagen, R. Oberacker, A. M. Segadães, and M. J. Hoffmann, Journal of Colloid and Interface Science **286**, 579–588 (2005).

[14] H. Khorasanizadeh, M. Nikfar, and J. Amani, European Journal of Mechanics B/Fluids **37**, 143–152 (2013).

International Conference on Mechanical Engineering 2015
(ICME 2015) 18 – 20 December, 2015, Dhaka, Bangladesh

Paper ID : 611

Effect of Reynolds and Grashof Numbers on Mixed Convection Inside a Lid-Driven Square Cavity Filled with Water-Al_2O_3 Nanofluid

Md. Shah Jaman, Showmic Islam, Sumon Saha[a)], Mohammad Nasim Hasan and Md. Quamrul Islam

Department of Mechanical Engineering, Bangladesh University of Engineering and Technology, Dhaka 1000, Bangladesh

[a)]Corresponding author: sumonsaha@me.buet.ac.bd

Abstract. A numerical analysis is carried out to study the performance of steady laminar mixed convection flow inside a square lid-driven cavity filled with water-Al_2O_3 nanofluid. The top wall of the cavity is moving at a constant velocity and is heated by an isothermal heat source. Two-dimensional Navier-stokes equations along with the energy equations are solved using Galerkin finite element method. Results are obtained for a range of Reynolds and Grashof numbers by considering with and without the presence of nanoparticles. The parametric studies for a wide range of governing parameters in case of pure mixed convective flow show significant features of the present problem in terms of streamline and isotherm contours, average Nusselt number and average temperature profiles. The computational results indicate that the heat transfer coefficient is strongly influenced by the above governing parameters at the pure mixed convection regime.

INTRODUCTION

Lid-driven cavities involving mixed convective flow are very common in various engineering applications such as cooling of electronic devices, furnaces, lubrication technologies, chemical processing equipment, drying technologies, etc. The influence of the governing parameters such as Reynolds number for characterising forced convection, and Grashof number for dominating natural convection, plays a vital role to investigate the thermal-fluid phenomenon of buoyancy forces due to temperature gradient and forced flow due to shear in mixed convection heat transfer.

Several researchers have presented a good number of articles to report the effect of either Reynolds or Grashof number on mixed convection problems in a lid-driven sqaure cavity. Most earlier work was reported by Moallemi and Jang [1] who considered the variation of Reynolds number on the thermal performance of lid-driven square cavity. Later, the individual effect of either Reynolds and Grashof numbers on average Nusselt number was investigated by Prasad and Koseff [2] while keeping one of these two parameters constant. Similar observations through the variation of Reynolds and Grashof numbers on the performance of mixed convection were made by Khanafer and Chamkha [3], Sivakumar *et al.* [4], Basak *et al.* [5]. Oztop and Dagtekin [6] studied the effect of Richardson number from 0.01 to 100 by changing Reynolds number while keeping Grashof number fixed. They concluded that Richardson number characterized the heat transfer regime in mixed convection of lid-driven cavity.

Cavities filled with nanofluid have a significant role in enhancing convective heat transfer. Nanofluid offers far greater heat transfer rate compare to the common fluid. Hence, mixed convection inside a nanofluid filled cavity has now become a popular topic among the researchers. Tiwari and Das [7] investigated numerically the behaviour of *Cu*-water nanofluid inside a two-sided lid-driven differentially heated square cavity to gain insight into convective re-circulation and flow processes induced by a nanofluid. It was found that both Richardson number and the direction of the moving walls affected the fluid flow and heat transfer in the cavity. Talebi, Mahmoudi, and Shahi [8] carried out a numerical investigation on laminar mixed convection flows through a square lid-driven cavity filled with copperwater nanofluid. They found that at the fixed Reynolds number, the solid concentration changed the flow pattern and thermal behavior particularly for a higher Rayleigh number and the effect of solid concentration decreased by the increase of

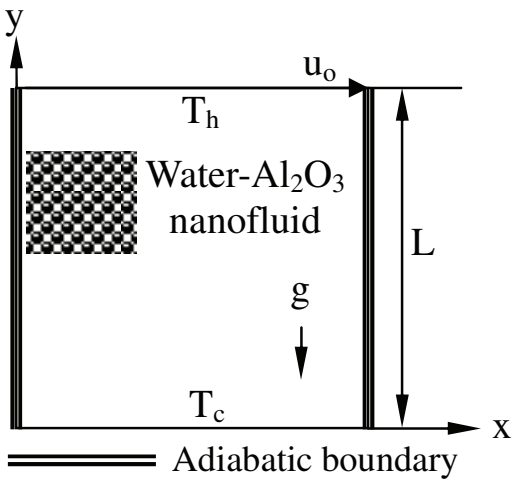

FIGURE 1. Schematic diagram of the square cavity with moving top wall and filled with water-Al_2O_3 nanofluid.

Reynolds number. Abu-Nada and Chamkha [9] focused on the numerical modeling of steady laminar mixed convection flow in a lid-driven inclined square enclosure filled with water-Al_2O_3 nanofluid. They noticed that heat transfer enhancement achieved significantly due to the presence of nanoparticles and that this was accentuated by inclination of the enclosure at moderate and large Richardson numbers. Sebdani, Mahmoodi, and Hashemi [10] investigated numerically the problem of mixed convection fluid flow and heat transfer of Al_2O_3-water nanofluid with temperature and nanoparticles concentration dependent thermal conductivity and effective viscosity inside a square cavity. Their results indicated that when the Reynolds number increased, while the Rayleigh number was kept constant, the forced convection became stronger that caused the heat transfer rate to increase. Most recently, Muthtamilselvan and Doh [11] considered the variation of Richardson number on steady state two-dimensional mixed convection in a lid-driven square cavity filled with *Cu*-water nanofluid and found that Richardson number strongly affected the fluid flow and heat transfer in the cavity.

The objective of the present study is to investigate steady-state laminar mixed convection inside a lid-driven square cavity filled with water-Al_2O_3 nanofluid. Initially, the governing equations related to the present problem are derived and then, a finite element formulation is applied to numerically solve these nonlinear partial differential equations. Parametric variation of two major governing parameters namely Reynolds and Grashof numbers is carried out to explore the nature of mixed convective flow inside the cavity with and without the presence of nanoparticle.

PHYSICAL PROBLEM

The present problem simulates the performance of heat transfer and fluid flow in a two-dimensional square cavity of length L as shown schematically in Fig. 1. A Cartesian coordinate system is considered where the origin is set at the lower-left corner of the cavity. The top wall of the cavity is moving in the positive x-direction at a constant speed, u_0. The vertical side walls of the cavity are kept insulated, while the top and the bottom walls are kept at constant high and low temperatures T_h and T_c, respectively. We assume that the nanofluid (water-Al_2O_3) is in thermal equilibrium, Newtonian and incompressible. The flow is assumed to be steady, two-dimensional, laminar and viscous dissipation, radiation effects and Joule heating are neglected in the present study.

MATHEMATICAL FORMULATION

Mixed convection is governed by the differential equations expressing conservation of mass, momentum and energy. In the present study, the properties of the nanofluid are also assumed to be constant expect the Boussinesq approximation which is invoked for the fluid properties to relate density changes to temperature changes and to couple in this way the temperature field to the flow field. The governing equations in non-dimensional form considering the above

TABLE 1. Boundary conditions in non-dimensional forms for the present study.

Parameter	$\mathbf{X = 0, 0 \le Y \le 1}$	$\mathbf{Y = 0, 0 \le X \le 1}$	$\mathbf{X = 1, 0 \le Y \le 1}$	$\mathbf{Y = 1, 0 \le X \le 1}$
Velocity	$U = V = 0$	$U = V = 0$	$U = V = 0$	$U = 1, V = 0$
Temperature	$\frac{\partial \Theta}{\partial Y} = 0$	$\Theta = 0$	$\frac{\partial \Theta}{\partial Y} = 0$	$\Theta = 1$

TABLE 2. Properties of water, Al_2O_3 and water-Al_2O_3 nanofluid used for the present simulation.

Property	**Water**	$\mathbf{Al_2O_3}$	**water-$\mathbf{Al_2O_3}$ nanofluid** ($\phi = \mathbf{0.1}$)
c_p (J/kg K)	4179	765	3131.9
ρ (kg/m^3)	997.1	3970	1294.4
k (W/m K)	0.613	25	0.80154
β (1/K)	2.1×10^{-4}	0.85×10^{-5}	1.482×10^{-4}
μ (Pa. s)	0.001003	-	0.0013053

assumptions are written as follows:

$$\frac{\partial U}{\partial X} + \frac{\partial V}{\partial Y} = 0, \tag{1}$$

$$U\frac{\partial U}{\partial X} + V\frac{\partial U}{\partial Y} = -\frac{\partial P}{\partial X} + \frac{\mu_{nf}}{\rho_{nf}\nu_f}\frac{1}{Re}\left(\frac{\partial^2 U}{\partial X^2} + \frac{\partial^2 U}{\partial Y^2}\right), \tag{2}$$

$$U\frac{\partial V}{\partial X} + V\frac{\partial V}{\partial Y} = -\frac{\partial P}{\partial Y} + \frac{\mu_{nf}}{\rho_{nf}\nu_f}\frac{1}{Re}\left(\frac{\partial^2 V}{\partial X^2} + \frac{\partial^2 V}{\partial Y^2}\right) + \frac{(\rho\beta)_{nf}}{\rho_{nf}\beta_f}Ri\Theta, \tag{3}$$

$$U\frac{\partial \Theta}{\partial X} + V\frac{\partial \Theta}{\partial Y} = \frac{\alpha_{nf}}{\alpha_f}\frac{1}{RePr}\left(\frac{\partial^2 \Theta}{\partial X^2} + \frac{\partial^2 \Theta}{\partial Y^2}\right). \tag{4}$$

Equations (1)-(4) are normalized using the following dimensionless scales:

$$X = \frac{x}{L}, Y = \frac{y}{L}, U = \frac{u}{u_0}, V = \frac{v}{u_0}, P = \frac{p}{\rho_{nf}{u_0}^2}, \Theta = \frac{T - T_L}{T_h - T_L}, \tag{5}$$

where x and y are the distances measured along the horizontal and the vertical directions, respectively; u and v are the velocity components in the x- and the y-directions, respectively; p is the pressure, T denotes the temperature; μ, ν, α, ρ, and β are dynamic viscosity, kinematic viscosity, thermal diffusivity, fluid density and coefficient of volumetric expansion and the thermal conductivity respectively. The subscripts 'f','s' and 'nf' are used to represent the properties of base fluid, solid nanoparticles and nanofluid respectively. The governing parameters in the above equations are Prandtl number (Pr) and Grashof number (Gr), Reynolds number (Re) and Richardson number (Ri) and those are defined as follows:

$$Pr = \frac{\nu_f}{\alpha_f}, Re = \frac{u_0 L}{\nu_f}, Gr = \frac{g\beta_f(T_h - T_c)L^3}{{\nu_f}^2}, Ri = \frac{Gr}{Re^2}. \tag{6}$$

The non-dimensional boundary conditions for the present problem are listed in Table 1. The thermo-physical properties of nanofluid (water-Al_2O_3) used in this study are computed by the relations provided in the reference of Saha *et al.* [12] and are listed in Table 2.

Nusselt number (Nu) is one of the important dimensionless parameters to be computed for heat transfer analysis in mixed convection flow. The average Nusselt number is calculated by integrating the non-dimensional temperature gradient over the heated wall as

$$Nu = -\frac{k_{nf}}{k_f}\int_0^1 \left(\frac{\partial \Theta}{\partial Y}\right)_{Y=1} dX \tag{7}$$

Similarly, the average fluid temperature inside the cavity, Θ_{av} is obtained by integrating the fluid temperature over the entire domain as

$$\Theta_{av} = \int_A \Theta dA, \tag{8}$$

where A is the non-dimensional area of the domain.

TABLE 3. Validation of the present numerical results with Abu-Nada and Chamkha [9].

		Nu($\phi = \mathbf{0}, \mathbf{0.1}$)		
Gr	*Ri*	Present Work	Abu-Nada and Chamkha [9]	Difference(%)
100	0.2	2.5449214, 3.0258367	2.644311, 3.098952	0.0993896, 0.0731153
100	0.5	2.1284957, 2.532299	2.183122, 2.554669	0.0546263, 0.02237
100	2	1.593388, 1.8970088	1.60701, 1.88441	0.013622, -0.0125988
100	5	1.3224441, 1.6066937	1.325823, 1.594969	0.0033789, -0.0117247

NUMERICAL PROCEDURE

Using Galerkin finite element formulation, the momentum and the thermal energy equations (1-4) result in a set of non-linear coupled algebraic equations for which an iterative scheme is adopted. To ensure convergence of the numerical algorithm, the following criteria is applied to all dependent variables over the solution domain

$$\sum \left| {\psi_{ij}}^{m} - {\psi_{ij}}^{m-1} \right| \leq 10^{-5}, \tag{9}$$

where ψ represents a dependent variable U, V, P and Θ; the indexes i, j indicate a grid point and the index m is the current iteration at the grid level.

Grid independence check is performed by comparing the results of different grid meshes for $Gr = 10^6$ and $Re = 10^3$, which are the highest Grashof and Reynolds numbers considered in the present simulation. Special attention is given on the convergence of the average Nusselt number, Nu at the heated surface with grid refinement for both plain and nanofluids. It is noticed that grid independence is obtained for 6561 mesh elements where there is an insignificant change in Nu, with further increase of element number.

In order to validate the numerical code, the present results are compared with those reported by Abu-Nada and Chamkha [9] obtained at some specific computational parameters. In Table 3, a comparison of the average Nusselt number between the present numerical scheme and the results of Abu-Nada and Chamkha [9] is presented. The comparison shows reasonable accuracy of the present numerical algorithm and thus validates the simulation results satisfactorily.

RESULTS AND DISCUSSIONS

From the numerical simulation, the flow and thermal fields inside a lid-driven square cavity filled with water-Al_2O_3 nanofluid are obtained for different governing parameters. The solid particle volume fraction for nanofluid is considered to be 10%. For first set of simulation, the range of Reynolds numbers is taken from 0.1 to 10^3 at fixed Grashof number ($Gr = 100$). In the second case, the Grashof number also varies from 0.1 to 10^6 for a constant Reynolds number ($Re = 100$). Finally, special attention is given at the pure mixed convection regime ($Ri = 1$), where the flow and heat transfer characteristics are investigated for the Grashof number ranges from 0.1 to 10^6 and the corresponding Reynolds number varies from $\sqrt{0.1}$ to 10^3.

Effect of Reynolds Number

In order to examine the effect of Reynolds numbers, a parametric study is carried out for a range of Reynolds number from 0.1 to 10^3 at fixed Grashof number ($Gr = 100$). Fig. 2 shows the contours of the streamlines and isotherms inside the cavity for some selective cases. In these cases, three different Reynolds numbers ($Re = 100, 10$ and 1) with the corresponding Richardson number, $Ri = 0.01, 1.0$ and 100 are selected. By definition, the value of Richardson number designates the dominance of the buoyancy driven natural convection over lid-driven forced convection. As depicted in the top of Fig. 2, during the forced convection dominated mode ($Ri = 0.01$), the streamline patterns represent a primary clockwise recirculating cell which is mainly induced by the moving lid and occupies most of the cavity space. Two very small secondary eddies are observed near the both side of the bottom wall corners. The flow features can be attributed to the fact that the buoyancy force is overwhelmed by the mechanical or shear effect of the moving top lid at lower values of Richardson number.

As shown in Fig. 2, the isotherms for the forced convection dominated mode are clustered closely near the bottom surface of the cavity which indicates sharp temperature gradient in the vertical direction in the region. However, in

the remaining region of the cavity especially near the moving lid, the temperature gradients are very little. This means the temperature is quite uniform in the interior region of the cavity due to vigorous effect of mechanically driven circulations. In the mixed convection dominated mode ($Ri = 1.0$), the buoyancy effect is comparable in magnitude to the mechanical effect of the moving lid. The distribution of streamlines consists of one large primary circulating cell of the cavity size with other two secondary eddies near the bottom wall corners. The spacing among isotherms becomes larger near the bottom wall at the same time they are being pushed upward. It indicates that the temperature gradient in the vertical direction decreases as compared to the forced convection dominated mode ($Ri = 0.01$). In the natural convection dominated mode ($Ri = 100$), the buoyancy effect is dominant over the mechanical effect of the moving lid. As the streamline distribution indicates, the flow field remains almost stagnant in the bulk of the cavity interior except near the moving top wall where the shear effect of the moving lid is confined. The contours of isotherms are nearly parallel lines with minimum distortion among three different cases under consideration. The heat transfer mechanism in this case resembles a conduction dominated convection process. Note that, with the decrease of the Reynolds number, the core of the primary circulating cell moves upward and the flow becomes weak which results in flat isotherms near the bottom wall. These phenomena ultimately decrease the heat transfer rate. The addition of nanoparticle has been found to affect the flow and thermal field inside the cavity as depicted in Fig. 2. With the addition of the nanoparticle, the maximum value of the stream function decreases at higher values of the Reynolds number. Moreover, the variation in the distribution of the isotherms with and without nanoparticle is very prominent at higher Reynolds number or at lower Richardson number.

Figure 3 depicts how the variation of Reynolds and Richardson number affect the heat transfer process inside the cavity with and without nanoparticle at a constant Grashof number ($Gr = 100$). The points considered herein is the average Nusselt number (Nu) over the hot moving wall and the average fluid temperature (θ_{av}) in the cavity. As shown in Fig. 3, the average Nusselt number changes with the Re. However, the change in Nu is not linear. For lower values of the Reynolds number, increase in the Reynold number does not result in any significant change in the Nusselt number This trend continues up to a critical value, $Re = 3$; after that, with the increase of the Reynolds number, the average Nusselt number increases significantly with the Reynolds number The addition of nanoparticle in the base fluid results in better heat transfer inside the cavity. However, this effect is more prominent at the higher values of the Reynolds number The average fluid temperature inside the cavity does not show any significant change with Reynolds number up to $Re = 1$. After that, with the increase of the Reynolds number, average fluid temperature inside the cavity increase sharply. Moreover, addition of nanoparticle decreases the average fluid temperature in the cavity which is due to better heat transfer.

Effect of Grashof Number

Fig. 4 describes the flow and temperature field inside the cavity in terms of the distribution of streamlines and isotherms when the Grashof number of the system is varied from 100 to 10^6 at a constant mechanical effect of the moving lid i.e. $Re = 100$. These result in the Richardson number of the system to vary from 0.01 to 100. As illustrated in Fig. 4, the variations in the flow field as well as in the temperature field inside the cavity with the Richardson number are drastically different to the corresponding cases ($Ri = 0.01, 1.0, 100$) described in Fig. 2. As the reference one, consider the forced convection dominated mode as depicted in Fig. 4 with $Gr = 100$ ($Ri = 0.01; Re = 100$). For this case, the flow field is mainly governed by a primary clockwise recirculating cell with two minor eddies near the bottom corners. As the Grashof number increases to 10^4, a strong secondary counter clockwise recirculating cell is found to appear near the bottom wall that occupies a significant volume of the cavity compared to the primary circulating cell as shown in Fig. 4. In other words, increased buoyancy effect causes the mechanical effect of the moving lid to push back to the upper part of the cavity. As the Grashof number is eventually increased to 10^6, the streamlines show four circulating cells throughout the cavity as in Fig. 4 where the flow induced by the moving lid is pushed up very near to the top moving lid. These changes in the flow field with Grashof number are also manifested in the distribution of isotherms inside the cavity. For the forced convection dominated mode with $Gr = 100$ ($Ri = 0.01; Re = 100$) as depicted in Fig. 4), the isotherms are clustered near the bottom wall where a large temperature gradient exists in the vertical direction. As the Grashof number increases to 10^4, ($Ri = 0.01; Re = 100$) the isotherms near the bottom wall take more space in their distribution as shown in Fig. 4. Also, the generation of the secondary recirculating cell near the bottom wall causes the isotherms to move down near the left wall. For the natural convection dominated mode with $Gr = 100$ ($Ri = 100; Re = 100$) as in Fig. 4, the isotherm distribution is very much similar to the case of conduction dominated convection case represented by parallel isotherms. Majority of the cavity is occupied by largely spaced undistorted isotherms while in a minor part of the cavity neat the top moving lid, the isotherms undergoes some sort of distortion.

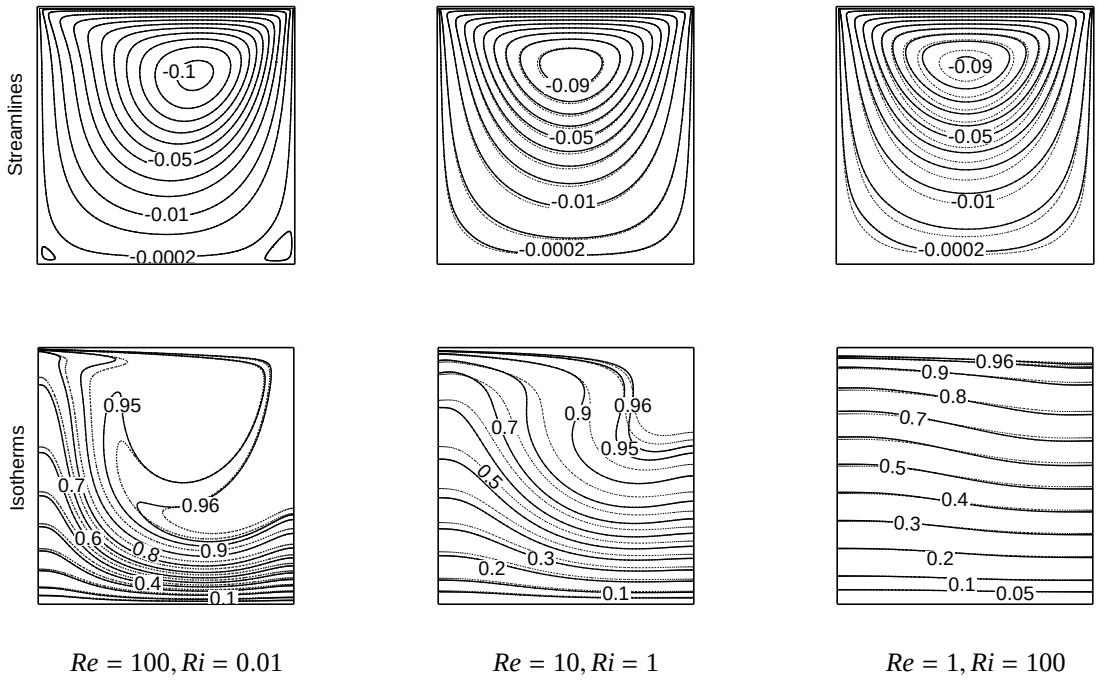

FIGURE 2. Streamlines and isotherms patterns for different Reynolds numbers ($Gr = 100$). Solid line represents plain base fluid ($\Phi = 0$) and dashed line represents nanofluid with ($\Phi = 0.1$).

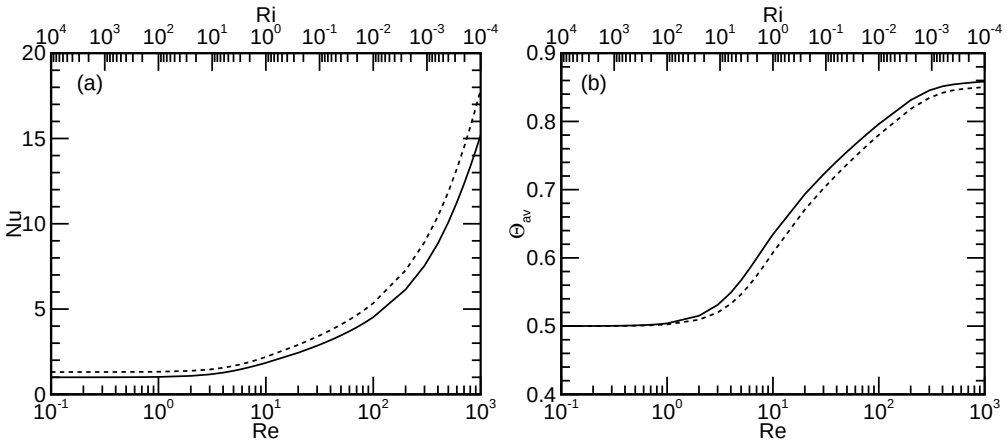

FIGURE 3. Effect of Reynolds number on (a) average Nusselt number of the heated wall and (b) average fluid temperature of the cavity for constant Grashof number, $Gr = 100$. Solid line represents plain base fluid ($\Phi = 0$) and dashed line represents nanofluid with $\Phi = 0.1$.

This is because of the fact that, the mechanically driven flow near the top moving lid got shrunk by the generation of the secondary recirculating cells beneath.These secondary recirculating cells offer much resistance to heat transfer from the hot moving wall as the primary recirculating flow which is mostly responsible for the transfer of energy gets trapped in between the top moving wall and secondary recirculating cells far away from the cold bottom wall i.e. the heat sink. Therefore, the isotherm distribution at high values of Grashof number recognizes heat transfer to take place in a very narrow space. The distribution of streamlines and isotherms with and without nanoparticle as depicted in Fig 5 indicates that both the fluid flow and heat transfer inside the cavity is influenced by the addition of nanoparticle.

Fig. 5 depicts the variation of average Nusselt number over the hot top moving lid and the average fluid temperature inside the cavity filled with base fluid or nanofluid for a wide range of Grashof number with a constant Reynolds number, $Re = 100$. As illustrated in Fig. 5(a), addition of the nanoparticle in the base fluid results in significant increase of the average Nusselt number which means heat transfer rate is enhanced. However, the trend of variation of the average Nusselt number with Grashof number is similar for both the base fluid and nanofluid. In both cases, the heat transfer rate i.e. the average Nusselt number remains almost constant with the increase of the Grashof number up to $Gr = 100$, and then started to decrease slowly at higher values of Grashof number This trend continues up to $Gr = 10^3$ after which the Nusselt number decreases very sharply with the Grashof number up to $Gr = 10^4$. After this, the average Nusselt number continues to decrease with increasing Grashof number slowly as compared with the earlier stage ($10^3 < Gr < 10^4$). As obtained in the present study, the average Nusselt number decreases up to 72% and 74% for the base fluid and nanofluid respectively as the Grashof number increases from 100 to 10^6. Therefore it might be concluded that, the formation of secondary recirculating cells in the cavity at higher Grashof number has intense influence on the heat transfer rate of the system. As depicted in Fig. 5(b), the average fluid temperature inside the cavity for base fluid is found to be higher than the nanofluid. This is because of enhanced heat transfer characteristics of nanofluid over base fluid. For both cases, the average fluid temperature remains constant with increasing Grashof number up to $Gr = 10^3$. For Grashof No. $Gr > 10^3$, the average fluid temperature in the cavity starts decreasing for both the base fluid and nanofluid as the heat transfer from the hot moving lid starts decreasing at higher Grashof No as indicated in Fig. 5(a). At very high Grashof number, the average fluid temperature in the cavity for base fluid and nanofluid assumes very small values as the effect of primary circulating flow inside the cavity prevails only in a very narrow region near the moving top lid while the flow and temperature field in the majority of cavity is governed by the secondary circulating flow. Moreover, the effect of nano particle on the average Nusselt number of the system is found to be deemed at very high values of Grashof number.

Combined Effect of Reynolds and Grashof Numbers

Figure 6 shows the contours of the streamlines and isotherms inside the cavity for the case of pure mixed convection heat transfer mode. The Reynolds number in this time is varied as 1, 10 and 10^3 while the Grashof number is varied accordingly as 1, 10^2 and 10^6 to have the Richardson number 1. In the case of pure mixed convection heat transfer mode with smaller mechanical effect of the moving lid and small buoyancy effect ($Re = 1$ and $Gr = 1$), as shown in Fig. 6, the flow field is mainly governed by a clockwise primary circulating cell with two minor eddies at the bottom corners. As both the mechanical effect and buoyancy effect is very low, the resultant flow field is very weak as indicated by the maximum value of the stream function. When both the mechanical effect of the moving lid and buoyancy effect increase ($Re = 10$ and $Gr = 10^4$) as depicted in Fig. 6, the strength of the flow field inside the cavity increase. However, the flow field still is characterized by a single clockwise primary recirculation cell. At much higher mechanical effect of the moving lid and buoyancy effect, ($Re = 10^3$ and $Gr = 10^6$), the flow field becomes even much stronger as indicated in Fig. 6. The flow field in this case clearly shows up two different flow circulations inside the cavity. The primary reirculation cell due to the moving top lid is found to reside at the top right location of the cavity as a secondary recirculation cell due to enhanced buoyancy appear at the bottom left location of the cavity. The variation in the magnitude of the Reynolds and Grashof number in pure mixed convection mode heat transfer also results in significant change of isotherm distribution inside the cavity as shown in Fig. 6. For the mixed convection case with small shear and buoyancy effect, ($Re = 1$ and $Gr = 1$), the isotherms take more space in their distribution through the cavity like a conduction dominated convection case. The isotherms undergo the minimum level of distortion in this case among all cases under consideration. In the second case ($Re = 10$ and $Gr = 10^4$) as shown in Fig 6, the isotherms near the right wall of the cavity are pushed down to the bottom wall as strong shear induced hot flow moves downward after being deflected from the right wall. This results in higher temperature gradient near the bottom wall. In the third case ($Re = 10^3$ and $Gr = 10^6$) as shown in Fig 6, the isotherms are much heavily clustered in a narrow space near the bottom wall. At the same time, a large portion of the cavity remains almost at constant temperature with very low

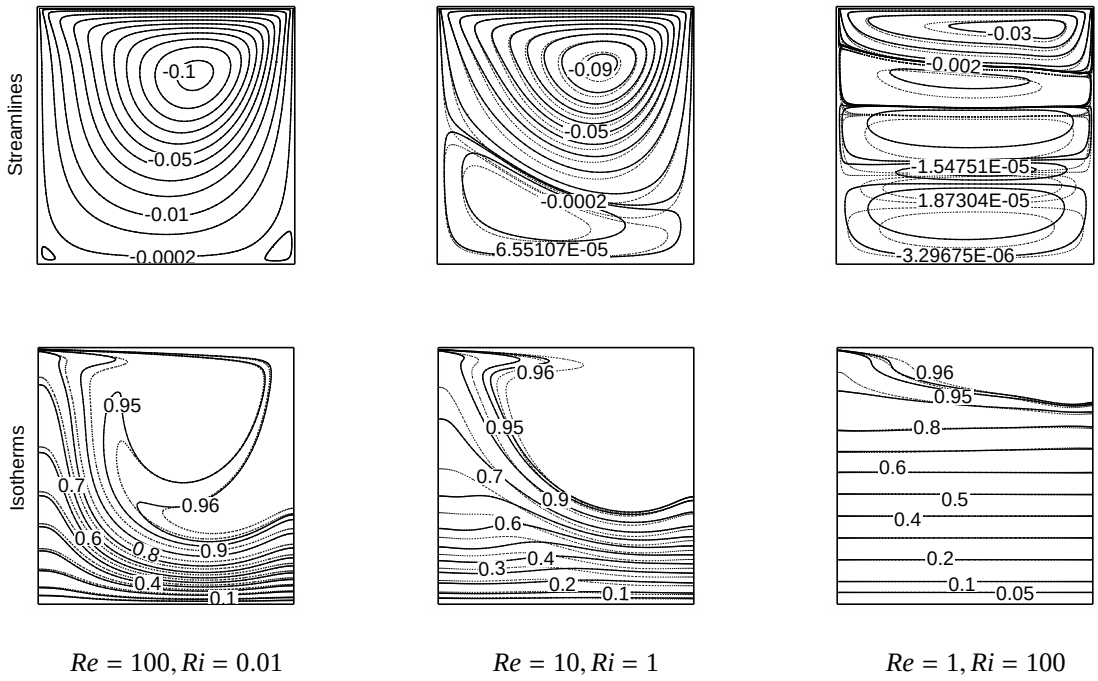

FIGURE 4. Streamlines and isotherms patterns for different Grashof numbers ($Re = 100$). Solid line represents plain base fluid ($\Phi = 0$) and dashed line represents nanofluid with ($\Phi = 0.1$)

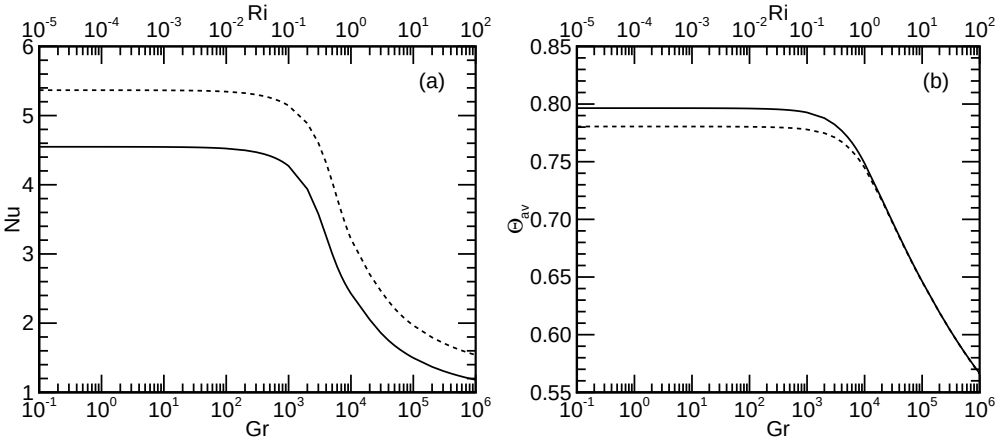

FIGURE 5. Effect of Grashof number on (a) average Nusselt number of the heated wall and (b) average fluid temperature of the cavity for constant Reynolds number, $Re = 100$. Solid line represents plain base fluid ($\Phi = 0$) and dashed line represents nanofluid with $\Phi = 0.1$.

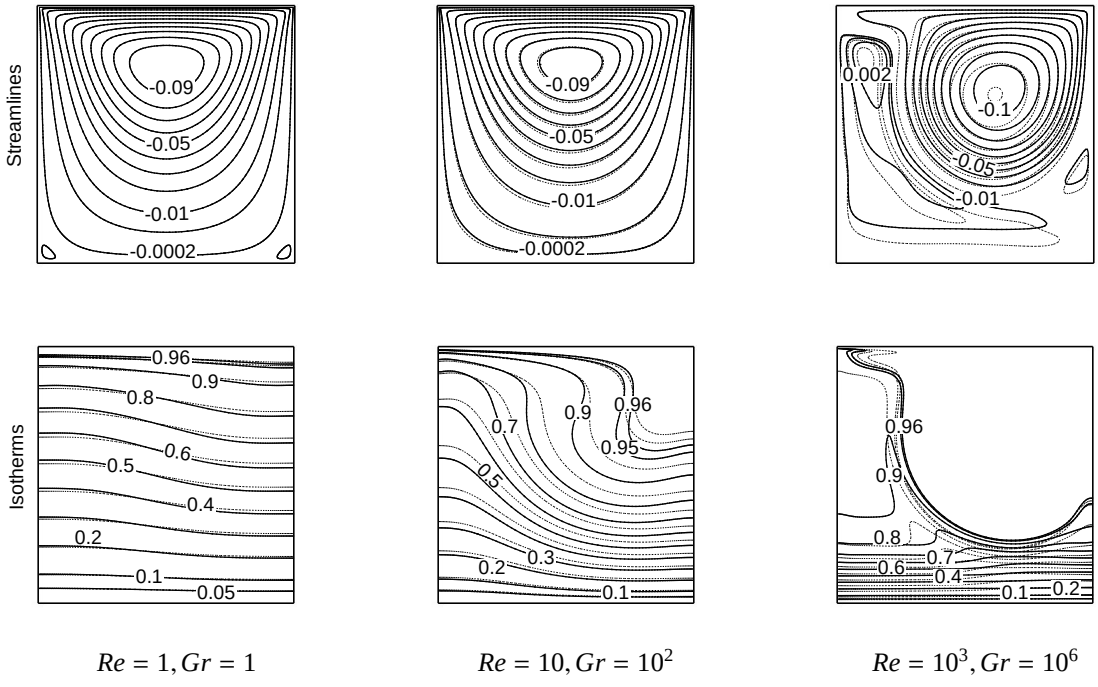

$Re = 1, Gr = 1$ $Re = 10, Gr = 10^2$ $Re = 10^3, Gr = 10^6$

FIGURE 6. Streamlines and isotherms patterns for different Reynolds and Grashof numbers for constant Richardson number ($Ri = 1$). Solid line represents plain base fluid ($\Phi = 0$) and dashed line represents nanofluid with $\Phi = 0.1$

temperature gradient. Due to the existence of strong secondary recirculation cell near the left wall, the isotherms are found to undergo reshaping in this region.

Fig. 7 illustrates the combined effect of the Reynolds and the Grashof numbers on the average Nusselt number of the heated wall and on the average fluid temperature inside the cavity with or without nanoparticle for the case of pure mixed convection corresponding to, $Ri = 1.0$. The addition of nano particle in the base fluid results in enhanced heat transfer from the hot wall within the range of Reynolds number ($10^{-0.5} - 10^3$) and Grashof number ($10^{-1} - 10^6$) as indicated in Fig. 7(a). However, the improvement in the heat transfer performance of nano fluid over base fluid is accentuated at higher values of the Reynolds and the Grashof number as manifested in Fig. 7(a). As seen in Fig. 7(a), the variation of the average Nusselt number with the Reynolds and the Grashof number is nonlinear for both the base fluid and nanofluid cases.

The variation of the average fluid temperature inside the cavity is also found to be greatly influenced the relative magnitudes of the Reynolds as well as the Grashof number for both the base fluid and the nano fluid cases. For very small values of the Reynolds and the Grashof number, the average temperature inside the cavity is very small for both the base fluid and nanofluid cases. Addition of nano particle in the base fluid does not show any significant variation of the average fluid temperature inside the cavity as shown in Fig. 7(b). For small values of the Reynolds and the Grashof number, the average temperature inside the cavity increases slowly for both the base fluid and nanofluid cases. For moderate values of the Reynolds and the Grashof number, the average temperature inside the cavity increases rapidly for both the base fluid and nanofluid cases while the rate of increase gets slow down. For very high values of the Reynolds and the Grashof number, the average temperature inside the cavity again starts increasing rapidly for both the base fluid and nanofluid cases. However, both the base fluid and nano fluid assume almost same average fluid temperature inside the cavity.

CONCLUSION

In this study, numerical simulation is performed for mixed convection inside a lid-driven square cavity under different conditions of *Re* and *Gr*. For the cases considered, where *Gr* was kept constant at 100, gives the most heat transfer. For

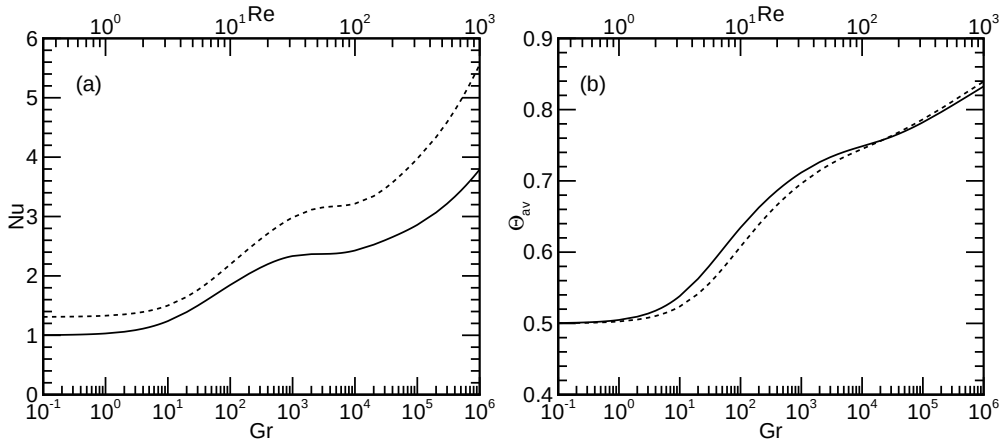

FIGURE 7. Combined effect of Reynolds and Grashof numbers on (a) average Nusselt number of the heated wall and (b) average fluid temperature of the cavity for constant Richardson number, $Ri = 1$. Solid line represents plain base fluid ($\Phi = 0$) and dashed line represents nanofluid with $\Phi = 0.1$.

this case heat transfer increases with the increase of *Re*. For the case where *Re* was kept fixed, heat transfer decreases with the increase of *Gr*. For pure mixed convection($Ri = 1$), heat transfer increases with the increase of *Gr* and *Ri* simultaneously. For all the cases, Nanofluid gives the higher heat transfer than the base fluid.

ACKNOWLEDGMENTS

The authors would like to thank the Department of Mechanical Engineering, Bangladesh University of Engineering and Technology (BUET), Bangladesh for the support provided during this research work.

REFERENCES

[1] M. K. Moallemi and K. S. Jang, International Journal of Heat and Mass Transfer **35**, 1881–1892 (1992).
[2] A. K. Prasad and J. R. Koseff, International Journal of Heat and Fluid Flow **17**, 460–467 (1996).
[3] K. M. Khanafer and A. J. Chamkha, International Journal of Heat and Mass Transfer **42**, 2465–2481 (1999).
[4] V. Sivakumar, S. Sivasankaran, P. Prakash, and J. Lee, Computers & Mathematics with Applications **59**, 3053–3065 (2010).
[5] T. Basak, S. Roy, P. K. Sharma, and I. Pop, International Journal of Heat and Mass Transfer **52**, 2224–2242 (2009).
[6] H. F. Oztop and I. Dagtekin, International Journal of Heat and Mass Transfer **47**, 1761–1769 (2004).
[7] R. K. Tiwari and M. K. Das, International Journal of Heat and Mass Transfer **50**, 2002–2018 (2007).
[8] F. Talebi, A. H. Mahmoudi, and M. Shahi, International Communications in Heat and Mass Transfer **37**, 79–90 (2010).
[9] E. Abu-Nada and A. J. Chamkha, European Journal of Mechanics-B/Fluids **29**, 472–482 (2010).
[10] S. M. Sebdani, M. Mahmoodi, and S. M. Hashemi, International Journal of Thermal Sciences **52**, 112–126 (2012).
[11] M. Muthtamilselvan and D. H. Doh, Applied Mathematical Modelling **38**, 3164–3174 (2014).
[12] S. Saha, S. Hossen, M. H. Hasib, and S. C. Saha, "Onset of transition in mixed convection of a lid-driven trapezoidal enclosure filled with water-Al_2O_3 nanofluid," in *19th Australasian Fluid Mechanics Conference* (Melbourne, Australia, 2014).